

12-17-2015

Synthetically Tailored Cyanines for Imaging and Therapy

Eric Owens

Follow this and additional works at: https://scholarworks.gsu.edu/chemistry_diss

Recommended Citation

Owens, Eric, "Synthetically Tailored Cyanines for Imaging and Therapy." Dissertation, Georgia State University, 2015.
https://scholarworks.gsu.edu/chemistry_diss/115

This Dissertation is brought to you for free and open access by the Department of Chemistry at ScholarWorks @ Georgia State University. It has been accepted for inclusion in Chemistry Dissertations by an authorized administrator of ScholarWorks @ Georgia State University. For more information, please contact scholarworks@gsu.edu.

SYNTHETICALLY TAILORED CYANINES FOR IMAGING AND THERAPY

by

ERIC ANDREW OWENS

Under the Direction of Maged M. Henary, Ph.D

ABSTRACT

This dissertation focuses on two fundamental yet unanswered questions in human health and disease concerning both diagnostics and therapeutics. The first half addresses the lack of optimized near-infrared fluorophores for image-guided surgery. Fluorescence imaging cameras and intraoperative imaging systems lack appropriately engineered contrast agents that allow the detection of sensitive normal tissue (i.e. endocrine and exocrine glands) for surgical avoidance. After systematically probing various fluorophore classes, we discovered promise in cyanine-based contrast agents. By altering functional groups of cyanine fluorophores, we, for the first time, report the selective targeting of many endocrine glands, exocrine glands, cartilage and bone using NIR fluorescence to visualize the targeted tissue. Secondly, this dissertation elaborates a new pathway for developing functional and fluorescent chemotherapeutics based on the targeting, stabilization and imaging of G-quadruplex DNA – a folding pattern commonly associated with cancer cell

proliferation through telomerase over-expression and oncogene promoter regions. Chromophores modified to assume quadruplex binding characteristics – planar cationic structures – have been developed that stabilize the quadruplex as evaluated through several complementary methods toward developing novel theranostic agents in the NIR visualization and treatment of human cancers.

INDEX WORDS: Carbocyanine, Fluorescence-guided cancer resection, Image-guided surgery, G-quadruplex DNA, Chemotherapeutics, Near-infrared.

SYNTHETICALLY TAILORED CYANINES FOR IMAGING AND THERAPY

by

ERIC ANDREW OWENS

A Dissertation Submitted in Partial Fulfillment of the Requirements for the Degree of

Doctor of Philosophy

in the College of Arts and Sciences

Georgia State University

2015

Copyright by
Eric Andrew Owens
2015

SYNTHETICALLY TAILORED CYANINES FOR IMAGING AND THERAPY

by

ERIC ANDREW OWENS

Committee Chair: Maged Henary

Committee: Donald Hamelberg

Suazette Mooring

Electronic Version Approved:

Office of Graduate Studies

College of Arts and Sciences

Georgia State University

December 2015

DEDICATION

This dissertation is wholly dedicated to my loving and supportive family who have always been there to celebrate in good times and pick me up during the bad.

ACKNOWLEDGEMENTS

I would like to acknowledge my dissertation committee (Dr. Donald Hamelberg, Dr. Suzette Mooring and Dr. Maged Henary) for overcoming scheduling conflicts and helping me throughout the entire process. Also, I would like to thank Drs. Binghe Wang and Jenny Yang for assisting me greatly with support and training through my University Fellowship from the Center for Diagnostics and Therapeutics at Georgia State University.

TABLE OF CONTENTS

ACKNOWLEDGEMENTS	v
LIST OF TABLES	xviii
LIST OF FIGURES	xx
1 INTRODUCTION TO NIR-FLUORESCENCE IMAGE-GUIDED SURGERY 1	
1.1 Abstract	1
1.2 Introduction	1
1.3 High Background in Molecular Imaging	2
1.4 Why Optical Imaging <i>via</i> Fluorescence?	4
1.5 NIR Window of Optical Clarity	5
1.6 Small Molecule Optical Contrast Agents	7
1.7 Classes of NIR Fluorophores.....	8
1.8 State-of-the-art in Image-Guided Surgery.....	11
1.9 Background Retention	12
1.10 Nonspecific Uptake and Persistent Background Retention (PBR)	15
1.11 Conclusions.....	15
1.12 References.....	16
2 SITE SPECIFIC NIR IMAGING: A REVIEW	25
2.1 Abstract	25
2.2 Introduction	26

2.2.1	<i>Near-Infrared Window</i>	28
2.2.2	<i>Requisite Design Parameters</i>	31
2.3	Methods for Obtaining Site-Specific Imaging.	34
2.4	Nanoparticles for <i>In Vivo</i> Imaging.	36
2.5	Subnano Imaging Agents.	38
2.6	Targeted Approach.	39
2.6.1	<i>Targeting Ligand</i>	40
2.6.2	<i>Isolating Linker</i>	40
2.6.3	<i>Effector and Balancing Domain.</i>	41
2.6.4	<i>Recent Literature on Targeted Imaging</i>	42
2.7	Structure-inherent Targeting.	47
2.8	Activatable NIR Imaging Agents.	53
2.9	Summary and Outlook.	63
2.10	Future Directions.	63
2.11	Conclusions.	64
2.12	References.	64
3	CORRELATING TISSUE LOCALIZATION OF HYDROPHOBIC CYANINES.	80
3.1	Abstract	80
3.2	Introduction	81

3.3	Results and Discussion	83
3.3.1	<i>Synthesis of Pentamethine Fluorophores</i>	83
3.3.2	<i>Optical and Physicochemical Properties</i>	84
3.3.3	<i>Structure-Inherent Targeting Ability of Hydrophobic NIR Fluorophores</i> . 88	
3.4	Experimental	95
3.4.1	<i>Chemicals, Reagents and Synthesis</i>	95
3.4.2	<i>Optical Property Measurements and Physicochemical Predictions</i>	105
3.4.3	<i>LC-MS Spectroscopy</i>	106
3.4.4	<i>Optical Imaging System and Fluorescence Microscopy</i>	106
3.5	Conclusions	107
3.6	References	107
4	ELECTRONIC FACTORS INFLUENCE BIODISTRIBUTION OF CYANINES	113
4.1	Abstract	113
4.2	Introduction	114
4.3	Results and Discussion	116
4.3.1	<i>Synthesis of Pentamethine Fluorophores</i>	116
4.3.2	<i>Optical and Physicochemical Properties</i>	118
4.3.3	<i>Structure-Inherent Targeting Ability of NIR Fluorophores</i>	121
4.4	Experimental	132

4.4.1	<i>Synthesis of pentamethine cyanine analogs.</i>	132
4.4.2	<i>General Synthetic Procedure for the formation of heterocyclic derivatives</i>	
1-5.		132
4.4.3	<i>Synthesis of heterocyclic salts 6-10.</i>	134
4.4.4	<i>Synthesis of Methine Precursor 11-13.</i>	135
4.4.5	<i>Synthesis of Methylated Pentamethine Cyanines 14-28, 31-33.</i>	135
4.4.6	<i>Optical and physicochemical property analyses.</i>	148
4.4.7	<i>LC-MS analysis.</i>	148
4.4.8	<i>Animal models and biodistribution.</i>	149
4.4.9	<i>Quantitative analysis.</i>	149
4.5	Conclusions	150
4.6	Acknowledgments	150
4.7	References	150
5	MICROWAVE ASSISTED SYNTHESIS OF NITROGEN CONTAINING HETEROCYCLES	154
5.1	Abstract	154
5.2	Introduction.	155
5.3	Pyrrrole-Containing Heterocyclic Compounds.	157
5.4	Indole	160
5.5	Pyridines	164

5.6	Conclusion.....	166
5.7	References	166
6	ENVIRONMENTALLY BENIGN SYNTHETIC APPROACHES—APPLIED TO FLUORESCENT DYES AND THEIR PRECURSORS	169
6.1	Abstract	169
6.2	Introduction	170
6.3	Results and Discussion.....	173
6.3.1	<i>Eco-friendly Synthesis of Pentamethine Cyanine Fluorophores.....</i>	<i>173</i>
6.3.2	<i>The Final Synthetic Step—Optimization</i>	<i>178</i>
6.3.3	<i>Microwave Assisted Organic Synthesis Application to a Systematic Library of Pentamethine Cyanines.....</i>	<i>183</i>
6.3.4	<i>Heterocyclic Variation Alters the Optical Properties of the Cyanine Fluorophores</i>	<i>184</i>
6.4	Conclusions	186
6.5	Experimental.....	186
6.5.1	<i>Synthesis</i>	<i>186</i>
6.5.2	<i>Classical synthesis of indolenine compounds 1 and 2.....</i>	<i>188</i>
6.5.3	<i>Microwave synthesis of indolenine compounds 1 and 2</i>	<i>188</i>
6.5.4	<i>Classical synthesis of indolenine salts 3-11</i>	<i>188</i>
6.5.5	<i>Microwave synthesis of indolenine salts 3-11.....</i>	<i>189</i>

6.5.6	<i>Classical bromination</i>	190
6.5.7	<i>Eco-friendly bromination</i>	191
6.5.8	<i>Classical cyclization</i>	191
6.5.9	<i>Microwave assisted cyclization</i>	192
6.5.10	<i>Classical alkylation</i>	192
6.5.11	<i>Microwave assisted alkylation</i>	192
6.5.12	<i>General classical synthesis for NIR dyes 17-25 and 26-28</i>	193
6.5.13	<i>General microwave assisted synthesis for NIR dyes</i>	194
6.5.14	<i>Computational Experimental</i>	197
6.5.15	<i>Analytical Instrumentation</i>	197
6.5.16	<i>Stock Solutions</i>	198
6.5.17	<i>Method of Determining Molar Absorptivity</i>	198
6.5.18	<i>Method of Determining Quantum Yield</i>	198
6.6	References	199
7	CARTILAGE AND BONE TARGETING FLUOROPHORES	200
7.1	Abstract	201
7.2	Introduction	201
7.3	Results and Discussion	203
7.4	Experimental Section	211
7.4.1	<i>Synthesis of C700 and C800 NIR fluorophores</i>	211

7.4.2	<i>Optical and physicochemical property analyses</i>	219
7.4.3	<i>NIR fluorescence imaging system</i>	220
7.4.4	<i>Animal models</i>	220
7.4.5	<i>Quantitative analysis</i>	220
7.4.6	<i>Histology and NIR fluorescence microscopy</i>	221
7.5	References	221
8	BROWN ADIPOSE TISSUE TARGETED NIR FLUOROPHORES	225
8.1	Abstract	225
8.2	Introduction	225
8.3	Results and Discussion	227
8.4	Conclusions.	231
8.5	Acknowledgments.....	231
8.6	Experimental.....	231
8.6.1	<i>Synthetic Procedures and Structural Characterizations</i>	232
8.7	References.	239
9	STRUCTURALLY STABLE AND ULTRA-BRIGHT SQUARINE DYES: THE ROLE OF QUATERNARY AMMONIUM CATIONS IN OXOCYCLOBUTANAL STABILIZATION	241
9.1	Abstract	241
9.2	Introduction	242

9.3	Results and Discussion	244
9.4	Conclusions	250
9.5	Experimental.....	251
9.6	References	255
10	QUADRUPLEX-DNA: HISTORY, FUNCTION AND THERAPEUTIC POTENTIAL.....	258
10.1	Abstract	258
10.2	Preface	259
10.3	Nucleic Acids as a Functional Therapeutic Target.....	260
10.4	The Double Edge Sword of Nucleic Acid Drug Targets.....	260
10.5	Duplex DNA	260
10.6	i-Motif DNA.....	262
10.7	Triplex DNA.....	263
10.8	Quadruplex DNA.....	263
10.9	Introduction to the G-Quadruplex Structure and Function	265
10.9.1	<i>Rationale for the Quadruplex as a Potent Anti-Cancer Target</i>	<i>265</i>
10.9.2	<i>Early Interest—Wrapped Up in Telomeric DNA.....</i>	<i>265</i>
10.9.3	<i>Second Generation Quadruplex Interest—Oncogene Promoter Regions 267</i>	
10.9.4	<i>How to Bind the Quadruplex with Specificity?</i>	<i>268</i>

10.9.5	<i>Binding Agents and Efficacy</i>	269
10.9.6	<i>Limitations of the Quadruplex as a Therapeutic Target</i>	275
10.10	Future Directions for this Field	276
10.11	Summary and Conclusion	276
10.12	Acknowledgements	277
10.13	References	277
11	TRIMETHINE CYANINES AS G-QUADRUPLEX STABILIZING COMPOUNDS	284
11.1	Abstract	284
11.2	Introduction	285
11.3	Results and Discussion	286
11.3.1	<i>UV-Vis Thermal Melting</i>	288
11.3.2	<i>Biosensor-Surface Plasmon Resonance studies (SPR)</i>	290
11.3.3	<i>Fluorescence studies</i>	295
11.4	Discussion	297
11.5	Experimental	299
11.5.1	<i>Synthesis of Cyanines</i>	299
11.5.2	<i>Nucleic Acids</i>	303
11.5.3	<i>UV-Thermal Melting</i>	303
11.5.4	<i>Biosensor-Surface Plasmon Resonance</i>	304

11.5.5	<i>Fluorescence titrations</i>	304
11.5.6	<i>Nuclear Magnetic Resonance</i>	305
11.6	Conclusions	305
11.7	References	306
12	PENTAMETHINE CYANINES WITH HIGH FIDELITY TO QUADRUPLEX DNA	310
12.1	Abstract	311
12.2	Introduction	312
12.3	Results	313
12.3.1	<i>Chemistry</i>	313
12.3.2	<i>Thermal Melting (T_m)</i>	314
12.3.3	<i>Surface Plasmon Resonance (SPR)</i>	316
12.3.4	<i>Mass Spectrometry (MS)</i>	318
12.4	Discussion	319
12.5	Conclusions	322
12.6	Experiments	322
12.6.1	<i>Pentamethine Dye Synthesis</i>	322
12.6.2	<i>DNA preparation</i>	329
12.6.3	<i>UV-thermal melting studies</i>	329
12.6.4	<i>Surface Plasmon Resonance</i>	330

12.6.5	<i>Mass spectrometry</i>	331
12.7	Acknowledgements	331
12.8	References.....	332
13	RIGIDITY IN HEPTAMETHINE CYANINES IMPROVES QUADRUPLEX BINDING	334
13.1	Abstract	334
13.2	Introduction	334
13.3	Synthesis	336
13.4	Ultra-Violet Thermal Melting	338
13.5	Nuclear Magnetic Resonance Spectroscopy	339
13.6	Molecular Modeling	340
13.7	Discussion	342
13.8	Experimental.....	343
13.9	References.....	346
14	SECOND GENERATION TRIMETHINE CYANINES	350
14.1	Abstract	350
14.2	Introduction	350
14.3	Synthesis	352
14.4	Nuclear Magnetic Resonance Spectroscopy	361
14.5	Discussion	365

14.6	Conclusions.....	365
14.7	Materials and Methods	366
	<i>14.7.1 Synthesis.....</i>	<i>367</i>
	<i>14.7.2 Nucleic Acids.....</i>	<i>381</i>
	<i>14.7.3 Thermal Melting</i>	<i>382</i>
	<i>14.7.4 Surface Plasmon Resonance</i>	<i>382</i>
14.8	References.....	383
	APPENDICES	386

LIST OF TABLES

Table 3-1 Optical properties of NIR fluorophores. All measurements were performed in several solvents, ethanol (EtOH), dimethyl sulfoxide (DMSO), phosphate-buffered saline (PBS), and fetal bovine serum (FBS), pH = 7.4 at 37 °C, and the fluorescence QY in FBS, pH = 7.4 at 37 °C. Abbreviations: λ_{abs}; maximum absorbance; λ_{em}; SS, Stokes shift; and QY, quantum yield.	85
Table 3-2 The Physicochemical descriptors and targeting ability for each contrast agent. 88	
Table 4-1. Optical properties of 700 nm emitting NIR fluorophores. All measurements were performed in dimethyl sulfoxide (DMSO), ethanol (EtOH), phosphate-buffered saline (PBS), and fetal bovine serum (FBS), pH = 7.4 at 37 °C. Abbreviations: λ_{abs}, wavelength of maximum absorbance; λ_{em}, wavelength of maximum emission; QY, quantum yield; and MB, molecular brightness.....	119
Table 4-2. <i>In silico</i> physicochemical properties of 700 nm emitting NIR fluorophores (LogD, TPSA and H-bond acceptors) calculated using Marvin and JChem calculator plugins (ChemAxon, Budapest, Hungary). LogD = partition coefficient at pH 7.4, TPSA = total polar surface area while molecular parameters (length, volume dipole and polarizability) were calculated using Spartan Wavefunction (V10) DFT starting with the minimized structural conformation of the lowest energy.	120
Table 4-3. Targeting properties and biodistribution of 700 nm emitting NIR fluorophores for specific organs/tissues at 4 h post-injection.	121
Table 6-1 Optimization Data for Pentamethine Carbocyanine Dye 18 with an ethyl group.	181
Table 6-2 Microwave Synthesis versus Conventional Synthesis	183

Table 6-3 The optical properties of propyl substituted dyes 17, 20, 23 and 26 with respect to different substituents on the heterocyclic backbone. The data presented was obtained in methanol from 1 mM stock solutions made in DMSO.	185
Table 12-1. Thermal melting studies of the cyanine analogs with telomeric quadruplex (Tel22) and a control duplex (AATT). The thermal melting values reported are reproducible within ± 1 °C. λ could not be accurately determined due to complex aggregation.	315
Table 12-2. Equilibrium binding constants of the cyanine analogs with quadruplex and duplex sequences obtained from SPR studies. The steady-state response obtained as a function of free ligand concentration was fitted to a two-site model to obtain K_1 and K_2. In all the cases, no duplex binding was observed suggesting a high selectivity of the ligands.	317

LIST OF FIGURES

- Figure 1-1. (a) PET imaging. 100 μ Ci of scVEGF/Cu (top row) or inVEGF/Cu (bottom row) were injected into 4T1luc tumor-bearing mice in the left axillary fat pads. Radioactivity for each resected organ was obtained 2 h post-injection. (b) SPECT imaging. 100 μ Ci of scVEGF/Tc (left) or inVEGF/Tc (right) were injected into 4T1luc tumor-bearing mice 1 h prior to imaging and resection. Arrows mark left mammary fat pad tumor; arrowheads and dotted boxes indicate nonspecific uptake. H, heart; L, liver; scale bar, 1 cm [Adapted from Backer *et al.*⁵ Copyright permission from Nature Publishing Group]..... 3**
- Figure 1-2. *In vivo* optical properties of injected fluorophores along with wavelength. 6**
- Figure 1-3. Chemical structures of various classes of small molecule fluorophores that have been explored for biophotonic imaging, their general hydrophobicity maps, highlighted characteristics concerning their potential for *in vivo* performance and the overall optical properties concerning the general core structure..... 9**
- Figure 1-4. Current state-of-the-art NIR fluorophores used in image-guided surgery. The chemical structures of three NIR fluorescent contrast agents and the corresponding optical properties. The negatively charged moieties are highlighted in red and the positively charged regions are designated in blue..... 12**
- Figure 1-5. Biodistribution and clearance of ICG and ZW800-1. ICG shows elevated nonspecific uptake in liver and duodenum, while ZW800-1 represents ultralow background and renal clearance. Animals were housed in an AAALAC-certified facility and were studied under the supervision of BIDMC IACUC in accordance with approved institutional protocols (#101-2011 for rodents and #046-2010 for pigs). NIR**

<p>fluorophores were injected intravenously into ~20 g CD-1 mice (10 nmol), ~250 g SD rats (50 nmol), and ~35 kg Yorkshire pigs (1 μmol) 1 h prior to imaging. Shown are color and 800 nm NIR fluorescence images of surgically exposed organs taken by the FLARE intraoperative imaging system.¹⁴⁻¹⁶ NIR fluorescence images have identical exposure times and normalizations. Abbreviations used are: Bl: bladder; BD: bile duct; Du: duodenum; In: intestine; Ki: kidneys; Li: liver; Sk: skin; St: stomach; Ur: ureter. Scale bars = 1 cm.</p>	14
<p>Figure 2-1. A simplified Jablonski diagram showing fluorescence and competing pathways for molecular relaxation from an excited state.</p>	27
<p>Figure 2-2. NIR Region and Characteristics. (A) The electromagnetic spectrum with a magnification of the visible and near-infrared region. (B) Imaging modalities, examples and their general characteristics with beneficial characteristics shown in blue and negative characteristics shown in red.....</p>	29
<p>Figure 2-3. The general schematic of dual channel image guided surgery and color video overlay for real-time imaging of the surgical field.....</p>	31
<p>Figure 2-4. The three main strategies for the imaging of a particular region of diseased or cancerous tissue.....</p>	35
<p>Figure 2-5. General overview for the modular approach to the design of targeting contrast agents/therapeutics.</p>	37
<p>Figure 2-6. (A) Compact modular design for preparing tissue-targeting imaging agents and (B) structure inherent imaging through the incorporation of targeting elements into the small molecule structure.....</p>	39

Figure 2-7. Small molecules and macromolecules used for tethering to direct NIR

fluorescent domains to particular targets for developing site-specific contrast agents.40

Figure 2-8. (A) The in vivo performance of ICG, and 3 ZW800 analogs with attributes

tabulated showing the net charge, availability for covalent targeting modification,

LogD (pH = 7.4), clearance route, clearance % after 4h., overall biodistribution (Li,

Liver; Du, duodenum; GB, gallbladder; Bl, bladder; Ki, kidney), and optical stability

in FBS after 24h. (B) The performance of ZW800-analog compared to Cy5.5 both

modified with cRGD *in vivo*. Adapted with the permission of The Royal Society of

Chemistry, the American Chemical Society and Nature Publishing Group..... 44

Figure 2-9. (A) The ZW700-1 structure that was prepared for the 700 nm channel of NIR

imaging guided surgery alongside the biodistribution in mice showing rapid

elimination after 4 hr. into the bladder (Bl), (B) The ZW700-1 conjugation to bovine

serum albumin which allowed for angiographic imaging using 700 nm channel which

was used alongside cRGD-ZW800-1 to target cancerous tumor in 800 nm channel and

the merged imaging provides real time image guidance with all three cameras

overlaid..... 45

Figure 2-10. Cy5-NP41 imaging of the sciatic nerve in transgenic mice engineered to

express yellow fluorescent protein with insets showing zoomed images in panels A-C.

(A) Normal color camera view of the sciatic nerve. (B) Same nerve visualized byYFP

fluorescence (pseudocolored yellow) superimposed on the visible video image (C) Cy5

fluorescence (pseudocolored cyan) superimposed on the brightfield image, showing

nerve labeling with Cy5-NP41. The arrows in panels B and C indicate improved Cy5

imaging of thin and obstructed nerve branches. (D-G) Cross sectional areas

corresponding to the nerve shown in panels A-C. (D) Cross-section of the sciatic nerve revealing myelin using differential interference contrast (DIC), pseudocolored blue.

(E) D Axoplasmic yellow fluorescent protein (YFP) pseudocolored green (arrows). (F)

Cy5-NP41 labeling (pseudocolored red) of epineurium (arrows) and endoneurium

(arrowheads). (G) Composite image of d, e and f showing that Cy5-NP41 labeling does

not colocalize with either myelin or axoplasm. Figure was adapted with permission

from Nature Publishing Group..... 46

Figure 2-11. The targeting ability of a pentamethine cyanine fluorophore showing site specific uptake through passive targeting. The biodistribution offers high SBR with excellent imaging of the thyroid gland (TG) in CD-1 mice and swine and the adrenal gland (AG) and ovaries (Ov) in CD-1 mice. 48

Figure 2-12. Physiological targets, molecular character, representative molecule and corresponding *in vivo* NIR images of subnano imaging agents that are tailored for imaging of cartilage and bone in pigs 4h post injection. Figure adapted with permission from Wiley Publishing. 50

Figure 2-13. Chemical structure of pancreas targeting and imaging of nearby structures with corresponding *in vivo* NIR images of subnano imaging agents that are tailored for imaging of specific tissues. Figure reproduced and adapted with permission from Theranostics and Ivyspring Publishing. 51

Figure 2-14. Molecular structure of NIR fluorescent imaging agents and corresponding *in vivo* NIR images for the subnano imaging agents that are tailored for imaging of thyroid and parathyroid in the same surgical space. Figure reproduced and adapted with permission from Nature Publishing Group. 52

Figure 2-15. Oxazine 4 as an exemplary nerve targeting agent with corresponding *in vivo* NIR images for both the brachial and sciatic nerves. Below the immunohistochemistry confirms the nerve targeting of Oxazine 4. Figure reproduced and adapted from Theranostics and Ivyspring Publishers..... 53

Figure 2-16. pH activatable BODIPY NIR imaging probes. (A) General strategy for targeting pH probes to tumor cells and activating fluorescence with a pH response, (B) two (of four, not shown) analogs of pH activatable and always on (control) compounds and their pH-fluorescence profile, (C) cellular imaging at time 0 h and time 24 h showing always on fluorescence and cell endocytosis mediated fluorescence activation (see A), and (D) *in vivo* imaging showing effective targeting of tumors in both always on and activatable contrast agents—SBR is much higher when using the activatable probe. Figure reproduced and adapted with permission of Nature Publishing Group. 55

Figure 2-17. Folate receptor-specific activatable (FSA) probe. (A) The design and structure of the final probes using in (B) cellular experiments in SKOV3 cells expressing the folic acid receptor without a folic acid receptor inhibitor present and with a folate acid receptor inhibitor present and (C) *in vivo* data showing rapid clearance of the free dye after 30 minutes and high SBR imaging of the tumor tissue when using the FSA probe. Figure reproduced and adapted with permission of the Royal Society of Chemistry.. 57

Figure 2-18. (left) Activatable cell penetrating peptides (ACPPs) that harness ion paired peptides and a cleavable segment for sites-specific imaging (right) further modification of ACPPs that incorporates a second fluorophore Cy7 for ratiometric activation (RACPP). 59

Figure 2-19. (A) Overall schematic for suitable imaging time points for A CPP contrast agent, (B) the improved surgical resection with several small tumors being located by the A CPP contrast agent that would have been missed using current techniques (i.e. eyesight, feel, etc.). Figure reproduced and adapted with permission of Nature Publishing Group..... 60

Figure 2-20. The characteristics and imaging capabilities for RACPP. (A) the emission spectra of uncleaved and cleaved RACPP1 (630 nm excitation in mouse plasma) before (black solid curve) and after (red dashed curve) peptide cleavage with MMP-9. The starting spectrum shows considerable quenching of the Cy5 peak at 670 nm which results in emission from Cy7 at 780 nm, whereas the final spectrum is almost purely that of Cy5, (B) general schematic showing the imaging timeline for RACPP, (C) Cy5 intensity images (ex 620 nm, em 670 nm) 2 hours after intravenous injection of RACPP1 or an uncleavable control into mice bearing either HT-1080 xenografts or subcutaneous LM-P syngeneic grafts after skin removal. Images are pseudocolored where pixels with only Cy5 emission are pseudocolored red (indicating cleavage of RACPP), whereas pixels with both Cy5 and Cy7 emission peaks are pseudocolored green indicating no cleavage, (D) RACPP1 (MMP2,9-selective) or RACPP3 (elastase-sensitive) contrast agents were administered via intravenous injection and the livers (PyMT 8119 GFP-positive metastases) were removed after 2 hours. The following images were obtained: GFP fluorescence images, Cy5 fluorescence images obtained by exciting Cy5 at 620 nm, Cy7 emission images obtained by exciting Cy5 and Cy5/Cy7 emission ratio images. Red indicates high Cy5/Cy7 fluorescence ratios and blue indicates low ratios. Arrows show regions that do not contain tumors which is

- indicated by low ratios of Cy5 to Cy7 fluorescence values. Figure reproduced and adapted with permission of Nature Publishing Group..... 62
- Figure 3-1.** Graphical representation for this section which covers the development of structure-inherent NIR fluorophores..... 81
- Figure 3-2.** The synthetic route to the final hydrophobic pentamethine fluorophores. 84
- Figure 3-3** The absorption and emission spectra for each of the evaluated compounds (0.3 μM) in 100% FBS supplemented with 50 mM HEPES buffer at 37 °C..... 87
- Figure 3-4.** Thyroid gland (TG)-targeted NIR fluorophores. 10 nmol of each fluorophore was injected intravenously into CD-1 mice 4 h prior to imaging and resection. Abbreviations used are: Du, duodenum; He, heart; In, intestine; Ki, kidney; Li, liver; Lu, lung; Mu, muscle; Pa, pancreas; SG, salvery gland, and Sp, spleen. Arrows indicate TGs. Scale bars = 1 cm..... 90
- Figure 3-5.** Adrenal gland (AG)-targeted NIR fluorophores. 10 nmol of each fluorophore was injected intravenously into CD-1 mice 4 h prior to imaging and resection. Abbreviations used are: Du, duodenum; He, heart; In, intestine; Ki, kidney; Li, liver; LN, lymph nodes; Lu, lung; Mu, muscle; Pa, pancreas; and Sp, spleen. Arrows indicate AGs. Scale bars = 1 cm..... 91
- Figure 3-6.** Pancreas (Pa)-targeted NIR fluorophores. 10 nmol of each fluorophore was injected intravenously into CD-1 mice 4 h prior to imaging and resection. Abbreviations used are: Du, duodenum; He, heart; In, intestine; Ki, kidney; Li, liver; Lu, lung; Mu, muscle; Pa, pancreas; and Sp, spleen. Arrows indicate Pa. Scale bars = 1 cm. 92

Figure 3-7. Lymph node (LN)-targeted fluorophores. A) Methylated benz[e]indolenine-based cyanines and B) ethylated benz[e]indolenine-based cyanines. 10 nmol of each fluorophore was injected intravenously into CD-1 mice 4 h prior to imaging and resection. Abbreviations used are: Du, duodenum; He, heart; In, intestine; Ki, kidney; Li, liver; Lu, lung; Mu, muscle; Pa, pancreas; and Sp, spleen. Arrows indicate LNs. Scale bars = 1 cm..... 94

Figure 4-1. Compounds 20-22, targeting to salivary glands and thyroid glands, and biodistribution of resected organs in CD-1 mice. 10 nmol of each fluorophore was injected intravenously into 25 g CD-1 mice 4 h prior to imaging and resection. Abbreviations used are: Du, duodenum; He, heart; In, intestine; Ki, kidneys; Li, liver; Lu, lungs; Mu, muscle; Pa, pancreas; SG, salivary gland, Sp, spleen. Arrows indicate the targeted gland. 124

Figure 4-2. Compounds 23-25, targeting to salivary glands and thyroid glands, and biodistribution of resected organs in CD-1 mice. 10 nmol of each fluorophore was injected intravenously into 25 g CD-1 mice 4 h prior to imaging and resection. Abbreviations used are: Du, duodenum; He, heart; In, intestine; Ki, kidneys; Li, liver; Lu, lungs; Mu, muscle; Pa, pancreas; SG, salivary gland, Sp, spleen. Arrowheads indicate the targeted gland..... 125

Figure 4-3. Compounds 26-28, targeting to thyroid glands and pituitary gland, and biodistribution of resected organs in CD-1 mice. 10 nmol of each fluorophore was injected intravenously into 25 g CD-1 mice 4 h prior to imaging and resection. Abbreviations used are: Du, duodenum; He, heart; In, intestine; Ki, kidneys; Li, liver; LN, lymph node; Lu, lungs; Mu, muscle; Pa, pancreas; SG, salivary gland, Sp, spleen.

Arrows indicate the targeted gland. For pituitary glands, arrowheads indicate the anterior portion, and arrows for posterior pituitary.....	127
Figure 4-4. Compounds 31-33, targeting to inguinal and lumbar lymph nodes, and biodistribution of resected organs in CD-1 mice. 10 nmol of each fluorophore was injected intravenously into 25 g CD-1 mice 4 h prior to imaging and resection. Abbreviations used are: Bl, bladder; Du, duodenum; He, heart; In, intestine; Ki, kidneys; Li, liver; LN, lymph node; Lu, lungs; Mu, muscle; Pa, pancreas; Sp, spleen. Arrows indicate the targeted gland.	129
Figure 4-5. Compounds 36-38, targeting to adrenal glands and pituitary gland, and biodistribution of resected organs in CD-1 mice. 10 nmol of each fluorophore was injected intravenously into 25 g CD-1 mice 4 h prior to imaging and resection. Abbreviations used are: Du, duodenum; He, heart; In, intestine; Ki, kidneys; Li, liver; Lu, lungs; Mu, muscle; Pa, pancreas; SG, salivary gland, Sp, spleen. Arrows indicate the targeted gland. Arrows indicate the targeted gland. For pituitary glands, arrowheads indicate the anterior portion, and arrows for posterior pituitary.....	131
Figure 5-1. General schematic for microwave energy.....	157
Figure 5-2. The chemical structures of porphobilinogen and atorvastatin.	158
Figure 5-3. Drugs bearing the indole (or similar) moiety.....	161
Figure 5-4. Drugs that exhibit a pyridine structure.....	164
Figure 6-1. Graphical representation for the microwave assisted green method for the preparation of pentamethine cyanines.....	170
Figure 6-2. The reaction intermediates and postulated degradation products that form during either the classical heating method of synthesis or purification of cyanine dyes	

that lead to difficulty in obtaining analytically pure compounds for biological testing.

.....	172
Figure 6-3. The new, green microwave assisted method for preparation of alkylated salts 3-11 based off of the indolenine heterocyclic structure.	174
Figure 6-4. The preparation the brominated ketone 12.	175
Figure 6-5. The preparation of the fused dioxolane heterocycle 13.	176
Figure 6-6. The proposed mechanism based off of an adaptation of the Bischler-Möhlau method for indole formation.	177
Figure 6-7. The microwave assisted preparation of a systematic set of pentamethine cyanines with variance in heterocyclic and N-alkyl groups.	179
Figure 6-8. Isolated yield (%) versus reaction temperature (°C) versus the three pentamethine carbocyanine dyes with varied lengths of the N-alkyl groups 17 (methyl, blue), 18 (ethyl, red), and 19 (propyl, green). Reactions were held at 20 min for the isolated yield.	180
Figure 6-9 DFT calculation results showing a decrease in the dipole moment as alkyl length increases.	182
Figure 6-10 Near infrared (NIR) absorbance of fluorophores in methanol at a 2.0 μM concentration.	184
Figure 6-11 In silico DFT calculations depicting the HOMO and LUMO for each compound 17 and 26 with corresponding energy levels (eV) shown below the structures.	185
Figure 7-1. Synthetic scheme (a) and physicochemical and optical properties (b) of C700 and C800 NIR fluorophores. In silico calculations of physicochemical properties were	

calculated using Marvin and JChem calculator plugins (ChemAxon, Budapest, Hungary). All optical measurements were performed at 37°C in 100% fetal bovine serum (FBS) buffered with 50 mM HEPES, pH 7.4. 205

Figure 7-2. In vivo cartilage targeting using C700 (a) and C800 (b) NIR fluorophores in mice. Each fluorophore was injected intravenously into 25 g CD-1 mice (10 nmol; 0.3 mg kg⁻¹) 4 h prior to imaging. SBR was calculated by the fluorescence intensity of costal cartilage tissues versus the signal intensity of neighboring muscle obtained over the imaging period (n = 3, mean ± s.d.). *P < 0.05, *P < 0.001. All NIR fluorescence images have identical exposure and normalizations. Scale bars = 1 cm. 206**

Figure 7-3. In vivo NIR imaging and histological analysis of cartilage tissues from ear (a), knee joint (b), and inside chest (c) in mice. C700-OMe and C800-OMe were intravenously injected into 25 g CD-1 mice (10 nmol; 0.4 mg/kg) 4 h prior to imaging. #1 (arrows) and #2 (arrowheads) in (c) indicate hyaline and fibrocartilage, respectively. Alcian Blue, H&E, and NIR images of resected cartilage tissues were obtained from the same animal. All NIR fluorescence images for each condition have identical exposure times and normalizations. Scale bars = 1 cm (for in vivo image) and 100 µm (for histology image). Images are representative of n = 3 independent experiments. 209

Figure 7-4. Dual-channel in vivo fluorescence imaging of cartilage and bone tissues by using C700-OMe and P800SO₃⁶ in the same animals. 10 nmol and 1 µmol of C700-OMe and P800SO₃ were intravenously injected into 25 g CD-1 mice (top; 0.4 mg kg⁻¹) and 35 kg Yorkshire pigs (bottom; 0.02 mg kg⁻¹), simultaneously, 4 h prior to imaging. All NIR fluorescence images for each condition have identical exposure times and

normalizations. Scale bars = 1 cm. Images are representative of n = 3 independent experiments. Pseudo-colored red and green colors were used for 700 nm and 800 nm channel images, respectively, in the color-NIR merged image.	210
Figure 8-1. General physiological and cellular diagrams of brown and white fat. (left) Presence and location of brown and white fat at different stages of development and health, (right) cellular differences between brown adipose tissues which are high in mitochondria with small fat deposits and white adipose tissues which contains mostly fat. Nucleus is represented by purple and fat is represented by white circles.	226
Figure 8-2. The numbering of 2-methylbenzothiazole and synthetic methods to final methylated cyanine chromophores for BAT targeting.....	228
Figure 8-3. The chemical structures, color video and 70 nm NIR fluorescence for final BAT targeting compounds.	229
Figure 8-4. The chemical structures, color video and 700 nm NIR fluorescence for final BAT targeting compounds.	230
Figure 9-1. (top) General overview of covalently labeling a biomolecule with a NIR-dye (bottom) commonly used fluorophores with benefits, in green, and negatives, in red, associated with their <i>in vivo</i> use.	244
Figure 9-2. Preparation of squaric acid dyes 9-12.	245
Figure 9-3. Final asymmetric compound 16-19 preparation.	246
Figure 9-4. Final carboxylate-modified zwitterionic squaric acid dye 22 preparation.	247
Figure 9-5. (top, left) The absorption and fluorescence spectra for each compounds in Fetal Bovine Serum supplemented with HEPES buffer at pH = 7.4 and warmed to physiological temperature (37 °C). (top, right) The absorption-based stability in light	

and under heat in FBS buffer for compounds 9, 16 and industry standard Cy5
 (bottom) Optical properties of the synthesized fluorophores in various solvents,
 dimethyl sulfoxide (DMSO), ethanol (EtOH, 200 proof), phosphate buffered saline
 (PBS, pH = 7.4) and fetal bovine serum (FBS, pH = 7.4, 37 °C) supplemented with
 HEPES buffer were utilized to show biological compatibility..... 249

Figure 9-6. DFT calculations (Wavefunction, Spartan, '10, B3LYP 6-311++G**) confirm
 the presence of a salt-bridge between the quaternary ammonium cation and the
 delocalized negative charge across the central oxygens in both the symmetric and
 asymmetric compounds..... 250

Figure 10-1 Duplex DNA and binding ligands. Diamidine structures effectively target the
 minor groove while the major groove is effectively bound through dimerization and
 the tetra-cationic cyanine dye can effectively intercalate between the base pairs of
dsDNA. 262

Figure 10-2. Cartoon quadruplex structure. The molecular structure of the quadruplex
 stabilized through hydrogen bonding interactions represented by a red-square with
 coordinated metal ion represented as a blue sphere. These planar tetrads will
 spontaneously stack *in vivo* much like the cartoon image on the right..... 264

Figure 10-3. 3D structure of the quadruplex. The top view and side view with the central
 quadruplex highlighted in red. The blue represents the loops of the quadruplex..... 264

Figure 10-4. Telomerase binding to and elongating the terminal TTAGGG segment of the
 telomere and the G-quadruplex DNA blocking telomerase binding..... 266

- Figure 10-5. The promoter region leads the expression of particular proteins, however, the quadruplex orientation prevents effective translation and can be an effective route toward the silencing of oncopromoting genes. 267**
- Figure 10-6. G-Quadruplex Binding Modes. Monocationic difluorinated compound effectively intercalates while the BRACO-analog interacts through loop binding and the macrocyclic telomestatin analog's nature and size stacks effectively on the top of the tetraplex. 269**
- Figure 10-7. A synthetic pathway toward trisubstituted acridine agents for the stabilization of G-quadruplex DNA and generic structure bearing three positions for substitution on the acridine core. 270**
- Figure 10-8. Acridine based compound BRACO-19 complexed to G-quadruplex. 271**
- Figure 10-9. Synthetic scheme to the final naphthalene diimide compounds for quadruplex binding. 272**
- Figure 10-10. Naphthalene diimide ligand and crystal structure rendering with quadruplex dimer (PDB 3UYH). 272**
- Figure 10-11. Core carbazole structure with positions of variation that have led to increased binding efficacy to quadruplex DNA. 273**
- Figure 10-12. General structure for carbocyanine compounds with points of modification shown by generic groups. 274**
- Figure 10-13. The parent structures with non-substituted heterocyclic moieties and quaternary substituents at the *N*-indolenyl site with representative SPR plots for cMYC in blue and human telomere in red. 275**

Figure 11-1. Synthetic scheme and chemical structure of the trimethine cyanine analogs used in the current study. The modifications performed on the parent cyanine (26) are highlighted in different colors (compounds 24-32). All compounds have one positive charge delocalized on the cyanine system with variance in charge on the heterocyclic rings and the nitrogen chain. 287

Figure 11-2. SPR sensorgrams and the steady-state binding plots for the parent cyanine (26, panel a) and the brominated analog (31, panel b) with Tel22 and cMYC19 quadruplex sequences. The injected concentration range for 26 is 10 nM - 10 μ M and for 31 is 10 nM - 1 μ M. The binding plots were obtained by fitting the steady-state response values (RU) as a function of free ligand concentration (C_{free}) and fit to a two-site binding model. The estimated equilibrium binding affinities (K_1 and K_2) are reported in Table 10-2. 292

Figure 11-3. Imino proton spectra of MYC22 quadruplex titrated with the parent cyanine 26 (a) and the brominated analogue 31 (b). Ligands were added to the quadruplex at the ratio indicated on the plot. Selected imino protons of 3'-end (9, red) middle (8, blue) and 5'-end (16, green) tetrads are marked. 294

Figure 11-4. (a) Schematic structure of the c-myc quadruplex MYC22 (Ambrus et al, 2005, [26]). For clarity the imino protons of the guanine tetrads are color coded. Red: 3'-end tetrad, blue: center tetrad, and green: 5'-end tetrad. Imino proton titration curves of 3'-end, middle and 5'-end tetrad for the parent cyanine (26, b) and the brominated analog (31, c)..... 295

Figure 11-5 Fluorescence emission spectra of the parent cyanine (26, panel a) and the brominated analog (31, panel b) with Tel22 and cMYC19 quadruplex sequences. The

arrow indicates increasing concentrations of DNA titrated into the ligand solution (1 μ M) until no further change in the fluorescence emission signal was detected. 296

Figure 12-1. The synthesis of the cyanine structures used in developing G-quadruplex binding agents..... 314

Figure 12-2. (A) SPR sensorgram of compound 13 with the two quadruplex as well as a reference duplex sequence. (B) Steady-state equilibrium binding plots of analogs 13 and 15. The solid colored lines are the fits obtained using a two-site model. In all cases, the steady-state response with duplex sequence was too low to fit reasonably. 317

Figure 12-3. Mass spectra of *c-myc* quadruplex with 0:1, 1:1, 2:1, 4:1 ratios (top to bottom) of parent dye 13 (A) and mono-brominated compound 15 (B)..... 319

Figure 13-1. The chemical structures of known binding quadruplex binding ligands..... 335

Figure 13-2. TEL-24 quadruplex titration with 15 (left), and 13 (right) followed with the imino proton spectra of TEL-24. NMR imino proton spectra (T=298 K) of the TEL-24 quadruplex are shown on the top of the figure. Compounds 13 and 15 were added to a constant amount of TEL-24 indicated in terms of their mole ratios. The DNA is mostly present as a hybrid-1 form in solution. Ligands were added to the quadruplex at the ratio indicated on the plot, where 1:0 ratio corresponds to the imino proton spectrum of TEL-24 with no ligand added. Schematic structures of TEL-24 are color coded according to the tetrad guanine imino protons affected in the titrations. Red residues are strongly affected, yellow are somewhat affected, and green are not affected..... 339

Figure 13-3. Molecular dynamics snapshots for the binding of compounds 11 and 15 to cMYC DNA (PU22, PDB ID: 1XAV). (A) Compound 11 with cMYC, and (B) Compound 15 with cMYC..... 341

- Figure 13-4. Molecular dynamics snapshots for the binding of compounds 11 and 15 to hTel DNA (hTel22, PDB ID:). (A) Compound 11 with cMYC, and (B) Compound 15 with cMYC..... 342**
- Figure 14-1. Molecular depictions of the most energetically favorable state for monomethine compound compared to trimethine analog showing drastically different twisting associated with the reduction of the polymethine-bridge and corresponding DTm measurements at 4:1 compound:Tel22 ratio. 357**
- Figure 14-2. Surface Plasmon Resonance Sensograms. The G4 binding agents 24 (methyl) and 28 (butyl) were examined with TEL22 and MYC19 DNA..... 360**
- Figure 14-3 TEL24 quadruplex titration with 22 (left) and 26 (right) followed with the imino proton spectra of TEL24. Ligands were added to the quadruplex at the ratio indicated on the plot, where 1:0 ratio corresponds to the imino proton spectrum of TEL24 with no ligand added. Schematic structures of TEL24 are color coded according to the imino protons affected in the titrations. Red residues are strongly affected, yellow are somewhat affected, and green are not affected. 362**
- Figure 14-4. Molecular dynamics and corresponding snapshots for the binding of compounds 24 and 28 to MYC DNA. (A) compound 24 with MYC, (B) compound 28 with MYC 364**
- Figure 14-5. Molecular dynamics and corresponding snapshots for the binding of compounds 24 and 28 to TEL22 DNA. (A) Compound 24 with TEL22, (B) Compound 28 with TEL22..... 365**

1 INTRODUCTION TO NIR-FLUORESCENCE IMAGE-GUIDED SURGERY

Note: This chapter has been adapted from the following publication in WIREs Nanomedicine and Nanobiotechnology. My contributions as first author were the design and figure/manuscript preparation.

Owens, E. A., Lee, S., Choi J, Henary, M, Choi, H.S. NIR Fluorescent Small Molecules for Intraoperative Imaging. **2015** WIREs Nanomedicine and Nanobiotechnology, Invited Focus Article In Press-Early View.

1.1 Abstract

Recent advances in bioimaging and nanomedicine have permitted the exploitation of molecular optical imaging in image-guided surgery; however, the parameters mediating optimum performance of contrast agents are not yet precisely determined. To develop ideal contrast agents for image-guided surgery, we need to consider the following criteria: 1) excitation and emission wavelengths in the NIR window, 2) optimized optical characteristics for high in vivo performance, 3) overcoming or harnessing biodistribution and clearance, and 4) reducing nonspecific uptake. The design considerations should be focused on optimizing the optical and physicochemical property criteria. Biodistribution and clearance should first be considered because they mediate the fate of a contrast agent in the body such as how long after intravenous injection a contrast agent reaches the peak signal-to-background ratio (SBR) and how long the signal lasts (retention).

1.2 Introduction

Despite advancements in oral medications, surgery remains the primary treatment option for controlling the progression of many diseases from dysplasia to carcinoma.¹⁻³ Surgeons currently perform complex long-duration surgical resections without the aid of real-time image guidance. The common colloquialism we use for “extremely precise” is surgical

precision, which is currently limited to anatomical structures and palpation with surgeons experience to perform complex surgeries.⁴ There are times, especially in the resection of cancerous tissues, when eyesight alone is not enough to complete a complicated surgical resection successfully—we define successful as the complete removal of disease tissue and the avoidance of nerves, blood vessels, and other vital tissues.⁵

Surgeons currently utilize many pre-surgical imaging modalities including computed tomography (CT), magnetic Resonance Image (MRI), single-photon emission computed tomography (SPECT), or positron emission tomography (PET)⁶⁻⁹ for deciphering the surgical field and for locating specific tissues, but subtle nuances after pre-surgical imaging can have severe consequences which could lead to additional surgical procedures, incomplete resection, poor patient outcomes or even death. It is undeniable that the development of biomedical imaging modalities has contributed significantly to the outcome of surgical procedures by locating the disease tissue prior to surgery. Unfortunately, the surgical field remains an ever-changing space where real-time imagery is required while the patient is undergoing an operation to minimize morbidity and mortality. To avoid this, we require the development of a real-time approach to the imaging of surgical field but there remain significant obstacles in developing successful optical contrast agents, including the high background associated with current molecular imaging technology.

1.3 High Background in Molecular Imaging

Molecular imaging exploits the radioactive property of various elements or compounds for visualization. Depending on the exact atomic or molecular characteristics, clinicians are able to observe the signal using positron or photon detecting equipment with appropriately radiolabeled contrast agents. In order for surgeons to clearly visualize their target, the molecular imaging contrast agent must offer high signal to background for optimum delineation of meaningful signal from surrounding tissue which offers a more precise image of

the surgical field leading to increased surgical efficacy. Most clinically utilized contrast agents including ^{18}F -FDG (PET) or $^{99\text{m}}\text{Tc}$ (SPECT) to target diseased tissue with properly detectable signal, however, the percent injected dose (%ID) taken up by non-target (normal) tissue and organ remaining in the body after several hours of circulation and clearance is still high, i.e., nonspecific background. As shown in Figure 1,⁵ elevated non-specific uptake of the contrast agent makes deducing meaningful signal more difficult. The major organs including liver, kidneys, spleen and lung display equal or higher signals compared to the targeted tumor. Reducing the background associated with any contrast agent remains a paramount and very difficult research endeavor. The perfect contrast agent would exhibit high signal to background in the desired tissue with the remaining amount being cleared through renal filtration or hepatobiliary clearance with minimal off-target absorption.

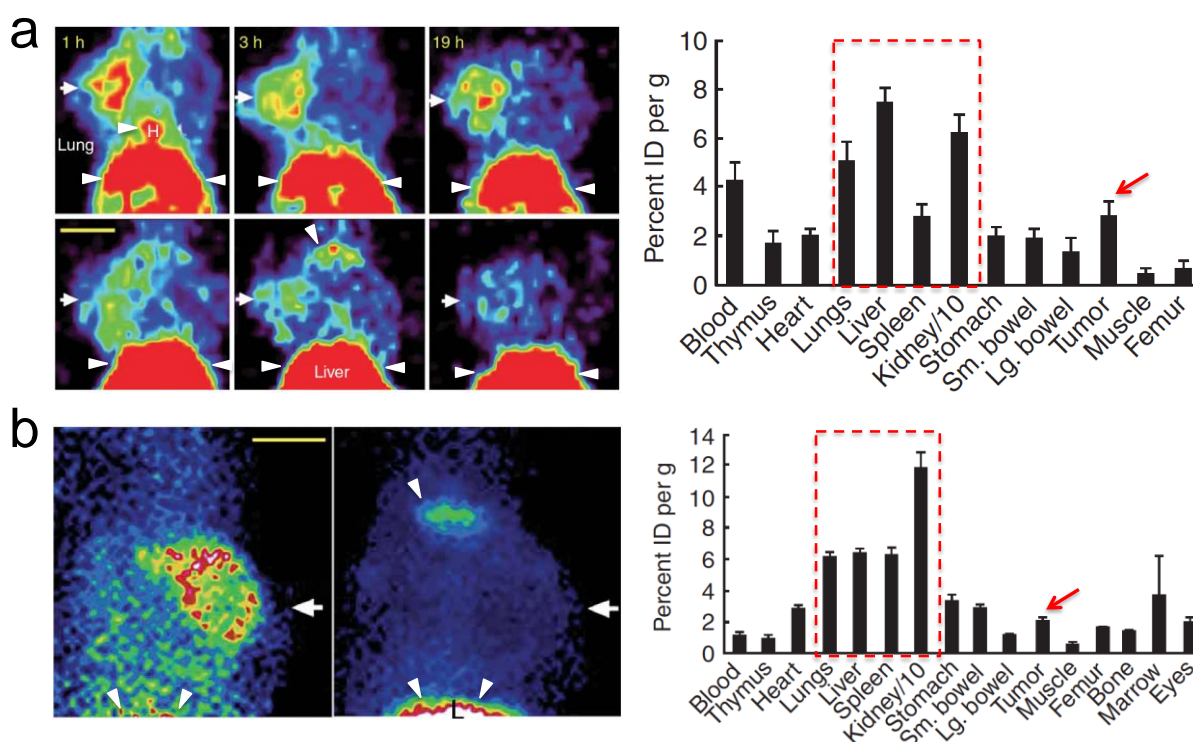


Figure 1-1. (a) PET imaging. 100 μCi of scVEGF/Cu (top row) or inVEGF/Cu (bottom row) were injected into 4T1 luciferase tumor-bearing mice in the left axillary fat pads. Radioactivity for each resected organ was obtained 2 h post-injection. (b) SPECT

imaging. 100 μ Ci of scVEGF/Tc (left) or inVEGF/Tc (right) were injected into 4T1luc tumor-bearing mice 1 h prior to imaging and resection. Arrows mark left mammary fat pad tumor; arrowheads and dotted boxes indicate nonspecific uptake. H, heart; L, liver; scale bar, 1 cm [Adapted from Backer *et al.*⁵ Copyright permission from Nature Publishing Group].

1.4 Why Optical Imaging *via* Fluorescence?

Conventional PET scan, as shown in Figure 1, provides whole body imaging to find disease target, commonly using radiolabeled ^{18}F -FDG or other radioactive contrast agents such as ^{15}O , ^{11}C and ^{64}Cu .^{10, 11} The proton-rich radionuclides spontaneously convert a proton to a neutron, resulting in the emission of a positron. This modality, similar to SPECT (usually exploits gamma rays emitted from $^{99\text{m}}\text{Tc}$, ^{123}I , ^{111}In , ^{201}Tl , ^{67}Ga or ^{133}Xe) poses significant safety concerns and must be utilized sparsely to avoid unhealthy radiation exposure to the patient. MRI utilizes high magnetic fields to noninvasively image diseased and healthy tissues. Unfortunately, these various imaging techniques fail to offer the desirable spatial resolution required for operative guidance and translating the currently employed imaging technology into a real-time setting exposes the patient and surgical team to harmful levels of radiation during long-term procedures. Research endeavors are underway to develop a harmless and effective strategy for surgical imaging—one of the most promising methods is optical-based imaging using NIR fluorescence and herein we discuss the design concepts that must be considered for the development of these fluorescent compounds.

1.5 NIR Window of Optical Clarity

Molecular imaging encompasses a highly broad category of techniques that; however, a more specific type of molecular imaging, optical imaging, relies on the photophysical properties of a contrast agent to report, usually through fluorescence, on the location of the targeted tissue. Optical imaging allows for a very detailed image with high spatial resolution to be obtained in real-time if the correct imaging agents are utilized. Furthermore, optical imaging has been shown to be useful for image-guided surgery and allows target specific tissues inside the body using laser light excitation combined with corresponding fluorophores with excitation and emission in the NIR region of optical clarity. The NIR window is the optical range of the electromagnetic spectrum which is characterized by wavelengths between 650 nm and 900 nm and is depicted in Figure 2. Absorption and scattering properties of tissue greatly affects the photon penetration into living tissue; however, the NIR region of the electromagnetic spectrum overcomes this obstacle and can significantly improve *in vivo* imaging. Understanding the NIR window and the optimized excitation and emission wavelengths along with the molecular characteristics required for NIR wavelengths are key in developing ideal contrast agents for image-guided surgery.

There are several advantages of working in the NIR region of the spectrum. First, the endogenous chromophores present in living tissues absorb and scatter visible light, limiting light penetration to only a few millimeters. However, NIR light has a much lower tissue absorption coefficient, which permits its deeper penetration to several centimeters. Since common biological systems do not feature the capacity to absorb this wavelength of light it is innocuous to human cells and tissue resulting in an inherently safer imaging modality. Additionally, the scattered light from the excitation source is greatly reduced in the NIR region since the scattering intensity is proportional to the inverse fourth power of the wavelength. Low

background noise and low scattering of NIR fluorescence result in a high SBR, thereby allowing highly sensitive detection. Further advantages of NIR imaging includes low interferences from Raman scattering and reduced possibility of sample degradation.

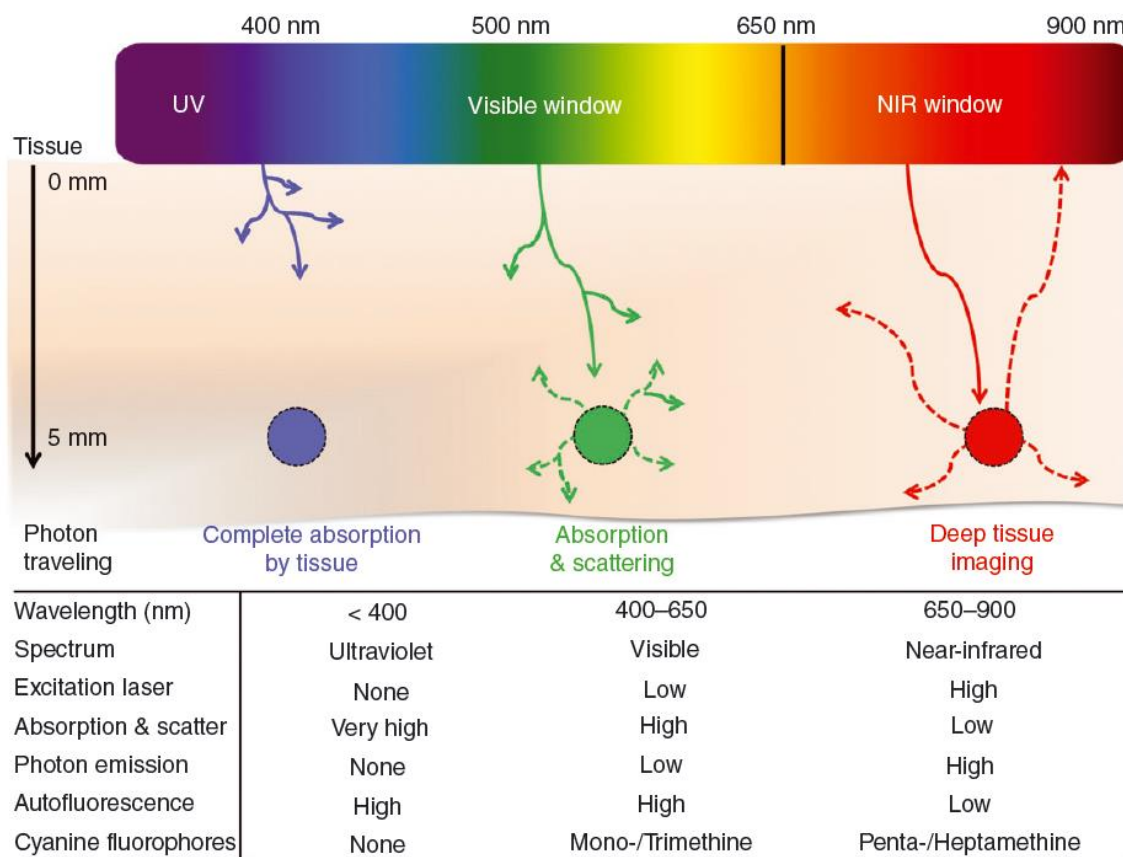


Figure 1-2. *In vivo* optical properties of injected fluorophores along with wavelength.

Many biological compounds fluoresce within the ultraviolet (< 400 nm) and visible (400-650 nm) regions which makes observing contrast agents in this range nearly impossible; however, NIR-fluorescent compounds avoid this issue by being spectrally distinct from the native biological fluorescence (autofluorescence) which offers outstanding SBR. It has been convincingly demonstrated that native tissue greatly interferes with the extraction of meaningful signal in the red-shifted visible region. Therefore, the lower limit (> 650 nm) of the NIR window is bound by biological autofluorescence. The upper end of the NIR region (< 900 nm) of optical clarity is bound by absorption arising from vibrational characteristics of water (> 950 nm). These advantages along with the availability and low cost of long-

wavelength diode lasers and detectors for the NIR light, have led to increasing research interest in the design, development, spectroscopic characterization and application of novel NIR fluorophores.¹²

1.6 Small Molecule Optical Contrast Agents

Engineering optical contrast agents that satisfy the physical, chemical and biological requirements is a difficult process but remains crucial in maximizing the surgical implementation of image-guided surgery.¹³ The performance of contrast agents depends strongly on their physicochemical properties (i.e. molecular weight, total polar surface area, hydrogen bond donors/acceptors, acidic/basic pKa, distribution/partition coefficient and stability), which heavily influence their *in vivo* fate with slight structural modifications posing significant biological perturbation.¹⁴⁻²³

Efficient optical properties are the very basic requirements for developing new contrast agents and there are several crucial parameters such as high solubility, high extinction coefficient, large Stokes' Shift, high quantum yield, and high photobleaching threshold that directly influence the potential obtainable signal during the imaging process.^{24, 25} Correspondingly, the first essential task is to optimize these parameters in the process of developing novel contrast agents.

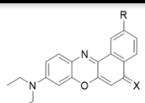
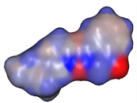
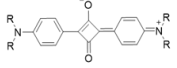
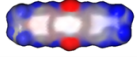
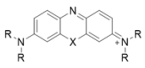
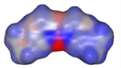
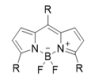

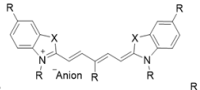
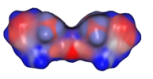
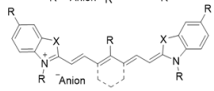
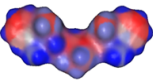
The aqueous optical profile and water solubility normally go hand-in-hand; therefore, the first design consideration is either to avoid a highly hydrophobic core or alternately incorporate a charged group onto the fluorophore. Following these design parameters drastically increases the aqueous solubility and can increase the quantum yield (up to 10x). Judicious placement of charge is necessary as superfluous intrinsic charge can reduce the efficacy of biological targeting moieties due to steric hindrance, electrostatic repulsion or general bio-incompatibility. Therefore, fluorophores should be designed to have high aqueous solubility, while maintaining target recognition.

Additionally large extinction coefficient and quantum yield values are paramount for optical contrast agents, especially at the tissue depths required for image-guided surgery. The extinction coefficient—measure of the absorption at a particular wavelength by a compound—accurately represents the ability of a compound to absorb radiation and can be determined using the Beer-Lambert equation²⁶. For optical imaging, typical satisfactory extinction coefficients in aqueous systems are between 100,000 and 200,000 M⁻¹cm⁻¹. This range of extinction coefficients results in reasonable photon absorption by the fluorophore.

Last but not least, high photobleaching threshold is a very important area of consideration. Conventional fluorophores are highly susceptible to photobleaching which places severe limitation on the fluence rate and consequently the sensitivity and length of detection. For example, the NIR fluorescent indocyanine green (ICG) rapidly photobleaches in warm serum when fluence rates exceed 50 mW/cm².²⁷ However, hybrid nanoparticles (quantum dots, etc.) and multivalent polymeric nanomaterials commonly have higher resistance to photobleaching compared to small molecules with ability to withstand fluence rates one to two orders of magnitude higher. Because fluence rates improve the signal-to-background, contrast agents with higher resistance to photobleaching will yield improved fluorophores.

1.7 Classes of NIR Fluorophores

Among the optical contrast agents explored to date, the NIR region has gained considerable numbers of ideal fluorophores with potential for translation in image-guided surgery. Fortunately, there are several classes of fluorophores that offer appealing characteristics for further modifications towards designing contrast agents within the NIR window. The general molecular structures seen in Figure 3 represent a selection of chromophores that fluoresce in the NIR region. These fluorophores have general properties that either make them more appealing or limit their overall utility as bioimaging agents.

Fluorophore	Chemical Structure	Hydrophobicity	General Characteristics	Wavelength, Φ , ϵ
Nile Red (X = O) Nile Blue (X = NH ₂ ⁺)			Highly solvatochromic and hydrophobic. Φ varies greatly according to R. Biodistribution is mostly unknown. Low modification potential.	X = O 530-600 nm, 40-80%, 60,000 M ⁻¹ cm ⁻¹ X = NH ₂ ⁺ 530-600 nm, 40-80%, 60,000 M ⁻¹ cm ⁻¹
Squaric Acid Fluorophores			High Φ and ϵ (molecular brightness). High yielding synthetic routes with large opportunity of modification. Not stable in the presence of proteins.	600-650 nm, 50-80%, 250,000 M ⁻¹ cm ⁻¹
Phenoxazine (X = O) Phenothiazine (X = S)			Structurally stable molecules that are generally synthetically low yielding. Low modification potential.	X = O 550-600 nm, 25-35%, 80,000 M ⁻¹ cm ⁻¹ X = S 640-680 nm, 9-15%, 45,000 M ⁻¹ cm ⁻¹
Boron-dipyrromethene (BODIPY)			Structurally stable but exhibits a broad abs spectrum with low Φ and ϵ . Highly amenable to diverse modifications.	480-750 nm, 15-35%, 80,000 M ⁻¹ cm ⁻¹
Pentamethine Cyanine Dyes			Structurally stable with comparatively high molar absorptivity and moderate quantum yield dependent on Rs. Highly modifiable.	650-700 nm, 20-60%, 200,000 M ⁻¹ cm ⁻¹
Heptamethine Cyanine Dyes			Structurally stable with central cyclic ring but otherwise chemically labile. Optical properties depend on Rs. Highly modifiable.	740-850 nm, 12-40%, 200,000 M ⁻¹ cm ⁻¹

Φ = quantum yield; ϵ = extinction coefficient

Figure 1-3. Chemical structures of various classes of small molecule fluorophores that have been explored for biophotonic imaging, their general hydrophobicity maps, highlighted characteristics concerning their potential for in vivo performance and the overall optical properties concerning the general core structure.

Nile red and nile blue are notoriously solvatochromic (change absorption spectrum when changing solvent or environment), highly hydrophobic fluorophores that can be modified in several positions to achieve water solubility;²⁸ however, analogs synthesized and evaluated to date fluoresce in the NIR albeit with low quantum yield in aqueous systems or in the presence of proteins. These limitations have precluded them from being extensively evaluated *in vivo*.²⁹⁻
³² Another class of compounds centers on the cyclic oxobutanol ring and is referred to as squaraine or squaric acid fluorophores.³³ The extreme electrophilicity of this cyclic butane ring is susceptible to nucleophilic attack, which irreversibly diminishes the optical properties of the compound, unless the core is protected by one of several methods including rotaxane encapsulation³⁴ which reduces the overall applicability in small molecule bioimaging. Contrary to the squaraine class of fluorophores, the tricyclic fused structures of phenoxazine

and phenothiazine are highly structurally and optically stable even in the presence of nucleophilic species due to the aromatic core. The synthetic difficulty associated with this class limits the versatility and overall applicability in image-guided surgery. Furthermore, the emission wavelengths of the oxazine class is too low and cannot be used due to interfering native tissue absorption and autofluorescence.^{35,36} The boron-dipyrromethane (BODIPY) class of fluorophores exhibits excellent characteristics from high stability and above-average quantum yield but suffers from having a highly hydrophobic core and broad absorption/emission spectra. These fluorophores have been successful *in vivo* due to their NIR emission, high quantum yield and ability to be synthetically tailored to several applications.^{23,37-41} currently, however, high background during intravenous injection limits the scope for this molecular class.²³

Cyanine fluorophores are broadly defined as two heterocyclic nitrogen atoms that are connected *via* an electron deficient polymethine bridge. Monomethine cyanines display one methine unit, in this case defined as (=CH-), between the heterocyclic structures, this class of compounds displays absorbance within the ultraviolet and visible regions with low fluorescence quantum yield. Elongating the central chromophore length by sets of 2 methylene groups yields tri-, penta-, and heptamethine cyanines. The wavelengths of most trimethine cyanines are too low to be effective in NIR imaging in biological systems; however, penta- and heptamethine cyanines have near-infrared absorbance and fluorescence characteristics that are a function of their exact heterocyclic structure and moieties within the polymethine chain which can be tuned to offer high quantum yield and molecular brightness with a high degree of structural amenability toward manipulating the pharmacophore in the generation of successful NIR fluorescent contrast agents.

1.8 State-of-the-art in Image-Guided Surgery

Figure 4 shows two of the most highly used optical contrast agents, methylene blue (MB), a fused phenothiazine compound, and ICG, a heptamethine cyanine dye. Surgeons have found ways to utilize the FDA approved ICG;⁴²⁻⁴⁷ however, the high background signal *in vivo*, structural and optical instability and the lack of ability for a targeting functionality has opened several avenues for the manipulation of the chemical structure. MB, perhaps the second most widely researched compound in image-guided surgery not because of its NIR fluorescence but its color staining properties^{48, 49} unfortunately suffers from non-dependable optical properties.⁵⁰⁻⁵⁷ The absorption and fluorescence characteristics are at appropriate wavelengths during *in vitro* experimentation; however, the redox state of the compound allows for the reduction of the central imine to the corresponding amine which destroys the NIR fluorescence of the compound. These non-optimum properties along with low extinction coefficient and non-amenability to the addition of a targeting ligand limit the overall utility of this particular contrast agent. In order to develop robust NIR fluorescent contrast agents for image guided surgery, the general structure of ICG was modified to include a central cyclic ring for increased optical and chemical stability along with a zwitterionic character to minimize cellular accumulation and prevent off-target localization.^{14, 15} Additionally, a reactive carboxylate moiety was added for structural manipulation toward targeted imaging.¹⁶ The engineered molecule is depicted in Figure 4 and is known as ZW800-1 and is among the carbocyanine class of NIR contrast agents for targeted imaging once conjugated to a biological targeting ligand.¹⁶

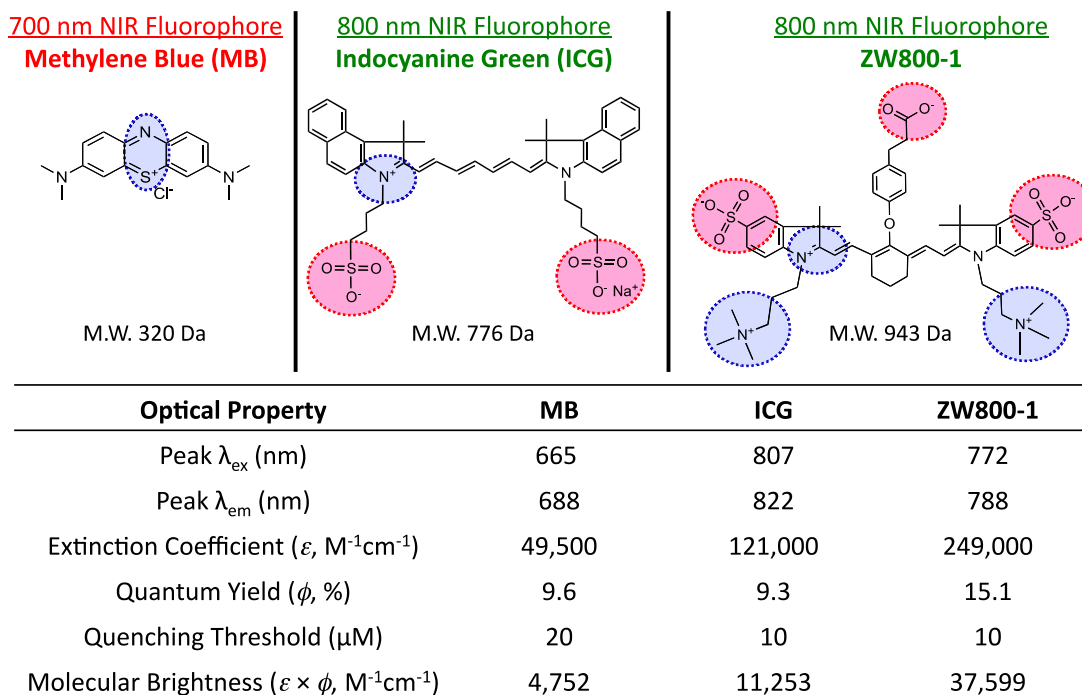


Figure 1-4. Current state-of-the-art NIR fluorophores used in image-guided surgery. The chemical structures of three NIR fluorescent contrast agents and the corresponding optical properties. The negatively charged moieties are highlighted in red and the positively charged regions are designated in blue.

1.9 Background Retention

Optical contrast agents have been designed to satisfy the optical property criteria and their capacity to luminesce using fluorescence light through skin and tissue has been convincingly demonstrated, but only a few fluorophores exhibit the ultralow background required for clinical translation.^{14-16, 25, 58-64} Obtaining this high signal to background depends on the clearance pathway from the body and there are structural constraints that allow compounds to be cleared through renal filtration—the pathway for obtaining clear background.

Renal clearance, involving the kidney, is the ideal route as it minimizes retention and toxicity risks within the body.⁶⁵ There are three steps that comprise the process of renal clearance: glomerular filtration, tubular secretion, and urinary excretion.^{66, 67} The molecular

shape, conformation, size and surface charges are important determinants of renal clearance, more specifically glomerular filtration.²⁴ Intravascular agents with a hydrodynamic diameter (HD) smaller than 6 nm are usually successfully filtered when the surface charges are neutral or zwitterionic, while injected molecules with an HD > 8 nm are not filtered through kidneys at all.^{58, 68} Large molecules or highly charged molecules undergo some level of hepatobiliary excretion, which generally involves catabolism and biliary excretion, and contaminates the gastrointestinal (GI) tract and increase non-specific uptake. Although the overall size is smaller than 6 nm, cationic charged molecules trap in the negatively charged filters and vasculature, and increase background signal significantly.

The comparison between ZW800-1 and ICG shows a prime example of the clearance pathway leading to elevated background signal. ZW800-1 displays unique and exciting biological and physiological properties *in vivo*.¹⁴⁻¹⁶ The highly charged yet neutral character prevents cellular accumulation and minimizes protein interactions allowing for complete and rapid clearance through renal filtration as shown in comparison to ICG in Figure 5. The biodistribution pattern associated with ICG is more common among alternate NIR fluorophores

with high non-specific uptake shown through the high signal in the liver and duodenum evidenced by the high fluorescence signal in Figure 5.

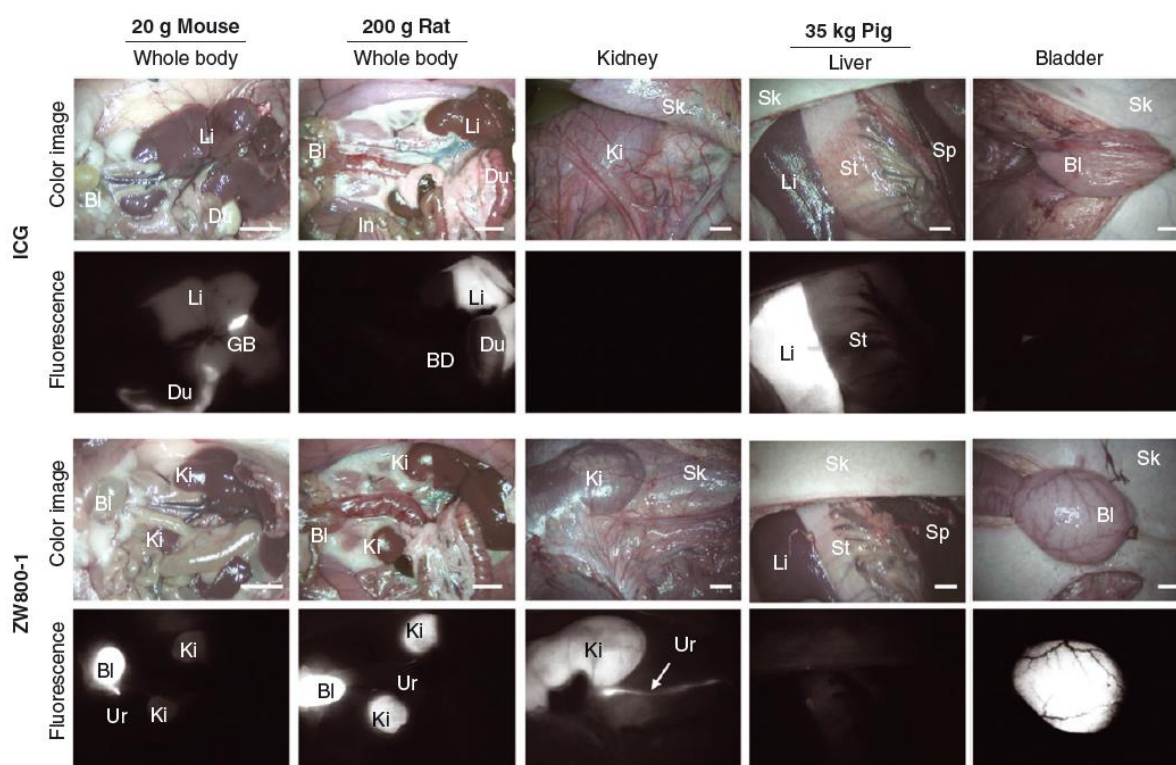


Figure 1-5. Biodistribution and clearance of ICG and ZW800-1. ICG shows elevated nonspecific uptake in liver and duodenum, while ZW800-1 represents ultralow background and renal clearance. Animals were housed in an AAALAC-certified facility and were studied under the supervision of BIDMC IACUC in accordance with approved institutional protocols (#101-2011 for rodents and #046-2010 for pigs). NIR fluorophores were injected intravenously into ~20 g CD-1 mice (10 nmol), ~250 g SD rats (50 nmol), and ~35 kg Yorkshire pigs (1 μ mol) 1 h prior to imaging. Shown are color and 800 nm NIR fluorescence images of surgically exposed organs taken by the FLARE intraoperative imaging system.¹⁴⁻¹⁶ NIR fluorescence images have identical exposure times and normalizations. Abbreviations used are: Bl: bladder; BD: bile duct; Du: duodenum; In: intestine; Ki: kidneys; Li: liver; Sk: skin; St: stomach; Ur: ureter. Scale bars = 1 cm.

1.10 Nonspecific Uptake and Persistent Background Retention (PBR)

The focal point of optical imaging combined with appropriate contrast agents is to produce a high SBR: increase the target signal while decreasing the background signal and noise. While the focus of optical imaging is typically on generating signal, it is the SBR, and more often background, which dictates the performance of an injected contrast agent. From the moment an exogenous contrast agent is injected intravenously, it is likely non-specifically contributing to background signal and degrading overall performance. The SBR is adequate for imaging only after specific binding to the desired target and clearance of this non-specific background from tissue.

Although virtually all published mathematical models of contrast agent biodistribution and clearance suggest that background is cleared in a relatively short period of time, especially for small molecule contrast agents, in reality there is a phenomenon of persistent background retention (PBR) that results in 10-30% of the injected dose remaining non-specifically in tissues throughout the body.^{69, 70} While the mechanism for PBR is presently unknown, it appears to be a strong function of molecular size, shape, charges, and charge-to-mass ratio.²⁴ Therefore, in order to improve the SBR of an injected molecule thus improve its intraoperative use, reducing PBR is desperately needed through structural manipulating of its size, charge, absorption and clearance as the rapid biodistribution and complete elimination.

1.11 Conclusions

Although surgery is the main path in curing almost half of all cancer patients, none can perfectly image the desired target due to high levels of background signal that results in extreme difficulty during surgery. Designing the best possible contrast agent is essential in maximizing the use of optical imaging to detect, target, and diagnose specific cancer cells *in vivo*. Therefore a thorough understanding of the molecular and tissue properties helps in designing the ideal contrast agent. Monitoring the surgical field through the visualization of near-infrared

fluorescence stands firm as a leading alternative and arguably most viable option for real-time-guided surgery.

1.12 References

1. Fujimura M, Niizuma K, Endo H, Sato K, Inoue T, Shimizu H, Tominaga T. Quantitative analysis of early postoperative cerebral blood flow contributes to the prediction and diagnosis of cerebral hyperperfusion syndrome after revascularization surgery for moyamoya disease. *Neurol Res* 2014;1743132814Y0000000432.
2. Nakahara M, Ito M, Hattori N, Magota K, Takahata M, Nagahama K, Sudo H, Kamishima T, Tamaki N, Iwasaki N. 18F-FDG-PET/CT better localizes active spinal infection than MRI for successful minimally invasive surgery. *Acta Radiol* 2014.
3. Mannu GS, Bhalerao A. A century of breast surgery: from radical to minimal. *Can J Surg* 2014, 57:E147-148.
4. Vahrmeijer AL, Hutteman M, van der Vorst JR, van de Velde CJ, Frangioni JV. Image-guided cancer surgery using near-infrared fluorescence. *Nat Rev Clin Oncol* 2013, 10:507-518.
5. Backer MV, Levashova Z, Patel V, Jehning BT, Claffey K, Blankenberg FG, Backer JM. Molecular imaging of VEGF receptors in angiogenic vasculature with single-chain VEGF-based probes. *Nat Med* 2007, 13:504-509.
6. Vag T, Slotta-Huspenina J, Rosenberg R, Bader FG, Nitsche U, Drecoll E, Rummeny EJ, Gaa J. Computerized analysis of enhancement kinetics for preoperative lymph node staging in rectal cancer using dynamic contrast-enhanced magnetic resonance imaging. *Clin Imaging* 2014.
7. Bal H, Guerin L, Casey ME, Conti M, Eriksson L, Michel C, Fanti S, Pettinato C, Adler S, Choyke P. Improving PET spatial resolution and detectability for prostate cancer imaging. *Phys Med Biol* 2014, 59:4411-4426.

8. Povoski SP, Hall NC, Martin EW, Jr., Walker MJ. Multimodality approach of perioperative 18F-FDG PET/CT imaging, intraoperative 18F-FDG handheld gamma probe detection, and intraoperative ultrasound for tumor localization and verification of resection of all sites of hypermetabolic activity in a case of occult recurrent metastatic melanoma. *World J Surg Oncol* 2008, 6:1.
9. Candell L, Campbell MJ, Shen WT, Gosnell JE, Clark OH, Duh QY. Ultrasound-guided methylene blue dye injection for parathyroid localization in the reoperative neck. *World J Surg* 2014, 38:88-91.
10. Lee S, Chen X. Dual-modality probes for in vivo molecular imaging. *Molecular imaging* 2009, 8:87-100.
11. Blasberg RG. In vivo molecular-genetic imaging: multi-modality nuclear and optical combinations. *Nuclear medicine and biology* 2003, 30:879-888.
12. Weissleder R. A clearer vision for in vivo imaging. *Nature biotechnology* 2001, 19:316-317.
13. Lee JH, Park G, Hong GH, Choi J, Choi HS. Design considerations for targeted optical contrast agents. *Quantitative imaging in medicine and surgery* 2012, 2:266-273.
14. Choi HS, Nasr K, Alyabyev S, Feith D, Lee JH, Kim SH, Ashitate Y, Hyun H, Patonay G, Streckowski L, et al. Synthesis and in vivo fate of zwitterionic near-infrared fluorophores. *Angewandte Chemie* 2011, 50:6258-6263.
15. Hyun H, Bordo MW, Nasr K, Feith D, Lee JH, Kim SH, Ashitate Y, Moffitt LA, Rosenberg M, Henary M, et al. cGMP-Compatible preparative scale synthesis of near-infrared fluorophores. *Contrast media & molecular imaging* 2012, 7:516-524.
16. Choi HS, Gibbs SL, Lee JH, Kim SH, Ashitate Y, Liu F, Hyun H, Park G, Xie Y, Bae S, et al. Targeted zwitterionic near-infrared fluorophores for improved optical imaging. *Nature biotechnology* 2013, 31:148-153.

17. Kim SH, Lee JH, Hyun H, Ashitate Y, Park G, Robichaud K, Lunsford E, Lee SJ, Khang G, Choi HS. Near-infrared fluorescence imaging for noninvasive trafficking of scaffold degradation. *Scientific reports* 2013, 3:1198.
18. Kim SH, Park G, Hyun H, Lee JH, Ashitate Y, Choi J, Hong GH, Owens EA, Henary M, Choi HS. Near-infrared lipophilic fluorophores for tracing tissue growth. *Biomedical materials* 2013, 8:014110.
19. Ashitate Y, Hyun H, Kim SH, Lee JH, Henary M, Frangioni JV, Choi HS. Simultaneous mapping of pan and sentinel lymph nodes for real-time image-guided surgery. *Theranostics* 2014, 4:693-700.
20. Choi HS. Nanoparticle assembly: building blocks for tumour delivery. *Nature nanotechnology* 2014, 9:93-94.
21. Hyun H, Wada H, Bao K, Gravier J, Yadav Y, Laramie M, Henary M, Frangioni JV, Choi HS. Phosphonated Near-Infrared Fluorophores for Biomedical Imaging of Bone. *Angewandte Chemie* 2014.
22. Park MH, Hyun H, Ashitate Y, Wada H, Park G, Lee JH, Njiojob C, Henary M, Frangioni JV, Choi HS. Prototype nerve-specific near-infrared fluorophores. *Theranostics* 2014, 4:823-833.
23. Salim MM, Owens EA, Gao T, Lee JH, Hyun H, Choi HS, Henary M. Hydroxylated near-infrared BODIPY fluorophores as intracellular pH sensors. *Analyst* 2014.
24. Choi HS, Frangioni JV. Nanoparticles for biomedical imaging: fundamentals of clinical translation. *Molecular imaging* 2010, 9:291-310.
25. Choi HS, Liu W, Liu F, Nasr K, Misra P, Bawendi MG, Frangioni JV. Design considerations for tumour-targeted nanoparticles. *Nature nanotechnology* 2010, 5:42-47.

26. Beckford G, Owens E, Henary M, Patonay G. The solvatochromic effects of side chain substitution on the binding interaction of novel tricarbocyanine dyes with human serum albumin. *Talanta* 2012, 92:45-52.
27. Yaqoob Z, McDowell E, Wu J, Heng X, Fingler J, Yang C. Molecular contrast optical coherence tomography: A pump-probe scheme using indocyanine green as a contrast agent. *J Biomed Opt* 2006, 11:054017.
28. Jose J, Ueno Y, Burgess K. Water-soluble Nile Blue derivatives: syntheses and photophysical properties. *Chemistry* 2009, 15:418-423.
29. Chen W, Sommerfeld M, Hu Q. Microwave-assisted Nile red method for in vivo quantification of neutral lipids in microalgae. *Bioresour Technol* 2011, 102:135-141.
30. Kuramitz H, Piruska A, Halsall HB, Seliskar CJ, Heineman WR. Simultaneous multiselective spectroelectrochemical sensing of the interaction between protein and its ligand using the redox dye Nile blue as a label. *Anal Chem* 2008, 80:9642-9648.
31. Sharma AK, Ahlawat DS, Mohan D, Singh RD. Concentration-dependent energy transfer studies in ternary dye mixture of Stilbene-420, Coumarin-540 and Nile Blue. *Spectrochim Acta A Mol Biomol Spectrosc* 2009, 71:1631-1633.
32. Lin CW, Shulok JR, Wong YK, Schanbacher CF, Cincotta L, Foley JW. Photosensitization, uptake, and retention of phenoxazine Nile blue derivatives in human bladder carcinoma cells. *Cancer Res* 1991, 51:1109-1116.
33. Sreejith S, Divya KP, Ajayaghosh A. A near-infrared squaraine dye as a latent ratiometric fluorophore for the detection of aminothiols in blood plasma. *Angew Chem Int Ed Engl* 2008, 47:7883-7887.
34. Hsueh SY, Lai CC, Liu YH, Wang Y, Peng SM, Chiu SH. Protecting a squaraine near-IR dye through its incorporation in a slippage-derived [2]rotaxane. *Org Lett* 2007, 9:4523-4526.

35. Nowakowska-Oleksy A, Soloducho J, Cabaj J. Phenoxazine based units--synthesis, photophysics and electrochemistry. *J Fluoresc* 2011, 21:169-178.
36. Karlsson KM, Jiang X, Eriksson SK, Gabrielsson E, Rensmo H, Hagfeldt A, Sun L. Phenoxazine dyes for dye-sensitized solar cells: relationship between molecular structure and electron lifetime. *Chemistry* 2011, 17:6415-6424.
37. Carlson JC, Meimetis LG, Hilderbrand SA, Weissleder R. BODIPY-tetrazine derivatives as superbright bioorthogonal turn-on probes. *Angew Chem Int Ed Engl* 2013, 52:6917-6920.
38. Ucuncu M, Emrullahoglu M. A BODIPY-based reactive probe for the detection of Au(III) species and its application to cell imaging. *Chem Commun (Camb)* 2014, 50:5884-5886.
39. Quan L, Sun T, Lin W, Guan X, Zheng M, Xie Z, Jing X. BODIPY fluorescent chemosensor for Cu²⁺ detection and its applications in living cells: fast response and high sensitivity. *J Fluoresc* 2014, 24:841-846.
40. Misra R, Jadhav T, Dhokale B, Gautam P, Sharma R, Maragani R, Mobin SM. Carbazole-BODIPY conjugates: design, synthesis, structure and properties. *Dalton Trans* 2014, 43:13076-13086.
41. Zhang HX, Chen JB, Guo XF, Wang H, Zhang HS. Highly sensitive determination of nitric oxide in biologic samples by a near-infrared BODIPY-based fluorescent probe coupled with high-performance liquid chromatography. *Talanta* 2013, 116:335-342.
42. Gilmore DM, Khullar OV, Gioux S, Stockdale A, Frangioni JV, Colson YL, Russell SE. Effective low-dose escalation of indocyanine green for near-infrared fluorescent sentinel lymph node mapping in melanoma. *Ann Surg Oncol* 2013, 20:2357-2363.
43. Hutteman M, Mieog JS, van der Vorst JR, Liefers GJ, Putter H, Lowik CW, Frangioni JV, van de Velde CJ, Vahrmeijer AL. Randomized, double-blind comparison of indocyanine

- green with or without albumin premixing for near-infrared fluorescence imaging of sentinel lymph nodes in breast cancer patients. *Breast Cancer Res Treat* 2011, 127:163-170.
44. Schaafsma BE, Mieog JS, Hutteman M, van der Vorst JR, Kuppen PJ, Lowik CW, Frangioni JV, van de Velde CJ, Vahrmeijer AL. The clinical use of indocyanine green as a near-infrared fluorescent contrast agent for image-guided oncologic surgery. *J Surg Oncol* 2011, 104:323-332.
45. Tummers QR, Verbeek FP, Prevoo HA, Braat AE, Baeten CI, Frangioni JV, van de Velde CJ, Vahrmeijer AL. First Experience on Laparoscopic Near-Infrared Fluorescence Imaging of Hepatic Uveal Melanoma Metastases Using Indocyanine Green. *Surg Innov* 2014.
46. van der Vorst JR, Hutteman M, Mieog JS, de Rooij KE, Kaijzel EL, Lowik CW, Putter H, Kuppen PJ, Frangioni JV, van de Velde CJ, et al. Near-infrared fluorescence imaging of liver metastases in rats using indocyanine green. *J Surg Res* 2012, 174:266-271.
47. van der Vorst JR, Schaafsma BE, Verbeek FP, Hutteman M, Mieog JS, Lowik CW, Liefers GJ, Frangioni JV, van de Velde CJ, Vahrmeijer AL. Randomized comparison of near-infrared fluorescence imaging using indocyanine green and 99(m) technetium with or without patent blue for the sentinel lymph node procedure in breast cancer patients. *Ann Surg Oncol* 2012, 19:4104-4111.
48. Gioux S, Choi HS, Frangioni JV. Image-guided surgery using invisible near-infrared light: fundamentals of clinical translation. *Molecular imaging* 2010, 9:237-255.
49. Merian J, Gravier J, Navarro F, Texier I. Fluorescent nanoprobes dedicated to in vivo imaging: from preclinical validations to clinical translation. *Molecules* 2012, 17:5564-5591.
50. Guay J, Grabs D. A cadaver study to determine the minimum volume of methylene blue or black naphthol required to completely color the nerves relevant for anesthesia during breast surgery. *Clin Anat* 2011, 24:202-208.

51. Moll X, Garcia F, Ferrer RI, Santos L, Aguilar A, Andaluz A. Distribution of methylene blue after injection into the epidural space of anaesthetized pregnant and non-pregnant sheep. *PLoS One* 2014, 9:e92860.
52. Shah-Khan MG, Lovely J, Degnim AC. Safety of methylene blue dye for lymphatic mapping in patients taking selective serotonin reuptake inhibitors. *Am J Surg* 2012, 204:798-799.
53. Ashitate Y, Lee BT, Laurence RG, Lunsford E, Hutteman M, Oketokoun R, Choi HS, Frangioni JV. Intraoperative prediction of postoperative flap outcome using the near-infrared fluorophore methylene blue. *Ann Plast Surg* 2013, 70:360-365.
54. Matsui A, Tanaka E, Choi HS, Kianzad V, Gioux S, Lomnes SJ, Frangioni JV. Real-time, near-infrared, fluorescence-guided identification of the ureters using methylene blue. *Surgery* 2010, 148:78-86.
55. Tummers QR, Verbeek FP, Schaafsma BE, Boonstra MC, van der Vorst JR, Liefers GJ, van de Velde CJ, Frangioni JV, Vahrmeijer AL. Real-time intraoperative detection of breast cancer using near-infrared fluorescence imaging and Methylene Blue. *Eur J Surg Oncol* 2014, 40:850-858.
56. van der Vorst JR, Schaafsma BE, Verbeek FP, Swijnenburg RJ, Tummers QR, Hutteman M, Hamming JF, Kievit J, Frangioni JV, van de Velde CJ, et al. Intraoperative near-infrared fluorescence imaging of parathyroid adenomas with use of low-dose methylene blue. *Head Neck* 2014, 36:853-858.
57. Verbeek FP, van der Vorst JR, Schaafsma BE, Swijnenburg RJ, Gaarenstroom KN, Elzevier HW, van de Velde CJ, Frangioni JV, Vahrmeijer AL. Intraoperative near infrared fluorescence guided identification of the ureters using low dose methylene blue: a first in human experience. *J Urol* 2013, 190:574-579.

58. Choi HS, Liu W, Misra P, Tanaka E, Zimmer JP, Ity Ipe B, Bawendi MG, Frangioni JV. Renal clearance of quantum dots. *Nature biotechnology* 2007, 25:1165-1170.
59. Ashitate Y, Stockdale A, Choi HS, Laurence RG, Frangioni JV. Real-time simultaneous near-infrared fluorescence imaging of bile duct and arterial anatomy. *The Journal of surgical research* 2012, 176:7-13.
60. Wu Z, Shao P, Zhang S, Bai M. Targeted zwitterionic near infrared fluorescent probe for improved imaging of type 2 cannabinoid receptors. *Journal of biomedical optics* 2014, 19:36006.
61. Liu J, Yu M, Ning X, Zhou C, Yang S, Zheng J. PEGylation and zwitterionization: pros and cons in the renal clearance and tumor targeting of near-IR-emitting gold nanoparticles. *Angewandte Chemie* 2013, 52:12572-12576.
62. Liu J, Yu M, Zhou C, Yang S, Ning X, Zheng J. Passive tumor targeting of renal-clearable luminescent gold nanoparticles: long tumor retention and fast normal tissue clearance. *Journal of the American Chemical Society* 2013, 135:4978-4981.
63. Zhou C, Long M, Qin Y, Sun X, Zheng J. Luminescent gold nanoparticles with efficient renal clearance. *Angewandte Chemie* 2011, 50:3168-3172.
64. van Dam GM, Themelis G, Crane LM, Harlaar NJ, Pleijhuis RG, Kelder W, Sarantopoulos A, de Jong JS, Arts HJ, van der Zee AG, et al. Intraoperative tumor-specific fluorescence imaging in ovarian cancer by folate receptor-alpha targeting: first in-human results. *Nature medicine* 2011, 17:1315-1319.
65. Longmire M, Choyke PL, Kobayashi H. Clearance properties of nano-sized particles and molecules as imaging agents: considerations and caveats. *Nanomedicine* 2008, 3:703-717.
66. Deen WM, Lazzara MJ, Myers BD. Structural determinants of glomerular permeability. *Am J Physiol Renal Physiol* 2001, 281:F579-596.

67. Ohlson M, Sorensson J, Haraldsson B. A gel-membrane model of glomerular charge and size selectivity in series. *Am J Physiol Renal Physiol* 2001, 280:F396-405.
68. Moghimi SM, Hunter AC, Murray JC. Long-circulating and target-specific nanoparticles: theory to practice. *Pharmacological reviews* 2001, 53:283-318.
69. Le Mignon MM, Chambon C, Warrington S, Davies R, Bonnemain B. Gd-DOTA. Pharmacokinetics and tolerability after intravenous injection into healthy volunteers. *Investigative radiology* 1990, 25:933-937.
70. van Hagen PM, Breeman WA, Bernard HF, Schaar M, Mooij CM, Srinivasan A, Schmidt MA, Krenning EP, de Jong M. Evaluation of a radiolabelled cyclic DTPA-RGD analogue for tumour imaging and radionuclide therapy. *International journal of cancer. Journal international du cancer* 2000, 90:186-198.

2 SITE SPECIFIC NIR IMAGING: A REVIEW

This chapter focuses on the design parameters and literature associated with developing contrast agents that selectively image diseased and native tissues for optical imaging. The chapter has been amended from the manuscript prepared for invited submission. My contributions from inception concerned the design, organization, deciding material for incorporation, making figures, writing manuscript from beginning to end.

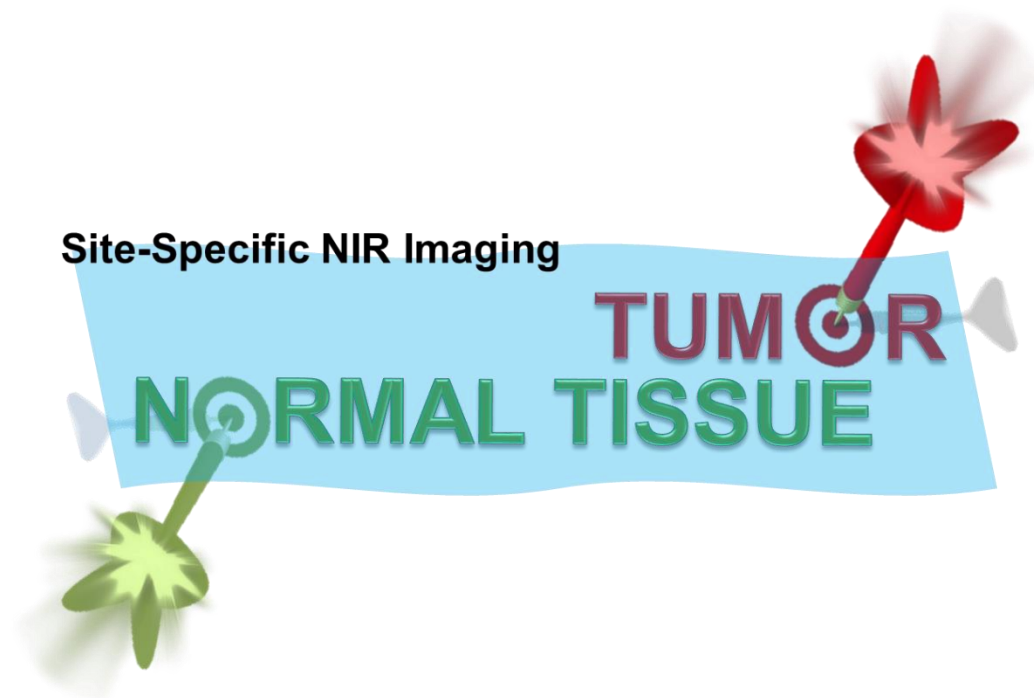
Owens, E.A., Henary, M., Choi, H.S., Site Specific NIR Imaging. Expected **2016**. Invited Review

2.1 Abstract

Clearly defining the physical margins of diseased tissue remains of paramount importance in intraoperative biomedical imaging. An equally noteworthy yet less researched goal is the ability to outline healthy tissues that should be carefully navigated without transection. Both of these paths require optimizing a gauntlet of design considerations to obtain an effective nano or subnano imaging agent that has the requisite NIR-absorbance and fluorescence wavelengths but also high quantum yield, water solubility, highly specific tissue-targeting and biocompatible characteristics. Recent advances offer promise toward fulfilling these stringent requirements for developing a successful catalog of successful imaging agents for illuminating both diseased and healthy tissue in the same surgical space by employing spectrally distinct fluorophores in a single injected dose in real-time.

Keywords. Disease-targeted imaging, native tissue imaging, structure inherent targeting, nanoparticles, fluorophores

TOC Graphic



2.2 Introduction

Long-term survival of surgical patients depends on the ability to fully resect diseased tissue and avoid sensitive tissues/nerves present on the surgical field. Currently, surgeons are limited to their eyesight and physical analyses to determine intra-operative intricacies on the surgical field, even in the performance of highly complicated resections. Toward offering surgeons a real-time method of visualization, the imaging community has pursued various avenues by translating spectral imaging modalities from extant pre-operative techniques that include single photon emission computed tomography (SPECT) or positron emission tomography (PET). [1-4]

Both of these molecular imaging methods have been explored with some success; however, high non-specific targeting leads to elevated background retention in non-targeted tissues which makes deciphering the surgical field challenging thus obviating potential benefits. Furthermore, ionizing radiation associated with these techniques limits the overall scope of their real-time translation. In response to this severe clinical need, alternate possibilities have been established, and they rely on the emission of light by molecules, usually

through fluorescence (i.e. the absorption and conversion of one wavelength of light to one of lower energy, Figure 1), for illuminating the surgical field.[5-16] In this review, we focus on detailing the requisite parameters required for the development of a site-specific chemical probe, the biological infrastructure that must be overcome or harnessed to achieve selective imaging.

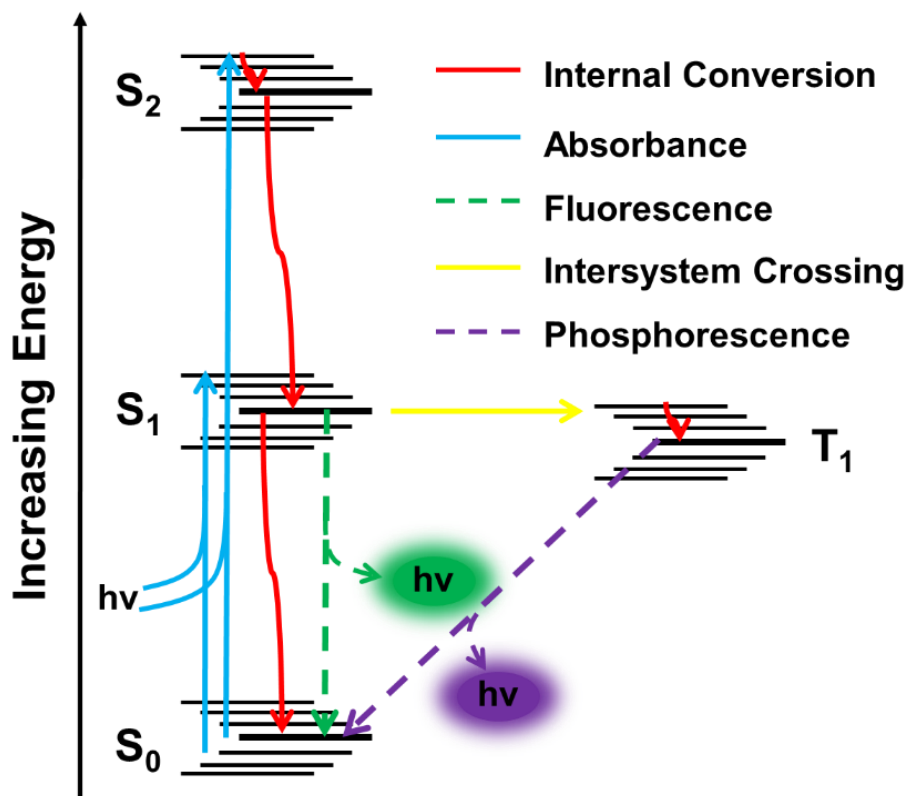


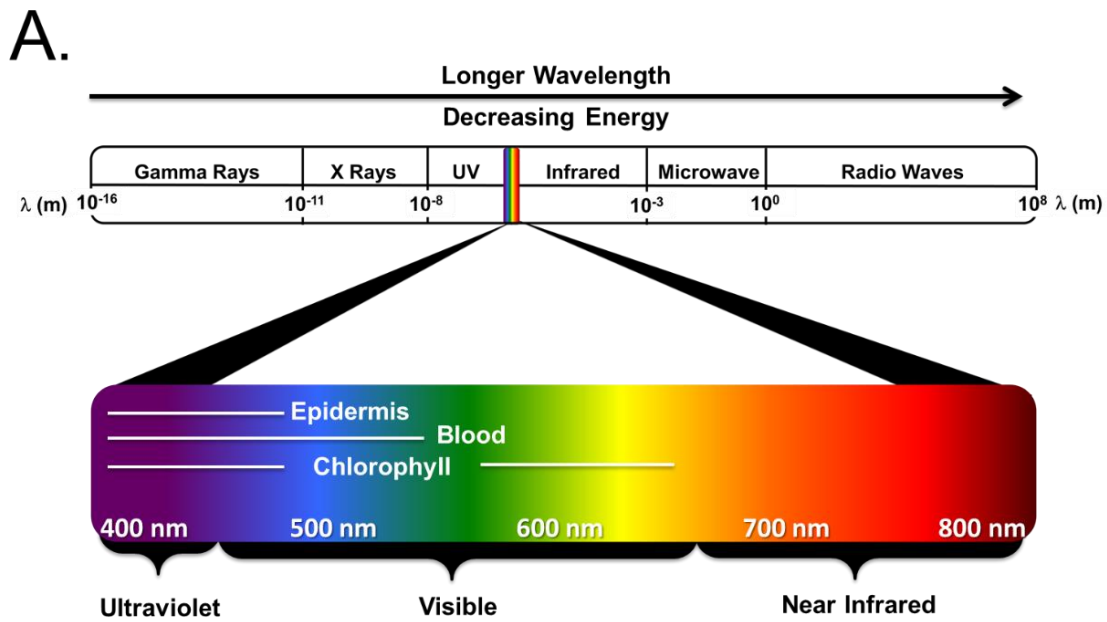
Figure 2-1. A simplified Jablonski diagram showing fluorescence and competing pathways for molecular relaxation from an excited state.

Fluorescence is only one of the pathways that may occur after an incident photon promotes a chemical species from ground state S_0 to excited S_1 , S_2 and beyond. Energetic relaxation occurs through several pathways. Shown in red (Figure 1) is internal conversion that correspond to molecular movements (vibration, stretching, twisting, etc.). Another competing pathway is the process of fluorescence, or the release of light of lower energy (higher wavelength) than that absorbed (energy difference is the origin of the Stokes shift). Lastly, the spin inversion from an excited singlet state to an excited triplet state can relax back to the spin

paired ground state through a time-lapsed phosphorescence pathway. In all systems these various pathways are in dynamic equilibrium with the chemical structure significantly influencing the efficiency of each pathway for energy release. Building on these principles, the chemical structure may be modified such that fluorescence dominates the alternate pathways which affords a high quantum yield of photon emission. This has proven to be very promising and the search for engineered fluorophores with optimum characteristics has been underway.

2.2.1 Near-Infrared Window

Molecular fluorescence relies on the emission of a photon from a molecule relaxing from an excited singlet state and compete with alternate relaxation pathways (i.e. phosphorescence, vibrational relaxation, etc.); the photon emission must be tuned to specific wavelengths using structural modifications. Fortunately, there exists a region where tissue features minimum absorption and fluorescence characteristics thus allowing engineered contrast agents to operate effectively by avoiding the disruptive background signal present at lower wavelengths. It has been well defined and established that near-infrared (NIR, 650-900 nm) light exhibits optimum characteristics for imaging applications *in vivo*, owing to the low tissue attenuation resulting in high penetration depth and minimum background autofluorescence. [17-31] These characteristics afford high signal to background (SBR) which is recognized as the paramount descriptor for successful site-specific contrast agents. The opportunity for high SBR paired with cost effective lasers/detectors and the inherent innocuous nature of NIR light makes it a promising technology for development. [32-38]



B.

Imaging Modality	Excitation	Signal	Characteristics
UV-Vis Fluorophore UV-Vis Absorption and Fluorescence (Rhodamines, Fluoresceins, Coumarins)	UV/Vis Light 350 – 650 nm 	Heat Minimal Target signal X Competing Biological Fluorophores	High Autofluorescence No Resolution Low Tissue Penetration DNA Damage at High Intensities
NIR Fluorophore NIR Absorption and Fluorescence (Cyanines, Phenothiazines, BODIPYs, Squaraines)	NIR Light 650 – 1000 nm 	Low Background High Signal 	No Autofluorescence High Resolution High Tissue Penetration Innocuous
Nuclear Imaging Agent PET, SPECT (^{99m} Tc, ¹¹¹ In, ¹²³ I, ²⁰¹ Tl, ¹¹ C, ¹³ N, ¹⁵ O, ¹⁸ F, ⁶⁴ Cu, ⁶² Cu, ¹²⁴ I, ⁷⁶ Br, ⁸² Rb and ⁶⁸ Ga)	Radiotracer 	Positron/Gamma Ray Emission Computed Tomography 	Low Resolution High Tissue Penetration Highly Ionizing Unsafe to Patient

Figure 2-2. NIR Region and Characteristics. (A) The electromagnetic spectrum with a magnification of the visible and near-infrared region. (B) Imaging modalities, examples and their general characteristics with beneficial characteristics shown in blue and negative characteristics shown in red.

The holy grail of NIR imaging exploits the large wavelength window and offers two distinct imaging channels (i.e. channel 1: 680-720 nm and channel 2: 780-820 nm, Figure 2) which would theoretically allow a single disease targeted fluorophore to be spectrally distinct from another contrast agent directed to sensitive tissues (i.e. nerves, etc.) - should the optimum contrast agents exist. The clinical platform that harnesses NIR irradiation is depicted in Figure 2. A broad spectrum excitation light source is used for brightening the surgical field and excitation of the two spectrally distinct targeted NIR fluorophores that have been intravenously injected. Optical filters facilitates the isolated detection of 700 nm, 800 nm and visible light which can be viewed independently or as an overlay to obtain a merged image (Figure 3). Highly specific targeting and knowing the wavelength for each targeted tissue (i.e. one channel for diseased tissues and the other for native tissue) affords a clear real-time visualization of the surgical field. However, in our quest toward obtaining the dual-channel pinnacle of real-time NIR imaging, we must design contrast agents within the requisite boundaries for developing any pharmaceutical or medicinally relevant agent.

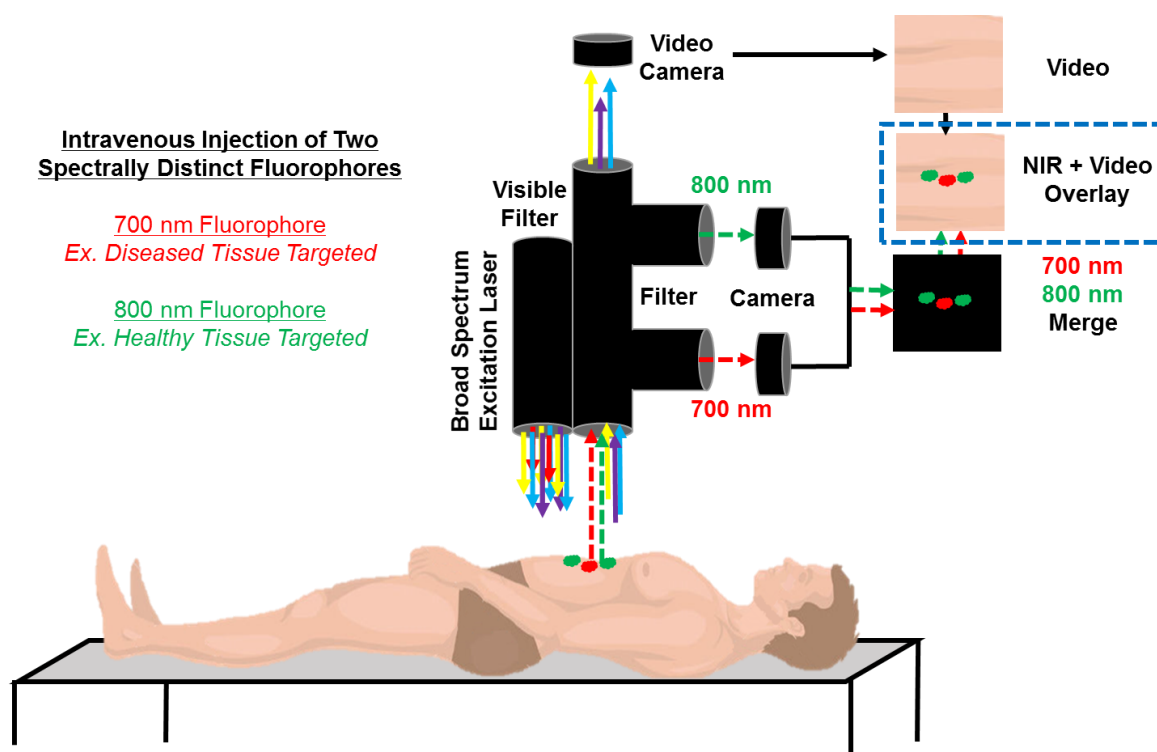


Figure 2-3. The general schematic of dual channel image guided surgery and color video overlay for real-time imaging of the surgical field.

2.2.2 Requisite Design Parameters

Before NIR imaging successfully emerges in the clinic, contrast agents must be designed to satisfy a very particular set of parameters that are requisite to future successes. Many classes of known fluorescent structures have been used successfully and they encompass three unique classes. One of the most studied is the small molecule fluorophore such as cyanines [39-48], porphyrin-based fluorophores [49-56], metal complexes [57, 58], xanthene dyes [59-65], squaraine rotaxanes [66-74], phenothiazine-based fluorophores [6, 7, 75-82]; 2) synthetic nanoparticles such as quantum dots (QDs) [83-90] and 3) biologics such as green fluorescent protein [91-103]. All of these representative contrast agents must be chemically tailored to assume particular characteristics in the body to be clinically relevant. The chemical structure must be engineered for stability, specificity and safety for human use.

The stability of a contrast agent *in vitro* and *in vivo* can be defined by the retention of the original chemical, physical and optical properties. If the molecular structure becomes compromised in the presence of proteins *in vivo*, the signal to background may be lessened or the entire molecular targeting capability may become impaired. These characteristics cannot be overlooked because long-duration surgeries require that the contrast agent remain visible in the diseased tissue for an extended period of time, this effect is known as enhanced permeation and retention (EPR). In order to fulfill this criterion, the molecule must be non-labile to nucleophilic thiol and amine species, resistant to photobleaching and changing redox conditions while simultaneously retaining biological activity. Once narrowing the design criteria to include robust chemical bonds, the specificity to the target-site must be considered.

Specificity is defined as the ability to differentiate between the targeted tissues and the non-targeted tissues. Specific targeting improves the overall image of the target tissue because it improves the target signal by lowering the signals around the target. The injected contrast agents' traveling path (biodistribution) needs to be traced to achieve accurate targeting and complete excretion. Once the contrast agents are introduced into the body, the molecules gather in specific targeting tissues and cells. There are two types of ways in which contrast agents amass in specific tissues: organ-specific targeting and subcellular-specific targeting (to be discussed in detail later).

Safety implies that contrast agents should not impart negative side effects or interfere with biological function in any way, but also, any potentially biodegraded products of the contrast agents should pose no harm to the surgical patient (re stability). Minimizing undesired negative consequences due to potentially toxic characteristics of the contrast agents can be partially controlled by manipulating their size, charge, absorption and elimination. Since cyanine-based contrast agents, for example, are inherently non-toxic, based on the clinical

evaluation of ICG, exploring this class as nontoxic and biocompatible contrast agents could have outstanding clinical significance.

Table 1. Mandatory Properties of Disease-Specific Probes

- 1. High Stability**
 - Physicochemical stability of targeted ligand
 - Optical stability of probe
 - Biological (*in vitro*) and physiological (*in vivo*) stability
- 2. High Sensitivity**
 - High target concentration
 - High molecular brightness of optical probe
 - High performance of imaging modality
- 3. High Specificity**
 - High signal-to-background (noise) ratio (SBR or SNR)
 - High affinity of ligand to the target (signal)
 - Low nonspecific binding to normal tissue (background)
- 4. Favorable delivery** to the target across biological barriers
 - Biodistribution (organ delivery with minimum nonspecific uptake)
 - Delivery across cell membranes (intracellular targets)
- 5. Favorable pharmacokinetics** and metabolism
 - Rapid accumulation to the target (bound molecules)
 - Sustained retention on the target (bound molecules)
 - Rapid clearance from nonspecific tissues (unbound molecules)
 - Rapid elimination from the body (unbound molecules)
- 6. Low toxicity**
 - Chemical, biological, physiological toxicity
 - Acute and chronic toxicity
 - Cytotoxicity and *in vivo* toxicity

These medicinal properties are highly important for future clinical translation and must be maintained throughout the developmental process of a contrast agent. The sensitivity, specificity, delivery, pharmacokinetics and toxicity depend highly on the targeting method used and the overall chemical composition of the contrast agent where the stability is also a determining factor to *in vivo* success, the chemical bonds and moieties present only limit the choices available for modification which does not directly influence the site-specific imaging characteristics.

In the pursuit of efficacious NIR contrast agents, the specificity (i.e. targetability and clearance) remains the dominating factor that determines the future outlook of an engineered fluorophore and there are several molecular blueprints that have been used to overcome this obstacle.

2.3 Methods for Obtaining Site-Specific Imaging.

Site-specificity is determined by the signal-to-background ratio (SBR). As a simple comparison of the signal in the targeted tissue to the signal in the surrounding area, this ratio (SBR) plays a fundamental yet crucial role in the imaging of small and otherwise undetectable tissues. For example, when contrast agents fail to display high tissue specificity resulting in low SBR, small tumors or occult metastases would remain invisible, and the imaging procedure would not afford meaningful guidance to perform a complete resection thus leading to multiple unwarranted surgeries or poor patient survival. Overcoming this obstacle has proved challenging and has been the focus of a recent thrust recent research. Throughout the years of developing targeted optical probes, various research labs have engineered contrast agents that exploit biological systems in various ways to achieve optimal signal-to-background ratio in desired tissues.

These different methods of harnessing/manipulating our biological systems to achieve site-specific imaging can be grouped into three categories (shown in Figure 4) which all have inherent positive and negative characteristics. These three methods are, 1) passive targeting *via* the enhanced permeability and retention (EPR) effect, 2) active targeting *via* biodistribution of known molecules and 3) activatable targeting through an internal stimulus.

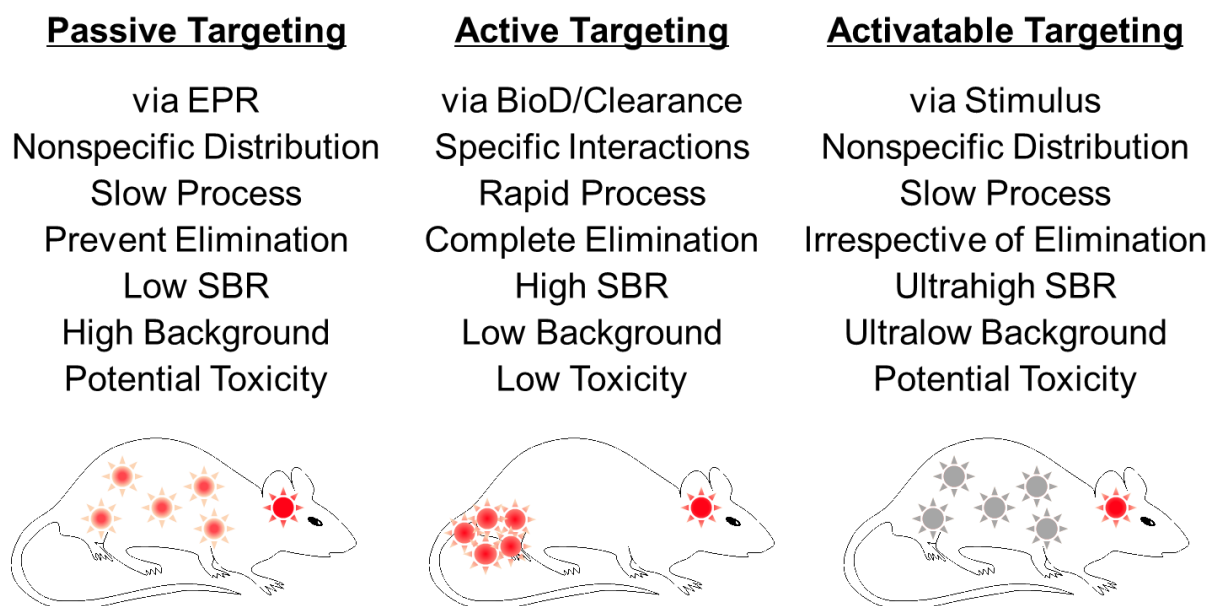


Figure 2-4. The three main strategies for the imaging of a particular region of diseased or cancerous tissue.

Passive targeting through EPR effect relies on the overall biodistribution of a NIR fluorescent contrast agent to achieve site selective imaging. For example, the leaky vasculature of tumors frequently allow larger molecules to enter compared to the more selective healthy tissue. In normal cells, the vasculature remains non-permeable allowing only those molecules of a particular size or bearing molecular recognition moiety through active transport. This preferential accumulation in the tumor offers a pathway for obtaining site specific imaging through the EPR effect. A contrast agent of the appropriate size, charge and pKa bearing certain hydrogen bond donors/acceptor characteristics and other physicochemical properties must be engineered to passively localize within tumor tissues with unbound contrast agent being cleared rapidly from the body. Unless careful design considerations are employed, this proves to be a relatively slow method that commonly results in nonspecific fluorophore distribution and high background signal resulting in reduced signal-to-background and loss in imaging clarity.

The perhaps most straightforward strategy for disease-specific targeting is through the active approach, which involves an engineered NIR fluorophore being synthetically tethered

to a targeting moiety which selectively binds the diseased tissue [104-127] . Surface biomarkers, specifically in cancer cells, have been effectively exploited for homing contrast agents directly to diseased tissues. This is a very rapid process with potential for high signal-to-background ratio and complete excretion associated with reduced non-specific binding. However, problems occur when the tumor does not express large quantities of the surface integrin which significantly lowers the overall signal-to-background ratio. Other factors also must be considered when designing compounds for active-targeting of diseased tissue, including the size molecular weight/size of the contrast domain and the excretion pathway.

The last method is when a contrast agent is activatable through a particular internal stimulus. Normally, when using this method the contrast agent's fluorescence is quenched using any number of methods (i.e. synthetically attached and biologically labile dinitro compounds, reduction of azides, pH-sensitive moieties, etc). Once injected, the molecules exhibiting diminished fluorescence intensity travel throughout the body and become activated at the target by a known stimulus commonly associated with the tissue or microenvironment (i.e. pH[128], concentration of metabolite, redox potential in hypoxic cells, etc.) and exhibits fluorescence. This is a very slow process with a nonspecific distribution of the molecules. This strategy displays very low background signal that results in an overall high signal-to-background ratio.

By developing distinct site-specific fluorophores with complete clearance of unbound contrast agent will afford surgeons a powerful real-time approach to complex surgeries and increased quality of care for surgical patients.

2.4 Nanoparticles for *In Vivo* Imaging.

The nanoparticle-based contrast agents for optical image-guided surgery are currently being developed and their total performance depends strongly on their molecular design, physiochemical and optical properties. [129-137] The molecular design must feature four

major components that are depicted in Figure 5. This modular schematic shows the effector domain, in this case a nanoparticle-based contrast agent, being attached to a targeting ligand through an isolating linker.[138-141] It is important that this isolating linker does not influence the biological recognition of the targeting ligand which could be a small molecule or peptide. This is achieved by the addition of a balancing domain that helps the effector domain achieve a particular size, shape or hydrophobicity to improve the pharmacokinetic properties and overall biodistribution/clearance of the effector domain. Ideally, the imaging agent without the targeting ligand would be cleared rapidly through renal filtration without non-specifically binding to tissues. Adding the homing device (targeting ligand) to this nano-imaging agent would afford high signal-to-background imaging when a successful ligand is employed in the presence of the targeted tissue.

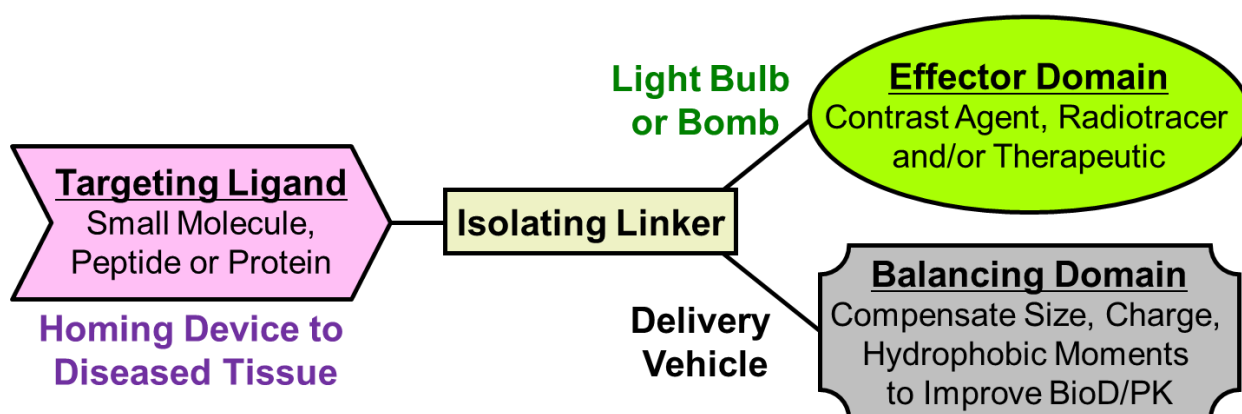


Figure 2-5. General overview for the modular approach to the design of targeting contrast agents/therapeutics.

Recent advancements in nanoparticle-based imaging suggest high promise in the future; currently, however, the intrinsic character of nanoparticles does not readily lend itself to biological compatibility.[142] Owing to this principle, rapid clinical translation is not common in the nanoparticle space. Though nanoparticles are slowly becoming accepted by regulation agencies, in the meantime, small molecule, (defined herein as subnano) imaging agents, offer a unique and appealing alternative with respect to the ability to synthesize a single chemical

entity with high reproducibility and purity. These characteristics lend themselves to FDA-approved clinical translation and predictably reproducible *in vivo* success. With the FDA approved indocyanine green, it is likely these subnano agents that will be the first clinically relevant contrast agents in site-specific imaging; therefore, the remainder of this review will focus on exciting and robust research in this area.

2.5 Subnano Imaging Agents.

Compared to the nanoparticle blueprint, a more simplistic modular design for disease or tissue specific imaging agents is shown in Figure 6A. Similar to the first schematic, there is a targeting ligand that serves as the homing beacon that delivers the imaging agent to the tissue of interest; however, the effector domain must remain either comparatively small (against the targeting ligand) or biologically silent through the synthetic incorporation of a balancing domain within the structure of the fluorophore. These two design approaches are not equal as reducing the effector domain size effectively limits the aromatic system resulting in blue-shifted absorbance/fluorescence wavelengths (i.e. non-NIR region); therefore, we are left with perfecting the balancing domain to achieve a biologically inert effector domain portion of the overall contrast agent. Above this, however, the Holy Grail of NIR imaging (dual channel imaging capability of the surgical field) requires the targeting of healthy tissue which requires the engineering of additional fluorophores that exhibit native tissue site-selectivity. Cellular surface receptors and subcellular targeting domains for native healthy tissue remain scarcely known within the literature; therefore, a tethered approach would not be an obvious choice for obtaining site-specific contrast agents for these tissues. The greatest success thus far in healthy tissue targeting has been obtained through structure inherent targeting which features a simplified molecular design.

Reducing the complexity in modular design even further, the isolating linker may be removed, leaving a single fluorophore with all three of the requisite characteristics expressed

on the one fluorophore domain—as shown in Figure 6B, known as structure inherent targeting. Both molecular blueprints have been exploited to assume excellent properties *in vivo*, and the design and structural requirements vary greatly depending on the targeted tissue (i.e. disease/tumor for resection or sensitive tissue for avoidance).

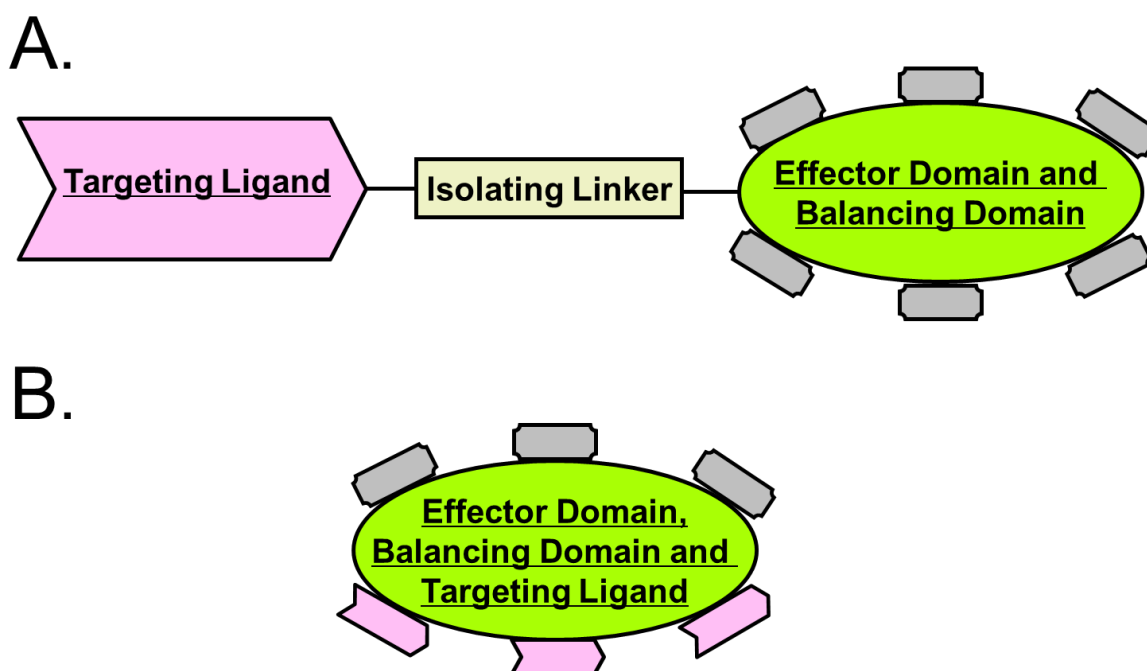


Figure 2-6. (A) Compact modular design for preparing tissue-targeting imaging agents and (B) structure inherent imaging through the incorporation of targeting elements into the small molecule structure.

2.6 Targeted Approach.

Numerous peptidyl-fluorophore tethering approaches have been recently explored with a varying degree of success. The three factors that are individually requisite in the *in vivo* performance of tethered fluorophores are shown in Figure 6A: the targeting ligand, the isolating linker and the dual-purposed fluorophore with an effector and balancing domain. Successful implementation of this approach requires several specific engineering hurdles.

2.6.1 Targeting Ligand.

Perhaps the most crucial aspect for the success of a targeted site-specific probe is the choice and overall efficacy of the targeting ligand—the homing beacon to the tissue of choice. Through direct covalent conjugation to the effector domain, this ligand may target and bind surface molecules or overexpressed receptors on the cell surface. Figure 7 depicts a non-exhaustive list of successful ligands that have shown promise in the targeting of various cell types.

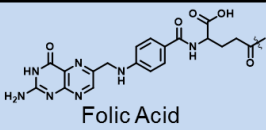
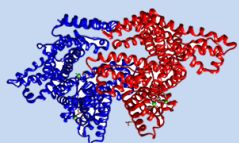
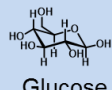
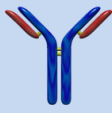
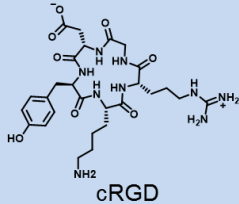
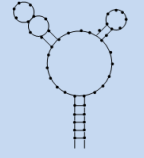
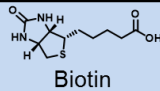
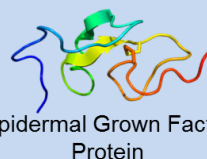
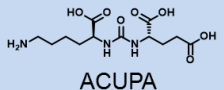
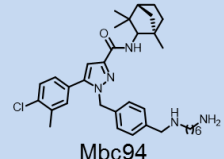
Small Molecules	Target	Macromolecules	Target
 Folic Acid	Overexpressed folate receptors on cancer cells	 Bovine Serum Albumin Protein	Main component in blood – angiography imaging for avoidance of blood vessels
 Glucose	Cancer's high rate of aerobic glycolysis. GLUT Transporter	 Trastuzumab Antibody	Over expressed HER2 receptor targeting common in breast cancers
 cRGD	$\alpha_v\beta_3$ surface integrin of cancer cells	 XQ-2c DNA Aptamer	Surface of pancreatic ductal adenocarcinoma (PDAC) cells
 Biotin	Tumor cells with biotin-selective transporters	 Epidermal Growth Factor Protein	Cancers that overexpress the epidermal growth factor receptor (EGFR) on the cell surface.
 ACUPA	Prostate specific membrane antigens		
 Mbc94	Type 2 cannabinoid receptor (CB2R) involved carcinogenesis		

Figure 2-7. Small molecules and macromolecules used for tethering to direct NIR fluorescent domains to particular targets for developing site-specific contrast agents.

2.6.2 Isolating Linker.

Upon first glance, the isolating linker's importance is immediately understated; however, the importance of optimizing the physicochemical, structural and dynamic properties cannot be underestimated. The isolating linker component of the entire contrast agent should

be sufficiently flexible to allow the targeting ligand and fluorophore to act independently but also satisfactorily rigid to keep these two domains physically separate in three dimensional conformational space. Furthermore, the isolating linker should be chemically inert to avoid unfavorable interactions with either domains but should be robust throughout the procedure. Most importantly, the isolating linker must impart either a positive or negligible effect on the physicochemical properties (i.e. overall pKa, net charge, logD, etc) which highly influence *in vivo* biodistribution. This concept is important in order to allow the targeting domain to remain the sole guiding force in the body. In balance with these design criteria, the isolating linker can also have a functional purpose as we will discuss later, wherein the linker may be enzymatically cleaved in tumor cells which can result in site-specific contrast through activatable fluorescence imaging, should the correct criteria be met.

2.6.3 Effector and Balancing Domain.

Satisfactory molecular brightness *in vivo* and clearance properties (pre-ligand attachment) are the major obstacles to perfecting characteristics for future implementation in the clinic (reviewed in [9]).

The optical profile, specifically regarding Stokes shift, extinction coefficient and quantum yield, is high dependent on the rigidity of the core fluorophore structure, specific modifications to the conjugated system and solvent-fluorophore effects (reviewed in [9]). Indeed these are design considerations that must be overcome in the pursuit of an efficient effector domain; however, when navigating this area, it is also necessary to structurally engineer a balancing domain that reduces the biological interactions that result in off target imaging.

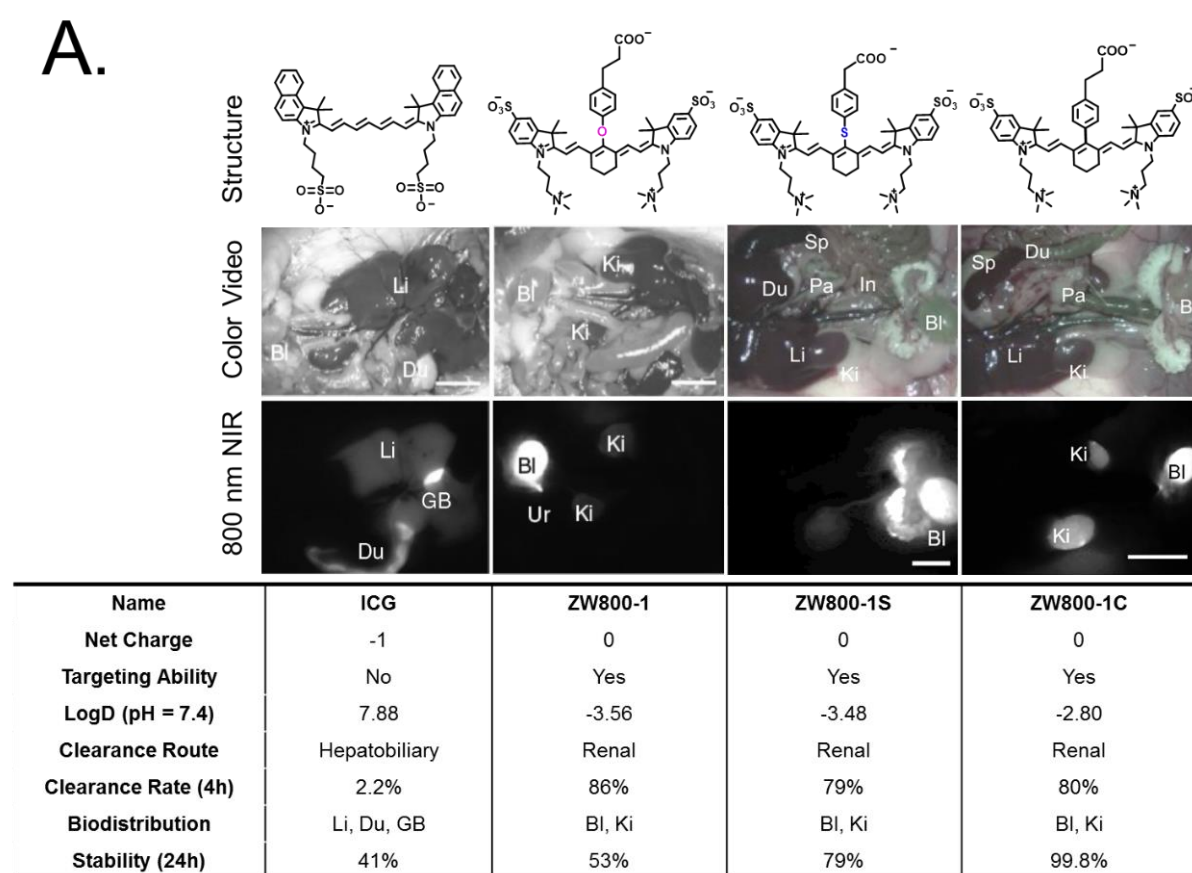
Their physicochemical properties (i.e. molecular weight, total polar surface area, hydrogen bond donors/acceptors, acidic/basic pKa, distribution/partition coefficient and stability) heavily influence their *in vivo* fate with slight structural modifications posing

significant biological perturbation. If correctly selected, these physicochemical descriptors may provide a shielding characteristic to the fluorophore allowing the targeting ligand to act independently of the optical contrast agent. In the most simplistic structural design, the targeting moieties and balancing domain must be well integrated into the overall molecular structure such that both properties are retained without jeopardizing site-selective targeting.

2.6.4 Recent Literature on Targeted Imaging.

Many of the fluorophores described to date have one or more detrimental fallbacks ranging from limited chemical/optical stability, insufficient fluorescence quantum yield in serum, or high background signal *in vivo* arising from non-specific binding to extracellular proteins. These chemical structures have been extensively modified for decades with only minor improvements to tissue affinity and background reduction. Choi *et al.*[143, 144] explored the importance of judiciously incorporating charge in the engineering of fluorophores for maximizing targeting efficacy by carefully incorporating zwitterionic character into a heptamethine cyanine chromophore which yielded the final fluorophore, **ZW800-1**, resulting in minimal fluorophore-serum protein interactions. This engineered characteristic imparts **ZW800-1** with the unique ability to allow any functional biological ligand to act independently thus effectively targeting the corresponding receptor. Building on this principle, Njiojob *et al.*[145] and Hyun *et al.*[146] developed analogous fluorophores bearing either a *meso*-thioether bond or central carbon-carbon bond respectively, with either an available carboxylate or primary amine for conjugation; these modifications have increased functionality and improved stability for long-term surgical measurements while exhibiting the unparalleled clearance properties arising from the zwitterionic surface charge. An immediate downfall of the commercial gold standard, indocyanine green (ICG), is the lack of a reactive handle for covalent modification with a targeting ligand, but ICG also demonstrates poor biodistribution and clearance properties with high background signal throughout the gastrointestinal tract. In

comparison, the **ZW800** analogs are rapidly cleared through renal filtration as shown in Figure 8. The benefits of rapid excretion cannot be understated. These data indicate that the zwitterionic balancing domain on the fluorophore is highly effective at preventing interactions with biological tissues and proteins. In theory, once this fluorophore is conjugated with a targeting ligand, the biodistribution would rely solely on the targeting ligand as the fluorophore has been engineered to exhibit minimal *in vivo* binding. In fact, when the commercial alternative, **Cy5.5**, and the **ZW800-1** analog are modified with cRGD, Choi *et al.* observed unparalleled tumor targeting with low non-specific background as seen in Figure 8B. [143]



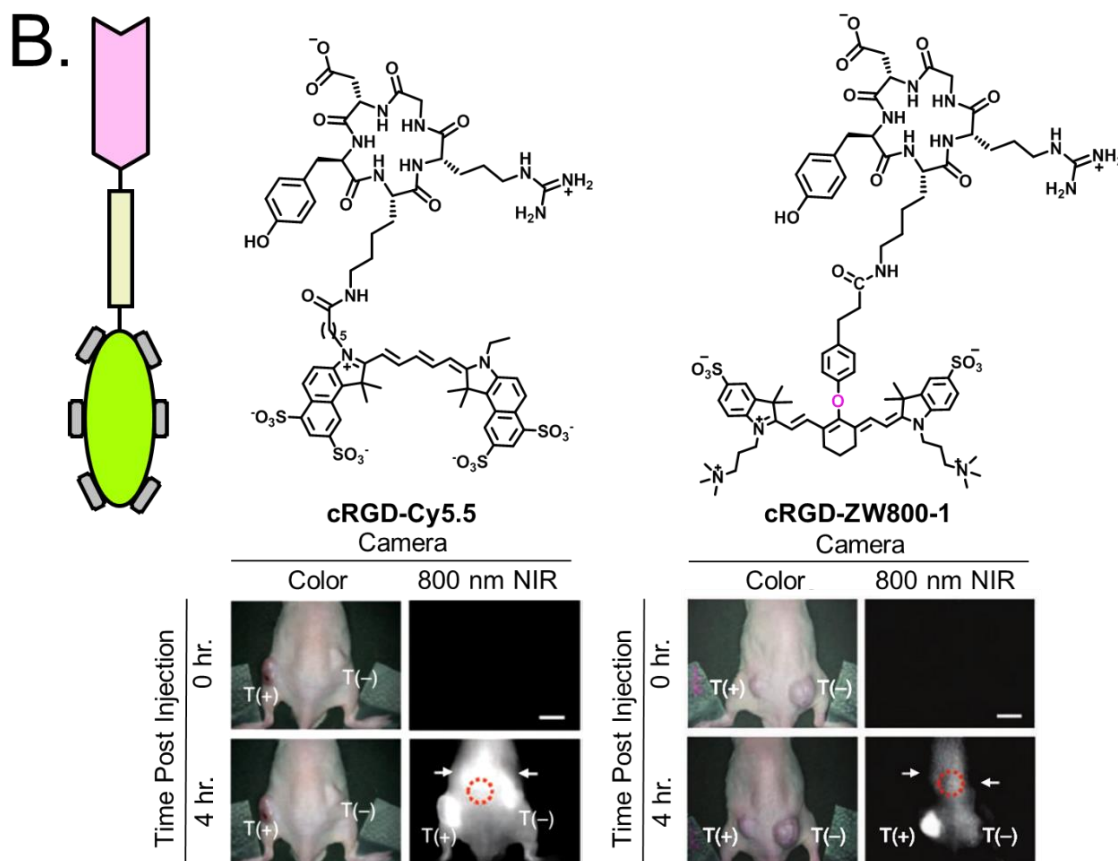


Figure 2-8. (A) The *in vivo* performance of ICG, and 3 ZW800 analogs with attributes tabulated showing the net charge, availability for covalent targeting modification, LogD (pH = 7.4), clearance route, clearance % after 4h., overall biodistribution (Li, Liver; Du, duodenum; GB, gallbladder; Bl, bladder; Ki, kidney), and optical stability in FBS after 24h. (B) The performance of ZW800-analog compared to Cy5.5 both modified with cRGD *in vivo*. Adapted with the permission of The Royal Society of Chemistry, the American Chemical Society and Nature Publishing Group.

These **ZW800** analogs have laid fundamental groundwork for the translation of NIR image guided surgery into the clinic. Building on these compounds, the Choi and Henry labs developed complementary analogs (i.e. **ZW700** compounds, Figure 9) for identical imaging at the lower wavelength channel. [147] The **ZW700-1** contrast agent was conjugated to bovine serum albumin which afforded effective imaging of the tumor angiography to identify major

blood vessels that should be avoided during cancer resection surgery. When this bioconjugate is paired with the **ZW800-cRGD**, surgeons are armed with a powerful and effective dual-channel imaging of both native and disease tissue in real-time without changing the look of the surgical field.

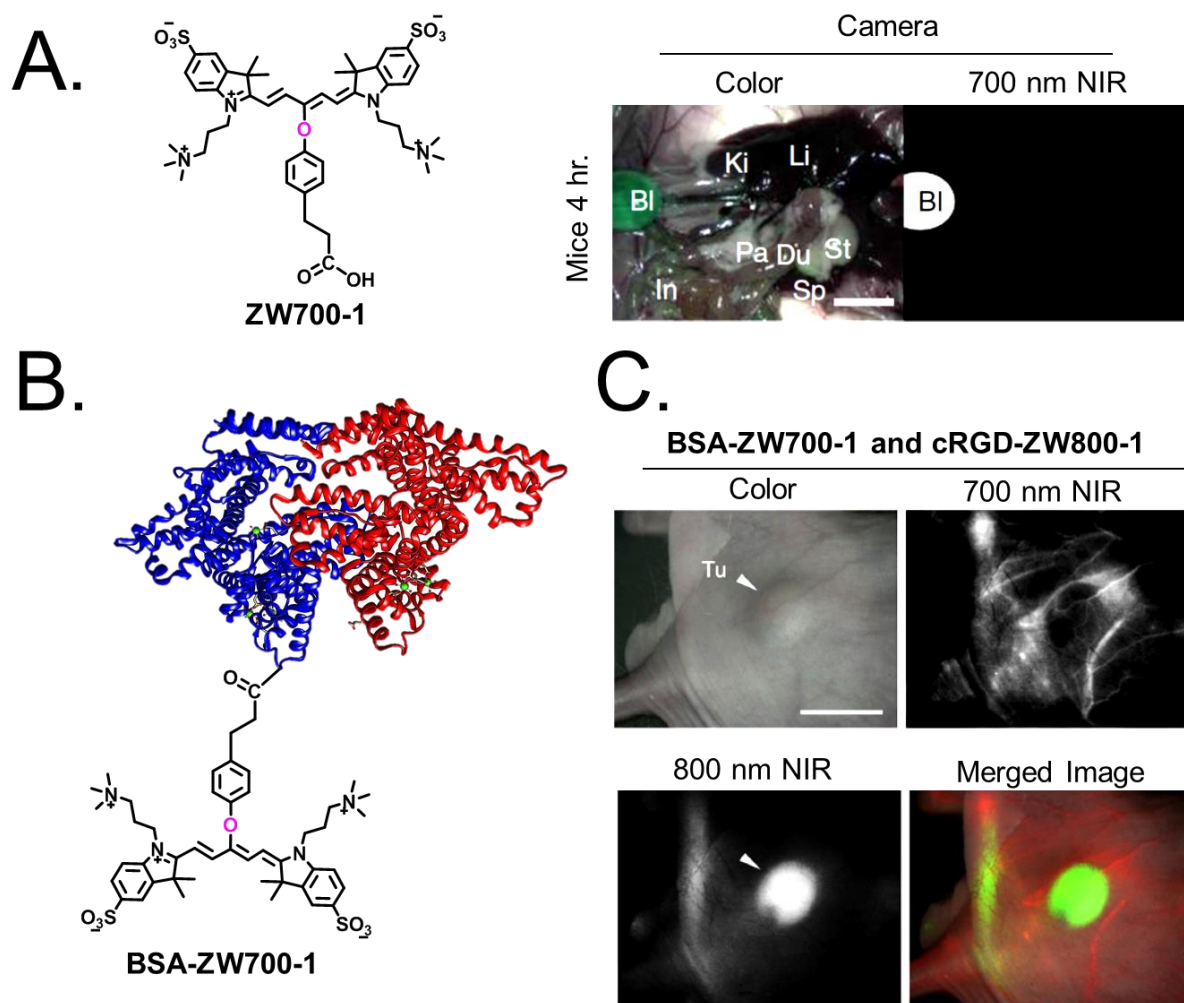


Figure 2-9. (A) The ZW700-1 structure that was prepared for the 700 nm channel of NIR imaging guided surgery alongside the biodistribution in mice showing rapid elimination after 4 hr. into the bladder (Bl), (B) The ZW700-1 conjugation to bovine serum albumin which allowed for angiographic imaging using 700 nm channel which was used alongside cRGD-ZW800-1 to target cancerous tumor in 800 nm channel and the merged imaging provides real time image guidance with all three cameras overlaid.

Similarly, the bioconjugated imaging agent relies heavily on the targeting moiety for site specificity and developing new targeting ligands is a critical barrier toward imaging native tissues in the body. Whitney *et al.* discovered new peptides that allow for the detection of nerves, NP41 (NTQTLAKAPEHT), that was conjugated to the pentamethine cyanine fluorophore Cy5. [148] The nerve imaging of this Cy5-NP41 targeted contrast agent is shown in Figure 10. In addition, the mice were genetically engineered to express yellow fluorescent protein in the axons of their nerves which is shown by the yellow fluorescence signal in Figure 10B. When a cross section of the nerves are examined, there is clear delineation of the axon and nerve shown in the composite image in Figure 10 panels E-G.

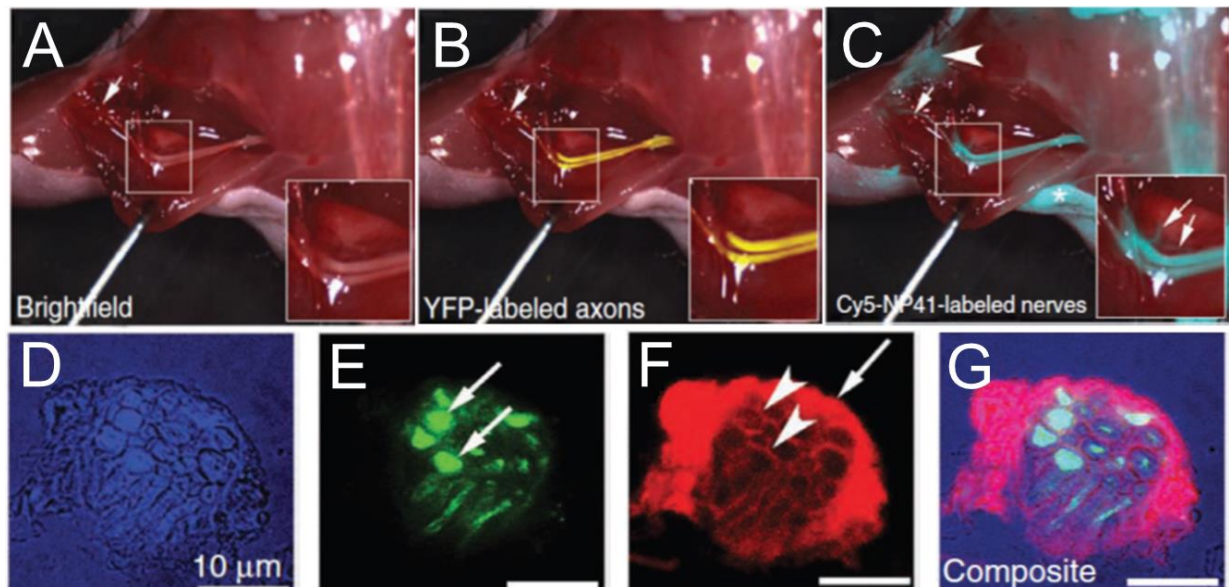


Figure 2-10. Cy5-NP41 imaging of the sciatic nerve in transgenic mice engineered to express yellow fluorescent protein with insets showing zoomed images in panels A-C. (A) Normal color camera view of the sciatic nerve. (B) Same nerve visualized by YFP fluorescence (pseudocolored yellow) superimposed on the visible video image (C) Cy5 fluorescence (pseudocolored cyan) superimposed on the brightfield image, showing nerve labeling with Cy5-NP41. The arrows in panels B and C indicate improved Cy5 imaging of thin and obstructed nerve branches. (D-G) Cross sectional areas corresponding to the nerve shown in panels A-C. (D) Cross-section of the sciatic nerve revealing myelin using differential interference contrast (DIC),

pseudocolored blue. (E) D Axoplasmic yellow fluorescent protein (YFP) pseudocolored green (arrows). (F) Cy5-NP41 labeling (pseudocolored red) of epineurium (arrows) and endoneurium (arrowheads). (G) Composite image of d, e and f showing that Cy5-NP41 labeling does not colocalize with either myelin or axoplasm. Figure was adapted with permission from Nature Publishing Group.

When fluorescent compounds are tethered to large biomolecules or even small molecules through an isolating linker it generates a large molecular complex that is retained in non-specific locations which reduces the clarity of imaging. While active targeting is an attractive and heavily researched field, there are also improvements that would come from reducing the size of the overall complex – this concept is embodied by structure inherent targeting.

2.7 Structure-inherent Targeting.

As previously discussed in Figure 4, the enhanced permeation and retention effect describes a contrast agents' ability to localize within one particular tissue versus another, usually based on the general biodistribution phenomenon. Recently, it has been postulated that the parent structures of various classes of fluorescent small molecules that have innate biodistribution pathways may be manipulated through the addition or removal of certain isolated functional groups to achieve site-selective imaging. [149-153] Taking advantage of the modification potential of several fluorophore classes, several reports now suggest that specific modifications may improve site-specificity. These modifiable chemical structures have been exploited to optimize the chemical structure and direct localization/imaging to diseased tissue or native organs. A structure inherent approach would help overcome the obstacles of targeting ligand-based contrast agent to native tissues and sensitive glands which remains a longstanding clinical problem in contrast agent development. Hyun *et al.*[152] and

Owens *et al.*[150] were two of the first suggestions in the literature that the molecular character may be modified and finely tuned to achieve selective uptake with high SBR in particular tissues using a structure-inherent approach which exploits chemical recognition to biological tissue for targeting and biodistribution. Selective modifications can direct the pharmacophore to distinct regions utilizing the structure-inherent chemical recognition to the targeted tissue. We observed that tuning the hydrophobicity of NIR fluorescent compounds allows for high uptake in the endocrine system.[150] Figure 11 shows **ESNF-10** that localizes in the thyroid gland, adrenal gland and ovaries in female mice with the same compound exhibiting high localization in identical tissues in swine—thyroid gland shown as an example in Figure 11.

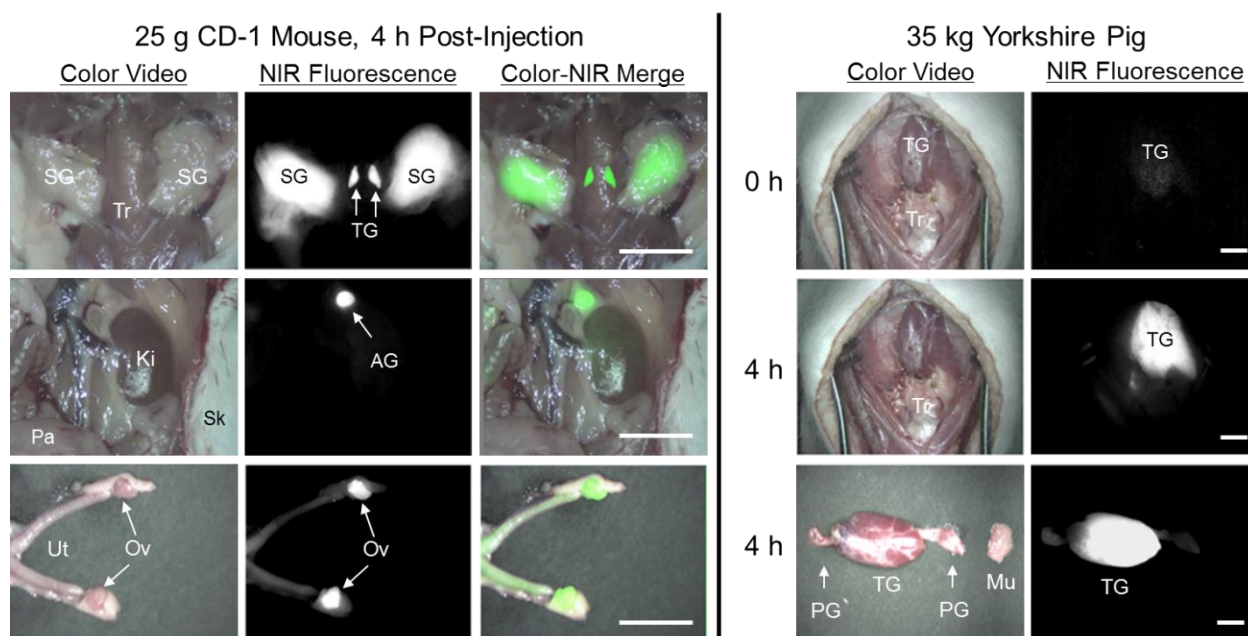


Figure 2-11. The targeting ability of a pentamethine cyanine fluorophore showing site specific uptake through passive targeting. The biodistribution offers high SBR with excellent imaging of the thyroid gland (TG) in CD-1 mice and swine and the adrenal gland (AG) and ovaries (Ov) in CD-1 mice.

Similar results have been achieved through tuning the physicochemical properties and rationally incorporating recognition elements into the compounds. Cartilage and bone imaging plays a crucial role toward more fully understanding the disease progression within these

particular tissues. Hyun *et al.* rationalized that the negatively charged sulfonate and carboxylate groups present in cartilage would be an effective characteristic to exploit for cartilage-selective imaging (Figure 12A). Selecting quaternary ammonium moieties for chondrocyte targeting in cartilage afforded a core pharmacophore that highlighted all types of cartilage very nicely without discriminating between the specific types of cartilage.[154] Figure 12B shows the 700 nm channel which highlights the cartilage imaging contrast agent seen in red in the merged image. Similarly, phosphonate groups in the non-resonant side chain of the contrast agent serves as the structure-inherent homing beacon to bone.[151, 153] The phosphonate structures interacts favorably with the hydroxyapatite in bone tissue – likely through calcium binding – and very clear imaging can be obtained for long durations as the contrast agent becomes incorporated within the bone matrix. These two contrast agents epitomize the desired success in dual-channel NIR imaging, and these two site-specific fluorophores have great potential in the monitoring of cartilage tissue engineering and therapeutics and also in the study of osteoblast formation and maturation in bone.

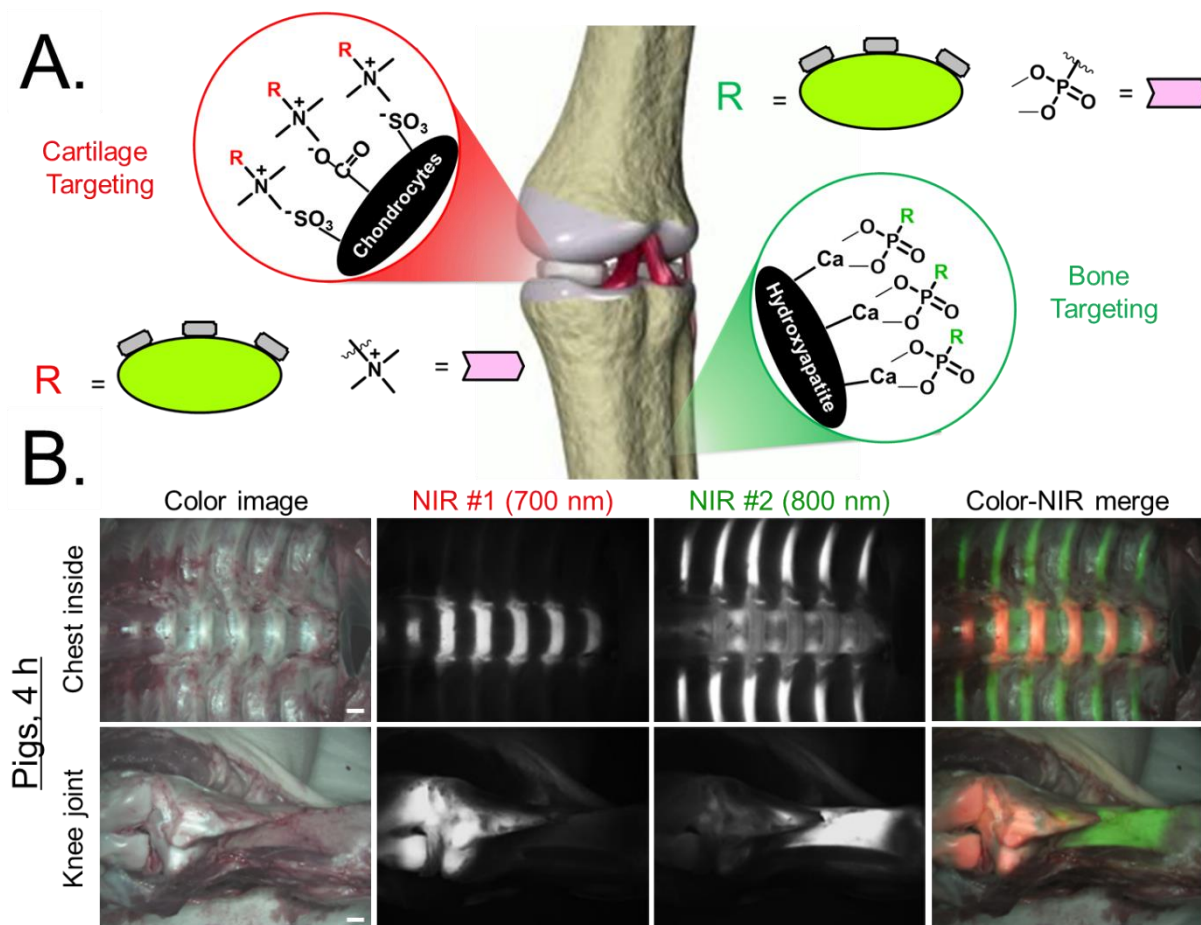


Figure 2-12. Physiological targets, molecular character, representative molecule and corresponding *in vivo* NIR images of subnano imaging agents that are tailored for imaging of cartilage and bone in pigs 4h post injection. Figure adapted with permission from Wiley Publishing.

Other native structures must be imaged during surgical resection, especially in the removal of pancreatic tumors where healthy tissue should not be jeopardized. Also, pancreas-related surgeries including peripancreatic lymph node resection, adrenalectomy, and nephrectomy currently show an intolerable level of risk. Towards alleviating this risk and affording surgeons real time imagery of the pancreas and surrounding tissue, Owens *et al.* and Wada *et al.* reported pentamethine fluorophores that target the pancreatic tissue with high SBR. Small and compact fluorophores with low hydrophobic character were found to be most

effective in the target-ability of pancreatic tissue. Figure 13 shows the chemical structure of 700 nm pancreatic targeting contrast agent used in two pancreatic surgeries, one surgery where the adrenal gland is targeted in the 800 nm channel using the hydrophobic heptamethine fluorophore and the other surgery imaging angiography using **ZW800-1**.

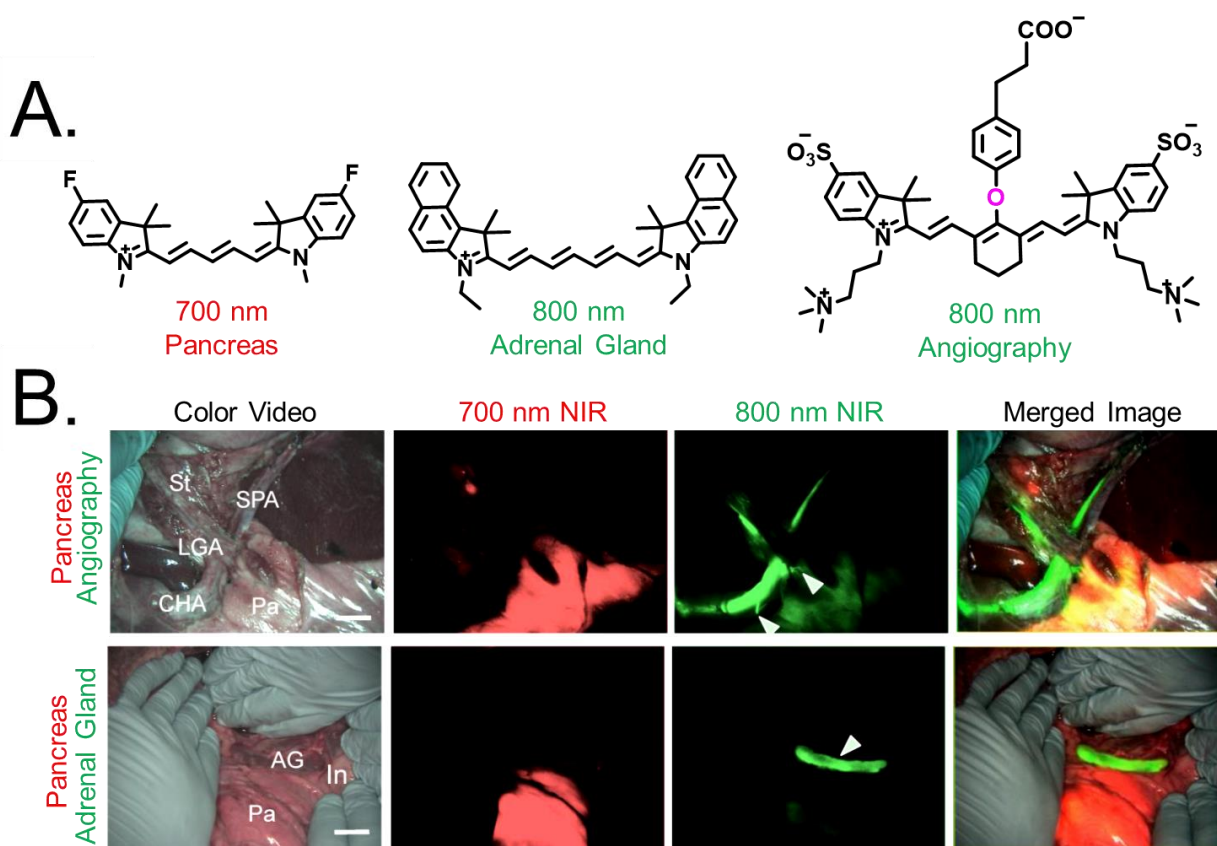


Figure 2-13. Chemical structure of pancreas targeting and imaging of nearby structures with corresponding *in vivo* NIR images of subnano imaging agents that are tailored for imaging of specific tissues. Figure reproduced and adapted with permission from Theranostics and Ivyspring Publishing.

Similarly, NIR fluorophores were developed that target the thyroid and parathyroid gland in identical surgical space using two fluorinated cyanine chromophores. It was found that the pentamethine compound (700 nm fluorescence) localized effectively in the thyroid gland and the heptamethine cyanine (800 nm fluorescence) became flushed from the thyroid to

the parathyroid gland (Figure 14). Dual channel imaging of these glands afforded a very clear delineation of these two glands for biopsy or surgical excision.

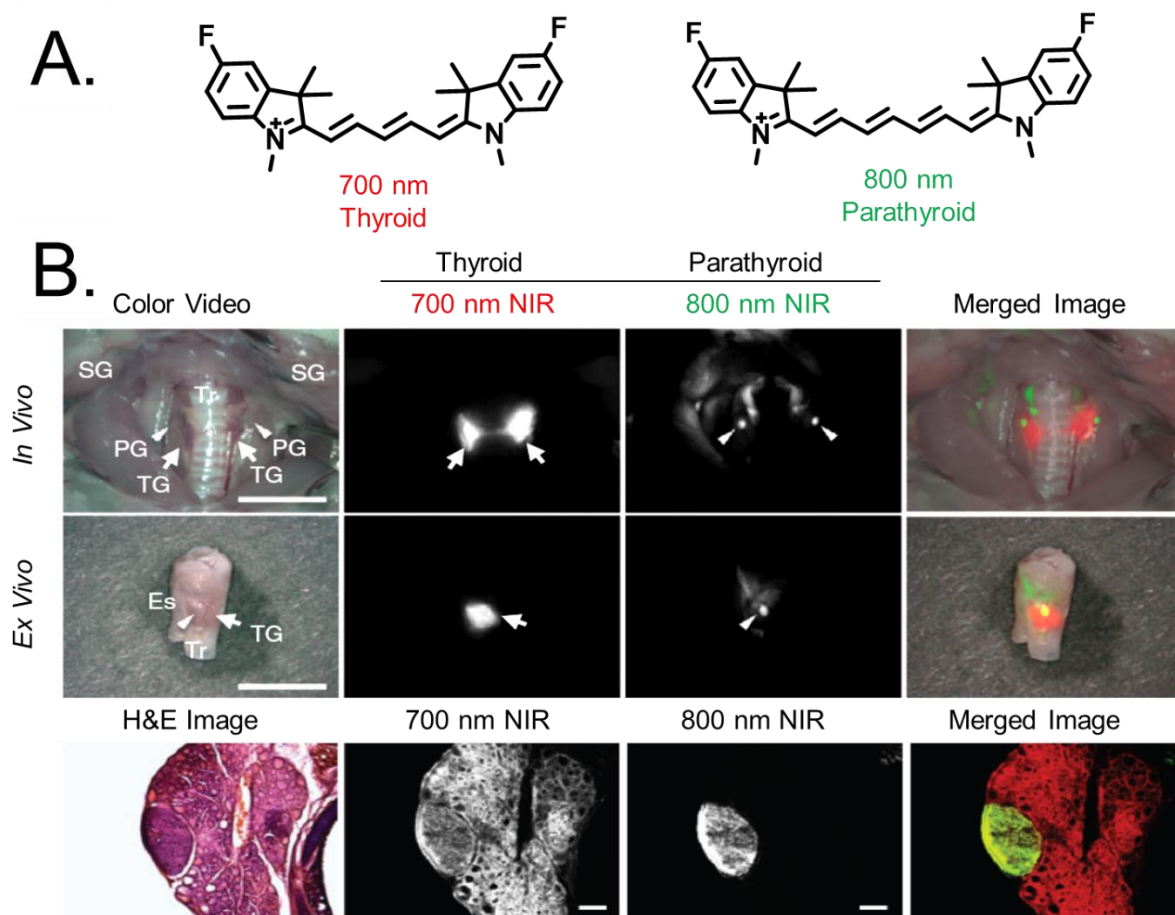


Figure 2-14. Molecular structure of NIR fluorescent imaging agents and corresponding *in vivo* NIR images for the subnano imaging agents that are tailored for imaging of thyroid and parathyroid in the same surgical space. Figure reproduced and adapted with permission from Nature Publishing Group.

Despite all of the small molecule derivatives that have been synthesized and tested throughout the literature, there are only scarce reports of nerve targeted contrast agents. A screening of phenoxazine based fluorophores has been reported by Park *et al.* that shows exciting nerve targeting properties for identification and avoidance. Shown in Figure 15, this

fluorophore successfully labels the brachial and sciatic nerve in mice with even small peripheral nerve endings being well visualized toward improving post operation patient prognosis. Amazingly, only minor perturbations in the chemical structure removed the nerve targeting ability of the fluorophore.

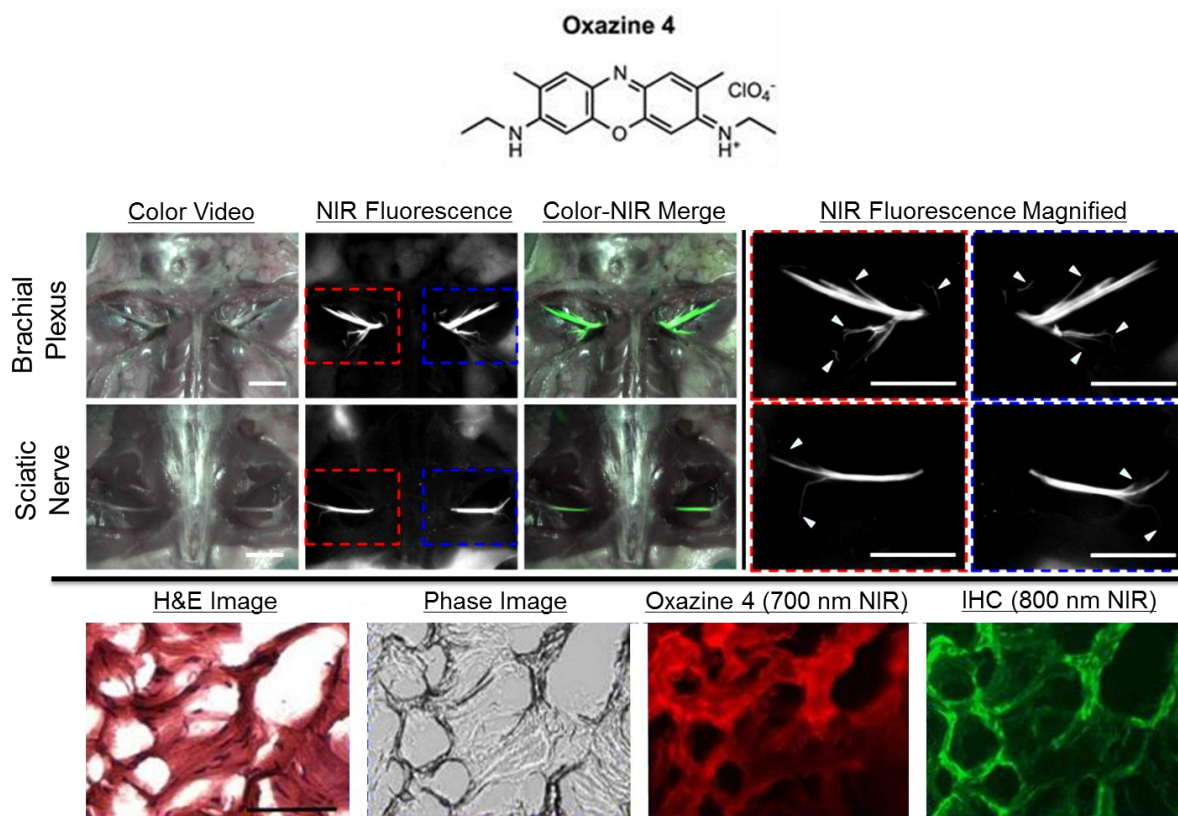


Figure 2-15. Oxazine 4 as an exemplary nerve targeting agent with corresponding *in vivo* NIR images for both the brachial and sciatic nerves. Below the immunohistochemistry confirms the nerve targeting of Oxazine 4. Figure reproduced and adapted from Theranostics and Ivyspring Publishers.

2.8 Activatable NIR Imaging Agents.

The development of successful paradigm shifting activatable NIR imaging probes has been slow compared to alternate approaches. This owes strongly to the complexity in design and increased requirements required for engineering these highly intelligent molecules. In this high-risk, high-reward situation, a successful imaging agent could dominate the optical imaging space; however, the site specificity of healthy tissues remains an unsolved

shortcoming of this approach though tumor targeting is well established. These well-established methods for targeting tumors exploit unique attributes of cancer cells, for example, the Urano and Kobayashi labs described pH activatable NIR fluorophores that are covalently linked to monoclonal antibody trastuzumab which binds to human epidermal growth factor receptor type 2 (HER2). After binding, the probe-antibody complex is internalized within cancer cells through a lysosomal degradation pathway (Figure 16A). This acidic environment causes protonation of the tertiary amine installed on the fluorophore core resulting in increased fluorescence compared to the non-protonated counterpart. Figure 16B shows the fluorescence images of pH activatable contrast agent and the always on version as a function of pH. Using these probes, we can see cellular turn-on of fluorescence in panel C in Figure 16 when the diethylamine is present; however, the always on probe retains fluorescence signal over time. The *in vivo* images (Figure 16D) show excellent tumor targeting but the always on probe shows high background in the tissue surrounding the tumors, but the activatable probe lowers the background signal which allows high SBR and a clear depiction of diseased tissue for surgical removal.

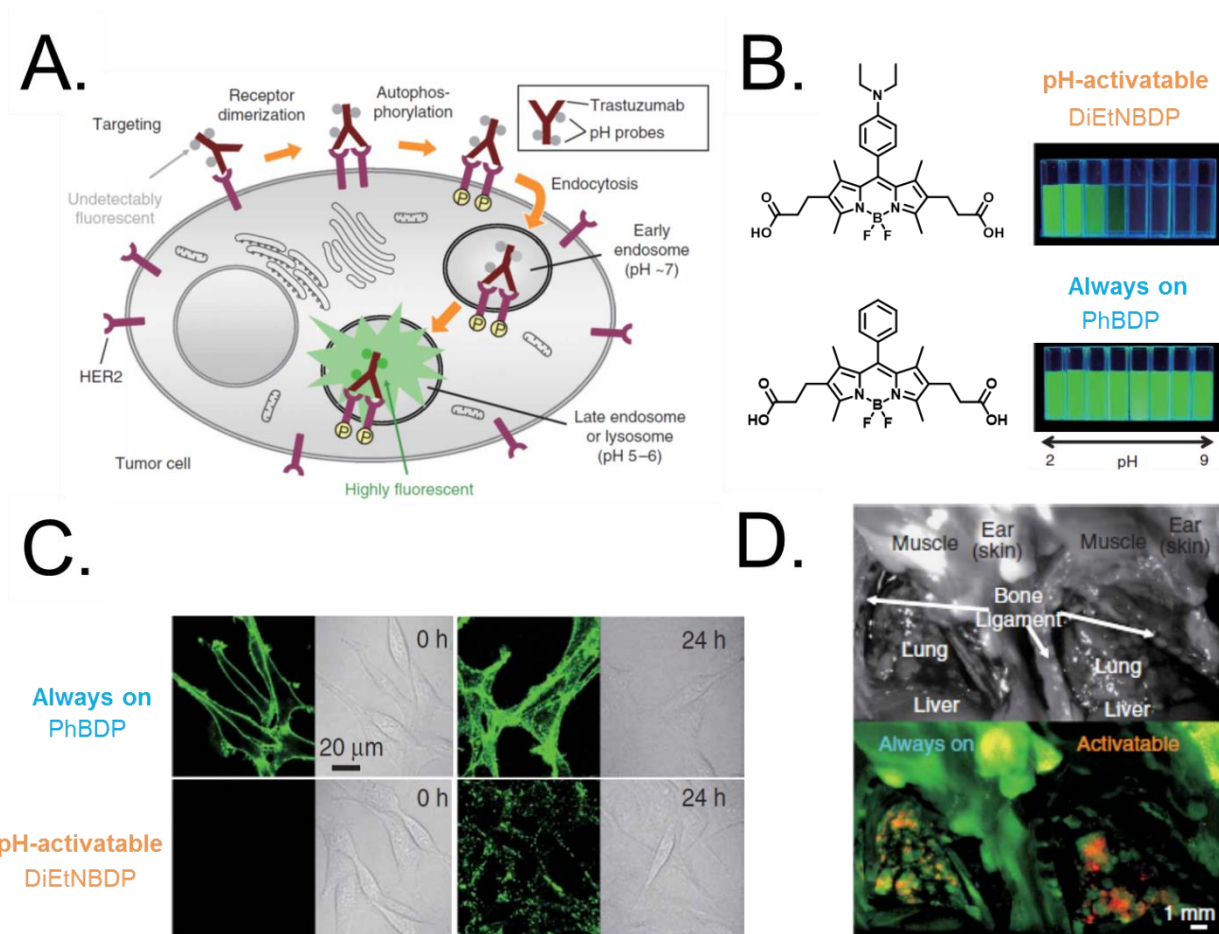


Figure 2-16. pH activatable BODIPY NIR imaging probes. (A) General strategy for targeting pH probes to tumor cells and activating fluorescence with a pH response, (B) two (of four, not shown) analogs of pH activatable and always on (control) compounds and their pH-fluorescence profile, (C) cellular imaging at time 0 h and time 24 h showing always on fluorescence and cell endocytosis mediated fluorescence activation (see A), and (D) *in vivo* imaging showing effective targeting of tumors in both always on and activatable contrast agents—SBR is much higher when using the activatable probe. Figure reproduced and adapted with permission of Nature Publishing Group.

The use of pH activation is a well described concept with this report embodying an excellent implementation of this approach. Despite this success, we require an arsenal of contrast agents for universal implementation of NIR imaging technology. Toward this goal, alternate designs have been explored that activate when reaching tumor sites. Increasing

evidence shows that folate receptors are overexpressed on the surface of many cancer cells and targeting these receptors through covalently tethering a folic acid moiety to a effector domain has been a longstanding concept.[155-172] Using this folic acid dually as a quenching moiety and homing beacon, Lee *et al.* [173] explored the targeting of ovarian cancer using an activatable probe that remains quenched through intramolecular charge transfer between the effector domain, dye ATTO655, and folic acid (shown in Figure 17A [173]). The isolating linker in this case is uniquely constructed to cleave in the presence of cathepsin B. After the folic acid domain recognizes the cellular target and the probe enters the cell, the linker is recognized and cleaved by lysosomal cathepsin B resulting in enhanced fluorescence. Cellular data that shows fluorescence “turn-on” in the presence of tumor cells and no fluorescence when a folate receptor inhibitor is added confirms the suspected mechanism of action. This enhanced fluorescence results in high signal to background imaging of tumors with small signal in the liver. The peptide and folic acid incorporation is critical in the targeting ability of this contrast agent as the dye alone is excreted rapidly from the body and does not preferentially accumulate in any particular organ or tissue based on the NIR images.

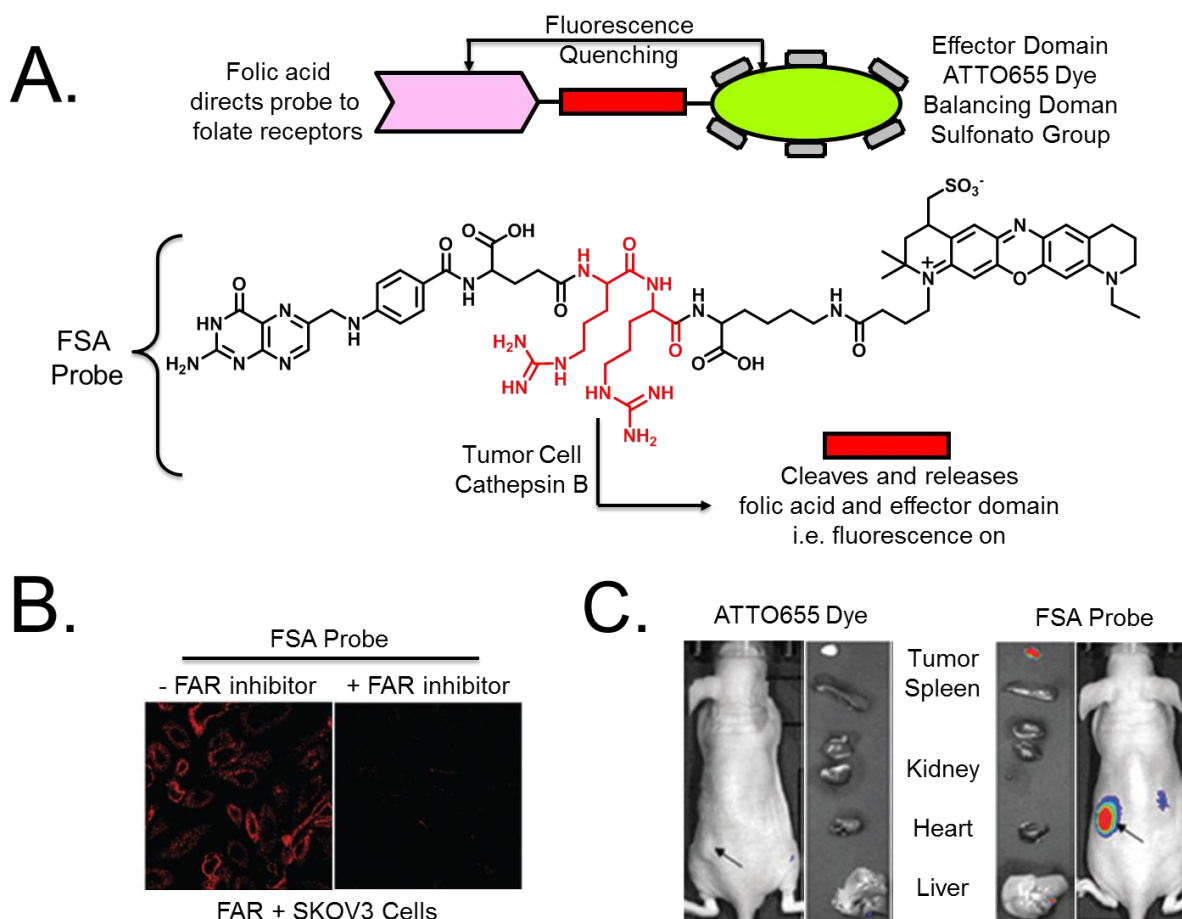


Figure 2-17. Folate receptor-specific activatable (FSA) probe. (A) The design and structure of the final probes using in (B) cellular experiments in SKOV3 cells expressing the folic acid receptor without a folic acid receptor inhibitor present and with a folate acid receptor inhibitor present and (C) *in vivo* data showing rapid clearance of the free dye after 30 minutes and high SBR imaging of the tumor tissue when using the FSA probe. Figure reproduced and adapted with permission of the Royal Society of Chemistry.

The peptide-cleavage activation of NIR imaging is indeed a long standing concept; however, an elegant approach was reported by Nguyen *et al.*[174] and Savariar *et al.* [175] which describes the use of (ACPPs) [174, 176-179] and ratiometric activatable cell penetrating peptides (RACPPs) [180], respectively. A general depiction of these strategies are shown in Figure 18 with the peptides in the developed contrast agent being ion paired to facilitate clearance and limit non-specific binding. When the cleavable peptide (shown in green) is

cleaved in the tumor environment, the cationic portion is retained within the tumor cell. The difference in these two – ACPs and RACPs – lies on the negatively charged peptide. The ACP diagram contains no additional domain on the negatively charged peptide (red) and is activatable in that tumor cells activate the peptide-portion and the signal is retained in the tumor tissue. However, the RACP goes another step further and incorporates another fluorophore of longer wavelength (Cy7) that allows highly specific imaging of tumor tissue. Specifically, energy transfer arising from the fluorescence of a lower wavelength fluorophore to a quenching moiety (molecule that absorbs the fluorescence energy) is a well-established method for designing an activatable probe that selectively images tissues that facilitate the spatial separation of these two molecules. The key concept is maintaining close proximity before cleavage to allow the energy transfer to occur. The ion-paired peptides help facilitate the orientation of these two fluorophores in the same space which allows the energy transfer from Cy5 to Cy7 (Cy5 quenching) to be efficient. If these two fluorophores were not close to each other, this phenomenon would not be observed making this a very unique and effective strategy for high signal to background imaging. Once the scissile peptide breaks, the two fluorophores are then allowed to separate through systemic circulation resulting in increased Cy5 fluorescence being retained in the tumor with diffusion of the Cy7-peptide segment resulting in diminishing Cy7 fluorescence.

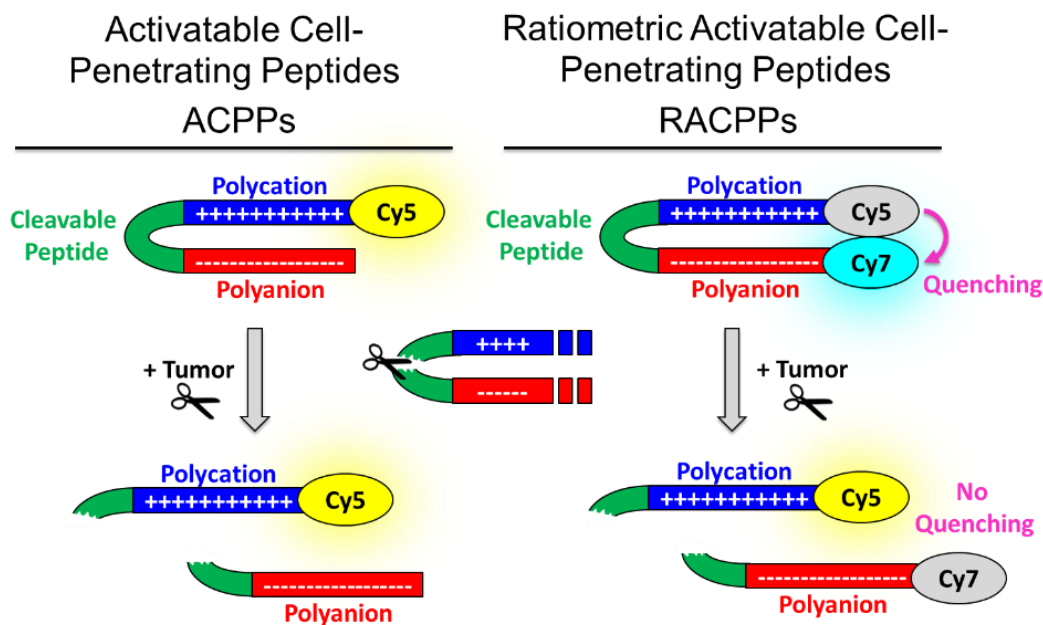


Figure 2-18. (left) Activatable cell penetrating peptides (ACPPs) that harness ion paired peptides and a cleavable segment for sites-specific imaging (right) further modification of ACPPs that incorporates a second fluorophore Cy7 for ratiometric activation (RACPP).

Figure 19A shows the timeline of tumor targeting for ACPPs that have been injected in to an organism containing tumor tissue. After 6 hours, the polycationic-Cy5 ligand is retained with high fluorescence while a large amount of uncleaved contrast agent is cleared by the body. This leads to good contrast in the delineation of tumor tissue on the surgical field. After 24 hours, however, the polycationic ligand begins to be excreted from the tumor cell resulting in equal signal in the tumor tissue and surroundings which reduces the SBR and makes imaging difficult. Choosing the correct imaging timepoint is therefore highly significant. Once all the procedures are optimized, it is possible to achieve proficient use of this technology resulting in the cancer surgery in Figure 19B where small remnants of tumor tissue was found using the ACPP NIR imaging method.

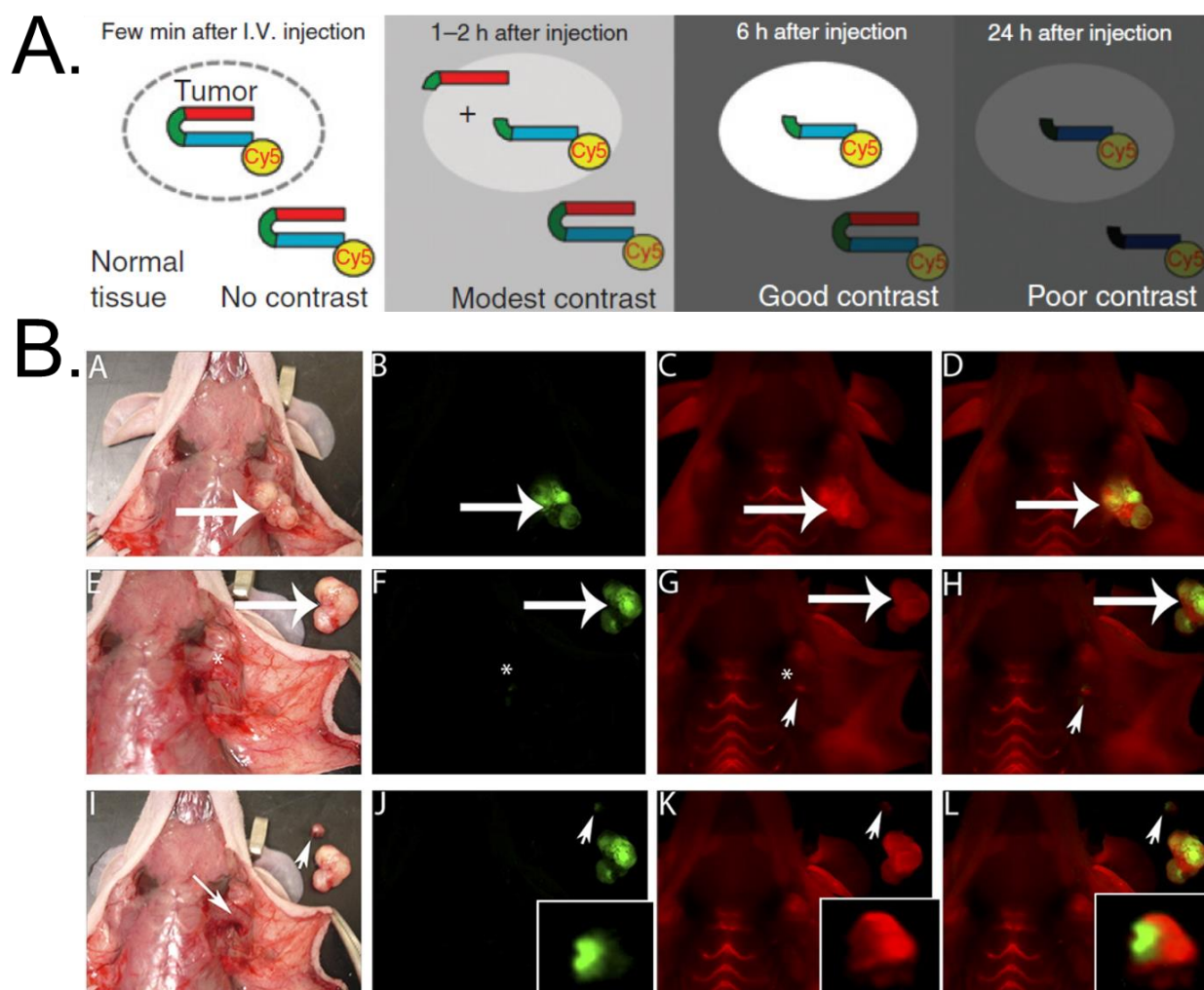


Figure 2-19. (A) Overall schematic for suitable imaging time points for ACPP contrast agent, (B) the improved surgical resection with several small tumors being located by the ACPP contrast agent that would have been missed using current techniques (i.e. eyesight, feel, etc.). Figure reproduced and adapted with permission of Nature Publishing Group.

Building on the activatable cell penetrating peptide scaffold, a second fluorophore was incorporated on the anionic peptide, creating a ratiometric activatable cell penetrating peptide. Figure 20A shows the fluorescence of the contrast agent before (black solid line) and after (red dashed line) peptide cleavage. In essence, before cleavage energy transfer occurs from Cy5 to Cy7 resulting in the 780 nm fluorescence. After peptide cleavage, the 670 nm fluorescence increases and the 780 nm fluorescence decreases due to an increase in distance. This approach allows for high contrast imaging according to the mechanistic schematic in Figure 20B.

Immediately post-injection the contrast agent will be in equal concentration in tumor and normal tissues which offers no ability to distinguish the tumor margins. After allowing more time for the peptide cleavage and clearance of unbound fluorophore, the Cy5-polycationic peptide fragment will be selectively retained in the cancer tissue. This offers high signal to background imaging as seen in Figure 20C without dependence on the specific cancer cell type as both pancreatic and fibrosarcoma are imaged with clear identification, especially in comparison to a control contrast agent that features an uncleavable peptide *in lieu* of the cleavable peptide resulting in a fluorophore that only displays Cy7 fluorescence. This ion-paired control compound is effectively cleared from the body as indicated by the low signal indicated by the green color in Figure 20C. The next logical technique would be to make cleavable peptides that respond to specific cancers. Indeed, they prepared two contrast agents that respond to different enzymatic reactions that are dependent and unique to the tumor. Specifically, RACPP1 (MMP2,9-selective) or RACPP3 (elastase-sensitive) contrast agents were used to image PyMT 8119 GFP-positive metastases in mice liver. After 2h, the livers were removed and the fluorescence values for GFP, Cy5, Cy7 and a ratio of Cy5/Cy7 were evaluated which indicated a higher and more accurate response for RACPP3 to identify tumor sites using high fluorescence ratios between Cy5 and Cy7.

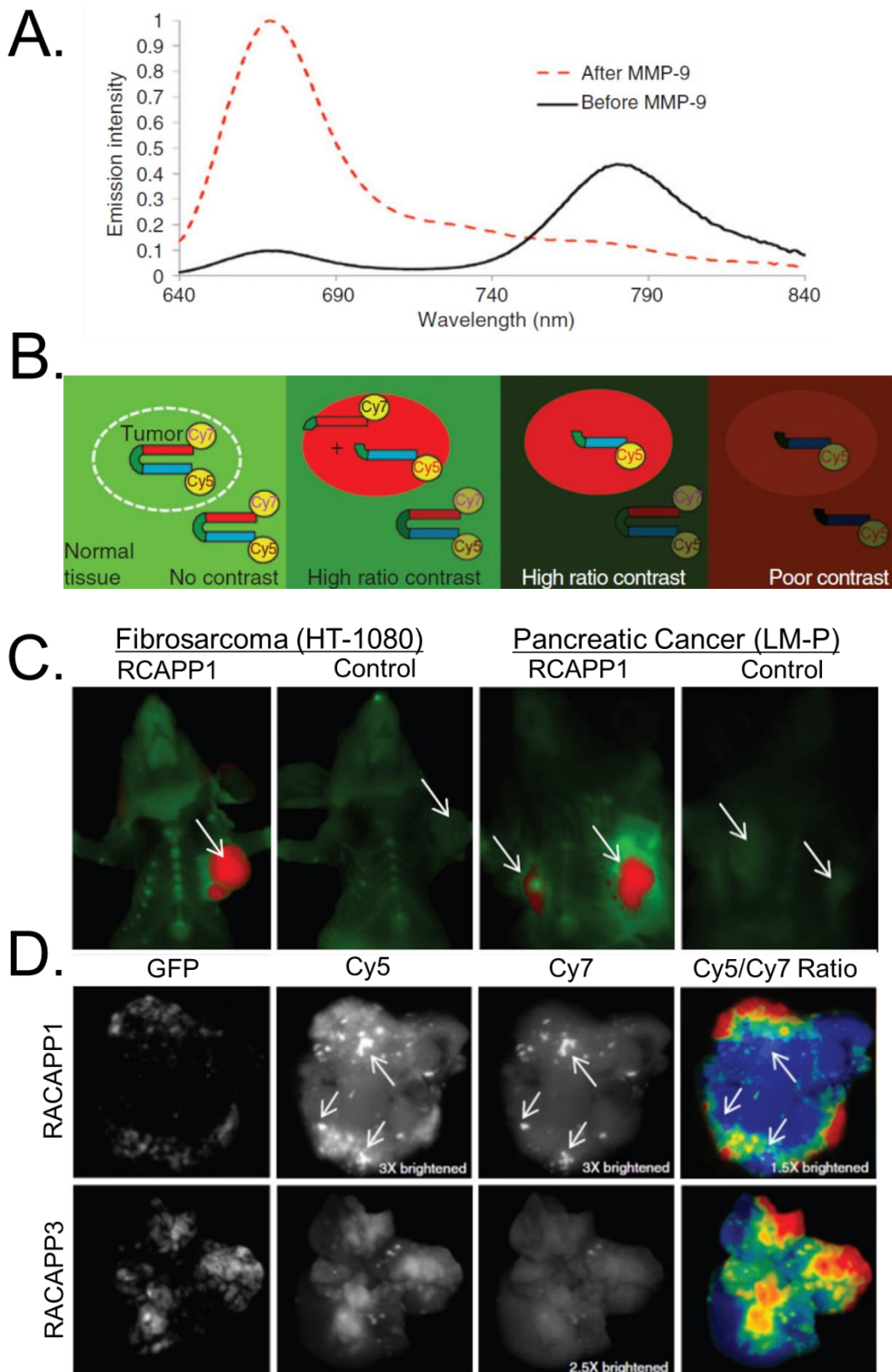


Figure 2-20. The characteristics and imaging capabilities for RACPP. (A) the emission spectra of uncleaved and cleaved RACPP1 (630 nm excitation in mouse plasma) before (black solid curve) and after (red dashed curve) peptide cleavage with MMP-9. The starting spectrum

shows considerable quenching of the Cy5 peak at 670 nm which results in emission from Cy7 at 780 nm, whereas the final spectrum is almost purely that of Cy5, (B) general schematic showing the imaging timeline for RACPP, (C) Cy5 intensity images (ex 620 nm, em 670 nm) 2 hours after intravenous injection of RACPP1 or an uncleavable control into mice bearing either HT-1080 xenografts or subcutaneous LM-P syngeneic grafts after skin removal. Images are pseudocolored where pixels with only Cy5 emission are pseudocolored red (indicating cleavage of RACPP), whereas pixels with both Cy5 and Cy7 emission peaks are pseudocolored green indicating no cleavage, (D) RACPP1 (MMP2,9-selective) or RACPP3 (elastase-sensitive) contrast agents were administered via intravenous injection and the livers (PyMT 8119 GFP-positive metastases) were removed after 2 hours. The following images were obtained: GFP fluorescence images, Cy5 fluorescence images obtained by exciting Cy5 at 620 nm, Cy7 emission images obtained by exciting Cy5 and Cy5/Cy7 emission ratio images. Red indicates high Cy5/Cy7 fluorescence ratios and blue indicates low ratios. Arrows show regions that do not contain tumors which is indicated by low ratios of Cy5 to Cy7 fluorescence values. Figure reproduced and adapted with permission of Nature Publishing Group.

2.9 Summary and Outlook.

The technological advancements in this field of subnano near-infrared fluorophores in imaging has exploded resulting in tremendous potential to shift clinical paradigms. With the sustained efficacious progress, as we have seen over the past five years, more in-human clinical trials will be seen and NIR imaging systems will become a more common technology in operating rooms. These advancements are, in turn, expected to solidify NIR fluorescence imaging technology and allow for the expanse into many surgical procedures.

2.10 Future Directions.

The influx of new site-specific NIR fluorescent contrast agents has great potential to revolutionize image guided surgery, but the NIR fluorescence imaging modality is limited to only intraoperative environments due to the signal loss through tissue. A single molecule that

allows for both whole-body imaging (i.e. PET/SPECT, MRI, etc.) paired with a disease-specific fluorescent domain would allow one chemical entity to be used during an entire surgical operation from identification to resection. Also, the ability to provide a structure-inherent imaging approach for site-selectivity opens the doors to new possibilities of therapeutic imaging agents in the quest for new theranostic agents using a single chemical entity thus obviating the need for separate therapeutic and imaging domains.

2.11 Conclusions.

With these recent advancements, the imaging community is appreciating NIR fluorescence as a unique alternative to current imaging techniques. Whole body pre-operative SPECT and PET imaging retains an important diagnostic utility, but they lack the efficacy of innocuous, targeted, subnano NIR fluorophores to simultaneously facilitate the real-time delineation of native and diseased tissue. The library of site-specific fluorophores available in the literature offers clinicians an array of possibilities that will undoubtedly improve intraoperative success and long-term post-operation prognosis.

2.12 References.

- [1] D.E. Cohn, N.C. Hall, S.P. Povoski, L.G. Seamon, W.B. Farrar, E.W. Martin, Jr., *Gynecologic oncology*, 110 (2008) 152-157.
- [2] I. Sarikaya, S.P. Povoski, O.H. Al-Saif, E. Kocak, M. Bloomston, S. Marsh, Z. Cao, D.A. Murrey, J. Zhang, N.C. Hall, M.V. Knopp, E.W. Martin, Jr., *World journal of surgical oncology*, 5 (2007) 80.
- [3] R.A. Olmos, S. Vidal-Sicart, O.E. Nieweg, *European journal of nuclear medicine and molecular imaging*, 36 (2009) 1-5.

[4] L. Vermeeren, W. Meinhardt, A. Bex, H.G. van der Poel, W.V. Vogel, C.A. Hoefnagel, S. Horenblas, R.A. Valdes Olmos, *Journal of nuclear medicine : official publication, Society of Nuclear Medicine*, 51 (2010) 376-382.

[5] Q.R. Tummers, C.E. Hoogstins, A.A. Peters, C.D. de Kroon, J.B. Trimbos, C.J. van de Velde, J.V. Frangioni, A.L. Vahrmeijer, K.N. Gaarenstroom, *PloS one*, 10 (2015) e0129766.

[6] Q.R. Tummers, A. Schepers, J.F. Hamming, J. Kievit, J.V. Frangioni, C.J. van de Velde, A.L. Vahrmeijer, *Surgery*, (2015).

[7] Q.R. Tummers, F.P. Verbeek, B.E. Schaafsma, M.C. Boonstra, J.R. van der Vorst, G.J. Liefers, C.J. van de Velde, J.V. Frangioni, A.L. Vahrmeijer, *European journal of surgical oncology : the journal of the European Society of Surgical Oncology and the British Association of Surgical Oncology*, 40 (2014) 850-858.

[8] S.L. Troyan, V. Kianzad, S.L. Gibbs-Strauss, S. Gioux, A. Matsui, R. Oketokoun, L. Ngo, A. Khamene, F. Azar, J.V. Frangioni, *Annals of surgical oncology*, 16 (2009) 2943-2952.

[9] E.A. Owens, S. Lee, J. Choi, M. Henary, H.S. Choi, *Wiley interdisciplinary reviews. Nanomedicine and nanobiotechnology*, (2015).

[10] V. Humblet, R. Lapidus, L.R. Williams, T. Tsukamoto, C. Rojas, P. Majer, B. Hin, S. Ohnishi, A.M. De Grand, A. Zaheer, J.T. Renze, A. Nakayama, B.S. Slusher, J.V. Frangioni, *Molecular imaging*, 4 (2005) 448-462.

[11] C.P. Parungo, S. Ohnishi, S.W. Kim, S. Kim, R.G. Laurence, E.G. Soltesz, F.Y. Chen, Y.L. Colson, L.H. Cohn, M.G. Bawendi, J.V. Frangioni, *The Journal of thoracic and cardiovascular surgery*, 129 (2005) 844-850.

[12] A.M. De Grand, J.V. Frangioni, *Technology in cancer research & treatment*, 2 (2003) 553-562.

[13] J.V. Frangioni, *Current opinion in chemical biology*, 7 (2003) 626-634.

- [14] A. Nakayama, F. del Monte, R.J. Hajjar, J.V. Frangioni, *Molecular imaging*, 1 (2002) 365-377.
- [15] A. Nakayama, A.C. Bianco, C.Y. Zhang, B.B. Lowell, J.V. Frangioni, *Molecular imaging*, 2 (2003) 37-49.
- [16] A. Zaheer, T.E. Wheat, J.V. Frangioni, *Molecular imaging*, 1 (2002) 354-364.
- [17] X. Zhang, S. Bloch, W. Akers, S. Achilefu, *Current protocols in cytometry / editorial board, J. Paul Robinson, managing editor ... [et al.]*, Chapter 12 (2012) Unit12 27.
- [18] M. Zhou, X. Zhang, M. Bai, D. Shen, B. Xu, J. Kao, G. Xia, S. Achilefu, *Rsc Adv*, 3 (2013) 6756-6758.
- [19] S. Zhu, J. Zhang, J. Janjanam, J. Bi, G. Vegesna, A. Tiwari, F.T. Luo, J. Wei, H. Liu, *Analytica chimica acta*, 758 (2013) 138-144.
- [20] X.D. Liu, C. Fan, R. Sun, Y.J. Xu, J.F. Ge, *Analytical and bioanalytical chemistry*, 406 (2014) 7059-7070.
- [21] Y. Ni, J. Wu, *Organic & biomolecular chemistry*, 12 (2014) 3774-3791.
- [22] C. Sun, P. Wang, L. Li, G. Zhou, X. Zong, B. Hu, R. Zhang, J. Cai, J. Chen, M. Ji, *Applied biochemistry and biotechnology*, 172 (2014) 1036-1044.
- [23] R. Tivony, L. Larush, O. Sela-Tavor, S. Magdassi, *Journal of biomedical nanotechnology*, 10 (2014) 1041-1048.
- [24] H. Wu, S. Krishnakumar, J. Yu, D. Liang, H. Qi, Z.W. Lee, L.W. Deng, D. Huang, *Chemistry, an Asian journal*, 9 (2014) 3604-3611.
- [25] J.B. Wu, C. Shao, X. Li, C. Shi, Q. Li, P. Hu, Y.T. Chen, X. Dou, D. Sahu, W. Li, H. Harada, Y. Zhang, R. Wang, H.E. Zhau, L.W. Chung, *Biomaterials*, 35 (2014) 8175-8185.
- [26] X. Yi, F. Wang, W. Qin, X. Yang, J. Yuan, *International journal of nanomedicine*, 9 (2014) 1347-1365.

- [27] J. Yu, X. Zhang, X. Hao, X. Zhang, M. Zhou, C.S. Lee, X. Chen, *Biomaterials*, 35 (2014) 3356-3364.
- [28] M. Gao, F. Yu, H. Chen, L. Chen, *Analytical chemistry*, 87 (2015) 3631-3638.
- [29] Z. Li, X. He, Z. Wang, R. Yang, W. Shi, H. Ma, *Biosensors & bioelectronics*, 63 (2015) 112-116.
- [30] T. Namikawa, T. Sato, K. Hanazaki, *Surgery today*, (2015).
- [31] R.M. Schols, N.J. Connell, L.P. Stassen, *World journal of surgery*, 39 (2015) 1069-1079.
- [32] C. Zhao, X. Li, F. Wang, *Chemistry, an Asian journal*, 9 (2014) 1777-1781.
- [33] D. Ishikawa, H. Shinzawa, T. Genkawa, S.G. Kazarian, Y. Ozaki, *Analytical sciences : the international journal of the Japan Society for Analytical Chemistry*, 30 (2014) 143-150.
- [34] C. Yue, P. Liu, M. Zheng, P. Zhao, Y. Wang, Y. Ma, L. Cai, *Biomaterials*, 34 (2013) 6853-6861.
- [35] V. Pansare, S. Hejazi, W. Faenza, R.K. Prud'homme, *Chemistry of materials : a publication of the American Chemical Society*, 24 (2012) 812-827.
- [36] K. Aita, T. Temma, Y. Kuge, K. Seki, H. Saji, *Luminescence : the journal of biological and chemical luminescence*, 25 (2010) 19-24.
- [37] L.S. Fournier, V. Lucidi, K. Berejnoi, T. Miller, S.G. Demos, R.C. Brasch, *Optics express*, 14 (2006) 6713-6723.
- [38] Z. Zhang, S. Achilefu, *Photochemistry and photobiology*, 81 (2005) 1499-1504.
- [39] X.T. Zhang, Z.Y. Gu, L. Liu, S. Wang, G.W. Xing, *Chemical communications*, 51 (2015) 8606-8609.
- [40] D.S. Pisoni, L. Todeschini, A.C. Borges, C.L. Petzhold, F.S. Rodembusch, L.F. Campo, *The Journal of organic chemistry*, 79 (2014) 5511-5520.

- [41] Z. Wang, X. Yue, Y. Wang, C. Qian, P. Huang, M. Lizak, G. Niu, F. Wang, P. Rong, D.O. Kiesewetter, Y. Ma, X. Chen, *Advanced healthcare materials*, 3 (2014) 1326-1333.
- [42] E.A. Owens, H. Hyun, S.H. Kim, J.H. Lee, G. Park, Y. Ashitate, J. Choi, G.H. Hong, S. Alyabyev, S.J. Lee, G. Khang, M. Henary, H.S. Choi, *Biomed Mater*, 8 (2013) 014109.
- [43] Z. Guo, G.H. Kim, I. Shin, J. Yoon, *Biomaterials*, 33 (2012) 7818-7827.
- [44] L. Wang, J. Jin, X. Chen, H.H. Fan, B.K. Li, K.W. Cheah, N. Ding, S. Ju, W.T. Wong, C. Li, *Organic & biomolecular chemistry*, 10 (2012) 5366-5370.
- [45] J.W. Park, Y. Kim, K.J. Lee, D.J. Kim, *Bioconjugate chemistry*, 23 (2012) 350-362.
- [46] B. Ebert, B. Riefke, U. Sukowski, K. Licha, *Journal of biomedical optics*, 16 (2011) 066003.
- [47] H. Langhals, A. Varja, P. Laubichler, M. Kernt, K. Eibl, C. Haritoglou, *J Med Chem*, 54 (2011) 3903-3925.
- [48] L.Q. Ying, B.P. Branchaud, *Bioconjugate chemistry*, 22 (2011) 865-869.
- [49] O. Taratula, M. Patel, C. Schumann, M.A. Naleway, A.J. Pang, H. He, O. Taratula, *International journal of nanomedicine*, 10 (2015) 2347-2362.
- [50] A.B. Attia, G. Balasundaram, W. Driessen, V. Ntziachristos, M. Olivo, *Biomedical optics express*, 6 (2015) 591-598.
- [51] E. Yaghini, F. Giuntini, I.M. Eggleston, K. Suhling, A.M. Seifalian, A.J. MacRobert, *Small*, 10 (2014) 782-792.
- [52] J.H. Park, J.E. Royer, E. Chagarov, T. Kaufman-Osborn, M. Edmonds, T. Kent, S. Lee, W.C. Trogler, A.C. Kummel, *Journal of the American Chemical Society*, 135 (2013) 14600-14609.

- [53] E. Ranyuk, N. Cauchon, K. Klarskov, B. Guerin, J.E. van Lier, *J Med Chem*, 56 (2013) 1520-1534.
- [54] M. Haruta, K. Yoshida, H. Kurata, S. Isoda, *Ultramicroscopy*, 108 (2008) 545-551.
- [55] R. Cubeddu, A. Pifferi, P. Taroni, A. Torricelli, G. Valentini, D. Comelli, C. D'Andrea, V. Angelini, G. Canti, *Photochemistry and photobiology*, 72 (2000) 690-695.
- [56] M.J. Witjes, A.J. Mank, O.C. Speelman, R. Posthumus, C.A. Nooren, J.M. Nauta, J.L. Roodenburg, W.M. Star, *Photochemistry and photobiology*, 65 (1997) 685-693.
- [57] A. Wragg, M.R. Gill, L. McKenzie, C. Glover, R. Mowll, J.A. Weinstein, X. Su, C. Smythe, J.A. Thomas, *Chemistry*, 21 (2015) 11865-11871.
- [58] K. Zelenka, L. Borsig, R. Alberto, *Bioconjugate chemistry*, 22 (2011) 958-967.
- [59] A. Katori, E. Azuma, H. Ishimura, K. Kuramochi, K. Tsubaki, *The Journal of organic chemistry*, 80 (2015) 4603-4610.
- [60] S. Kamino, M. Murakami, M. Tanioka, Y. Shirasaki, K. Watanabe, J. Horigome, Y. Ooyama, S. Enomoto, *Organic letters*, 16 (2014) 258-261.
- [61] A. Nandakumar, P.T. Perumal, *Organic letters*, 15 (2013) 382-385.
- [62] I.K. Astakhova, J. Wengel, *Chemistry*, 19 (2013) 1112-1122.
- [63] H. Kato, K. Komagoe, Y. Nakanishi, T. Inoue, T. Katsu, *Photochemistry and photobiology*, 88 (2012) 423-431.
- [64] L.M. Wysocki, J.B. Grimm, A.N. Tkachuk, T.A. Brown, E. Betzig, L.D. Lavis, *Angewandte Chemie*, 50 (2011) 11206-11209.
- [65] J.M. Cardenas-Maestre, R.M. Sanchez-Martin, *Organic & biomolecular chemistry*, 9 (2011) 1720-1722.
- [66] E.L. Cole, E. Arunkumar, S. Xiao, B.A. Smith, B.D. Smith, *Organic & biomolecular chemistry*, 10 (2012) 5769-5773.

- [67] M. Xue, Y.S. Su, C.F. Chen, *Chemistry*, 16 (2010) 8537-8544.
- [68] S.Y. Hsueh, C.C. Lai, S.H. Chiu, *Chemistry*, 16 (2010) 2997-3000.
- [69] J.J. Gassensmith, J.M. Baumes, B.D. Smith, *Chemical communications*, (2009) 6329-6338.
- [70] N. Fu, J.M. Baumes, E. Arunkumar, B.C. Noll, B.D. Smith, *The Journal of organic chemistry*, 74 (2009) 6462-6468.
- [71] J.J. Gassensmith, L. Barr, J.M. Baumes, A. Paek, A. Nguyen, B.D. Smith, *Organic letters*, 10 (2008) 3343-3346.
- [72] J.R. Johnson, N. Fu, E. Arunkumar, W.M. Leevy, S.T. Gammon, D. Piwnicka-Worms, B.D. Smith, *Angewandte Chemie*, 46 (2007) 5528-5531.
- [73] E. Arunkumar, N. Fu, B.D. Smith, *Chemistry*, 12 (2006) 4684-4690.
- [74] E. Arunkumar, C.C. Forbes, B.C. Noll, B.D. Smith, *Journal of the American Chemical Society*, 127 (2005) 3288-3289.
- [75] T. Simon, M. Potara, A.M. Gabudean, E. Licarete, M. Banciu, S. Astilean, *ACS applied materials & interfaces*, 7 (2015) 16191-16201.
- [76] W. Kim, B.E. Applegate, *Optics letters*, 40 (2015) 1426-1429.
- [77] Q.R. Tummers, M.C. Boonstra, J.V. Frangioni, C.J. van de Velde, A.L. Vahrmeijer, B.A. Bonsing, *International journal of surgery case reports*, 6C (2015) 150-153.
- [78] J.R. van der Vorst, B.E. Schaafsma, F.P. Verbeek, R.J. Swijnenburg, Q.R. Tummers, M. Hutteman, J.F. Hamming, J. Kievit, J.V. Frangioni, C.J. van de Velde, A.L. Vahrmeijer, *Head & neck*, 36 (2014) 853-858.
- [79] P. Schafer, S. van de Linde, J. Lehmann, M. Sauer, S. Doose, *Analytical chemistry*, 85 (2013) 3393-3400.

- [80] J.R. van der Vorst, A.L. Vahrmeijer, M. Hutteman, T. Bosse, V.T. Smit, C.J. van de Velde, J.V. Frangioni, B.A. Bonsing, *World journal of gastrointestinal surgery*, 4 (2012) 180-184.
- [81] X. He, X. Wu, K. Wang, B. Shi, L. Hai, *Biomaterials*, 30 (2009) 5601-5609.
- [82] M. Muslumanoglu, T. Terzioglu, S. Ozarmagan, S. Tezelman, R. Guloglu, *La Radiologia medica*, 90 (1995) 444-447.
- [83] W. Bian, F. Wang, Y. Wei, L. Wang, Q. Liu, W. Dong, S. Shuang, M.M. Choi, *Analytica chimica acta*, 856 (2015) 82-89.
- [84] J. Lee, Y. Choi, Y. Cho, R. Song, *Journal of nanoscience and nanotechnology*, 13 (2013) 417-422.
- [85] J.I. Kim, J. Kim, J. Lee, D.R. Jung, H. Kim, H. Choi, S. Lee, S. Byun, S. Kang, B. Park, *Nanoscale research letters*, 7 (2012) 482.
- [86] K.S. Kim, W. Hur, S.J. Park, S.W. Hong, J.E. Choi, E.J. Goh, S.K. Yoon, S.K. Hahn, *ACS nano*, 4 (2010) 3005-3014.
- [87] M.S. Choi, *Nature nanotechnology*, 4 (2009) 347-348.
- [88] H.S. Choi, B.I. Ipe, P. Misra, J.H. Lee, M.G. Bawendi, J.V. Frangioni, *Nano letters*, 9 (2009) 2354-2359.
- [89] W. Liu, H.S. Choi, J.P. Zimmer, E. Tanaka, J.V. Frangioni, M. Bawendi, *Journal of the American Chemical Society*, 129 (2007) 14530-14531.
- [90] H.S. Choi, W. Liu, P. Misra, E. Tanaka, J.P. Zimmer, B. Itty Ipe, M.G. Bawendi, J.V. Frangioni, *Nature biotechnology*, 25 (2007) 1165-1170.
- [91] C.L. Walker, K.A. Lukyanov, I.V. Yampolsky, A.S. Mishin, A.S. Bommarius, A.M. Duraj-Thatte, B. Azizi, L.M. Tolbert, K.M. Solntsev, *Current opinion in chemical biology*, 27 (2015) 64-74.
- [92] V. Venkatachalam, A.E. Cohen, *Biophysical journal*, 107 (2014) 1554-1563.

- [93] Y. Kikuchi, T. Fukatsu, *Molecular ecology*, 23 (2014) 1445-1456.
- [94] L. Yuan, W. Lin, H. Chen, S. Zhu, L. He, *Angewandte Chemie*, 52 (2013) 10018-10022.
- [95] M. Frizler, I.V. Yampolsky, M.S. Baranov, M. Stirnberg, M. Gutschow, *Organic & biomolecular chemistry*, 11 (2013) 5913-5921.
- [96] G.D. Malo, L.J. Pouwels, M. Wang, A. Weichsel, W.R. Montfort, M.A. Rizzo, D.W. Piston, R.M. Wachter, *Biochemistry*, 46 (2007) 9865-9873.
- [97] N. Daigle, J. Ellenberg, *Nature methods*, 4 (2007) 633-636.
- [98] C. Shannon, M. Salter, R. Fern, *Journal of anatomy*, 210 (2007) 684-692.
- [99] G. Halet, *Biology of the cell / under the auspices of the European Cell Biology Organization*, 97 (2005) 501-518.
- [100] A. Miyawaki, *Current opinion in neurobiology*, 13 (2003) 591-596.
- [101] D. Ehrhardt, *Current opinion in plant biology*, 6 (2003) 622-628.
- [102] P.C. Goodwin, *Methods in cell biology*, 58 (1999) 343-367.
- [103] J. Haseloff, *Methods in cell biology*, 58 (1999) 139-151.
- [104] N.K. Tafreshi, X. Huang, V.E. Moberg, N.M. Barkey, V.K. Sondak, H. Tian, D.L. Morse, J. Vagner, *Bioconjugate chemistry*, 23 (2012) 2451-2459.
- [105] I.R. Corbin, K.K. Ng, L. Ding, A. Jurisicova, G. Zheng, *Nanomedicine*, 8 (2013) 875-890.
- [106] S.K. Ghosh, M. Uchida, B. Yoo, A.W. Ross, S.J. Gendler, J. Gong, A. Moore, Z. Medarova, *International journal of cancer. Journal international du cancer*, 132 (2013) 1860-1867.
- [107] X. Wu, S.M. Burden-Gulley, G.P. Yu, M. Tan, D. Lindner, S.M. Brady-Kalnay, Z.R. Lu, *Bioconjugate chemistry*, 23 (2012) 1548-1556.

[108] L. Wang, W. Su, Z. Liu, M. Zhou, S. Chen, Y. Chen, D. Lu, Y. Liu, Y. Fan, Y. Zheng, Z. Han, D. Kong, J.C. Wu, R. Xiang, Z. Li, *Biomaterials*, 33 (2012) 5107-5114.

[109] L. Liu, K.T. Yong, I. Roy, W.C. Law, L. Ye, J. Liu, J. Liu, R. Kumar, X. Zhang, P.N. Prasad, *Theranostics*, 2 (2012) 705-713.

[110] R.Y. Lin, K. Dayananda, T.J. Chen, C.Y. Chen, G.C. Liu, K.L. Lin, Y.M. Wang, *Contrast media & molecular imaging*, 7 (2012) 7-18.

[111] N.A. Jager, J. Westra, G.M. van Dam, N. Teteloshvili, R.A. Tio, J.C. Breek, R.H. Slart, H. Boersma, P.S. Low, M. Bijl, C.J. Zeebregts, *Journal of nuclear medicine : official publication, Society of Nuclear Medicine*, 53 (2012) 1222-1229.

[112] R. Huang, J. Vider, J.L. Kovar, D.M. Olive, I.K. Mellinshoff, P. Mayer-Kuckuk, M.F. Kircher, R.G. Blasberg, *Clinical cancer research : an official journal of the American Association for Cancer Research*, 18 (2012) 5731-5740.

[113] J. Geng, K. Li, K.Y. Pu, D. Ding, B. Liu, *Small*, 8 (2012) 2421-2429.

[114] Z. Liu, N. Chen, C. Dong, W. Li, W. Guo, H. Wang, S. Wang, J. Tan, Y. Tu, J. Chang, *ACS applied materials & interfaces*, 7 (2015) 18997-19005.

[115] T. Zako, M. Yoshimoto, H. Hyodo, H. Kishimoto, M. Ito, K. Kaneko, K. Soga, M. Maeda, *Biomaterials science*, 3 (2015) 59-64.

[116] J.B. Wu, C. Shi, G.C. Chu, Q. Xu, Y. Zhang, Q. Li, J.S. Yu, H.E. Zhau, L.W. Chung, *Biomaterials*, 67 (2015) 1-10.

[117] S. Zhang, P. Shao, X. Ling, L. Yang, W. Hou, S.H. Thorne, W. Beaino, C.J. Anderson, Y. Ding, M. Bai, *American journal of nuclear medicine and molecular imaging*, 5 (2015) 246-258.

[118] N. Li, T. Li, C. Hu, X. Lei, Y. Zuo, H. Han, *ACS applied materials & interfaces*, (2015).

- [119] M.J. Uddin, B.C. Crews, K. Ghebreselasie, C.K. Daniel, P.J. Kingsley, S. Xu, L.J. Marnett, *Journal of biomedical optics*, 20 (2015) 50502.
- [120] L. Fu, C. Sun, L. Yan, *ACS applied materials & interfaces*, 7 (2015) 2104-2115.
- [121] R. Tang, J. Xue, B. Xu, D. Shen, G.P. Sudlow, S. Achilefu, *ACS nano*, 9 (2015) 220-230.
- [122] T. Liu, S. Luo, Y. Wang, X. Tan, Q. Qi, C. Shi, *Drug design, development and therapy*, 8 (2014) 1287-1297.
- [123] X. Wang, S.S. Huang, W.D. Heston, H. Guo, B.C. Wang, J.P. Basilion, *Molecular cancer therapeutics*, 13 (2014) 2595-2606.
- [124] J. Tian, L. Ding, H. Ju, Y. Yang, X. Li, Z. Shen, Z. Zhu, J.S. Yu, C.J. Yang, *Angewandte Chemie*, 53 (2014) 9544-9549.
- [125] R. Ruger, F.L. Tansi, M. Rabenhold, F. Steiniger, R.E. Kontermann, A. Fahr, I. Hilger, *Journal of controlled release : official journal of the Controlled Release Society*, 186 (2014) 1-10.
- [126] Z. Wu, P. Shao, S. Zhang, M. Bai, *Journal of biomedical optics*, 19 (2014) 36006.
- [127] A. Dutour, V. Jossierand, D. Jury, S. Guillermet, A.V. Decouvelaere, F. Chotel, T. Pointecouteau, P. Rizo, J.L. Coll, J.Y. Blay, *Bone*, 62 (2014) 71-78.
- [128] Y. Urano, D. Asanuma, Y. Hama, Y. Koyama, T. Barrett, M. Kamiya, T. Nagano, T. Watanabe, A. Hasegawa, P.L. Choyke, H. Kobayashi, *Nature medicine*, 15 (2009) 104-109.
- [129] G.J. Chen, C. Hsu, J.H. Ke, L.F. Wang, *Journal of biomedical nanotechnology*, 11 (2015) 951-963.
- [130] Z.Y. Ma, Y.P. Liu, L.Y. Bai, J. An, L. Zhang, Y. Xuan, X.S. Zhang, Y.D. Zhao, *Dalton transactions*, 44 (2015) 16304-16312.
- [131] M. Yu, J. Zheng, *ACS nano*, 9 (2015) 6655-6674.

[132] Z. Liu, P. Rong, L. Yu, X. Zhang, C. Yang, F. Guo, Y. Zhao, K. Zhou, W. Wang, W. Zeng, *Molecular pharmaceutics*, 12 (2015) 3119-3128.

[133] S. Capolla, C. Garrovo, S. Zorzet, A. Lorenzon, E. Rampazzo, R. Sprez, G. Pozzato, L. Nunez, C. Tripodo, P. Macor, S. Biffi, *International journal of nanomedicine*, 10 (2015) 4099-4109.

[134] L. Prodi, E. Rampazzo, F. Rastrelli, A. Speghini, N. Zaccheroni, *Chemical Society reviews*, 44 (2015) 4922-4952.

[135] J.E. Chung, S. Tan, S.J. Gao, N. Yongvongsoontorn, S.H. Kim, J.H. Lee, H.S. Choi, H. Yano, L. Zhuo, M. Kurisawa, J.Y. Ying, *Nature nanotechnology*, 9 (2014) 907-912.

[136] H.S. Choi, *Nature nanotechnology*, 9 (2014) 93-94.

[137] H.S. Choi, W. Liu, F. Liu, K. Nasr, P. Misra, M.G. Bawendi, J.V. Frangioni, *Nature nanotechnology*, 5 (2010) 42-47.

[138] W. Shi, S.M. Ogbomo, N.K. Wagh, Z. Zhou, Y. Jia, S.K. Brusnahan, J.C. Garrison, *Biomaterials*, 35 (2014) 5760-5770.

[139] C. Zhu, Q. Xu, D. Pan, Y. Xu, P. Liu, R. Yang, L. Wang, X. Sun, S. Luo, M. Yang, *Contrast media & molecular imaging*, (2015).

[140] L. Zhang, T. Navaratna, J. Liao, G.M. Thurber, *Bioconjugate chemistry*, 26 (2015) 329-337.

[141] M. Benesova, M. Schafer, U. Bauder-Wust, A. Afshar-Oromieh, C. Kratochwil, W. Mier, U. Haberkorn, K. Kopka, M. Eder, *Journal of nuclear medicine : official publication, Society of Nuclear Medicine*, 56 (2015) 914-920.

[142] Y. Barenholz, *Journal of controlled release : official journal of the Controlled Release Society*, 160 (2012) 117-134.

[143] H.S. Choi, S.L. Gibbs, J.H. Lee, S.H. Kim, Y. Ashitate, F. Liu, H. Hyun, G. Park, Y. Xie, S. Bae, M. Henary, J.V. Frangioni, *Nature biotechnology*, 31 (2013) 148-153.

[144] H.S. Choi, K. Nasr, S. Alyabyev, D. Feith, J.H. Lee, S.H. Kim, Y. Ashitate, H. Hyun, G. Patonay, L. Strekowski, M. Henary, J.V. Frangioni, *Angewandte Chemie*, 50 (2011) 6258-6263.

[145] C.N. Njiojob, E.A. Owens, L. Narayana, H. Hyun, H.S. Choi, M. Henary, *J Med Chem*, 58 (2015) 2845-2854.

[146] H. Hyun, E.A. Owens, L. Narayana, H. Wada, J. Gravier, K. Bao, J.V. Frangioni, H.S. Choi, M. Henary, *Rsc Adv*, 4 (2014) 58762-58768.

[147] H. Hyun, M. Henary, T. Gao, L. Narayana, E. Owens, J. Lee, G. Park, H. Wada, Y. Ashitate, J. Frangioni, H. Choi, *Molecular Imaging and Biology*, (2015) 1-10.

[148] M.A. Whitney, J.L. Crisp, L.T. Nguyen, B. Friedman, L.A. Gross, P. Steinbach, R.Y. Tsien, Q.T. Nguyen, *Nat Biotech*, 29 (2011) 352-356.

[149] H. Hyun, E.A. Owens, H. Wada, A. Levitz, G. Park, M.H. Park, J.V. Frangioni, M. Henary, H.S. Choi, *Angewandte Chemie*, 54 (2015) 8648-8652.

[150] E.A. Owens, H. Hyun, J.G. Tawney, H.S. Choi, M. Henary, *J Med Chem*, 58 (2015) 4348-4356.

[151] K. Bao, K.A. Nasr, H. Hyun, J.H. Lee, J. Gravier, S.L. Gibbs, H.S. Choi, *Theranostics*, 5 (2015) 609-617.

[152] H. Hyun, M.H. Park, E.A. Owens, H. Wada, M. Henary, H.J. Handgraaf, A.L. Vahrmeijer, J.V. Frangioni, H.S. Choi, *Nature medicine*, 21 (2015) 192-197.

[153] H. Hyun, H. Wada, K. Bao, J. Gravier, Y. Yadav, M. Laramie, M. Henary, J.V. Frangioni, H.S. Choi, *Angewandte Chemie*, 53 (2014) 10668-10672.

[154] H. Hyun, E.A. Owens, H. Wada, A. Levitz, G. Park, M.H. Park, J.V. Frangioni, M. Henary, H.S. Choi, *Angewandte Chemie*, (2015).

[155] H. Jiang, G. Xu, Y. Sun, W. Zheng, X. Zhu, B. Wang, X. Zhang, G. Wang, *Chemical communications*, 51 (2015) 11810-11813.

- [156] M. Ocak, A.G. Gillman, J. Bresee, L. Zhang, A.M. Vlad, C. Muller, R. Schibli, W.B. Edwards, C.J. Anderson, H.M. Gach, *Molecular pharmaceutics*, 12 (2015) 542-553.
- [157] A. Polyak, I. Hajdu, M. Bodnar, G. Dabasi, R.P. Joba, J. Borbely, L. Balogh, *International journal of pharmaceutics*, 474 (2014) 91-94.
- [158] J. Kim, C.H. Tung, Y. Choi, *Chemical communications*, 50 (2014) 10600-10603.
- [159] C. Muller, R. Schibli, *Journal of nuclear medicine : official publication, Society of Nuclear Medicine*, 52 (2011) 1-4.
- [160] C.Y. Ke, C.J. Mathias, M.A. Green, *Advanced drug delivery reviews*, 56 (2004) 1143-1160.
- [161] W. Guo, G.H. Hinkle, R.J. Lee, *Journal of nuclear medicine : official publication, Society of Nuclear Medicine*, 40 (1999) 1563-1569.
- [162] Y. Yamada, H. Nakatani, H. Yanaihara, M. Omote, *Annals of nuclear medicine*, (2015).
- [163] D. Shao, J. Li, Y. Pan, X. Zhang, X. Zheng, Z. Wang, M. Zhang, H. Zhang, L. Chen, *Biomaterials science*, 3 (2015) 833-841.
- [164] H. Li, K. Yan, Y. Shang, L. Shrestha, R. Liao, F. Liu, P. Li, H. Xu, Z. Xu, P.K. Chu, *Acta biomaterialia*, 15 (2015) 117-126.
- [165] M.H. Kim, W.H. Kim, C.G. Kim, D.W. Kim, *Nuclear medicine and molecular imaging*, 49 (2015) 200-207.
- [166] L.E. Kelderhouse, S. Mahalingam, P.S. Low, *Molecular imaging and biology : MIB : the official publication of the Academy of Molecular Imaging*, (2015).
- [167] E. de Boer, L.M. Crane, M. van Oosten, B. van der Vegt, T. van der Sluis, P. Kooijman, P.S. Low, A.G. van der Zee, H.J. Arts, G.M. van Dam, J. Bart, *PloS one*, 10 (2015) e0135012.

[168] M. Zheng, P. Zhao, Z. Luo, P. Gong, C. Zheng, P. Zhang, C. Yue, D. Gao, Y. Ma, L. Cai, *ACS applied materials & interfaces*, 6 (2014) 6709-6716.

[169] E.H. Tsai, B.Z. Bentz, V. Chelvam, V. Gaiind, K.J. Webb, P.S. Low, *Biomedical optics express*, 5 (2014) 2662-2678.

[170] T. Nakamura, K. Kawano, K. Shiraishi, M. Yokoyama, Y. Maitani, *Biological & pharmaceutical bulletin*, 37 (2014) 521-527.

[171] A.H. Maurer, P. Elsinga, S. Fanti, B. Nguyen, W.J. Oyen, W.A. Weber, *Journal of nuclear medicine : official publication, Society of Nuclear Medicine*, 55 (2014) 701-704.

[172] Y. Chen, H. Guo, F. Xie, J. Lu, *Journal of labelled compounds & radiopharmaceuticals*, 57 (2014) 12-17.

[173] H. Lee, J. Kim, H. Kim, Y. Kim, Y. Choi, *Chemical communications*, 50 (2014) 7507-7510.

[174] Q.T. Nguyen, E.S. Olson, T.A. Aguilera, T. Jiang, M. Scadeng, L.G. Ellies, R.Y. Tsien, *Proceedings of the National Academy of Sciences of the United States of America*, 107 (2010) 4317-4322.

[175] E.N. Savariar, C.N. Felsen, N. Nashi, T. Jiang, L.G. Ellies, P. Steinbach, R.Y. Tsien, Q.T. Nguyen, *Cancer research*, 73 (2013) 855-864.

[176] S.R. MacEwan, A. Chilkoti, *Wiley interdisciplinary reviews. Nanomedicine and nanobiotechnology*, 5 (2013) 31-48.

[177] E.S. Olson, M.A. Whitney, B. Friedman, T.A. Aguilera, J.L. Crisp, F.M. Baik, T. Jiang, S.M. Baird, S. Tsimikas, R.Y. Tsien, Q.T. Nguyen, *Integrative biology : quantitative biosciences from nano to macro*, 4 (2012) 595-605.

[178] X. Yuan, X. Lin, G. Manorek, S.B. Howell, *BMC cancer*, 11 (2011) 61.

[179] E.S. Olson, T. Jiang, T.A. Aguilera, Q.T. Nguyen, L.G. Ellies, M. Scadeng, R.Y. Tsien, Proceedings of the National Academy of Sciences of the United States of America, 107 (2010) 4311-4316.

[180] C.A. Metildi, C.N. Felsen, E.N. Savariar, Q.T. Nguyen, S. Kaushal, R.M. Hoffman, R.Y. Tsien, M. Bouvet, Annals of surgical oncology, 22 (2015) 2082-2087.

3 CORRELATING TISSUE LOCALIZATION OF HYDROPHOBIC CYANINES

This chapter has been reprinted from the following publication in the Journal of Medicinal Chemistry. My contributions as first author were the design, synthesis, optical property determination, molecular modeling and computational experiments, data interpretation and figure/manuscript preparation. **Owens, E. A.**, Hyun, H., Tawney, J. G., Choi, H. S., Henary, M. Correlating Molecular Character of NIR Imaging Agents with Endocrine-Specific Uptake **2015** *Journal of Medicinal Chemistry*

3.1 Abstract

Near-infrared (NIR) fluorescent nanoprobe are emerging in optical imaging as sensitive, cost effective and non-harmful alternatives to current agents that emit harmful ionizing radiation. Surgeons require these NIR-based nanoprobe to visualize sensitive vital tissues to selectively avoid them during surgical resection of diseased tissue; therefore, developing spectrally distinct fluorophores is of great significance to lower morbidity in the clinic. In response to this clinical need, we report the synthetic variation of pentamethine cyanine fluorophores with systematic modifications of physicochemical properties towards prompting tissue-specific uptake into sensitive tissues (i.e., endocrine glands). Tissue-specific targeting and biodistribution studies revealed localization of intravenously injected nanoprobe in the adrenal glands, pituitary glands, pancreas and lymph nodes with strong dependence on the molecular characteristics. Heterocyclic modification involved the use of indolenine and benz[e]indolenine moieties to increase the logD of the compounds. Furthermore, incorporation of hydrophobic alkyl groups to the *N*-indolenyl site and halogens to the *meso*-carbon of the methine-bridge allowed a fine tuning capability to the hydrophobic character and overall dipole moment for observing perturbation in biological activity in response to minor structural

alterations. These NIR nanoprobcs have potential for clinical translation for intraoperative imaging in the delineation of delicate glands.

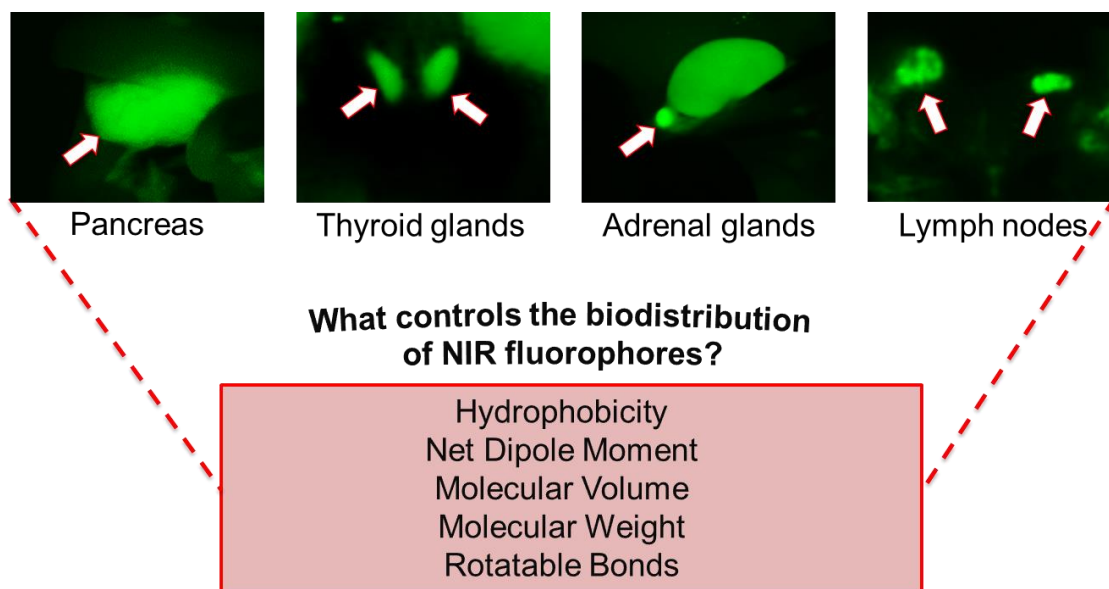


Figure 3-1. Graphical representation for this section which covers the development of structure-inherent NIR fluorophores.

3.2 Introduction

Molecular imaging agents that display selectivity toward various tissues are among paramount importance for use in image-guided surgery.¹⁻⁷ For instance, visualizing native endocrine glands during head and neck surgery remains of high clinical significance as current imaging agents being explored utilize the emission of harmful ionizing radiation and place the patient and caregiver at undesirable levels of exposure.^{8, 9} Additional disadvantages of common molecular imaging modalities, such as positron emission tomography (PET) and single-photon emission computed tomography (SPECT), include their low spatial resolution of tissue and inability to conduct surgery in real-time with image capture.¹⁰ Optical imaging using near-infrared (NIR) light, however, is harmless as human tissues do not absorb these wavelengths of the electromagnetic spectrum.⁶ Developing fluorophores in the NIR window also helps to minimize the optical background that arises from fluorescence from native

biological tissue.¹¹⁻¹⁷ This autofluorescence increases background signal which reduces the all-important signal-to-background ratio (SBR) and makes delineating meaningful signal more difficult.

Many groups have utilized a number of approaches for directing molecular imaging agents to particular organs using receptors attached to a reactive moiety residing on the fluorophore.¹⁸⁻²¹ These moieties normally include a carboxylic acid or amine for amide coupling or alkyne/azide for click chemistry which can be synthetically challenging. However, only a few methods have been explored for chemically tailoring a class of fluorophore for site-specific uptake by glands and tissues using physicochemical predictors to systematically synthesize, evaluate and harness the inherent biodistribution of the fluorophores.²² To date, only one NIR fluorescent compound, indocyanine green (ICG), has been approved for clinical use by the U.S. Food and Drug Administration (FDA).²³ Indeed the exact molecular structure does not offer appealing biodistribution properties or potential for additional chemical modifications, it serves to validate the cyanine class as an excellent choice for further optimization.²⁴ Cyanine dyes are a unique class of compounds that are generally represented by two nitrogen-containing heterocycles linked *via* an electron-deficient conjugated polymethine bridge.^{25, 26} The absorption and fluorescence properties of these compounds can be tailored, and the two main subclasses of NIR-fluorescing cyanine compounds include pentamethine (~700 nm emission) and heptamethine backbones (~800 nm emission). These compounds have appealing optical properties, including their red-shifted fluorescence, elevated quantum yields and high stability in serum.

The FLARE (Fluorescence-Assisted Resection and Exploration) imaging system used for intraoperative NIR imaging utilizes two video channels (700 and 800 nm fluorescence) merged with a color video image.^{27, 28} We have previously reported a heptamethine cyanine dye (800 nm fluorescence) with unparalleled clearance properties that, after conjugation,

selectively images cancerous tissues.^{29, 30} For native endocrine-tissue imaging, therefore, we have reserved the lower 700 nm channel for dual imaging of the surgical field. Previously, we elucidated that cyanine chromophores have various binding strengths to serum albumin depending on their hydrophobicity³¹; therefore, we hypothesized that we could harness this interaction to manipulate the biodistribution of these compounds. Herein, we report the development of pentamethine cyanine imaging agents that display tissue-specific uptake into various endocrine glands resulted from the modification of the heterocyclic nitrogen and methine-bridge.

3.3 Results and Discussion

3.3.1 *Synthesis of Pentamethine Fluorophores.*

Using our optimized synthetic strategy for preparing pentamethine cyanines that exhibit varied hydrophobic character, we began by reacting either mucochloric **1** or mucobromic **2** acid with aniline in warm ethanol and upon cooling and dilution with diethyl ether, the intermediate salts **4** and **5** precipitated as yellow solids with precursor **3** being commercially obtained. In parallel, heterocyclic derivatives **8-15** were prepared from 2,3,3-trimethylindolenine **6** and 1,1,2-trimethyl-1H-benzo[*e*]indole **7** using the corresponding alkyl halide in boiling acetonitrile. Subsequently, the reaction of individual salts **8-15** with intermediate **3-5** formed the final pentamethine cyanines that were purified by open column chromatography or *via* our precipitation procedure from methanol using dilution with either diethyl ether or methyl *tert*-butyl ether until analytical purity was obtained for evaluating these compounds in bio-distribution experiments.

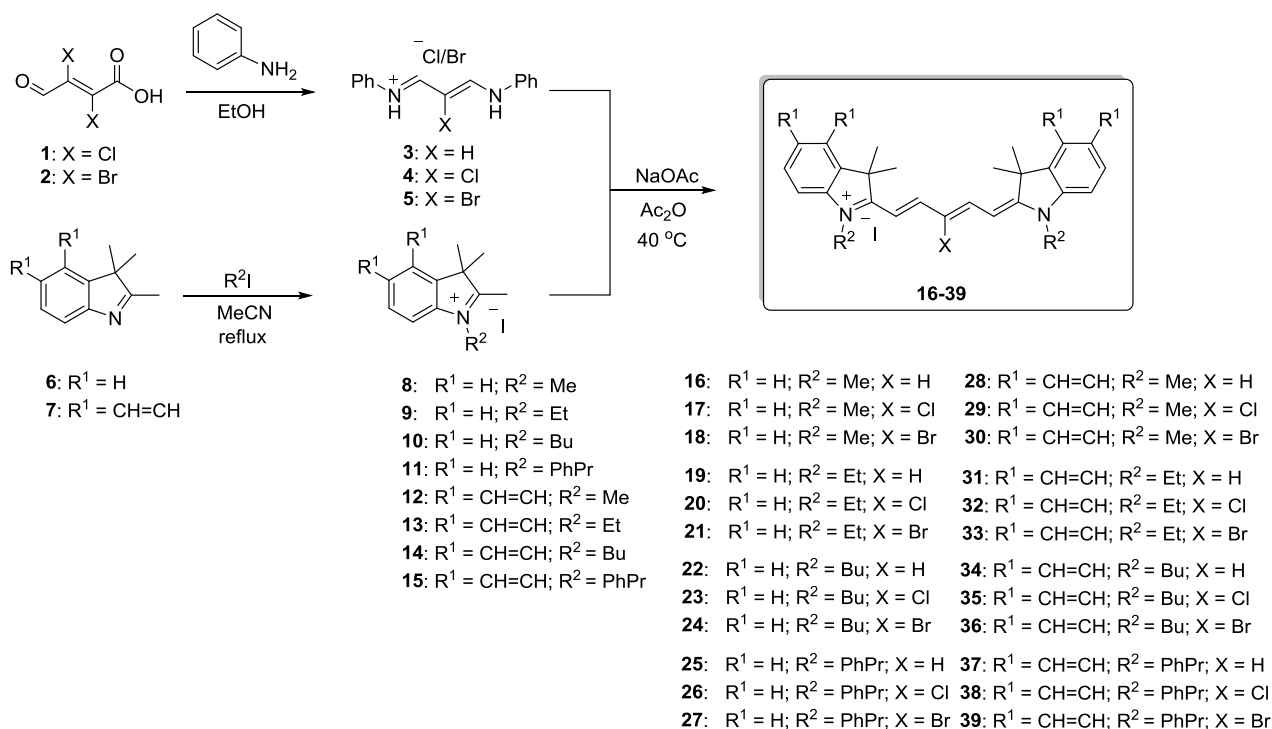


Figure 3-2. The synthetic route to the final hydrophobic pentamethine fluorophores.

Note: Cellular experiments were conducted regarding the following compounds and are previously referred to using ESNF nomenclature: **16** (ESNF-10), **22** (ESNF-11), **25** (ESNF-12) and **31** (ESNF-14).³² Herein, we will discuss the animal studies concerning the entire systematic set of fluorophores and will be referred to by their numbers in the synthetic scheme.

3.3.2 Optical and Physicochemical Properties.

The optical properties, shown in Table 2.1, including λ_{\max} (ethanol and FBS), λ_{em} (ethanol and FBS), extinction coefficient (ethanol, DMSO, PBS and FBS), and fluorescence quantum yield (FBS) of the synthesized fluorophores were determined to ensure compatibility and visibility with the FLARE imaging. All compounds showed excellent extinction coefficients in the near-infrared region in all four of the studied solvents with many compounds having very promising properties in serum.

Table 3-1 Optical properties of NIR fluorophores. All measurements were performed in several solvents, ethanol (EtOH), dimethyl sulfoxide (DMSO), phosphate-buffered saline (PBS), and fetal bovine serum (FBS), pH = 7.4 at 37 °C, and the fluorescence QY in FBS, pH = 7.4 at 37 °C. Abbreviations: λ_{abs} ; maximum absorbance; λ_{em} ; SS, Stokes shift; and QY, quantum yield.

ID	λ_{abs} (nm)	λ_{em} (nm)	SS (nm)	Extinction Coefficient ($\text{M}^{-1}\text{cm}^{-1}$)				QY (%)
	EtOH/FBS	EtOH/FBS	EtOH/FBS	EtOH	DMSO	PBS	FBS	FBS
16	645/649	660/662	15/13	212,500	248,200	218,800	184,500	31.0
17	644/638	659/665	15/27	235,300	207,800	171,000	168,800	28.8
18	641/634	657/660	16/26	257,330	253,200	204,400	211,700	43.6
19	645/637	667/665	22/28	246,500	235,000	179,800	193,300	17.0
20	646/649	662/659	16/10	262,200	237,000	213,600	204,000	25.5
21	642/636	655/656	13/20	211,400	210,000	176,800	147,300	43.7
22	644/640	666/668	22/28	210,200	182,800	177,600	140,200	16.0
23	649/644	665/661	16/17	231,400	143,600	80,600	123,900	14.8
24	646/640	661/660	15/20	218,300	134,600	73,600	135,200	15.7
25	655/646	669/666	14/20	229,700	178,000	56,600	139,200	17.7
26	652/653	664/665	12/12	254,500	228,200	62,000	113,000	22.1
27	650/648	665/660	15/12	241,800	211,200	61,200	117,000	28.6
28	680/688	701/711	21/23	177,500	167,600	60,000	168,400	17.5
29	681/689	697/702	16/13	218,200	206,400	77,200	214,900	18.0
30	676/682	699/699	23/17	164,800	173,400	54,600	161,100	17.9
31	682/691	702/705	20/14	233,400	203,200	97,600	202,400	13.8
32	684/690	700/705	16/15	215,200	172,800	86,000	207,400	21.9
33	681/682	695/698	14/17	182,000	202,600	68,200	177,200	11.8

34	684/691	706/711	22/20	255,500	237,000	76,200	193,300	8.9
35	685/691	703/702	18/11	233,800	201,200	56,600	157,100	12.0
36	683/689	702/699	19/10	222,800	212,600	62,800	170,300	22.7
37	685/698	711/710	26/12	194,200	95,800	39,400	166,700	14.5
38	687/697	705/707	18/10	164,000	158,600	42,600	143,400	17.9
39	685/695	704/709	19/14	285,200	220,200	56,400	133,900	12.9

The more hydrophobic fluorophores displayed a second blue-shifted absorption maximum due to H-aggregation in the highly polar FBS (Figure 2.2). Fortunately, we did not encounter loss in signal resulting from fluorescence quenching from microaggregation *in vivo*.

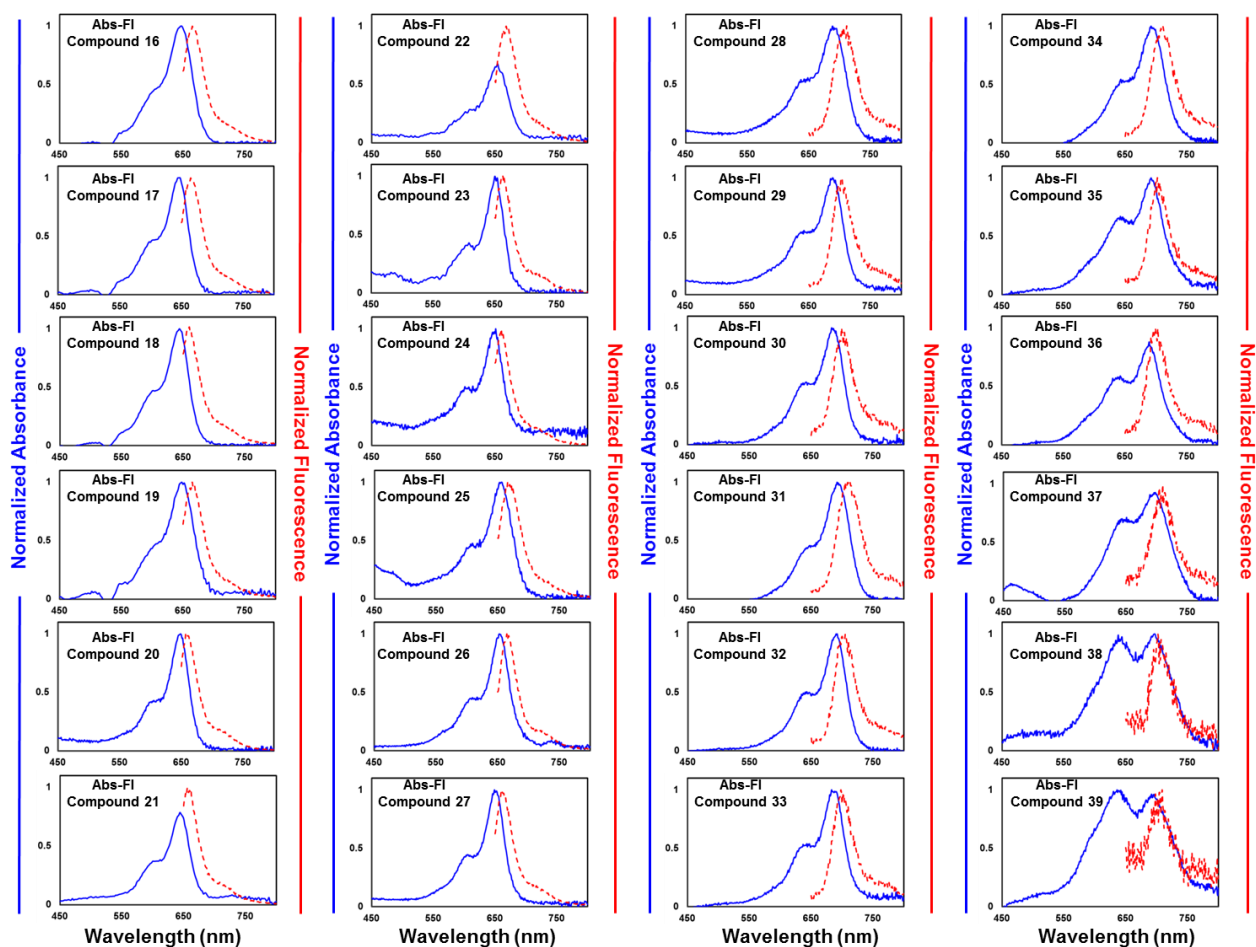


Figure 3-3 The absorption and emission spectra for each of the evaluated compounds (0.3 μM) in 100% FBS supplemented with 50 mM HEPES buffer at 37 $^{\circ}\text{C}$.

The quantum yield values are very high in serum suggesting great applicability in NIR-fluorescence imaging. In order to correlate *in vivo* biodistribution to the molecular characteristics of the synthesized fluorophores, the physicochemical properties (LogD, molecular weight and rotatable bonds) were predicted using ChemAxon (JChem plugin) with molecular dipole moment and volume being calculated using Spartan '10 (Wavefunction, Inc., Irvine, CA). The molecular weight values are independent of counter ion as the fluorophore and anion would become disassociated *in vivo*. The molecular weight values fall between 383.55 and 770.86 and the distribution coefficient numbers fall between 3.56 and 10.85 with the halogenation at the central carbon, heterocyclic variation and alkyl length alteration

providing fine tuning characteristics to the hydrophobicity of the compounds for observing minor perturbation to the biological profile. Similarly, the molecular volume for the synthesized compounds fall between 445.39 and 806.74 and the compounds exhibit 0, 4 or 8 rotatable bonds.

3.3.3 Structure-Inherent Targeting Ability of Hydrophobic NIR Fluorophores.

In order to assess the *in vivo* performance of the newly prepared pentamethine cyanines, we injected them into CD-1 mice and observed the passive localization and overall biodistribution. The synthesized compounds displayed very appealing structure-inherent endocrine targeting of biological tissues for intra-operative guidance using NIR light. Surgeons require precise visualization of sensitive tissues to avoid accidental transection and we have focused our biodistribution study on the thyroid glands, adrenal glands, pancreas and lymph nodes.

Table 3-2 The Physicochemical descriptors and targeting ability for each contrast agent.

ID	LogD (pH 7.4)	Volume (Å ³)	Rotatable Bonds	Dipole (debye)	MW (g/mol)	Targeted Tissues				Biodistribution				
						TG	AG	Pa	LN	Li	Ki	Lu	Sp	SG
16	3.56	445.39	0	3.26	383.55	++	+++	+++	+	-	+++	+	-	++
17	3.79	458.97	0	1.88	417.99	++	+	++	+	+	+++	++	-	+++
18	3.96	462.36	0	1.50	462.45	++	+	+	+	+	+++	++	-	++
19	4.27	482.09	4	2.10	411.60	+++	+	++	+	+	+++	++	-	+++
20	4.51	495.44	4	0.32	446.05	++	-	++	+	++	+++	++	-	+++
21	4.67	499.85	4	1.35	490.5	+	-	++	+	+++	+++	+++	-	+++
22	6.20	573.88	8	2.12	467.71	+++	+++	++	+	++	+++	++	+	++
23	6.44	587.27	8	3.47	502.15	++	++	++	+++	+++	++	+++	++	++
24	6.61	591.69	8	3.44	546.60	-	++	++	+++	+++	++	+++	++	++
25	8.47	686.97	8	3.42	591.85	-	++	+	++	++	++	+++	++	+

26	8.71	700.36	8	5.05	626.29	-	+	+	++	+++	++	+++	+++	+
27	8.87	704.78	8	5.43	670.74	-	+	+	+	+++	++	+++	+++	+
28	5.54	546.41	0	4.45	483.67	++	+++	+	+	+++	++	+++	++	+
29	5.77	559.86	0	1.83	518.11	++	+	+	+++	+++	++	+++	++	+
30	5.94	564.29	0	0.67	562.56	++	+	+	+++	+++	++	+++	+++	+
31	6.25	583.80	4	3.84	511.72	++	+++	+	+	+++	++	+++	++	++
32	6.49	597.23	4	1.36	546.16	++	++	+	+++	++	++	++	++	++
33	6.65	601.67	4	0.30	590.62	+	++	+	+++	+++	++	++	++	++
34	8.18	657.21	8	0.71	567.83	+	+++	+	++	+++	++	+++	++	++
35	8.42	670.60	8	1.04	602.27	+	++	+	++	+++	++	+++	+++	++
36	8.59	675.02	8	1.04	646.72	+	-	+	++	+++	++	+++	+++	+
37	10.45	787.63	8	2.88	691.96	-	+++	+	+++	++	-	+	+	+
38	10.69	800.94	8	4.42	726.41	+	+	+	+++	+++	++	+++	+++	+
39	10.85	806.74	8	5.82	770.86	+	+	+	+++	+++	++	+++	+++	++

In order to draw conclusions from these results and optimize a model for predicting the *in vivo* performance of NIR fluorophores, we attempted to correlate calculated physicochemical predictors with the biodistribution and localization within the targeted tissues. We have noticed a general trend for all of the tissues where the overall hydrophobicity (LogD, pH 7.4) greatly controls the *in vivo* fate of the molecules. Specifically, thyroid gland (TG) targeting seems to be effective within a range of LogD values. Observing the trend in Table 2, we see that the optimum hydrophobicity falls with 3.56 to 6.49. Exemplifying this, we compared the butylated set of indolenine compounds **22-24** that spans the upper range we have set for TG targeting.

Thyroid Gland Targeting NIR Fluorophores

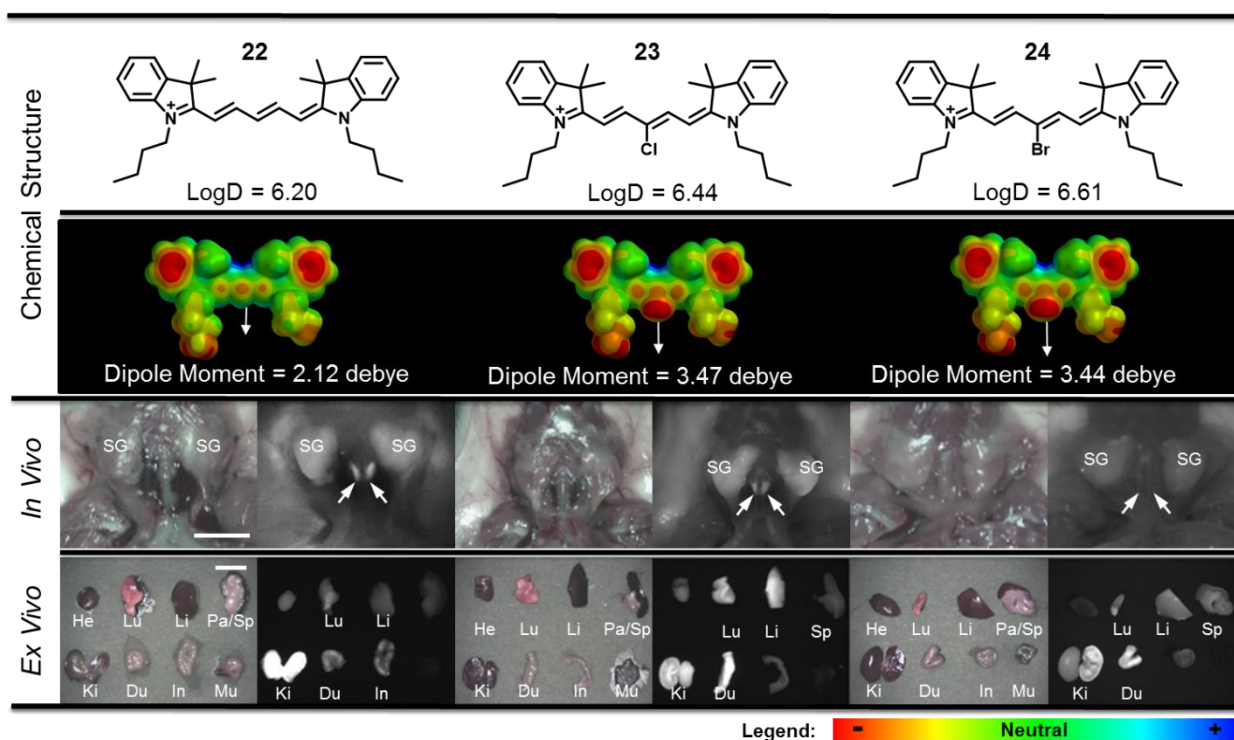


Figure 3-4. Thyroid gland (TG)-targeted NIR fluorophores. 10 nmol of each fluorophore was injected intravenously into CD-1 mice 4 h prior to imaging and resection. Abbreviations used are: Du, duodenum; He, heart; In, intestine; Ki, kidney; Li, liver; Lu, lung; Mu, muscle; Pa, pancreas; SG, salivary gland, and Sp, spleen. Arrows indicate TGs. Scale bars = 1 cm.

The compound with a *meso*-hydrogen atom **22** localizes effectively in the thyroid gland as seen in Figure 2. The addition of *meso*-halogens to the butylated indolenine set of compounds **22-24** drastically lowers the thyroid targeting ability in deference to non-specific uptake in the lung resulting from an increase in hydrophobicity and higher enveloping by macrophages which carry the fluorophore to the liver for destruction and filtration.

Similarly, we expected that since the TG and adrenal gland (AG) are both integrated into the endocrine system, they may be effectively targeted using similar molecular character. When comparing the adrenal gland uptake of compounds **34-36**, all containing a

benzo[*e*]indoleine heterocyclic scaffold with a highly hydrophobic butyl group, we notice that the addition of *meso* halogens greatly reduces the successful targeting abilities. Further examining the AG targeting set, we see that a wide range of LogD values spanning the entire set of compounds (3.56 to 10.85) are tolerated; however, *meso*-halogenation universally reduces the AG retention as seen in Table 2.

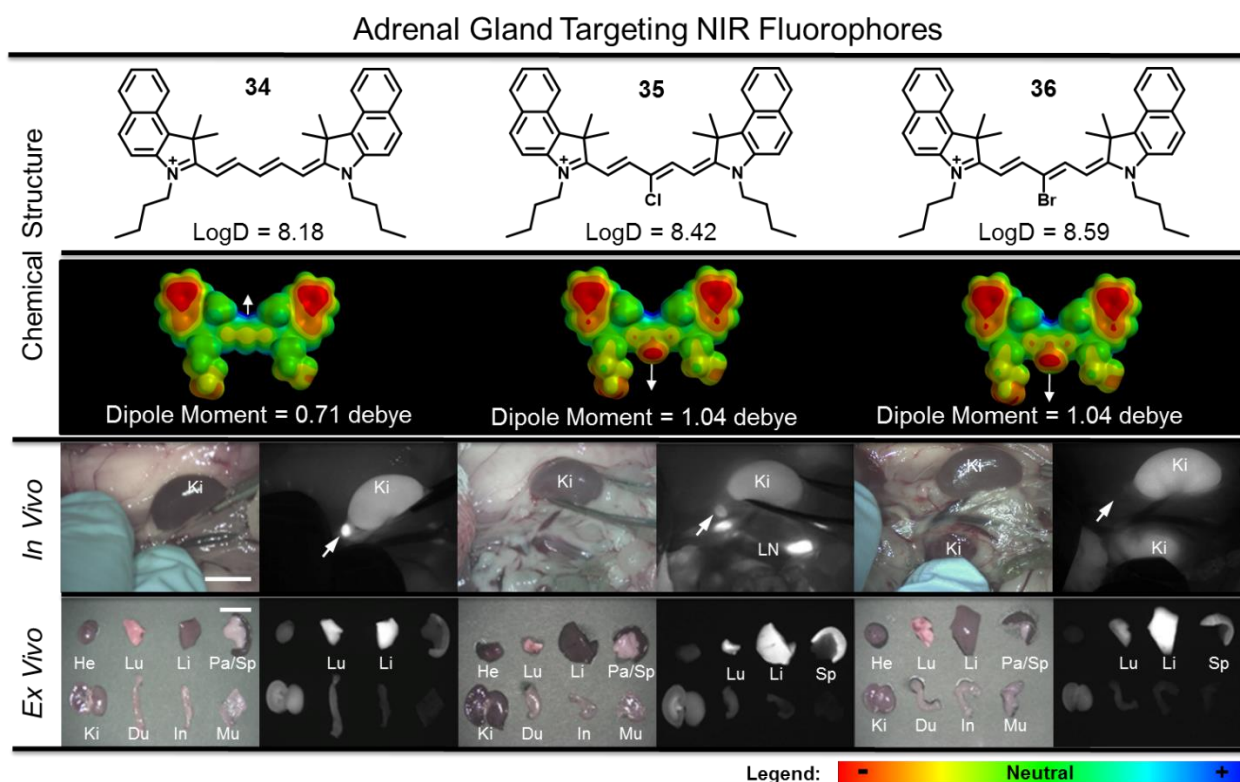


Figure 3-5. Adrenal gland (AG)-targeted NIR fluorophores. 10 nmol of each fluorophore was injected intravenously into CD-1 mice 4 h prior to imaging and resection. Abbreviations used are: Du, duodenum; He, heart; In, intestine; Ki, kidney; Li, liver; LN, lymph nodes; Lu, lung; Mu, muscle; Pa, pancreas; and Sp, spleen. Arrows indicate AGs. Scale bars = 1 cm.

The methylated dyes, **16-18**, showed an interesting trend in pancreatic tissue (Pa) targeting (Figure 4). The non-halogenated **16** (LogD = 3.56) displays increased signal in the pancreas compared to background signal with most of the fluorophore molecules being cleared

through renal filtration; correspondingly, the halogenated compounds, with slightly increased hydrophobicity (LogD = 3.79 and 3.96 respectively) and lower overall dipole moment shown in the electrostatic maps, shows slightly decreased SBR in the pancreas compared to **16**.

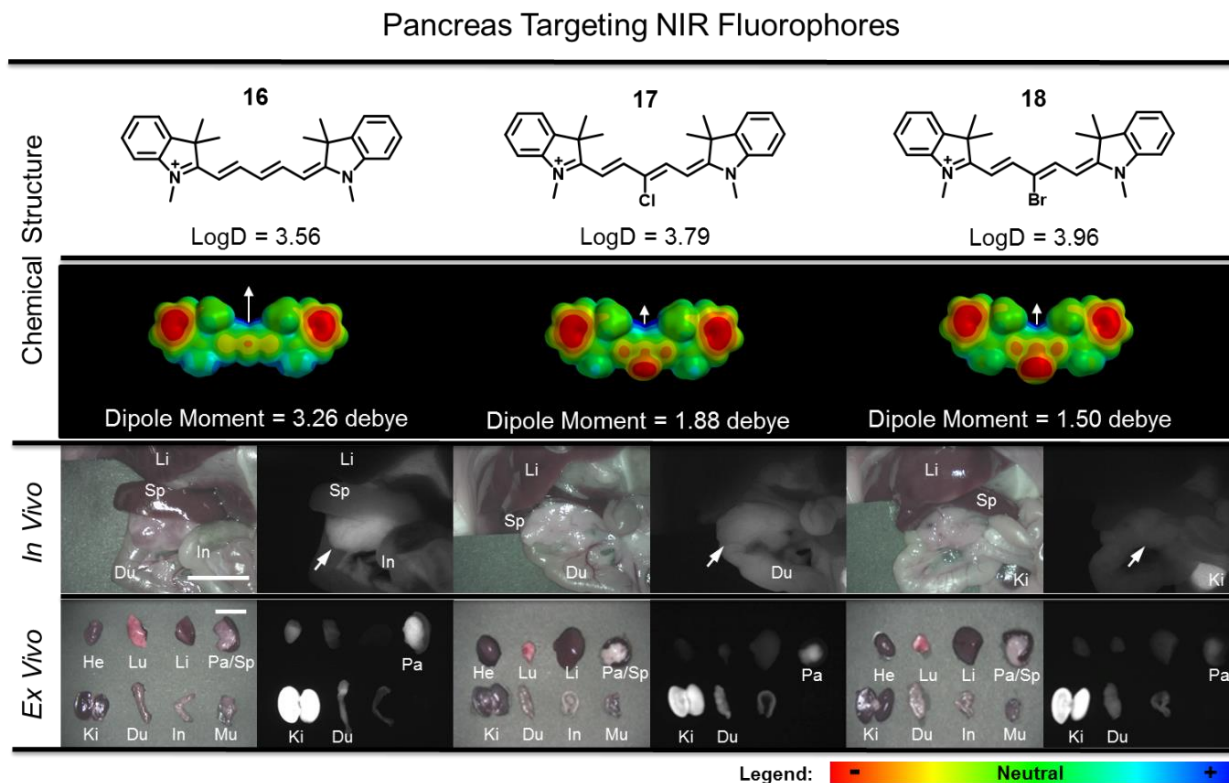


Figure 3-6. Pancreas (Pa)-targeted NIR fluorophores. 10 nmol of each fluorophore was injected intravenously into CD-1 mice 4 h prior to imaging and resection. Abbreviations used are: Du, duodenum; He, heart; In, intestine; Ki, kidney; Li, liver; Lu, lung; Mu, muscle; Pa, pancreas; and Sp, spleen. Arrows indicate Pa. Scale bars = 1 cm.

Observing the entire set of synthesized fluorophores, we observe that the lower LogD compounds with smaller molecular volume and smaller molar mass exhibit higher pancreatic uptake with compound **16** showing excellent localization.

The last tissues that we aimed to target were the lymph nodes (LN), which are critical in locating during surgery to either remove, biopsy or avoid. We see that as a general trend, the compounds exhibiting higher hydrophobicity localize within the LN with higher SBR

compared to more hydrophilic fluorophores; however, closely observing the correlation between LN targeting and LogD reveals that LN localization cannot be solely attributed to the hydrophobic character—though we have observed that the general hydrophobic nature of a compound greatly controls the *in vivo* fate in previous glands.

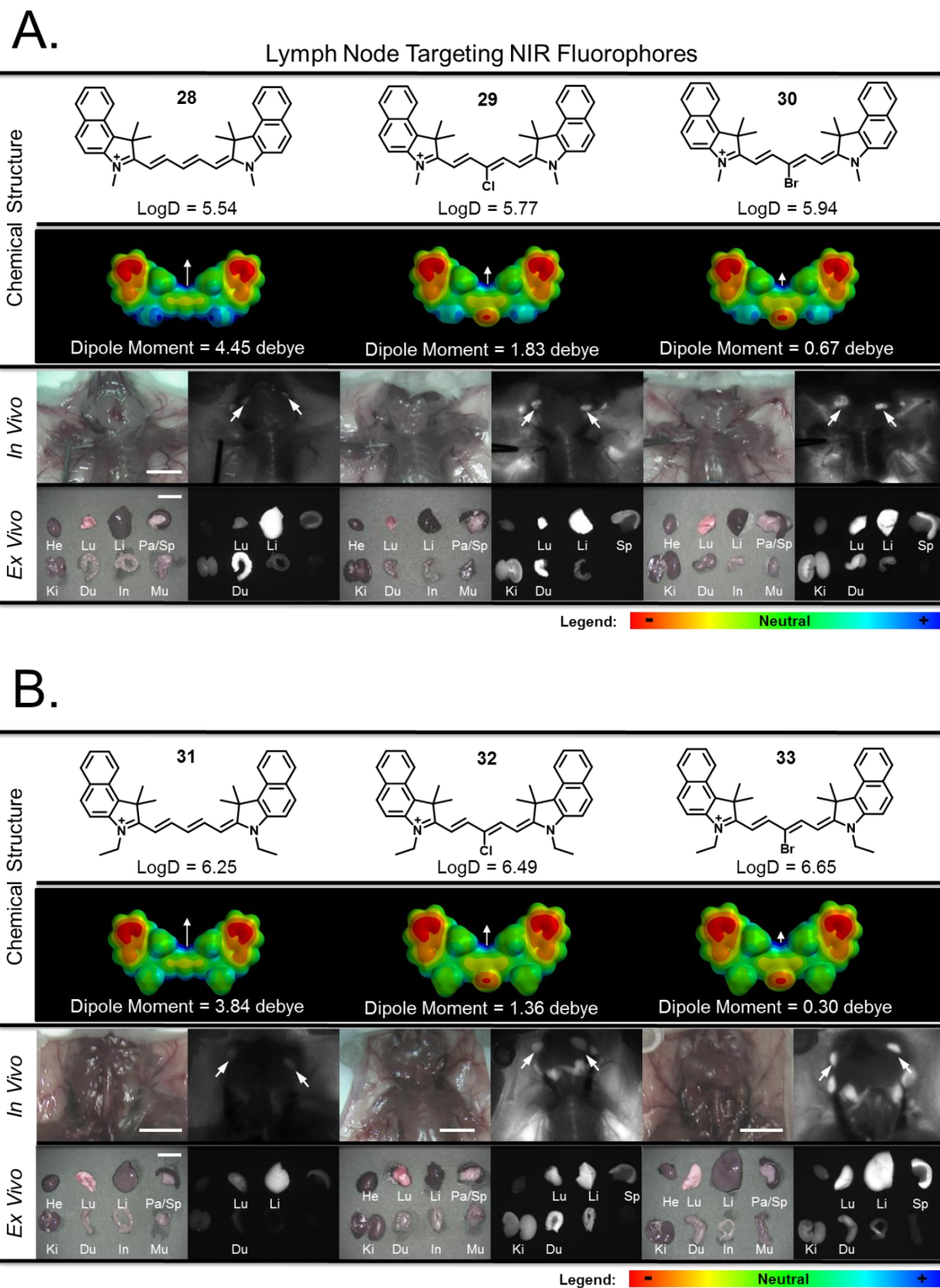


Figure 3-7. Lymph node (LN)-targeted fluorophores. A) Methylated benz[e]indolenine-based cyanines and B) ethylated benz[e]indolenine-based cyanines. 10

nmol of each fluorophore was injected intravenously into CD-1 mice 4 h prior to imaging and resection. Abbreviations used are: Du, duodenum; He, heart; In, intestine; Ki, kidney; Li, liver; Lu, lung; Mu, muscle; Pa, pancreas; and Sp, spleen. Arrows indicate LNs. Scale bars = 1 cm.

Building on this principle, we have noticed that the localization within the lymph node is dependent on hydrophobicity with overall dipole moment acting as a fine-tuning characteristic. It has been previously reported that altering the dipole moment of steroid-based compounds drastically alters the overall biodistribution pattern³³, and we have noticed a similar trend when comparing compounds **28-33**. Compounds bearing a *meso*-hydrogen atom **28** and **31** display very high dipole moments ($\mu > 3.80$ debye); however, the *meso*-halogenated compounds display comparatively low dipole moments ($\mu < 1.85$ debye) due to the inductive electron withdrawing characteristics acting adversely to the overall dipole. Of all the physicochemical descriptors, only net dipole offers an effective explanation for the observation that only *meso*-halogen-bearing compounds localize effectively within the lymph node versus the hydrogen-containing parent compound within the effective LogD range.

3.4 Experimental

3.4.1 Chemicals, Reagents and Synthesis

The chemical reagents used in the synthesis of these compounds were obtained from Acros Organics, Alfa Aesar and Matrix Scientific. The reactions were followed using silica gel 60 F₂₅₄ thin layer chromatography plates (Merck EMD Millipore, Darmstadt, Germany). Open column chromatography was utilized for the purification of all final compounds using 60-200 μ , 60A classic column silica gel (Dynamic Adsorbents, Norcross, GA). The ¹H NMR and ¹³C NMR spectra were obtained using high quality Kontes NMR tubes (Kimble Chase, Vineland,

NJ) rated to 500 MHz and were recorded on a Bruker Avance (400 MHz) spectrometer using DMSO-*d*₆ or MeOD-*d*₄ containing tetramethylsilane (TMS) as an internal calibration standard set to 0.0 ppm. UV-Vis/NIR absorption spectra were recorded on a Varian Cary 50 spectrophotometer. High-resolution accurate mass spectra (HRMS) were obtained either at the Georgia State University Mass Spectrometry Facility using a Waters Q-TOF micro (ESI-Q-TOF) mass spectrometer or utilizing a Waters Micromass LCT TOF ES+ Premier Mass Spectrometer. Liquid chromatography utilized a Waters 2487 single wavelength absorption detector with wavelengths set between 640 and 700 nm depending on the particular photophysical properties. The column used in LC was a Waters Delta-Pak 5 μ M 100A 3.9 x 150 mm reversed phase C₁₈ column. Evaporative light scattering detection analyzes trace impurities that cannot be observed by alternate methods; a SEDEX 75 ELSD was utilized in tandem with liquid chromatography to confirm purity.

Synthesis of pentamethine cyanine precursors 4 and 5. The synthesis of these two reagents has been previously reported by our laboratory, and they were obtained in 88% and 75% yield, respectively.³⁴

General synthetic procedure for the formation of alkylated heterocycles. The alkylation of the commercially obtained heterocyclic structures has been previously reported by our group.³⁵

Synthesis of pentamethine cyanines with varied hydrophobic character. A mixture of individual salts (2 molar equivalents), either malonaldehyde bisphenylimine monohydrochloride **3**, chlorinated analog **4** or brominated analog **5** (1 molar equivalent) and sodium acetate (3 equivalents) were heated to 40 °C for 2-6 hrs in acetic anhydride under

nitrogen atmosphere and then allowed to cool to room temperature. The reaction mixture was concentrated *in vacuo* and the resulting residue was dissolved in a minimum amount of methanol and precipitated after dilution with diethyl ether. The final fluorophores were obtained in analytical purity after column chromatography with 2-5% methanol in DCM as the eluting solvent depending on the relative hydrophobicity of the compound.

1,3,3-Trimethyl-2-((1E,3E,5E)-5-(1,3,3-trimethylindolin-2-ylidene)penta-1,3-dien-1-yl)-3H-indol-1-ium iodide (16): Yield 64%, MP >260 °C, ¹H NMR (400 MHz, MeOD-*d*₄) δ: 1.71 (s, 12H), 3.63 (s, 6H), 6.28 (d, *J* = 16 Hz, 2H), 6.65 (t, *J* = 12 Hz, 1H), 7.24 (t, *J* = 8 Hz, 2H), 7.29 (d, *J* = 8 Hz, 2H), 7.39 (t, *J* = 8 Hz, 2H), 7.48 (d, *J* = 8 Hz, 2H), 8.25 (t, *J* = 12 Hz, 2H); ¹³C NMR (100 MHz, MeOD-*d*₄) δ 27.90, 31.71, 50.50, 104.44, 111.83, 123.31, 126.20, 129.71, 142.56, 144.29, 155.52, 175.28. Accurate mass TOF HRMS *m/z* [M]⁺ calculated for [C₂₇H₃₁N₂]⁺ 383.2487, found 383.2474.

2-((1E,3Z,5E)-3-Chloro-5-(1,3,3-trimethylindolin-2-ylidene)penta-1,3-dien-1-yl)-1,3,3-trimethyl-3H-indol-1-ium iodide (17): Yield 64%, MP 230-232 °C, ¹H NMR (400 MHz, MeOD-*d*₄) δ 1.76 (s, 12H), 3.71 (s, 6H), 6.435 (d, *J* = 12 Hz, 2H), 7.32 (t, *J* = 8 Hz, 2H), 7.39 (d, *J* = 8 Hz, 2H), 7.45 (t, *J* = 8 Hz, 2H), 7.54 (d, *J* = 8 Hz, 2H), 8.345 (d, *J* = 12 Hz, 2H). ¹³C NMR (100 MHz, MeOD-*d*₄) δ 25.03, 29.53, 48.55, 98.93, 110.02, 121.00, 121.86, 124.55, 127.43, 140.42, 141.67, 146.72, 174.28. Accurate mass TOF HRMS *m/z* [M]⁺ calculated for [C₂₇H₃₀N₂Cl]⁺ 417.2098 found 417.2107.

2-((1E,3Z,5E)-3-Bromo-5-(1,3,3-trimethylindolin-2-ylidene)penta-1,3-dien-1-yl)-1,3,3-trimethyl-3H-indol-1-ium iodide (18): Yield 61%, MP 230-232 °C, ¹H NMR (400 MHz, CDCl₃-*d*₁) δ 1.91 (s, 12H), 3.82 (s, 6H), 6.36 (d, 8 Hz, 2H), 7.16 (d, 8 Hz, 2H), 7.26-7.31 (m,

4H), 7.39-7.44 (m, 4H) 8.93 (d, 12 Hz, 2H). ^{13}C NMR (100 MHz, DMSO- d_6) δ 27.04, 31.98, 49.85, 102.61, 112.19, 115.98, 122.94, 125.97, 128.93, 141.78, 143.02, 149.64, 175.14. Accurate mass TOF HRMS m/z $[\text{M}]^+$ calculated for $[\text{C}_{27}\text{H}_{30}\text{N}_2\text{Br}]^+$ 461.1592 found 461.1585.

1-Ethyl-2-((1E,3E,5E)-5-(1-ethyl-3,3-dimethylindolin-2-ylidene)penta-1,3-dien-1-yl)-3,3-dimethyl-3H-indol-1-ium iodide (19): Yield: 62%, MP > 260°C, ^1H NMR (400 MHz, DMSO- d_6) δ : 1.27 (t, $J = 8$ Hz, 6H), 1.68 (s, 12H), 4.14 (d, $J = 8$ Hz, 4H), 6.30 (d, $J = 16$ Hz), 6.57 (t, $J = 12$ Hz, 1H), 7.26 (s, 2H), 7.39 (s, 4H), 7.62 (d, $J = 8$ Hz, 2H), 8.34 (t, $J = 12$ Hz, 2H). ^{13}C NMR (100 MHz, DMSO- d_6) δ : 12.14, 27.05, 48.90, 102.74, 110.85, 122.47, 124.69, 125.35, 128.44, 141.21, 141.55, 154.16, 172.20. Accurate mass TOF HRMS m/z $[\text{M}]^+$ calculated for $[\text{C}_{29}\text{H}_{35}\text{N}_2]^+$ 411.2880 found 411.2820.

2-((1E,3Z,5E)-3-Chloro-5-(1-ethyl-3,3-dimethylindolin-2-ylidene)penta-1,3-dien-1-yl)-1-ethyl-3,3-dimethyl-3H-indol-1-ium iodide (20): Yield 71%, MP >260 °C ^1H NMR (400 MHz, DMSO- d_6) δ 1.35 (d, $J = 6.8$ Hz, 6H), 1.74 (s, 12H), 4.23 (q, $J = 6.8$ Hz, 4H), 6.32 (d, $J = 13.2$ Hz, 2H), 7.32 (t, $J = 7.2$ Hz, 2H), 7.45 (t, $J = 7.2$ Hz, 2H), 7.50 (d, $J = 7.2$ Hz, 2H), 7.67 (d, $J = 7.2$ Hz, 2H), 8.45 (d, $J = 13.2$ Hz, 2H). ^{13}C NMR (100 MHz, DMSO- d_6) δ 12.46, 27.20, 39.65, 49.97, 99.93, 112.04, 122.71, 123.05, 126.02, 129.04, 141.82, 142.05, 148.05, 174.30. Accurate mass TOF HRMS m/z $[\text{M}]^+$ calculated for $[\text{C}_{29}\text{H}_{34}\text{N}_2\text{Cl}]^+$ 446.0462 found 446.0496.

2-((1E,3Z,5E)-3-Bromo-5-(1-ethyl-3,3-dimethylindolin-2-ylidene)penta-1,3-dien-1-yl)-1-ethyl-3,3-dimethyl-3H-indol-1-ium iodide (21): Yield 59%, MP >250°C, ^1H NMR (400 MHz, DMSO- d_6): δ 1.32 (s, 6H), 1.70 (s, 12H), 4.21 (s, 4H), 6.31(d, $J = 12$ Hz, 2H), 7.31 (s, 2H), 7.43 (d, 2H), 7.50 (s, 2H), 7.69 (d, $J = 8$ Hz, 2H), 8.50 (d, $J = 16$ Hz, 2H); ^{13}C NMR (100 MHz, DMSO- d_6): δ 11.52, 26.11, 48.99, 101.17, 111.08, 115.09, 122.17, 125.07, 128.07,

140.78, 140.98, 148.96, 173.28. Accurate mass TOF HRMS m/z $[M]^+$ calculated for $[C_{29}H_{34}N_2Br]^+$ 489.1900 found 489.1879.

1-Butyl-2-((1E,3E,5E)-5-(1-butyl-3,3-dimethylindolin-2-ylidene)penta-1,3-dien-1-yl)-3,3-dimethyl-3H-indol-1-ium iodide (22): Yield: 48%, MP > 260°C, 1H NMR (400 MHz, DMSO- d_6) δ : 0.91 (t, $J = 8$ Hz, 6H), 1.37 (q, $J = 8$ Hz, 4H), 1.66 (s, 16H), 4.08 (s, 4H), 6.3 (d, $J = 16$ Hz, 2H), 6.59 (t, $J = 12$ Hz, 1H), 7.23 (s, 2H), 7.38 (s, 4H), 7.60 (d, $J = 8$ Hz, 2H), 8.33 (t, $J = 12$ Hz, 2H). ^{13}C NMR (100 MHz, DMSO- d_6) δ : 13.39, 19.11, 26.80, 28.73, 42.84, 48.52, 102.81, 110.74, 122.09, 124.31, 125.25, 128.07, 140.75, 141.65, 153.65, 172.26. Accurate mass TOF HRMS m/z $[M]^+$ calculated for $[C_{33}H_{43}N_2]^+$ 467.3426 found 467.3412

1-Butyl-2-((1E,3Z,5E)-5-(1-butyl-3,3-dimethylindolin-2-ylidene)-3-chloropenta-1,3-dien-1-yl)-3,3-dimethyl-3H-indol-1-ium iodide (23): Yield 60%, MP 206-208 °C, 1H NMR (400 MHz, MeOD- d_4) δ 1.07 (t, 7.4 Hz, 6H), 1.48-1.58 (m, 4H), 1.78 (s, 12H), 1.83 (p, 7.6 Hz, 4H), 4.22 (t, 8.0 Hz, 4H), 6.50 (d, 13.6 Hz, 2H), 7.35 (t, 8.0 Hz, 2H), 7.41 (d, 8.0 Hz, 2H), 7.47 (t, 8.0 Hz, 2H), 7.57 (d, 7.2 Hz, 2H), 8.38 (d, 13.6 Hz, 2H). ^{13}C NMR (100 MHz, DMSO- d_6) δ 14.02, 19.96, 27.28, 29.43, 44.23, 49.94, 100.38, 112.26, 122.77, 123.01, 126.02, 129.02, 141.92, 142.28, 147.83, 174.75. Accurate mass TOF HRMS m/z $[M]^+$ calculated for $[C_{33}H_{42}N_2Cl]^+$ 501.3037 found 501.3059.

2-((1E,3Z,5E)-3-Bromo-5-(1-butyl-3,3-dimethylindolin-2-ylidene)penta-1,3-dien-1-yl)-1-butyl-3,3-dimethyl-3H-indol-1-ium iodide (24): Yield 73%, MP 192-194 °C, 1H NMR (400 MHz, DMSO- d_6): δ 0.95 (t, $J = 8$ Hz, 6H), 1.43-1.35 (m, 4H), 1.81-1.70 (m, 16 H), 4.18 (t, $J = 8$ Hz, 4H), 6.355 (d, $J = 12$ Hz, 2H), 7.32 (t, $J = 8$ Hz, 2H), 7.45 (t, $J = 8$ Hz, 2H), 7.52 (d, $J = 8$ Hz, 2H), 7.68 (d, $J = 8$ Hz, 2H), 8.505 (d, $J = 12$ Hz, 2H). ^{13}C NMR (100 MHz,

DMSO- d_6): δ 14.15, 20.03, 27.17, 29.40, 44.21, 49.96, 102.62, 112.30, 116.14, 123.09, 126.06, 129.04, 141.87, 142.80, 174.80. Accurate mass TOF HRMS m/z $[M]^+$ calculated for $[C_{33}H_{42}N_2Br]^+$ 545.2531 found 545.2532.

2-((1*E*,3*E*,5*E*)-5-(3,3-Dimethyl-1-(3-phenylpropyl)indolin-2-ylidene)penta-1,3-dien-1-yl)-3,3-dimethyl-1-(3-phenylpropyl)-3*H*-indol-1-ium iodide (**25**): Yield 49%, MP 185-187°C, 1H NMR (400 MHz, DMSO- d_6) δ 1.68 (s, 12H), 2.01 (t, $J = 8$ Hz, 4H), 2.74 (t, $J = 8$ Hz, 4H), 4.15 (t, $J = 8$ Hz, 4H), 6.075 (d, $J = 12$ Hz, 2H), 6.46 (t, $J = 12$ Hz, 1H), 7.40-7.24 (m, 16H), 7.62 (d, $J = 8$ Hz, 2H), 8.33 (t, $J = 12$ Hz, 2H). ^{13}C NMR (100 MHz, DMSO- d_6) δ 27.60, 29.16, 32.58, 43.55, 49.40, 103.58, 111.47, 122.93, 125.19, 125.19, 125.97, 128.71, 128.91, 141.43, 141.43, 142.46, 154.54, 173.11. Accurate mass TOF HRMS m/z $[M]^+$ calculated for $[C_{43}H_{47}N_2]^+$ 591.3739, found 591.3741.

2-((1*E*,3*Z*,5*E*)-3-Chloro-5-(3,3-dimethyl-1-(3-phenylpropyl)indolin-2-ylidene)penta-1,3-dien-1-yl)-3,3-dimethyl-1-(3-phenylpropyl)-3*H*-indol-1-ium iodide (**26**): Yield 53%, MP 125-127 °C, 1H NMR (400 MHz, $CDCl_3$ - d_1) δ 1.94 (s, 12H), 2.20 (t, $J = 8.0$ Hz, 4H), 2.84 (t, $J = 8.0$ Hz, 4H), 4.05 (t, $J = 8.0$ Hz, 4H), 6.24 (d, $J = 16.0$ Hz, 2H), 6.97 (d, $J = 8.0$ Hz, 2H), 7.21-7.38 (m, 16H), 9.05 (d, $J = 12.0$ Hz, 2H). ^{13}C NMR (100 MHz, DMSO- d_6) δ 27.24, 28.68, 32.66, 44.07, 49.93, 100.26, 112.14, 122.88, 123.00, 126.02, 126.58, 128.69, 128.95, 128.99, 141.10, 141.93, 142.24, 147.96, 174.63 Accurate mass TOF HRMS m/z $[M]^+$ calculated for $[C_{43}H_{46}ClN_2]^+$ 625.3350 found 625.3369.

2-((1*E*,3*Z*,5*E*)-3-Bromo-5-(3,3-dimethyl-1-(3-phenylpropyl)indolin-2-ylidene)penta-1,3-dien-1-yl)-3,3-dimethyl-1-(3-phenylpropyl)-3*H*-indol-1-ium iodide (**27**): Yield 31%, MP 189-191°C, 1H NMR (400 MHz, DMSO- d_6) δ 1.69 (s, 12H), 2.05 (t, $J = 8$ Hz, 4H), 2.77 (t, J

= 8 Hz, 4H), 4.16 (t, $J = 8$ Hz, 4H), 6.155 (d, $J = 12$ Hz, 2H), 7.49-7.25 (m, 16H), 7.68 (d, $J = 8$ Hz, 2H), 8.485 (t, $J = 12$ Hz, 2H). ^{13}C NMR (100 MHz, DMSO- d_6) δ 27.21, 28.70, 32.75, 44.18, 49.96, 102.60, 112.17, 116.28, 123.02, 126.05, 126.59, 128.74, 128.98, 141.10, 141.92, 142.23, 149.91, 174.80. Accurate mass TOF HRMS m/z $[\text{M}]^+$ calculated for $[\text{C}_{43}\text{H}_{46}\text{BrN}_2]^+$ 669.2839, found 669.1030.

1,1,3-Trimethyl-2-((1E,3E,5E)-5-(1,1,3-trimethyl-1H-benzo[e]indol-2(3H)-ylidene)penta-1,3-dien-1-yl)-1H-benzo[e]indol-3-ium iodide (28): Yield 80%, MP >260 °C, ^1H NMR (400 MHz, DMSO- d_6) δ 1.95 (s, 12H), 3.73 (s, 6H), 6.325 (d, $J = 12$ Hz, 2H), 6.59 (t, $J = 12.0$ Hz, 1H), 7.52 (t, $J = 8.0$ Hz, 2H), 7.67 (t, $J = 8.0$ Hz, 2H), 7.74 (d, $J = 8.0$ Hz, 2H), 8.06 (t, $J = 8.0$ Hz, 4H), 8.24 (d, $J = 8.0$ Hz, 2H), 8.465 (t, $J = 12.0$ Hz, 2H). ^{13}C NMR (100 MHz, DMSO- d_6) δ 26.61, 31.47, 50.58, 102.98, 111.53, 122.09, 124.65, 125.26, 127.48, 127.66, 129.87, 130.12, 131.23, 132.90, 140.39, 152.77, 174.114. Accurate mass TOF HRMS m/z $[\text{M}]^+$ calculated for $[\text{C}_{35}\text{H}_{35}\text{N}_2]^+$ 483.2800, found 483.2818.

2-((1E,3Z,5E)-3-Chloro-5-(1,1,3-trimethyl-1H-benzo[e]indol-2(3H)-ylidene)penta-1,3-dien-1-yl)-1,1,3-trimethyl-1H-benzo[e]indol-3-ium iodide (29): Yield 53%, MP 206-208 °C, ^1H NMR (400 MHz, DMSO- d_6) δ 2.00 (s, 12H), 3.83 (s, 6H), 6.365 (d, 12.0 Hz, 2H), 7.56 (t, 8.0 Hz, 2H), 7.72 (t, 8.0 Hz, 2H), 7.85 (d, 8.0 Hz, 2H), 8.08-8.15 (m, 4H), 8.29 (d, 8.0 Hz, 2H), 8.60 (d, 16.0 Hz, 2H). ^{13}C NMR (100 MHz, DMSO- d_6) δ 26.73, 32.36, 51.50, 99.98, 112.27, 122.58, 122.67, 125.59, 127.80, 128.34, 130.39, 130.77, 132.05, 134.10, 140.61, 146.66, 175.96. Accurate mass TOF HRMS m/z $[\text{M}]^+$ calculated for $[\text{C}_{35}\text{H}_{34}\text{N}_2\text{Cl}]^+$ 517.2411, found 517.2401.

2-((1E,3Z,5E)-3-Bromo-5-(1,1,3-trimethyl-1H-benzo[e]indol-2(3H)-ylidene)penta-1,3-dien-1-yl)-1,1,3-trimethyl-1H-benzo[e]indol-3-ium iodide (30): Yield 90%, MP 229-230 °C, ¹H NMR (400 MHz, DMSO-*d*₆) δ 1.97 (s, 12H), 3.80 (s, 6H), 6.345 (d, *J* = 12 Hz, 2H), 7.53 (t, 8 Hz, 2H), 7.69 (t, *J* = 8 Hz, 2H), 7.83 (d, *J* = 8 Hz, 2H), 8.12-8.07 (m, 4H), 8.26 (d, *J* = 8 Hz, 2H), 8.635 (d, *J* = 12 Hz, 2H). ¹³C NMR (100 MHz, DMSO-*d*₆) δ 25.91, 31.56, 50.78, 101.49, 111.54, 115.27, 121.88, 124.78, 127.01, 127.51, 129.61, 129.95, 131.27, 133.26, 139.85, 147.91, 175.31. Accurate mass TOF HRMS *m/z* [M]⁺ calculated for [C₃₅H₃₄N₂Br]⁺ 561.1905 found 561.1914

3-Ethyl-2-((1E,3E,5E)-5-(3-ethyl-1,1-dimethyl-1H-benzo[e]indol-2(3H)-ylidene)penta-1,3-dien-1-yl)-1,1-dimethyl-1H-benzo[e]indol-3-ium iodide (31): Yield 79%, MP 266-268 °C, ¹H NMR (400 MHz, DMSO-*d*₆) δ 1.333 (t, *J* = 8 Hz, 6H), 1.962 (s, 12H), 4.297 (t, *J* = 8 Hz, 4H), 6.37 (d, *J* = 12 Hz, 2H), 6.637 (t, *J* = 12 Hz, 1H), 7.51 (t, *J* = 8 Hz, 2H), 6.68 (t, *J* = 8 Hz, 2H), 7.74 (d, *J* = 8 Hz, 2H), 8.08 (t, *J* = 8 Hz, 4H), 8.25 (d, *J* = 8 Hz, 2H), 8.46 (t, *J* = 12 Hz, 2H). ¹³C NMR (100 MHz, DMSO-*d*₆) δ 11.96, 26.17, 48.04, 50.19, 102.05, 110.90, 121.58, 124.20, 125.07, 127.11, 127.19, 129.39, 129.83, 130.76, 132.72, 138.77, 152.54, 172.71. Accurate mass TOF HRMS *m/z* [M]⁺ calculated for [C₃₇H₃₉N₂]⁺ 511.3113, found 511.3098.

2-((1E,3Z,5E)-3-Chloro-5-(3-ethyl-1,1-dimethyl-1H-benzo[e]indol-2(3H)-ylidene)penta-1,3-dien-1-yl)-3-ethyl-1,1-dimethyl-1H-benzo[e]indol-3-ium iodide (32): Yield 68%, MP 231-233 °C, ¹H NMR (400 MHz, DMSO-*d*₆): δ 1.39 (s, 6H), 2.00 (s, 12H), 4.37 (s, 4H), 6.38 (d, *J* = 16 Hz, 2H), 7.55 (t, 2H), 7.73 (t, 2H), 7.84 (d, *J* = 8 Hz, 2H), 8.12 (m, 4H), 8.27 (d, *J* = 4 Hz, 2H) 8.65 (d, *J* = 16 Hz, 2H); ¹³C NMR (100 MHz, DMSO-*d*₆): δ 11.81, 25.80, 50.72, 98.52, 111.19, 121.60, 121.71, 124.67, 126.96, 127.37, 129.47, 130.01, 131.15,

133.41, 138.56, 146.10, 174.17. Accurate mass TOF HRMS m/z $[M]^+$ calculated for $[C_{37}H_{38}N_2Cl]^+$ 545.2724, found 545.2717.

2-((1E,3Z,5E)-3-Bromo-5-(3-ethyl-1,1-dimethyl-1H-benzo[e]indol-2(3H)-ylidene)penta-1,3-dien-1-yl)-3-ethyl-1,1-dimethyl-1H-benzo[e]indol-3-ium iodide (33): Yield 50%. MP 226-229 °C, 1H NMR (400 MHz, MeOD- d_4) δ 1.553 (t, 7.2 Hz, 6H), 2.091 (s, 12H), 4.404 (q, 7.6 Hz, 4H), 6.588 (d, 13.6 Hz, 2H), 7.567 (t, 8 Hz, 2H), 7.736 (t, 8 Hz, 2H), 8.066 (d, 8.4 Hz, 2H), 8.104 (d, 8.8 Hz, 2H), 8.3115 (d, 8.4 Hz, 2H), 8.561 (d, 13.6 Hz, 2H). ^{13}C NMR (100 MHz, DMSO- d_6) δ 12.65, 26.79, 51.72, 101.80, 112.07, 116.01, 122.65, 125.71, 127.94, 128.05, 128.37, 130.44, 131.01, 132.14, 134.46, 139.46, 148.98, 175.39. Accurate mass TOF HRMS m/z $[M]^+$ calculated for $[C_{37}H_{38}N_2Br]^+$ 589.2218 found 589.2204.

3-Butyl-2-((1E,3E,5E)-5-(3-butyl-1,1-dimethyl-1H-benzo[e]indol-2(3H)-ylidene)penta-1,3-dien-1-yl)-1,1-dimethyl-1H-benzo[e]indol-3-ium iodide (34): Yield 74%, MP 164-166 °C, 1H NMR (400 MHz, DMSO- d_6) δ 0.940 (t, 6.8 Hz, 6H), 1.42-1.44 (m, 4H), 1.725 (bs, 4H), 1.955 (s, 12H), 4.240 (bs, 4H), 6.380 (d, 13.6 Hz, 2H), 6.687 (t, 13.6 Hz, 1H), 7.495 (t, 6.8 Hz, 2H), 7.650 (t, 6.8 Hz, 2H), 7.745 (d, 8.4 Hz, 2H), 8.056 (t, 8.8 Hz, 4H), 8.245 (d, 8.4 Hz, 2H), 8.474 (t 12.8 Hz, 2H). ^{13}C NMR (100 MHz, DMSO- d_6) δ 14.28, 19.79, 27.28, 29.87, 43.71, 51.17, 103.45, 103.48, 112.09, 122.61, 125.05, 125.22, 128.06, 128.13, 128.21, 130.36, 130.76, 130.83, 131.72, 133.63, 140.16, 174.10. Accurate mass TOF HRMS m/z $[M]^+$ calculated for $[C_{41}H_{47}N_2]$ 567.3734 found 567.3718.

3-Butyl-2-((1E,3Z,5E)-5-(3-butyl-1,1-dimethyl-1H-benzo[e]indol-2(3H)-ylidene)-3-chloropenta-1,3-dien-1-yl)-1,1-dimethyl-1H-benzo[e]indol-3-ium iodide (35): Yield 67%, MP 160-163 °C, 1H NMR (400 MHz, DMSO- d_6) δ 1.00 (t, 8 Hz, 6H), 1.42-1.49 (m, 4H), 1.81 (p,

8 Hz, 4H), 2.01 (s, 12H), 4.34 (t, 8 Hz, 4H), 6.42 (d, 16 Hz, 2H), 7.57 (t, 8 Hz, 2H), 7.73 (t, 8 Hz, 2H), 8.12 (d, 12 Hz, 2H), 8.29 (8 Hz, 2H), 8.63 (d, 16 Hz, 2H). ^{13}C NMR (100 MHz, DMSO- d_6) δ 14.11, 19.94, 26.91, 29.67, 44.29, 51.64, 99.97, 112.29, 122.68, 125.72, 127.88, 128.39, 130.42, 130.95, 132.09, 134.34, 139.90, 146.80, 173.03, 175.67. Accurate mass TOF HRMS m/z $[\text{M}]^+$ calculated for $[\text{C}_{41}\text{H}_{46}\text{N}_2\text{Cl}]^+$ 601.3350 found 601.3350.

2-((1E,3Z,5E)-3-Bromo-5-(3-butyl-1,1-dimethyl-1H-benzo[e]indol-2(3H)-ylidene)penta-1,3-dien-1-yl)-3-butyl-1,1-dimethyl-1H-benzo[e]indol-3-ium iodide (36): Yield 74%, MP 153-156 °C, ^1H NMR (400 MHz, DMSO- d_6) δ 0.96 (t, $J = 8$ Hz, 6H), 1.46-1.40 (m, 4H), 1.83-1.75 (m, 4H), 1.99 (s, 12H), 4.30 (s, 4H), 6.405 (d, $J = 12$ Hz, 2H), 7.55 (d, $J = 8$ Hz, 2H), 7.70 (t, $J = 8$ Hz, 2H), 7.845 (d, $J = 12$ Hz, 2H), 7.10 (t, $J = 12$ Hz, 4H), 8.27 ($J = 8$ Hz, 2H), 8.655 (d, $J = 12$ Hz, 2H). ^{13}C NMR (100 MHz, DMSO- d_6) δ 13.36, 19.19, 26.05, 28.82, 50.89, 101.49, 111.55, 121.89, 124.89, 127.07, 127.55, 129.61, 130.12, 131.29, 133.46, 139.13, 148.01, 174.93 Accurate mass TOF HRMS m/z $[\text{M}]^+$ calculated for $[\text{C}_{41}\text{H}_{46}\text{N}_2\text{Br}]^+$ 645.2844 found 645.2866.

2-((1E,3E,5E)-5-(1,1-Dimethyl-3-(3-phenylpropyl)-1H-benzo[e]indol-2(3H)-ylidene)penta-1,3-dien-1-yl)-1,1-dimethyl-3-(3-phenylpropyl)-1H-benzo[e]indol-3-ium iodide (37): Yield 33%, MP 95-98 °C, ^1H NMR (400 MHz, DMSO- d_6) δ 1.95 (s, 12H), 2.05 (t, 8.4 Hz, 4H), 2.78 (t, $J = 8.0$ Hz, 4H), 4.29 (t, $J = 6.8$ Hz, 4H), 6.27 (d, $J = 13.6$, 2H), 6.55 (t, $J = 12.4$ Hz, 1H), 7.31-7.17 (m, 10H), 7.49 (t, $J = 11.2$ Hz, 2H), 7.72-7.64 (m, 4H), 8.07-8.03 (m, 4H), 8.24 (d, $J = 8.4$, 2H), 8.49 (t, $J = 13.2$, 2H). ^{13}C NMR (100 MHz, DMSO- d_6) δ 27.24, 29.53, 32.55, 43.74, 51.19, 103.40, 112.01, 119.44, 122.59, 125.21, 125.54, 128.05, 128.19, 128.73, 128.90, 130.38, 130.75, 131.74, 133.63, 140.13, 141.49, 153.41, 174.13. Accurate mass TOF HRMS m/z $[\text{M}]^+$ calculated for $[\text{C}_{51}\text{H}_{51}\text{N}_2]^+$ 691.4052 found 691.4028.

2-((1E,3Z,5E)-3-Chloro-5-(1,1-dimethyl-3-(3-phenylpropyl)-1H-benzo[e]indol-2(3H)-ylidene)penta-1,3-dien-1-yl)-1,1-dimethyl-3-(3-phenylpropyl)-1H-benzo[e]indol-3-ium iodide

(38): Yield 47%, MP 134-136 °C, ¹H NMR (400 MHz, DMSO-*d*₆) δ 1.98 (s, 12H), 2.04 (t, 4 Hz, 4H), 2.82 (t, 4 Hz, 4H), 4.31 (t, 8 Hz, 4H), 6.235 (d, 16 Hz, 2H), 7.23-7.36 (m, 10H), 7.57 (t, 8 Hz, 2H), 7.72 (t, 8 Hz, 2H), 7.82 (d, 8 Hz, 2H), 8.12 (t, 8 Hz, 4H), 8.28 (d, 8 Hz, 2H), 8.585 (d, 12 Hz, 2H). ¹³C NMR (100 MHz, DMSO-*d*₆) δ 27.65, 29.77, 33.39, 44.93, 52.44, 100.59, 112.99, 123.47, 123.60, 126.49, 127.42, 128.68, 129.17, 129.55, 129.80, 131.22, 131.73, 132.90, 135.16, 140.62, 141.89, 147.75, 176.31. Accurate mass TOF HRMS m/z [M]⁺ calculated for [C₅₁H₅₀N₂Cl]⁺ 725.3663 found 725.3663.

2-((1E,3Z,5E)-3-Bromo-5-(1,1-dimethyl-3-(3-phenylpropyl)-1H-benzo[e]indol-2(3H)-ylidene)penta-1,3-dien-1-yl)-1,1-dimethyl-3-(3-phenylpropyl)-1H-benzo[e]indol-3-ium iodide

(39): Yield 58%, MP 143-145 °C, ¹H NMR (400 MHz, DMSO-*d*₆) δ 1.98 (s, 12H), 2.13 (t, 8 Hz, 4H), 2.83 (t, 8 Hz, 4H), 4.31 (t, 8 Hz, 4H), 6.24 (d, 12 Hz, 2H), 7.23-7.36 (m, 10H), 7.57 (t, 8 Hz, 2H), 7.72 (t, 8 Hz, 2H), 7.83 (d, 8 Hz, 2H), 8.12 (t, 8 Hz, 4H), 8.28 (d, 8 Hz, 2H), 8.615 (d, 12 Hz, 2H); ¹³C NMR (100 MHz, DMSO-*d*₆) δ 26.96, 28.99, 32.76, 44.41, 51.72, 102.30, 112.30, 112.21, 116.44, 122.68, 125.68, 126.60, 127.96, 128.35, 128.77, 128.99, 130.42, 130.92, 132.21, 134.41, 139.89, 141.13, 148.91, 175.78. Accurate mass TOF HRMS m/z [M]⁺ calculated for [C₅₁H₅₀N₂Br]⁺ 769.3157, found 769.3138.

3.4.2 Optical Property Measurements and Physicochemical Predictions.

All optical measurements were performed in various solvents, including ethanol (200 proof, Fischer Chemical), dimethyl sulfoxide (DMSO, 99.9% Acros Organics), phosphate buffered saline (PBS, pH 7.4, Fischer Scientific) and at 37°C in 100% fetal bovine serum (FBS,

Fischer Scientific) buffered with 50 mM HEPES, pH 7.4. Absorbance and fluorescence emission spectra of the series of NIR fluorophores were measured using Varian Cary 50 absorbance spectrophotometer (190–1100 nm) and Shimadzu RF-5301PC spectrofluorometer (350–1000 nm). For fluorescence quantum yield (QY) measurements, rhodamine 800 in absolute ethanol (QY = 28%) was used as a calibration standard, under conditions of matched absorbance at 640 nm. *In silico* calculations of physicochemical distribution coefficient (logD at pH 7.4) was calculated using Marvin and JChem calculator plugins (ChemAxon, Budapest, Hungary). Electrostatic maps were calculated using Spartan DFT calculations at the B3LYP level.

3.4.3 LC-MS Spectroscopy.

The purity of all compounds was measured using liquid chromatography-mass spectrometry (LC-MS) on a Waters system consisting of a 1525 binary HPLC pump with a manual 7725i Rheodyne injector, a 996 Photodiode Array (PDA) detector, and a 2475 multiwavelength fluorescence detector. The column eluent was divided in 2 using a flow splitter (Upchurch Scientific). A portion of the eluent flowed into an ELSD (Richards Scientific) while the rest flowed into a Micromass LCT ESI-TOF spectrometer (Waters) equipped with a Symmetry (R) C18 (4.6 x 150 mm, 5 μ m) reverse-phase HPLC column. For mass spectrometry mobile phase was solvent A = 0.1% formic acid (FA) in water and solvent B = CH₃CN with 95% A for 5 min and a linear gradient from 5% to 40% CH₃CN (from A to B for 30 min) at a flow rate of 1 mL/min, capillary voltage was -3317V, and sample cone voltage was -50V.

3.4.4 Optical Imaging System and Fluorescence Microscopy.

The real-time intraoperative FLARE imaging system has been described in detail previously.^{27, 28} In this study, 670 nm excitation was used at a fluence rate of 4 mW/cm², with white light (400-650 nm) at 40,000 lx. Color and NIR fluorescence images were acquired

simultaneously with custom software at rates up to 15 Hz over a 15 cm diameter field of view. The imaging system was positioned at a distance of 18 inches from the surgical field. The wavelength used for excitation and emission filters was 650 ± 22 nm.

3.5 Conclusions

As the clinical need for intraoperative NIR contrast agents reaches a critical level, we have successfully generated a series of pentamethine cyanine fluorophores for the targeting of vital tissues that should be carefully avoided during surgery. The targetability of these compounds represents the first successful correlation of tissue-specific contrast agents with their physicochemical properties reported to date that could help solve an unmet clinical need in image-guided surgery. We are currently investigating the cellular targets that explain this interesting phenomenon which will be thoroughly explored in subsequent publications. Additionally, it should be noted that the physiological filtration and clearance pathways of these compounds are highly consistent with the Lipinski's rules with the more hydrophobic compounds being observed in the liver and the less hydrophobic contrast agents being cleared through renal filtration.

3.6 References

1. Zhu, N.; Mondal, S.; Gao, S.; Achilefua, S.; Gruev, V.; Liang, R. Dual-mode optical imaging system for fluorescence image-guided surgery. *Opt Lett* **2014**, 39, 3830-2.
2. Chae, Y. S.; Lee, S. H.; Lee, H. K.; Kim, M. Y. Optical coordinate tracking system using afocal optics for image-guided surgery. *Int J Comput Assist Radiol Surg* **2014**.
3. Levy, L. L.; Vila, P. M.; Park, R. W.; Schwarz, R.; Polydorides, A. D.; Teng, M. S.; Gurudutt, V. V.; Genden, E. M.; Miles, B.; Anandasabapathy, S.; Gillenwater, A. M.; Richards-Kortum, R.; Sikora, A. G. High-Resolution Optical Imaging of Benign and Malignant Mucosa

in the Upper Aerodigestive Tract: An Atlas for Image-Guided Surgery. *ISRN Minim Invasive Surg* **2012**, 2012.

4. Keereweer, S.; Sterenborg, H. J.; Kerrebijn, J. D.; Van Driel, P. B.; Baatenburg de Jong, R. J.; Lowik, C. W. Image-guided surgery in head and neck cancer: current practice and future directions of optical imaging. *Head Neck* **2012**, 34, 120-6.

5. Mieog, J. S.; Vahrmeijer, A. L.; Hutteman, M.; van der Vorst, J. R.; Drijfhout van Hooff, M.; Dijkstra, J.; Kuppen, P. J.; Keijzer, R.; Kaijzel, E. L.; Que, I.; van de Velde, C. J.; Lowik, C. W. Novel intraoperative near-infrared fluorescence camera system for optical image-guided cancer surgery. *Mol Imaging* **2010**, 9, 223-31.

6. Keereweer, S.; Kerrebijn, J. D.; van Driel, P. B.; Xie, B.; Kaijzel, E. L.; Snoeks, T. J.; Que, I.; Hutteman, M.; van der Vorst, J. R.; Mieog, J. S.; Vahrmeijer, A. L.; van de Velde, C. J.; Baatenburg de Jong, R. J.; Lowik, C. W. Optical image-guided surgery--where do we stand? *Mol Imaging Biol* **2011**, 13, 199-207.

7. Matsui, A.; Lomnes, S. J.; Frangioni, J. V. Optical clearing of the skin for near-infrared fluorescence image-guided surgery. *J Biomed Opt* **2009**, 14, 024019.

8. Yokoyama, J.; Fujimaki, M.; Ohba, S.; Anzai, T.; Yoshii, R.; Ito, S.; Kojima, M.; Ikeda, K. A feasibility study of NIR fluorescent image-guided surgery in head and neck cancer based on the assessment of optimum surgical time as revealed through dynamic imaging. *Oncotargets Ther* **2013**, 6, 325-30.

9. Tomura, N.; Watanabe, O.; Omachi, K.; Sakuma, I.; Takahashi, S.; Otani, T.; Kidani, H.; Watarai, J. Image fusion of thallium-201 SPECT and MR imaging for the assessment of recurrent head and neck tumors following flap reconstructive surgery. *Eur Radiol* **2004**, 14, 1249-54.

10. Wall, J.; Richey, T.; Williams, A.; Stuckey, A.; Osborne, D.; Martin, E.; Kennel, S. Comparative Analysis of Peptide p5 and Serum Amyloid P Component for Imaging AA

Amyloid in Mice Using Dual-Isotope SPECT. *Molecular Imaging and Biology* **2012**, 14, 402-407.

11. Aita, K.; Temma, T.; Kuge, Y.; Seki, K.; Saji, H. NIR fluorescent ytterbium compound for in vivo fluorescence molecular imaging. *Luminescence* **2010**, 25, 19-24.

12. Cao, J.; Zhu, H.; Deng, D.; Xue, B.; Tang, L.; Mahounga, D.; Qian, Z.; Gu, Y. In vivo NIR imaging with PbS quantum dots entrapped in biodegradable micelles. *J Biomed Mater Res A* **2012**, 100, 958-68.

13. Jose, I.; Deodhar, K. D.; Desai, U. B.; Bhattacharjee, S. Early detection of breast cancer: synthesis and characterization of novel target specific NIR-fluorescent estrogen conjugate for molecular optical imaging. *J Fluoresc* **2011**, 21, 1171-7.

14. Karunakaran, S. C.; Babu, P. S.; Madhuri, B.; Marydasan, B.; Paul, A. K.; Nair, A. S.; Rao, K. S.; Srinivasan, A.; Chandrashekar, T. K.; Rao Ch, M.; Pillai, R.; Ramaiah, D. In vitro demonstration of apoptosis mediated photodynamic activity and NIR nucleus imaging through a novel porphyrin. *ACS Chem Biol* **2013**, 8, 127-32.

15. Kim, J. S.; Cho, K. J.; Tran, T. H.; Nurunnabi, M.; Moon, T. H.; Hong, S. M.; Lee, Y. K. In vivo NIR imaging with CdTe/CdSe quantum dots entrapped in PLGA nanospheres. *J Colloid Interface Sci* **2011**, 353, 363-71.

16. Koide, Y.; Urano, Y.; Hanaoka, K.; Piao, W.; Kusakabe, M.; Saito, N.; Terai, T.; Okabe, T.; Nagano, T. Development of NIR fluorescent dyes based on Si-rhodamine for in vivo imaging. *J Am Chem Soc* **2012**, 134, 5029-31.

17. Luo, S.; Zhang, E.; Su, Y.; Cheng, T.; Shi, C. A review of NIR dyes in cancer targeting and imaging. *Biomaterials* **2011**, 32, 7127-38.

18. Seela, F.; Pujari, S. S. Azide-alkyne "click" conjugation of 8-aza-7-deazaadenine-DNA: synthesis, duplex stability, and fluorogenic dye labeling. *Bioconjug Chem* **2010**, 21, 1629-41.

19. Seela, F.; Xiong, H.; Leonard, P.; Budow, S. 8-Aza-7-deazaguanine nucleosides and oligonucleotides with octadiynyl side chains: synthesis, functionalization by the azide-alkyne 'click' reaction and nucleobase specific fluorescence quenching of coumarin dye conjugates. *Org Biomol Chem* **2009**, *7*, 1374-87.
20. Seela, F.; Sirivolu, V. R. Pyrrolo-dC oligonucleotides bearing alkynyl side chains with terminal triple bonds: synthesis, base pairing and fluorescent dye conjugates prepared by the azide-alkyne "click" reaction. *Org Biomol Chem* **2008**, *6*, 1674-87.
21. Seela, F.; Sirivolu, V. R.; Chittepu, P. Modification of DNA with octadiynyl side chains: synthesis, base pairing, and formation of fluorescent coumarin dye conjugates of four nucleobases by the alkyne--azide "click" reaction. *Bioconjug Chem* **2008**, *19*, 211-24.
22. Wada, H.; Hyun, H.; Vargas, C.; Gravier, J.; Park, G.; Gioux, S.; Frangioni, J. V.; Henary, M.; Choi, H. S. Pancreas-Targeted NIR Fluorophores for Dual-Channel Image-Guided Abdominal Surgery *Theranostics* **2015**, *5*, 1-11.
23. Holt, D.; Okusanya, O.; Judy, R.; Venegas, O.; Jiang, J.; DeJesus, E.; Eruslanov, E.; Quatromoni, J.; Bhojnagarwala, P.; Deshpande, C.; Albelda, S.; Nie, S.; Singhal, S. Intraoperative Near-Infrared Imaging Can Distinguish Cancer from Normal Tissue but Not Inflammation. *PLoS ONE* **2014**, *9*, e103342.
24. Flower, R. W.; Lim, J. I. An ICG angiogram-based clinical method for characterizing the choroidal circulation used to assess the hemorrheologic effects of pentoxifylline. *J Fr Ophthalmol* **2000**, *23*, 756-62.
25. Lin, Y.; Weissleder, R.; Tung, C. H. Novel near-infrared cyanine fluorochromes: synthesis, properties, and bioconjugation. *Bioconjug Chem* **2002**, *13*, 605-10.
26. Sowell, J.; Agnew-Heard, K. A.; Mason, J. C.; Mama, C.; Strekowski, L.; Patonay, G. Use of non-covalent labeling in illustrating ligand binding to human serum albumin via affinity

capillary electrophoresis with near-infrared laser induced fluorescence detection. *J Chromatogr B Biomed Sci Appl* **2001**, 755, 91-9.

27. Lee, B. T.; Hutteman, M.; Gioux, S.; Stockdale, A.; Lin, S. J.; Ngo, L. H.; Frangioni, J. V. The FLARE intraoperative near-infrared fluorescence imaging system: a first-in-human clinical trial in perforator flap breast reconstruction. *Plast Reconstr Surg* **2010**, 126, 1472-81.

28. Troyan, S. L.; Kianzad, V.; Gibbs-Strauss, S. L.; Gioux, S.; Matsui, A.; Oketokoun, R.; Ngo, L.; Khamene, A.; Azar, F.; Frangioni, J. V. The FLARE intraoperative near-infrared fluorescence imaging system: a first-in-human clinical trial in breast cancer sentinel lymph node mapping. *Ann Surg Oncol* **2009**, 16, 2943-52.

29. Choi, H. S.; Nasr, K.; Alyabyev, S.; Feith, D.; Lee, J. H.; Kim, S. H.; Ashitate, Y.; Hyun, H.; Patonay, G.; Streckowski, L.; Henary, M.; Frangioni, J. V. Synthesis and In Vivo Fate of Zwitterionic Near-Infrared Fluorophores. *Angewandte Chemie International Edition* **2011**, 50, 6258-6263.

30. Choi, H. S.; Gibbs, S. L.; Lee, J. H.; Kim, S. H.; Ashitate, Y.; Liu, F.; Hyun, H.; Park, G.; Xie, Y.; Bae, S.; Henary, M.; Frangioni, J. V. Targeted zwitterionic near-infrared fluorophores for improved optical imaging. *Nat Biotechnol* **2013**, 31, 148-53.

31. Beckford, G.; Owens, E.; Henary, M.; Patonay, G. The solvatochromic effects of side chain substitution on the binding interaction of novel tricyanocyanine dyes with human serum albumin. *Talanta* **2012**, 92, 45-52.

32. Kim, J. J.; Choi, H. S.; Lee, M. Y.; Ryu, C. J. Characterization of monoclonal antibodies recognizing 130 kDa surface proteins on human embryonic stem cells and cancer cell lines. *Monoclon Antib Immunodiagn Immunother* **2013**, 32, 136-9.

33. Ali, H.; Rousseau, J.; van Lier, J. E. Synthesis, receptor binding and biodistribution of the gem-21-chloro-21-iodovinylestradiol derivatives. *J Steroid Biochem Mol Biol* **1993**, 46, 613-22.

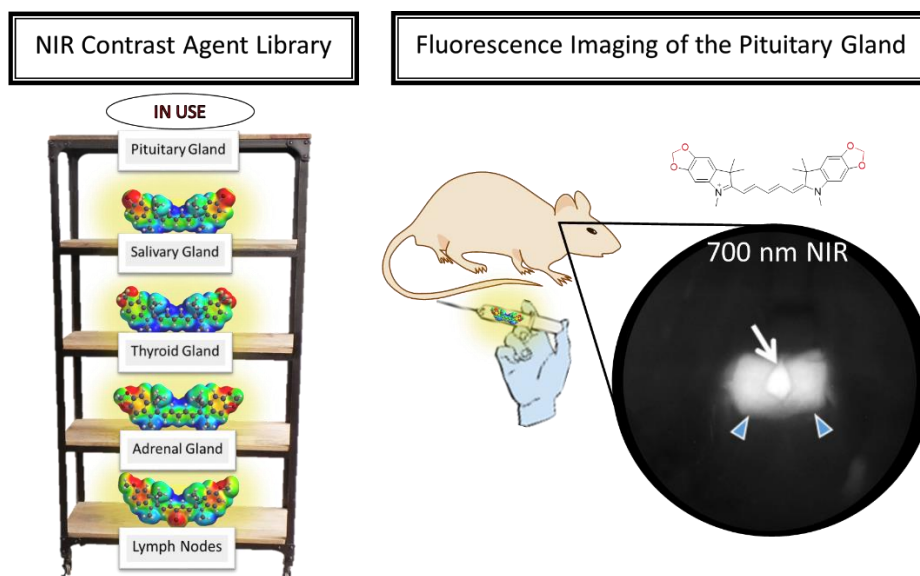
34. Nanjunda, R.; Owens, E. A.; Mickelson, L.; Alyabyev, S.; Kilpatrick, N.; Wang, S.; Henary, M.; Wilson, W. D. Halogenated pentamethine cyanine dyes exhibiting high fidelity for G-quadruplex DNA. *Bioorg Med Chem* **2012**, 20, 7002-11.
35. Sinha, S. H.; Owens, E. A.; Feng, Y.; Yang, Y.; Xie, Y.; Tu, Y.; Henary, M.; Zheng, Y. G. Synthesis and evaluation of carbocyanine dyes as PRMT inhibitors and imaging agents. *Eur J Med Chem* **2012**, 54, 647-59.

4 ELECTRONIC FACTORS INFLUENCE BIODISTRIBUTION OF CYANINES

This chapter focuses on altering the electron effects on pentamethine cyanines and observing the overall perturbation in biodistribution. By observing these effects, it is possible to design additional contrast agents targeted using the inherent chemical structure. My contributions as first author were the design, synthesis, optical property determination, molecular modeling and computational experiments, data interpretation and figure/manuscript preparation. This manuscript is prepared and is awaiting submission to the Journal of Medicinal Chemistry. **Owens, E.A.**, Hyun, H., Dost, T, Choi, H.S., Henary, M., NIR Illumination of Native Tissues for Image-Guided Surgery. Prepared for Submission to J. Med Chem. **2015**

4.1 Abstract

Our initial efforts to prepare tissue-specific near-infrared (NIR) fluorescent compounds generated successful correlation between physicochemical properties and global uptake in major organs after systemic circulation and biodistribution. Herein, we focus on the effects on biodistribution based on modulating electronic influencing moieties from donating to withdrawing moieties at both the heterocyclic site and through *meso*-substitution of pentamethine cyanine fluorophores. These selected modifications harnessed innate biodistribution pathways through the structure-inherent targeting resulting in effective imaging of the adrenal glands, pituitary gland, lymph nodes, pancreas, thyroid and salivary glands. These native-tissue contrast agents will arm surgeons with a powerful and versatile arsenal for intraoperative NIR imaging in real time.



4.2 Introduction

During endocrine surgeries and intricate surgical resections, surgeons mostly rely on their naked eye and experience during often-lengthy procedures to avoid sensitive glands and tissues.¹⁻³ Neglecting to carefully navigate the surgical field can lead to poor patient prognosis even morbidity.⁴⁻¹¹ Endocrine and exocrine tissues regulate the body's hormone levels and any perturbation, especially transection, can jeopardize the patient's ability to recover after surgery and maintain proper hormone levels.¹²⁻¹⁵ The important task of avoiding sensitive tissues is often difficult as these small and imperative glands are often obscured by blood and surrounding tissues. Surgeons require an imaging modality that can allow them to visualize these tissues during cancer resection surgeries to improve the surgical success rate, lower overall fatalities and advance patient prognoses.

Near-infrared (NIR) fluorescence guided resection of cancerous tissues has demonstrated significant promise with increasing advancements being reported over the recent years.¹⁵⁻²⁵ Unfortunately, the research efforts have been overwhelmingly concentrated on developing cancer-specific NIR-fluorophores with optimal optical, physicochemical and targeting properties. This only satisfies one-half of the main objective: the ability to

simultaneously image the surgical field with both a disease-targeted fluorophore and a native-tissue targeted fluorophore of distinct wavelengths that can both be simultaneously and separately detected for direct dual-target imaging in real time.

Significant advancements have been made to develop NIR-fluorescent compounds that target sensitive endogenous tissue and help surgeons avoid these hormonal glands in real time without changing the overall look of the surgical field. The class of NIR-fluorescent cyanine dyes has shown excellent promise in the area of NIR-fluorescence image guided surgery for *in vivo* tumor targeting. Cyanine chromophores are broadly defined by having two nitrogen-containing heterocycles that are connected through an electron deficient polymethine bridge with a delocalized monocation conjugated between both nitrogen atoms. The wavelengths associated with these compounds are heavily dependent on the length of the polymethine-bridge and the terminal heterocyclic moieties. Polymethine cyanines are chemically stable NIR-fluorescent compounds, and we have investigated the pentamethine class of compounds previously^{16, 20} and herein for laying the groundwork for endogenous tissue targeting. The heptamethine cyanine class (~800 nm fluorescence) has been more extensively explored for disease targeting through the development of cRGD-ZW800-1.^{10, 21, 22} The longer NIR wavelengths (i.e. 800 nm) are more easily detected against the background and usually reserved to detect occult cancerous metastasis due to the minimal autofluorescence. We plan to further exploit the 700 nm channel (pentamethine cyanines) for native tissue imaging for dual channel intraoperative imaging.

Toward achieving this goal, we have continued to harness the structure-inherent tissue affinity to determine the innate biodistribution and targeting by modulating overall molecular characteristics such as hydrophobicity (determined through LogD calculations), total polar surface area, molecular size/weight and the electronic contributions (electron donating/withdrawing characteristics). The compounds synthesized and analyzed herein vary

by their heterocyclic moieties (electron donating or withdrawing) and various halogenation at the central carbon atom of the polymethine chain which alters the net dipole, volume, polarization and even overall shape of the compounds. We expect these selected modifications to offer biological perturbation toward understanding the molecular characteristics for targeting specific tissues. Correlating these molecular descriptors with *in vivo* biodistribution is expected to result in a clinically significant paradigm in the quest of translating NIR-targeted contrast agents into the clinic, and every analyzed compound offers another evidentiary piece to the puzzle.

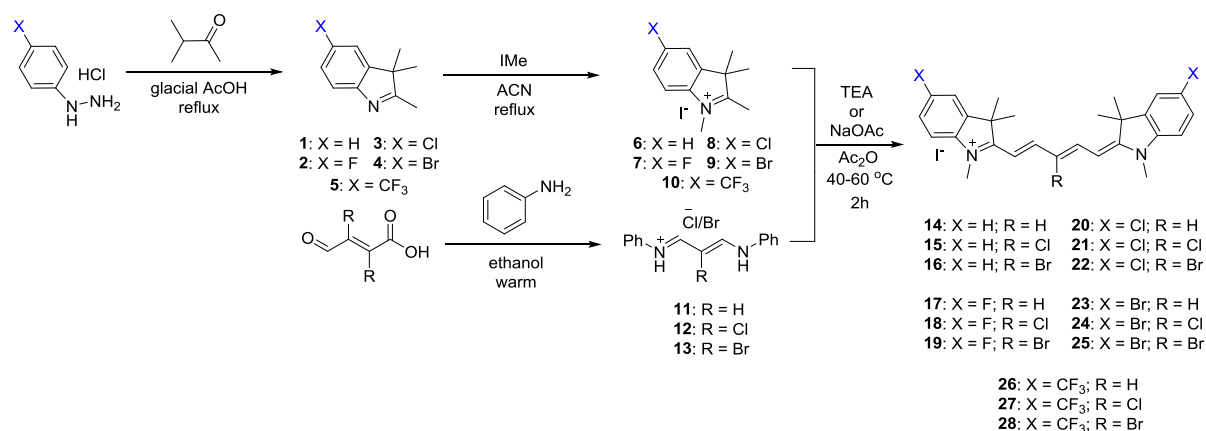
4.3 Results and Discussion

4.3.1 Synthesis of Pentamethine Fluorophores.

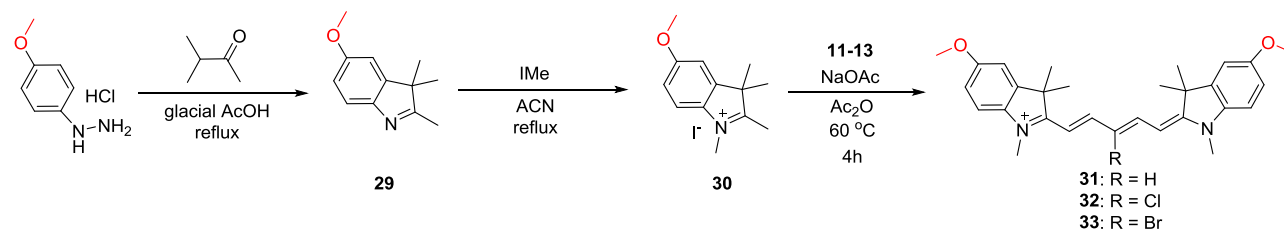
Since it has been previously reported that halogenated hydrocarbons localize in higher concentration within endocrine and exocrine glands compared to their non-halogenated counterparts,¹⁶ we decided to probe the effect of halogenation on pentamethine cyanines for endocrine and exocrine tissue targeting. For a direct comparison, we synthesized electron-donating counterparts that could offer insight into how potential electronic factors present in the compounds may influence biodistribution.

We have developed several optimized synthetic routes for maximizing the structural diversity in the pentamethine cyanine pharmacophore. The compounds with neutral effects and electron withdrawing groups are synthesized starting with the corresponding phenyl hydrazine salts being refluxed in the presence of 3-methyl-2-butanone in acidic conditions. This reaction furnishes the indolenines **2-5** in excellent yield. We then alkylated the obtained oil using iodomethane in acetonitrile, which yields the cationic salt **6-10** bearing an acidic methylene proton. We also separately react aniline with a warm ethanolic solution of either mucochloric or mucobromic acid to obtain the pentamethine precursor **12** or **13** with **11** being commercially obtained. These two compounds are individually combined in the presence of acetic anhydride

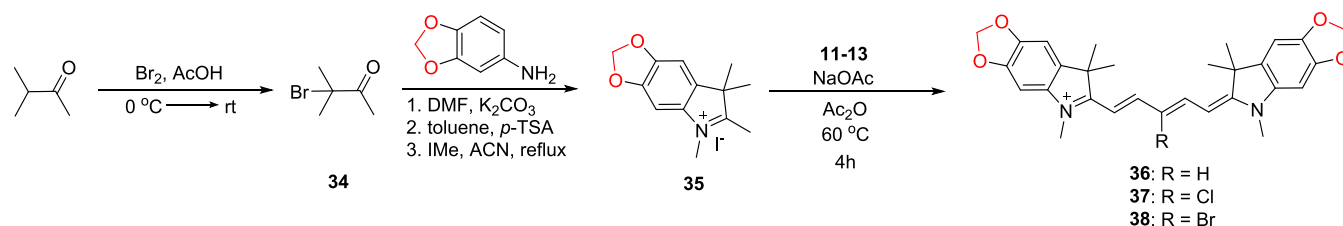
and either triethylamine (fluorine-containing compounds) or sodium acetate and are heated to afford the brilliant blue pentamethine fluorophores.



Scheme 1. The synthesis of 700 nm emitting pentamethine cyanines featuring neutral (X = H) and electron withdrawing (X = F, Cl, Br, CF₃) moieties.



Scheme 2. The synthesis of 700 nm emitting pentamethine cyanines featuring electron donating methoxy groups.



Scheme 3. The synthesis of 700 nm emitting pentamethine cyanines featuring electron donating methylene dioxy substitution on the phenyl rings.

The electron donating-containing methoxy-substituted compounds are prepared through an identical synthetic route; however, the final step requires a longer reaction time at a slightly elevated temperature, due to the methoxy group electron donating effects which

increases the pKa of the methylene proton resulting in reduced reactivity of the methylene carbon. We also designed a complementary set of compounds bearing heterocyclic donating groups features the methylene dioxy ring shown in compounds **36-38**. These compounds are prepared using an alternate synthetic strategy beginning with the acidic bromination of 3-methyl-2-butanone followed by S_N1 replacement of the tertiary bromine by the methylene dioxyaniline compound. Upon heating in the presence of acid catalyst, paratoluenesulphonic acid, the compound forms the cyclic methylene dioxy 2,3,3-trimethylindolenine ring through a largely unexplored Bischler-Möhlau method that can be alkylated using aforementioned conditions for the formation of compound **35**. The final methylene dioxy compounds **36-38** were synthesized using similar chemistry as the methoxy group.

4.3.2 *Optical and Physicochemical Properties.*

The optical properties, shown in Table 1, were performed in several solvents to determine the *in vivo* success for the fluorophores. We can see that the compounds with hydrogen, chlorine, bromide and methoxy groups (**14-25**, **31-33**) exhibit sharp and NIR absorbance bands with very high molar absorptivity all being greater than 100,000 M⁻¹cm⁻¹ which suggests that these fluorophores will satisfactorily absorb NIR wavelengths *in vivo* and will be compatible with the intraoperative imaging system. As expected, the methylenedioxy compounds exhibited slightly lower molar absorptivity due to a broadening of the absorption profile which results from a more widely dispersed sub-energy levels. Similarly, the trifluoromethyl substituted compounds are very poor at absorbing light at their wavelength of maximum absorbance as indicated by their low molar absorptivity values in Table 1. We attribute this to the high electron withdrawing characteristics of the trifluoromethyl groups which lowers the overall probability of electron movement across the methine-bridge connecting the aza-heterocycles. The *in vivo* success of these compounds also depends of the

quantum yield, and more importantly the molecular brightness (determined as the product of extinction coefficient and quantum yield), of the compounds in serum; therefore, we examined the quantum yield of these fluorophores in FBS. Compounds **14-28**, **31-33** exhibit high quantum yield values in serum which is very appealing. All of the synthesized compounds have sufficiently high molecular brightness values in serum with many compounds exhibiting molecular brightness values of >20,000. We observed an overall trend for the majority of compounds that as the size of the central halogen increases, the molecular brightness decreases. When analyzing the minimized three-dimensional structures, we see that the *meso*-halogenation perturbs the *trans*-alkene angles and the elongated structure of the fluorophore which actually shortens the overall length and perturbs the conjugated bridge. This is an interesting finding since upon first glance, it seems that adding larger groups to the middle of the compound should result in an elongation of the compound simply because it would force the neighboring hydrogen atoms apart. Another potential explanation for the decrease in molecular brightness is the heavy atom effect that can effectively stabilize the triplet state allowing for other competing decay processes (i.e. phosphorescence or energy transfer).

Table 4-1. Optical properties of 700 nm emitting NIR fluorophores. All measurements were performed in dimethyl sulfoxide (DMSO), ethanol (EtOH), phosphate-buffered saline (PBS), and fetal bovine serum (FBS), pH = 7.4 at 37 °C. Abbreviations: λ_{abs} , wavelength of maximum absorbance; λ_{em} , wavelength of maximum emission; QY, quantum yield; and MB, molecular brightness.

ID	λ_{abs} (nm)				Extinction Coefficient ($\epsilon, \text{M}^{-1} \text{cm}^{-1}$)				λ_{em} (nm)		Stokes Shift		QY (Φ , %)		MB ($\epsilon \times \Phi$)	
	DMSO	EtOH	PBS	FBS	DMSO	EtOH	PBS	FBS	EtOH	FBS	EtOH	FBS	EtOH	FBS	EtOH	FBS
14	647	645	640	649	212,500	248,200	218,800	184,500	660	662	15	13	32.7	31.0	81,161	57,195
15	645	644	642	638	235,300	207,800	171,000	168,800	659	665	15	27	29.2	28.8	60,677	48,614
16	645	641	638	634	257,330	253,200	204,400	211,700	657	660	16	26	30.1	43.6	76,213	92,301
17	645	641	638	649	216,700	225,800	196,500	164,400	663	662	22	13	31.6	35.2	71,352	58,868
18	646	643	638	638	210,900	233,700	193,400	193,400	658	660	15	22	16.5	15.3	38,561	29,590

19	642	641	635	644	173,200	210,500	170,900	145,800	658	658	17	14	16.3	11.9	34,312	17,350
20	652	649	645	660	183,400	204,200	174,200	136,000	658	669	19	9	41.5	57.5	84,743	78,200
21	653	652	647	658	192,800	207,800	140,200	136,000	664	666	14	8	18.3	28.5	38,027	38,760
22	650	648	643	655	233,100	250,600	185,000	153,700	665	663	17	12	15.4	17.4	38,592	26,744
23	653	650	653	662	181,200	174,500	144,800	141,100	670	671	20	9	42.4	57.0	73,988	80,427
24	655	653	660	648	140,200	189,600	121,500	119,700	667	671	14	23	20.8	23.0	39,437	27,531
25	643	641	635	644	169,000	169,600	166,900	159,600	657	663	16	21	15.5	11.8	26,288	18,833
26	642	638	636	648	41,200	45,200	28,700	30,600	656	654	18	6	58.7	89.2	26,532	27,295
27	644	640	638	649	72,000	114,900	56,300	19,500	656	655	16	6	20.5	47.4	23,555	9,243
28	641	638	635	644	32,400	49,700	19,600	8,400	653	651	15	7	21.1	29.0	10,487	2,436
31	671	668	658	674	152,300	205,000	133,600	135,000	696	696	28	22	9.6	11.9	19,680	16,070
32	672	671	658	676	148,100	210,000	135,900	162,000	694	692	23	16	3.9	9.7	8,190	15,710
33	669	669	655	676	94,200	154,000	82,100	109,000	689	688	20	12	5.1	9.7	7,218	10,570
36	691	690	680	698	107,200	108,100	89,200	85,900	705	716	15	18	4.7	6.5	5,081	5,584
37	689	690	678	693	147,200	156,600	127,100	117,800	716	712	26	19	3.0	4.2	4,698	4,948
38	687	687	675	691	154,900	165,800	135,700	125,000	715	716	28	25	2.9	3.1	4,808	3,875

Table 4-2. *In silico* physicochemical properties of 700 nm emitting NIR fluorophores (LogD, TPSA and H-bond acceptors) calculated using Marvin and JChem calculator plugins (ChemAxon, Budapest, Hungary). LogD = partition coefficient at pH 7.4, TPSA = total polar surface area while molecular parameters (length, volume dipole and polarizability) were calculated using Spartan Wavefunction (V10) DFT starting with the minimized structural conformation of the lowest energy.

ID	Physicochemical Properties							
	MW (g/mol)	LogD (pH 7.4)	= TPSA	H-bond acceptors	Length (Å)	Volume (Å ³)	Dipole (debye)	Polarizability
14	383.548	3.56	6.25	1	18.665	445.51	1.95	76.14
15	417.994	3.79	6.25	1	18.530	458.45	0.89	77.21
16	462.445	3.96	6.25	1	18.453	462.96	0.79	77.55
17	419.529	3.84	6.25	2	18.684	455.28	4.23	76.95
18	453.974	4.08	6.25	3	18.536	468.22	3.32	78.02
19	498.425	4.24	6.25	3	18.475	472.73	3.26	78.36
20	452.439	4.77	6.25	2	18.674	472.01	3.55	78.30
21	486.884	5.00	6.25	3	18.539	484.95	2.58	79.37
22	531.335	5.17	6.25	3	18.464	489.45	2.52	79.71
23	541.341	5.09	6.25	2	18.665	481.25	3.74	79.05
24	575.786	5.33	6.25	3	18.517	494.19	2.79	80.12
25	620.237	5.50	6.25	3	18.340	498.70	2.73	80.40
26	519.544	5.31	6.25	6	20.188	511.26	8.04	81.47
27	553.989	5.55	6.25	7	19.547	524.14	7.58	82.54
28	598.440	5.70	6.25	7	19.406	528.65	7.62	82.88

31	443.600	3.24	24.71	2	20.631	500.23	4.10	80.61
32	478.045	3.48	24.71	3	20.527	513.28	3.04	81.68
33	522.496	3.64	24.71	3	20.142	517.72	2.89	82.02
36	471.577	2.80	43.17	4	21.203	496.69	2.69	80.33
37	506.019	3.04	43.17	5	20.847	509.64	1.77	81.39
38	550.473	3.21	43.17	5	20.680	514.15	1.72	81.74

4.3.3 Structure-Inherent Targeting Ability of NIR Fluorophores.

As native tissue targeting remains predominantly understudied, we focused our attention to the salivary, thyroid, pituitary, adrenal glands, lymph nodes and pancreas. As these tissues facilitate the regulation of human hormone levels they are important for long-term health and should be carefully avoided during surgical resection in surrounding areas.

After *in vivo* studies, we found compounds that exhibited high SBR in targeted tissues (high is designated as a ratio of target signal to surrounding tissue being >2.0). Without surface or subcellular receptors readily available for the particular native tissues, it has been difficult to infer mechanistic insight of how these fluorophores localize within their respective tissues. However, we have found several key structural components that help facilitate structure-inherent biodistribution and localization in important tissues, including the salivary, thyroid, pituitary, adrenal glands, lymph nodes and pancreas.

Table 4-3. Targeting properties and biodistribution of 700 nm emitting NIR fluorophores for specific organs/tissues at 4 h post-injection.

Targeted Tissues							Biodistribution					
ID	AG	Pa	PG	SG	TG	LN	Li	Ki	He	Lu	Sp	Bo
14	–	+++	++	+++	++	++	–	+++	+	–	–	++
15	–	+++	+	+++	+	+	+	+++	–	–	–	+
16	+	++	–	+++	+	+	+	+++	–	–	–	+
17	–	+++	++	+++	+++	++	–	+++	–	+	–	+
18	+	++	+	++	++	++	++	+++	–	+	–	–
19	–	+	–	+	+	–	++	+++	–	+	–	–
20	++	+++	+++	+++	+++	+++	–	+++	+	++	–	++
21	+	+	+	++	+	–	+++	++	–	–	–	–

22	+	+	-	+	+	-	++++	++	-	+	-	-
23	+	+++	+++	+++	+++	+++	++	+++	+	++	-	++
24	+	+	+	++	+	+	+++	++	-	+	-	+
25	+	+	-	+	+	-	+++	++	-	+	-	-
26	-	++	+++	++	++	-	+++	++	-	-	-	-
27	-	+	+	+	-	++	+++	++	-	-	-	-
28	+	+	-	+	-	-	+++	+	-	-	-	-
31	++	+++	++	+++	++	++	+	+++	+	+	-	+
32	++	++	++	++	++	+++	+++	+++	-	-	-	-
33	+	+	++	++	+	+++	+++	+++	-	+	+	-
36	++	+++	+++	++	+	+	++	+++	+	+	-	-
37	++	+++	++	++	++	+	+++	++	-	-	-	-
38	++	+++	++	++	++	+	+++	++	-	-	-	-

Abbreviations used are: AG, adrenal gland; Pa, pancreas; PG, pituitary gland; TG, thyroid gland; SG, salivary gland; Li, liver; Ki, kidneys; He, heart; Lu, lungs; Sp, spleen; Bo, bone; LN, lymph node. The SBR of each organ/tissue relative to the abdominal wall was quantified and labeled as -, 1 to 2; +, 2 to 3; ++, 3 to 5; and +++, > 5.

In surgical resections such as thyroidectomies, it is crucial to remove the entire thyroid gland while maintaining complete integrity of the parathyroid gland. Selective thyroid gland imaging is paramount in the ability to avoid partial thyroid resection or accidental parathyroid transection which can cause several abnormal human conditions such as hypocalcemia.

The common clinical indications of salivary gland imaging are pain and swelling. Imaging is useful in identifying the masses of salivary glands and also in differentiating them from the masses/pathologies of adjacent cervical spaces. In proven case of salivary gland tumors, imaging helps in delineating the extent of the lesion and invasion of adjacent cervical spaces. Cancerous tissues in this area can grow quickly and surgical resection of the diseased tissue is needed while sparing excision of the exocrine salivary glands themselves.

Toward finding the thyroid and salivary glands targeting by using NIR fluorophores, we evaluated the imaging capability of these compounds in thyroid and salivary glands. Table 3 shows the thyroid and salivary glands targeting for the entire set of compounds. The targeting of these two tissues seemed to parallel each other suggesting a biological connection between these two tissues, though despite an extensive literature review, an explanation for this remains unclear. Among the entire set of prepared compounds we found that central halogenation reduced the targeting efficacy into these glands. Surprisingly, the parent set of compounds (**14-16**) all targeted the salivary gland with superior SBR. From our data, we can see overall that the salivary glands are sensitive to the central halogenation but remain tolerant to the heterocyclic halogen incorporation. Compounds **20-25** exhibit the halogen trend we observed. With the heterocyclic halogen substitution the salivary gland targeting remains high; however, when the central halogen is incorporated within the same compounds we have a severely diminished targeted ability (i.e. from compound **20** with SBR of >5 to compounds **21** and **22** with SBR of 1-2). Specifically compounds **17-25** shown in Figures 1 and 2 exemplify this trend. Compounds **17, 20, 23** do not feature halogens at the central carbon of the polymethine

chain and exhibit the most effective thyroid and salivary glands localization. As the halogen incorporation increases, the thyroid and salivary glands localization is forfeited in deference to non-specific accumulation and high liver uptake due to hepatobiliary clearance arising from the increase in hydrophobicity.

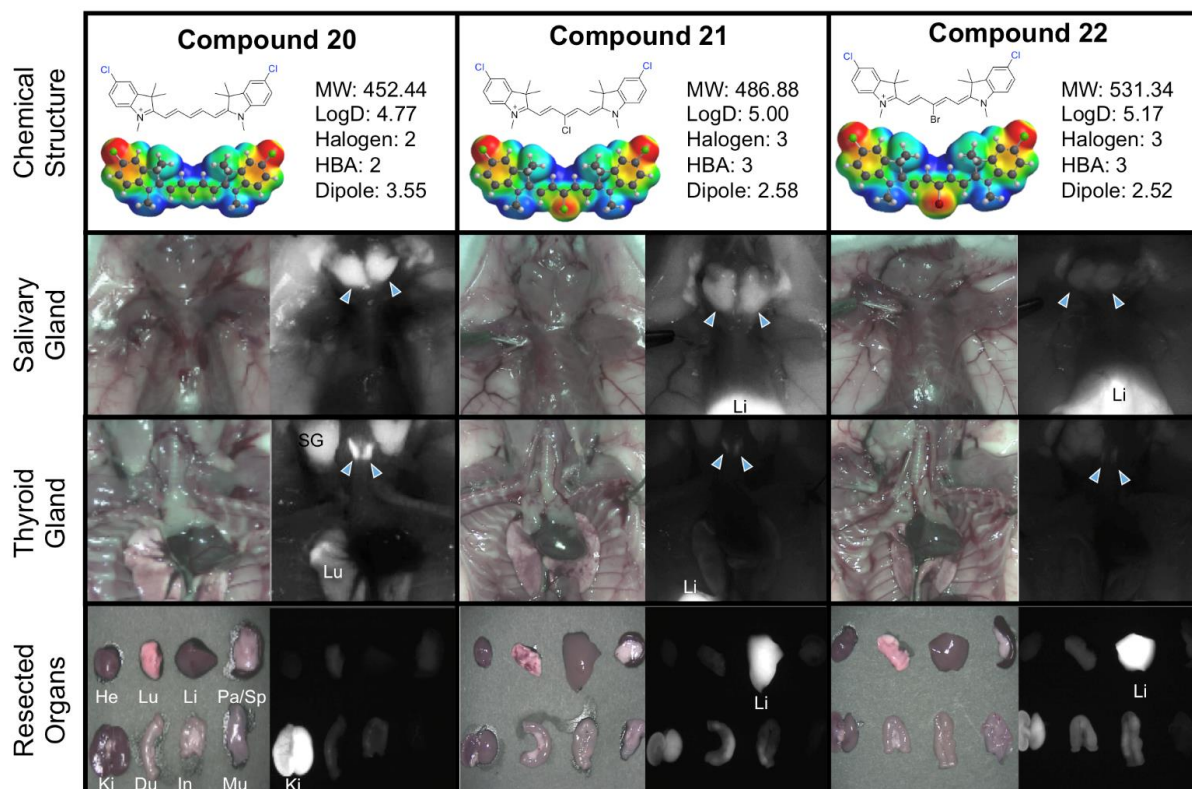


Figure 4-1. Compounds 20-22, targeting to salivary glands and thyroid glands, and biodistribution of resected organs in CD-1 mice. 10 nmol of each fluorophore was injected intravenously into 25 g CD-1 mice 4 h prior to imaging and resection. Abbreviations used are: Du, duodenum; He, heart; In, intestine; Ki, kidneys; Li, liver; Lu, lungs; Mu, muscle; Pa, pancreas; SG, salivary gland, Sp, spleen. Arrows indicate the targeted gland.

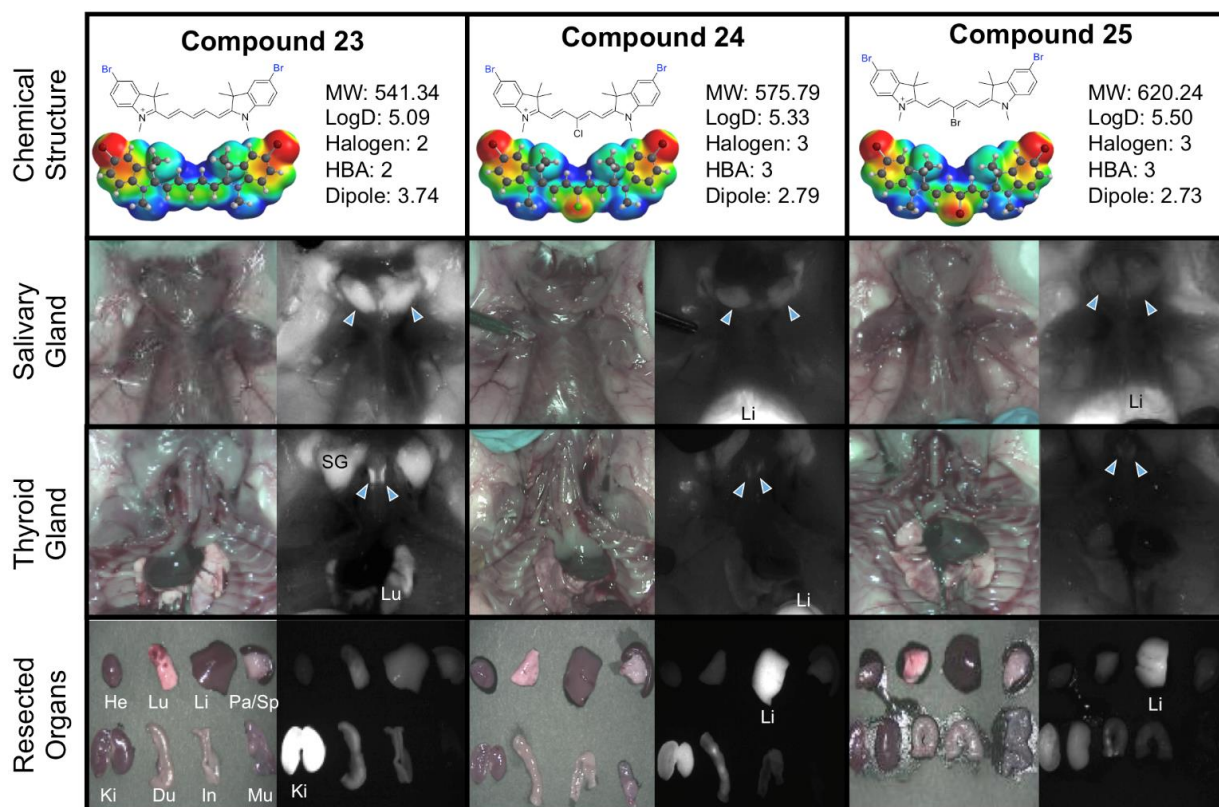


Figure 4-2. Compounds 23-25, targeting to salivary glands and thyroid glands, and biodistribution of resected organs in CD-1 mice. 10 nmol of each fluorophore was injected intravenously into 25 g CD-1 mice 4 h prior to imaging and resection. Abbreviations used are: Du, duodenum; He, heart; In, intestine; Ki, kidneys; Li, liver; Lu, lungs; Mu, muscle; Pa, pancreas; SG, salivary gland, Sp, spleen. Arrowheads indicate the targeted gland.

As one of the important endocrine glands, the pituitary gland (dubbed the master gland) is responsible for controlling the hormonal release of signaling chemicals throughout the body. Transecting this precious gland during surgery causes lasting side effects from hormone dysregulation with imbalances perpetuating during the lifetime of the patient. Tumors associated with the pituitary gland can interfere with signaling the release of many hormones such as thyroid-stimulating hormone which directly influences metabolic activity, energy levels, growth hormones and the nervous system. Efforts to remove pituitary gland tumors must critically and clearly image the native tissue to prevent accidental damage. We found excellent pituitary gland targeting with the trifluoromethyl compounds **26-28** (Figure 3). The trifluoromethyl substitutions increase the dipole of the compound considerably (Table 2) which we anticipated to elicit a drastic biological response compared to the alternate halogenated counterparts. Indeed, the vast change in electronic dipole from 1-4 debye (other compounds) to >7.5 debye in the trifluoromethyl substituted compounds lowered the target recognition to some endocrine tissues; however, the thyroid gland targeting remained elevated when the central position was halogen-free.

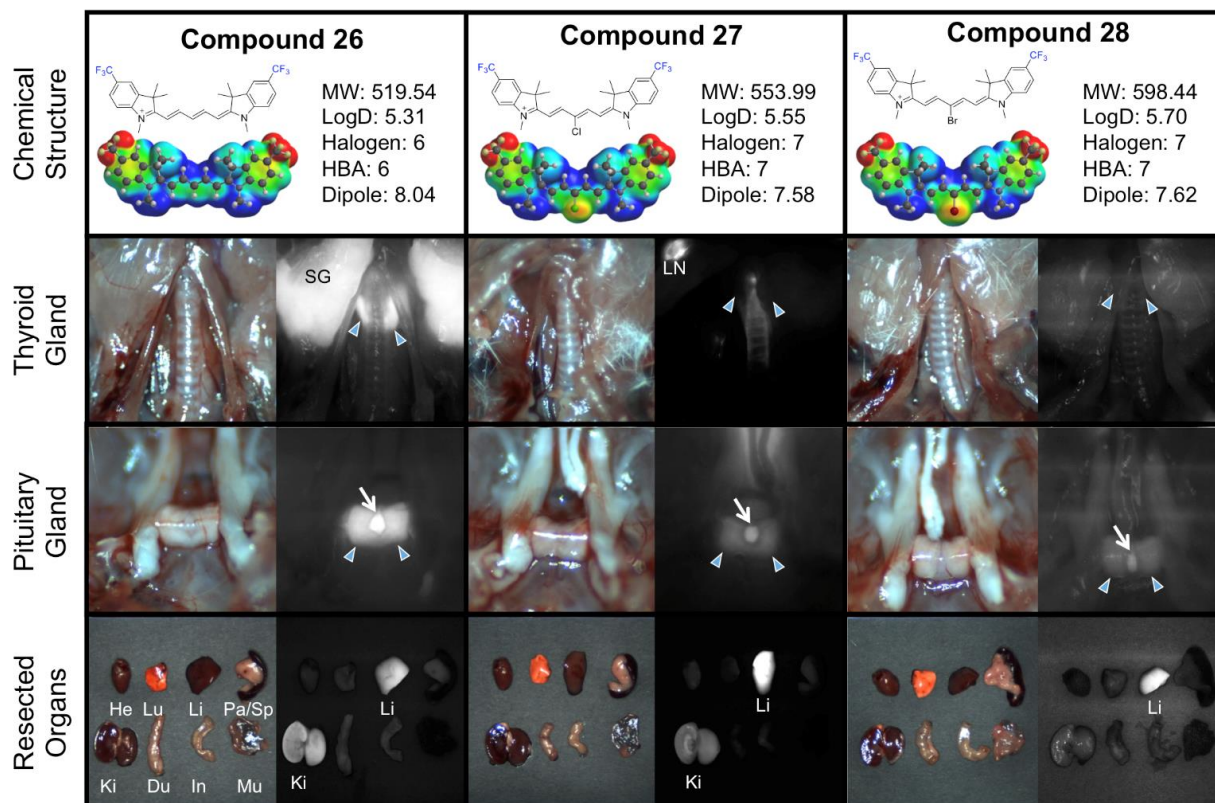


Figure 4-3. Compounds 26-28, targeting to thyroid glands and pituitary gland, and biodistribution of resected organs in CD-1 mice. 10 nmol of each fluorophore was injected intravenously into 25 g CD-1 mice 4 h prior to imaging and resection. Abbreviations used are: Du, duodenum; He, heart; In, intestine; Ki, kidneys; Li, liver; LN, lymph node; Lu, lungs; Mu, muscle; Pa, pancreas; SG, salivary gland, Sp, spleen. Arrows indicate the targeted gland. For pituitary glands, arrowheads indicate the anterior portion, and arrows for posterior pituitary.

Lymph nodes are widely distributed and are responsible for immune system function and can indicate an abnormal physiological condition. For example, an increase in size may indicate leukemia due to increased trafficking of lymphocytes from the blood into the lymph nodes. Additionally, thorough examination of the lymph nodes is crucial for the staging of cancer as tumor metastases normally first localize in sentinel lymph nodes. For surgical avoidance and the frequent necessity to biopsy, a NIR imaging technique to visualize this tissue is highly important. In the developed set of compounds, we noticed effective targeting of the lymph node by the methoxy derivatives **31-33** which is surprising in the context of the methylene dioxy compounds **36-38** exhibiting low lymph node targeting. Interestingly we see an inverse effect of the previous set of compounds where the *meso* halogenation increases the imaging signal as compared to the surrounding tissue in the lymph node with **32** and **33** having a SBR of >5 as indicated by the +++ in Table 3. Figure 4 shows two successful examples of nodal imaging in the inguinal and lumbar nodes with compound **33** exhibiting excellent targeting characteristics.

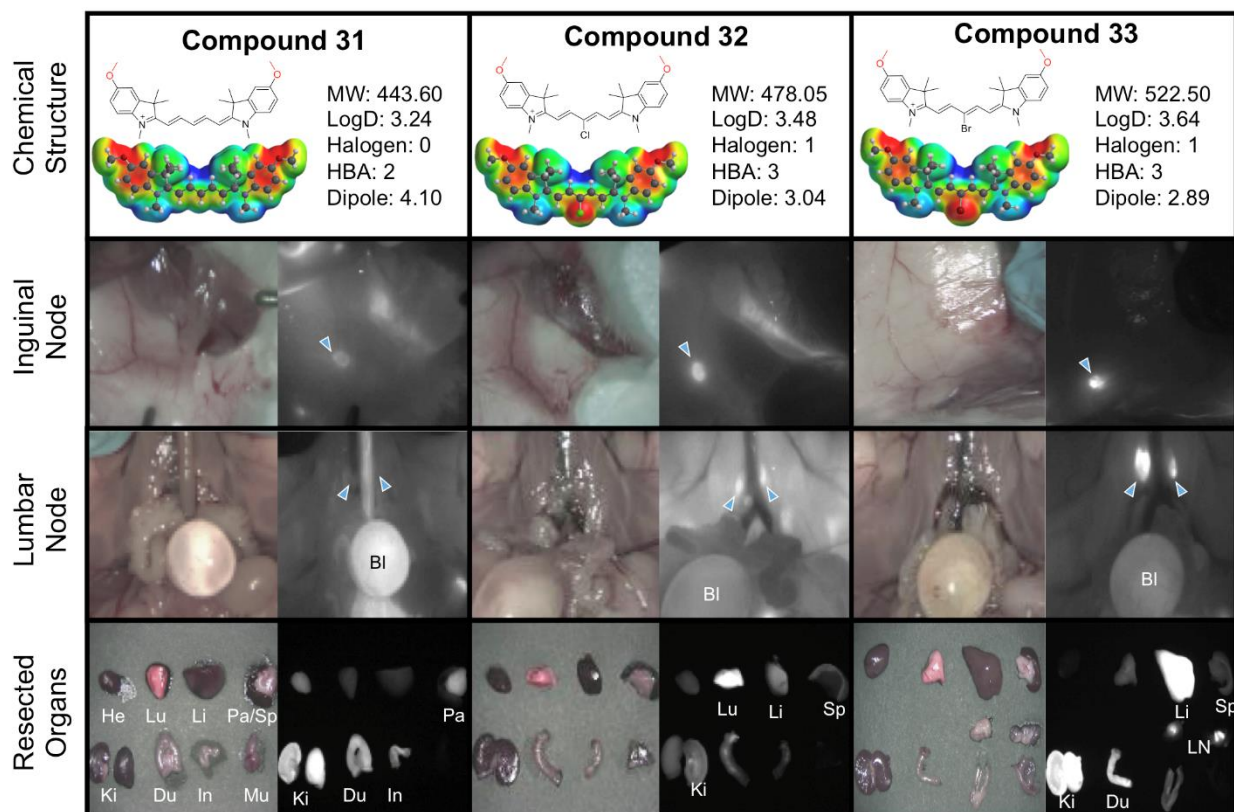


Figure 4-4. Compounds 31-33, targeting to inguinal and lumbar lymph nodes, and biodistribution of resected organs in CD-1 mice. 10 nmol of each fluorophore was injected intravenously into 25 g CD-1 mice 4 h prior to imaging and resection. Abbreviations used are: Bl, bladder; Du, duodenum; He, heart; In, intestine; Ki, kidneys; Li, liver; LN, lymph node; Lu, lungs; Mu, muscle; Pa, pancreas; Sp, spleen. Arrows indicate the targeted gland.

The adrenal glands, located above the kidney, produce essential and nonessential hormones that primarily control the body's metabolism, blood pressure and stress response. In Figure 5, we observed that the methylene dioxy compounds **36-38** exhibited adrenal gland targeting characteristics (++, SBR 3-5) that also seemed to be tolerant to the addition of *meso*-halogens. It seems that the logD values predominantly govern the localization of these compounds as the 5 compounds (**31, 32, 36-38**) with the lowest logD were the most effective at targeting this tissue with the methylene dioxy compounds **36-38** prevailing as the best contrast agents for the adrenal gland across the series. This finding is also true in their pancreas targeting ability as all three compounds within this set exhibit excellent SBR in pancreatic tissue. Interestingly, the small change from methoxy **31-33** to the locked ring structure of **36-38** alters the targeting ability of the compound (i.e. comparing **33** and **38**). This finding also corroborates our previous results that pancreatic targeting requires low comparative logD values. Indeed the highest pancreas targeting characteristics are from compounds exhibiting comparatively low logD values (i.e. compounds **36-38**, logD 2.80-3.21). Additionally, the central halogenation seems to lower pancreas-targeting substantially except for the methylene dioxy set of compounds. It is very interesting that independent halogenation (either central or terminal heterocycles) does not seem to greatly perturb the pancreatic tissue uptake, except for when the trifluoromethyl group is incorporated. Halogenating both positions, however, has a detrimental effect on the compound-pancreas localization. For example, compounds **15, 16, 17, 20, 23** are all effective at pancreas targeting and only have halogens at either the heterocycles or bridge. Compounds **18, 19, 21, 22, 24, 25** with all sites halogenated exhibit reduced pancreas uptake. We attribute this effect to an increase in overall hydrophobicity imparted by too many halogens on the core structure. Additionally, structures with higher

molecular weight in addition to greater hydrophobic character seem to be poor at pancreatic localization.

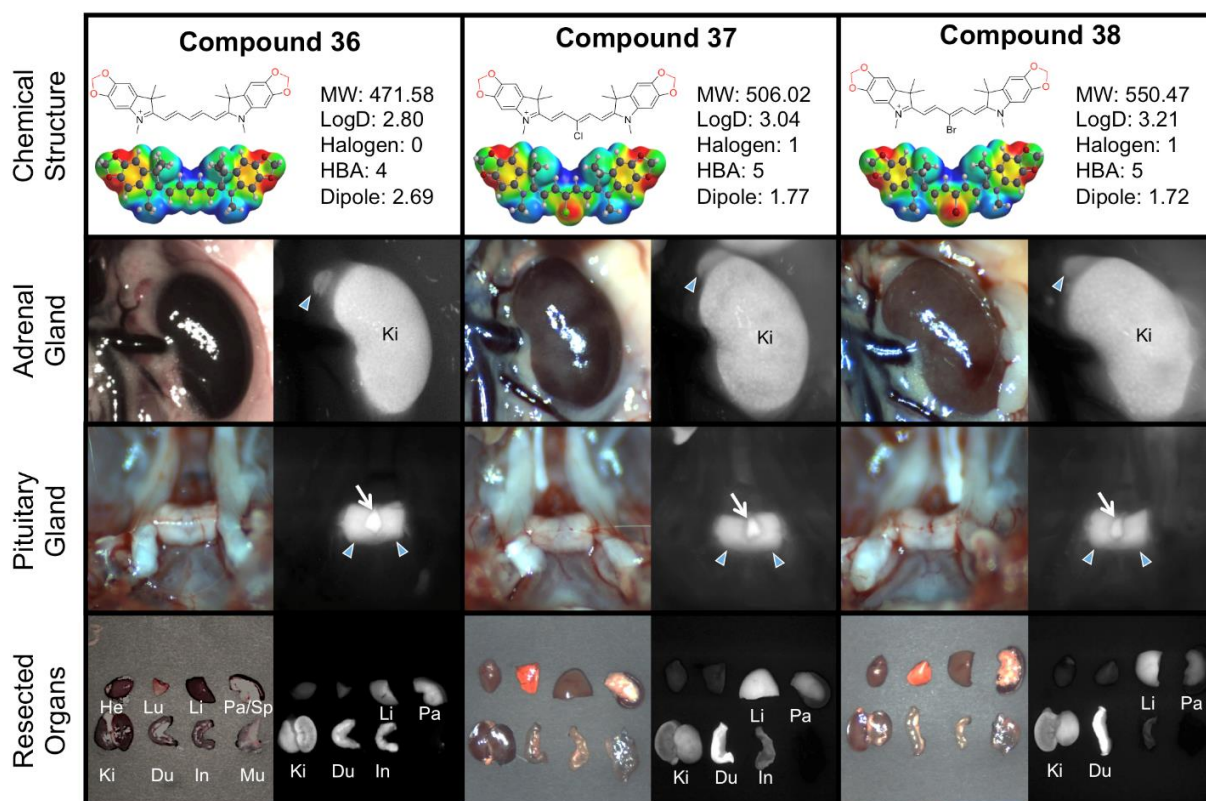


Figure 4-5. Compounds 36-38, targeting to adrenal glands and pituitary gland, and biodistribution of resected organs in CD-1 mice. 10 nmol of each fluorophore was injected intravenously into 25 g CD-1 mice 4 h prior to imaging and resection. Abbreviations used are: Du, duodenum; He, heart; In, intestine; Ki, kidneys; Li, liver; Lu, lungs; Mu, muscle; Pa, pancreas; SG, salivary gland, Sp, spleen. Arrows indicate the targeted gland. Arrows indicate the targeted gland. For pituitary glands, arrowheads indicate the anterior portion, and arrows for posterior pituitary.

4.4 Experimental

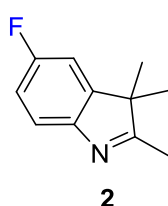
4.4.1 *Synthesis of pentamethine cyanine analogs.*

The chemical reagents used in the synthesis of these compounds were obtained from Acros Organics, Alfa Aesar and Matrix Scientific. The reactions were followed using silica gel 60 F₂₅₄ thin layer chromatography plates (Merck EMD Millipore, Darmstadt, Germany). Open column chromatography was utilized for the purification of all final compounds using 60-200 μm , 60A, classic column silica gel (Dynamic Adsorbents, Norcross, GA). The ¹H NMR and ¹³C NMR spectra were obtained using high quality Kontes NMR tubes (Kimble Chase, Vineland, NJ) rated to 500 MHz and were recorded on a Bruker Avance (400 MHz) spectrometer using DMSO-*d*₆ or MeOD-*d*₄ containing tetramethylsilane (TMS) as an internal calibration standard set to 0.0 ppm. UV-Vis/NIR absorption spectra were recorded on a Varian Cary 50 spectrophotometer. High-resolution accurate mass spectra (HRMS) were obtained either at the Georgia State University Mass Spectrometry Facility using a Waters Q-TOF micro (ESI-Q-TOF) mass spectrometer or utilizing a Waters Micromass LCT TOF ES+ Premier Mass Spectrometer. Liquid chromatography utilized a Waters 2487 single wavelength absorption detector with wavelengths set between 640 and 700 nm depending on the particular photophysical properties. The column used in LC was a Waters Delta-Pak 5 μM 100A 3.9 x 150 mm reversed phase C₁₈ column. Evaporative light scattering detection analyzes trace impurities that cannot be observed by alternate methods; a SEDEX 75 ELSD was utilized in tandem with liquid chromatography to confirm purity.

4.4.2 *General Synthetic Procedure for the formation of heterocyclic derivatives 1-5.*

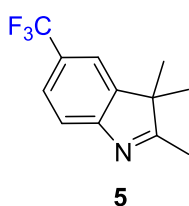
Appropriate 4-substituted phenylhydrazine hydrochloride derivative (20 g) was slowly added to a 250-mL round bottom flask containing 150-mL of vigorously stirring warm glacial acetic acid. After a heterogenous mixture was observed, 3-methyl-2-butanone (3 mol. equiv.) was added. The light brown solution was allowed to heat at reflux for 48-72 h. The reddish

brown mixture was concentrated on a rotary evaporator to form a viscous oil after removal of acetic acid. The oil was dissolved in dichloromethane (35 mL) and washed with water (3 x 25 mL) and saturated sodium bicarbonate (3 x 50 mL). The organic layer was extracted, dried over sodium sulfate and obtained, after solvent removal, as a deep-reddish brown oil (Note: fluorine-containing indolenine analog **2** was obtained as a red solid). Compound **1** was a commercially obtained starting material and was not synthesized.



5-fluoro-2,3,3-trimethyl-3H-indole (2): Yield 84%, MP 146-149 °C ; ^1H NMR (400 MHz, DMSO- d_6) δ : 1.24 (s, 6H), 2.19 (s, 3H), 7.09-7.04 (m, 1H), 7.33 (d, J = 8.0 Hz, 1H), 7.41 (br s, 1H).

5-chloro-2,3,3-trimethyl-3H-indole (3) and *5-bromo-2,3,3-trimethyl-3H-indole (4)* have been previously reported by our group.¹

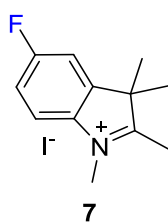


2,3,3-trimethyl-5-(trifluoromethyl)-3H-indole (5): Yield 43%, ^1H NMR (400 MHz, DMSO- d_6) δ : 1.32 (s, 6H), 2.60 (s, 3H), 7.89 (br s, 1H), 8.01 (br s, 1H), 8.24 (br s, 1H).

4.4.3 Synthesis of heterocyclic salts 6-10.

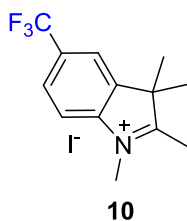
The methylated heterocyclic salts were synthesized using a general method by dissolving the viscous indolenine oil in anhydrous acetonitrile (25 mL) and heated to reflux in the presence of iodomethane (3 mol eq) for 12-18 h. The reaction mixture was allowed to cool to room temperature and the acetonitrile was removed under reduced pressure to afford a red residue. The crude was dissolved in methanol and diethyl ether was added to the solution to afford a light brown solid which was suction filtered and dried to obtain the final product.

1,2,3,3-tetramethyl-3H-indol-1-ium iodide (**6**) was commercially obtained and used in the dye syntheses without purification.



5-fluoro-1,2,3,3-tetramethyl-3H-indol-1-ium iodide (**7**): Yield 81%, ^1H NMR (400 MHz, DMSO- d_6) δ : 1.29 (s, 6H), 2.31 (s, 3H), 4.11 (s, 3H), 7.21-7.16 (m, 1H), 7.80 (d, J = 8.0 Hz, 1H), 7.99 (br s, 1H).

5-chloro-1,2,3,3-tetramethyl-3H-indol-1-ium iodide (**8**) and *5-bromo-1,2,3,3-tetramethyl-3H-indol-1-ium iodide* (**9**) were synthesized as previously described.



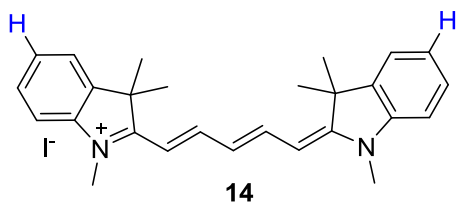
1,2,3,3-tetramethyl-5-(trifluoromethyl)-3H-indol-1-ium iodide (10): Yield 33%, ^1H NMR (400 MHz, $\text{DMSO-}d_6$) δ : 1.59 (s, 6H), 2.84 (s, 3H), 4.02 (s, 3H), 8.07 (br s, 1H), 8.15 (br s, 1H), 8.37 (br s, 1H).

4.4.4 Synthesis of Methine Precursor 11-13.

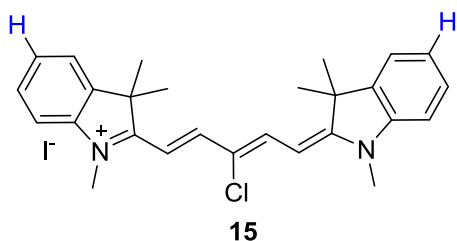
Precursor **11** was obtained commercially from Acros Organics and was used as obtained without modification. Compounds **12** and **13** have been previously described by our laboratory and the compounds were synthesized as described.

4.4.5 Synthesis of Methylated Pentamethine Cyanines 14-28, 31-33.

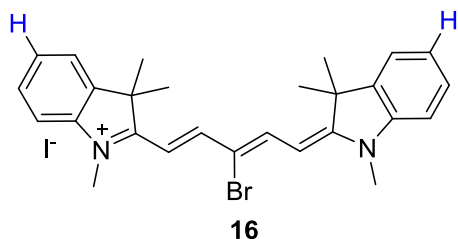
A mixture of indolium salt **6-10** (1 mmol), bis-iminium salt **11-13** (0.5 mmol), sodium acetate (0.23 mmol) and acetic anhydride (1 mL) was added to an oven dried round bottom flask with magnetic stirring bar. The reaction mixture was heated using a standard oil bath for a particular reaction time and was followed using TLC and UV-Vis-NIR absorption in ethanol. After starting materials were consumed, the reaction was allowed to cool to room temperature. Diethyl ether was added to the round bottom flask resulting in an oily metallic blue residue. The diethyl ether was decanted and the oil was dissolved in a minimal amount of methanol followed by the addition of diethyl ether (50 mL) resulting in the formation of light blue crystals, which were filtered. The crystals were dissolved in dichloromethane leaving unreacted sodium acetate on the funnel. The dichloromethane was removed *in vacuo*. Silica-gel column chromatography eluting with 2-5% methanol in dichloromethane afforded the various pentamethine cyanines in their respective yield.



1,3,3-Trimethyl-2-((1E,3E,5E)-5-(1,3,3-trimethylindolin-2-ylidene)penta-1,3-dien-1-yl)-3H-indol-1-ium iodide (14): Yield 64%, MP >260 °C ; ^1H NMR (400 MHz, MeOD- d_4) δ : 1.71 (s, 12H), 3.63 (s, 6H), 6.28 (d, $J = 16.0$ Hz, 2H), 6.65 (t, $J = 12.0$ Hz, 1H), 7.24 (t, $J = 8.0$ Hz, 2H), 7.29 (d, $J = 8.0$ Hz, 2H), 7.39 (t, $J = 8.0$ Hz, 2H), 7.48 (d, $J = 8.0$ Hz, 2H), 8.25 (t, $J = 12.0$ Hz, 2H); ^{13}C NMR (100 MHz, MeOD- d_4) δ 27.90, 31.71, 50.50, 104.44, 111.83, 123.31, 126.20, 129.71, 142.56, 144.29, 155.52, 175.28. TOF HRMS m/z $[\text{M}]^+$ calculated for $[\text{C}_{27}\text{H}_{31}\text{N}_2]^+$ 383.2487, found 383.2474.

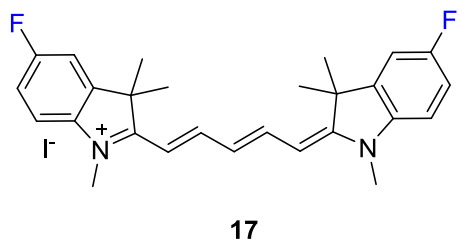


2-((1E,3Z,5E)-3-chloro-5-(1,3,3-trimethylindolin-2-ylidene)penta-1,3-dien-1-yl)-1,3,3-trimethyl-3H-indol-1-ium iodide (15): Yield 64%, M.P. 230-232 °C, ^1H NMR (400 MHz, MeOD- d_4) δ 1.76 (s, 12H), 3.71 (s, 6H), 6.435 (d, $J = 12$ Hz, 2H), 7.32 (t, $J = 8$ Hz, 2H), 7.39 (d, $J = 8$ Hz, 2H), 7.45 (t, $J = 8$ Hz, 2H), 7.54 (d, $J = 8$ Hz, 2H), 8.345 (d, $J = 12$ Hz, 2H). ^{13}C NMR (100 MHz, MeOD- d_4) δ 25.03, 29.53, 48.55, 98.93, 110.02, 121.00, 121.86, 124.55, 127.43, 140.42, 141.67, 146.72, 174.28. TOF HRMS m/z $[\text{M}]^+$ calculated for $[\text{C}_{27}\text{H}_{30}\text{N}_2\text{Cl}]^+$ 417.2098 found 417.2107.



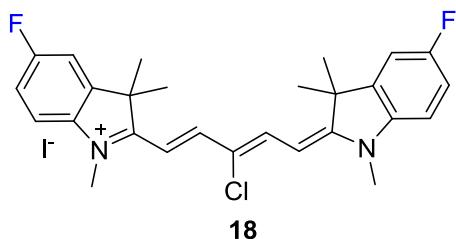
2-((1E,3Z,5E)-3-Bromo-5-(1,3,3-trimethylindolin-2-ylidene)penta-1,3-dien-1-yl)-

1,3,3-trimethyl-3H-indol-1-ium iodide (16): Yield 61%, M.P. 230-232 °C ; ^1H NMR (400 MHz, CDCl_3-d_1) δ 1.91 (s, 12H), 3.82 (s, 6H), 6.36 (d, $J = 8$ Hz, 2H), 7.16 (d, $J = 8.0$ Hz, 2H), 7.26-7.31 (m, 4H), 7.39-7.44 (m, 4H) 8.93 (d, $J = 12$ Hz, 2H). ^{13}C NMR (100 MHz, $\text{DMSO}-d_6$) δ 27.04, 31.98, 49.85, 102.61, 112.19, 115.98, 122.94, 125.97, 128.93, 141.78, 143.02, 149.64, 175.14. TOF HRMS m/z $[\text{M}]^+$ calculated for $[\text{C}_{27}\text{H}_{30}\text{N}_2\text{Br}]^+$ 461.1592 found 461.1585.

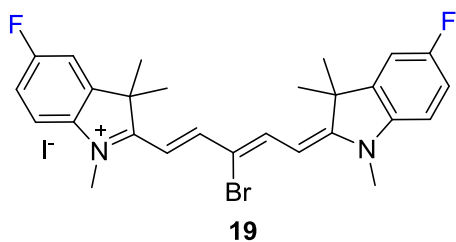


5-Fluoro-2-((1E,3E,5E)-5-(5-fluoro-1,3,3-trimethylindolin-2-ylidene)penta-1,3-dien-

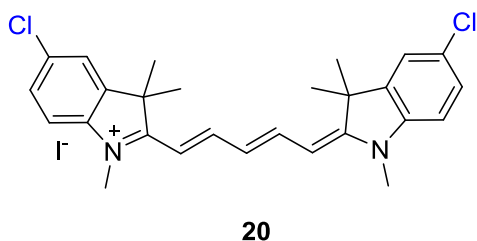
1-yl)-1,3,3-trimethyl-3H-indol-1-ium iodide (17): Yield 78%, MP >260 °C, ^1H -NMR(400 MHz, $\text{DMSO}-d_6$) δ 1.68 (s, 12H), 3.59 (s, 6H), 6.23 (d, $J = 12.0$ Hz, 2H), 6.52 (s, 1H), 7.24 (s, 2H), 7.39 (s, 2H), 7.62 (s, 2H), 8.29 (s, 2H). ^{13}C -NMR (100 MHz, $\text{DMSO}-d_6$) δ : 27.27, 31.85, 49.54, 103.64, 103.76, 110.82, 111.07, 112.43, 112.49, 112.59, 112.66, 115.15, 125.54, 139.55, 143.60, 143.69, 154.27, 154.29, 159.32, 161.72, 173.64. TOF HR-MS ESI m/z $[\text{M}]^+$ calculated for $[\text{C}_{27}\text{H}_{29}\text{F}_2\text{N}_2]^+$ 419.2299, found 419.2296.



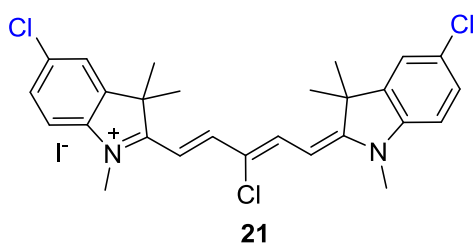
2-((1*E*,3*Z*,5*E*)-3-chloro-5-(5-fluoro-1,3,3-trimethylindolin-2-ylidene)penta-1,3-dien-1-yl)-5-fluoro-1,3,3-trimethyl-3*H*-indol-1-ium (**18**): Yield 37%, MP >260 °C, ¹H-NMR(400 MHz, DMSO-*d*₆) δ : 1.72 (s, 12H), 3.67 (s, 6H), 6.26 (d, *J* = 14 Hz, 2H), 7.29,7.31 (t, *J* = 6.8 Hz, 8.8 Hz, 2H), 7.52-7.54 (m, 2H), 7.70 (d, *J* = 6 Hz, 2H), 8.41 (d, *J* = 14 Hz, 2H). ¹⁹F NMR (375 MHz, DMSO- *d*₆) δ : -116.67 (s, 2F). TOF HR-MS ESI *m/z* [M]⁺ calculated for [C₂₇H₂₉F₂ClN₂]⁺ 453.1909 found 453.1914.



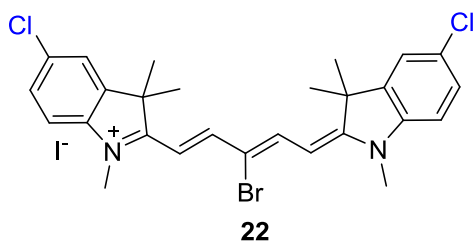
2-((1*E*,3*Z*,5*E*)-3-Bromo-5-(5-fluoro-1,3,3-trimethylindolin-2-ylidene)penta-1,3-dien-1-yl)-5-fluoro-1,3,3-trimethyl-3*H*-indol-1-ium (**19**) Yield 52%, ¹H-NMR(400 MHz, DMSO-*d*₆) δ : 1.72 (s, 12H), 3.67 (s, 6H), 6.26 (d, *J* = 13.2 Hz, 2H), 7.32 (t, *J* = 8.8 Hz, 2H), 7.55-7.52 (m, 2H), 7.70 (d, *J* = 7.6, 2H), 8.46 (d, *J* = 13.6, 2H). ¹⁹F NMR (375 MHz, DMSO- *d*₆) δ : -116.67 (s, 2F). TOF HR-MS ESI *m/z* [M]⁺ calculated [C₂₇H₂₉F₂N₂Br]⁺ was 497.1404 found 497.1394.



5-Chloro-2-((1E,3E,5E)-5-(5-chloro-1,3,3-trimethylindolin-2-ylidene)penta-1,3-dien-1-yl)-1,3,3-trimethyl-3H-indol-1-ium iodide (20): Yield 59%, MP >260 °C, ¹H-NMR(400 MHz, DMSO-*d*₆) δ: 1.69 (s, 12H), 3.59 (s, 6H), 6.27 (d, *J* = 14 Hz, 2H), 6.551 (t, *J* = 12.4, 12.0 Hz, 1H), 7.39 (d, *J* = 8.8 Hz, 2H), 7.46 (d, *J* = 8.4 Hz, 2H), 7.80 (s, 2H), 8.32 (t, *J* = 13.2 Hz, 2H). ¹³C-NMR (100 MHz, DMSO-*d*₆) δ: 27.30, 31.84, 49.51, 104.09, 112.87, 123.29, 126.16, 128.67, 129.50, 142.23, 143.54, 154.72, 173.65. TOF HR-MS ESI *m/z* [M]⁺ calculated for [C₂₇H₂₉Cl₂N₂]⁺ 451.1708, found 451.1722.

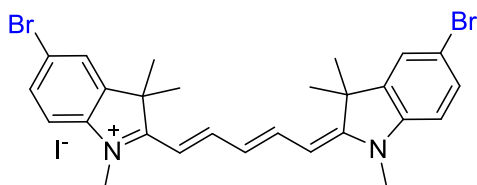


5-chloro-2-((1E,3Z,5E)-3-chloro-5-(5-chloro-1,3,3-trimethylindolin-2-ylidene)penta-1,3-dien-1-yl)-1,3,3-trimethyl-3H-indol-1-ium (21): Yield 53%, MP >260 °C, ¹H-NMR(400 MHz, DMSO-*d*₆) δ: 1.72 (s, 12H), 3.67 (s, 6H), 6.26 (d, *J* = 14 Hz, 2H), 7.52 (m, 4H), 7.89 (s, 2H), 8.43 (d, *J* = 13.6, 2H). ¹³C-NMR (100 MHz, DMSO-*d*₆) δ: 26.81, 32.15, 49.98, 100.72, 113.62, 123.06, 123.49, 128.80, 130.31, 142.02, 143.83, 147.96, 174.97. TOF HR-MS ESI *m/z* [M]⁺ calculated for [C₂₇H₂₉Cl₃N₂]⁺ 485.1318 found 485.1317.

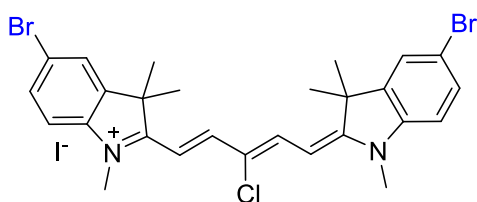


2-((1E,3Z,5E)-3-Bromo-5-(5-chloro-1,3,3-trimethylindolin-2-ylidene)penta-1,3-dien-1-yl)-5-chloro-1,3,3-trimethyl-3H-indol-1-ium iodide (22) Yield 69%, MP 252-254 °C ¹H-

NMR(400 MHz, DMSO- d_6) δ : 1.73 (s, 12H), 3.67 (s, 6H), 6.28 (d, $J = 13.2$ Hz, 2H), 7.52 (m, 4H), 7.89 (s, 2H), 8.47 (d, $J = 13.2$ Hz, 2H). ^{13}C -NMR (100 MHz, DMSO- d_6) δ : 26.79, 32.16, 50.03, 102.96, 113.65, 116.40, 123.51, 128.82, 130.35, 141.99, 143.83, 149.98, 175.15. TOF HR-MS ESI m/z $[\text{M}]^+$ calculated $[\text{C}_{27}\text{H}_{28}\text{BrN}_2\text{Cl}_2]^+$ was 529.0813 found 529.0810.

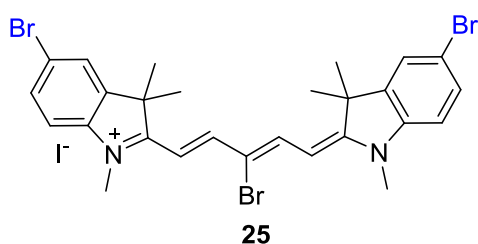
**23**

5-Bromo-2-((1E,3E,5E)-5-(5-bromo-1,3,3-trimethylindolin-2-ylidene)penta-1,3-dien-1-yl)-1,3,3-trimethyl-3H-indol-1-ium iodide (23): Yield 62%, MP >260 °C, ^1H -NMR(400 MHz, DMSO- d_6) δ : 1.69 (s, 12H), 3.58 (s, 6H), 6.27 (d, $J = 14$ Hz, 2H), 6.56 (t, $J = 12.4$, 12 Hz, 1H), 7.35 (d, $J = 8.4$ Hz, 2H), 7.59 (d, $J = 8.4$, 2H), 7.93 (s, 2H), 8.33 (t, $J = 13.2$ Hz, 2H). ^{13}C -NMR (100 MHz, DMSO- d_6) δ 27.25, 31.71, 49.48, 104.07, 113.33, 117.45, 126.09, 131.51, 142.63, 143.85, 154.86, 173.45. TOF HR-MS ESI m/z $[\text{M}]^+$ calculated for $[\text{C}_{27}\text{H}_{29}\text{Br}_2\text{N}_2]^+$ 539.0697, found 539.0695.

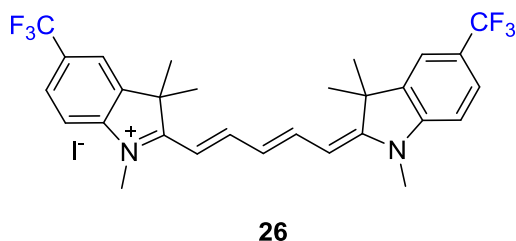
**24**

5-Bromo-2-((1E,3Z,5E)-5-(5-bromo-1,3,3-trimethylindolin-2-ylidene)-3-chloropenta-1,3-dien-1-yl)-1,3,3-trimethyl-3H-indol-1-ium (24): Yield 72%, MP >260 °C, ^1H -NMR(400 MHz, DMSO- d_6) δ : 1.72 (s, 12H), 3.67 (s, 6H), 6.28 (d, $J = 12.0$ Hz, 2H), 7.47 (d, $J = 8.0$ Hz, 2H), 7.63 (d, $J = 8.0$ Hz, 2H), 8.01 (s, 2H), 8.43 (d, $J = 12.0$ Hz, 2H). ^{13}C -NMR (100 MHz, DMSO- d_6) δ : 26.81, 32.17, 49.96, 100.69, 114.05, 118.37, 123.13, 126.26, 131.63, 142.40,

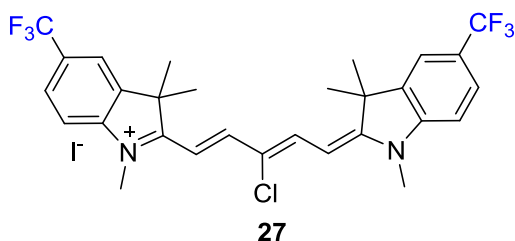
144.11, 147.96, 174.78. TOF HR-MS ESI m/z $[M]^+$ calculated for $[C_{27}H_{28}Br_2N_2Cl]^+$ 573.0308, found 573.0316.



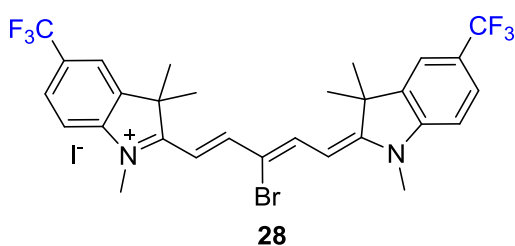
5-bromo-2-((1E,3Z,5E)-3-bromo-5-(5-bromo-1,3,3-trimethylindolin-2-ylidene)penta-1,3-dien-1-yl)-1,3,3-trimethyl-3H-indol-1-ium iodide (25): Yield 46%, MP 231-232 °C, 1H -NMR(400 MHz, DMSO- d_6) δ : 1.72 (s, 12H), 3.66 (s, 6H), 6.28 (d, $J = 13.2$ Hz, 2H), 7.47 (d, $J = 8.0$ Hz, 2H), 6.64 (d, $J = 8.4$ Hz, 2H), 8.01 (s, 2H), 8.48 (d, $J = 13.6$ Hz, 2H). ^{13}C -NMR (100 MHz, DMSO- d_6) δ : 26.79, 32.11, 50.03, 102.97, 114.07, 116.47, 118.42, 126.27, 131.65, 142.40, 144.13, 150.03, 175.01. TOF HR-MS ESI m/z $[M]^+$ calculated $[C_{27}H_{28}Br_3N_2]^+$ was 616.9803, found 616.9814



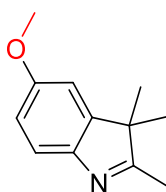
1,3,3-trimethyl-5-(trifluoromethyl)-2-((1E,3E)-5-((E)-1,3,3-trimethyl-5-(trifluoromethyl)indolin-2-ylidene)penta-1,3-dien-1-yl)-3H-indol-1-ium iodide (26): Yield 55%, MP 218-221°C, 1H NMR (400 MHz, $CDCl_3$): δ 1.81 (s, 12H), 3.79 (s, 6H), 6.53 (d, $J = 13.6$ Hz, 2H), 7.11 (t, $J = 13.6$ Hz, 1H), 7.21(d, $J = 8.4$ Hz, 2H), 7.60 (s, 2H), 7.70 (d, $J = 7.6$ Hz, 2H), 8.02 (t, $J = 13.6$, 2H). ^{19}F NMR: (375 MHz, DMSO- d_6): δ 62.00. TOF HRMS m/z $[M]^+$ calculated for $[C_{29}H_{29}N_2F_6]^+$ 519.2297, found 519.2393



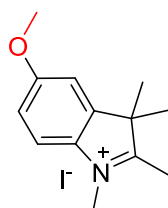
2-((1E,3Z)-3-chloro-5-((E)-1,3,3-trimethyl-5-(trifluoromethyl)indolin-2-ylidene)penta-1,3-dien-1-yl)-1,3,3-trimethyl-5-(trifluoromethyl)-3H-indol-1-ium iodide (27): Yield 71%, MP 226-228 °C, ¹H NMR (400 MHz, CDCl₃): δ 1.91 (s, 12H), 3.87 (s, 6H), 6.47 (d, *J* = 13.6 Hz, 2 H), 7.30 (s, 2H), 7.65 (m, 4H), 8.90 (d, *J* = 10.4 Hz, 2H). ¹⁹F NMR (375 MHz, DMSO-*d*₆): δ 62.05. TOF HRMS *m/z* [M]⁺ calculated for [C₂₉H₂₈N₂F₆Cl]⁺ 553.1840, found 553.1996.



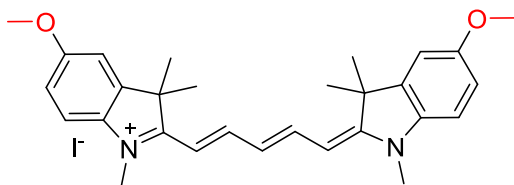
2-((1E,3Z)-3-bromo-5-((E)-1,3,3-trimethyl-5-(trifluoromethyl)indolin-2-ylidene)penta-1,3-dien-1-yl)-1,3,3-trimethyl-5-(trifluoromethyl)-3H-indol-1-ium iodide (28): Yield 71%, MP 226-228 °C, ¹H NMR (400 MHz, CDCl₃): δ 1.91 (s, 12H), 3.87 (s, 6H), 6.46 (bs, 2H), 7.30 (s, 2H), 7.69 (m, 4H), 8.91 (d, *J* = 7.2 Hz, 2H). ¹⁹F NMR (375 MHz, DMSO-*d*₆): δ: 62.01. TOF HRMS *m/z* [M]⁺ calculated for [C₂₉H₂₈N₂F₆Br]⁺ 597.1335, found 597.1597.

**29**

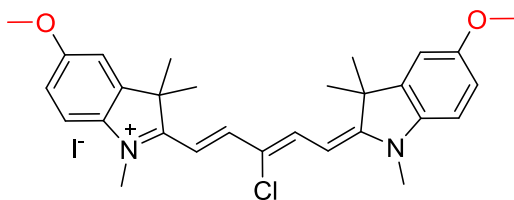
5-methoxy-2,3,3-trimethyl-3H-indole (29): Yield 78%, reddish brown oil; ^1H NMR (400MHz, DMSO- d_6) δ 1.17 (s, 6H), 2.16 (s, 3H), 3.68 (s, 3H), 6.74 (m, 2H), 7.38 (s, 1H).

**30**

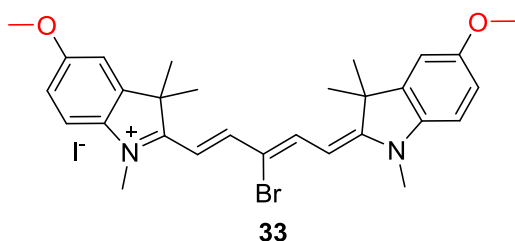
5-methoxy-1,2,3,3-tetramethyl-3H-indol-1-ium iodide (30): ^1H NMR (400 MHz, DMSO- d_6) δ 1.51 (s, 6H), 2.71 (s, 3H), 3.86 (s, 3H), 3.94 (s, 3H), 7.14 (d, $J = 8.0$ Hz, 1H), 7.47 (s, 1H), 7.81 (d, $J = 8.0$ Hz, 1H).

**31**

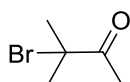
5-Methoxy-2-((1E,3E,5E)-5-(5-methoxy-1,3,3-trimethylindolin-2-ylidene)penta-1,3-dien-1-yl)-1,3,3-trimethyl-3H-indol-1-ium iodide (31): Yield 75%, MP 228-230 °C, ^1H NMR (400 MHz, DMSO- d_6): δ 1.66 (s, 12H), 3.56 (s, 3H), 3.81 (s, 6H), 6.17 (d, $J = 12$ Hz, 2H), 6.46 (t, $J = 12$ Hz, 1H), 6.95 (d, $J = 8$ Hz, 2H), 7.30-7.28 (m, 4H), 8.23 (t, $J = 12$ Hz, 2H). ^{13}C NMR (100 MHz, DMSO- d_6): δ 26.48, 30.62, 48.45, 55.29, 102.06, 108.43, 111.02, 112.84, 123.73, 135.80, 142.15, 151.94, 156.98, 171.55. TOF HRMS m/z $[\text{M}]^+$ calculated for $[\text{C}_{29}\text{H}_{35}\text{N}_2\text{O}_2]^+$ 443.2699, found 443.2692.

**32**

2-((1*E*,3*Z*,5*E*)-3-Chloro-5-(5-methoxy-1,3,3-trimethylindolin-2-ylidene)penta-1,3-dien-1-yl)-5-methoxy-1,3,3-trimethyl-3*H*-indol-1-ium iodide (**32**): Yield 80%, MP 235-237 °C, ¹H NMR (400 MHz, MeOD-*d*₄) δ 1.73 (s, 12H), 3.67 (s, 6H), 3.85 (s, 6H), 6.34 (d, *J* = 12 Hz, 2H), 6.99 (d, *J* = 8.0 Hz, 2H), 7.14 (s, 2H), 7.29 (d, *J* = 8.0 Hz, 2H), 8.23 (d, *J* = 12 Hz, 2H). ¹³C NMR (100 MHz, DMSO-*d*₆) δ 27.05, 31.96, 49.88, 56.33, 99.74, 109.36, 112.76, 114.07, 121.81, 136.50, 143.49, 146.18, 158.51, 173.76. TOF HRMS *m/z* [M]⁺ calculated for [C₂₉H₃₄N₂O₂Cl]⁺ 477.2309; found 477.2327.

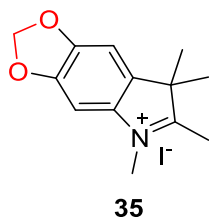


2-((1*E*,3*Z*,5*E*)-3-Bromo-5-(5-methoxy-1,3,3-trimethylindolin-2-ylidene)penta-1,3-dien-1-yl)-5-methoxy-1,3,3-trimethyl-3*H*-indol-1-ium iodide (**33**): Yield 55%, MP 214-216 °C, ¹H NMR (400 MHz, DMSO-*d*₆): δ 1.69 (s, 12H), 3.63 (s, 6H), 3.81 (s, 6H), 6.18 (d, *J* = 12 Hz, 2H), 6.97 (d, *J* = 8.0 Hz, 2H), 7.35 (s, 2H), 7.40 (d, *J* = 8 Hz, 2H), 8.38 (d, *J* = 12 Hz, 2H). ¹³C NMR (100 MHz, DMSO-*d*₆): δ 26.20, 31.16, 49.13, 55.53, 101.20, 108.56, 112.00, 113.28, 114.41, 135.67, 142.68, 147.32, 157.72, 173.09. TOF HRMS *m/z* [M]⁺ calculated for [C₂₉H₃₄N₂O₂Br]⁺ 521.1804 found 521.1801.



3-bromo-3-methyl-2-butanone (**34**): A mixture of 3-methylbutan-2-one (25.00 mL, 233.65 mmol) and acetic acid (38.00 mL) was added to a three-neck oven-dried round bottom flask and maintained at a temperature of 5 °C. Next, both molecular bromine (12.03 mL,

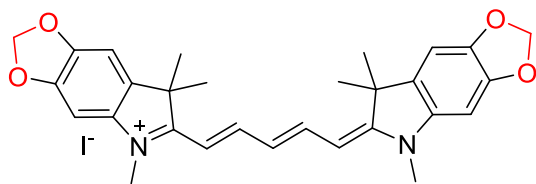
233.65 mmol) and acetic acid (13.00 mL) was combined in an addition funnel and added dropwise to the round bottom flask. When all of the bromine was added the reaction mixture was allowed to stir overnight at room temperature. To the resulting mixture, water (100 mL) was added, then transferred to a separatory funnel where another 100 mL of water was added and the organic layer was extracted with diethyl ether (3 x 150 mL). The compound was then washed with cold, saturated sodium bicarbonate (4 x 100 mL), dried over anhydrous sodium sulfate, and the reaction mixture was concentrated *in vacuo* to afford a yellow oil. The crude product was further purified *via* vacuum distillation (52 °C, ~ 25 mmHg) to yield a colorless oil. Yield 34%. ¹H NMR (400 MHz, CDCl₃) δ: 1.824 (s, 6H), 2.401 (s, 3H).



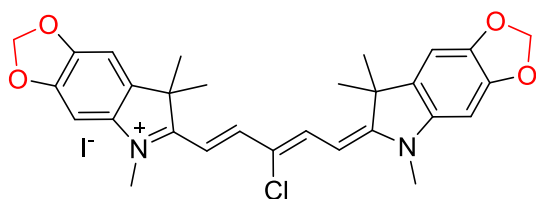
6,7,7-trimethyl-7H-[1,3]dioxolo[4,5-f]indole: A solution of DMF, (8 mL), aniline (1.56 g, 11.38 mmol), and potassium carbonate (1.05 g, 6.8 mmol) was brought to 45 °C in a two-neck round bottom flask with small magnetic stir-bar. 3-Bromo-3-methylbutan-2-one (**34**, 1.86 g, 1 mL) was added to the solution overnight with a syringe pump (Kd Scientific, Model 100). After addition was completed, solution was stirred for 24 h at 45 °C and monitored by TLC. After TLC showed that the starting material was consumed, dimethylformamide was evaporated *in vacuo*, and concentrate was extracted with toluene (5 x 20 mL) and was washed with deionized water. Toluene was concentrated to an amount of 10-20 mL, and *p*-methyltoluenesulfonic acid (0.110 g, 0.1 mol equiv.) was added to solution. Solution was allowed to reflux for 24h, until TLC showed an absence of starting material. Toluene was evaporated *in vacuo*, and dichloromethane (20 mL) was added to the reaction mixture. Solution was washed with a saturated solution of sodium carbonate (5 x 50 mL) until the organic layer was a red/brown color. DCM was removed under reduced pressure and the resulting red/brown

oil was recovered and the crude cyclic intermediate (obtained in 57% yield) was used without purification. *5,6,7,7-Tetramethyl-7H-[1,3]dioxolo[4,5-f]indol-5-ium iodide (35)*: This crude product was added to a round bottom flask with acetonitrile (50 mL) and iodomethane (3 mol. eq.). The mixture was heated to 60 °C for 4h. until the starting material was consumed. The reaction mixture was allowed to cool to rt and diethyl ether (80 mL) was added to the solution resulting in a dark brown oil. Several precipitations from methanol by diluting with diethyl ether afforded a light grey pure solid. Yield 60%, ¹H NMR (400 MHz, DMSO-*d*₆) δ : 1.48 (s, 6H) 2.70 (br. s., 3H) 3.90 (s, 3H) 6.19 (s, 2H) 7.48 (s, 1H) 7.64 (s, 1H), ¹³C NMR (100 MHz, DMSO-*d*₆) δ : 15.43, 21.48, 23.05, 53.61, 55.34, 101.44, 103.34, 125.76, 128.64, 129.34, 139.90, 145.50, 146.91, 147.91, 187.11.

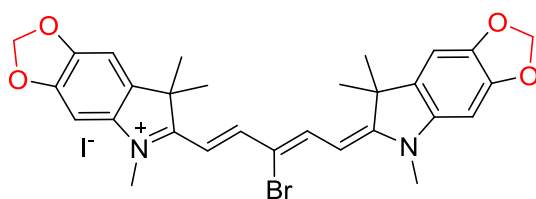
A mixture of indolium salt **35** (1 mmol), bis-iminium salt **11-13** (0.5 mmol), sodium acetate (0.23 mmol) and acetic anhydride (1 mL) was added to an oven dried round bottom flask with magnetic stirring bar. The reaction mixture was heated using a standard oil bath for a particular reaction time and was followed using TLC and UV-Vis-NIR absorption in ethanol. After starting materials were consumed, the reaction was allowed to cool to room temperature. Diethyl ether was added to the round bottom flask resulting in an oily metallic blue residue. The diethyl ether was decanted and the oil was dissolved in a minimal amount of methanol followed by the addition of diethyl ether (50 mL) resulting in the formation of light blue crystals, which were filtered. The crystals were dissolved in dichloromethane leaving unreacted sodium acetate on the funnel. The dichloromethane was removed *in vacuo*. Silica-gel column chromatography eluting with 2-5% methanol in dichloromethane afforded the various pentamethine cyanines **36-38** in their respective yield.

**36**

5,7,7-Trimethyl-6-((1E,3E,5Z)-5-(5,7,7-trimethyl-5H-[1,3]dioxolo[4,5-f]indol-6(7H)-ylidene)penta-1,3-dien-1-yl)-7H-[1,3]dioxolo[4,5-f]indol-5-ium iodide (36): Yield 38%, ^1H NMR (400 MHz, $\text{DMSO-}d_6$) δ : 1.63 (s, 12H), 3.54 (s, 6H), 6.06 (s, 4H), 6.18 (d, $J = 16.0$ Hz, 2H), 6.46 (t, $J = 16.0$ Hz, 1H), 7.13 (s, 2H), 7.28 (s, 2H), 8.16 (t, $J = 15$ Hz, 2H). ^{13}C NMR (100 MHz, $\text{DMSO-}d_6$) δ : 27.59, 31.89, 49.29, 94.35, 102.18, 103.40, 104.03, 125.11, 134.93, 137.52, 145.55, 148.02, 152.68, 173.32. TOF HRMS m/z $[\text{M}]^+$ calculated for $[\text{C}_{29}\text{H}_{31}\text{O}_4\text{N}_2]^+$ 471.2278 found 471.2268.

**37**

6-((1E,3Z,5E)-3-chloro-5-(5,7,7-trimethyl-5,7-dihydro-6H-[1,3]dioxolo[4,5-f]indol-6-ylidene)penta-1,3-dien-1-yl)-5,7,7-trimethyl-7H-[1,3]dioxolo[4,5-f]indol-5-ium (37): Yield 39%, ^1H NMR (400 MHz, $\text{DMSO-}d_6$) δ : 1.66 (s, 12H), 3.63 (s, 6H), 6.10 (s, 4H), 6.21 (d, $J = 13.6$ Hz, 2H), 7.29 (s, 2H), 7.38 (s, 2H), 8.30 (d, $J = 13.6$ Hz, 2H). ^{13}C NMR (100 MHz, $\text{DMSO-}d_6$) δ : 27.10, 32.20, 49.70, 94.92, 100.10, 102.34, 104.12, 135.49, 137.25, 146.04, 146.12, 148.10, 174.41. TOF HRMS m/z $[\text{M}]^+$ calculated for $[\text{C}_{29}\text{H}_{30}\text{N}_2\text{O}_4\text{Cl}]^+$ 505.1894 found 505.1871.

**38**

6-((1*E*,3*Z*,5*E*)-3-bromo-5-(5,7,7-trimethyl-5,7-dihydro-6*H*-[1,3]dioxolo[4,5-*f*]indol-6-ylidene)penta-1,3-dien-1-yl)-5,7,7-trimethyl-7*H*-[1,3]dioxolo[4,5-*f*]indol-5-ium (**38**): Yield 27%, ¹H NMR (400 MHz, DMSO-*d*₆) δ: 1.66 (s, 12H), 3.62 (s, 6H), 6.10 (s, 4H), 6.21 (d, *J* = 13.6 Hz, 2H), 7.29 (s, 2H), 7.39 (s, 2H), 8.36 (d, *J* = 13.6 Hz, 2H). ¹³C NMR (100 MHz, DMSO-*d*₆) δ: 27.08, 32.20, 49.76, 94.94, 102.34, 104.14, 113.95, 135.50, 137.22, 146.16, 146.16, 148.02, 174.59. TOF HRMS *m/z* [M]⁺ calculated for [C₂₉H₃₀N₂O₄Br]⁺ 549.1389 found 549.1368.

4.4.6 Optical and physicochemical property analyses.

All optical measurements were performed in various solvents, including ethanol, dimethyl sulfoxide (DMSO), phosphate buffered saline (PBS, pH 7.4) and at 37°C in 100% fetal bovine serum (FBS) buffered with 50 mM HEPES, pH 7.4. Absorbance and fluorescence emission spectra of the series of NIR fluorophores were measured using Varian Cary 50 absorbance spectrophotometer (190–1100 nm) and Shimadzu RF-5301PC spectrofluorometer (350–1000 nm). For fluorescence quantum yield (QY) measurements, rhodamine 800 in absolute ethanol (QY = 28%) was used as a calibration standard, under conditions of matched absorbance at 640 nm. *In silico* calculations of physicochemical distribution coefficient (logD at pH 7.4) was calculated using Marvin and JChem calculator plugins (ChemAxon, Budapest, Hungary). Electrostatic maps were calculated using Spartan DFT calculations at the B3LYP level.

4.4.7 LC-MS analysis.

The purity of all compounds was measured using liquid chromatography-mass spectrometry (LC-MS) on a Waters system consisting of a 1525 binary HPLC pump with a manual 7725i Rheodyne injector, a 996 Photodiode Array (PDA) detector, and a 2475 multiwavelength fluorescence detector. The column eluent was divided in 2 using a flow

splitter (Upchurch Scientific). A portion of the eluent flowed into an ELSD (Richards Scientific) while the rest flowed into a Micromass LCT ESI-TOF spectrometer (Waters) equipped with a Symmetry (R) C18 (4.6 x 150 mm, 5 μ m) reverse-phase HPLC column. For mass spectrometry mobile phase was solvent A = 0.1% formic acid (FA) in water and solvent B = CH₃CN with 95% A for 5 min and a linear gradient from 5% to 40% CH₃CN (from A to B for 30 min) at a flow rate of 1 mL/min, capillary voltage was -3317V, and sample cone voltage was -50V.

4.4.8 Animal models and biodistribution.

Animals were housed in an AAALAC-certified facility and were studied under the supervision of BIDMC's IACUC in accordance with the approved institutional protocol #057-2014. Male CD-1 mice (20–30 g, 6-8 weeks, Charles River Laboratories, Wilmington, MA) were anesthetized with 100 mg/kg ketamine and 10 mg/kg xylazine intraperitoneally (Webster Veterinary, Fort Devens, MA). For intraoperative imaging and biodistribution, the imaging system equipped with a custom filter set (Chroma Technology Corporation, Brattleboro, VT) composed of a 650 ± 22 nm excitation filter, a 680 nm dichroic mirror, and an 710 ± 25 nm emission filter was used at a fluence rate of 4 mW/cm², with white light (400-650 nm) at 40,000 lx. Color and NIR fluorescence images were acquired simultaneously with custom software at rates up to 15 Hz over a 15 cm diameter field of view. The imaging system was positioned at a distance of 18 inches from the surgical field. For each experiment, camera exposure time and image normalization was held constant.

4.4.9 Quantitative analysis.

At each time point, the fluorescence and background intensity of a region of interest (ROI) over each tissue was quantified using custom imaging software and ImageJ software (NIH, Bethesda, MD) version 1.45q. The signal-to-background ratio (SBR) was calculated as

SBR = fluorescence/background, where background is the signal intensity of neighboring tissues such as muscle or skin obtained over the period of imaging time. All NIR fluorescence images for a particular fluorophore were normalized identically for all conditions of an experiment. At least three animals were analyzed at each time point. Statistical analysis was carried out using the unpaired Student's *t*-test or one-way analysis of variance (ANOVA). Results were presented as mean \pm s.d. and curve fitting was performed using Prism version 4.0a software (GraphPad, San Diego, CA).

4.5 Conclusions

Toward satisfying the clinical need for native tissue targeted contrast agents in real-time NIR image-guided surgery, we present compounds that are effective at imaging the salivary, thyroid, pituitary, adrenal glands, lymph nodes and pancreas. We are confident that this work will lay the foundation for development of native tissue contrast agents for clinical use.

4.6 Acknowledgments

This study was supported by a Georgia State University dissertation grant (E.A.O.), the Brains and Behavior grant (M.H.) and the NIH/NIBIB grant #R01-EB-011523 (H.S.C.). EAO was supported through a pre-doctoral fellowship from the Center for Diagnostics and Therapeutics (CDT). Thank you Andrew Levitz and Nicholas Bruschi for helping with the synthesis.

4.7 References

1. Yokoyama, J.; Fujimaki, M.; Ohba, S.; Anzai, T.; Yoshii, R.; Ito, S.; Kojima, M.; Ikeda, K. A feasibility study of NIR fluorescent image-guided surgery in head and neck cancer based on the assessment of optimum surgical time as revealed through dynamic imaging. *Onco Targets Ther* **2013**, *6*, 325-30.

2. Ris, F.; Hompes, R.; Cunningham, C.; Lindsey, I.; Guy, R.; Jones, O.; George, B.; Cahill, R. A.; Mortensen, N. J. Near-infrared (NIR) perfusion angiography in minimally invasive colorectal surgery. *Surg Endosc* **2014**, *28*, 2221-6.
3. Li, C.; Cao, L.; Zhang, Y.; Yi, P.; Wang, M.; Tan, B.; Deng, Z.; Wu, D.; Wang, Q. Preoperative Detection and Intraoperative Visualization of Brain Tumors for More Precise Surgery: A New Dual-Modality MRI and NIR Nanoprobe. *Small* **2015**, *11*, 4517-25.
4. Zhu, N.; Huang, C. Y.; Mondal, S.; Gao, S.; Huang, C.; Gruev, V.; Achilefu, S.; Liang, R. Compact wearable dual-mode imaging system for real-time fluorescence image-guided surgery. *J Biomed Opt* **2015**, *20*, 96010.
5. Chan, H. H.; Siewerdsen, J. H.; Vescan, A.; Daly, M. J.; Prisman, E.; Irish, J. C. 3D Rapid Prototyping for Otolaryngology-Head and Neck Surgery: Applications in Image-Guidance, Surgical Simulation and Patient-Specific Modeling. *PLoS One* **2015**, *10*, e0136370.
6. Zheng, J.; Muhanna, N.; De Souza, R.; Wada, H.; Chan, H.; Akens, M. K.; Anayama, T.; Yasufuku, K.; Serra, S.; Irish, J.; Allen, C.; Jaffray, D. A multimodal nano agent for image-guided cancer surgery. *Biomaterials* **2015**, *67*, 160-8.
7. Ramakrishnan, V. R.; Kingdom, T. T. Does Image-Guided Surgery Reduce Complications? *Otolaryngol Clin North Am* **2015**, *48*, 851-9.
8. Al-Qudah, M. Image-Guided Sinus Surgery in Sinonasal Pathologies With Skull Base/Orbital Erosion. *J Craniofac Surg* **2015**, *26*, 1606-8.
9. Xi, L.; Jiang, H. Image-guided surgery using multimodality strategy and molecular probes. *Wiley Interdiscip Rev Nanomed Nanobiotechnol* **2015**.
10. Njiojob, C. N.; Owens, E. A.; Narayana, L.; Hyun, H.; Choi, H. S.; Henary, M. Tailored near-infrared contrast agents for image guided surgery. *J Med Chem* **2015**, *58*, 2845-54.

11. Hill, T. K.; Abdulahad, A.; Kelkar, S. S.; Marini, F. C.; Long, T. E.; Provenzale, J. M.; Mohs, A. M. Indocyanine green-loaded nanoparticles for image-guided tumor surgery. *Bioconjug Chem* **2015**, *26*, 294-303.
12. Liang, C. H.; Di, W. Y.; Ren, J. P.; Zhou, F. M.; Hu, Y.; Mao, H. J.; Han, D. M. Imaging, clinical and pathological features of salivary gland adenolymphoma. *Eur Rev Med Pharmacol Sci* **2014**, *18*, 3638-44.
13. Santhanam, P.; Oakley, C. Pet imaging of the adrenal gland-utility and pitfalls. *Endocr Pract* **2014**, *20*, 375-7.
14. Sumi, M.; Van Cauteren, M.; Sumi, T.; Obara, M.; Ichikawa, Y.; Nakamura, T. Salivary gland tumors: use of intravoxel incoherent motion MR imaging for assessment of diffusion and perfusion for the differentiation of benign from malignant tumors. *Radiology* **2012**, *263*, 770-7.
15. Hyun, H.; Park, M. H.; Owens, E. A.; Wada, H.; Henary, M.; Handgraaf, H. J.; Vahrmeijer, A. L.; Frangioni, J. V.; Choi, H. S. Structure-inherent targeting of near-infrared fluorophores for parathyroid and thyroid gland imaging. *Nat Med* **2015**, *21*, 192-7.
16. Owens, E. A.; Hyun, H.; Tawney, J. G.; Choi, H. S.; Henary, M. Correlating molecular character of NIR imaging agents with tissue-specific uptake. *J Med Chem* **2015**, *58*, 4348-56.
17. Owens, E. A.; Lee, S.; Choi, J.; Henary, M.; Choi, H. S. NIR fluorescent small molecules for intraoperative imaging. *Wiley Interdiscip Rev Nanomed Nanobiotechnol* **2015**.
18. Wada, H.; Hyun, H.; Vargas, C.; Gravier, J.; Park, G.; Gioux, S.; Frangioni, J. V.; Henary, M.; Choi, H. S. Pancreas-targeted NIR fluorophores for dual-channel image-guided abdominal surgery. *Theranostics* **2015**, *5*, 1-11.
19. Salim, M. M.; Owens, E. A.; Gao, T.; Lee, J. H.; Hyun, H.; Choi, H. S.; Henary, M. Hydroxylated near-infrared BODIPY fluorophores as intracellular pH sensors. *Analyst* **2014**, *139*, 4862-73.

20. Park, M. H.; Hyun, H.; Ashitate, Y.; Wada, H.; Park, G.; Lee, J. H.; Njiojob, C.; Henary, M.; Frangioni, J. V.; Choi, H. S. Prototype nerve-specific near-infrared fluorophores. *Theranostics* **2014**, *4*, 823-33.
21. Choi, H. S.; Nasr, K.; Alyabyev, S.; Feith, D.; Lee, J. H.; Kim, S. H.; Ashitate, Y.; Hyun, H.; Patonay, G.; Strekowski, L.; Henary, M.; Frangioni, J. V. Synthesis and in vivo fate of zwitterionic near-infrared fluorophores. *Angew Chem Int Ed Engl* **2011**, *50*, 6258-63.
22. Choi, H. S.; Gibbs, S. L.; Lee, J. H.; Kim, S. H.; Ashitate, Y.; Liu, F.; Hyun, H.; Park, G.; Xie, Y.; Bae, S.; Henary, M.; Frangioni, J. V. Targeted zwitterionic near-infrared fluorophores for improved optical imaging. *Nat Biotechnol* **2013**, *31*, 148-53.
23. Ashitate, Y.; Kim, S. H.; Tanaka, E.; Henary, M.; Choi, H. S.; Frangioni, J. V.; Flaumenhaft, R. Two-wavelength near-infrared fluorescence for the quantitation of drug antiplatelet effects in large animal model systems. *J Vasc Surg* **2012**, *56*, 171-80.
24. Wada, H.; Hyun, H.; Vargas, C.; Genega, E. M.; Gravier, J.; Gioux, S.; Frangioni, J. V.; Choi, H. S. Sentinel Lymph Node Mapping of Liver. *Ann Surg Oncol* **2015**.
25. Ashitate, Y.; Hyun, H.; Kim, S. H.; Lee, J. H.; Henary, M.; Frangioni, J. V.; Choi, H. S. Simultaneous mapping of pan and sentinel lymph nodes for real-time image-guided surgery. *Theranostics* **2014**, *4*, 693-700.

5 MICROWAVE ASSISTED SYNTHESIS OF NITROGEN CONTAINING HETEROCYCLES

This chapter serves to introduce microwave assisted organic synthetic methods for the application toward various nitrogenous heterocycles. Using these advancements, we have developed a green route using microwave irradiation to synthesize a series of pentamethine cyanines in the following chapter. This is an excerpt from a review article that has been prepared about many different microwave reactions and we are planning to publish the article in *Med Chem Comm*. My contributions as first author were the structural design, data interpretation and figure/manuscript preparation as well as guiding the other authors in looking up articles and preparing their individual portions of the manuscript.

Owens, E.A., Kananda, C., Holder, C, Ma, X., Bruschi, N., Henary, M. Microwave Synthesis of Drug-like Nitrogen Containing Heterocycles. Prepared for submission to *MedChemComm*. **2015**.

5.1 Abstract

Heterocyclic compounds are of immense research interest because they are found frequently in natural compounds and exhibit a wide range of interesting biological activities. The prominence of such compounds makes it vital to develop methods to increase the efficiency of their synthesis and probe effects of their modifications on biological efficacy. It is often these occur in a combinatorial manner, and many medicinal chemists have employed microwave-assisted organic synthesis (MAOS) in their laboratories as a way of efficiently and time-effectively synthesizing various heterocycles. Microwave assisted synthesis is of growing popularity amongst medicinal chemists and has proved more efficient in terms of reaction yield, time, purity and environmental friendliness for many reactions when compared to conventional thermal methods—especially in forming carbon-nitrogen heterocyclic ring systems. The importance of nitrogen-containing ring systems in medicine cannot be

understated as such ring systems have shown to have applicability ranging from vitamins and herbicides to anti-fungal, anti-bacterial and anti-cancer agents, among other things. The significance of these applications has created an unprecedented need for more efficient synthetic methods. This review presents the most recent and pressing advancements made in the field of microwave-assisted synthesis for the formation of small and medium nitrogen-containing heterocycles, including pyrrole, indole, pyridine, pyrrolidine, imidazole and pyrazoline structures and their corresponding biological profile.

5.2 Introduction.

Heterocyclic ring systems have attracted a great deal of attention from medicinal chemists due to their prominent use in several significant biologically active small molecules. A brief survey of the most active pharmacological heterocyclic atoms shows that nitrogen-based heterocycles are the most prevalent in biologically relevant small molecules. Heterocyclic compounds containing these atoms are of current research interest because they are building scaffolds for compounds that exhibit interesting biological activities and are used for many different pharmacological applications. Such ring systems have shown to have various applications ranging from vitamins and herbicides to anti-fungal, anti-bacterial and anti-cancer agents, among other things, and it is because of their wide range of applications that a more proficient method of synthesis should be developed. The development of efficient methods for their synthesis has been an ongoing quest. In the past few years, synthetic chemists have developed various methods for the preparation of heterocyclic compounds with many utilizing expensive palladium, gold or other equally expensive and environmentally polluting reagents. In this context, the need for improving reaction conditions has shown that microwave irradiation is particularly beneficial in generating heterocyclic compounds in elevated yield with a reduction or elimination of caustic reagents.

Microwave assisted organic synthesis (MAOS) use a different type of heating distinct to the external heating source used in conventional methods. This “superman heat vision” effect is based on temperature increase by dielectric heating which happens through two means: dipolar polarization and ionic conduction. Microwave dielectric heating drives chemical reactions by taking advantage of the ability of the medium to transform electromagnetic radiation into heat. It happens when the dipoles or ions present in the reaction mixture align in an applied electric field as a result to microwave irradiation. As the electric field oscillates, the dipoles or ion field tend to realign itself with the oscillating electric field, in the process, losing energy in the form of heat, due to molecular friction and dielectric losses. The microwave energy passes through the walls of the reaction vessel, heating the reactants and solvents by coupling directly with the molecules of the entire reaction mixture, consequently, the tendency for the initiation of boiling is reduced, and superheating above the boiling point of the solvent is possible. A properly designed cavity allows the temperature increase to be uniform throughout the sample, leading to reduction of reaction time, typically from days or hours to minutes or even seconds, and this method usually results in a direct increase in product yields, purity and atom efficiency—if the correct conditions are optimized. Additionally, these benefits lend themselves directly toward developing green methods for the production of medicinal compounds in an environmentally friendly approach. In order to maximize the effective use of microwave chemistry, one must judiciously select reagents (i.e. reactants, solvents, etc.) as well as understand the benefits yet also design around the inherent limitations of microwave assisted methods. One important concept is the dipole effect which is responsible for the dielectric heating afforded by microwave irradiation.

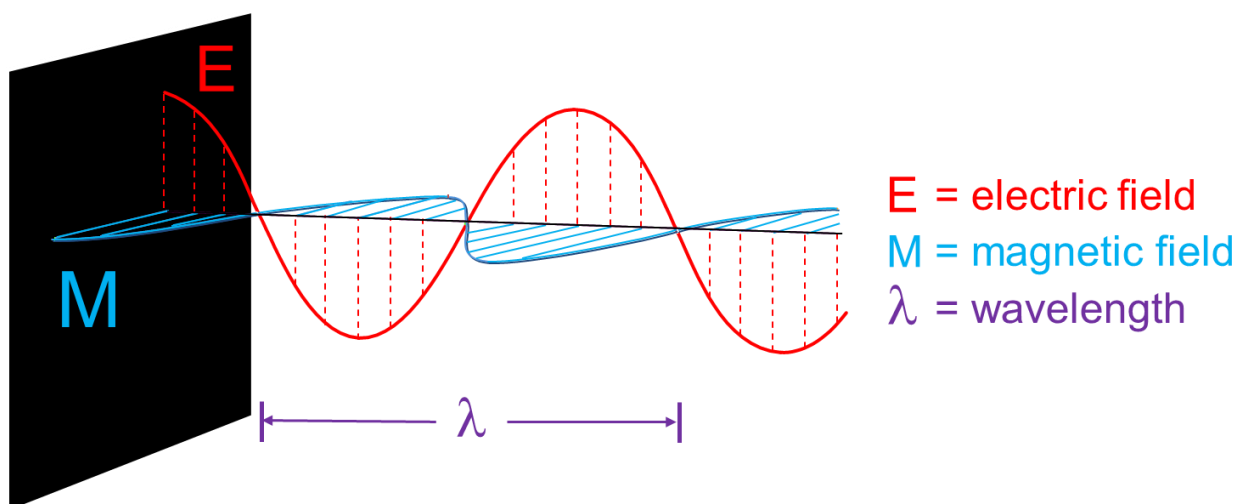


Figure 5-1. General schematic for microwave energy.

Microwave synthesis generally allows for one pot sequences for many reaction processes in the formation of such compounds. It can also be incorporated as a step in the overall scheme of pre-existing reactions. This review article presents the most recent and pressing advancements made in the field of microwave-assisted synthesis for the formation of small and medium nitrogen-containing heterocycles, including pyrrole, indole, pyridine, pyrrolidine, imidazole and pyrazoline structures among others. We are confident that medicinal chemists will be able to utilize these reactions toward the synthesis of new and promising therapeutic compounds.

5.3 Pyrrole-Containing Heterocyclic Compounds

The pyrrole ring has extreme notoriety in all aspects of the chemical industry; it is among the most frequently observed heterocyclic system in the structure of natural products and synthetic materials. Both the blood respiratory pigment heme and the photosynthesis pigment chlorophyll are biosynthesized from the pyrrole porphobilinogen; furthermore, Atorvastatin known commercially as Lipitor, a drug used to treat high cholesterol, is also a very well-known pyrrole-containing derivative(Figure 2) ¹. There are many classic protocols for the synthesis of pyrroles including the Knorr, Pall- Knorr, Hantzsch condensation and

Clauson-Kaas synthesis. The yields and conditions for performing this chemistry has been improved through microwave assistance.

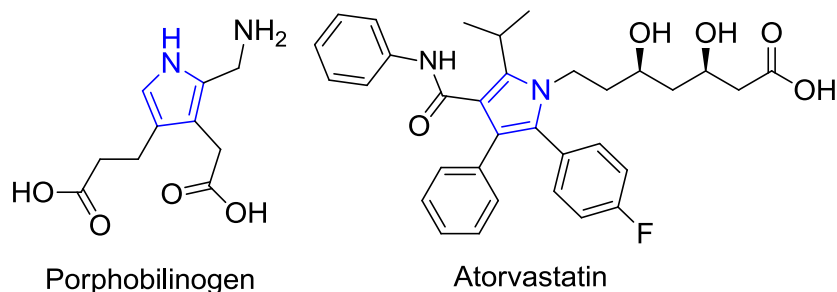
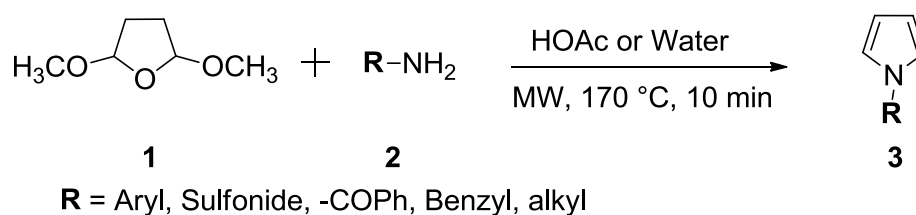


Figure 5-2. The chemical structures of porphobilinogen and atorvastatin.

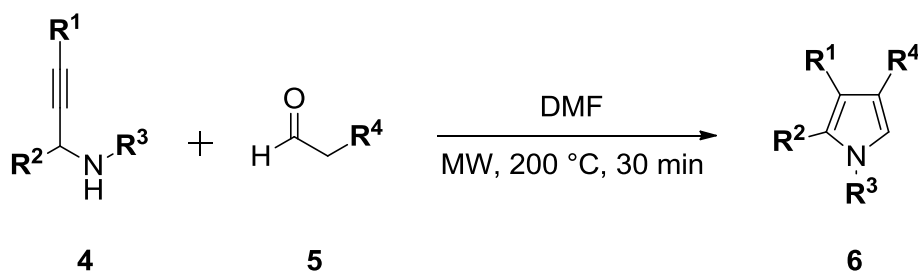
Miles *et al.* [10] adopted the Clauson-Kaas synthesis by reacting 2,5-dialkoxytetrahydrofurans **1** with a variety of nitrogen derivatives **2** using microwave irradiation at 170 °C for 10 minutes in either acetic acid or water as both solvent and promoter to produce *N*-substituted pyrroles **3** in good yields (Equation 1). In this reaction, higher yields (70-96%) were obtained when acetic acid was used as a solvent compared to water (12-74%). For the water solvated reactions, the yield and purity were found higher when the amine reacted were anilines or sulfonamides.



Equation 1.

Pyrrole derivatives bearing higher order substitution compared to **3** have been reported by Bremner *et al.* [11]. They described a novel method for the synthesis of pyrrole derivatives consisting of the reaction of various secondary propargylamines **4** with aldehydes **5** in DMF using microwave irradiation at 200 °C for 30 minutes to yield pyrrole compounds **6** (Equation

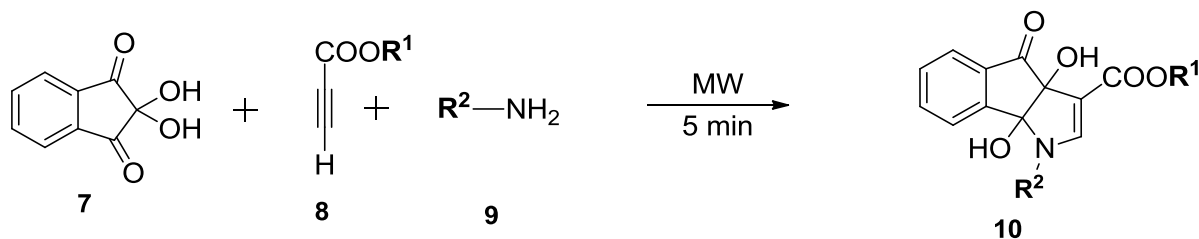
2). The following methodology exploits a tandem condensation/aza-Claisen rearrangement/cyclization sequence. It is highly tolerable to bulky aliphatic groups substituted on the R³ position, as well as pharmaceutically relevant functionality such as nitrogen and sulfur heterocycles at the acetylenic position.



R¹ = H, Ph, Pyrimidinyl, thiophenyl
 R² = H, Et, Bn, c-hex
 R³ = Bn, Me, OMe, But, c-hex, *i*prop
 R⁴ = H, Me, Ph, *i*prop, SMe, Ph-Et

Equation 2.

Hatamjafari *et al*² described a short and efficient 3-component reaction of ninhydrins **7**, alkyl propiolates **8**, and simple primary amines **9** under solvent free MW irradiation for 5 minutes for the synthesis of a series of tetrahydro-dihydroxy-oxoindeno[1,2-b]pyrroles **10** with good yield 60-87% (Equation 3). These polyhydroxylated pyrroles are very interesting pyrrole derivatives as they structurally resemble the sugar moiety of monosaccharide carbohydrates and can be used as potent inhibitors for enzymes that are involved in a wide range of important biological processes.



R¹ = Et, Me,

R² = Ben, n-But, cHex, Me, Et

Equation 3.

5.4 Indole

In the hierarchy of biologically privileged structures the indole ring system is one of the most prevalent³. Indole nuclei are prevalent in many bioactive natural products and medicinally important synthetics. The search for an efficient construction of indole skeletons of chemical and biomedical importance has remained a prevailing theme in organic synthesis⁴. One of the most robust and proven methods is Fisher indole synthesis—the reaction of a ketone with phenyl hydrazine in acidic media. Toward optimizing this effective route, microwave synthesis methods have been employed for maximizing the atom efficiency, yield, purity and scope toward the synthesis of natural products and medicines.

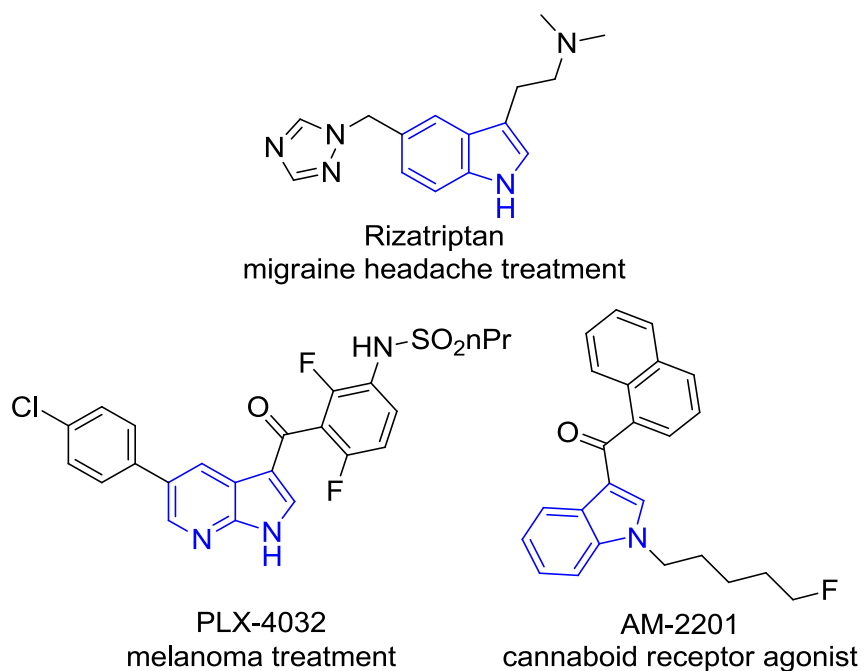
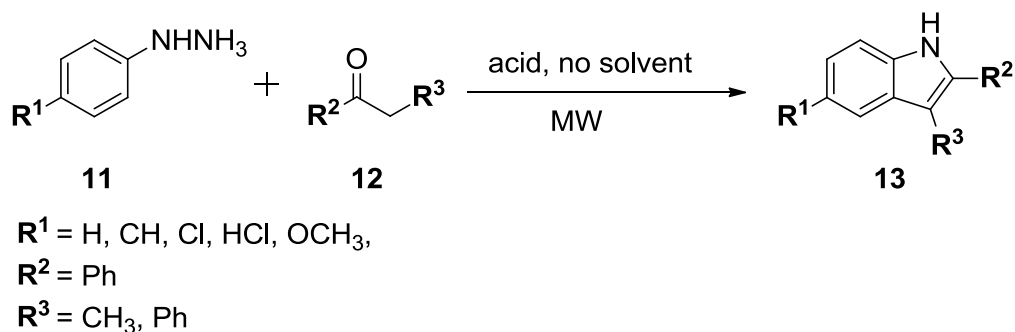


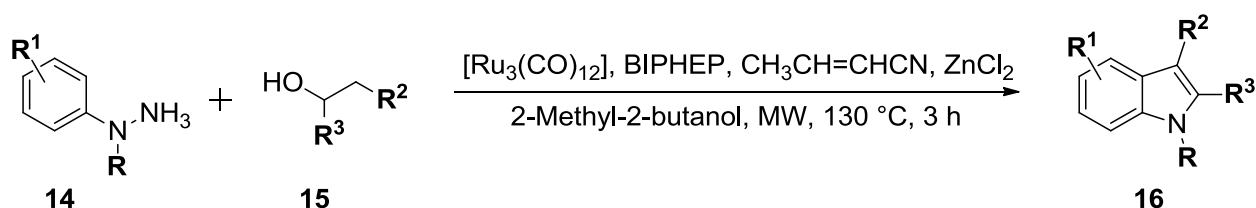
Figure 5-3. Drugs bearing the indole (or similar) moiety.

Creencia *et al.* described the synthesis of substituted indole **13** by a one-pot-one-step, solvent-free, microwave-assisted Fischer indole reaction using various readily available substituted phenylhydrazines **11** and enolizable ketones **12** (Equation 4). This synthesis method does not require the preparation and isolation of unstable arylhydrazones because commercially available precursors are used as starting reagents. Good product yields were obtained at shorter reaction times compared to the non-microwave assisted methods that generally offer complex mixtures in extended reaction timescales.



Equation 4.

The robust and diverse Fischer indole reaction was again utilized by Porcheddu and his co-workers⁵ starting from readily available alcohols. This reaction was carried out under \square W irradiation, combining the classical Fischer indole synthesis with the innovative hydrogen auto transfer technology to catalytically oxidize primary or secondary alcohols **15** in the presence of phenylhydrazine **14** and a protic or Lewis acid, using Ru and ZnCl₂ as a metal catalyst at 130 °C to give the corresponding indoles **16** (Equation 5). This method allows the formation of substituted indole rings using less toxic, and cheaper starting material.



R = H, Bn, Bu, Ph

R¹ = H

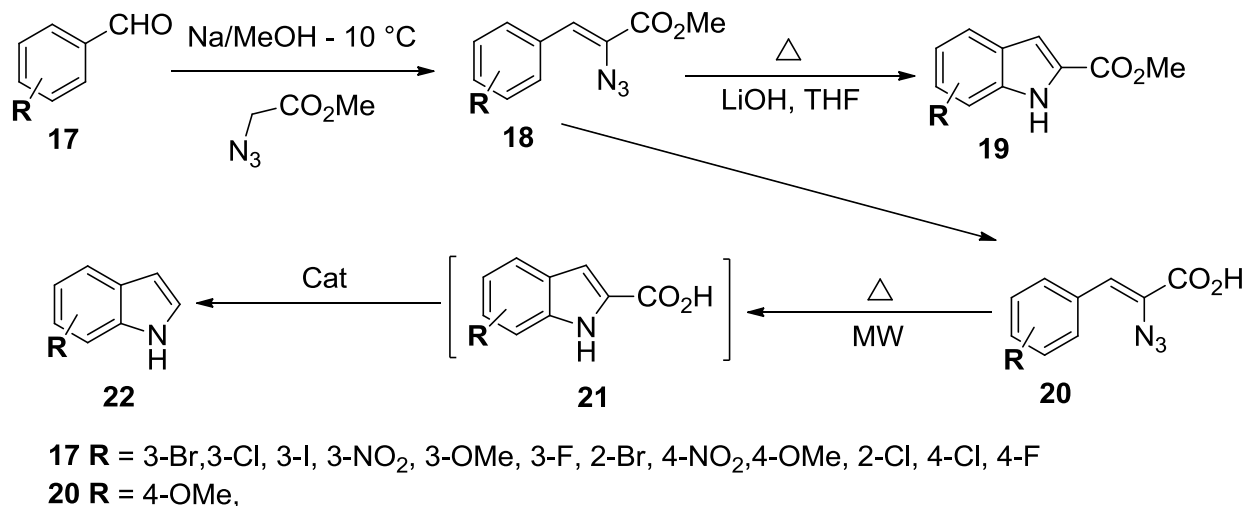
R² = Me, Prop, But, Pent, Bn, Ph

R³ = H, Me, Et, But,

Equation 5.

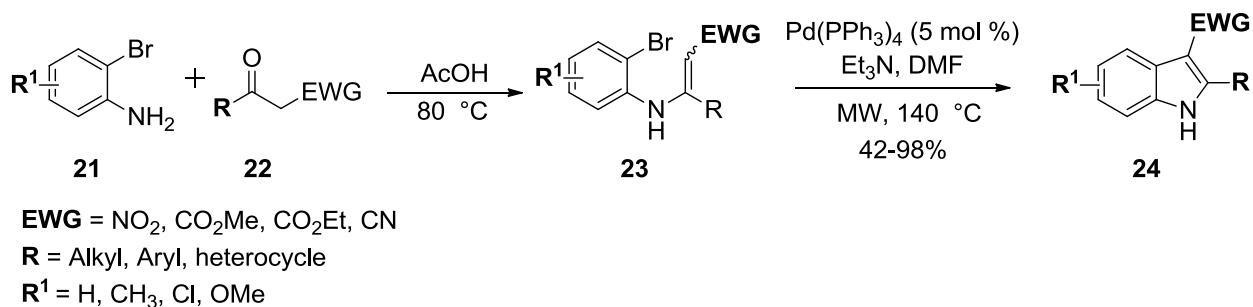
Ranasinghe *et al.*⁶ applied microwave, flow chemistry, and a combination of both methodologies through the Hemetsberger– Knittel (HK) indole synthesis to produce a number of substituted indoles. A series of azidoesters **18** were converted to the corresponding indole-2-carboxylates **19** under a variety of conditions. The use of microwave gave good yields at the optimal temperature of 200 °C for 10 min using toluene as solvent. A tandem HK-decarboxylation sequence was also performed by converting substrate **18** to the corresponding indole **22**. The process involved the conversion of the azidoester to azidoacid **20**, which was then subjected to \square W irradiation under optimal conditions in the presence of a catalyst to yield the substituted indole presumably through intermediate **21**, which could only be isolated using the Rh based catalyst (Scheme 1). An extension of the HK decarboxylation sequence reaction

involved the synthesis of analogs of agent PLX-4032 (Figure 3), an azaindoles recently approved as an anti-melanoma agent, and also used in peptide tagging.



Scheme 1.

Nguyen et al.⁷ described the versatility of tetrakis triphenylphosphine palladium(0) ($\text{Pd}(\text{PPh}_3)_4$) for the intermolecular Heck cyclization of *N*-aryl β -nitroenamines **23** as a route to the synthesis of functionalized 3-nitroindoles **24** using microwave irradiation at 140 °C (Scheme 2). This methodology utilized catalytic amount of the ubiquitous $\text{Pd}(\text{PPh}_3)_4$ and enamines readily available in one synthetic step from commercially available **21** o-bromoanilines and aryl and alkyl ketones. This method also allows for the synthesis of indoles bearing alternate and diverse electron-withdrawing groups (EWG) at 3-C.



Scheme 2.

5.5 Pyridines

Pyridine-based chemical compounds rank among the most highly represented in the pharmaceutical industry with many having several key biological characteristics—such as antibacterial, anti-inflammatory and analgesics⁸. Figure 4 shows three important compounds that utilize the pyridine structure in the pharmaceutical mendicant, among them are some of the most successful drugs in the market—particularly esomeprazole (Nexium™) ranks as 2nd in leading the U.S. pharmaceutical market in sales. Consequently, the development of methods for the preparation of substituted pyridine derivatives is of importance to synthetic and medicinal chemistry.

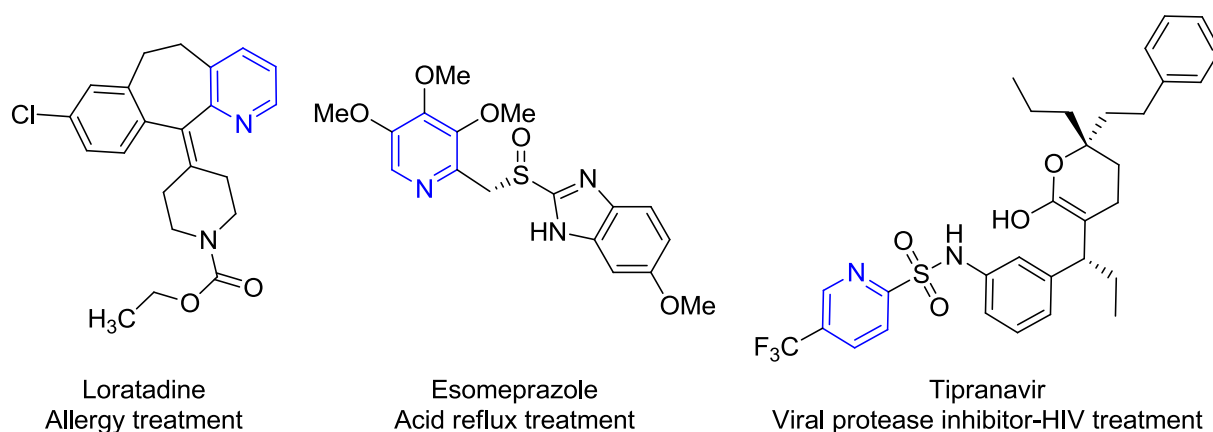
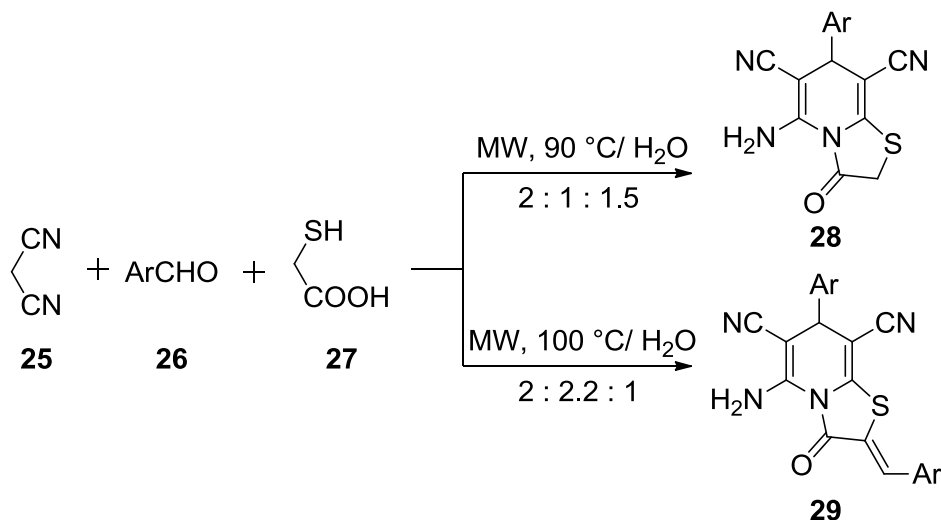


Figure 5-4. Drugs that exhibit a pyridine structure.

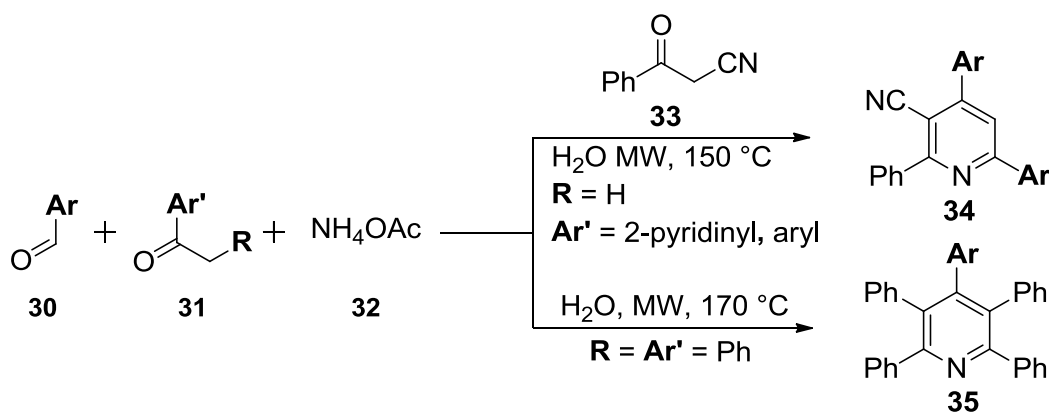
In response to the need for developing methods for the microwave synthesis of pyridine compounds, Shi *et al.*⁹ reported the optimization of the chemo selective synthesis of novel thiazolo[3,2-a]pyridines derivatives **28** and **29** *via* microwave-assisted three-component reactions of malononitrile **25**, aromatic aldehydes **26** and 2-mercaptoacetic acid **27** in water

(Scheme 3). These pyridine derivatives were examined for their antioxidant and cytotoxic activities. The novel class of thiazolo[3,2-a]pyridine derivatives, possess electron acceptors and donors that exhibited potent antioxidant activity and selective tumor cytotoxicity.



Scheme 3.

Jiang *et al.*¹⁰ developed a new improved reaction that offered a simple and efficient route for diversity-oriented synthesis, DOS, of highly functionalized 2 pyridine collections (Krohnke pyridines). The goal of diversity-oriented synthesis is the facile preparation of collections of structurally complex and diverse compounds from simple starting materials¹¹. This methodology involved the variation of aromatic aldehydes **30**, 3-oxo-3-phenylpropanenitrile **33** and 2-acetylpyridine substrates **31** in the presence of ammonium acetate using microwave heating at optimized reaction conditions to form highly functionalized pyridine derivatives (2, 2'-bipyridines, unsymmetrical 2,4,6-triarylpyridines) **34** and penta-aryl pyridines **35** (Scheme 4). The DOS methodology under microwave heating provides rapid access to pyridines with predictable control to selectively introduce various substituents.



Scheme 4.

5.6 Conclusion.

The need for the improvement of reaction condition in the synthesis of organic heterocyclic compounds is certainly a very current topic that has promoted the quest for methodologies that will alleviate the many hurdles encountered. The microwave assisted organic synthesis seems to clear some obstacles by enabling for the formation of many compounds in shorter reaction times, with higher yields and purity that either do not occur under conventional heating or occur at much higher temperatures. This article highlights some key applications of microwave assisted organic synthesis in the ring formation of organic heterocyclic for the development of N, O, and S based systems in the past 4 years. The many benefits of microwave-assisted organic synthesis are pushing it to become a key component in many step for the formation of many heterocyclic systems. The examples cited above are impressive and provide a good insight of the use of microwave-assisted organic synthesis in the field of heterocyclic chemistry.

5.7 References

1. Michlik, S.; Kempe, R., A sustainable catalytic pyrrole synthesis. *Nat. Chem.* **2013**, *5* (2), 140-144.

2. Hatamjafari, F.; Montazeri, N., Three-component process for the synthesis of some pyrrole derivatives under microwave irradiation. *Turk. J. Chem.* **2009**, *33* (6), 797-802.
3. Simoneau, C. A.; Strohl, A. M.; Ganem, B., One-pot synthesis of polysubstituted indoles from aliphatic nitro compounds under mild conditions. *Tetrahedron Lett.* **2007**, *48* (10), 1809-1811.
4. Fu, L. P.; Shi, Q. Q.; Shi, Y.; Jiang, B.; Tu, S. J., Three-component domino reactions for regioselective formation of bis-indole derivatives. *ACS combinatorial science* **2013**, *15* (2), 135-40.
5. Porcheddu, A.; Mura, M. G.; De, L. L.; Pizzetti, M.; Taddei, M., From Alcohols to Indoles: A Tandem Ru Catalyzed Hydrogen-Transfer Fischer Indole Synthesis. *Org. Lett.* **2012**, *14* (23), 6112-6115.
6. Ranasinghe, N.; Jones, G. B., Extending the versatility of the Hemetsberger-Knittel indole synthesis through microwave and flow chemistry. *Bioorganic & medicinal chemistry letters* **2013**, *23* (6), 1740-2.
7. Nguyen, H. H.; Kurth, M. J., Microwave-Assisted Synthesis of 3-Nitroindoles from N-Aryl Enamines via Intramolecular Arene-Alkene Coupling. *Organic Letters* **2012**, *15* (2), 362-365.
8. Dutta, M.; Saikia, P.; Gogoi, S.; Boruah, R. C., Microwave-promoted and Lewis acid catalysed synthesis of steroidal A- and D-ring fused 4,6-diarylpyridines. *Steroids* **2013**, *78* (4), 387-95.
9. Shi, F.; Li, C.; Xia, M.; Miao, K.; Zhao, Y.; Tu, S.; Zheng, W.; Zhang, G.; Ma, N., Green chemoselective synthesis of thiazolo[3,2-a]pyridine derivatives and evaluation of their antioxidant and cytotoxic activities. *Bioorganic & medicinal chemistry letters* **2009**, *19* (19), 5565-8.

10. Jiang, B.; Hao, W.-J.; Wang, X.; Shi, F.; Tu, S.-J., Diversity-Oriented Synthesis of Kröhnke Pyridines. *J Comb Chem* **2009**, *11* (5), 846-850.
11. Ciolli, C. J., Diversity-Oriented Synthesis. **2002**.

6 ENVIRONMENTALLY BENIGN SYNTHETIC APPROACHES—APPLIED TO FLUORESCENT DYES AND THEIR PRECURSORS

The chapter has been adapted from the publication in *Dyes and Pigments* concerning the application microwave and green methods to the synthesis of carbocyanine compounds and many calculations to begin predicting microwave energetics in reactions as well as HOMO LUMO associations with bathochromically shifted fluorophores. My contributions as first author were the design, synthesis, optical property determination, molecular modeling and computational experiments, data interpretation and figure/manuscript preparation.

Owens, E.A., Bruschi, N., Tawney, J. G., Henary, M. M. A Microwave-Assisted and Environmentally Benign Approach to the Synthesis of Near-Infrared Fluorescent Pentamethine Cyanine Dyes **2015** *Dyes and Pigments* 113, 27-37.

6.1 Abstract

A time-efficient and eco-conscious microwave methodology was developed and applied to synthesize a systematic library of pentamethine cyanine dyes and their corresponding precursors. The synthesis outlined herein drastically reduced the reaction pathway for pentamethine carbocyanine dye syntheses from days to min, as well as producing increased yields (89-98%) to the conventional heating method (18-64%). Twelve examples of pentamethine cyanine dyes were synthesized by means of microwave-assisted organic synthesis which provided excellent yield in expedited reaction time and were obtained using facile isolation methods. Furthermore, three cyanines were prepared with a novel methylene dioxy heterocyclic structure which imparted an approximately 40 nm bathochromic shift compared to unsubstituted counterparts; these results were shown to be in agreement with DFT calculations and HOMO-LUMO energy differences.

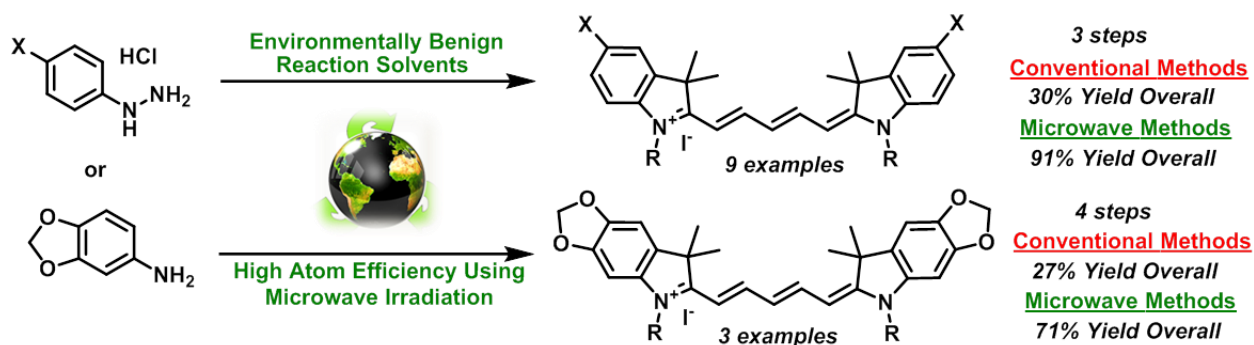


Figure 6-1. Graphical representation for the microwave assisted green method for the preparation of pentamethine cyanines.

6.2 Introduction

Mother Nature provides our atmosphere to breathe, food required to eat and beautiful scenery to enjoy. Protecting and nurturing our environment should be a task shared by all in the research community. There are many methods for helping to preserve our precious natural resources which include the following: (1) using green solvents, (2) reducing heating times to conserve energy, (3) increasing atom efficiency by using higher yielding reaction conditions and (4) eliminating wasteful purification steps by using optimized methods that reduce side-products. These principles have been applied to the synthesis of many classes of compounds that are interesting to a broad population of the scientific community. Correspondingly, we have chosen to develop a completely benign synthetic route for the synthesis of near-infrared fluorescent compounds that have shown excellent promise in biological imaging, solar-cell technology, as chemodosimeters in sensing biologically relevant species and for non-covalent labeling of biomolecules.

Near-infrared (NIR, 640-900 nm) fluorescent chromophores have garnered considerable research interest for biomolecular labeling because of their unique red-shifted optical properties. [1-4] The majority of fluorescent sensors have shown to emit light in the visible region (400-600 nm), which forces unwanted competition with background noise that arises from inherent biomolecular auto-fluorescence. This competition disrupts the meaningful

signal and can lead to extreme difficulty in signal delineation often with undesirable results. [5] To avoid the problems associated with visible-light-emitting fluorophores, molecules which absorb and emit light in the near-infrared region have been of significant interest to the scientific community. [1-3, 5-7]

Specifically among the NIR emitting dyes, immense interest has been placed in the particular class of chromophores known as cyanine dyes, and they have shown extensive applications in cancer imaging, nucleic acid detection, biomolecular labeling, photographic processes, information storage and dye lasers. [7-10] Possessing relatively high molar absorption coefficients and a broad range of tunable fluorescence wavelengths (650-900 nm) cyanine dyes have been synthesized to emit light in the NIR range while maintaining biological efficacy. [4, 5, 8-11] Chiefly among these fluorophores, pentamethine cyanine dyes have shown significant promise for image guided surgery using NIR light. [1] Specifically, we reported several pentamethine cyanine dyes that have been shown to specifically locate various tissues of clinical importance during image-guided surgery. [1] Expanding upon the synthesis of pentamethine cyanine dyes as biomolecular imaging agents has been a focus of many bioorganic research labs worldwide. [12, 13]

The design and synthesis of various substituted pentamethine cyanines has been achieved in a combinatorial manner by changing the N-alkyl substituent or functionalizing different positions of the heterocyclic backbone. [2, 4] It has been observed that minor structural alterations elicits a drastic biological response which makes synthesis of highly varied chemical structures very important.[1] This provides a significant rationale for developing a fast, facile and effective method for generating a library of pentamethine cyanines with high purity levels.

Synthesis of various pentamethine cyanine dyes with slightly altered connectivity has been shown to take hours to days by the conventional oil bath heating method with lengthy,

difficult column chromatography that generates environmentally polluting solvent waste. [2, 6, 14] Cyanine dyes are sensitive to the acidic nature of silica gel, photodegrade during purification steps and cleave in the basic solutions required for their synthesis (Figure 4-2); therefore, expediting the reaction time and increasing purity levels is of highly important.

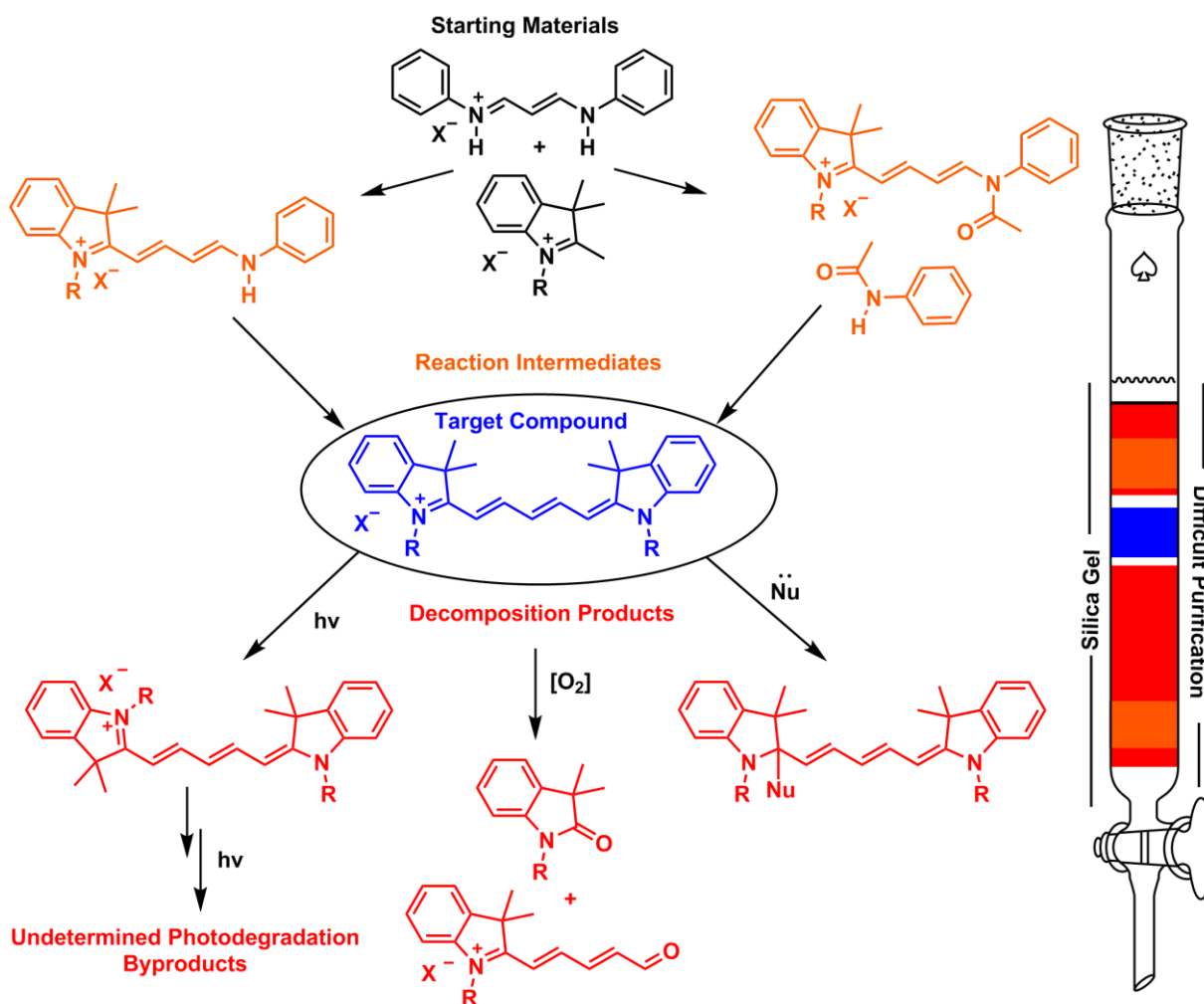


Figure 6-2. The reaction intermediates and postulated degradation products that form during either the classical heating method of synthesis or purification of cyanine dyes that lead to difficulty in obtaining analytically pure compounds for biological testing.

Recently, the implementations of microwave chemistry has helped speed reactions and decrease the environmentally harmful waste common in organic labs; it has received interest

throughout the scientific community and it is very desirable to conduct synthetic protocol under microwave irradiation.

In order to implement this technology in cyanine synthesis, we have harnessed the ability of our reaction mixture to absorb microwave energy. Electromagnetic irradiation of molecules results in rapid, volumetric heating caused by the dielectric effect which yields the final compounds without the need for column purification that may jeopardize the chemical integrity of the compounds from photodegradation or decomposition on the silica matrix [9]. The pentamethine class of cyanine dyes has not been optimized using MAOS. Utilizing a green approach, an entire synthetic pathway has been designed to prepare pentamethine cyanines with diverse chemical structures. Specifically, in the final synthetic step, using the CEM Discover LabMate several different substituted pentamethine cyanine dyes have been synthesized within 20 min in analytical purity without column purification. In comparison to the conventional heating method, the syntheses described herein provide drastically decreased reaction times and comparable or increased yields (89-98% in the final step, 80-91% overall).

6.3 Results and Discussion

6.3.1 Eco-friendly Synthesis of Pentamethine Cyanine Fluorophores

The common synthetic method for the preparation of pentamethine cyanines begins with the formation of the terminal heterocyclic moieties. The four heterocycles used to afford the compounds were synthesized according to Figures 4-3 and 4-4. We optimized each step for the synthesis beginning with heterocyclic formation and begins when substituted phenylhydrazines are refluxed in glacial acetic acid with 3-methyl-2-butanone to afford **1** and **2**.

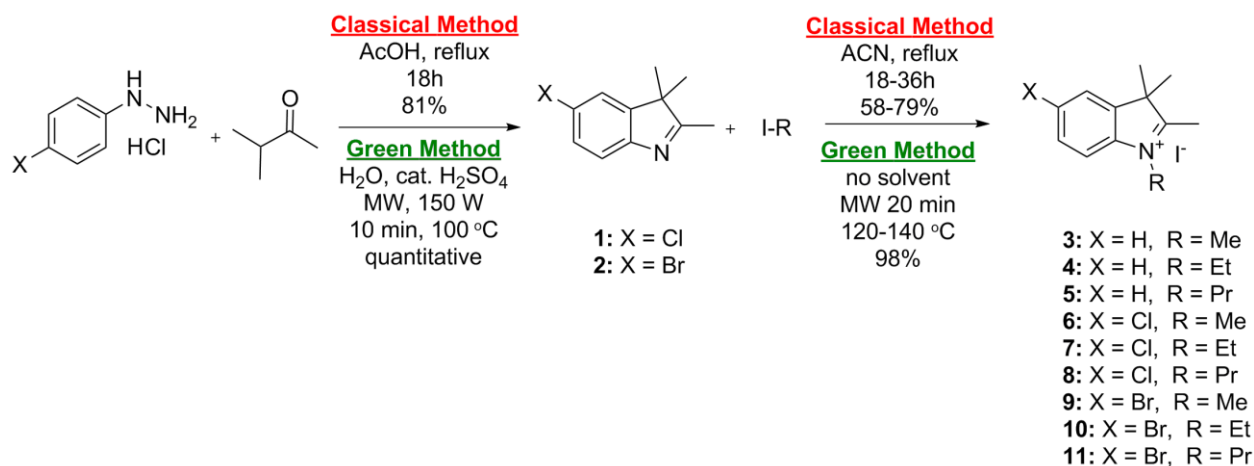


Figure 6-3. The new, green microwave assisted method for preparation of alkylated salts 3-11 based off of the indolenine heterocyclic structure.

This reaction affords the desired indolenine compounds in good yield, but this method requires extended periods of reaction time exceeding 24 hours and excess acetic acid as solvent. Our green microwave method employs water as an environmentally conscious solvent and a catalytic (0.1 mol. eq.) amount of sulfuric acid to achieve quantitative conversion in 10 min. The second synthetic step is the quaternization of the indolenine nitrogen atom. A classical method for this synthesis is mixing the two reagents in acetonitrile and refluxing until the reaction goes to completion. The volatile nature of short chain alkyl halides limits the reaction scope and many molar equivalents should be used to completely react with the heterocyclic starting materials. This leads to low atom efficiency and the use of an unnecessarily high quantity of alkylating agent. Our optimized alkylation is effective at a 1.2 molar equivalency of alkyl iodide (Me, iodomethane, Et, iodoethane, Pr, iodopropane) without the use of harmful solvents at a drastically reduced reaction time. After 20 min, the corresponding quaternary salts precipitate in >98% yield as a fine powder and can be utilized in the next reaction without purification procedures.

Achieving new heterocyclic building blocks for the synthesis of cyanine dyes has been limited by the number of commercially available hydrazine hydrochlorides. The synthesis of hydrazines with a number of interesting substitutions has remained scarce throughout the literature; however, utilizing a modified Bischler-Möhlau approach, we can achieve the synthesis of an acidic methylene proton with the quaternized nitrogen through a facile microwave-assisted approach (accessing the scope of this reaction using additional heterocycles are explored in another paper, Owens et al. manuscript in preparation). Our model compound was the dioxolane structure.

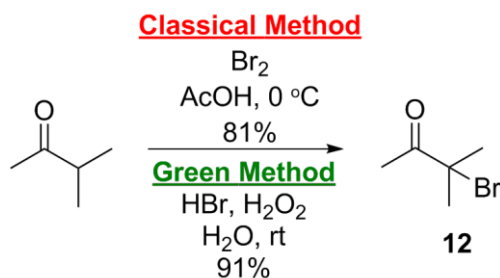


Figure 6-4. The preparation the brominated ketone 12.

The initial precursor to the dioxolane heterocyclic unit, 3-bromo-3-methylbutan-2-one (shown in Figure 5-4), was classically prepared beginning with bromination of 3-methyl-2-butanone under acidic conditions at 0 °C. The high volatility and dangerous nature of working with molecular bromine requires the use of an alternate and environmentally friendly route. Applying the the bromine “on water” method reported by the Iskra lab [15], we achieved selective and high yielding bromination of 3-methy-2-butanone to afford **12**.

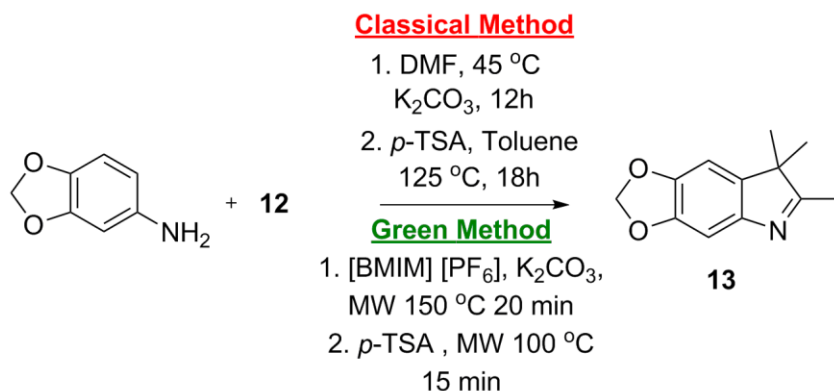


Figure 6-5. The preparation of the fused dioxolane heterocycle **13.**

The cyclic product **13** is formed through treatment of the commercially available 3,4-(methylenedioxy)aniline with intermediate **12** in DMF with potassium carbonate followed by addition of para-toluenesulfonic acid in toluene at 125 °C (Equation 2).

In order to develop a green-method for the formation of this dioxolane, we began by examining the mechanism of this reaction. From a mechanistic point-of-view, this reaction is very interesting. In basic conditions, the anilino-amine is highly nucleophilic substituting the tertiary bromine alpha to the carbonyl of **12** through an S_N1 pathway. Monoalkylation of the arylamine is successful due to high steric hindrance from the dimethyl groups. Treatment of this intermediate with para-toluenesulfonic acid in the presence of excess catalytic aniline yields the dehydrated arylimine intermediate that undergoes loss of aniline through electrophilic aromatic substitution and re-aromatization yields the heterocyclic precursor **13**.

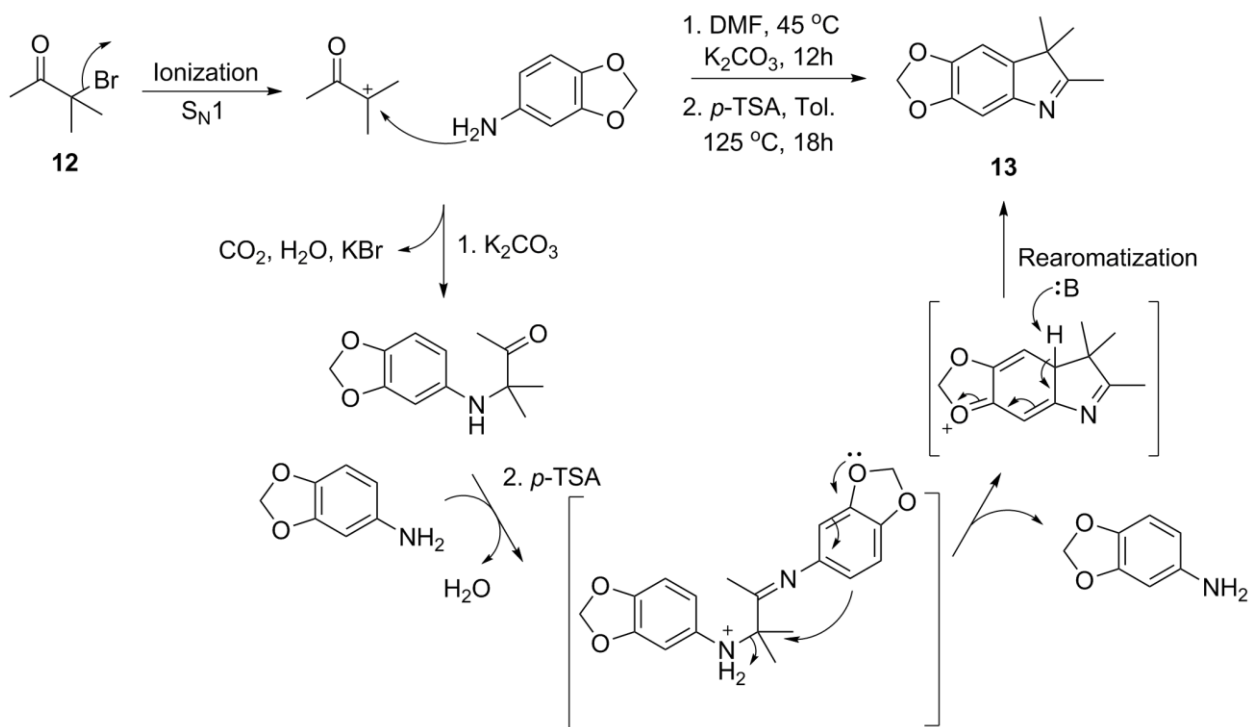
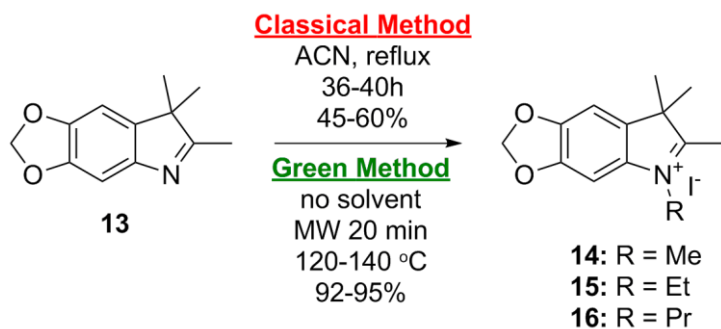


Figure 6-6. The proposed mechanism based off of an adaptation of the Bischler-Möhlau method for indole formation.

We postulated that this may work satisfactorily using eco-friendly conditions through microwave irradiation and successfully replaced the organic solvents with the ionic liquid [BMIM][PF₆] and we maintained the use of potassium carbonate as the base. The first part of the reaction was completed using microwave irradiation (150W) at $150^\circ C$ followed by treatment with para-toluene sulphonic acid as the catalytic activation of the carbonyl and cyclization of the ring. The alkylation of **13** was performed using the methodology previously employed in Figure 5-3 and the salts **14-16** were obtained in moderate yield with classical reflux methods and excellent yield using MAOS (Figure 4-5).



Equation 3: The preparation of the alkylated fused dioxolane heterocycles **14-16**.

6.3.2 The Final Synthetic Step—Optimization

In the final synthetic step, shown in Scheme 3, two equivalents of individual monocationic salt were allowed to react with malonaldehyde bis(phenylimine) monohydrochloride in the presence of sodium acetate and acetic anhydride open vessel classical oil-heating causes a wide variety of decomposition and incomplete reaction products and results in a substantial net loss of product, yielding between 18% and 64%. In order to optimize the microwave-assisted reaction temperature, we first anticipated that the optimum reaction temperatures would be most heavily dependent on the length of the N-indolenyl substituent. We performed the synthesis of a representative fluorophore with various alkyl lengths on the indolenyl nitrogen to obtain the correct temperature to employ for all of the pentamethine cyanines.

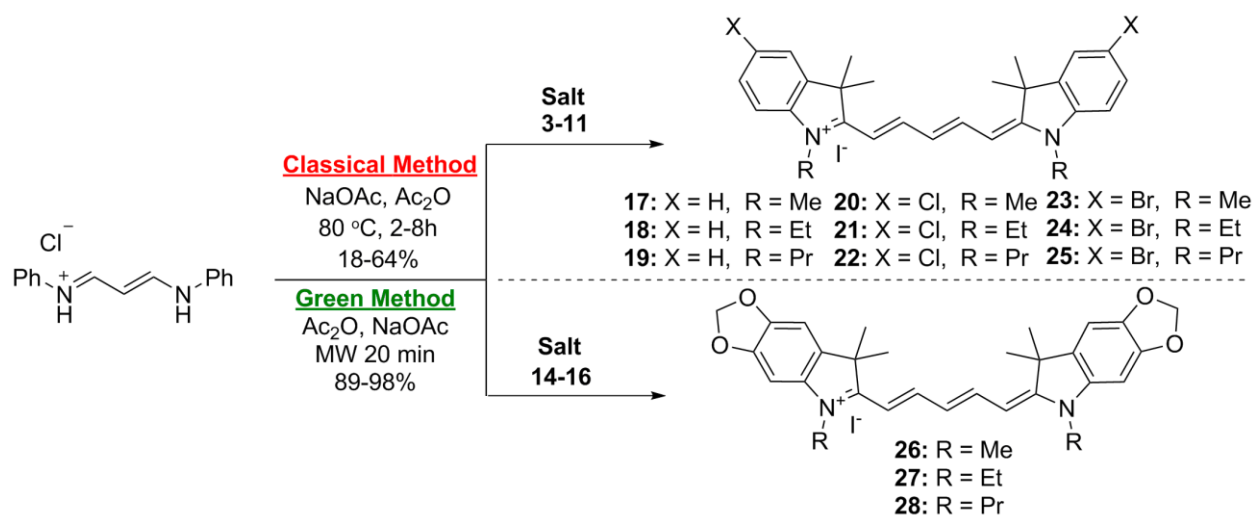


Figure 6-7. The microwave assisted preparation of a systematic set of pentamethine cyanines with variance in heterocyclic and N-alkyl groups.

As the alkyl length increases, the insulation properties of the compound also increase. In order to determine the optimal temperature, the systematic set of dyes 17-19 were tested at a range of temperatures. The isolated yield for each of the reactions are shown as a function of temperature in Figure 2 and shows a correlation as the alkyl group becomes longer, the most desirable reaction temperature also increases.

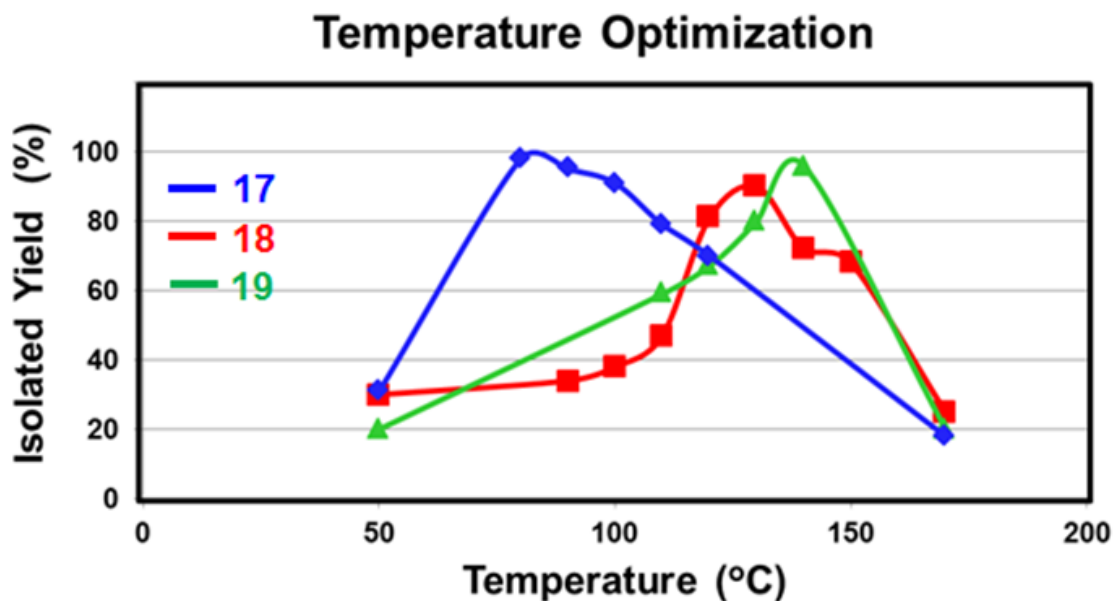


Figure 6-8. Isolated yield (%) versus reaction temperature (°C) versus the three pentamethine carbocyanine dyes with varied lengths of the N-alkyl groups **17** (methyl, blue), **18** (ethyl, red), and **19** (propyl, green). Reactions were held at 20 min for the isolated yield.

The medium length N-substituted ethyl dye **18** was chosen as a model for discussing optimal reaction temperatures. As shown in Table 1, multiple trials were conducted varying temperature by 10 °C increments starting with 90 °C while alternating reaction time for 10 and 20 min.

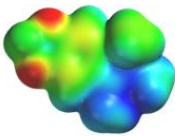
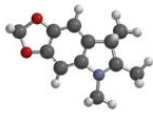
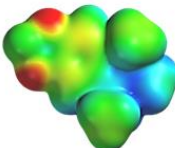

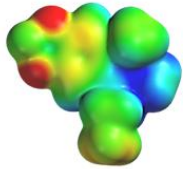
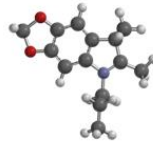
Table 6-1 Optimization Data for Pentamethine Carbocyanine Dye 18 with an ethyl group.

Trial	Temp (°C)	Reaction Time (min)	Yield (%)
1	50	10	25
2	50	20	31
3	90	10	32
4	90	20	36
5	100	10	38
6	100	20	38
7	110	10	40
8	110	20	47
9	120	10	73
10	120	20	81
11	130	10	89
12	130	20	95
13	140	10	76
14	140	20	72
15	150	10	70
16	150	20	68
17	170	10	35
18	170	20	25
19	130	25	91
20	130	30	84

Conducting the reaction at temperatures between 50 °C and 90 °C showed comparatively low yields. The optimum temperature was observed as a maximum and heating above this temperature resulted in undesirable byproducts and decomposition of the product, which decreased yield shown in Figure 2 this method was applied to the synthesis of compounds **17** and **19**. Methyl substituted dye, **17** was shown to reach a maximum yield at 80 °C, ethyl **18** at 130 °C and propyl **19** at 140 °C. Continuing the reaction time past 20 min to 25 min and 30 min also resulted in reduced percentage isolated yield.

We suspected that the increasing N-alkyl chain length was corresponded to a decrease in overall dipole moment of the corresponding indolinium salt, causing a reduced microwave energy absorption which required an increase in thermal energy to attain a comparable reaction

yield [9]. We became intrigued with this observation and performed DFT calculations at the BLYP 6-31G* level beginning with the conformer of the lowest energy.

Compound ID	Electrostatic Potential Map	Molecular Skeleton	Calculated Dipole Moment (debye)
14			3.39
15			2.48
16			1.69


-  +

Figure 6-9 DFT calculation results showing a decrease in the dipole moment as alkyl length increases.

The electrostatic maps qualitatively show less polarization and the decrease in dipole moment corresponds directly to the decrease in microwave energy absorbed by the compound. In order for the molecule to react in the microwave, a higher amount of energy is required. The salt containing a methyl group has a dipole moment of 3.39 debye which is more than double the dipole moment of the salt with a propyl substituent which was calculated to be only 1.69 debye. This is in agreement with the thermal energy required to form the final product with methyl and propyl; the methyl salt required only 80 °C to form the final compound in optimized yield whereas the propyl compound was optimized at 140 °C.

6.3.3 Microwave Assisted Organic Synthesis Application to a Systematic Library of Pentamethine Cyanines

After optimizing the reaction conditions for each of the three sets of pentamethine cyanines (Me, Et and Pr), we subjected the other structures with heterocyclic variation to the same reaction conditions and isolated the compounds using precipitation and facile recrystallization techniques. Notably, the reaction time, shown in Table 2, is drastically reduced in some cases more than 13-fold. Additionally, the purified yield increased, especially for compound 23 which showed an increase from 32% to 98%; correspondingly, compound 28, which was difficult to purify and obtain an 18% overall yield using classical methods, precipitated as a nearly analytically pure solid after initial workup in 89% yield.

Table 6-2 Microwave Synthesis versus Conventional Synthesis

Dye Structure	M.W. Time (min)	Conventional Time (min)	Microwave Yield ¹	Conventional Yield ¹
17	20	120	98 %	64 %
18	20	180	95 %	62 %
19	20	220	96 %	61 %
20	20	190	95 %	36 %
21	20	180	96 %	58 %
22*	20	250	94 %	64 %
23	20	240	98 %	32 %
24	20	270	98 %	60 %
25*	20	340	96 %	55 %
26*	20	480	90 %	27 %
27*	20	480	92 %	21 %
28*	20	480	89 %	18 %

The conventional synthetic method affords numerous byproducts which are not efficiently removed from the desired compound; however, the microwave methods developed herein have avoided the undesirable side reactions which have led to much reduced solvent waste with substantially less time and hazardous solvent waste spent on purification.

6.3.4 Heterocyclic Variation Alters the Optical Properties of the Cyanine Fluorophores

The effect of changing the *N*-alkyl chain length of cyanine dyes has been shown by our laboratory to minimally alter optical properties [2]; therefore, we will not concentrate on re-evaluating this phenomenon. However, while keeping the alkyl groups constant, differences in absorbance, emission, molar absorptivity (extinction coefficient) and relative quantum yield were observed for dyes containing heterocyclic variations, including chlorine, bromine and methylene dioxy groups (Table 3).

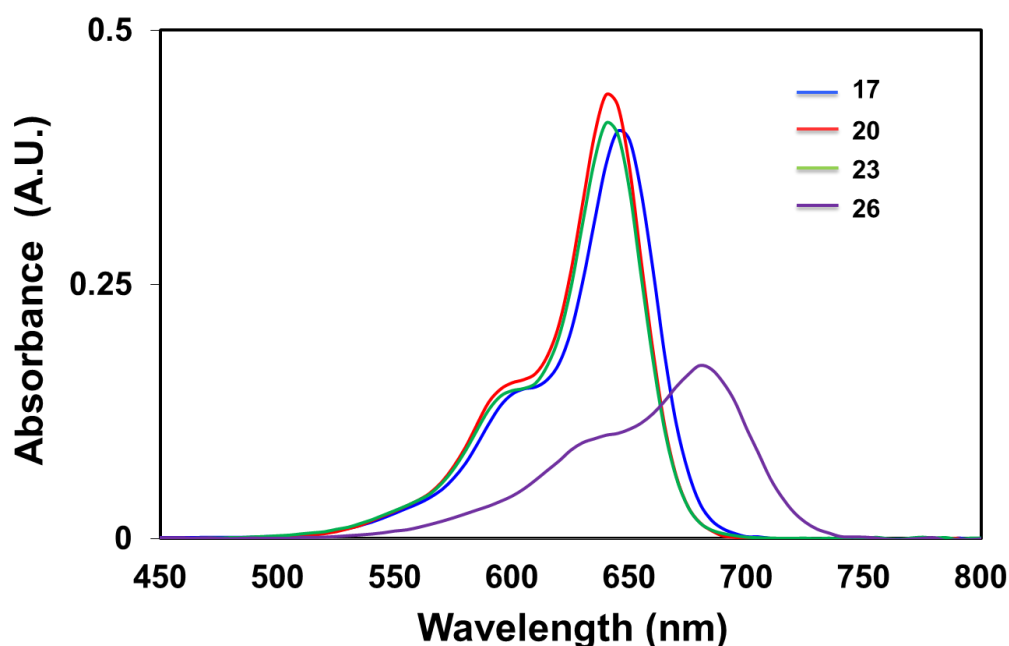


Figure 6-10 Near infrared (NIR) absorbance of fluorophores in methanol at a 2.0 μM concentration.

The effect of chlorine **20** and bromine **23** was almost negligible in methanol along with except for an increased Stoke's Shift from 22 nm to 32/34 nm (Table 3). The addition of the methylene dioxy group **26** was shown to red shift the dye 35 nm, where the Stokes' Shift was observed to increase to 43 nm. Extinction coefficients for all dyes were shown to be favorably large, (85,100 to 222,800 $\text{M}^{-1}\text{cm}^{-1}$) while quantum yields ranged from 30.5 to 9.5% (Table 3).

The quantum yield of the dioxy compound **26** is lower due to the possibility for non-radiative energy decay associated with the non-aromatic substituents on the heterocyclic ring.

Table 6-3 The optical properties of propyl substituted dyes **17**, **20**, **23** and **26** with respect to different substituents on the heterocyclic backbone. The data presented was obtained in methanol from 1 mM stock solutions made in DMSO.

Dye	λ_{abs} (nm)	λ_{em} (nm)	ϵ (M ⁻¹ cm ⁻¹)	Φ (%)
17	644	666	212, 500	30.5
20	640	674	222, 800	29.4
23	640	672	210, 100	16.9
26	679	722	85, 100	9.5

In order to confirm the observed red-shift of the methylene-dioxy substituted compounds, and knowing the *N*-alkyl substitution does not significantly alter the optical properties of the chromophore, we performed density functional theory calculations on the synthesized compounds **17** and **26** to look at the HOMO and LUMO levels to determine energetic differences between the compounds. The calculations were performed at the BLYP 6-31G* level starting from the most energetically stable state.

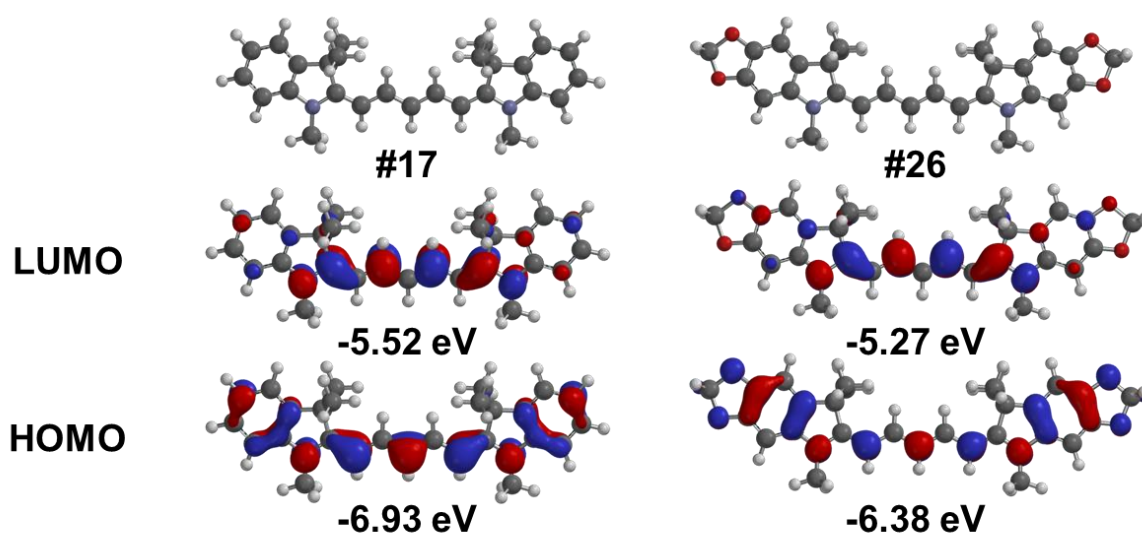


Figure 6-11 In silico DFT calculations depicting the HOMO and LUMO for each compound **17** and **26** with corresponding energy levels (eV) shown below the structures.

The DFT calculations reveal a larger energy gap for compound **17** (E_{gap} (eV) = 1.41 eV) predicting a blue-shifted absorption spectrum compared to the small energy barrier for compound **26** (E_{gap} (eV) = 1.11 eV) which displays a 41 nm bathochromic shift. These results corroborate the observed bathochromic shift of compound **26** and we can use similar computational methods for predicting a red or blue shift before synthesizing additional compounds (Figure 5).

6.4 Conclusions

The complete synthetic route for various substituted pentamethine carbocyanine dyes was completed using microwave-based green eco-conscious methods including the preparation of a novel methylene dioxy heterocyclic structure. Optimal reaction conditions were found at a constant reaction time of 20 min for all dyes with increasing alkyl lengths resulting in increased optimal reaction temperatures. The benefits associated with our methodology include decreased reaction time with significantly improved yield and outstanding purity (based on ^1H NMR spectra) without the need for lengthy purification methods. Additionally, the red-shifted compounds dioxymethylene compounds were shown, through DFT calculations, to have small HOMO-LUMO energy differences resulting in the red-shifted optical profile. As NIR fluorophores continue to garner increasing interest in the scientific community, the optimized synthetic protocol will help to increase efficiency while simultaneously reducing the environmental impact.

6.5 Experimental

6.5.1 Synthesis

The chemical reagents used in the synthesis of these compounds were obtained from Acros Organics (Geel, Belgium), Alfa Aesar and Matrix Scientific. Microwave irradiation was

completed using a Discover LabMate apparatus interfaced to a PC using the provided Synergy software to monitor reaction temperature, pressure, wattage and simultaneous cooling. Scale-up reactions of indolenine salts were performed using the open-vessel accessories and the same protocol as detailed in the experimental with similar yield. All classical method reactions were kept under a positive pressure of nitrogen during the entirety of the reaction. Microwave-assisted reaction vessels were purged with nitrogen before the reaction was initially subjected to irradiation. The reactions were followed using silica gel 60 F₂₅₄ thin layer chromatography plates (Merck EMD Millipore, Darmstadt, Germany) with 5% methanol in DCM as the mobile phase. Open column chromatography was utilized for the purification of the final compounds needing additional purification using 60-200u, 60A classic column silica gel (Dynamic Adsorbents, Norcross, GA). The ¹H NMR and ¹³C NMR spectra were obtained using high quality Kontes NMR tubes (Kimble Chase, Vineland, NJ) rated to 500 MHz and were recorded on a 400 MHz Bruker Avance (at either 400 MHz or 100 MHz for ¹H NMR and ¹³C NMR, respectively) spectrometer using DMSO-*d*₆ or CDCl₃ containing tetramethylsilane (TMS) as an internal calibration standard. High-resolution accurate mass spectra (HRMS) were obtained either at the Georgia State University Mass Spectrometry Facility using a Waters Q-TOF micro (ESI-Q-TOF) mass spectrometer or utilizing a Waters Micromass LCT TOF ES+ Premier Mass Spectrometer. Liquid chromatography utilized a Waters 2487 single wavelength absorption detector with wavelengths set between 640 and 700 nm depending on the dye's photophysical properties. The column used in LC was a Waters Delta-Pak 5 μm 100Å 3.9 × 150 mm reversed phase C18 column. Evaporative light scattering detection analyzes trace impurities that cannot be observed by alternate methods; a SEDEX 75 ELSD (Olivet, France) was utilized in tandem with liquid chromatography to confirm purity.

2,3,3-trimethylindolenine was commercially obtained and used in the alkylation reaction without purification.

6.5.2 *Classical synthesis of indolenine compounds 1 and 2*

Substituted phenylhydrazine hydrochloride heterocyclic starting materials (1 g) were added to an oven dried and nitrogen flushed round bottom flask. Acetic acid (15 mL) was added to the flask and the reaction mixture was heated using an oil bath to reflux. Ketone, 3-methyl-2-butanone (1.5 mol. eq.), was added to the reaction mixture. The mixture was allowed to heat for 12-48h until TLC indicated a consumption of starting materials. After the reaction was completed, the acetic acid and excess ketone was removed under high vacuum rotary evaporation at elevated temperature. The resulting reddish oil was dissolved in dichloromethane and a saturated aqueous solution of sodium bicarbonate was added carefully to the organic layer. The organic layer was washed with sodium bicarbonate (3 x 10 mL), the organic layer was extracted, dried over magnesium sulfate and concentrated to afford the final compounds in 76% and 81% yield, respectively.

6.5.3 *Microwave synthesis of indolenine compounds 1 and 2*

Heterocyclic phenylhydrazine hydrochloride (1 g) was added to a 10-mL microwave vessel equipped with a micro magnetic stir bar along with 3-methyl-2-butanone (1.2 mol. eq.). Deionized water (3 mL) and sulfuric acid (0.1 mol. eq.) was added to the reaction mixture. The reaction vessel was securely capped and then subjected to microwave irradiation for 10 min at 100 °C allowing for the complete transformation of the starting material. The water was decanted off and a saturated solution of sodium bicarbonate (3 mL) was added. The flask was sonicated for 10 min to quench the reactive acid. The liquid was poured off and the resulting oil was dissolved in minimum dichloromethane dried over sodium sulfate for 30 min, gravity filtered and concentrated to yield the corresponding products in quantitative yield.

6.5.4 *Classical synthesis of indolenine salts 3-11*

Individual indolenine derivative **1-3** was added to a 50 mL round bottom flask with a magnetic stir bar along with appropriate alkyl iodide (3 mol. eq) and acetonitrile (10 mL). The

low boiling point of the alkyl iodide limits the reaction temperature; also, some of the alkylating agent will evaporate during the reactions, higher equivalents are needed in the classical methods. The reaction mixtures were heated to reflux for 48-72h. After TLC indicated a consumption of the starting materials, the reaction was allowed to cool and the mixture was concentrated under reduced pressure. Diethyl ether (25 mL) was added to the flask resulting in an oily residue. Acetone (5 mL) was added to the residue and the reaction mixture was sonicated for 10 min resulting in a free flowing solid which was filtered, washed with diethyl ether and hexanes and dried under vacuum. The compounds were obtained in 58-79% yield.

6.5.5 *Microwave synthesis of indolenine salts 3-11*

Individual indolenine derivative, 2,3,3-trimethylindolenine, **1**, or **2** was added to a 10-mL microwave vessel equipped with a micro magnetic stir bar along with appropriate alkyl iodide (1.2 mol. eq.). The reaction vessel was securely capped and then subjected to microwave irradiation for 20 min allowing for the complete transformation of the heterocyclic starting material to the corresponding salt. The resulting residue was filtered, dried overnight on vacuum and the corresponding salts were obtained in 98%+ yield in excellent purity as determined by NMR (^1H and ^{13}C) spectroscopy.

Salts **3**, **4**, **6**, **7**, **9** and **10** are previously published compounds and the data agrees with the literature values.¹⁰⁵

2,3,3-Trimethyl-1-propyl-3H-indol-1-ium iodide (5): ^1H NMR (400 MHz, DMSO- d_6) δ : 1.00 (t, $J = 7.20$ Hz, 3H), 1.56 (s, 6H) 1.80 - 1.98 (m, 2H), 2.88 (s, 3H), 4.47 (t, $J = 7.45$ Hz, 2H) 7.63 (d, $J = 5.05$, $J = 3.28$ Hz, 2H), 7.82 - 7.92 (m, 1H), 7.96 - 8.07 (m, 1H), ^{13}C NMR (100 MHz, DMSO- d_6) δ : 10.76, 14.22, 20.78, 22.06, 48.83, 54.14, 115.53, 123.51, 128.90, 129.37, 141.06, 141.82, 196.54

5-Chloro-2,3,3-trimethyl-1-propyl-3H-indol-1-ium iodide (8): ^1H NMR (400 MHz, CDCl_3) δ : 1.05 (t, $J = 8.00$ Hz, 3H) 1.65 (s, 6H) 1.93 - 2.10 (m, 2H) 3.09 (s, 3H) 4.62 (t, $J = 8.0$ Hz, 2H) 7.48 - 7.60 (m, 2H) 7.79 (d, $J = 8.0$ Hz, 1H). ^{13}C NMR (100 MHz, $\text{DMSO}-d_6$) δ : 11.22, 14.77, 21.22, 22.35, 49.52, 54.92, 118.01, 123.29, 127.41, 132.32, 140.94, 144.64, 197.61.

5-Bromo-2,3,3-trimethyl-1-propyl-3H-indol-1-ium iodide (11): ^1H NMR (400 MHz, $\text{DMSO}-d_6$) δ : 0.99 (t, $J = 7.20$ Hz, 3H) 1.57 (s, 6H) 1.86 (d, $J = 7.33$ Hz, 2H) 2.81 - 2.91 (m, 3H) 4.37 - 4.55 (m, 2H) 7.86 (s, 1H) 8.00 (d, $J = 8.59$ Hz, 1H) 8.21 (s, 1H), ^{13}C NMR (100 MHz, $\text{DMSO}-d_6$) δ : 11.24, 14.86, 21.24, 22.17, 22.36, 49.56, 54.92, 118.03, 123.29, 127.41, 132.32, 140.94, 144.64, 182.07, 188.62, 197.60.

6.5.6 Classical bromination

3-bromo-3-methyl-2-butanone (12): A mixture of 3-methylbutan-2-one (25.00 mL, 233.65 mmol) and acetic acid (38.00 mL) was added to a three-neck oven-dried round bottom flask and maintained at a temperature of 5 °C. Next, both molecular bromine (1.2 mL, 23.4 mmol) and acetic acid (5.0 mL) was combined in an addition funnel and added dropwise to the round bottom flask. When all of the bromine was added the reaction mixture was allowed to stir overnight at room temperature. To the resulting mixture, water (10 mL) was added, and then transferred to a separatory funnel where another 10 mL of water was added and the organic layer was extracted with diethyl ether (3 x 15 mL). The compound was then washed with cold, saturated sodium bicarbonate (4 x 10 mL), dried over anhydrous sodium sulfate, and the reaction mixture was concentrated *in vacuo* to leave yellow oil. The crude product was further purified via vacuum distillation (52 °C, ~ 25 mmHg) to yield a colorless oil, 3.14 g (81%). ^1H NMR (400 MHz, CDCl_3) δ : 1.824 (s, 6H), 2.401 (s, 3H).

6.5.7 *Eco-friendly bromination*

3-bromo-3-methyl-2-butanone (**12**): 3-methylbutan-2-one (20.1 mmol) was added to water (10 mL) a round bottom flask at room temperature. The round bottom flask was enveloped in aluminum foil to prevent light-induced interactions. A 48% aqueous solution of HBr (30.2 mmol) was added to the stirring mixture. After 10 min of stirring at room temperature, a solution of H₂O₂ (30% in water, 40.2 mmol) was added to the reaction mixture. The clear solution was allowed to stir for 18h. After full consumption of the starting materials, the reaction was quenched by adding excess saturated sodium bicarbonate solution and the final brominated compound was extracted in diethyl ether. After concentration under reduced pressure, the resulting oil was vacuum distilled (52 °C , ~ 25 mmHg) to afford the final compound in 91% yield.

6.5.8 *Classical cyclization*

6,7,7-trimethyl-7H-[1,3]dioxolo[4,5-f]indole (**13**): A solution of DMF, (8 mL), aniline (1.56 g, 11.38 mmol), and potassium carbonate (1.05 g, 6.8 mmol) was brought to 45 °C in a two-neck round bottom flask with small magnetic stir-bar. 3-Bromo-3-methylbutan-2-one (**12**, 1.86 g, 1 mL) was added to the solution overnight with a syringe pump (Kd Scientific, Model 100). After addition was completed, solution was stirred for 24 h at 45 °C and monitored by TLC. After TLC showed that the starting material was consumed, dimethylformamide was evaporated *in vacuo*, and concentrate was extracted with toluene (5 x 20 mL) and was washed with deionized water. Toluene was concentrated to an amount of 10-20 mL, and *p*-methyltoluenesulfonic acid (0.110 g, 0.1 mol equiv.) was added to solution. Solution was allowed to reflux for 24h, until TLC showed an absence of starting material. Toluene was evaporated *in vacuo*, and dichloromethane (20 mL) was added to the reaction mixture. Solution was washed with a saturated solution of sodium carbonate (5 x 50 mL) until the organic layer

was a red/brown color. DCM was removed under reduced pressure and the resulting red/brown oil was recovered and the crude **13** (obtained in 57% yield) was used without purification.

6.5.9 Microwave assisted cyclization

6,7,7-trimethyl-7H-[1,3]dioxolo[4,5-f]indole (13): A solution of [BMIM][PF₆] (4 mL), potassium carbonate (1.2 mol. eq.) and aniline (1.2 mol. eq.) was added to a microwave vessel (10 mL). 3-Bromo-3-methylbutan-2-one (1.0 mol. eq.) was added to the microwave vessel. The contents were subjected to microwave irradiation at 150 W, 150 °C for 20 min. Approximately 90% of the reactive aniline (100% of the butanone was consumed) was allowed to go to completion leaving an additional amount to participate in the imine formation seen in the mechanism. Para-toluene sulphonic acid was added to the vessel (0.2 mol. eq.) and the reaction was heated to 100 °C for 20 min. The brown solution was dissolved in DCM (10 mL) and washed with saturated solution of sodium bicarbonate (3 x 15 mL). The organic layer was dried over magnesium sulfate and was evaporated under reduced pressure to afford the final heterocyclic dioxolane. The compound was obtained in 92% yield.

6.5.10 Classical alkylation

The classical alkylation of *6,7,7-trimethyl-7H-[1,3]dioxolo[4,5-f]indole* was achieved using identical procedures found above and the respective yields are found below.

6.5.11 Microwave assisted alkylation

Dioxyindolenine was added to a 10-mL microwave vessel equipped with a micro magnetic stir bar along with appropriate alkyl iodide (1.2 mol. eq.). The reaction vessel was securely capped and then subjected to microwave irradiation for 20 min allowing for the complete transformation of the heterocyclic starting material to the corresponding salt. The resulting residue was filtered, dried overnight on vacuum and the corresponding salts were obtained in 98% yield in excellent purity as determined by NMR (¹H and ¹³C) spectroscopy.

5,6,7,7-Tetramethyl-7H-[1,3]dioxolo[4,5-f]indol-5-ium iodide (14): Classical Yield 60%, Microwave Yield 95%. ^1H NMR (400 MHz, DMSO- d_6) δ : 1.48 (s, 6H) 2.70 (br. s., 3H) 3.90 (s, 3H) 6.19 (s, 2H) 7.48 (s, 1H) 7.64 (s, 1H), ^{13}C NMR (100 MHz, DMSO- d_6) δ : 15.43, 21.48, 23.05, 53.61, 55.34, 101.44, 103.34, 125.76, 128.64, 129.34, 139.90, 145.50, 146.91, 147.91, 187.11.

5-Ethyl-6,7,7-trimethyl-7H-[1,3]dioxolo[4,5-f]indol-5-ium (15): Classical Yield 53%, Microwave Yield 94%. ^1H NMR (400 MHz, DMSO- d_6) δ : 1.48 (s, 6H) 2.70 (br. s., 3H) 3.90 (s, 3H) 6.19 (s, 2H) 7.48 (s, 1H) 7.64 (s, 1H), ^{13}C NMR (100 MHz, DMSO- d_6) δ : 13.28, 14.33, 22.37, 43.71, 54.33, 97.77, 103.21, 104.52, 134.88, 137.31, 148.54, 149.29, 194.54

6,7,7-Trimethyl-5-propyl-7H-[1,3]dioxolo[4,5-f]indol-5-ium (16): Classical Yield 45%, Microwave Yield 92%. ^1H NMR (400 MHz, DMSO- d_6) δ : 0.85 - 1.06 (m, 3H) 2.79 (s, 6H) 4.38 (br. s., 1H) 6.20 (s, 4H) 7.51 (s, 1H) 7.75 (s, 1H), ^{13}C NMR (100 MHz, DMSO- d_6) δ : 11.14, 14.50, 21.35, 22.55, 49.39, 54.36, 97.65, 103.23, 104.44, 135.27, 137.24, 148.55, 149.34, 195.03.

6.5.12 General classical synthesis for NIR dyes 17-25 and 26-28

A mixture of indolium salt (40 mg, 0.154 mmol), bis-iminium salt (20 mg, 0.077 mmol), NaOAc (17 mg, 0.23 mmol) and acetic anhydride (1 mL) was added to an oven dried round bottom flask with stirring bar. The reaction mixture was heated using a standard oil bath for a particular reaction time (refer to Table 1). After starting materials were consumed, the reaction was allowed to cool to room temperature. Diethyl ether was added to the round bottom flask resulting in an oily metallic blue residue. The diethyl ether was decanted and the oil was dissolved in a minimal amount of methanol followed by the addition of diethyl ether (50 mL) resulting in the formation of light blue crystals, which were filtered. The crystals were dissolved in dichloromethane leaving unreacted sodium acetate on the funnel. The dichloromethane was removed *in vacuo*. Many compounds needed additional purification

methods. Silica-gel column chromatography eluting with 2-5% methanol in dichloromethane afforded the various pentamethine cyanines in their respective yield.

6.5.13 General microwave assisted synthesis for NIR dyes

A mixture of indolium salt (40 mg, 0.154 mmol), bis-iminium salt (20 mg, 0.077 mmol), NaOAc (17 mg, 0.23 mmol) and acetic anhydride (1 mL) was placed in sealed microwave vessel with stirring bar. Sealed vessel was placed in single-mode microwave (CEM Discover) on standard power setting, at indicated temperature, see Table 1 for 20 min resulting in increased pressure (40-100 psi). Reaction mixture was diluted with diethyl ether (10-20 mL) and filtered *in vacuo*. Solid was washed twice with diethyl ether (5 mL). A clean filter flask was attached to the funnel and the resulting solid was dissolved with dichloromethane (10-15 mL) leaving unreacted sodium acetate crystals on the filter funnel. The filtrate was transferred to a clean round bottom flask and dichloromethane was removed with a rotary evaporator. Metallic blue/green crystals were formed after solvent removal resulting in the yield of individual compounds reported in Table 2. Compounds **17-21**, **23** and **24** have been previously reported by conventional method.¹⁰⁵

1,3,3-Trimethyl-2-((1E,3E,5E)-5-(1,3,3-trimethylindolin-2-ylidene)penta-1,3-dien-1-yl)-3H-indol-1-ium iodide (17): ¹H NMR (400 MHz, DMSO-*d*₆) δ 1.71 (s, 12H), 3.63 (s, 6H), 6.28 (d, *J* = 16.0 Hz, 2H), 6.65 (t, *J* = 12.0 Hz, 1H), 7.24 (t, *J* = 8.0 Hz, 2H), 7.29 (d, *J* = 8.0 Hz, 2H), 7.39 (t, *J* = 8.0 Hz, 2H), 7.48 (d, *J* = 8.0 Hz, 2H), 8.25 (t, *J* = 12.0 Hz, 2H)

1-Ethyl-3,3-trimethyl-2-((1E,3E,5E)-5-(1,3,3-trimethylindolin-2-ylidene)penta-1,3-dien-1-yl)-3H-indol-1-ium iodide (18): ¹H NMR (400 MHz, DMSO-*d*₆) δ 1.27 (t, *J* = 4.0, 6H), 1.68 (s, 12H), 4.15 (d, *J* = 8.0, 4H), 6.57 (t, *J* = 12.0, 1H), 7.26 (t, *J* = 4.0, 2H), 7.39 (s, 4H), 7.63 (d, *J* = 8.0, 2H), 8.34 (t, *J* = 12.0, 2H).

1-Propyl-3,3-dimethyl-2-((1E,3E,5E)-5-(1-propyl,3,3-dimethylindolin-2-ylidene)penta-1,3-dien-1-yl)-3H-indol-1-ium iodide (19): ^1H NMR (400 MHz, DMSO- d_6) δ 0.95 (t, $J = 4.0$ Hz, 6H), 1.69 (s, 12H), 4.08 (m, $J = 4.0$ Hz, 4H), 6.35 (d, $J = 16.0$ Hz, 2H), 6.60 (t, $J = 12.0$ Hz, 1H), 7.25 (d, $J = 8.0$ Hz, 2H), 7.42 (s, 4H), 7.64 (d, $J = 8.0$ Hz, 2H), 8.34 (t, $J = 12.0$ Hz, 2H). HR-MS calculated for $[\text{C}_{31}\text{H}_{39}\text{N}_2]^+$ 439.3108 found 439.3093.

2-((1E,3Z,5E)-3-Chloro-5-(1,3,3-trimethylindolin-2-ylidene)penta-1,3-dien-1-yl)-1,3,3-trimethyl-3H-indol-1-ium iodide (20): ^1H NMR (400 MHz, DMSO- d_6) δ 1.69, (s, 12H), 3.58 (s, 6H), 6.29 (d, $J = 12.0$ Hz, 2H), 6.55 (t, $J = 12.0$ Hz, 1H), 7.39 (d, $J = 8.0$ Hz, 2H), 7.46 (d, $J = 8.0$ Hz, 2H), 7.81 (s, 2H), 8.33 (t, $J = 12.0$ Hz, 2H).

2-((1E,3Z,5E)-3-Chloro-5-(1-ethyl-3,3-dimethylindolin-2-ylidene)penta-1,3-dien-1-yl)-1-ethyl-3,3-dimethyl-3H-indol-1-ium iodide (21): ^1H NMR (400 MHz, DMSO- d_6) δ 1.25 (s, 6H), 1.69 (s, 12H), 4.13 (s, 4H), 6.33 (d, $J = 12.0$ Hz, 2H), 6.58 (t, $J = 12.0$ Hz, 1H), 7.46 (m, $J = 12.0$ Hz, 2H), 7.89 (s, 2H), 8.35 (t, $J = 12.0$ Hz, 2H).

2-((1E,3Z,5E)-3-Chloro-5-(1-propyl-3,3-dimethylindolin-2-ylidene)penta-1,3-dien-1-yl)-1-propyl-3,3-dimethyl-3H-indol-1-ium iodide (22): ^1H NMR (400 MHz, DMSO- d_6) δ 0.94 (t, $J = 8.0$ Hz, 6H), 1.70 (s, 16H), 4.07 (t, $J = 8.0$ Hz, 4H), 6.35 (d, $J = 12.0$ Hz, 2H), 6.65 (t, $J = 12.0$ Hz, 1H), 7.45 (s, 4H), 7.83 (s, 2H), 8.35 (t, $J = 12.0$ Hz, 2H). ^{13}C NMR (100 MHz, DMSO- d_6) δ : 0.57, 11.39, 20.80, 27.43, 45.33, 49.57, 104.08, 113.08, 123.50, 128.75, 129.48, 141.53, 143.65, 154.93, 173.20. HR-MS calculated for $[\text{C}_{31}\text{H}_{37}\text{N}_2\text{Cl}_2]^+$ 507.2328 found 507.2315.

2-((1*E*,3*Z*,5*E*)-3-Bromo-5-(1,3,3-trimethylindolin-2-ylidene)penta-1,3-dien-1-yl)-1,3,3-trimethyl-3*H*-indol-1-ium iodide (**23**): ¹H NMR (400 MHz, DMSO-*d*₆) δ 1.91 (s, 12H), 3.82 (s, 6H), 6.36 (d, *J* = 8.0 Hz, 2H), 7.16 (d, *J* = 8.0 Hz, 2H), 7.26-7.31 (m, 4H), 7.39-7.44 (m, 4H), 8.93 (d, *J* = 12.0 Hz, 2H).

2-((1*E*,3*Z*,5*E*)-3-Bromo-5-(1-ethyl-3,3-dimethylindolin-2-ylidene)penta-1,3-dien-1-yl)-1-ethyl-3,3-dimethyl-3*H*-indol-1-ium iodide (**24**): ¹H NMR (400 MHz, DMSO-*d*₆) δ 1.25 (m, *J* = 4.0 Hz, 6H), 1.69 (s, 12H), 4.12 (m, *J* = 8.0 Hz, 4H), 6.30 (d, *J* = 16.0 Hz, 2H), 6.58 (t, *J* = 8.0 Hz, 1H), 7.37 (t, *J* = 8.0 Hz, 2H), 7.59 (d, *J* = 8.0 Hz, 2H), 7.94 (s, 2H), 8.35 (d, *J* = 12.0 Hz, 2H).

2-((1*E*,3*Z*,5*E*)-3-Bromo-5-(1-propyl-3,3-dimethylindolin-2-ylidene)penta-1,3-dien-1-yl)-1-propyl-3,3-dimethyl-3*H*-indol-1-ium iodide (**25**): ¹H NMR (400 MHz, DMSO-*d*₆) δ 0.94 (t, *J* = 4.0 Hz, 6H), 1.70 (m, *J* = 12.0 Hz, 16H), 4.06 (t, *J* = 4.0 Hz, 4H), 6.35 (d, *J* = 12.0 Hz, 2H), 6.65 (t, *J* = 12.0 Hz, 1H), 7.40 (d, *J* = 8.0 Hz, 2H), 7.59 (d, *J* = 8.0 Hz, 2H), 7.95 (s, 2H), 8.35 (t, *J* = 12.0 Hz, 2H). ¹³C NMR (100 MHz, DMSO-*d*₆) δ : 11.39, 20.79, 27.43, 45.29, 49.56, 104.09, 113.53, 117.49, 126.26, 126.60, 131.59, 141.95, 143.97, 154.97, 173.06. HR-MS calculated for [C₃₁H₃₇N₂Br₂]⁺ 595.1318 found 595.1311.

5,7,7-Trimethyl-6-((1*E*,3*E*,5*Z*)-5-(5,7,7-trimethyl-5*H*-[1,3]dioxolo[4,5-*f*]indol-6(7*H*)-ylidene)penta-1,3-dien-1-yl)-7*H*-[1,3]dioxolo[4,5-*f*]indol-5-ium iodide (**26**): ¹H NMR (400 MHz, DMSO-*d*₆) δ 1.63 (s, 12H), 3.54 (s, 6H), 6.06 (s, 4H), 6.18 (d, *J* = 16.0 Hz, 2H), 6.46 (t, *J* = 16.0 Hz, 1H), 7.13 (s, 2H), 7.28 (s, 2H), 8.16 (t, *J* = 15 Hz, 2H). HR-MS calculated for [C₂₉H₃₁O₄N₂]⁺ 471.2278 found 471.2268.

5-Ethyl-7,7-dimethyl-6-((1E,3E,5Z)-5-(5-ethyl-7,7-dimethyl-5H-[1,3]dioxolo[4,5-f]indol-6(7H)-ylidene)penta-1,3-dien-1-yl)-7H-[1,3]dioxolo[4,5-f]indol-5-ium iodide (27): ¹H NMR (400 MHz, DMSO-*d*₆) δ 1.24 (t, *J* = 4.0 Hz, 6H), 1.63 (s, 12H), 4.08 (m, *J* = 4.0 Hz, 4H), 6.07 (s, 4H), 6.22 (d, *J* = 16.0 Hz, 2H), 6.48 (t, *J* = 12.0 Hz, 1H), 7.18 (s, 2H), 7.32 (s, 2H), 8.20 (t, *J* = 12.0 Hz, 2H). ¹³C NMR (100 MHz, DMSO-*d*₆) δ 12.68, 27.55, 49.34, 94.24, 102.17, 102.95, 104.30, 135.15, 136.19, 145.50, 148.05, 152.99, 172.22. HR-MS calculated for [C₃₁H₃₅O₄N₂]⁺ 499.2591 found 499.2577.

5-Propyl-7,7-dimethyl-6-((1E,3E,5Z)-5-(5-propyl-7,7-dimethyl-5H-[1,3]dioxolo[4,5-f]indol-6(7H)-ylidene)penta-1,3-dien-1-yl)-7H-[1,3]dioxolo[4,5-f]indol-5-ium iodide (28): ¹H NMR (400 MHz, DMSO-*d*₆) δ 0.93 (t, *J* = 8.0 Hz, 6H), 1.63 (m, 16H), 4.01 (s, 4H), 6.07 (s, 4H), 6.24 (d, *J* = 16.0 Hz, 2H), 6.50 (t, *J* = 12.0 Hz, 1H), 7.21 (s, 2H), 7.32 (s, 2H), 8.20 (t, *J* = 16.0 Hz, 2H). ¹³C NMR (100 MHz, DMSO-*d*₆) δ: 11.35, 20.89, 27.69, 49.06, 49.32, 94.49, 102.19, 103.42, 104.20, 135.01, 136.77, 145.50, 148.04, 152.81, 172.78. HR-MS calculated for [C₃₃H₃₉O₄N₂]⁺ 527.2904 found 527.2883.

6.5.14 Computational Experimental

Spartan Computational Modeling Software was utilized to draw the chemical structures and calculations were performed using Density Functional Theory at the B3LYP level. Chemical structures were minimized to the conformer of the lowest energy and calculations were performed using appropriately applied charges in a vacuum.

6.5.15 Analytical Instrumentation

Absorbance spectra were measured using a Varian Cary 50 UV-Visible Spectrophotometer interfaced to a PC, with a spectral bandwidth of 2 nm. Fluorescence spectra for the pentamethine cyanine dyes were obtained using a Shimadzu RF-1501 Spectrofluorophotometer (Shimadzu Scientific Instruments, Columbia, MD) interfaced to a

PC, with spectral bandwidths for both excitation and emission set to 10 nm and the sensitivity set to “high”. Disposable absorbance and fluorescence cuvettes were used with a pathlength of 1.00 cm. All calculations were performed on Microsoft Excel 2010, (Microsoft Corporation, Redmond, WA).

6.5.16 Stock Solutions

Stock solutions of the dyes in 1 mM concentration were prepared by weighing the dye on a 5-digit analytical balance directly into a brown glass vial and adding DMSO, (98.5% Spectroscopy grade, Sigma Aldrich) with an auto pipette (100-1000 uL, Eppendorf). The stock solutions were vortexed for 30 sec, and subsequently sonicated for 20 min to ensure complete dissolution.

6.5.17 Method of Determining Molar Absorptivity

Stock solutions were used to prepare six to seven samples in methanol with various concentrations such that absorbance values remained less than 1. Samples were prepared in 5.00 mL of DMSO having used 5-50 uL, 10-100uL, and 100-1000 uL Micropipettes, (Eppendorf). Samples were prepared in disposable glass test tubes, (10 mL, Fischer Scientific) and vortexed for 20 seconds to ensure dissolution. Appropriate measurements were chosen to ensure the absorbance values were less than 1.0 but greater than 0.1. Five measurements were taken and the recorded absorbance values versus concentration were plotted and the linear regression was determined to obtain the molar absorptivity according to Beer’s law.

6.5.18 Method of Determining Quantum Yield

Rhodamine 800, (99.9 % Fluorescence grade, Sigma Aldrich) was used as a standard within the given range of absorbance maxima, (648-682 nm). Samples of the dyes and their respective standards were prepared from stock solutions such that their absorbance maxima were less than 0.1. The absorbance and fluorescence spectra of each sample were obtained

concurrently to minimize experimental error from photobleaching. Each dye was diluted accordingly, to ensure fluorescence was below 1000 units.

6.6 References

[1] Y. Ashitate, S.H. Kim, E. Tanaka, M. Henary, H.S. Choi, J.V. Frangioni, R. Flaumenhaft, Two-wavelength near-infrared fluorescence for the quantitation of drug antiplatelet effects in large animal model systems, *Journal of Vascular Surgery*, 56 (2012) 171-180.

[2] G. Chapman, M. Henary, G. Patonay, The Effect of Varying Short-Chain Alkyl Substitution on the Molar Absorptivity and Quantum Yield of Cyanine Dyes, *Analytical Chemistry Insights*, 6 (2011) 29-36.

[3] A.M. Mehranpour, S. Hashemnia, R. Maghamifar, Synthesis and Characterization of New γ -Substituted Pentamethine Cyanine Dyes, *Synthetic Communications*, 40 (2010) 3594-3602.

[4] G. Patonay, J. Salon, J. Sowell, L. Strekowski, Noncovalent Labeling of Biomolecules with Red and Near- Infrared Dyes, *Molecules*, 9 (2004) 40-49.

[5] S. Luo, E. Zhang, Y. Su, T. Cheng, C. Shi, A review of NIR dyes in cancer targeting and imaging, *Biomaterials*, 32 (2011) 7127-7138.

[6] R. Nanjunda, E.A. Owens, L. Mickelson, S. Alyabyev, N. Kilpatrick, S. Wang, M. Henary, W.D. Wilson, Halogenated pentamethine cyanine dyes exhibiting high fidelity for G-quadruplex DNA, *Bioorganic & Medicinal Chemistry*, 20 (2012) 7002-7011.

[7] D. Oushiki, H. Kojima, T. Terai, M. Arita, K. Hanaoka, Y. Urano, T. Nagano, Development and Application of a Near-Infrared Fluorescence Probe for Oxidative Stress Based on Differential Reactivity of Linked Cyanine Dyes, *J Am Chem Soc*, 132 (2010) 2795-2801.

[8] R.B. Mujumdar, L.A. Ernst, S.R. Mujumdar, C.J. Lewis, A.S. Waggoner, Cyanine dye labeling reagents: Sulfoindocyanine succinimidyl esters, *Bioconjugate Chemistry*, 4 (1993) 105-111.

[9] M. Levitus, S. Ranjit, Cyanine dyes in biophysical research: the photophysics of polymethine fluorescent dyes in biomolecular environments, *Quarterly Reviews of Biophysics*, 44 (2011) 123-151.

[10] J.O. Escobedo, O. Rusin, S. Lim, R.M. Strongin, NIR dyes for bioimaging applications, *Current Opinion in Chemical Biology*, 14 (2010) 64-70.

[11] F. Shao, H. Yuan, L. Josephson, R. Weissleder, S.A. Hilderbrand, Facile synthesis of monofunctional pentamethine carbocyanine fluorophores, *Dyes and Pigments*, 90 (2011) 119-122.

[12] X. Yang, C. Shi, R. Tong, W. Qian, H.E. Zhau, R. Wang, G. Zhu, J. Cheng, V.W. Yang, T. Cheng, M. Henary, L. Streckowski, L.W.K. Chung, Near IR Heptamethine Cyanine Dye-Mediated Cancer Imaging, *Clinical Cancer Research*, 16 (2010) 2833-2844.

[13] B. Ebert, B. Riefke, U. Sukowski, K. Licha, Cyanine dyes as contrast agents for near-infrared imaging in vivo: acute tolerance, pharmacokinetics, and fluorescence imaging, *BIOMEDO*, 16 (2011) 066003-066003-066009.

[14] A. Samanta, M. Vendrell, R. Das, Y.-T. Chang, Development of photostable near-infrared cyanine dyes, *Chem Commun (Camb)*, 46 (2010) 7406-7408.

[15] A. Podgoršek, S. Stavber, M. Zupan, J. Iskra, Bromination of ketones with H₂O₂-HBr "on water", *Green chemistry*, 9 (2007) 1212-1218.

7 CARTILAGE AND BONE TARGETING FLUOROPHORES

This chapter was adapted from the following publication in which I was designated co-first author for my contributions in the design, synthesis, optical determinations and manuscript preparation.

Hyun, H.*, **Owens, E.A.***, Wada, H., Levitz, A., Park, G., Park, M., H., Frangioni, J. V., Henary, M., Choi, H. S., Cartilage-Specific Near-Infrared Fluorophores for Biomedical

Imaging **2015** Accepted by Angewandte Chemie—Hot Article—Top 10% of Publications.

*Co-First Authors.

7.1 Abstract

Almost every human tissue develops abnormalities that inflict pain as physically debilitating conditions that are detrimental in an emotional, familial, societal and even economic sense. Over 27 million United States citizens are afflicted by osteoarthritis and other conditions that relate primarily to cartilage and bone. Unfortunately, these diseases and proposed treatment regimens are either poorly understood or currently unavailable. This lack of knowledge concerning disease progression and treatment impact stems from an inability to image the degradation or repair of bone and cartilage tissue (i.e. osteoblast activity and chondrocyte maturation). Since near-infrared fluorescence imaging has been recognized as an established real-time tracking protocol for imaging in live tissue, we sought to develop NIR fluorescent contrast agents for cartilage and bone imaging that allows simultaneous delineation of both tissues in the same surgical space in real-time.

7.2 Introduction

To achieve direct in vivo imaging of cartilage tissues, positively charged contrast agents using magnetic resonance (MR) and computed tomography (CT) imaging systems have recently been designed. Presently, however, it is still a challenge to design near-infrared (NIR) emitting optical probes that bind to cartilage tissue after an intravenous injection and highlight its location and quantity. The NIR fluorescent light can penetrate millimeters to centimeters inside living tissue in real-time, then researchers and clinicians could, for the first time, detect and measure cartilage noninvasively during surgery. In this study, we report a new class of cationic NIR fluorescent agents that could highlight various cartilage tissues in small and large animals based on structure-inherent targeting. The results from in vivo and histological assessments demonstrate the high affinity of quaternary ammonium cations to cartilage tissues

with little to no nonspecific uptake. This new strategy for cartilage-specific imaging has the potential to revolutionize tissue engineering, joint surgery, and cartilage-specific drug development.

Intravital near-infrared (NIR) fluorescence imaging technique is a promising method that allows us to investigate complex vital physiological and biological phenomena *in vivo*.^{1,2} In particular, discovery and development of targeted contrast agents in conjunction with appropriate equipment such as FLARE imaging system enable visualization of the behavior and function of specific tissues/organs inside the living body.³ Currently, NIR fluorophores are developed to target various vital tissues such as pan and sentinel lymph nodes,⁴ peripheral nerves,⁵ bone,⁶ pancreas,⁷ thyroid and parathyroid glands⁸ as well as many tumorous tissues.⁹ Furthermore, design of novel tissue-specific NIR fluorophores is continuously required for image-guided surgery.

Most recently, we have developed NIR fluorophores specific to bone components such as hydroxylapatite and calcium phosphate, which are able to be incorporated into the bone matrix without interfering with normal bone deposition.⁶ Armed with this data, we aimed to develop a therapeutic solution for osteoarthritis, which is a degenerative joint disease caused by destruction of cartilage on the articular surfaces of joints accompanying severe pain and debilitation.¹⁰ The clinical challenge is a lack of cartilage-targeted contrast agents. Cartilage is an essential component of the human body, being found on the articular surfaces of joints, in the rib cage, in the intervertebral spaces, protecting the trachea, and giving structure to the ears and nose. Because cartilage cannot regenerate like bone, replacement therapy using tissue engineering, and pharmacologic treatment using drugs that prevent destruction, are being intensely explored. However, without the ability to monitor and quantify cartilage in living animals, these treatment approaches have yet to reach their full potential. In addition, during traumatic injury to joints, cartilage fragments can lead to chronic joint pain, which requires

arthroscopic removal of rough surfaces. Once, again, direct imaging of cartilage could have a major impact on the time required for the procedure and its efficacy.

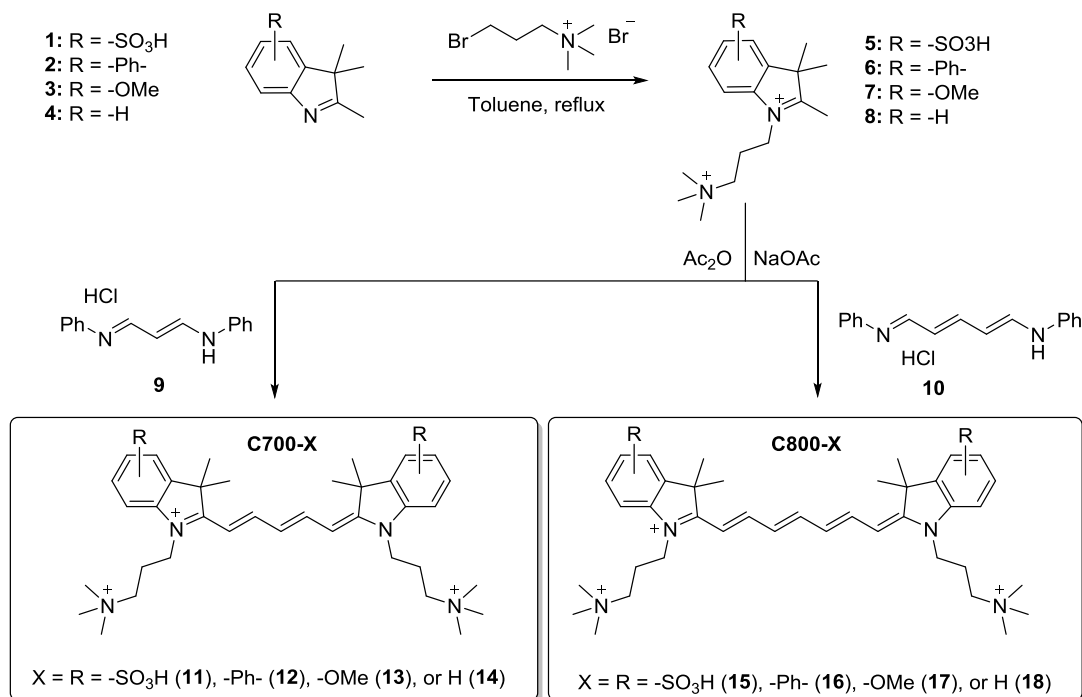
Despite its extreme importance, cartilage is difficult to image. So far, most efforts to image and quantify cartilage have focused on magnetic resonance imaging (MRI),¹¹ however, the water-deficient composition of cartilage makes it a poor target for MRI.¹² Low x-ray absorption also makes cartilage a relatively poor target for clinical computed tomography (CT), and when using conventional microCT it is essentially invisible.¹³ There is one single-photon emission computed tomography (SPECT) radiotracer for cartilage described in the literature in 2001,¹⁴ ^{99m}Tc-labeled N-(triethylammonium)-3-propyl-[15]ane-N5, but no clinical studies have been followed and recently published preclinical studies show poor image quality.¹⁵

7.3 Results and Discussion

To date, there isn't a single optical contrast agent for cartilage, and certainly not one in the NIR wavelength range of 650 nm to 900 nm. NIR light has certain key advantages for biomedical imaging including relatively low tissue absorption, reduced scatter, and minimal autofluorescence.¹⁻³ Thus, unlike visible light, which only penetrates a few hundred microns below a tissue surface, NIR light can penetrate millimeters to centimeters into living tissue. Therefore, the use of NIR fluorophores, i.e., molecules that convert one NIR wavelength into another, permits a high signal-to-background ratio (SBR) to be produced.³

For cartilage-specific targeting, it is known that the surface chemical group of imaging molecules should be positively charged to prevent the coulombic repulsion between the contrast agents and anionic glycosaminoglycans (GAGs) and induce the electrostatic interactions.¹⁶⁻¹⁸ GAG, a key component of the extracellular matrix in the articular cartilage, bears a high density of fixed negative charges owing to a number of sulfates and carboxylates, and hence strong hydrophilicity to retain a large amount of water in the tissue.¹⁶ Based on the theory, we therefore hypothesized that cationic groups substituted on a NIR fluorophore could

interact with the anionic cartilage tissues. Herein, we explored this hypothesis by using the quaternary ammonium cations (quats) as the primary modification and also studied the ability of other substituents, such as sulfonates, phenyl rings, and methoxy groups, to enhance the performance of the final molecules.



700 nm Fluorophores	C700-SO ₃	C700-Ph	C700-OMe	C700-H
Molecular Weight (Da)	713.97	655.98	615.91	555.86
LogD at pH 7.4	-2.20	-2.63	-4.93	-4.61
Total Polar Surface Area (Å ²)	120.65	6.25	24.71	6.25
Extinction Coefficient (M ⁻¹ cm ⁻¹)	85,000	131,000	96,500	110,400
Absorbance Maximum (nm)	650	691	666	646
Emission Maximum (nm)	668	716	692	665
Stokes Shift (nm)	18	25	26	19
Quantum Yield (%)	11.5	12.4	9.7	10.8

800 nm Fluorophores	C800-SO ₃	C800-Ph	C800-OMe	C800-H
Molecular Weight (Da)	740.01	682.01	641.95	581.90
LogD at pH 7.4	-1.67	-2.10	-4.40	-4.08
Total Polar Surface Area (Å ²)	120.65	6.25	24.71	6.25
Extinction Coefficient (M ⁻¹ cm ⁻¹)	128,000	179,000	121,000	101,500
Absorbance Maximum (nm)	765	800	770	745
Emission Maximum (nm)	788	818	804	767
Stokes Shift (nm)	23	18	34	22
Quantum Yield (%)	10.4	10.8	11.5	7.2

Figure 7-1. Synthetic scheme (a) and physicochemical and optical properties (b) of C700 and C800 NIR fluorophores. In silico calculations of physicochemical properties were calculated using Marvin and JChem calculator plugins (ChemAxon, Budapest, Hungary). All optical measurements were performed at 37°C in 100% fetal bovine serum (FBS) buffered with 50 mM HEPES, pH 7.4.

As shown in **Figure 1a**, a series of cationic NIR fluorophores were synthesized from a pentamethine core for 700 nm fluorescence and a heptamethine core for 800 nm fluorescence, with the addition of three different substituents as indicated. The synthetic pathways for C700 and C800 were detailed in **Experimental**. The physicochemical and optical properties of all NIR fluorophores are summarized in **Figure 1b**. By modulating the side chains of the polymethine core, final NIR fluorophores could be systematically altered in terms of hydrophobicity, polarity, and electron-resonance properties without affecting the emission

wavelength in the range of 650 to 800 nm, which together could potentially minimize tissue autofluorescence and maximize fluorescence signal.¹⁹

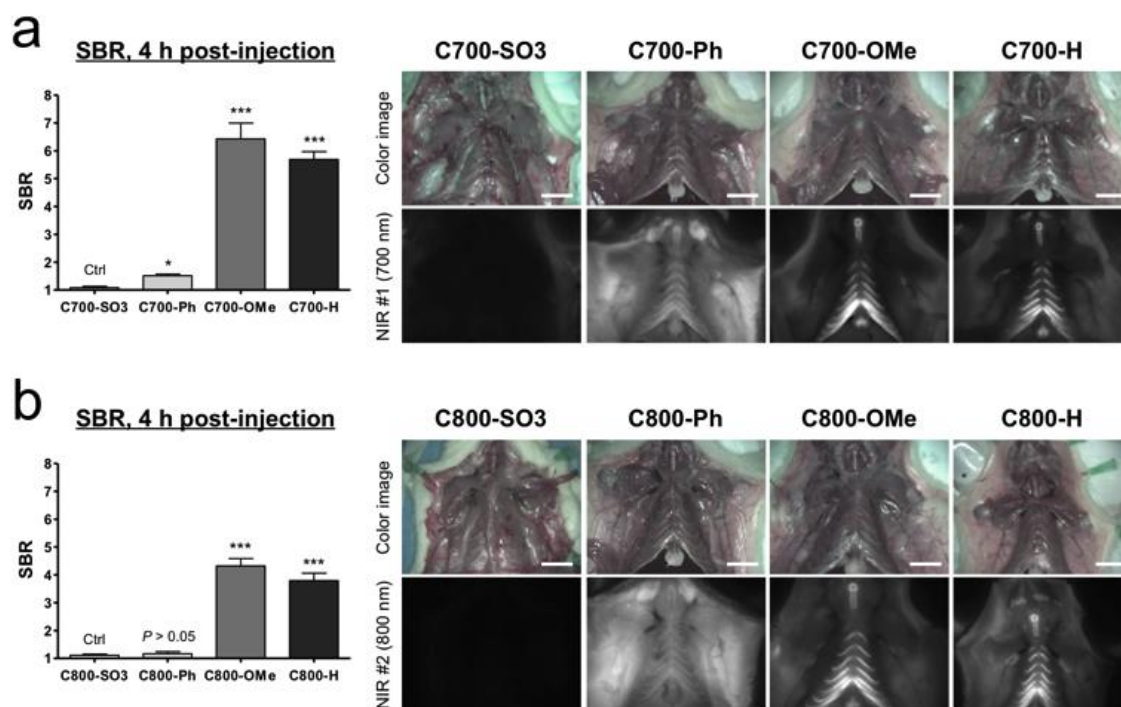


Figure 7-2. In vivo cartilage targeting using C700 (a) and C800 (b) NIR fluorophores in mice. Each fluorophore was injected intravenously into 25 g CD-1 mice (10 nmol; 0.3 mg kg⁻¹) 4 h prior to imaging. SBR was calculated by the fluorescence intensity of costal cartilage tissues versus the signal intensity of neighboring muscle obtained over the imaging period (n = 3, mean ± s.d.). *P < 0.05, ***P < 0.001. All NIR fluorescence images have identical exposure and normalizations. Scale bars = 1 cm.

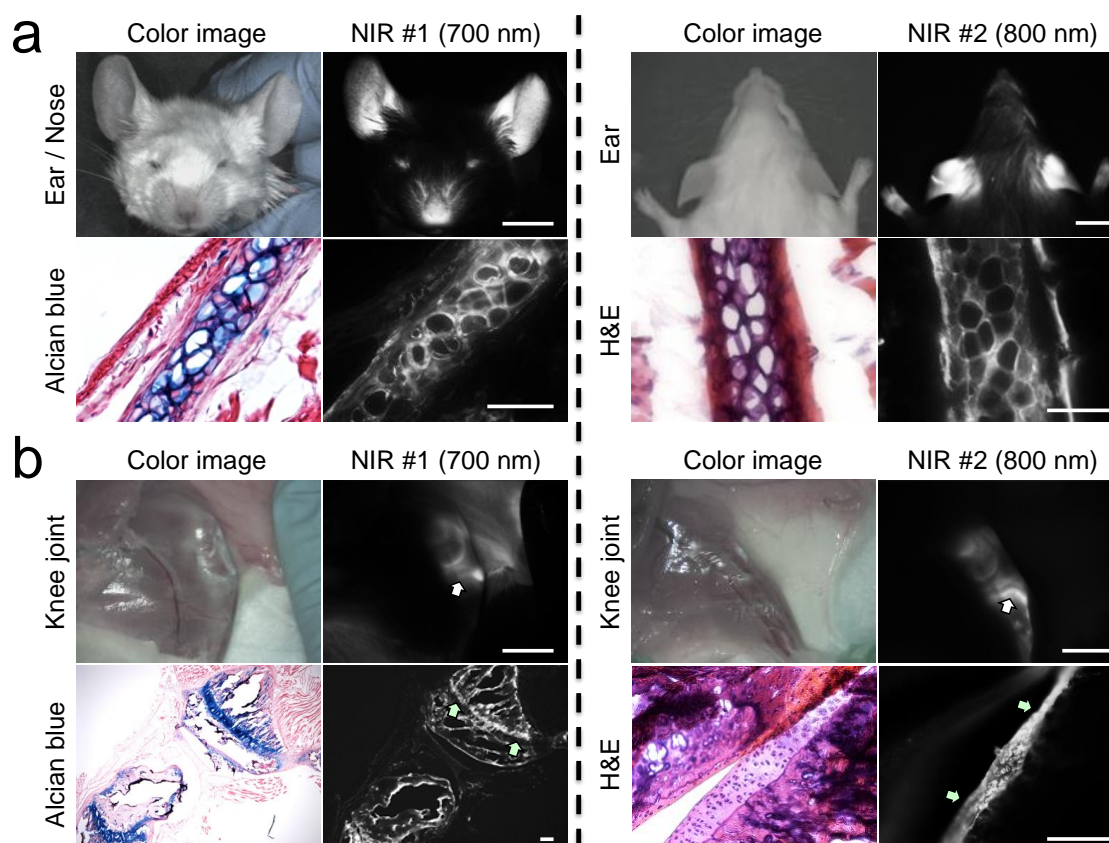
As a preliminary *in vivo* test for cartilage targeting, C700 and C800 NIR fluorophores were intravenously injected into CD-1 mice (10 nmol; 0.3 mg kg⁻¹) imaged after 4 h, and the fluorescent signals in costal cartilage tissues were respectively quantified (**Figure 2**). Interestingly, C700-OMe and C800-OMe showed the highest SBR (calculated by fluorescence intensities between costal cartilage and neighboring muscle) values compared to the other molecules, and both C700-H and C800-H showed significantly high signals in cartilage tissues. Although the synergy of methoxy groups on the cationic polymethine structure for efficient

cartilage binding is not well understood, methoxy groups improve hydrophilicity (LogD at pH $7.4 < -4.0$) and increase polar surface area properly (24.71 \AA). In contrast, the addition of sulfonates and phenyl groups on the polymethine backbone diminished the cartilage-specific targeting of the final fluorophores. C700-Ph and C800-Ph showed high nonspecific background signals everywhere due to the increased hydrophobicity and imbalanced 3D conformation (data not shown), whereas the entire surface charges of C700-SO₃ and C800-SO₃ are geometrically balanced between sulfonates and quaternary ammonium groups resulting in no cartilage tissue uptake. In addition, the polarity values of sulfonated fluorophores are close to the 120 \AA^2 , which tend to be poor at permeating cell membranes.²⁰

Because C700-OMe and C800-OMe showed the highest SBR for cartilage tissues among the different side chains, we selected these methoxy-substituted NIR fluorophores for further *in vivo* study. To confirm if their targeting ability exhibits in other types of cartilage including hyaline, elastic or fibrocartilage, we observed all the major cartilage tissues at 4 h post-injection of C700-OMe and C800-OMe in CD-1 mice (**Figure 3**). After a single intravenous injection of each agent, all cartilage tissues were visualized clearly including ears/nose, knee joints, sternum, and intervertebral discs. Since the compositions of each cartilage tissue are different, we further performed histological evaluations using Alcian Blue and Hematoxylin and Eosin (H&E) staining. As shown in **Figure 3**, the histology and NIR fluorescence images obtained from the same animals prove clearly where the fluorescence signals came from. Alcian Blue mainly stained acidic GAGs in cartilages as a dark blue color, where strong NIR fluorescence observed. The histology data also prove that those cationic NIR fluorophores have high affinities with not only hyaline cartilage but also elastic and fibrocartilage. Since the cartilage tissues are all produced by chondrocytes (or more precisely chondroblasts until entrapment within their own extracellular matrix) and differ mainly in the

relative amounts of collagen, proteoglycans, and elastin present, we believe the intravenously injected molecules mainly target chondrocytes in all types of cartilage tissues.

Interestingly, as shown in **Figure 3b**, the growth (epiphyseal) plate (arrows) was also targeted in company with fibrocartilage of knee joint. Growth plate is also one of hyaline cartilage tissues located in the metaphysis at each end of a long bone. The plate is typically found in children and adolescents, that is, we could observe the unexpected fluorescence signal at the growth plate because of the use of relatively young mice (8 wk) in this study. This result indicates that cationic NIR fluorophores can specifically bind to all cartilage tissues present in the body, even at the development stage.



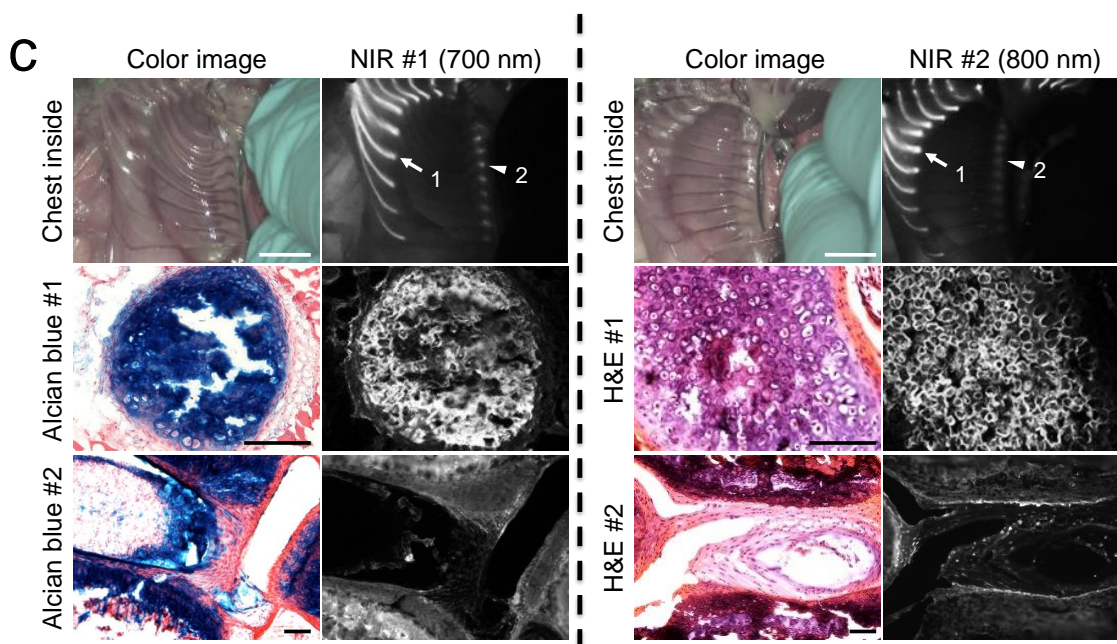


Figure 7-3. In vivo NIR imaging and histological analysis of cartilage tissues from ear (a), knee joint (b), and inside chest (c) in mice. C700-OMe and C800-OMe were intravenously injected into 25 g CD-1 mice (10 nmol; 0.4 mg/kg) 4 h prior to imaging. #1 (arrows) and #2 (arrowheads) in (c) indicate hyaline and fibrocartilage, respectively. Alcian Blue, H&E, and NIR images of resected cartilage tissues were obtained from the same animal. All NIR fluorescence images for each condition have identical exposure times and normalizations. Scale bars = 1 cm (for in vivo image) and 100 μm (for histology image). Images are representative of $n = 3$ independent experiments.

Finally, we exploited the dual-NIR channel capability of the FLARE imaging system to highlight cartilage and bone tissues simultaneously in real time. Since the bone-targeting NIR fluorophores (e.g., P800SO3) have been previously developed by our group,⁶ the combination of C700-OMe (emitting at 700 nm) and P800SO3⁶ (emitting at 800 nm) were used by injecting both agents together into mice and pigs, respectively. As shown in **Figure 4**, cartilage tissues were identified by C700-OMe in 700 nm channel, whereas bone tissues were visualized by P800SO3 in 800 nm channel, independently, despite the co-injection. This approach is especially important in complex surgery when resection of the damaged tissues

(i.e., using one NIR channel) needs to be performed, while neighboring critical structures need to be preserved (i.e., using the second NIR channel).

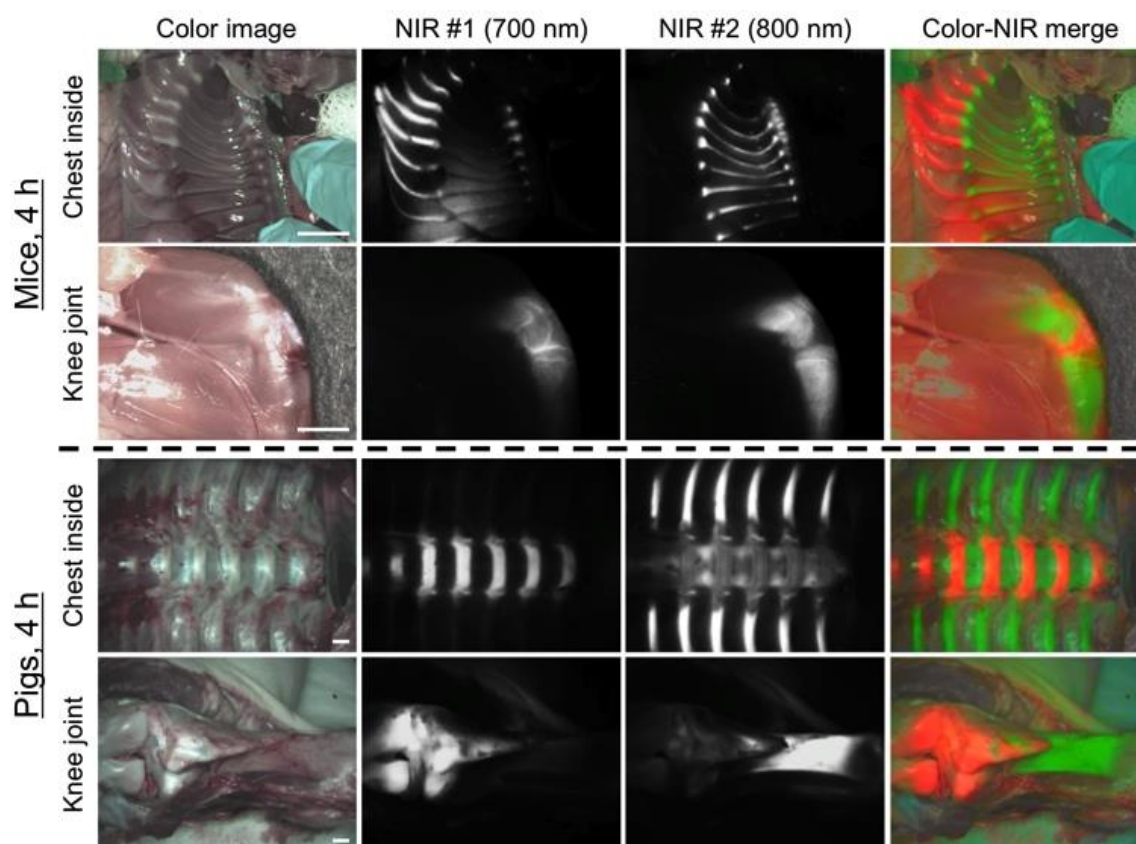


Figure 7-4. Dual-channel in vivo fluorescence imaging of cartilage and bone tissues by using C700-OMe and P800SO₃⁶ in the same animals. 10 nmol and 1 μ mol of C700-OMe and P800SO₃ were intravenously injected into 25 g CD-1 mice (top; 0.4 mg kg⁻¹) and 35 kg Yorkshire pigs (bottom; 0.02 mg kg⁻¹), simultaneously, 4 h prior to imaging. All NIR fluorescence images for each condition have identical exposure times and normalizations. Scale bars = 1 cm. Images are representative of n = 3 independent experiments. Pseudo-colored red and green colors were used for 700 nm and 800 nm channel images, respectively, in the color-NIR merged image.

In summary, by incorporating low affinity quats into the polymethine backbone, we could design a new class of high affinity cartilage-targeted NIR fluorescent agents. “Structure-

inherent targeting” was initially reported in our previous paper⁸ for thyroid and parathyroid targeting, and now we expand this concept for cartilage specific targeting and imaging. The high affinity of cationic NIR fluorophores for cartilage provides high-quality tissue visualization, ultralow background signal, and low injected dose. Hence, this method complements other imaging modalities being explored for cartilage imaging, including MR imaging and CT. In addition, this technique may be useful for assessment in longitudinal animal models of cartilage degeneration without destructive methods often used for biochemical analysis. We anticipate that this finding of the cationic NIR fluorophores will form the basis of further development of optical contrast agents and give guidance to the early noninvasive diagnosis and treatment of cartilage diseases.

7.4 Experimental Section

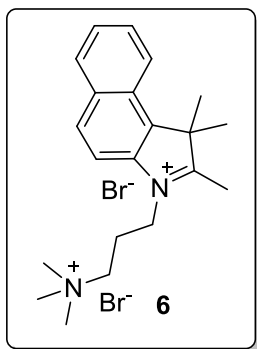
7.4.1 *Synthesis of C700 and C800 NIR fluorophores*

All chemicals and solvents were of American Chemical Society grade or HPLC purity and were used as received. HPLC grade acetonitrile (CH₃CN) and water were purchased from VWR International (West Chester, PA) and American Bioanalytic (Natick, MA), respectively. All other chemicals were purchased from Fisher Scientific (Pittsburgh, PA, USA), Sigma-Aldrich (Saint Louis, MO) and Acros Organics. The reactions were followed using silica gel 60 F₂₅₄ thin layer chromatography plates (Merck EMD Millipore, Darmstadt, Germany). Open column chromatography was utilized for the purification of all hydrophobic final compounds using 60-200u, 60A classic column silica gel (Dynamic Adsorbents, Norcross, GA). Highly charged final products were isolated using reversed phase C18 column chromatography (Fluka). The ¹H NMR and ¹³C NMR spectra were obtained using high quality Kontes NMR tubes (Kimble Chase, Vineland, NJ) rated to 500 MHz and were recorded on a Bruker Avance (400 MHz) spectrometer using D₂O, DMSO-*d*₆ or MeOD-*d*₄ containing tetramethylsilane (TMS) as an internal calibration standard set to 0.0 ppm. NMR abbreviations used throughout the

experimental section are as follows, s = singlet, d = doublet, t = triplet, q = quartet, p = pentet, m = multiplet, dd = doublet doublets, and bs = broad singlet. UV-Vis/NIR absorption spectra were recorded on a Varian Cary 50 spectrophotometer. High-resolution accurate mass spectra (HRMS) were obtained either at the GSU Mass Spectrometry Facility using a Waters Q-TOF micro (ESI-Q-TOF) mass spectrometer or utilizing a Waters Micromass LCT TOF ES+ Premier Mass Spectrometer. The purity of each compound tested was determined by using LC/MS instrument possessing a Waters 2487 single wavelength absorption detector with wavelengths set between 640 and 700 nm depending on the particular photophysical properties. The column used in LC was a Waters Delta-Pak 5 μ M 100A 3.9 x 150 mm reversed phase C₁₈ column, with a flow rate of 1mL/min employing a 5-100% acetonitrile/water/0.1 formic acid gradient; a SEDEX 75 Evaporative light scattering detection (ELSD) was also utilized in tandem with liquid chromatography to confirm purity. All compounds tested were > 95% pure.

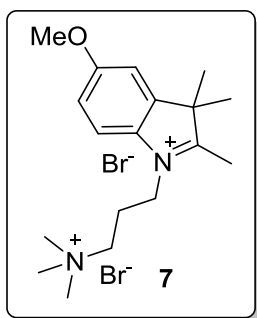
Synthesis of heterocyclic salts 6 and 7.

Compounds **5** and **8** have been previously described by our laboratory. Heterocyclic starting material **2** or **3** (1 mol. eq.) was added to an oven dried and nitrogen purged 250-mL round bottom flask. Toluene (100 mL) was added to the round bottom flask under a positive pressure of nitrogen. (3-Bromopropyl)trimethylammonium bromide (1.2 mol. eq.) was quickly added to the reaction vessel to avoid absorption of water from the atmosphere. The reaction was heated to reflux for 72 h. under heavy stirring. After 72 h., the reaction vessel was allowed to cool to rt. The toluene was evaporated *in vacuo* and the residue was dissolved in methanol and subsequently diluted with diethyl ether to afford the corresponding salt which was suction filtered and washed with diethyl ether, ethyl acetate and acetone to obtain the pure compounds. The powdered solids were dried under high vacuum for >24h.



1,1,2-Trimethyl-3-(3-(trimethylammonio)propyl)-1H-benzo[e]indolium bromide (6).

Yield 52%; $^1\text{H-NMR}$ (400 MHz, $\text{DMSO-}d_6$), δ : 1.79 (s, 6H), 2.42-2.37 (m, 2H), 3.03 (s, 3H), 3.41 (s, 9H), 3.65 (t, $J = 8.0$ Hz, 2H), 4.64 (t, $J = 8.0$ Hz, 2H), 7.82-7.75 (m, 2H), 8.26 (t, $J = 8.8$ Hz, 2H), 8.33 (d, $J = 8.8$ Hz, 1H), 8.39 (d, $J = 8.8$ Hz, 1H).



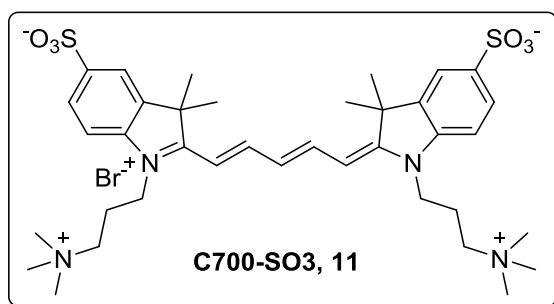
5-Methoxy-2,3,3-trimethyl-1-(3-(trimethylammonio)propyl)-3H-indolium bromide (7).

Yield 88%; $^1\text{H-NMR}$ (400 MHz, $\text{DMSO-}d_6$) δ 1.55 (s, 6H), 2.33 (m, 2H), 2.87 (s, 3H), 3.12 (s, 9H), 3.63 (t, $J = 8.4$ Hz, 2H), 3.87 (s, 3H), 4.48 (t, $J = 8.4$ Hz, 2H), 7.16 (d, $J = 8.8$ Hz, 1H), 7.58 (s, 1H), 8.03 (d, $J = 8.8$ Hz, 1H).

Synthesis of Cartilage Targeting C700 (11-14) and C800 (15-18) Fluorophores.

Individual heterocyclic salt **5-8** (2 mol. eq.) were added to a clean, dry and nitrogen cooled round bottom flask (25-mL) along with a magnetic stir bar followed by acetic anhydride (5 mL) and sodium acetate (4 mol. eq.). The resulting mixture was heated to 40 °C under vigorous stirring with a maintained positive pressure of nitrogen. Individual malonaldehyde

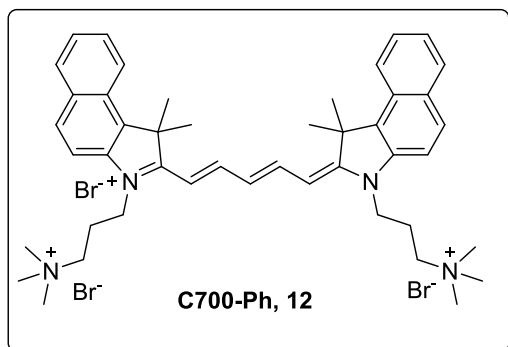
bis(phenylimine) monohydrochloride **9** or *N*-[5-(phenylamino)-2,4-pentadienyldiene]aniline monohydrochloride **10** (1 mol. eq.) was added to the reaction mixture. The reaction was then heated to 60 °C and kept for 2-6 hr. depending on the dye structure. The reactions were monitored by Vis/NIR spectrophotometry by analyzing the change in absorption spectrum, *i.e.* increase in characteristic absorbance >600 nm (product) and corresponding decrease <500 nm (starting materials). After the absorbance signature indicated the completion of the reaction, the reaction mixture was allowed to cool to room temperature. Diethyl ether was added to the reaction mixture under heavy stirring resulting in a fine powder which was suction filtered, washed with acetone, ethyl acetate and diethyl ether and placed on heavy vacuum for 24 h. The compounds were purified on either reversed phase C₁₈ silica gel with 5% acetonitrile:water as the eluting solvent or *via* multiple precipitation by dissolving the compounds in methanol and diluting with ether. The purification steps afforded the final **C700** and **C800** compounds in excellent purity.



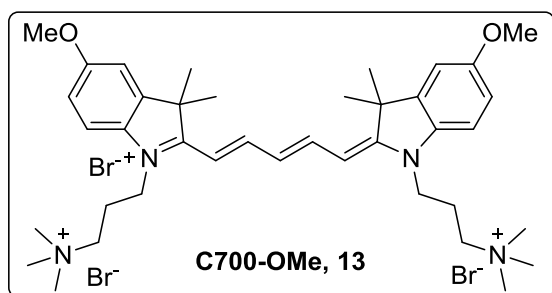
2-((1*E*,3*E*)-5-((*E*)-3,3-dimethyl-5-sulfonato-1-(3-(trimethylammonio)propyl)indolin-2-ylidene)penta-1,3-dien-1-yl)-3,3-dimethyl-1-(3-(trimethylammonio)propyl)-3*H*-indol-1-ium-5-sulfonate bromide (**C700-SO₃, 11**). Yield 90%; MP >260 °C; ¹H NMR (400 MHz, D₂O) δ 1.579 (s, 12H), 2.232 (bs, 4H), 3.046 (bs, 4H), 3.427 (s, 18H), 3.728 (bs, 4H), 4.103 (bs, 4H), 6.271 (d, *J* = 14.0 Hz, 2H), 6.606 (t, *J* = 11.2 Hz, 1H), 7.235 (d, *J* = 6.8 Hz, 2H), 7.765-7.703 (m, 4H), 8.058 (t, *J* = 12.0 Hz, 2H). ¹³C NMR (100 MHz, D₂O) δ 21.29, 27.37, 41.01, 49.66,

53.59, 63.79, 104.67, 111.06, 120.41, 126.92, 127.09, 140.30, 142.18, 144.05, 155.90, 175.13.

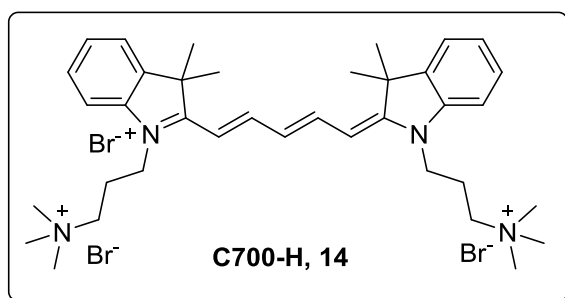
High-resolution electrospray ionization (ESI) accurate mass spectra calculated m/z for $[C_{37}H_{53}N_4O_6S_2]^{3+}$ 713.9730 found 713.9751.



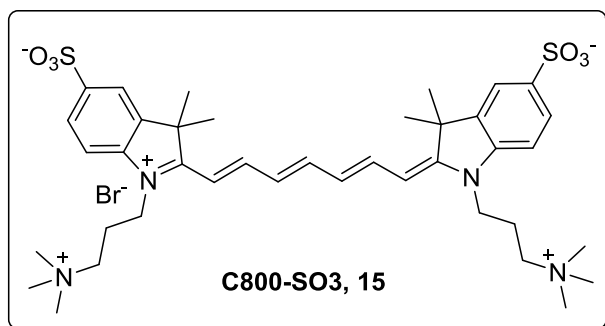
2-((1*E*,3*E*,5*E*)-5-(1,1-dimethyl-3-(3-(trimethylammonio)propyl)-1*H*-benzo[*e*]indol-2(3*H*)-ylidene)penta-1,3-dien-1-yl)-1,1-dimethyl-3-(3-(trimethylammonio)propyl)-1*H*-benzo[*e*]indolium bromide (**C700-Ph, 12**). Yield 60%; MP 250-252 °C; 1H NMR (400 MHz, MeOD-*d*4) δ 2.04 (s, 12H), 2.39 (m, 4H), 3.23 (s, 18H), 3.80 (s, 4H), 4.38 (s, 4H), 6.65 (t, $J = 12.8$ Hz, 2H), 7.17 (m, 1H), 7.49 (m, 2H), 7.62 (m, 2H), 7.73 (t, $J = 9.2$ Hz, 2H), 8.08-7.97 (m, 4H), 8.26 (t, $J = 9.2$ Hz, 2H), 8.41 (m, 2H). ^{13}C NMR (100 MHz, MeOD-*d*4) δ 21.30, 26.32, 40.7, 51.02, 52.62, 63.10, 103.28, 110.79, 121.97, 124.68, 126.55, 127.35, 128.06, 129.63, 130.46, 132.02, 132.02, 133.70, 139.16, 153.57, 174.48. High-resolution ESI accurate mass spectra calculated m/z for $[C_{45}H_{59}N_4]^{3+}$ 218.4908 found 218.4383; calculated m/z for $[C_{45}H_{59}N_4]^{2+}$ 327.7365, found 327.1663.



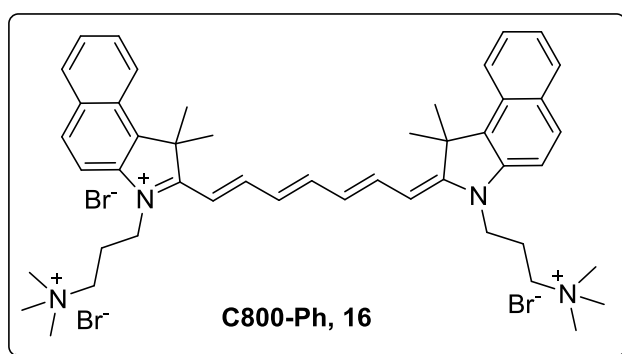
5-Methoxy-2-((1E,3E,5E)-5-(5-methoxy-3,3-dimethyl-1-(3-(trimethylammonio)propyl)indolin-2-ylidene)penta-1,3-dien-1-yl)-3,3-dimethyl-1-(3-(trimethylammonio)propyl)-3H-indolium bromide (C700-OMe, 13). Yield 81%; MP 235-237°C; ¹HNMR (400 MHz, DMSO-*d*₆) δ 1.70 (s, 12H), 2.10 (s, 4H), 3.12 (s, 18H), 3.65 (t, *J* = 8.0 Hz, 4H), 3.80 (s, 6H), 4.15 (t, *J* = 8.0 Hz, 4H), 6.37 (d, *J* = 13.6 Hz, 2H), 6.65 (t, *J* = 12.0 Hz, 1H), 6.94 (d, *J* = 8.8 Hz, 2H), 7.33 (s, 2H), 7.45 (d, *J* = 8.8 Hz, 2H), 8.30 (t, *J* = 13.6 Hz, 2H). ¹³CNMR (100 MHz, DMSO-*d*₆) δ 21.30, 27.63, 41.17, 49.63, 52.95, 56.39, 62.82, 103.31, 109.64, 112.21, 114.00, 125.69, 135.73, 143.32, 153.80, 158.13, 172.34. High-resolution ESI accurate mass spectra calculated *m/z* for [C₃₉H₅₉N₄O₂]³⁺ 205.1541 found 205.1466; calculated *m/z* for [C₃₉H₅₉N₄O₂]²⁺ 307.2314, found 307.2271.



2-((1E,3E,5E)-5-(3,3-dimethyl-1-(3-(trimethylammonio)propyl)indolin-2-ylidene)penta-1,3-dien-1-yl)-3,3-dimethyl-1-(3-(trimethylammonio)propyl)-3H-indolium bromide (C700-H, 14). Yield 71%; MP 218-221 °C; ¹H NMR (400 MHz, MeOD-*d*₄) δ 1.78 (s, 12H), 2.35-2.38 (m, 4H), 3.24 (s, 18H), 3.75 (t, *J* = 8.4 Hz, 4H), 4.25 (t, *J* = 7.6 Hz, 4H), 6.62 (d, *J* = 13.6 Hz, 2H), 7.14 (t, *J* = 12.4 Hz, 1H), 7.28-7.32 (m, 2H), 7.43-7.48 (m, 4H), 7.54 (d, *J* = 7.6 Hz, 2H), 8.34 (t, *J* = 13.2 Hz, 2H). ¹³CNMR (100 MHz, MeOD-*d*₄) δ 20.93, 26.56, 40.26, 49.22, 52.49, 63.08, 103.72, 110.41, 122.20, 125.07, 127.11, 128.50, 141.23, 141.76, 154.80, 173.47. High-resolution ESI accurate mass spectra calculated *m/z* for [C₃₇H₅₅N₄]³⁺ 185.1470 found 185.1070; calculated *m/z* for [C₃₇H₅₅N₄]²⁺ 277.7208, found 277.1687.

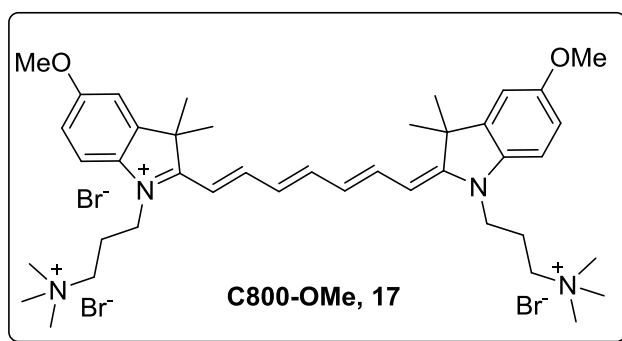


2-((1*E*,3*E*,5*E*,7*E*)-7-(3,3-dimethyl-5-sulfonato-1-(3-(trimethylammonio)propyl)indolin-2-ylidene)hepta-1,3,5-trien-1-yl)-3,3-dimethyl-1-(3-(trimethylammonio)propyl)-3*H*-indol-1-ium-5-sulfonate bromide (**C800-SO₃, 15**) Yield 53%; MP >260 °C; ¹H NMR (400 MHz, DMSO-*d*₆) δ 1.68 (s, 12 H), 2.16 (m, 4 H), 3.10 (s, 18 H), 3.51 (t, *J* = 7.6 Hz, 4 H), 4.14 (t, *J* = 7.6 Hz, 4 H), 6.44 (d, *J* = 13.6 Hz, 2 H), 6.58 (t, *J* = 13.2 Hz, 2 H), 7.36 (d, *J* = 8.0 Hz, 2 H), 7.68 (d, *J* = 8.4 Hz, 2 H), 7.79 (s, 2 H), 8.91 (m, 3 H). ¹³C NMR (100 MHz, DMSO-*d*₆) δ 21.30, 27.63, 41.24, 49.25, 52.98, 62.95, 110.45, 120.39, 126.59, 140.77, 142.31, 145.93. High-resolution ESI accurate mass spectra calculated *m/z* for [C₃₉H₅₅N₄O₆S₂]³⁺ 739.3558 found 739.3571.

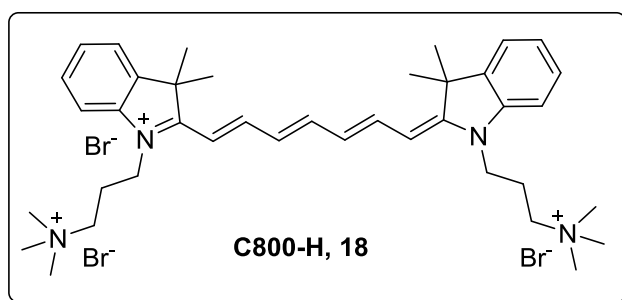


2-((1*E*,3*E*,5*E*,7*E*)-7-(1,1-dimethyl-3-(3-(trimethylammonio)propyl)-1*H*-benzo[*e*]indol-2(3*H*)-ylidene)hepta-1,3,5-trien-1-yl)-1,1-dimethyl-3-(3-(trimethylammonio)propyl)-1*H*-benzo[*e*]indol-3-ium bromide (**C800-Ph, 16**). Yield 62%; MP 219-221 °C; ¹H NMR (400 MHz, DMSO-*d*₆) δ 1.92 (s, 12 H), 2.20 (m, 4 H), 3.16 (s, 18 H), 3.76 (t, *J* = Hz, 4 H), 4.13 (t, *J* = Hz, 4 H), 6.74 (m, 4 H), 7.50 (t, *J* = 7.2 Hz, 2 H), 7.65 (t, *J*

= 7.2 Hz, 2 H), 7.87 (m, 3 H), 8.07 (m, 6 H), 8.26 (d, $J = 8.4$, 2 H). ^{13}C NMR (100 MHz, DMSO- d_6) δ 21.61, 27.27, 50.89, 53.02, 62.81, 104.43, 112.03, 122.67, 122.67, 125.22, 126.66, 128.06, 128.17, 130.35, 130.77, 131.74, 133.52, 140.05, 172.74. High-resolution ESI accurate mass spectra calculated m/z for $[\text{C}_{47}\text{H}_{61}\text{N}_4]^{3+}$ 227.1627, found 227.1599.



5-methoxy-2-((1E,3E,5E,7E)-7-(5-methoxy-3,3-dimethyl-1-(3-(trimethylammonio)propyl)indolin-2-ylidene)hepta-1,3,5-trien-1-yl)-3,3-dimethyl-1-(3-(trimethylammonio)propyl)-3H-indol-1-ium bromide (C800-OMe, 17). Yield 15%; MP 183-185 °C; ^1H NMR (400 MHz, MeOD- d_4) δ 1.65 (s, 12 H), 2.30 (m, 4 H), 3.25 (s, 18 H), 3.78 (s, 6 H), 3.84 (t, $J = 8.4$ Hz, 4 H), 4.32 (t, $J = 8.4$ Hz, 4 H), 6.66 (t, $J = 12$ Hz, 2 H), 6.93 (d, $J = 8.4$ Hz, 2 H), 7.08 (s, 2 H), 7.43 (m, 3 H), 7.77 (d, $J = 10.8$ Hz, 2 H). ^{13}C NMR (100 MHz, MeOD- d_4) δ 20.95, 26.66, 40.53, 49.02, 52.51, 54.99, 63.16, 108.77, 111.25, 113.27, 125.90, 135.44, 142.77, 150.61, 158.28, 170.65. High-resolution ESI accurate mass spectra calculated m/z for $[\text{C}_{41}\text{H}_{61}\text{N}_4\text{O}_2]^{3+}$ 213.8260 found 213.7877.



2-((1E,3E,5E,7E)-7-(3,3-dimethyl-1-(3-(trimethylammonio)propyl)indolin-2-ylidene)hepta-1,3,5-trien-1-yl)-3,3-dimethyl-1-(3-(trimethylammonio)propyl)-3H-indol-1-ium bromide (**C800-H, 18**). Yield 46%; MP 191-193 °C; ¹H NMR (400 MHz, MeOD-*d*₄) δ 1.69 (s, 12 H), 2.32 (m, 4 H), 3.25 (s, 18 H), 3.85 (t, *J* = 8.0 Hz, 4 H), 4.32 (t, *J* = 7.6 Hz, 4 H), 6.62 (d, *J* = 13.2 Hz, 2 H), 6.77 (t, *J* = 12 Hz, 2 H), 7.23 (t, *J* = 7.2 Hz, 2 H), 7.40 (t, *J* = 7.6 Hz, 2 H), 7.49 (t, *J* = 8.0 Hz, 4 H) 7.61 (t, *J* = 12 Hz, 1 H), 7.91 (t, *J* = 11.6 Hz, 2 H). ¹³C NMR (100 MHz, MeOD-*d*₄) δ 20.93, 26.70, 40.39, 48.93, 52.48, 52.52, 52.56, 63.11, 110.58, 122.08, 124.75, 126.63, 128.46, 141.02, 141.93, 152.22, 171.63. High-resolution ESI accurate mass spectra calculated *m/z* for [C₃₉H₅₇N₄]³⁺ 193.8189 found 193.7919.

7.4.2 Optical and physicochemical property analyses

All optical measurements were performed at 37°C in 100% fetal bovine serum (FBS) buffered with 50 mM HEPES, pH 7.4. Absorbance and fluorescence emission spectra NIR fluorophores were measured using fiber optic HR2000 absorbance (200–1100 nm) and USB2000FL fluorescence (350–1000 nm) spectrometers (Ocean Optics, Dunedin, FL). NIR excitations were provided by 5 mW of 655 nm red laser pointer (Opcom Inc., Xiamen, China) and 8 mW of 765 nm NIR laser diode light source (Electro Optical Components, Santa Rosa, CA) coupled through a 300 μm core diameter, NA 0.22 fiber (Fiberguide Industries, Stirling, NJ). For fluorescence quantum yield (QY) measurements, oxazine 725 in ethylene glycol (QY = 19%) and ICG in DMSO (QY = 13%) were used as calibration standards, under conditions of matched absorbance at 655 and 765 nm, respectively. *In silico* calculations for surface molecular charge, the partition coefficient (logD at pH 7.4) and total polar surface area (TPSA) were calculated using Marvin and JChem calculator plugins (ChemAxon, Budapest, Hungary).

7.4.3 NIR fluorescence imaging system

The dual-NIR channel FLARE imaging system has been described in detail previously.^{21,22} In this study, 4 mW/cm² of 670 nm excitation light and 11 mW/cm² of 760 nm excitation light were used with white light (400–650 nm) at 40,000 lx. Color and NIR fluorescence images were acquired simultaneously with custom software at rates up to 15 Hz over a 15 cm diameter field of view. The imaging system was positioned at a distance of 18 inches from the surgical field. For each experiment, camera exposure time and image normalization was held constant.

7.4.4 Animal models

Animals were housed in an AAALAC-certified facility and were studied under the supervision of BIDMC IACUC in accordance with approved institutional protocols (#101-2011 for rodents and #034-2013 for pigs). Male CD-1 mice (25–30 g, 8 weeks, Charles River Laboratories, Wilmington, MA) were anesthetized with 100 mg/kg ketamine and 10 mg/kg xylazine intraperitoneally (Webster Veterinary, Fort Devens, MA). Female Yorkshire pigs (E.M. Parsons and Sons, Hadley, MA) averaging 35 kg were induced with 4.4 mg/kg intramuscular Telazol (Fort Dodge Labs, Fort Dodge, IA), intubated, and maintained with 2% isoflurane (Baxter Healthcare Corp., Deerfield, IL). Following anesthesia, electrocardiogram, heart rate, pulse oximetry, and body temperature were monitored throughout surgery.

7.4.5 Quantitative analysis

At each time point, the fluorescence and background intensity of a region of interest (ROI) over each tissue was quantified using custom FLARE software. The signal-to-background ratio (SBR) was calculated as $SBR = \text{fluorescence}/\text{background}$, where background is the signal intensity of neighboring tissues, such as muscle or skin, obtained over the imaging period. All NIR fluorescence images for a particular fluorophore were normalized identically for all conditions of an experiment. At least 3 animals were analyzed at each time point.

Statistical analysis was carried out using the unpaired Student's *t*-test or one-way analysis of variance (ANOVA). Results were presented as mean \pm s.d. and curve fitting was performed using Prism version 4.0a software (GraphPad, San Diego, CA).

7.4.6 *Histology and NIR fluorescence microscopy*

Cartilage tissues were placed in 2% paraformaldehyde in PBS for 30 min before mounting in Tissue-Tek OCT compound (Fisher Scientific, Pittsburgh, PA) and flash-freezing in liquid nitrogen. Frozen samples were cryosectioned (10 μ m per slice), observed by NIR fluorescence microscopy, and also stained with alcian blue or hematoxylin and eosin (H&E), respectively. NIR fluorescence microscopy was performed on a 4-filter Nikon Eclipse TE300 microscope system as previously described.^{23, 24} The microscope was equipped with a 100 W mercury light source (Chiu Technical Corporation, Kings Park, NY), NIR-compatible optics, and a NIR-compatible 10X Plan Fluor objective lens and a 100X Plan Apo oil immersion objective lens (Nikon, Melville, NY). Images were acquired on an Orca-AG (Hamamatsu, Bridgewater, NJ). Image acquisition and analysis was performed using iVision software (BioVision Technologies, Exton, PA). Two custom filter sets (Chroma Technology Corporation, Brattleboro, VT) composed of 650 ± 22 nm and 750 ± 25 nm excitation filters, 675 nm and 785 nm dichroic mirrors, and 710 ± 25 nm and 810 ± 20 nm emission filters were respectively used to detect C700-OMe and C800-OMe signals in the frozen tissue samples.

7.5 References

1. Achilefu, S. The insatiable quest for near infrared fluorescent probes for molecular imaging. *Angew. Chem. Int. Ed.* **2010**, 49, 9816-9818.
2. Kobayashi, H.; Ogawa, M.; Alford, R.; Choyke, P. L.; Urano, Y. New strategies for fluorescent probe design in medical diagnostic imaging. *Chem. Rev.* **2010**, 110, 2620-2640.

3. Vahrmeijer, A. L.; Hutteman, M.; van der Vorst, J. R.; van de Velde, C. J.; Frangioni, J. V. Image-guided cancer surgery using near-infrared fluorescence. *Nat. Rev. Clin. Oncol.* **2013**, *10*, 507-518.
4. Ashitate, Y.; Hyun, H.; Kim, S. H.; Lee, J. H.; Henary, M.; Frangioni, J. V.; Choi, H. S. Simultaneous mapping of pan and sentinel lymph nodes for real-time image-guided surgery. *Theranostics* **2014**, *4*, 693-700.
5. Park, M. H.; Hyun, H.; Ashitate, Y.; Wada, H.; Park, G.; Lee, J. H.; Njiojob, C.; Henary, M.; Frangioni, J. V.; Choi, H. S. Prototype nerve-specific near-infrared fluorophores. *Theranostics* **2014**, *4*, 823-833.
6. Hyun, H.; Wada, H.; K., B.; Gravier, J.; Yadav, Y.; Laramie, M.; Henary, M.; Frangioni, J. V.; Choi, H. S. Phosphonated near-infrared fluorophores for biomedical imaging of bone. *Angew. Chem. Int. Ed.* **2014**, *53*, 10668-10672.
7. Wada, H.; Hyun, H.; Vargas, C.; Gravier, J.; Park, G.; Gioux, S.; Frangioni, J. V.; Henary, M.; Choi, H. S. Pancreas-targeted NIR fluorophores for dual-channel image-guided abdominal surgery. *Theranostics* **2015**, *5*, 1-11.
8. Hyun, H.; Park, M. H.; Owens, E. A.; Wada, H.; Henary, M.; Handgraaf, H. J. M.; Vahrmeijer, A. L.; Frangioni, J. V.; Choi, H. S. Structure-inherent targeting of near-infrared fluorophores for parathyroid and thyroid gland imaging. *Nature Medicine* **2015**, *21*, 104-U9.
9. Choi, H. S.; Gibbs-Strauss, S. L.; Lee, J. H.; Kim, S. H.; Ashitate, Y.; Liu, F.; Hyun, H.; Park, G.; Xie, Y.; Bae, S.; Henary, M.; Frangioni, J. V. Targeted zwitterionic near-infrared fluorophores for improved optical imaging. *Nat. Biotechnol.* **2013**, *31*, 148-153.
10. Murphy, L.; Helmick, C. G. The impact of osteoarthritis in the United States: a population-health perspective: A population-based review of the fourth most common cause of hospitalization in U.S. adults. *Orthop. Nurs.* **2012**, *31*, 85-91.

11. Ding, C.; Zhang, Y.; Hunter, D. Use of imaging techniques to predict progression in osteoarthritis. *Curr. Opin. Rheumatol.* **2013**, *25*, 127-135.
12. Crema, M. D.; Roemer, F. W.; Marra, M. D.; Burstein, D.; Gold, G. E.; Eckstein, F.; Baum, T.; Mosher, T. J.; Carrino, J. A.; Guermazi, A. Articular cartilage in the knee: current MR imaging techniques and applications in clinical practice and research. *Radiographics* **2011**, *31*, 37-61.
13. Ruan, M. Z.; Dawson, B.; Jiang, M. M.; Gannon, F.; Heggeness, M.; Lee, B. H. Quantitative imaging of murine osteoarthritic cartilage by phase contrast micro-computed tomography. *Arthritis Rheum.* **2013**, *65*, 388-396.
14. Ollier, M.; Maurizis, J. C.; Nicolas, C.; Bonafous, J.; de Latour, M.; Veyre, A.; Madelmont, J. C. Joint scintigraphy in rabbits with 99mTc-N-[3-(triethylammonio)propyl]-15ane-N5, a new radiodiagnostic agent for articular cartilage imaging. *J. Nucl. Med.* **2001**, *42*, 141-145.
15. Miot-Noirault, E.; Guicheux, J.; Vidal, A.; Gauthier, O.; Auzeloux, P.; Lesoeur, J.; Cachin, F.; Askienazy, S.; Chezal, J. M.; Vinatier, C. In vivo experimental imaging of osteochondral defects and their healing using (99m)Tc-NTP 15-5 radiotracer. *Eur. J. Nucl. Med. Mol. Imaging* **2012**, *39*, 1169-1172.
16. Freedman, J. D.; Lusic, H.; Snyder, B. D.; Grinstaff, M. W. Tantalum oxide nanoparticles for the imaging of articular cartilage using x-ray computed tomography: Visualization of ex vivo/in vivo murine tibia and ex vivo human index finger cartilage. *Angew. Chem. Int. Ed.* **2014**, *53*, 8406-8410.
17. Irie, T.; Oda, K.; Shiino, A.; Kubo, M.; Morikawa, S.; Urushiyama, N.; Aonuma, S.; Kimura, T.; Inubushi, T.; Oohashi, T.; Komatsu, N. Design, synthesis, and preliminary ex vivo and in vivo evaluation of cationic magnetic resonance contrast agent for rabbit articular cartilage imaging. *Med. Chem. Commun.* **2013**, *4*, 1508-1512.

18. Stewart, R. C.; Bansal, P. N.; Entezari, V.; Lusic, H.; Nazarian, R. M.; Snyder, B. D.; Grinstaff, M. W. Contrast-enhanced CT with a high-affinity cationic contrast agent for imaging ex vivo bovine, intact ex vivo rabbit, and in vivo rabbit cartilage. *Radiology* **2013**, 266, 141-150.
19. Lee, J. H.; Park, G.; Hong, G. H.; Choi, J.; Choi, H. S. Design considerations for targeted optical contrast agents. *Quantitative imaging in medicine and surgery* **2012**, 2, 266-73.
20. Kim, S. H.; Park, G.; Hyun, H.; Lee, J. H.; Ashitate, Y.; Choi, J.; Hong, G. H.; Owens, E. A.; Henary, M.; Choi, H. S. Near-infrared lipophilic fluorophores for tracing tissue growth. *Biomedical materials* **2013**, 8, 014110.
21. Ashitate, Y.; Kim, S. H.; Tanaka, E.; Henary, M.; Choi, H. S.; Frangioni, J. V.; Flaumenhaft, R. Two-wavelength near-infrared fluorescence for the quantitation of drug antiplatelet effects in large animal model systems. *J. Vasc. Surg.* **2012**, 56, 171-180.
22. Gioux, S.; Choi, H. S.; Frangioni, J. V. Image-guided surgery using invisible near-infrared light: fundamentals of clinical translation. *Mol. Imaging* **2010**, 9, 237-255.
23. Choi, H. S.; Ashitate, Y.; Lee, J. H.; Kim, S. H.; Matsui, A.; Insin, N.; Bawendi, M. G.; Semmler-Behnke, M.; Frangioni, J. V.; Tsuda, A. Rapid translocation of nanoparticles from the lung airspaces to the body. *Nat. Biotechnol.* **2010**, 28, 1300-1303.
24. Choi, H. S.; Ipe, B. I.; Misra, P.; Lee, J. H.; Bawendi, M. G.; Frangioni, J. V. Tissue- and organ-selective biodistribution of NIR fluorescent quantum dots. *Nano Lett.* **2009**, 9, 2354-2359.

8 BROWN ADIPOSE TISSUE TARGETED NIR FLUOROPHORES

8.1 Abstract

The prevalence of brown adipose tissue in human health and disease is being unraveled; however, detection methods remain critically scarce for the longitudinal monitoring of this important tissue. As near-infrared fluorescence imaging has emerged as a leading alternative to other harmful and non-spatially resolved imaging techniques, we have explored small molecule fluorophores that report on the location of brown adipose tissue for longitudinal monitoring.

8.2 Introduction

Similar to, yet more effective than, its skeletal muscle relative, brown adipose tissue (BAT) helps newborns and hibernating animals avoid hypothermic conditions when they are unable to effectively regulate their internal temperature.¹⁻³ BAT uniquely combats hypothermia through two structural characteristics, 1) a large population of mitochondria which is responsible for increased temperature through thermogenesis and 2) a disproportionately high concentration of UCP1 (uncoupled protein 1, also referred to as thermogenin) located within the mitochondrial inner membrane.^{4,5} UCP1 affords the efficient heat-generating mechanism of BAT by dissipating the proton electrochemical gradient within the inner mitochondrial membrane causing reduction in the rate of ATP synthesis. It had been long assumed that BAT lacked a prevailing presence in adults in large part because of developed thermoneutrality or the ability for adults to maintain their body temperatures in alternate ways (i.e. clothes, air conditioning/heat, fire, etc.).⁶⁻⁸ Importantly, it was recently discovered that BAT persists into adulthood and is responsible for maintaining metabolism and plays a vital role in the propensity to gain weight and develop obesity.

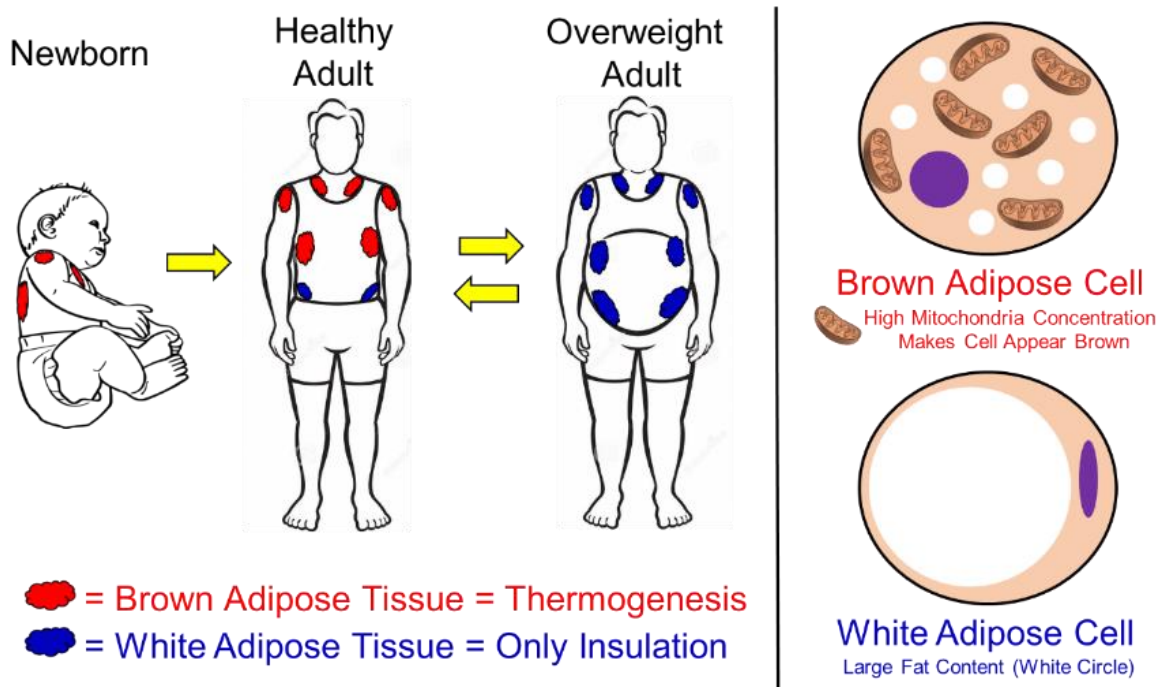


Figure 8-1. General physiological and cellular diagrams of brown and white fat. (left) Presence and location of brown and white fat at different stages of development and health, (right) cellular differences between brown adipose tissues which are high in mitochondria with small fat deposits and white adipose tissues which contains mostly fat. Nucleus is represented by purple and fat is represented by white circles.

The highly ubiquitous nature of BAT, the extremely important interplay with the global obesity epidemic and the unknown mechanism for production/dissipation of BAT demands a technique for effective real-time monitoring of this important tissue. This task has been difficult as the three dimensional structures for targetable molecular receptors remain critically unknown; therefore, engineering contrast agents that specifically target BAT remains a significant unmet clinical need and a challenging research endeavor. Clinicians have relied on position emission tomography (PET) and magnetic resonance imaging (MRI) for studying the location and lifetime-dynamics of brown adipose tissue. PET experiments should be limited for patients due to their

characteristically harmful irradiation; similarly, the spatial resolution of these techniques cannot provide accurate, real-time longitudinal studies for analysis of brown adipose tissue.⁹⁻¹² Our lab focuses on an emerging imaging technique using optical fluorescence of targeted small molecules (fluorophores). Correctly engineered fluorophores are required for *in vivo* use. They must be synthetically modified to assume near-infrared (NIR) absorbance and fluorescence properties. The NIR region is unique in that it features a minimum of human tissue absorbance and fluorescence characteristics—this offers an appealing potential for imaging with low background, reduced tissue attenuation and high signal given the contrast agent exists for a particular tissue. Utilizing a NIR-fluorescent BAT-targeted contrast agent would allow long-term and real-time analysis of brown adipose tissue *in vivo*. Recently, Azhdarinia *et al.*¹³ probed potential BAT-targeted peptides systematically in a combinatorial manner. These peptides were covalently conjugated to a cyanine dye (Cy5) and shows whole-body imaging of BAT. This longstanding approach of fluorophore-dye conjugation has been substantially researched; however, owing to low success in clinical translation, a new approach has been actively researched—structure-inherent targeting. Toward this goal, we realized that mitochondria-targeted small molecules are commonly lipophilic cations and since BAT cells are enriched with high levels of mitochondria we started with fluorophore structures featuring lipophilic cations.

8.3 Results and Discussion

After a systematic screening of >300 small molecules that feature a hydrophobic core with a central cation, we were able to define a generic pharmacophore that showed appealing BAT localization.

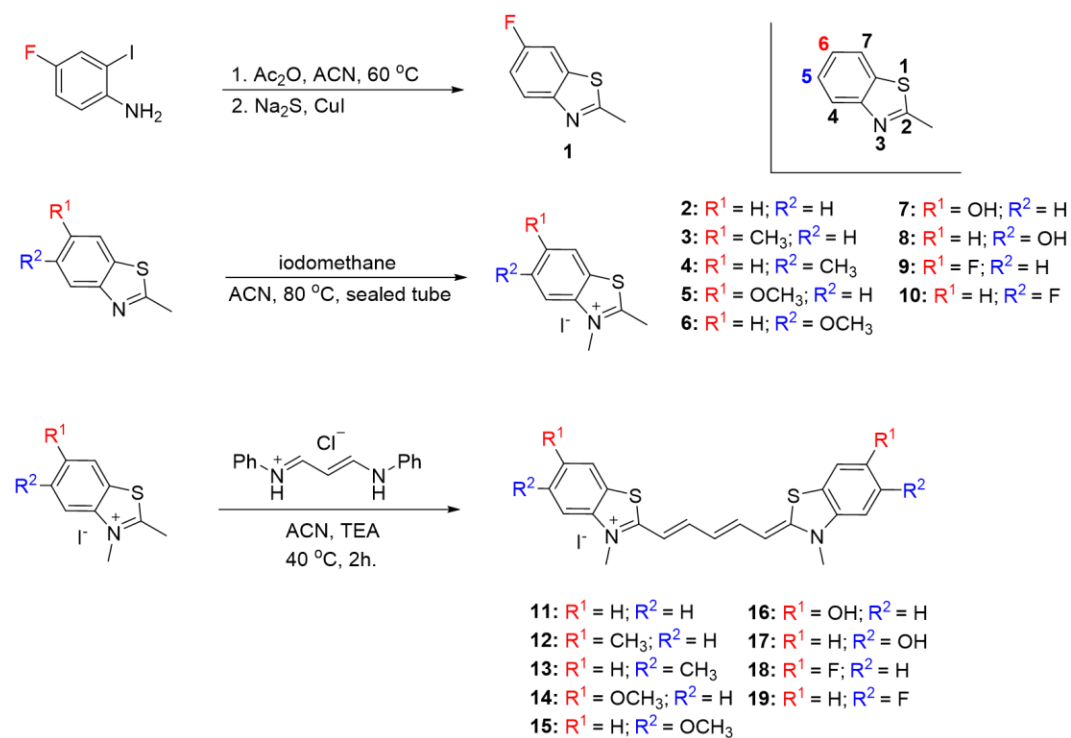


Figure 8-2. The numbering of 2-methylbenzothiazole and synthetic methods to final methylated cyanine chromophores for BAT targeting.

We then directed our focus to modifying this lead compound by systematically installing selected heterocyclic and alkyl modifications that directly influence the all-important lipophilic character for BAT targeting. After screening and analyzing a structure activity relationship for a large series of fluorophores (>300 chemical structures), we identified an overall pharmacophore of pentamethine cyanines bearing the benzothiazole heterocycle. After this general pharmacophore was found, we began systematically modifying the heterocyclic units from hydrophilic (-OH and -OMe) to hydrophobic (methyl, fluorine) to observe potential perturbation in BAT accumulation. The preparation of these fluorophores is shown in Figure 2. We initially began with the commercially available benzothiazoles that were subjected to a facile alkylation with iodomethane in a sealed tube. This quaternization proceeded in near quantitative yield to afford the salts **2-10**. The fluorine heterocycle was prepared from the starting 4-fluoro-2-

iodoaniline which was acetylated and the cyclization reaction was performed in the presence of catalytic copper iodide.

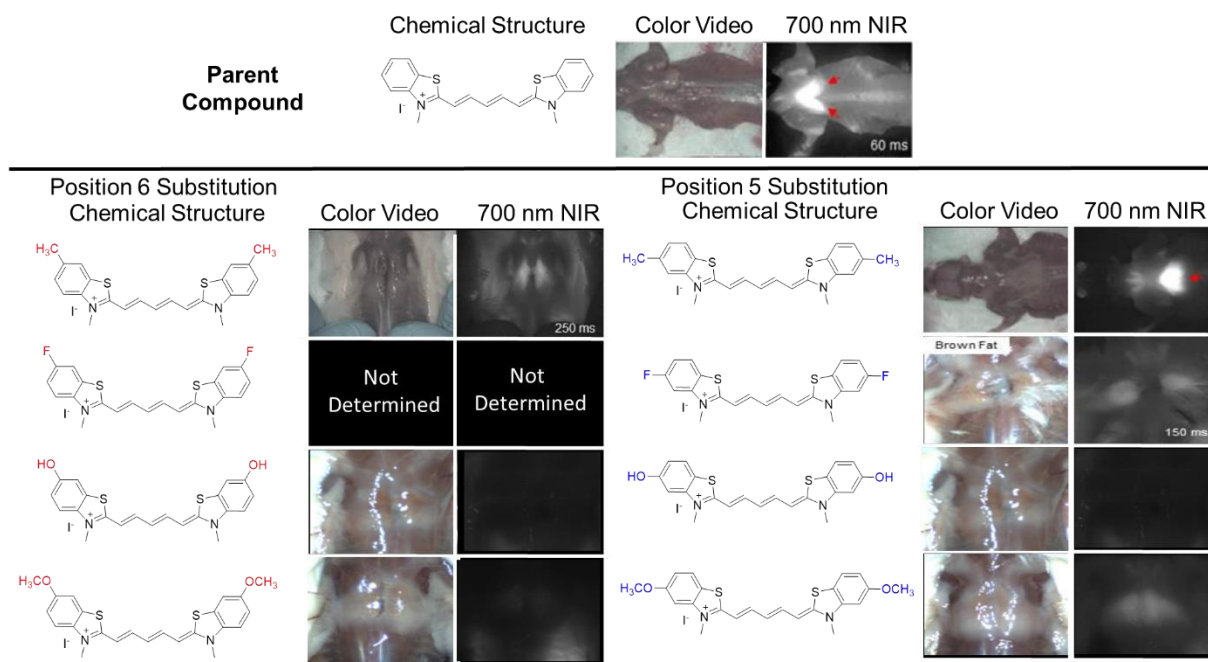


Figure 8-3. The chemical structures, color video and 70 nm NIR fluorescence for final BAT targeting compounds.

Since we observed that both the unsubstituted parent and the 5-methyl substituted compound offered an appealing increase in BAT targeting and began modifying the heterocyclic nitrogen alkyl chains while maintaining the active heterocyclic units. As mitochondria is the major component of brown adipose tissues, and mitochondrial targeting small molecules are lipophilic cations with heavy dependence on the molecular character of the lipophilic cation and related physicochemical descriptors (i.e. LogD, etc.) for their efficacy. Elongating the alkyl chains and increasing the hydrophobic character was thought to direct the compound to areas on increased lipophilic environments while maintaining the BAT targeting character of the heterocyclic unit.

We have found in our previous work on developing structure inherent targeting small molecule fluorophores that minor structural alterations can cause significant and often beneficially serendipitous biological results. Elongating the alkyl chain focused on moving from methyl to ethyl, butyl and phenylpropyl for fully examining a broad range of lipophilic groups.

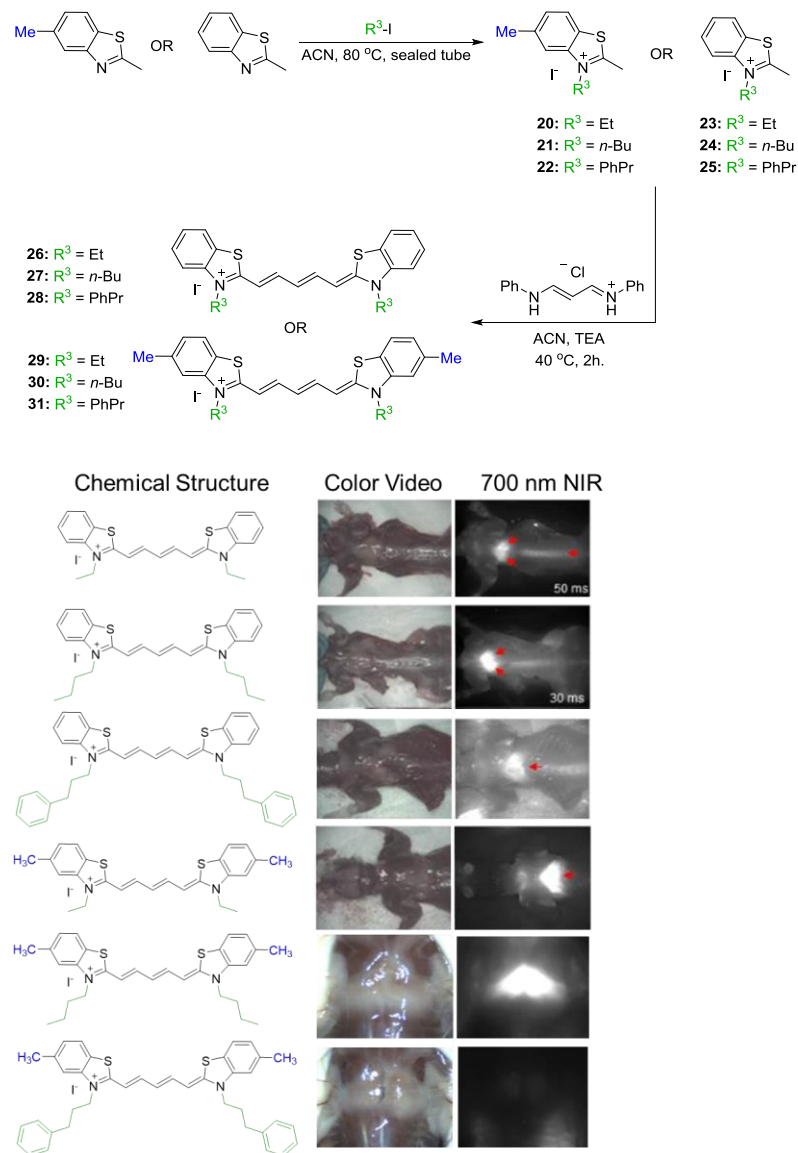


Figure 8-4. The chemical structures, color video and 700 nm NIR fluorescence for final BAT targeting compounds.

When the BAT localization is examined, the butyl side-chains seems to be most effective at selective and high signal brown adipose tissue targeting with the 5-methyl benzothiazole exhibiting higher signal compared to the non-modified heterocyclic analog.

8.4 Conclusions.

For the first time, structure inherent targeting has been successfully applied to the fluorescence imaging of brown adipose tissue. By fine tuning the hydrophobicity in conjunction with heterocyclic manipulation, we achieved highly specific imaging with low surrounding background. These optimized contrast agents can be readily employed for longitudinal monitoring and research toward fully elucidating the intricate nature and therapeutic potential of brown adipose tissue.

8.5 Acknowledgments.

This study was supported by a Georgia State University dissertation grant (E.A.O.), the Brains and Behavior grant (M.H.) and the NIH/NIBIB grant #R01-EB-011523 (H.S.C.). EAO was supported through a pre-doctoral fellowship from the Center for Diagnostics and Therapeutics (CDT).

8.6 Experimental.

Chemicals and Reagents. The chemical reagents used in the synthesis of these compounds were obtained from Acros Organics, Alfa Aesar and Matrix Scientific. The reactions were followed using silica gel 60 F₂₅₄ thin layer chromatography plates (Merck EMD Millipore, Darmstadt, Germany). Open column chromatography was utilized for the purification of all final compounds using 60-200u, 60A, classic column silica gel (Dynamic Adsorbents, Norcross, GA). The ¹H NMR and ¹³C NMR spectra were obtained using high quality Kontes NMR tubes (Kimble

Chase, Vineland, NJ) rated to 500 MHz and were recorded on a Bruker Avance (400 MHz) spectrometer using DMSO- d_6 or MeOD- d_4 containing tetramethylsilane (TMS) as an internal calibration standard set to 0.0 ppm. UV-Vis/NIR absorption spectra were recorded on a Varian Cary 50 spectrophotometer. High-resolution accurate mass spectra (HRMS) were obtained either at the Georgia State University Mass Spectrometry Facility using a Waters Q-TOF micro (ESI-Q-TOF) mass spectrometer or utilizing a Waters Micromass LCT TOF ES+ Premier Mass Spectrometer. Liquid chromatography utilized a Waters 2487 single wavelength absorption detector with wavelengths set between 640 and 700 nm depending on the particular photophysical properties. The column used in LC was a Waters Delta-Pak 5 μ M 100A 3.9 x 150 mm reversed phase C₁₈ column. Evaporative light scattering detection analyzes trace impurities that cannot be observed by alternate methods; a SEDEX 75 ELSD was utilized in tandem with liquid chromatography to confirm purity (>95% as determined by LC-ELSD-MS).

8.6.1 Synthetic Procedures and Structural Characterizations.

General Procedure for preparation of salts

These compounds were synthesized with slight modification of the previously published procedure.^{14, 15} A mixture of 2-methylbenzothiazole (1 eq.) and alkyl halide (3 eq.) was heated at 80°C for 6 to 18 hours. The mixture was cooled to room temperature and resulting crude solid was subjected for purification by precipitation from methanol and diethyl ether (10 mL, 1:4). The precipitated solid was then filtered and dried *in vacuo*.

2,3-dimethylbenzo[d]thiazol-3-ium iodide: Yield 81%; ¹H NMR (DMSO- d_6 , 400 MHz): δ 8.49 (d, J = 8 Hz, 1H), 8.31 (d, J = 8.4 Hz, 1H), 7.89 (q, J_1 = 7.2 Hz, J_2 = 0.8Hz, 1H), 7.80 (t, J_1 = 8.4

Hz, $J_2 = 7.2$ Hz, 1H), 4.24 (s, 3H), 3.22 (s, 3H). ^{13}C NMR (DMSO- d_6 , 100 MHz): δ 177.04, 141.47, 129.15, 128.58, 127.93, 124.47, 116.70, 36.44, 17.48.

2, 3, 5-trimethylbenzo[d]thiazol-3-ium iodide: Yield 76%; ^1H NMR (DMSO- d_6 , 400 MHz): δ 8.31 (d, $J = 8.4$ Hz, 1H), 8.15 (s, 1H), 7.62 (d, $J = 8.4$ Hz, 1H), 4.18 (s, 3H), 3.17 (s, 3H), 2.56 (s, 3H). ^{13}C NMR (DMSO- d_6 , 100 MHz): δ 176.73, 141.79, 139.75, 129.45, 125.75, 124.00, 123.90, 116.51, 116.37, 36.29, 21.14, 17.32.

General procedure for synthesis of BAT targeted compounds

A mixture of benzothiazole quaternary salt (2 eq.) and malonaldehyde bis(phenylimine) monohydrochloride (1 eq.) were heated to 45 $^{\circ}\text{C}$ in presence of triethylamine (2 eq.) in acetonitrile for 2 hours. The solution was cooled down to room temperature and resulting solid was filtered. The resulting crude solid was purified by precipitation from DMF–diethyl ether (20 mL, 1:4).

3-methyl-2-((1E,3E,5Z)-5-(3-methylbenzo[d]thiazol-2(3H)-ylidene)penta-1,3-dien-1-yl)benzo[d]thiazol-3-ium iodide: Yield 68% (0.21 g); m.p. >260 $^{\circ}\text{C}$; ^1H NMR (DMSO- d_6 , 400 MHz): δ 7.98 (d, $J = 8$ Hz, 2H), 7.75~7.67 (m, 4H), 7.55 (t, $J = 7.2$ Hz, 2H), 7.38 (t, $J = 7.6$ Hz, 2H), 6.53~6.50 (m, 3H), 3.80 (s, 6H). ^{13}C NMR (DMSO- d_6 , 100 MHz): δ 164.01, 150.28, 142.02, 127.95, 125.14, 124.94, 122.93, 113.35, 100.62, 33.48. ESI-HRMS m/z : calc. for $(\text{C}_{21}\text{H}_{19}\text{N}_2\text{S}_2)^+$ 363.0990, found 363.1004. $\lambda_{\text{abs}} = 650$ nm $\lambda_{\text{fluo}} = 670$ nm

2-((1E,3E,5Z)-5-(3,5-dimethylbenzo[d]thiazol-2(3H)-ylidene)penta-1,3-dien-1-yl)-3,5-dimethylbenzo[d]thiazol-3-ium iodide: Yield 63% (0.15 g); m.p. >260 $^{\circ}\text{C}$; ^1H NMR (DMSO- d_6 , 400 MHz): δ 7.83 (d, $J = 8$ Hz, 2H), 7.70 (t, $J = 12$ Hz, 2H), 7.52 (s, 2H), 7.21 (d, $J = 8$ Hz, 2H), 6.50~6.42 (m, 3H), 3.77 (s, 6H), 2.43 (s, 6H). ^{13}C NMR (DMSO- d_6 , 100 MHz): δ

164.05, 149.90, 142.14, 138.03, 125.94, 122.47, 122.02, 113.53, 100.54, 33.36, 21.11. ESI-HRMS m/z: calc. for (C₂₃H₂₃N₂S₂)⁺ 391.1297, found 391.1308. $\lambda_{\text{abs}} = 654 \text{ nm}$ $\lambda_{\text{fluo}} = 678 \text{ nm}$

6-hydroxy-2-((1E,3E,5Z)-5-(6-hydroxy-3-methylbenzo[d]thiazol-2(3H)-ylidene)penta-1,3-dien-1-yl)-3-methylbenzo[d]thiazol-3-ium 4-methylbenzenesulfonate:

Yield 61% (0.16 g); m.p. >260 °C; ¹H NMR (DMSO-*d*₆, 400 MHz): δ 10.06 (s, 2H), 7.61~7.46 (m, 5H), 7.35 (s, 2H), 7.10 (d, *J* = 7.6 Hz, 1H), 6.96 (d, *J* = 6.96 Hz, 2H), 6.40~6.34 (m, 3H), 3.73 (m, 6H), 2.28 (s, 1H). ¹³C NMR (DMSO-*d*₆, 100 MHz): δ 162.04, 155.25, 148.70, 134.80, 127.90, 126.32, 125.37, 115.69, 113.86, 108.63, 99.62, 33.28, 20.73. ESI-HRMS m/z: calc. for (C₂₁H₁₉N₂O₂S₂)⁺ 395.0888, found 395.0893. $\lambda_{\text{abs}} = 665 \text{ nm}$ $\lambda_{\text{fluo}} = 688 \text{ nm}$

Repeat of salt synthesis procedure from above:

3-ethyl-2-methylbenzo[d]thiazol-3-ium iodide: Yield 72%; ¹H NMR (DMSO-*d*₆, 400 MHz): δ 8.47 (d, *J* = 8 Hz, 1H), 8.35 (d, *J* = 8.4 Hz, 1H), 7.92 ~ 7.79 (m, 2H), 4.78 (q, *J* = 7.2 Hz, 2H), 3.23 (s, 3H), 1.46 (t, *J* = 7.2 Hz, 3H). ¹³C NMR (DMSO-*d*₆, 100 MHz): δ 176.87, 140.46, 129.37, 129.14, 128.05, 124.69, 116.68, 44.74, 16.79, 13.22.

3-butyl-2-methylbenzo[d]thiazol-3-ium iodide: Yield 50%; ¹H NMR (DMSO-*d*₆, 400 MHz): δ 8.47 (d, *J* = 8 Hz, 1H), 8.35 (d, *J* = 8.8 Hz, 1H), 7.88~7.78 (m, 2H), 4.72 (t, *J* = 7.6 Hz, 2H), 3.23 (s, 3H), 1.89~1.78 (m, 2H), 1.50 ~ 1.41 (m, 2H), 0.93 (t, *J* = 7.2 Hz, 3H). ¹³C NMR (DMSO-*d*₆, 100 MHz): δ 176.98, 140.81, 129.33, 129.05, 128.05, 124.64, 116.88, 49.06, 29.77, 19.27, 16.99, 13.52.

3-ethyl-2,5-dimethylbenzo[d]thiazol-3-ium iodide: Yield 65%; ^1H NMR (DMSO- d_6 , 400 MHz): δ 8.32 (d, $J = 8.4$ Hz, 1H), 8.20 (s, 1H), 7.64 (d, $J = 8.4$ Hz, 1H), 4.73 (q, $J = 7.2$ Hz, 2H), 3.21 (s, 3H), 2.58 (s., 3H), 1.46 (t, $J = 7.2$ Hz, 3H). ^{13}C NMR (DMSO- d_6 , 100 MHz): δ 176.45, 140.76, 140.01, 129.52, 126.25, 124.15, 116.33, 44.60, 21.17, 16.73, 13.21.

General Procedure for synthesis of alkylated BAT agents:

A mixture of benzothiazole quaternary salts (2 eq.) and malonaldehyde bis(phenylimine) monohydrochloride (1 eq.) were heated to 45 $^{\circ}\text{C}$ in presence of triethylamine (2 eq.) in acetonitrile for 2 hours. The solution was cooled to room temperature and the resulting solid was filtered. It was then purified by precipitation from DMF–diethyl ether (20 mL, 1:4).

3-ethyl-2-((1E,3E,5Z)-5-(3-ethylbenzo[d]thiazol-2(3H)-ylidene)penta-1,3-dien-1-yl)benzo[d]thiazol-3-ium iodide: Yield 65% (0.19 g); m.p. >260 $^{\circ}\text{C}$; ^1H NMR (DMSO- d_6 , 400 MHz): δ 7.98 (d, $J = 7.6$ Hz, 2H), 7.77~7.69 (m, 4H), 7.53 (t, $J = 7.6$ Hz, 2H), 7.37 (t, $J = 7.6$ Hz, 2H), 6.55~6.46 (m, 3H), 4.38 (q, $J = 6.8$ Hz, 4H), 1.30 (t, $J = 7.2$ Hz, 3H). ^{13}C NMR (DMSO- d_6 , 100 MHz): δ 163.22, 150.57, 140.93, 128.00, 125.39, 124.91, 123.05, 120.74, 113.09, 100.06, 41.28, 12.65. ESI-HRMS m/z : calc. for $(\text{C}_{23}\text{H}_{23}\text{N}_2\text{S}_2)^+$ 391.1297, found 391.1298. $\lambda_{\text{abs}} = 650$ nm
 $\lambda_{\text{fluo}} = 673$ nm

3-butyl-2-((1E,3E,5Z)-5-(3-butylbenzo[d]thiazol-2(3H)-ylidene)penta-1,3-dien-1-yl)benzo[d]thiazol-3-ium iodide: Yield 62% (0.14 g); m.p. 240 - 242 $^{\circ}\text{C}$; ^1H NMR (DMSO- d_6 , 400 MHz): δ 7.99 (d, $J = 8$ Hz, 2H), 7.79~7.71 (m, 4H), 7.55 (t, $J = 7.6$ Hz, 2H), 7.39 (t, $J = 7.6$ Hz, 2H), 6.55~6.48 (m, 3H), 4.34 (brt, $J = 7.2$ Hz, 4H), 1.71 (m, 4H), 1.41 (m, 4H), 0.94 (t, $J = 7.2$ Hz, 6H). ^{13}C NMR (DMSO- d_6 , 100 MHz): δ 163.34, 150.26, 141.23, 127.89, 125.21, 124.82,

122.95, 120.91, 113.26, 100.36, 45.82, 29.38, 19.29, 13.63. ESI-HRMS m/z: calc. for (C₂₇H₃₁N₂S₂)⁺ 447.1923, found 447.1933. $\lambda_{\text{abs}} = 655 \text{ nm}$ $\lambda_{\text{fluo}} = 673 \text{ nm}$

3-(3-phenylpropyl)-2-((1E,3E,5Z)-5-(3-(3-phenylpropyl)benzo[d]thiazol-2(3H)-ylidene)penta-1,3-dien-1-yl)benzo[d]thiazol-3-ium bromide: Yield 63% (0.17 g); m.p. 130 - 132 °C; ¹H NMR (DMSO-*d*₆, 400 MHz): δ 7.97 (d, *J* = 8 Hz, 2H), 7.73 ~ 7.52 (m, 6H), 7.39 ~ 7.21 (m, 10H), 6.42 ~ 6.39 (m, 3H), 4.35 (brt, *J* = 6.8 Hz, 4H), 2.76 (t, *J* = 7.6 Hz, 4H), 2.03 (m, 4H). ¹³C NMR (DMSO-*d*₆, 100 MHz): δ 163.56, 150.40, 141.31, 140.77, 128.40, 128.21, 127.94, 126.09, 125.31, 124.93, 123.01, 120.77, 113.21, 100.26, 45.65, 31.81, 28.79. ESI-HRMS m/z: calc. for (C₃₇H₃₅N₂S₂)⁺ 571.2236, found 571.2240. $\lambda_{\text{abs}} = 655 \text{ nm}$ $\lambda_{\text{fluo}} = 674 \text{ nm}$

3-ethyl-2-((1E,3E,5Z)-5-(3-ethyl-5-methylbenzo[d]thiazol-2(3H)-ylidene)penta-1,3-dien-1-yl)-5-methylbenzo[d]thiazol-3-ium iodide: Yield 56% (0.16 g); m.p. >260 °C; ¹H NMR (DMSO-*d*₆, 400 MHz): δ 7.85 (d, *J* = 8 Hz, 2H), 7.73 (t, *J* = 12.4 Hz, 2H), 7.57 (s, 2H), 7.22 (d, *J* = 7.6 Hz, 2H), 6.54~6.42 (m, 3H), 4.36 (brd, *J* = 6.4 Hz, 4H), 2.44 (s, 6H), 1.31 (t, *J* = 6.8 Hz, 6H). ¹³C NMR (DMSO-*d*₆, 100 MHz): δ 163.36, 150.14, 141.05, 138.14, 125.94, 125.53, 122.20, 113.22, 99.91, 41.10, 21.02, 12.56. ESI-HRMS m/z: calc. for (C₂₅H₂₇N₂S₂)⁺ 419.1610, found 419.1602. $\lambda_{\text{abs}} = 660 \text{ nm}$ $\lambda_{\text{fluo}} = 679 \text{ nm}$

Optical and Physicochemical Property Analyses. All optical measurements were performed in various solvents, including ethanol (200 proof, Fischer Chemical), dimethyl sulfoxide (DMSO, 99.9% Acros Organics), phosphate buffered saline (PBS, pH 7.4, Fischer Scientific) and at 37°C in 100% fetal bovine serum (FBS, Fischer Scientific) buffered with 50 mM HEPES, pH 7.4. Absorbance and fluorescence emission spectra of the series of NIR fluorophores were measured using Varian Cary 50 absorbance spectrophotometer (190–1100 nm) and Shimadzu RF-5301PC spectrofluorometer (350–1000 nm). For fluorescence quantum yield (QY)

measurements, rhodamine 800 in absolute ethanol (QY = 28%) was used as a calibration standard, under conditions of matched absorbance at 640 nm. *In silico* calculations of physicochemical distribution coefficient (logD at pH 7.4) was calculated using Marvin and JChem calculator plugins (ChemAxon, Budapest, Hungary). Electrostatic maps were calculated using Spartan DFT calculations at the B3LYP level.

LC-MS Analysis. The purity of all compounds was measured using liquid chromatography-mass spectrometry (LC-MS) on a Waters system consisting of a 1525 binary HPLC pump with a manual 7725i Rheodyne injector, a 996 Photodiode Array (PDA) detector, and a 2475 multiwavelength fluorescence detector. The column eluent was divided in 2 using a flow splitter (Upchurch Scientific). A portion of the eluent flowed into an ELSD (Richards Scientific) while the rest flowed into a Micromass LCT ESI-TOF spectrometer (Waters) equipped with a Symmetry (R) C18 (4.6 x 150 mm, 5 μ m) reverse-phase HPLC column. For mass spectrometry mobile phase was solvent A = 0.1% formic acid (FA) in water and solvent B = CH₃CN with 95% A for 5 min and a linear gradient from 5% to 40% CH₃CN (from A to B for 30 min) at a flow rate of 1 mL/min, capillary voltage was -3317V, and sample cone voltage was -50V.

Optical Imaging System and Fluorescence Assisted Surgical Resection. The real-time intraoperative FLARE imaging system has been described in detail previously.^{16, 17} In this study, 670 nm excitation was used at a fluence rate of 4 mW/cm², with white light (400-650 nm) at 40,000 lx. Color and NIR fluorescence images were acquired simultaneously with custom software at rates up to 15 Hz over a 15 cm diameter field of view. The imaging system was positioned at a distance of 18 inches from the surgical field. The wavelength used for excitation and emission filters was 650 \pm 22 nm.

Animal models. Animals were housed in an AAALAC-certified facility and were studied under the supervision of BIDMC's IACUC in accordance with the approved institutional protocol #057-2014. Male CD-1 mice (20–30 g, 6-8 weeks, Charles River Laboratories, Wilmington, MA) were anesthetized with 100 mg/kg ketamine and 10 mg/kg xylazine intraperitoneally (Webster Veterinary, Fort Devens, MA). For intraoperative imaging and biodistribution, the imaging system equipped with a custom filter set (Chroma Technology Corporation, Brattleboro, VT) composed of a 650 ± 22 nm excitation filter, a 680 nm dichroic mirror, and an 710 ± 25 nm emission filter was used at a fluence rate of 4 mW/cm^2 , with white light (400-650 nm) at 40,000 lx. Color and NIR fluorescence images were acquired simultaneously with custom software at rates up to 15 Hz over a 15 cm diameter field of view. The imaging system was positioned at a distance of 18 inches from the surgical field. For each experiment, camera exposure time and image normalization was held constant.

Quantitative analysis. At each time point, the fluorescence and background intensity of a region of interest (ROI) over each tissue was quantified using custom imaging software and ImageJ software (NIH, Bethesda, MD) version 1.45q. The signal-to-background ratio (SBR) was calculated as $\text{SBR} = \text{fluorescence}/\text{background}$, where background is the signal intensity of neighboring tissues such as muscle or skin obtained over the period of imaging time. All NIR fluorescence images for a particular fluorophore were normalized identically for all conditions of an experiment. At least three animals were analyzed at each time point. Statistical analysis was carried out using the unpaired Student's *t*-test or one-way analysis of variance (ANOVA). Results were presented as mean \pm s.d. and curve fitting was performed using Prism version 4.0a software (GraphPad, San Diego, CA).

8.7 References.

1. Santhanam, P.; Solnes, L.; Hannukainen, J. C.; Taieb, D. Adiposity-Related Cancer and Functional Imaging of Brown Adipose Tissue. *Endocr Pract* **2015**.
2. Zhang, X.; Tian, Y.; Zhang, H.; Kavishwar, A.; Lynes, M.; Brownell, A. L.; Sun, H.; Tseng, Y. H.; Moore, A.; Ran, C. Curcumin analogues as selective fluorescence imaging probes for brown adipose tissue and monitoring browning. *Sci Rep* **2015**, 5, 13116.
3. Izzi-Engbeaya, C.; Salem, V.; Atkar, R. S.; Dhillon, W. S. Insights into Brown Adipose Tissue Physiology as Revealed by Imaging Studies. *Adipocyte* **2015**, 4, 1-12.
4. Puigserver, P.; Vazquez, F.; Bonet, M. L.; Pico, C.; Palou, A. In vitro and in vivo induction of brown adipocyte uncoupling protein (thermogenin) by retinoic acid. *Biochem J* **1996**, 317 (Pt 3), 827-33.
5. Jacobsson, A.; Muhleisen, M.; Cannon, B.; Nedergaard, J. The uncoupling protein thermogenin during acclimation: indications for pretranslational control. *Am J Physiol* **1994**, 267, R999-1007.
6. Peng, X. G.; Ju, S.; Fang, F.; Wang, Y.; Fang, K.; Cui, X.; Liu, G.; Li, P.; Mao, H.; Teng, G. J. Comparison of brown and white adipose tissue fat fractions in ob, seipin, and Fsp27 gene knockout mice by chemical shift-selective imaging and (1)H-MR spectroscopy. *Am J Physiol Endocrinol Metab* **2013**, 304, E160-7.
7. Weber, W. A. Brown adipose tissue and nuclear medicine imaging. *J Nucl Med* **2004**, 45, 1101-3.
8. Dellagiacomma, G.; Sbarbati, A.; Rossi, M.; Zancanaro, C.; Benati, D.; Merigo, F.; Baldassarri, A.; Boicelli, A. Brown adipose tissue: magnetic resonance imaging and ultrastructural studies after transplantation in syngeneic rats. *Transplant Proc* **1992**, 24, 2986.

9. Hwang, J. J.; Yeckel, C. W.; Gallezot, J. D.; Aguiar, R. B.; Ersahin, D.; Gao, H.; Kapinos, M.; Nabulsi, N.; Huang, Y.; Cheng, D.; Carson, R. E.; Sherwin, R.; Ding, Y. S. Imaging human brown adipose tissue under room temperature conditions with $(11)\text{C-MRB}$, a selective norepinephrine transporter PET ligand. *Metabolism* **2015**, *64*, 747-55.
10. Borga, M.; Virtanen, K. A.; Romu, T.; Leinhard, O. D.; Persson, A.; Nuutila, P.; Enerback, S. Brown adipose tissue in humans: detection and functional analysis using PET (positron emission tomography), MRI (magnetic resonance imaging), and DECT (dual energy computed tomography). *Methods Enzymol* **2014**, *537*, 141-59.
11. Hong, T. S.; Shamma, A.; Charron, M.; Zukotynski, K. A.; Drubach, L. A.; Lim, R. Brown adipose tissue 18F-FDG uptake in pediatric PET/CT imaging. *Pediatr Radiol* **2011**, *41*, 759-68.
12. Basu, S. Functional imaging of brown adipose tissue with PET: can this provide new insights into the pathophysiology of obesity and thereby direct antiobesity strategies? *Nucl Med Commun* **2008**, *29*, 931-3.
13. Azhdarinia, A.; Daquinag, A. C.; Tseng, C.; Ghosh, S. C.; Ghosh, P.; Amaya-Manzanares, F.; Sevic-Muraca, E.; Kolonin, M. G. A peptide probe for targeted brown adipose tissue imaging. *Nat Commun* **2013**, *4*, 2472.
14. Poronik, Y. M.; Hugues, V.; Blanchard-Desce, M.; Gryko, D. T. Octupolar Merocyanine Dyes: A New Class of Nonlinear Optical Chromophores. *Chemistry – A European Journal* **2012**, *18*, 9258-9266.
15. Kuramoto, N.; Natsukawa, K.; Asao, K. Synthesis and characterization of deep-coloured squarylium dyes for laser optical recording media. *Dyes and Pigments* **1989**, *11*, 21-35.
16. Troyan, S. L.; Kianzad, V.; Gibbs-Strauss, S. L.; Gioux, S.; Matsui, A.; Oketokoun, R.; Ngo, L.; Khamene, A.; Azar, F.; Frangioni, J. V. The FLARE intraoperative near-infrared

fluorescence imaging system: a first-in-human clinical trial in breast cancer sentinel lymph node mapping. *Ann Surg Oncol* **2009**, 16, 2943-52.

17. Lee, B. T.; Hutteman, M.; Gioux, S.; Stockdale, A.; Lin, S. J.; Ngo, L. H.; Frangioni, J. V. The FLARE intraoperative near-infrared fluorescence imaging system: a first-in-human clinical trial in perforator flap breast reconstruction. *Plast Reconstr Surg* **2010**, 126, 1472-81.

9 STRUCTURALLY STABLE AND ULTRA-BRIGHT SQUARINE DYES: THE ROLE OF QUATERNARY AMMONIUM CATIONS IN OXOCYCLOBUTANAL STABILIZATION

This chapter is a manuscript that has been prepared for publication for submission as a communication to *Angewandte Chemie* based on the stability and biological tagging applications of new ultrabright squaraine dyes. My co-first author designation is for the design of the project, the molecular modeling, NMR studies to confirm the modeling (not currently shown), the manuscript/figure preparation and the synthesis of final asymmetric compounds for later biological applications.

Yadav, Y. *, **Owens, E. A.***, Henary, M., Near-infrared Fluorescent Squaric Acid Dyes with Unparalleled Brightness and Stability in Serum **2015** Submitted to *Angewandte Chemie*. *Co-First Authors

9.1 Abstract

Highly stable symmetric and asymmetric squaric acid fluorophores have been synthesized featuring an internal salt bridge between a quaternary ammonium cation and the central oxycyclobutenolate ring of the chromophore. The newly synthesized symmetric and asymmetric compounds display increased molar absorptivity (DMSO: symmetric average $447,325 \text{ M}^{-1}\text{cm}^{-1}$

and asymmetric average $333,725 \text{ M}^{-1}\text{cm}^{-1}$; Fetal Bovine Serum: $398,050 \text{ M}^{-1}\text{cm}^{-1}$ and $375,100 \text{ M}^{-1}\text{cm}^{-1}$, respectively), quantum yield in serum (symmetric average $\phi = 45\%$, asymmetric average $\phi = 79\%$), and thermal/photochemical stability over previously reported squaric acid based dyes. Consequently, both classes show great promise in re-surfacing the normally environment-labile squaric acid dyes as novel imaging agents and scaffolds for fluorescence sensing. Furthermore, incorporating a covalent attachment point away from the conjugated system allows for biological tagging applications without disturbing the optimum optical characteristics of the newly designed fluorophore.

9.2 Introduction

Biological sensors and imaging agents that absorb and fluoresce within the near-infrared (NIR) region of the electromagnetic spectrum continue to garner sustained research interest due to their inherent optical clarity for *in vivo* and *in vitro* use. The NIR region features a reduction in light scattering, low light absorption by biomolecules and the removal of fluorescence signal competition arising from biological sources. Designing a NIR-absorbing and fluorescing compound must satisfy an array of diverse and crucial characteristics, including, (1) the compound must display absorbance and fluorescence above 630 nm which is red-shifted enough to be easily filtered from lower wavelength biomolecular autofluorescence, (2) a sufficient extinction coefficient and quantum yield in serum/water to be used in living/aqueous systems, (3) sustained water solubility to avoid micro-crystallization and reduction in optical performance and (4) high photo- and chemical stability to retain absorbance and fluorescence abilities in harsh conditions. Many fluorophore subclasses, including fluorescein^{1,2}, BODIPY³⁻⁵ and aminocoumarin^{6,7} based fluorophores (Figure 1) satisfy some of these characteristics, and they have been explored with great interest. These fluorophores display non-optimum optical properties, limited water

solubility, difficult synthetic protocols or tedious purification methods, which limit their widespread utility. One particularly interesting class of NIR fluorescent compound centers on an oxocyclobutenolate ring and are called squaric acid dyes.⁸⁻¹⁰ These compounds are characterized by extremely high fluorescence quantum yield (20-40%) which is highly desirable for increasing meaningful signal; however, since their initial discovery, they have been reported by various researchers to be unstable due to their highly chemically and photolytically labile oxocyclobutenolate ring which quickly diminishes their widespread utility.¹¹ The delocalized cation between the terminal heterocyclic rings helps to resolve this but adds only minor stability to the overall structure; however, various strategies such as dye polymerization¹², rotaxane-protection of the squaraine-core¹³, polymer-incorporation¹⁴ or dextran enveloping¹⁵ have been employed to harness the characteristically remarkable quantum yield of these compounds. All of these methods have been shown to impart a subtle increase on the stability by protecting the electrophilic core of the chromophore, but these low-yielding (10%) and tedious manufacturing processes have not offered a substantial breakthrough in increasing squaraine dye stability or overall utility. In addition, these fluorophores cannot be utilized for many specific labeling techniques that require a relatively small molecular size—such as imaging *in vivo* or in biomolecular labeling which renders squaric acid compounds useless in these highly demanding applications¹⁶⁻¹⁸. Many efforts have been exhausted in the attempt to develop a system for increasing the stability of squaric acid fluorophores and herein, we report a facile scaffold for producing the most stable squaric acid compounds synthesized to date with unparalleled brightness in serum as determined by their measured extinction coefficients (ϵ), quantum yield (ϕ) and optical brightness ($\epsilon\phi$). Using our generic fluorophore platform, we are able to harness the optical prowess of squaric acid-based NIR fluorophores without sacrificing stability.

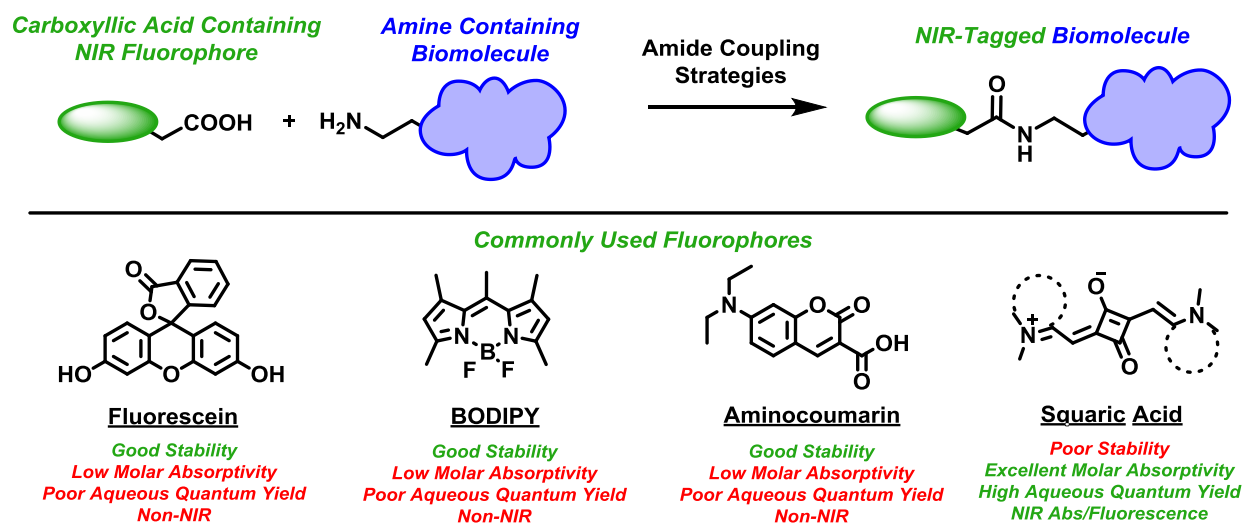


Figure 9-1. (top) General overview of covalently labeling a biomolecule with a NIR-dye (bottom) commonly used fluorophores with benefits, in green, and negatives, in red, associated with their *in vivo* use.

9.3 Results and Discussion

We initiated this finding by synthesizing water-soluble squaric acid fluorophores (Figure 9-2) for image guided surgery. To begin, we utilized Fischer indole synthesis, which proceeds well in acetic acid, to install various halogens on the ring for influencing physicochemical descriptors for *in vivo* studies. Alkylating the heterocyclic nitrogen with a propyl based quaternary ammonium side chain is followed by the corresponding dicationic salt is allowed to react with squaric acid under dean-stark conditions. Having the final fluorophores in hand we initially confirmed that we successfully installed improved water solubility; however, we were skeptical that our squaric acid dyes would be able to survive intravenous injection and we investigated the optical profile. To our serendipitous advantage, when observing the photo-stability, we found retained optical performance after continuous irradiation for 10 hours.

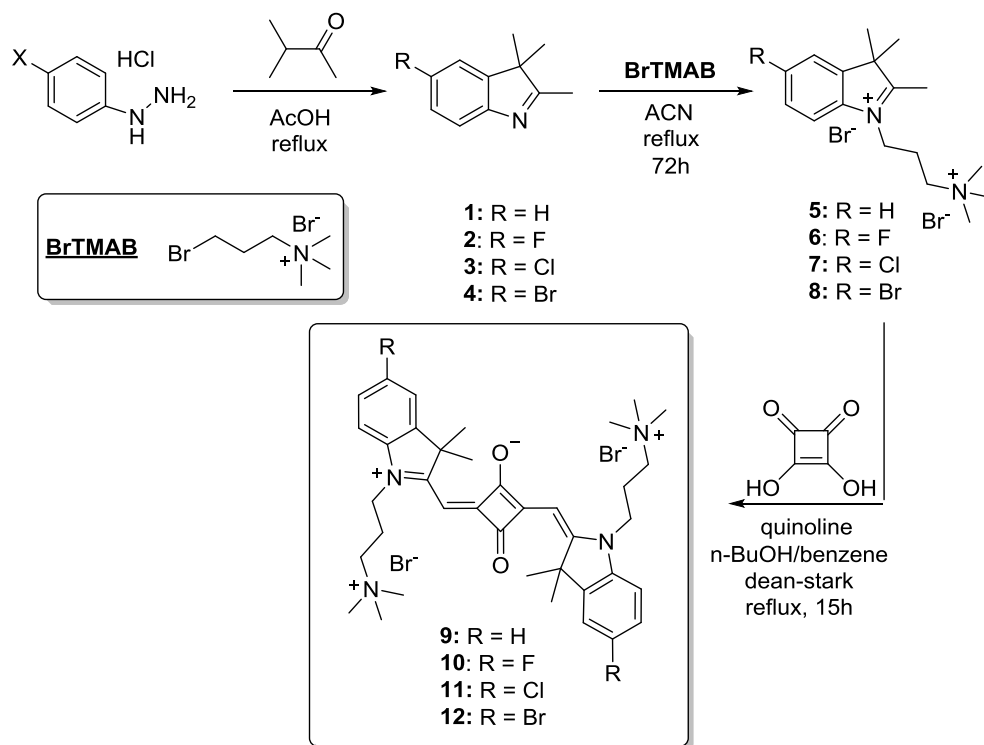


Figure 9-2. Preparation of squaric acid dyes 9-12.

Similarly to the above synthesis, we prepared additional analogs containing only a single quaternary ammonium arm, shown in Figure 9-3. The synthetic route begins with methylation and subjecting the precursor **13** to a reaction with diisopropyl squarate. Careful reaction monitoring and using triethyl amine affords the single heterocyclic adduct which is then reacted with an ethanolic sodium hydroxide solution which prepares the intermediate **15** for reaction with a second heterocyclic equivalent (**5-8**) under identical reaction conditions—this yields the final asymmetric dyes **16-19** in good to excellent yield.

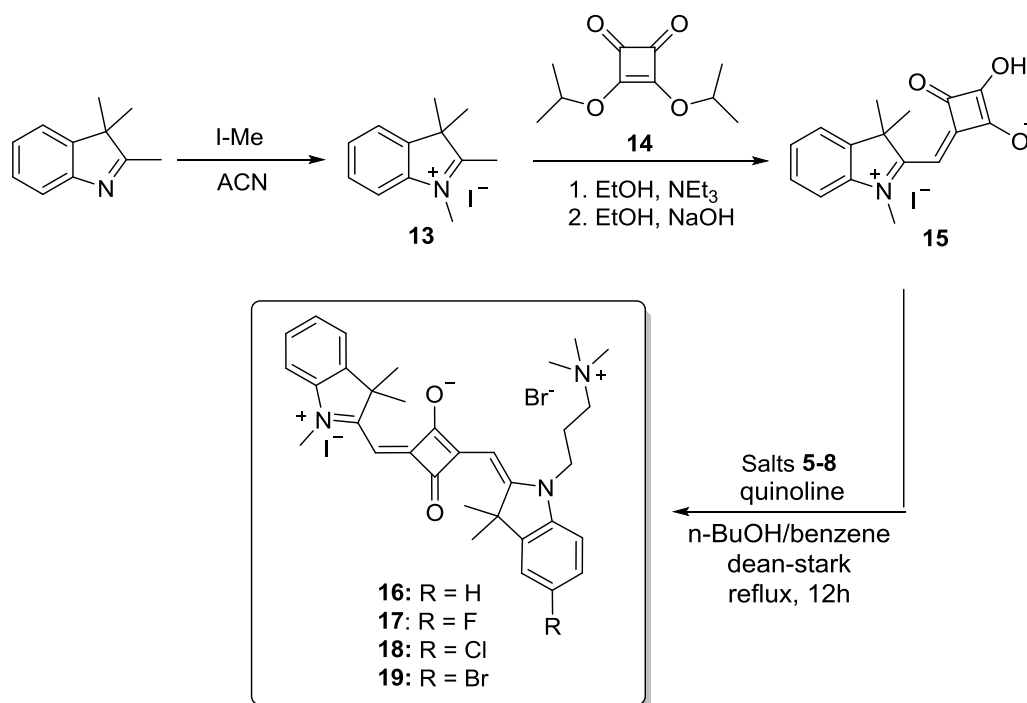


Figure 9-3. Final asymmetric compound 16-19 preparation.

Similar stability tests confirmed that the asymmetric compounds exhibited excellent stability compared to previously known squaric acid dyes and we began to realize that we could, in fact, use these *in vivo* and take full advantage of the elevated optical brightness. Biological experiments often require a reactive handle for covalent attachment of a fluorophore and, at this point, our compounds lacked a reactive functionality; therefore, using the chemistry optimized in Scheme 2, we prepared the derivative **22** (Figure 9-3) bearing the reactive carboxylic acid functionality for further covalent modification. Having confirmed that we could synthesize a biologically relevant squaric acid dye, we fully examined the optical profile in various solvents (ethanol, dimethylsulfoxide, phosphate buffered saline and fetal bovine serum) to confirm the near-infrared properties and ensure our scaffold still featured the positive properties of squaric acid dyes with improved stability.

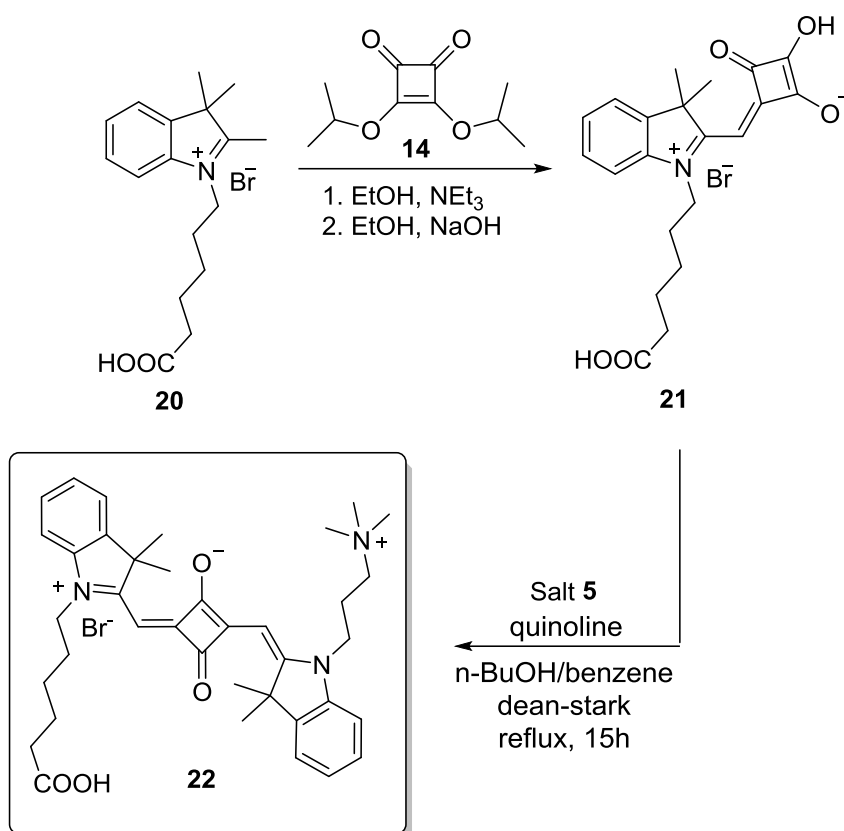


Figure 9-4. Final carboxylate-modified zwitterionic squaric acid dye 22 preparation.

All dyes dissolve immediately in aqueous systems without the need for a co-solvent and show near-infrared absorption and fluorescence characteristics with common Stokes' Shift values (8-15 nm). The sharpness of the absorption band in serum is highly remarkable as other fluorophores display signature aggregation which reduces their *in vivo* applicability. Common molar absorptivity of squaric acid dyes has been reported around 300,000-340,000 in organic solvents which decreases drastically in aqueous and protein-based media. We found that our newly prepared fluorophores display the highest extinction coefficient values observed to date with some greater than 450,000 M⁻¹cm⁻¹ (Figure 9-5) probably due to the rigidity associated with the electrostatic interaction between the ammonium cation and the partially negative central oxygen atoms (Figures 9-5 and 9-6). Common intermolecular salt bridge distances are less than 4Å which

larger spatial separation being too large for ionic interactions to occur. DFT calculations suggest that the quaternary ammonium arms fold back onto the central core of the electrophilic chain to within 4Å. In Figure 9-6, we show these intermolecular distances and the electrostatic maps associated with both the symmetric and asymmetric fluorophores. All distances for the compounds' quaternary ammonium nitrogen and corresponding central oxygen are less than 3.7Å with representative compounds **10** and **17** shown for example. This adds the rigidity and stability by locking the conformational state of the squaric acid fluorophore. We suspect that this rigidization of the conjugated system of the compounds owes to the increase in quantum yield as well with some measured values approaching unity (compound **16** ϕ (FBS) = 93%). We noted, however, that bromine incorporation reduced the overall quantum yield, especially in serum. Finally, the paramount issue associated with squaric acid dyes is their inherent lability. The stability tests to determine the stability of these fluorophores bearing an internal salt bridge included irradiation using a high energy light while the compound was dissolved in FBS and heating the compound in FBS to 37 °C to determine stability at physiological temperature in the presence of proteins. The optical half-life recognized by absorbance reaching half of the original value for each of the compounds **9** and **16** was not reached after 72h; however, the industry standard, Cy5 (inherently more stable than previously known squaric acid dyes) was depleted of >75% of the absorption measurements after the same timeframe. We noted an increase in stability of the symmetric version over the asymmetric compound however the difference was not substantial as even the asymmetric compound is vastly more stable compared to previously published squaric acid compounds.

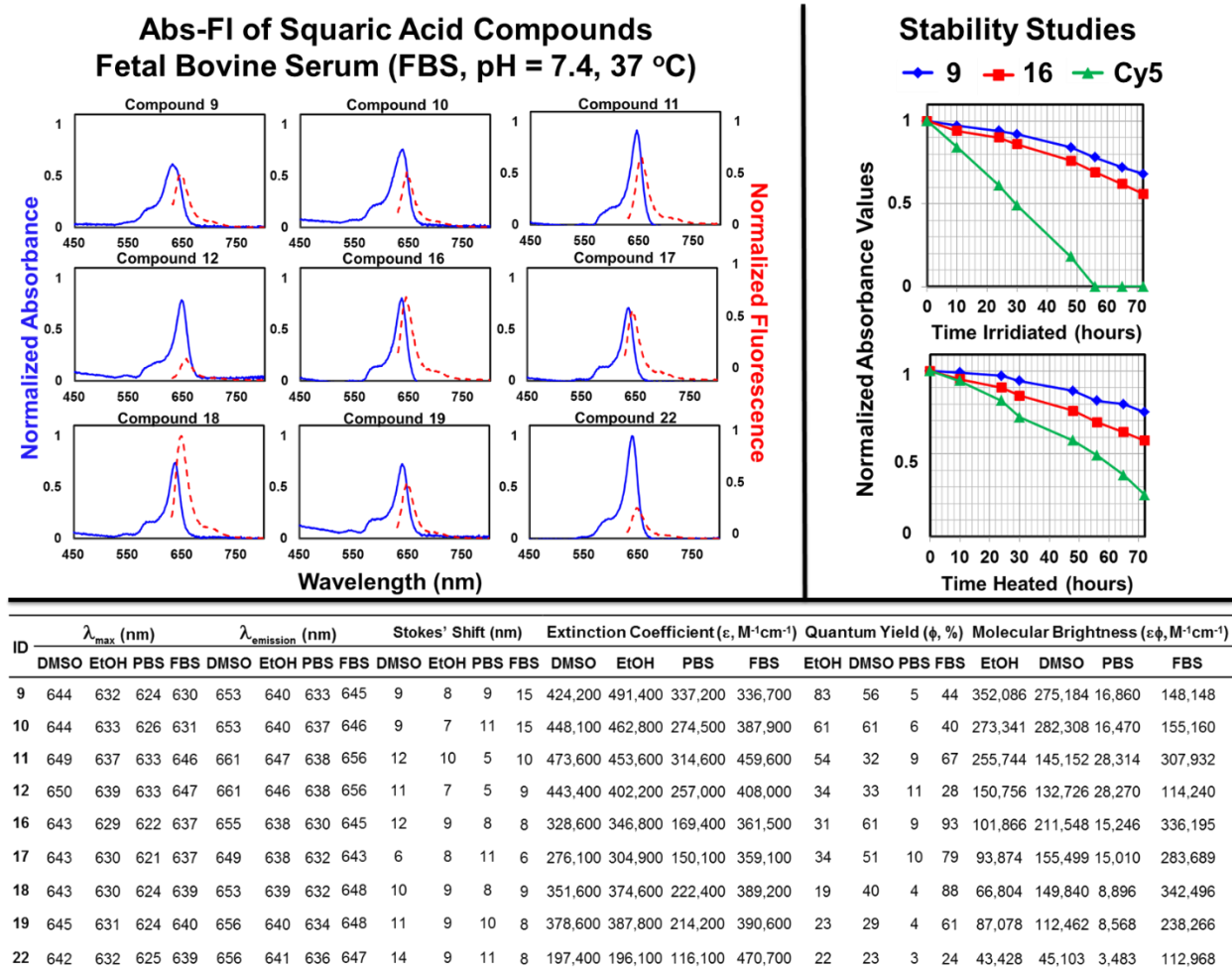


Figure 9-5. (top, left) The absorption and fluorescence spectra for each compounds in Fetal Bovine Serum supplemented with HEPES buffer at pH = 7.4 and warmed to physiological temperature (37 °C). (top, right) The absorption-based stability in light and under heat in FBS buffer for compounds 9, 16 and industry standard Cy5 (bottom) Optical properties of the synthesized fluorophores in various solvents, dimethyl sulfoxide (DMSO), ethanol (EtOH, 200 proof), phosphate buffered saline (PBS, pH = 7.4) and fetal bovine serum (FBS, pH = 7.4, 37 °C) supplemented with HEPES buffer were utilized to show biological compatibility.

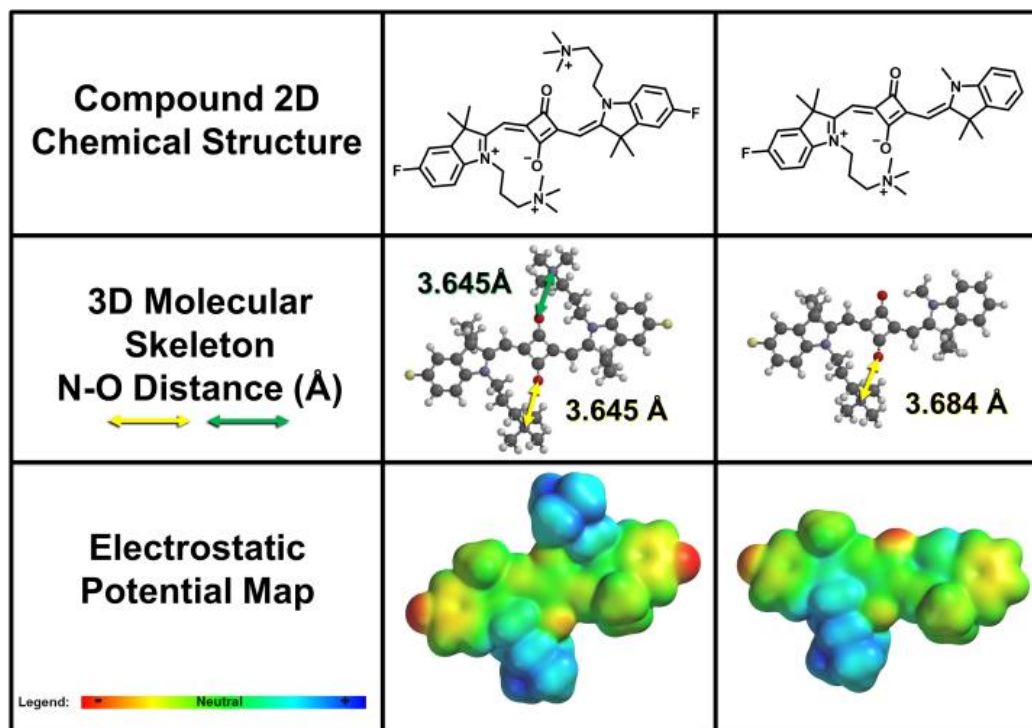


Figure 9-6. DFT calculations (Wavefunction, Spartan, '10, B3LYP 6-311++G**) confirm the presence of a salt-bridge between the quaternary ammonium cation and the delocalized negative charge across the central oxygens in both the symmetric and asymmetric compounds.

9.4 Conclusions

To conclude, we have synthesized and evaluated the ability of an intermolecular salt bridge to protect the central oxocyclobutenolate ring of squaric acid fluorophores and increase the molar absorptivity and quantum yield owing to increased rigidity associated with the locked structure. The asymmetric compounds were shown to have unparalleled optical brightness in serum and were modified to include a carboxylic acid moiety was optimum for all biological labeling experiments which require high NIR extinction coefficients and quantum yield. These findings offer a facile

solution to squaric acid stability while finally increasing the *in vivo* appeal of squaric acid fluorophores.

9.5 Experimental

General procedure for the synthesis of symmetric squaric acid fluorophores: A mixture of the corresponding indolenine salt (1.0 mol. eq.) and squaric acid (0.5 mol. eq.) and quinoline (5.0 mol. eq.) was refluxed in a mixture of n-butanol and benzene (40ml, 1:1) with azeotropic distillation using dean stark apparatus for 15 hr. Reaction mixture was monitoring by Vis/NIR spectrophotometry. The solvent was removed under reduced pressure. The residue was stirred in ethyl acetate (100 mL). The precipitated product was filtered, washed with ethyl acetate, acetone and dried under vacuum. The crude material was dissolved in methanol (10 mL), and poured into ethyl acetate (100 mL). The precipitated product was filtered and dried under vacuum. This precipitation procedure was repeated once more and the obtained pure product was dried under vacuum.

Mono((Z)-4-((3,3-dimethyl-1-(3-(trimethylammonio)propyl)-3H-indol-1-ium-2-yl)methylene)-2-((E)-(3,3-dimethyl-1-(3-(trimethylammonio)propyl)indolin-2-ylidene) methyl)-3-oxocyclobut-1-enolate) tribromide (9) Yield 70%. MP >260°C ¹H NMR (400 MHz, DMSO) δ 1.71 (s, 6H, CH₃), 2.15 (s, 2H, CH₂), 3.12 (s, 9H, CH₃), 3.57-3.61 (s, 2H, CH₂), 4.16 (s, 2H, CH₂), 5.86 (s, 1H, CH), 7.20 (t, *J* = 7.2 Hz, 1H, ArH), 7.38 (t, *J* = 8.0 Hz, 1H, ArH), 7.46 (d, *J* = 8.0 Hz, 1H, ArH), 7.55 (d, *J* = 7.2 Hz, 1H, ArH) ¹³C NMR (100 MHz, DMSO) δ 21.0, 27.1, 49.3, 53.0, 63.2, 86.8, 110.8, 122.7, 124.3, 128.4, 141.8, 142.4, 169.6, 180.4, 181.0. MS for C₃₈H₅₂N₄O₂²⁺ calculated 298.2, found 298.3.

Mono((Z)-4-((5-fluoro-3,3-dimethyl-1-(3-(trimethylammonio)propyl)-3H-indol-1-ium-2-yl)methylene)-2-((E)-(5-fluoro-3,3-dimethyl-1-(3-(trimethylammonio)propyl)indolin-2-

ylidene)methyl)-3-oxocyclobut-1-enolate) tribromide (10) Yield 64%. MP >260°C ¹H NMR (400 MHz, DMSO) δ 1.71 (s, 12H, CH₃), 2.13 (s, 4H, CH₂), 3.10 (s, 18H, CH₃), 3.55 (s, 4H, CH₂), 4.14 (s, 4H, CH₂), 5.83 (s, 2H, CH), 7.21-7.25 (s, 2H, Ar-H), 7.46 (brs, 2H, Ar-H), 7.53-7.54 (m, 2H, ArH) ¹³C NMR (100 MHz, DMSO) δ 20.7, 26.5, 40.8, 49.5, 53.3, 63.3, 86.4, 110.4, 110.6, 111.7, 111.8, 115.0, 115.2, 138.1, 143.8, 143.9, 159.0, 161.4, 170.9, 175.8, 182.7 HRMS for C₃₈H₅₀F₂N₄O₂²⁺ calculated 316.1946, found 316.1965

Mono((Z)-4-((5-chloro-3,3-dimethyl-1-(3-(trimethylammonio)propyl)-3H-indol-1-ium-2-yl)methylene)-2-((E)-(5-chloro-3,3-dimethyl-1-(3-(trimethylammonio)propyl)indolin-2-ylidene)methyl)-3-oxocyclobut-1-enolate) tribromide (11) Yield 75%. MP >260°C ¹H NMR (400 MHz, DMSO) δ 1.71 (s, 12H, CH₃), 2.13 (s, 4H, CH₂), 3.10 (s, 18H, CH₃), 3.54 (s, 4H, CH₂), 4.15 (s, 4H, CH₂), 5.86 (s, 2H, CH), 7.43-7.49 (s, 4H, Ar-H), 7.70 (s, 2H, Ar-H), ¹³C NMR (100 MHz, DMSO) δ 21.0, 26.9, 49.0, 49.5, 53.1, 63.3, 87.3, 112.2, 123.1, 128.3, 128.8, 141.4, 143.9, 169.6, 180.9, 181.2.

Mono((Z)-4-((5-bromo-3,3-dimethyl-1-(3-(trimethylammonio)propyl)-3H-indol-1-ium-2-yl)methylene)-2-((E)-(5-bromo-3,3-dimethyl-1-(3-(trimethylammonio)propyl)indolin-2-ylidene)methyl)-3-oxocyclobut-1-enolate) tribromide (12) Yield 62%. MP >260°C ¹H NMR (400 MHz, DMSO) δ 1.70 (s, 12H, CH₃), 2.12 (s, 4H, CH₂), 3.09 (s, 18H, CH₃), 3.54 (s, 4H, CH₂), 4.14 (s, 4H, CH₂), 5.85 (s, 2H, CH), 7.43-7.55 (s, 4H, Ar-H), 7.80 (s, 2H, Ar-H), ¹³C NMR (100 MHz, DMSO) δ 20.9, 26.9, 49.5, 53.0, 63.1, 87.3, 112.8, 116.5, 125.9, 131.2, 141.8, 144.2, 159.4, 162.3, 169.3, 180.9 HRMS for C₃₈H₅₀Br₂N₄O₂²⁺ calculated 377.1135, found 378.1139.

(Z)-2-hydroxy-3-oxo-4-((1,3,3-trimethyl-3H-indol-1-ium-2-yl)methylene)cyclobut-1-enolate iodide (15) Methylindolium salt (4.0 mol), 3,4-diisopropoxycyclobutane-1,2-dione (4.0mol) and triethylamine (1.0 ml) was heated in EtOH for 3 hr. After the reaction was completed,

the reaction was cooled and removes the solvent under reduced pressure. The crude product was purified by silicagel column chromatography (CH₂Cl₂/MeOH). Yield 65%; purified Compound (1.0 mol) was dissolved in ethanol (10 ml) and NaOH (40%, 0.5 ml) was added. The mixture was heated at 70°C for 30 min. After the reaction was completed, the mixture was cooled and 2N HCl (5 ml) was added. The product was purified by silicagel column chromatography (MeOH/DCM 1:9).

General procedure for the synthesis of asymmetric squaric acid fluorophores: A mixture of the corresponding indolenine salt (1.0 mol. eq.) and mono squaric acid modified compound **15** or **21** (1 mol. eq.) and quinoline (5.0 mol. eq.) was refluxed in a mixture of n-butanol and benzene (40 ml, 1:1) with azeotropic distillation using dean stark apparatus for 12 hr. Reaction mixture was monitoring by Vis/NIR spectrophotometry. The solvent was removed under reduced pressure. The residue was stirred in ethyl acetate (100 mL). The precipitated product was filtered, washed with ethyl acetate, acetone and dried under vacuum. The crude material was dissolved in methanol (10 mL), and poured into ethyl acetate (100 mL). The precipitated product was filtered and dried under vacuum. This precipitation procedure was repeated once more and the obtained pure product was dried under vacuum.

Mono((Z)-2-((E)-(3,3-dimethyl-1-(3-(trimethylammonio)propyl)indolin-2-ylidene) methyl)-3-oxo-4-((1,3,3-trimethyl-3H-indol-1-ium-2-yl)methylene)cyclobut-1-enolate mono bromide mono iodide (16) Yield 37%. MP >198-200°C ¹H NMR (400 MHz, MeOD) δ 1.76-1.77 (m, 12H, CH₃), 2.34 (brs, 2H, CH₂), 3.22 (s, 9H, CH₃), 3.63-3.67 (m, 5H, CH₃&CH₂), 4.23 (brs, 2H, CH₂), 5.89 (s, 1H, CH), 5.99 (s, 1H, CH), 7.21-7.26 (m, 2H, Ar-H), 7.32-7.43 (m, 4H, Ar-H), 7.46-7.50 (m, 2H, Ar-H), ¹³C NMR (100 MHz, MeOD) δ 20.6, 25.6, 26.1, 30.3, 40.0, 49.0, 49.4,

52.5, 52.8, 62.3, 63.3, 109.8, 110.3, 121.9, 122.0, 123.9, 124.6, 128.0, 129.2, 130.0, 135.2, 141.3, 141.8, 142.6, 144.6, 147.5, 182.7. HRMS for $C_{33}H_{40}N_3O_2^+$ calculated 510.3115, found 510.8995

Mono((Z)-2-((E)-(5-fluoro-3,3-dimethyl-1-(3-(trimethylammonio)propyl)indolin-2-ylidene)methyl)-3-oxo-4-((1,3,3-trimethyl-3H-indol-1-ium-2-yl)methylene)cyclobut-1-enolate) mono bromide monoiodide (17) Yield 43%. 1H NMR (400 MHz, MeOD) δ 1.76 (s, 12H, CH_3), 2.32 (s, 2H, CH_2), 3.22 (s, 9H, CH_3), 3.62-3.70 (m, 5H, CH_3 & CH_2), 4.20 (s, 2H, CH_2), 5.85 (s, 1H, CH), 5.99 (s, 1H, CH), 7.13 (t, $J = 8.0$ Hz, 1H, ArH), 7.25-7.29 (m, 2H, Ar-H), 7.32-7.36 (m, 2H, Ar-H), 7.40-7.43 (m, 1H, Ar-H), 7.50 (t, $J = 7.6$ Hz, 1H, ArH), ^{13}C NMR (100 MHz, MeOD) δ 20.5, 25.5, 26.1, 30.3, 40.1, 52.5, 63.5, 85.3, 86.2, 109.8, 110.1, 110.2, 110.3, 114.0, 114.3, 121.8, 124.7, 127.9, 138.2, 141.9, 142.7, 169.0, 173.4, 173.9, 177.8, 183.0 HRMS for $C_{33}H_{39}FN_3O_2^+$ calculated 528.3021, found 528.2086

Mono((Z)-2-((E)-(5-chloro-3,3-dimethyl-1-(3-(trimethylammonio)propyl)indolin-2-ylidene)methyl)-3-oxo-4-((1,3,3-trimethyl-3H-indol-1-ium-2-yl)methylene)cyclobut-1-enolate) mono bromide monoiodide (18) Yield 31%. 1H NMR (400 MHz, MeOD) δ 1.75 (s, 12H, CH_3), 2.30-2.31 (m, 2H, CH_2), 3.23 (s, 9H, CH_3), 3.63-3.65 (m, 2H, CH_2), 3.71 (s, 3H, CH_3), 4.17-4.21 (m, 2H, CH_2), 5.84 (s, 1H, CH), 6.01 (s, 1H, CH), 7.26-7.36 (m, 4H, ArH), 7.40-7.42 (m, 1H, Ar-H), 7.44-7.46 (m, 1H, Ar-H), 7.49-7.51 (m, 1H, Ar-H), ^{13}C NMR (100 MHz, MeOD) δ 20.4, 25.5, 26.2, 30.4, 40.0, 49.7, 52.5, 63.5, 85.5, 86.6, 110.5, 121.9, 122.5, 124.9, 127.8, 128.0, 128.8, 141.0, 142.0, 142.6, 143.1, 168.0, 173.9, 183.0 HRMS for $C_{33}H_{39}ClN_3O_2^+$ calculated 544.2725, found 545.1194

Mono((Z)-2-((E)-(5-bromo-3,3-dimethyl-1-(3-(trimethylammonio)propyl)indolin-2-ylidene)methyl)-3-oxo-4-((1,3,3-trimethyl-3H-indol-1-ium-2-yl)methylene)cyclobut-1-enolate) mono bromide monoiodide (19) Yield 36%. M.P. 204-206 °C 1H NMR (400 MHz, MeOD) δ 1.75-

1.76 (m, 12H, CH₃), 2.31 (s, 2H, CH₂), 3.23 (s, 9H, CH₃), 3.71-3.72 (m, 5H, CH₃&CH₂), 4.17 (s, 2H, CH₂), 5.84 (s, 1H, CH), 6.01 (s, 1H, CH), 7.28-7.32 (m, 2H, Ar-H), 7.35-7.37 (m, 1H, Ar-H), 7.40-7.43 (m, 1H, Ar-H), 7.49-7.51 (m, 2H, Ar-H), 7.58-7.61 (m, 1H, Ar-H), ¹³C NMR (100 MHz, MeOD) δ 20.4, 25.5, 26.1, 30.4, 39.9, 49.6, 52.5, 63.3, 85.5, 86.6, 110.6, 111.1, 116.0, 121.9, 124.9, 125.4, 128.0, 130.8, 141.4, 142.0, 142.5, 173.6, 178.2, 182.9 HRMS for C₃₃H₃₉BrN₃O₂⁺ calculated 588.2220, found 589.6223

9.6 References

1. Plange, N.; Remky, A.; Arend, K. O. Potential diagnostic value of fluorescein angiography and color Doppler imaging in primary open-angle glaucoma. *Eur J Ophthalmol* **2010**, *20*, 1091-2; author reply 1092.
2. Fluorescein-conjugated human serum albumin. In *Molecular Imaging and Contrast Agent Database (MICAD)*, Bethesda (MD), 2004.
3. Chen, J.; Mizumura, M.; Shinokubo, H.; Osuka, A. Functionalization of boron dipyrin (BODIPY) dyes through iridium and rhodium catalysis: a complementary approach to alpha- and beta-substituted BODIPYs. *Chemistry* **2009**, *15*, 5942-9.
4. Cakmak, Y.; Akkaya, E. U. Phenylethynyl-BODIPY oligomers: bright dyes and fluorescent building blocks. *Org Lett* **2009**, *11*, 85-8.
5. Wu, L.; Burgess, K. A new synthesis of symmetric boraindacene (BODIPY) dyes. *Chem Commun (Camb)* **2008**, 4933-5.
6. Krystkowiak, E.; Dobek, K.; Maciejewski, A. An intermolecular hydrogen-bonding effect on spectral and photophysical properties of 6-aminocoumarin in protic solvents. *Photochem Photobiol Sci* **2013**, *12*, 446-55.

7. Diallo, S.; Bastard, P.; Prognon, P.; Dauphin, C.; Hamon, M. A new spectrofluorimetric microdetermination of nitrite in water after derivatization with 4-methyl-7-aminocoumarin. *Talanta* **1996**, *43*, 359-64.
8. Wu, N.; Lan, J.; Yan, L.; You, J. A sensitive colorimetric and fluorescent sensor based on imidazolium-functionalized squaraines for the detection of GTP and alkaline phosphatase in aqueous solution. *Chem Commun (Camb)* **2014**, *50*, 4438-41.
9. Delcamp, J. H.; Shi, Y.; Yum, J. H.; Sajoto, T.; Dell'Orto, E.; Barlow, S.; Nazeeruddin, M. K.; Marder, S. R.; Gratzel, M. The role of pi bridges in high-efficiency DSCs based on unsymmetrical squaraines. *Chemistry* **2013**, *19*, 1819-27.
10. Mayerhoffer, U.; Fimmel, B.; Wurthner, F. Bright near-infrared fluorophores based on squaraines by unexpected halogen effects. *Angew Chem Int Ed Engl* **2012**, *51*, 164-7.
11. Inoue, T.; Pandey, S. S.; Fujikawa, N.; Yamaguchi, Y.; Hayase, S. Synthesis and characterization of squaric acid based NIR dyes for their application towards dye-sensitized solar cells. *Journal of Photochemistry and Photobiology a-Chemistry* **2010**, *213*, 23-29.
12. Völker, S. F.; Uemura, S.; Limpinsel, M.; Mingeback, M.; Deibel, C.; Dyakonov, V.; Lambert, C. Polymeric Squaraine Dyes as Electron Donors in Bulk Heterojunction Solar Cells. *Macromolecular Chemistry and Physics* **2010**, *211*, 1098-1108.
13. Collins, C. G.; Peck, E. M.; Kramer, P. J.; Smith, B. D. Squaraine rotaxane shuttle as a ratiometric deep-red optical chloride sensor. *Chemical Science* **2013**, *4*, 2557-2563.
14. Völker, S. F.; Dellermann, T.; Ceymann, H.; Holzapfel, M.; Lambert, C. Synthesis, electrochemical, and optical properties of low band gap homo- and copolymers based on squaraine dyes. *Journal of Polymer Science Part A: Polymer Chemistry* **2014**, *52*, 890-911.

15. Ullman, E. F.; Kirakossian, H.; Singh, S.; Wu, Z. P.; Irvin, B. R.; Pease, J. S.; Switchenko, A. C.; Irvine, J. D.; Dafforn, A.; Skold, C. N. Luminescent oxygen channeling immunoassay: measurement of particle binding kinetics by chemiluminescence. *Proceedings of the National Academy of Sciences* **1994**, 91, 5426-5430.
16. Grabolle, M.; Brehm, R.; Pauli, J.; Dees, F. M.; Hilger, I.; Resch-Genger, U. Determination of the labeling density of fluorophore-biomolecule conjugates with absorption spectroscopy. *Bioconjug Chem* **2012**, 23, 287-92.
17. Morales, A. R.; Yanez, C. O.; Schafer-Hales, K. J.; Marcus, A. I.; Belfield, K. D. Biomolecule labeling and imaging with a new fluorenyl two-photon fluorescent probe. *Bioconjug Chem* **2009**, 20, 1992-2000.
18. Kostenko, O. M.; Kovalska, V. B.; Volkova, K. D.; Shaytanov, P.; Kocheshev, I. O.; Slominskiy, Y. L.; Pisareva, I. V.; Yarmoluk, S. M. New method for covalent fluorescent biomolecule labeling with hemicyanine dye. *J Fluoresc* **2006**, 16, 589-93.

10 QUADRUPLEX-DNA: HISTORY, FUNCTION AND THERAPEUTIC POTENTIAL

This chapter is an excerpt from a review article that I initiated for the gathering of ligands associated with binding the quadruplex with a high affinity and specificity. My role has been universal since inception.

Owens, E. A., Henary, M. G-Quadruplex DNA: History, Function and Potent Target for New Chemotherapeutics **2015** *In Preparation*.

10.1 Abstract

Nucleic acids have always been an attractive target for developing novel drugs targeting the information machinery to arrest translation into biologically active proteins; however, specificity and efficacy have limited the success of this field. Recently, however, the discovery of G-quadruplex and development of small molecules that stabilize this structure has opened a novel avenue to target cancer cells as they are often located in oncogene promoter regions. The classes of compounds used to target this structure are diverse, but after a screening of the literature, elongated planar compounds with a high degree of cationic character were the most effective at binding the tetraplex structure. Also, with a diverse array of folding patterns, there are many different binding modes that these compounds can assume depending on the particular ligand. We present an analysis and a critical review of the synthetic development of compounds identified to be quadruplex binding agents, the degree and mode of quadruplex binding, the specificity to quadruplex DNA over other duplex-forming sequences and the biological efficacy concerning the medicinal chemistry properties of the evaluated compounds.

Keywords: G-quadruplex, chemotherapeutics, DNA-targeted therapies.

10.2 Preface

The medical community has long drawn on the foundations of scientific physical, chemical and biological research to provide powerful targets and therapeutics to fight against malignancies in human disease. As the incidence rate of cancer is ever increasing, we continue to search for new routes with a high aptitude for killing tumors while sparing the formation and proliferation of native tissues toward increasing the quality of our patients' lives. Decades have past searching for a miracle cure ubiquitous for all cancers, but this Holy Grail of modern medicine continues to elude researchers despite most valiant scientific efforts paired with an unthinkable amount of funding. The National Cancer Institute (NCI) issues approximately \$5 billion per annum in the fight against cancer with many insitutions focused on inhibiting proteins in distitnct cellular pathways, but ... could it be that targeting the proteins and molecular machinery that propel cancer cells isn't the most attractive therapeutic target? Maybe the answer lies within the realm of nucleic acids—killing cancer through the manipulation of the genetic code. One recently recognized therapeutic target is the G-quadruplex folding region seen spontaneously forming in DNAs and RNAs with dependence on salt concentration. Due to the emerging importance of the G-quadruplex, researchers have synthesized and tested compounds with many performing with higher efficacy. The main concern centers around compound specificity to quadruplex-forming regions rather than binding linear and alternate folding patterns of DNA. This review focuses on the discovery, hypothesized *in vivo* functions, anti-cancer drug targeting, clinical translation and the future directions of the G-quadruplex as a potent target for new chemotherapeutics.

10.3 Nucleic Acids as a Functional Therapeutic Target

Ever since Watson, Crick, Wilkins and Franklin helped de-mystify the information storage vehicle known as DNA, we as a scientific community have considered it, since the 1953 publication, an overwhelmingly appealing target for designing therapeutics.¹ The thought of controlling disease on a genetic level remains a paramount research field; however, multiple experimental failures from lack of sequence specificity and *in vivo* shortcomings have led interest away from the utilization of DNA as an efficacious therapeutic target^{2,3}; however, in recent years, the resurgence of nucleic acid drug targets has been prompted by the overwhelming support that alternate folding patterns of DNA occur spontaneously *in vivo*.⁴⁻⁹ These findings allow an alternate avenue for the utilization of DNA as a potent drug target.

10.4 The Double Edge Sword of Nucleic Acid Drug Targets

DNAs fold in very peculiar ways and they have all been postulated and probed for various therapeutic efficacy.^{4,10} These folding patterns are notoriously difficult for being unrelentingly selective and only rarely allow ligands to bind while maintaining discrimination against all other DNAs. Knocking down genetic anomalies has numerous benefits but also numerous negative aspects that must be overcome in the pursuit of potent nucleic acid-targeted therapeutics. To fully understand and begin analyzing the various aspects of this field, we must consider the alternate folding patterns of DNA and how to choose binding characteristics and selectively modify a potential binding agent for targeting a specific type of DNA.

10.5 Duplex DNA

Duplex DNA as a therapeutic drug target relies on the recognition of exact sequences through either electrostatic interactions, width of the minor/major groove or the twisting

conformation arising from the particular sequence. The binding modes of B-form DNA targeting agents rely on three basic principles: minor groove binding, major groove binding and intercalation – these binding principles are exemplified in Figure 10-1. Minor groove binding molecules exhibit a curved structure with H-bonding capable sites directed toward the nucleotides with terminal cations helping with interactions with the phosphate backbone. The exact 3-dimensional structure of the small molecule must be well suited with planarity and a curved geometry that matches the curve of the minor groove of DNA. This approach is in stark contrast to major groove binding agents that tend to dimerize as most small molecules do not have the necessary size to fully fill the spatial opening posed by the major groove. Similar to minor groove binding, intercalating agents must be highly planar and bind with an extremely high affinity; thermodynamically speaking, the intercalated compound must be more energetically favorable than the formation of B-form DNA itself.

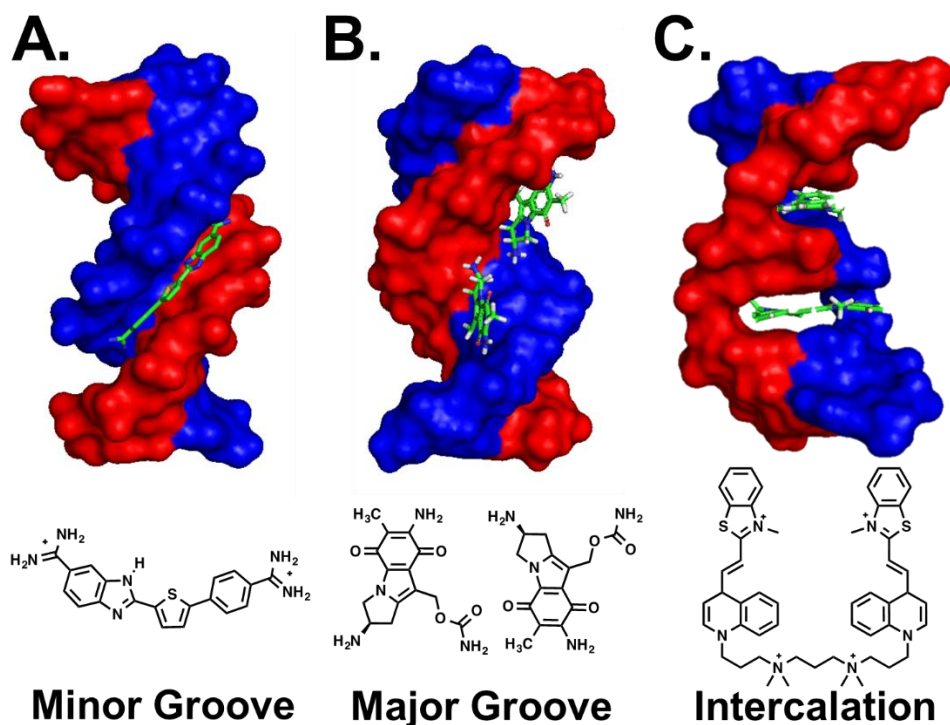


Figure 10-1 Duplex DNA and binding ligands. Diamidine structures effectively target the minor groove while the major groove is effectively bound through dimerization and the tetra-cationic cyanine dye can effectively intercalate between the base pairs of *dsDNA*.

10.6 i-Motif DNA

The intercalated motif (i-motif) is a helical hemi-protonated structure marked by cytosine-rich segments that were first reported in 1993 by Gehring *et al.* Fortunately, this DNA morphology has been extensively employed in nanotechnology, especially employing the sensitivity to pH for intracellular monitoring of pH changes. Despite advances in exploiting this folding pattern, there are limited explanations that explain *in vivo* functions or biological significance of the i-motif, nonetheless, binding ligands have been explored to probe exact biological functions though at this point, little is known about the potential to employ this route as a target for designing biologically relevant therapeutics.

10.7 Triplex DNA

Triple-stranded DNA characterized by three oligonucleotides with one strand binding uniquely antiparallel to a common *dsDNA* structure. Since the discovery of DNA, it had been postulated that triplex DNA could form but several predictions discounted this theory in early years. Throughout the years, it has been increasingly recognized to exist in nature; however, there is no concrete evidence that triplex DNA exists selectively in either diseased or native tissues which limits the therapeutic relevance of this toward the treatment of disease. Several exciting studies do show potential of triplex DNA as a therapeutic but not a therapeutic target which is a highly similar situation with holliday junction DNA.

10.8 Quadruplex DNA

The scientific community has recently tapped the emerging area of G-quadruplex targeted therapeutics.¹¹⁻¹⁷ The quadruplex is defined as a three dimensional folding pattern marked by four guanine nucleotides interacting through hydrogen bonds on both the Watson and Crick face and Hoogsteen face.¹⁸ These four guanine nucleotides form a planar surface that then stack on top of each other around a central stabilizing cation (either sodium or potassium) as shown in cartoon view in Figure 10-2 and 3D view (with cation removed for clarity) in Figure 10-3.

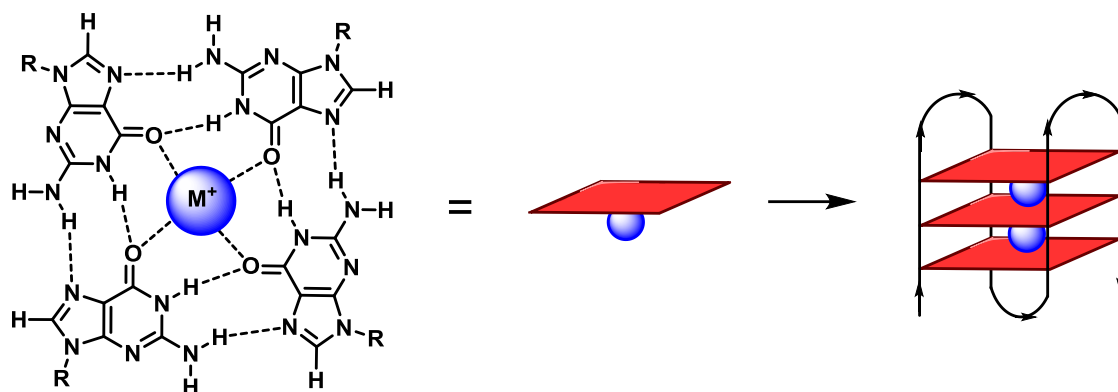


Figure 10-2. Cartoon quadruplex structure. The molecular structure of the quadruplex stabilized through hydrogen bonding interactions represented by a red-square with coordinated metal ion represented as a blue sphere. These planar tetrads will spontaneously stack *in vivo* much like the cartoon image on the right.

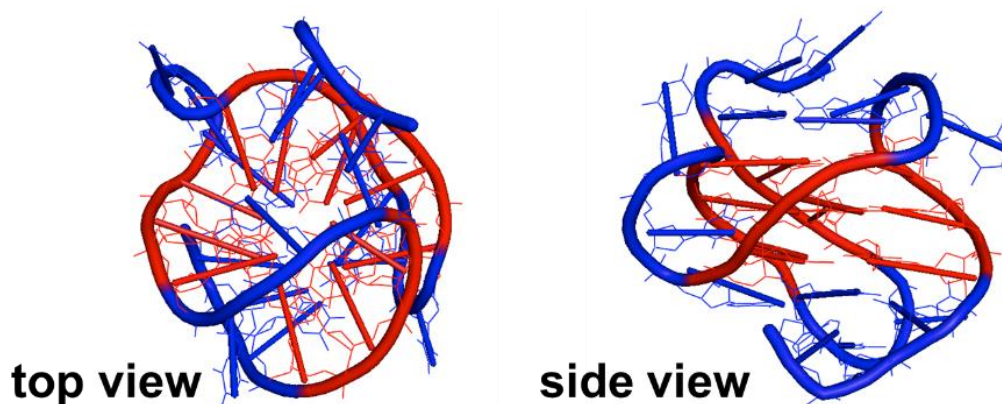


Figure 10-3. 3D structure of the quadruplex. The top view and side view with the central quadruplex highlighted in red. The blue represents the loops of the quadruplex.

This folded G-rich structure has been found greatly interesting and has propelled in recent years to one of the most heavily researched areas of nucleic acid-targeted therapeutics for many reasons which will be more thoroughly explained in the subsequent sections.

10.9 Introduction to the G-Quadruplex Structure and Function

The quadruplex has very diverse structural arrangements that are directly related to the sequence of the linear nucleic acid sequence; the tetraplex can arrange in either parallel or antiparallel configuration or either interstranded or intrastranded. Bioinformatics has helped deduce which linear sequences display high propensity for the formation of quadruplex structure. The exact biological function of the quadruplex remains highly mysterious and ever elusive. As we start to piece together the complex puzzle, we unravel more questions.

10.9.1 Rationale for the Quadruplex as a Potent Anti-Cancer Target

Chemotherapeutic design hinges on the ability to reduce off-target interactions that results in debilitating side-effects in the clinic. Fortunately, the quadruplex represents a potential target that offers the required specificity should we be able to capitalize on this strategic route through structural manipulation based on well-established medicinal chemistry.

10.9.2 Early Interest—Wrapped Up in Telomeric DNA

Initial interest in quadruplex DNA was heavily interested in the human telomere which protects chromosomal degradation that could occur through nuclear replication. The biochemical replication pathway results in non-coding nucleic acid segments being cleaved *in lieu* of the biologically necessary segments, these overhanging structures are called telomeres. Telomeres in mammalian cells are usually marked by repeating guanine-rich segments (5'-TTAGGG-3') units that can extend 5-15 kb. As these well-placed non-coding segments are systematically removed, the chromosomal degradation barrier becomes critically short and the cell undergoes apoptotic senescence to protect the cells vital information. A reverse transcriptase ribonucleoprotein complex, telomerase, helps to restore the telomere by binding to the linear G-rich telomeric sequence and catalyzing the elongation of the telomere by tandem TTAGGG repeats (Figure 10-

4). Unfortunately, this enzyme is over expressed in approximately 85% of cancer cells which bestows upon them limitless replication processes and the ability to evade normal apoptotic protocol; consequently, discovering a route toward inhibiting this enzyme was hypothesized to be a potent anti-cancer target. The most effective strategy came-to-light when the G-rich telomeric strand was discovered to spontaneously form folded a quadruplex structure *in vivo*. In line with this discovery, many laboratories began synthesizing binding agents to the telomeric quadruplex that could effectively stabilize the tertiary structure and prevent the enzyme from recognizing the linear binding domain.

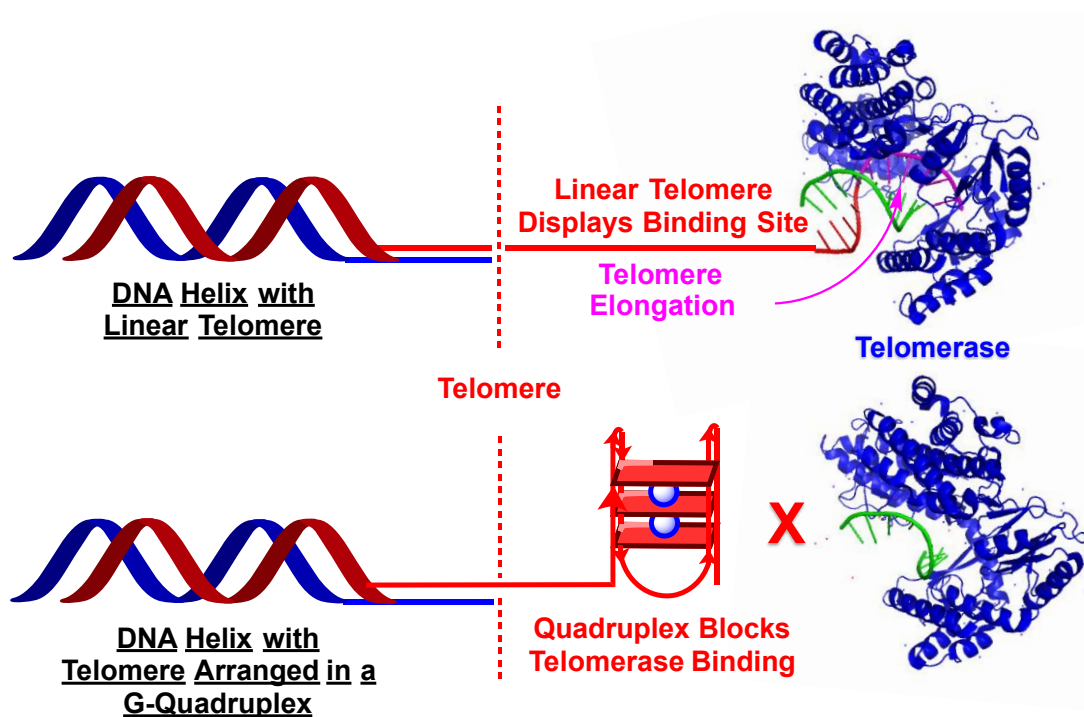


Figure 10-4. Telomerase binding to and elongating the terminal TTAGGG segment of the telomere and the G-quadruplex DNA blocking telomerase binding.

10.9.3 Second Generation Quadruplex Interest—Oncogene Promoter Regions

First generation telomere-quadruplex binding enticed the drug design community but shortly thereafter biological geneticists uncovered that many sequences of DNA throughout the genome have high propensity to form quadruplex structures. The quadruplex has been observed to form in the genetic code associated with several cancer-related proteins that are highlighted within the "hallmarks of cancer." Figure 10-5 shown the formation of quadruplex structure in promoter region and when the quadruplex is present, the transcriptional gene expression in effective silenced leading to reduced synthesis of the respective protein. Should a binding ligand interact with a quadruplex that forms in a oncogene promoter region, a strong and medicinally tolerable binding ligand would directly correlate to chemotherapeutic proterties by reducing the cellular machinery needed for the proliferation of cancer cells.

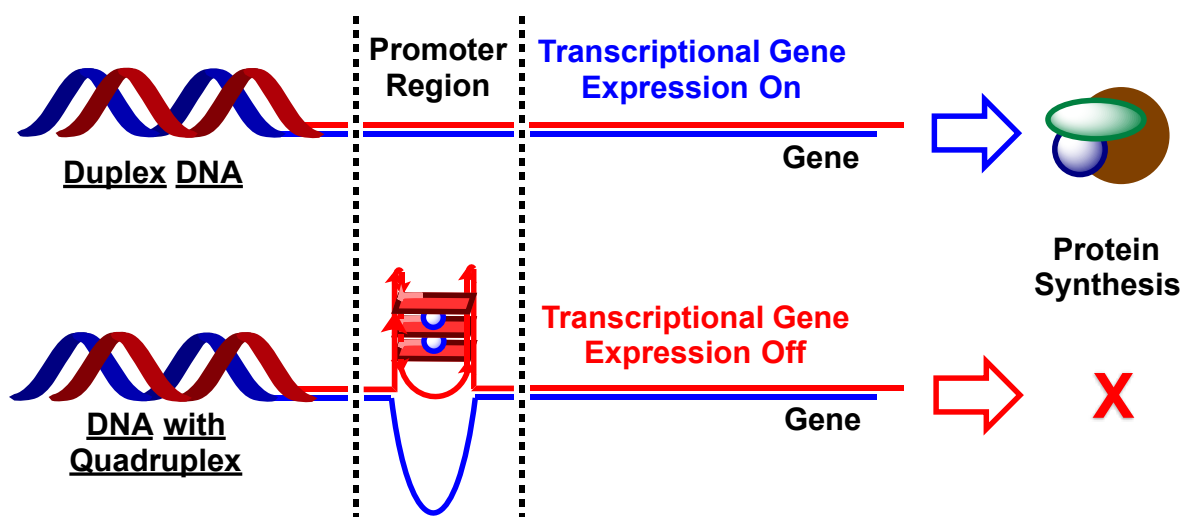


Figure 10-5. The promoter region leads the expression of particular proteins, however, the quadruplex orientation prevents effective translation and can be an effective route toward the silencing of oncopromoting genes.

10.9.4 How to Bind the Quadruplex with Specificity?

The quadruplex has three common binding modes that can be exploited in targeting this structure; however, this realization is problematic in that duplex DNA, which controls the information machinery for all of our natural and much needed proteins, has similar structural constraints for binding. Fortunately, we have found several avenues that may be exploited to generate high affinity quadruplex binding compounds with minimal duplex interactions. Incorporating several design parameters into the molecular structure alleviates the *dsDNA* binding in favor of strong quadruplex interactions. Since we have covered *dsDNA* binding in Figure 1, we now need to look at the quadruplex-binding ligand interactions that show us through nuclear magnetic resonance and x-ray crystallography the mode of interaction shown in Figure 6. The three main interactions that we have observed are intercalation, loop binding and end-stacking. Intercalating compounds for the quadruplex display very similar characteristics when comparing them to *dsDNA* intercalators—entirely planar and monocationic. The second mode of binding is through loop interactions. We see the BRACO-derivative synthesized by the Neidle lab seemingly hugging the blue-colored loop of the quadruplex. Since *dsDNA* does not contain loops within the helical structure, this avenue could possibly be a route for obtaining selectivity. Lastly, we have observed telomestatin among other macrocyclic and non-cyclic ligands that bind quite favorably through aromatic π - π stacking with the top tetrad. In this case, a telomestatin-based analog sits quite well on the top tetrad with two cationic primary amine functionalities interacting quite strongly with the phosphate backbone of the quadruplex. The size of the telomestatin-analog and cyclic nature greatly limit *dsDNA* interactions which is another design strategy for exploiting molecular structure for obtaining medically relevant selectivity to the quadruplex over *dsDNA*.

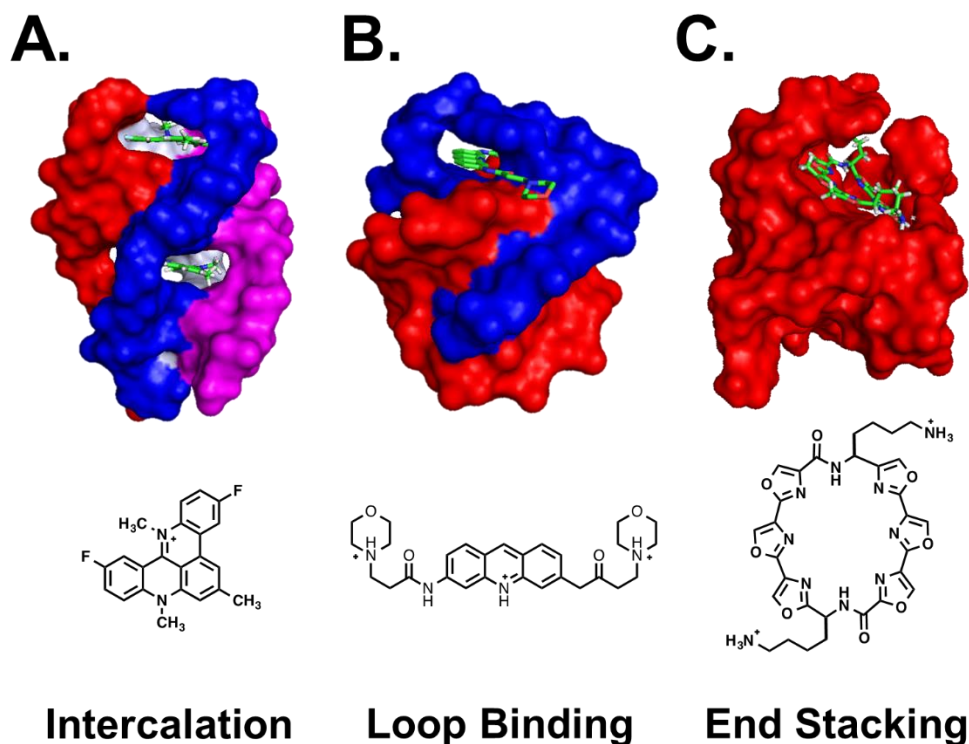


Figure 10-6. G-Quadruplex Binding Modes. Monocationic difluorinated compound effectively intercalates while the BRACO-analog interacts through loop binding and the macrocyclic telomestatin analog's nature and size stacks effectively on the top of the tetraplex.

10.9.5 Binding Agents and Efficacy

Since we have observed some of the binding ligands in the previous sections to demonstrate the different binding modes to the plethora of folding patterns of DNA, we will now delve into the different routes taken to optimize the biophysical interactions and the medicinal properties for clinically utilized therapeutics. One class of compounds has been heavily researched and are based off the the tricyclic anthracene core.

10.9.5.1 Acridine

Acridine compounds are marked by having a tricyclic nitrogen containing core that is highly modifiable and the Neidle lab, among others, has pioneered the functionalization and thorough evaluation of the acridine core for targeting the quadruplex and inducing a medically relevant biological response. The compounds they have developed are highlighted in brief in the synthetic scheme.¹⁹

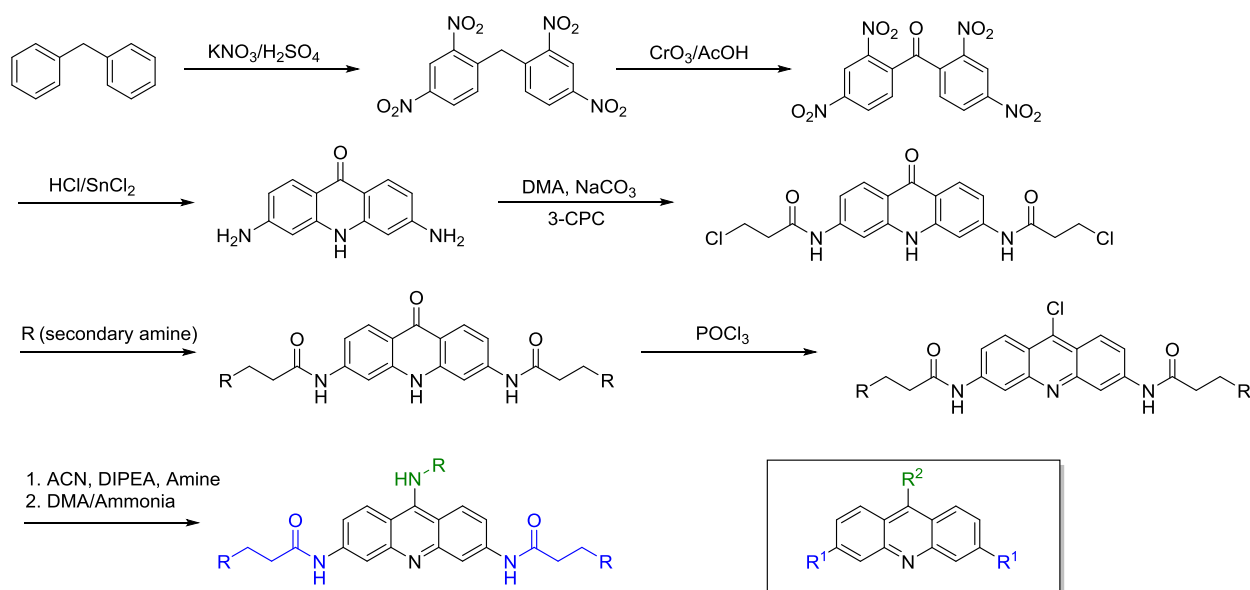


Figure 10-7. A synthetic pathway toward trisubstituted acridine agents for the stabilization of G-quadruplex DNA and generic structure bearing three positions for substitution on the acridine core.

A vast number of structural studies, NMR and crystallography, allowed them to fine tune the chemical structure to include a central 4-dimethylaminophenyl substituent at the R^2 position of the general structure.²⁰⁻³² These structural manipulations afforded the compound-DNA complex shown in Figure 10-8 that depicts strong end-stacking, loop binding and the well placed dimethylamine moiety finding an open pocket formed by the loop of the quadruplex top. These

interactions together form a highly potent quadruplex interacting ligand that has and continue to serve as a design scaffold for further design considerations.

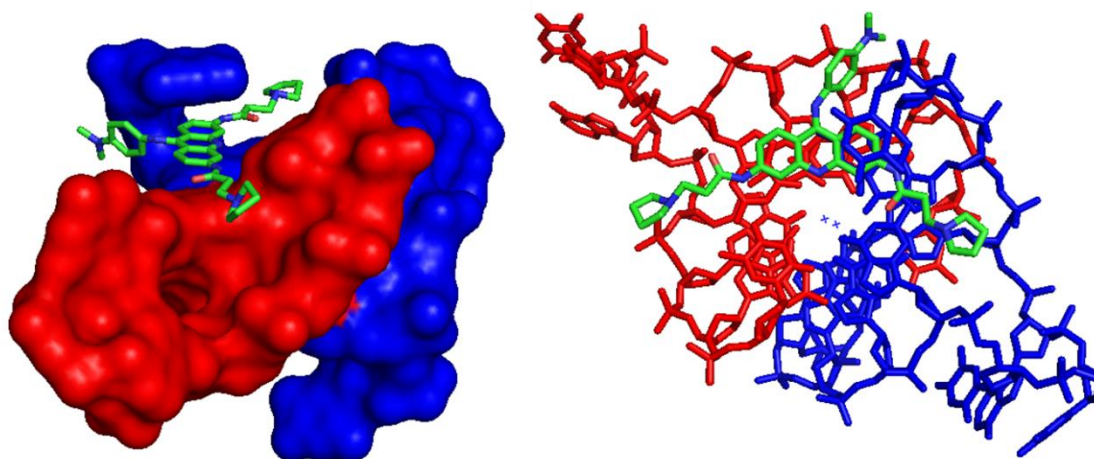


Figure 10-8. Acridine based compound BRACO-19 complexed to G-quadruplex.

10.9.5.2 Naphthalene Diimide Compounds

Naphthalene is defined as two fused benzene rings that share two aromatic carbon atoms as a part of the 10-carbon structure. These characteristics afford a high planar ring system that serves as a promising starting scaffold for development in quadruplex binding compounds. The 1,4,5,8-naphthalenetetracarboxylic dianhydride structure seen in Figure 9 serves as the starting material for diverse modifications. Bromination and amine modifications afford the general structure with various R groups. Figure 10 depicts a successful binding ligand that targets the quadruplex. The naphthalene diimide structure features morpholine groups on the imide nitrogen atoms and methylpiperazine substituents on the naphthalene rings. All of these substitutions maintain a mostly planar core thus embodying the design features that are requisite for quadruplex targeting compounds.

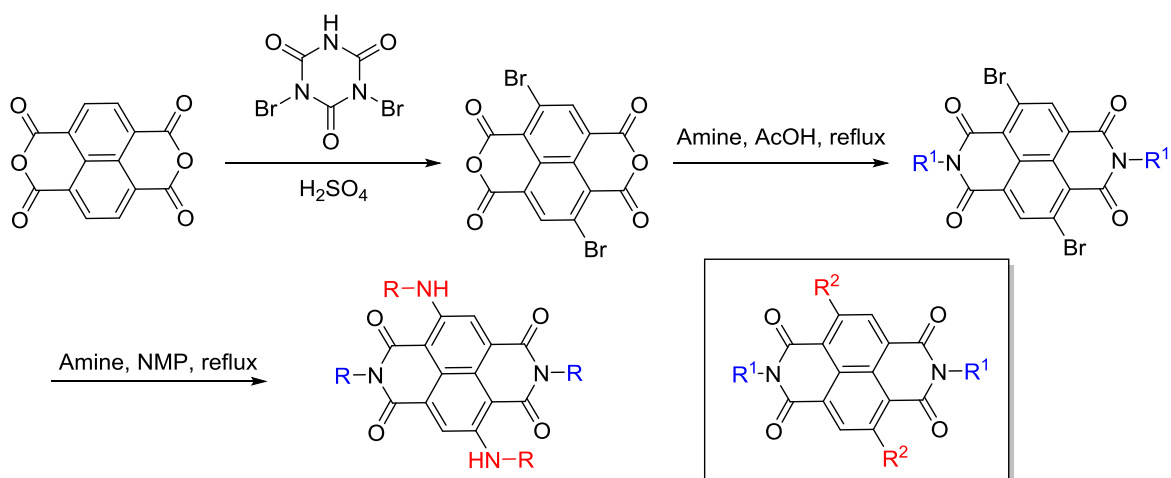


Figure 10-9. Synthetic scheme to the final naphthalene diimide compounds for quadruplex binding.

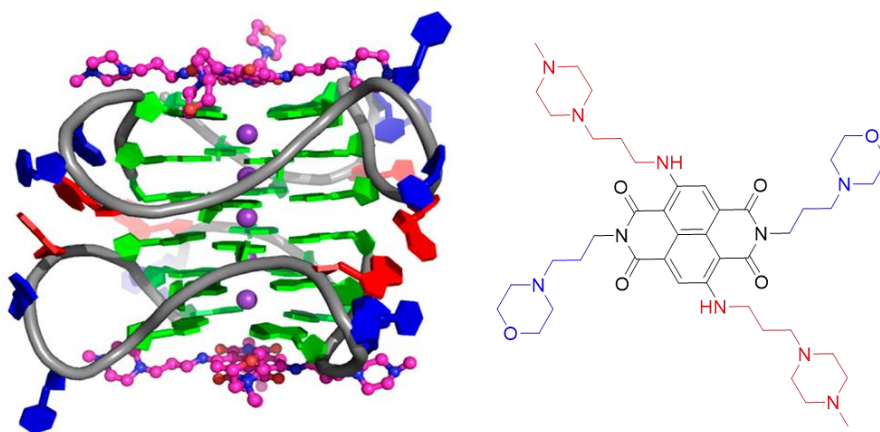


Figure 10-10. Naphthalene diimide ligand and crystal structure rendering with quadruplex dimer (PDB 3UYH).

The naphthalene core features the highly planar pi-pi stacking abilities that are necessary for potent quadruplex interacting ligands. Additionally, the tertiary amines serve as excellent phosphate interacting ligands at physiological pH. The diimides within the core structure are properly located to position the morpholine and piperazine moieties at effective positions to bind well to the

quadruplex. Melting temperatures for this model compound are higher than most other naphthalene diimide compounds studied with nanomolar IC_{50} inhibition of cancer cell lines.

10.9.5.3 Carbazole-centered Compounds

Carbazole, the planar tricyclic heterocyclic compound has the potential for diverse modification, especially *para* to the nitrogen atom.

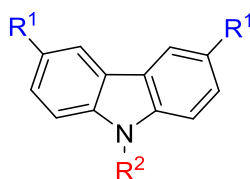


Figure 10-11. Core carbazole structure with positions of variation that have led to increased binding efficacy to quadruplex DNA.

A few groups have exploited the planarity and amenability of this heterocycle for tailoring quadruplex interacting ligands. Specifically among them, a dicationic carbazole compound termed 3,6-bis(1-methyl-4-vinylpyridium)carbazole diiodide (**BMVC**) was the first to be reported and showed excellent fluorescence enhancement upon titration with G4-forming DNA sequences (Hum24).³⁹ The facile synthesis of this compound exploits the robust palladium(II)acetate catalyzed Heck coupling between 3,6-dibromocarbazole and 4-vinylpyridine followed by usual methylation procedures to afford the dicationic **BMVC**.⁴⁰ Researchers have been building on this work considerably and have designed alternate compounds including **BPBC** that contains an increased number of hydrogen bond donors and acceptors and an extended aromatic surface for π - π interactions with the tetrad's surface. The medicinal potential is higher as the **BPBC** compound contains ionizable side arms that may form cations in an environment of the proper pH compared

to the static and unchanging cations present in **BMVC** which may hamper the *in vivo* success due to decreased cellular permeability and increased off-target effects.

10.9.5.4 Cyanines

Derived from the work in Greek ‘cyanos’ meaning blue, these are defined as two nitrogen containing heterocyclic rings that are connected through an electron deficient polymethine (methine is equivalent to $-\text{CH}=\text{}$) bridge with a delocalized monocation. These cyanine compounds are mostly known for their red-shifted absorption and fluorescence wavelengths that are a direct function of the polymethine bridge and the heterocyclic units with modifications to both moieties allowing for structural diversity. Through structural modifications, cyanines have been modified to serve as effective nucleic acid stains for several decades with sequence specificity being attained for the minor groove of DNA. Similarly, several groups have pioneered the avenue of examining this exciting class of compounds toward developing novel G4 binding compounds for either probing G4 DNA or for developing therapeutics.

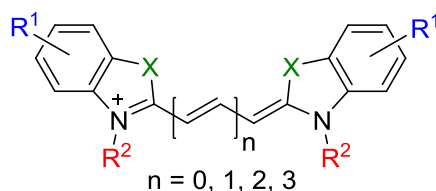


Figure 10-12. General structure for carbocyanine compounds with points of modification shown by generic groups.

The Henary and Wilson lab have pioneered the development of dimethylindolenine-based cyanines that show paramount selectivity toward quadruplex forming sequences versus *dsDNA* arising from two structural modifications – the trimethyl ammonium substituents and the dimethyl groups on the indolenine rings.

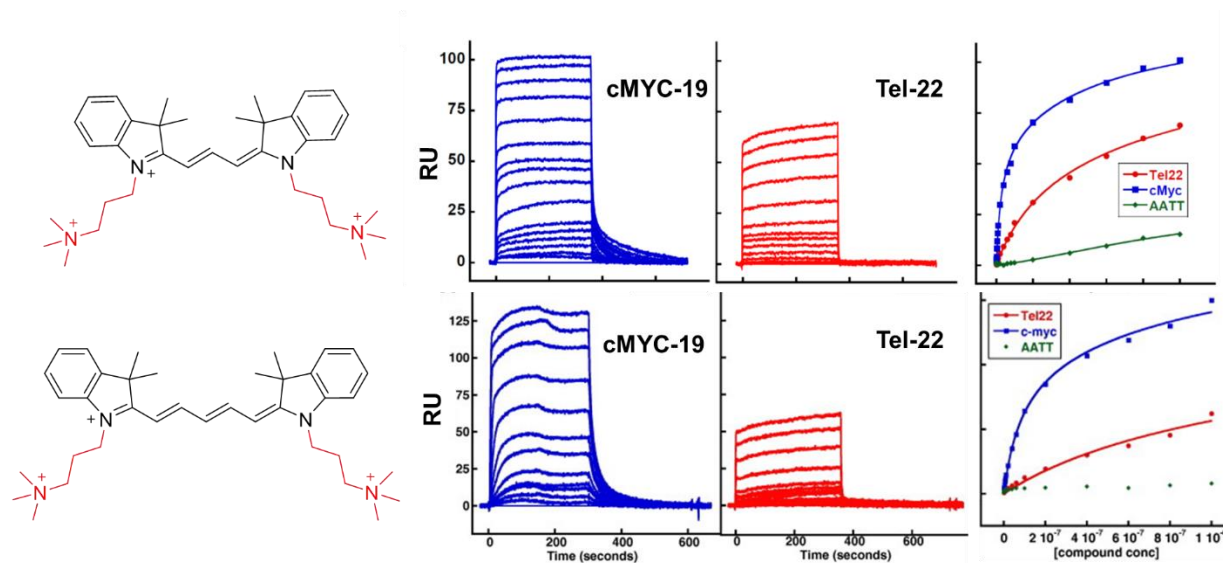


Figure 10-13. The parent structures with non-substituted heterocyclic moieties and quaternary substituents at the *N*-indolenyl site with representative SPR plots for cMYC in blue and human telomere in red.

10.9.6 Limitations of the Quadruplex as a Therapeutic Target

Despite the recent progresses in the field of quadruplex-targeted compounds, we still have to consider the harsh reality. The first limitation is that the nucleus of the cell maintains the genetic code and to reach it, compounds must display a particular size and set of molecular physicochemical properties that facilitate its permeation of the nuclear envelope. Secondly, more broadly, the pharmacokinetics and dynamics of the compounds tested to date not been effective at offering hope with Quarfloxin potentially offering too many dangerous side effects to be taken into the clinic with low top line efficacy. Lastly and potentially a more minor limitation is the ability to synthesize, from the standpoint of an organic chemist standpoint, some of the active compounds that require demainingly harsh conditions for their preparation (i.e. porphyrns). The

low yields combined with the difficulty in purification limit their overall utility in clinically-translatable medications.

10.10 Future Directions for this Field

Currently, the field of G4-targeted therapeutics has great momentum in various avenues; specifically, the determination of various binding modes and more importantly, the molecular characteristics, conformations and configurations that allow quadruplex binding and specific binding to occur are continuously being unraveled. Despite always suspecting that RNA would form quadruplexes, we now have evidence that they are highly likely to stack in G-tetrads.⁴⁵⁻⁴⁹ This has great implications in the field of quadruplex-targeted therapeutics as the nucleus no longer must be targeted and some ligands should be tested against these newly discovered RNA-G4 sequences.

10.11 Summary and Conclusion

In conclusion, we have demonstrated that the quadruplex is likely, based on bioinformatics, to be heavily involved in oncogene promoter regions and play a pivotal role in the initiation and proliferation of carcinogenic tissue. In line with this finding, quadruplex structures are potent targets for the design of new chemotherapeutic agents and several lead compounds have been identified as binding the quadruplex with high specificity and affinity. The medicinal properties of these compounds and *in vivo* efficacy leave much to be desired and further research efforts are required to modify and optimize the hit compounds.

10.12 Acknowledgements

This work was supported by a predoctoral fellowship awarded to E.A.O through the Center for Diagnostics and Therapeutics at Georgia State University. M.H. would like to thank the Brains and Behavior program through the Neuroscience Institute for their support.

10.13 References

1. Watson, J. D.; Crick, F. H. Molecular structure of nucleic acids; a structure for deoxyribose nucleic acid. *Nature* **1953**, 171, 737-8.
2. Chen, Y. Y.; Smolke, C. D. From DNA to targeted therapeutics: bringing synthetic biology to the clinic. *Sci Transl Med* **2011**, 3, 106ps42.
3. Saraswat, P.; Soni, R. R.; Bhandari, A.; Nagori, B. P. DNA as therapeutics; an update. *Indian J Pharm Sci* **2009**, 71, 488-98.
4. Hurley, L. H. Secondary DNA structures as molecular targets for cancer therapeutics. *Biochem Soc Trans* **2001**, 29, 692-6.
5. Kelley, M. R.; Fishel, M. L. DNA repair proteins as molecular targets for cancer therapeutics. *Anticancer Agents Med Chem* **2008**, 8, 417-25.
6. Miller, K. M.; Rodriguez, R. G-quadruplexes: selective DNA targeting for cancer therapeutics? *Expert Rev Clin Pharmacol* **2011**, 4, 139-42.
7. Nimmagadda, S.; Shields, A. F. The role of DNA synthesis imaging in cancer in the era of targeted therapeutics. *Cancer Metastasis Rev* **2008**, 27, 575-87.
8. Patel, D. J.; Phan, A. T.; Kuryavyi, V. Human telomere, oncogenic promoter and 5'-UTR G-quadruplexes: diverse higher order DNA and RNA targets for cancer therapeutics. *Nucleic Acids Res* **2007**, 35, 7429-55.

9. Patil, S. D.; Rhodes, D. G.; Burgess, D. J. DNA-based therapeutics and DNA delivery systems: a comprehensive review. *AAPS J* **2005**, *7*, E61-77.
10. Siddiqui-Jain, A.; Hurley, L. H. DNA structure: Visualizing the quadruplex. *Nat Chem* **2013**, *5*, 153-5.
11. Frank-Kamenetskii, M. DNA structure. The turn of the quadruplex? *Nature* **1989**, 342, 737.
12. Taylor, J. P. Neurodegenerative diseases: G-quadruplex poses quadruple threat. *Nature* **2014**, *507*, 175-7.
13. Welsh, S. J.; Dale, A. G.; Lombardo, C. M.; Valentine, H.; de la Fuente, M.; Schatzlein, A.; Neidle, S. Inhibition of the hypoxia-inducible factor pathway by a G-quadruplex binding small molecule. *Sci Rep* **2013**, *3*, 2799.
14. Nasiri, H. R.; Bell, N. M.; McLuckie, K. I.; Husby, J.; Abell, C.; Neidle, S.; Balasubramanian, S. Targeting a c-MYC G-quadruplex DNA with a fragment library. *Chem Commun (Camb)* **2014**, *50*, 1704-7.
15. Ohnmacht, S. A.; Neidle, S. Small-molecule quadruplex-targeted drug discovery. *Bioorg Med Chem Lett* **2014**, *24*, 2602-12.
16. Ohnmacht, S. A.; Varavipour, E.; Nanjunda, R.; Pazitna, I.; Di Vita, G.; Gunaratnam, M.; Kumar, A.; Ismail, M. A.; Boykin, D. W.; Wilson, W. D.; Neidle, S. Discovery of new G-quadruplex binding chemotypes. *Chem Commun (Camb)* **2014**, *50*, 960-3.
17. Lavrado, J.; Borralho, P. M.; Ohnmacht, S. A.; Castro, R. E.; Rodrigues, C. M.; Moreira, R.; Santos, D. J.; Neidle, S.; Paulo, A. Synthesis, G-Quadruplex Stabilisation, Docking Studies, and Effect on Cancer Cells of Indolo[3,2-b]quinolines with One, Two, or Three Basic Side Chains. *ChemMedChem* **2013**.

18. Hsu, S. T.; Varnai, P.; Bugaut, A.; Reszka, A. P.; Neidle, S.; Balasubramanian, S. A G-rich sequence within the c-kit oncogene promoter forms a parallel G-quadruplex having asymmetric G-tetrad dynamics. *J Am Chem Soc* **2009**, 131, 13399-409.
19. Martins, C.; Gunaratnam, M.; Stuart, J.; Makwana, V.; Greciano, O.; Reszka, A. P.; Kelland, L. R.; Neidle, S. Structure-based design of benzylamino-acridine compounds as G-quadruplex DNA telomere targeting agents. *Bioorganic & Medicinal Chemistry Letters* **2007**, 17, 2293-2298.
20. Liao, S. R.; Zhou, C. X.; Wu, W. B.; Ou, T. M.; Tan, J. H.; Li, D.; Gu, L. Q.; Huang, Z. S. 12-N-Methylated 5,6-dihydrobenzo[c]acridine derivatives: a new class of highly selective ligands for c-myc G-quadruplex DNA. *Eur J Med Chem* **2012**, 53, 52-63.
21. Ferreira, R.; Artali, R.; Farrera-Sinfreu, J.; Albericio, F.; Royo, M.; Eritja, R.; Mazzini, S. Acridine and quindoline oligomers linked through a 4-aminoproline backbone prefer G-quadruplex structures. *Biochim Biophys Acta* **2011**, 1810, 769-76.
22. Collie, G. W.; Sparapani, S.; Parkinson, G. N.; Neidle, S. Structural basis of telomeric RNA quadruplex--acridine ligand recognition. *J Am Chem Soc* **2011**, 133, 2721-8.
23. Campbell, N. H.; Smith, D. L.; Reszka, A. P.; Neidle, S.; O'Hagan, D. Fluorine in medicinal chemistry: beta-fluorination of peripheral pyrrolidines attached to acridine ligands affects their interactions with G-quadruplex DNA. *Org Biomol Chem* **2011**, 9, 1328-31.
24. Bazzicalupi, C.; Chioccioli, M.; Sissi, C.; Porcu, E.; Bonaccini, C.; Pivetta, C.; Bencini, A.; Giorgi, C.; Valtancoli, B.; Melani, F.; Gratteri, P. Modeling and biological investigations of an unusual behavior of novel synthesized acridine-based polyamine ligands in the binding of double helix and G-quadruplex DNA. *ChemMedChem* **2010**, 5, 1995-2005.

25. Ferreira, R.; Avino, A.; Perez-Tomas, R.; Gargallo, R.; Eritja, R. Synthesis and g-quadruplex-binding properties of defined acridine oligomers. *J Nucleic Acids* **2010**, 2010.
26. Zambre, V. P.; Murumkar, P. R.; Giridhar, R.; Yadav, M. R. Structural investigations of acridine derivatives by CoMFA and CoMSIA reveal novel insight into their structures toward DNA G-quadruplex mediated telomerase inhibition and offer a highly predictive 3D-model for substituted acridines. *J Chem Inf Model* **2009**, 49, 1298-311.
27. Campbell, N. H.; Parkinson, G. N.; Reszka, A. P.; Neidle, S. Structural basis of DNA quadruplex recognition by an acridine drug. *J Am Chem Soc* **2008**, 130, 6722-4.
28. Nagesh, N.; Krishnaiah, A.; Dhople, V. M.; Sundaram, C. S.; Jagannadham, M. V. Noncovalent interaction of G-quadruplex DNA with acridine at low concentration monitored by MALDI-TOF mass spectrometry. *Nucleosides Nucleotides Nucleic Acids* **2007**, 26, 303-15.
29. Martins, C.; Gunaratnam, M.; Stuart, J.; Makwana, V.; Greciano, O.; Reszka, A. P.; Kelland, L. R.; Neidle, S. Structure-based design of benzylamino-acridine compounds as G-quadruplex DNA telomere targeting agents. *Bioorg Med Chem Lett* **2007**, 17, 2293-8.
30. Casals, J.; Debethune, L.; Alvarez, K.; Risitano, A.; Fox, K. R.; Grandas, A.; Pedroso, E. Directing quadruplex-stabilizing drugs to the telomere: synthesis and properties of acridine-oligonucleotide conjugates. *Bioconjug Chem* **2006**, 17, 1351-9.
31. Nagesh, N.; Krishnaiah, A. A comparative study on the interaction of acridine and synthetic bis-acridine with G-quadruplex structure. *J Biochem Biophys Methods* **2003**, 57, 65-74.
32. Alberti, P.; Ren, J.; Teulade-Fichou, M. P.; Guittat, L.; Riou, J. F.; Chaires, J.; Helene, C.; Vigneron, J. P.; Lehn, J. M.; Mergny, J. L. Interaction of an acridine dimer with DNA quadruplex structures. *J Biomol Struct Dyn* **2001**, 19, 505-13.

33. Casagrande, V.; Alvino, A.; Bianco, A.; Ortaggi, G.; Franceschin, M. Study of binding affinity and selectivity of perylene and coronene derivatives towards duplex and quadruplex DNA by ESI-MS. *J Mass Spectrom* **2009**, *44*, 530-40.
34. Pivetta, C.; Lucatello, L.; Krapcho, A. P.; Gatto, B.; Palumbo, M.; Sissi, C. Perylene side chains modulate G-quadruplex conformation in biologically relevant DNA sequences. *Bioorg Med Chem* **2008**, *16*, 9331-9.
35. Franceschin, M.; Lombardo, C. M.; Pascucci, E.; D'Ambrosio, D.; Micheli, E.; Bianco, A.; Ortaggi, G.; Savino, M. The number and distances of positive charges of polyamine side chains in a series of perylene diimides significantly influence their ability to induce G-quadruplex structures and inhibit human telomerase. *Bioorg Med Chem* **2008**, *16*, 2292-304.
36. Franceschin, M.; Pascucci, E.; Alvino, A.; D'Ambrosio, D.; Bianco, A.; Ortaggi, G.; Savino, M. New highly hydrosoluble and not self-aggregated perylene derivatives with three and four polar side-chains as G-quadruplex telomere targeting agents and telomerase inhibitors. *Bioorg Med Chem Lett* **2007**, *17*, 2515-22.
37. Tuntiwechapikul, W.; Taka, T.; Bethencourt, M.; Makonkawkeyoon, L.; Randall Lee, T. The influence of pH on the G-quadruplex binding selectivity of perylene derivatives. *Bioorg Med Chem Lett* **2006**, *16*, 4120-6.
38. Rossetti, L.; Franceschin, M.; Schirripa, S.; Bianco, A.; Ortaggi, G.; Savino, M. Selective interactions of perylene derivatives having different side chains with inter- and intramolecular G-quadruplex DNA structures. A correlation with telomerase inhibition. *Bioorg Med Chem Lett* **2005**, *15*, 413-20.

39. Chang, C.-C.; Wu, J.-Y.; Chien, C.-W.; Wu, W.-S.; Liu, H.; Kang, C.-C.; Yu, L.-J.; Chang, T.-C. A Fluorescent Carbazole Derivative: High Sensitivity for Quadruplex DNA. *Analytical Chemistry* **2003**, *75*, 6177-6183.
40. Chang, C.-C.; Wu, J.-Y.; Chang, T.-C. A Carbazole Derivative Synthesis for Stabilizing the Quadruplex Structure. *Journal of the Chinese Chemical Society* **2003**, *50*, 185-188.
41. Wei, C.; Jia, G.; Zhou, J.; Han, G.; Li, C. Evidence for the binding mode of porphyrins to G-quadruplex DNA. *Phys Chem Chem Phys* **2009**, *11*, 4025-32.
42. Wei, C.; Wang, L.; Jia, G.; Zhou, J.; Han, G.; Li, C. The binding mode of porphyrins with cation side arms to (TG4T)₄ G-quadruplex: spectroscopic evidence. *Biophys Chem* **2009**, *143*, 79-84.
43. Ishikawa, Y.; Higashi, E.; Morioka, H. Molecular docking of porphyrins with cationic limbs on intramolecular G-quadruplex. *Nucleic Acids Symp Ser (Oxf)* **2007**, 247-8.
44. Goncalves, D. P.; Ladame, S.; Balasubramanian, S.; Sanders, J. K. Synthesis and G-quadruplex binding studies of new 4-N-methylpyridinium porphyrins. *Org Biomol Chem* **2006**, *4*, 3337-42.
45. Zamiri, B.; Reddy, K.; Macgregor, R. B., Jr.; Pearson, C. E. TMPyP4 porphyrin distorts RNA G-quadruplex structures of the disease-associated r(GGGGCC)_n repeat of the C9orf72 gene and blocks interaction of RNA-binding proteins. *J Biol Chem* **2014**, *289*, 4653-9.
46. von Hacht, A.; Seifert, O.; Menger, M.; Schutze, T.; Arora, A.; Konthur, Z.; Neubauer, P.; Wagner, A.; Weise, C.; Kurreck, J. Identification and characterization of RNA guanine-quadruplex binding proteins. *Nucleic Acids Res* **2014**, *42*, 6630-44.
47. Xu, Y.; Suzuki, Y.; Ishizuka, T.; Xiao, C. D.; Liu, X.; Hayashi, T.; Komiyama, M. Finding a human telomere DNA-RNA hybrid G-quadruplex formed by human telomeric 6-mer RNA and

16-mer DNA using click chemistry: A protective structure for telomere end. *Bioorg Med Chem* **2014**.

48. Yu, C. H.; Teulade-Fichou, M. P.; Olsthoorn, R. C. Stimulation of ribosomal frameshifting by RNA G-quadruplex structures. *Nucleic Acids Res* **2014**, 42, 1887-92.

49. Zhang, J. Y.; Zheng, K. W.; Xiao, S.; Hao, Y. H.; Tan, Z. Mechanism and manipulation of DNA:RNA hybrid G-quadruplex formation in transcription of G-rich DNA. *J Am Chem Soc* **2014**, 136, 1381-90.

11 TRIMETHINE CYANINES AS G-QUADRUPLEX STABILIZING COMPOUNDS

This chapter was adapted from the following publication. My contributions to the manuscript consisted of the synthesis of binding ligands, data analysis, figure and manuscript preparation and recurring discussions concerning the project. Drs. Wilson and Germann labs wholly contributed to the biophysical and NMR studies. Nanjunda, R., **Owens, E. A.**, Mickelson, L., Dost, T. L., Stroeve, E. M., Huynh, H. T., Germann, M. W., Henary, M. M., Wilson W. D., Selective G-Quadruplex DNA Recognition by a New Class of Designed Cyanines **2013 *Molecules*** 18,11, 13588-13607. Invited Article

11.1 Abstract

A variety of cyanines provide versatile and sensitive agents as DNA stains and sensors and have been structurally modified to bind in the DNA minor groove in a sequence dependent manner. Similarly, we are developing a new set of cyanines that have been designed with the goal of achieving highly selective binding to DNA G-quadruplexes with much weaker binding to DNA duplexes. A systematic set of structurally analogous trimethine cyanines has been synthesized and evaluated for quadruplex targeting. The results reveal that elevated quadruplex binding and specificity are highly sensitive to the polymethine chain length, heterocyclic structure and intrinsic charge of the compound. Biophysical experiments show that the compounds display significant selectivity for quadruplex binding with a higher preference for parallel stranded quadruplexes, such as cMYC. NMR studies revealed the primary binding through an end-stacking mode and SPR studies showed the strongest compounds have primary K_D values below 100 nM that are nearly 100 times higher for duplexes. The high selectivity of these newly designed trimethine cyanines for quadruplexes as well their ability to discriminate between different quadruplexes are extremely promising features to develop them as novel probes for targeting quadruplexes structures *in vivo*.

11.2 Introduction

G-quadruplexes are higher order DNA structures formed by either intra or intermolecular association of guanine-rich sequences into a stacked array of G-tetrads and stabilized by Hoogsteen hydrogen bonds as well as coordinated monovalent cations^{1,2}. The formation and stabilization of these unique structural motifs are implicated in diverse biological functions such as gene regulation and chromosomal stability^{3,4}; therefore, these structures have garnered immense interest as a viable platform for the development of quadruplex-specific small-molecule drugs for therapeutic purposes^{5,6}. Furthermore, with the recent exciting evidence showing the formation of G-quadruplexes during various stages of mammalian cell cycle *in vivo* as well as convincing evidence that small molecules can indeed induce and stabilize quadruplexes *in vivo*, these unique structures are undoubtedly a novel and promising target for the design and development of anticancer therapeutic agents using small molecules^{7,8}. In fact, a wide range of quadruplex-specific small molecules have been reported so far with some compounds showing very promising biological activities⁹⁻¹¹.

Cyanines are a class of small molecules that are being developed as potential G-quadruplex targeting agents in addition to their wide-range of applications as cancer imaging agents and nucleic acid stains^{12,13}. The synthetic ability to structurally tailor cyanines as well as their many therapeutically favorable features, such as low toxicity, renders them ideal candidates also for their potential development as quadruplex targeting agents. Previously we had reported a new class of indolenine scaffold based cyanine molecules with highly favorable quadruplex interactions¹⁴. The pentamethine linker between the two indolenine rings provided the needed flexibility for efficient stacking at the terminal tetrads of the quadruplex, whereas the dimethyl groups on the indolenine rings considerably reduced the intercalation or stacking of the cyanines in the duplex minor groove.

The halogen substitutions at different positions on the aromatic core further increased their quadruplex affinity. The highly promising results of the pentamethine cyanines as quadruplex specific agents encouraged us to further explore the conformational space of cyanine molecules for increased quadruplex affinity and selectivity. In the current study, a series of cyanine molecules (Figure 1) with reduced methine linker length were synthesized to probe the effects on quadruplex binding while maintaining the dimethyl and halogen substitutions. Using a series of powerful biophysical techniques, we show that these newly designed trimethine cyanines exhibit more favorable quadruplex binding while maintaining a very low duplex affinity. The results are highly promising and encouraging towards the development of cyanine-based small molecules as highly specific quadruplex targeting agents.

11.3 Results and Discussion

The synthesis of trimethine quadruplex binding agents based off of the symmetric cyanine model consists of heterocyclic derivation installed through the formation of the dimethyl indolenine rings by Fisher indole synthesis from the starting 4-substituted hydrazine compounds. After the heterocyclic rings are prepared, facile S_N2 quaternization of the heterocyclic enamine results in the cationic salts bearing the groups shown in Figure 10-1. The carbon attached to the 2-position of the ring contains acidic protons due to the positively charged electron sink of the salt. The deprotonation at this position initiates the reaction with triethylorthoformate which produces ethoxide thus promoting further reaction. Two salts condense with a triethyl orthoformate molecule which results in the final products **24-32**.

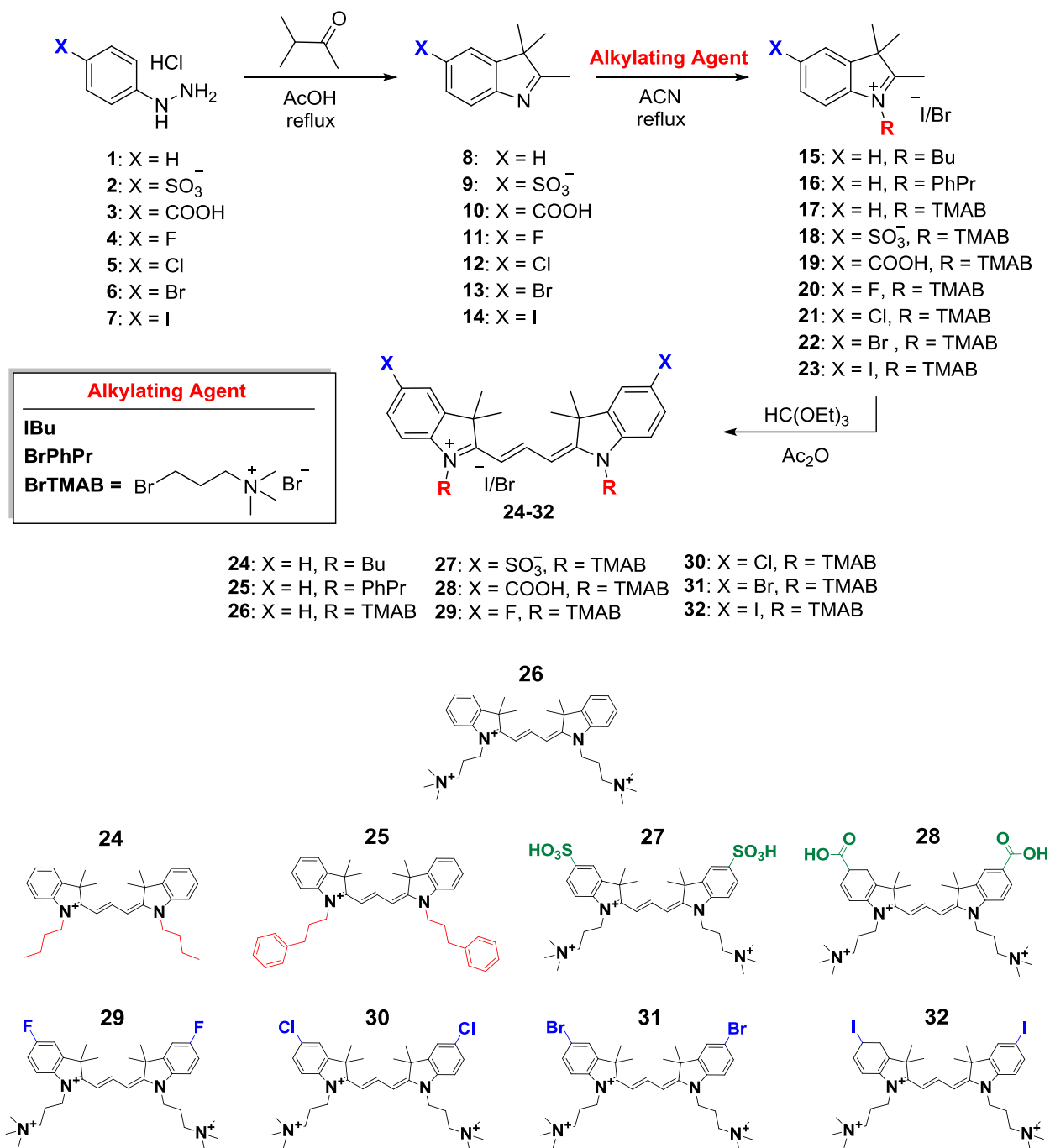


Figure 11-1. Synthetic scheme and chemical structure of the trimethine cyanine analogs used in the current study. The modifications performed on the parent cyanine (26) are highlighted in different colors (compounds 24-32). All compounds have one positive charge delocalized

on the cyanine system with variance in charge on the heterocyclic rings and the nitrogen chain.

11.3.1 UV-Vis Thermal Melting

UV-Thermal melting is a rapid and robust screening technique to determine selectivity as well as to rank the ligand-induced relative stability of quadruplex-ligand complexes^{15, 16}. Preliminary T_m analysis of a synthetic set of symmetric trimethine cyanines containing different substituents on the indolenine rings (Figure 1) were conducted with a well-characterized telomeric quadruplex sequence (Tel22) and a control hairpin duplex sequence (AATT) that is quite favorable for detection of either minor groove or intercalative binding to duplexes. The increase in the thermal stability of the complexes upon ligand binding (ΔT_m) at different ligand-DNA ratios is listed in Table 1. A range of ligand-DNA mole ratios were employed to ensure saturation of binding sites on the quadruplex as well as duplex motifs. Drug-DNA ratios beyond 6:1 resulted in inconsistent melting curves in some cases due to possible aggregation of cyanines. The trimethine-linked parent cyanine, compound **26**, exhibited a favorable increase in the thermal stability of the Tel22 sequence with increasing ratios. This increase in thermal stability of **26** with Tel22 is slightly improved compared to the ΔT_m of a similar cyanine with a pentamethine linker reported previously (Table 1: compare ΔT_m s of **26** and **a**)¹⁴. Replacing the propyl-(trimethyl ammonium) groups on both indolenine rings of **26** with hydrophobic propyl-phenyl groups, **25**, slightly reduced the thermal stability of the Tel22 complex. A similar replacement with an n-butyl group, **24**, dramatically reduced the thermal stability of the complex compared to **26**. This suggests the importance of charge on the substituents to maintain favorable electrostatic interactions with the backbone of the anionic quadruplex motif. While retaining the propyl-(trimethyl ammonium)

groups, various substitutions were made on the indolenine rings to probe their effect on quadruplex binding. Substitutions with either a sulfonato ($-\text{SO}_3\text{H}$, **27**) or carboxylic acid ($-\text{COOH}$, **28**), which have negative charges under the experimental conditions, resulted in a minimal increase in the thermal stability of Tel22, probably due to unfavorable electrostatic interactions with the negatively charged backbone. In accordance with the design principles established in the previous studies to enhance quadruplex interactions by halogenation of cyanines, systematic halogen substitutions on the indolenine rings in the current trimethine series showed a highly favorable increase in the thermal stability of the telomeric quadruplex (compounds **29-32**). Furthermore, the trimethine chloro (**30**) and bromo (**31**) analogs showed a more favorable increase in the thermal stability of Tel22 compared to the similar halogen-substituted pentamethine analogs (Table 1, compounds **b** and **c**). The trimethine-linker scaffold might be a better optimized system than the pentamethine-linker cyanines for more favorable interactions with a quadruplex unit. All the trimethine halogen derivatives, however, exhibited very similar increases in the thermal stability of the quadruplex motif suggesting a minimal effect of the size of the halogens.

One of the important features observed with these cyanine molecules is their very low binding to duplex-DNA sequences (Table 1, ΔT_m of an AATT sequence that is favorable for minor groove or intercalation binding mode). The trimethine cyanines exhibited a very small-to-zero increase in the thermal stability with duplex-DNA even at relatively high ligand-DNA ratios. The dimethyl substituents on the terminal indolenine rings, as predicted, provide the necessary steric hindrance and reduce any possible interaction with duplex-DNA. In line with the previous studies on pentamethine cyanines, these newly designed trimethine cyanines show an important step in further expanding the cyanine scaffolds as a novel quadruplex-targeting class of small molecules with reduced duplex-DNA selectivity.

Table 10-1. Thermal melting studies of trimethine cyanine analogs with telomeric quadruplex (Tel22) and a control duplex (AATT)

Compound/ Drug:DNA Ratio	Tel22				AATT duplex			
	1:1	2:1	4:1	6:1	1:1	2:1	4:1	6:1
24	1	1	1	0	ND			
25	1	2	4	11	0	2	2	2
26	2	4	9	14	0	1	1	2
27	2	1	1	1	ND			
28	1	1	3	7	1	1	2	3
29	3	8	12	16	0	1	1	2
30	3	7	15	19	0	0	1	1
31	1	5	14	24	0	0	0	0
32	3	7	17	21	1	1	3	3

The thermal melting values reported are an average of two independent trials and are reproducible within ± 0.5 °C. ND = Not Determined.

11.3.2 Biosensor-Surface Plasmon Resonance studies (SPR)

Biosensor-SPR is an effective technique to determine the equilibrium binding affinity and kinetics, as well as the stoichiometry and cooperativity of biomolecular interactions in real-time^{17, 18}. To determine the relative binding strength of the trimethine cyanine analogs, SPR experiments were performed with biotinylated quadruplex and duplex sequences. In addition to the Tel22 quadruplex, a well-characterized oncogenic promoter quadruplex sequence from *c-myc*, cMYC19, was also employed to determine if the compounds can exhibit any selectivity for different quadruplex architectures. Figure 2 shows representative SPR sensorgrams and the corresponding steady-state affinity plots for the parent cyanine (**26**) and the brominated analog (**31**) with both quadruplex-forming sequences. The sensorgrams show very fast association and dissociation of the compounds and were characteristic of all the analogs, except for compound **24**

which did not exhibit any binding with either quadruplex sequences. The equilibrium binding affinities for all the analogs were determined using a two-site binding model and are listed in Table 2. All the compounds exhibit reasonable binding to both quadruplex sequences with a primary strong binding (K_1) followed by a weaker binding (K_2) with an affinity, ca. 10X lower. The halogenated analogs (**29-32**) showed impressive 5-15 times stronger binding affinities with the telomeric quadruplex compared to the parent compound (**26**, $K_1 = 3.9 \times 10^5 \text{ M}^{-1}$) and are in agreement with the T_m studies. With the parallel cMYC19 quadruplex, compound **26** showed a more favorable 10 times increase in binding affinity compared to the telomeric quadruplex, however, the brominated analogs exhibited only a 2-5 fold increase in the binding affinity. The anionic substitution analogs (**27** and **28**) showed a 2-fold increase in the binding affinity with Tel22 compared to the parent cyanine (**26**), a trend that was not observed in T_m studies. In general, all the strong binding ligands showed a higher preference for the parallel *c-myc* quadruplex over the hybrid telomeric quadruplex. The binding affinities with the duplex sequence were either too low ($K_A < 10^5 \text{ M}^{-1}$) or could not be reasonably determined due to very low steady-state response values for the same concentration range (data not shown). SPR results, thus, conclusively show the selectivity of the trimethine analogs for quadruplex structures with different folding topologies as well as the selectivity over duplex sequences and in agreement with thermal melting studies. The two-site fitting model predicted two predominantly bound ligands per quadruplex unit probably stacked at the terminal tetrads (discussed below in NMR section), a common mode and stoichiometry of binding exhibited by a majority of quadruplex targeting ligands^{9, 19-24}.

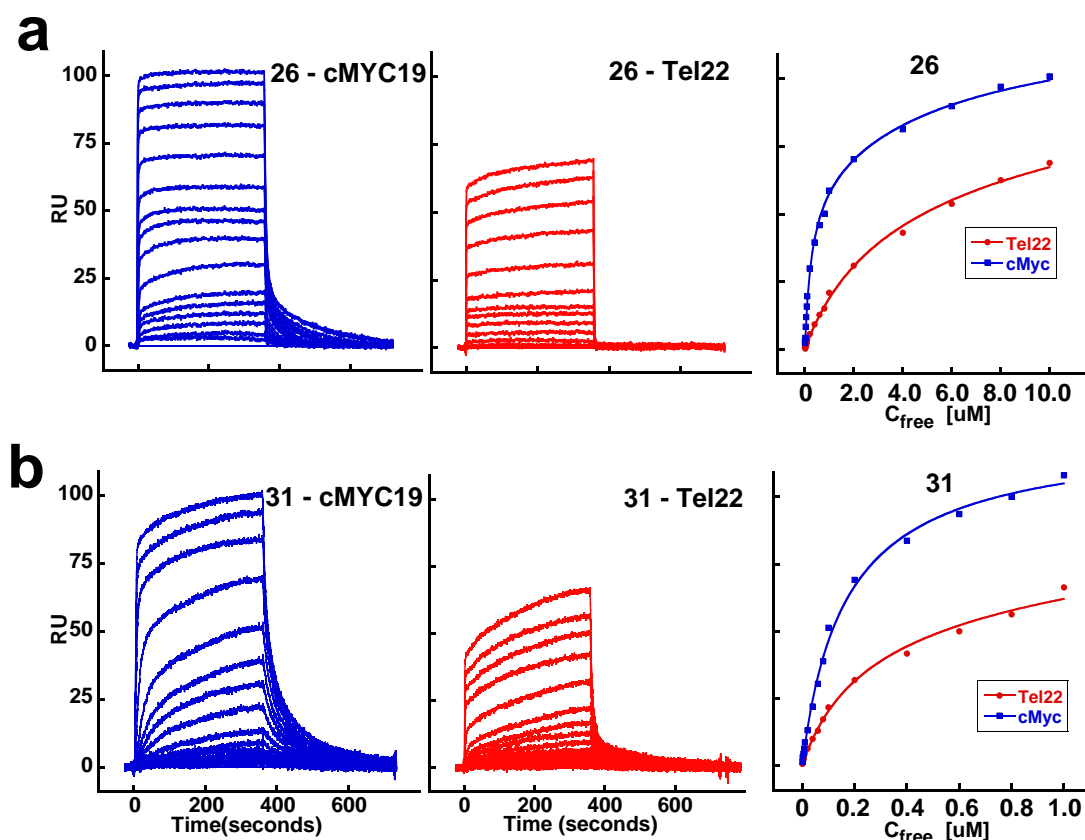


Figure 11-2. SPR sensorgrams and the steady-state binding plots for the parent cyanine (26, panel a) and the brominated analog (31, panel b) with Tel22 and cMYC19 quadruplex sequences. The injected concentration range for 26 is 10 nM - 10 μ M and for 31 is 10 nM - 1 μ M. The binding plots were obtained by fitting the steady-state response values (RU) as a function of free ligand concentration (C_{free}) and fit to a two-site binding model. The estimated equilibrium binding affinities (K_1 and K_2) are reported in Table 10-2.

2.4. Nuclear Magnetic Resonance studies (NMR)

NMR studies were carried out to locate the binding site(s) on the quadruplex structure and the imino proton spectra of a modified *c-myc* variant, MYC22, with the parent and brominated

analogues are shown in Figure 4. The imino protons of MYC22 were previously assigned²⁵ and serve as a convenient monitor to determine the mode of interaction and stoichiometry. Based on the imino proton shifts on titration, the primary binding site for compound **26** is the 3'-end tetrad of MYC22 (G9, G13, G18, and G22; Figure 4A and 5B). A secondary binding site at the 5'-end tetrad (G7, G11, G16, and G20) is evident after the top face approaches saturation. Remarkably, no precipitation was observed even at a 10-fold excess of either compound. With the exception of G8 imino proton, the middle tetrad is less affected by the binding on either terminal tetrad. However, it is noted that the shift of G8 imino proton parallels that of G16 imino proton which monitors binding to the 5'-end tetrad. This suggests that the binding to the 5'-end tetrad causes the chemical shift change of G8 imino proton. A similar binding sequence (first 3'-end and then 5'-end) is also observed for compound **31** (Figure 4B and 5C). Interestingly, the presence of the bulkier bromine substituent results in a much smaller effect on the central tetrad, as shown for G8 imino proton. This is in marked contrast to the result obtained for compound **26** and indicates that there are differences in the binding orientation of **26** and **31** (on the 5'-end tetrad). The NMR results, which demonstrate binding to the terminal tetrads of MYC22, are consistent with the CD results for **26** and **31** which indicate end-stacking interactions as well as small structural perturbations in the quadruplex upon complex formation.

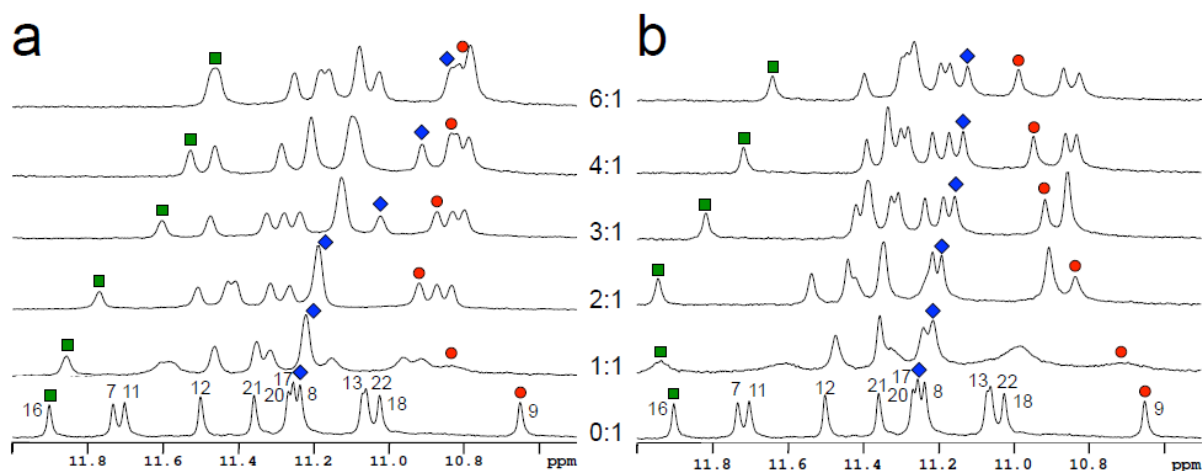


Figure 11-3. Imino proton spectra of MYC22 quadruplex titrated with the parent cyanine 26 (a) and the brominated analogue 31 (b). Ligands were added to the quadruplex at the ratio indicated on the plot. Selected imino protons of 3'-end (9, red) middle (8, blue) and 5'-end (16, green) tetrads are marked.

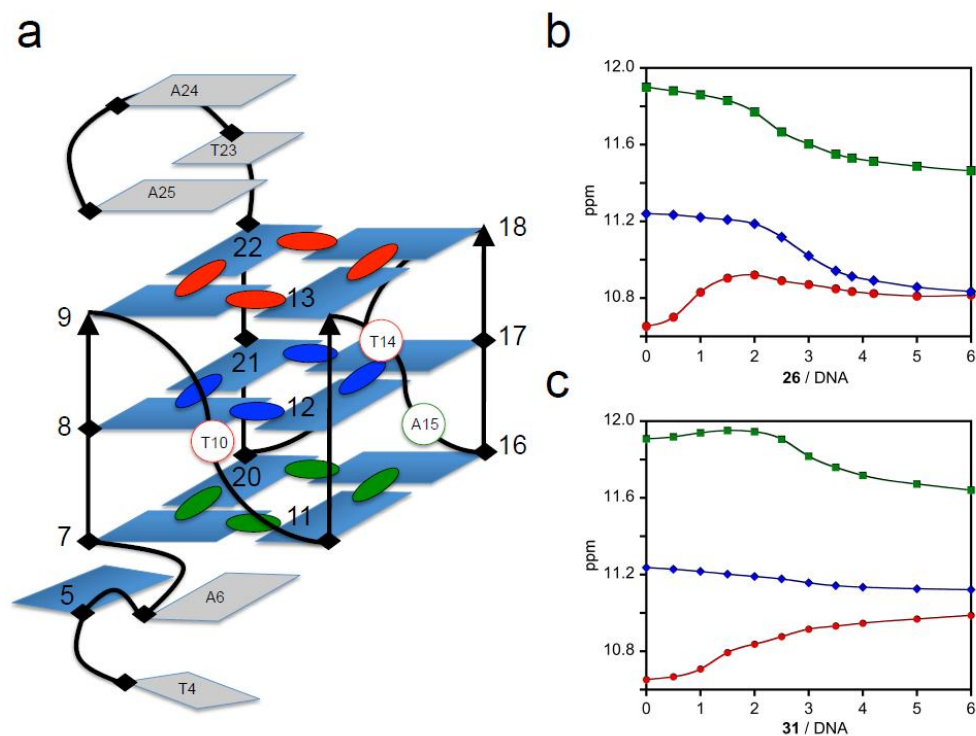


Figure 11-4. (a) Schematic structure of the c-myc quadruplex MYC22 (Ambrus et al, 2005, [26]). For clarity the imino protons of the guanine tetrads are color coded. Red: 3'-end tetrad, blue: center tetrad, and green: 5'-end tetrad. Imino proton titration curves of 3'-end, middle and 5'-end tetrad for the parent cyanine (26, b) and the brominated analog (31, c).

11.3.3 Fluorescence studies

Development of fluorescence probes that are highly selective for quadruplex structures is an additional promising area given the involvement of quadruplex motifs in several important biochemical processes. The trimethine cyanines were tested for their fluorescence properties with both Tel22 and cMYC19 quadruplex structures and the fluorescence spectra of the parent cyanine (26) and the brominated analog (31) are shown in Figure 6. From the spectra, it can be readily seen that the compounds exhibit enhancement in fluorescence intensities with both quadruplex

structures with increasing concentrations of DNA. However, it is strikingly apparent that the compounds exhibit very different fluorescence enhancements with both sequences. The enhancement in fluorescence intensity is significantly higher with the *c-myc* quadruplex compared to telomeric quadruplex. The preferential signal enhancement with *c-myc* quadruplex was observed with all the trimethine cyanine analogs. It is very clear that the ligands have a much stronger preference for the parallel over hybrid quadruplex.

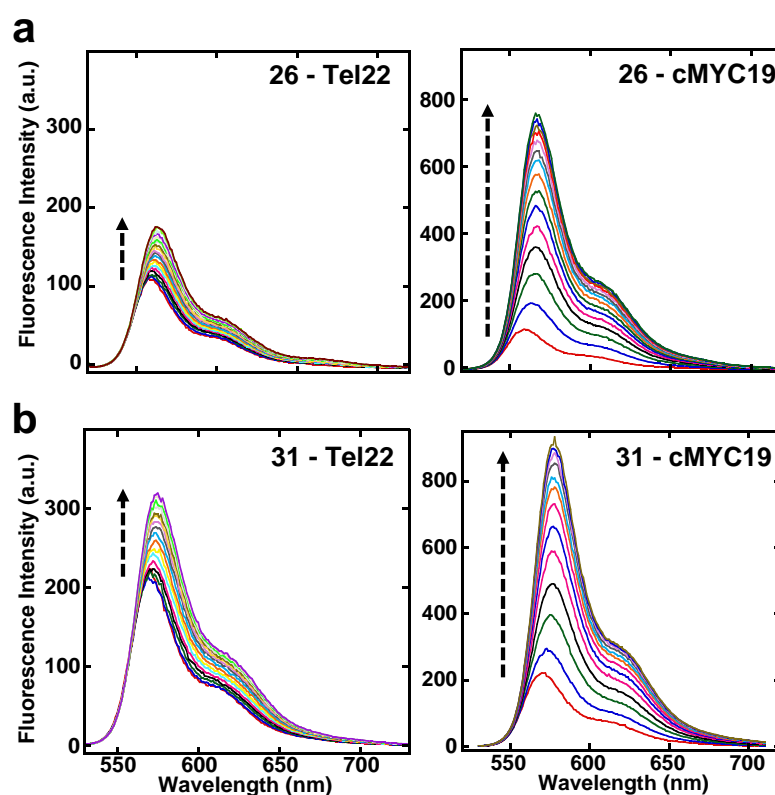


Figure 11-5 Fluorescence emission spectra of the parent cyanine (26, panel a) and the brominated analog (31, panel b) with Tel22 and cMYC19 quadruplex sequences. The arrow indicates increasing concentrations of DNA titrated into the ligand solution (1 μ M) until no further change in the fluorescence emission signal was detected.

11.4 Discussion

G-quadruplex structures are associated in many important biological processes such as gene regulation and protection against chromosome degradation^{3, 26, 27}. The recent and very exciting evidence showing the formation of G-quadruplex structures *in vivo* as well as the small-molecule mediated stabilization of these unique structures *in vivo* has further driven the need to develop potent quadruplex-targeting agents⁷. Various classes of small molecules have been developed using a G-quadruplex platform as a strategy for improved therapeutic potential as well as for enhancing the fundamental understanding of quadruplex-ligand interactions. Cyanines are one class of small molecules that have the potential as quadruplex-specific agents²⁸⁻³⁰. Previously, we have described the binding specificity and affinity of various pentamethine cyanine dyes with the telomeric and the *c-myc* oncogenic quadruplex forming sequences¹⁴. The pentamethine analogs exhibited a 2:1 binding stoichiometry with an end-stacking binding mode with a preferential binding for parallel *c-myc* over hybrid telomeric G-quadruplexes. The dimethyl substitutions on both indolenine rings considerably reduce their affinity for duplex systems. The 2:1 complex formation was shown to be entropically-driven, as is observed for many end-stacking quadruplex binders. With the success in developing rationally designed pentamethine cyanine scaffolds for quadruplex targeting, we have extended the study with the development of a new series of cyanine molecules with reduced linker length between the aromatic cores of the cyanine scaffold. Herein, we probe the sensitivity and selectivity of binding to the polymethine chain length by shortening the distance between the heterocyclic nitrogen atoms by two carbon units.

Preliminary screening studies of the new trimethine cyanines showed considerable improvements in the thermal stability of the Tel22 quadruplex compared to the pentamethine analogs. The compounds also showed significant selectivity over duplex sequences in accord with

the design principles established by the introduction of dimethyl scaffolds to reduce duplex interactions. Effectively targeting the relatively lower abundance quadruplex motifs in an essentially duplex-rich genome is a challenging task, and therefore, appropriate scaffolds with reduced duplex-DNA interactions can provide alternate platforms to develop further selective quadruplex-specific agents. This is especially true if any weak duplex interactions, such as non-specific electrostatic bindings, do not generate significant biological effects. Biosensor-SPR studies showed compound binding to different quadruplex motifs with a 2:1 binding stoichiometry and a higher preference for parallel-type quadruplex folds over hybrid quadruplexes. The more exposed terminal tetrad surface of the *c-myc* quadruplex might be more conducive for favorable stacking interactions. NMR imino proton chemical shifts provide specific evidence for cyanine stacking on both ends of the cMYC quadruplex structure. In addition, the NMR results shows that the two ends are saturated with cyanines at different ratios in agreement with the two binding affinity values (K_1 and K_2) observed in SPR studies. The NMR spectral changes for the parent (**26**) and the brominated derivative (**31**) suggest different stacking geometries by the two molecules. This is a very interesting result that will be very helpful in compound design as more structural details are obtained in more detailed NMR analyses.

One of the attractive features of cyanine molecules is their highly favorable fluorescence properties and their extensive application as dyes in the detection of biomolecules³¹⁻³³. Benzothiazole based cyanines have been generally developed as fluorescent dyes for duplex-DNA, however, their strong interactions with duplex-DNA have limited their development as quadruplex-specific fluorescence probes. Furthermore, given the different types of quadruplex structures formed by guanine-rich sequences from various genomic regions, it is highly desirable to develop fluorescent probes that are not only selective for quadruplex structures over duplex-

DNA but also discriminate between different quadruplex topologies. Very interestingly, the trimethine cyanines in the current study exhibit differential fluorescence behavior with quadruplex sequences. The significantly favorable fluorescence emission property of trimethine cyanine dyes with *c-myc* quadruplex is highly promising for their development as potential biomarkers for oncogenic-quadruplex-mediated cellular processes. The propensity of different guanine-rich sequences throughout the genome to fold into diverse quadruplex conformations will require the design of improved ligands that can discriminate among quadruplex topologies and show preferential binding with high selectivity³⁴⁻³⁶.

11.5 Experimental

11.5.1 Synthesis of Cyanines

The chemical reagents used in the synthesis of cyanine dyes were obtained from Acros Organics, Alfa Aesar and Matrix Scientific. The reactions were followed using silica gel 60 F₂₅₄ thin layer chromatography plates (Merck EMD Millipore, Darmstadt, Germany) with 5% methanol in DCM as the mobile phase. Open column chromatography was utilized for the purification of all final compounds using 60-200u, 60A classic column silica gel (Dynamic Adsorbents, Norcross, GA). The ¹H NMR and ¹³C NMR spectra were obtained using high quality Kontes NMR tubes (Kimble Chase, Vineland, NJ) rated to 500 MHz and were recorded on a Bruker Avance (400 MHz) spectrometer using D₂O containing tetramethylsilane (TMS) as an internal calibration standard. ¹⁹F NMR spectra were recorded using hexafluorobenzene as an internal standard. UV-Vis/NIR absorption spectra were recorded on a Varian Cary 50 spectrophotometer. High-resolution accurate mass spectra (HRMS) were obtained either at the Georgia State University Mass Spectrometry Facility using a Waters Q-TOF micro (ESI-Q-TOF) mass spectrometer or utilizing a Waters Micromass LCT TOF ES+ Premier Mass Spectrometer. Liquid chromatography

utilized a Waters 2487 single wavelength absorption detector with wavelengths set between 640 and 700 nm depending on the dye's photophysical properties. The column used in LC was a Waters Delta-Pak 5 μ M 100A 3.9 x 150 mm reversed phase C₁₈ column. Evaporative light scattering detection analyzes trace impurities that cannot be observed by alternate methods; a SEDEX 75 ELSD was utilized in tandem with liquid chromatography to confirm purity.

The preparation of the heterocyclic precursors **8-14** has been described by our laboratory and the compounds were used in the synthesis of the charged salts **15-23**.

General Synthesis for the alkylated indolenine salts 15-23:

Individual 2,3,3-indolenine heterocyclic precursor **8-14** was dissolved in anhydrous acetonitrile (50 mL) and was heated to 40 °C followed by the addition of the appropriate alkylating agent in 3 molar excess and was then heated to reflux for 72h. The reaction progress was followed by TLC eluting with DCM/methanol/acetic acid (40/58/2). The reaction mixture was allowed to cool and the solvent was partially removed *in vacuo*. The final compounds were obtained by precipitation from methanol by diluting with acetone, ethyl acetate and diethyl ether. The hygroscopic compounds were allowed to dry for several hours on high vacuum.

General Synthesis for the trimethine cyanine binding agents 24-32:

Individual alkylated indolenine salts **15-23** were dissolved in acetic anhydride (50 mL) followed by the addition of triethylorthoformate in a 2:1 molar ratio. The reaction was heated at 110 °C for 30 minutes and followed using UV-Vis spectroscopy diluted in methanol. The mixture was allowed to cool and was crystallized using hexanes/ethyl acetate/diethyl ether. A colored precipitate was filtered, washed and collected. Compounds **24-32** were dried for several hours under high vacuum.

Compounds **24** and **25** have been previously reported by our lab and were used directly in the quadruplex binding interaction studies without any additional modifications.

The product **26** was obtained in 89% yield. MP 105-107 °C; ^1H NMR (400 MHz, D_2O), δ : 1.62 (s, 12H), 2.27 (t, $J = 7.6$ Hz, 4H), 3.08 (s, 18H), 3.49-3.57 (m, 4H), 4.13 (t, $J = 7.2$ Hz, 4H), 6.52 (d, $J = 13.2$ Hz, 2H), 7.18-7.28 (m, 4H), 7.36 (d, $J = 7.6$ Hz, 2H), 7.47 (d, $J = 7.2$ Hz, 2H), 8.47 (t, $J = 13.2$ Hz, 1H). ^{13}C NMR (100 MHz, D_2O), δ : 21.0, 27.3, 40.5, 49.2, 53.1, 63.2, 102.7, 110.9, 122.5, 125.7, 128.8, 140.8, 141.3, 151.8, 175.1.

The product **27** was obtained in 92% yield. MP 295-297 °C; ^1H NMR (400 MHz, D_2O), δ : 1.66 (s, 12H), 2.26 (t, $J = 6.0$ Hz, 4H), 3.09 (s, 18H), 3.44-3.54 (m, 4H), 4.14 (t, $J = 7.2$ Hz, 4H), 6.44 (d, $J = 13.2$ Hz, 2H), 7.28 (d, $J = 8.4$ Hz, 2H), 7.74 (d, $J = 8.4$ Hz, 2H), 7.83 (s, 2H), 8.50 (t, $J = 13.2$ Hz, 1H). ^{13}C NMR (100 MHz, D_2O), δ : 20.9, 21.2, 30.2, 40.8, 49.5, 53.2, 63.1, 103.7, 111.1, 120.0, 126.7, 139.9, 141.5, 143.6, 153.0, 176.4. Combustion C, H N analysis calculated for $\text{C}_{35}\text{H}_{51}\text{BrN}_4\text{O}_6\text{S}_2$ ($4\text{H}_2\text{O}$): C, 50.05; H, 7.08; N, 6.67. Found: C, 50.30; H, 6.83; N, 6.56.

The product **28** was obtained in 55% yield. MP more than 350 °C; ^1H NMR (400 MHz, D_2O), δ : 1.64 (s, 12H), 2.22 (t, $J = 6.0$ Hz, 4H), 3.11 (s, 18H), 3.43- 3.53 (m, 4H), 4.16 (t, $J = 7.2$ Hz, 4H), 6.46 (d, $J = 13.2$ Hz, 2H), 7.35 (d, $J = 8.4$ Hz, 2H), 7.88 (d, $J = 8.4$ Hz, 2H), 7.93 (s, 2H), 8.55 (t, $J = 13.2$ Hz, 1H). ^{13}C NMR (100 MHz, D_2O), δ : 20.4, 21.3, 30.4, 41.8, 47.5, 54.6, 64.1, 106.7, 111.6, 122.1, 127.3, 134.9, 141.6, 147.2, 154.5, 177.4, 179.9.

The product **29** was obtained in 33% yield MP >260 °C. ; ^1H NMR (400 MHz, D_2O), δ : 1.70 (s, 12H), 2.29 (t, $J = 7.8$ Hz, 4H), 3.08 (s, 18H), 3.48 (tt, $J = 7.8$ Hz, $J = 7.8$ Hz, 4H), 4.15 (t, $J = 7.8$ Hz, 4H), 6.34 (d, $J = 13.6$ Hz, 2H), 7.14 (t, $J = 9.2$ Hz, 2H), 7.242-7.12 (m, 2H), 7.30 (d, 6.0 Hz, 2H), 8.49 (t, $J = 13.6$ Hz, 1H) . ^{19}F NMR (135 MHz, D_2O , C_6F_6 standard), δ : -118.8. HR-MS calculated for $[\text{C}_{35}\text{H}_{51}\text{N}_4\text{F}_2\text{Br}]^+$ 644.3265, found 644.3278.

The product **30** was obtained in 77% yield. MP 255-257 °C; ¹HNMR (400 MHz, D₂O), δ: 1.81 (s, 12H), 2.36 (t, *J* = 7.8 Hz, 4H), 3.29 (s, 18H), 3.95 (tt, *J* = 7.8 Hz, *J* = 7.8 Hz, 4H), 4.29 (t, *J* = 7.8 Hz, 4H), 7.21 (d, *J* = 13.4 Hz, 2H), 7.49 (d, *J* = 8.0 Hz, 2H), 7.59 (d, *J* = 8.0 Hz, 2H), 7.66 (s, 2H), 8.60 (t, *J* = 13.4 Hz, 1H). ¹³CNMR (100 MHz, D₂O), δ: 22.4, 28.4, 42.4, 50.9, 54.2, 64.2, 105.7, 114.0, 124.4, 130.2, 132.6, 141.9, 144.2, 153.3, 176.1. Combustion C, H N analysis calculated for C₃₅H₅₁Br₃Cl₂N₄ (2H₂O): C, 48.07; H, 6.34; N, 6.41. Found: C, 48.13; H, 6.31; N, 6.43.

The product **31** was obtained in 87% yield. MP 245-247 °C; ¹HNMR (400 MHz, D₂O), δ: 1.71 (s, 12H), 2.16 (t, *J* = 7.4 Hz, 4H), 3.16 (s, 18H), 3.83-3.93 (m, 4H), 4.13 (t, *J* = 7.6 Hz, 4H), 7.30 (d, *J* = 13.2 Hz, 2H), 7.57 (dd, *J* = 6.4 Hz, *J* = 4.0 Hz, 2H), 7.69 (d, *J* = 6.4 Hz, 2H), 7.99 (d, *J* = 4.0 Hz, 2H), 8.38 (t, *J* = 13.2 Hz, 1H). ¹³CNMR (100 MHz, D₂O), δ: 21.2, 31.1, 41.6, 49.5, 53.1, 62.5, 104.5, 113.9, 118.2, 126.3, 131.8, 141.4, 151.2, 172.4, 174.2. Combustion C, H N analysis calculated for C₃₅H₅₁Br₅N₄ (3H₂O): C, 42.84; H, 5.85; N, 5.71. Found: C, 43.09; H, 5.65; N, 5.61.

The product **32** was obtained in 92% yield. MP 260-262 °C; ¹HNMR (400 MHz, D₂O), δ: 1.69 (s, 12H), 2.15 (t, *J* = 7.8 Hz, 4H), 3.15 (s, 18H), 3.88 (tt, *J* = 7.8 Hz, *J* = 8.0 Hz, 4H), 4.11 (t, *J* = 8.0 Hz, 4H), 7.28 (d, *J* = 13.4 Hz, 2H), 7.44 (d, *J* = 8.0 Hz, 2H), 7.82 (d, *J* = 8.0 Hz, 2H), 8.08 (s, 2H), 8.37 (t, *J* = 13.4 Hz, 1H);. ¹³CNMR (100 MHz, D₂O), δ: 20.7, 27.2, 41.0, 48.8, 52.6, 62.0, 89.8, 103.9, 113.7, 131.2, 137.1, 141.4, 143.0, 150.6, 173.2. Combustion C, H N analysis calculated for C₃₅H₅₁Br₃I₂N₄ (2H₂O): C, 39.76; H, 5.24; N, 5.30. Found: C, 39.83; H, 5.18; N, 5.38.

11.5.2 Nucleic Acids

The DNA oligonucleotides: Tel22 d[AGGG(TTAGGG)₃], cMYC19 d[(AGGGTGGGG)₂A], and AATT hairpin duplex control d[CGAATTCGTTTTTCGAATTCG] with and without 5'-biotin labels were purchased from Integrated DNA Technologies (Coralville, IA) with HPLC purification and mass spectrometry characterization. For NMR studies, a modified *c-myc* sequence, MYC22, d[TG(AGGGTGGGG)₂AA] was used. The concentration of all the oligonucleotides was calculated using the absorbance at 260 nm and the manufacturer provided extinction coefficients determined by the nearest-neighbor method³⁷. Stock solutions of the oligonucleotides and the dyes were prepared in deionized water and diluted using appropriate experimental buffer prior to use. Experiments were conducted in 10 mM TRIS, or 10 mM HEPES for SPR, containing 50 mM KCl and 3 mM EDTA adjusted to pH 7.3.

11.5.3 UV-Thermal Melting

Thermal stability studies of the ligand-DNA complexes were performed with a Cary 300 BIO UV-visible spectrophotometer in 1 cm pathlength quartz cuvettes. Samples of ligand-DNA complexes were prepared in Tris buffer at different ratios (0:1 up to 6:1) and were mounted in a 6x6 Series II thermal block. The change in the absorbance of the complexes was monitored (at 295 nm for quadruplex samples and 260 nm for duplex samples) as a function of temperature with computer-controlled heating and cooling rates of 0.5 °C/min. A total of four scans for each sample were collected with automatic buffer correction. The buffer corrected scans were normalized and the T_m values were determined by using a combination of the derivative function and graphical estimation. The reported ΔT_m values are averaged over two independent experiments and are reproducible within ±1 °C.

11.5.4 Biosensor-Surface Plasmon Resonance

Biosensor-SPR studies were performed with a four-channel Biacore 2000 optical biosensor system (GE Healthcare, Sweden) using streptavidin-derivatized sensor chips (SA). The biotinylated oligonucleotides were prepared in HEPES buffer and were immobilized using the previously described procedure ¹⁷. A series of ligand solutions (10 nM – 10 μM) prepared in HEPES buffer were injected over the DNA immobilized sensor chip at a flow rate of 25 μL/min for an association and dissociation period of 5 minutes each. After the dissociation phase, the sensor-chip surface was regenerated with 10 mM glycine solution (pH 2.5) for a short period and was followed by a series of buffer injections to obtain a stable baseline for the next series of ligand injections. The equilibrium steady-state response values (RU_{obs}) at each injected ligand concentration (C_{free}) were obtained and the values were fitted to a two-site binding model by non-linear least squares method using the following equation:

$$RU_{obs} = RU_{max/ligand} (K_1 C_{free} + 2K_1 K_2 C_{free}^2) / (1 + K_1 C_{free} + K_1 K_2 C_{free}^2) \dots\dots\dots(1)$$

where $RU_{max/ligand}$ is the predicted response for a single ligand binding. K_1 and K_2 are binding affinities for two different binding sites.

11.5.5 Fluorescence titrations

A UV-Vis absorbance scan was obtained by scanning the ligand solutions (5 μM) in Tris buffer over 800 nm to 200 nm at a rate of 60 nm/min with a 1 nm slit width to determine their maximum excitation wavelength (λ_{max}). Fluorescence experiments were performed with a Cary Eclipse Fluorescence Spectrometer (Walnut Creek, CA) at 25 °C using an excitation and emission slit widths of 5 nm and the λ_{max} of each ligand. Preannealed quadruplex DNA solutions in Tris buffer were incrementally titrated (0.05 μM) into the cuvettes containing 1 μM compound and the fluorescence emission was monitored over 500 – 800 nm wavelength range. Scans of the

quadruplex-ligand samples were collected until no further change in the fluorescence intensity was observed upon further DNA titration. The spectra were processed and plotted with Kaleidagraph 4.0 software.

11.5.6 Nuclear Magnetic Resonance

Samples for NMR (100 μ M) were prepared in 90% H₂O/10% D₂O and 20 mM potassium phosphate, pH 6.02. 4,4-dimethyl-4-silapentane-1-sulphonic acid (DSS) was added as an internal reference. NMR experiments were performed on a Avance 600 spectrometer, equipped with a 5mm QXI ¹H{³¹P,¹³C,¹⁵N} probe (Bruker). Imino proton spectra (1024 scans) were collected at 308 K using a WATERGATE w5 pulse sequence and a sweep width of 24 ppm.

11.6 Conclusions

Herein we are reporting the design, synthesis and characterization of novel series of trimethine cyanine molecules with different substituents on the indolenine rings to probe the effects on quadruplex binding. Analogous to our previous studies with penthamethine-linked cyanines, current molecules exhibit elevated quadruplex binding with considerably reduced duplex affinity. The halogen substitutions significantly increase the thermal stability and binding affinity with the quadruplex sequences with favorable preference for the parallel quadruplex motif. NMR and SPR studies show a 2:1 binding stoichiometry of the ligands while NMR and CD results support a stacking complex at the terminal tetrads of the quadruplex. The significant fluorescence enhancement observed for the parallel quadruplex over the hybrid type is a highly attractive feature of these ligands in discriminating different quadruplex folds. In summary, the current study significantly advances our knowledge in developing novel cyanine scaffolds for targeting quadruplex structures and their possible development as novel probes for G-quadruplex detection *in vivo*.

11.7 References

1. Neidle, S.; Balasubramanian, S. *Quadruplex nucleic acids*. RSC Publishers: Cambridge, UK, 2006; p 301-315.
2. Burge, S.; Parkinson, G. N.; Hazel, P.; Todd, A. K.; Neidle, S. Quadruplex DNA: sequence, topology and structure. *Nucl. Acids Res.* **2006**, 34, 5402-5415.
3. Paeschke, K.; Simonsson, T.; Postberg, J.; Rhodes, D.; Lipps, H. J. Telomere end-binding proteins control the formation of G-quadruplex DNA structures in vivo. *Nature Structural & Molecular Biology* **2005**, 12, 847-854.
4. Schaffitzel, C.; Postberg, J.; Paeschke, K.; Lipps, H. Probing Telomeric G-Quadruplex DNA Structures in Cells with In Vitro Generated Single-Chain Antibody Fragments. In *G-Quadruplex DNA*, Baumann, P., Ed. Humana Press: New York, N.Y., 2010; Vol. 608, pp 159-181.
5. Neidle, S.; Parkinson, G. N. Quadruplex DNA crystal structures and drug design. *Biochimie* **2008**, 90, 1184-96.
6. Hurley, L.; Wheelhouse, R.; Sun, D.; Kerwin, S.; Salazar, M.; Fedoroff, O.; Han, F.; Han, H.; Izbicka, E.; Von Hoff, D. G-quadruplexes as targets for drug design. *Pharmacology & Therapeutics* **2000**, 85, 141-158.
7. Biffi, G.; Tannahill, D.; McCafferty, J.; Balasubramanian, S. Quantitative visualization of DNA G-quadruplex structures in human cells. *Nat Chem* **2013**, 5, 182-186.
8. Balasubramanian, S.; Hurley, L. H.; Neidle, S. Targeting G-quadruplexes in gene promoters: a novel anticancer strategy? *Nature Reviews: Drug Discovery* **2011**, 10, 261-275.
9. Monchaud, D. A hitchhiker's guide to G-quadruplex ligands. *Organic & biomolecular chemistry* **2008**, 6, 627-636.

10. Shin-ya, K.; Wierzba, K.; Matsuo, K.-i.; Ohtani, T.; Yamada, Y.; Furihata, K.; Hayakawa, Y.; Seto, H. Telomestatin, a Novel Telomerase Inhibitor from *Streptomyces anulatus*. *Journal of the American Chemical Society* **2001**, *123*, 1262-1263.
11. Drygin, D.; Siddiqui-Jain, A.; O'Brien, S.; Schwaebe, M.; Lin, A.; Bliesath, J.; Ho, C. B.; Proffitt, C.; Trent, K.; Whitten, J. P.; Lim, J. K. C.; Von Hoff, D.; Anderes, K.; Rice, W. G. Anticancer Activity of CX-3543: A Direct Inhibitor of rRNA Biogenesis. *Cancer Research* **2009**, *69*, 7653-7661.
12. Henary, M.; Mojzych, M. Stability and Reactivity of Polymethine Dyes in Solution. In *Heterocyclic Polymethine Dyes*, Streckowski, L., Ed. Springer: Berlin, Germany, 2008; Vol. 14, pp 221-238.
13. Mojzych, M.; Henary, M. Synthesis of Cyanine Dyes. In *Heterocyclic Polymethine Dyes*, Streckowski, L., Ed. Springer: Berlin, Germany, 2008; Vol. 14, pp 1-9.
14. Nanjunda, R.; Owens, E. A.; Mickelson, L.; Alyabyev, S.; Kilpatrick, N.; Wang, S.; Henary, M.; Wilson, W. D. Halogenated pentamethine cyanine dyes exhibiting high fidelity for G-quadruplex DNA. *Bioorganic and Medicinal Chemistry* **2012**, *20*, 7002-7011.
15. Fox, K. R. *Drug-DNA Interaction Protocols*. 2nd ed.; Humana Press: New York, N.Y., 2010; p 318-329.
16. Nanjunda, R.; Musetti, C.; Kumar, A.; Ismail, M. A.; Farahat, A. A.; Wang, S.; Sissi, C.; Palumbo, M.; Boykin, D. W.; Wilson, W. D. Heterocyclic Dications as a New Class of Telomeric G-Quadruplex Targeting Agents. *Current Pharmaceutical Design* **2012**, *18*, 1934-1947.
17. Nanjunda, R.; Munde, M.; Liu, Y.; Wilson, W. D. Real-Time Monitoring of Nucleic Acid Interactions with Biosensor-Surface Plasmon Resonance. In *Methods for Studying Nucleic Acid/Drug Interactions*, Tor, Y.; Wanunu, M., Eds. CRC Press: Boca Raton, 2011; pp 91-134.

18. Munde, M.; Kumar, A.; Nhili, R.; Depauw, S.; David-Cordonnier, M.-H.; Ismail, M. A.; Stephens, C. E.; Farahat, A. A.; Batista-Parra, A.; Boykin, D. W.; Wilson, W. D. DNA Minor Groove Induced Dimerization of Heterocyclic Cations: Compound Structure, Binding Affinity, and Specificity for a TTAA Site. *Journal of Molecular Biology* **2010**, 402, 847-864.
19. Dai, J.; Carver, M.; Hurley, L. H.; Yang, D. Solution Structure of a 2:1 Quindoline–c-MYC G-Quadruplex: Insights into G-Quadruplex-Interactive Small Molecule Drug Design. *Journal of the American Chemical Society* **2011**, 133, 17673-17680.
20. Barbieri, C. M.; Srinivasan, A. R.; Rzuczek, S. G.; Rice, J. E.; LaVoie, E. J.; Pilch, D. S. Defining the mode, energetics and specificity with which a macrocyclic hexaoxazole binds to human telomeric G-quadruplex DNA. *Nucl. Acids Res.* **2007**, 35, 3272-3286.
21. Chung, W. J.; Heddi, B.; Tera, M.; Iida, K.; Nagasawa, K.; Phan, A. T. Solution structure of an intramolecular (3+1) human telomeric G-quadruplex bound to a telomestatin derivative. *Journal of the American Chemical Society* **2013**.
22. Hounsou, C.; Guittat, L.; Monchaud, D.; Jourdan, M.; Saettel, N.; Mergny, J.-L.; Teulade-Fichou, M.-P. G-Quadruplex Recognition by Quinacridines: a SAR, NMR, and Biological Study. *ChemMedChem* **2007**, 2, 655-666.
23. Campbell, N. H.; Parkinson, G. N.; Reszka, A. P.; Neidle, S. Structural Basis of DNA Quadruplex Recognition by an Acridine Drug. *Journal of the American Chemical Society* **2008**, 130, 6722-6724.
24. Blankson, G. A.; Pilch, D. S.; Liu, A. A.; Liu, L. F.; Rice, J. E.; LaVoie, E. J. Macrocyclic biphenyl tetraoxazoles: Synthesis, evaluation as G-quadruplex stabilizers and cytotoxic activity. *Bioorganic and Medicinal Chemistry* **2013**, 21, 4511-4520.

25. Ambrus, A.; Chen, D.; Dai, J.; Jones, R. A.; Yang, D. Solution Structure of the Biologically Relevant G-Quadruplex Element in the Human c-MYC Promoter. Implications for G-Quadruplex Stabilization. *Biochemistry* **2005**, *44*, 2048-2058.
26. Moyzis, R. K.; Buckingham, J. M.; Cram, L. S.; Dani, M.; Deaven, L. L.; Jones, M. D.; Meyne, J.; Ratliff, R. L.; Wu, J. R. A highly conserved repetitive DNA sequence, (TTAGGG)_n, present at the telomeres of human chromosomes. *Proceedings of the National Academy of Sciences of the United States of America* **1988**, *85*, 6622-6.
27. Makarov, V. L.; Hirose, Y.; Langmore, J. P. Long G tails at both ends of human chromosomes suggest a C strand degradation mechanism for telomere shortening. *Cell* **1997**, *88*, 657-66.
28. Yang, Q.; Xiang, J.; Yang, S.; Zhou, Q.; Li, Q.; Tang, Y.; Xu, G. Verification of specific G-quadruplex structure by using a novel cyanine dye supramolecular assembly: I. Recognizing mixed G-quadruplex in human telomeres. *Chemical Communications* **2009**, 1103-1105.
29. David, W. M.; Brodbelt, J.; Kerwin, S. M.; Thomas, P. W. Investigation of quadruplex oligonucleotide-drug interactions by electrospray ionization mass spectrometry. *Analytical Chemistry* **2002**, *74*, 2029-33.
30. Kerwin, S. M.; Sun, D.; Kern, J. T.; Rangan, A.; Thomas, P. W. G-Quadruplex DNA binding by a series of carbocyanine dyes. *Bioorganic and Medicinal Chemistry Letters* **2001**, *11*, 2411-2414.
31. Kovalska, V.; Losytskyy, M.; Yarmoluk, S.; Lubitz, I.; Kotlyar, A. Mono and Trimethine Cyanines Cyan 40 and Cyan 2 as Probes for Highly Selective Fluorescent Detection of Non-canonical DNA Structures. *Journal of Fluorescence* **2011**, *21*, 223-230.

32. Kanony, C.; Åkerman, B.; Tuite, E. Photobleaching of Asymmetric Cyanines Used for Fluorescence Imaging of Single DNA Molecules. *Journal of the American Chemical Society* **2001**, *123*, 7985-7995.
33. Mohammed, H. S.; Delos Santos, J. O.; Armitage, B. Noncovalent binding and fluorogenic response of cyanine dyes to DNA homoquadruplex and PNA-DNA heteroquadruplex structures. *Artificial DNA: PNA & XNA* **2011**, *2*, 43-49.
34. Dai, J.; Carver, M.; Yang, D. Polymorphism of human telomeric quadruplex structures. *Biochimie* **2008**, *90*, 1172-1183.
35. Phan, A. T.; Kuryavyi, V.; Patel, D. J. DNA architecture: from G to Z. *Current Opinion in Structural Biology* **2006**, *16*, 288-98.
36. Hamon, F.; Largy, E.; Guédin-Beaurepaire, A.; Rouchon-Dagois, M.; Sidibe, A.; Monchaud, D.; Mergny, J.-L.; Riou, J.-F.; Nguyen, C.-H.; Teulade-Fichou, M.-P. An Acyclic Oligoheteroaryle That Discriminates Strongly between Diverse G-Quadruplex Topologies. *Angewandte Chemie (International Edition)* **2011**, *50*, 8745-8749.
37. Fasman, G. D. *Handbook of Biochemistry and Molecular Biology, Nucleic Acids*. CRC Press: Cleveland, 1975; Vol. 1, p 589.

12 PENTAMETHINE CYANINES WITH HIGH FIDELITY TO QUADRUPLEX DNA

This chapter is adapted from my publication in Bioorganic and Medicinal Chemistry in collaboration with Dr. David Wilson's lab at Georgia State University. My contributions as co-

first author included the synthesis of the binding ligands, interpretation of data, experimental design and manuscript preparation.

Nanjunda, R.*, Owens, E.A.*, Alyaybev, S., Mickelson, L., Wilson, W. D., Henary, M., Synthesis and Biophysical Analyses of the Interactions of Diverse Pentamethine Cyanine Dyes with G-Quadruplex DNA **2012** *Bioorg. & Med. Chem.* 20, 24, 7002-11. *Co-First Authors

12.1 Abstract

Design and optimization of quadruplex-specific small molecules is developing into an attractive strategy for anti-cancer therapeutics with some promising candidates in clinical trials. A number of therapeutically favorable features of cyanine molecules can be effectively exploited to develop them as promising quadruplex-targeting agents. Herein, the design, synthesis and evaluation of a series of dimethylindoliene cyanine dyes with varying halogen substitutions are reported. Their interactions with telomeric and *c-myc* quadruplexes as well as a reference duplex sequence have been evaluated using thermal melting analysis, biosensor-surface plasmon resonance, circular dichroism spectroscopy, isothermal titration calorimetry and mass spectrometry. Thermal melting analysis indicates that these ligands exhibit significant quadruplex stabilization and a very low duplex binding, with the dimethyl incorporation being of utmost importance for decreased duplex affinity. Circular dichroism studies showed that the interaction of cyanines with quadruplex structures are primarily through stacking at one or both ends of the terminal tetrads with the two (trimethylammonium)propyl groups interacting in the accessible quadruplex grooves. Surface plasmon resonance and mass spectral studies shows the formation of an initial strong 1:1 complex followed by a significantly weaker secondary binding. Isothermal calorimetry studies show that the interaction of cyanines is predominantly entropy driven. In line

with the design principles, this work provides new insights for further developing potent, highly selective cyanines as promising quadruplex-specific agents.

12.2 Introduction

It has now been convincingly demonstrated that small molecules that target quadruplexes can have cellular anticancer activity and this area is promising for new drug development.[1-4] One compound has entered clinical trials with encouraging initial results against neuroendocrine cancer.[5] In spite of this success, additional quadruplex targeting compounds that display appealing pharmacodynamics with selective quadruplex binding remain highly desirable. A review of quadruplex-targeting structures illustrates a dominance of planar aromatic substituents and an overall cationic nature.[6-9] The charged groups are frequently located on a flexible chain that is linked to the aromatic system. A common binding mode for compounds displaying this motif is stacking of the aromatic moiety on the terminal tetrads of the quadruplex and the flexible cationic group(s) in one or more of the quadruplex grooves. With this model in mind a systematic set of new cationic carbocyanines (Figure 1) were designed and synthesized as potentially selective ligands for DNA quadruplexes.

Cyanine dyes have extensive applications including cancer imaging, nucleic acid detection, photographic processes, and nonlinear optical materials that utilize their outstanding photophysical properties.[10, 11] Synthetic cyanines have characteristics, such as low toxicity and stability towards chemical decomposition, that make their cellular use extremely appealing. Additionally, this class of compounds displays excellent biocompatibility while being amenable to diverse chemical modifications.[10] With multiple synthetically active sites, there exist a multitude of carbocyanine dyes that can be designed and tested. Various cyanine supramolecular assemblies have been shown to probe the presence of the G-quadruplex structure in human telomere

sequences.[12] Cyanine dyes have been explored as fluorescent tags to observe the three-dimensional folding properties of G-quadruplex DNA structures and dyes based on the benzothiazole heterocyclic moiety have been shown to inhibit telomerase *via* a suggested G-quadruplex stabilization mechanism.[13] The benzothiazole cyanines, however, generally have very strong DNA duplex minor groove interactions; therefore, a systematic set of dimethylindolenine-based pentamethine cyanine dyes were synthesized to induce steric hindrance toward insertion of the compound into the duplex minor groove. Ammonium cations were introduced to the heterocyclic nitrogen to enhance solubility and increase quadruplex affinity by electrostatic interactions. Further structural diversity was achieved by halogenation at the 5-position and the *meso*-carbon of the polymethine-bridge. The interactions of these cyanine analogs with quadruplex and duplex DNA were evaluated using a variety of powerful biophysical techniques, including: DNA thermal melting screening, biosensor-surface plasmon resonance, circular dichroism, isothermal calorimetry and mass spectrometry. These methods reveal encouraging results as these cyanine structures bind strongly to quadruplexes with excellent selectivity over duplex DNA.

12.3 Results

12.3.1 Chemistry

In order to optimize the binding specificity and strength, we utilized the general 2,3,3-trimethylindolenine heterocyclic scaffold with heterocyclic halogenation and a 3-(trimethyl ammonium)propyl bromide substituent on the indolenine nitrogen. The synthetic pathway for obtaining the final pentamethine structures begins with Fischer-indole synthesis utilizing hydrazine derivatives **1-3** with 3-methyl-2-butanone to form modified Fischer-bases **4-6** (Figure 1). These obtained indolenine derivatives **4-6** were alkylated with (3-bromopropyl) trimethylammonium

bromide in anhydrous acetonitrile yielding dicationic salts **7-9**. Reagent **10** was commercially obtained and compounds **11** and **12** were prepared by decarboxylation of either mucochloric or mucobromic acid by aniline. Salts **7-9** were individually reacted with **10-12** in absolute ethanol under basic conditions to yield the nine corresponding tricationic pentamethine carboycyanine dyes **13-21** with varied halogen substituents.

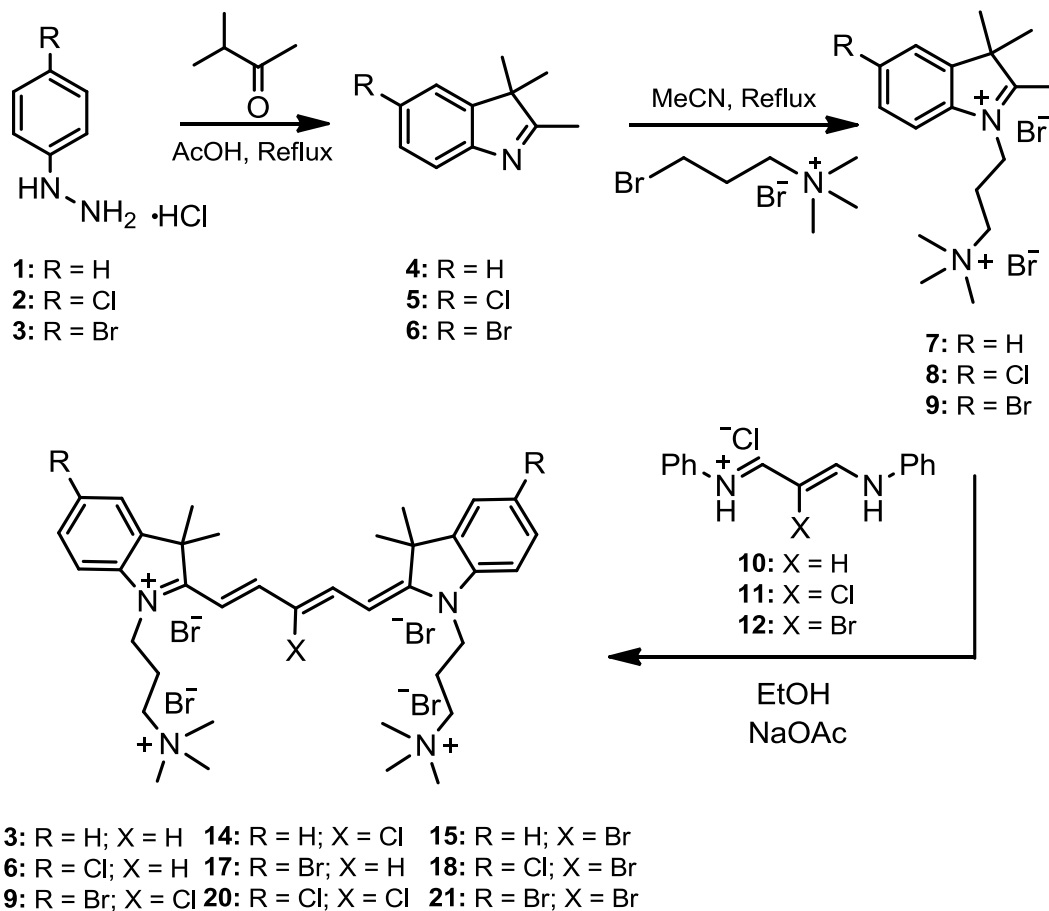


Figure 12-1. The synthesis of the cyanine structures used in developing G-quadruplex binding agents.

12.3.2 Thermal Melting (T_m)

An initial comparison of the interaction of all cyanines with Tel22 quadruplex and duplex DNA was done using UV thermal melting studies as a screening assay. Thermal melting studies

were done only with the telomeric G-quadruplex because the melting temperature of *c-myc* quadruplex is too high under the currently studied salt conditions (50 mM KCl) and the changes in T_m for most of the compounds go beyond the measurable limit. The ΔT_m results at ratios of cyanine to DNA ranging from 2:1 to 6:1 are shown in Table 1. The parent cyanine, compound **13**, shows a relatively low ΔT_m for Tel22. Adding chlorine (**14**) or bromine (**15**) atom to the central carbon of the pentamethine chain resulted in a large increase in ΔT_m with no significant difference between the Cl or Br compounds. Pentamethine cyanines with heterocyclic halogenation were then tested. Di-halogenated compounds (with terminal Cl and Br, compounds **16** and **17** respectively) do not show any increase in ΔT_m over the mono-substituted derivatives. The tricationic pentamethine structure was then synthesized with the incorporation of three halogen substituents (**18-21**) and these showed a substantial increase in the ΔT_m with no significant difference between the Cl and Br derivatives. In summary, pentamethine cyanines with multiple halogen substituents bind to the telomeric quadruplex much more strongly than the unsubstituted parent and with very high selectivity over duplex DNA. The selectivity of these compounds is clearly very promising.

Table 12-1. Thermal melting studies of the cyanine analogs with telomeric quadruplex (Tel22) and a control duplex (AATT). The thermal melting values reported are reproducible within ± 1 °C. \$ could not be accurately determined due to complex aggregation.

Compound	Tel22 (2:1, 4:1, 6:1 ratios)	Duplex (6:1 ratio)
13	2.1, 4.6, 8.7	0
14	4.6, 12.2, 13.2	2.8
15	4.6, 11.6, 15.6	0.1
16	3.1, 8.9, 13.2	0.5
17	2.5, 15.6, --- ^{\$}	1.1
18	8.0, 17.0, 20.0	1.8
19	9.0, 16.0, 21.0	2.5

20	7.0, 15.0, 19.0	2.3
21	8.0, 16.2, 20.3	1.2

12.3.3 Surface Plasmon Resonance (SPR)

Biosensor-SPR studies were conducted with biotinylated, sensor-surface captured quadruplex and duplex sequences to quantitatively evaluate the binding affinity, selectivity and stoichiometry of the cyanine analogs. Figure 2 shows the SPR sensorgrams and the steady-state affinity plots for the parent compound (**13**), with the two quadruplex and reference duplex DNA sequences, and the binding affinities of all cyanine derivatives are summarized in Table 2. All the compounds exhibited an initial strong binding followed by a weaker (ca. 5 – 50 fold) secondary binding for both quadruplex sequences, while binding to the duplex sequence was quite low to negligible for all the compounds. The binding kinetics were rapid under the experimental conditions with both association and dissociation reactions occurring near the instrument injection mixing limit. Among the mono-substituted analogs, the bromo substitution (**15**) resulted in a slight increase in the binding affinity ($K_1 = 1.7 \times 10^6 \text{ M}^{-1}$) relative to the parent compound ($K_1 = 1.3 \times 10^6 \text{ M}^{-1}$), whereas, the chloro substitution (**14**) resulted in a decrease in the affinity with the Tel22 quadruplex. Among the symmetric, tri-substituted and mixed halogen derivatives, no improvement in the binding was observed relative to the parent compound (Table 2).

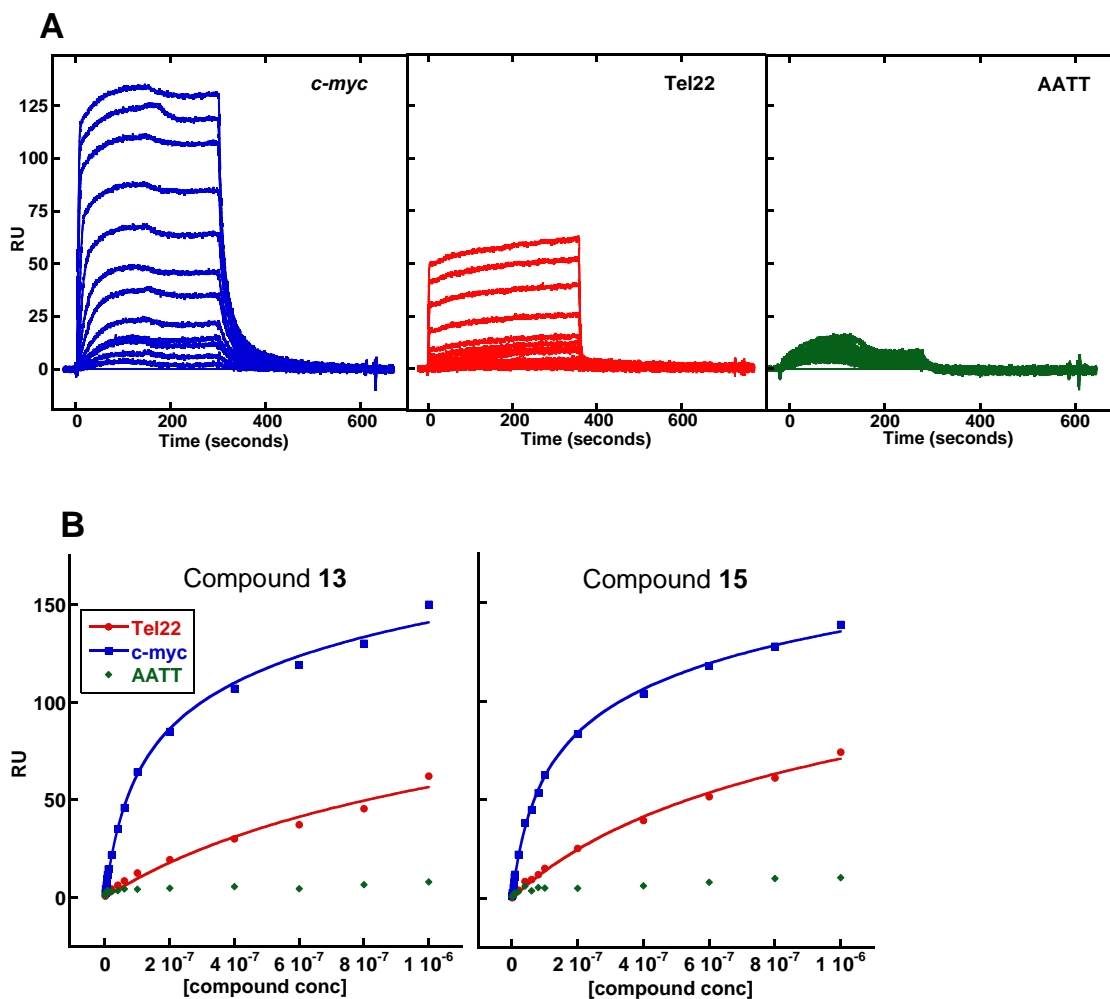


Figure 12-2. (A) SPR sensorgram of compound 13 with the two quadruplex as well as a reference duplex sequence. (B) Steady-state equilibrium binding plots of analogs 13 and 15. The solid colored lines are the fits obtained using a two-site model. In all cases, the steady-state response with duplex sequence was too low to fit reasonably.

Table 12-2. Equilibrium binding constants of the cyanine analogs with quadruplex and duplex sequences obtained from SPR studies. The steady-state response obtained as a function of free

ligand concentration was fitted to a two-site model to obtain K_1 and K_2 . In all the cases, no duplex binding was observed suggesting a high selectivity of the ligands.

Compound	Tel22 (K_1, K_2) x 10^6 M ⁻¹	<i>c-myc</i> (K_1, K_2) x 10^6 M ⁻¹	Duplex
13	1.3, 0.17	11.9, 0.07	< 10 ⁵
14	0.56, 0.08	9.7, 0.60	< 10 ⁵
15	1.7, 0.74	13.0, 0.07	< 10 ⁵
16	No binding	No binding	No binding
17	0.79, 0.59	5.5, 3.6	No binding
18	1.0, 0.13	7.2, 0.25	< 10 ⁵
19	0.35, 0.05	4.8, 0.20	< 10 ⁵
20	0.59, 0.08	8.0, 0.23	< 10 ⁵
21	0.39, 0.06	9.7, 2.0	< 10 ⁵

Interestingly, all the compounds exhibited a similar trend in the relative binding affinities with the *c-myc* quadruplex but with a significantly stronger binding (ca. 10 – 25 fold higher than the telomere) and a similar weak secondary binding. The duplex binding in all the cases was too low to detect in the concentration range that was tested. These results show a high selectivity for quadruplex sequences and confirm the selectivity observed in thermal melting studies. The lack of an increase in affinity for the halogens, relative to the parent, as expected from the T_m results, may be due to some absorption of the halogen derivatives to the sensor surface and resulting decrease in the compound concentration.

12.3.4 Mass Spectrometry (MS)

To quantitatively and directly evaluate complex stoichiometry, mass spectrometry was done on the complexes at several compound:DNA ratios to obtain an independent determination of binding stoichiometry. Experiments were conducted with all three bromo compounds and results for compounds **13** and **15** are shown in Figure 3. For free DNA, the -4 and -5 charge species dominate and are of similar magnitude. On addition of the compound, a 1:1 complex peak can be

seen. As the ratio is increased, the 1:1 peak grows in intensity and a smaller 2:1 peak can be seen at higher ratios. It is clear from the mass spectrometry results that the binding is a two site non-cooperative interaction in agreement with the SPR analysis.

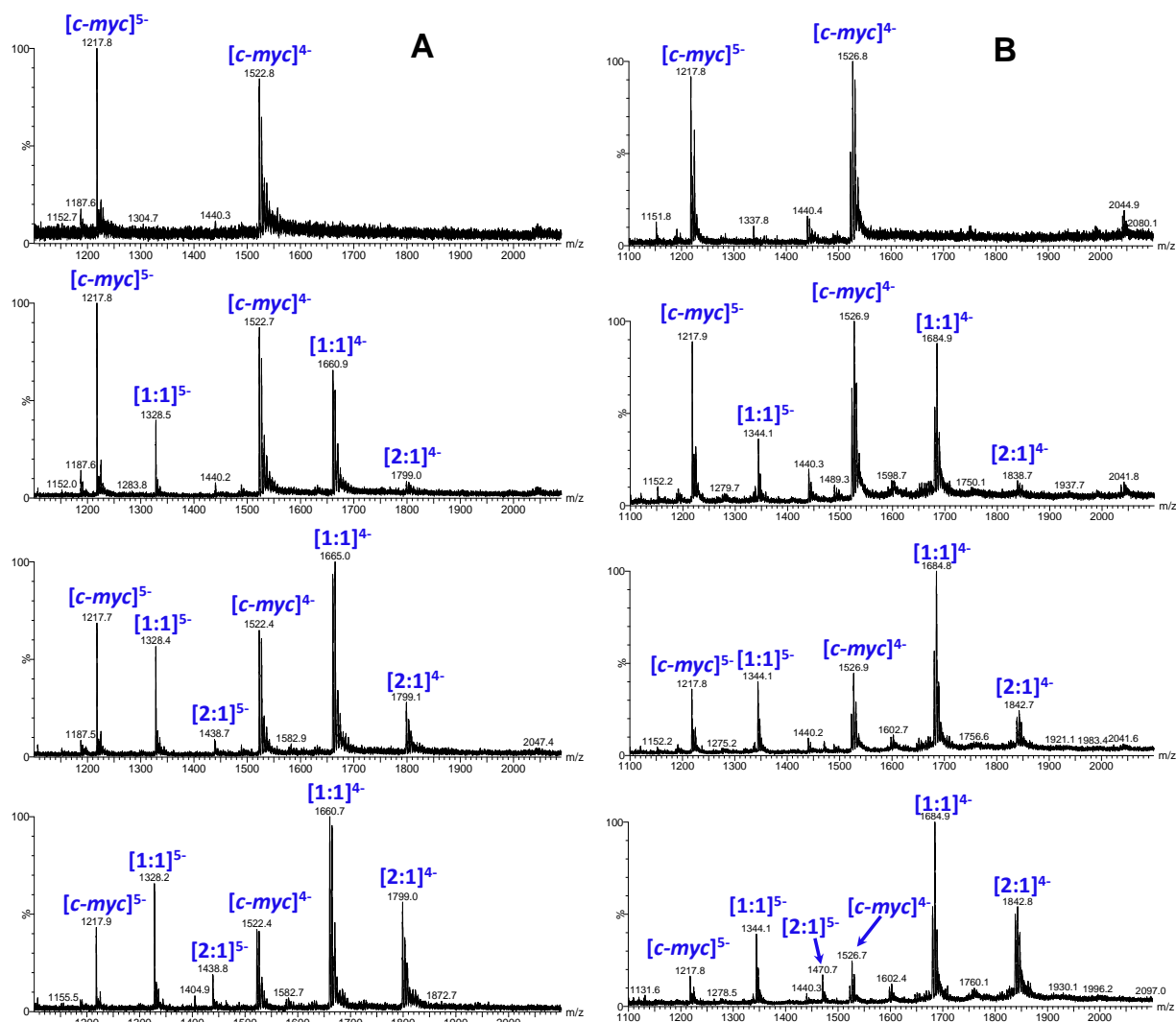


Figure 12-3. Mass spectra of *c-myc* quadruplex with 0:1, 1:1, 2:1, 4:1 ratios (top to bottom) of parent dye 13 (A) and mono-brominated compound 15 (B).

12.4 Discussion

The discovery of G-quadruplex structures and their potential involvement in important biological pathways as well as cancer development has significantly extended our understanding

of the importance of non-B-form DNA structures in cell function. In addition, such non-B structures can provide an alternate platform for developing structure-specific small molecules as part of a new therapeutic approach. To use the DNA quadruplex structure as a platform for anticancer drug development, it is essential to design and discover new agents that can discriminate between quadruplex and duplex structures with very high selectivity. Furthermore, the diversity of quadruplex conformations found in the genome also makes the development of ligands that can discriminate between different quadruplex folds quite attractive.[2, 14, 15] The dimethylindolenine cyanine scaffold was selected based on the concepts that it could not fit into the minor groove, as with planar cyanines, but could stack on the terminal tetrads of quadruplex structure with cationic chains in the quadruplex grooves. A survey of all the approved drugs that are currently being used as well as the drug candidates that are in clinical development shows that a majority of the drugs have halogen atoms incorporated to increase the pharmacological properties of the drug molecule.[16-18] While fluorine and chlorine are the most prevalent halogens used, brominated drugs can also increase the desired pharmacological features.[19] With this in mind for an initial test series, coupled with a number of features of cyanine molecules that are considered to be therapeutically favorable, a series of pentamethine-bridged cyanine analogs with various combinations of chlorine and bromine substitutions on the core aromatic system as well as on the meso-carbon of the pentamethine chain were synthesized. Their quadruplex binding potential and selectivity over duplex binding were evaluated using a complementary series of biophysical techniques.

The initial screening with thermal melting showed a very high selectivity by all the cyanine analogs for the quadruplex over duplex structures. This very promising finding is consistent with the design principles aimed at the development of strong quadruplex and weaker duplex binding.

The thermal stability of the quadruplex sequence further increased with the addition of halogens and with the tri-halogenated analogs inducing the highest stability. The introduction of either chlorine or bromine clearly increased the stabilization potential as compared to the parent molecule, however, no significant difference in the thermal melting values were found between the Cl or Br analogs as they both bound strongly to quadruplexes. The presence of polar atoms such as chlorine and bromine clearly has a positive and an additive effect on the binding to the quadruplex sequence. The lack of significant selectivity between Cl and Br suggests that the unfavorable steric contributions are minimal for these substitutions. Furthermore, the presence of two bulky methyl groups on both aromatic rings provides a steric hindrance to minimize binding to the duplex sequence.

Circular dichroism analysis indicates an end-stacking binding mode for all the ligands with quadruplex structures, based on the presence of characteristic weak ICD signals in the compound absorbance region upon complex formation (data not shown). This weak ICD is a commonly observed pattern for ligands that either intercalate with duplex sequences or stack on the terminal tetrads of quadruplex motifs.[9, 20-22] The two 3-(trimethylammonium)propyl substituents on these cyanine systems (Figure 1) can favorably interact with the accessible grooves of the quadruplex. These results are further supported by the presence of an initial strong binding site detected by SPR studies. The two-site model predicted an initial strong binding that can be attributed to end-stacking and a significantly weaker secondary binding. This stoichiometry analysis was strongly supported by the mass spectral results where the formation of a predominant 1:1 complex species and a weaker 2:1 complex was observed.

12.5 Conclusions

In conclusion, a series of halogenated cyanine dyes were systematically designed, synthesized and tested for their interaction potential with quadruplex sequences using complementary lines of biophysical techniques. In conjunction with the design principles, to enhance quadruplex specificity with low duplex affinity, several of the cyanine analogs in this study showed elevated binding to both telomeric and *c-myc* quadruplex structures while maintaining a very low duplex selectivity. The dimethyl substitutions on both indolenine rings provide the necessary steric hindrance for the cyanine moiety to decrease duplex groove interactions, while the more polar halogen substitutions enhanced quadruplex binding. Thermal melting studies showed a relative increase in quadruplex stability as the number of halogen substitutions was increased. The small ICD signal observed upon complex formation indicates that the cyanines are interacting with the quadruplex structure primarily through end-stacking mode. The formation of a strong 1:1 complex as observed in SPR and mass spectral studies further supports the end-stacking binding mode of the ligands. The currently designed ligands provide the necessary platform in developing further potent cyanine molecules as promising quadruplex-specific agents.

12.6 Experiments

12.6.1 Pentamethine Dye Synthesis

Sigma Aldrich or TCI America were the commercial sources for the starting materials utilized in the presented synthesis and the reagents were used without purification. The ^1H NMR and ^{13}C NMR spectra were recorded on a Bruker Avance (400 MHz) spectrometer using DMSO- d_6 or MeOD- d_4 containing tetramethylsilane (TMS) as an internal calibration standard. UV-Vis/NIR absorption spectra were recorded on a Varian Cary 50 spectrophotometer. High-

resolution accurate mass spectra (HRMS) were obtained either at the Georgia State University Mass Spectrometry Facility using a Waters Q-TOF micro (ESI-Q-TOF) mass spectrometer or utilizing a Waters Micromass LCT TOF ES+ Premier Mass Spectrometer. Liquid chromatography (LC) utilized a Waters 2487 single wavelength absorption detector with wavelengths set between 640 and 700 nm depending on the dye's photophysical properties. The column used in LC was a Waters Delta-Pak 5 μ M 100A 3.9 x 150 mm reversed phase C₁₈ column. Evaporative light scattering detection analyzes trace impurities that cannot be observed by alternate methods; a SEDEX 75 ELSD was utilized in tandem with liquid chromatography to observe and confirm purity.

5-chloro-2,3,3-trimethyl-3H-indole (**5**) and *5-bromo-2,3,3-trimethyl-3H-indole* (**6**) were prepared using the procedure published by Zimmermann *et. al.*⁶ They were obtained as reddish brown oils in 71% and 90% yield, respectively.

General Synthetic Procedure for Preparation of Heterocyclic Salts:

A mixture of corresponding indole derivative **4-6** (31.4 mmol) and 3-bromopropyl trimethylammonium bromide (9.0 g, 34.5 mmol) was refluxed for 72 hrs in anhydrous acetonitrile (100 mL) under nitrogen. The reaction was cooled to room temperature and solid product precipitated after 4 hours. The precipitate was filtered and was washed with acetone and diethyl ether.

2,3,3-trimethyl-1-(3-(trimethylammonio)propyl)-3H-indol-1-ium bromide (**7**) was synthesized by our group and is previously reported.⁷

5-chloro-2,3,3-trimethyl-1-(3-(trimethylammonio)propyl)-3H-indol-1-ium bromide (**8**)
Yield 82%; M.P. 215-217 °C; ¹HNMR (400 MHz, DMSO-*d*₆), δ : 1.65 (s, 6H), 2.56 (t, *J* = 8.0 Hz, 2H), 3.25 (s, 9H), 3.73 (tt, *J* = 8.0 Hz, *J* = 8.0 Hz, 2H), 4.64 (t, *J* = 8.0 Hz, 2H), 4.80 (s, 3H), 7.69

(dd, $J = 8.8$ Hz, $J = 2.0$ Hz, 1H), 7.84-7.92 (m, 2H); ^{13}C NMR (100 MHz, DMSO- d_6): δ 12.2, 20.0, 20.7, 43.3, 52.1, 53.2, 61.5, 115.9, 123.3, 128.8, 134.3, 138.2, 142.3, 197.9. Composition in theory: C(44.91%), H(5.99%), N(6.16%); Composition found: C(45.01%), H(6.29%), N(6.08%); HRMS (ESI) calculated for $[\text{C}_{17}\text{H}_{27}\text{ClN}_2]^{2+}$ m/z 147.4356, found m/z 146.9909, 148.0421

5-bromo-2,3,3-trimethyl-1-(3-(trimethylammonio)propyl)-3H-indol-1-ium bromide (9)

Yield 81%; M.P. 225-227 °C; ^1H NMR (400 MHz, DMSO- d_6), δ : 1.57 (s, 6H), 2.27 (s, 9H), 3.02 (s, 3H), 3.83 (t, $J = 8.0$ Hz, 2H), 4.57 (t, $J = 8.0$ Hz, 2H), 7.61 (m, 2H), 7.88 (t, $J = 5.6$ Hz, 1H). ^{13}C NMR (100 MHz, DMSO- d_6): δ 15.2, 22.0, 25.5, 30.6, 52.3, 54.3, 63.9, 115.6, 123.5, 128.8, 129.3, 140.9, 141.7, 197.7. Composition in theory: C(40.91%), H(5.45%), N(5.61%); Composition found: C(40.84%), H(5.48%), N(5.94%); HRMS (ESI) calculated for $[\text{C}_{17}\text{H}_{27}\text{BrN}_2]^{2+}$ m/z 169.6611, found m/z 169.7002.

General Synthetic Procedure for the Preparation of Methine Bridge Reagent

(E)-N-((Z)-2-chloro-3-(phenylamino)allylidene) benzenaminium chloride (11) was synthesized using the reported procedure. 88% yield; M.P. 214-216°C.

(E)-N-((Z)-2-bromo-3-(phenylamino)allylidene) benzenaminium chloride (12): Mucobromic acid (5.940 g, 23.04 mmol) was dissolved in ethanol (40 mL) and aniline (4.286 g, 4.2 mL, 46.1 mmol), diluted with ethanol (20 mL), was added dropwise over a 10-minute period. The reaction vessel was under vigorous stirring and was gently heated to 40 °C. After the addition of aniline was finished, CO_2 (g) was further produced indicating the reaction was not complete. Upon completion of CO_2 (g) evolution, the golden brown reaction mixture was cooled in an ice bath. Diethyl ether (50 mL) was added slowly at reduced temperature under heavy stirring until a bright yellow solid precipitated. The resulting solid was filtered, washed with ether, dried and was used without purification in subsequent reactions. Yield 75%; M.P. 189-191°C; ^1H NMR (400

MHz, DMSO- d_6): δ 7.330 (t, J = 7.2 Hz, 2H), 7.496 (t, J = 8 Hz, 4H), 7.708 (d, J = 8 Hz, 4H), 9.559 (s, 2H), 11.513 (s, 2H); ^{13}C NMR (100 MHz, DMSO- d_6): δ 89.3, 119.5, 123.9, 126.0, 129.2, 129.6, 138.5, 157.4.

General procedure for obtaining tricationic pentacarbocyanines **13-21**

A mixture of individual salts **7-9** (2 equivalents), either malonaldehyde bisphenylimine monohydrochloride **10**, chlorinated analog **11** or brominated analog **12** (1 equivalent) and sodium acetate (3 equivalents) were refluxed for 6 hrs in anhydrous ethanol under nitrogen atmosphere and then cooled to room temperature. The reaction mixture was concentrated *in vacuo*. The crude product was dissolved in deionized water and the target compounds **9-12** were isolated using silica gel 40-63 μm 90Å C_{18} reversed phase column chromatography using 20% methanol in water as eluting solvent.

2-((1E,3E,5E)-5-(3,3-dimethyl-1-(3-(trimethylammonio)propyl)indolin-2-ylidene)penta-1,3-dien-1-yl)-3,3-dimethyl-1-(3-(trimethylammonio)propyl)-3H-indol-1-ium bromide (13) Yield 71%; M.P. 218-221 °C; ^1H NMR (400 MHz, MeOD- d_4): δ 1.781 (s, 12H), 2.359-2.380 (m, 4H), 3.248 (s, 18H), 3.750 (t, J = 8.4 Hz, 4H), 4.254 (t, J = 7.6 Hz, 4H), 6.628 (d, J = 13.6 Hz, 2H), 7.140 (t, J = 12.4 Hz, 1H), 7.287-7.327 (m, 2H), 7.436-7.486 (m, 4H), 7.540 (d, J = 7.6 Hz, 2H), 8.345 (t, J = 13.2 Hz, 2H); ^{13}C NMR (400 MHz, MeOD- d_4): δ 20.93, 26.56, 40.26, 49.22, 52.49, 63.08, 103.72, 110.41, 122.20, 125.07, 127.11, 128.50, 141.23, 141.76, 154.80, 173.47. High-resolution electrospray ionization (ESI) accurate mass spectra calculated m/z for $\text{C}_{37}\text{H}_{55}\text{N}_4\text{Br}_2$ 713.2793, found 713.2767.

2-((1E,3Z,5E)-3-chloro-5-(3,3-dimethyl-1-(3-(trimethylammonio)propyl)indolin-2-ylidene)penta-1,3-dien-1-yl)-3,3-dimethyl-1-(3-(trimethylammonio)propyl)-3H-indol-1-ium bromide (14) Yield 46%; M.P. 225-227°C; ^1H NMR (400 MHz, DMSO- d_6): δ 1.81 (s, 12H), 2.40

(t, $J = 7.4$ Hz, 4H), 3.26 (s, 18H), 3.71-3.79 (m, 4H), 4.38 (t, $J = 7.6$ Hz, 4H), 6.55 (d, $J = 13.4$ Hz, 2H), 7.36 (t, $J = 7.2$ Hz, 2H), 7.50 (t, $J = 7.6$ Hz, 2H), 7.58 (d, $J = 7.6$ Hz, 2H), 7.63 (d, $J = 7.6$ Hz, 2H), 8.50 (d, $J = 13.4$ Hz, 2H); ^{13}C NMR (100 MHz, DMSO- d_6), δ : 20.9, 26.0, 40.7, 49.4, 52.5, 63.0, 100.9, 111.9, 122.2, 123.2, 125.6, 128.6, 141.4, 141.7, 148.2, 175.1. Composition in theory: (x3H₂O): C (50.27%), H (6.84%), N (6.34%); Composition found: C (50.16%), H (6.78%), N (6.26%); HRMS (ESI) calculated for [C₃₇H₅₄ClN₄]³⁺ m/z 196.7742, found m/z 194.9509, 197.1837.

2-((1E,3Z,5E)-3-bromo-5-(3,3-dimethyl-1-(3-(trimethylammonio)propyl)indolin-2-ylidene)penta-1,3-dien-1-yl)-3,3-dimethyl-1-(3-(trimethylammonio)propyl)-3H-indol-1-ium bromide (15) Yield 66%; M.P. 174-176°C; ^1H NMR (400 MHz, DMSO- d_6): δ 1.77 (s, 12H), 2.31 (t, $J = 7.1$ Hz, 4H), 3.13 (s, 18H), 3.58-3.68 (m, 4H), 4.34 (t, $J = 7.0$ Hz, 4H), 6.40 (d, $J = 13.2$ Hz, 2H), 7.61 (d, $J = 8.6$ Hz, 2H), 7.76 (d, $J = 8.6$ Hz, 2H), 8.11 (s, 2H), 8.61 (d, $J = 13.2$ Hz); ^{13}C NMR (100 MHz, DMSO- d_6), δ : 22.4, 27.6, 42.2, 51.8, 54.0, 64.2, 112.3, 118.3, 123.2, 127.1, 130.8, 143.6, 151.3, 176.1. Composition in theory: C (50.82), H (6.22), N (6.41); Composition found: C (50.48), H (6.75), N (6.45). High-resolution electrospray ionization (ESI) accurate mass spectra calculated m/z for C₃₇H₅₄N₄Br₂ 712.2715, found 712.2722.

5-chloro-2-((1E,3E,5E)-5-(5-chloro-3,3-dimethyl-1-(3-(trimethylammonio)propyl)indolin-2-ylidene)penta-1,3-dien-1-yl)-3,3-dimethyl-1-(3-(trimethylammonio)propyl)-3H-indol-1-ium bromide (16) Yield 88%; ^1H NMR (400 MHz, MeOD- d_4): δ 1.78 (s, 12H), 2.32 (s, 4H), 3.25 (s, 18H), 3.75 (t, $J = 8.4$ Hz, 4H), 4.24 (t, $J = 7.6$ Hz, 4H), 6.60 (d, $J = 13.2$ Hz, 2H), 7.11 (t, $J = 12.4$ Hz, 1H), 7.50-7.43 (m, 4H), 7.58 (s, 2H), 8.35 (t, $J = 13.2$ Hz, 2H). ^{13}C NMR (400 MHz, MeOD- d_4): δ 20.89, 26.50, 40.58, 49.35, 52.57, 63.05, 104.20, 111.92, 122.72, 127.75, 128.49, 130.54, 140.59, 143.15, 155.05, 173.28. High-resolution

electrospray ionization (ESI) accurate mass spectra calculated m/z for $[C_{37}H_{53}N_4Cl_2]^{3+}$ 207.7877 found 207.7555; calculated m/z for $[C_{37}H_{53}N_4Cl_2]^{2+}$ 311.6818, found 311.1284.

5-bromo-2-((1E,3E,5E)-5-(5-bromo-3,3-dimethyl-1-(3-(trimethylammonio)propyl)indolin-2-ylidene)penta-1,3-dien-1-yl)-3,3-dimethyl-1-(3-(trimethylammonio)propyl)-3H-indol-1-ium bromide (17) Yield 62%; M.P. 237-240 °C; 1H NMR (400 MHz, MeOD- d_4): δ 1.782 (s, 12H), 2.318 (t, $J = 7.1$ Hz, 4H), 3.241 (s, 18H), 3.707-3.750 (m, 4H), 4.224 (t, $J = 7.2$ Hz, 4H), 6.642 (d, $J = 13.6$ Hz, 2H), 7.176 (t, $J = 12.8$ Hz, 1H), 7.384 (d, $J = 8.4$ Hz, 2H), 7.611 (d, $J = 8.4$ Hz, 2H), 7.735 (s, 2H), 8.362 (t, $J = 12.8$ Hz, 2H); ^{13}C NMR (400 MHz, MeOD- d_4): δ 20.89, 26.06, 26.50, 40.55, 49.32, 52.60, 63.03, 104.27, 112.25, 117.93, 125.63, 131.45, 141.04, 143.44, 155.07, 173.11 High-resolution electrospray ionization (ESI) accurate mass spectra calculated m/z for $C_{37}H_{52}N_4Br_2$ 710.2559, found 710.2552.

2-((1E,3Z,5E)-3-bromo-5-(5-chloro-3,3-dimethyl-1-(3-(trimethylammonio)propyl)indolin-2-ylidene)penta-1,3-dien-1-yl)-5-chloro-3,3-dimethyl-1-(3-(trimethylammonio)propyl)-3H-indol-1-ium bromide (18) Yield 88%; M.P. 238-240°C; 1H NMR (400 MHz, DMSO- d_6): δ 1.77 (s, 12H), 2.19 (t, $J = 7.6$ Hz, 4H), 3.13 (s, 18H), 3.63 (tt, $J = 7.6$ Hz, $J = 7.8$ Hz, 4H), 4.25 (t, $J = 7.8$ Hz, 4H), 6.34 (d, $J = 13.4$ Hz, 2H), 7.53 (d, $J = 8.0$ Hz, 2H), 7.68 (d, $J = 8.0$ Hz, 2H), 7.94 (s, 2H), 8.61 (d, $J = 13.4$ Hz, 2H); ^{13}C NMR (400 MHz, DMSO- d_6), δ : 18.5, 20.6, 26.4, 41.4, 49.8, 52.3, 62.2, 102.7, 113.3, 117.0, 123.2, 128.3, 130.1, 140.5, 143.4, 150.3, 174.4. Composition in theory: (x3H₂O): C (44.56%), H (5.86%), N (5.62%); Composition found: C (44.54%), H (5.78%), N (5.56%); HRMS (ESI) calculated for $[C_{37}H_{52}BrCl_2N_4]^{3+}$ m/z 234.5546, found m/z 234.0587, 236.0536.

5-bromo-2-((1E,3Z,5E)-5-(5-bromo-3,3-dimethyl-1-(3-(trimethylammonio)propyl)indolin-2-ylidene)-3-chloropenta-1,3-dien-1-yl)-3,3-dimethyl-1-(3-

(trimethylammonio)propyl)-3*H*-indol-1-ium bromide (**19**) Yield 80%; M.P. 227-229°C; ¹HNMR (400 MHz, DMSO-*d*₆): δ 1.76 (s, 12H), 2.17 (t, *J* = 7.0 Hz, 4H), 3.12 (s, 18H), 3.58-3.68 (m, 4H), 4.26 (t, *J* = 6.8 Hz, 4H), 6.35 (d, *J* = 13.4 Hz, 2H), 7.61 (d, *J* = 8.6 Hz, 2H), 7.65 (d, *J* = 8.6 Hz, 2H), 8.05 (s, 2H), 8.56 (d, *J* = 13.4 Hz, 2H); ¹³CNMR (400 MHz, DMSO-*d*₆), δ: 20.7, 26.4, 41.2, 49.7, 52.3, 62.2, 100.3, 113.7, 118.1, 123.5, 126.0, 131.3, 140.4, 143.5, 148.7, 174.9. Composition in theory: (x3H₂O): C (42.65%), H (5.61%), N (5.38%); Composition found: C (42.09%), H (5.80%), N (5.26%); HRMS (ESI) calculated for [C₃₇H₅₂Br₂ClN₄]³⁺ *m/z* 249.3716, found *m/z* 248.9238, 251.0310.

5-chloro-2-((1*E*,3*Z*,5*E*)-3-chloro-5-(5-chloro-3,3-dimethyl-1-(3-*(trimethylammonio)propyl*)indolin-2-ylidene)penta-1,3-dien-1-yl)-3,3-dimethyl-1-(3-*(trimethylammonio)propyl*)-3*H*-indol-1-ium bromide (**20**) Yield 77%; M.P. 222-224°C; ¹HNMR (400 MHz, DMSO-*d*₆): δ 1.76 (s, 12H), 2.17 (t, *J* = 7.2 Hz, 4H), 3.13 (s, 18 H), 3.65 (tt, *J* = 7.6 Hz, *J* = 7.2 Hz, 4H), 4.27 (t, *J* = 7.6 Hz, 4H), 6.34 (d, *J* = 13.6 Hz, 2H), 7.51 (d, *J* = 8.4 Hz, 2H), 7.70 (d, *J* = 8.4 Hz, 2H), 7.93 (s, 2H), 8.73 (d, *J* = 13.6 Hz, 2H); ¹³CNMR (100 MHz, DMSO-*d*₆), δ: 20.7, 26.4, 41.3, 49.7, 52.3, 62.1, 100.3, 113.3, 123.2, 123.5, 128.3, 130.0, 140.5, 143.4, 148.4, 174.3. Composition in theory: (x3H₂O): C (46.63%), H (6.13%), N (5.88%); Composition found: C (46.22%), H (6.12%), N (5.78%); HRMS (ESI) calculated for [C₃₇H₅₂Cl₃N₄]³⁺ *m/z* 219.7376, found *m/z* 219.1727, 221.4561, 223.3207.

5-bromo-2-((1*E*,3*Z*,5*E*)-3-bromo-5-(5-bromo-3,3-dimethyl-1-(3-*(trimethylammonio)propyl*)indolin-2-ylidene)penta-1,3-dien-1-yl)-3,3-dimethyl-1-(3-*(trimethylammonio)propyl*)-3*H*-indol-1-ium bromide (**21**) Yield 77.6%; M.P. 232-234°C; ¹HNMR (400 MHz, DMSO-*d*₆): δ 1.76 (s, 12H), 2.18 (t, *J* = 7.1 Hz, 4H), 3.12 (s, 18H), 3.55-3.65 (m, 4H), 4.24 (t, *J* = 7.0 Hz, 4H), 6.34 (d, *J* = 13.2 Hz, 2H), 7.60 (d, *J* = 8.6 Hz, 2H), 7.66 (d, *J* = 8.6 Hz,

2H), 8.06 (s, 2H), 8.60 (d, $J = 13.2$ Hz, 2H); ^{13}C NMR (400 MHz, DMSO- d_6), δ : 20.66, 26.46, 41.37, 49.79, 52.35, 62.25, 102.70, 113.74, 116.99, 118.22, 126.03, 131.24, 140.93, 143.72, 150.42, 174.34. Composition in theory: (3xH₂O): C (40.91) H (5.38), N (5.16); Composition found: C (40.56), H (5.37), N (5.07). High-resolution electrospray ionization (ESI) accurate mass spectra calculated m/z for C₃₇H₅₂N₄Br₄ 868.0925, found 868.0930.

12.6.2 DNA preparation

DNA oligonucleotides: Tel22, d[AGGG(TTAGGG)₃]; *c-myc*, d[(AGGGTGGGG)₂A]; control duplex, d[CGAATTCGTTTTTCGAATTCG] with and without 5'-biotin labels were purchased from Integrated DNA Technologies (Coralville, IA) with HPLC. NMR and mass spectral analysis performed on these sequences further confirmed the purity. The concentration of oligonucleotides was determined from absorbance at 260 nm with extinction coefficients calculated by the nearest-neighbor method.[23] Appropriate stock solutions of each compound were prepared in double deionized water and diluted with the experimental buffer prior to use. Experiments were performed in 10 mM HEPES buffer containing 50 mM KCl and 3 mM EDTA adjusted to pH 7.3 using 1N HCl.

12.6.3 UV-thermal melting studies

Thermal denaturation studies were conducted on a Cary 300 BIO UV-visible spectrophotometer in quartz cuvettes of 1 cm pathlength. DNA solutions were prepared at single-strand concentrations in the range of 2-3 μM . Samples of compound to DNA ratios ranging from 0:1 to 6:1 was prepared. The absorbance of the oligonucleotides and the complexes was monitored at the recommended wavelength of 295 nm for Tel22 and 260 nm for duplex DNA sequences as a function of temperature. Cuvettes were mounted in a thermal block, and the solution temperatures were monitored by a thermistor in a reference cuvette with computer-controlled heating and

12.6.4 Surface Plasmon Resonance

Biosensor-SPR experiments were performed with a four-channel Biacore 2000 optical biosensor system (GE Healthcare, Sweden). The streptavidin-derivatized gold chip (SA chip from BIAcore) was prepared for use by conditioning with a series of 60 second injections of 1 M NaCl in 50 mM NaOH followed by extensive washing with buffer. Biotinylated DNA samples (25-50 nM) in HEPES buffer were immobilized on the flow cell surface by non-covalent capture as previously described[24]. Flow cell 1 was left blank as a reference, while flow cells 2-4 were immobilized with 5'-biotinylated DNA by manual injection of DNA stock solutions (flow rate of 1 μ L/min) until the desired amount of DNA response units was obtained (350-400 RU). Typically, a series of different ligand concentrations (1 nM to 1 μ M) were injected onto the chip (flow rate of 25 μ L/min, 5 min) until a constant steady-state response was obtained followed by a dissociation period (running buffer, 5 min). After every cycle, the chip surface was regenerated with 10 mM glycine solution (pH 2.5 for 30 seconds) followed by multiple buffer injections to obtain a stable baseline for following cycles.

The observed response (RU_{obs}) in the steady-state region is proportional to the amount of bound drug and was typically determined by linear averaging over 10-20 seconds or longer time span. The predicted maximum response per bound compound ($RU_{max/ligand}$) was calculated from the DNA molecular weight, the compound molecular weight, the amount of DNA immobilized on the flow cell, and the refractive index gradient ratio of the compound and DNA, as previously described.[24, 25] The $RU_{max/ligand}$ value is required to convert RU_{obs} to determine the moles of drug bound to DNA. The RU_{obs} was plotted as a function of free ligand concentration (C_{free}) and the equilibrium binding constants were determined using a two-site interaction model, $RU_{max/ligand} * (K_1 C_{free} + 2K_1 K_2 C_{free}^2) / (1 + K_1 C_{free} + K_1 K_2 C_{free}^2)$ using nonlinear least-squares optimization to

obtain an optimal fit with BIAevaluation (BIAcore Inc.) and Kaleidagraph (Synergy Software) softwares. K_1 and K_2 are equilibrium binding constants for two types of binding sites.

12.6.5 Mass spectrometry

The mass spectrometry analysis was performed on a Waters Q-TOF micromass spectrometer equipped with electrospray ionization source (ESI) in negative mode (Waters Corporate, Milford, MA). The mass range was from 500-3000 Da (displayed range in Figure 3 is from 1100 – 2100 m/z). Since mass spectrometry generally requires DNA sequences dissolved in a volatile salt solution, all the sequences tested with mass spectrometry were dialyzed several times with a 1000 Da cut-off membrane (Spectrum Laboratories Inc., Rancho Dominguez, CA, USA) in 50 mM ammonium acetate buffer at pH 7.2 in order to remove any low molecular weight impurities from DNA. The final concentrations of the dialyzed DNA were determined as above. Samples containing 25-30 μM *c-myc* sequence and appropriate amounts of ligands in the desired molar ratios to DNA were prepared in 50 mM ammonium acetate buffer with the final volume of 100 μL . The samples were introduced into the ion source through direct infusion at 5 $\mu\text{l}/\text{min}$ flow rate. The instrument parameters were as follows: capillary voltage of 2200 V, sample cone voltage of 30 V, extraction cone voltage of 2.5 V, desolvation temperature of 70 $^{\circ}\text{C}$ and source temperature of 100 $^{\circ}\text{C}$. Nitrogen was used as nebulizing and drying gas. Spectra were collected for 10 minutes and the last two minutes of the scan were used for data analysis. Data analysis and interpretation were performed using MassLynx 4.1 software.

12.7 Acknowledgements

The biophysical studies on cyanine-DNA interactions were supported by NIH NIAID Grant AI-064200 (WDW). The compound synthesis for this study was supported by a Georgia

Research Alliance grant (MH). EAO was supported through internal funds from the Research Initiation and Mentor Grants at GSU and MH appreciates the Georgia State University Center for Diagnostics and Therapeutics for their support.

12.8 References

- [1] S. Neidle, S. Balasubramanian, *Quadruplex nucleic acids*, RSC Pub, Cambridge, 2006.
- [2] S. Neidle, G.N. Parkinson, *Biochimie*, 90 (2008) 1184-1196.
- [3] S. Neidle, D.E. Thurston, *Nat. Rev. Cancer*, 5 (2005) 285-296.
- [4] H. Han, L. Hurley, *Trends Pharmacol. Sci.*, 21 (2000) 136 - 142.
- [5] D. Drygin, A. Siddiqui-Jain, S. O'Brien, M. Schwaebe, A. Lin, J. Bliesath, C.B. Ho, C. Proffitt, K. Trent, J.P. Whitten, J.K.C. Lim, D. Von Hoff, K. Anderes, W.G. Rice, *Cancer Res*, 69 (2009) 7653-7661.
- [6] D. Monchaud, *Org. Biomol. Chem.*, 6 (2008) 627-636.
- [7] D.F. Shi, R.T. Wheelhouse, D. Sun, L.H. Hurley, *J. Med. Chem.*, 44 (2001) 4509-4523.
- [8] E.W. White, F. Tanious, M.A. Ismail, A.P. Reszka, S. Neidle, D.W. Boykin, W.D. Wilson, *Biophys. Chem.*, 126 (2007) 140-153.
- [9] R. Nanjunda, C. Musetti, A. Kumar, M.A. Ismail, A.A. Farahat, S. Wang, C. Sissi, M. Palumbo, D.W. Boykin, W. Wilson, *Curr. Pharm. Des.*, 18 (2012) 1934.
- [10] M. Henary, M. Mojzych, *Stability and Reactivity of Polymethine Dyes in Solution Heterocyclic Polymethine Dyes*, in: L. Strekowski (Ed.), Springer Berlin / Heidelberg2008, pp. 221-238.
- [11] M. Mojzych, M. Henary, *Synthesis of Cyanine Dyes Heterocyclic Polymethine Dyes*, in: L. Strekowski (Ed.), Springer Berlin / Heidelberg2008, pp. 1-9.

- [12] Q. Yang, J. Xiang, S. Yang, Q. Zhou, Q. Li, Y. Tang, G. Xu, *Chem. Comm.*, (2009) 1103-1105.
- [13] S.M. Kerwin, D. Sun, J.T. Kern, A. Rangan, P.W. Thomas, *Bioorg. Med. Chem. Lett.*, 11 (2001) 2411-2414.
- [14] A.T. Phan, V. Kuryavyi, D.J. Patel, *Curr. Opin. Struct. Biol.*, 16 (2006) 288-298.
- [15] L. Hurley, R. Wheelhouse, D. Sun, S. Kerwin, M. Salazar, O. Fedoroff, F. Han, H. Han, E. Izbicka, D. Von Hoff, *Pharmacol. Ther.*, 85 (2000) 141-158.
- [16] S. Buchini, A. Buschiazzo, S.G. Withers, *Angew. Chem. Int. Ed. Engl.*, 47 (2008) 2700-2703.
- [17] H. Maehr, *Bioorg. Med. Chem.*, 5 (1997) 473-491.
- [18] G. Chessari, A.J. Woodhead, *Drug Discov. Today*, 14 (2009) 668-675.
- [19] M.Z. Hernandez, S.M. Cavalcanti, D.R. Moreira, F. Azevedo, A.C. Leite, *Curr. Drug Targets*, 11 (2010) 303-314.
- [20] E.D. Horowitz, N.V. Hud, *J. Am. Chem. Soc.*, 128 (2006) 15380-15381.
- [21] H.-K. Kim, J.-M. Kim, S.K. Kim, A. Rodger, B. Nordén, *Biochemistry*, 35 (1996) 1187-1194.
- [22] E.M. Rezler, J. Seenisamy, S. Bashyam, M.-Y. Kim, E. White, W.D. Wilson, L.H. Hurley, *J. Am. Chem. Soc.*, 127 (2005) 9439-9447.
- [23] G.D. Fasman, *Handbook of Biochemistry and Molecular Biology, Nucleic Acids*, CRC Press, Cleveland, 1975.
- [24] R. Nanjunda, M. Munde, Y. Liu, W. Wilson, *Real-Time Monitoring of Nucleic Acid Interactions with Biosensor-Surface Plasmon Resonance*, in: Y. Tor, M. Wanunu (Eds.) *Methods for Studying Nucleic Acid/Drug Interactions*, CRC Press, Boca Raton, 2011, pp. 91-134.
- [25] T.M. Davis, W.D. Wilson, *Anal. Biochem.*, 284 (2000) 348-353.

13 RIGIDITY IN HEPTAMETHINE CYANINES IMPROVES QUADRUPLEX BINDING

This chapter has been prepared as a publication for submission to MedChemComm in collaboration with Dr. Donald Hamelberg, Dr. Germann, and Dr. David Wilson's lab at Georgia State University. My contributions as co-first author included the synthesis of the binding ligands, interpretation of data, experimental design and manuscript preparation.

13.1 Abstract

Carbocyanine dyes have been long understood to bind strongly in the minor groove of DNA through H-aggregation and through electrostatic interactions with varied degrees of sequence specificity. Through carefully placed structural manipulations, we have prepared heptamethine cyanine structures that display strong and selective binding to G-quadruplex DNA. In corroboration with our previous reports, we observe a direct correlation with polymethine length and intrinsic charge of the binding agent.

13.2 Introduction

Within the past few years, it has been increasingly recognized that the G-quadruplex could be a potent target for the design of novel chemotherapeutics.¹ The quadruplex structure is characterized by four guanine nucleotides bound through both Hoogsteen hydrogen bonds and by those recognized by the Watson and Crick face. Early developments in the biological significance of this nucleic acid structure include the inhibition of the enzyme telomerase which is overactive in a number of cancer cells^{2, 3}; however, the field has moved toward the more appealing arena concerning oncogenetic suppression using the quadruplex as an effective silencing mechanism.⁴⁻⁸ Oncogenetic promoter regions are employed in the biological prevalence of several cancer-promoting proteins, including c-myc, RET, c-kit and VEGF, which are able to be targeted by the

stabilization of the corresponding quadruplex. Specifically, the MYC oncogene is responsible for Burkitt's Lymphoma⁹⁻¹¹ and it becomes active as the Epstein-Barr virus alters native B-cells into MYC-expressive cancerous cells. In line with this observation, the therapeutic potential of the quadruplex has been extensively researched with many hit compounds being reported as binding this structure with high affinity as measured by a number of complementary biological and biophysical techniques. Unfortunately, the Achilles heel of this approach remains a significant structural challenge—achieving discrimination against the minor groove of duplex DNA without jeopardizing desirable quadruplex affinity.

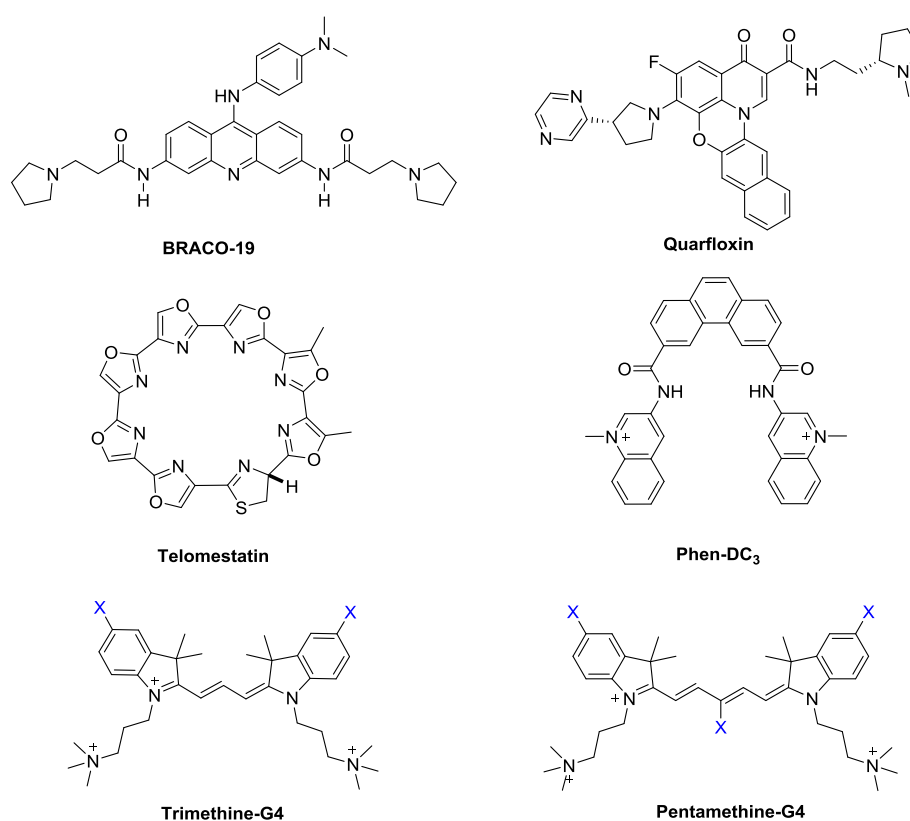


Figure 13-1. The chemical structures of known binding quadruplex binding ligands.

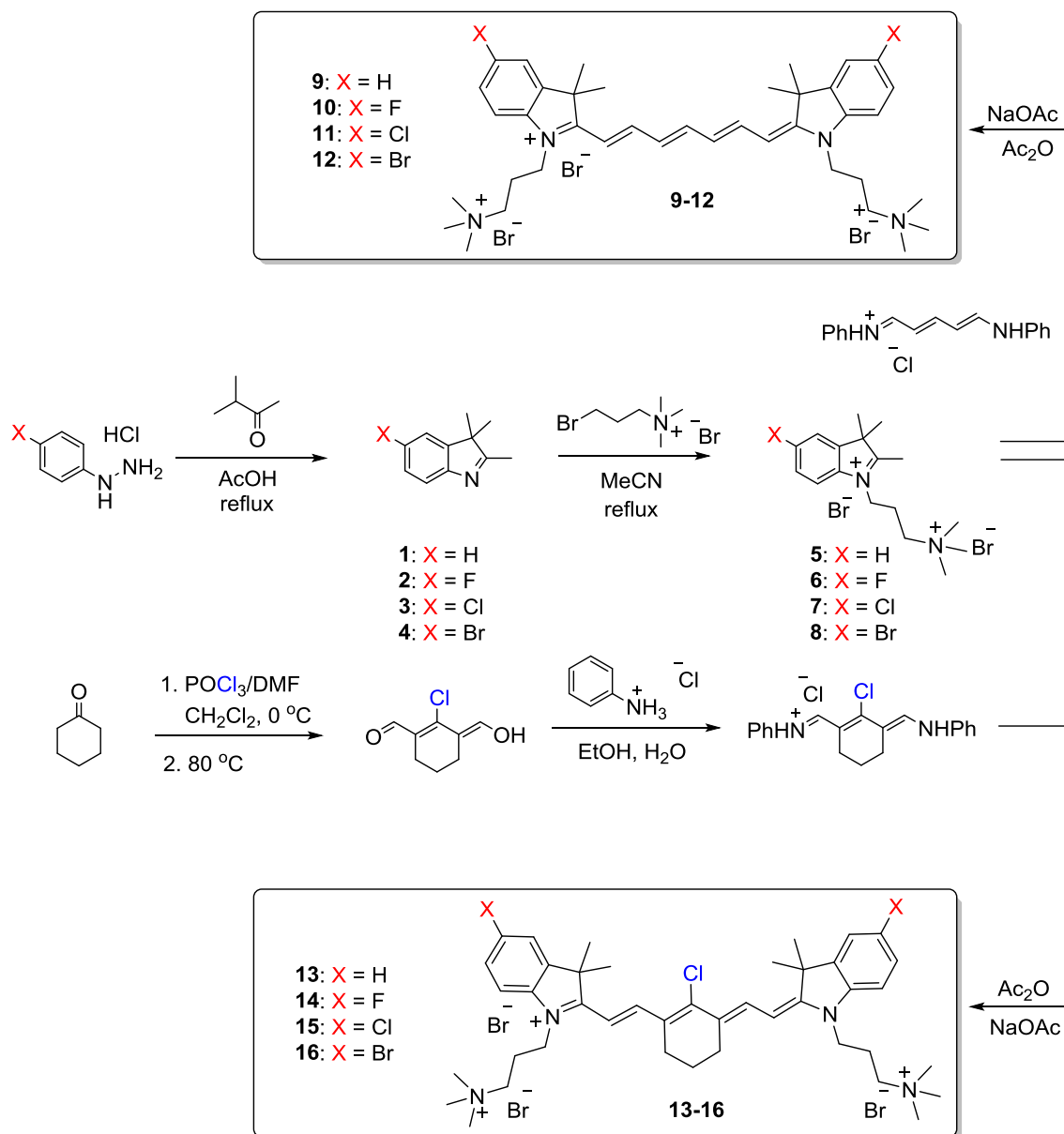
Cyanine dyes have been long recognized as effective nucleic acid labels owing to their inherent ability to bind to the minor groove and offer strong fluorescence signal.¹²⁻¹⁵ These

compounds have been diversely modified to achieve strong binding affinity to both duplex and quadruplex DNA based off of the benzothiazole nucleus. Initially, we postulated that incorporating a steric restraint to duplex binding could lead to quadruplex specific binding affinity and reported tri- and pentamethine cyanines with dimethyl indolenine heterocycles replacing the benzothiazole moieties. We found out that this molecular design when paired with terminal propyl quaternary ammonium cations and heterocyclic halogenations increased the binding affinity while maintaining the highly desirable quadruplex selectivity. The exact position of these binding moieties (cations and halogens) was thought to have a significant impact on the binding affinity to the quadruplex. It seemed logical to elongate the polymethine chain of the cyanine chromophore by an additional vinylene unit and compare them directly to the previously studied cyanine binding ligands. Heptamethine cyanines are the longest of the most common (of mono, tri, penta and hepta) and were needed to discover the optimum length for quadruplex binding. Heptamethines are very well known compounds across various disciplines including near-infrared imaging.¹⁶⁻²³

13.3 Synthesis

In synthetic pursuit of heptamethine cyanine dyes with similar structural characteristics as our previously reported tri and pentamethine cyanines, we prepared the heterocyclic salts for covalent attachment on both ends of the commercially obtained linking intermediate. Fischer-indole conditions starting with the corresponding halogenated hydrazine and 3-methyl-2-butanone yield heterocyclic compounds in excellent yield. Applying usual S_N2 chemistry in extra dry conditions affords the di-quaternary ammonium cation salts as a highly hygroscopic solid followed by condensation in acetic anhydride. As preparing open-chain heptamethine cyanines with a *meso*-halogen is synthetically difficult, we instead chose to incorporate a cyclohexene ring within the polymethine chain bearing a *meso*-chlorine atom. We began this synthetic route with the

formylation of cyclohexanone to afford the intermediate. After treatment with anilinium chloride, we obtain the Vilsmeier-Haack reagent in excellent yield which is then reacted with the dicationic salts using similar chemistry as previously described. The final heptamethine cyanines were obtained with a cyclic ring and *meso*-chlorine atom.



Scheme 1: The synthetic pathway for the preparation of diverse halogenated heptamethine cyanines bearing an open polymethine chain (**9-12**) and a ridged cyclohexene core (**13-16**).

13.4 Ultra-Violet Thermal Melting

In order to determine the degree of binding for the newly prepared heptamethine binding agents, we first use UV thermal melting to screen the compounds for activity against a human telomere sequence to gauge the potential for interaction with quadruplex sequences. The DNA melting curve is analyzed without binding agents and with binding ligand in different compound:DNA ratios (1:1, 2:1, 4:1, 6:1). Similarly, a duplex forming AT rich sequence is used to determine the potential for interaction with duplex DNA.

Table 1: T_m changes of heptamethine cyanine binding agents with telomeric quadruplex (Tel22) and a control duplex sequence (AATT). Previously published penta^a- and trimethine^b cyanines are listed for direct comparison. ND = Not determined

Compound ID	Tel22 (Compound:DNA)				AATT (Compound:DNA)
	(1:1)	(2:1)	(4:1)	(6:1)	(4:1)
9	3	5	9	12	1
9^a	ND	2	5	9	1
9^b	2	4	9	14	0
10	ND	ND	9	ND	1
10^b	3	8	12	16	1
11	ND	ND	10	ND	2
11^a	ND	3	9	13	0
11^b	3	7	15	19	1
12	ND	ND	12	ND	1
12^a	ND	3	16	ND	0
12^b	1	5	14	24	0
13	4	13	23	25	ND
13^a	ND	5	12	13	3
14	ND	ND	12	ND	1
15	ND	ND	21	ND	3
15^a	ND	7	15	19	2

16	3	6	22	ND	0
16^a	ND	9	16	21	3

ND = Not Determined

13.5 Nuclear Magnetic Resonance Spectroscopy

NMR spectroscopy is an excellent tool for deciphering the orientation and mode of chemical complexation with nucleic acids and proteins. Titrating DNA with varied ratios of binding ligand allows us to determine the location and degree of binding to the quadruplex. From the NMR data we can see strong interactions with the bottom of the quadruplex surface.

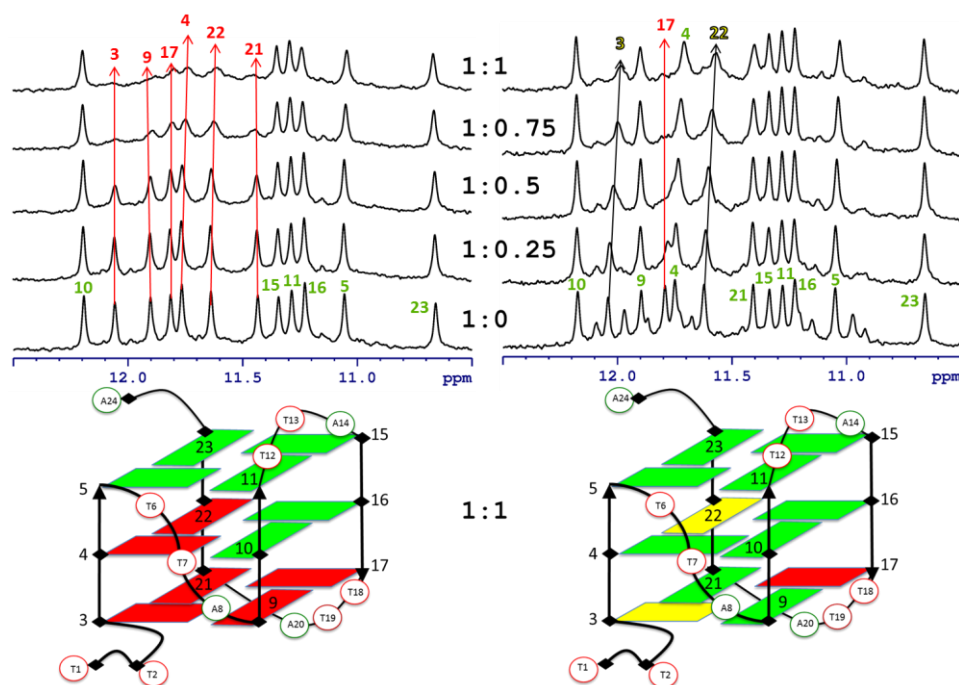
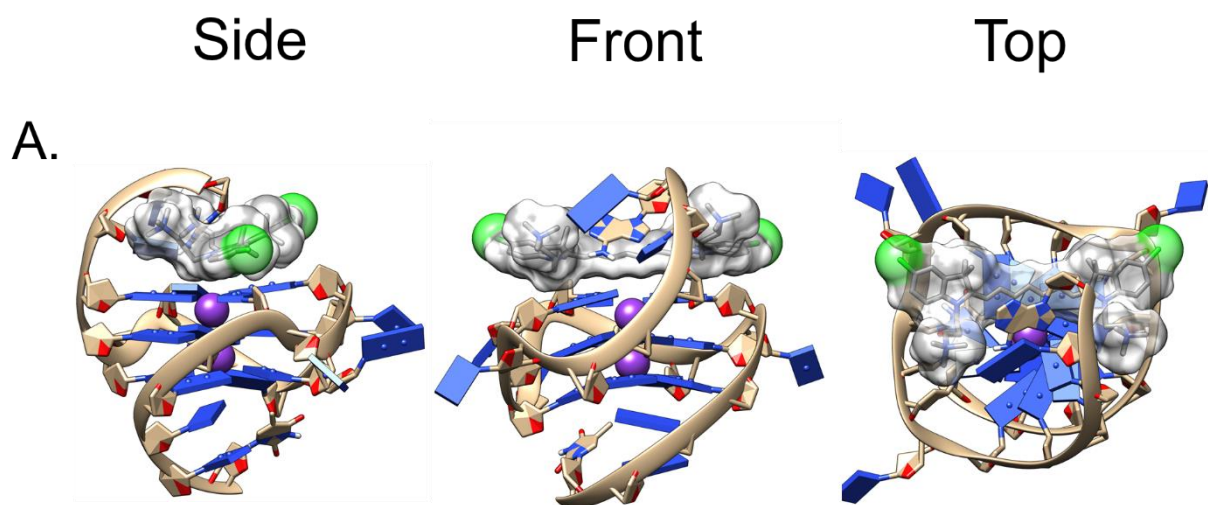


Figure 13-2. TEL-24 quadruplex titration with 15 (left), and 13 (right) followed with the imino proton spectra of TEL-24. NMR imino proton spectra (T=298 K) of the TEL-24 quadruplex are shown on the top of the figure. Compounds 13 and 15 were added to a constant amount of TEL-24 indicated in terms of their mole ratios. The DNA is mostly present as a hybrid-1 form in solution. Ligands were added to the quadruplex at the ratio

indicated on the plot, where 1:0 ratio corresponds to the imino proton spectrum of TEL-24 with no ligand added. Schematic structures of TEL-24 are color coded according to the tetrad guanine imino protons affected in the titrations. Red residues are strongly affected, yellow are somewhat affected, and green are not affected.

13.6 Molecular Modeling

After determining the qualitative binding mode through NMR titrations, we utilized the AMBER suite of computational dynamics software to more precisely visualize the binding to both hTel and cMYC DNA



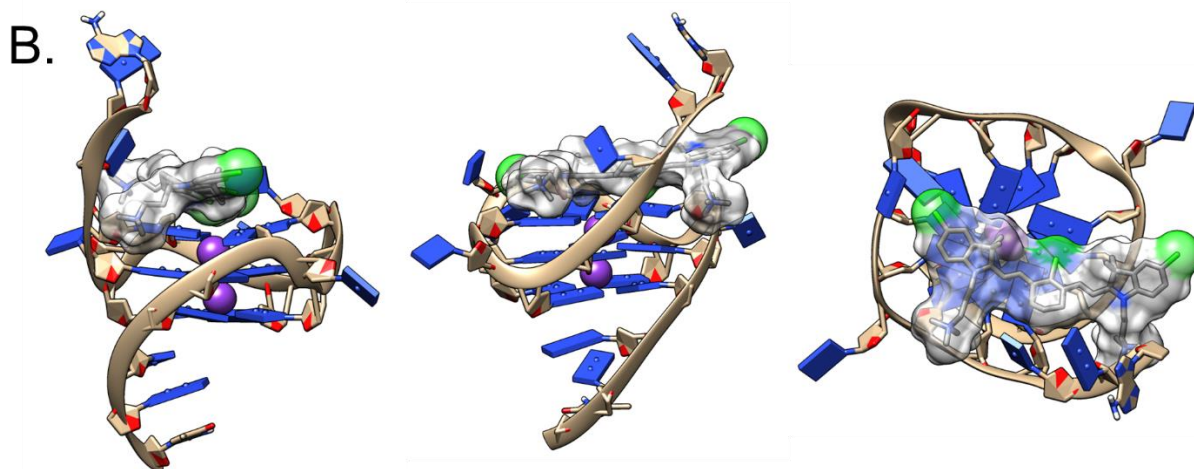


Figure 13-3. Molecular dynamics snapshots for the binding of compounds 11 and 15 to cMYC DNA (PU22, PDB ID: 1XAV). (A) Compound 11 with cMYC, and (B) Compound 15 with cMYC.

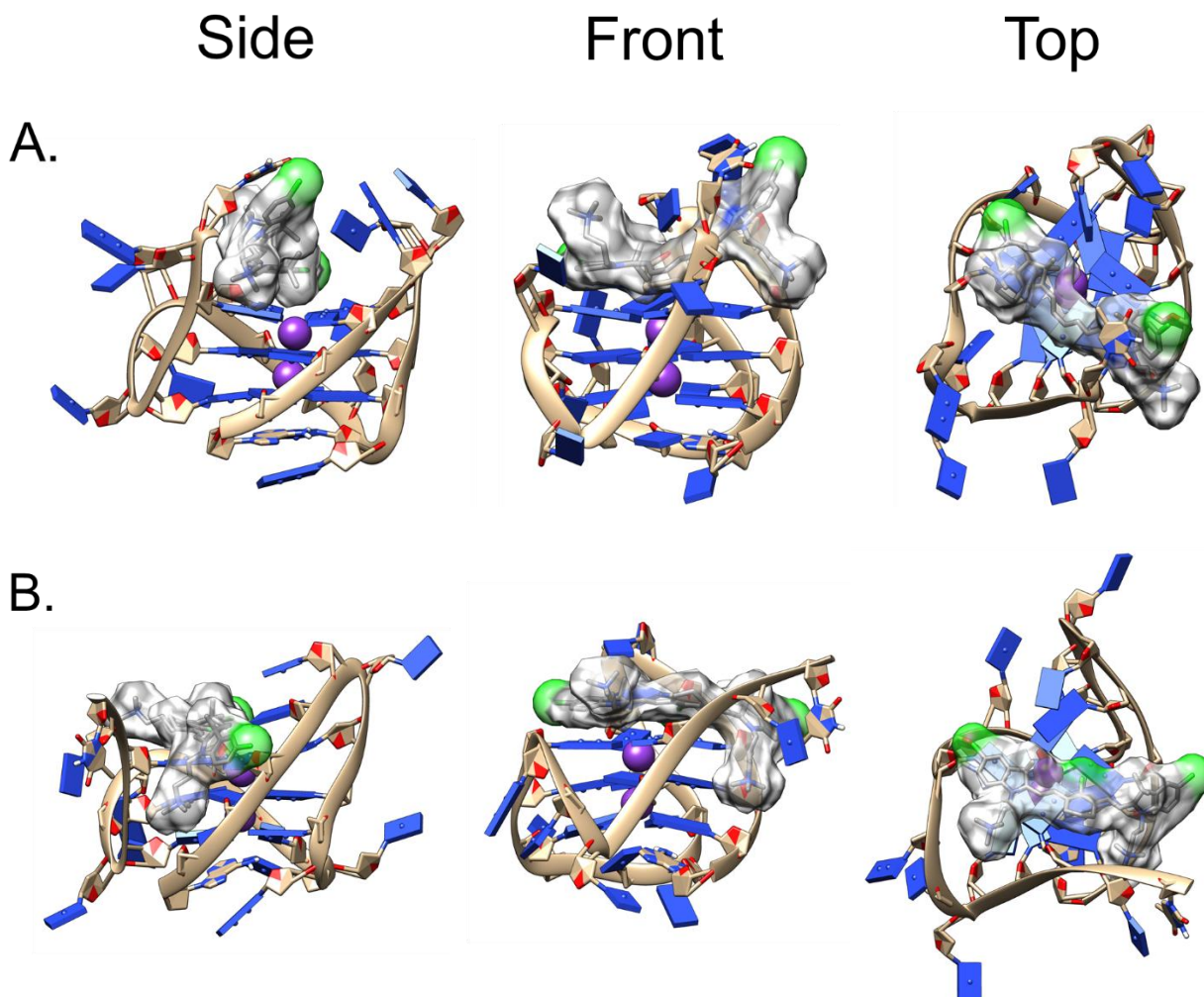


Figure 13-4. Molecular dynamics snapshots for the binding of compounds 11 and 15 to hTel DNA (hTel22, PDB ID:). (A) Compound 11 with cMYC, and (B) Compound 15 with cMYC.

13.7 Discussion

Our previous attempts to obtain selective and strongly-interacting quadruplex ligands led with the pentamethine and trimethine classes, respectively. The heptamethine class of cyanines has been long reserved for *in vivo* imaging or protein labeling. After modifying the aforementioned compounds through the addition of halogens on the heterocyclic units, we observed an increase in the overall interaction as indicated by SPR-Kd and ΔT_m measurements. We then hypothesized

that the overall length between heterocyclic units should be altered to observe the most appealing binding length for increasing quadruplex interactions and if this structural perturbation would increase, decrease or not affect the overall selectivity. This rationale led us to synthesize the heptamethine compounds shown in Scheme 1. Having these analogous quadruplex ligands in hand, they were subjected to an initial screening measurement using DNA uv thermal melting which robustly can determine a general order of magnitude binding strength owing to an increase in melting temperature of the quadruplex. Immediately a trend emerges between the two overall sets of compounds—the cyclohexene ring in the middle of compounds **13-16** results in an unexpected increase in quadruplex affinity with DTm measurements almost doubling from 12 °C to 23 °C.

13.8 Experimental

Synthesis. All starting reagents were obtained commercially from Sigma Aldrich or Matrix Scientific and were used without purification. Nuclear magnetic resonance experiments were performed on a Bruker Avance 400 MHz spectrometer and processed using Topspin 3.1. Chemical shift values are reported versus tetramethylsilane as an internal standard purchased in the commercially obtained deuterated solvents (Cambridge Isotope Laboratory). The reactions were followed using silica gel 60 F₂₅₄ thin layer chromatography plates (Merck EMD Millipore, Darmstadt, Germany). Open column chromatography was utilized for the purification of all final compounds using 60-200u, 60A, classic column silica gel (Dynamic Adsorbents, Norcross, GA).. UV-Vis/NIR absorption spectra were recorded on a Varian Cary 50 spectrophotometer. High-resolution accurate mass spectra (HRMS) were obtained either at the Georgia State University Mass Spectrometry Facility using a Waters Q-TOF micro (ESI-Q-TOF) mass spectrometer or utilizing a Waters Micromass LCT TOF ES+ Premier Mass Spectrometer. Liquid chromatography

utilized a Waters 2487 single wavelength absorption detector with wavelengths set between 640 and 700 nm depending on the particular photophysical properties. The column used in LC was a Waters Delta-Pak 5 μ M 100A 3.9 x 150 mm reversed phase C₁₈ column. Evaporative light scattering detection analyzes trace impurities that cannot be observed by alternate methods; a SEDEX 75 ELSD was utilized in tandem with liquid chromatography to confirm purity (>95% as determined by LC-ELSD-MS).

Synthetic preparation of open-chain heptamethine binding agents 9-12. Individual heterocyclic salt and corresponding starting linker were placed in an oven dry and nitrogen purged round bottom flask. Acetic anhydride (3 mL) was added and the reaction mixture was warmed to 40 °C for 10 minutes. Sodium acetate (2 mol. eq.) was added to the reaction mixture. The reaction was followed using both UV-Vis-NIR spectroscopy, monitoring the appearance of a absorbance band >700nm and the disappearance of absorbance characteristics below 600nm. TLC using neutral alumina coated glass and 5% methanol in DCM afforded efficient separation of the highly charged compounds. The reactions were followed to completion. After the disappearance of starting materials, the reaction mixture was added to a stirring mixture of acetone and ethyl acetate (1:1, 30 mL). The resulting solid was vacuum filtered and quickly dried under high vacuum. The compounds were purified by substantial washing with acetone or open column chromatography using alumina gel and a gradient of DCM to 1-5% methanol in DCM as the eluting solvent. The final compounds were obtained in the indicated yields of >95% purity as determined by tandem LC-ELSD-MS.

5-fluoro-2-((1E,3E,5E)-7-((E)-5-fluoro-3,3-dimethyl-1-(3-(trimethylammonio)propyl)indolin-2-ylidene)hepta-1,3,5-trien-1-yl)-3,3-dimethyl-1-(3-(trimethylammonio)propyl)-3H-indol-1-ium bromide (10): ¹H NMR (400 MHz, D₂O) δ 1.964 (s,

12H), 2.602 (bs, 4H), 3.404 (s, 18H), 3.763 (t, $J = 6.0$ Hz, 4H), 4.455 (bs, 4H), 6.529 (d, $J = 12.4$ Hz, 2H), 6.868 (t, $J = 12.8$ Hz, 2H), 7.497-7.473 (m, 4H), 7.616 (d, $J = 8.0$ Hz, 2H), 7.832 (t, $J = 12.4$ Hz, 1H), 8.200 (t, $J = 13.2$ Hz, 2H). ^{19}F NMR (375 MHz, D_2O , ref C_6F_6) $\delta -117.48$.

5-chloro-2-((1E,3E,5E)-7-((E)-5-chloro-3,3-dimethyl-1-(3-(trimethylammonio)propyl)indolin-2-ylidene)hepta-1,3,5-trien-1-yl)-3,3-dimethyl-1-(3-(trimethylammonio)propyl)-3H-indol-1-ium bromide (11): ^1H NMR (400 MHz, $\text{DMSO-}d_6$) δ 1.635 (s, 12H), 2.111 (bs, 4H), 3.148 (s, 18H), 3.775 (bs, 4H), 4.197 (bs, 4H), 6.726 (d, $J = 12.4$ Hz, 4H), 7.436 (d, $J = 8.4$ Hz, 2H), 7.603 (d, $J = 7.6$ Hz, 2H), 7.744 (s, 3H), 7.857 (bs, 2H).

2-((E)-2-((E)-2-chloro-3-(2-((E)-3,3-dimethyl-1-(3-(trimethylammonio)propyl)indolin-2-ylidene)ethylidene)cyclohex-1-en-1-yl)vinyl)-3,3-dimethyl-1-(3-(trimethylammonio)propyl)-3H-indol-1-ium bromide (12): ^1H NMR (400 MHz, $\text{DMSO-}d_6$) δ 1.653 (s, 12H), 2.309 (bs, 4H), 3.286 (s, 18H), 3.975 (t, $J = 8.0$ Hz, 4H), 4.426 (t, $J = 6.8$ Hz, 4H), 6.776-6.671 (m, 4H), 7.583-7.472 (m, 5H), 7.624 (s, 2H), 7.807 (t, $J = 12.4$ Hz, 3H).

5-bromo-2-((1E,3E,5E)-7-((E)-5-bromo-3,3-dimethyl-1-(3-(trimethylammonio)propyl)indolin-2-ylidene)hepta-1,3,5-trien-1-yl)-3,3-dimethyl-1-(3-(trimethylammonio)propyl)-3H-indol-1-ium bromide (13): ^1H NMR (400 MHz, $\text{DMSO-}d_6$) δ 1.714 (s, 12H), 1.882 (bs, 2H), 2.195 (bs, 4H), 2.793 (s, 4H), 3.125 (s, 18H), 3.613 (s, 4H), 4.289 (s, 4H), 6.378 (d, $J = 14.0$ Hz, 2H), 7.315 (t, $J = 7.6$ Hz, 2H), 7.458 (t, $J = 6.8$ Hz, 2H), 7.558 (d, $J = 7.2$ Hz, 2H), 7.659 (d, $J = 7.2$ Hz, 2H), 8.315 (d, $J = 13.6$ Hz, 2H).

2-((E)-2-((E)-2-chloro-3-(2-((E)-5-fluoro-3,3-dimethyl-1-(3-(trimethylammonio)propyl)indolin-2-ylidene)ethylidene)cyclohex-1-en-1-yl)vinyl)-5-fluoro-3,3-dimethyl-1-(3-(trimethylammonio)propyl)-3H-indol-1-ium bromide (14): ^{13}C NMR (100MHz, $\text{DMSO-}d_6$) 20.97, 21.41, 26.82, 27.94, 41.88, 49.84, 53.13, 62.95, 102.61, 110.97, 111.23, 113.42,

113.51, 115.49, 115.73, 127.12, 143.82, 148.92, 159.69, 162.10, 172.95. ^{19}F NMR (375 MHz, D_2O , ref C_6F_6) δ -119.19.

5-chloro-2-((E)-2-((E)-2-chloro-3-(2-((E)-5-chloro-3,3-dimethyl-1-(3-(trimethylammonio)propyl)indolin-2-ylidene)ethylidene)cyclohex-1-en-1-yl)vinyl)-3,3-dimethyl-1-(3-(trimethylammonio)propyl)-3H-indol-1-ium bromide (15): ^1H NMR (400 MHz, $\text{DMSO}-d_6$) δ 1.708 (s, 12H), 1.839 (bs, 2H), 2.159 (bs, 4H), 2.806 (s, 4H), 3.139 (s, 18H), 3.698 (s, 4H), 4.309 (s, 4H), 6.424 (d, $J = 14.0$ Hz, 2H), 7.498 (d, $J = 8.4$ Hz, 2H), 7.674 (d, $J = 7.6$ Hz, 2H), 7.845 (s, 2H), 8.274 (d, $J = 14.0$ Hz, 2H).

5-bromo-2-((E)-2-((E)-3-(2-((E)-5-bromo-3,3-dimethyl-1-(3-(trimethylammonio)propyl)indolin-2-ylidene)ethylidene)-2-chlorocyclohex-1-en-1-yl)vinyl)-3,3-dimethyl-1-(3-(trimethylammonio)propyl)-3H-indol-1-ium bromide (16): ^1H NMR (400 MHz, $\text{MeOD}-d_4$) δ 1.792 (s, 12H), 1.993 (bs, 2H), 2.347 (bs, 4H), 2.865 (s, 4H), 3.236 (s, 18H), 3.732 (d, $J = 7.6$ Hz, 4H), 4.329 (d, $J = 6.8$ Hz, 4H), 6.438 (d, $J = 14.0$ Hz, 2H), 7.670 (d, $J = 8.4$ Hz, 2H), 7.625 (d, $J = 8.4$ Hz, 2H), 7.765 (s, 2H), 8.487 (d, $J = 14.0$ Hz, 2H).

13.9 References.

1. Zheng, X. H.; Zhong, Y. F.; Tan, C. P.; Ji, L. N.; Mao, Z. W. Pt(II) squares as selective and effective human telomeric G-quadruplex binders and potential cancer therapeutics. *Dalton Trans* **2012**, 41, 11807-12.
2. Maji, B.; Kumar, K.; Muniyappa, K.; Bhattacharya, S. New dimeric carbazole-benzimidazole mixed ligands for the stabilization of human telomeric G-quadruplex DNA and as telomerase inhibitors. A remarkable influence of the spacer. *Org Biomol Chem* **2015**, 13, 8335-48.

3. Xu, C. X.; Zheng, Y. X.; Zheng, X. H.; Hu, Q.; Zhao, Y.; Ji, L. N.; Mao, Z. W. V-shaped dinuclear Pt(II) complexes: selective interaction with human telomeric G-quadruplex and significant inhibition towards telomerase. *Sci Rep* **2013**, *3*, 2060.
4. Lavrado, J.; Brito, H.; Borralho, P. M.; Ohnmacht, S. A.; Kim, N. S.; Leitao, C.; Pisco, S.; Gunaratnam, M.; Rodrigues, C. M.; Moreira, R.; Neidle, S.; Paulo, A. KRAS oncogene repression in colon cancer cell lines by G-quadruplex binding indolo[3,2-c]quinolines. *Sci Rep* **2015**, *5*, 9696.
5. Miyazaki, T.; Pan, Y.; Joshi, K.; Purohit, D.; Hu, B.; Demir, H.; Mazumder, S.; Okabe, S.; Yamori, T.; Viapiano, M.; Shin-ya, K.; Seimiya, H.; Nakano, I. Telomestatin impairs glioma stem cell survival and growth through the disruption of telomeric G-quadruplex and inhibition of the proto-oncogene, c-Myb. *Clin Cancer Res* **2012**, *18*, 1268-80.
6. Ma, Y.; Ou, T. M.; Tan, J. H.; Hou, J. Q.; Huang, S. L.; Gu, L. Q.; Huang, Z. S. Quinolino-benzo-[5, 6]-dihydroisoquinolium compounds derived from berberine: a new class of highly selective ligands for G-quadruplex DNA in c-myc oncogene. *Eur J Med Chem* **2011**, *46*, 1906-13.
7. Liu, Y.; Zheng, B.; Xu, X.; Yuan, G. Probing the binding affinity of small-molecule natural products to the G-quadruplex in C-myc oncogene by electrospray ionization mass spectrometry. *Rapid Commun Mass Spectrom* **2010**, *24*, 3072-5.
8. Hsu, S. T.; Varnai, P.; Bugaut, A.; Reszka, A. P.; Neidle, S.; Balasubramanian, S. A G-rich sequence within the c-kit oncogene promoter forms a parallel G-quadruplex having asymmetric G-tetrad dynamics. *J Am Chem Soc* **2009**, *131*, 13399-409.
9. Suk, F. M.; Lin, S. Y.; Lin, R. J.; Hsine, Y. H.; Liao, Y. J.; Fang, S. U.; Liang, Y. C. Bortezomib inhibits Burkitt's lymphoma cell proliferation by downregulating sumoylated hnRNP K and c-Myc expression. *Oncotarget* **2015**, *6*, 25988-26001.

10. Spender, L. C.; Inman, G. J. Developments in Burkitt's lymphoma: novel cooperations in oncogenic MYC signaling. *Cancer Manag Res* **2014**, *6*, 27-38.
11. Scheller, H.; Tobollik, S.; Kutzera, A.; Eder, M.; Unterlehberg, J.; Pfeil, I.; Jungnickel, B. c-Myc overexpression promotes a germinal center-like program in Burkitt's lymphoma. *Oncogene* **2010**, *29*, 888-97.
12. Kretschy, N.; Somoza, M. M. Comparison of the sequence-dependent fluorescence of the cyanine dyes Cy3, Cy5, DyLight DY547 and DyLight DY647 on single-stranded DNA. *PLoS One* **2014**, *9*, e85605.
13. Bohlander, P. R.; Wagenknecht, H. A. Synthesis and evaluation of cyanine-styryl dyes with enhanced photostability for fluorescent DNA staining. *Org Biomol Chem* **2013**, *11*, 7458-62.
14. Mohammed, H. S.; Delos Santos, J. O.; Armitage, B. A. Noncovalent binding and fluorogenic response of cyanine dyes to DNA homoquadruplex and PNA-DNA heteroquadruplex structures. *Artif DNA PNA XNA* **2011**, *2*, 43-49.
15. Mahmood, T.; Paul, A.; Ladame, S. Synthesis and spectroscopic and DNA-binding properties of fluorogenic acridine-containing cyanine dyes. *J Org Chem* **2010**, *75*, 204-7.
16. Nani, R. R.; Shaum, J. B.; Gorka, A. P.; Schnermann, M. J. Electrophile-integrating Smiles rearrangement provides previously inaccessible C4'-O-alkyl heptamethine cyanine fluorophores. *Org Lett* **2015**, *17*, 302-5.
17. Cheng, G.; Fan, J.; Sun, W.; Cao, J.; Hu, C.; Peng, X. A near-infrared fluorescent probe for selective detection of HClO based on Se-sensitized aggregation of heptamethine cyanine dye. *Chem Commun (Camb)* **2014**, *50*, 1018-20.

18. Xiao, L.; Zhang, Y.; Yue, W.; Xie, X.; Wang, J. P.; Chordia, M. D.; Chung, L. W.; Pan, D. Heptamethine cyanine based (64)Cu-PET probe PC-1001 for cancer imaging: synthesis and in vivo evaluation. *Nucl Med Biol* **2013**, 40, 351-60.
19. Zheng, H.; Yan, M.; Fan, X. X.; Sun, D.; Yang, S. Y.; Yang, L. J.; Li, J. D.; Jiang, Y. B. A heptamethine cyanine-based colorimetric and ratiometric fluorescent chemosensor for the selective detection of Ag⁺ in an aqueous medium. *Chem Commun (Camb)* **2012**, 48, 2243-5.
20. Yang, X.; Shi, C.; Tong, R.; Qian, W.; Zhau, H. E.; Wang, R.; Zhu, G.; Cheng, J.; Yang, V. W.; Cheng, T.; Henary, M.; Streckowski, L.; Chung, L. W. Near IR heptamethine cyanine dye-mediated cancer imaging. *Clin Cancer Res* **2010**, 16, 2833-44.
21. Bouit, P. A.; Aronica, C.; Toupet, L.; Le Guennic, B.; Andraud, C.; Maury, O. Continuous symmetry breaking induced by ion pairing effect in heptamethine cyanine dyes: beyond the cyanine limit. *J Am Chem Soc* **2010**, 132, 4328-35.
22. Lee, H.; Mason, J. C.; Achilefu, S. Heptamethine cyanine dyes with a robust C-C bond at the central position of the chromophore. *J Org Chem* **2006**, 71, 7862-5.
23. Peng, X.; Song, F.; Lu, E.; Wang, Y.; Zhou, W.; Fan, J.; Gao, Y. Heptamethine cyanine dyes with a large stokes shift and strong fluorescence: a paradigm for excited-state intramolecular charge transfer. *J Am Chem Soc* **2005**, 127, 4170-1.

14 SECOND GENERATION TRIMETHINE CYANINES

This chapter has been prepared for submission to *Chemistry—A European Journal* and has been the work of several labs collaborating across the Georgia State Campus. My contributions as first author of this manuscript have included the synthesis/characterization of binding ligands, molecular modeling, manuscript/figure preparation, data interpretation, project implementation, and overall project management.

14.1 Abstract

Second generation trimethine cyanines have been synthesized and evaluated for their quadruplex binding properties. Incorporating a benz[*c,d*]indolenine heterocyclic unit increased overall quadruplex binding and elongating the alkyl length increases the quadruplex-to-duplex binding specificity. Additionally the modification of the alkyl length increased the binding affinity to MYC DNA and lowered the targeting of Tel22 resulting in a highly MYC-specific binding ligand which is highly important in the recognition of particular quadruplex topologies.

14.2 Introduction

Effective drug targets are paramount in the rational design of new therapeutics for improving human health. Over the years, DNA has remained an appealing target due to its ubiquitous involvement that permeates biological processes—both native and diseased. Selectively inhibiting the translation and/or transcription of nucleic acids would give rise to personalized medications that would act by silencing the very creation of proteins that eventually lead to diseased states. Unfortunately, we are very far from making this a reality. Throughout recent years, alternate folding patterns of DNA (i.e. holliday junction, triplex, quadruplex, etc) have been extensively and excitingly explored as offering a favorable route toward effectively targeting the nucleic acid machinery of diseased cells. In line with this current trend, we have been

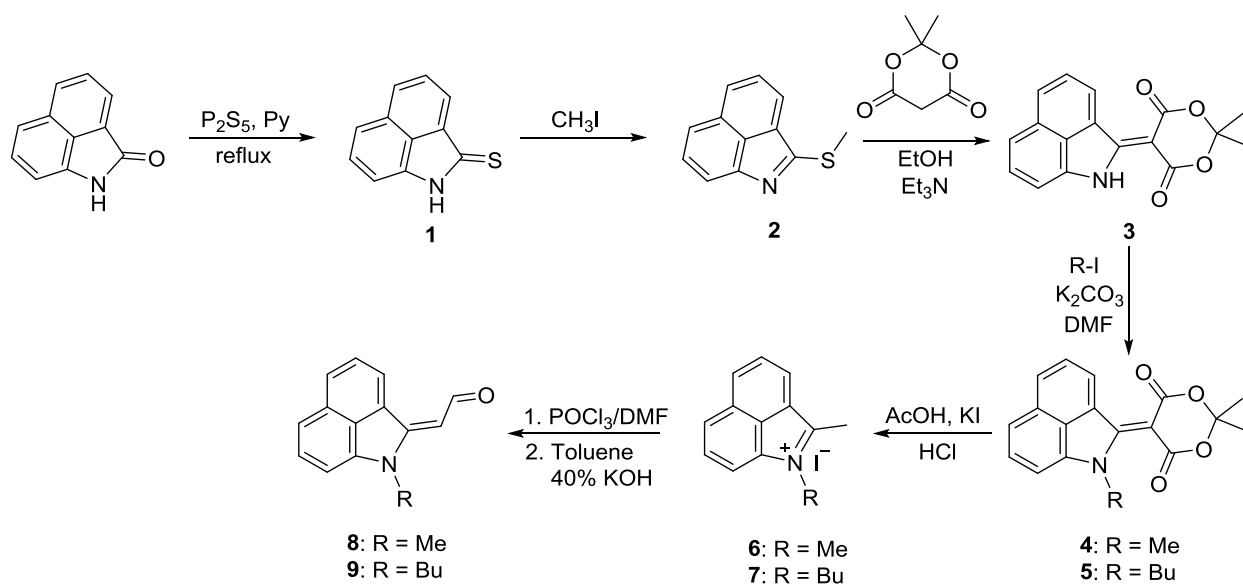
exploring ligands that bind and stabilize the G-quadruplex structure. The quadruplex is defined as a stacked tetrad of self-associated guanine nucleotides that assemble around a stabilizing cation.¹⁻

⁷ Bioinformatics suggests that quadruplex-forming sequences prevail in oncogene promoter regions and within the telomere domain; both quadruplex associations lend themselves to be relevant in the design of new chemotherapeutics targeting either the translation of oncogene associated proteins or the enzymatic inhibition of telomerase, which is overexpressed in cancer cells and is responsible for limitless replication processes through telomere elongation.

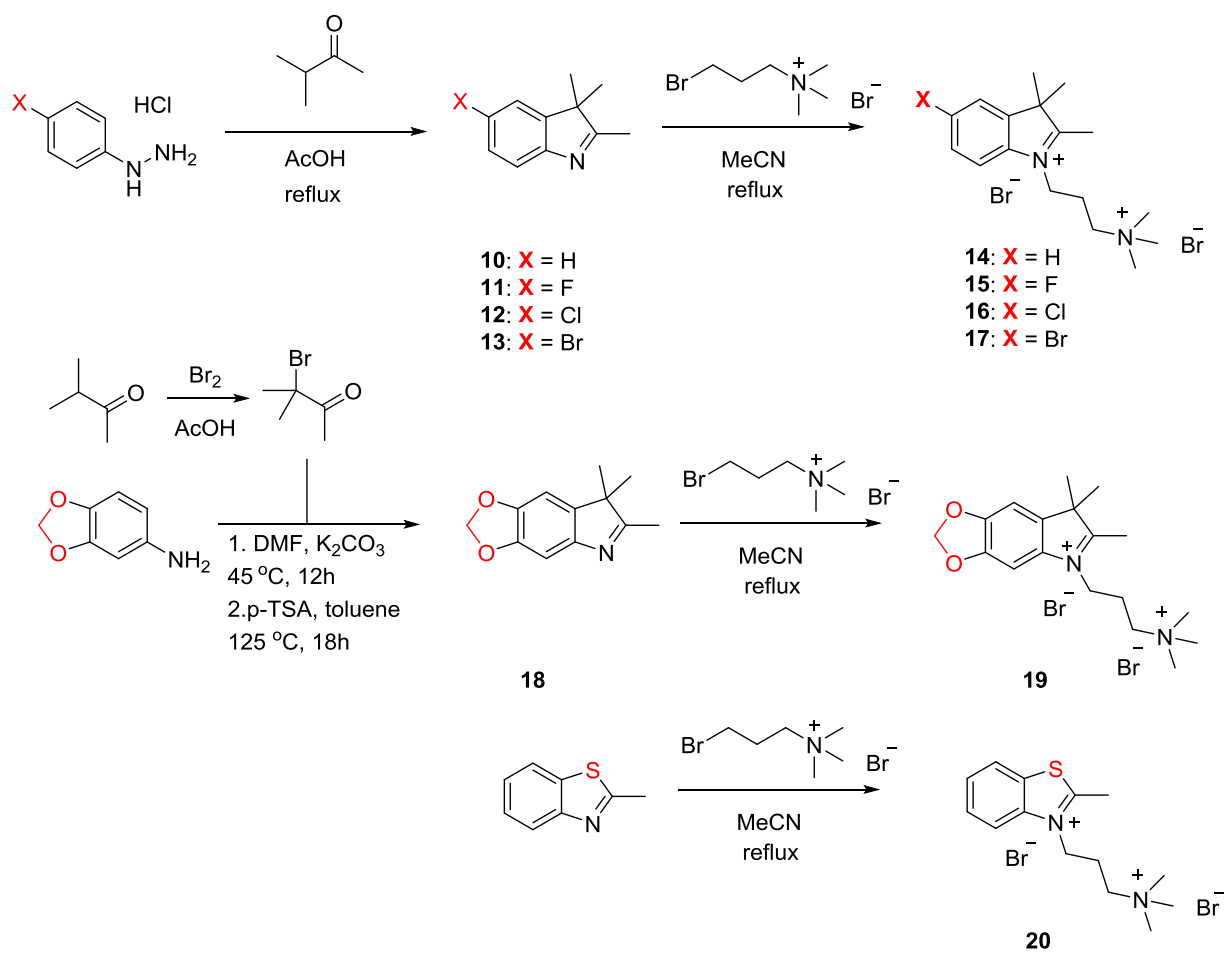
Developing a compound that strongly and selectively binds and stabilizes relevant quadruplex sequences could lead to non-toxic and potent chemotherapeutic.⁸⁻¹² Towards achieving this goal, we have previously reported the synthesis and biophysical evaluation of several symmetric cyanines that feature tricationic character with steric restraints toward duplex interactions and selectively bind the quadruplex.^{13, 14} Our binding mode, however, suggests that an asymmetric compound would be better suited for increasing quadruplex interactions. Asymmetric cyanines are widely employed as nucleic acid labels and noncovalent probes after systematically manipulating their core structure to suit individualized needs.¹⁵⁻²⁰ Their remarkable amenability to these diverse modifications furthers their applicability in nucleic acid targeting. It has been extensively reported that benzothiazole-based compounds bind with a high degree of affinity within the minor groove of DNA and, through systematic modifications, some degree of sequence specificity may be obtained. Through a reverse engineering of these compounds, we have removed the duplex binding affinity through well-placed steric restraints and incorporated a planar heterocyclic moiety for effective end-stacking with the quadruplex.

14.3 Synthesis

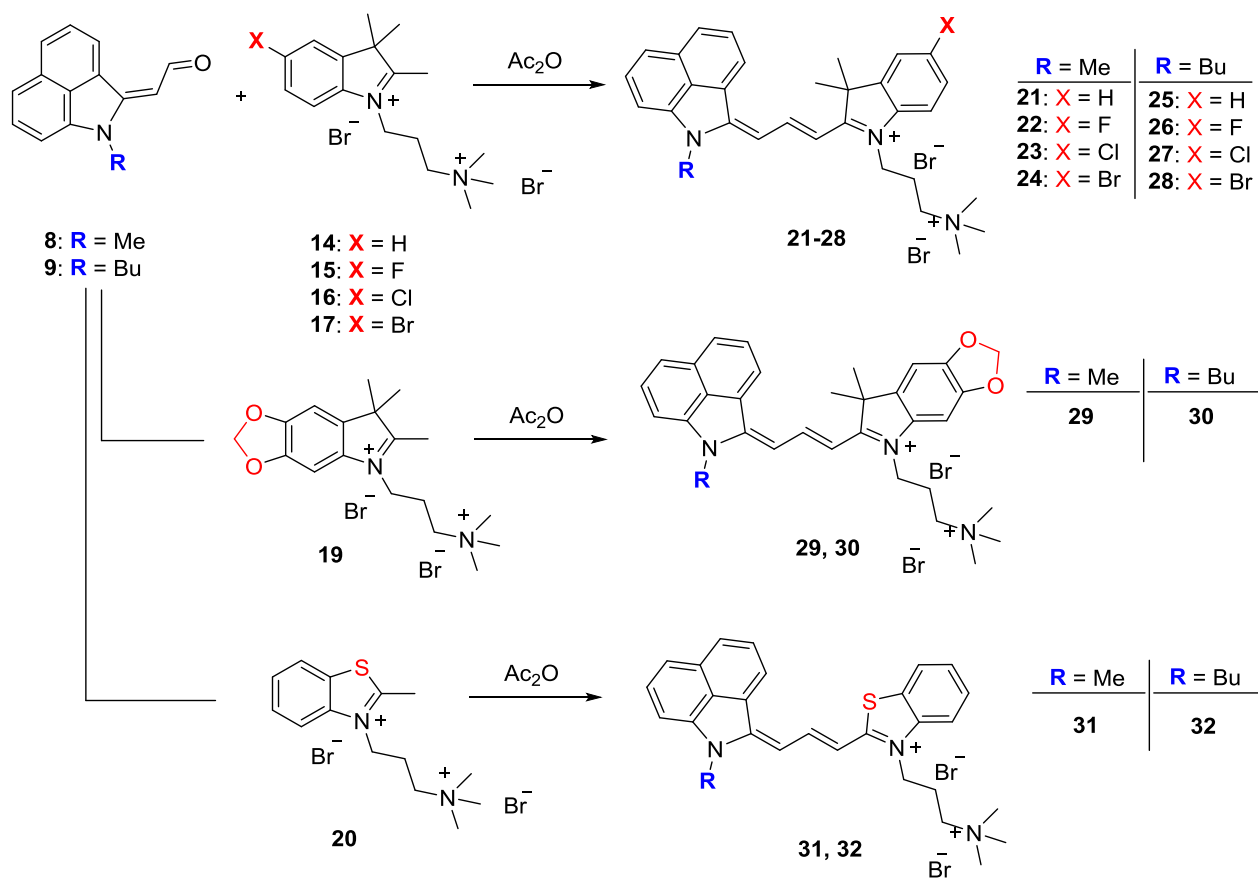
Our effective route toward second generation trimethine cyanine quadruplex binding agents begins with the commercially available benz[*c,d*]indol-2(1H)-one. Treatment of this reagent with phosphorous pentasulfide effectively yields the corresponding thione which is activated through simple alkylation using iodomethane. Meldrum's acid in a highly basic environment will replace the methanethiol affording the enamine intermediate. At this point, the heterocyclic nitrogen is activated to perform S_N2 chemistry in basic media. Alkylation was performed using either iodomethane or iodobutane to afford the tertiary amine. The reactive and acidic methyl group was obtained through thermal and acidic decomposition of the protecting Meldrum's acid group leaving the terminal methyl moiety for further modification. Subjecting the reactive methyl group to the Vilsmeier formylation reaction followed by alkaline cleavage affords the intermediate for half of the final binding ligand. The alternate half is formed through the well-established Fischer-indole reaction with halogenated phenyl hydrazine salts and 3-methyl-2-butanone which, in the presence of refluxing acetic acid, effectively affords the bicyclic products through a hydrazone intermediate followed by a pericyclic rearrangement. Alkylation of this heterocyclic precursor in dry acetonitrile with the corresponding bromopropyl trimethylammonium bromide affords the highly hygroscopic dicationic salts for the second half of the target binding agents. Combining each of the heterocyclic precursors in acetic anhydride yields the final bright blue colored asymmetric cyanine binding ligands.



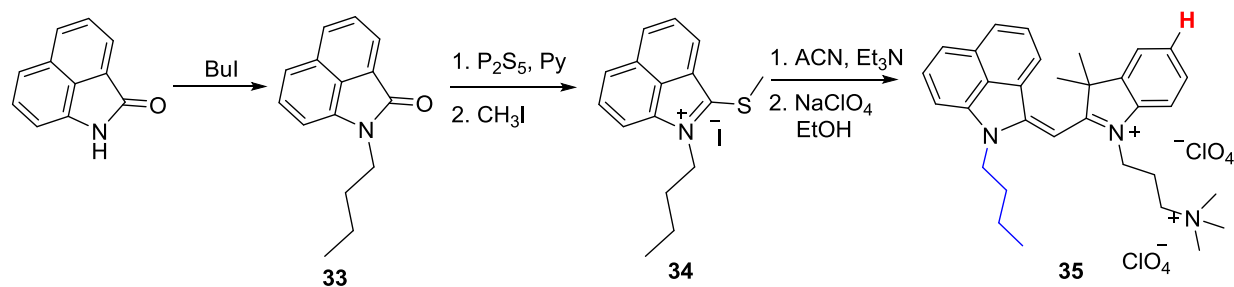
Scheme 1. Formation of the aldehyde intermediate of the benz[*c,d*]indolenine heterocyclic unit for reaction to form the final quadruplex binding ligands.



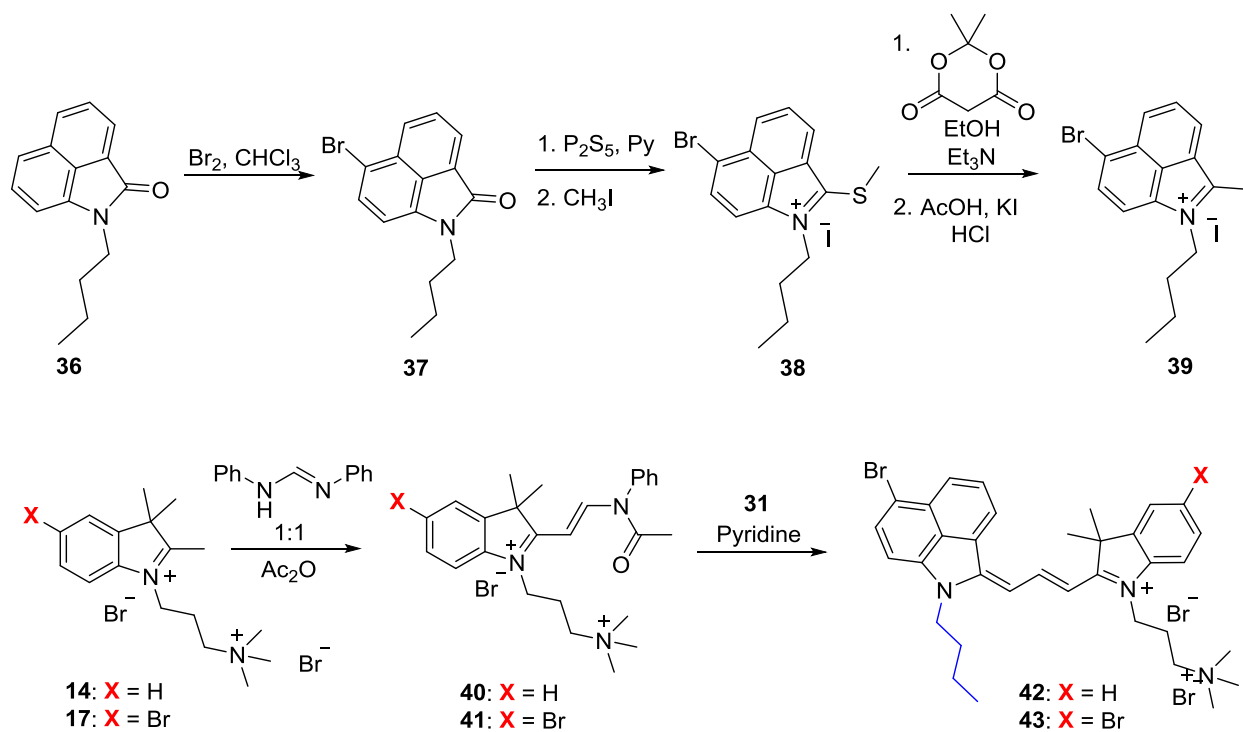
Scheme 2. Preparation of dicationic salts **14-17**, **19**, **20**.



Scheme 3. Final synthetic step for compounds 21-32.



Scheme 4. Preparation of the monomethine cyanine compound for quadruplex binding.



Scheme 5. Synthetic route for the brominated benz[*c,d*]indole ring and formation of the trimethine cyanine structure.

Routes to two synthetic precursors were employed to generate potential quadruplex binding agents based on our results in previous publications. We have seen that the length between heterocycles can influence the binding interactions; additionally, heterocyclic halogenations were observed to increase the binding strength to the quadruplex. We were interested in whether shortening the polymethine bridge by one vinylene ($-\text{CH}=\text{CH}-$) unit would make a substantial change in the thermal melting data. The benzo[*c,d*]indole-intermediate was alkylated and in basic conditions, the dicationic salt **14** is nucleophilic enough to displace the thiomethane group to afford the monomethine cyanine. Surprisingly, the binding efficacy was completely removed when shortening the compound by a subtle 2.96 angstroms (as determined by measurements of the lowest energy structures minimized using DFT calculations with the B3LYP basis set) and we therefore we discontinued the pursuit of monomethine cyanines as strong quadruplex interacting

agents. This 2.96 angstrom difference requires the three-dimensional form of the monomethine compound to twist out of plane in comparison to the highly planar trimethine cyanine compounds. In order to strengthen the quadruplex interactions, we thought that incorporating heterocyclic halogenations on the trimethine benz[*c,d*]indolenine heterocyclic portion should yield an increase in binding interaction as we previously found.

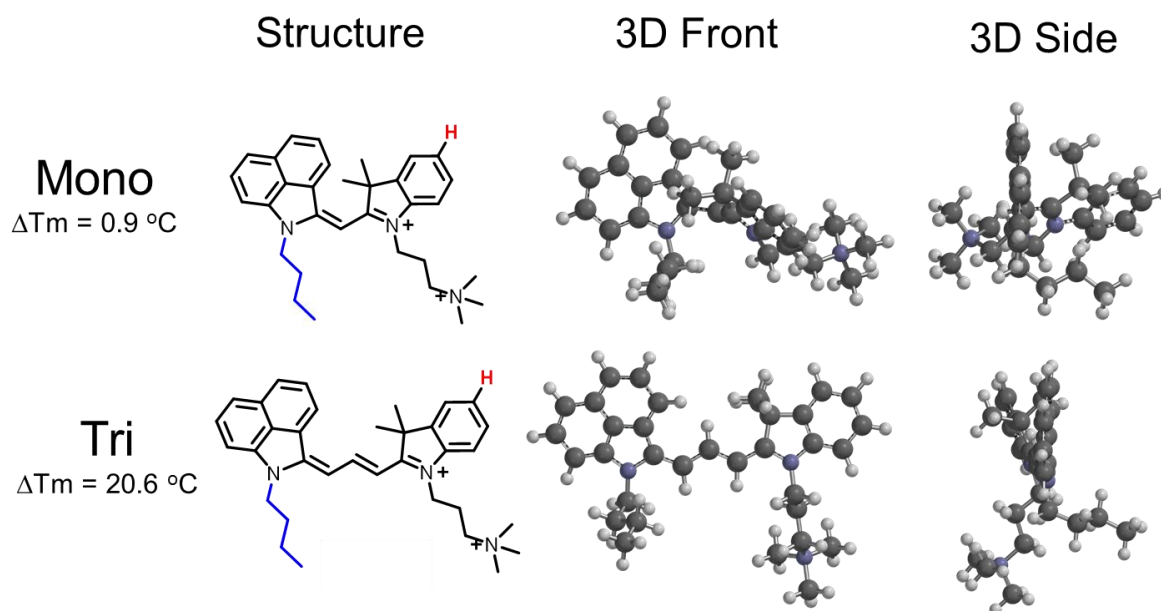


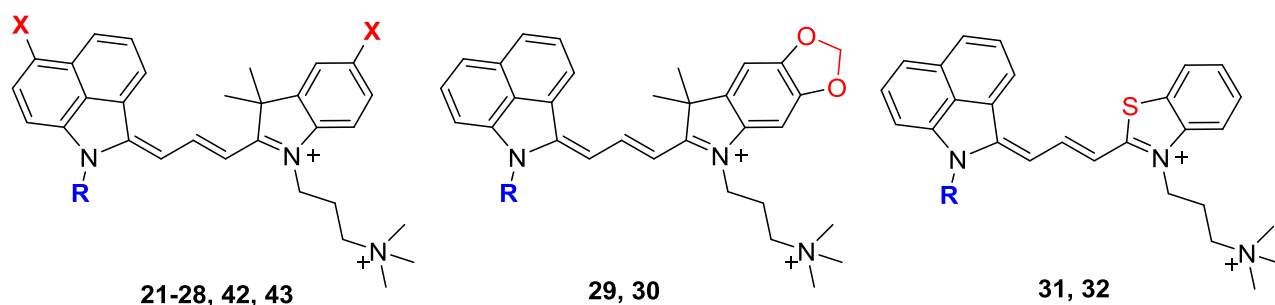
Figure 14-1. Molecular depictions of the most energetically favorable state for monomethine compound compared to trimethine analog showing drastically different twisting associated with the reduction of the polymethine-bridge and corresponding ΔT_m measurements at 4:1 compound:Tel22 ratio.

The synthesis of these brominated compounds (monobromo **34** and dibromo **35**) involves a varied synthetic route starting with the alkylation of the thioester compound affording the butyl derivative—as it showed improved G4 binding compared to the methyl counterpart. The heterocyclic portion, *para* to the tertiary amide nitrogen, was found to be sufficiently activated for effective bromination. This intermediate was prepared and reacted in similar fashion as previously described to afford the methylene intermediate. Correspondingly, the reaction of dicationic salts

(**14** and **17**) with diphenylformamidine in a 1:1 molar ratio in boiling acetic anhydride with careful reaction monitoring affords the half-reacted compound which undergoes loss of acetanilide by nucleophilic displacement by the brominated benzo[*c,d*]-containing analog.

Biophysical Evaluation. In order to screen for initial efficacy in quadruplex DNA binding affinity and corresponding selectivity against duplex DNA, we utilized UV-thermal melting. Thermal melting provide a quick scan for a quick selection of compounds for further analysis. Next, surface plasmon resonance was done to dyes with high change in thermal melting with quadruplex DNA while little to no binding with duplex DNA. Surface plasmon resonance is beneficial in quantitatively analyzing the affinity as well as the binding kinetics with two types of quadruplex motifs (parallel or mixed)

Table 1: General molecular structures and T_m changes of new unsymmetrical trimethine cyanine binding agents with telomeric quadruplex (TEL22) and a control duplex sequence (AATT).



ID	Heterocyclic Modifications		Tel22 (Compound:DNA)				AATT (Compound:DNA)
	Benz[<i>c,d</i>]	Other	(1:1)	(2:1)	(4:1)	(6:1)	(4:1)
21	Methyl, -H	-H	4.4	9.9	17.4	22.5	3.6
22	Methyl, -H	-F	4.3	9.9	18.0	22.0	3.4
23	Methyl, -H	-Cl	0.0	7.4	16.5	22.1	3.5
24	Methyl, -H	-Br	2.7	9.0	16.4	21.8	3.3
25	Butyl, -H	-H	2.1	7.8	20.6	26.3	2.3
26	Butyl, -H	-F	1.1	2.9	19.8	25.3	1.1
27	Butyl, -H	-Cl	4.2	9.2	22.8	23.3	2.2
28	Butyl, -H	-Br	2.5	11.2	20.9	23.3	2.2
29	Methyl, -H	-O-CH ₂ -O-	2.2	5.7	6.3	ND	ND
30	Butyl, -H	-O-CH ₂ -O-	1.1	4.1	ND	24.8	2.0
31	Methyl, -H	-S-	2.5	6.1	ND	ND	5.6
32	Butyl, -H	-S-	2.5	9.5	ND	ND	ND
35	Butyl, -H	-H	1.0	0.5	0.9	1.4	0.3
42	Butyl, -Br	-H	1.0	2.0	8.7	ND	2.3
43	Butyl, -Br	-Br	1.1	4.3	ND	ND	0.6

ND = Not Determined

Thermal melting screening data was followed by more sophisticated techniques to determine binding constants for these compounds to quadruplex DNA (Tel22 and MYC19). Surface plasmon resonance spectroscopy help to determine the exact binding association constants

of ligands to the quadruplex. When the methylated compound was examined, the SPR response indicated a strong binding affinity to both MYC19 and Tel22; however, the butylated counterpart revealed higher affinity for the MYC19 quadruplex forming sequence compared to the methyl analog. Additionally, the butyl-substituted ligand displayed remarkable selectivity with the binding affinity to MYC19 being orders of magnitude higher when analyzed through the steady-state binding plot. These results fully agree with the T_m measurements and offer more concrete and quantitative insight into the binding strength of these asymmetric trimethine compounds to the two different quadruplex forming sequences.

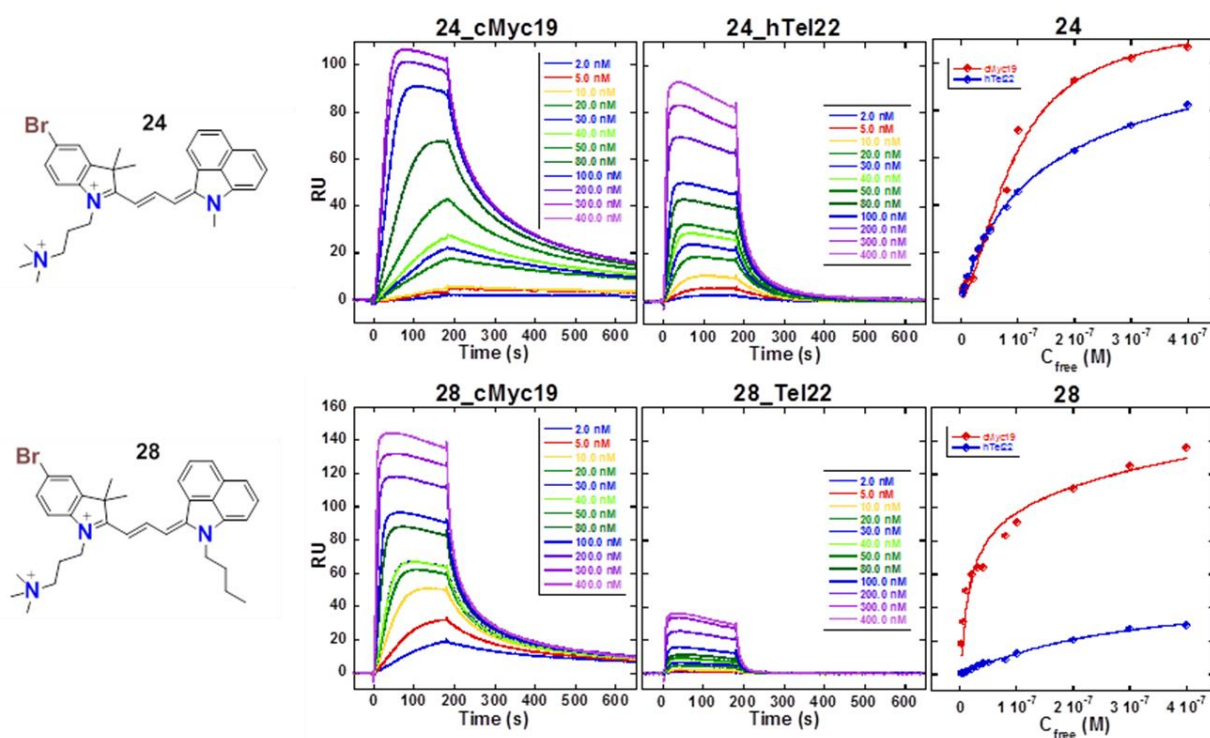


Figure 14-2. Surface Plasmon Resonance Sensograms. The G4 binding agents 24 (methyl) and 28 (butyl) were examined with TEL22 and MYC19 DNA.

14.4 Nuclear Magnetic Resonance Spectroscopy

In order to accurately determine the binding localization on the quadruplex and to guide molecular modeling studies, NMR titrations were performed with Tel24 (Figure 3) and MYC (data not shown). Tel24 was selected for NMR studies because there is only a single form in solution versus Tel22 which has an unknown major fold. Several folding patterns associated with Tel22 complicates the imino proton spectrum and makes deciphering the binding more difficult. We are confident that the two quadruplex sequences are similar enough to be comparable as thermal melting data (Supporting Information) shows similar results between Tel22 and Tel24 indicating similar binding affinity which suggests similar binding modes. The imino proton NMR spectra in Figure 3 shows two binding ligands, compound 22 on the left and 26 on the right, and the guanine nucleotides that show perturbations in the spectra when the ratio of compound:DNA is increased from 1:0 to 1:1. The disappearance of the NMR peaks indicates an interaction between the compound and the DNA at the location corresponding to the affected imino proton. For example, imino protons corresponding to 3, 9 and 17 shift the most as indicated by the red arrows and corresponding red coloring on the cartoon schematic.

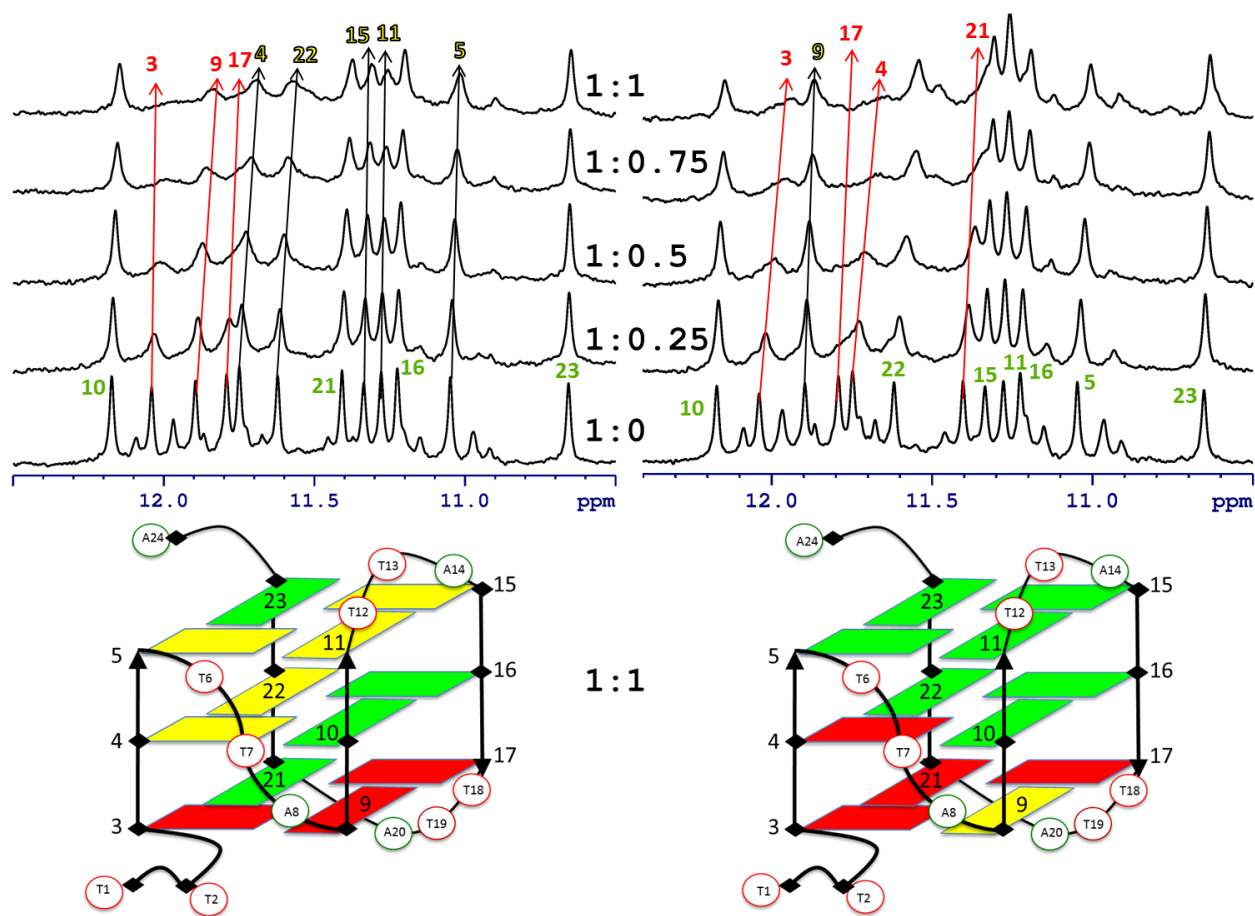
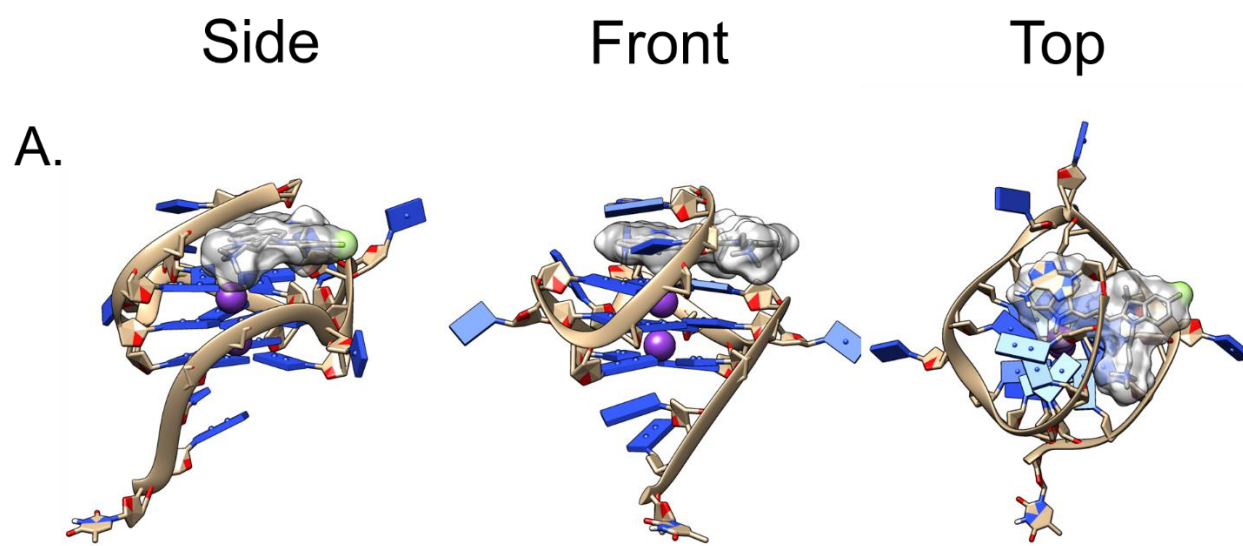


Figure 14-3 TEL24 quadruplex titration with 22 (left) and 26 (right) followed with the imino proton spectra of TEL24. Ligands were added to the quadruplex at the ratio indicated on the plot, where 1:0 ratio corresponds to the imino proton spectrum of TEL24 with no ligand added. Schematic structures of TEL24 are color coded according to the imino protons affected in the titrations. Red residues are strongly affected, yellow are somewhat affected, and green are not affected.

Molecular Modeling.

Using the NMR data as a template, we proceeded with molecular dynamics simulations in order to examine the binding mode and exact points of contact with the quadruplex. We see that the planar benz[cd] heterocyclic portion inserts under the quadruplex loop which is logical based on the steric restraints between the tetraplex surface and the dynamic look. The alternate heterocycle bearing the ammonium arm aligns itself well with the edge of the quadruplex and the quaternary ammonium group inserts itself in the available groove of the quadruplex. This binding paradigm is conserved in both the methylated and butylated compounds.



B.

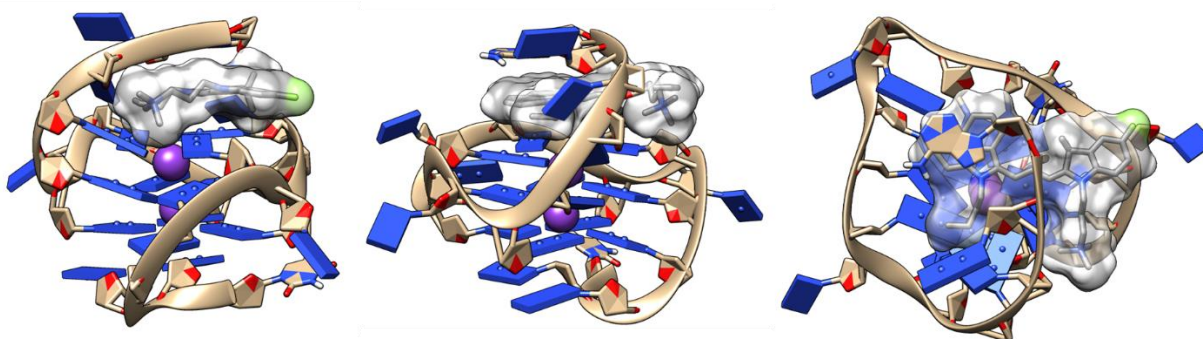


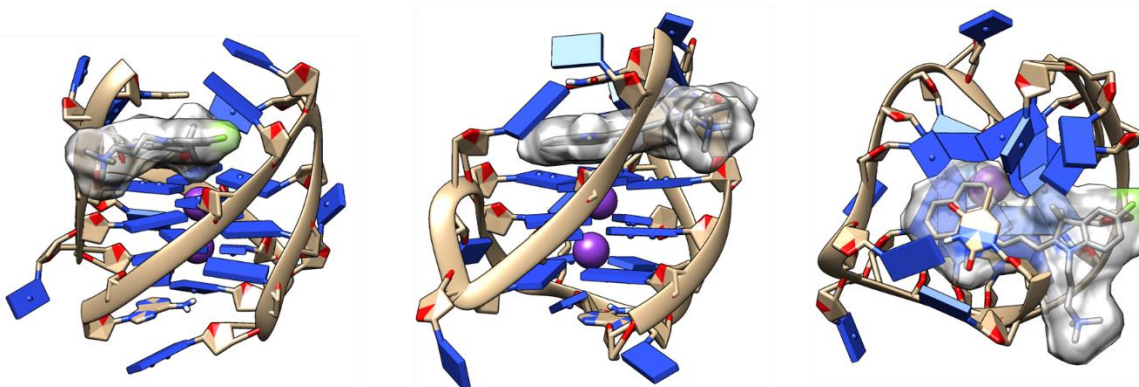
Figure 14-4. Molecular dynamics and corresponding snapshots for the binding of compounds 24 and 28 to MYC DNA. (A) compound 24 with MYC, (B) compound 28 with MYC

Side

Front

Top

A.



B.

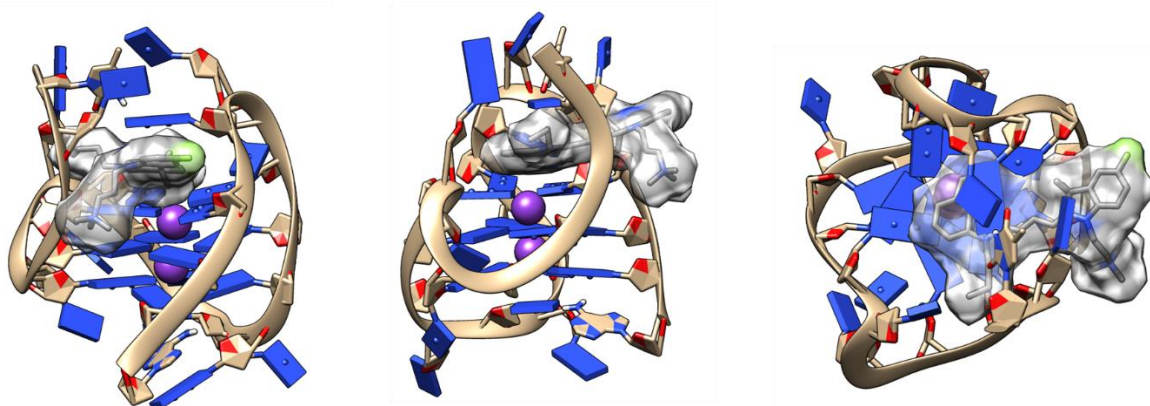


Figure 14-5. Molecular dynamics and corresponding snapshots for the binding of compounds 24 and 28 to TEL22 DNA. (A) Compound 24 with TEL22, (B) Compound 28 with TEL22.

14.5 Discussion

The benz[*c,d*]indole displays a highly planar surface that could interact by both stacking with the quadruplex end and intercalating between the base-pairs of AT-rich DNA sequences, especially when the heterocyclic nitrogen atom bears a single methyl group. We have observed that by elongating this alkyl chain, we help to discriminate against AT duplex binding probably due to the steric repulsion provided by the butyl chain which repels the heterocyclic unit from intercalation with the duplex DNA nucleotides and interacts favorably with the quadruplex groove. Dyes that have butyl chain are also showed to bind with parallel and discriminating against mixed quadruplex DNA using binding affinity data from SPR. In addition the kinetic of the SPR also showed that butyl chain have longer dissociation time with parallel quadruplex, this mean that the dyes: DNA interaction are tighter.

14.6 Conclusions

Through an optimized synthetic route, we have prepared second generation trimethine cyanines that display higher binding affinity to quadruplex DNA with high selectivity over the

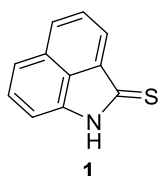
AATT rich sequences. NMR guided molecular modeling results have given an interesting end stacking binding mode with groove interactions being achieved by the quaternary ammonium arm. These structures suggest that developing asymmetric binding ligands may help take advantage of the asymmetry involved in many quadruplex forming sequences. SPR experimental results of dyes binding to quadruplex showed that there are more than one sites interaction where the primary sites is stronger while other binding sites weaker than 10-fold. Selectivity using SPR data also showed that these set of dyes have more binding and stability with parallel (MYC19) over antiparallel quadruplex structure (Tel22).

14.7 Materials and Methods

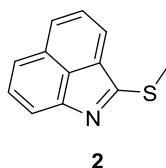
All starting reagents were obtained commercially from Sigma Aldrich or Matrix Scientific and were used without purification. Nuclear magnetic resonance experiments were performed on a Bruker Avance 400 MHz spectrometer and processed using Topspin 3.1. Chemical shift values are reported versus tetramethylsilane as an internal standard purchased in the commercially obtained deuterated solvents (Cambridge Isotope Laboratory). The reactions were followed using silica gel 60 F₂₅₄ thin layer chromatography plates (Merck EMD Millipore, Darmstadt, Germany). Open column chromatography was utilized for the purification of all final compounds using 60-200u, 60A, classic column silica gel (Dynamic Adsorbents, Norcross, GA). UV-Vis/NIR absorption spectra were recorded on a Varian Cary 50 spectrophotometer. High-resolution accurate mass spectra (HRMS) were obtained either at the Georgia State University Mass Spectrometry Facility using a Waters Q-TOF micro (ESI-Q-TOF) mass spectrometer or utilizing a Waters Micromass LCT TOF ES+ Premier Mass Spectrometer. Liquid chromatography utilized a Waters 2487 single wavelength absorption detector with wavelengths set between 640 and 700 nm depending on the particular photophysical properties. The column used in LC was a Waters

Delta-Pak 5 μ M 100A 3.9 x 150 mm reversed phase C₁₈ column. Evaporative light scattering detection analyzes trace impurities that cannot be observed by alternate methods; a SEDEX 75 ELSD was utilized in tandem with liquid chromatography to confirm purity (>95% as determined by LC-ELSD-MS).

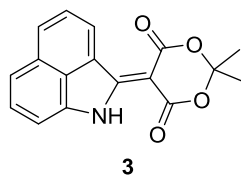
14.7.1 Synthesis.



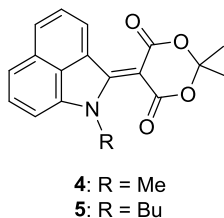
Benzo[cd]indole-2(1H)-thione (1): Freshly distilled pyridine (200 ml) was added to commercially obtained benzo[*c,d*]indol-2(1H)-one (53.9 g, 0.24 mol) and phosphorus pentasulfide (80 g, 0.36 mol). This mixture was heated at 110° C for 2h and then cooled to room temperature. DI water (650 ml) was added to the reaction mixture and the resulting suspension was allowed to stand for 1h. An oily residue was obtained which was extracted with diethyl ether (3 x 350 ml) and the organic layer was washed with 1M HCl solution followed by brine. The organic layer was collected and dried over MgSO₄. The solvent was evaporated to afford the product as orange oil (53.1 g) which was used in the next step without additional purification.



2-(methylthio)benzo[cd]indole (2): A solution of **2** (53.1 g, 0.22 mol) was added to a solution of iodomethane (70 ml). The resulting solution was stirred at room temperature for 24 h. The precipitate was filtered off, washed with diethyl ether (3 x 50 ml) and acetone (2 x 50 ml). Yield 91%.

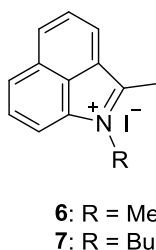


Compound **3** was synthesized as previously reported.



A mixture of compound **3** (10.2 mmol), alkyl iodide (30.6 mmol) and K_2CO_3 (30.6 mmol) were heated in DMF (40 mL) at 90 °C for 18 h under a nitrogen atmosphere. The mixture was cooled to room temperature and then filtered. The filtrate was concentrated under reduced pressure. The residue was purified on silica gel (flash column chromatography, using EtOAc–hexanes, 1:2 as an eluent).

(**5**): Yield 74%, 1H NMR (400 MHz, $DMSO-d_6$) δ 0.86 (t, $J = 7.6$ Hz, 3H), 1.27 (q, $J = 7.6$, 2H), 1.75 (s, 6H), 1.82 (p, $J = 7.2$ Hz, 2H), 3.39 (t, $J = 7.6$ Hz, 2H), 7.79 (t, $J = 7.6$ Hz, 1H), 7.94 (t, $J = 8.0$ Hz, 1H), 8.02 (d, $J = 7.2$ Hz, 1H), 8.06 (d, $J = 8.4$ Hz, 1H), 8.45 (d, $J = 8.0$ Hz, 1H), 8.91 (d, $J = 7.2$ Hz, 1H).



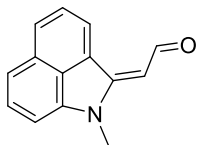
Ester **4-5** (2.9 mmol) was dissolved in acetic acid (4 mL) and the mixture was refluxed for 20 min. Concentrated HCl (4 mL) was added dropwise to the refluxing mixture until the color

changed from red to green. The mixture was cooled to room temperature, and saturated KI solution was added until the product started to precipitate. The product was filtered off, washed with ether, and dried *in vacuo* affording quaternary ammonium salts **6-7** in good yield.

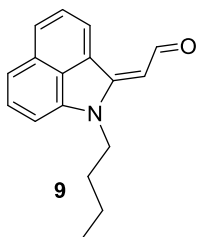
(**7**): Yield 82%, ^1H NMR (400 MHz, DMSO- d_6) δ 0.86 (t, $J = 7.2$ Hz 3H), 1.27 (m, 2H), 1.75 (s, 6H), 1.82 (p, $J = 6.8$ Hz, 2H), 4.39 (t, $J = 7.6$ Hz, 2H), 7.79 (t, $J = 8.0$ Hz, 1H), 7.94 (t, $J = 7.6$ Hz, 1H), 8.02 (d, $J = 7.2$ Hz, 1H), 8.07 (d, $J = 8.4$ Hz, 1H), 8.45 (d, $J = 8.0$ Hz, 1H), 8.91 (d, $J = 7.2$ Hz, 1H).

Synthesis of Benz[cd]indole aldehydes **8-9**

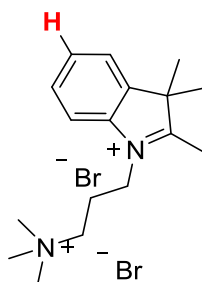
Individual alkylated compound was subjected to Vilsmeier formylation. DMF (5 mL) was added to an oven dried and nitrogen cooled round bottom flask and allowed to stir at 0 °C. Phosphorous oxychloride (1.5 mol. eq.) was added dropwise to the cold solution under high stirring. The reaction mixture was allowed to warm to room temperature while stirring for 20 minutes. After 20-30 minutes at room temperature, the reaction mixture is cooled to 0 °C again. The individual alkylated benz[cd]indole compound was added to the cooled reaction mixture dropwise *via* syringe. The reaction was then allowed to warm to room temperature and heated to 80 °C for 8h. After the starting material was consumed by monitoring with TLC eluting in 5% methanol in dichloromethane, the reaction mixture was allowed to cool. The resulting mixture was added to a cold 40% sodium perchlorate solution in water. The solution was left in the freezer for 6h. The precipitate was then filtered and added to a 50% KOH solution in water and the reaction mixture was heated to reflux to hydrolyzed the dimethyl amine moiety and synthesize the aldehyde moiety. After 12h., the reaction mixture was allowed to cool and the product was extracted in DCM and the solvent was removed under reduced pressure to afford the dark green/brown solid in the indicated yield.

**8**

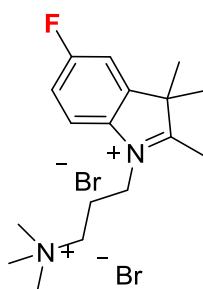
(*E*)-2-(1-methylbenzo[cd]indol-2(1*H*)-ylidene)acetaldehyde (**8**): Yield 20%; mp 149-151°C; ¹H NMR (400 MHz, DMSO-*d*₆): δ 3.48 (s, 3H), 5.79 (d, *J* = 7.6 Hz, 1H), 7.15 (m, 1H), 7.51-7.70 (m, 2H), 7.71 (t, *J* = 8.9 Hz, 1H), 8.05 (d, *J* = 8.0 Hz, 1H), 8.58 (d, *J* = 7.2 Hz, 1H), 10.30 (d, *J* = 7.6 Hz, 1H). ¹³C NMR (100 MHz, DMSO-*d*₆): δ 30.08, 102.92, 105.17, 119.29, 125.74, 126.52, 129.54, 129.57, 130.11, 130.26, 143.16, 156.32, 186.25.

**9**

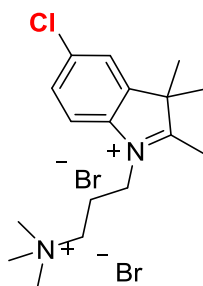
(*E*)-2-(1-butylbenzo[cd]indol-2(1*H*)-ylidene)acetaldehyde (**9**): Yield 41%; mp 178-180°C; ¹H NMR (400 MHz, DMSO-*d*₆): δ 0.19 (t, *J* = 7.6 Hz, 3H), 1.41-1.36 (m, 2H), 1.64 (p, *J* = 7.2 Hz, 2H), 3.98 (t, *J* = 7.6 Hz, 2H), 5.83 (d, *J* = 7.6 Hz, 1H), 7.13 (t, *J* = 7.2 Hz, 1H), 7.50 (s, 2H), 7.72 (t, *J* = 7.6 Hz, 1H), 8.06 (d, *J* = 8.0 Hz, 1H), 8.59 (d, *J* = 7.2 Hz, 1H), 10.32 (d, *J* = 7.6 Hz, 1H). ¹³C NMR (100 MHz, DMSO-*d*₆): δ 14.22, 20.07, 29.82, 42.60, 102.96, 105.34, 119.27, 126.70, 129.59, 130.17, 130.38, 142.82, 155.37, 186.36.

**14**

2,3,3-Trimethyl-1-(3-(trimethylammonio)propyl)-3H-indol-1-ium bromide (14): (2.52 g, 61%); MP 197-199°C. ^1H NMR (400 MHz, DMSO- d_6): δ 1.58 (s, 6H), 2.41 (m, 2H), 2.99 (s, 3H), 3.17 (s, 9H), 3.98 (t, $J = 7.6$ Hz, 2H), 4.57 (t, $J = 7.6$ Hz, 2H), 7.45 (m, 2H), 7.86 (d, $J = 5.2$ Hz, 1H), 8.19 (d, $J = 5.2$ Hz, 1H). ^{13}C NMR (100 MHz, DMSO- d_6): δ 21.3, 22.0, 25.4, 44.6, 52.5, 61.9, 64.9, 115.6, 123.5, 129.0, 129.4, 140.9, 141.8, 197.8. HRMS (ESI) calculated for $[\text{C}_{17}\text{H}_{27}\text{N}_2]^+$ m/z 259.2174, found m/z 259.2177.

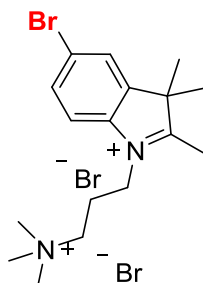
**15**

5-Fluoro-2,3,3-trimethyl-1-(3-(trimethylammonio)propyl)-3H-indol-1-ium bromide (15): Yield 90%; mp 237-240 °C; ^1H NMR (400 MHz, D $_2$ O): δ 1.56 (s, 6H), 2.47 (t, $J = 8.8$ Hz, 2H), 3.17 (s, 9H), 3.65 (tt, $J = 8.4$ Hz, $J = 8.4$ Hz, 2H), 4.53 (t, $J = 8.0$ Hz, 2H), 7.34 (t, $J = 9.2$ Hz, 1H), 7.82 (dd, $J = 8.8$ Hz, $J = 4.0$ Hz, 2H). ^{13}C NMR (100 MHz, DMSO- d_6): δ 12.2, 20.0, 20.7, 43.3, 52.1, 53.2, 61.5, 115.9, 123.3, 128.8, 134.3, 138.2, 142.3, 197.9.

**16**

5-Chloro-2,3,3-trimethyl-1-(3-(trimethylammonio)propyl)-3H-indol-1-ium bromide (16): Yield 82%; mp 215–217 °C; ^1H NMR (400 MHz, DMSO- d_6): δ 1.65 (s, 6H), 2.56 (t, $J = 8.0$ Hz,

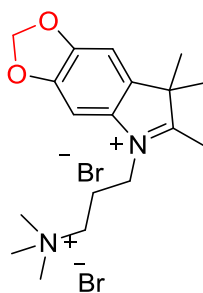
2H), 3.25 (s, 9H), 3.73 (tt, $J = 8.0$ Hz, $J = 8.0$ Hz, 2H), 4.64 (t, $J = 8.0$ Hz, 2H), 4.80 (s, 3H), 7.69 (dd, $J = 8.8$ Hz, $J = 2.0$ Hz, 1H), 7.84–7.92 (m, 2H); ^{13}C NMR (100 MHz, $\text{DMSO-}d_6$): δ 12.2, 20.0, 20.7, 43.3, 52.1, 53.2, 61.5, 115.9, 123.3, 128.8, 134.3, 138.2, 142.3, 197.9. Composition in theory: C(44.91%), H(5.99%), N(6.16%); Composition found: C(45.01%), H(6.29%), N(6.08%); HRMS (ESI) calculated for $[\text{C}_{17}\text{H}_{27}\text{ClN}_2]^{2+}$ m/z 147.4356, found m/z 146.9909, 148.0421



17

5-Bromo-2,3,3-trimethyl-1-(3-(trimethylammonio)propyl)-3H-indol-1-ium bromide (17):

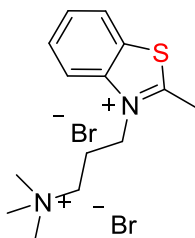
Yield 81%; MP 225–227 C; ^1H NMR (400 MHz, $\text{DMSO-}d_6$): δ 1.57 (s, 6H), 2.27 (s, 9H), 3.02 (s, 3H), 3.83 (t, $J = 8.0$ Hz, 2H), 4.57 (t, $J = 8.0$ Hz, 2H), 7.61 (m, 2H), 7.88 (t, $J = 5.6$ Hz, 1H). ^{13}C NMR (100 MHz, $\text{DMSO-}d_6$): δ 15.2, 22.0, 25.5, 30.6, 52.3, 54.3, 63.9, 115.6, 123.5, 128.8, 129.3, 140.9, 141.7, 197.7. Composition in theory: C(40.91%), H(5.45%), N(5.61%); Composition found: C(40.84%), H(5.48%), N(5.94%); HRMS (ESI) calculated for $[\text{C}_{17}\text{H}_{27}\text{BrN}_2]^{2+}$ m/z 169.6611, found m/z 169.7002.



19

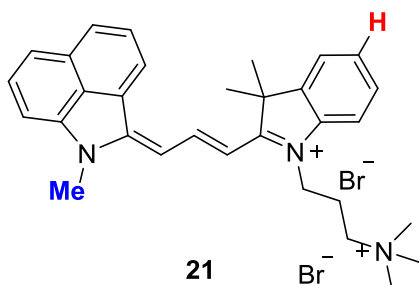
6,7,7-trimethyl-5-(3-(trimethylammonio)propyl)-7H-[1,3]dioxolo[4,5-f]indol-5-ium

bromide (19): Yield 70%; Mp 255-257 °C; ¹H NMR (400 MHz, D₂O), δ: 1.48 (s, 6H), 2.45-2.40 (m, 2H), 3.14 (s, 9H), 3.59 (t, *J* = 8.8 Hz, 2H), 4.44 (t, *J* = 8.0 Hz, 2H), 6.07 (s, 2H), 7.16 (s, 1H), 7.31 (s, 1H). ¹³C NMR (100 MHz, D₂O), δ: 21.50, 21.85, 44.45, 53.26, 54.48, 62.56, 62.59, 96.56, 103.02, 103.84, 134.31, 137.03, 148.49, 149.67, 195.93.



20

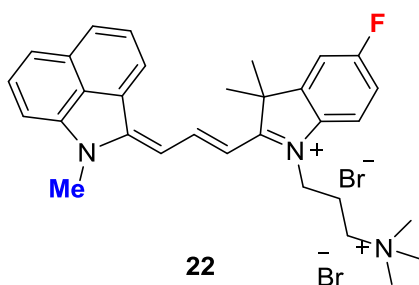
2-methyl-3-(3-(trimethylammonio)propyl)benzo[d]thiazol-3-ium bromide (20): Yield 93%; Mp >260 °C; ¹H NMR (400 MHz, DMSO-*d*₆), δ: 2.35 (bs, 2H), 3.07 (s, 9H), 3.19 (s, 3H), 3.62 (t, *J* = 8.4 Hz, 2H), 4.73 (t, *J* = 8.0 Hz, 2H), 7.76 (t, *J* = 7.6 Hz, 1H), 7.86 (t, *J* = 7.6 Hz, 1H), 8.31 (t, *J* = 7.6 Hz, 1H). ¹³C NMR (100 MHz, DMSO-*d*₆), δ: 17.54, 22.04, 46.12, 53.23, 62.26, 116.95, 124.69, 128.80, 129.18, 130.23, 140.94, 177.87.



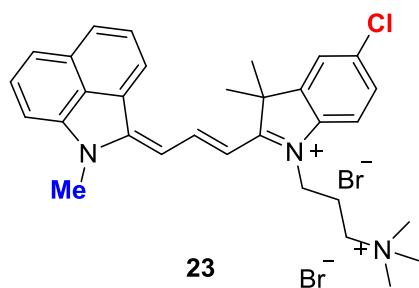
21

3,3-Dimethyl-2-((1E,3E)-3-(1-methylbenzo[cd]indol-2(1H)-ylidene)prop-1-en-1-yl)-1-(3-(trimethylammonio)propyl)-3H-indol-1-ium bromide (21): Yield 33%; Mp >245-247 °C; ¹H NMR (400 MHz, DMSO-*d*₆): 1.79 (s, 6H), 2.23 (t, *J* = 7.2 Hz, 2H), 3.17 (s, 9H), 3.80 (t, *J* = 7.2 Hz, 2H), 3.87 (s, 3H), 4.29 (t, *J* = 7.2 Hz, 2H), 4.64 (t, *J* = 8.0 Hz, 2H), 7.17 (d, *J* = 8.0 Hz, 1H), 7.27

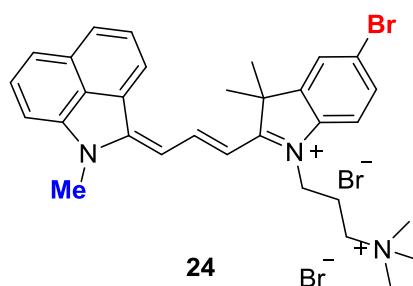
(d, $J = 12.0$ Hz, 1H), 7.37 (d, $J = 8.0$ Hz, 1H), 7.51 (t, $J = 8.0$ Hz, 1H), 7.56 (t, $J = 8.0$ Hz, 1H), 7.63 (d, $J = 12.0$ Hz, 1H), 7.84-7.79 (m, 2H), 7.97 (d, $J = 12.0$ Hz, 1H), 8.08 (d, $J = 8.0$ Hz, 1H), 8.15 (d, $J = 8.0$ Hz, 1H), 8.25 (d, $J = 8.0$ Hz, 1H), 8.79 (t, $J = 12.0$ Hz, 1H). ^{13}C NMR (100 MHz, MeOD- d_4): 21.22, 23.22, 27.77, 40.91, 49.67, 52.42, 62.96, 105.74, 108.48, 109.82, 111.37, 122.34, 122.40, 122.93, 123.10, 125.88, 126.76, 127.75, 128.83, 129.29, 129.54, 129.96, 131.47, 141.38, 141.55, 149.66, 149.68, 149.70, 174.83.



5-Fluoro-3,3-dimethyl-2-((1E,3E)-3-(1-methylbenzo[cd]indol-2(1H)-ylidene)prop-1-en-1-yl)-1-(3-(trimethylammonio)propyl)-3H-indol-1-ium bromide (22): Yield 49%; Mp >260 °C; ^1H NMR (400 MHz, MeOD- d_4), δ : 1.88 (s, 6H), 2.41 (bs, 2H), 3.21 (bs, 2H), 3.29 (s, 9H), 3.83 (s, 3H), 4.36 (t, $J = 7.6$ Hz, 2H), 7.10 (t, $J = 14.4$ Hz, 2H), 7.28 (t, $J = 8.8$ Hz, 1H), 7.43 (d, $J = 7.2$ Hz, 1H), 7.49 (d, $J = 7.6$ Hz, 1H), 7.66-7.60 (m, 2H), 7.73 (d, $J = 8.9$ Hz, 1H), 7.86 (t, $J = 7.6$ Hz, 1H), 8.16 (d, $J = 8.0$ Hz, 1H), 8.21 (d, $J = 7.2$ Hz, 1H), 8.79 (t, $J = 13.6$ Hz, 1H). ^{19}F NMR (375 MHz, DMSO- d_6), δ : 114.09.

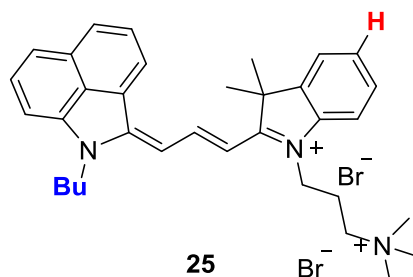


5-Chloro-3,3-dimethyl-2-((1E,3E)-3-(1-methylbenzo[cd]indol-2(1H)-ylidene)prop-1-en-1-yl)-1-(3-(trimethylammonio)propyl)-3H-indol-1-ium bromide (23): Yield 76%; Mp >260 °C; ^1H NMR (400 MHz, DMSO- d_6), δ : 1.30 (s, 6H), 1.91 (bs, 2H), 3.16 (s, 9H), 3.75 (t, $J = 8.0$ Hz, 2H), 3.89 (s, 3H), 4.25 (t, $J = 7.6$ Hz, 2H), 7.16 (d, $J = 14.4$ Hz, 1H), 7.29 (d, $J = 13.2$ Hz, 1H), 7.57 (d, $J = 7.6$ Hz, 1H), 7.74-7.66 (m, 3H), 7.86 (d, $J = 7.6$ Hz, 1H), 7.90 (s, 1H), 8.02 (t, $J = 8.9$ Hz, 1H), 7.86 (t, $J = 7.6$ Hz, 1H), 8.33 (d, $J = 8.0$ Hz, 1H), 8.40 (d, $J = 7.2$ Hz, 1H), 8.71 (t, $J = 13.6$ Hz, 1H). ^{13}C NMR (100 MHz, DMSO- d_6): 21.46, 28.44, 49.91, 53.09, 62.08, 62.64, 106.83, 111.23, 113.82, 123.62, 123.77, 124.75, 129.05, 129.88, 130.12, 130.47, 130.70, 132.28, 141.04, 141.78, 143.73, 149.56, 156.44, 174.23.

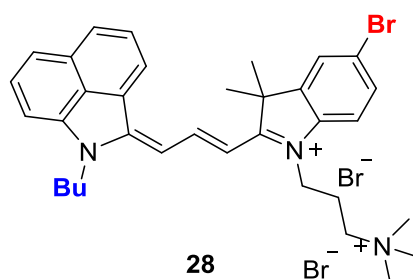


5-Bromo-3,3-dimethyl-2-((1E,3E)-3-(1-methylbenzo[cd]indol-2(1H)-ylidene)prop-1-en-1-yl)-1-(3-(trimethylammonio)propyl)-3H-indol-1-ium bromide (24): Yield 24%; Mp >260 °C; ^1H NMR (400 MHz, DMSO- d_6), δ : 1.80 (s, 6H), 2.19 (bs, 2H), 3.12 (s, 9H), 3.65 (t, $J = 7.2$ Hz, 2H), 3.89 (s, 3H), 4.23 (bs, 2H), 7.04 (d, $J = 13.2$ Hz, 1H), 7.11 (d, $J = 13.2$ Hz, 1H), 7.60 (d, $J = 8.8$ Hz, 1H), 7.76-7.72 (m, 3H), 7.88 (d, $J = 6.8$ Hz, 1H), 7.90 (s, 1H), 8.06 (m, 2H), 7.35 (d, $J = 8.0$ Hz, 1H), 8.42 (d, $J = 7.2$ Hz, 1H), 8.72 (t, $J = 13.2$ Hz, 1H). ^{13}C NMR (100 MHz, DMSO- d_6): 22.57, 29.21, 32.12, 42.42, 51.01, 54.11, 64.41, 106.95, 110.22, 114.29, 119.98, 125.23, 126.25,

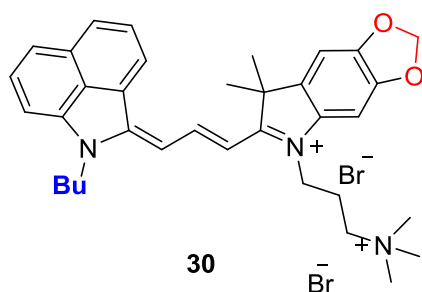
127.30, 128.85, 130.73, 130.89, 131.19, 131.49, 133.22, 133.47, 142.35, 142.84, 144.86, 151.32, 158.77, 175.22.



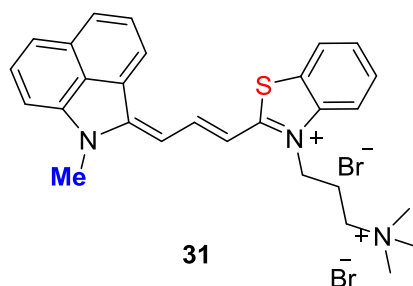
2-((1*E*,3*E*)-3-(1-butylbenzo[*cd*]indol-2(1*H*)-ylidene)prop-1-en-1-yl)-3,3-dimethyl-1-(3-(trimethylammonio)propyl)-3*H*-indol-1-ium bromide (**25**): Yield 54%; Mp 164-165 °C; ^1H NMR (400 MHz, CDCl_3): 0.98 (t, $J = 8.0$ Hz, 3H), 1.60 (q, $J = 8.0$ Hz, 2H), 1.79 (s, 6H), 1.93 (t, $J = 8.0$ Hz, 2H), 2.43 (t, $J = 8.0$ Hz, 2H), 3.41 (s, 9H), 4.36 (t, $J = 8.0$ Hz, 2H), 4.46 (t, $J = 8.0$ Hz, 2H), 4.64 (t, $J = 8.0$ Hz, 2H), 7.17 (d, $J = 8.0$ Hz, 1H), 7.27 (d, $J = 12.0$ Hz, 1H), 7.37 (d, $J = 8.0$ Hz, 1H), 7.51 (t, $J = 8.0$ Hz, 1H), 7.56 (t, $J = 8.0$ Hz, 1H), 7.63 (d, $J = 12.0$ Hz, 1H), 7.84-7.79 (m, 2H), 7.97 (d, $J = 12.0$ Hz, 1H), 8.08 (d, $J = 8.0$ Hz, 1H), 8.15 (d, $J = 8.0$ Hz, 1H), 8.25 (d, $J = 8.0$ Hz, 1H), 8.79 (t, $J = 12.0$ Hz, 1H). ^{13}C NMR (100 MHz, CDCl_3): 13.61, 19.94, 21.46, 28.69, 30.90, 40.99, 44.28, 48.92, 53.85, 61.90, 107.24, 108.77, 110.09, 113.14, 121.34, 122.28, 125.10, 125.60, 125.81, 129.02, 129.07, 129.39, 129.75, 130.71, 140.05, 141.02, 141.11, 149.16, 155.06, 173.29



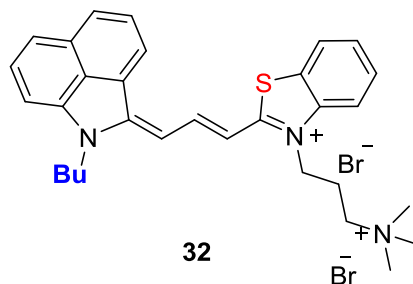
5-Bromo-2-((1E,3E)-3-(1-butylbenzo[cd]indol-2(1H)-ylidene)prop-1-en-1-yl)-3,3-dimethyl-1-(3-(trimethylammonio)propyl)-3H-indol-1-ium bromide (28): Yield 50%; Mp >260 °C; ^1H NMR (400 MHz, DMSO- d_6): 0.93 (t, $J = 8.0$ Hz, 3H), 1.50 (t, $J = 8.0$ Hz, 2H), 1.80 (s, 8H), 2.22 (s, 2H), 3.16 (s, 9H), 3.80 (bs, 2H), 4.25 (bs, 2H), 4.39 (bs, 2H), 7.31 (d, $J = 12.0$ Hz, 1H), 7.46 (d, $J = 8.0$ Hz, 1H), 7.72-7.69 (m, 3H), 7.87 (bs, 1H), 8.01 (t, $J = 8.0$ Hz, 1H), 8.34 (d, $J = 8.0$ Hz, 1H), 8.41 (d, $J = 8.0$ Hz, 1H), 8.75 (d, $J = 12.0$ Hz, 1H). ^{13}C NMR (100 MHz, DMSO- d_6): 14.30, 20.08, 21.46, 28.50, 31.30, 41.80, 44.33, 49.88, 53.09, 62.71, 107.01, 109.35, 111.36, 114.21, 118.52, 123.77, 124.78, 126.35, 128.36, 129.60, 129.99, 130.18, 130.76, 131.88, 132.33, 141.28, 141.47, 144.05, 149.73, 155.70, 174.03.



6-((1E,3E)-3-(1-butylbenzo[cd]indol-2(1H)-ylidene)prop-1-en-1-yl)-7,7-dimethyl-5-(3-(trimethylammonio)propyl)-7H-[1,3]dioxolo[4,5-f]indol-5-ium bromide (30): Yield 63%; Mp >260 °C; ^1H NMR (400 MHz, DMSO- d_6), δ : 0.94 (t, $J = 7.2$ Hz, 3H), 1.50-1.46 (m, 2H), 1.79-1.75 (m, 8H), 2.21 (bs, 2H), 3.15 (s, 9H), 3.74 (d, $J = 7.6$ Hz, 2H), 4.28 (t, $J = 8.8$ Hz, 2H), 6.15 (s, 2H), 7.28-7.18 (m, 2H), 7.47 (d, $J = 8.8$ Hz, 2H), 7.69 (t, $J = 8.0$ Hz, 1H), 7.75 (d, $J = 7.6$ Hz, 1H), 7.98 (t, $J = 7.6$ Hz, 1H), 8.31-8.25 (m, 2H), 8.64 (t, $J = 12.0$ Hz, 1H). ^{13}C NMR (100 MHz, MeOD- d_4): 12.94, 19.90, 21.31, 27.81, 30.83, 41.35, 43.71, 49.77, 52.62, 62.86, 94.11, 102.36, 103.14, 106.48, 107.82, 109.15, 122.35, 125.01, 126.33, 129.28, 129.46, 129.61, 130.20, 130.93, 135.52, 135.56, 141.22, 147.16, 148.30, 148.78, 154.79, 174.94.

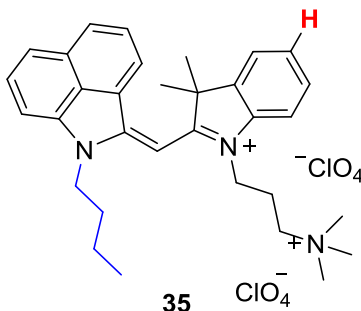


2-((1*E*,3*E*)-3-(1-methylbenzo[*cd*]indol-2(1*H*)-ylidene)prop-1-en-1-yl)-3-(3-(trimethylammonio)propyl)benzo[*d*]thiazol-3-ium bromide (**31**): Yield 37%; Mp 230-232 °C; ¹H NMR (400 MHz, DMSO-*d*₆), δ : 2.28 (bs, 2H), 3.05 (s, 2H), 3.16 (s, 9H), 3.72 (s, 2H), 4.62 (t, *J* = 7.2 Hz, 2H), 6.81 (d, *J* = 13.2 Hz, 1H), 7.41 (d, *J* = 6.8 Hz, 1H), 7.59 (d, *J* = 13.2 Hz, 1H), 7.59 (d, *J* = 13.2 Hz, 1H), 7.75-7.71(m, 4H), 7.87 (t, *J* = 8.0 Hz, 1H), 8.12 (d, *J* = 8.4 Hz, 1H), 8.20 (t, *J* = 8.8 Hz, 2H), 8.45 (d, *J* = 6.8 Hz, 1H), 8.59 (t, *J* = 13.2 Hz, 1H). ¹³C NMR (100 MHz, MeOD-*d*₄): 21.71, 29.52, 43.59, 52.59, 62.56, 105.28, 107.66, 113.78, 121.34, 122.80, 124.89, 126.05, 127.92, 128.58, 128.94, 129.31, 129.55, 129.60, 129.82, 130.18, 140.68, 141.39, 146.38, 154.03, 167.34. HRMS (ESI) calculated for [C₁₇H₂₇BrN₂] ²⁺ m/z 169.6611, found m/z 169.7002.



2-((1*E*,3*E*)-3-(1-butylbenzo[*cd*]indol-2(1*H*)-ylidene)prop-1-en-1-yl)-3-(3-(trimethylammonio)propyl)benzo[*d*]thiazol-3-ium bromide (**32**): Yield 56%; Mp 247-249°C; ¹H NMR (400 MHz, DMSO-*d*₆), δ : 0.94 (t, *J* = 7.2 Hz, 3H), 1.51-1.42 (m, 2H), 1.76 (p, *J* = 7.2, 2H), 2.30 (bs, 2H), 3.12 (s, 9H), 3.80 (s, 2H), 4.21 (t, *J* = 7.2 Hz, 2H), 4.61 (t, *J* = 7.6 Hz, 2H), 7.03 (d, *J* = 11.2 Hz, 1H), 7.41 (d, *J* = 7.2 Hz, 1H), 7.68-7.58 (m, 4H), 7.73 (t, *J* = 7.6 Hz, 1H), 7.89 (t, *J* =

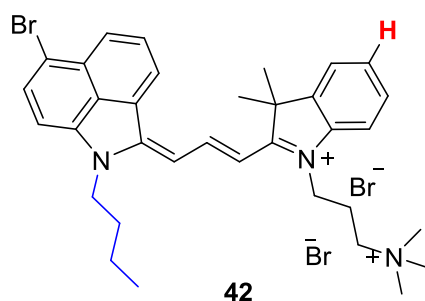
8.0 Hz, 1H), 8.12 (d, $J = 8.4$ Hz, 1H), 8.17 (t, $J = 8.8$ Hz, 2H), 8.44 (d, $J = 6.8$ Hz, 1H), 8.64 (t, $J = 12.4$ Hz, 1H). ^{13}C NMR (100 MHz, DMSO- d_6), δ : 14.32, 20.14, 22.29, 30.83, 43.57, 44.57, 53.11, 62.43, 105.94, 107.77, 108.32, 115.38, 121.40, 124.05, 125.35, 126.87, 127.08, 129.16, 130.01, 130.09, 130.24, 130.61, 141.50, 141.96, 147.06, 152.69, 168.33, 168.37. HRMS (ESI) calculated for $[\text{C}_{17}\text{H}_{27}\text{BrN}_2]^{2+}$ m/z 169.6611, found m/z 169.7002.



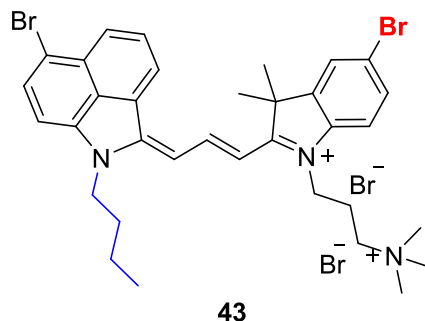
(E)-2-((1-butylbenzo[*cd*]indol-2(1*H*)-ylidene)methyl)-3,3-dimethyl-1-(3-

trimethylammonio)propyl)-3*H*-indol-1-ium perchlorate (**35**): A suspension of **34** (0.57g, 2.5 mmol) and corresponding indolium salt **14** (2.5 mmol) in acetonitrile (15 ml) was added to triethylamine (1 ml) and then refluxed for 1h. The reaction mixture was cooled to room temperature and diethyl ether (75 ml) was added and then allowed to stand for 1h. Precipitated dye was filtered off, washed with diethyl ether (2x50ml) and crude product was purified by anion-exchange reaction with saturated ethanolic solution of sodium perchlorate. Yield 31%; MP > 250° C. ^1H NMR (DMSO- d_6): δ 8.38 (d, $J = 8.0$ Hz, 1H), 8.03 (d, $J = 8.0$ Hz, 1H), 7.93-7.88 (m, 2H), 7.78-7.71 (m, 4H), 7.58 (t, $J = 8.0$ Hz, 1H), 7.45 (t, $J = 8.0$ Hz, 1H), 6.27 (s, 1H), 4.48 (t, $J = 8.0$ Hz, 2H), 4.23 (t, $J = 8.0$ Hz, 2H), 3.14-3.05 (m, 2H), 2.90 (s, 9H), 2.06 (t, $J = 8.0$ Hz, 2H), 1.86 (t, $J = 8.0$ Hz, 2H), 1.67 (s, 6H), 1.47 (q, $J = 8.0$ Hz, 2H), 0.96 (t, $J = 8.0$ Hz, 3H). ^{13}C NMR (DMSO- d_6): 180.35, 156.35, 141.52, 140.63, 140.54, 132, 96, 130.16, 130.08, 129.60, 129.25, 128.59, 128.56, 126.41, 123.91, 123.71, 123.25, 113.99, 111.53, 83.60, 61.90, 52.24, 51.71, 46.86, 43.74, 30.00, 25.77, 21.27, 19.49, 13.76.

General Procedure for the Synthesis of Trimethine Cyanines 42 and 43. A suspension of indolium salt **14** or **17** (1.2 mmol) and diphenyl formamidine (1.2 mmol) in acetic anhydride (5 ml) was heated at 120° C for 0.5h and then cooled to room temperature. This deep red reaction mixture was allowed to cool and a suspension of **31** (0.45g, 1.2mmol) in pyridine (8 ml) was added. This mixture was stirred at rt for 2h and was monitored using UV-Vis spectrophotometry and alumina TLC plates eluting with 5% methanol in DCM. Diethyl ether (50 ml) was added to a blue-colored reaction mixture and the solution was allowed to stand for 30 min. The ether layer was decanted and this precipitation procedure was repeated twice. Dyes were purified by open column chromatography using neutral alumina gel, eluent MeOH/DCM from 1/25 to 1/10.



3-(6-bromo-1-butylbenzo[cd]indol-2(1H)-ylidene)prop-1-enyl-3,3-dimethyl-1-(3-(trimethylammonio)propyl)-3H-indolium dibromide (42): Yield 31%; MP >250° C. ¹H NMR (400 MHz, DMSO-d₆): δ 8.73 (t, *J* = 12.0 Hz, 1H), 8.33 (d, *J* = 8.0 Hz, 1H), 8.14 (d, *J* = 8.0 Hz, 1H), 8.07 (t, *J* = 8.0 Hz, 1H), 7.91 (d, *J* = 8.0 Hz, 1H), 7.76 (t, *J* = 8.0 Hz, 2H), 7.55 (t, *J* = 8.0 Hz, 1H), 7.44-7.35 (m, 4H), 4.32 (t, *J* = 8.0 Hz, 4H), 3.84 (t, *J* = 8.0 Hz, 2H), 3.17 (s, 9H), 2.44 (t, *J* = 8.0 Hz, 2H), 1.81 (s, 6H), 1.75 (t, *J* = 8.0 Hz, 2H), 1.48 (q, *J* = 8.0 Hz, 2H), 0.91 (t, *J* = 8.0 Hz, 3H). ¹³C NMR (100 MHz, DMSO-d₆): δ 175.90, 153.75, 149.29, 142.19, 141.71, 141.29, 132.91, 131.79, 129.73, 129.30, 129.20, 128.20, 126.84, 126.09, 123.16, 115.30, 112.99, 110.68, 108.65, 108.31, 62.56, 53.12, 50.20, 43.96, 41.87, 30.91, 28.43, 21.59, 19.99, 14.23.



5-Bromo-3-(6-bromo-1-butylbenzo[cd]indol-2(1H)-ylidene)prop-1-enyl-3,3-dimethyl-1-(3-(trimethylammonio)propyl)-3H-indolium dibromide (43): Yield 18%; MP 241-242° C. ¹H NMR (400 MHz, DMSO-*d*₆): δ 8.70 (m, 1H), 8.37 (m, 1H), 8.16 (m, 1H), 8.12-8.05 (m, 2H), 7.93 (m, 1H), 7.71 (m, 2H), 7.49 (m, 3H), 4.32 (m, 4H), 3.85 (m, 2H), 3.17 (s, 9H), 2.23 (m, 2H), 1.80 (m, 8H), 1.47 (q, *J* = 8.0 Hz, 2H), 0.93 (t, *J* = 8.0 Hz, 3H). ¹³C NMR (100 MHz, DMSO-*d*₆): δ 174.44, 153.63, 149.00, 143.69, 140.62, 132.34, 131.29, 129.39, 128.66, 127.94, 125.75, 125.41, 118.47, 115.15, 114.04, 110.63, 109.09, 107.87, 61.88, 52.41, 49.56, 43.52, 41.42, 30.42, 27.84, 27.64, 20.93, 19.33, 13.63.

14.7.2 Nucleic Acids

The DNA oligonucleotides: Tel22 d[AGGG(TTAGGG)₃], MYC19 d[(AGGGTGGGG)₂A], and AATT hairpin duplex control d[CGAATTCGTTTTTCGAATTCG] with and without 5'-biotin labels were purchased from Integrated DNA Technologies (Coralville, IA, USA) with HPLC purification and mass spectrometry characterization. For NMR studies, a modified c-myc sequence, MYC22, d[TG(AGGGTGGGG)₂AA] was used. The concentration of all the oligonucleotides was calculated using the absorbance at 260 nm and the manufacturer provided extinction coefficients determined by the nearest-neighbor method [ref]. Stock solutions of the oligonucleotides and the dyes were prepared in deionized water and diluted using

appropriate experimental buffer prior to use. Experiments were conducted in 10 mM TRIS, or 10 mM HEPES for SPR, containing 50 mM KCl and 1 mM EDTA adjusted to pH 7.3.

14.7.3 Thermal Melting

DNA in TRIS K⁺ buffer and a specific ratios of cyanine dyes:DNA (0:1 to 6:1) in a 1 cm path length quartz cells. The experiment were conducted on a Cary Varian 300 BIO UV-Vis thermal melting spectrophotometer (Santa Clara, CA) with monitored heating and cooling rates of 0.5 °C/min. The controlled wavelength of were set at 295 and 260 nm for quadruplex and duplex, respectively. The corrected data were normalized and the T_m were determined using combination of derivative function and graphical estimation. The reported ΔT_m are reproducible within ± 1 °C.

14.7.4 Surface Plasmon Resonance

Biosensor SPR experiments were performed with two-channel BIAcore X100 optical biosensor system (BIAcore, Inc.) and streptavidin-coated sensor chips. The chips preparation were done by an extensive wash of HBS-EP+ buffer (GE Healthcare, Inc.) followed by activation buffer (1 M NaCl and 50 mM NaOH) and again extensive washing of HBS-EP+ buffer. Injection of single stranded biotinylated DNA until the change in RU_{max} reach 330 - 350. Compound serial dilutions were prepared in HEPES experimental buffer (10 mM HEPES, 50 mM KCl, 1 mM EDTA, 0.005% (v/v) P20 (GE Healthcare, Inc.), pH 7.4). The experiment were set so that the contact time are 180s, the dissociation time are 900s and the regeneration contact time of 60s with stabilization period of 180s, and the constant temperature of 25 °C. Two-site fitting model (equation below) was used to fit the sensorgrams curve in Kaleidagraph 4.0 software to obtain the dissociation constant. K_1 and K_2 are equilibrium constants for first and second binding sites respectively and C_{free} are compound concentrations in equilibrium.

$$r = (K_1 C_{free} + 2 K_1 K_2 C_{free}^2) / (1 + K_1 C_{free} + K_1 K_2 C_{free}^2)$$

14.8 References

1. Ray, S.; Bandaria, J. N.; Qureshi, M. H.; Yildiz, A.; Balci, H. G-quadruplex formation in telomeres enhances POT1/TPP1 protection against RPA binding. *Proc Natl Acad Sci U S A* **2014**, *111*, 2990-5.
2. Kim, I. S.; Seo, Y. J. Probe development for detection of TERRA 1 intramolecular G-quadruplex formation using a fluorescent adenosine derivative. *Bioorg Med Chem Lett* **2014**, *24*, 1589-91.
3. Zhang, D.; Yin, L.; Meng, Z.; Yu, A.; Guo, L.; Wang, H. A sensitive fluorescence anisotropy method for detection of lead (II) ion by a G-quadruplex-inducible DNA aptamer. *Anal Chim Acta* **2014**, *812*, 161-7.
4. Islam, M. A.; Thomas, S. D.; Murty, V. V.; Sedoris, K. J.; Miller, D. M. c-Myc quadruplex-forming sequence Pu-27 induces extensive damage in both telomeric and nontelomeric regions of DNA. *J Biol Chem* **2014**, *289*, 8521-31.
5. Zavyalova, E.; Golovin, A.; Pavlova, G.; Kopylov, A. Module-activity relationship of G-quadruplex based DNA aptamers for human thrombin. *Curr Med Chem* **2013**, *20*, 4836-43.
6. Fotticchia, I.; Giancola, C.; Petraccone, L. G-quadruplex unfolding in higher-order DNA structures. *Chem Commun (Camb)* **2013**, *49*, 9488-90.
7. Zhuang, X. Y.; Yao, Y. G. Mitochondrial dysfunction and nuclear-mitochondrial shuttling of TERT are involved in cell proliferation arrest induced by G-quadruplex ligands. *FEBS Lett* **2013**, *587*, 1656-62.
8. Satyanarayana, M.; Kim, Y. A.; Rzuczek, S. G.; Pilch, D. S.; Liu, A. A.; Liu, L. F.; Rice, J. E.; LaVoie, E. J. Macrocyclic hexaoxazoles: Influence of aminoalkyl substituents on RNA and DNA G-quadruplex stabilization and cytotoxicity. *Bioorg Med Chem Lett* **2010**, *20*, 3150-4.

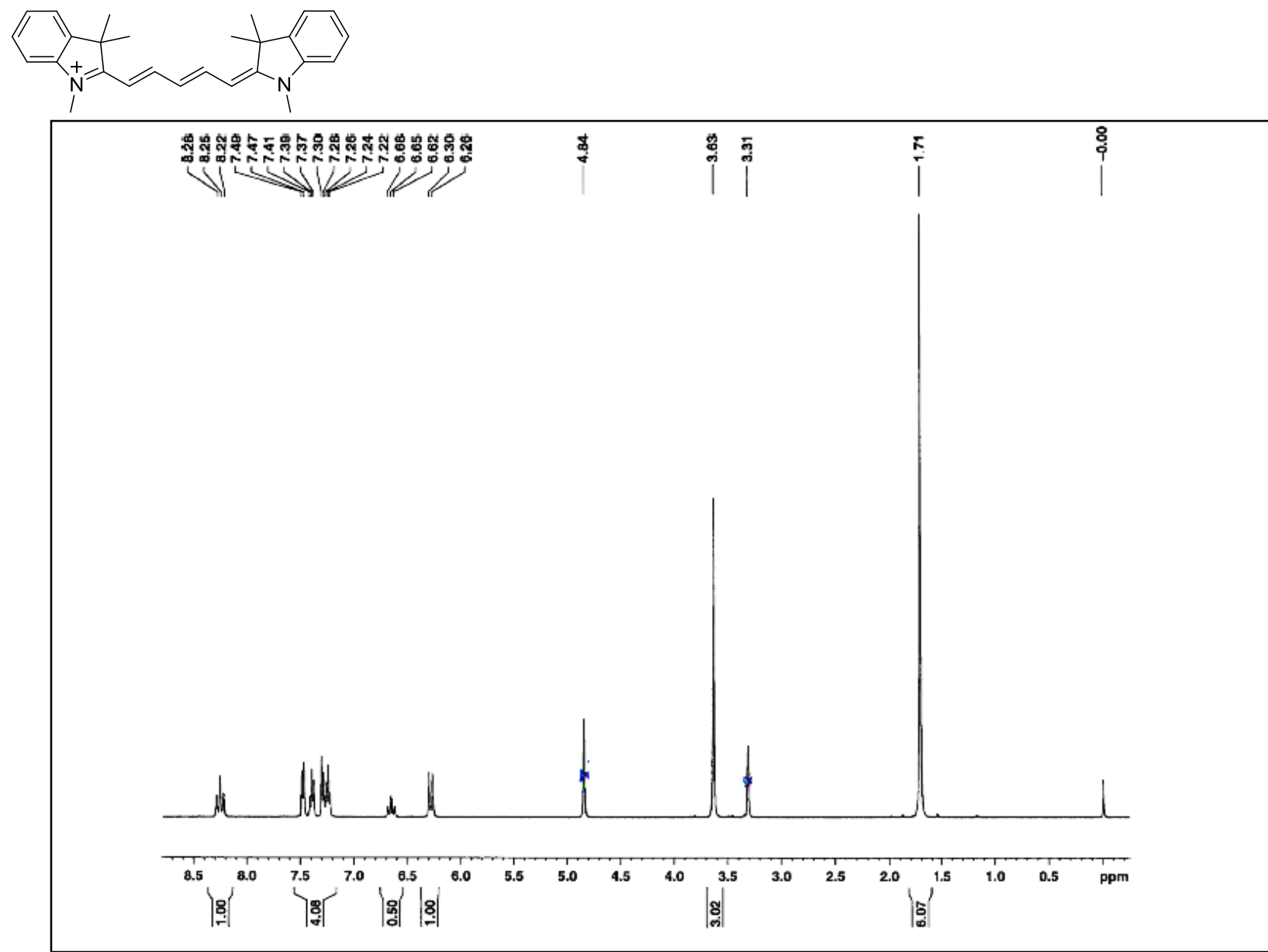
9. Schaffitzel, C.; Postberg, J.; Paeschke, K.; Lipps, H. J. Probing telomeric G-quadruplex DNA structures in cells with in vitro generated single-chain antibody fragments. *Methods Mol Biol* **2010**, 608, 159-81.
10. Schiavone, D.; Guilbaud, G.; Murat, P.; Papadopoulou, C.; Sarkies, P.; Prioleau, M. N.; Balasubramanian, S.; Sale, J. E. Determinants of G quadruplex-induced epigenetic instability in REV1-deficient cells. *EMBO J* **2014**, 33, 2507-20.
11. Sun, D.; Liu, Y.; Liu, D.; Zhang, R.; Yang, X.; Liu, J. Stabilization of G-quadruplex DNA, inhibition of telomerase activity and live cell imaging studies of chiral ruthenium(II) complexes. *Chemistry* **2012**, 18, 4285-95.
12. Suntharalingam, K.; Gupta, D.; Sanz Miguel, P. J.; Lippert, B.; Vilar, R. Synthesis, structural characterisation and quadruplex DNA binding studies of a new gold(III) pyrazolylpyridine complex. *Chemistry* **2010**, 16, 3613-6.
13. Nanjunda, R.; Owens, E. A.; Mickelson, L.; Dost, T. L.; Stroeva, E. M.; Huynh, H. T.; Germann, M. W.; Henary, M. M.; Wilson, W. D. Selective G-quadruplex DNA recognition by a new class of designed cyanines. *Molecules* **2013**, 18, 13588-607.
14. Nanjunda, R.; Owens, E. A.; Mickelson, L.; Alyabyev, S.; Kilpatrick, N.; Wang, S.; Henary, M.; Wilson, W. D. Halogenated pentamethine cyanine dyes exhibiting high fidelity for G-quadruplex DNA. *Bioorg Med Chem* **2012**, 20, 7002-11.
15. Hamann, F. M.; Brehm, R.; Pauli, J.; Grabolle, M.; Frank, W.; Kaiser, W. A.; Fischer, D.; Resch-Genger, U.; Hilger, I. Controlled modulation of serum protein binding and biodistribution of asymmetric cyanine dyes by variation of the number of sulfonate groups. *Mol Imaging* **2011**, 10, 258-69.

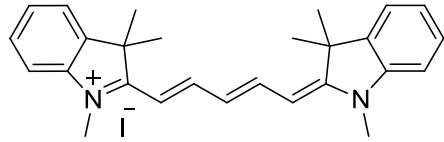
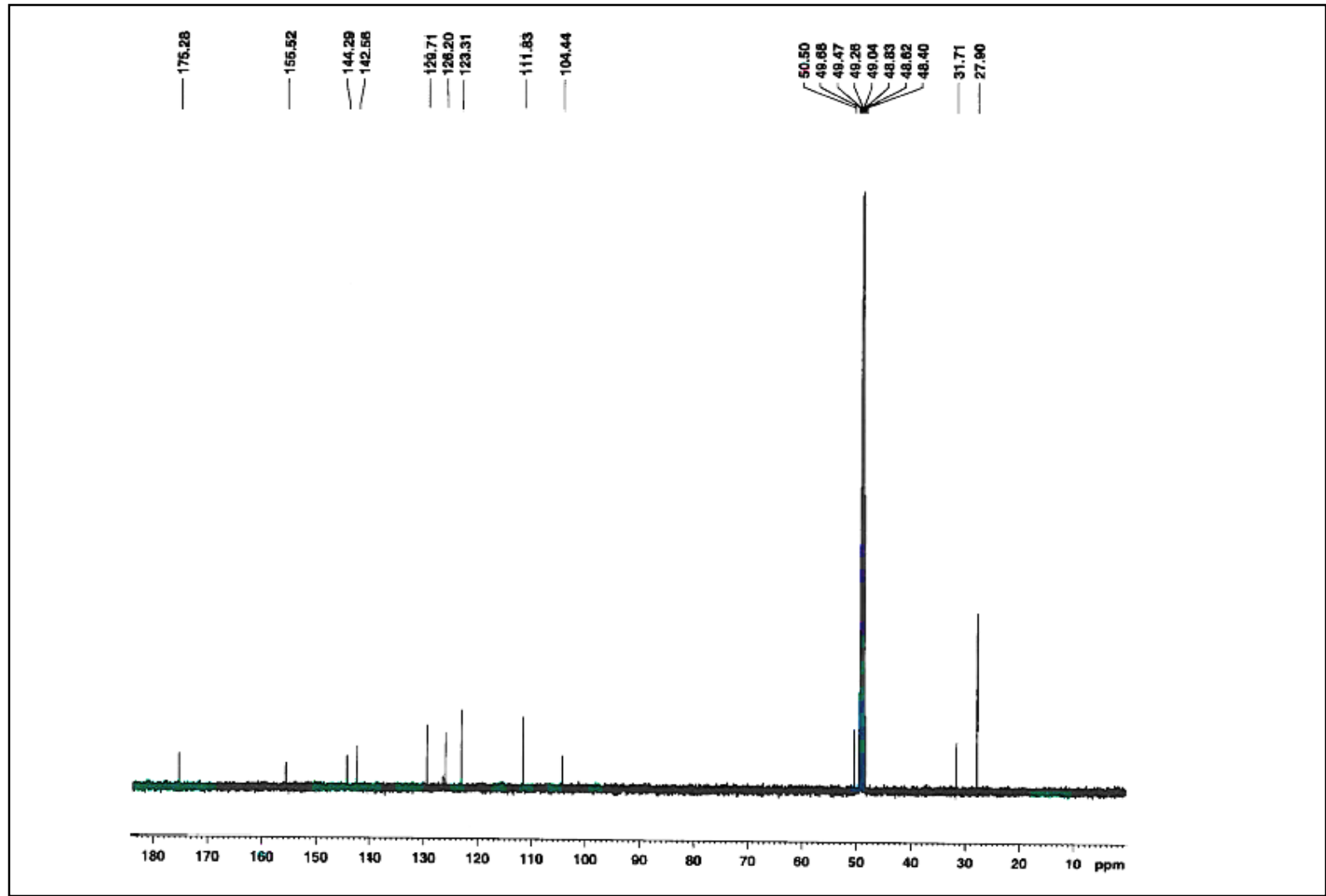
16. Bengtsson, M.; Karlsson, H. J.; Westman, G.; Kubista, M. A new minor groove binding asymmetric cyanine reporter dye for real-time PCR. *Nucleic Acids Res* **2003**, 31, e45.
17. Karlsson, H. J.; Lincoln, P.; Westman, G. Synthesis and DNA binding studies of a new asymmetric cyanine dye binding in the minor groove of [poly(dA-dT)]₂. *Bioorg Med Chem* **2003**, 11, 1035-40.
18. Asato, A. E.; Watanabe, D. T.; Liu, R. S. The use of prochiral centers for demonstrating asymmetric stacking in aggregates of azulenylazulenium cyanine dyes. *Org Lett* **2000**, 2, 2559-62.
19. Timcheva, II; Maximova, V. A.; Deligeorgiev, T. G.; Gadjev, N. I.; Sabnis, R. W.; Ivanov, I. G. Fluorescence spectral characteristics of novel asymmetric monomethine cyanine dyes in nucleic acid solutions. *FEBS Lett* **1997**, 405, 141-4.
20. Rye, H. S.; Yue, S.; Wemmer, D. E.; Quesada, M. A.; Haugland, R. P.; Mathies, R. A.; Glazer, A. N. Stable fluorescent complexes of double-stranded DNA with bis-intercalating asymmetric cyanine dyes: properties and applications. *Nucleic Acids Res* **1992**, 20, 2803-12.

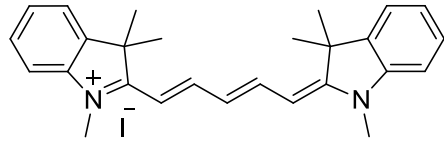
APPENDICES

The following appendices contain the supplemental information including NMR, MS and biological data.

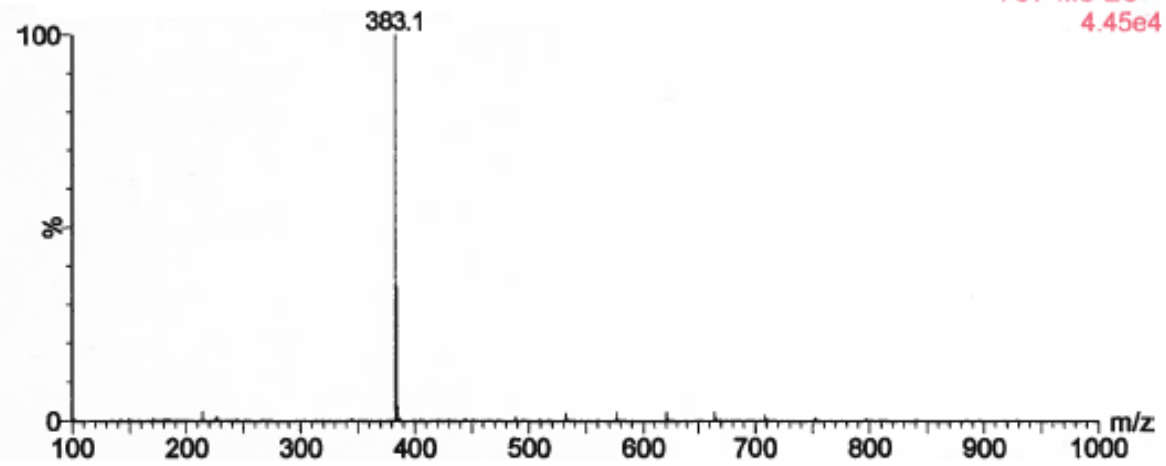
Experimental Data for Chapter 3 -- CORRELATING TISSUE LOCALIZATION OF HYDROPHOBIC CYANINES

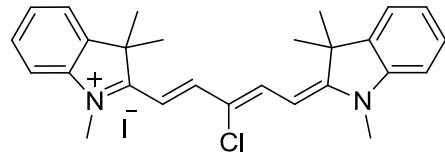
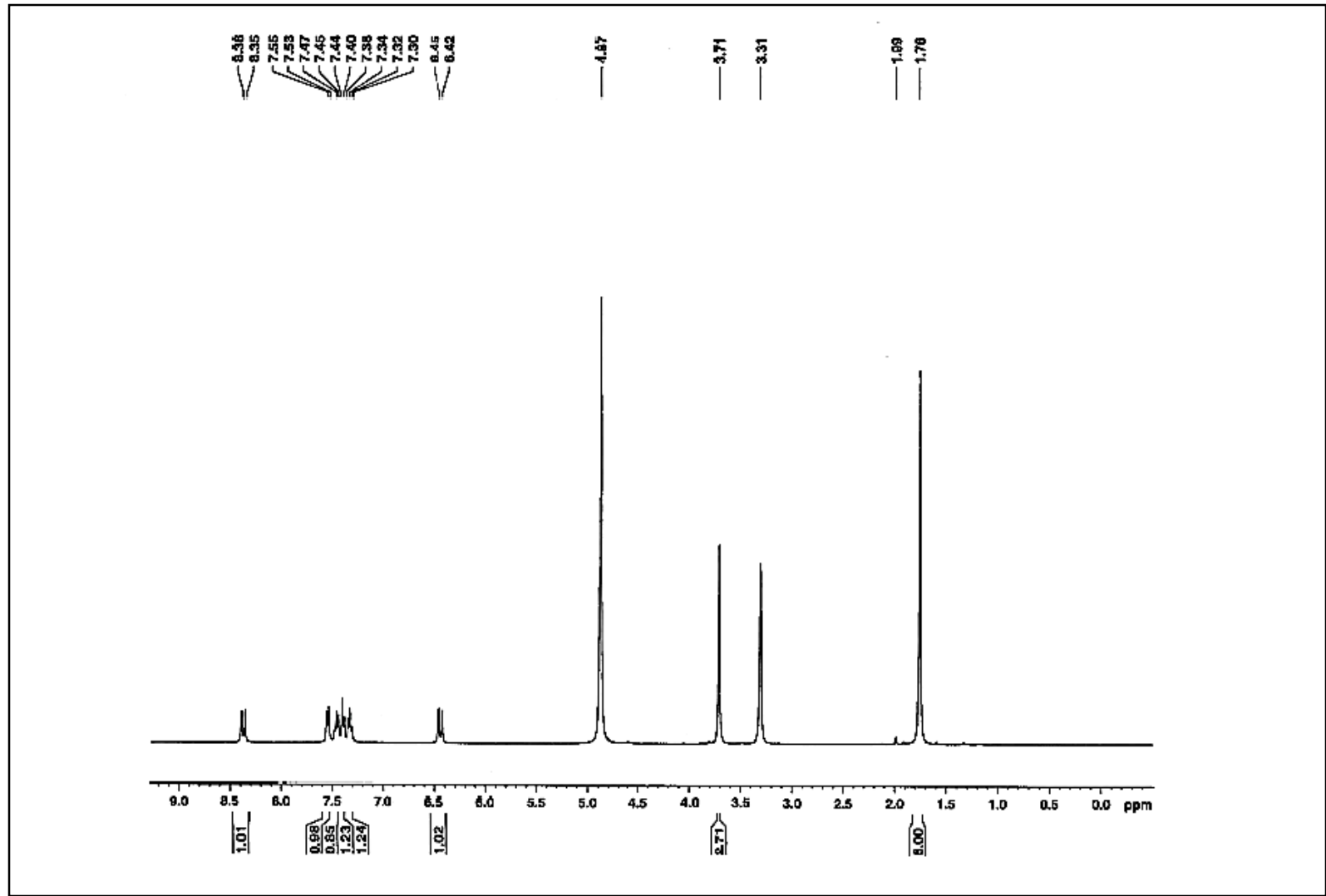


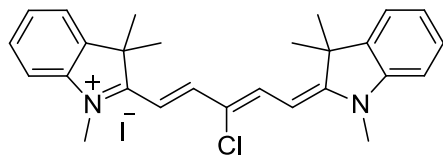
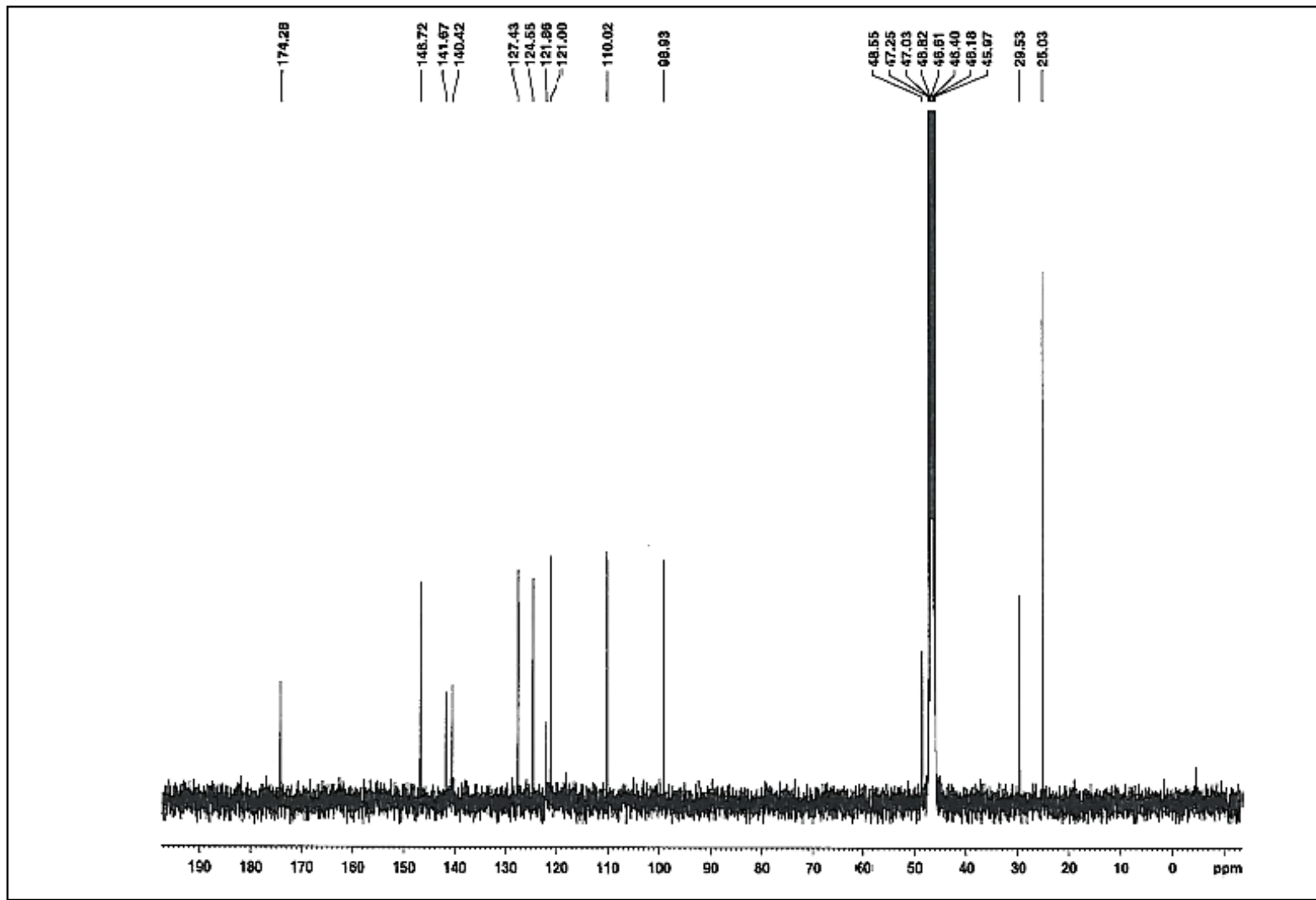
MeOD- d_4 

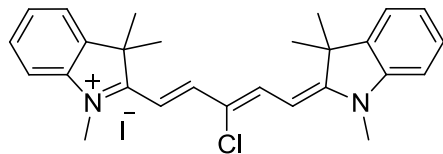


50%MeOH+0.1%HCOOH

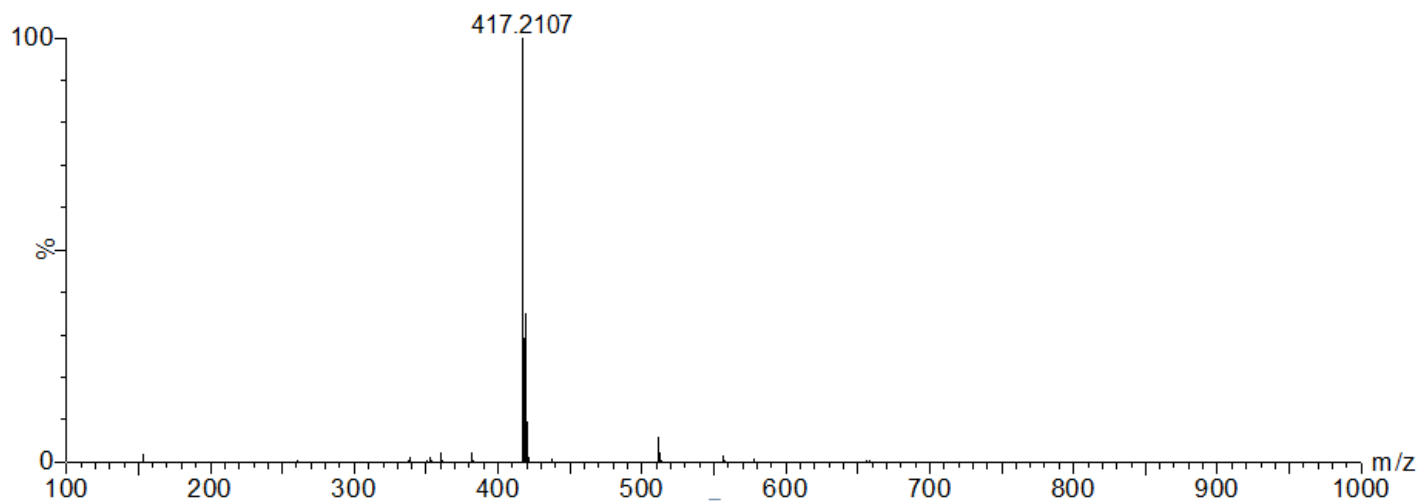


MeOD-*d*₄

MeOD- d_4 

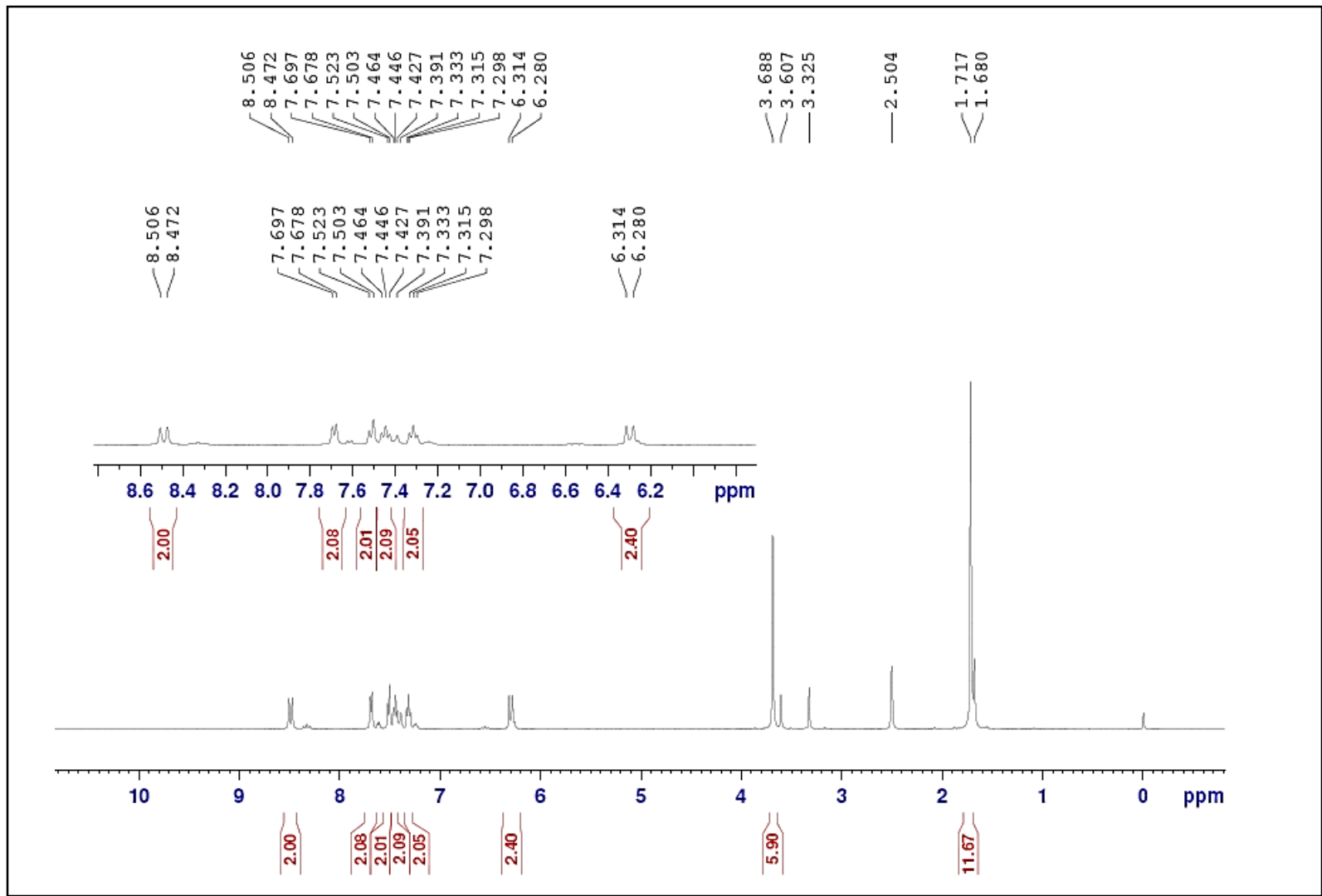
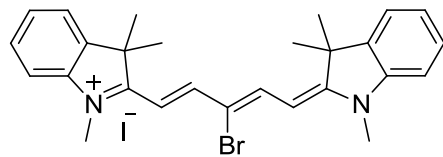


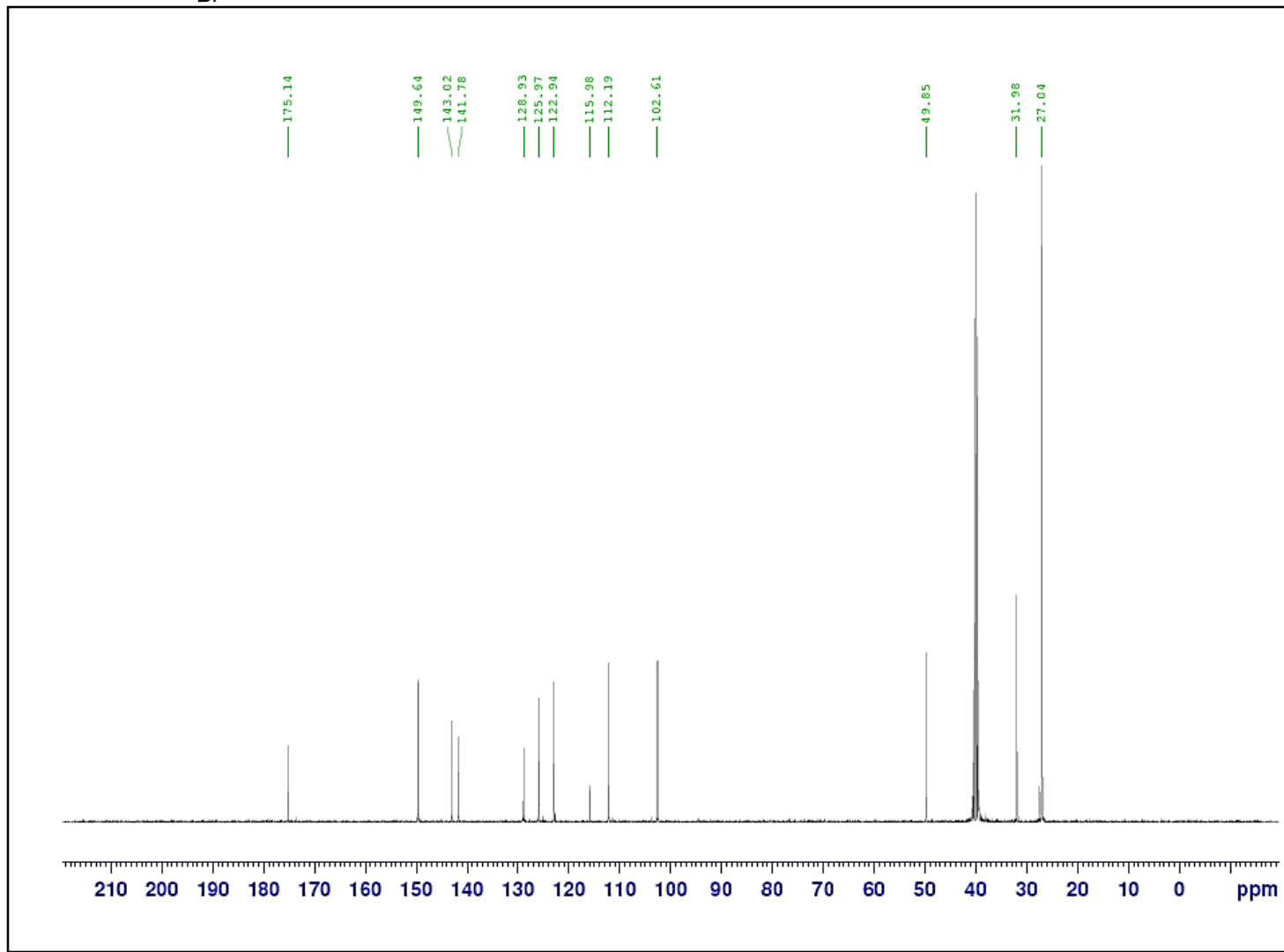
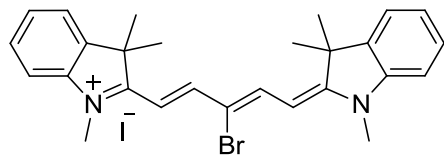
100%MeOH+0.1%HCOOH

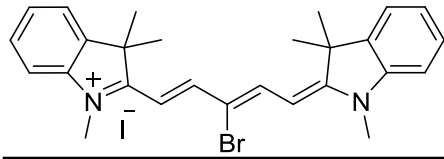


Elemental Composition Report

Mass	Calc. Mass	mDa	PPM	DBE	i-FIT	Formula
417.2107	417.2098	0.9	2.2	13.5	9.6	C ₂₇ H ₃₀ N ₂ Cl





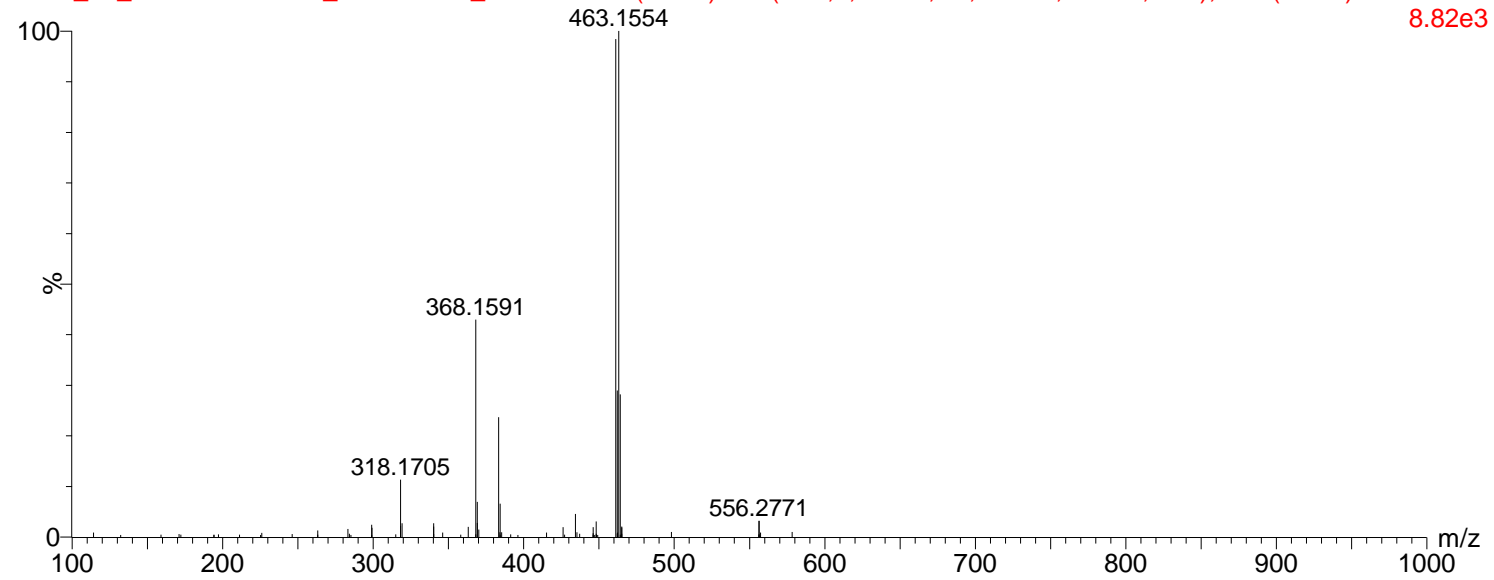


diluted in 80%MeOH

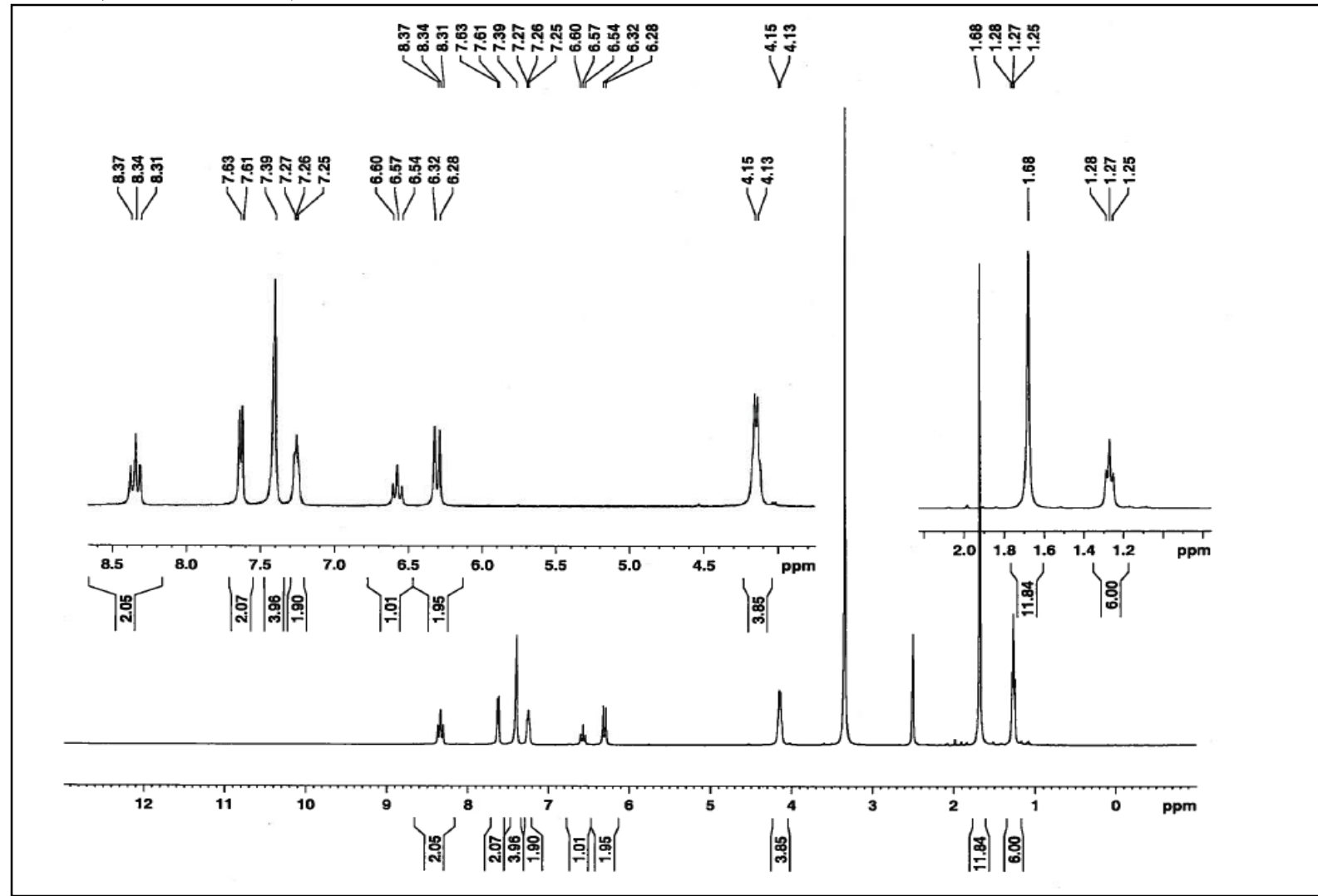
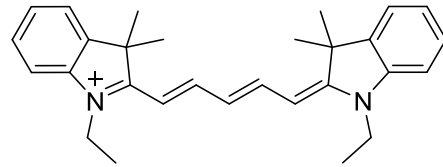
15:28:12 01-Feb-2013

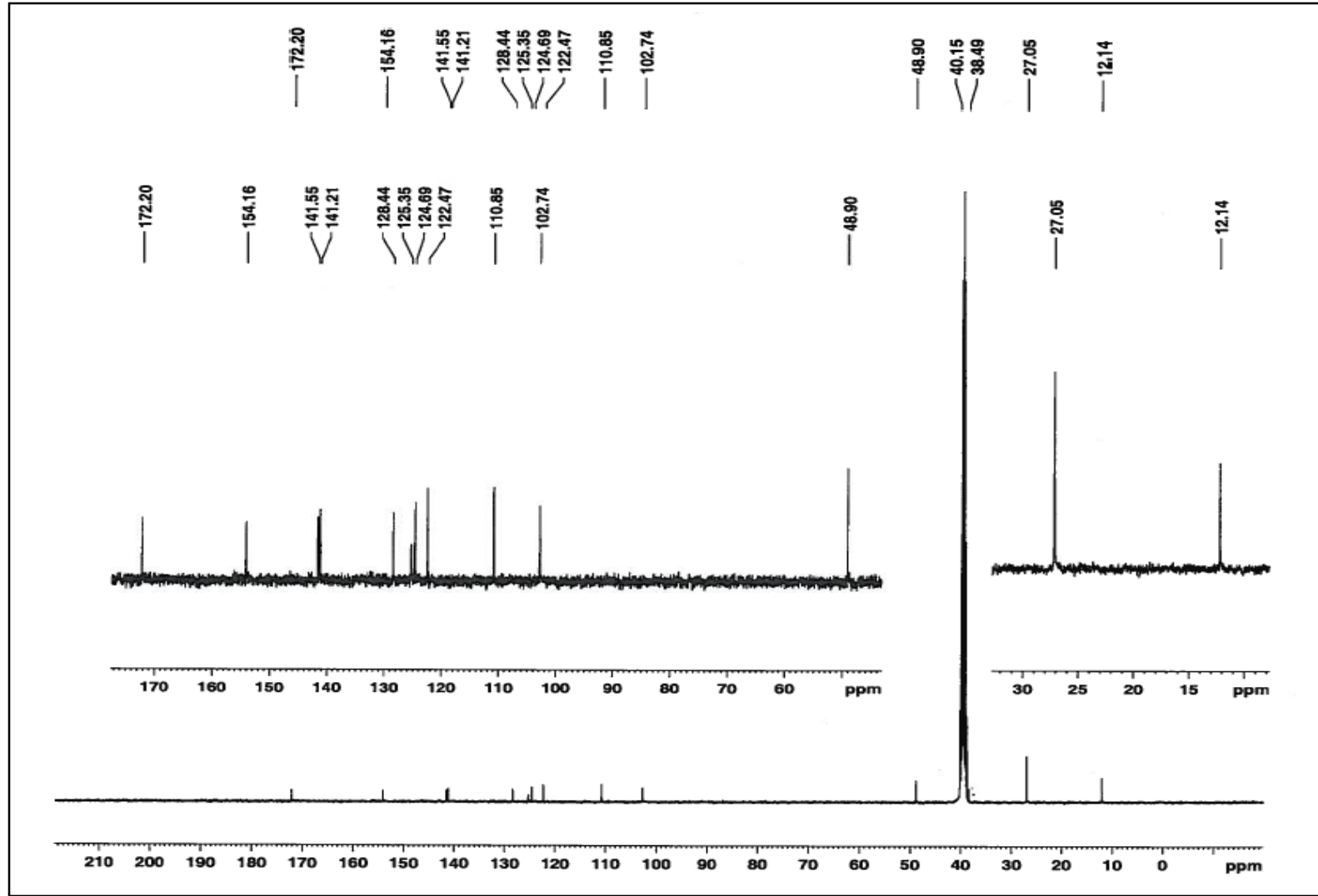
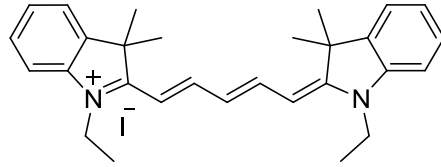
ERIC_32_HENARY-ACCU_02-01-2013_ESI-POS 59 (1.177) AM (Gen,2, 80.00, Ar,5000.0,556.28,0.70); Cm (56:60)

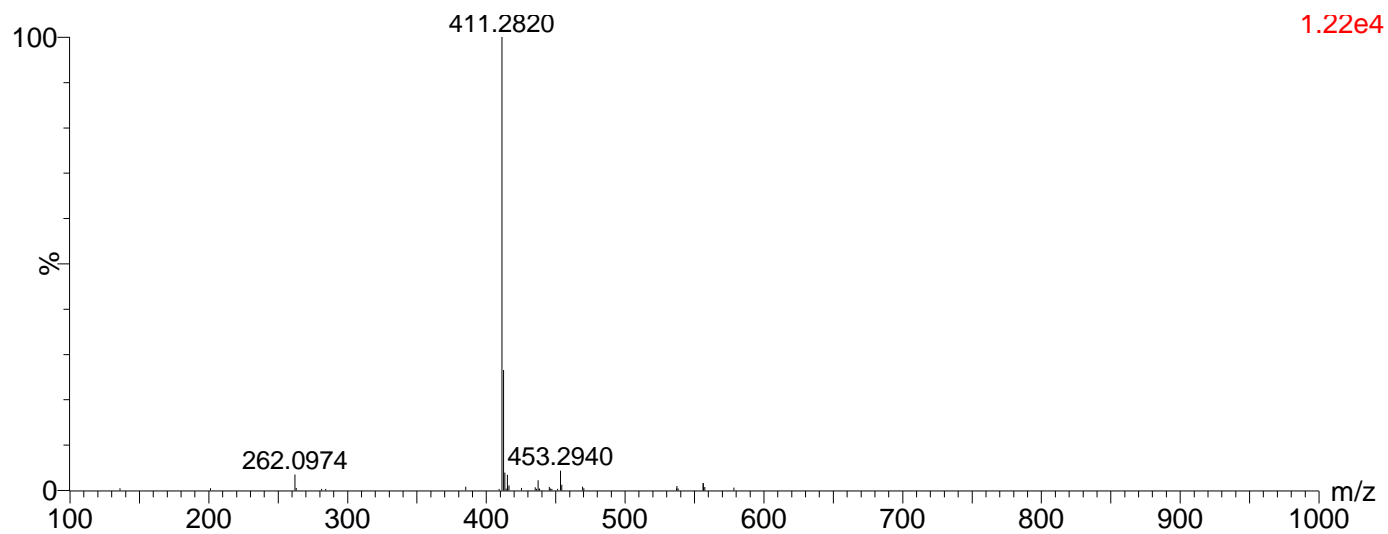
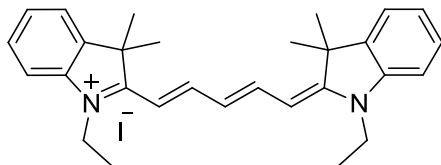
8.82e3



Mass	Calc. Mass	mDa	PPM	DBE	i-FIT	Formula
461.1585	461.1592	-0.7	-1.5	13.5	4.5	C27 H30 N2 Br

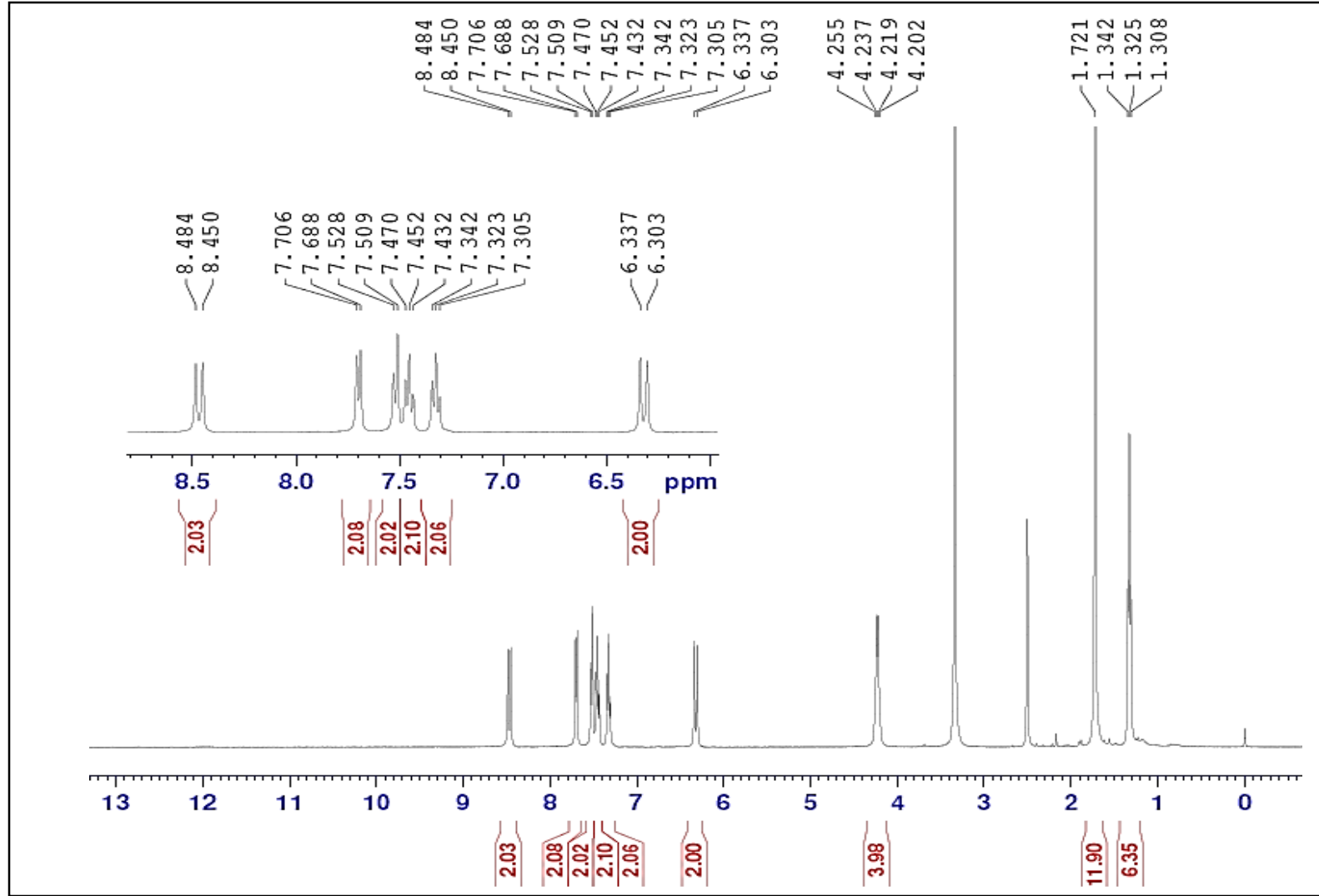
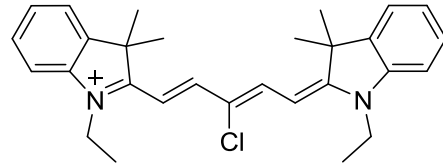


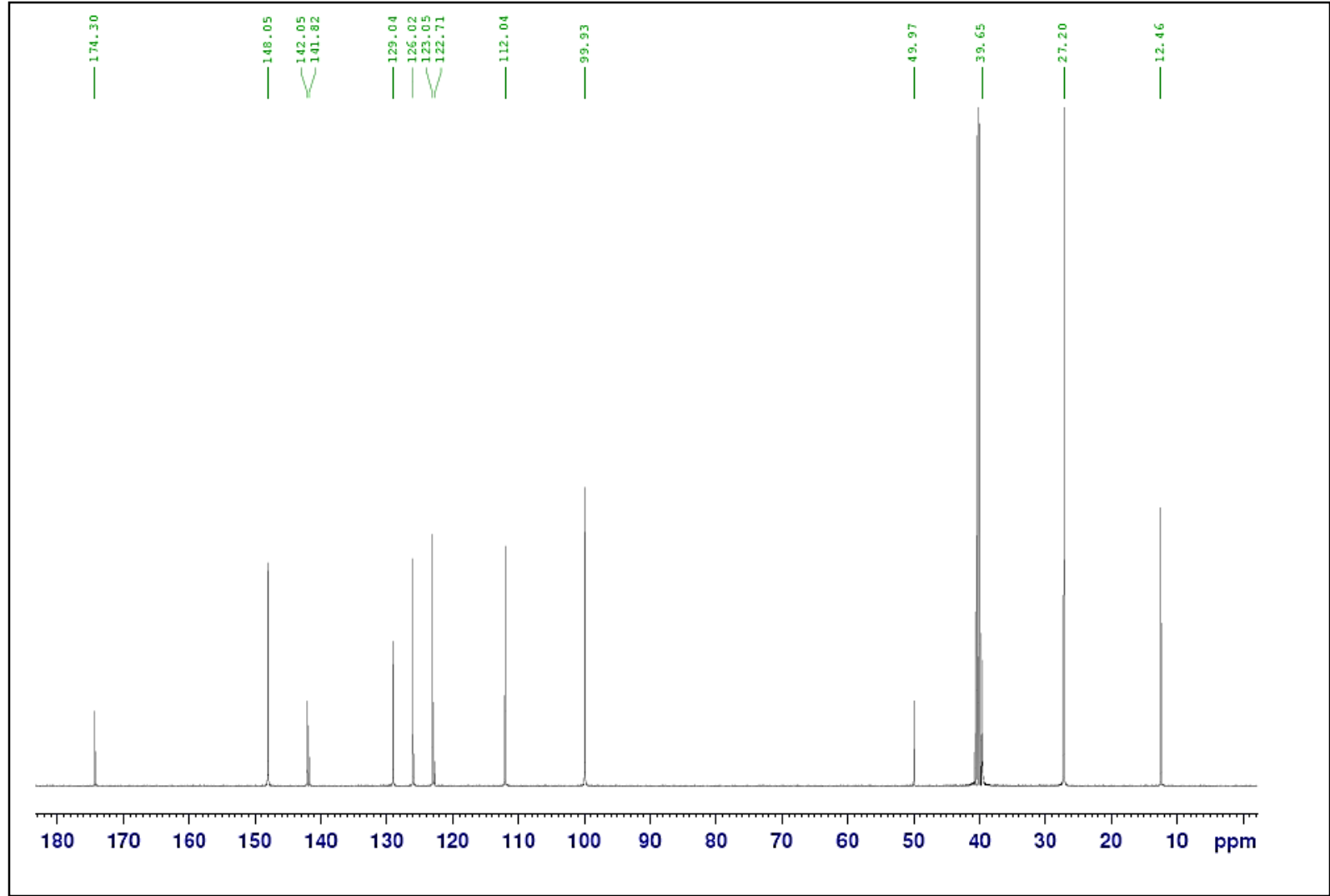
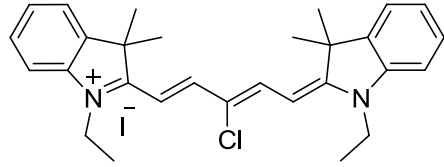


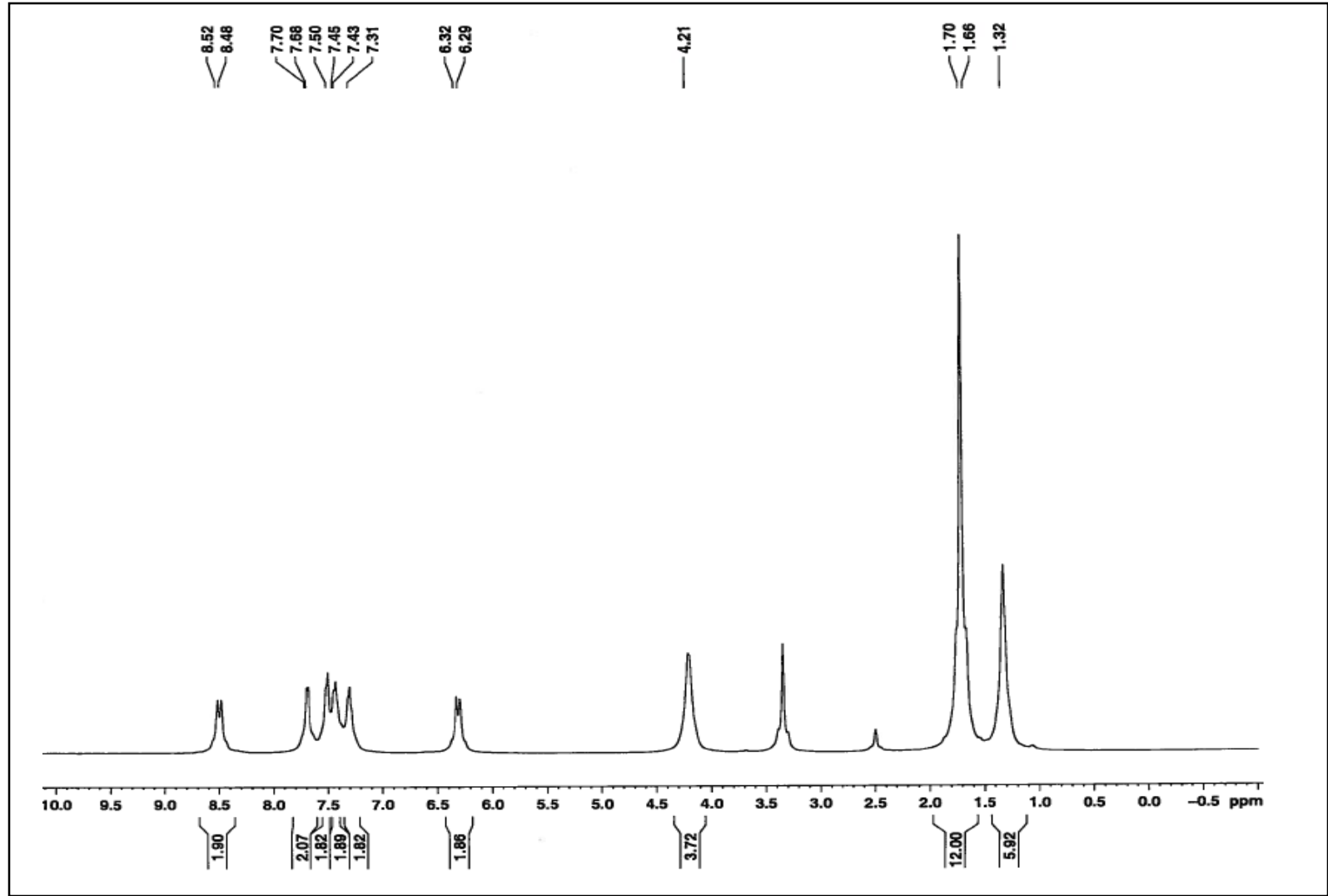
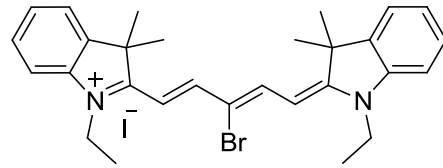


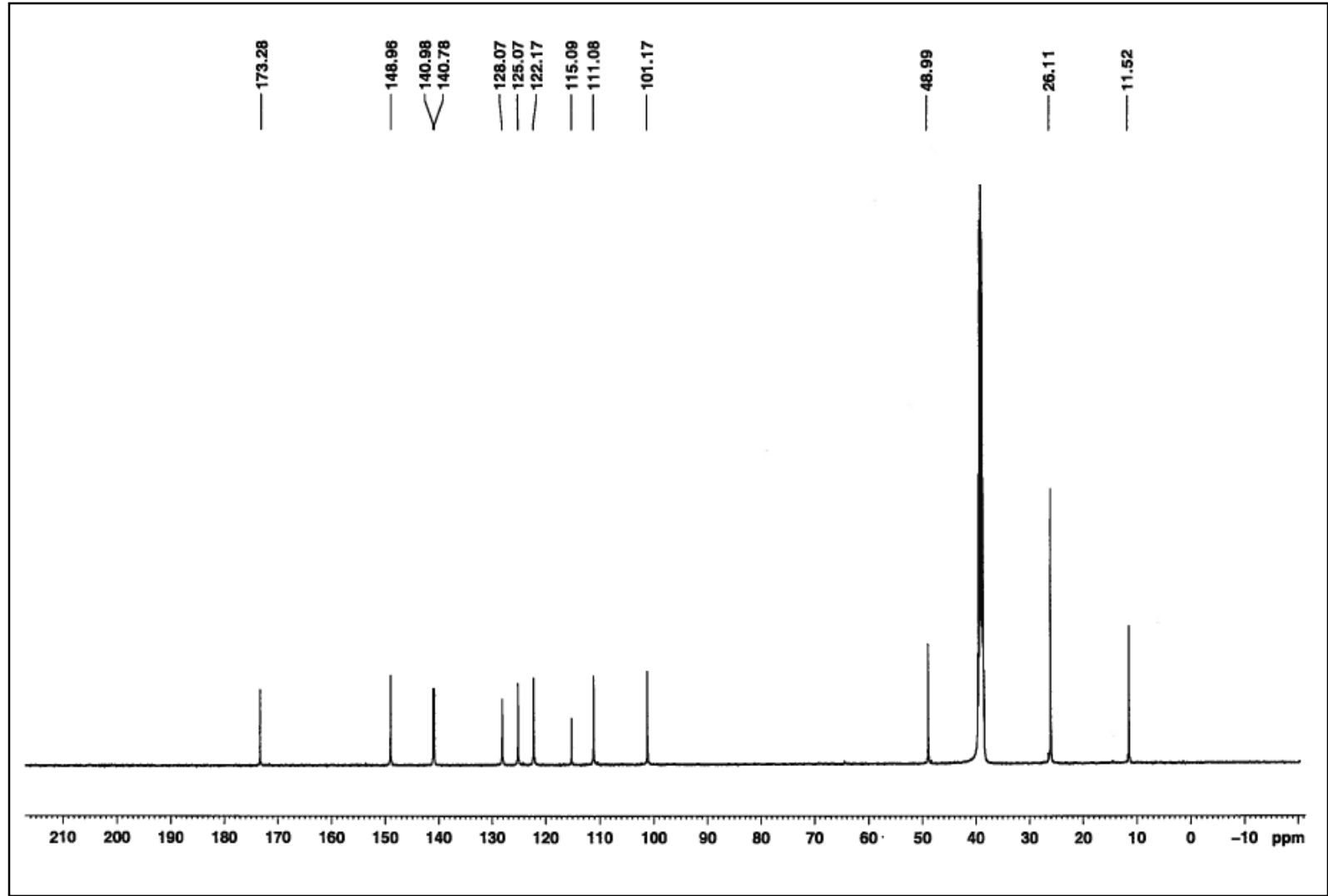
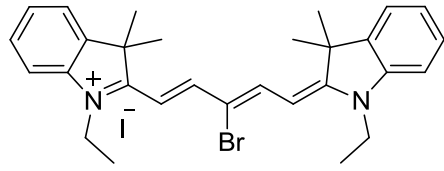
Elemental Composition Report

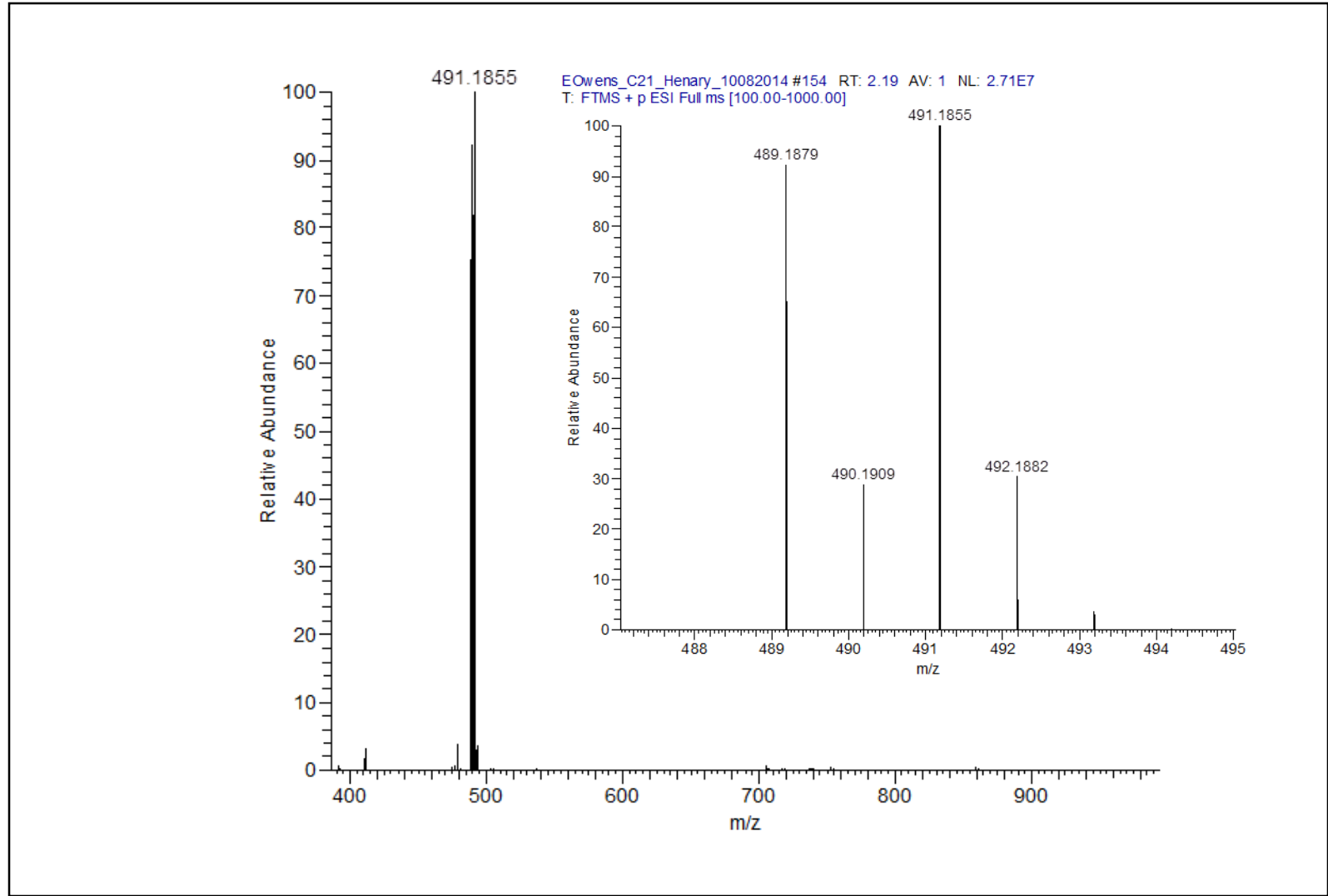
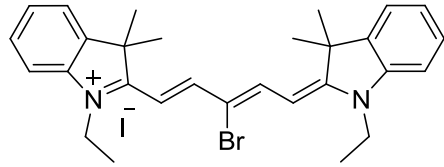
Mass	Calc. Mass	mDa	PPM	DBE	i-FIT	Formula
411.2820	411.2800	2.0	4.9	13.5	100.6	C ₂₉ H ₃₅ N ₂

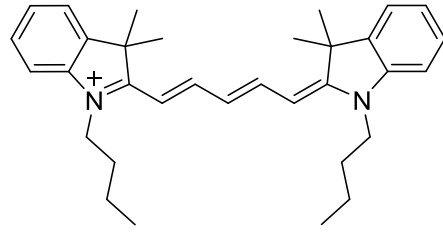
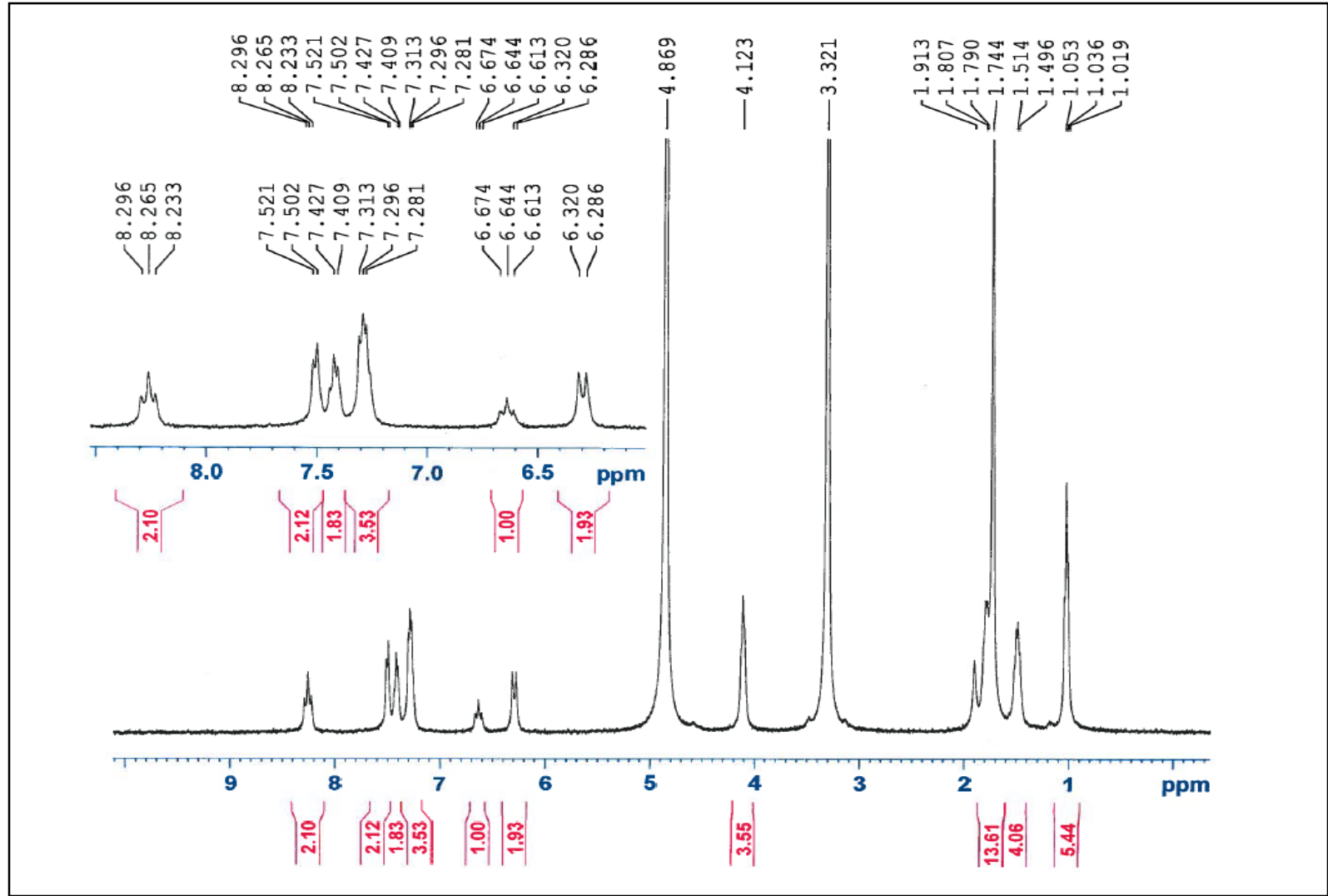


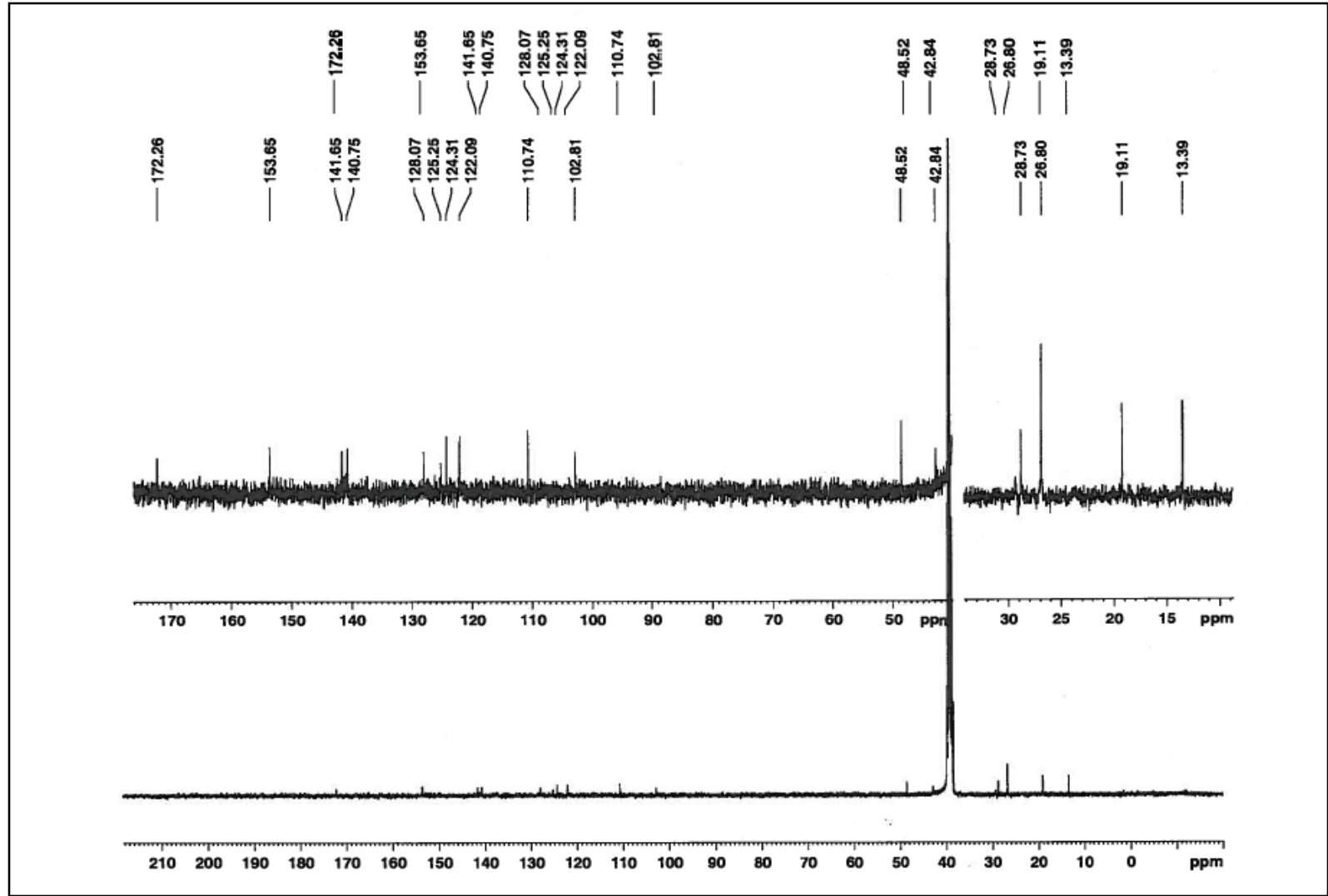
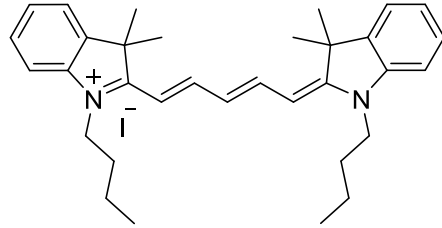


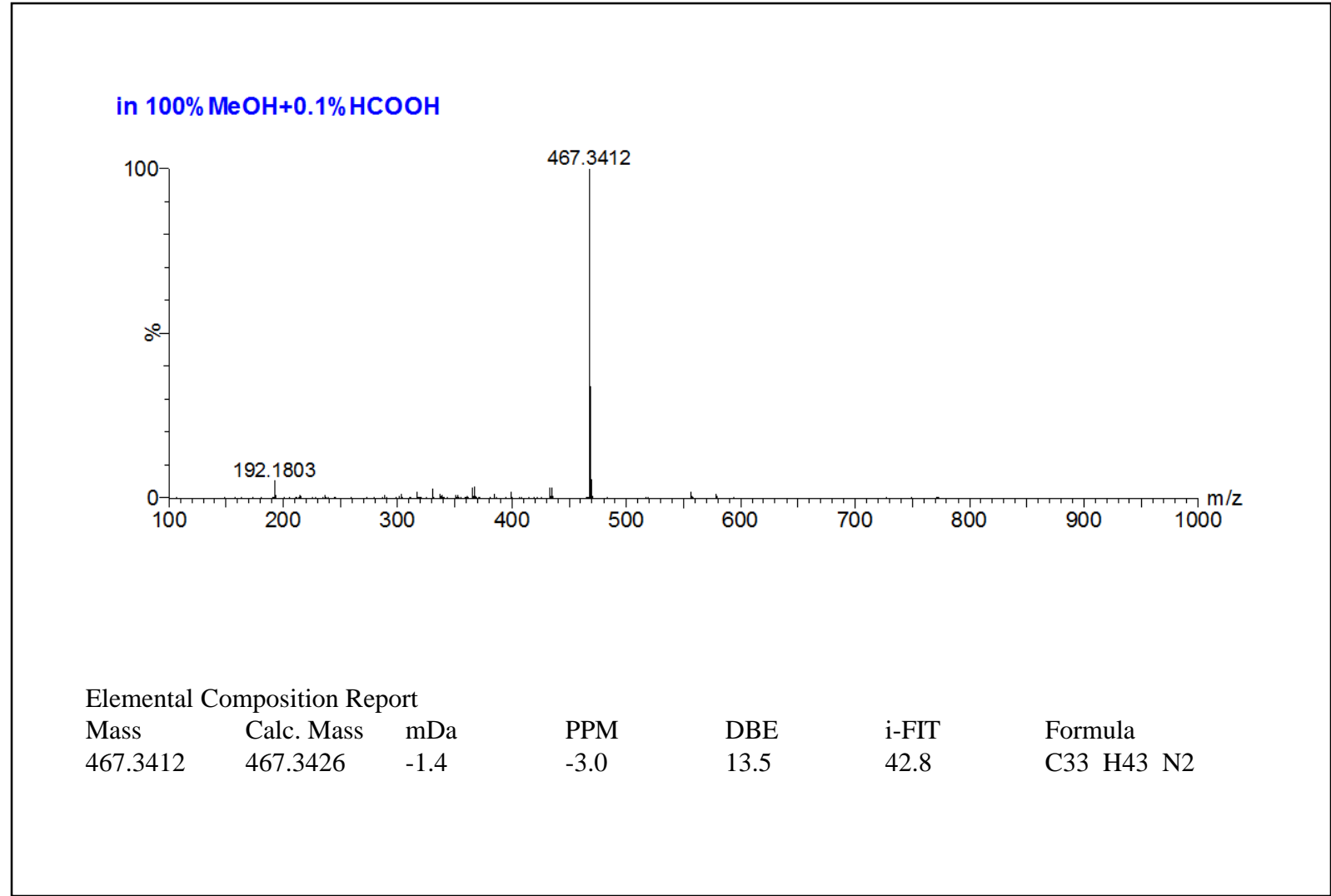
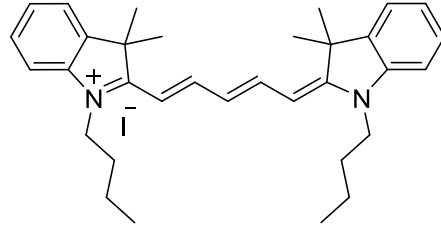


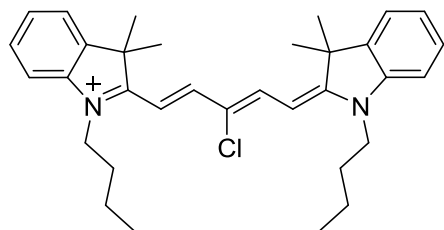
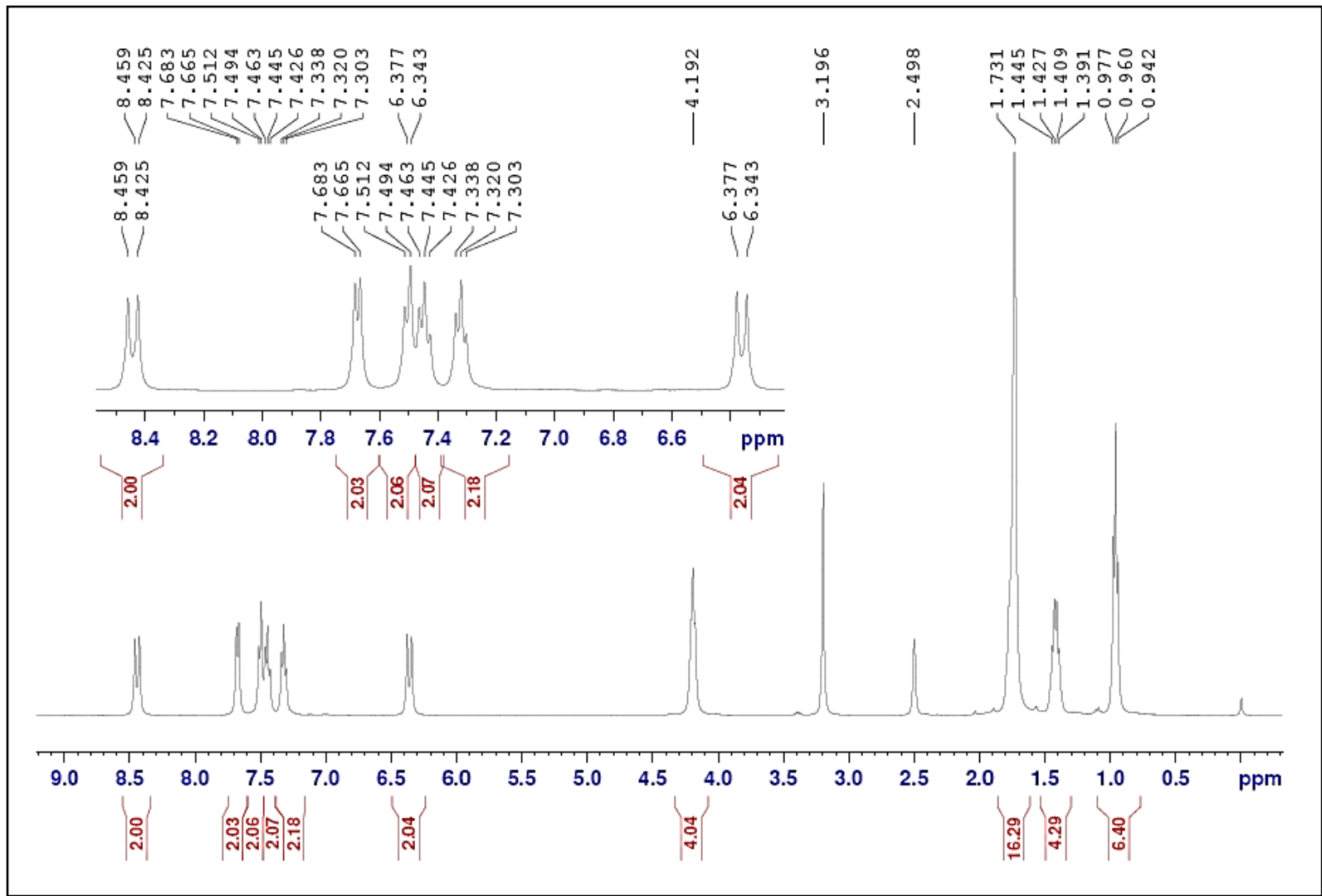


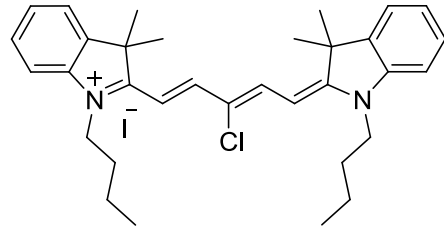
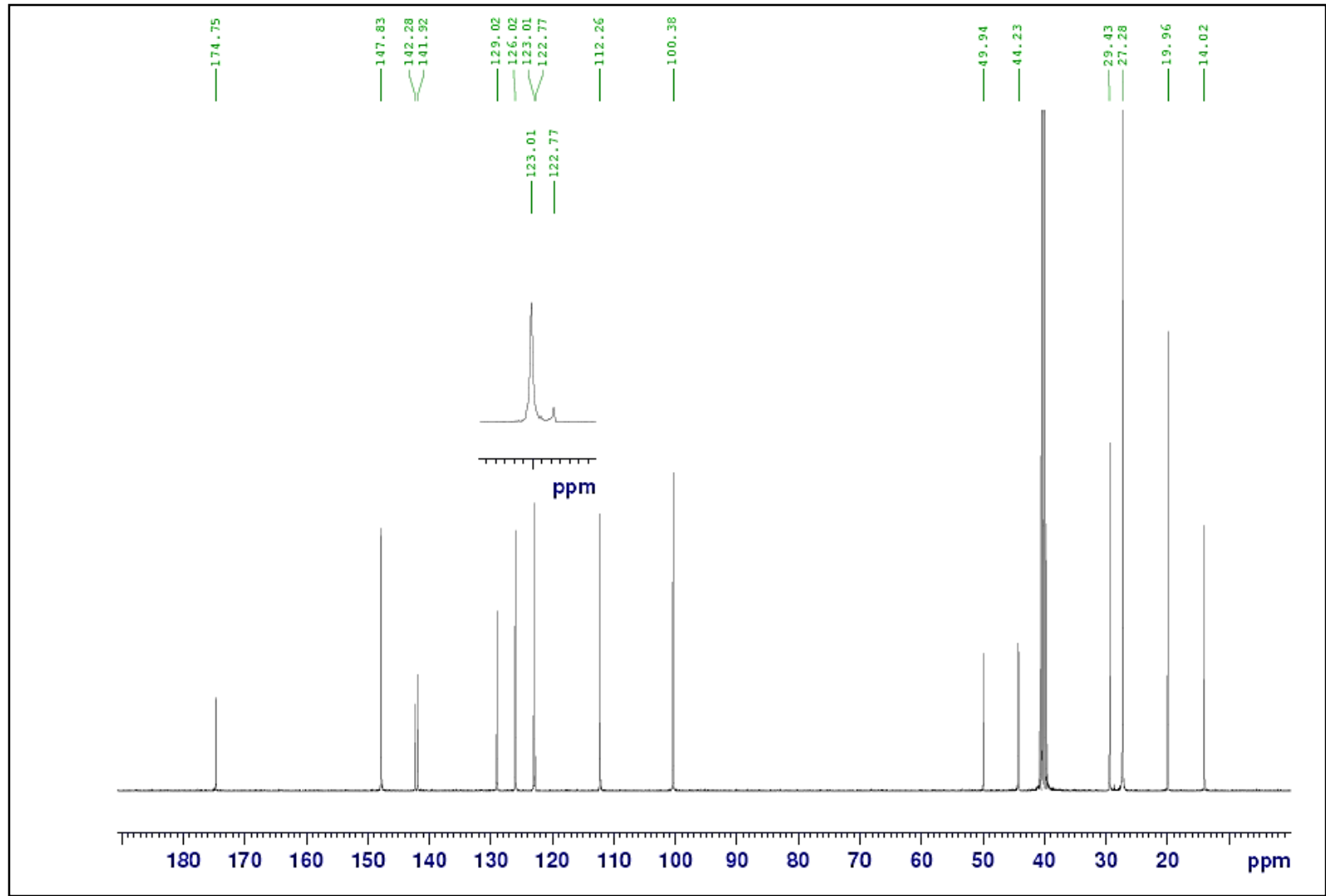


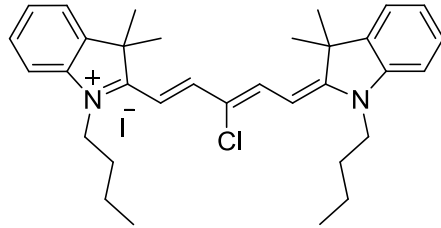
MeOD- d_4 



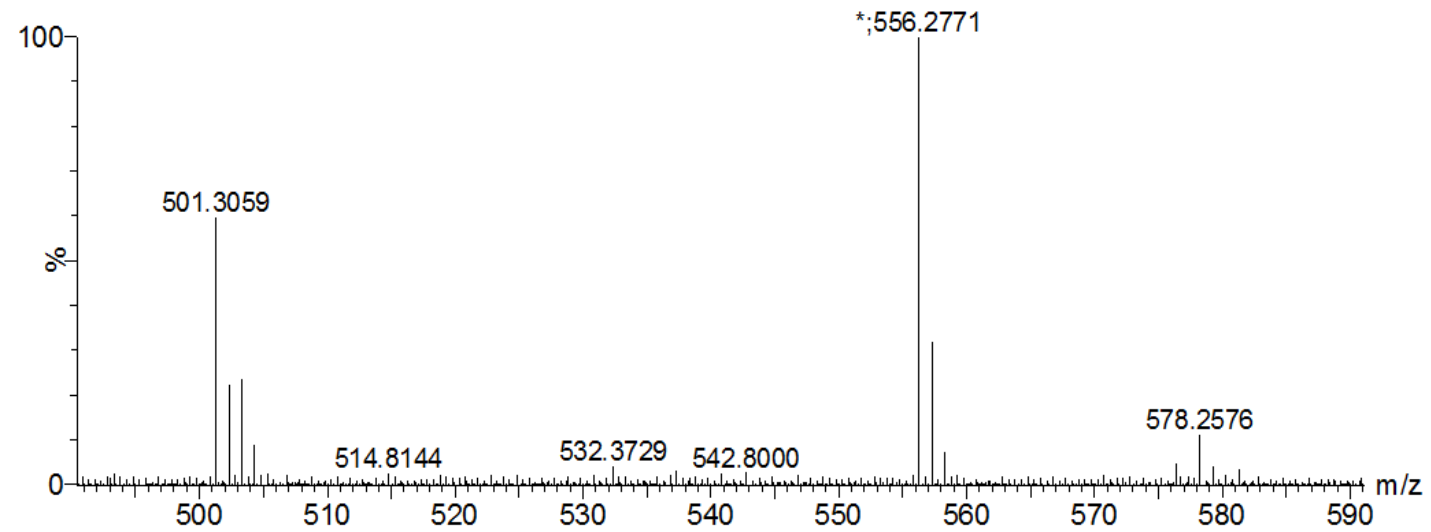


DMSO- d_6 

DMSO- d_6 

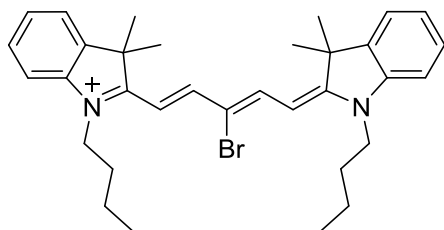
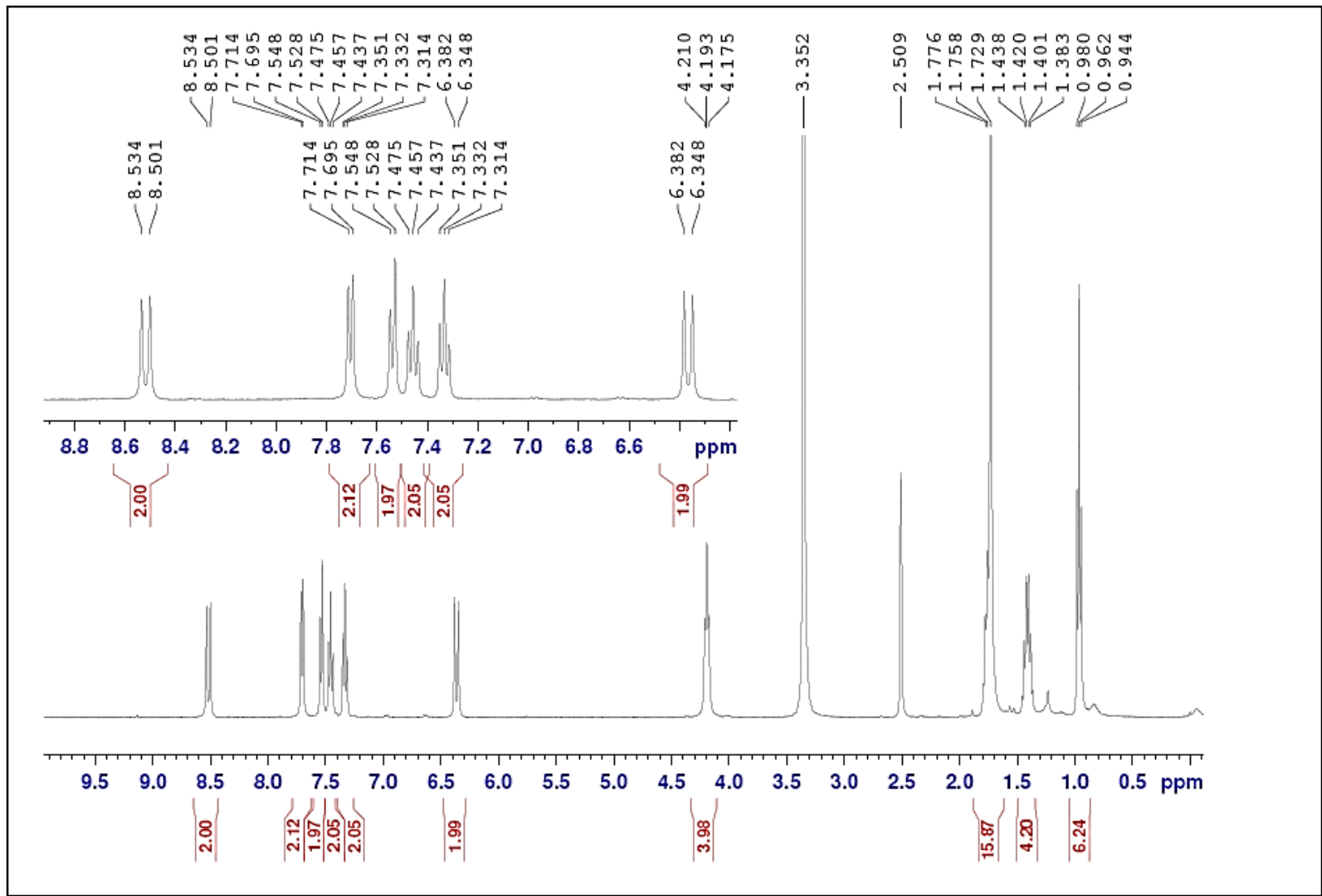


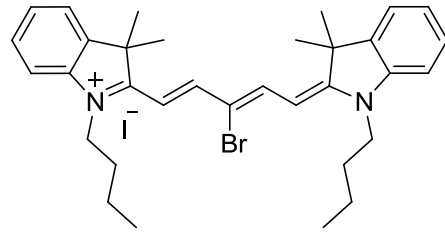
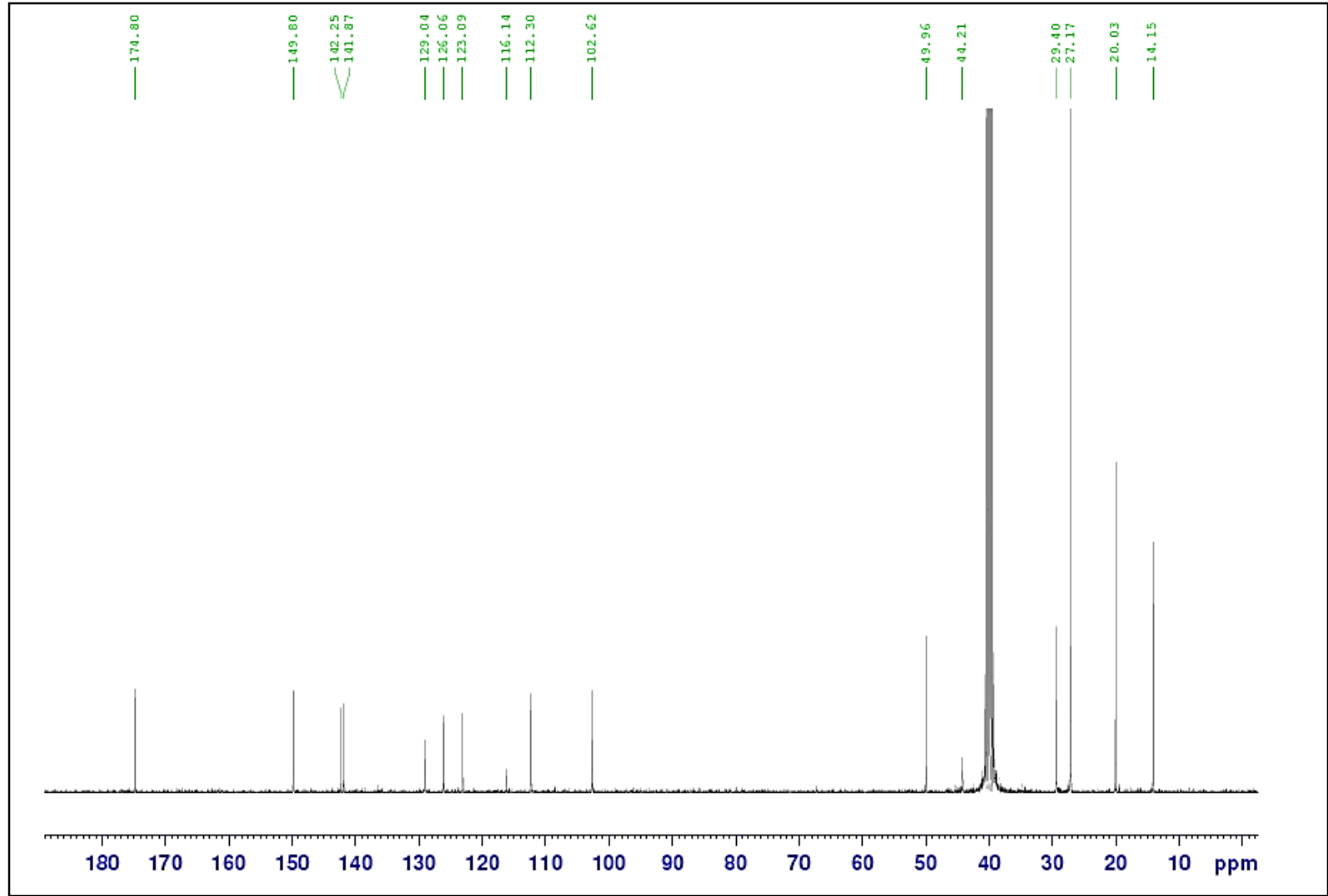
50% MeOH+0.1% HCOOH, Leuink as ITSD

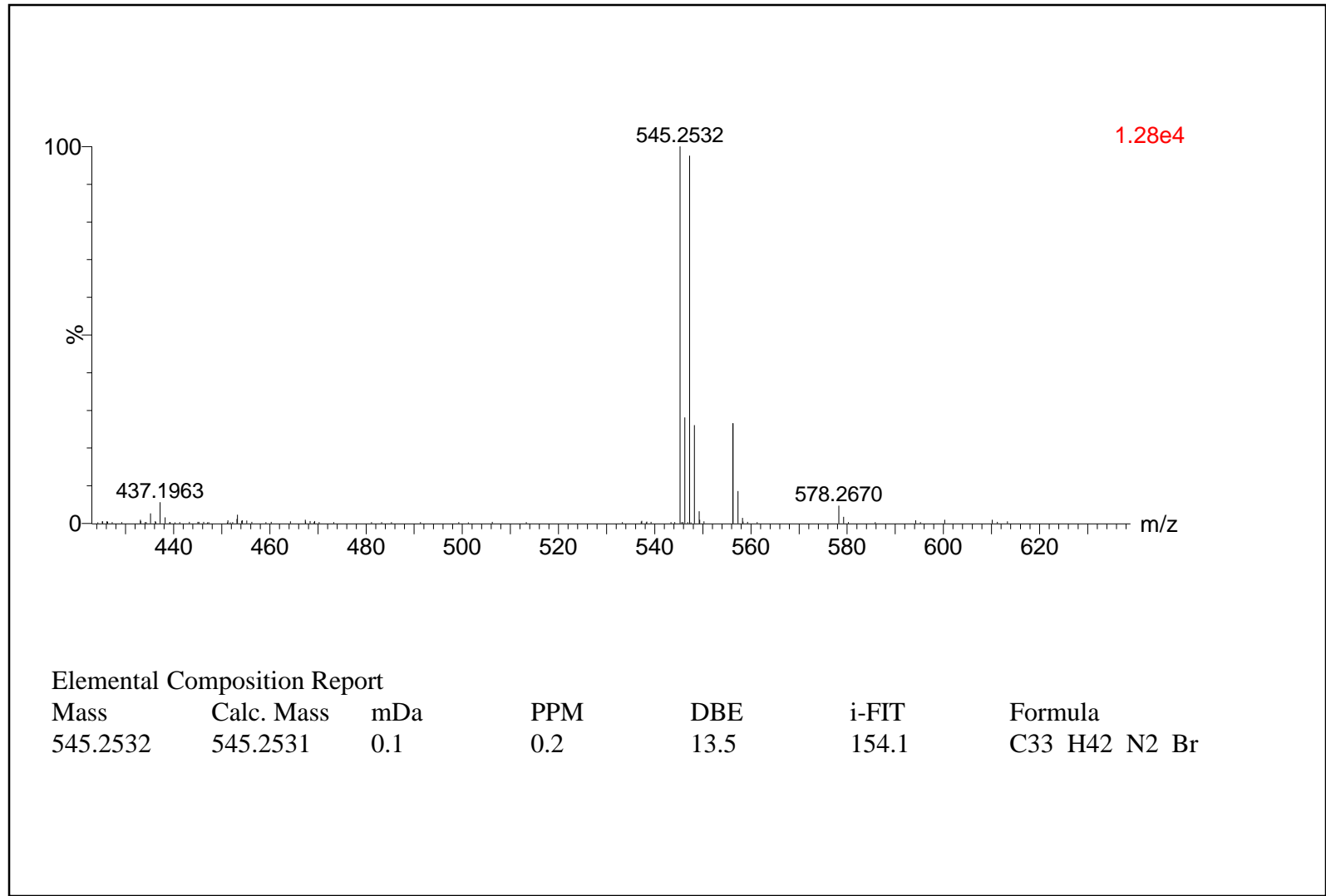
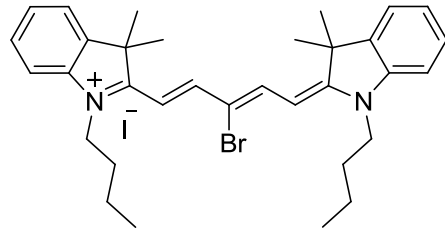


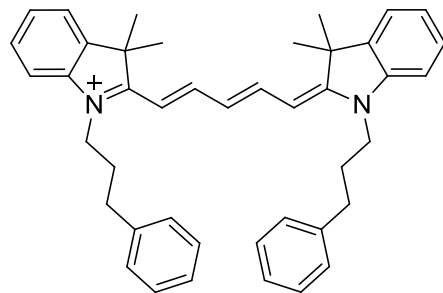
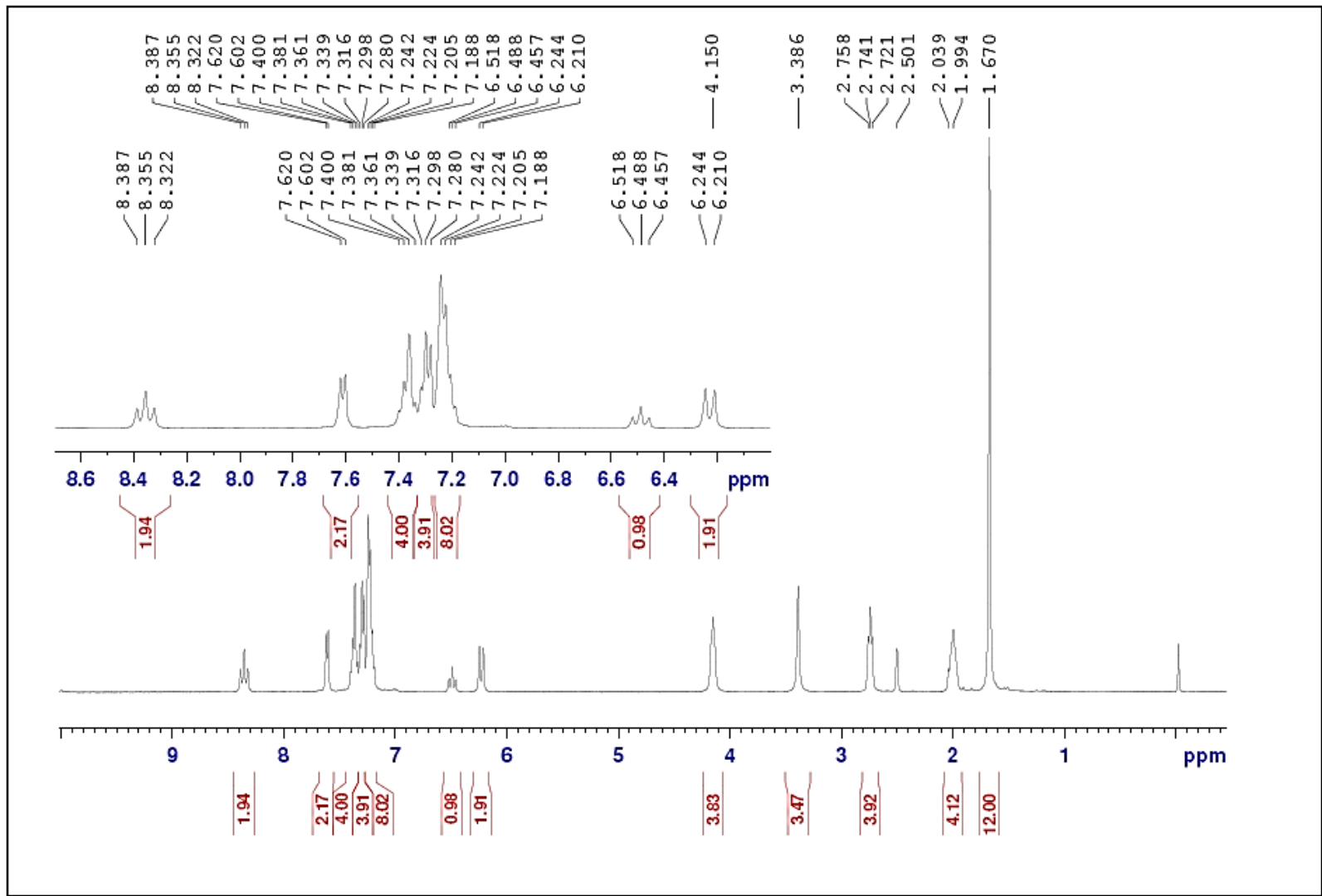
Elemental Composition Report

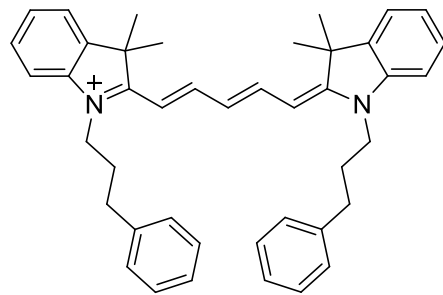
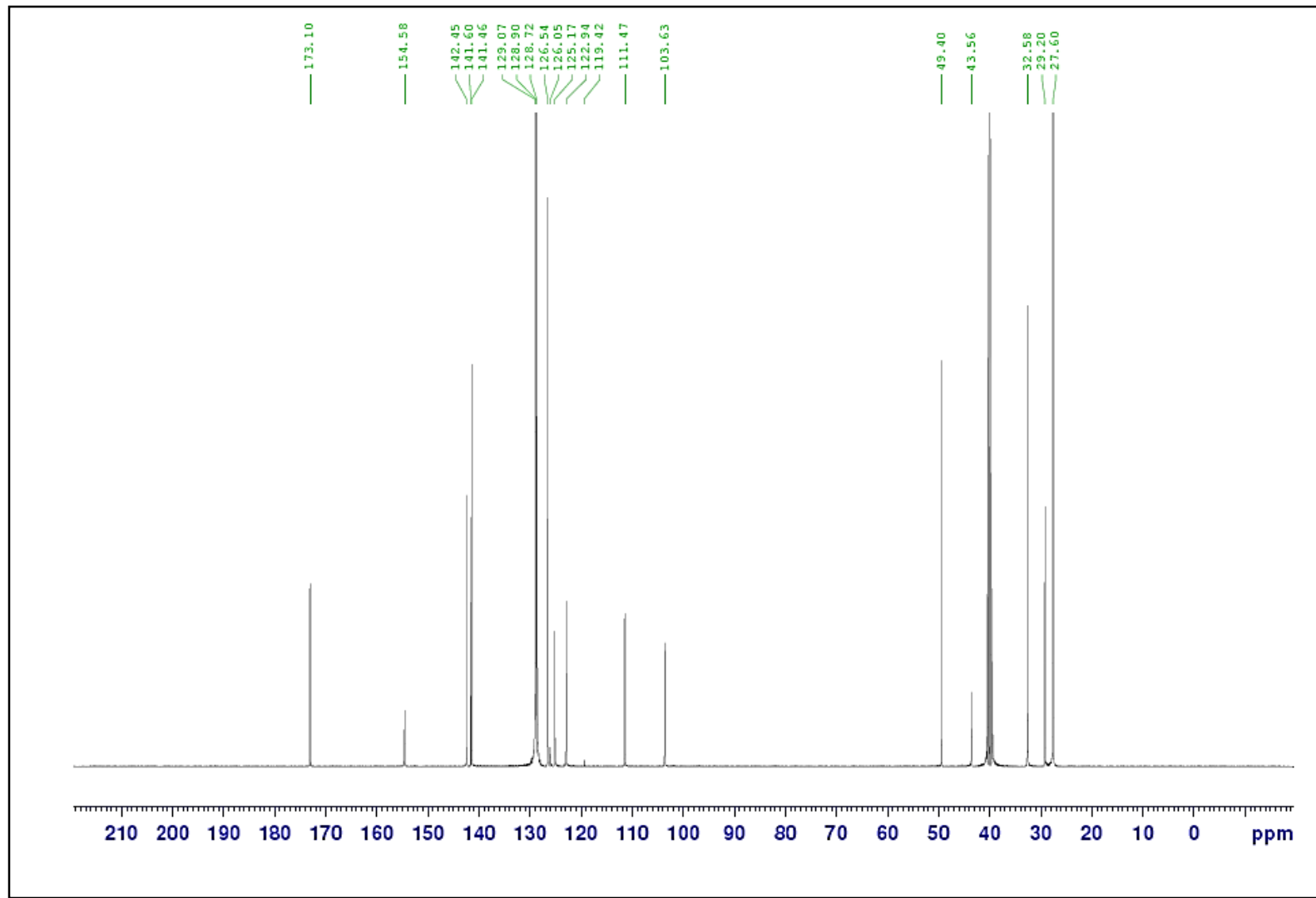
Mass	Calc. Mass	mDa	PPM	DBE	i-FIT	Formula
501.3059	501.3037	2.2	4.4	13.5	1.0	C ₃₃ H ₄₂ N ₂ Cl

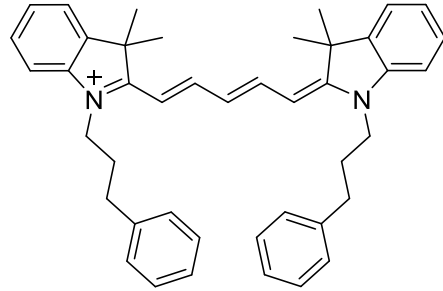
DMSO- d_6 

DMSO- d_6 

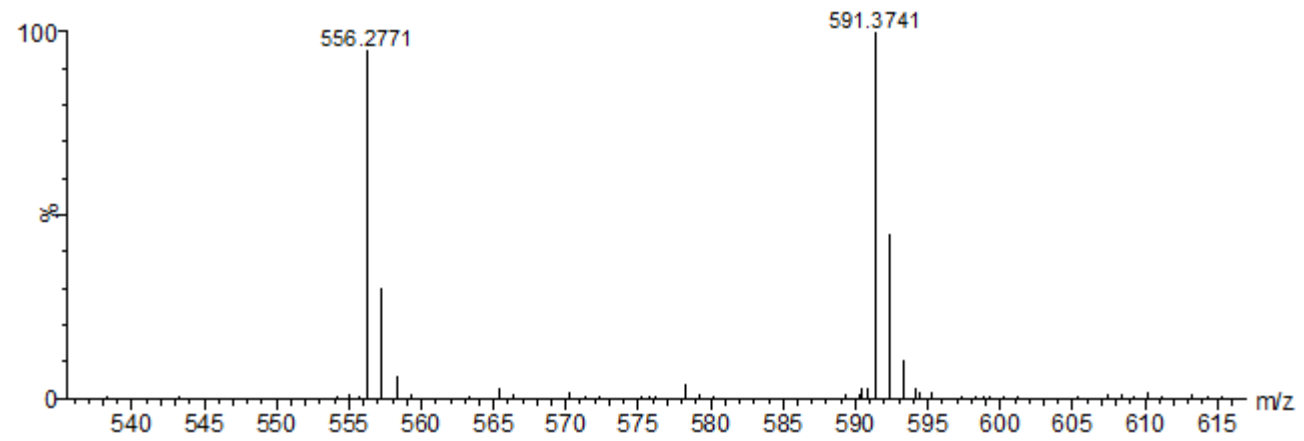


DMSO- d_6 

DMSO- d_6 

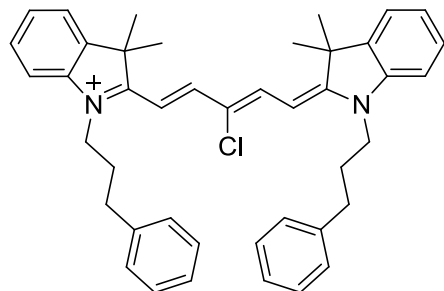
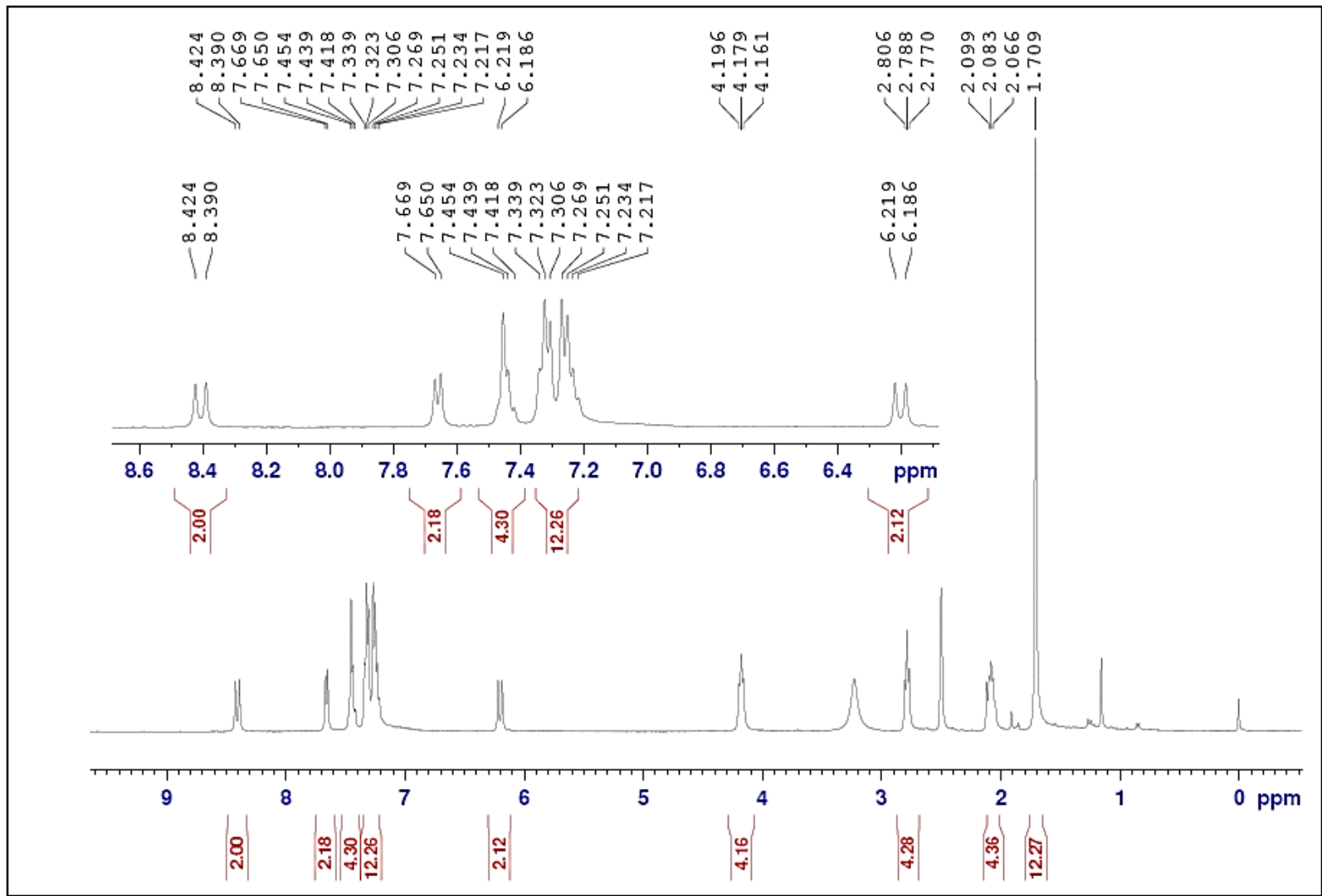


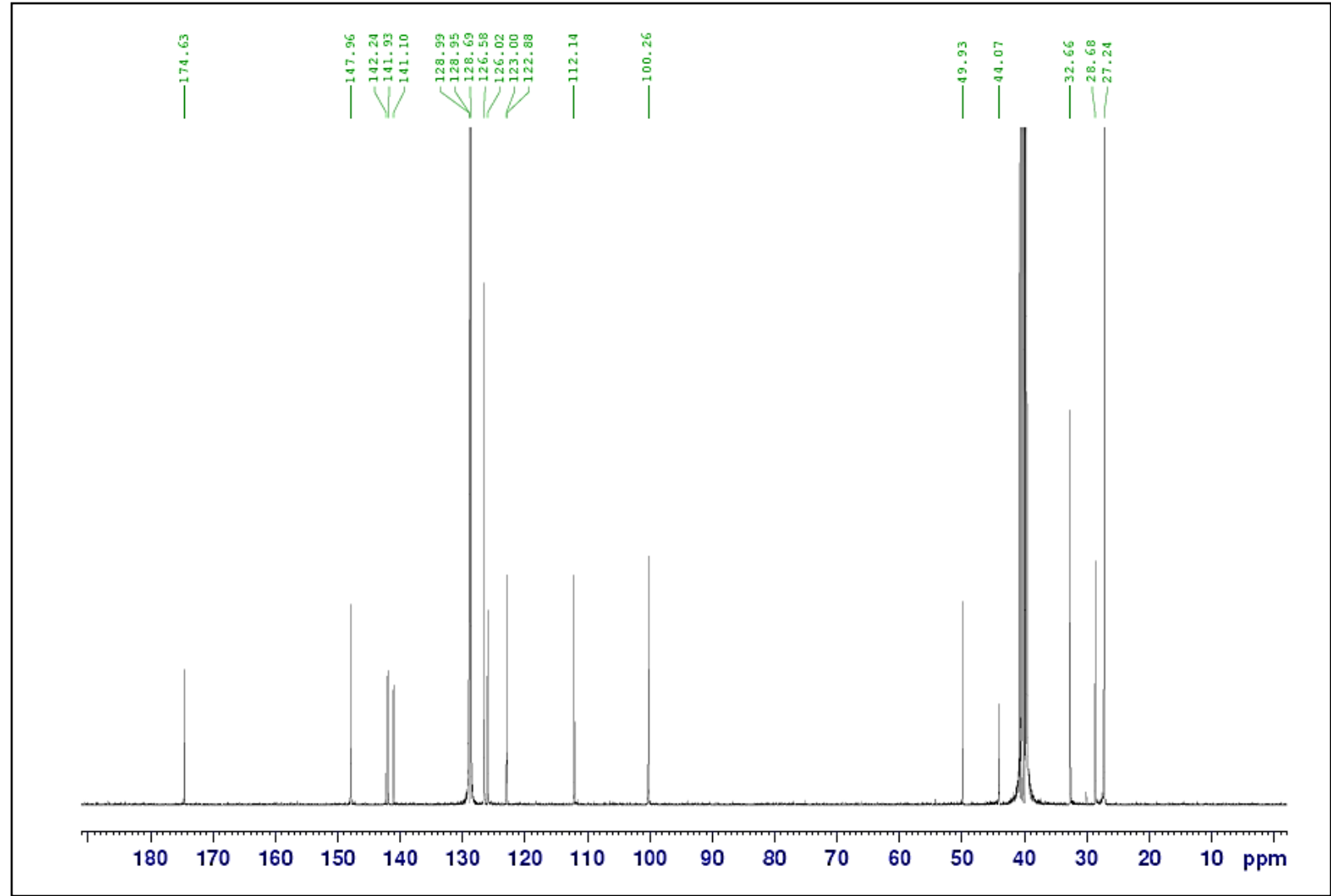
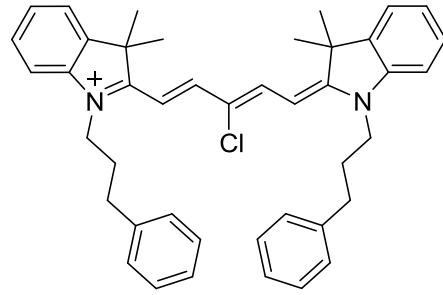
100% MeOH+0.1% HCOOH

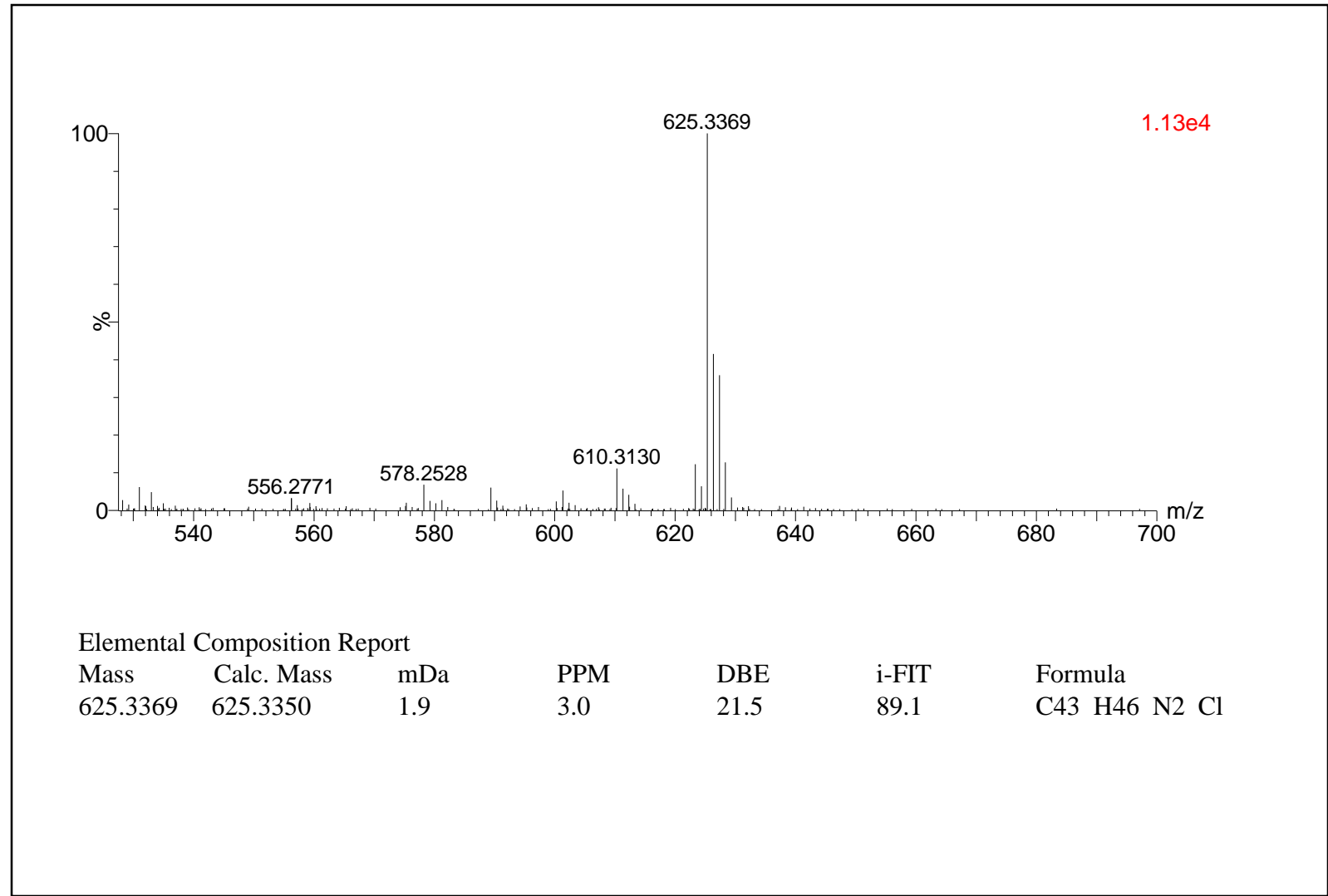
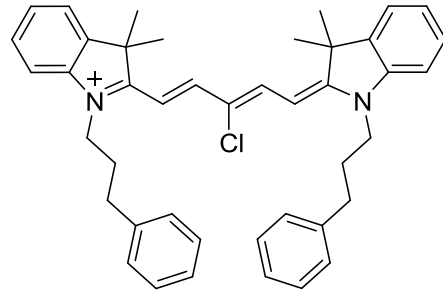


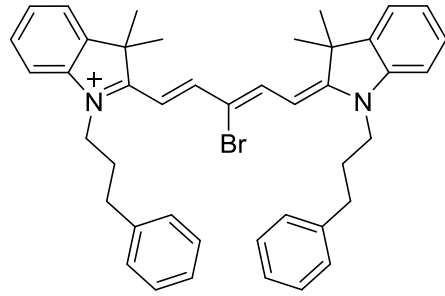
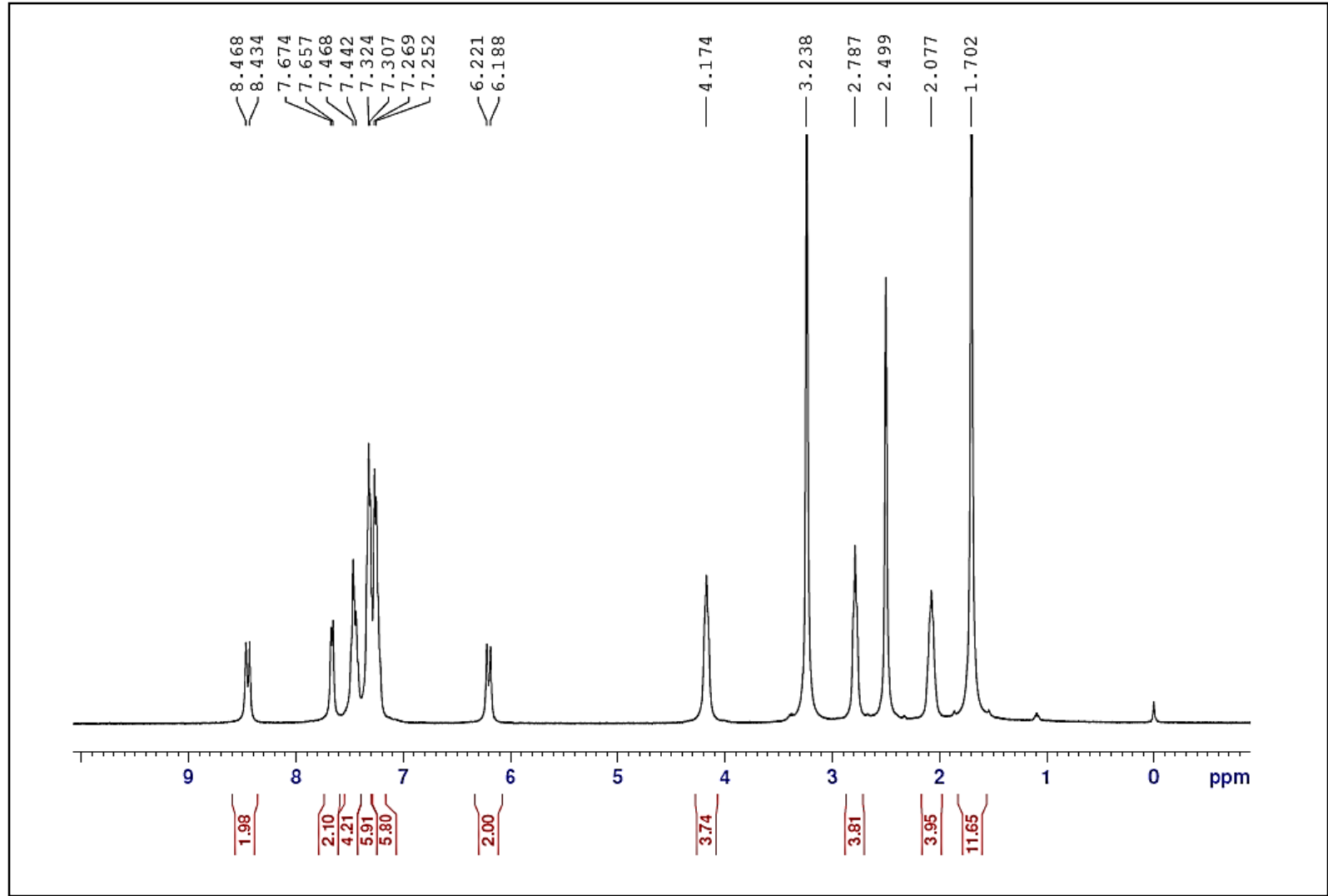
Elemental Composition Report

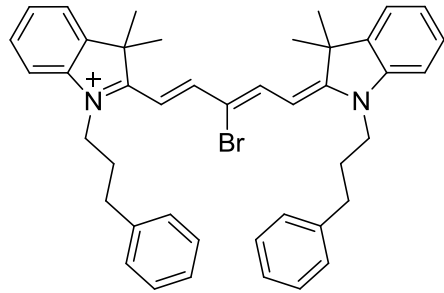
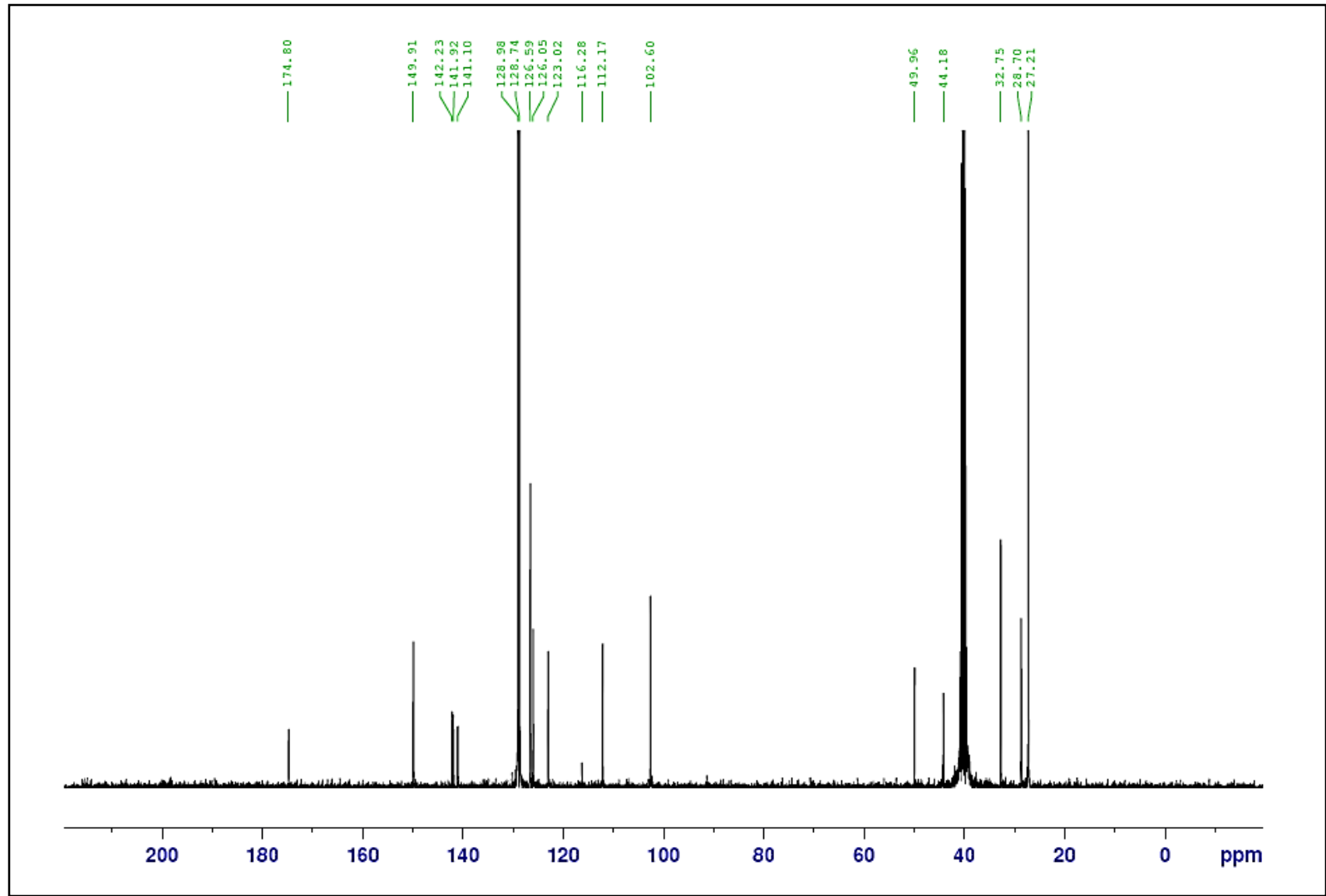
Mass	Calc. Mass	mDa	PPM	DBE	i-FIT	Formula
591.3741	591.3739	0.2	0.3	21.5	84.6	C43 H47 N2

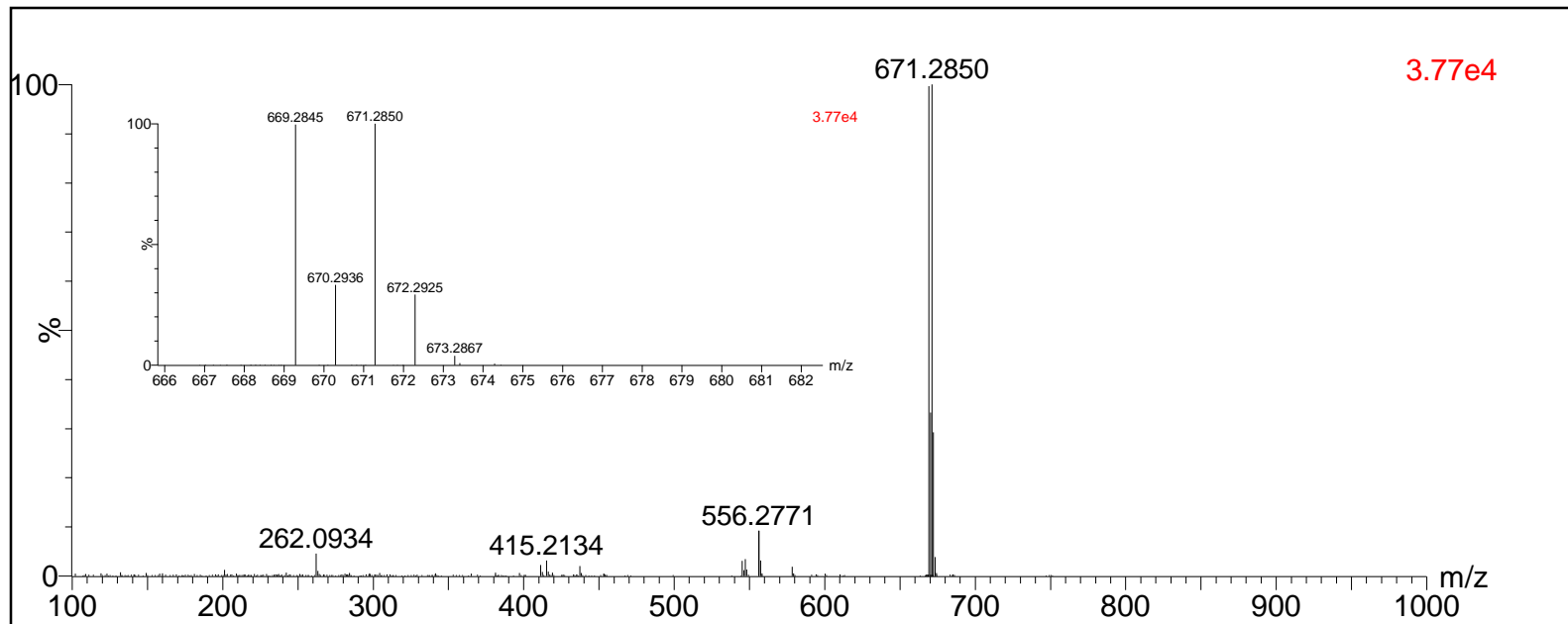
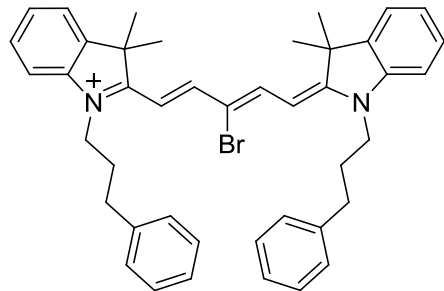
DMSO- d_6 





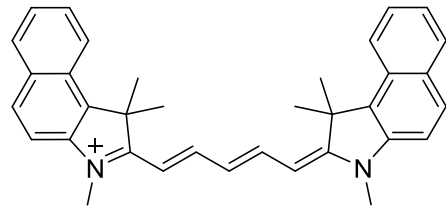
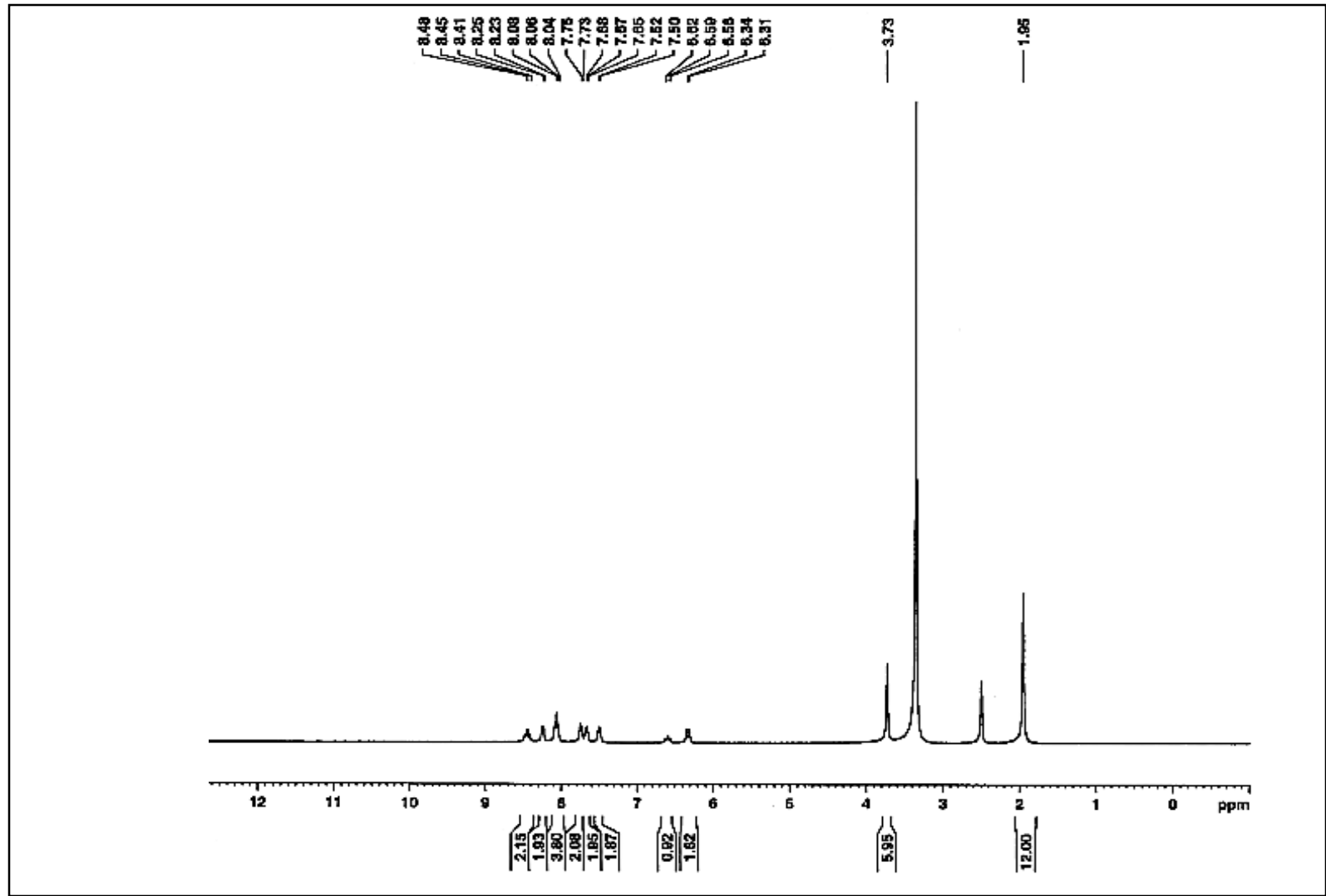
DMSO- d_6 

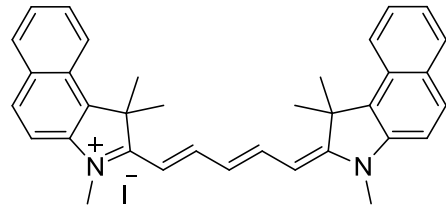
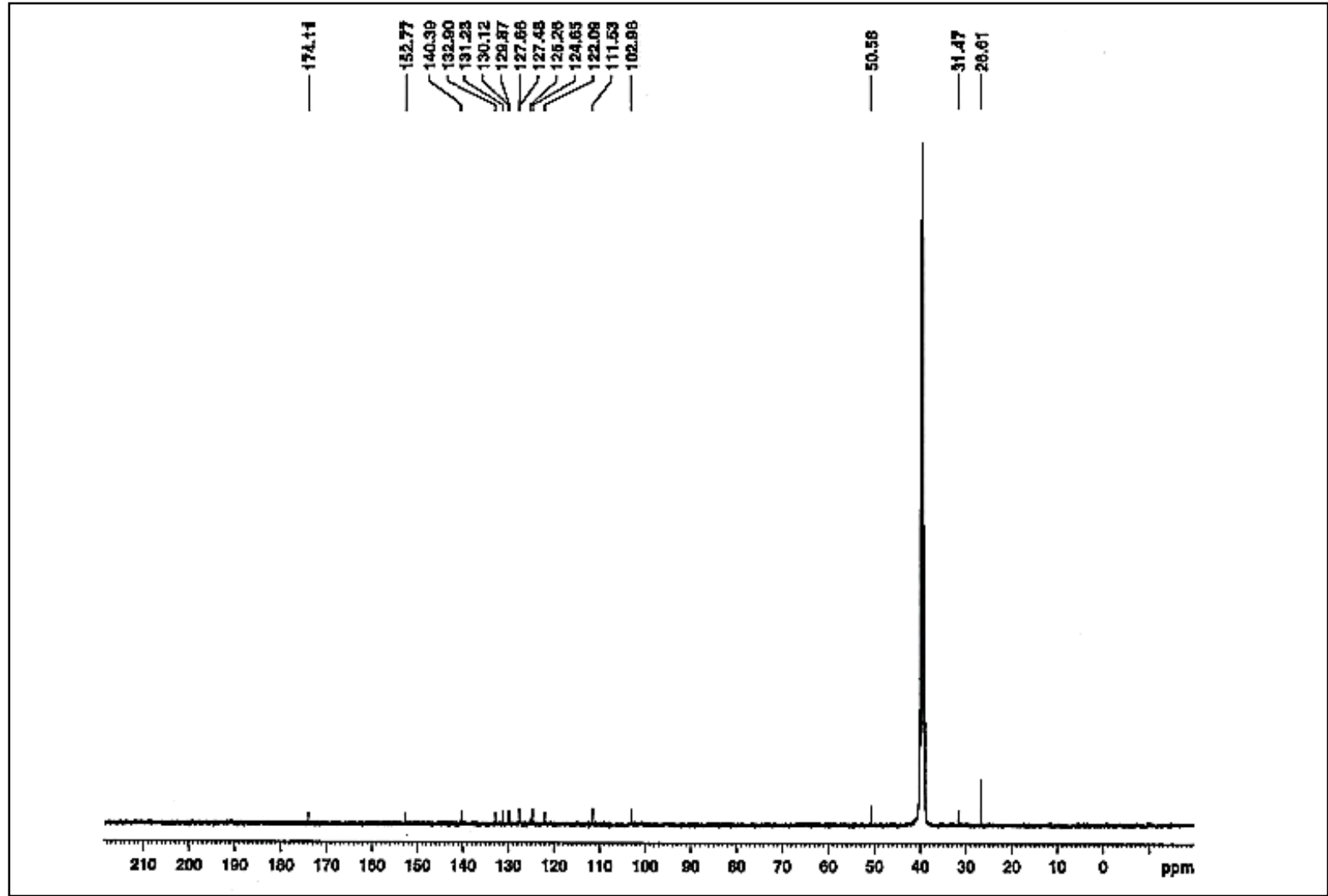
DMSO- d_6 

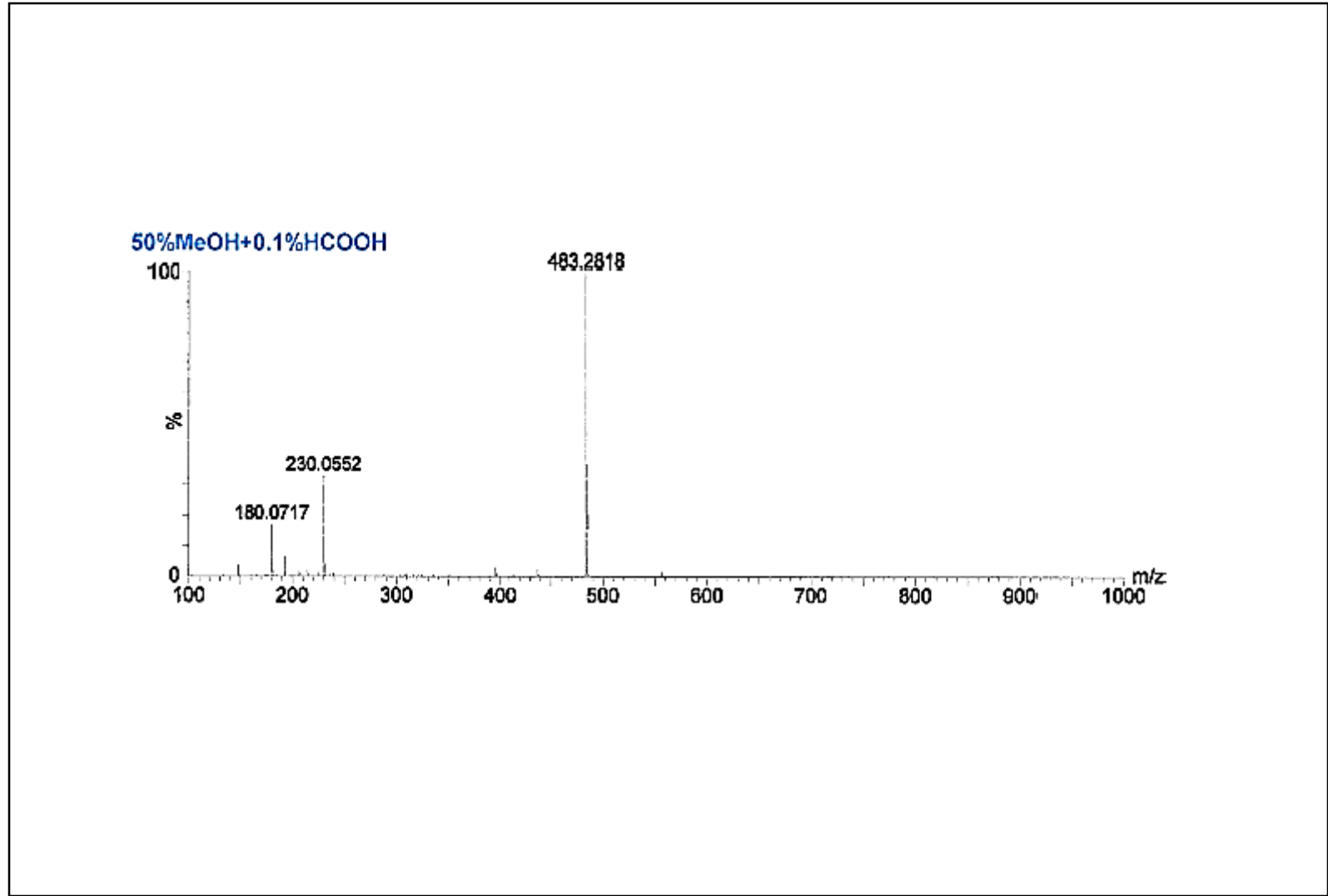
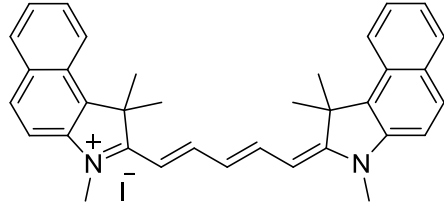


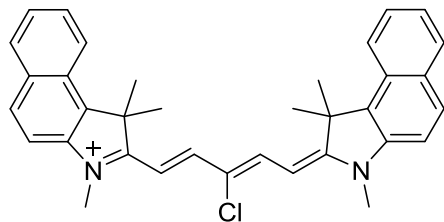
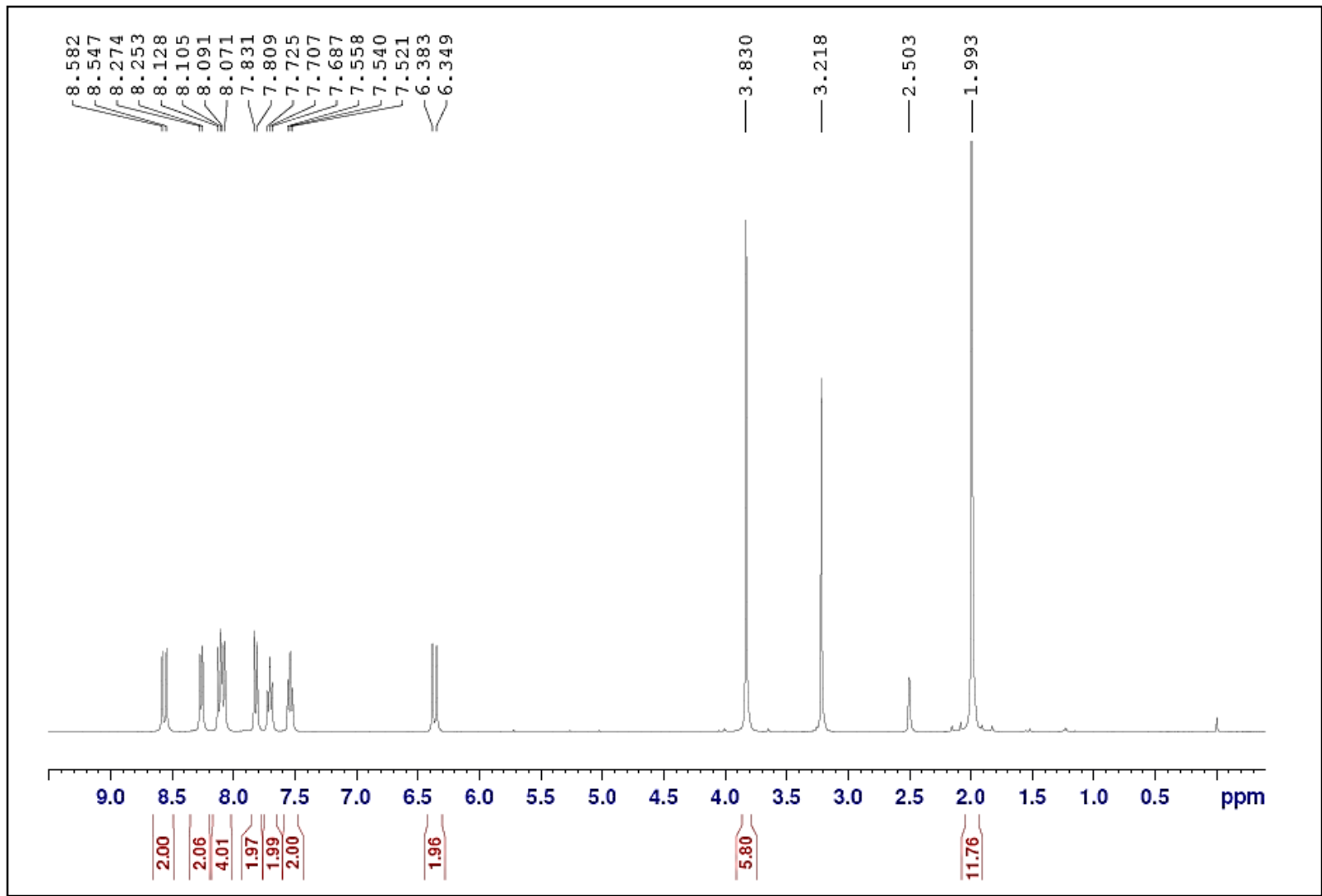
Elemental Composition Report

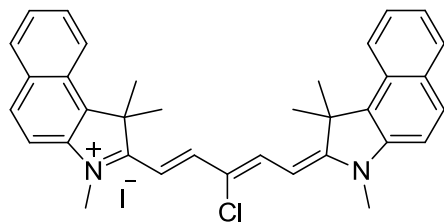
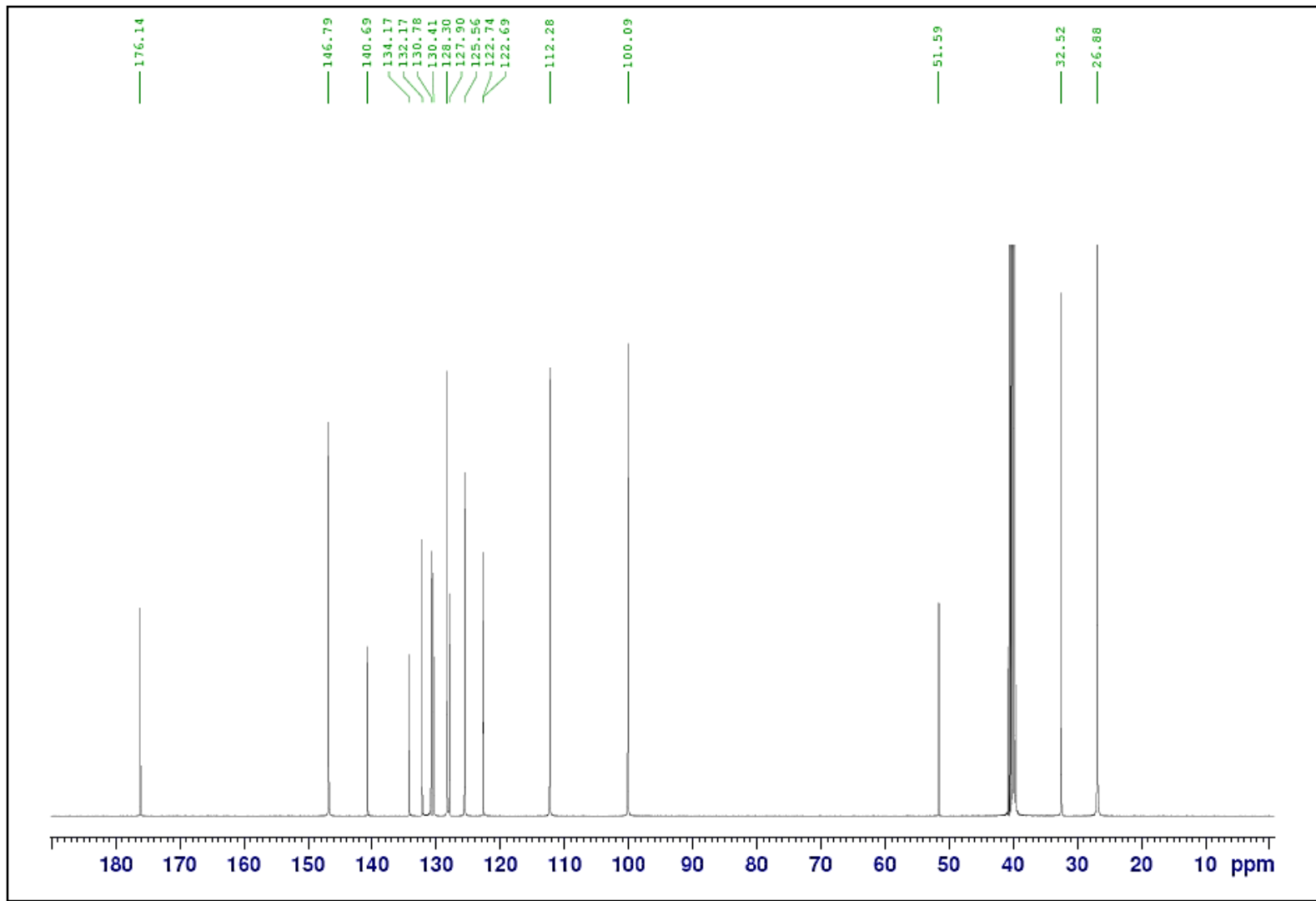
Mass	Calc. Mass	mDa	PPM	DBE	i-FIT	Formula
669.2845	669.2844	0.1	0.1	21.5	870.8	C43 H46 N2 Br

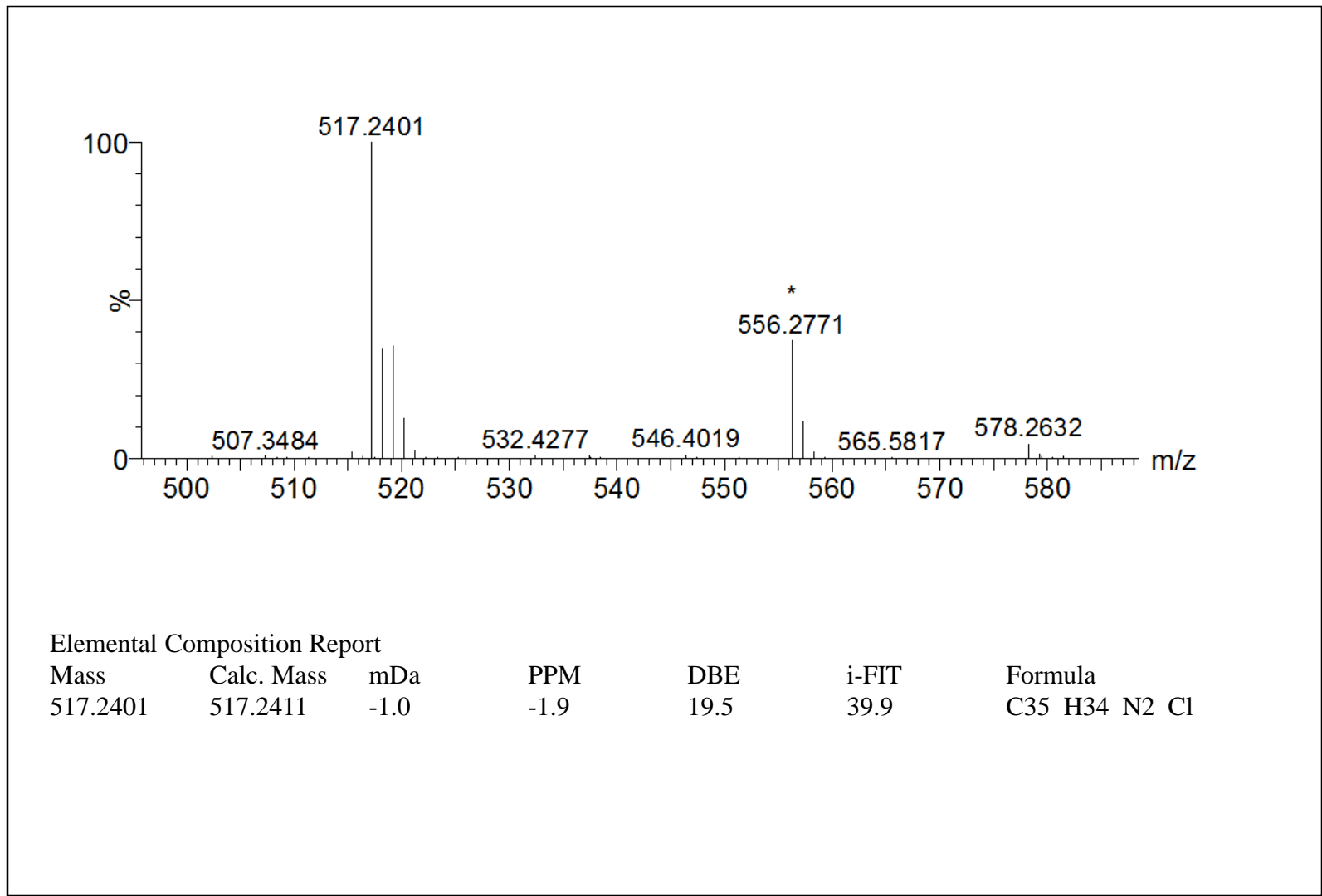
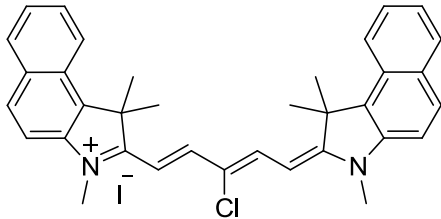
DMSO- d_6 

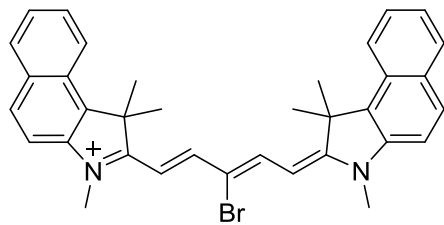
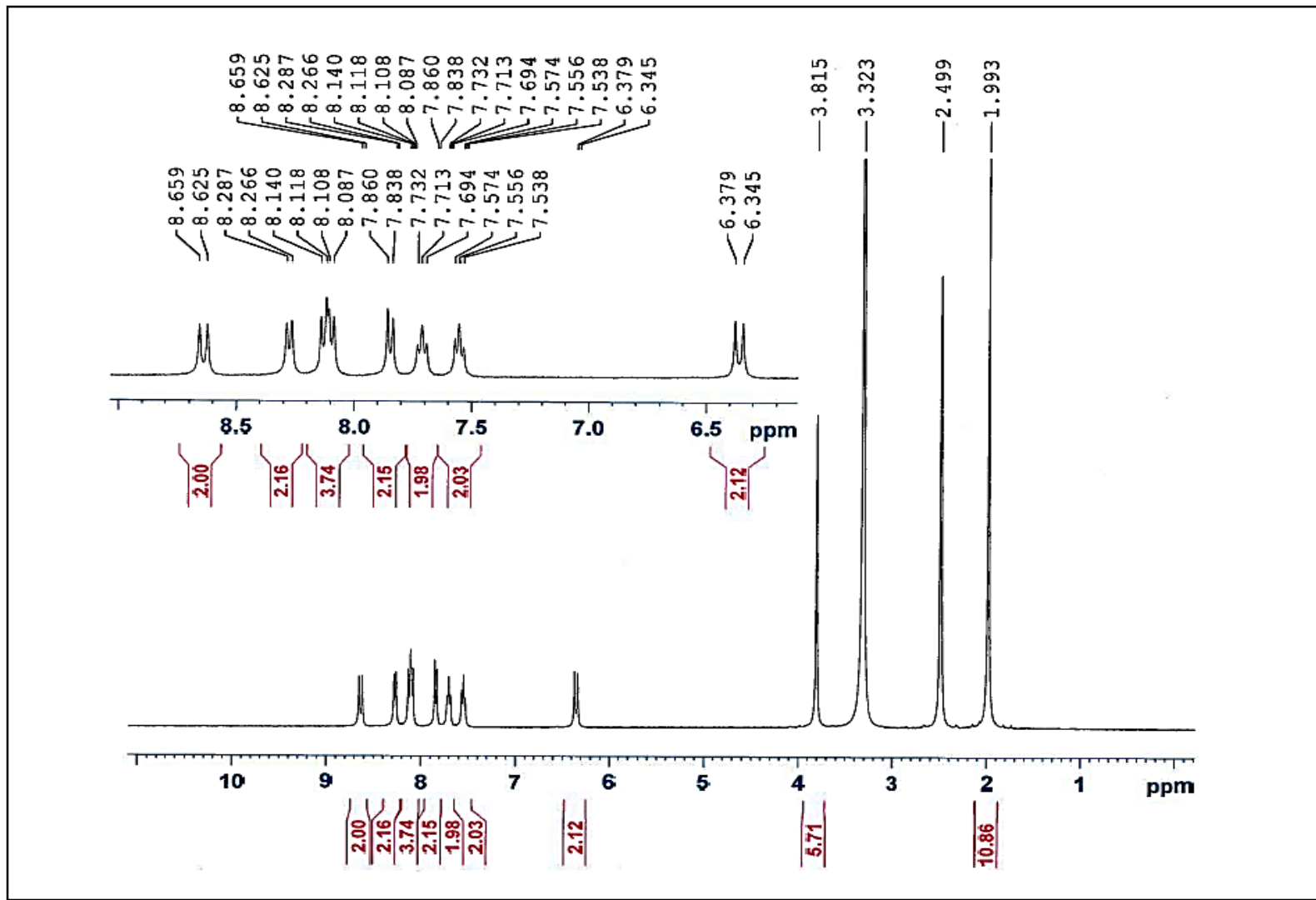
DMSO- d_6 

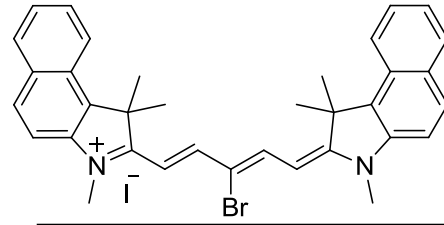
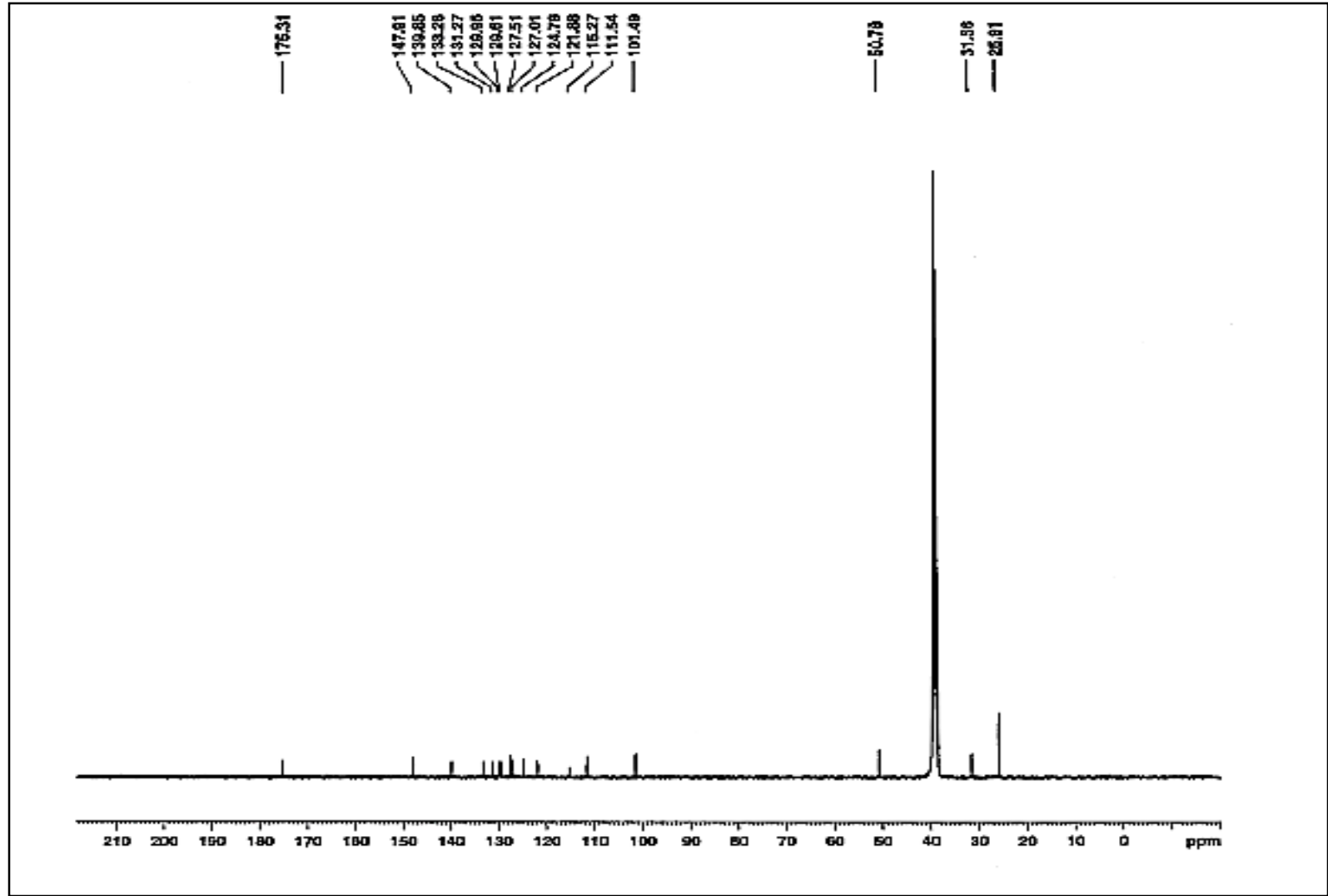


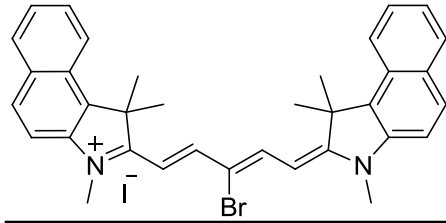
DMSO- d_6 at 50 °C

DMSO-*d*₆ at 50 °C

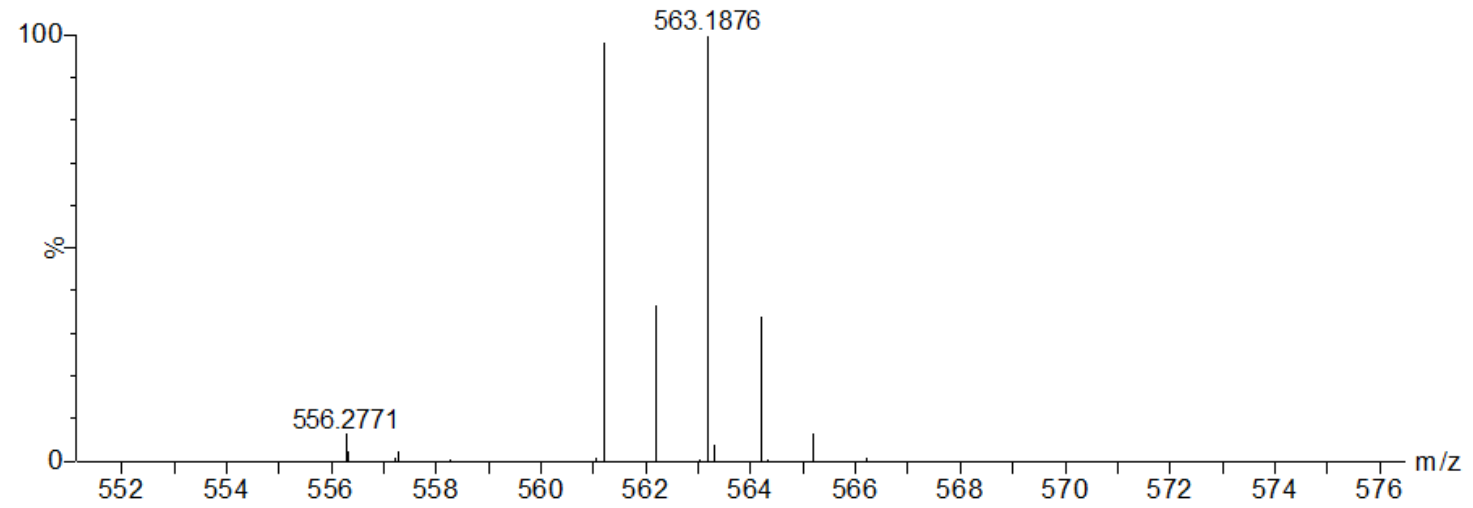


DMSO- d_6 

DMSO- d_6 

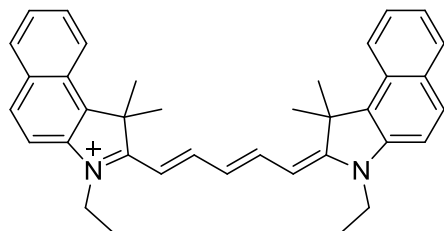
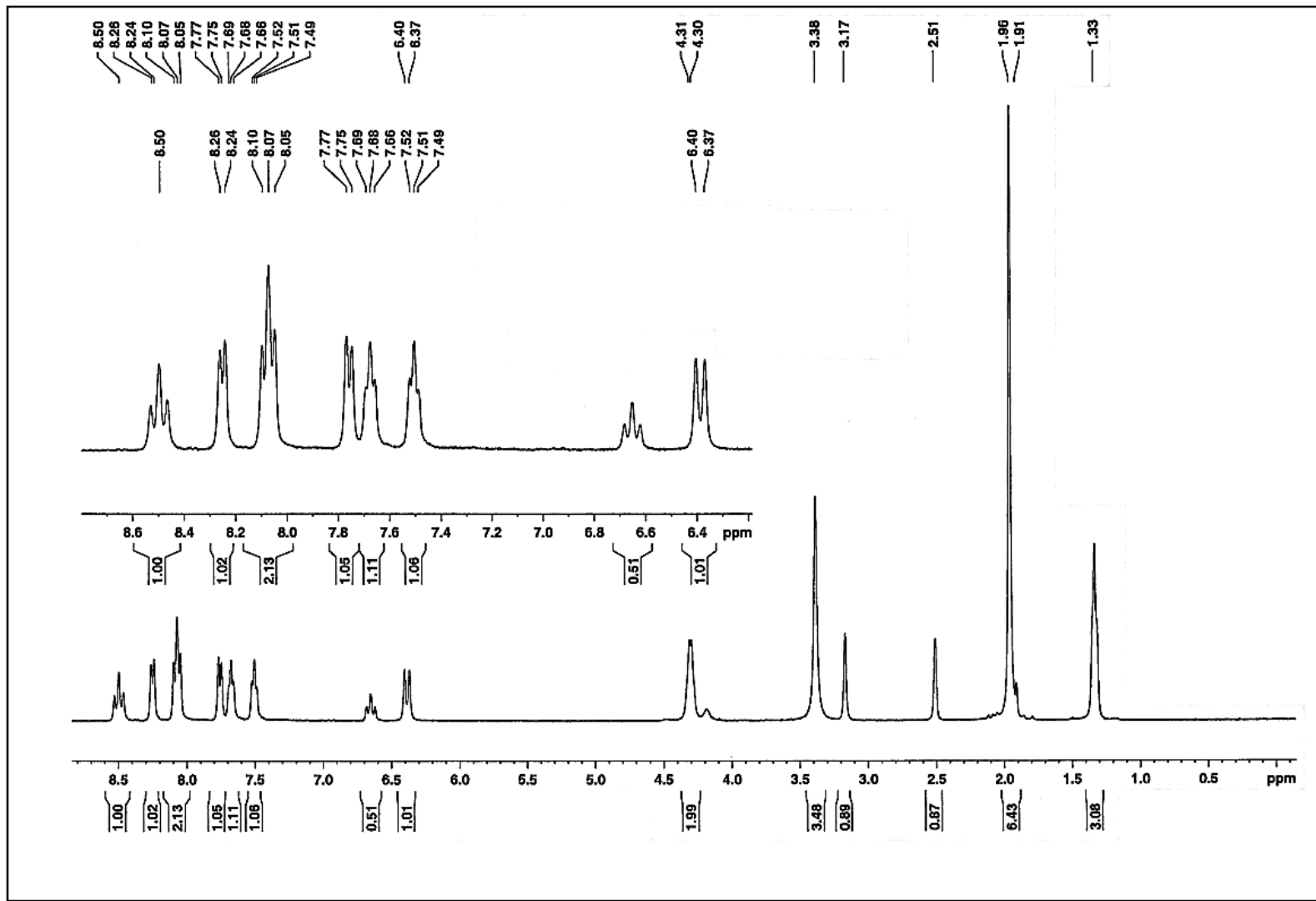


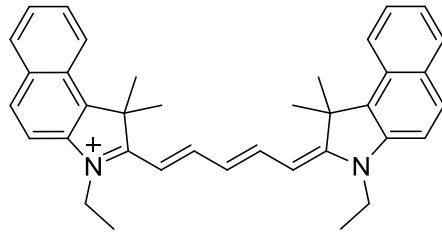
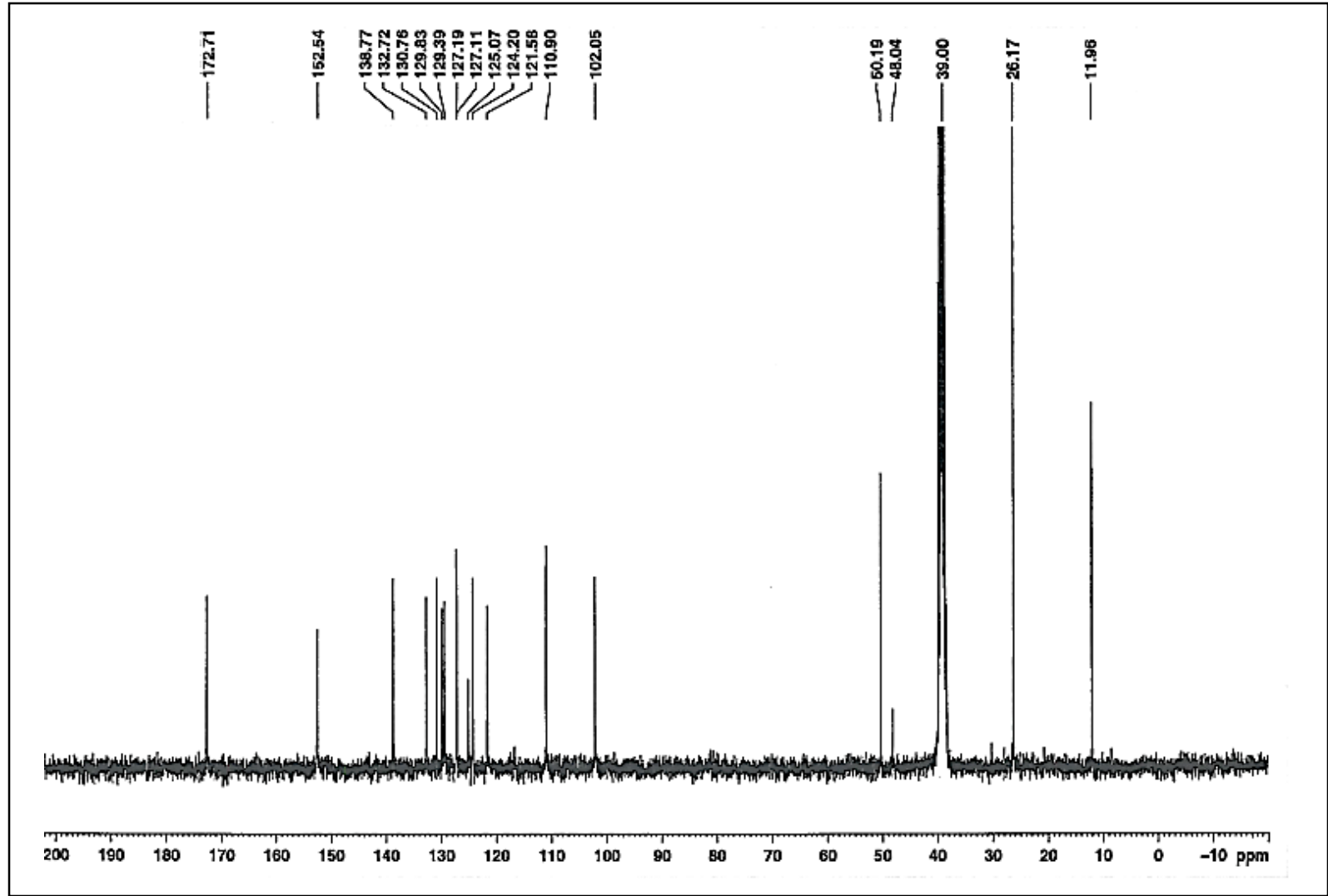
in 100%MeOH+0.1%HCOOH

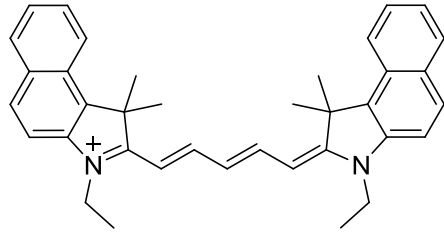


Elemental Composition Report

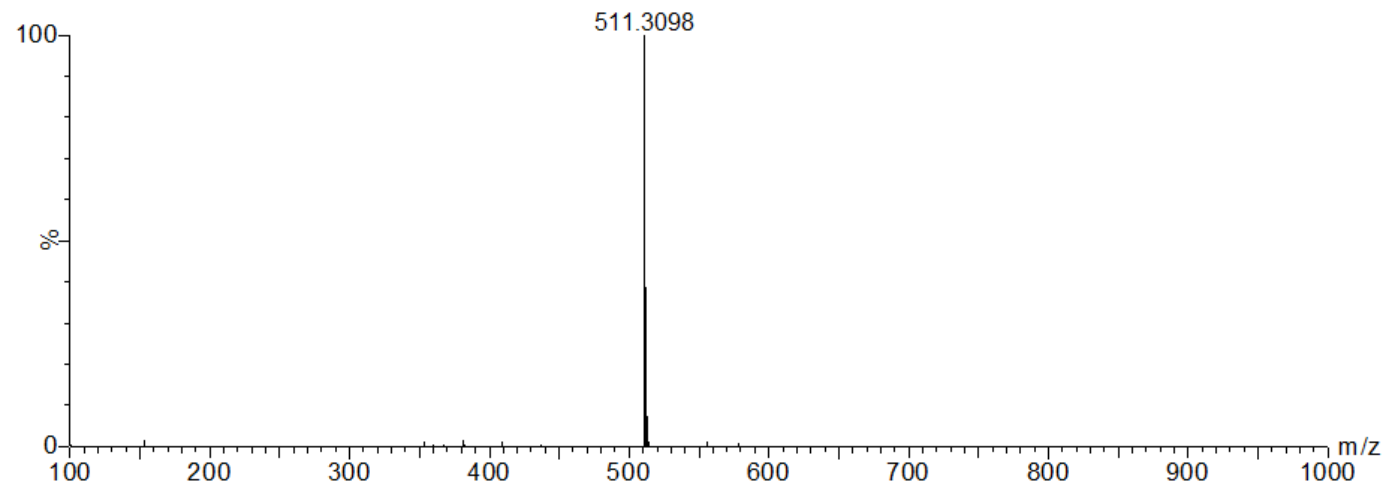
Mass	Calc. Mass	mDa	PPM	DBE	i-FIT	Formula
561.1914	561.1905	0.9	1.6	19.5	7.3	C ₃₅ H ₃₄ N ₂ Br

DMSO- d_6 

DMSO- d_6 

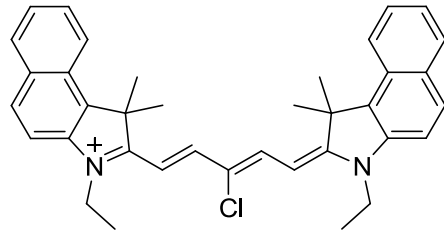
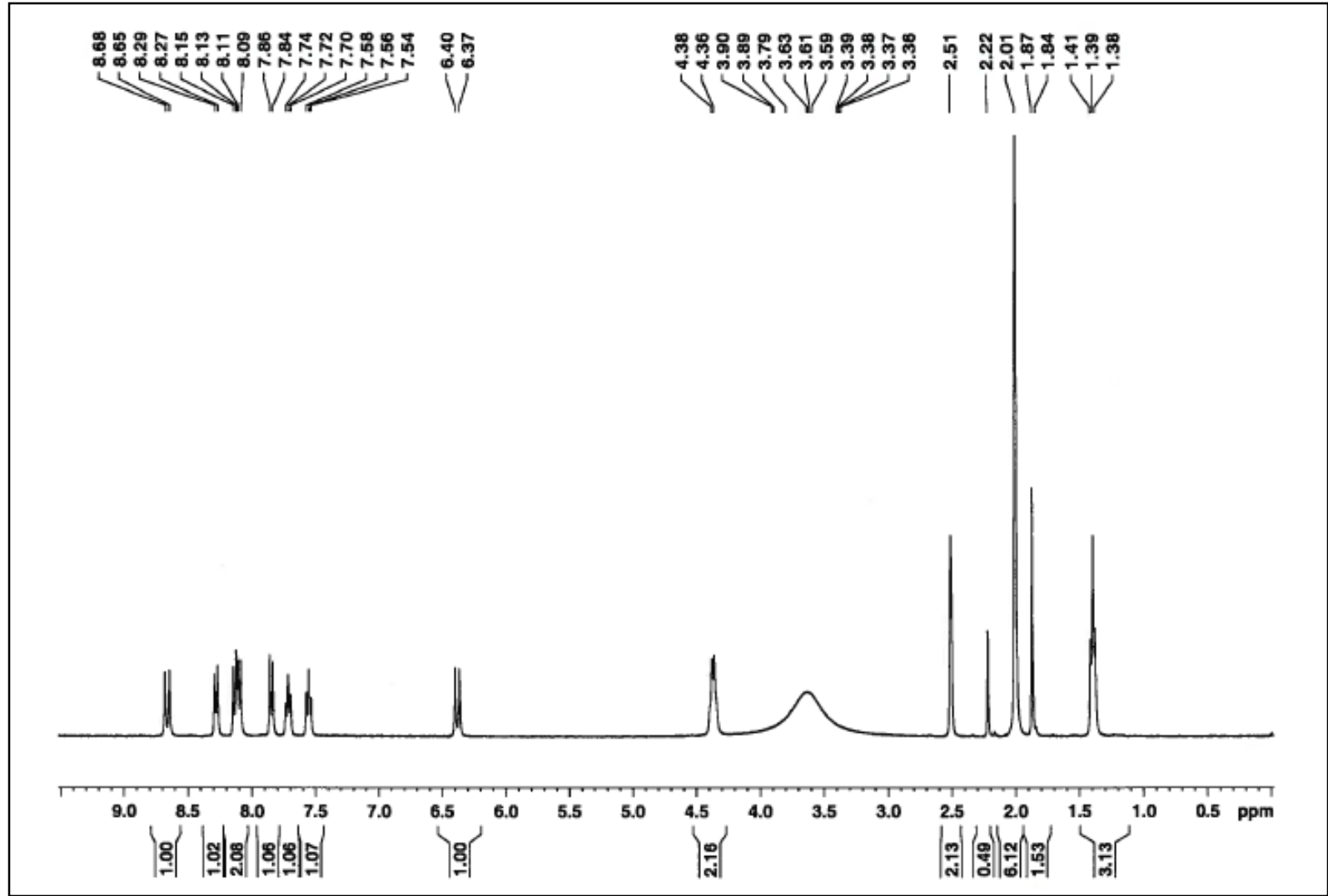


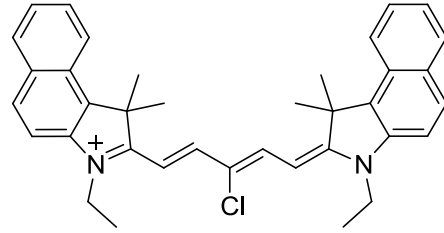
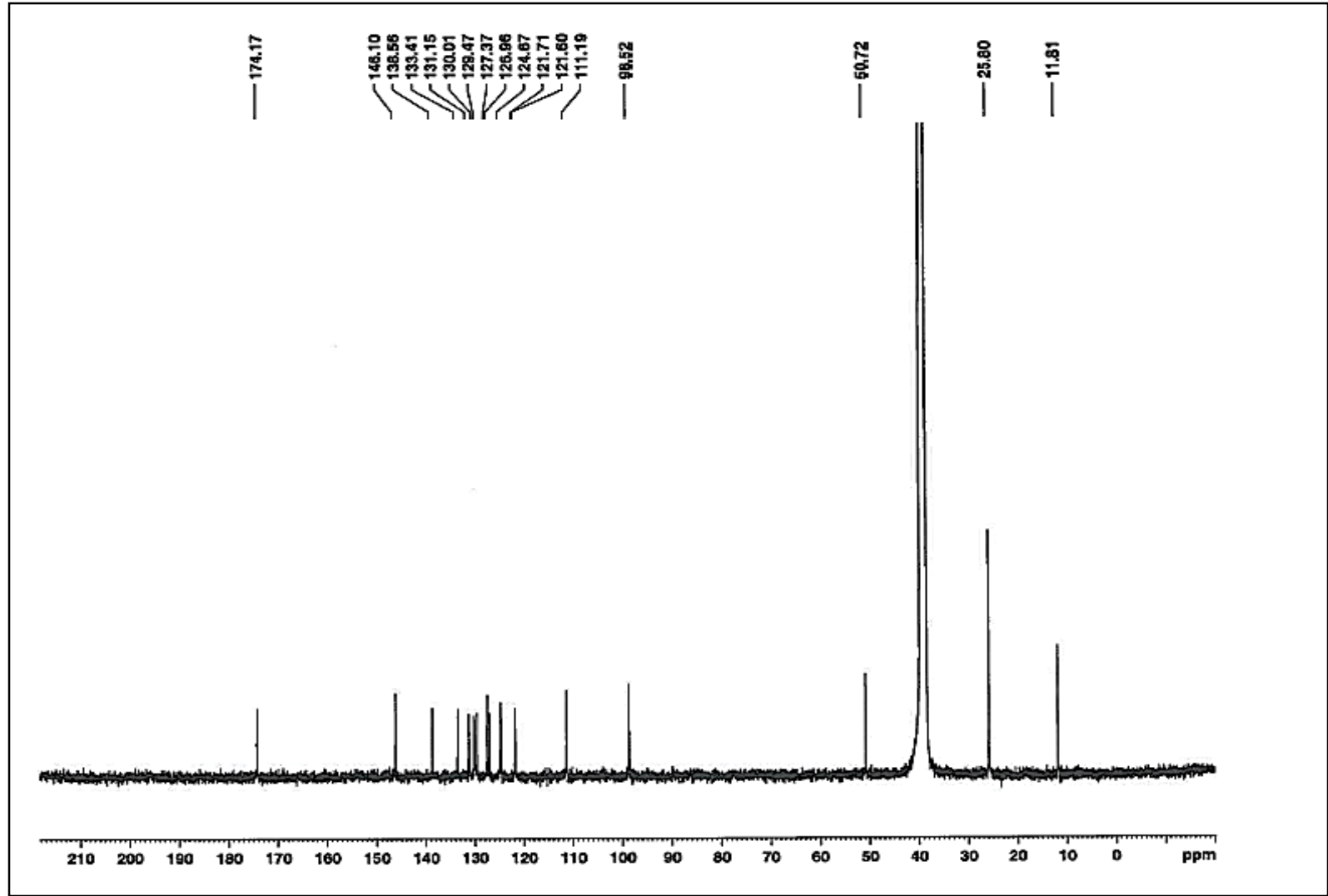
100%MeOH+0.1%HCOOH

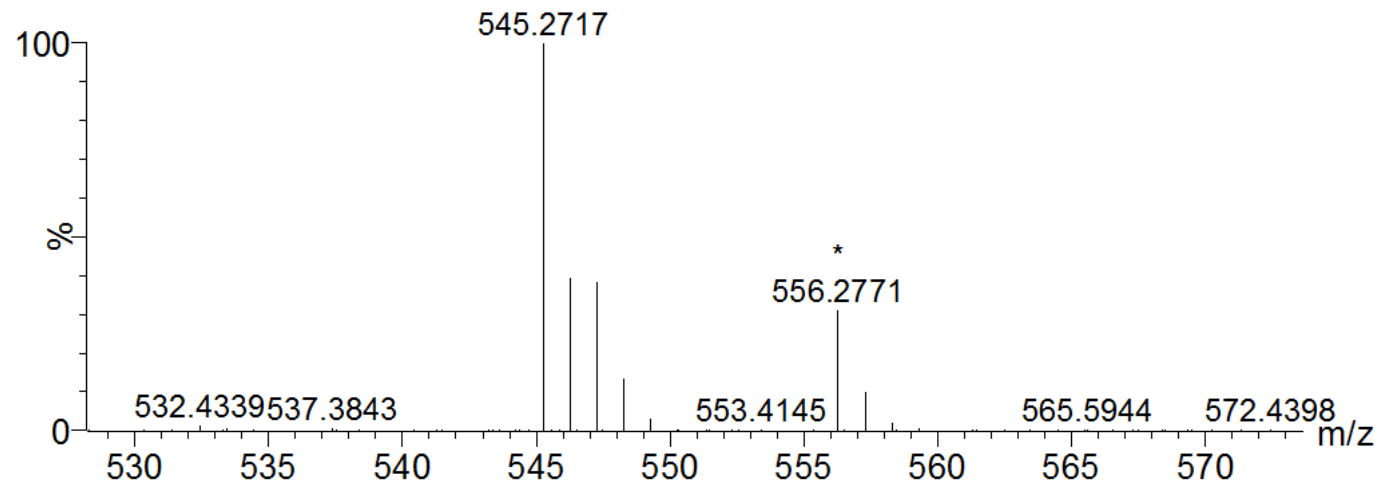
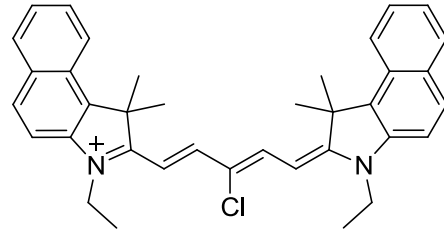


Elemental Composition Report

Mass	Calc. Mass	mDa	PPM	DBE	i-FIT	Formula
511.3098	511.3113	-1.5	-2.9	19.5	25.7	C37 H39 N2

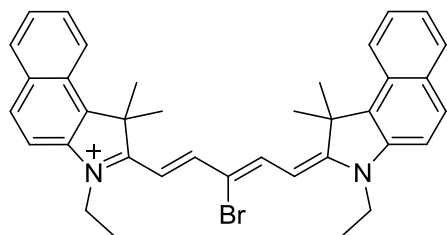
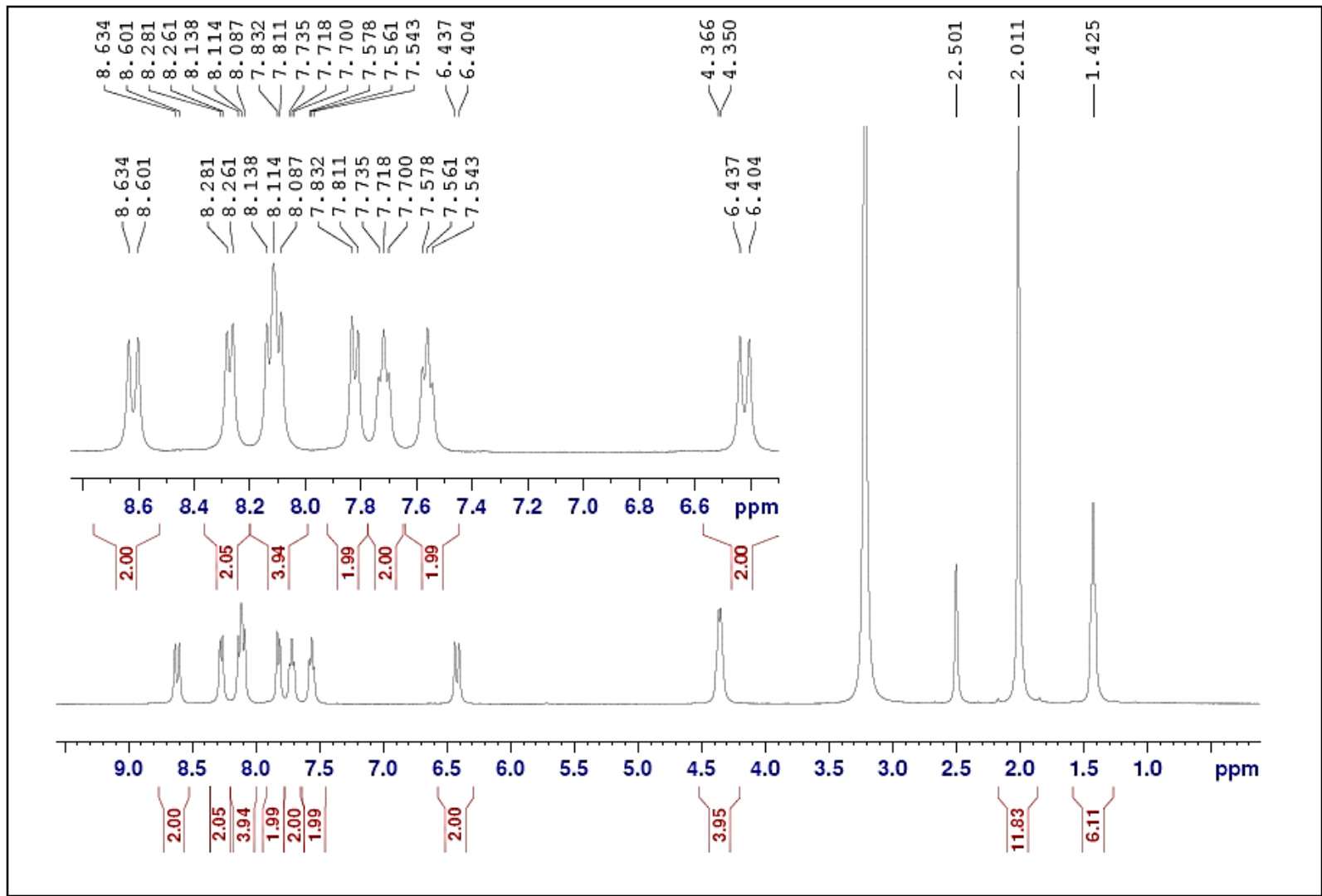
DMSO- d_6 

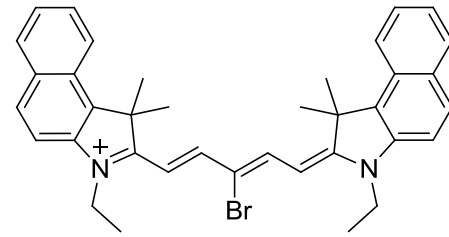
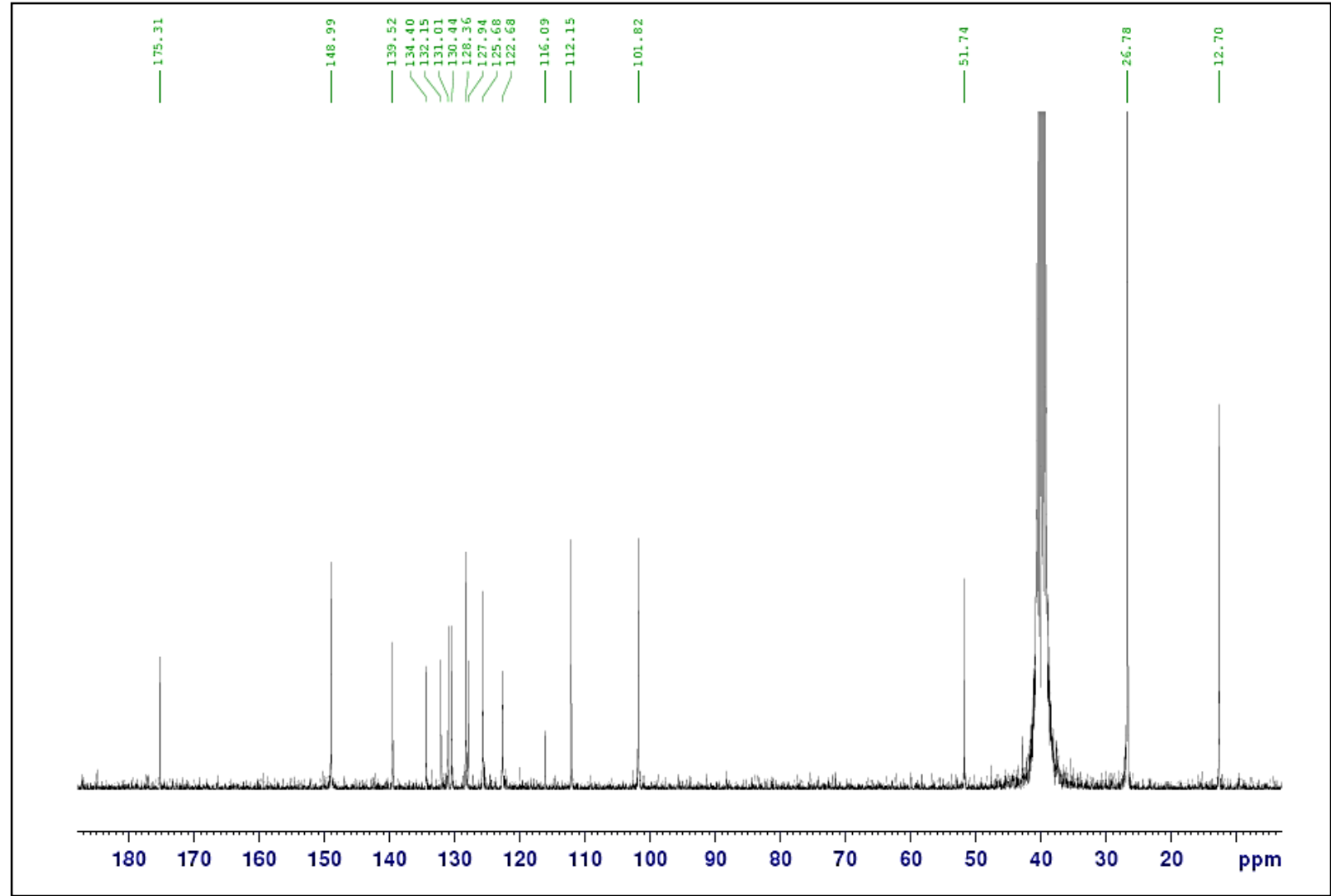
DMSO- d_6 

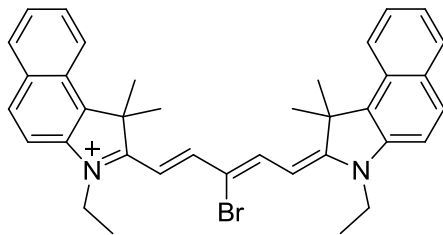


Elemental Composition Report

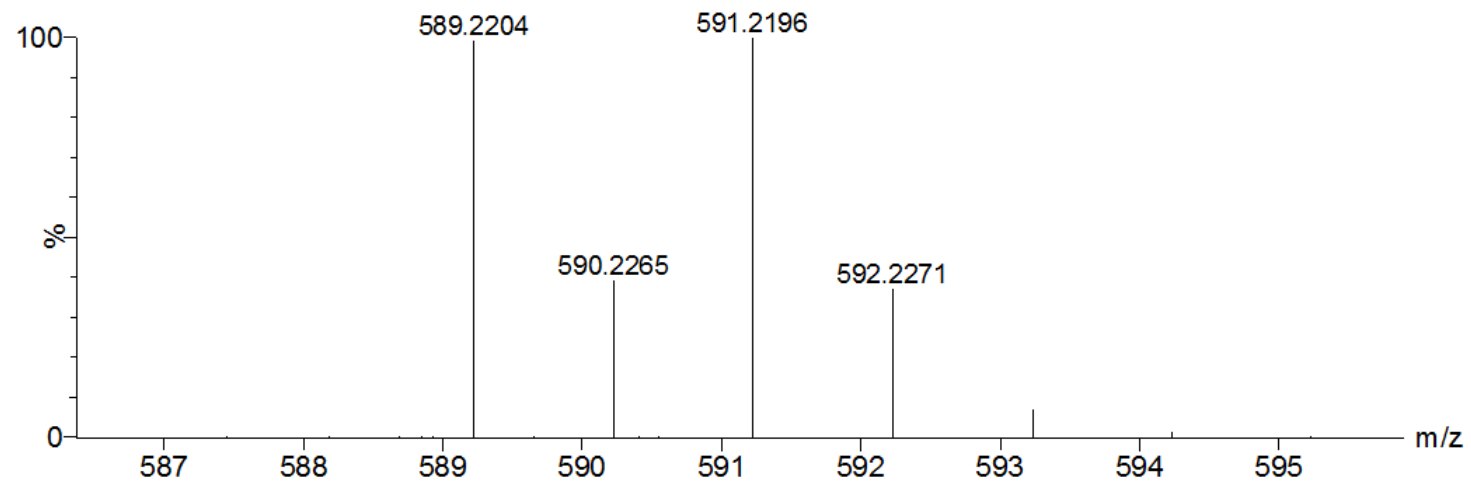
Mass	Calc. Mass	mDa	PPM	DBE	i-FIT	Formula
545.2717	545.2724	-0.7	-1.3	19.5	6.3	C ₃₇ H ₃₈ N ₂ Cl

DMSO- d_6 

DMSO-*d*₆

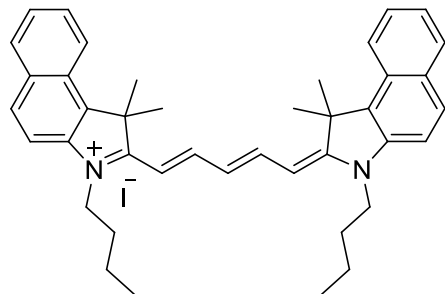
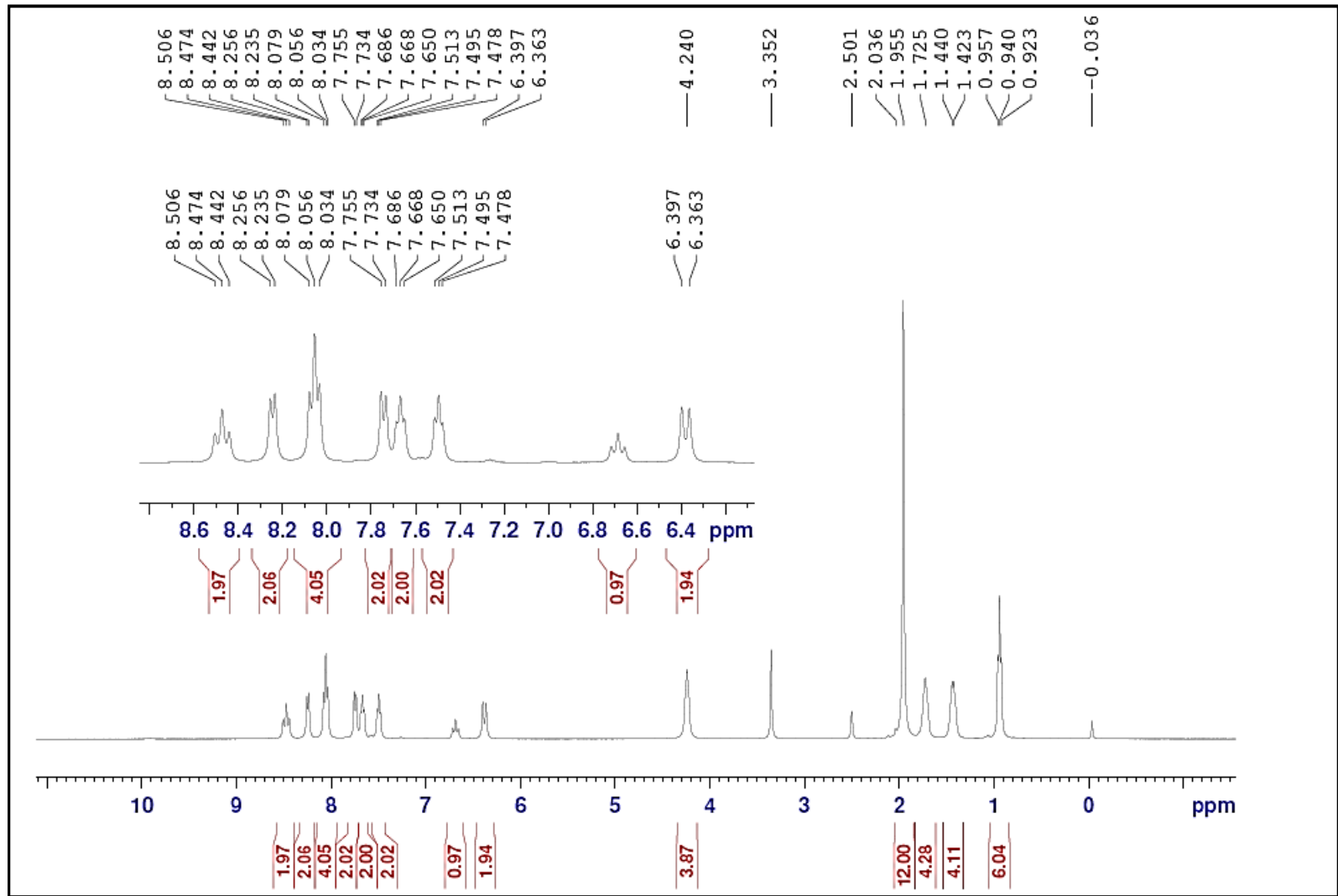


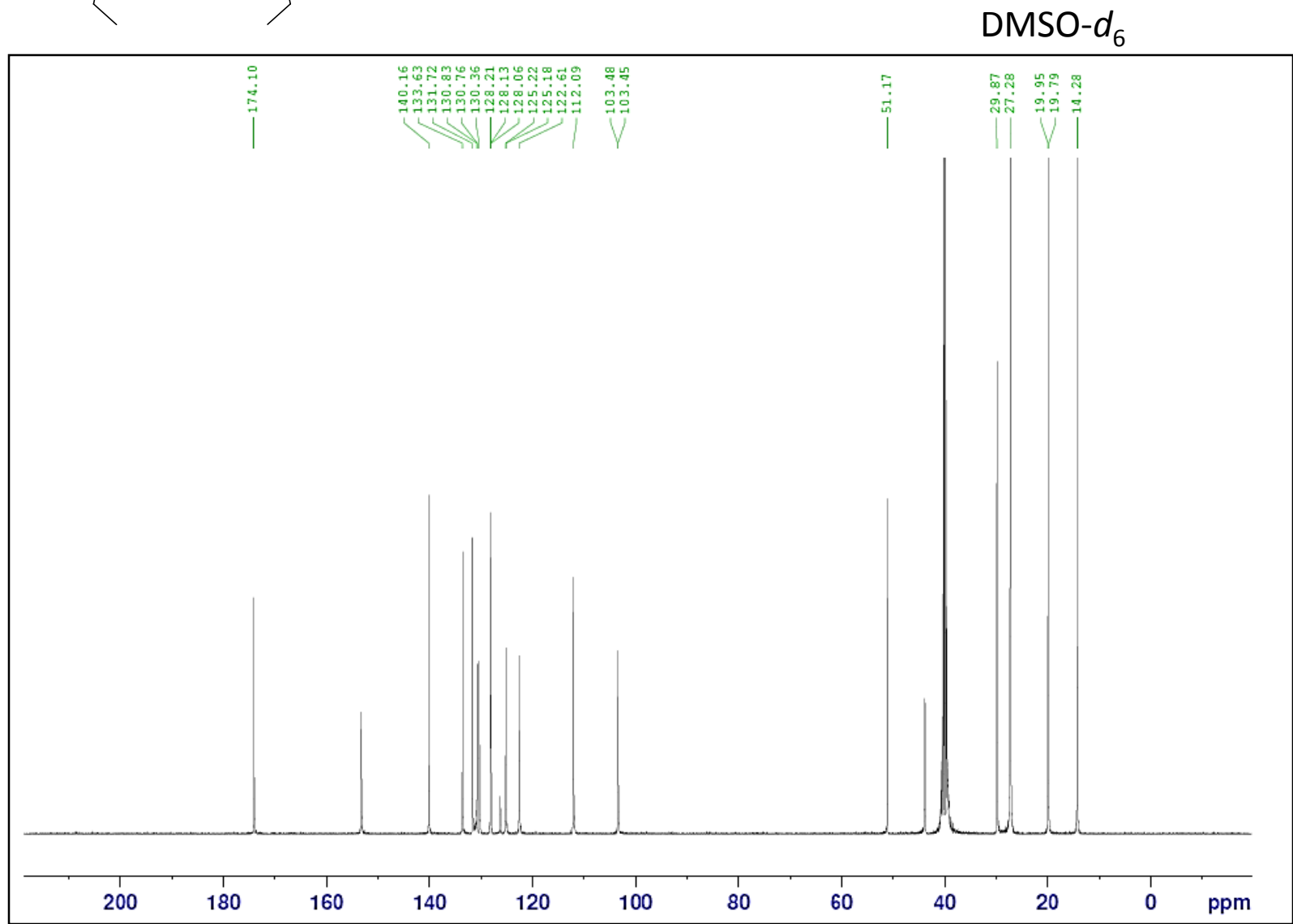
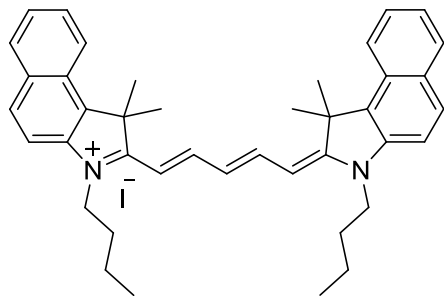
100% MeOH+0.1% HCOOH, Leuink as ITSD

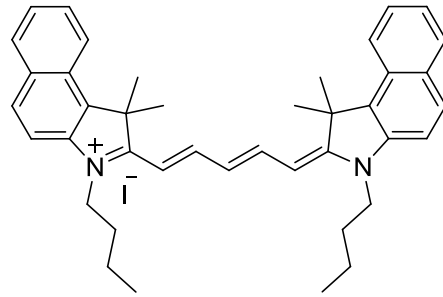


Elemental Composition Report

Mass	Calc. Mass	mDa	PPM	DBE	i-FIT	Formula
589.2204	589.2218	-1.4	-2.4	19.5	4.4	C ₃₇ H ₃₈ N ₂ Br

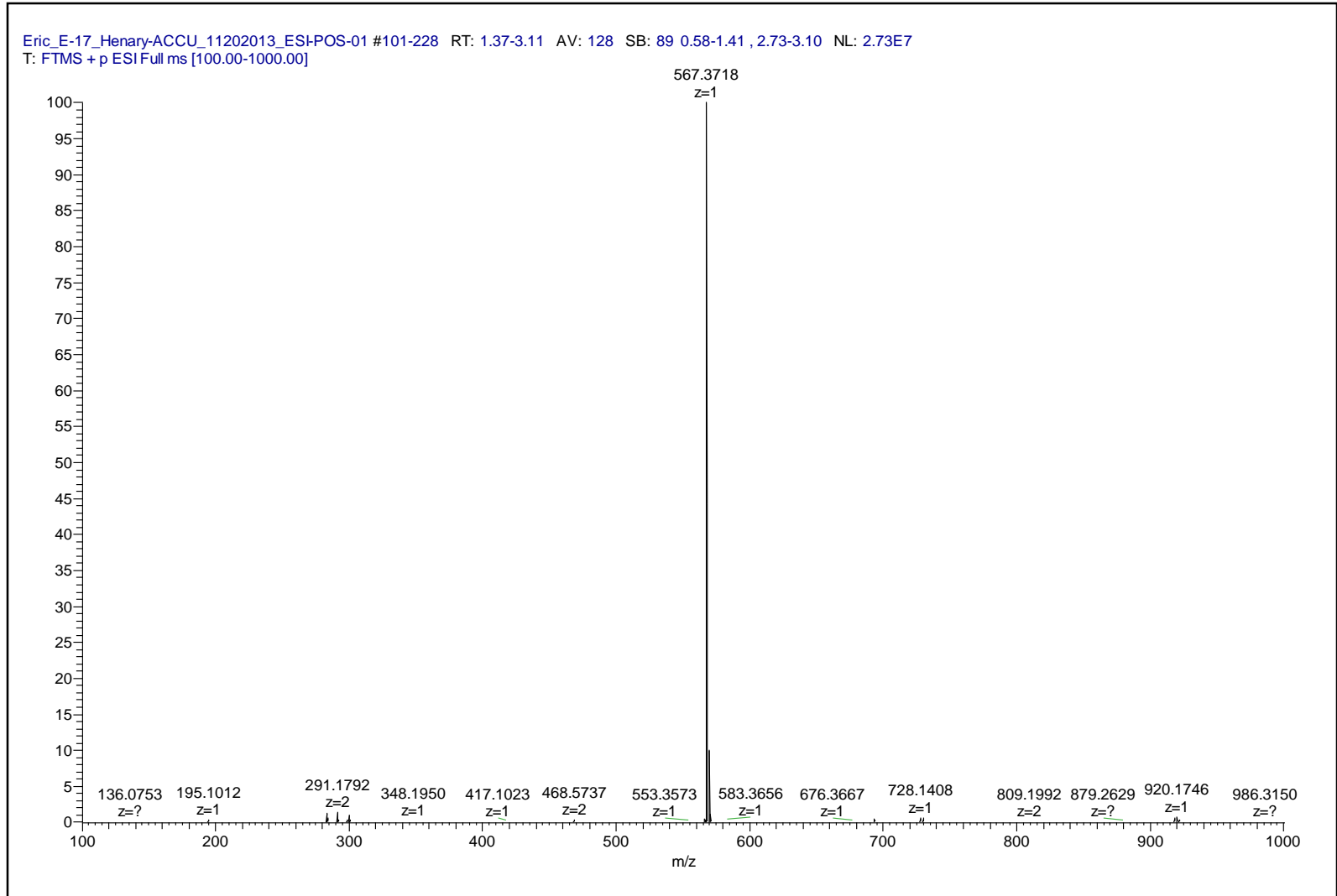
DMSO- d_6 

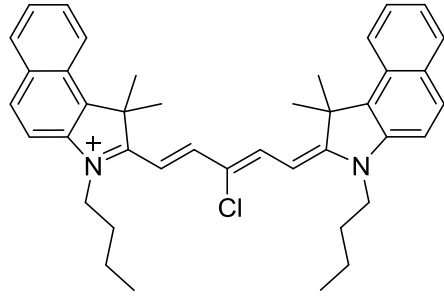
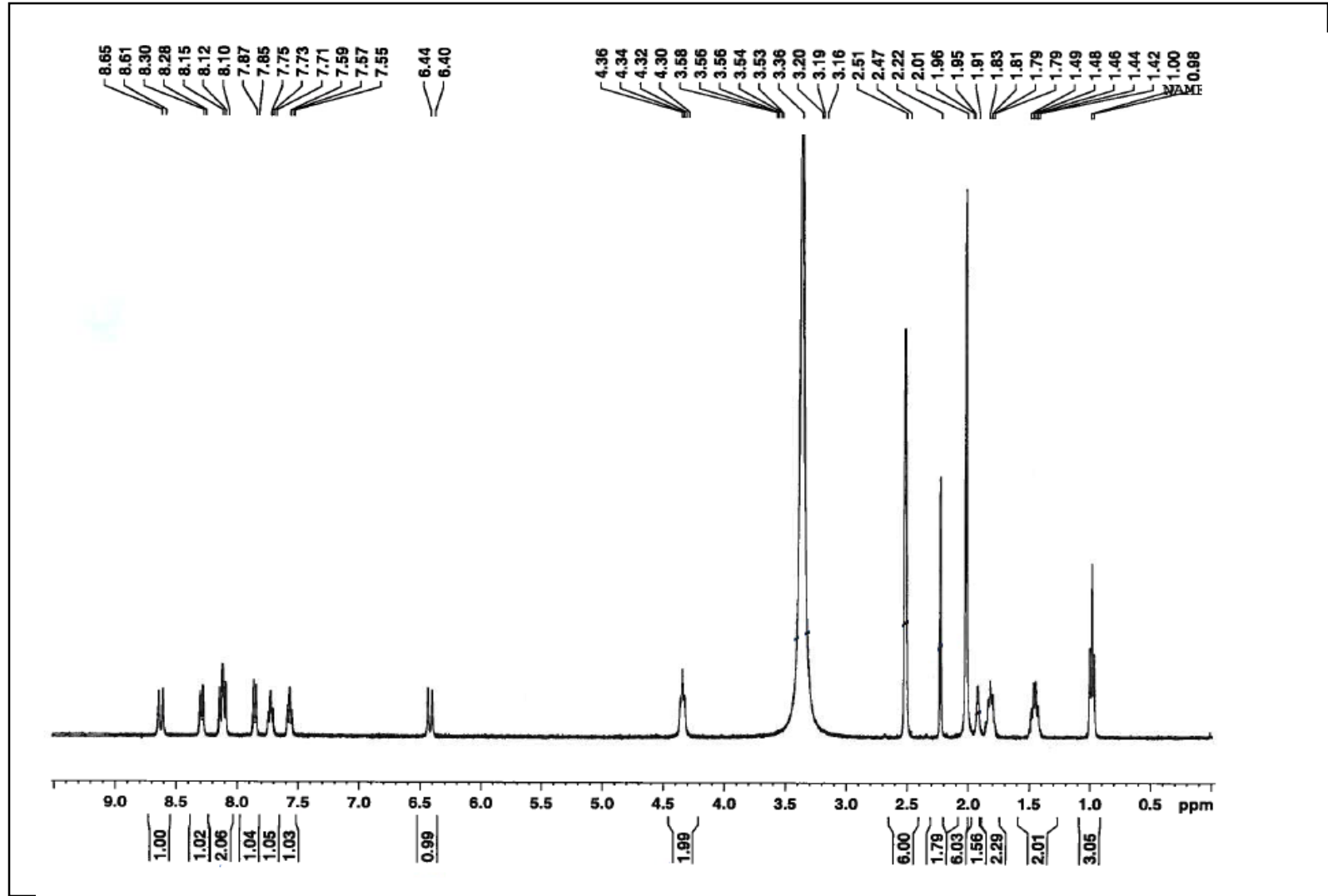


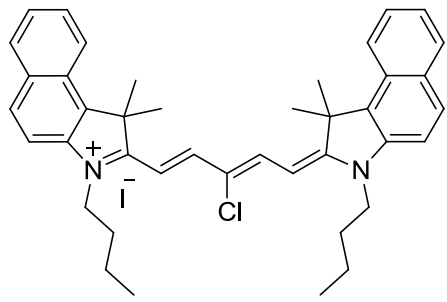
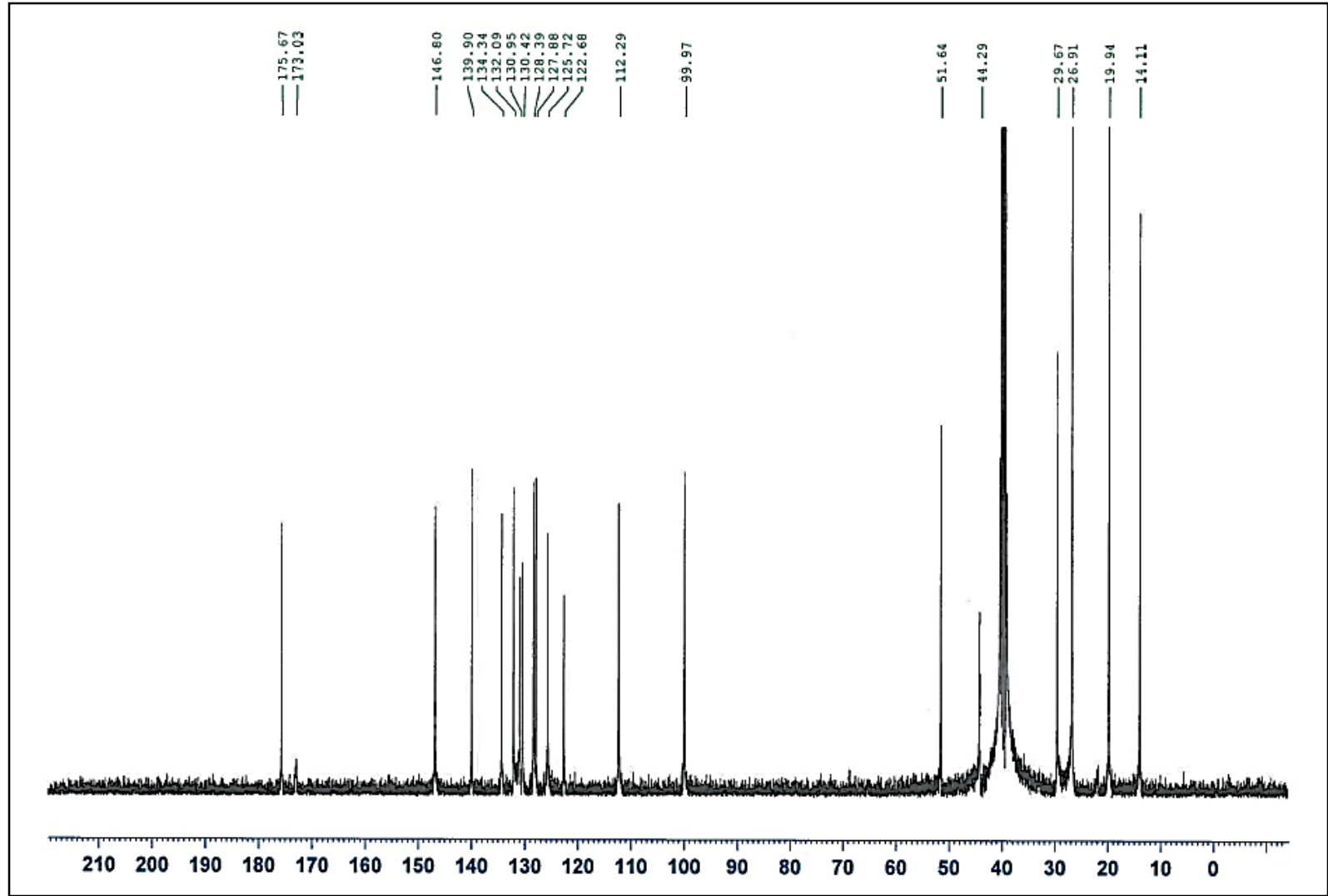


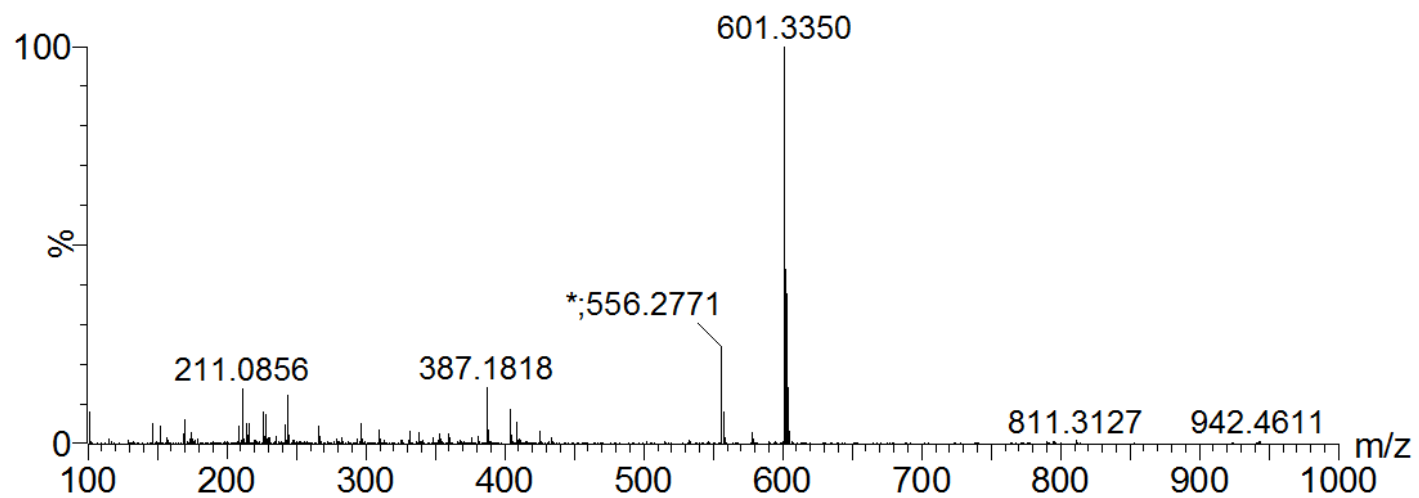
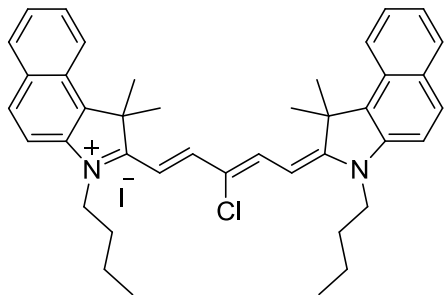
m/z	Theo. Mass	Delta (ppm)	RDB equiv.	Composition
567.3718	567.3734	-2.81	19.5	C41 H47 N2

Eric_E-17_Henary-ACCU_11202013_ESI-POS-01 #101-228 RT: 1.37-3.11 AV: 128 SB: 89 0.58-1.41, 2.73-3.10 NL: 2.73E7
T: FTMS + p ESI Full ms [100.00-1000.00]



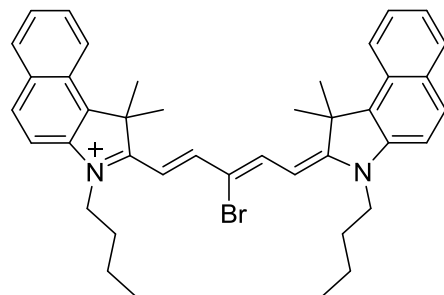
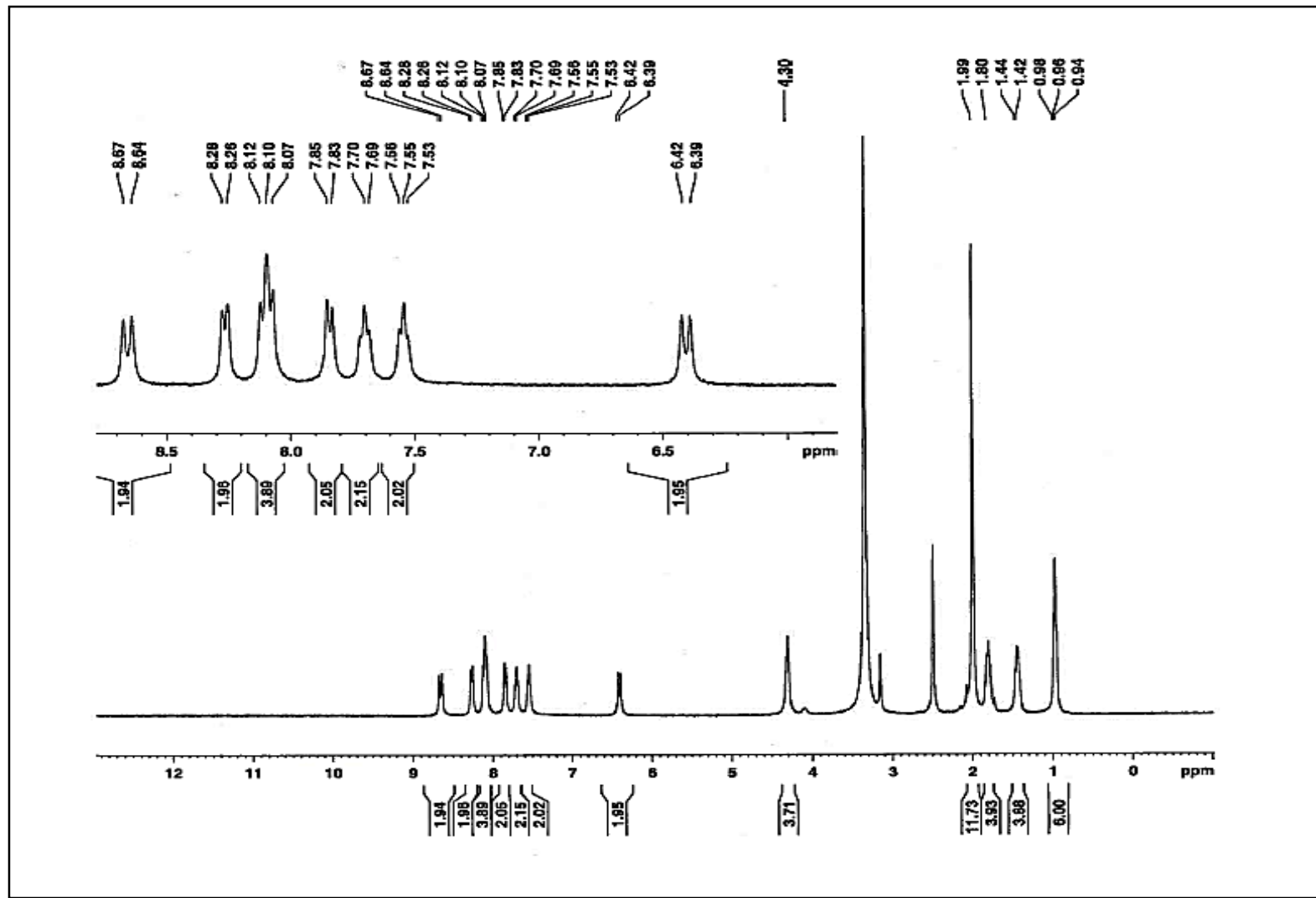
DMSO- d_6 

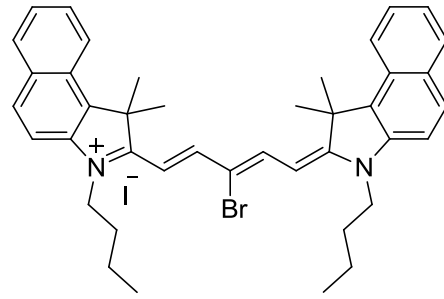
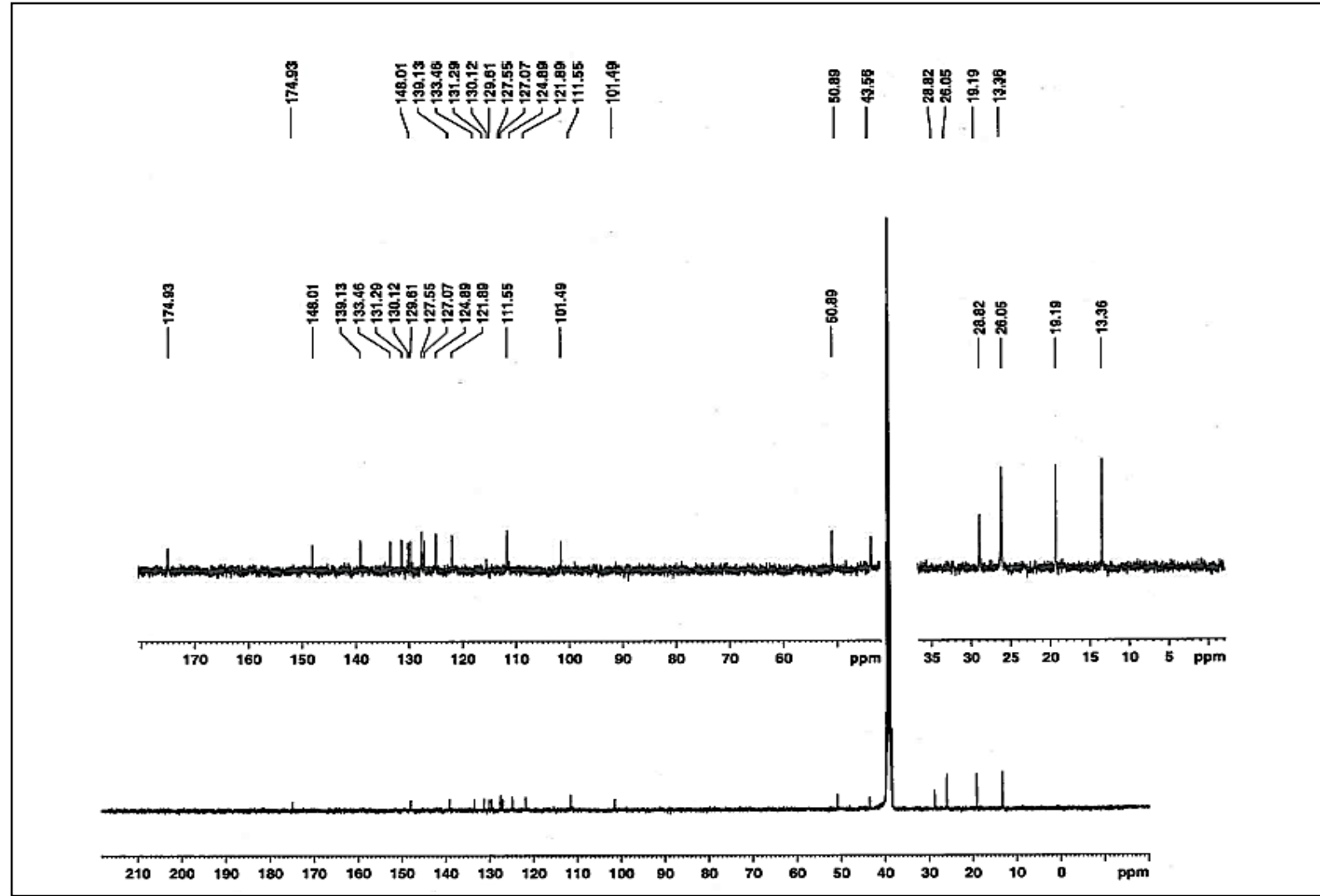
DMSO-*d*₆

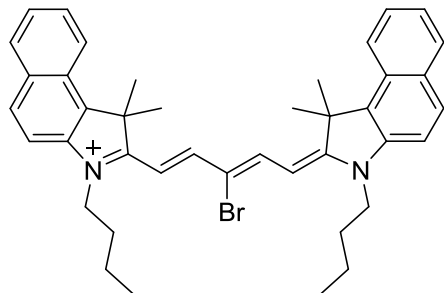


Elemental Composition Report

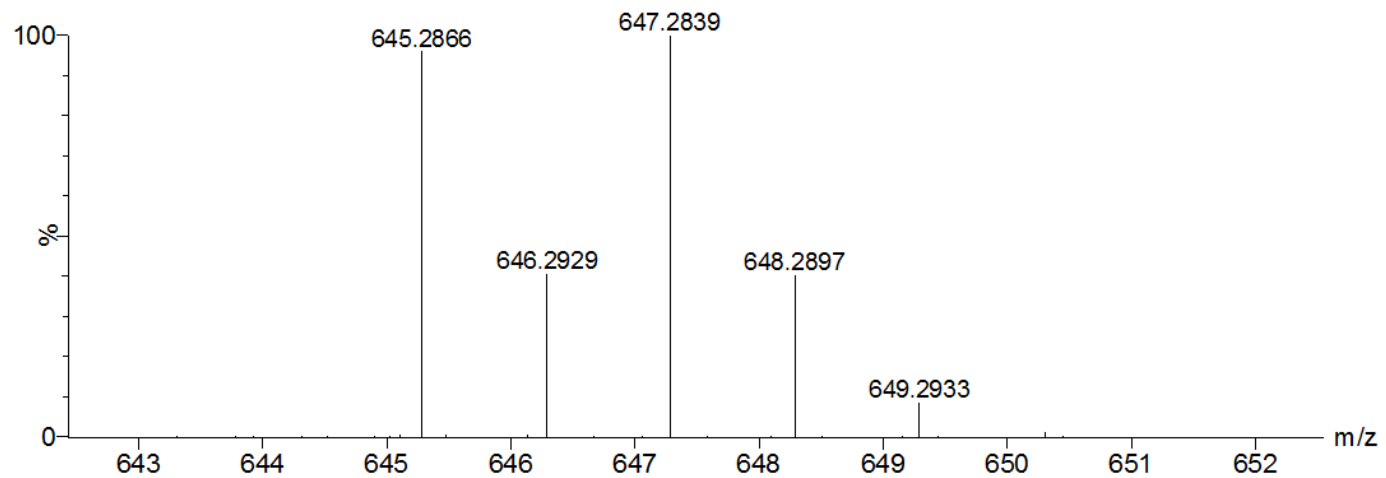
Mass	Calc. Mass	mDa	PPM	DBE	i-FIT	Formula
601.3350	601.3350	0.0	0.0	19.5	36.1	C ₄₁ H ₄₆ N ₂ Cl

DMSO- d_6 

DMSO-*d*₆

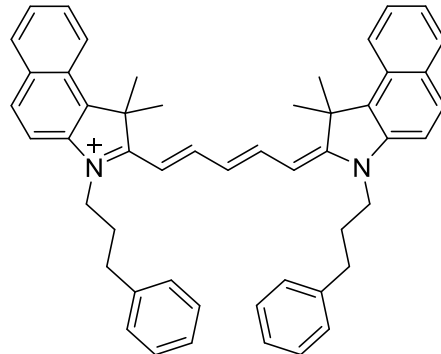
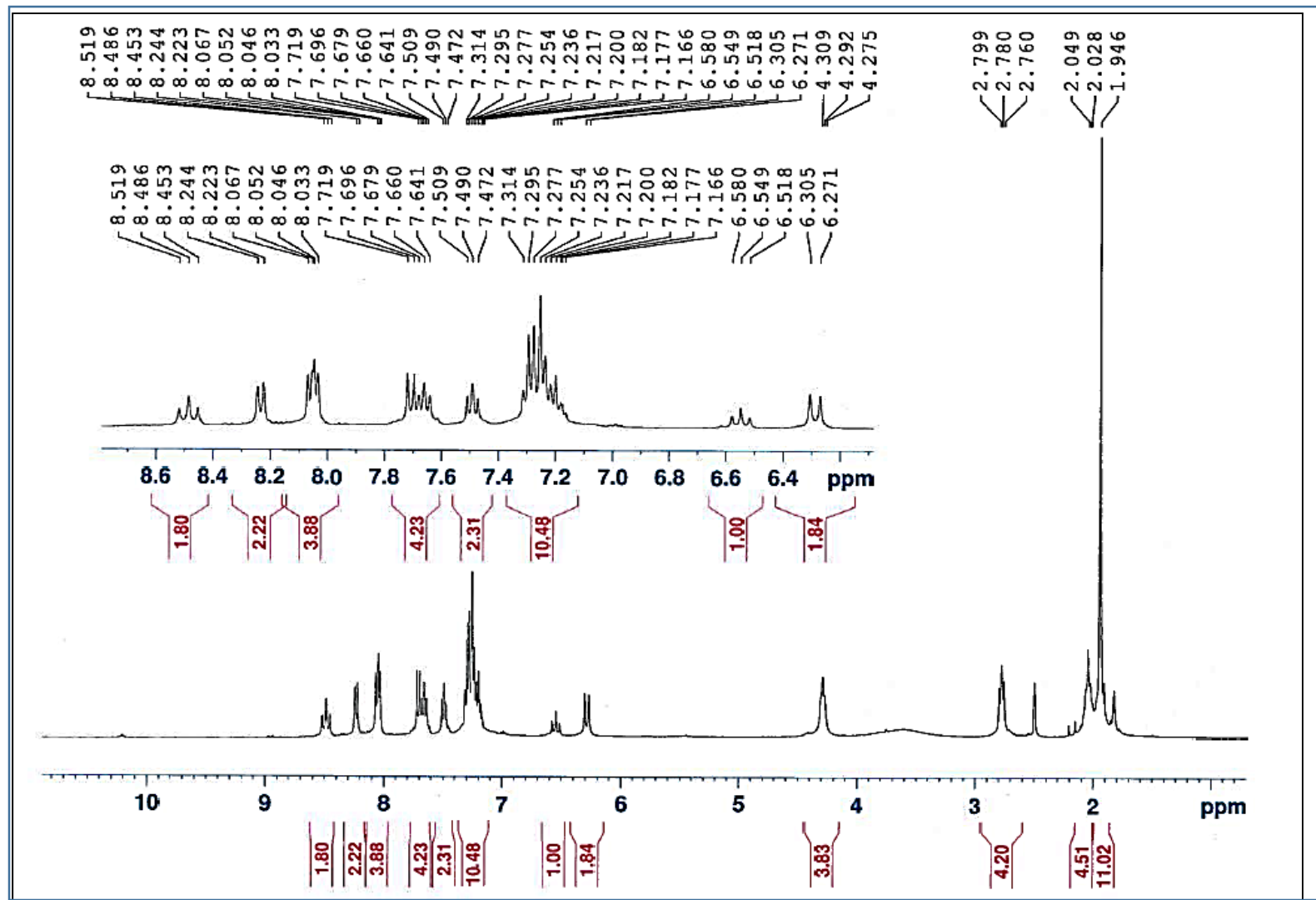


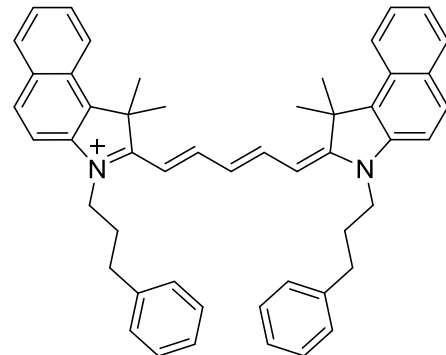
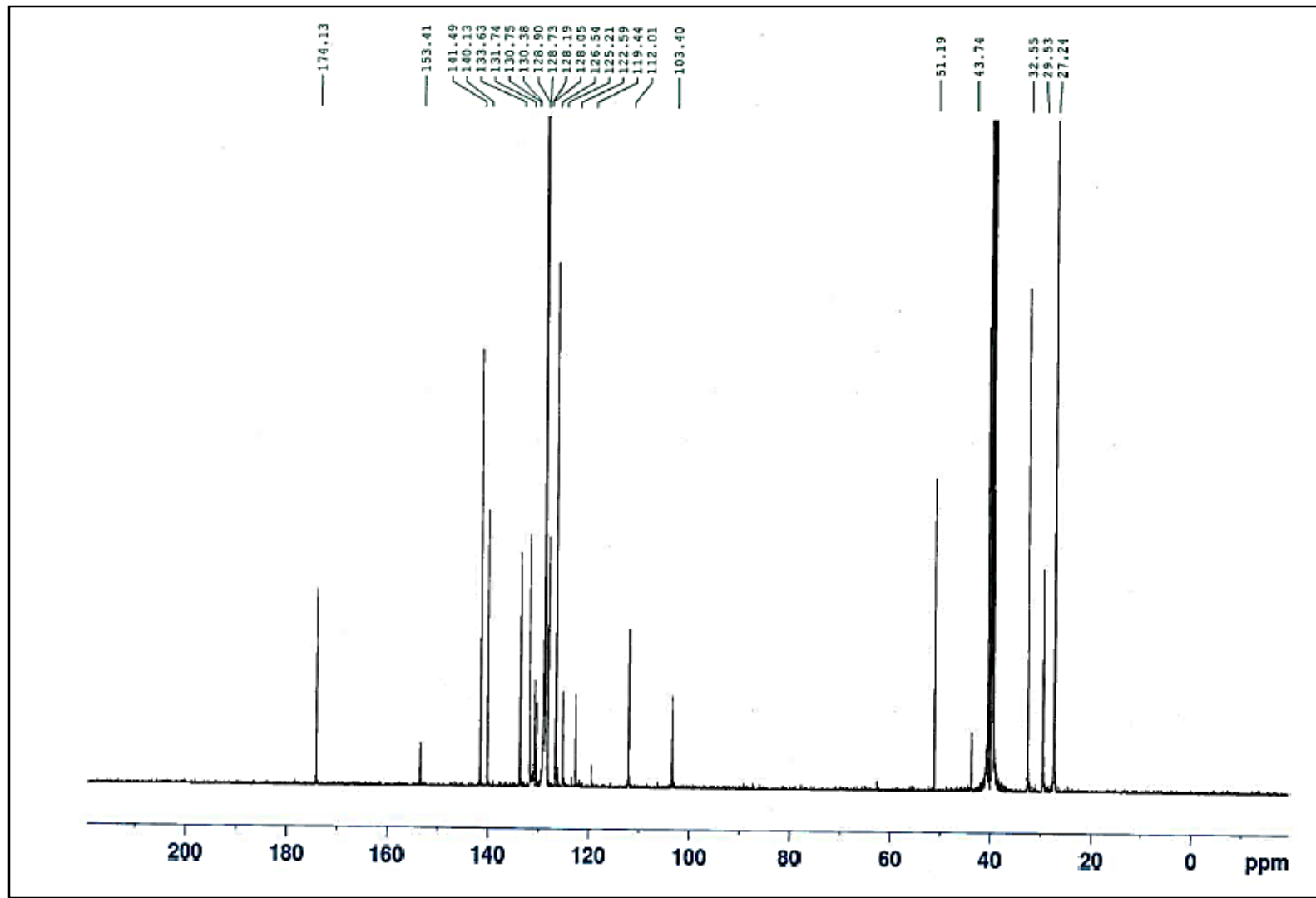
in 100% MeOH+0.1% HCOOH

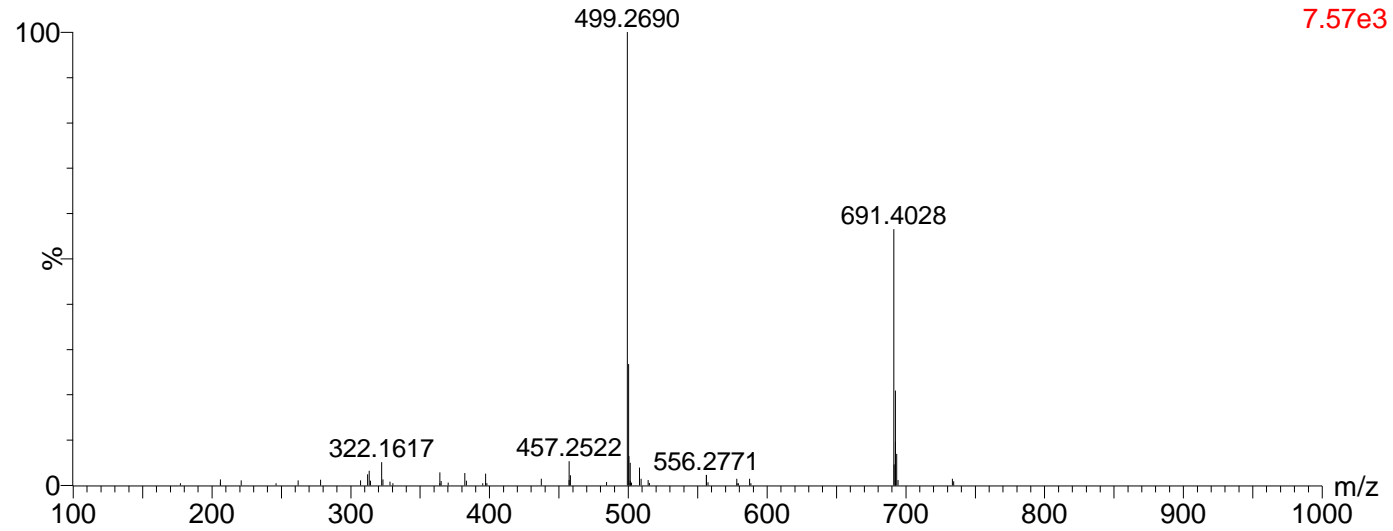
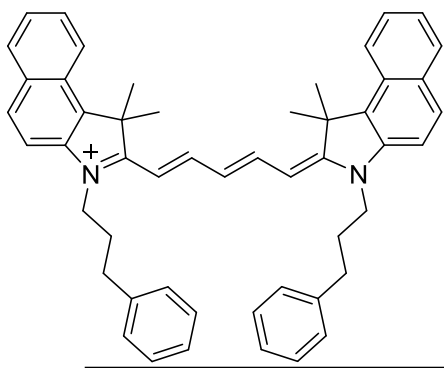


Elemental Composition Report

Mass	Calc. Mass	mDa	PPM	DBE	i-FIT	Formula
645.2866	645.2844	2.2	3.4	19.5	20.4	C41 H46 N2 Br

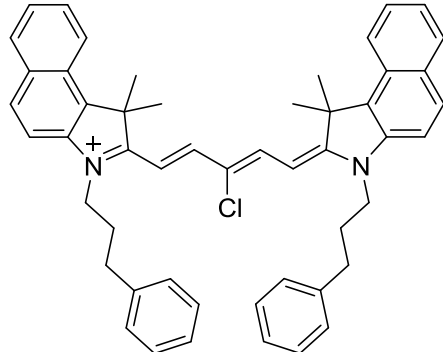
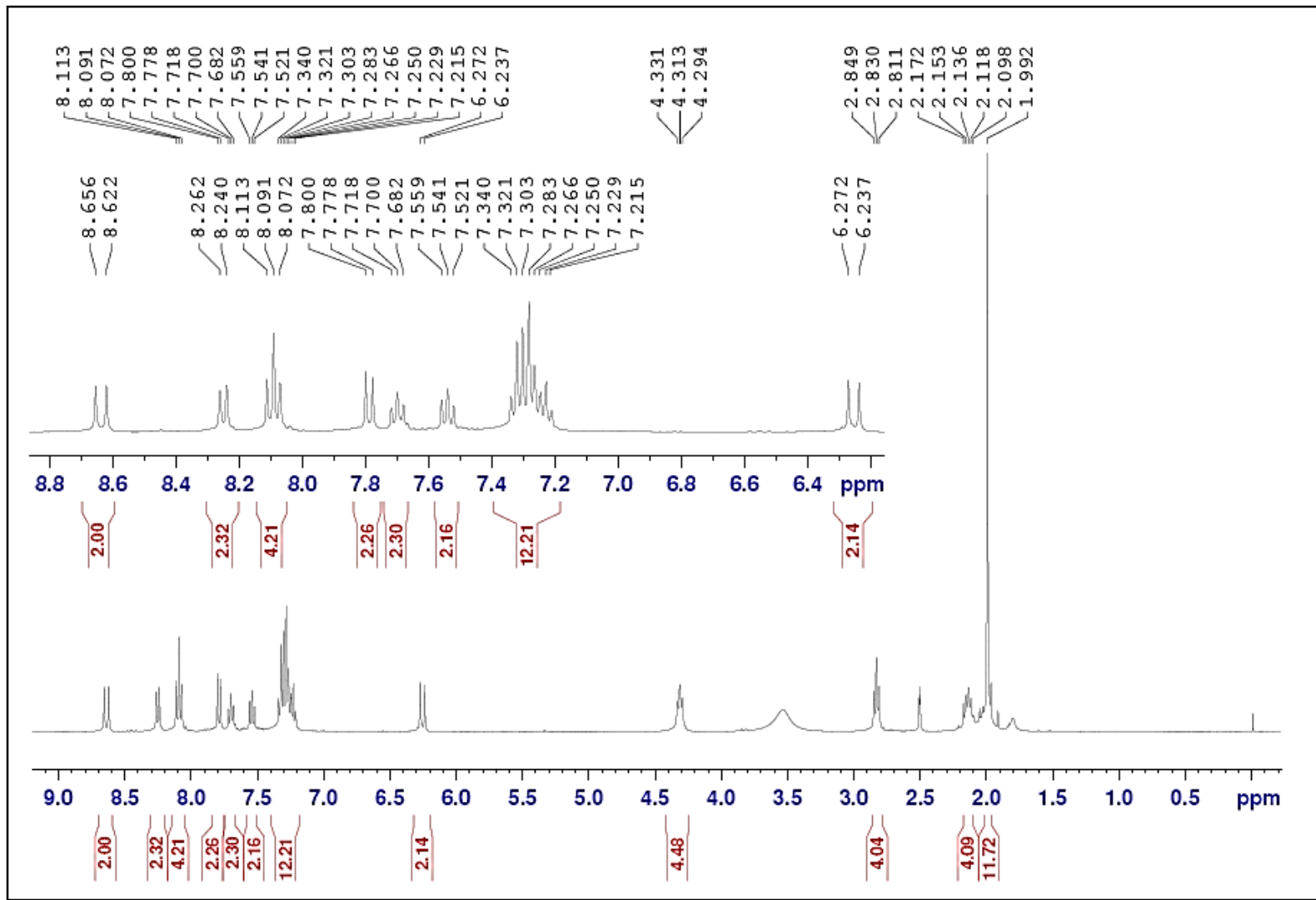
DMSO- d_6 

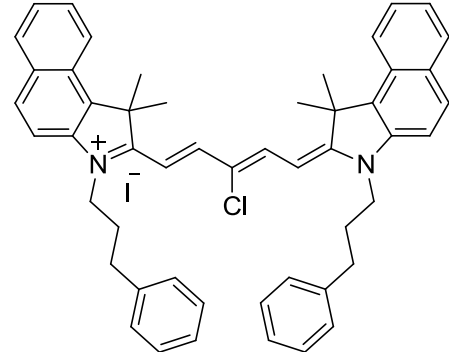
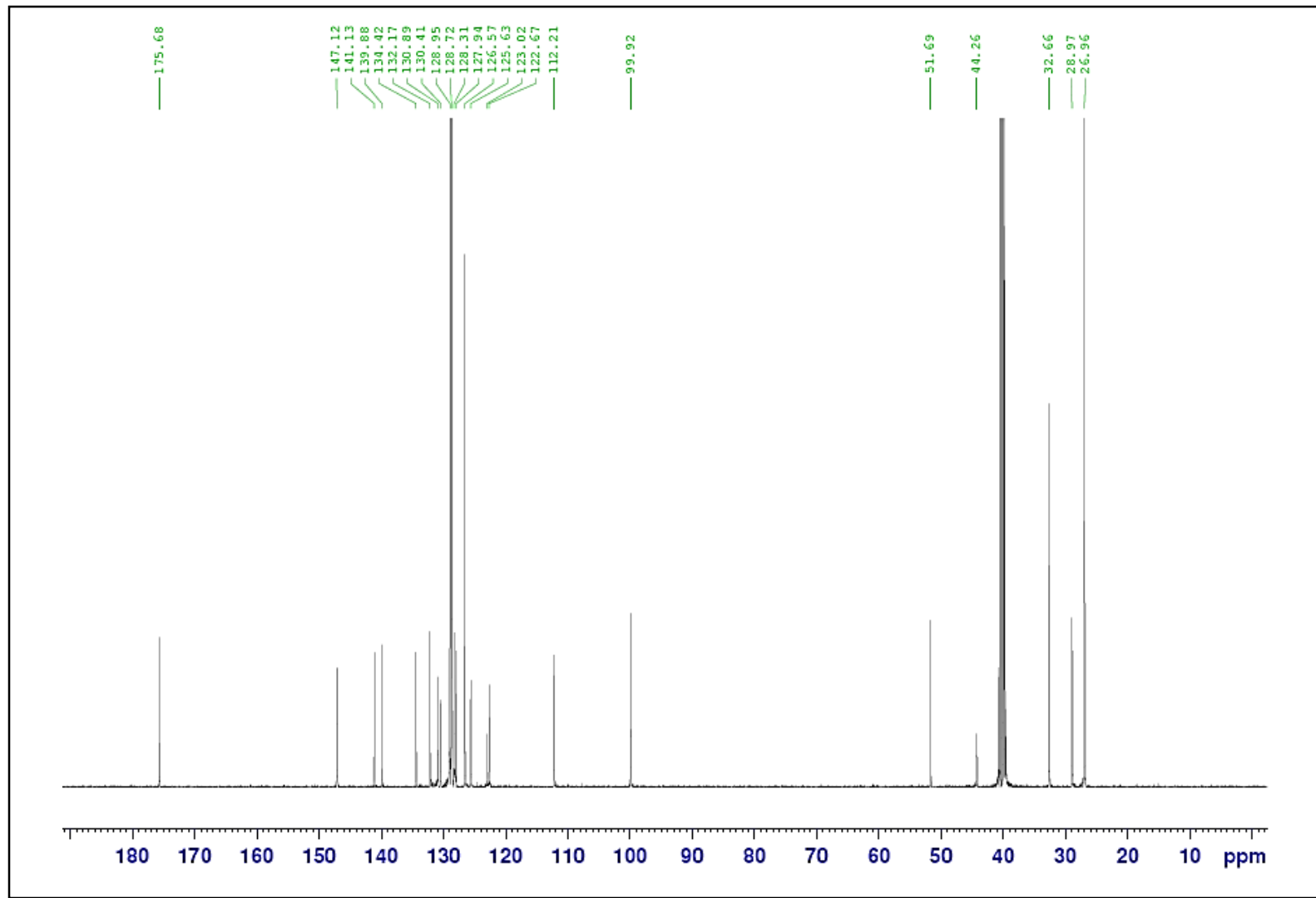
DMSO- d_6 

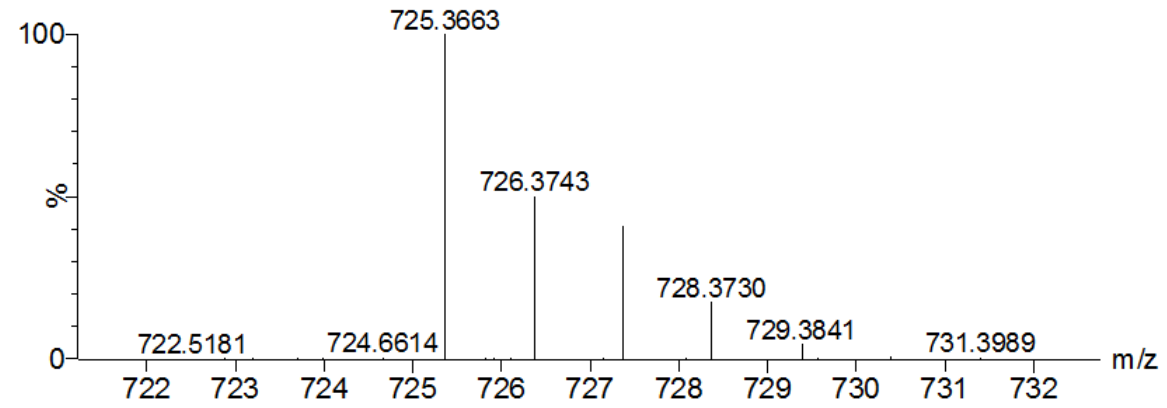
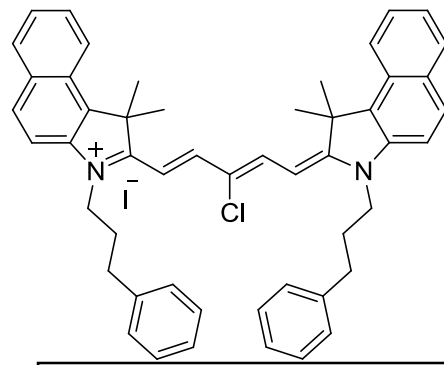


Elemental Composition Report

Mass	Calc. Mass	mDa	PPM	DBE	i-FIT	Formula
691.4028	691.4052	-2.4	-3.5	27.5	142.0	C51 H51 N2

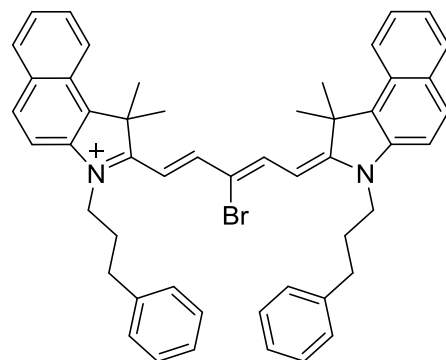
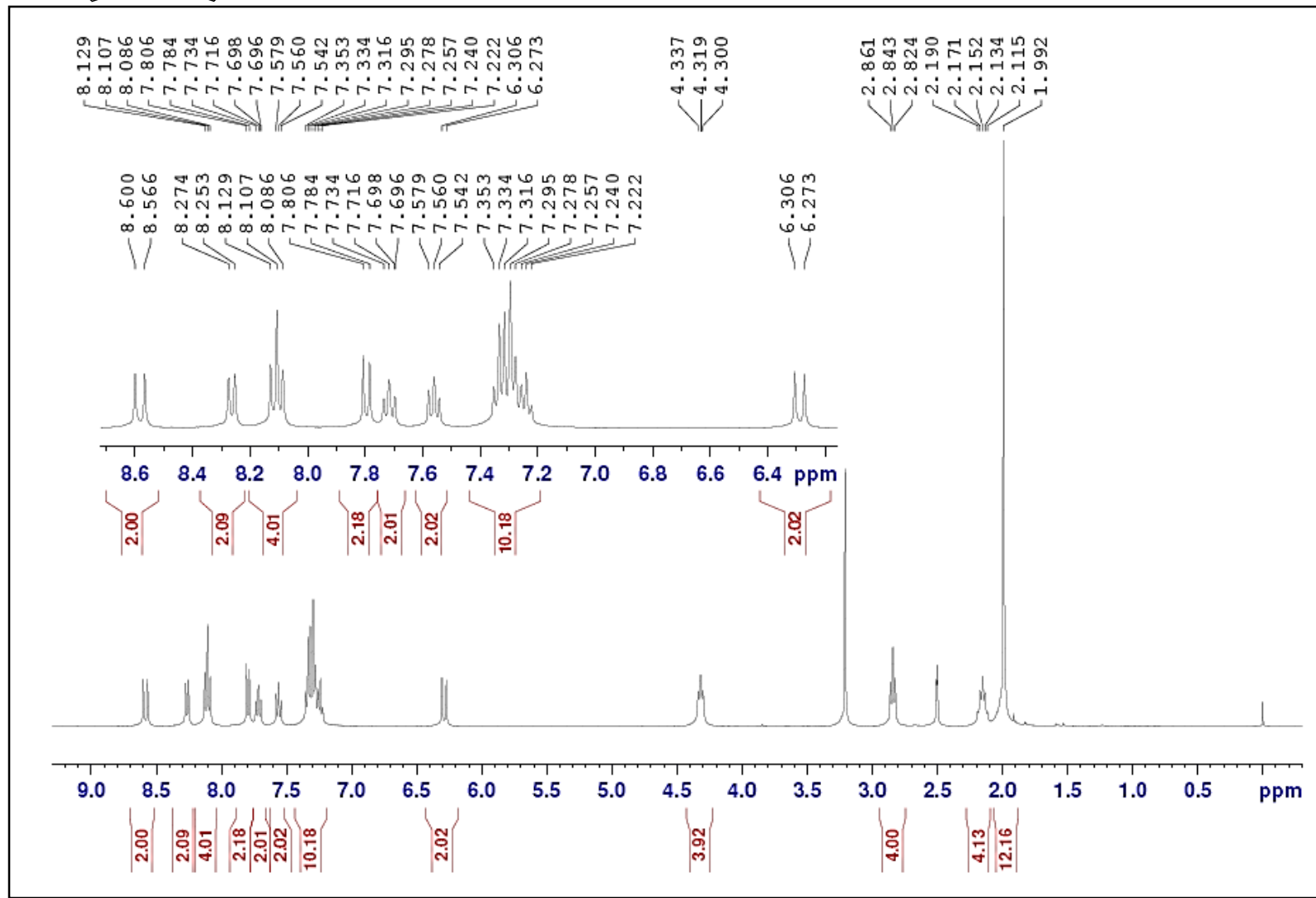
DMSO- d_6 

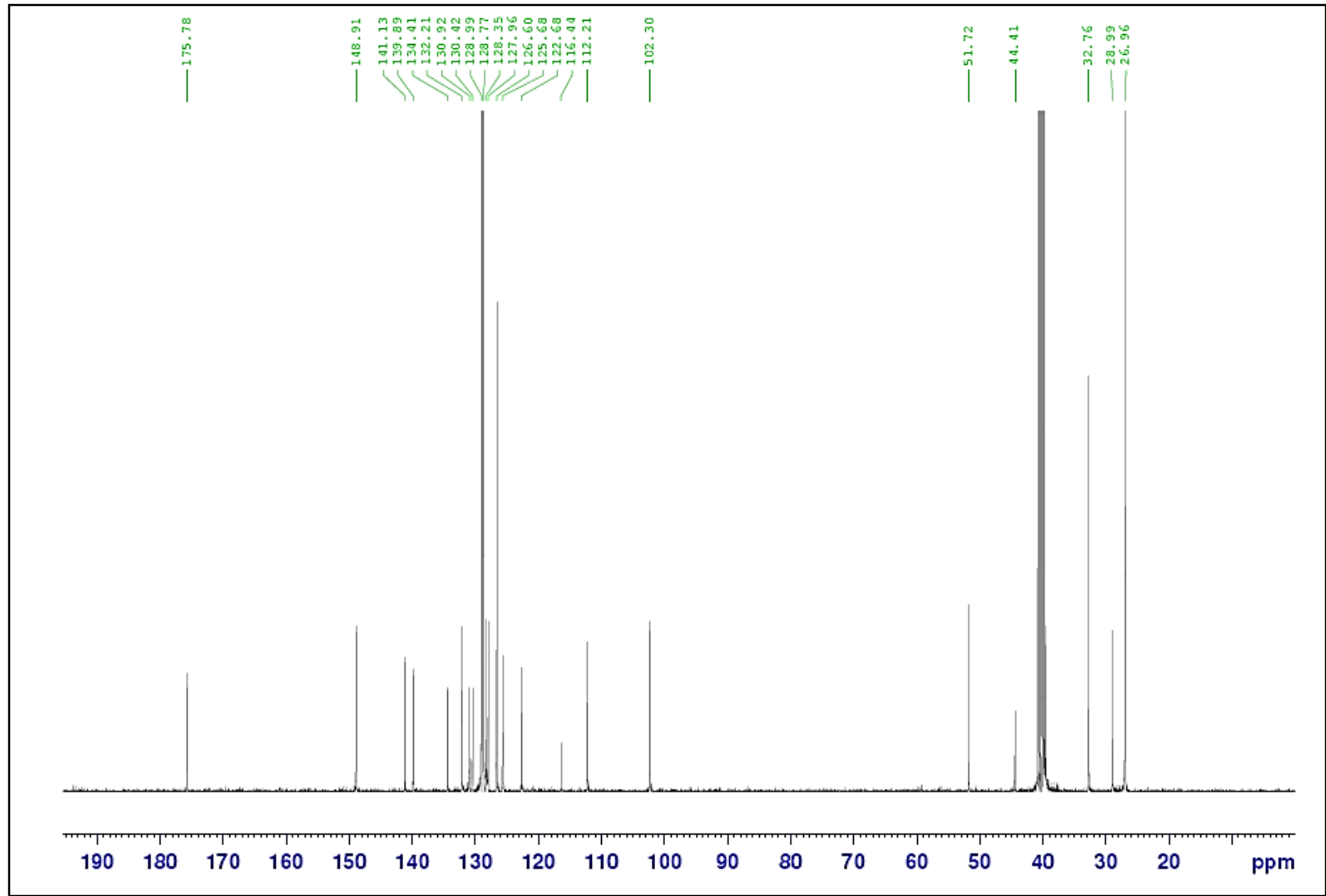
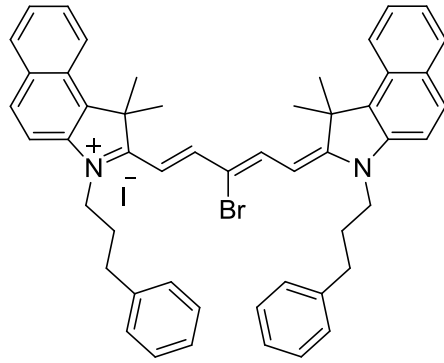
DMSO- d_6 



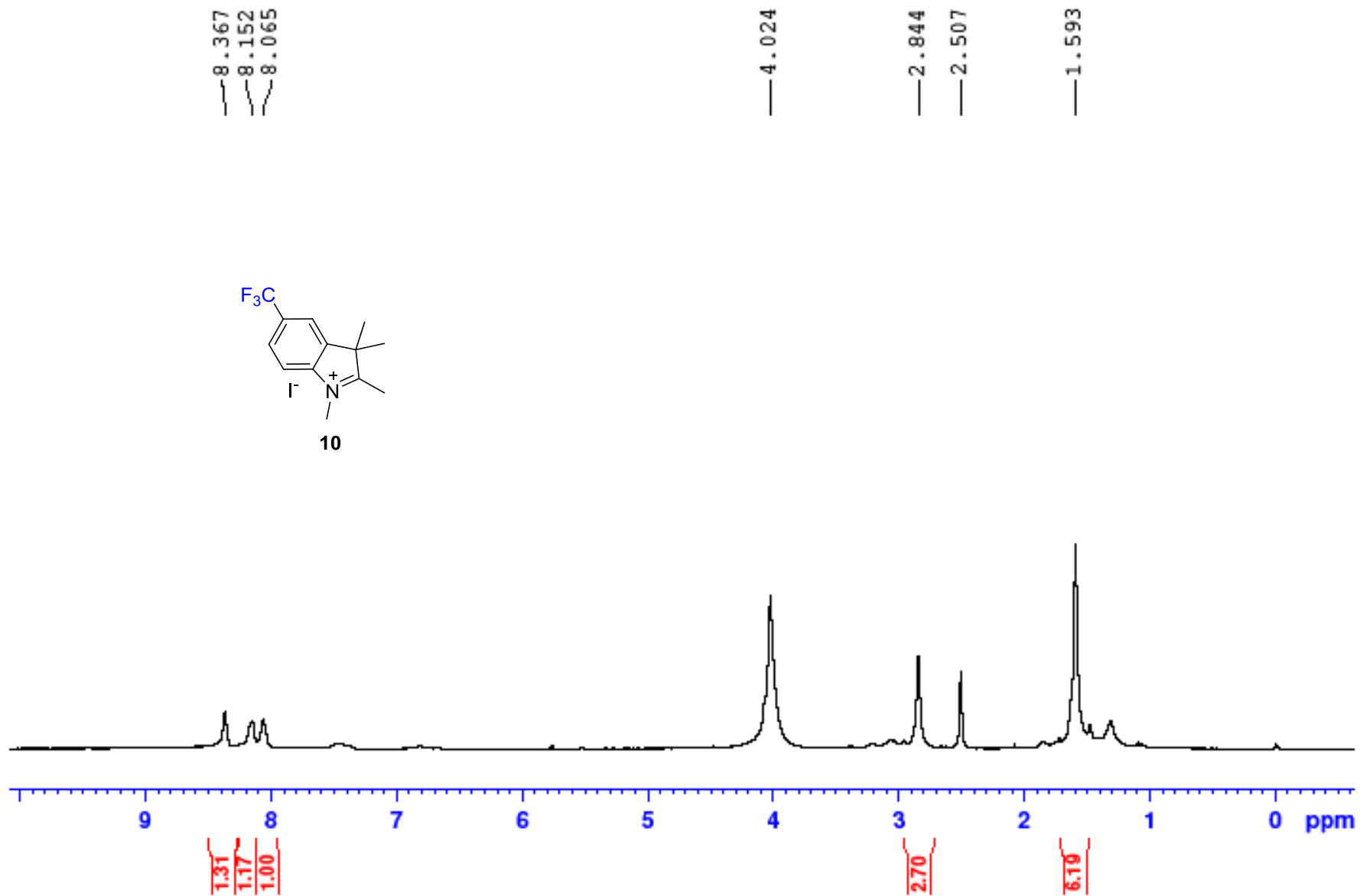
Elemental Composition Report

Mass	Calc. Mass	mDa	PPM	DBE	i-FIT	Formula
725.3663	725.3663	0.0	0.0	27.5	69.7	C ₅₁ H ₅₀ N ₂ Cl

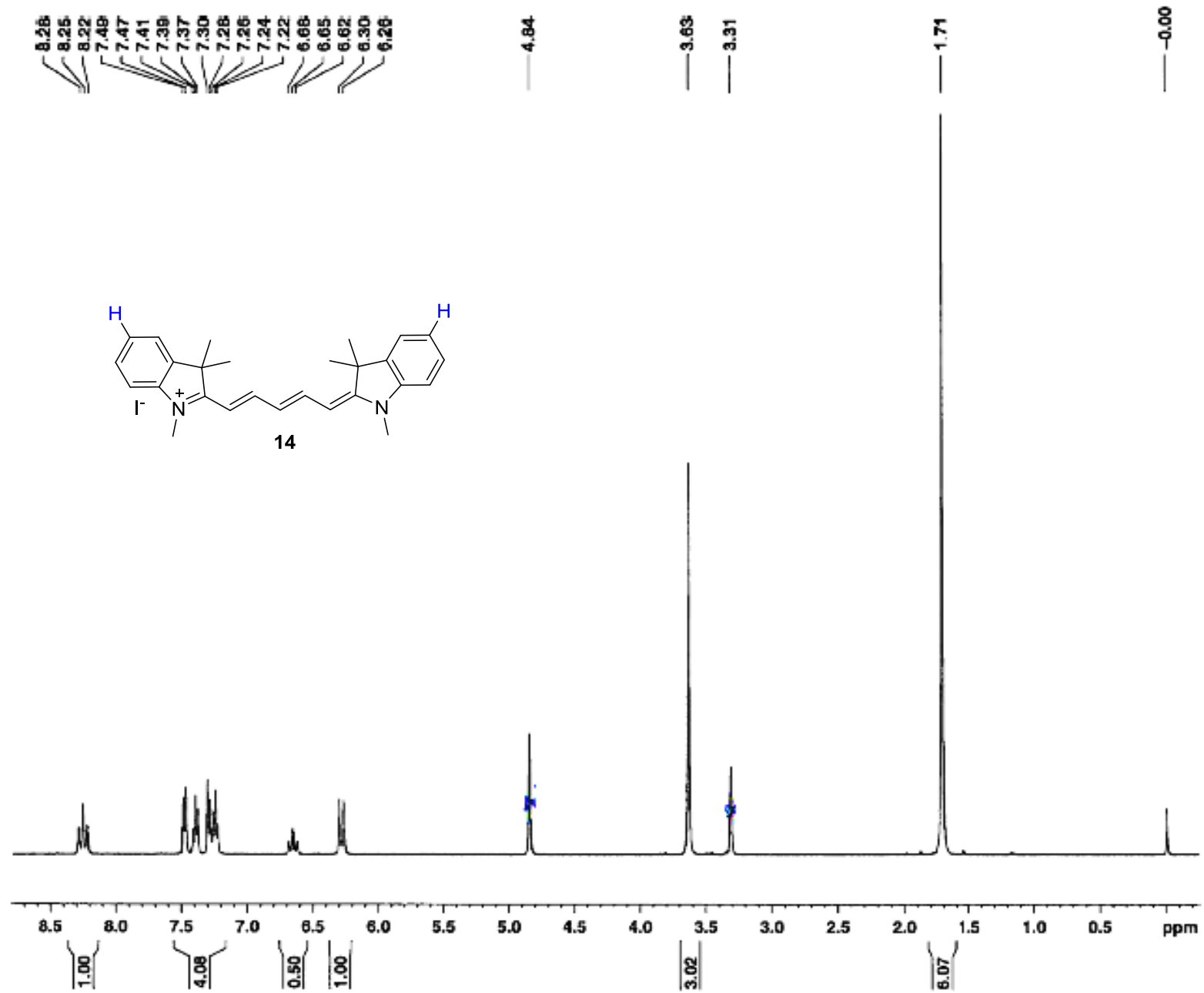
DMSO- d_6 

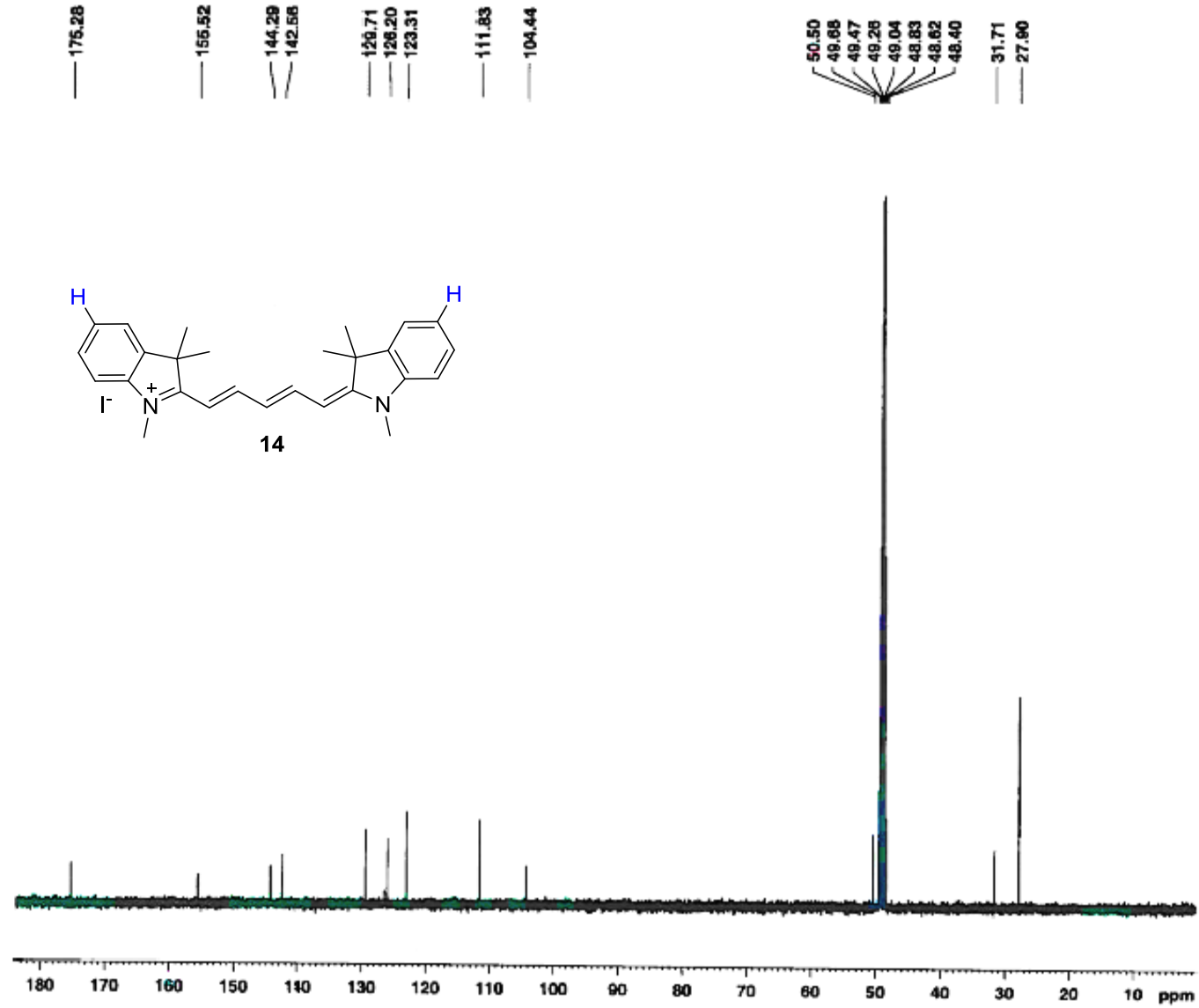


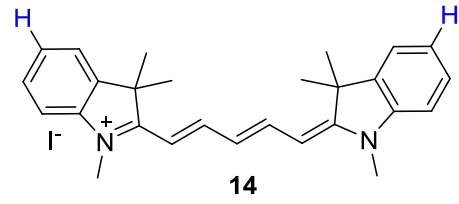
Experimental Data for Chapter 4 -- ELECTRONIC FACTORS INFLUENCE BIODISTRIBUTION OF CYANINES



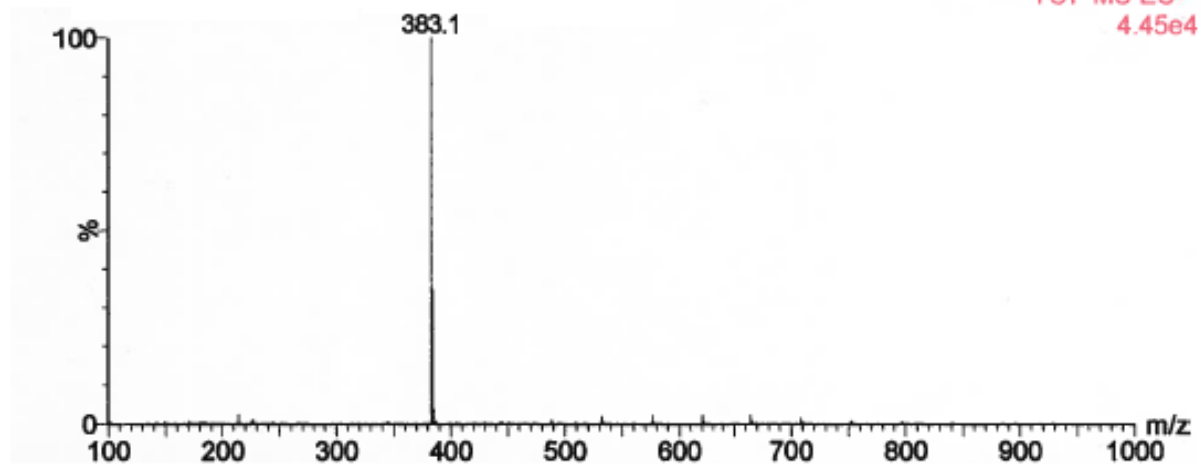
MeOD- d_4

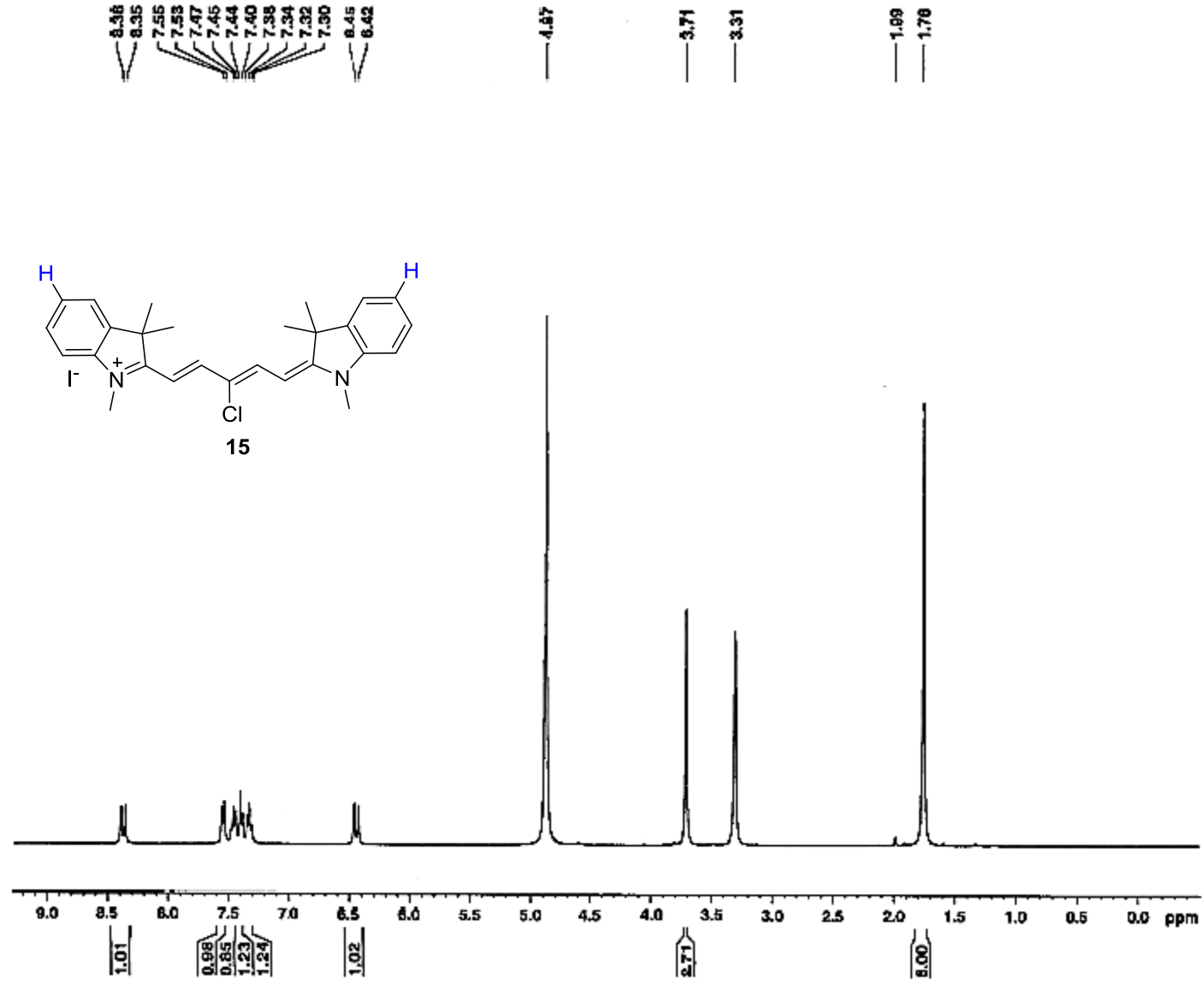


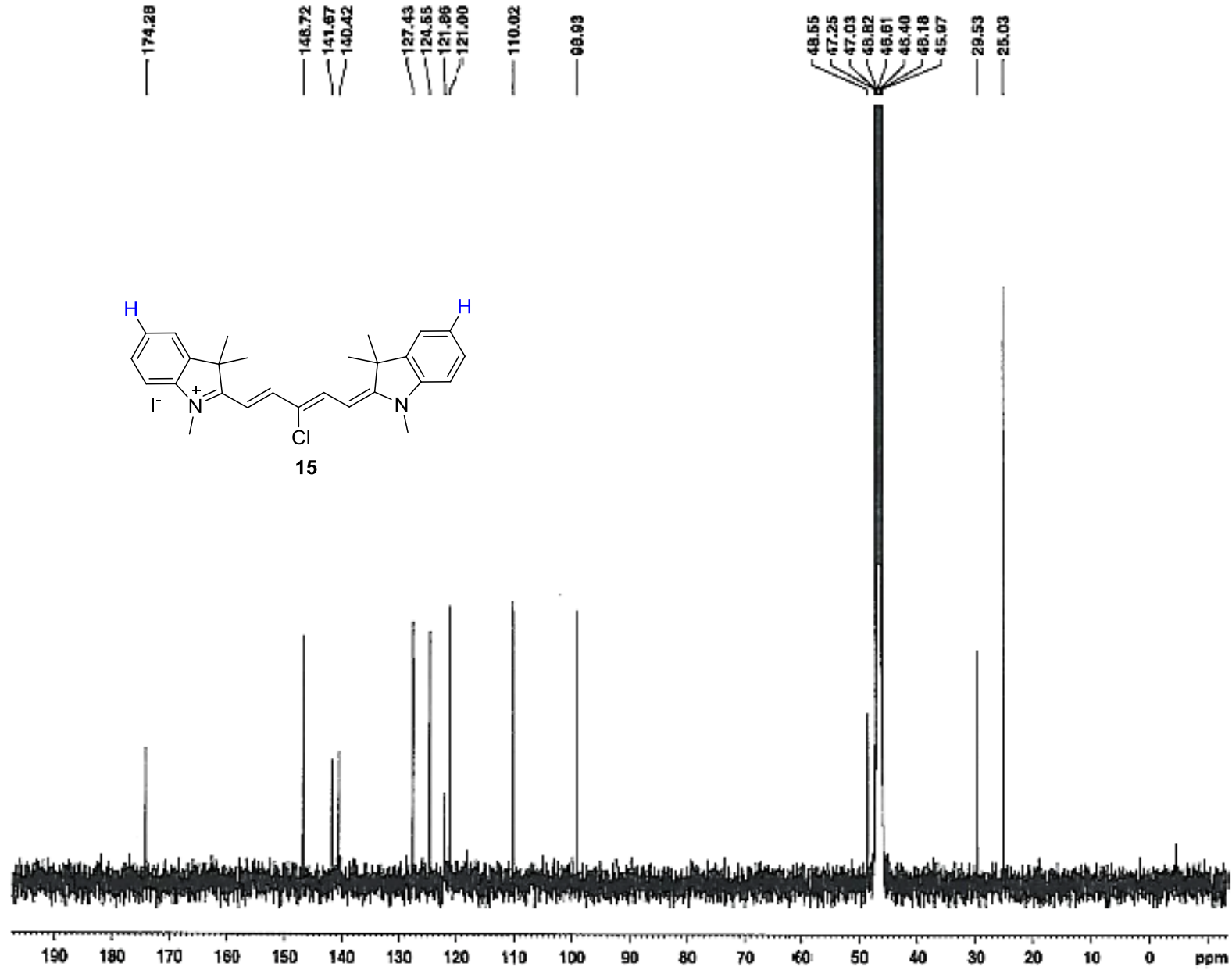


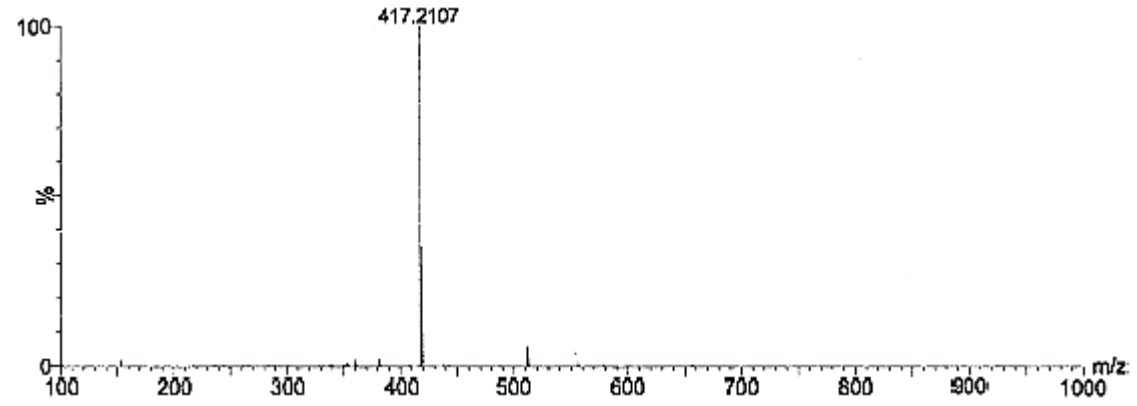
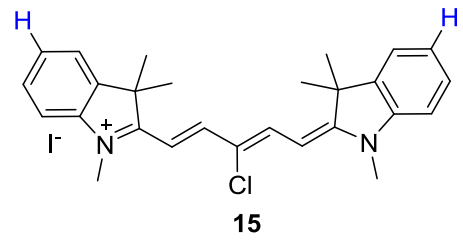


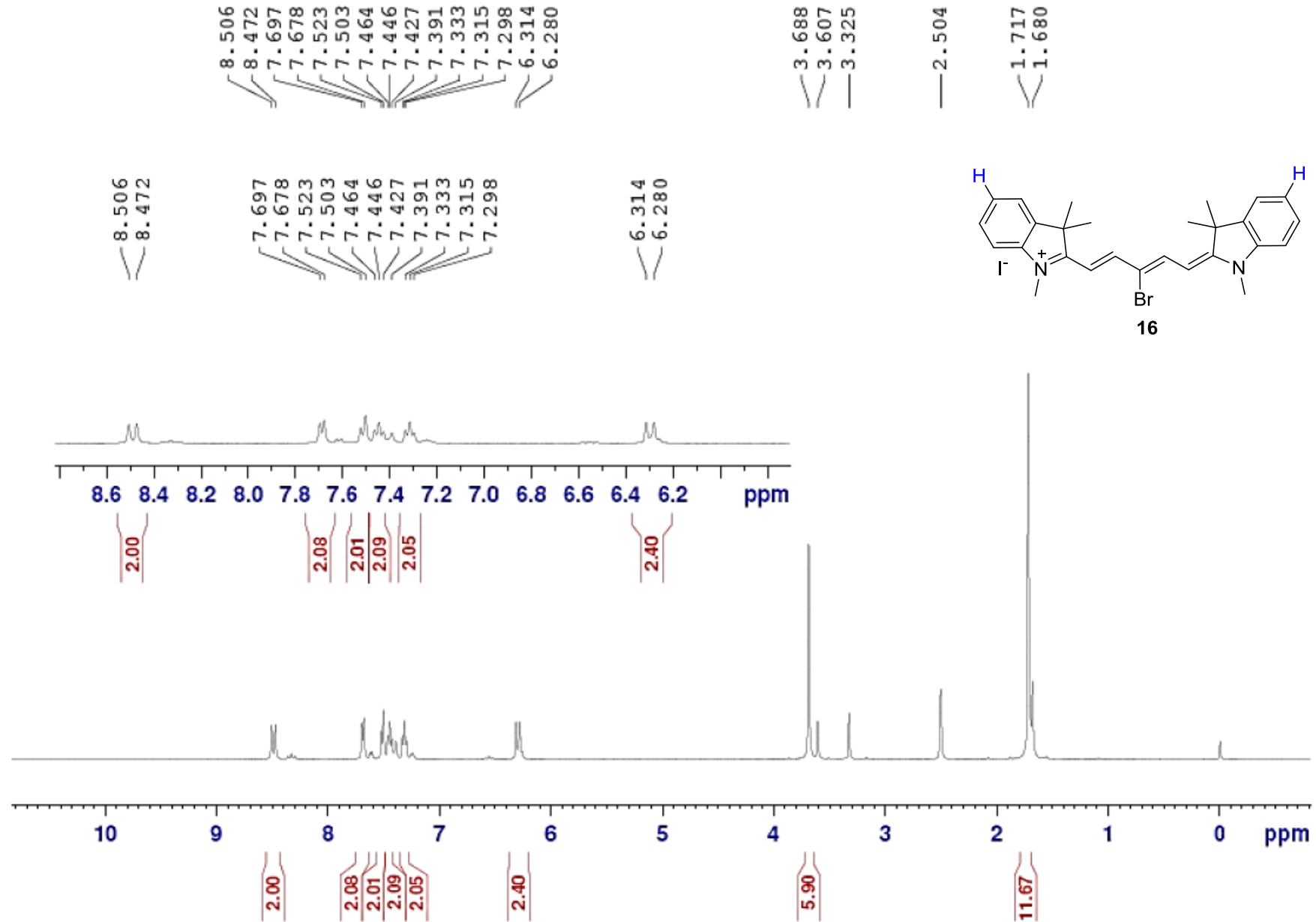
50%MeOH+0.1%HCOOH

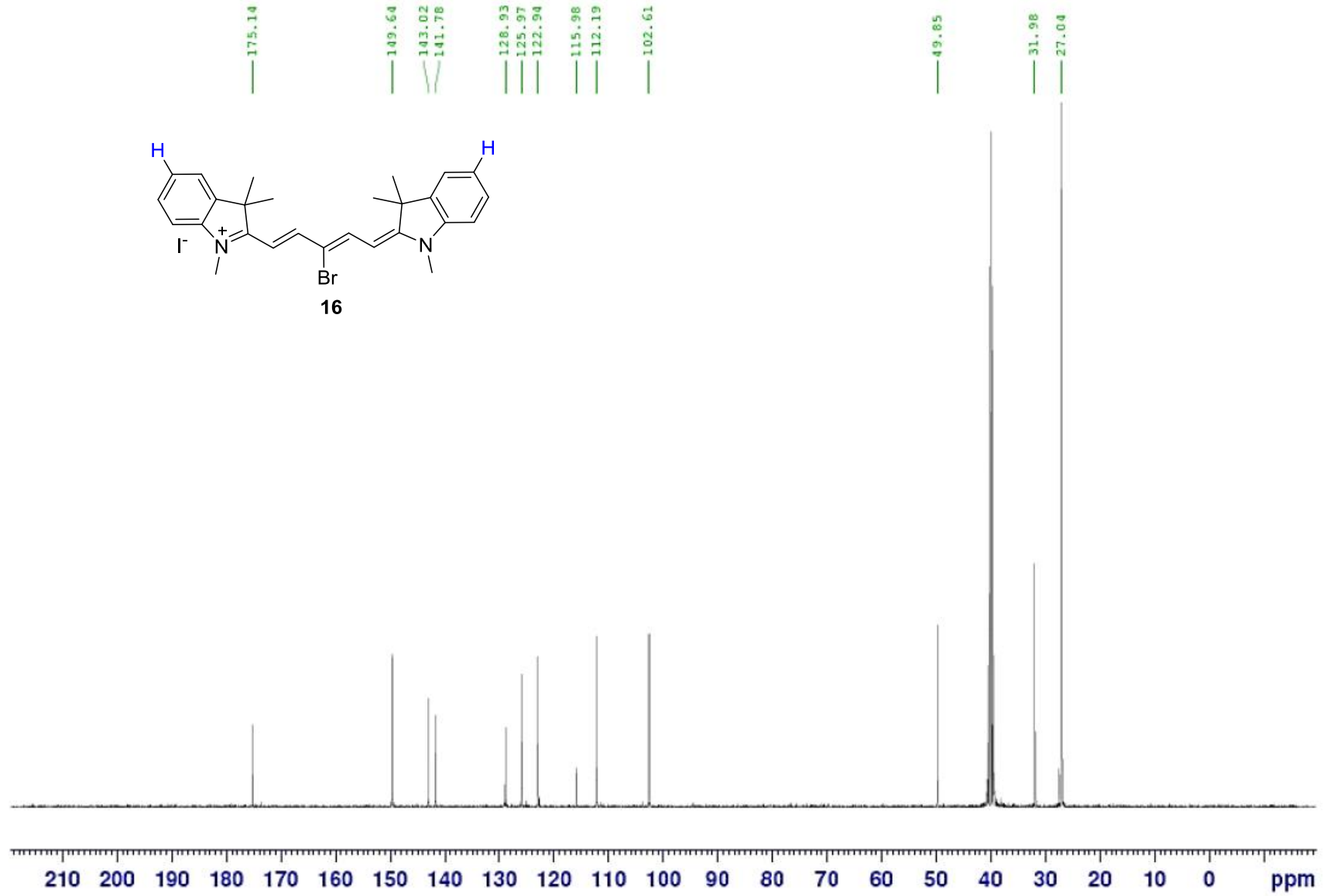










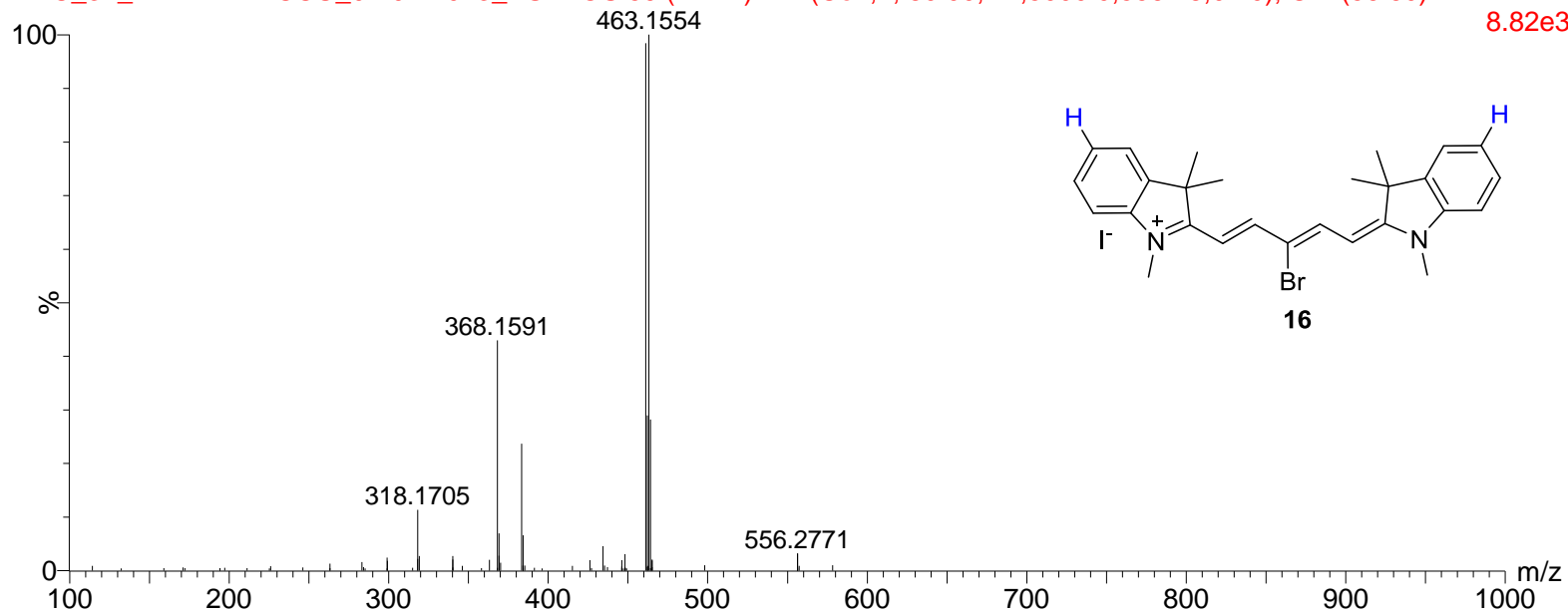


diluted in 80%MeOH

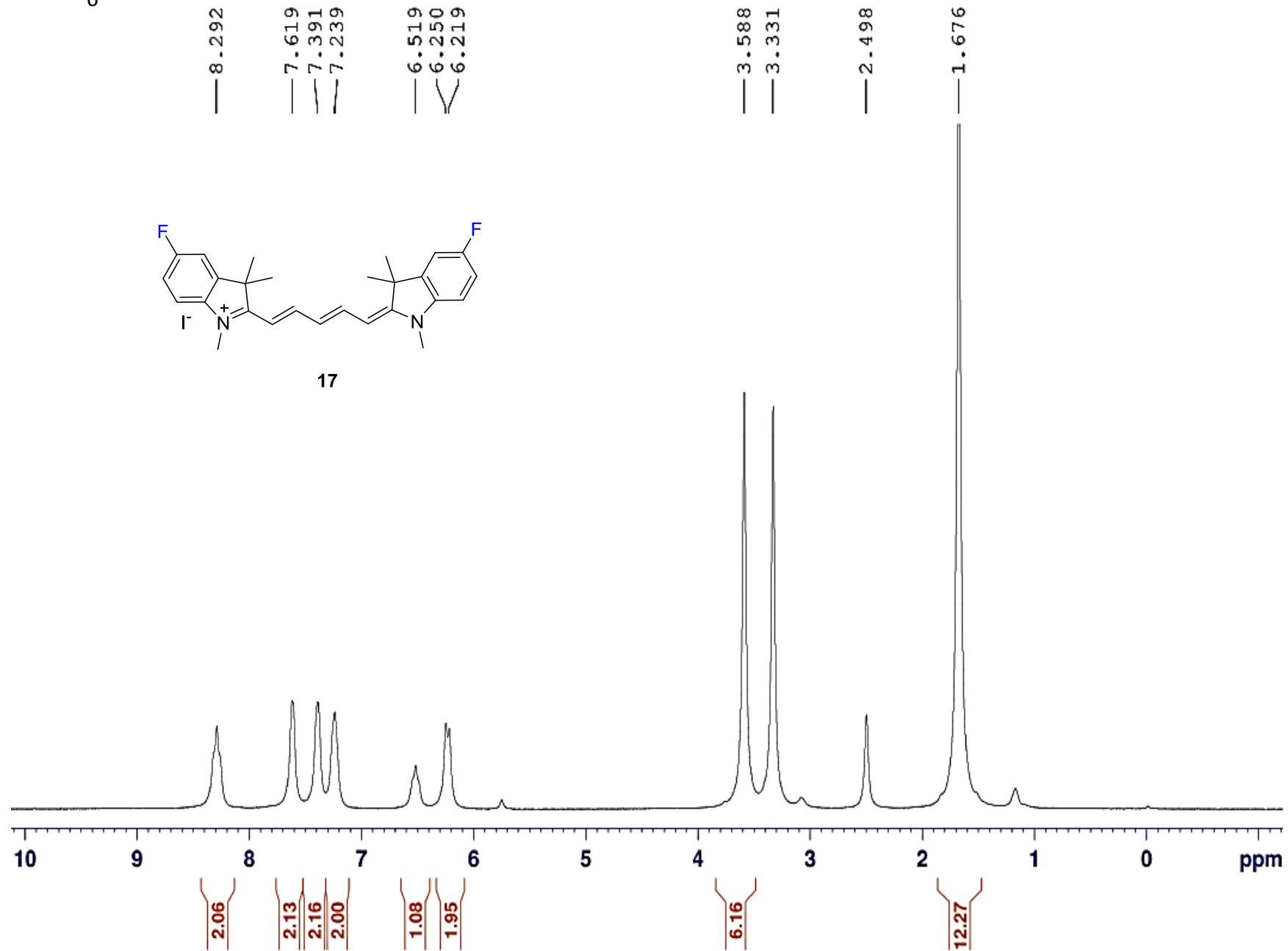
15:28:12 01-Feb-2013

ERIC_32_HENARY-ACCU_02-01-2013_ESI-POS 59 (1.177) AM (Cen,2, 80.00, Ar,5000.0,556.28,0.70); Cm (56:60)

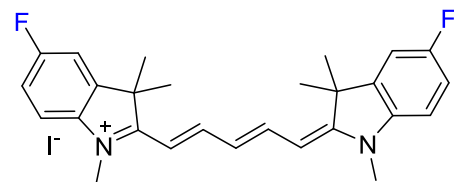
8.82e3



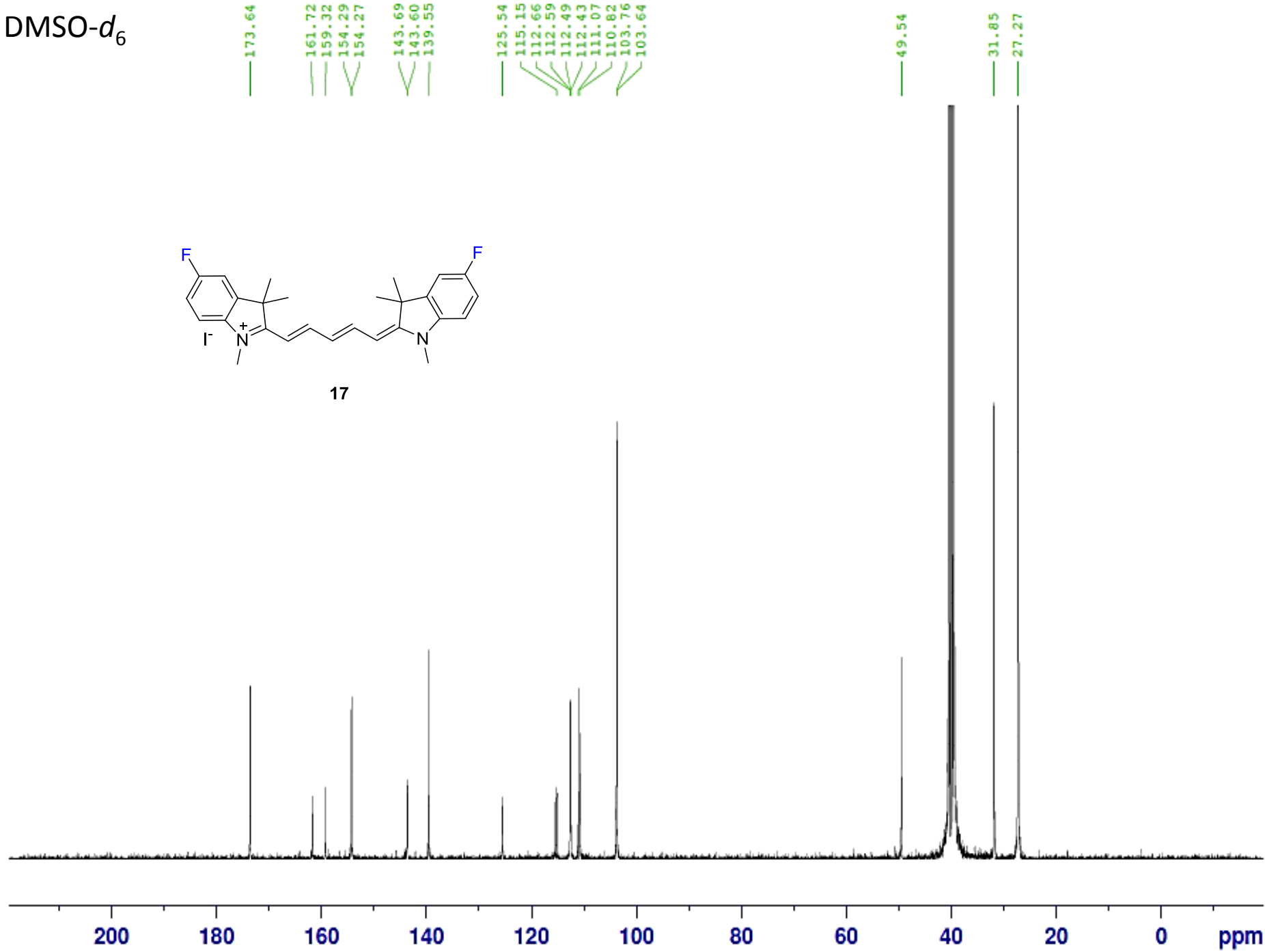
Mass	Calc. Mass	mDa	PPM	DBE	i-FIT	Formula
461.1585	461.1592	-0.7	-1.5	13.5	4.5	C27 H30 N2 Br



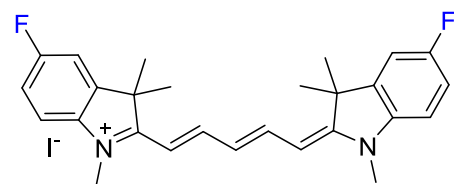
DMSO- d_6



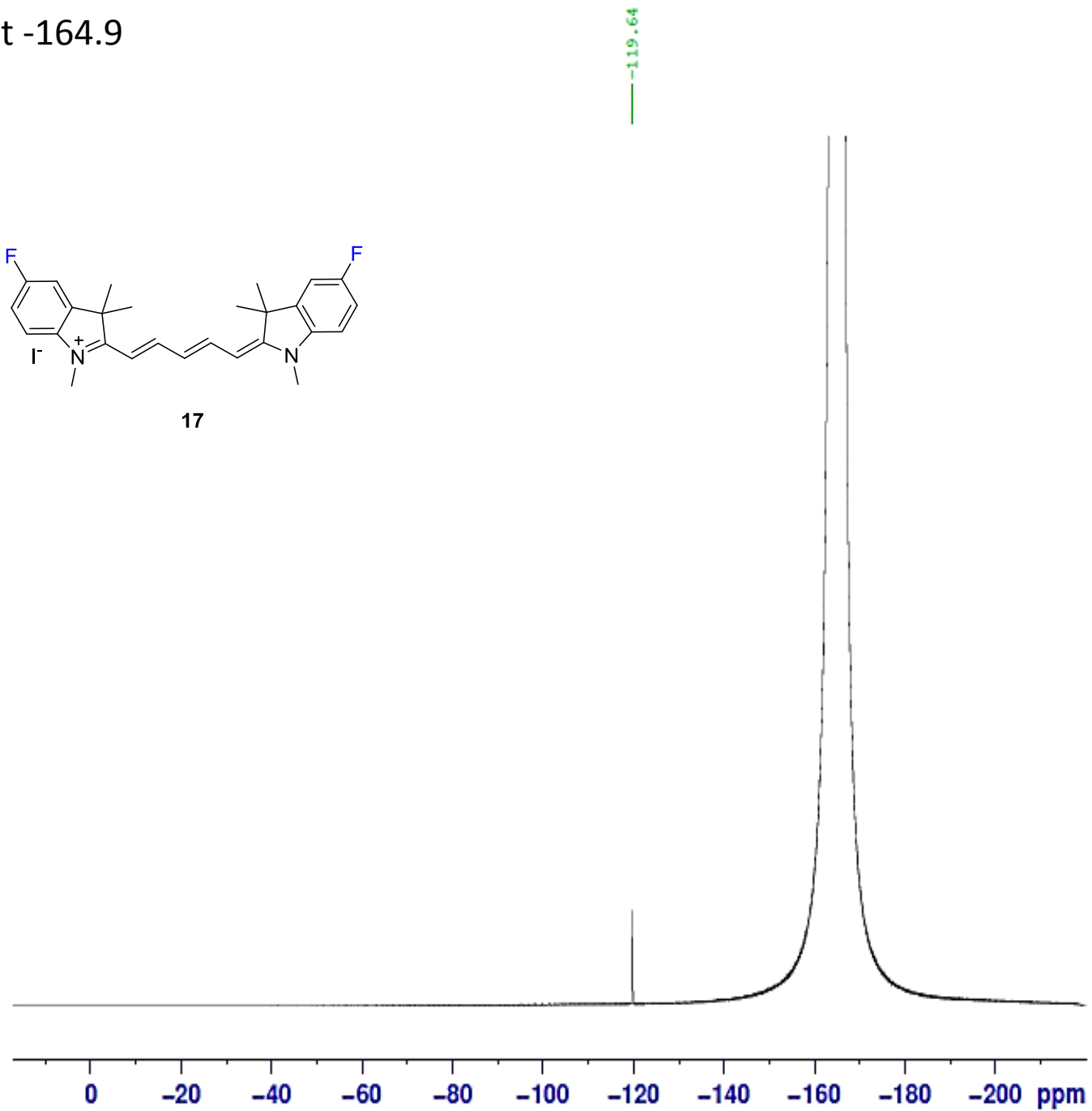
17

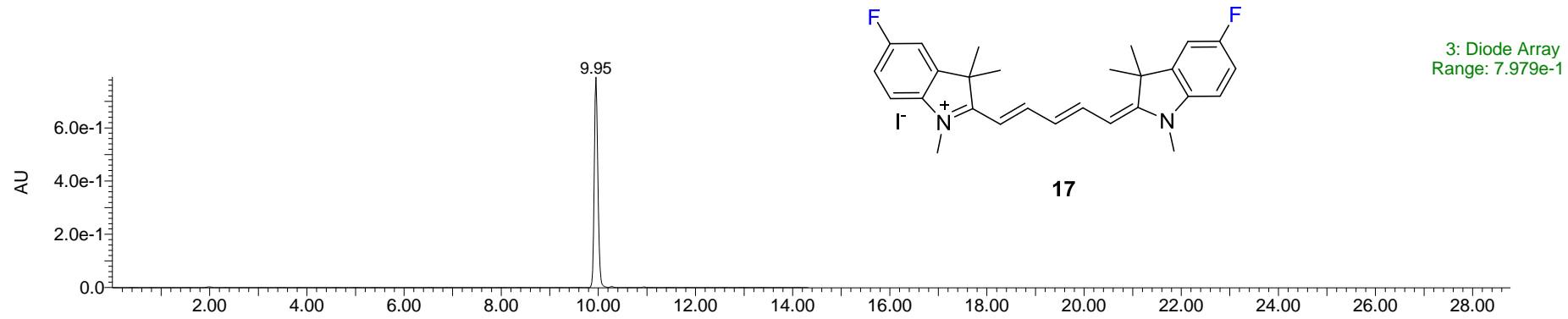


DMSO- d_6 with Hexafluorobenzene ^{19}F Standard
Referenced at -164.9



17



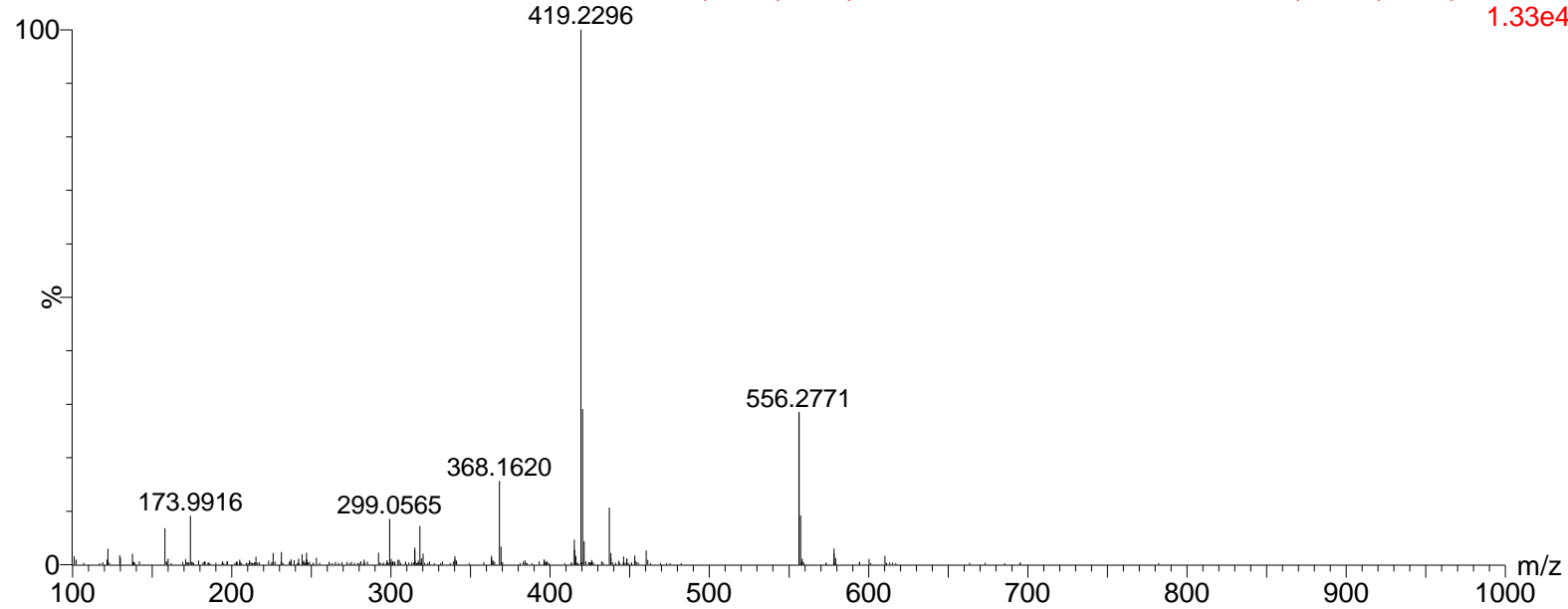


diluted in 80%MeOH

17:23:31 01-Feb-2013

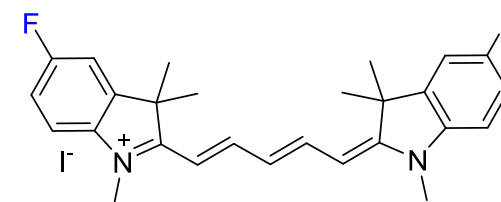
ERIC_22_HENARY-ACCU_02-01-2013_ESI-POS01 23 (0.458) AM (Cen,2, 80.00, Ar,5000.0,556.28,0.70); Cm (21:25)

1.33e4

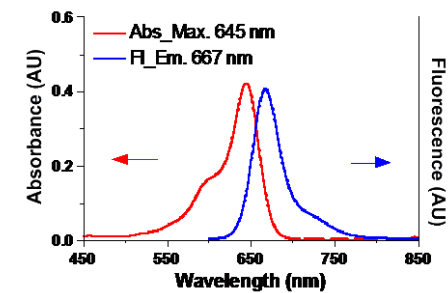


Mass	Calc. Mass	mDa	PPM	DBE	i-FIT	Formula
419.2296	419.2299	-0.3	-0.7	13.5	9.4	C27 H29 N2 F2

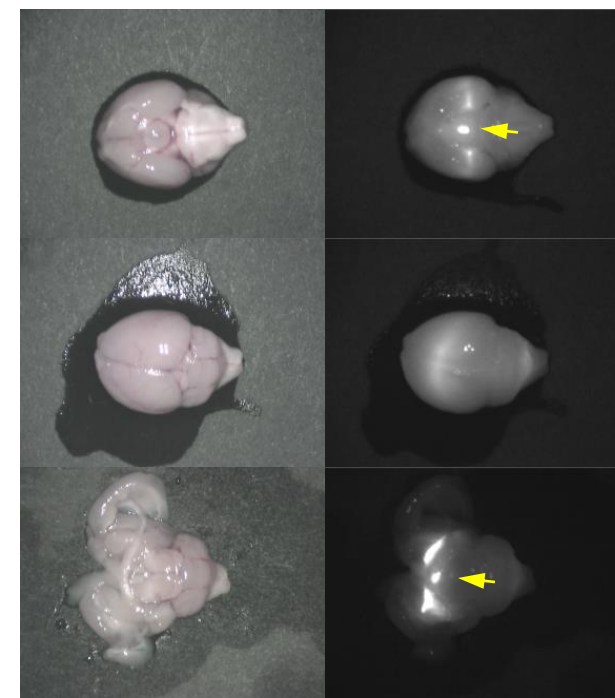
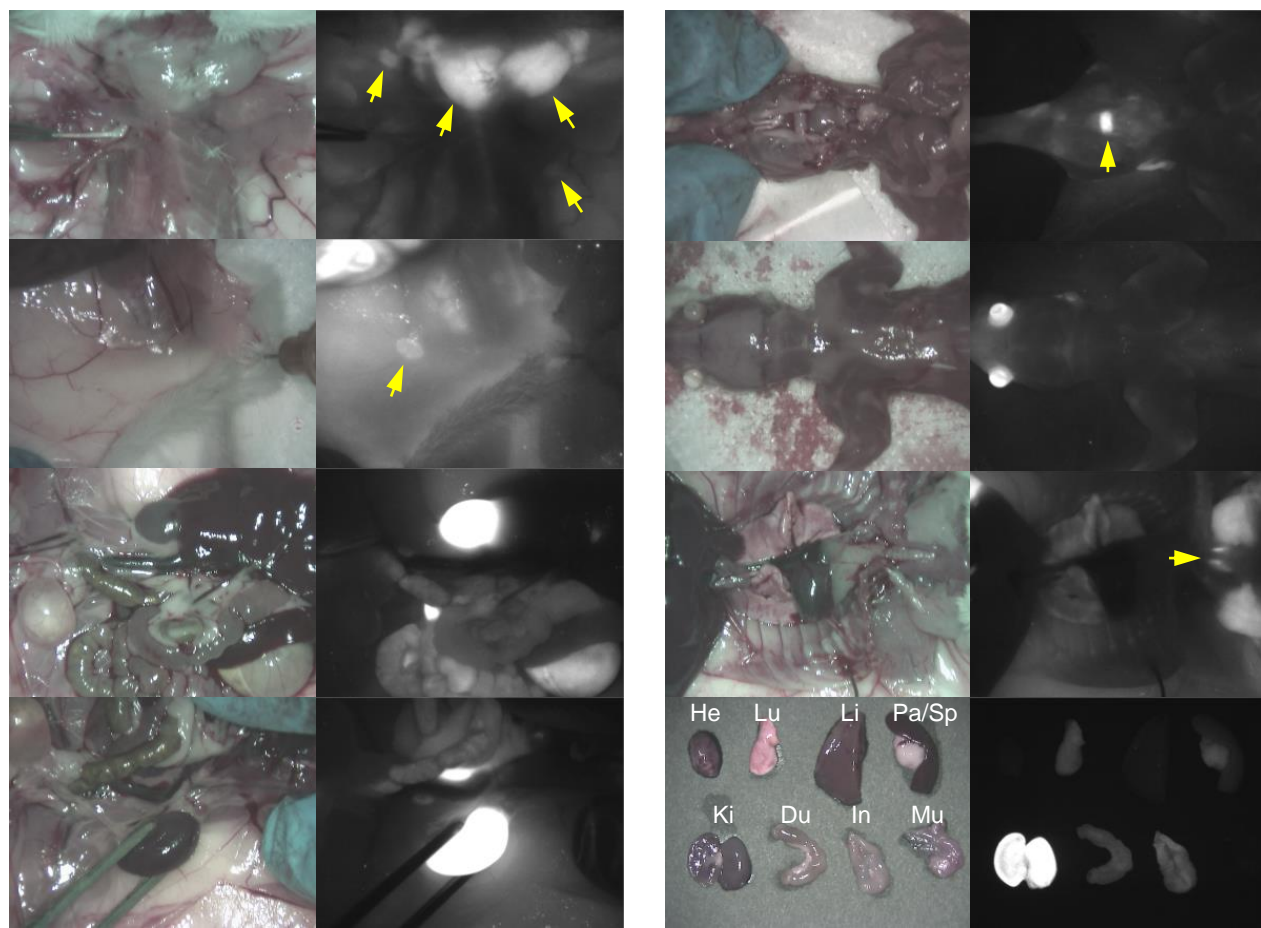
BioD result of Compound 17										
Endocrine Gland	Salivary		Adrenal		Thyroid		Pituitary		Mammary	
	++		-		++		+++		-	
Lymph node	Neck		Axillary		Groin		Lumbar		Kidney	
	+		+		+		+		-	
Organ & Tissue	He	Lu	Li	Pa/Sp	Ki	Du	In	Mu	Brain (CP)	Brown fat
	-	+	-	+/-	+++	+	+	-	+++	-

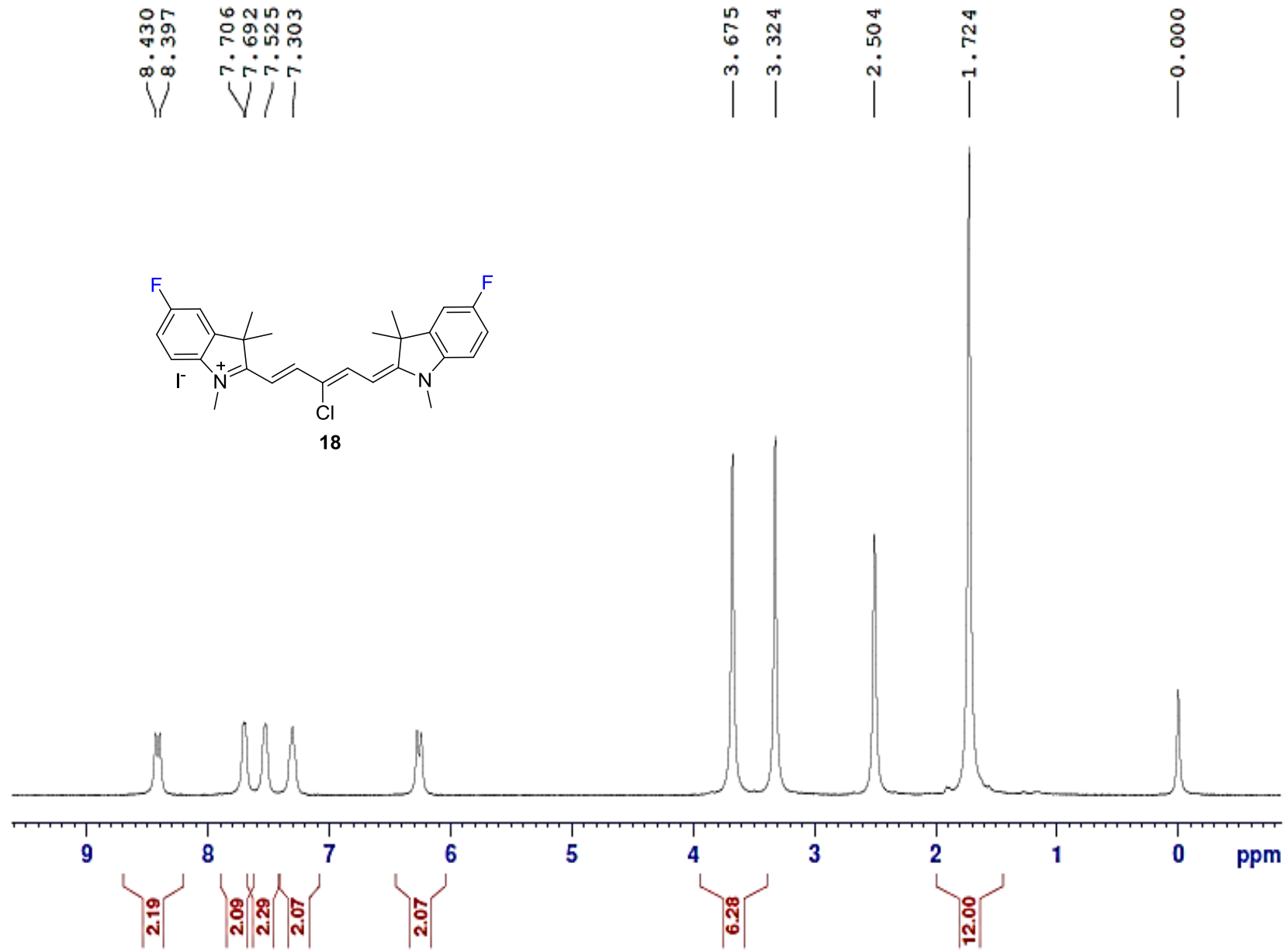


17

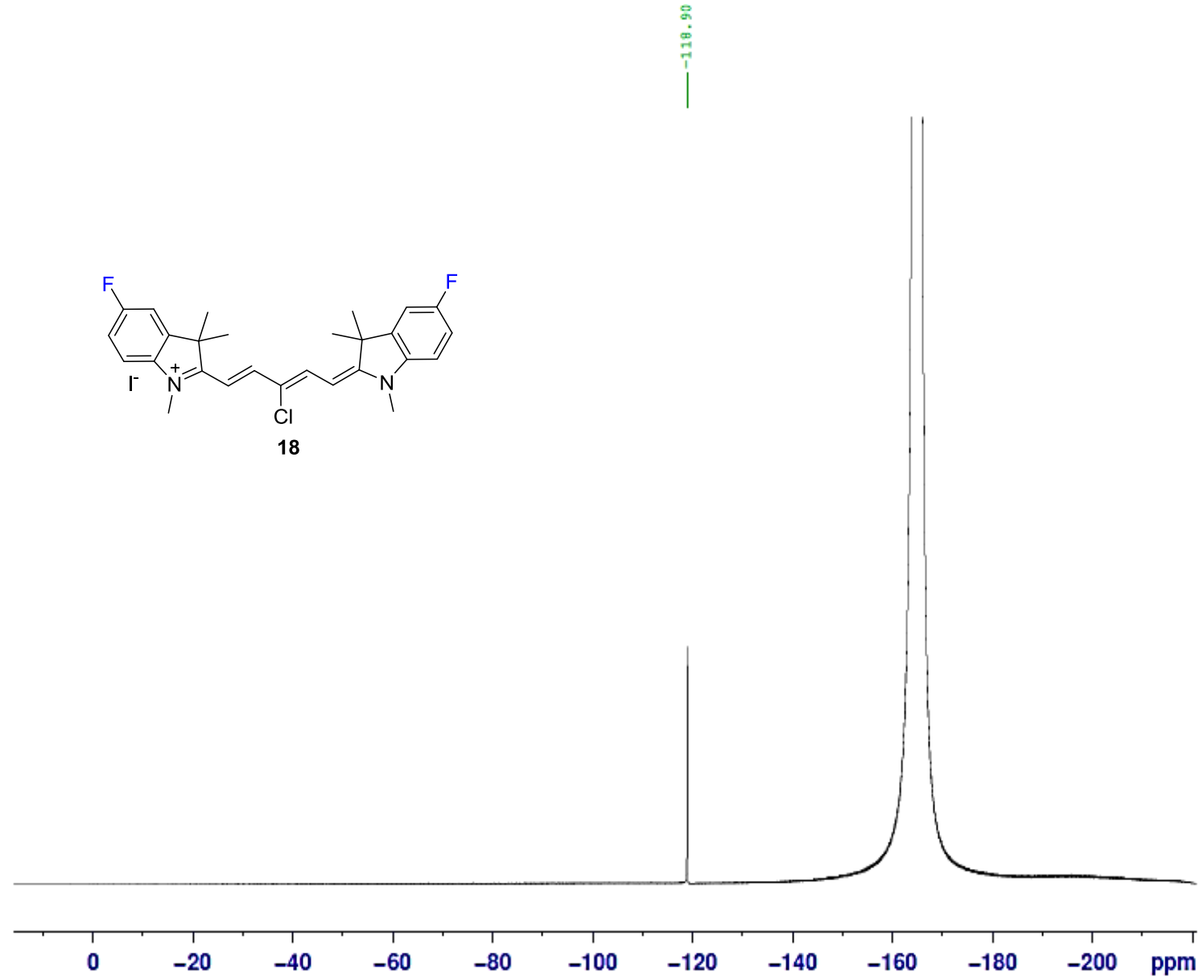


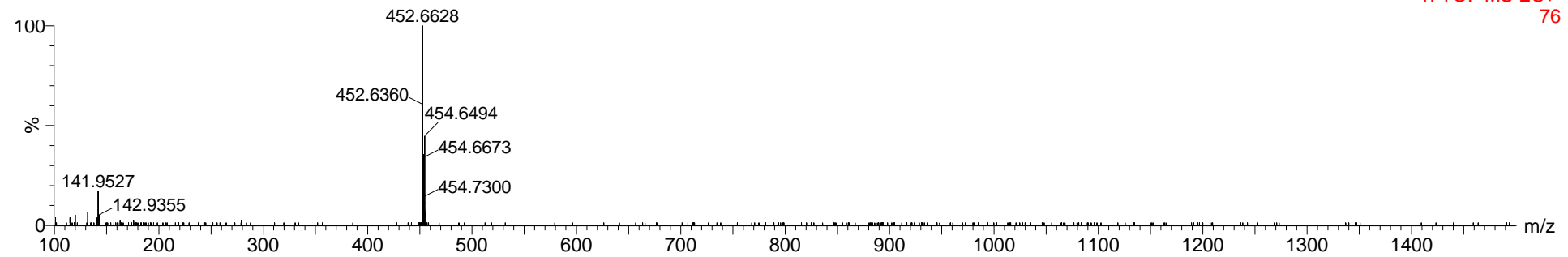
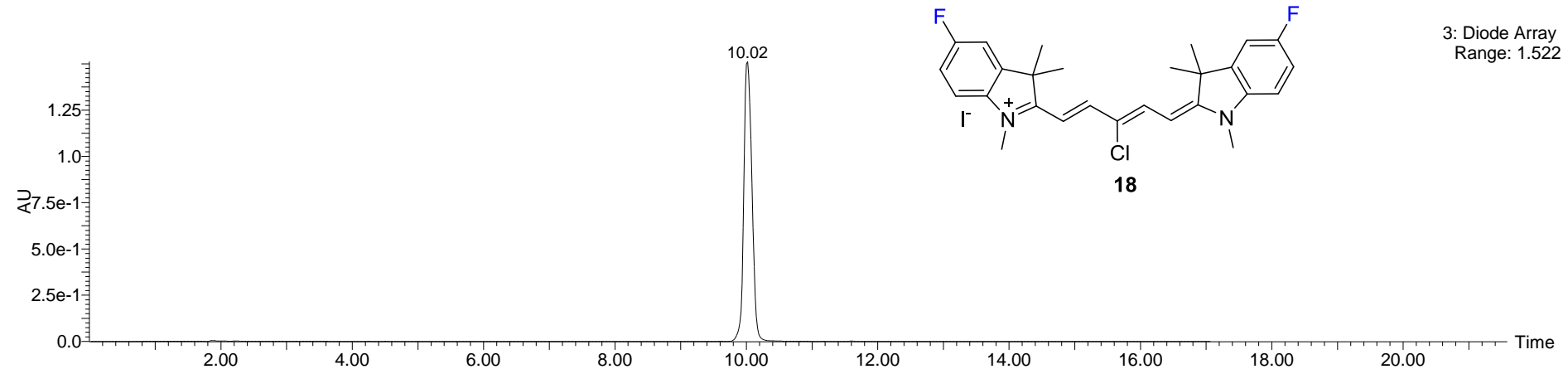
logD at pH 7.4 : (3.84)



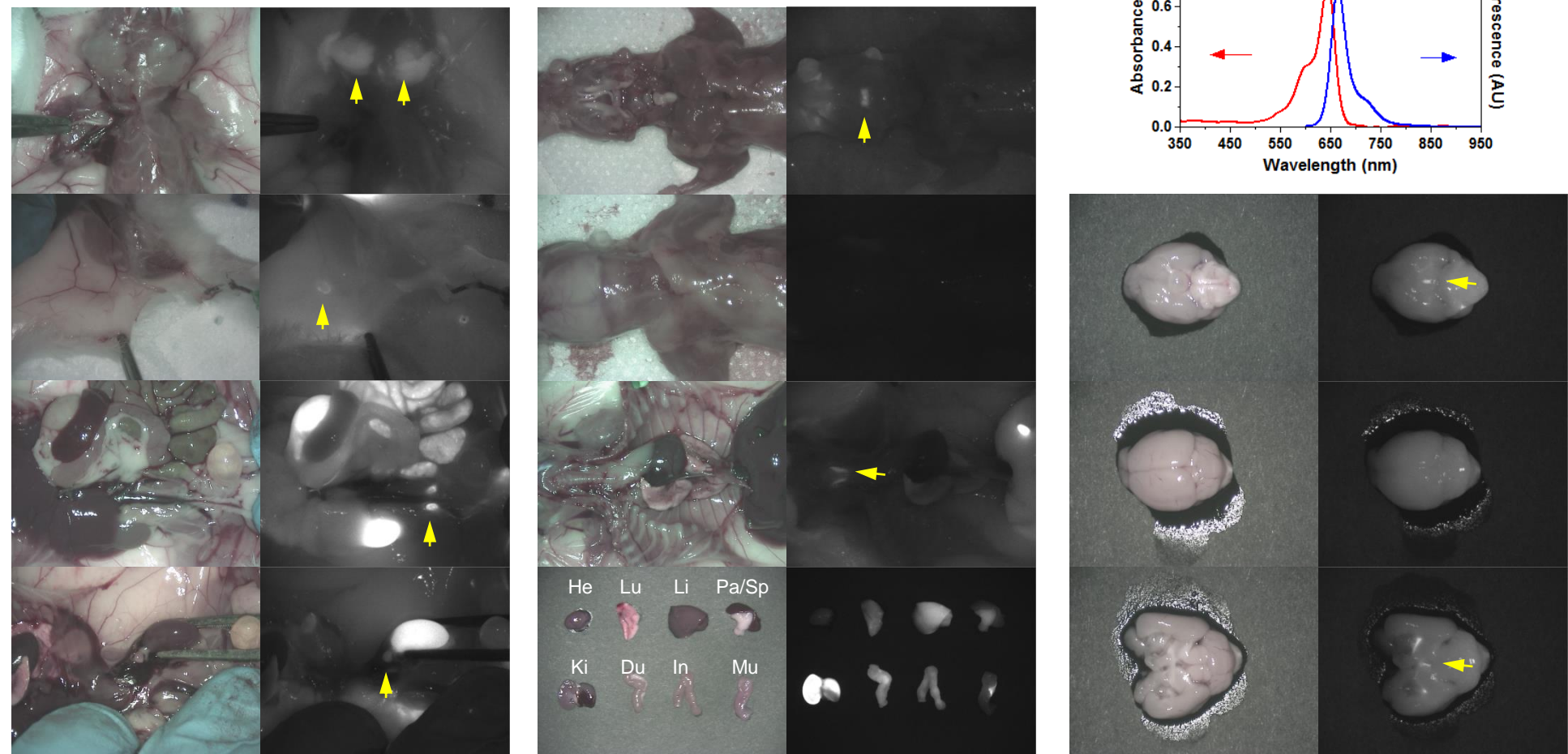
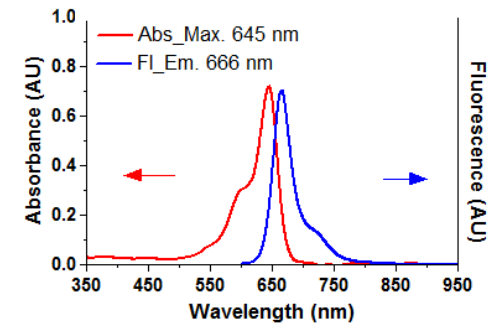
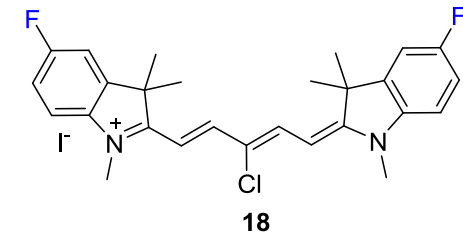


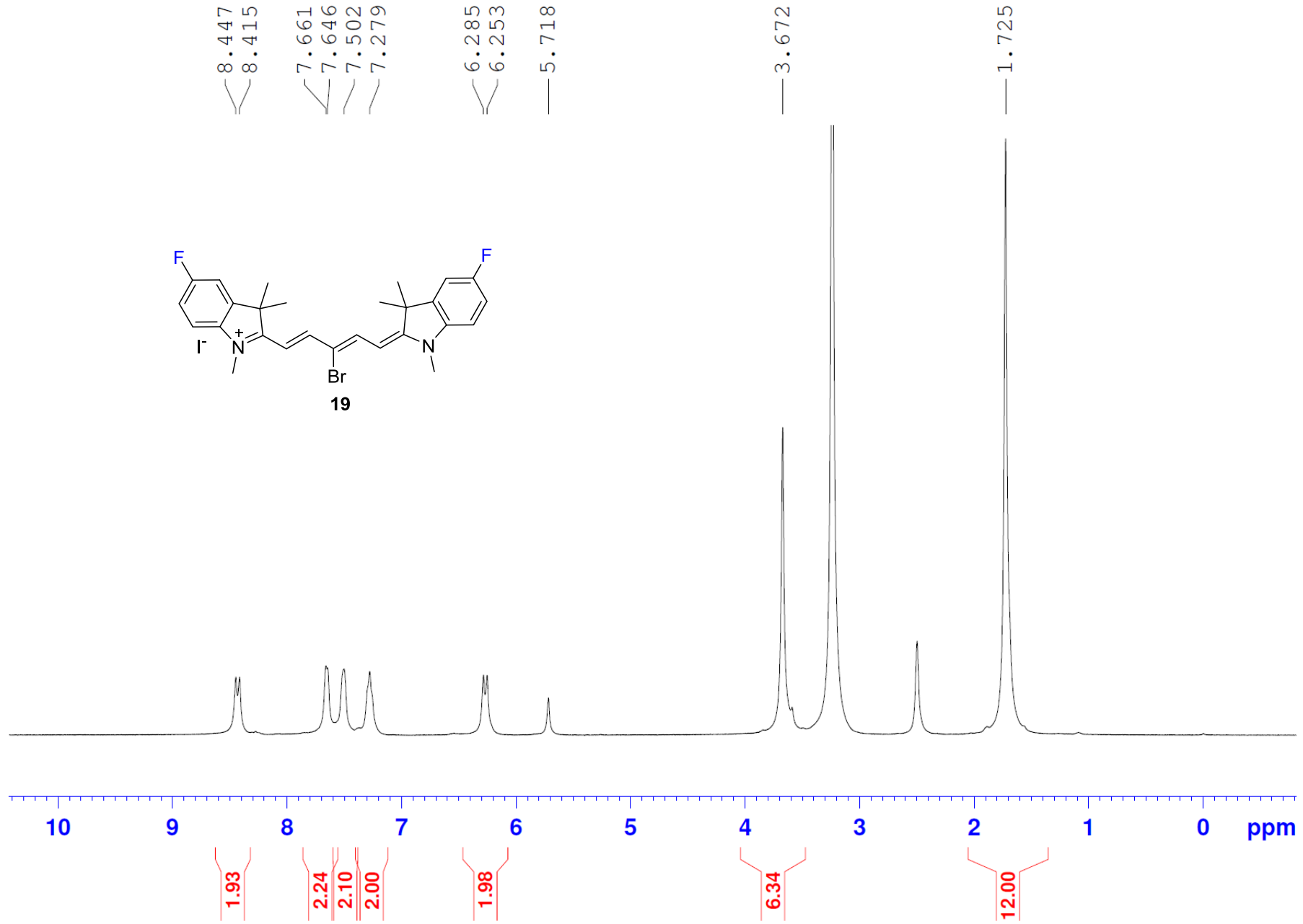
DMSO- d_6 with Hexafluorobenzene ^{19}F Standard
Referenced at -164.9



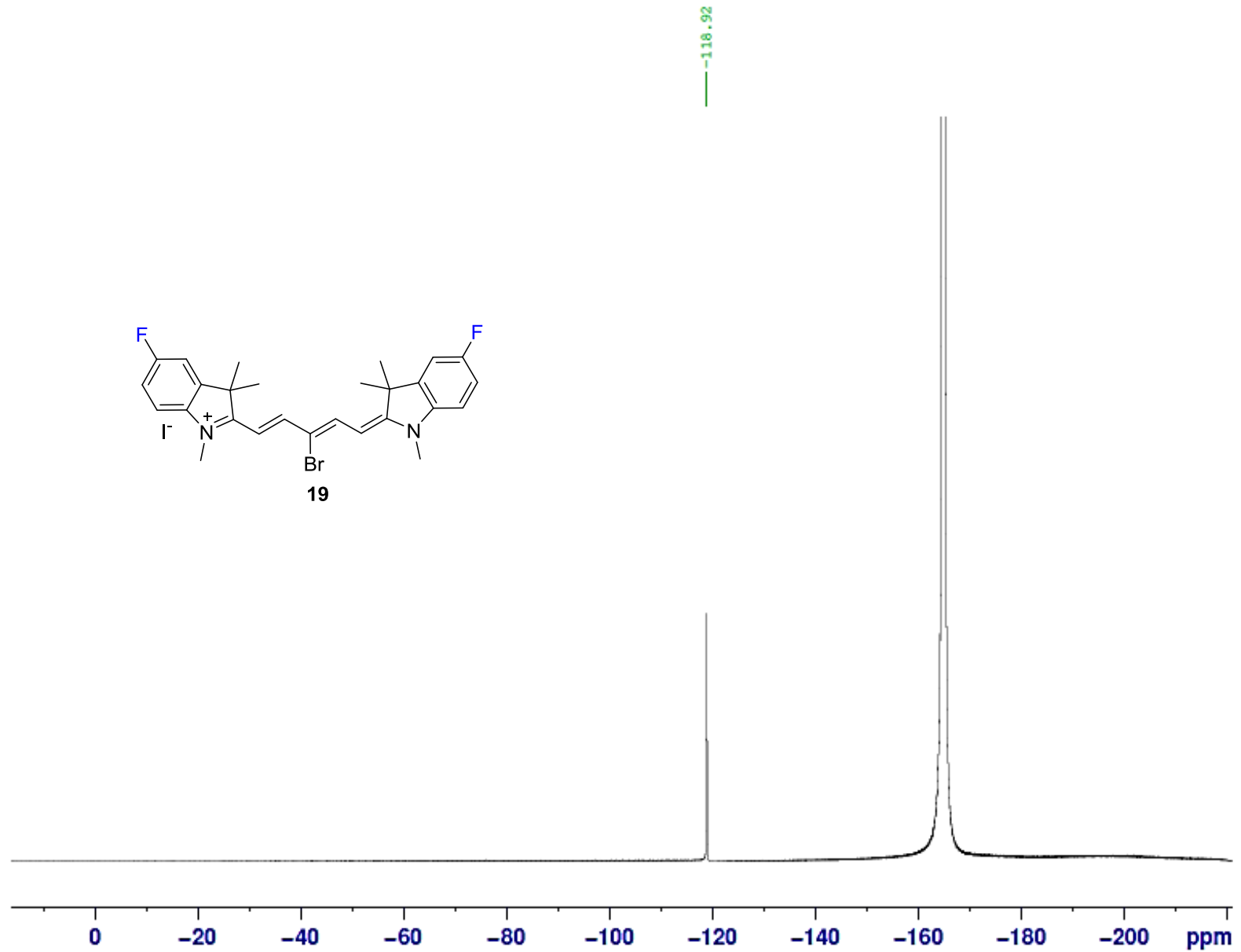


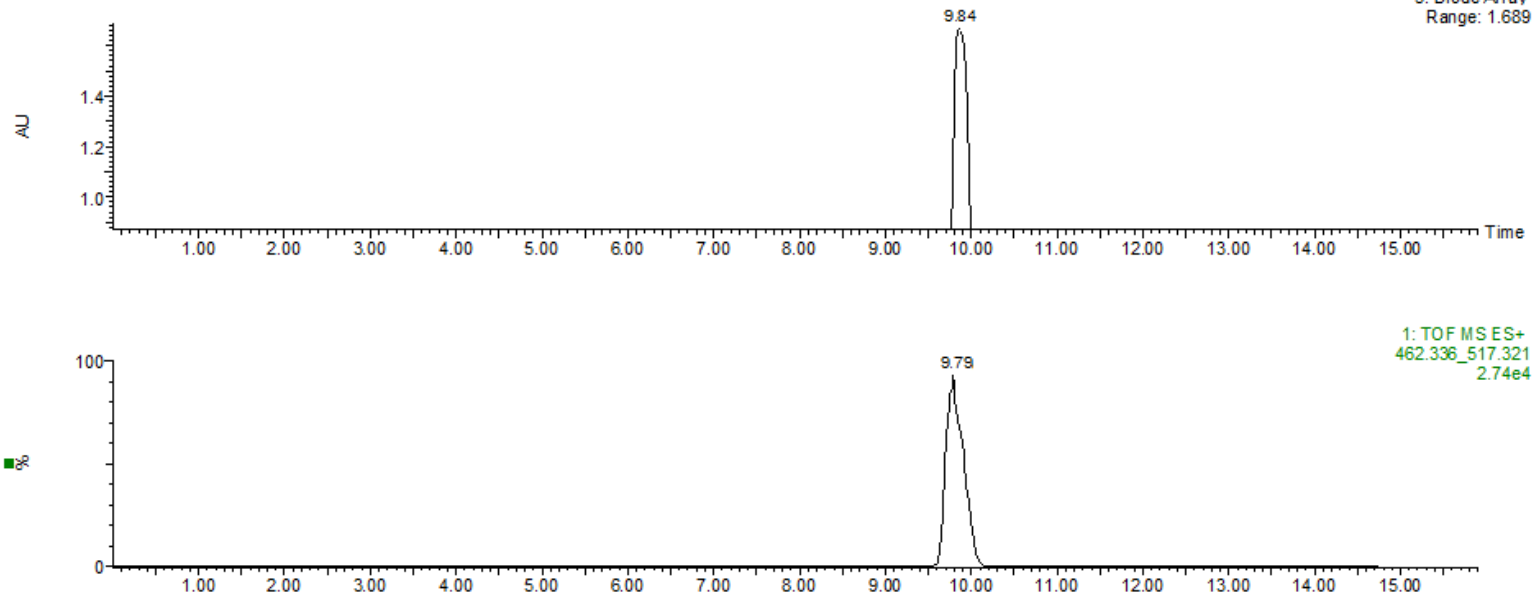
BioD result of Compound 18										
Endocrine Gland	Salivary		Adrenal		Thyroid		Pituitary		Mammary	
	++		+		++		++		-	
Lymph node	Neck		Axillary		Groin		Lumbar		Kidney	
	-		-		+		++		-	
Organ & Tissue	He	Lu	Li	Pa/Sp	Ki	Du	In	Mu	Brain (CP)	Brown fat
	-	+	++	++/-	+++	+	+	-	+	-





DMSO- d_6 with Hexafluorobenzene ^{19}F Standard
Referenced at -164.9

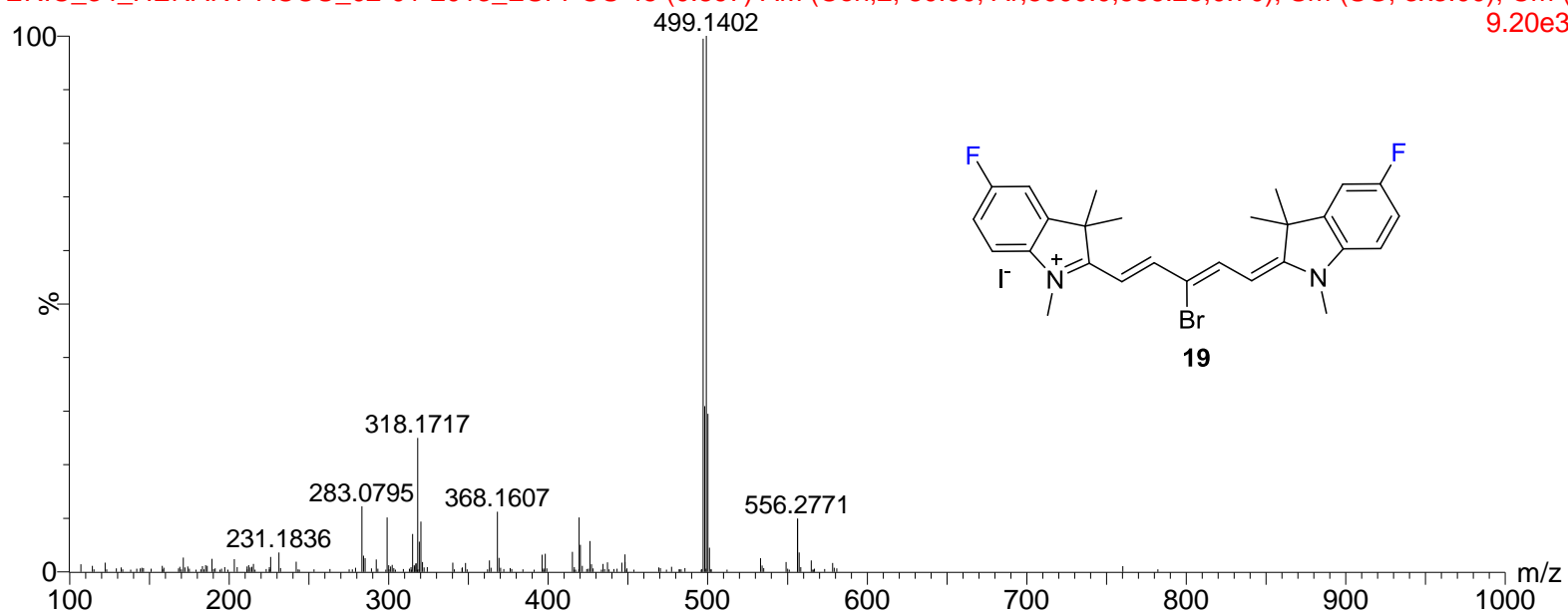




diluted in 80%MeOH

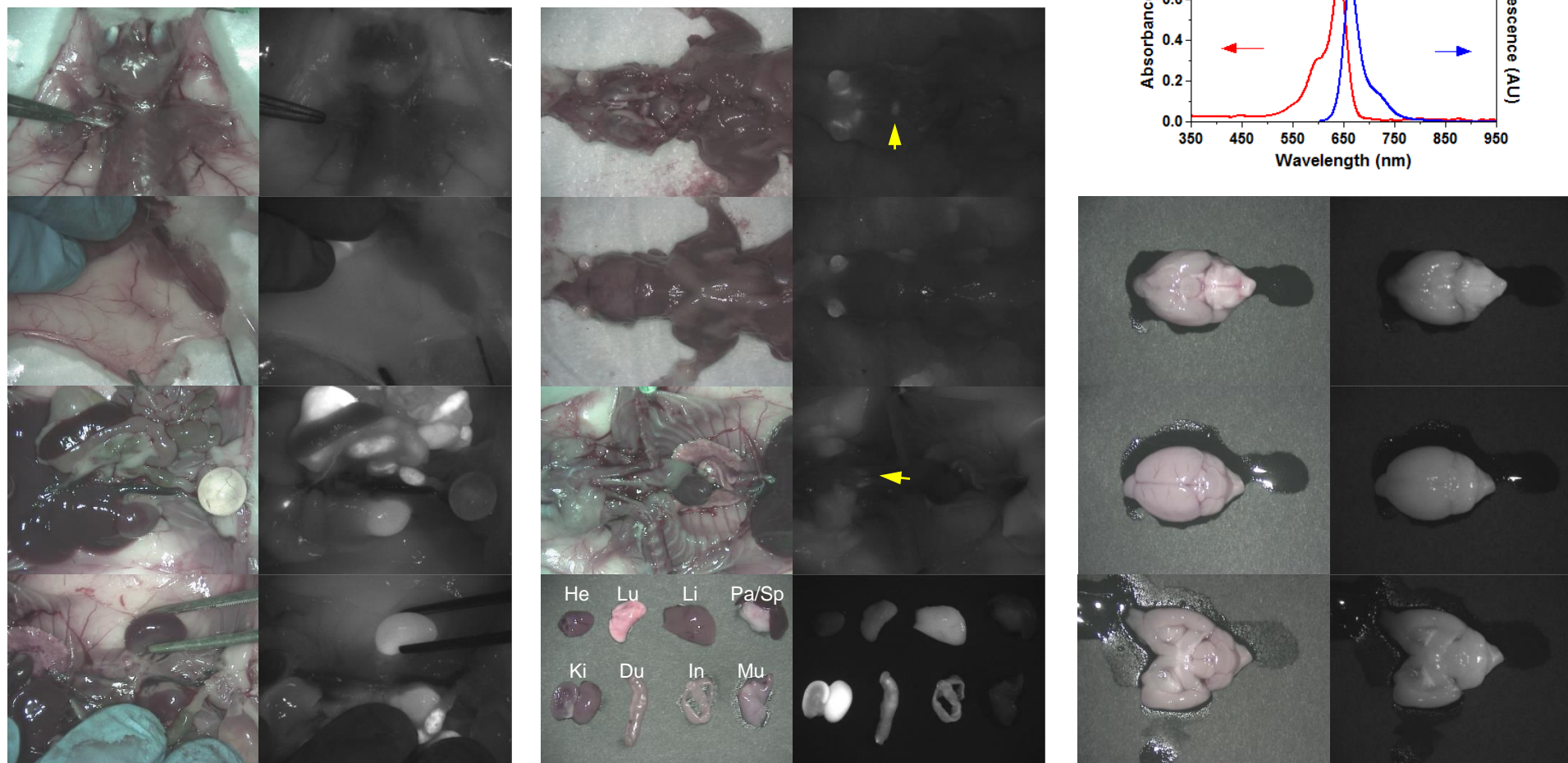
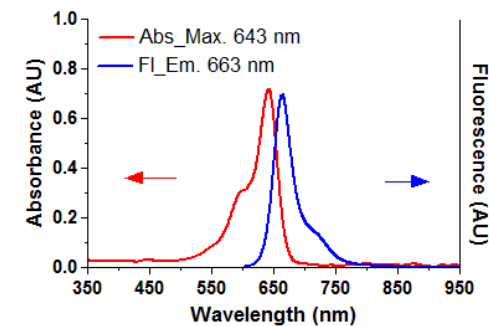
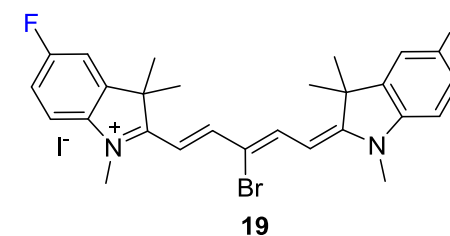
15:58:33 01-Feb-2013

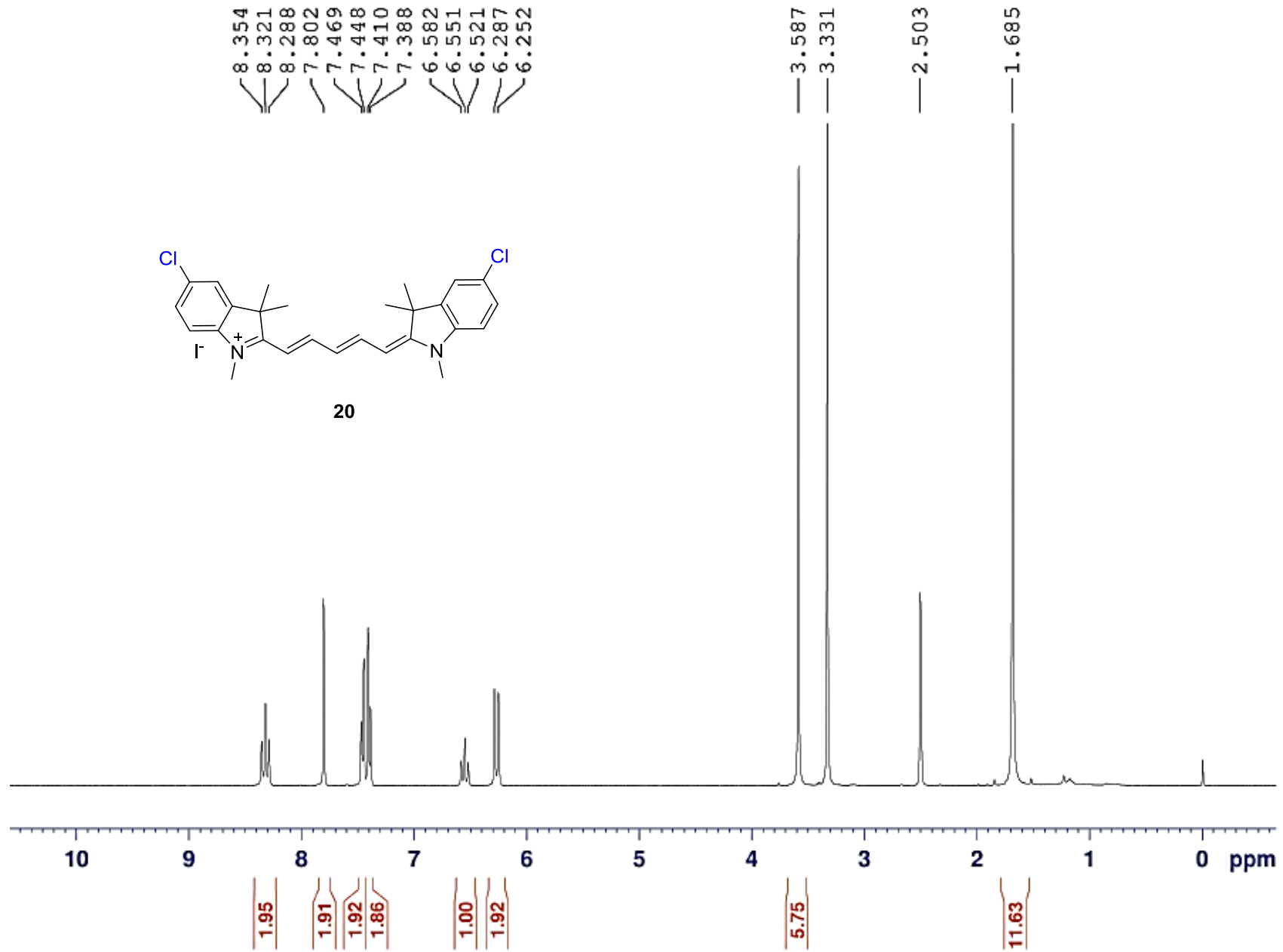
ERIC_34_HENARY-ACCU_02-01-2013_ESI-POS 45 (0.897) AM (Cen,2, 80.00, Ar,5000.0,556.28,0.70); Sm (SG, 3x3.00); Cm (-9.20e3

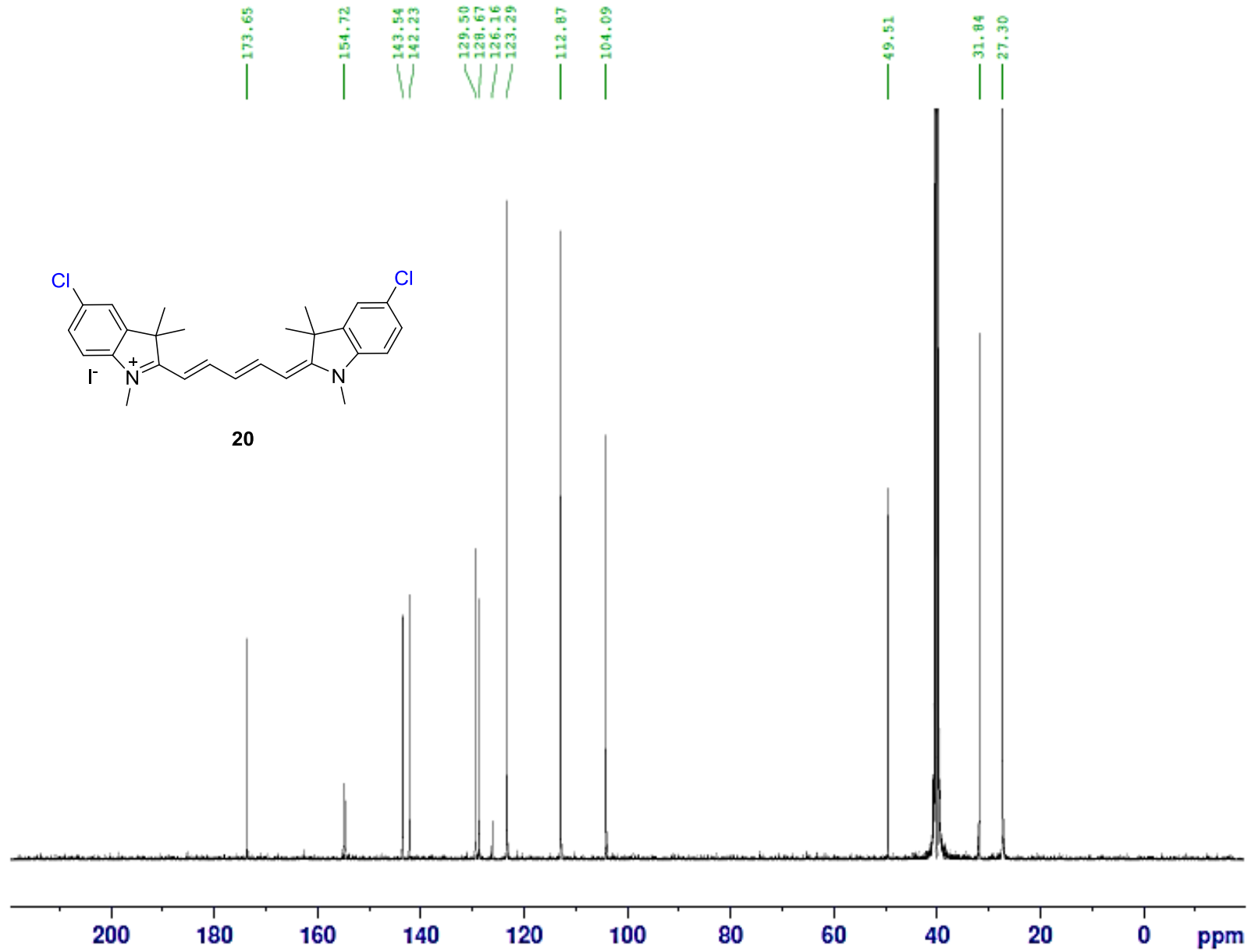


Mass	Calc. Mass	mDa	PPM	DBE	i-FIT	Formula
497.1394	497.1404	-1.0	-2.0	13.5	0.8	C27 H28 N2 F2 Br

BioD result of Compound 19										
Endocrine Gland	Salivary		Adrenal		Thyroid		Pituitary		Mammary	
	+		-		+		+		-	
Lymph node	Neck		Axillary		Groin		Lumbar		Kidney	
	-		-		-		-		-	
Organ & Tissue	He	Lu	Li	Pa/Sp	Ki	Du	In	Mu	Brain (CP)	Brown fat
	-	+	+	-/-	++	+	+	-	-	-





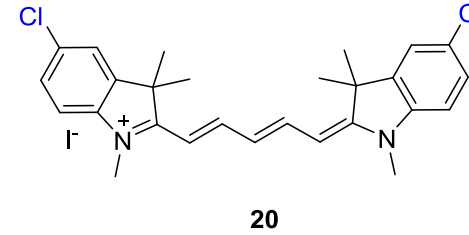
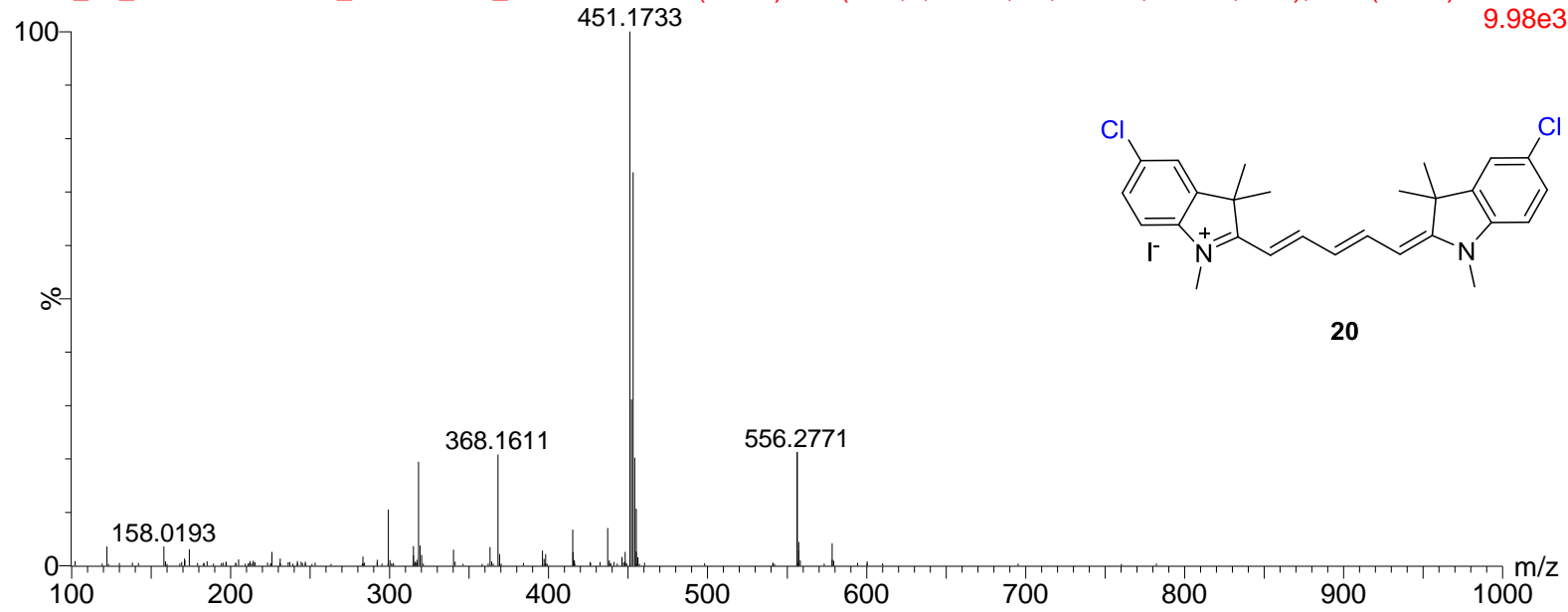


diluted in 80%MeOH

17:14:54 01-Feb-2013

ERIC_23_HENARY-ACCU_02-01-2013_ESI-POS01 72 (1.429) AM (Cen,2, 80.00, Ar,5000.0,556.28,0.70); Cm (72:78)

9.98e3

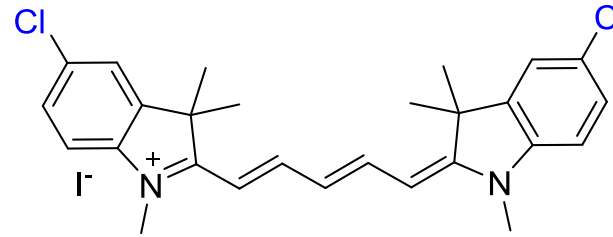


Mass	Calc. Mass	mDa	PPM	DBE	i-FIT	Formula
451.1722	451.1708	1.4	3.1	13.5	17.7	C27 H29 N2 Cl2

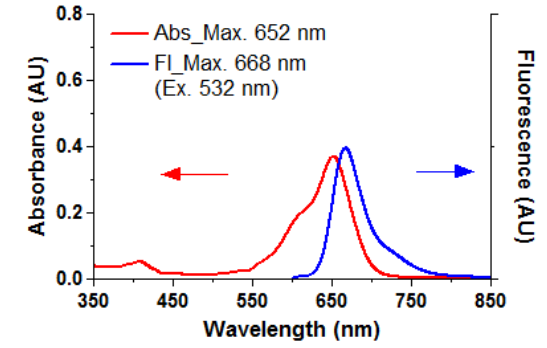
Compound 20

(4h post-injection)

Injection solution: 30% FBS in saline
 Animal: CD-1 mouse
 Injection route: Penial vein
 Dose: 25 nmol (250 µM x 100 µL)



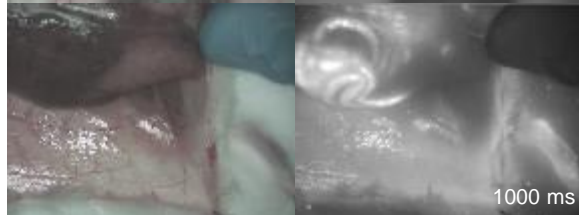
20



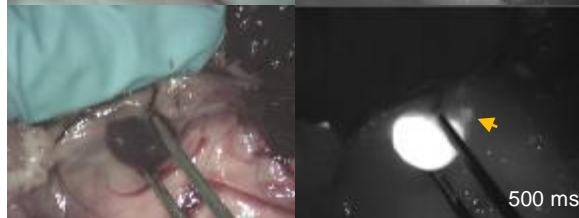
Neck&Axillary LN



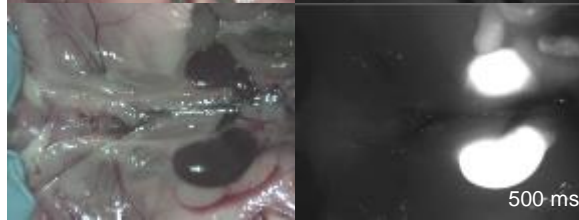
Groin LN



Adrenal GL



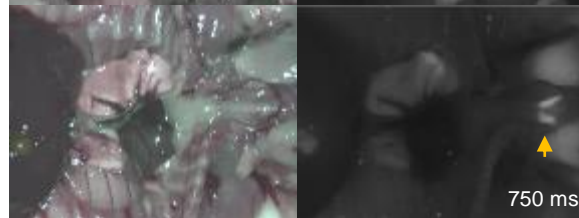
Lumbar LN



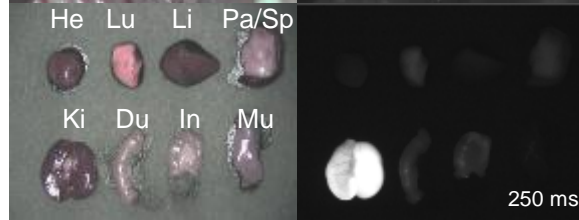
Abdomen



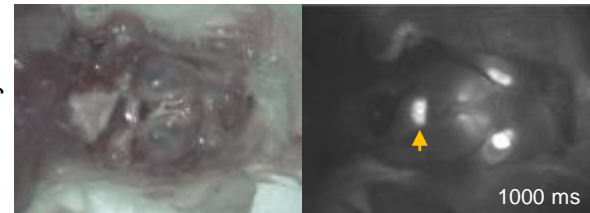
Chest



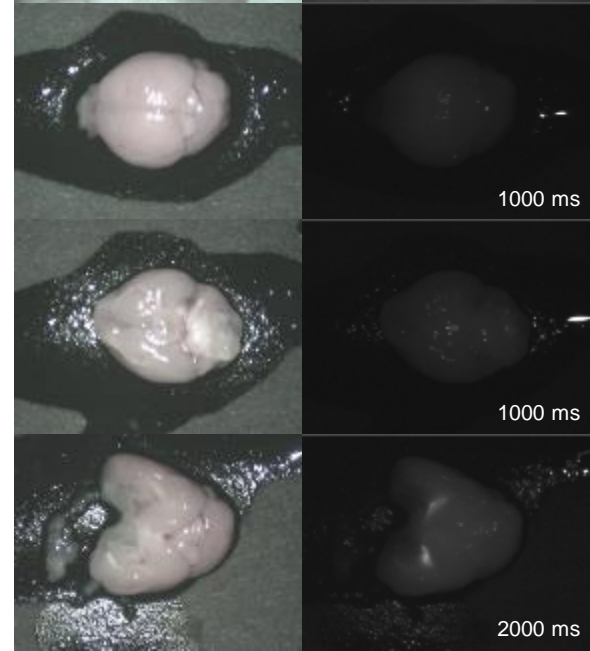
Organs

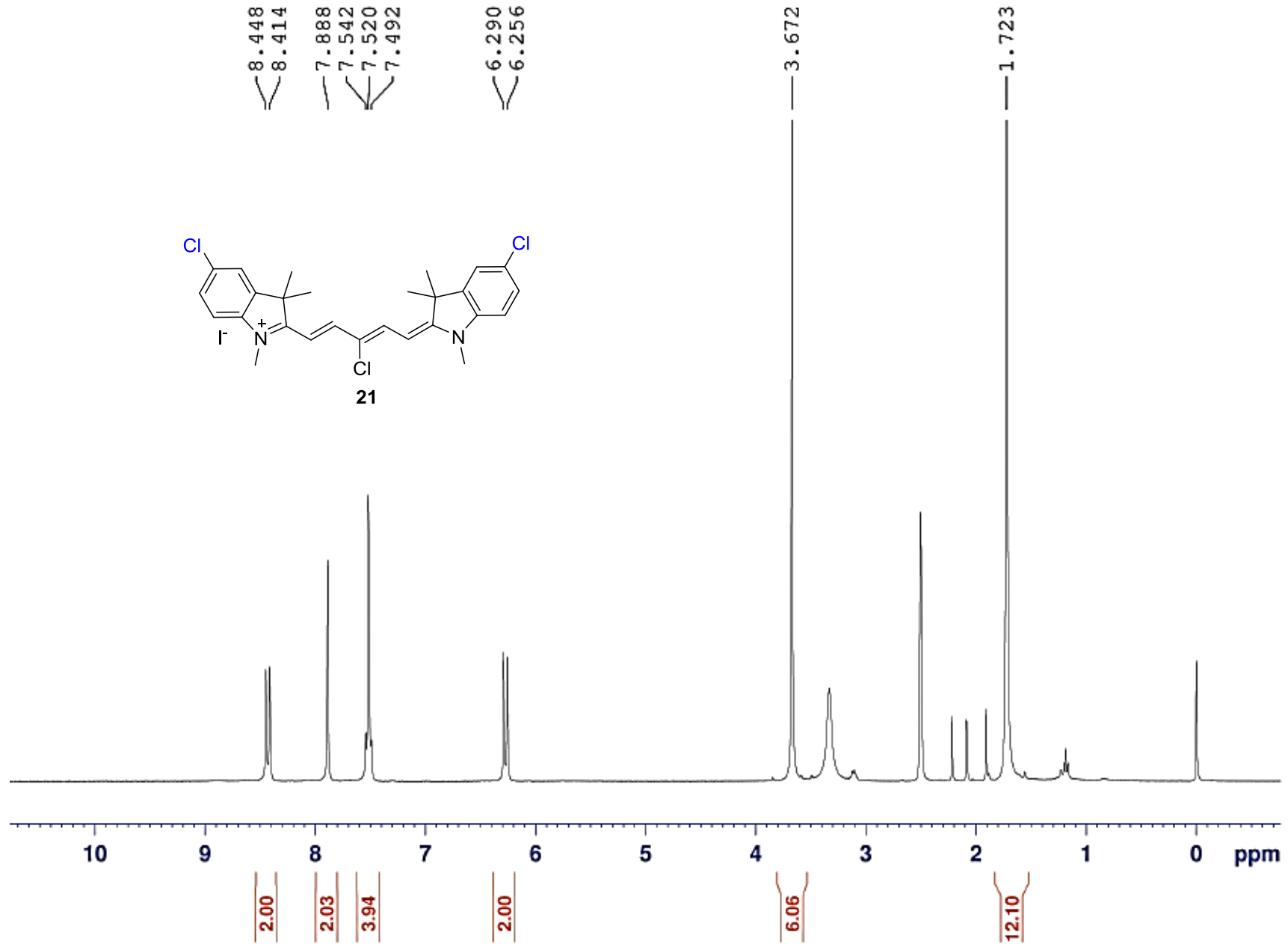


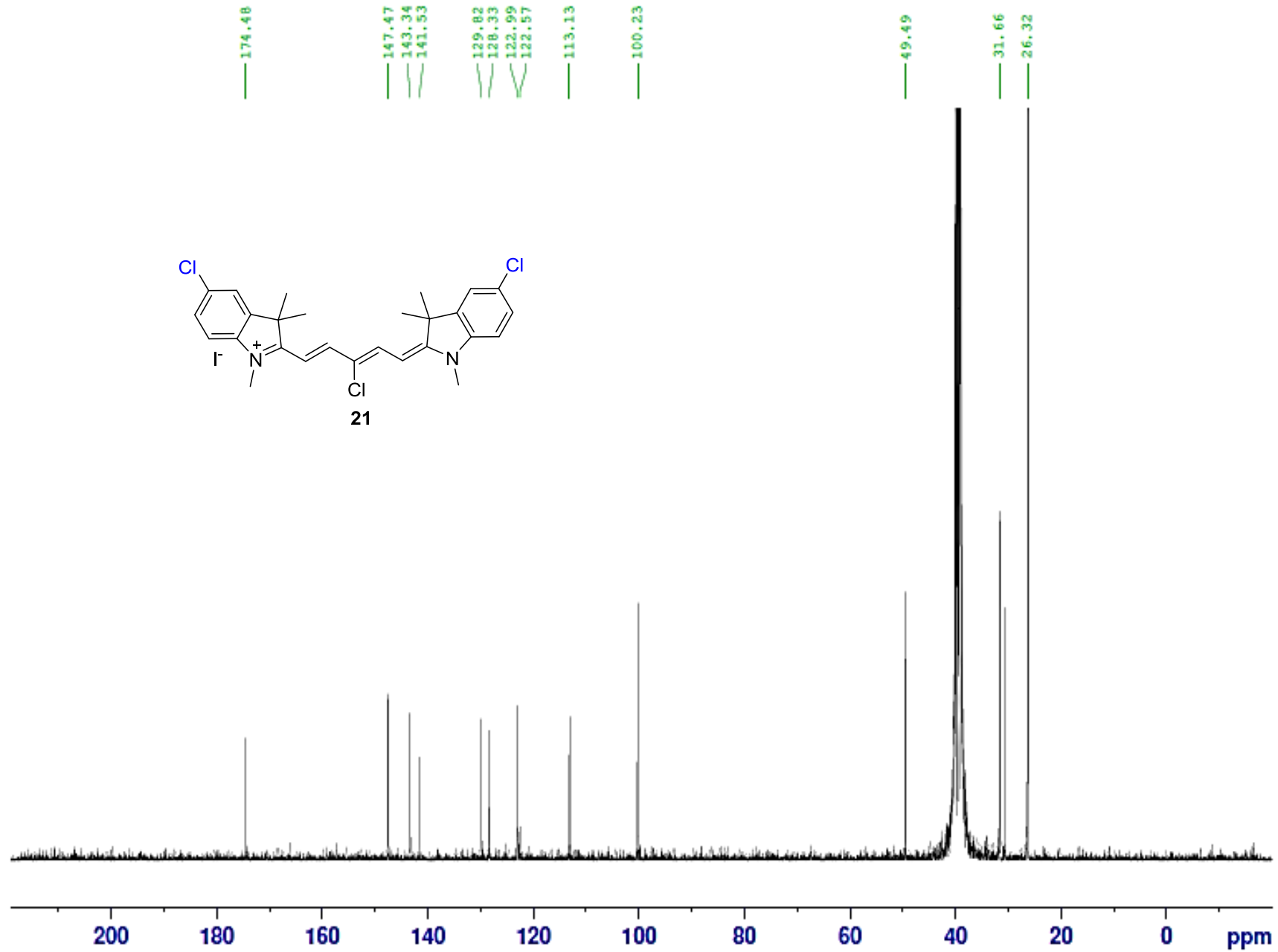
Pituitary GL

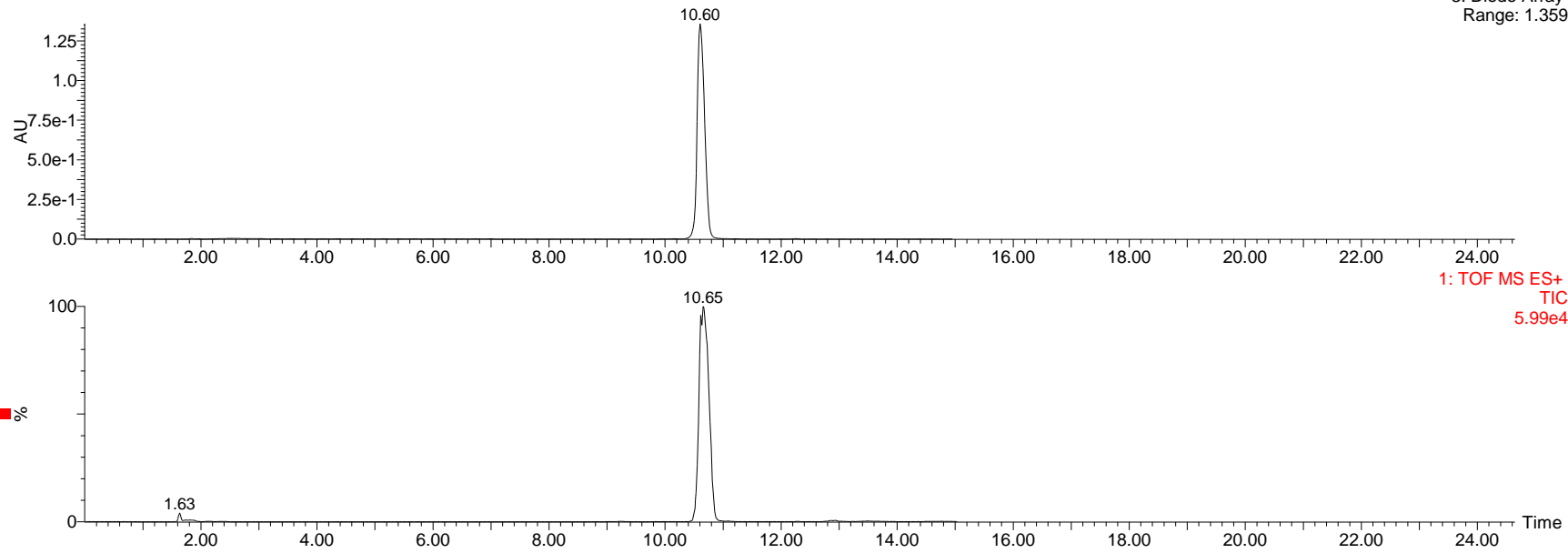


Brain





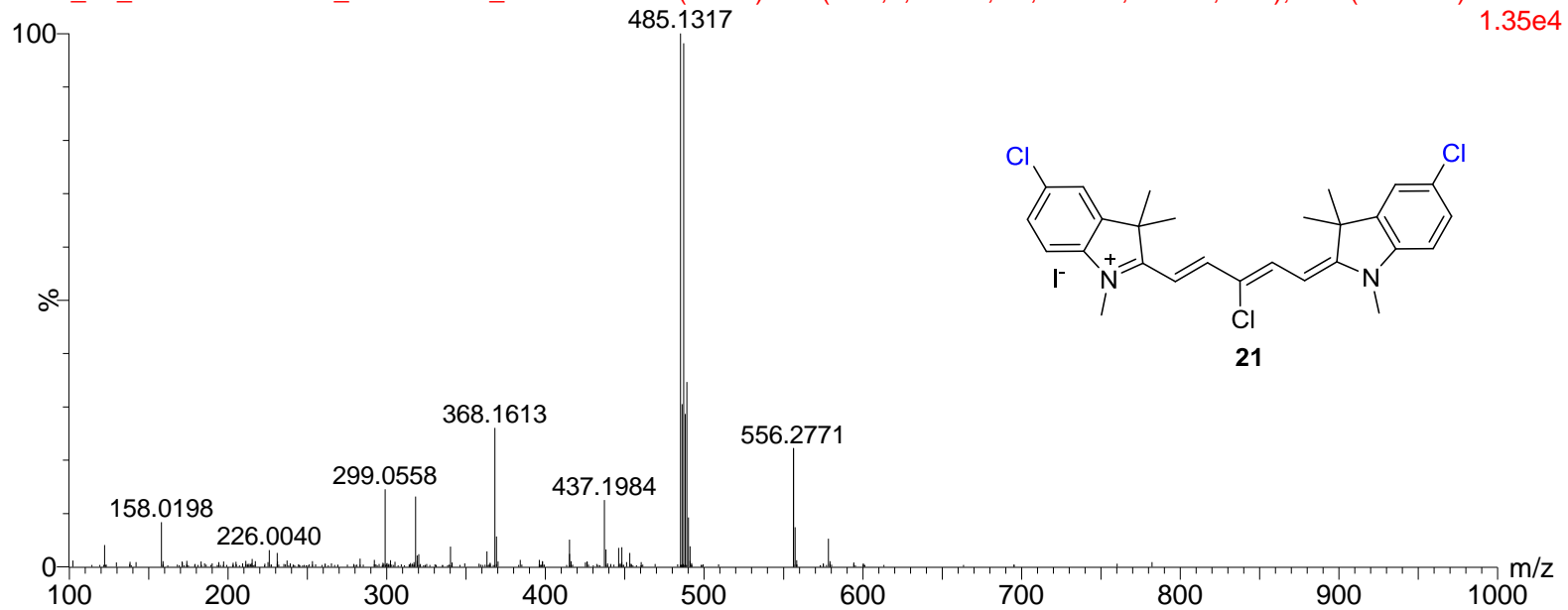




diluted in 80%MeOH

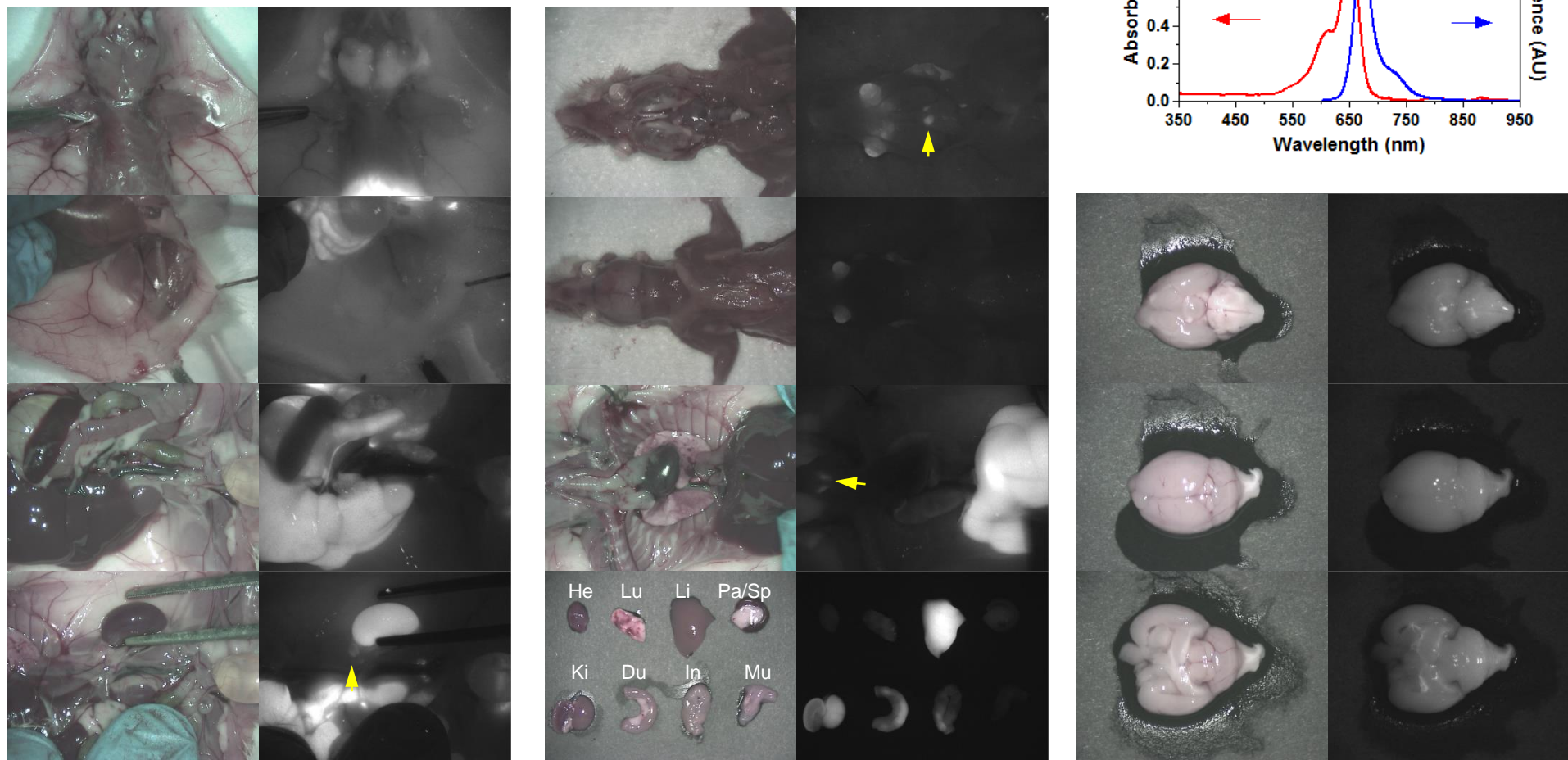
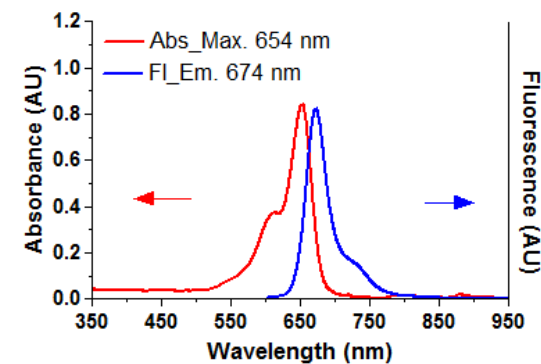
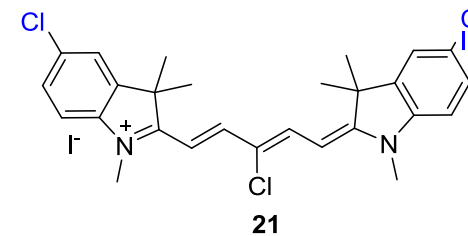
16:44:36 01-Feb-2013

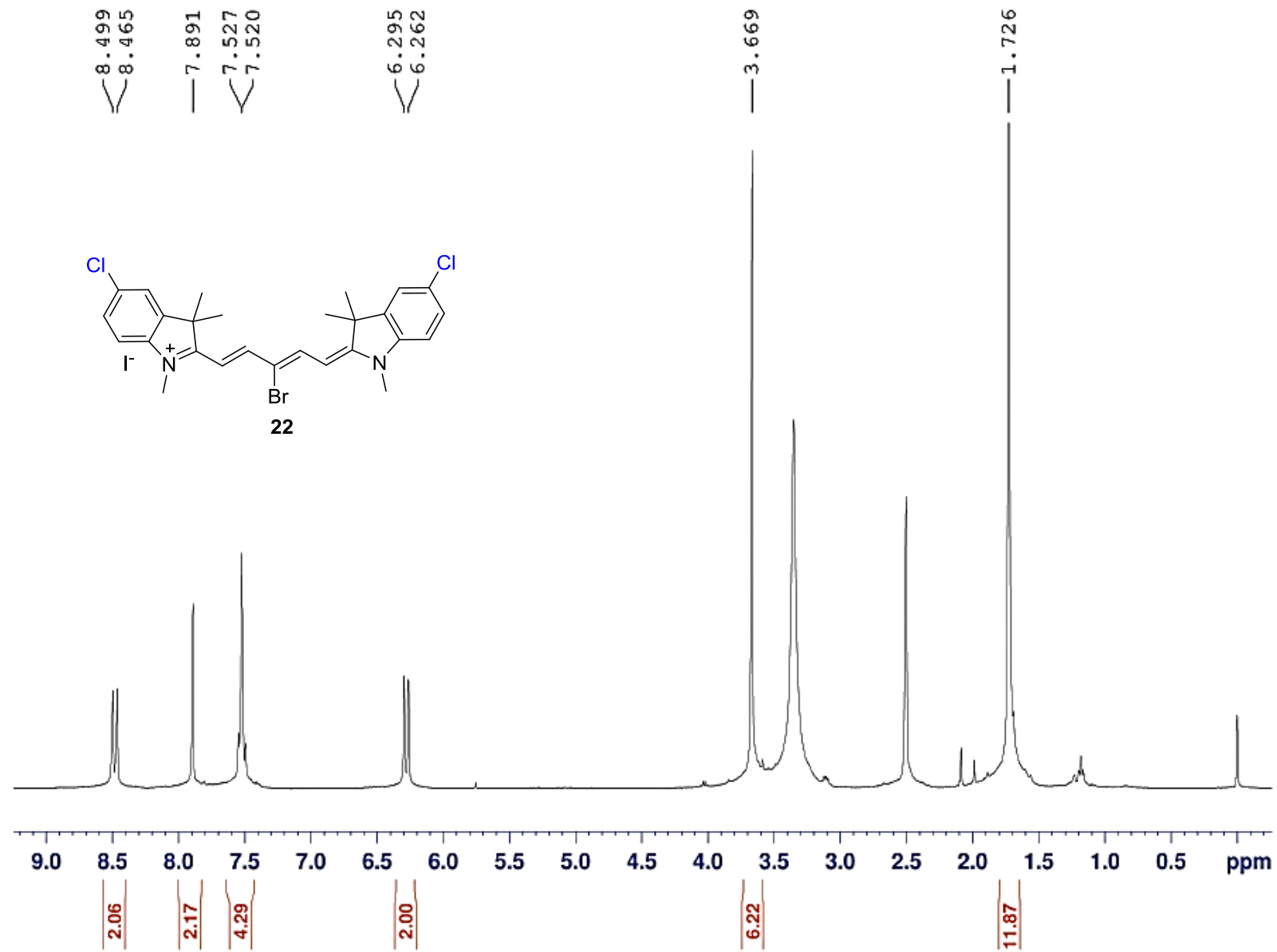
ERIC_29_HENARY-ACCU_02-01-2013_ESI-POS 120 (2.394) AM (Cen,2, 80.00, Ar,5000.0,556.28,0.70); Cm (117:123)

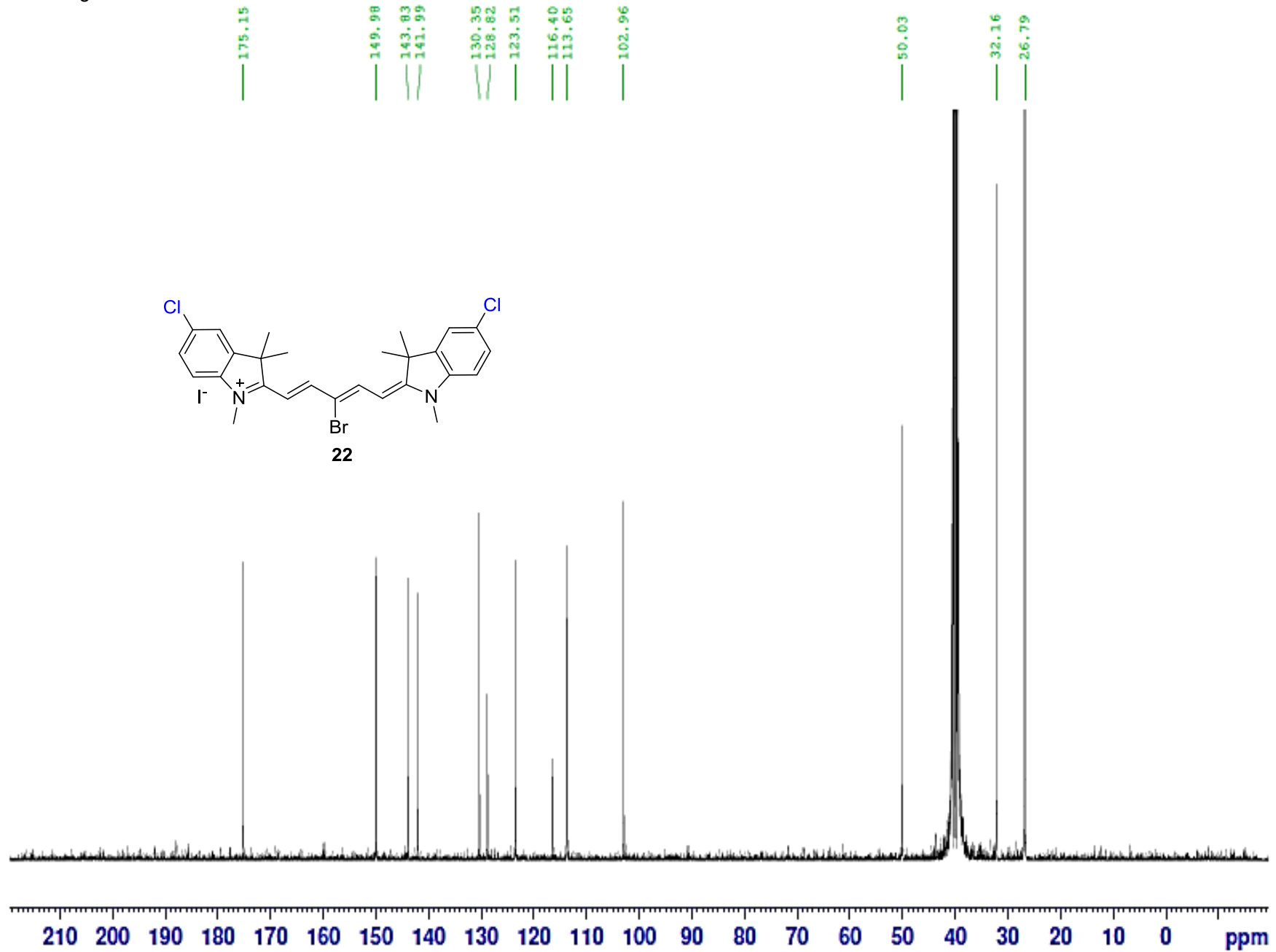


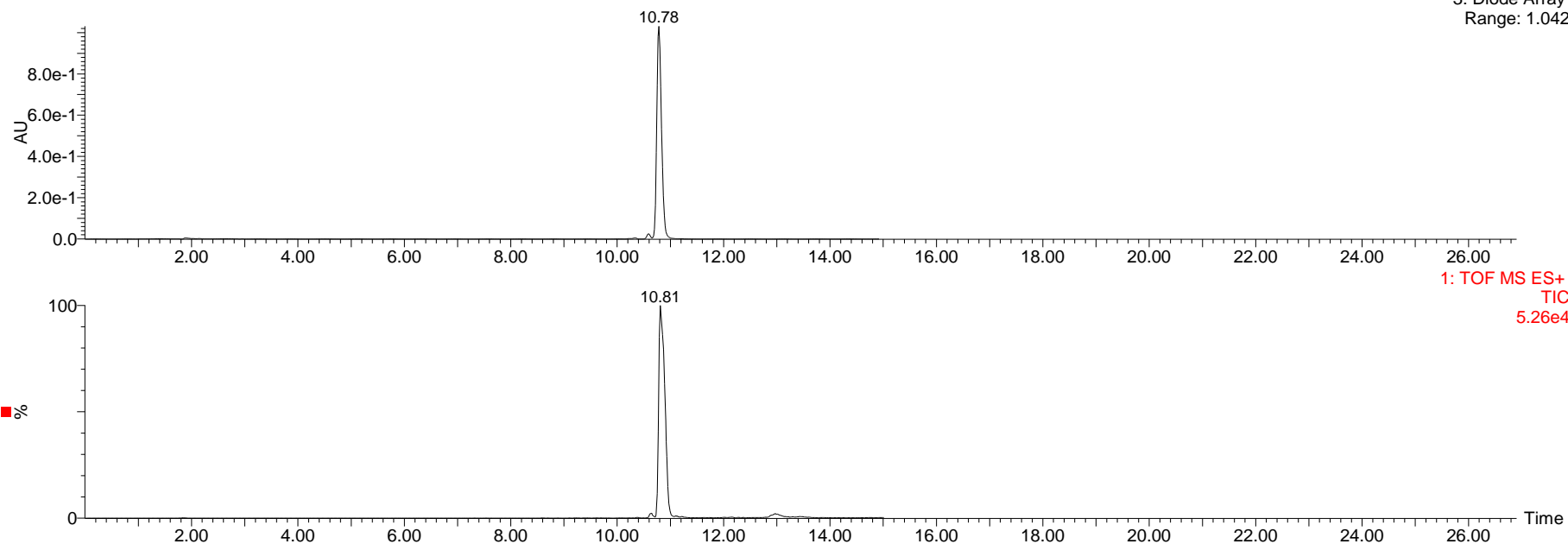
Mass	Calc. Mass	mDa	PPM	DBE	i-FIT	Formula
485.1317	485.1318	-0.1	-0.2	13.5	2.3	C27 H28 N2 Cl3

BioD result of Compound 21										
Endocrine Gland	Salivary		Adrenal		Thyroid		Pituitary		Mammary	
	+		+		+		+		-	
Lymph node	Neck		Axillary		Groin		Lumbar		Kidney	
	-		-		-		+		-	
Organ & Tissue	He	Lu	Li	Pa/Sp	Ki	Du	In	Mu	Brain (CP)	Brown fat
	-	-	+++	-/-	++	+	-	-	+	-







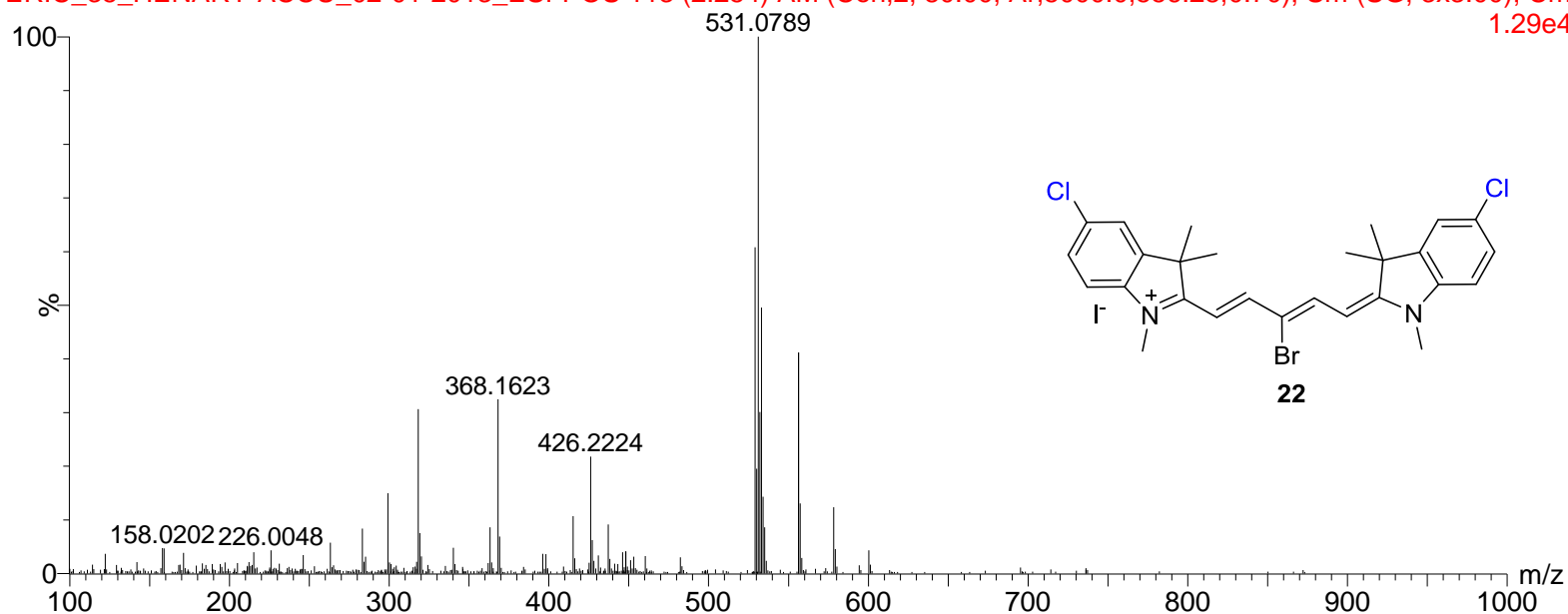


diluted in 80%MeOH

15:36:17 01-Feb-2013

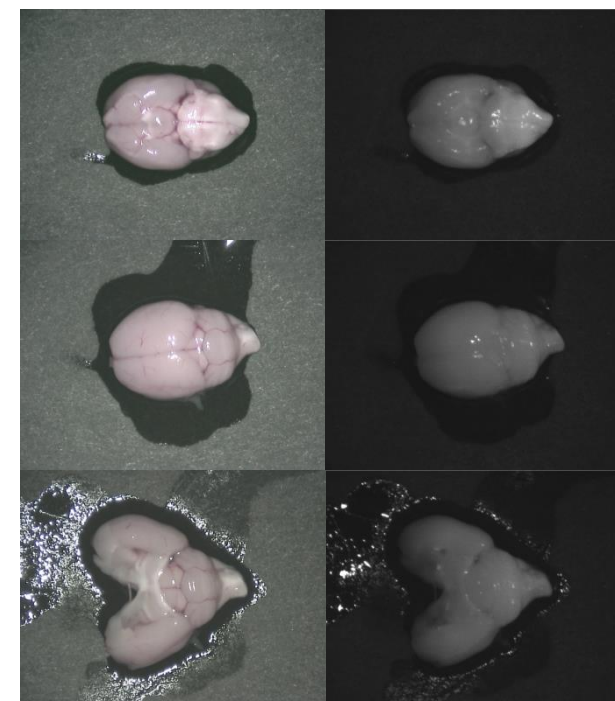
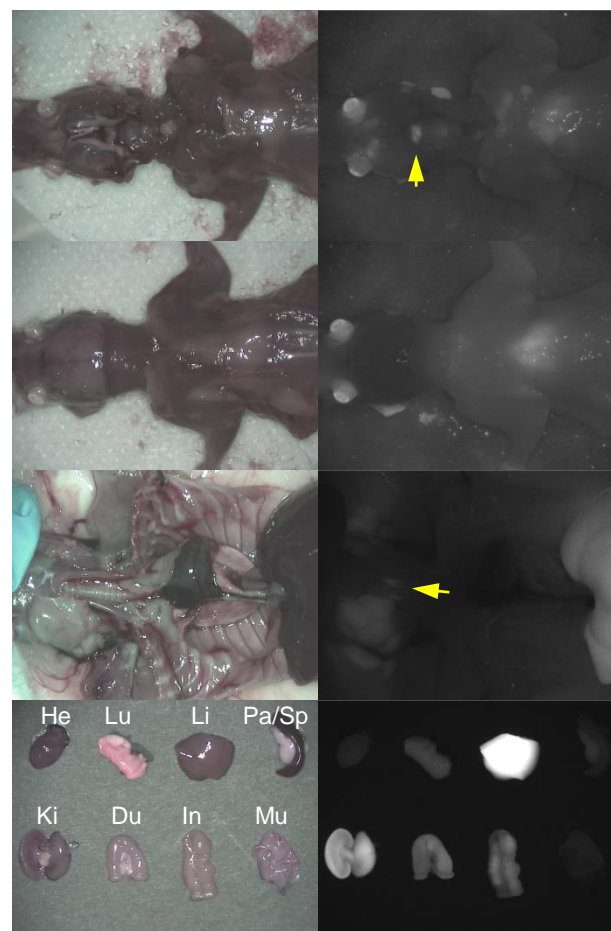
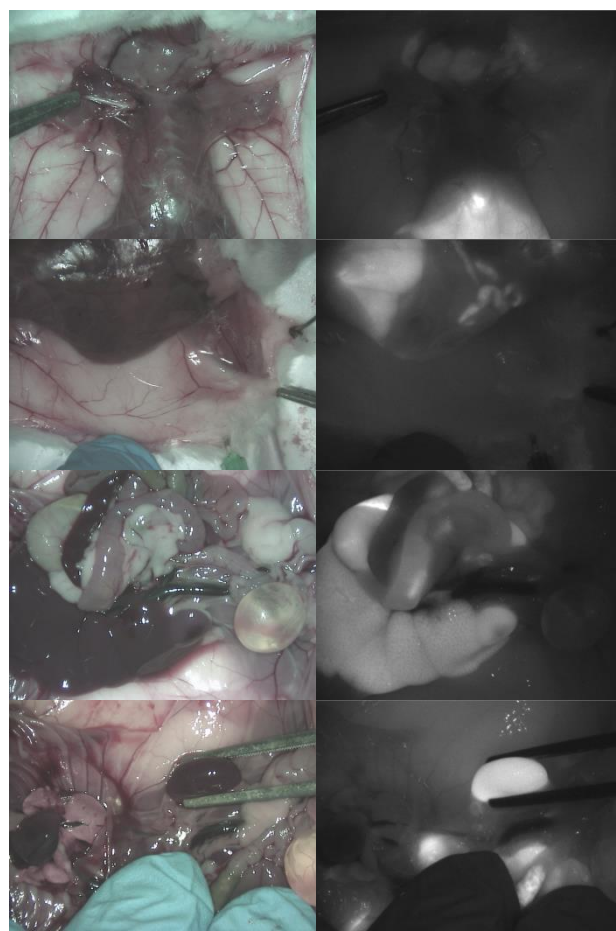
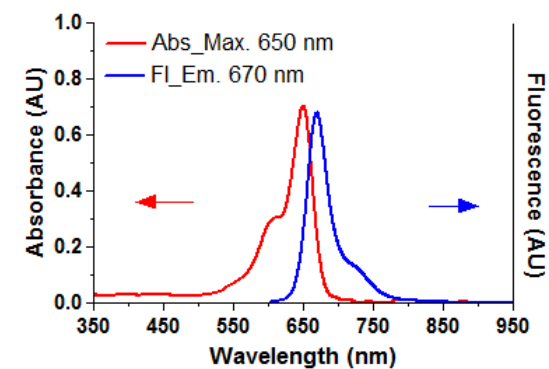
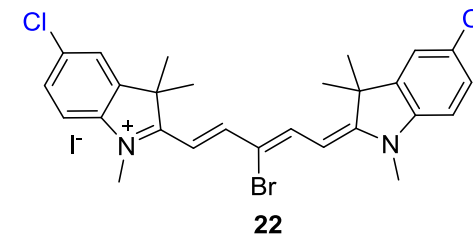
ERIC_35_HENARY-ACCU_02-01-2013_ESI-POS 113 (2.254) AM (Cen,2, 80.00, Ar,5000.0,556.28,0.70); Sm (SG, 3x3.00); Cm

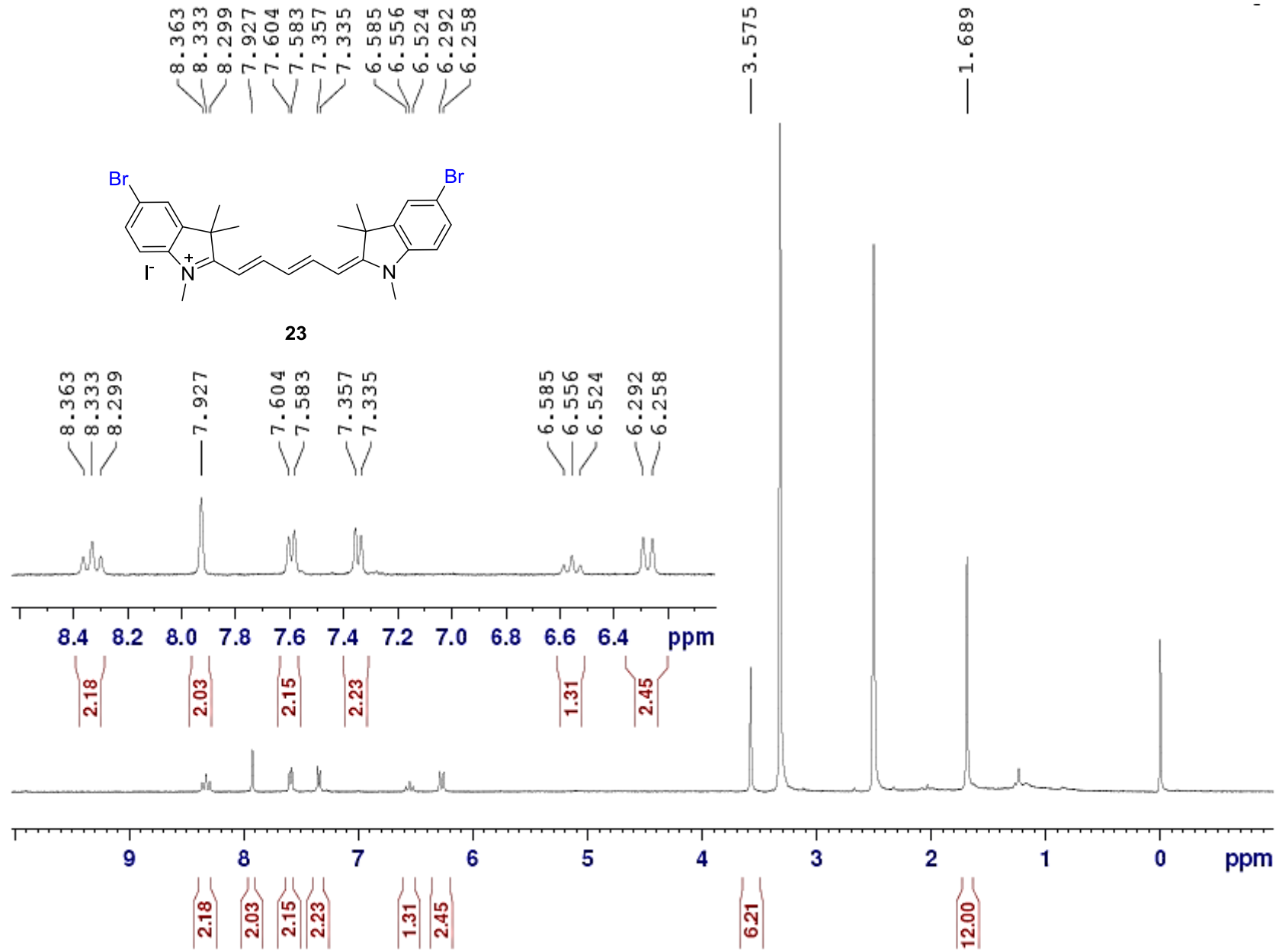
1.29e4

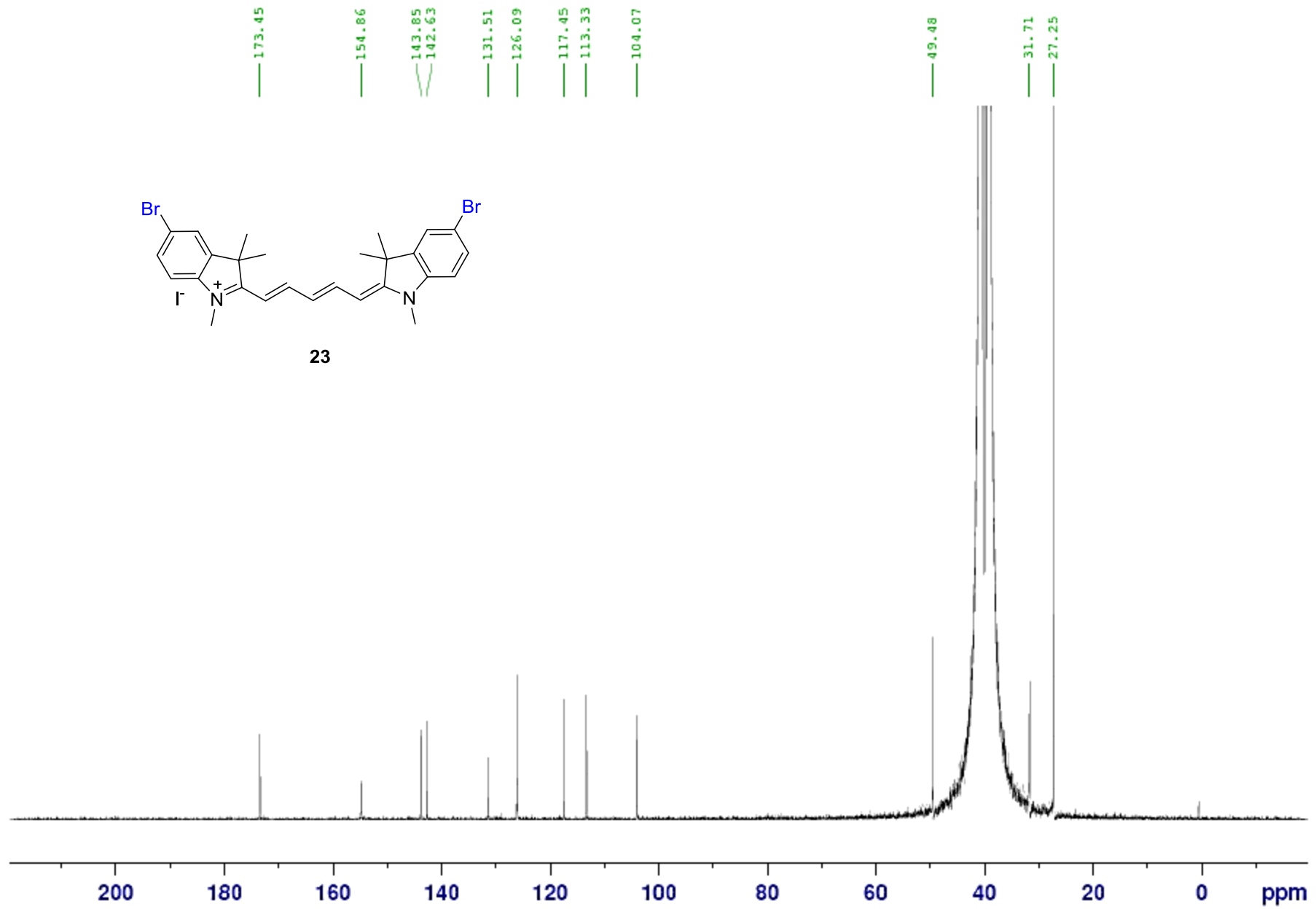


Mass	Calc. Mass	mDa	PPM	DBE	i-FIT	Formula
529.0810	529.0813	-0.3	-0.6	13.5	1.4	C27 H28 N2 Cl2 Br

BioD result of Compound 22										
Endocrine Gland	Salivary		Adrenal		Thyroid		Pituitary		Mammary	
	+		+		+		+		-	
Lymph node	Neck		Axillary		Groin		Lumbar		Kidney	
	-		-		-		+		-	
Organ & Tissue	He	Lu	Li	Pa/Sp	Ki	Du	In	Mu	Brain (CP)	Brown fat
	-	+	+++	+/-	++	+	+	-	-	-

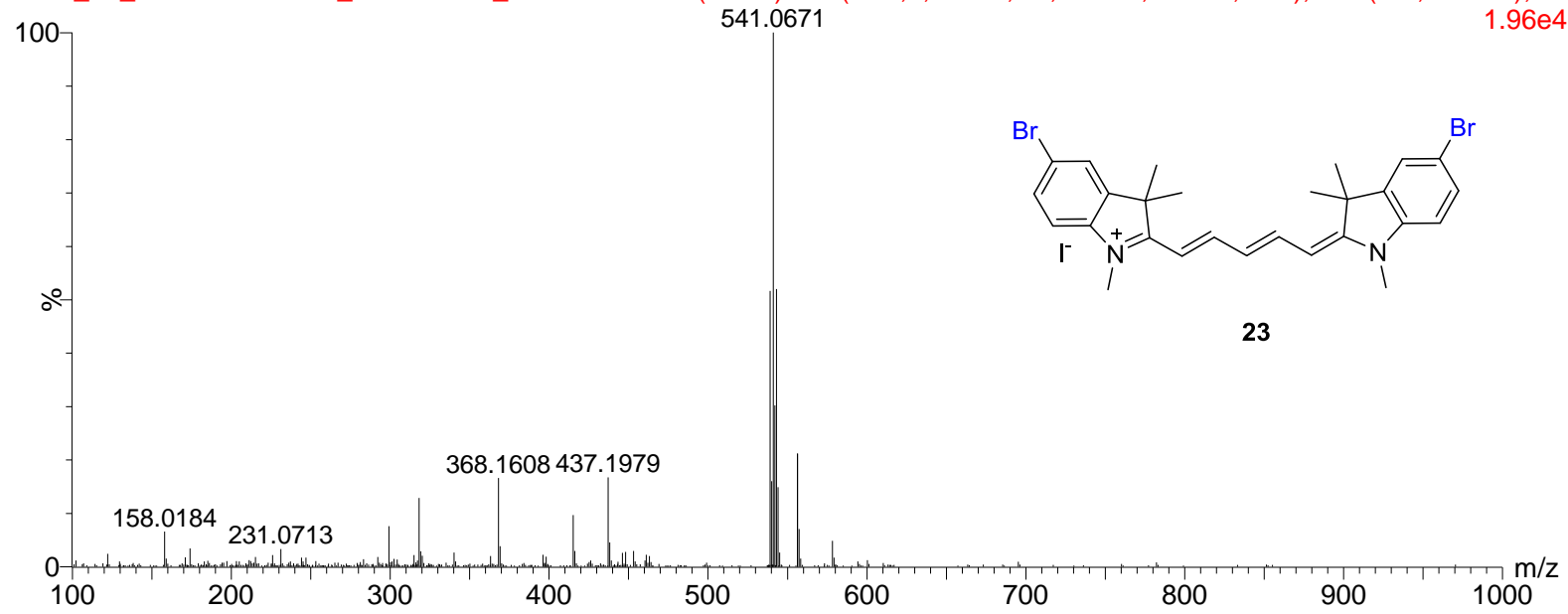






diluted in 80%MeOH

17:10:50 01-Feb-2013

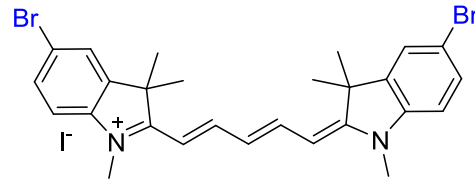
ERIC_24_HENARY-ACCU_02-01-2013_ESI-POS01 22 (0.437) AM (Cen,2, 80.00, Ar,5000.0,556.28,0.70); Sm (SG, 3x3.00); Cn
1.96e4

Mass	Calc. Mass	mDa	PPM	DBE	i-FIT	Formula
539.0695	539.0697	-0.2	-0.4	13.5	2.8	C27 H29 N2 Br2

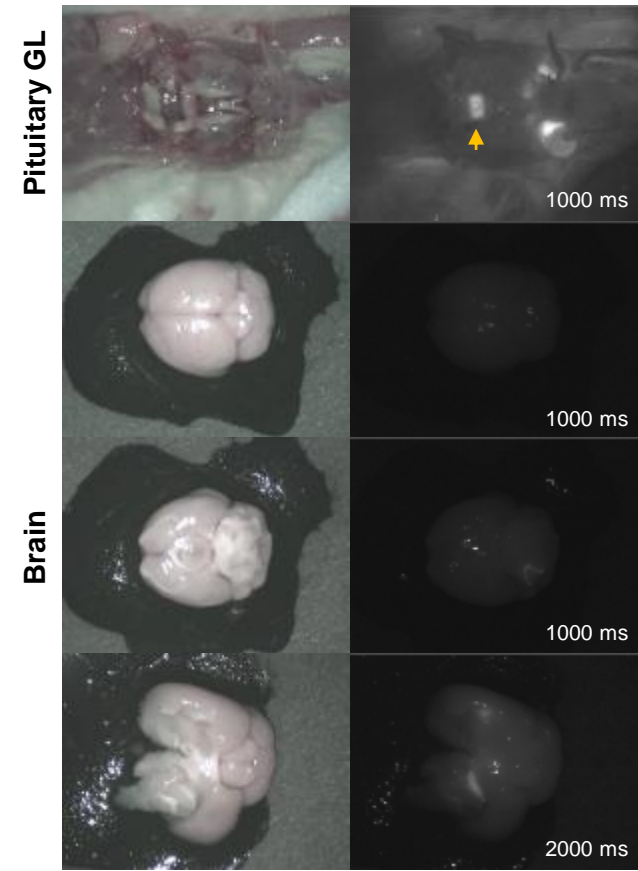
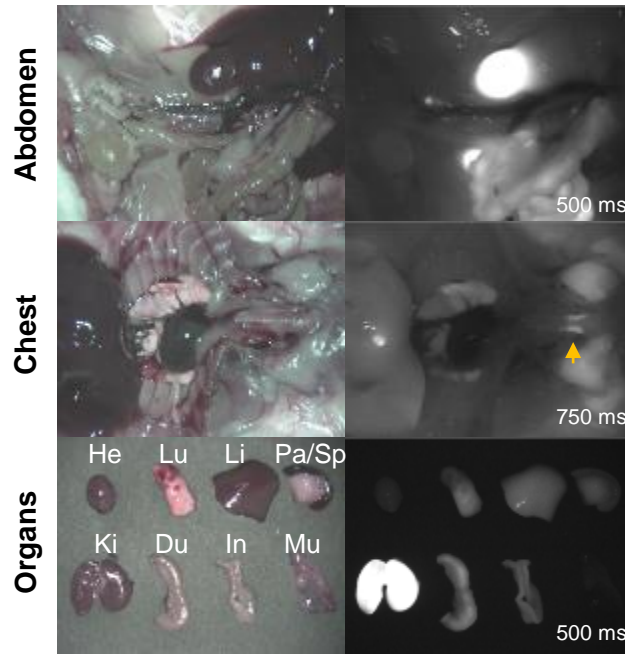
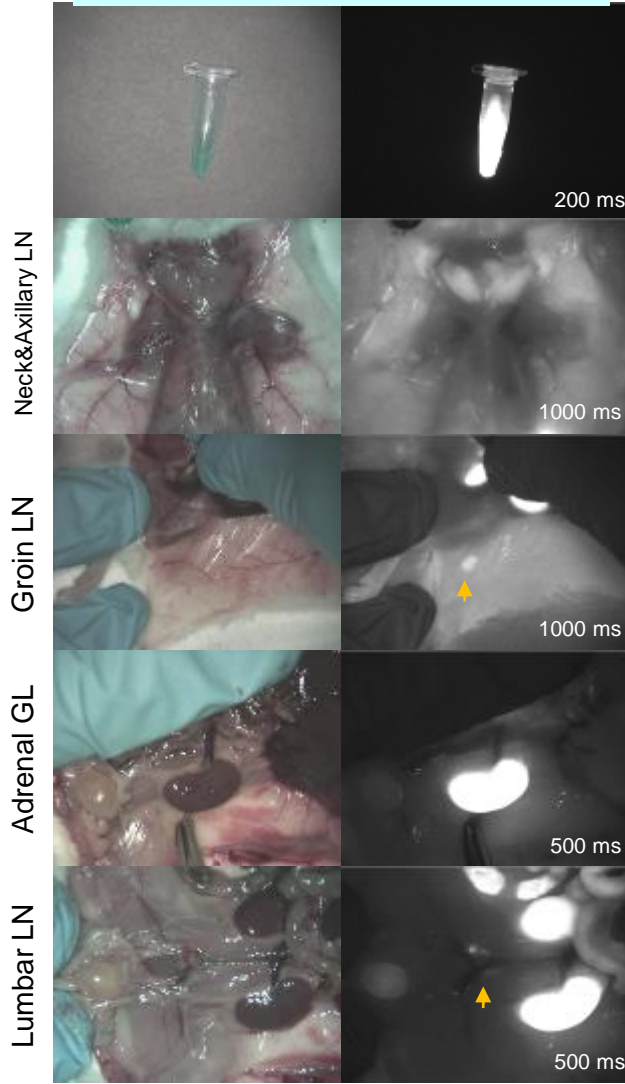
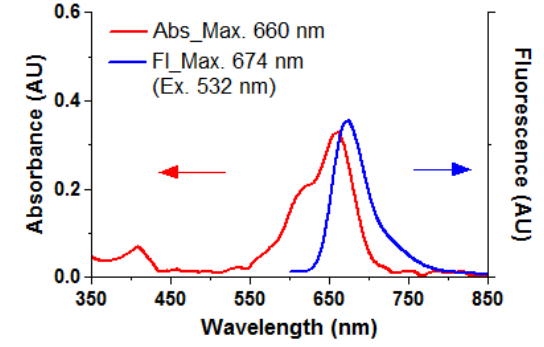
BioD of Compound 23

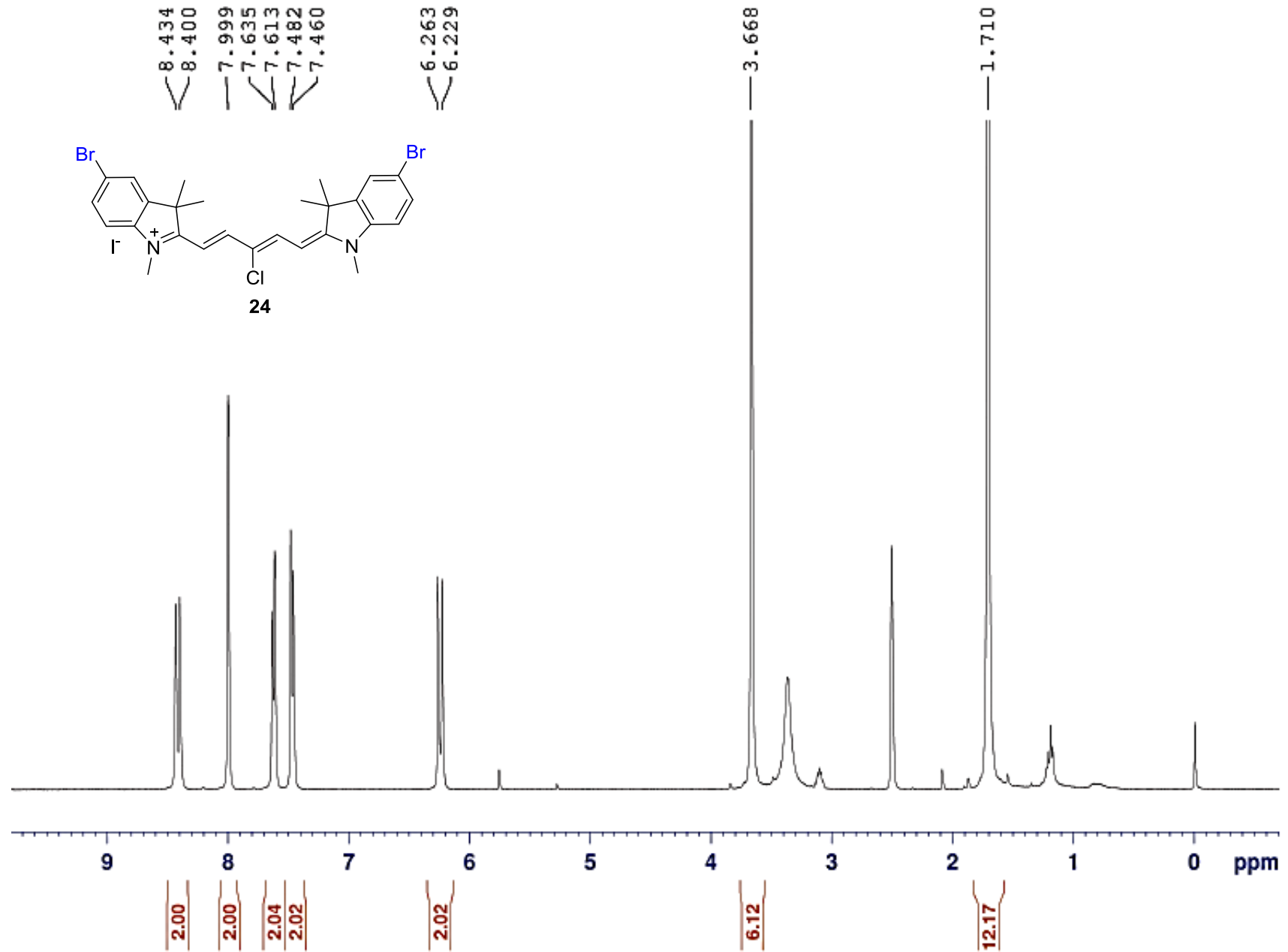
(4h post-injection)

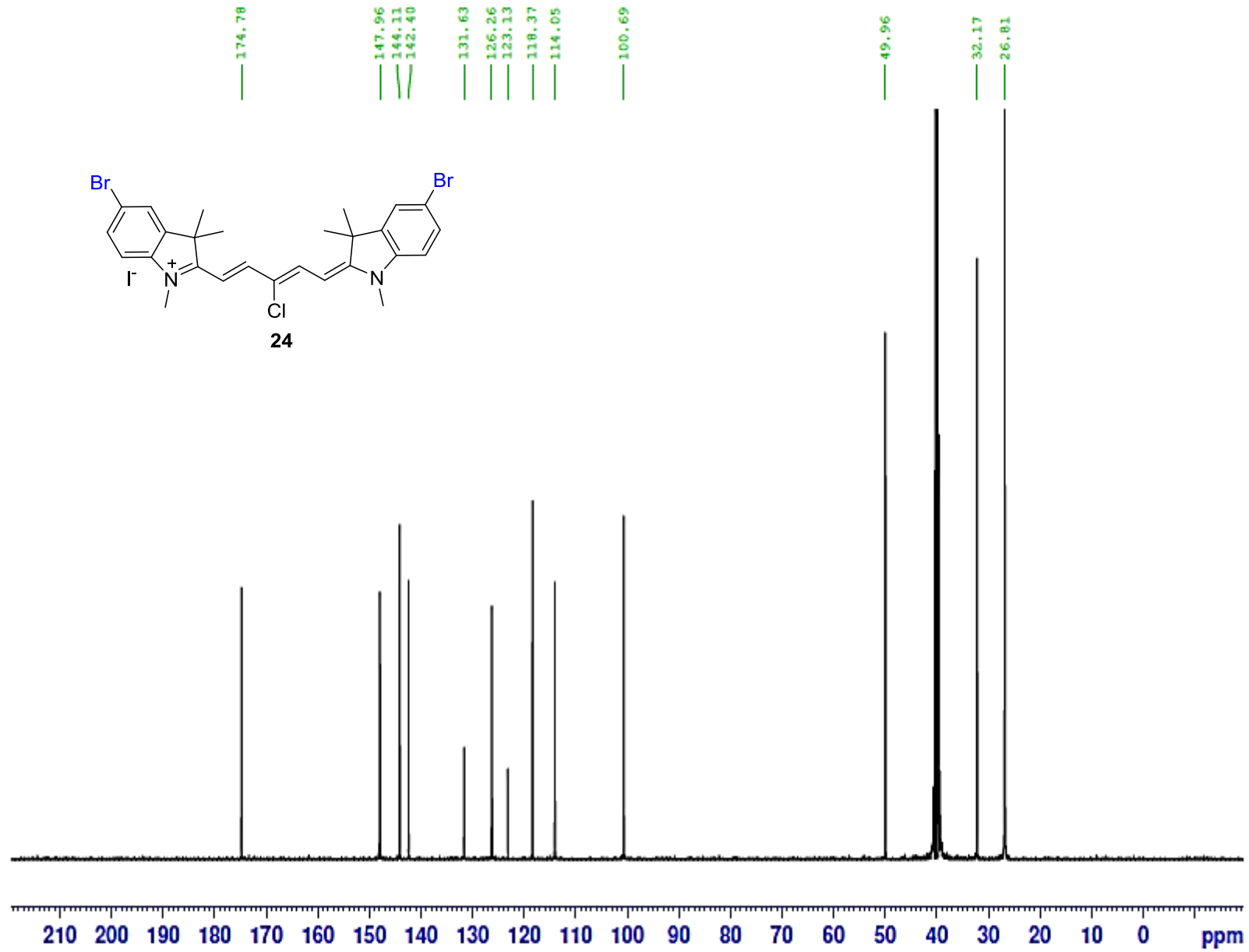
Injection solution: 30% FBS in saline
 Animal: CD-1 mouse
 Injection route: Penial vein
 Dose: 25 nmol (250 μ M x 100 μ L)

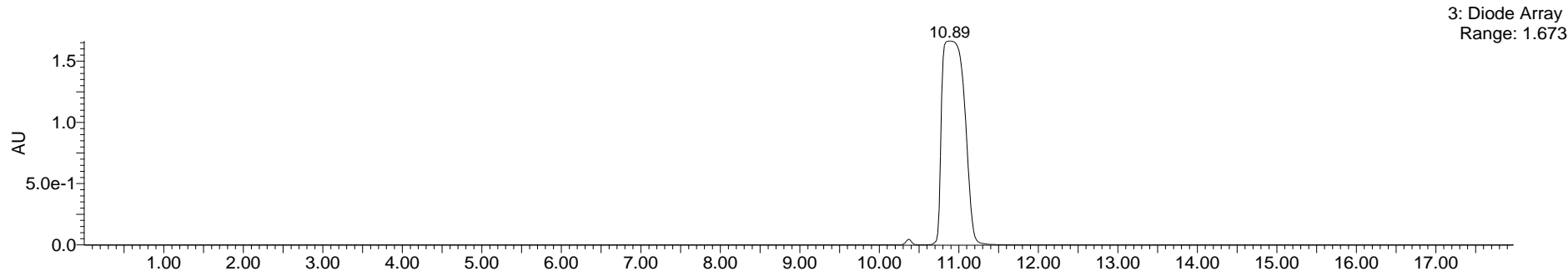


23





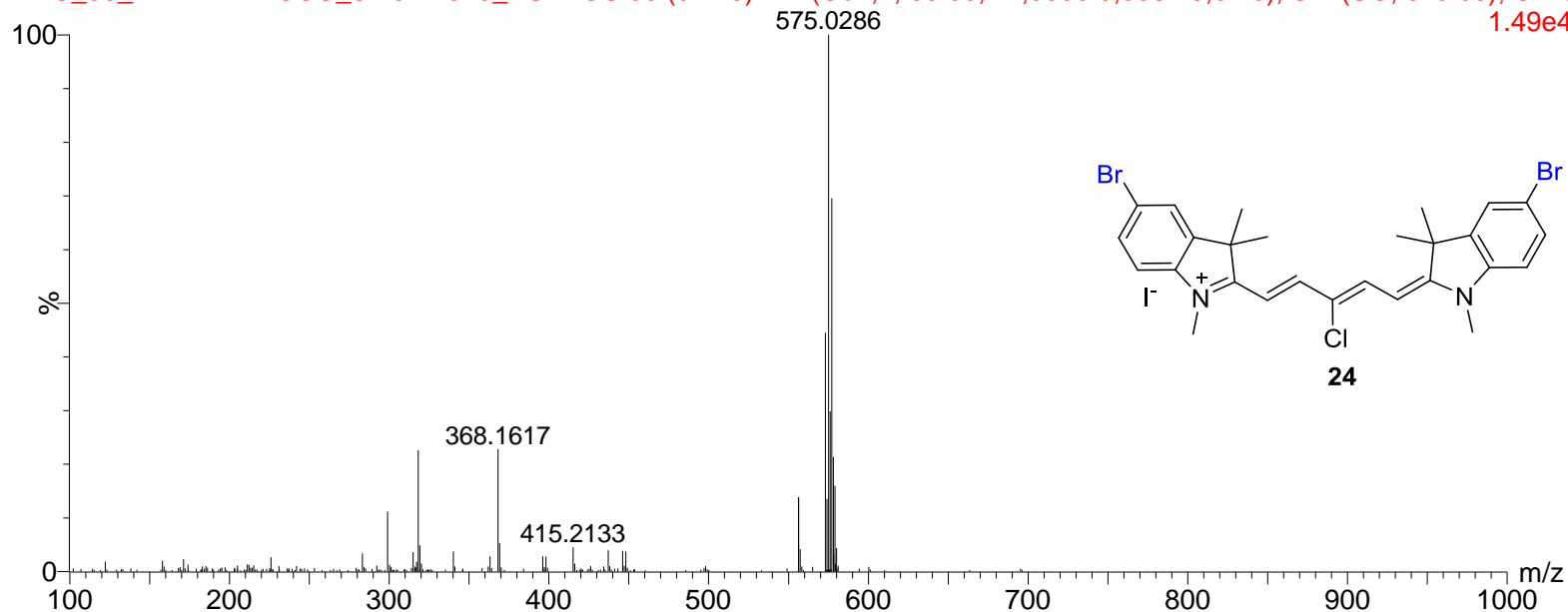




diluted in 80%MeOH

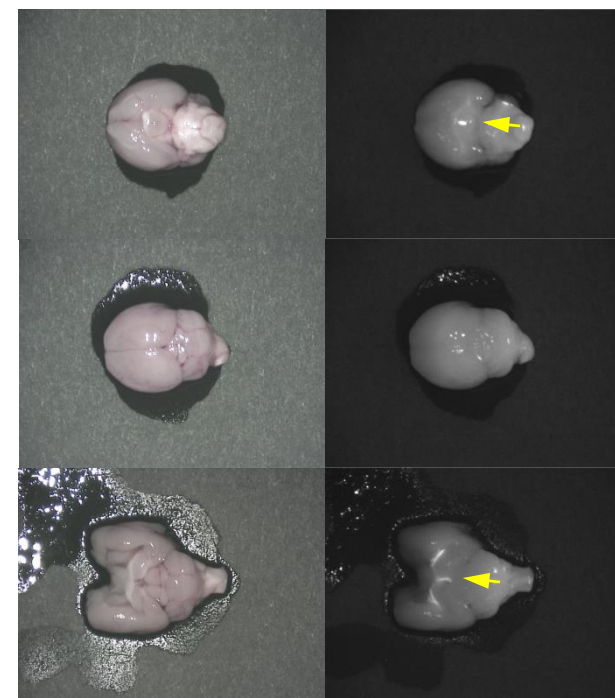
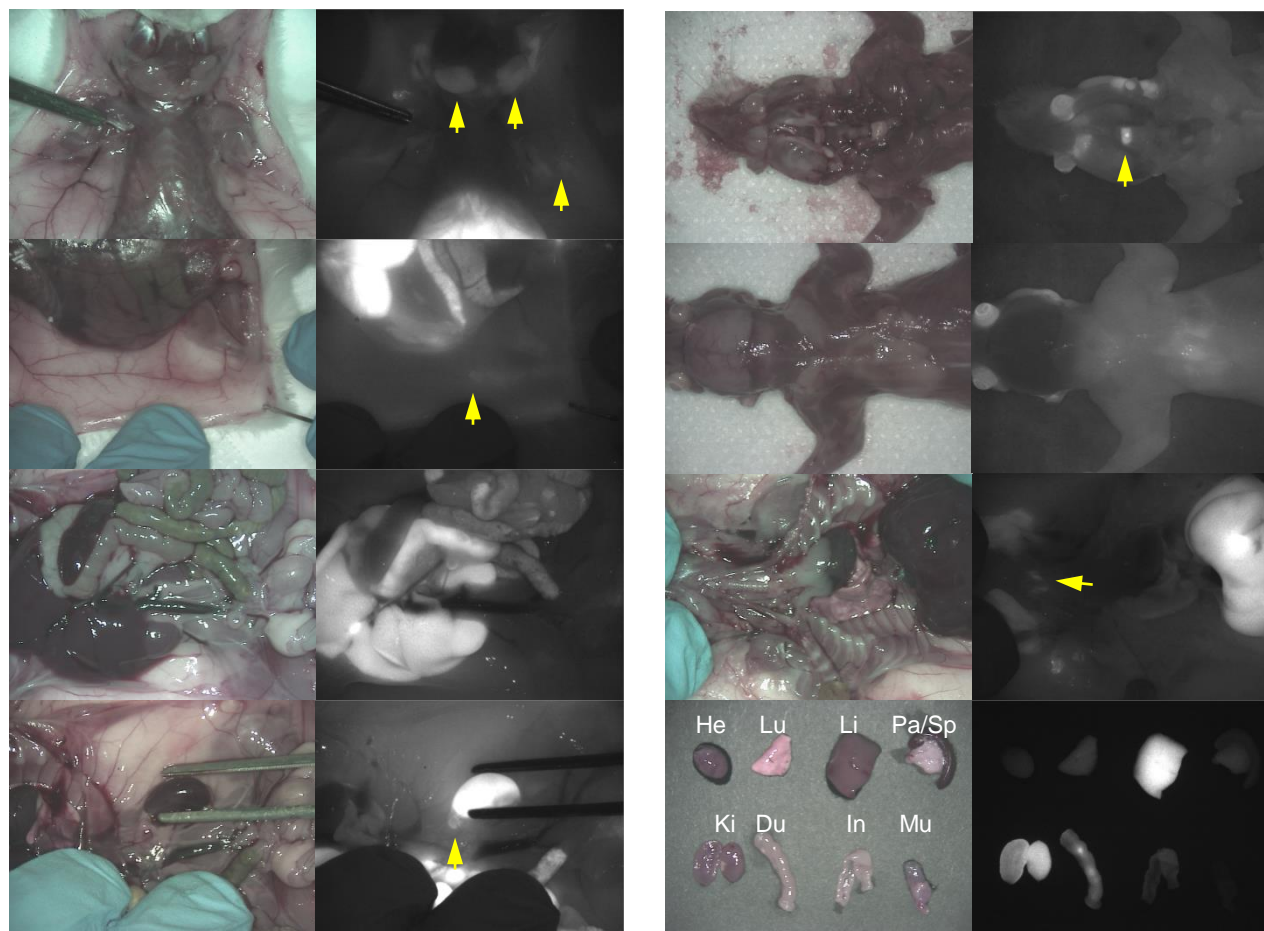
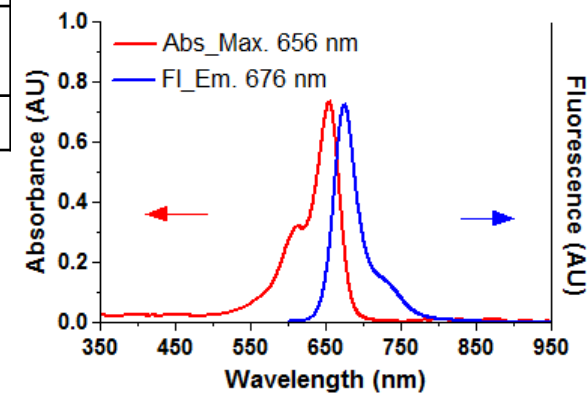
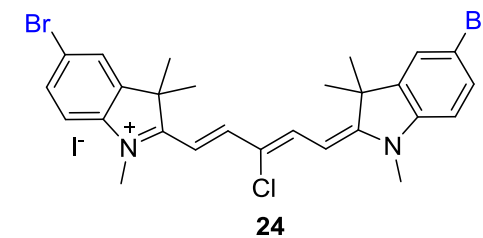
16:40:08 01-Feb-2013

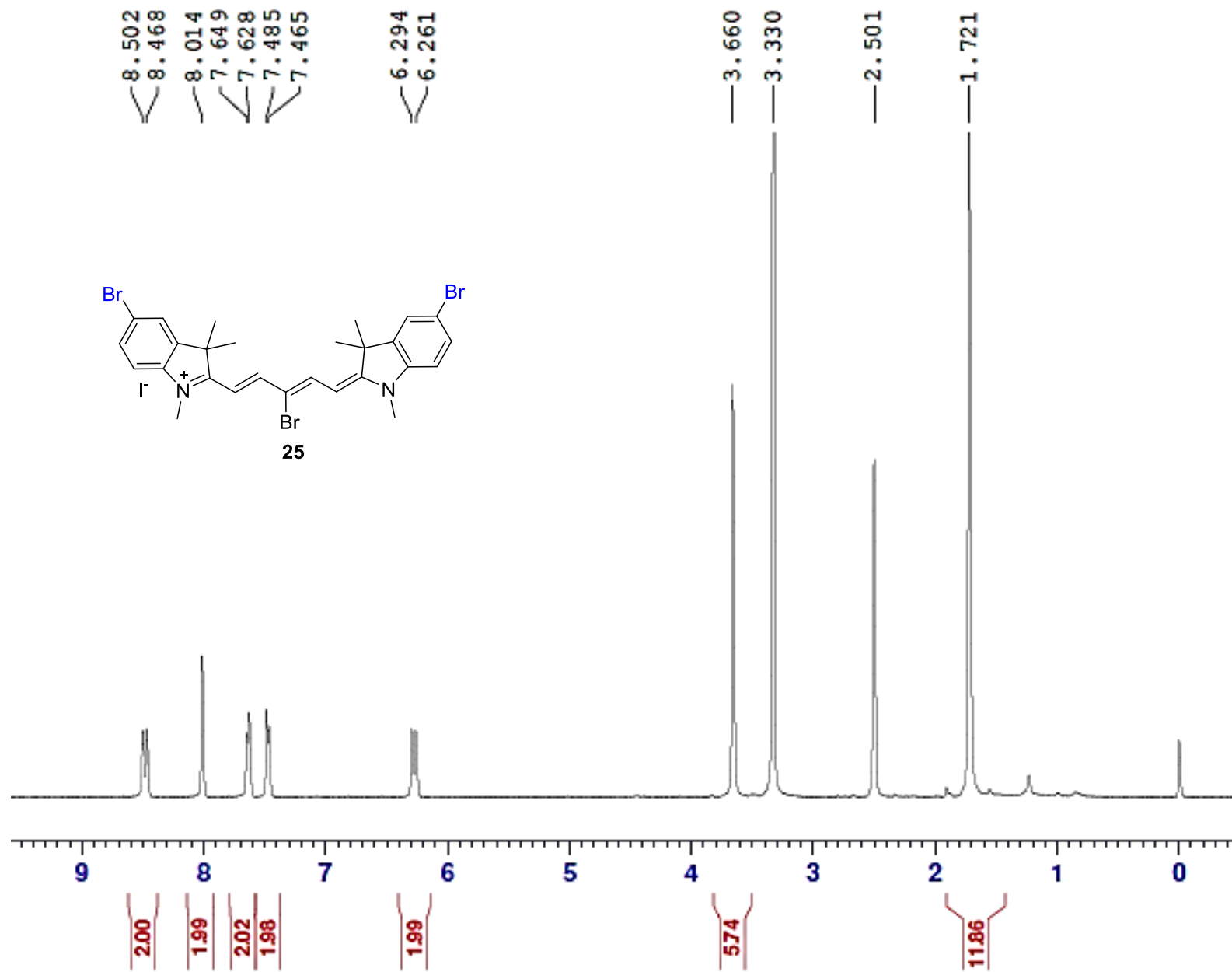
ERIC_30_HENARY-ACCU_02-01-2013_ESI-POS 39 (0.779) AM (Cen,2, 80.00, Ar,5000.0,556.28,0.70); Sm (SG, 3x3.00); Cm (:
1.49e4

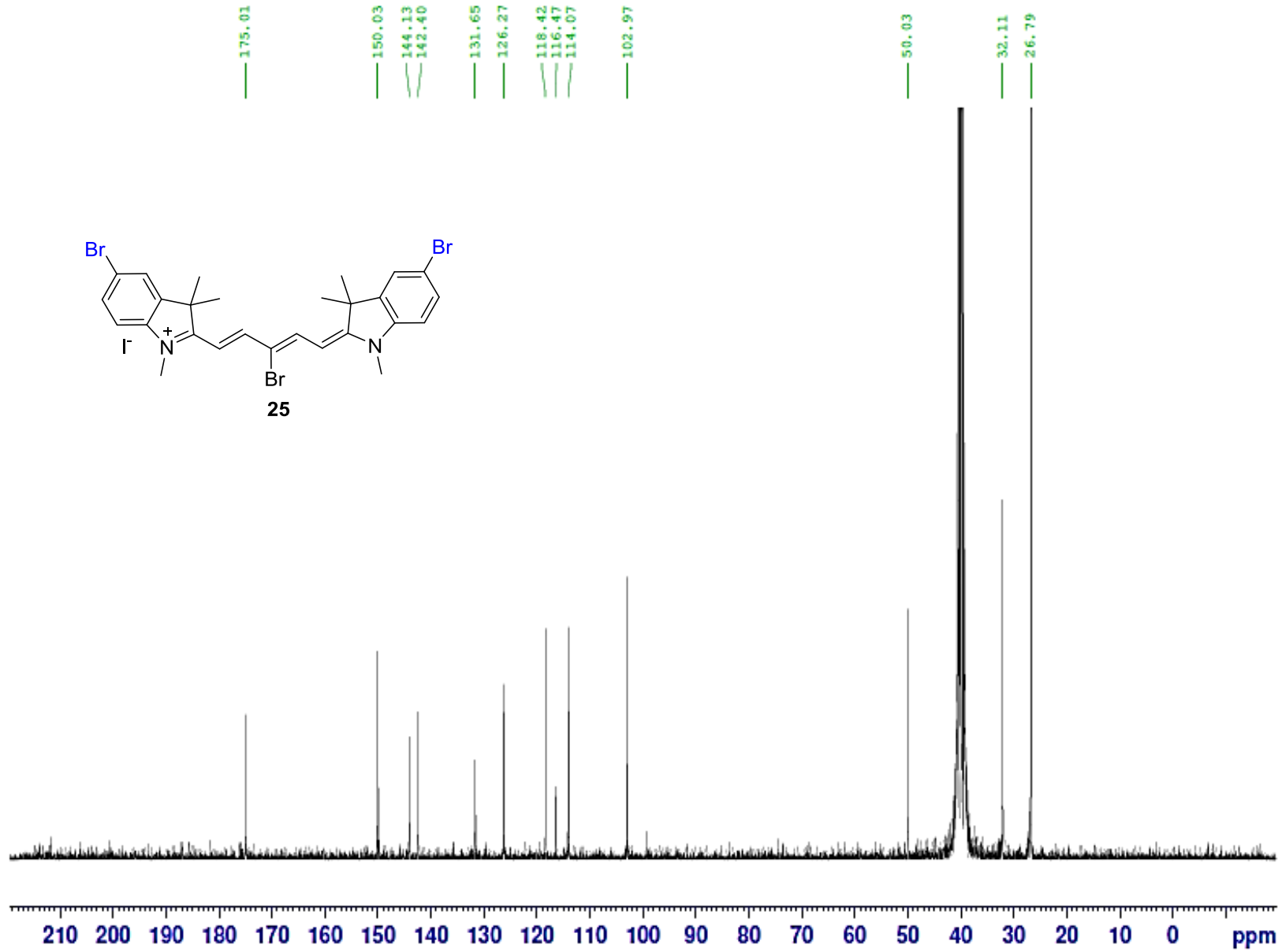


Mass	Calc. Mass	mDa	PPM	DBE	i-FIT	Formula
573.0316	573.0308	0.8	1.4	13.5	2.2	C ₂₇ H ₂₈ N ₂ Cl Br ₂

BioD result of Compound 24										
Endocrine Gland	Salivary		Adrenal		Thyroid		Pituitary		Mammary	
	++		+		++		++		-	
Lymph node	Neck		Axillary		Groin		Lumbar		Kidney	
	-		+		+		-		-	
Organ & Tissue	He	Lu	Li	Pa/Sp	Ki	Du	In	Mu	Brain (CP)	Brown fat
	-	+	+++	+/-	+++	+	+	-	+	-

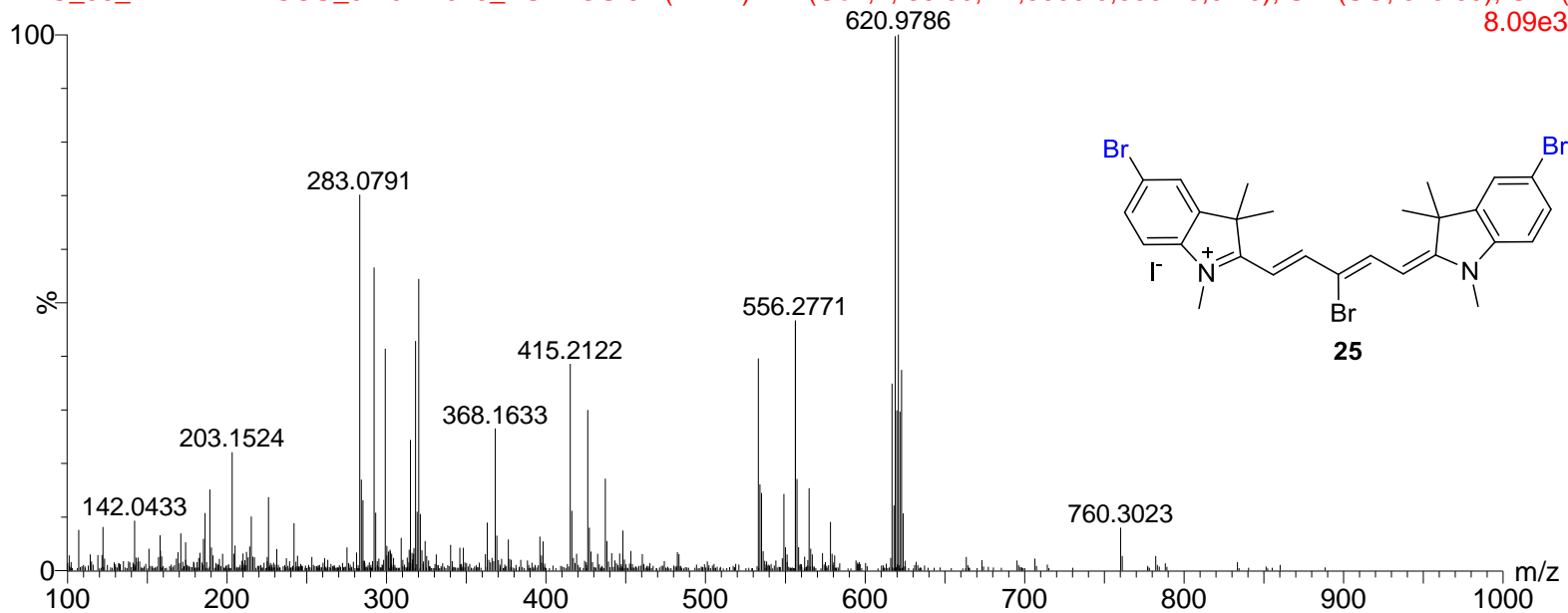






diluted in 80%MeOH

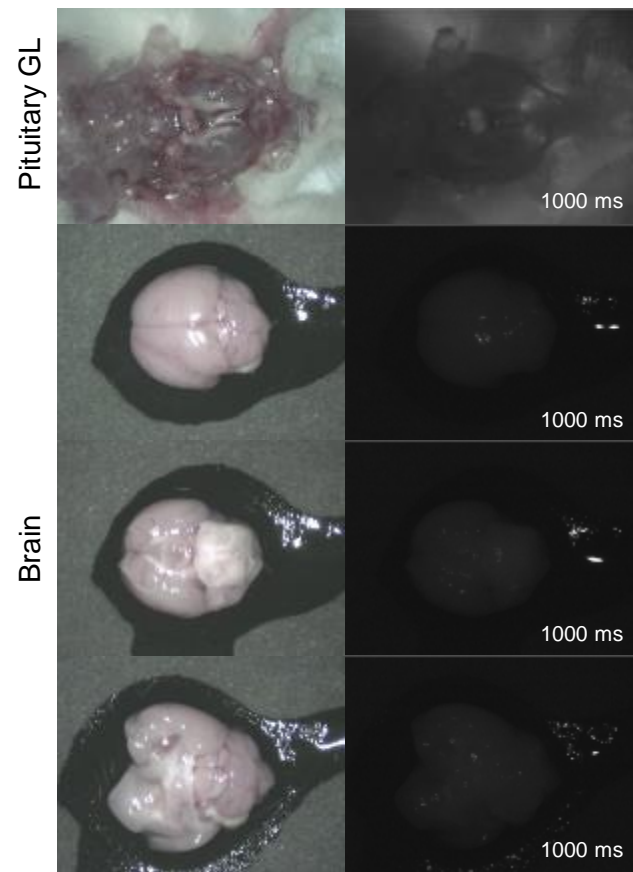
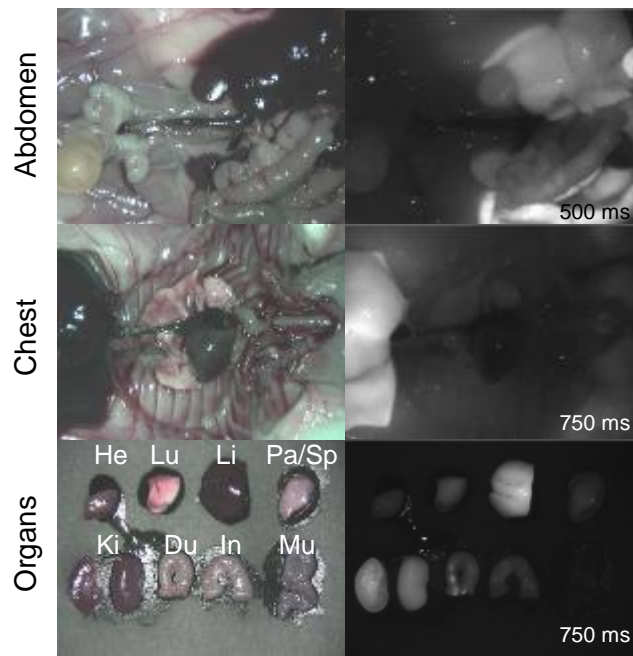
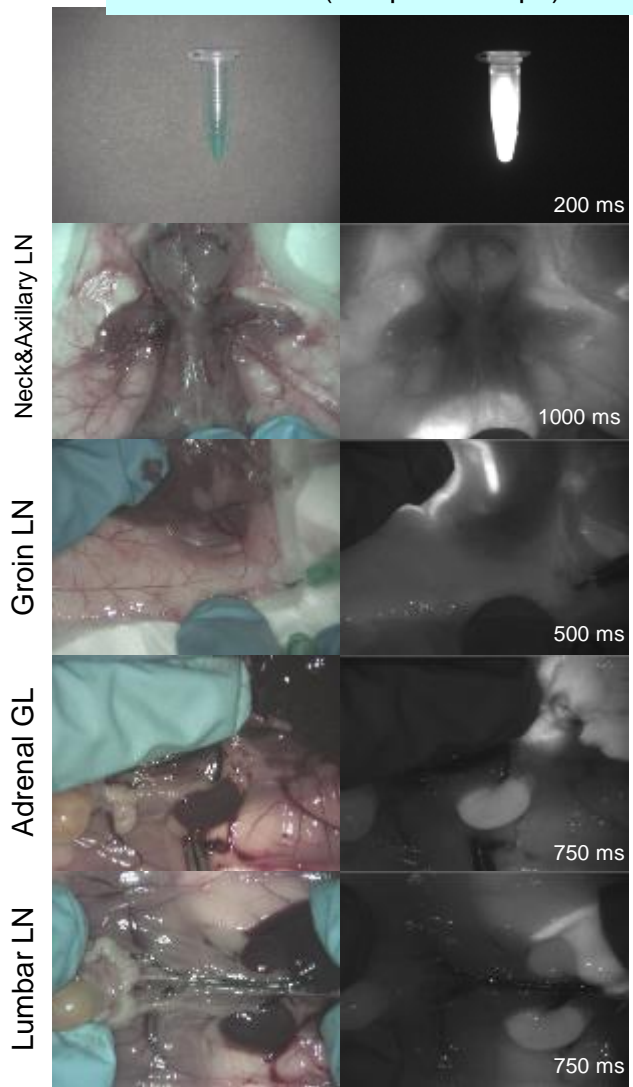
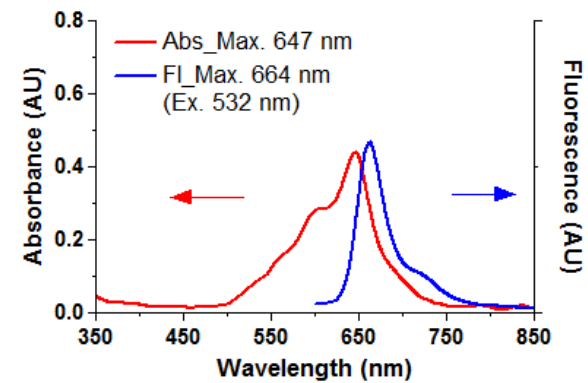
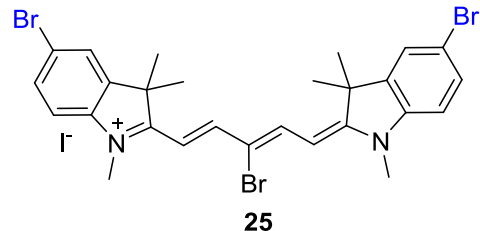
15:51:38 01-Feb-2013

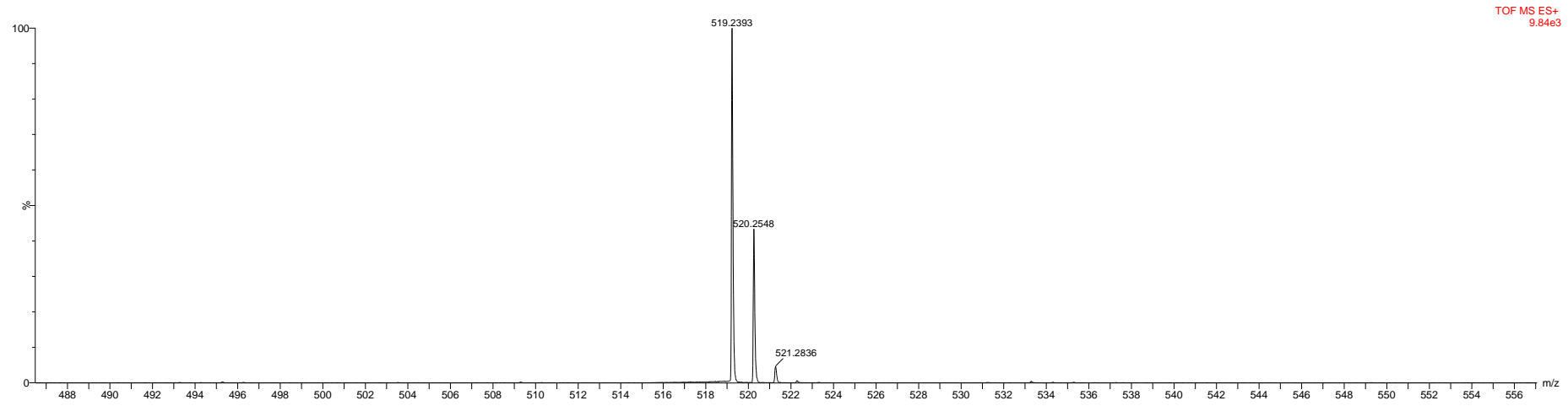
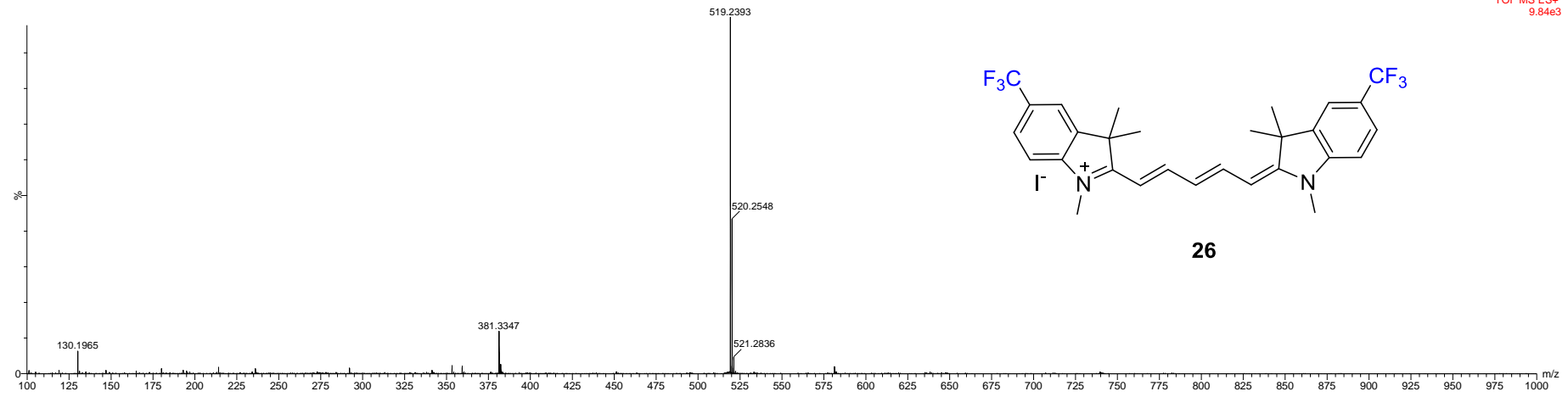
ERIC_36_HENARY-ACCU_02-01-2013_ESI-POS 64 (1.277) AM (Cen,2, 80.00, Ar,5000.0,556.28,0.70); Sm (SG, 3x3.00); Cm (I
8.09e3

Mass	Calc. Mass	mDa	PPM	DBE	i-FIT	Formula
616.9814	616.9803	1.1	1.8	13.5	9.0	C27 H28 N2 Br3

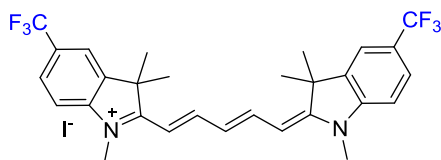
BioD result of Compound 25 (4h post-injection)

Injection solution: 30% FBS in saline
 Animal: CD-1 mouse
 Injection route: Penial vein
 Dose: 25 nmol (250 μM x 100 μL)



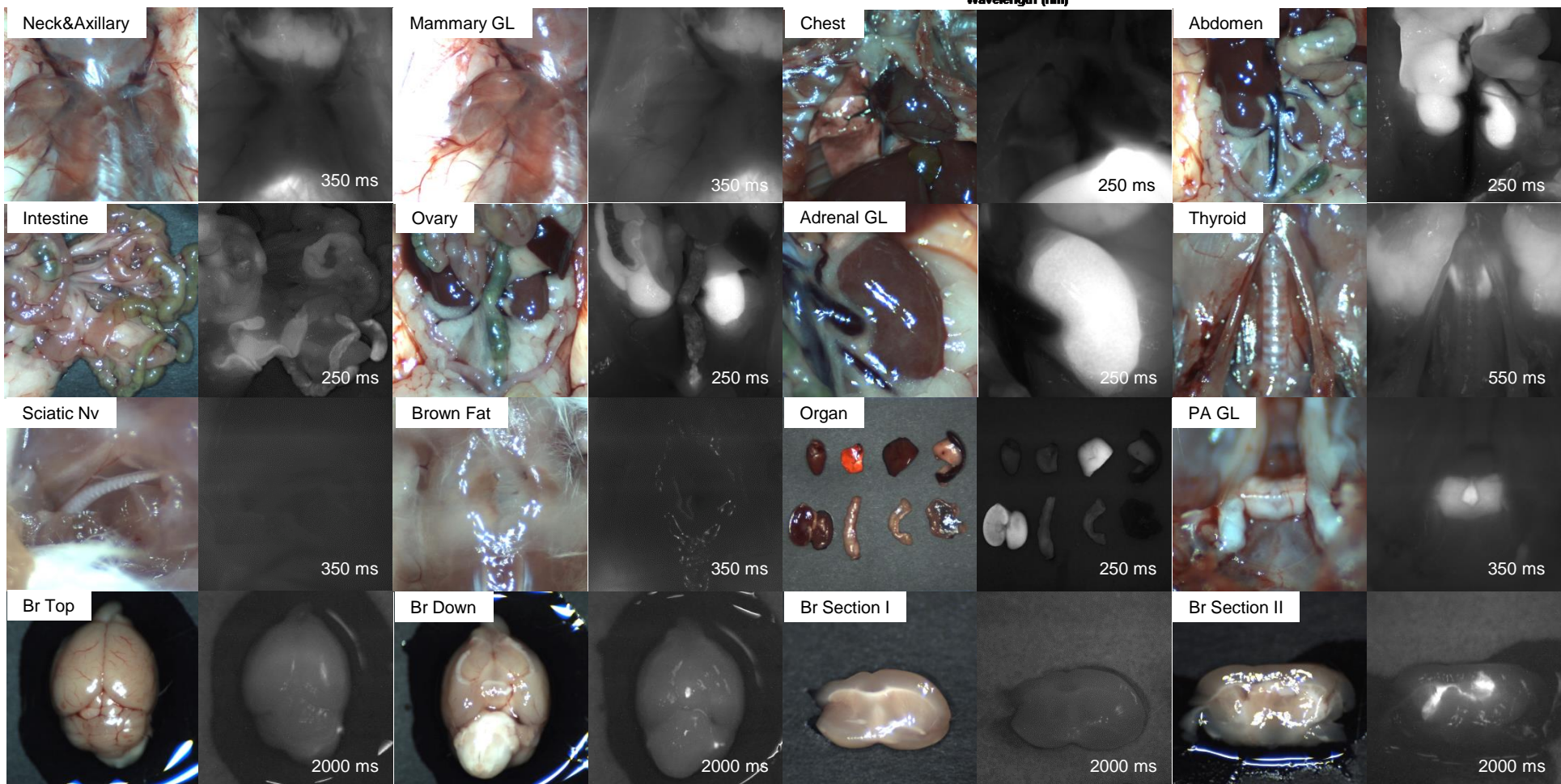
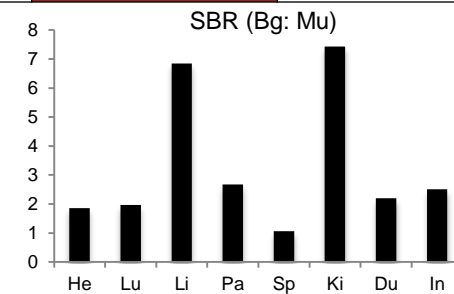
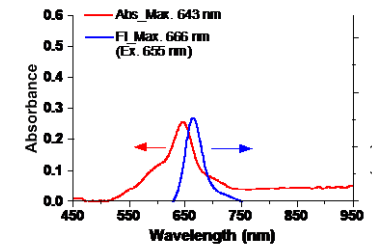


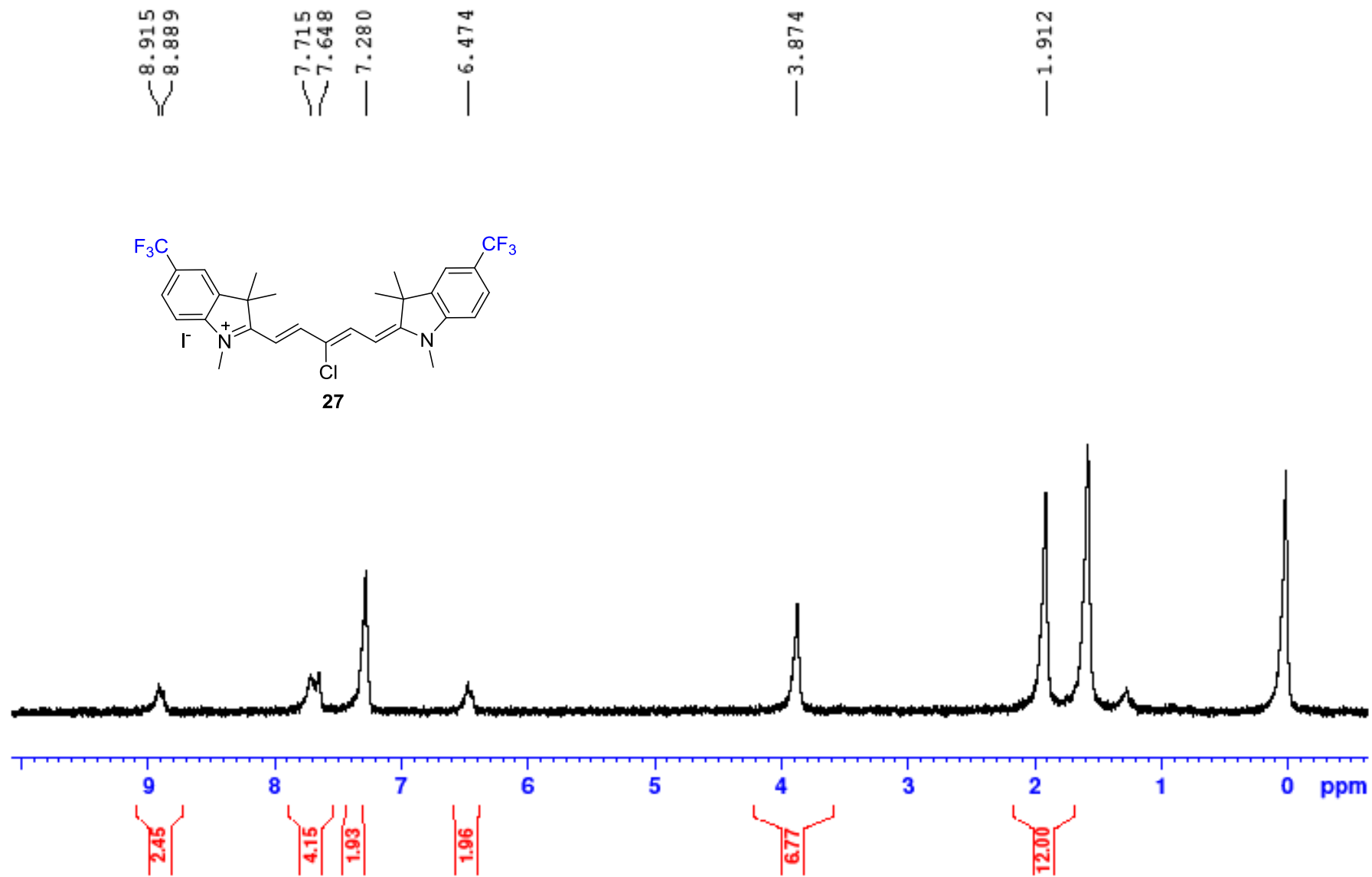
FLARE Parameters				Study Info.				Measurement	
Model	K-FLARE™ Zoom	Channel	700 nm	Chemical	26	Formulation	C-D5W	FOV	5 / 3.3 / 2 cm
Fluence rate	0.54 mW at 660 nm	Filter	660-20/673lpxr/Dual BP (710-50 and 781lp)	Animal	CD-1	Inj. route	R.O.	ROI	13
Working Dt.	9 in	Bit depth	16	Gender	Female	Anesthesia	K+X	Acquisition time	1 h post inj.
Gain	12 dB	Matrix size	512x512	Dose	100 nmol	Body Weight	25-30 g	Exp. Time (msec)	L, M, H

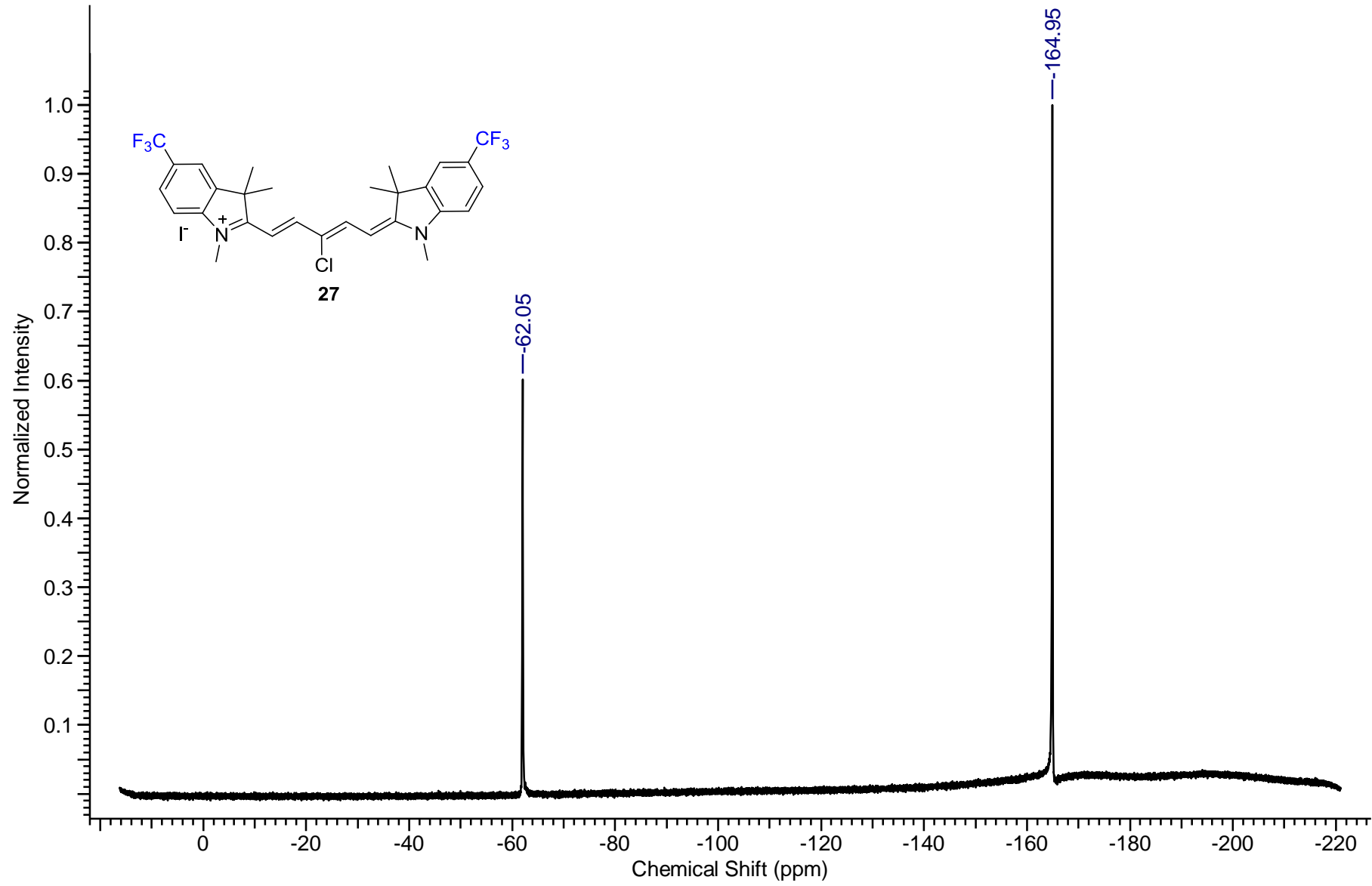


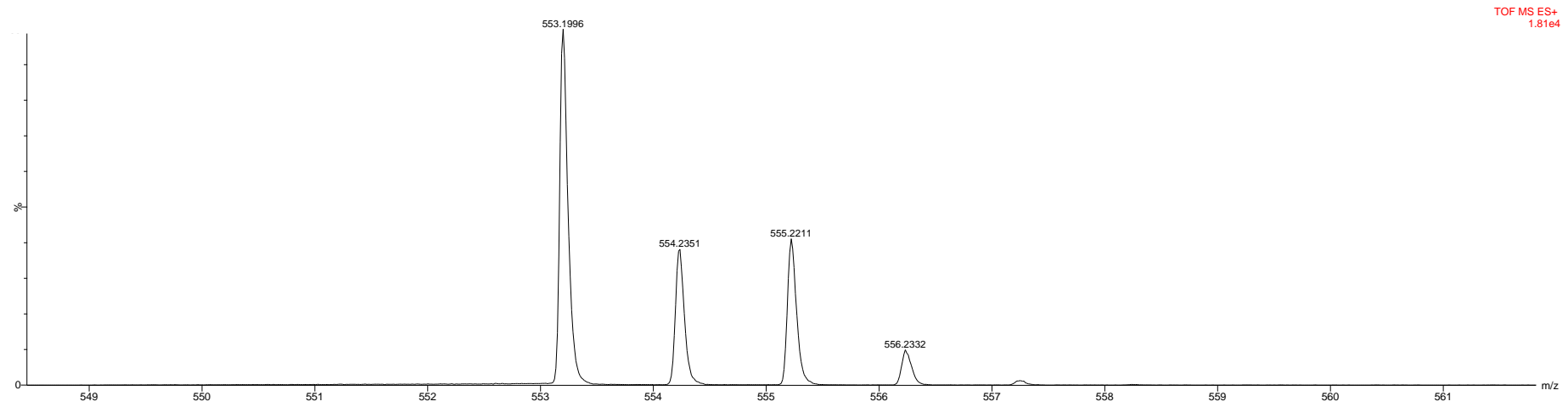
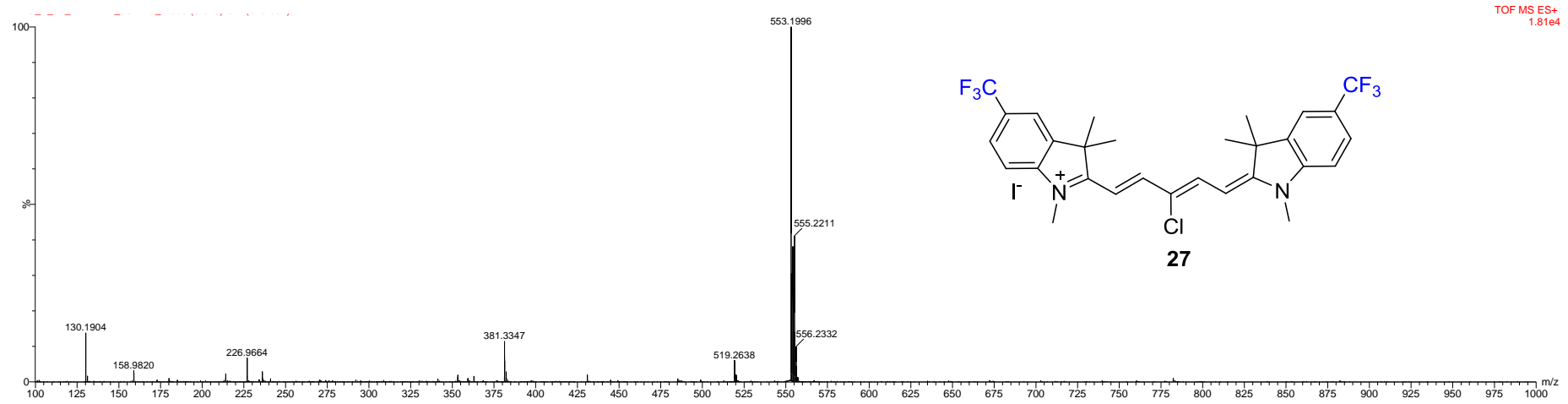
26

Exact Mass	519.22
LogD at 7.4	5.31
TPSA	6.25
HBD	0.00
HBA	1.00
Total Charge	1.00
Refractivity	151.00
Rotatable Bond	5.00
SB pKa	1.39
SA pKa	0.00

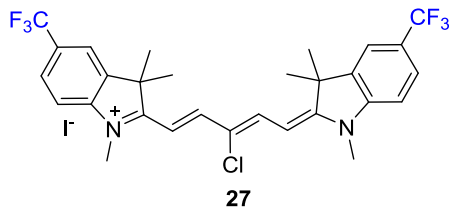




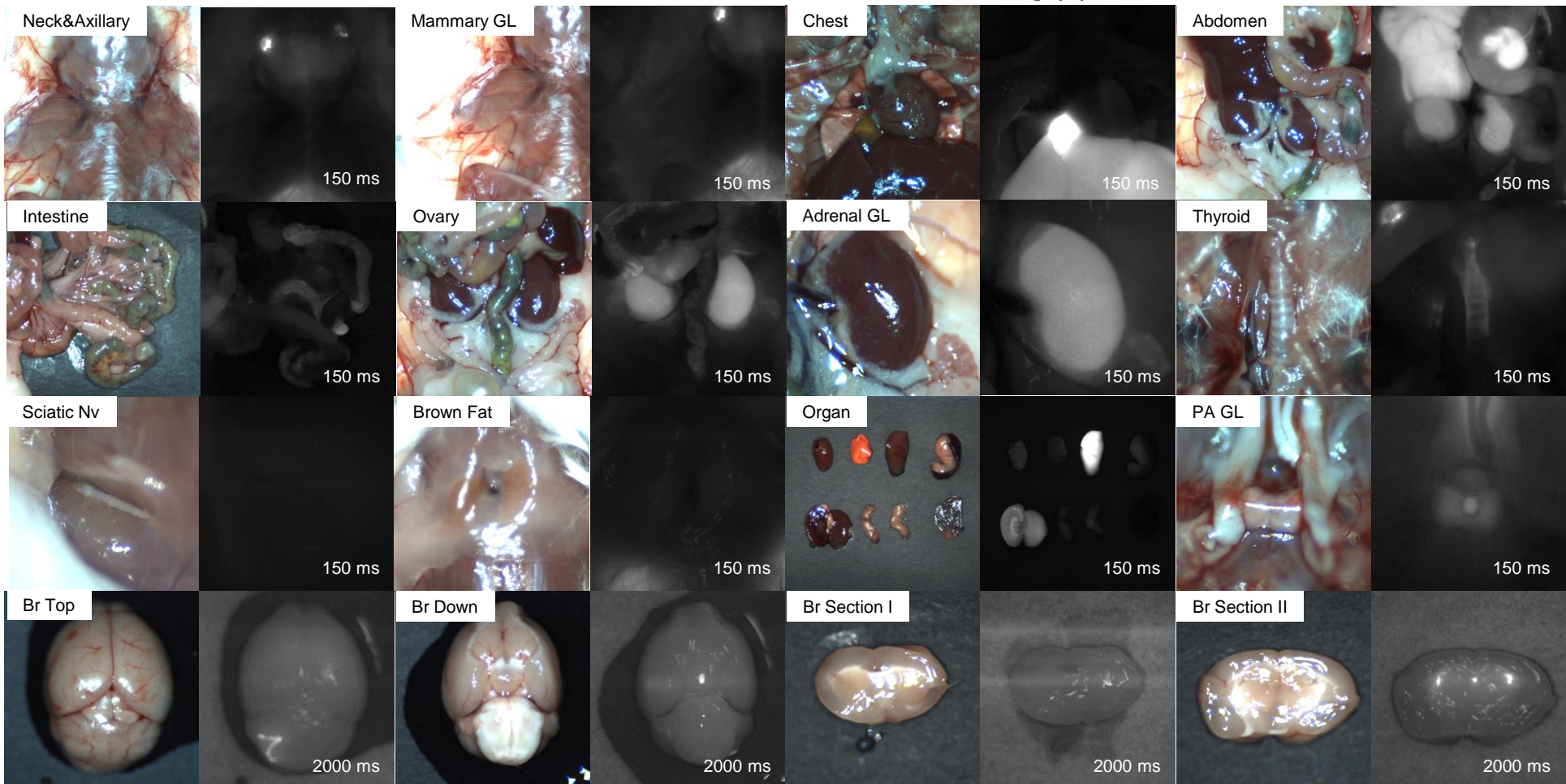
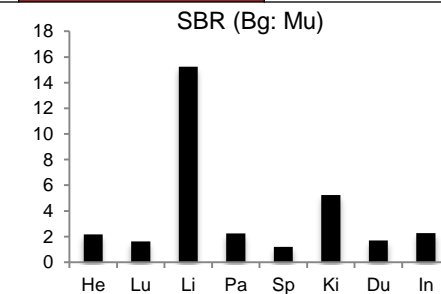
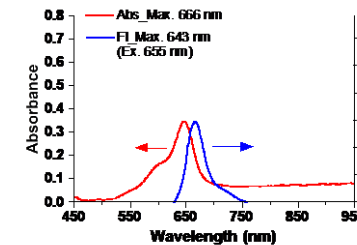


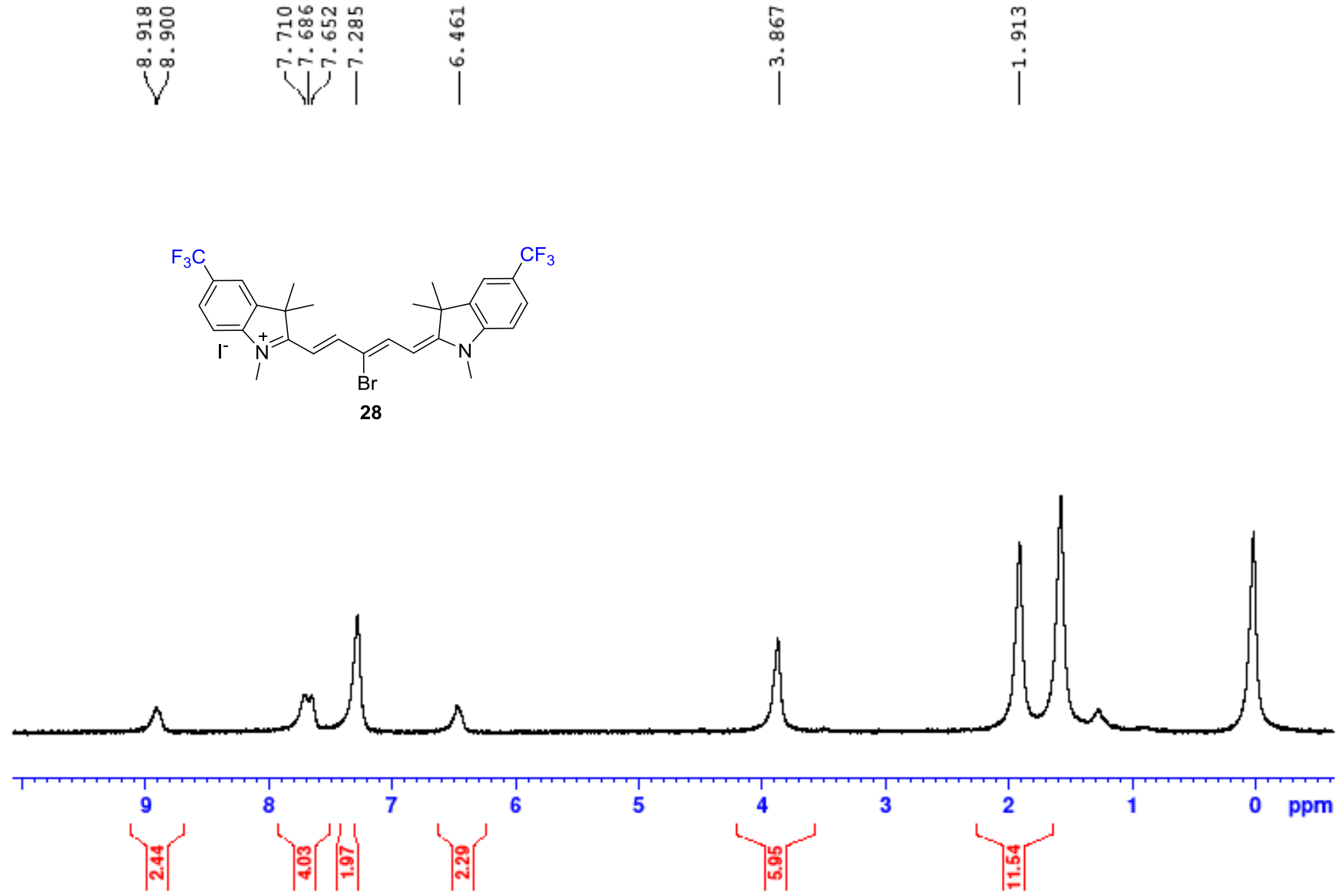


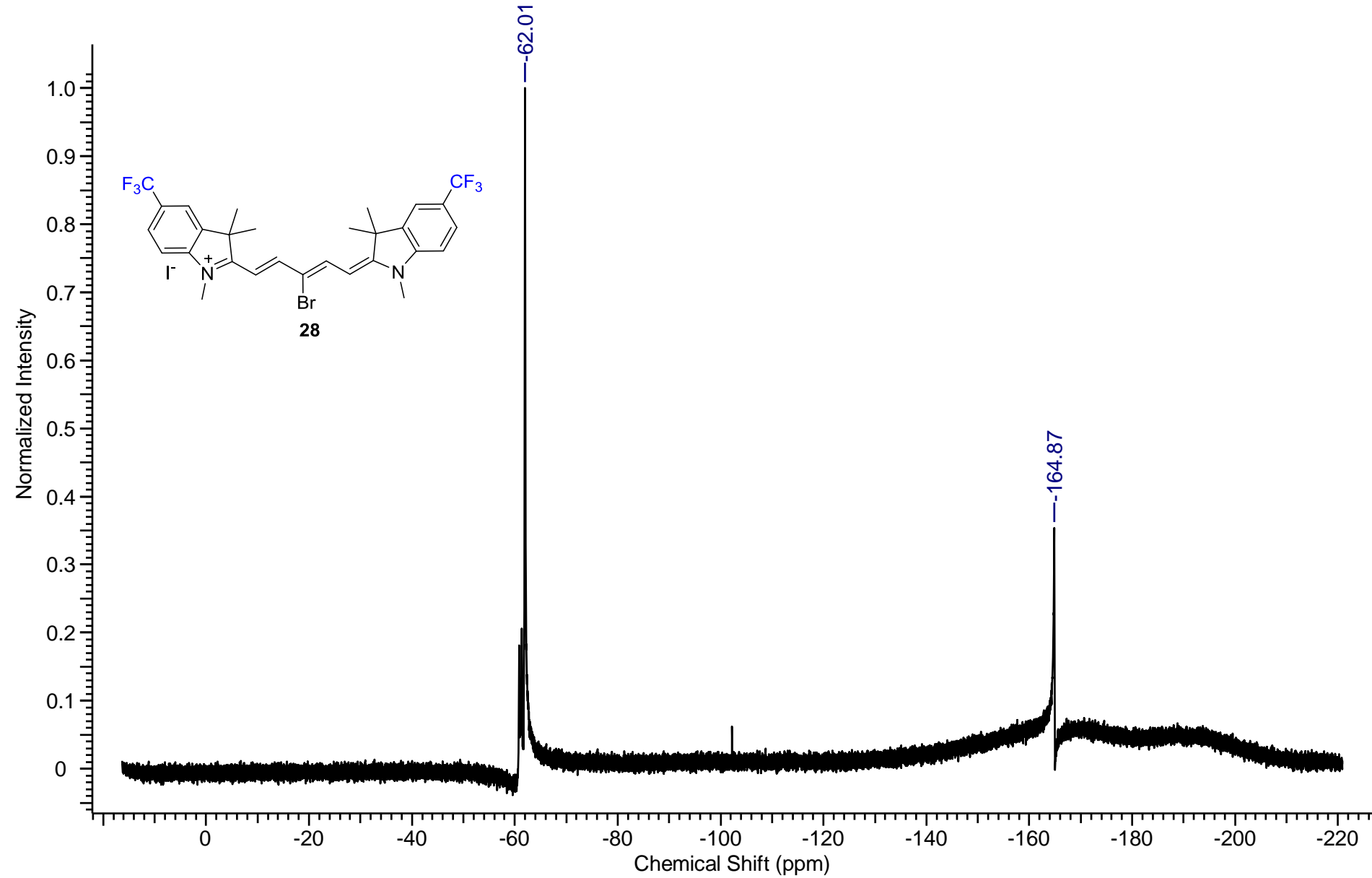
FLARE Parameters				Study Info.				Measurement	
Model	K-FLARE™ Zoom	Channel	700 nm	Chemical	27	Formulation	C-D5W	FOV	5 / 3.3 / 2 cm
Fluence rate	0.54 mW at 660 nm	Filter	660-20/673lpxr/Dual BP (710-50 and 781lp)	Animal	CD-1	Inj. route	R.O.	ROI	13
Working Dt.	9 in	Bit depth	16	Gender	Female	Anesthesia	K+X	Acquisition time	1 h post inj.
Gain	12 dB	Matrix size	512x512	Dose	100 nmol	Body Weight	25-30 g	Exp. Time (msec)	L, M, H

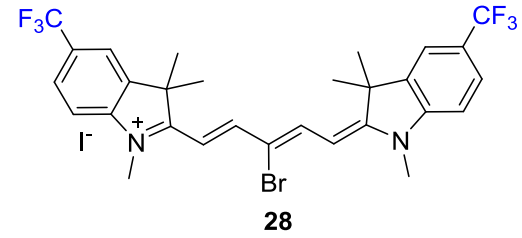
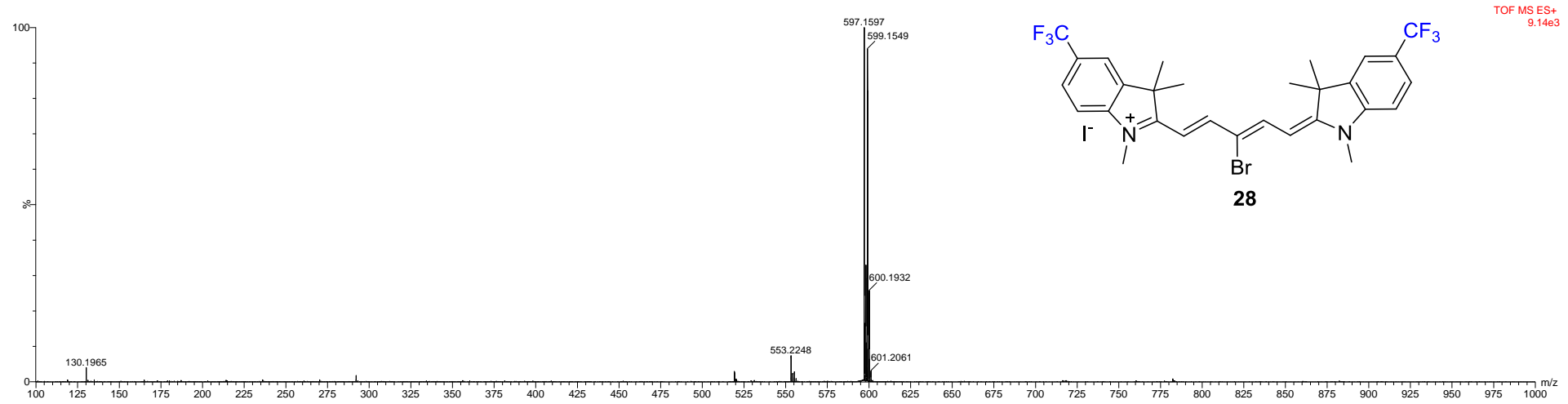
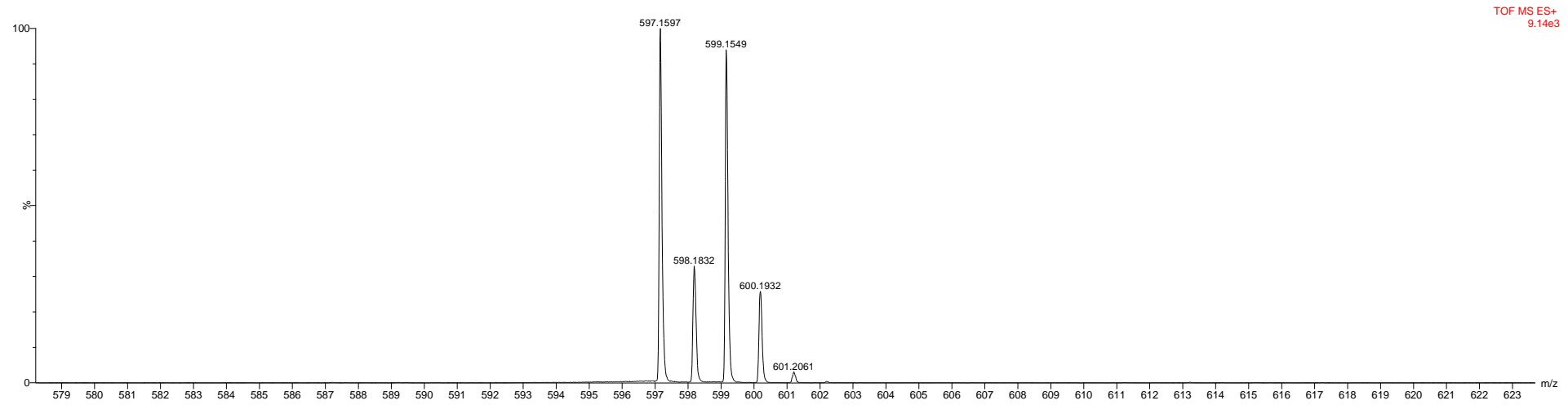


Exact Mass	553.18
LogD at 7.4	5.55
TPSA	6.25
HBD	0.00
HBA	1.00
Total Charge	1.00
Refractivity	156.00
Rotatable Bond	5.00
SB pKa	1.31
SA pKa	0.00

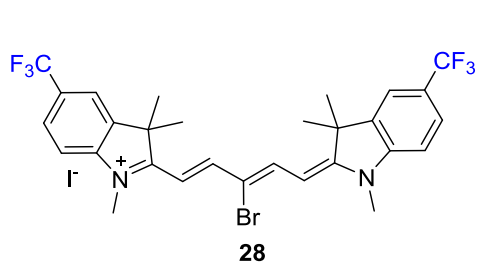




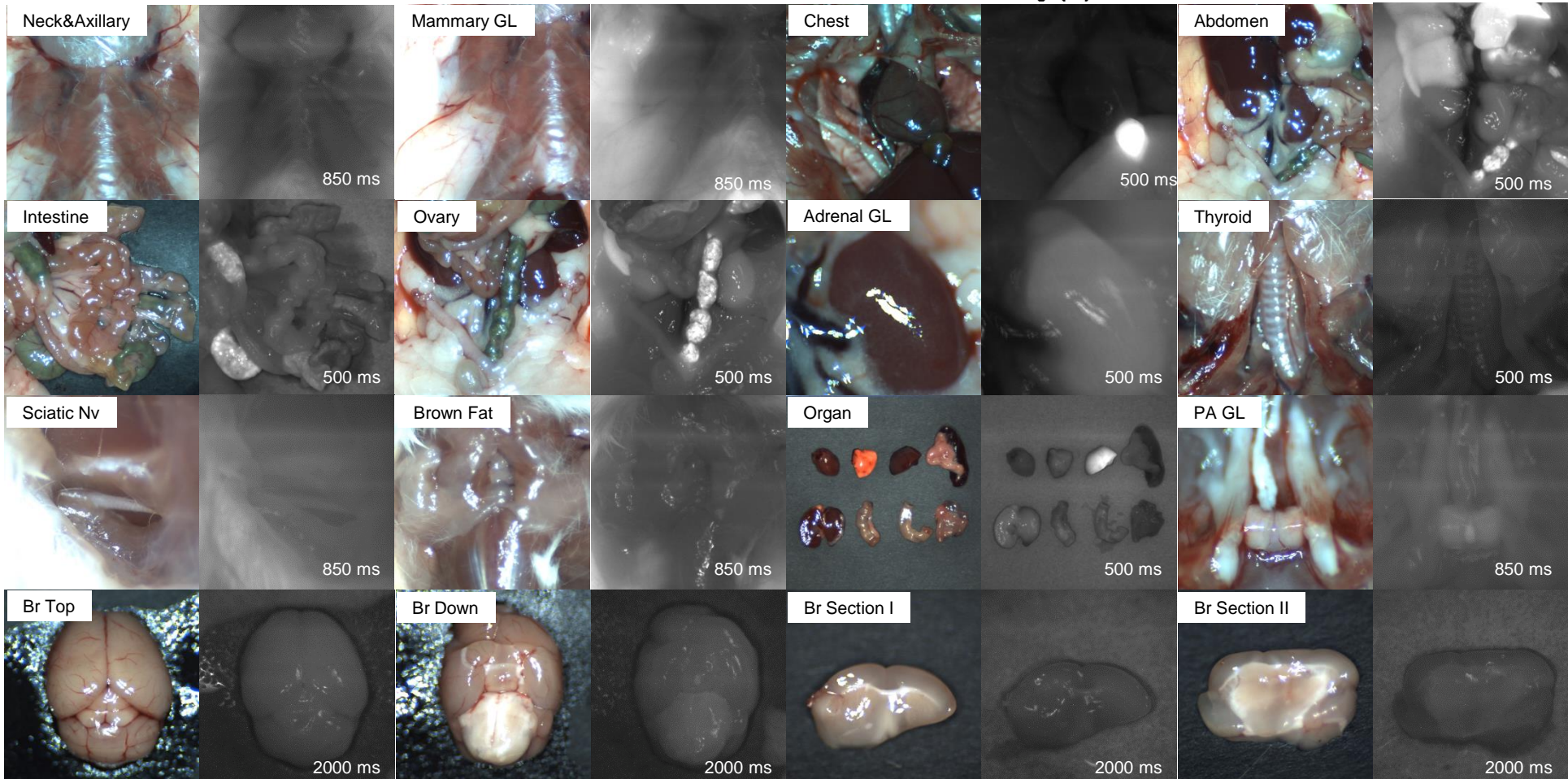
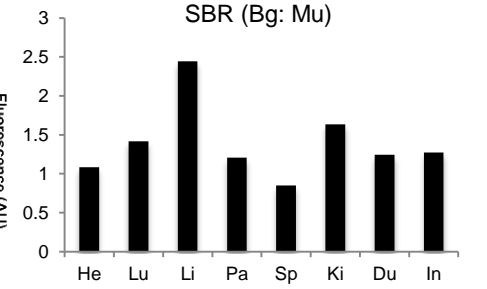
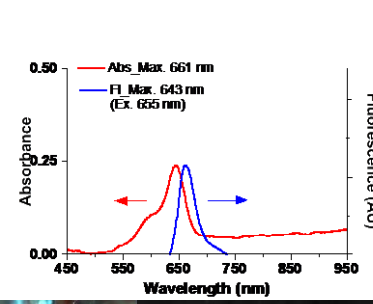


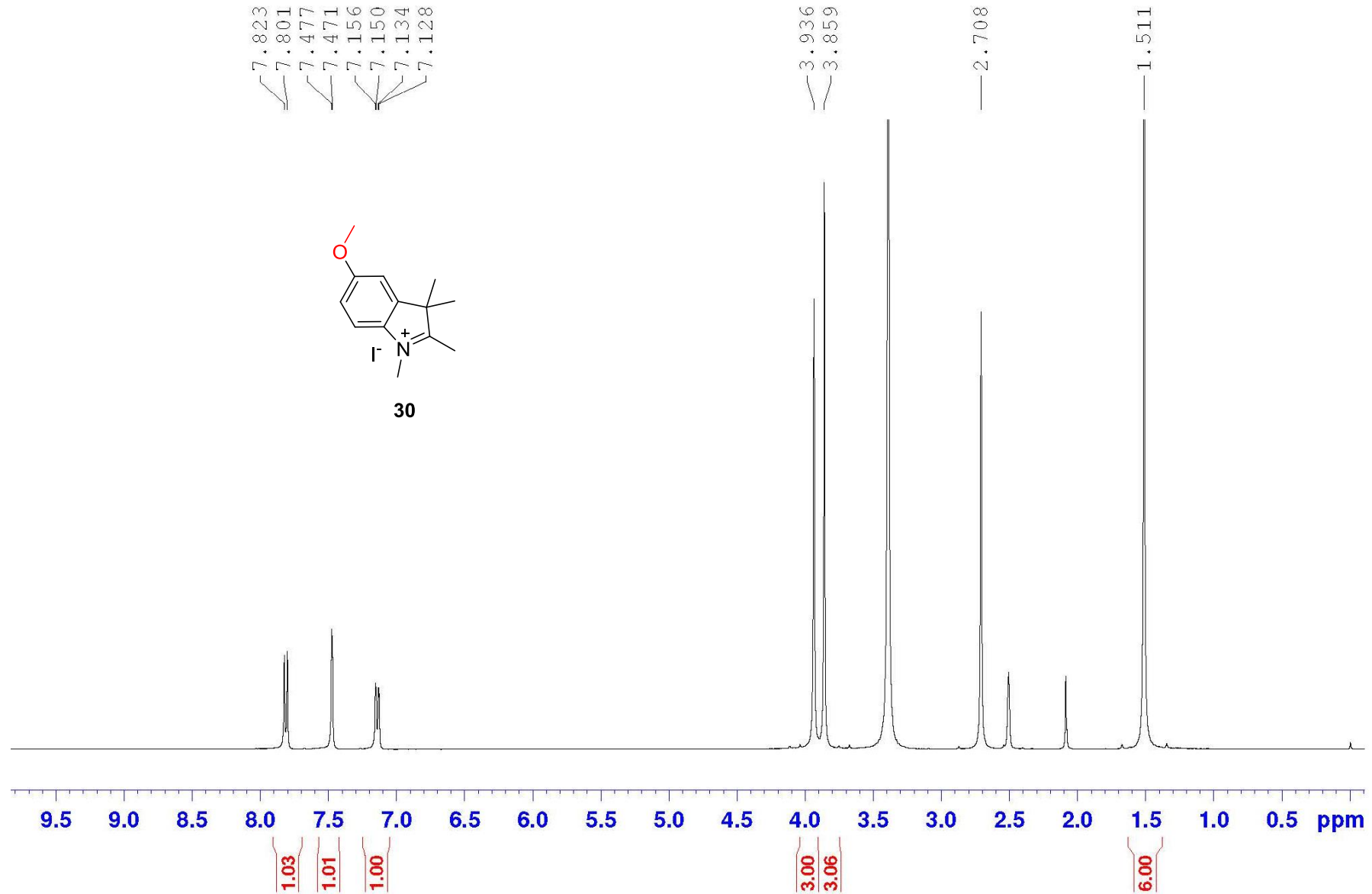
TOF MS ES+
9.14e3TOF MS ES+
9.14e3

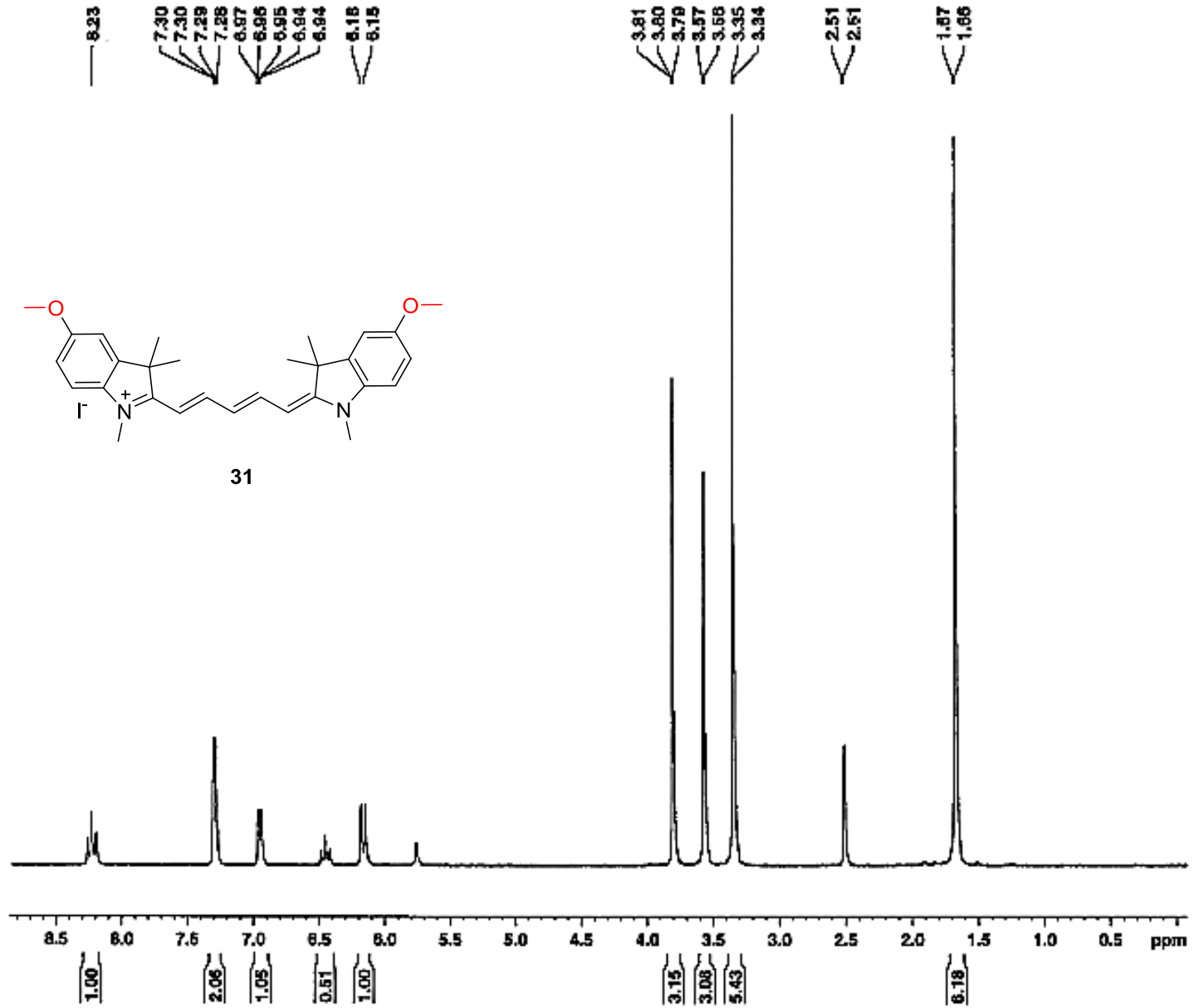
FLARE Parameters				Study Info.				Measurement	
Model	K-FLARE™ Zoom	Channel	700 nm	Chemical	28	Formulation	C-D5W	FOV	5 / 3.3 / 2 cm
Fluence rate	0.54 mW at 660 nm	Filter	660-20/673lpxr/Dual BP (710-50 and 781lp)	Animal	CD-1	Inj. route	R.O.	ROI	13
Working Dt.	9 in	Bit depth	16	Gender	Female	Anesthesia	K+X	Acquisition time	1 h post inj.
Gain	12 dB	Matrix size	512x512	Dose	100 nmol	Body Weight	25-30 g	Exp. Time (msec)	L, M, H

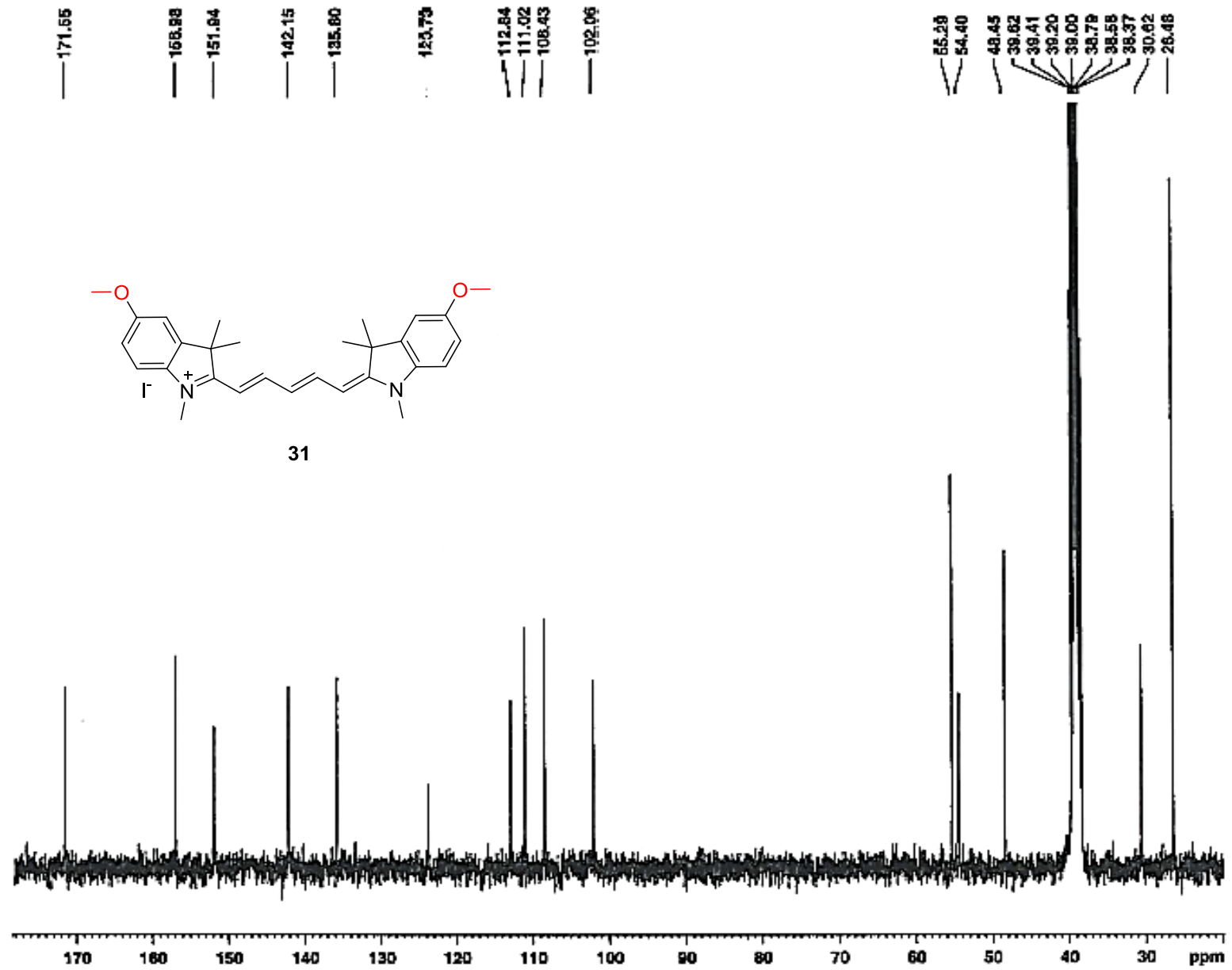


Exact Mass	597.13
LogD at 7.4	5.71
TPSA	6.25
HBD	0.00
HBA	1.00
Total Charge	1.00
Refractivity	158.00
Rotatable Bond	5.00
SB pKa	1.33
SA pKa	0.00







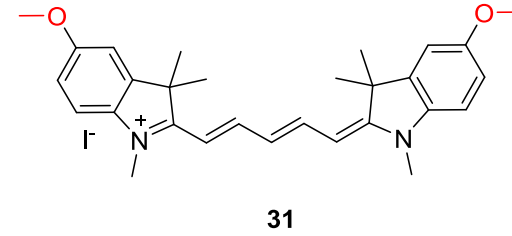
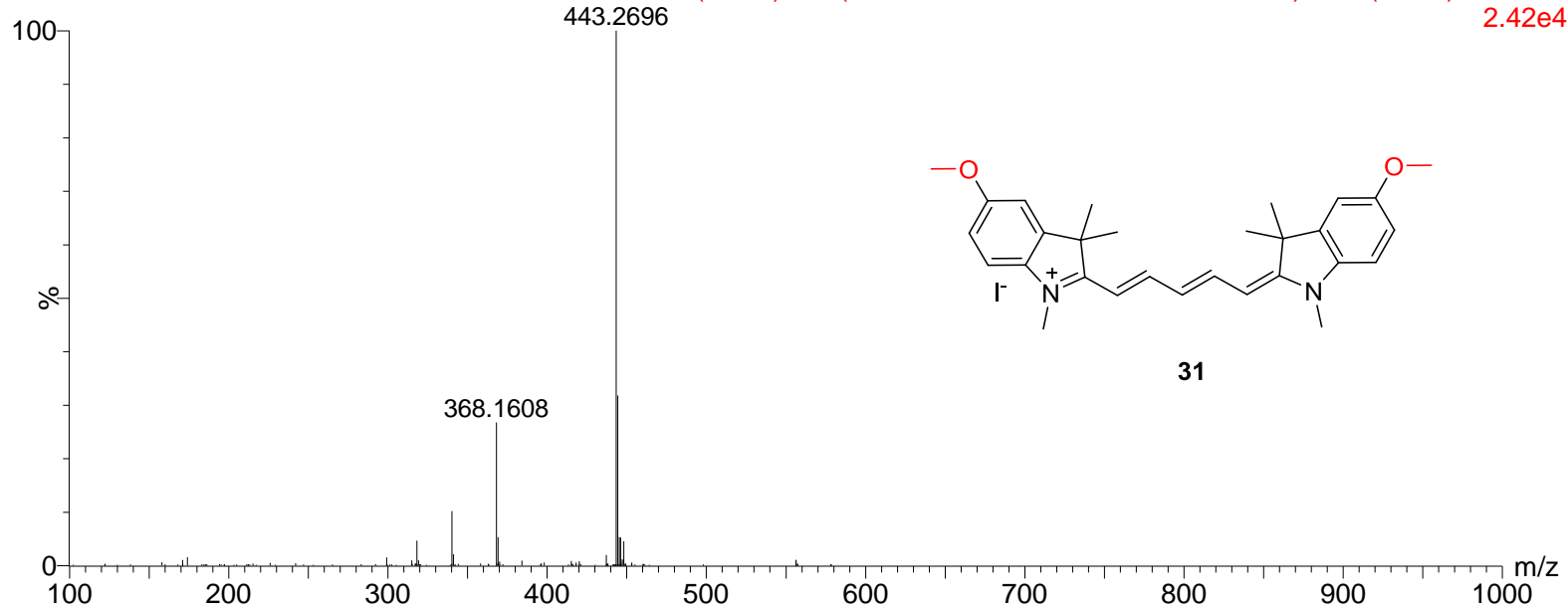


diluted in 80%MeOH

17:00:53 01-Feb-2013

ERIC_25_HENARY-ACCU_02-01-2013_ESI-POS01 61 (1.215) AM (Cen,2, 80.00, Ar,5000.0,556.28,0.70); Cm (61:80)

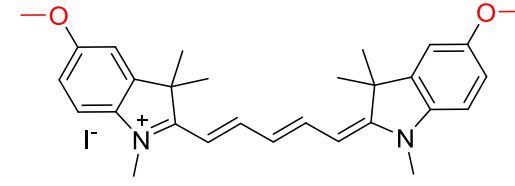
2.42e4



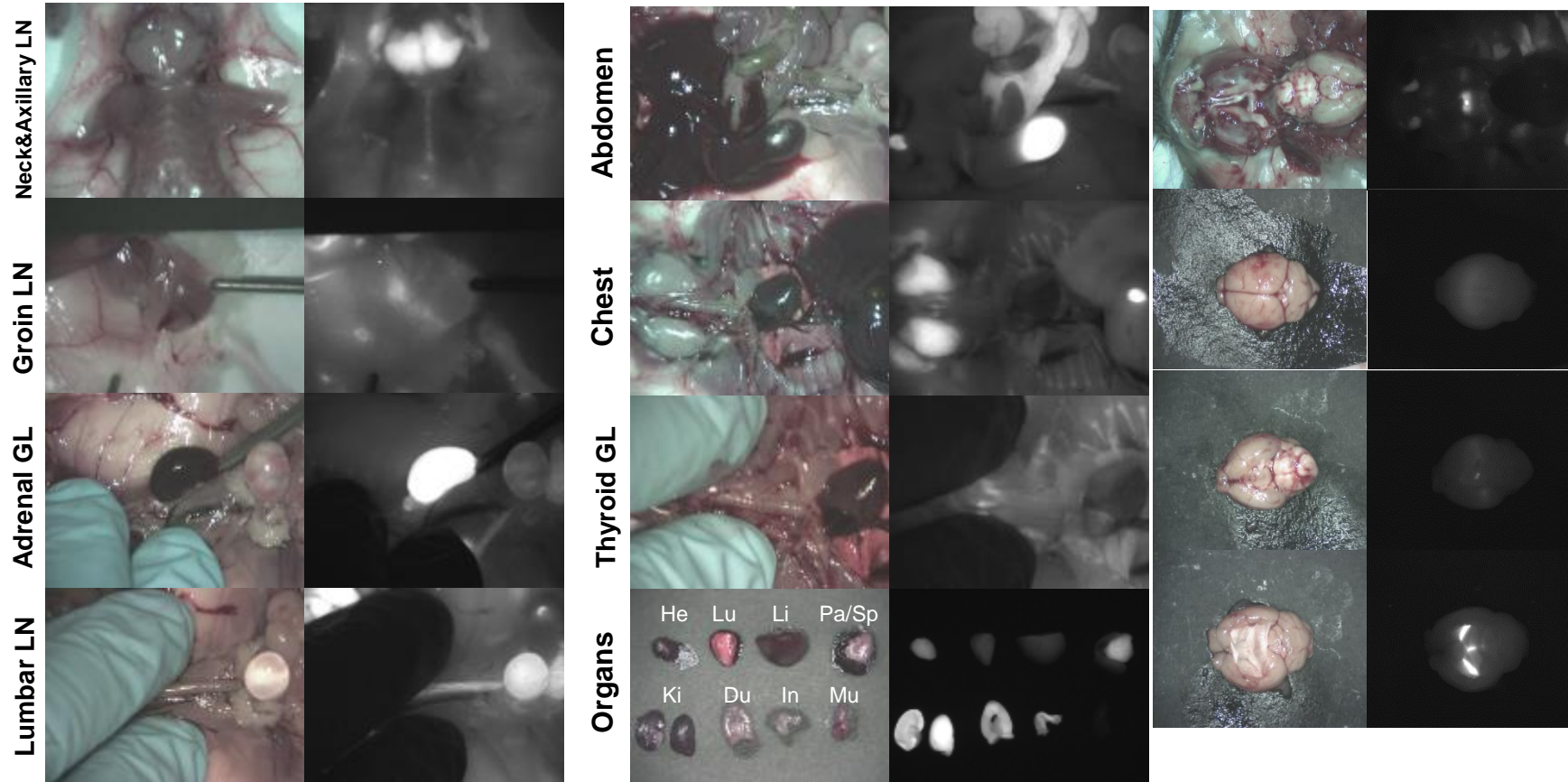
Mass	Calc. Mass	mDa	PPM	DBE	i-FIT	Formula
443.2696	443.2699	-0.3	-0.7	13.5	14.0	C ₂₉ H ₃₅ N ₂ O ₂

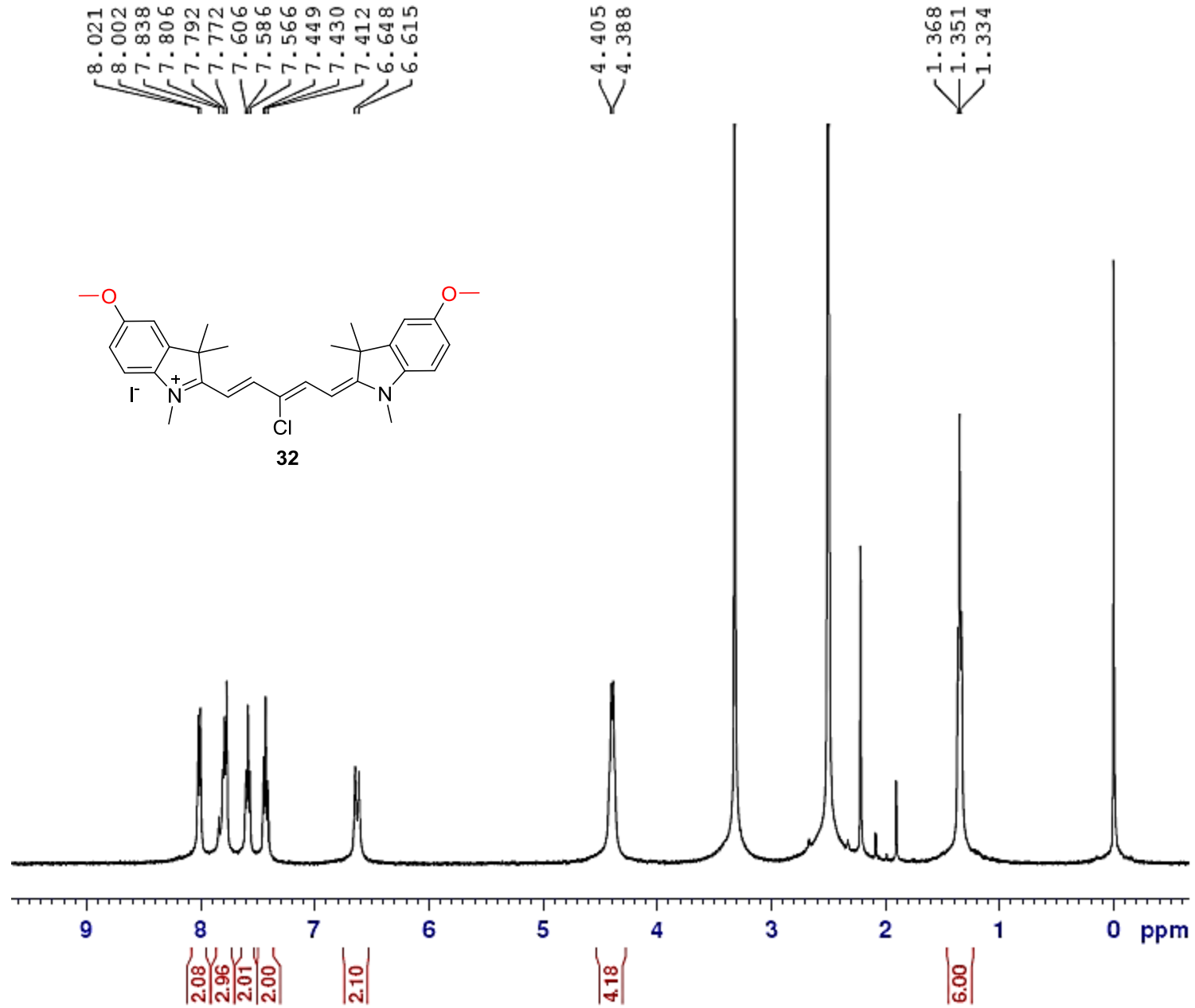
BioD of Compound 31

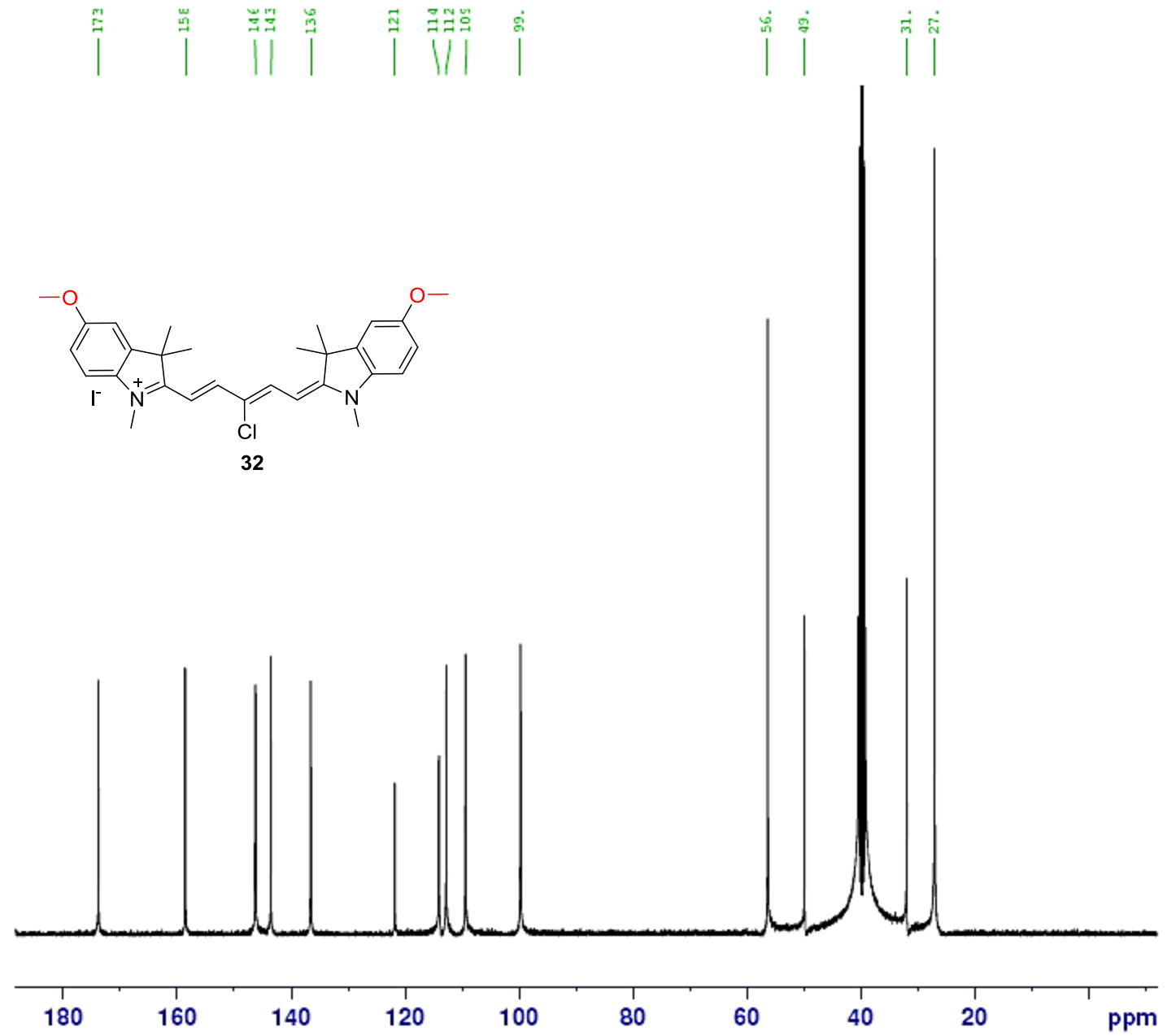
(4h post-injection)

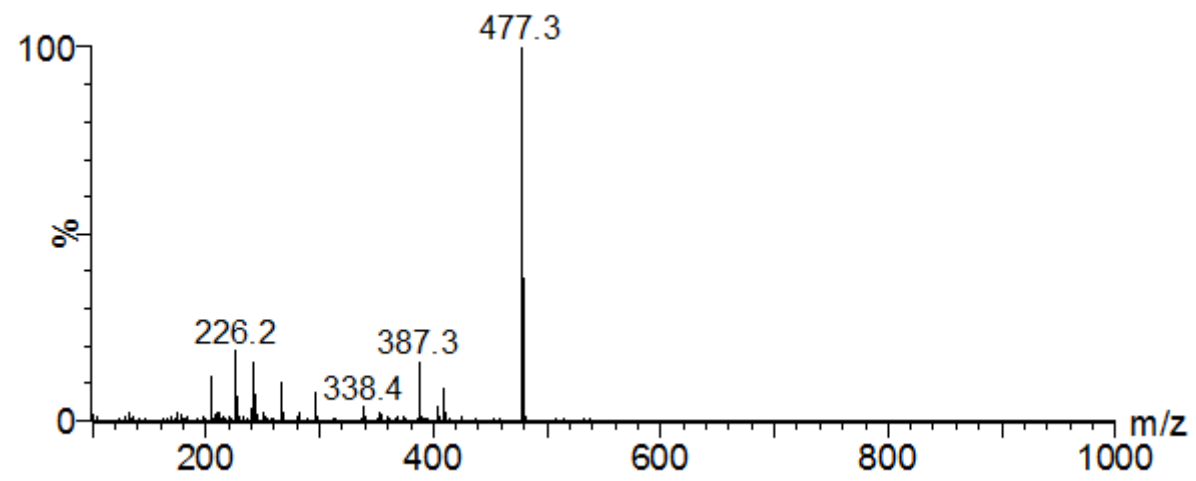
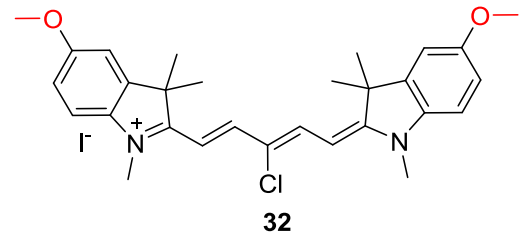


31



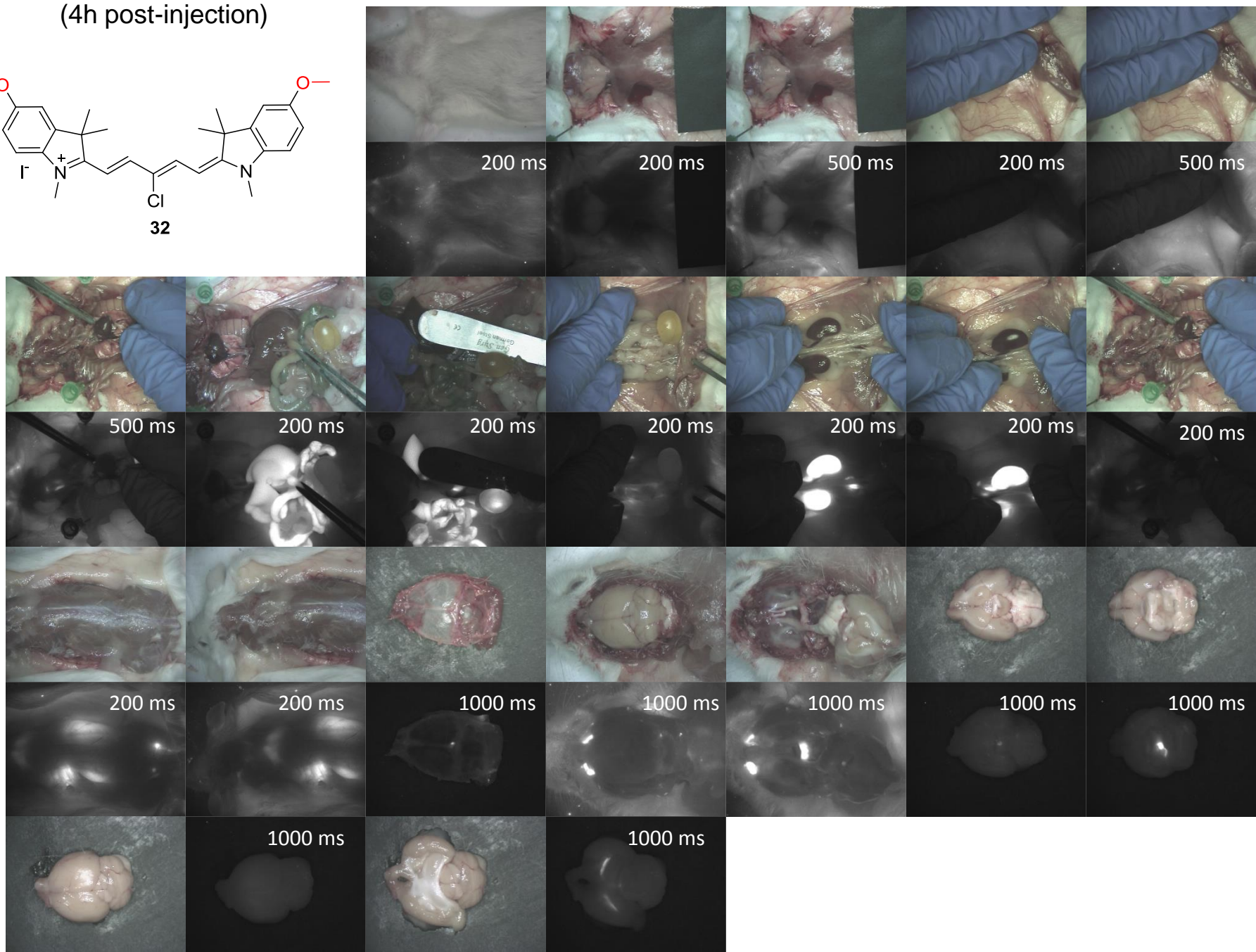
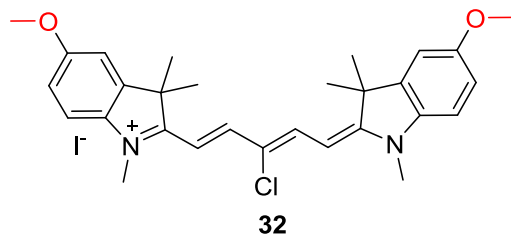


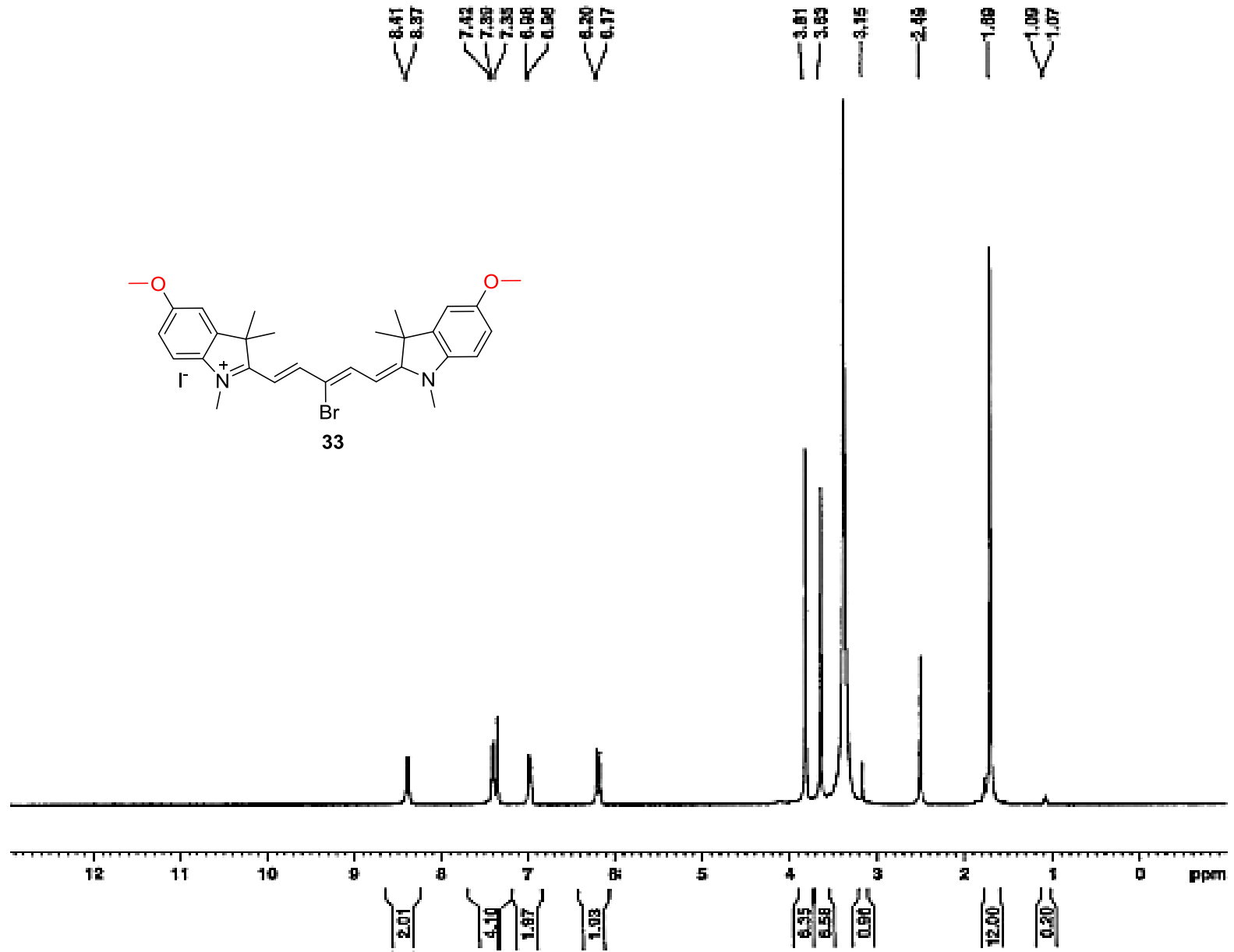


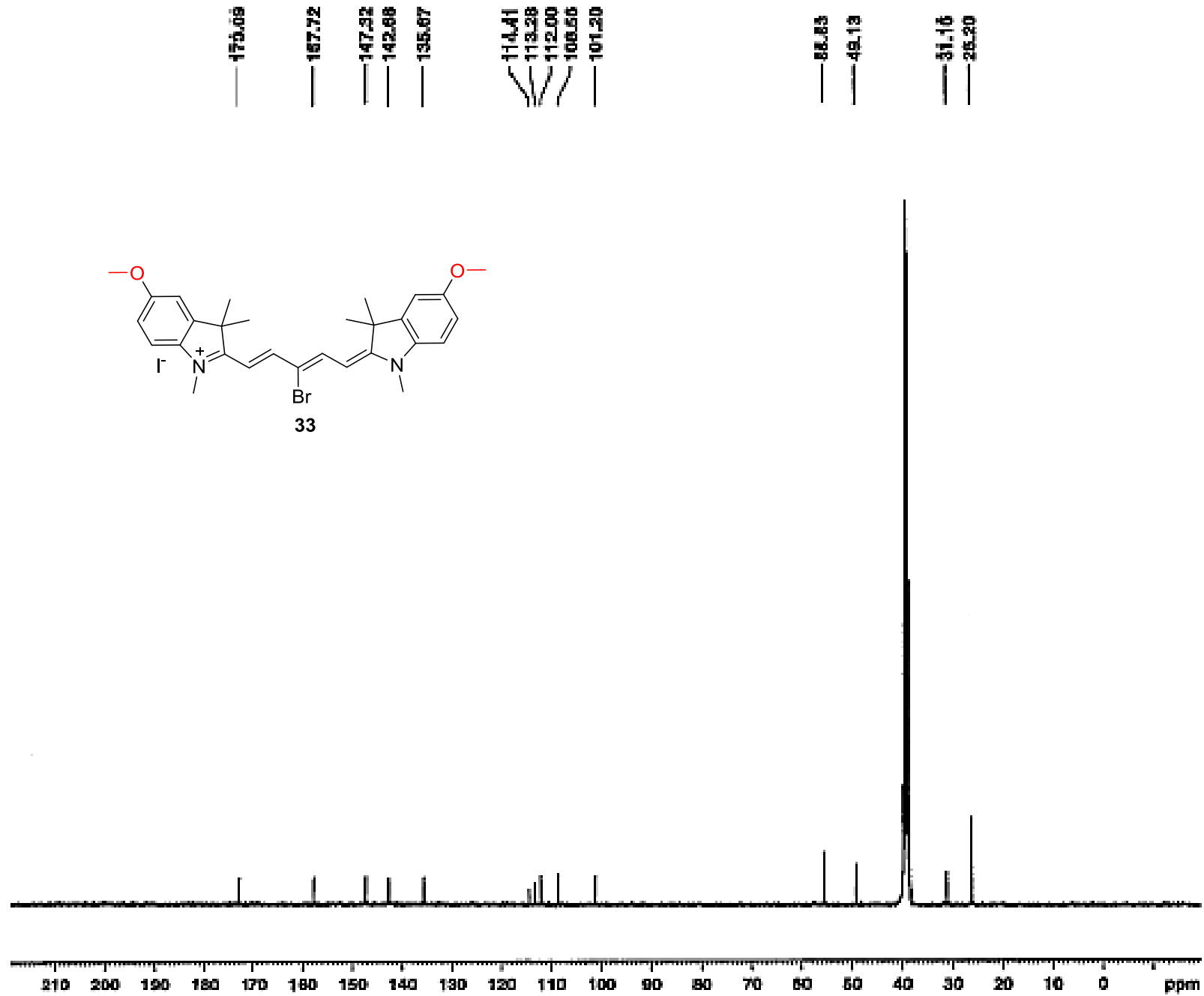


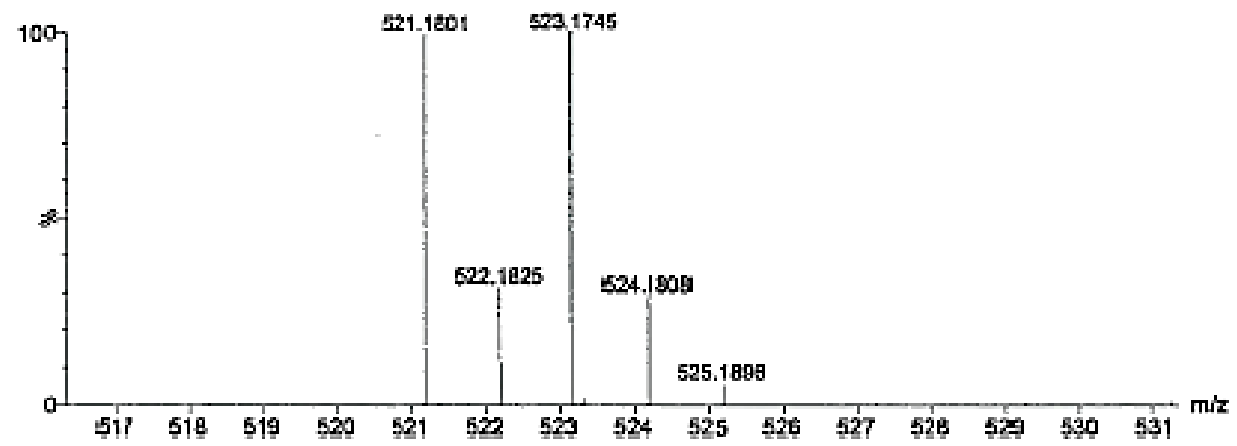
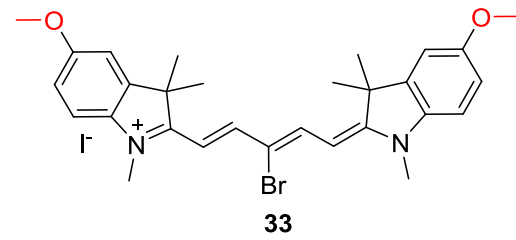
BioD of Compound 32

(4h post-injection)

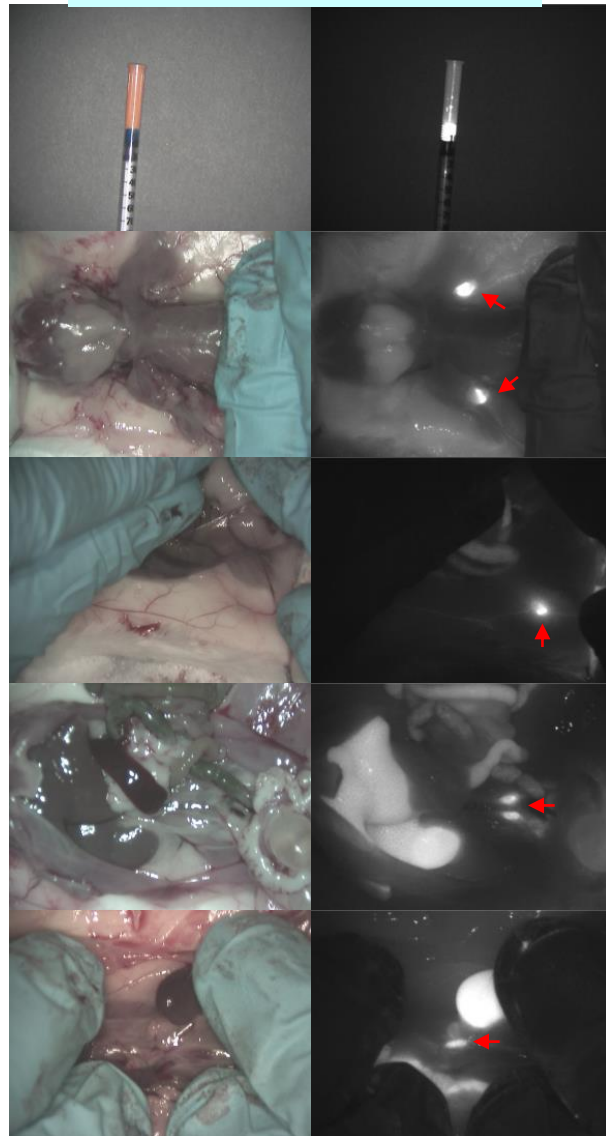




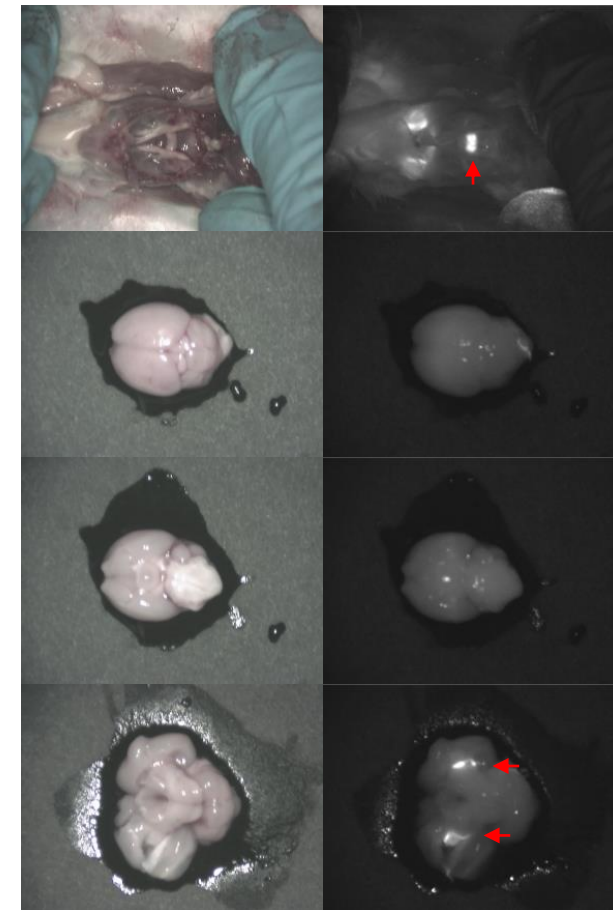
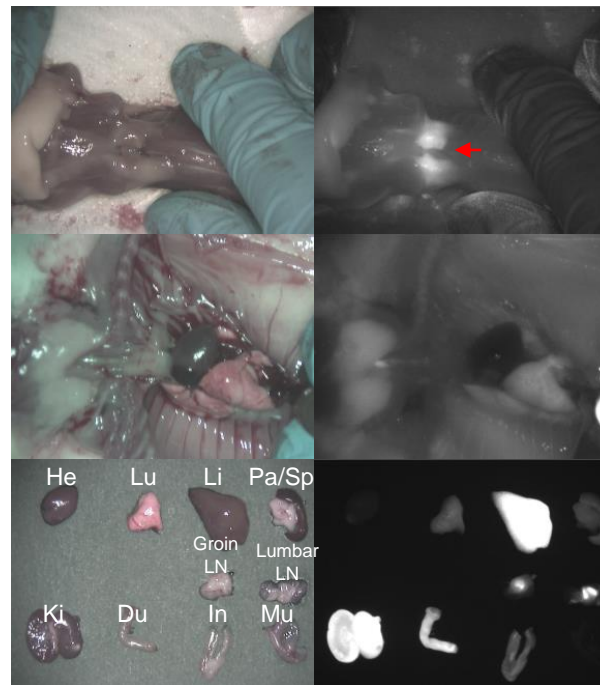
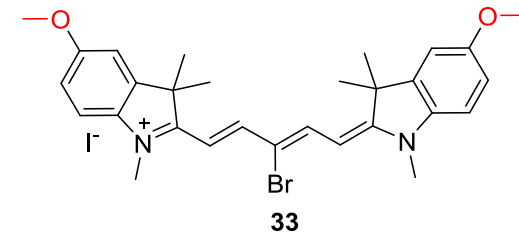


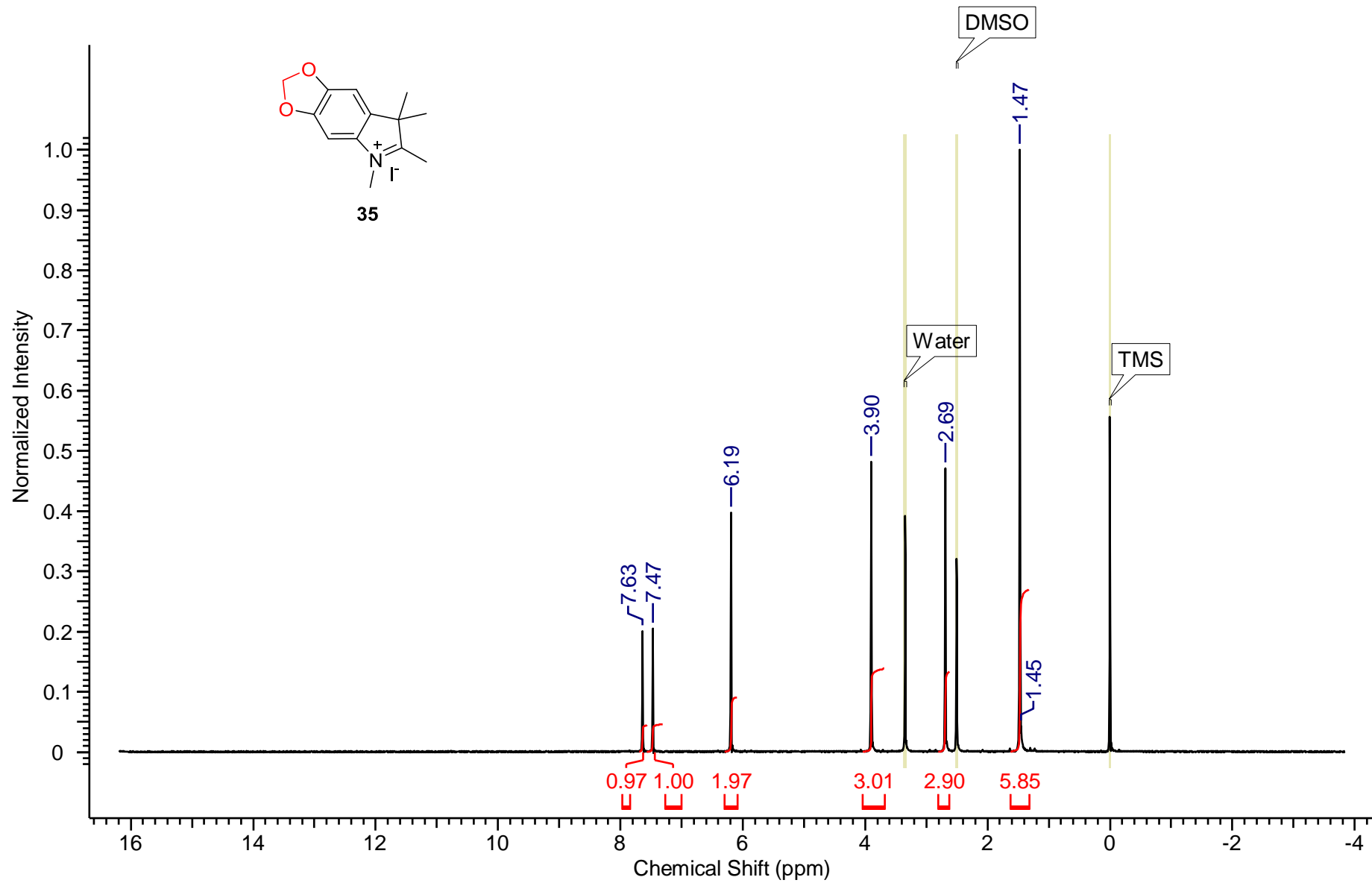


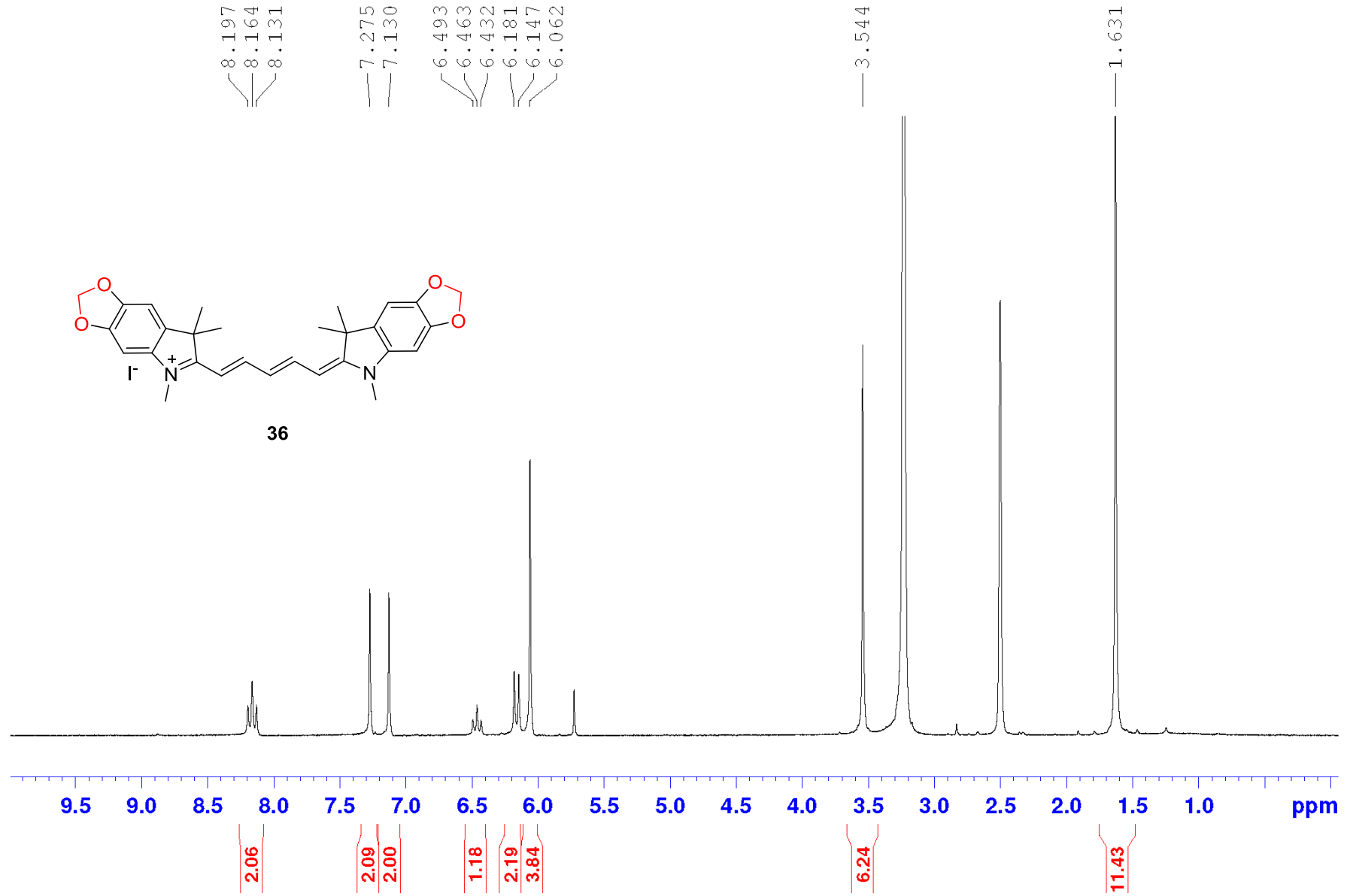
Injection solution: 30% FBS in saline
 Animal: CD-1 mouse (n=1)
 Injection route: Penial vein
250 μM x 100 μL (25 nmol)

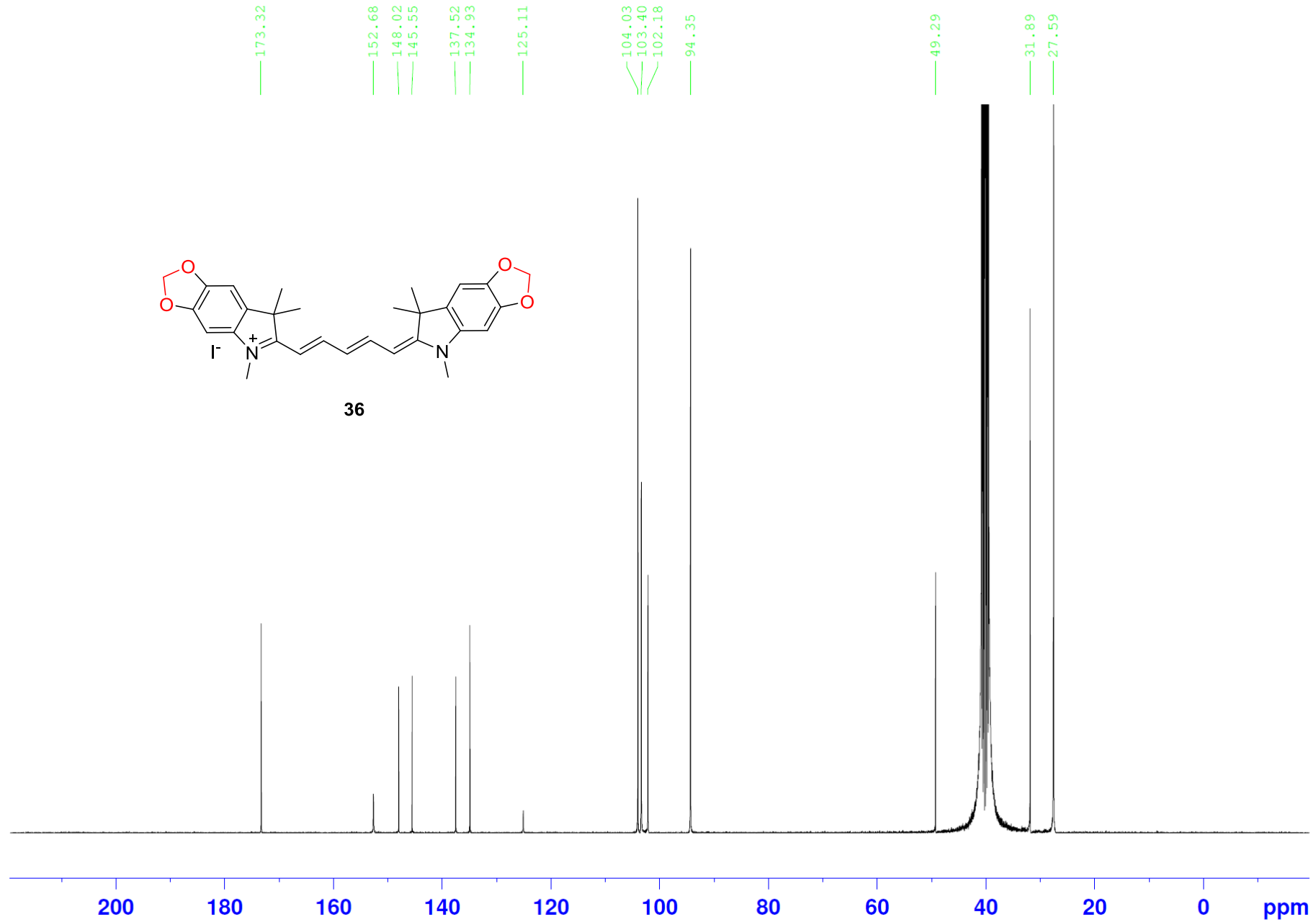


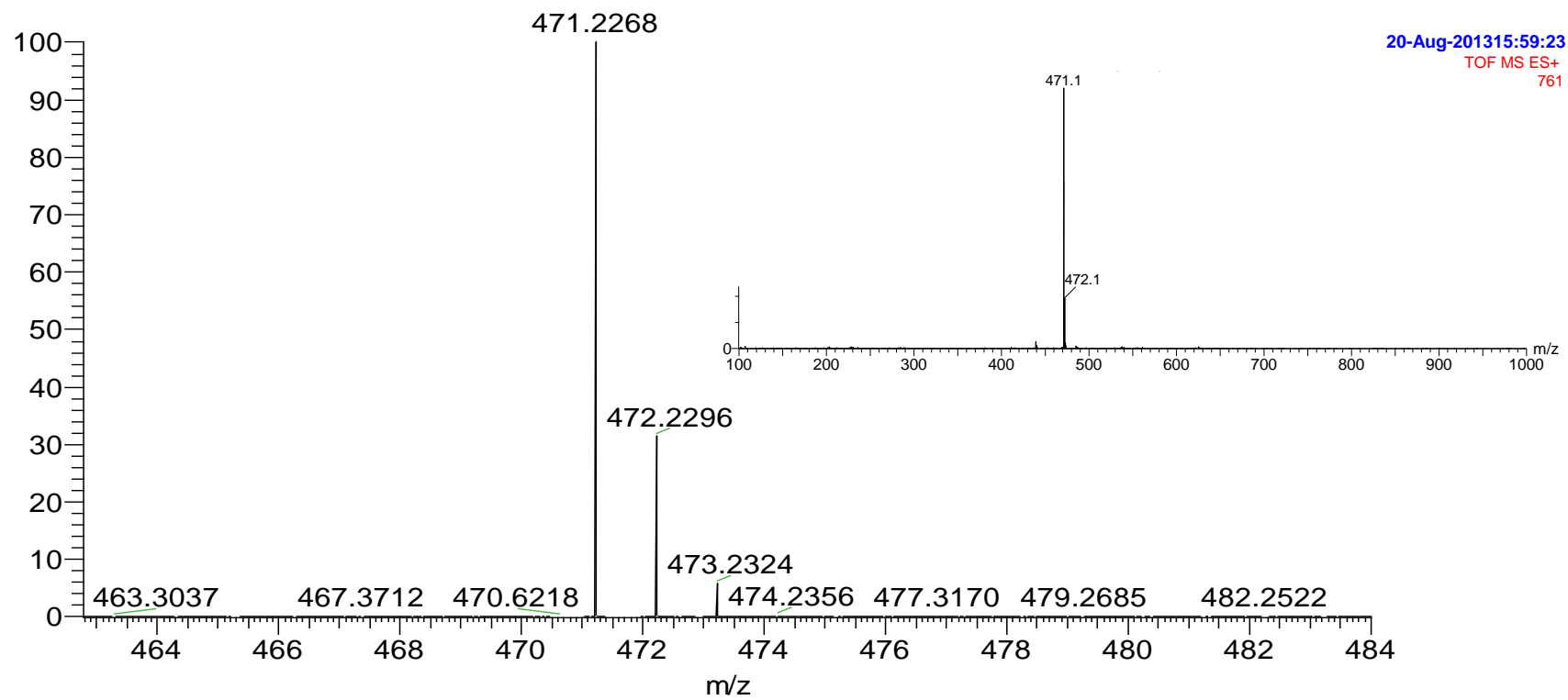
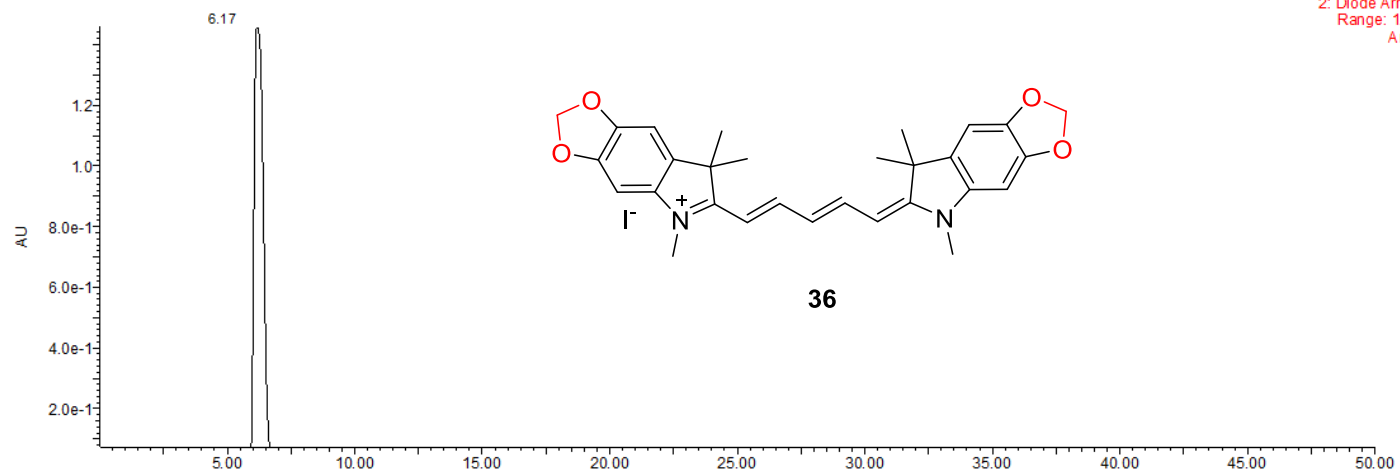
BioD result for Compound 33	
Endocrine Targeting	Adrenal GL +++ Pituitary GL +++
Lymph node	Axillary +++ Groin +++ Lumbar +++
Brain	Choroid plexus ++
Organ	Lung ++ Liver +++ Pa/Sp ++ Duodenum +++ Kidney +++
Tissue	Brown fat +++



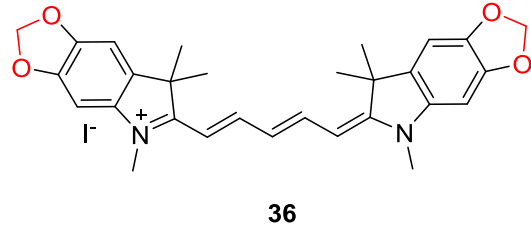




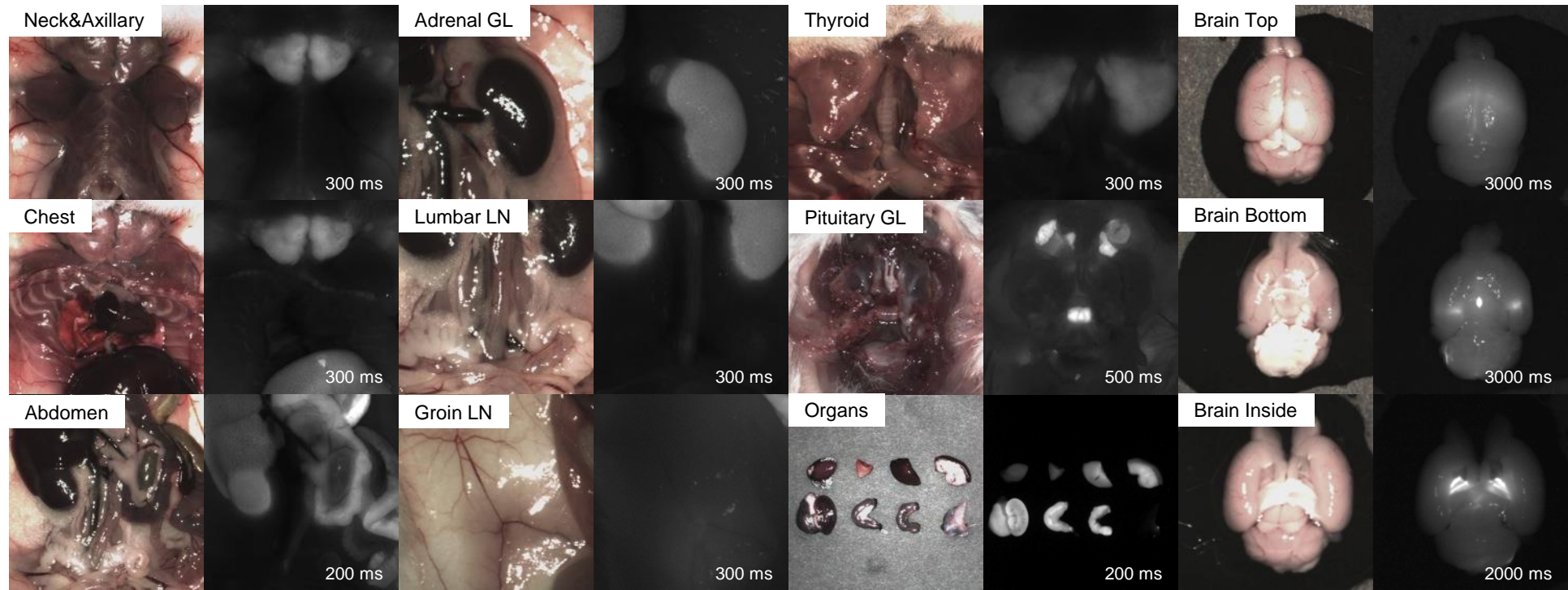
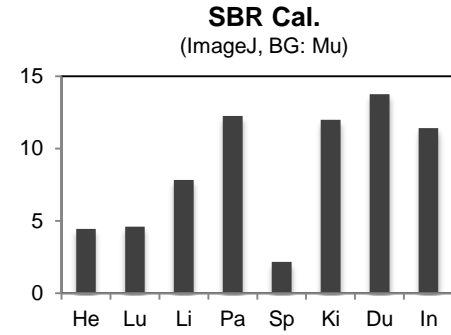
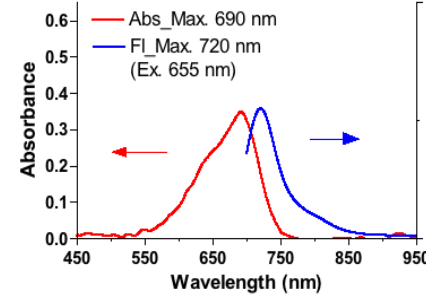


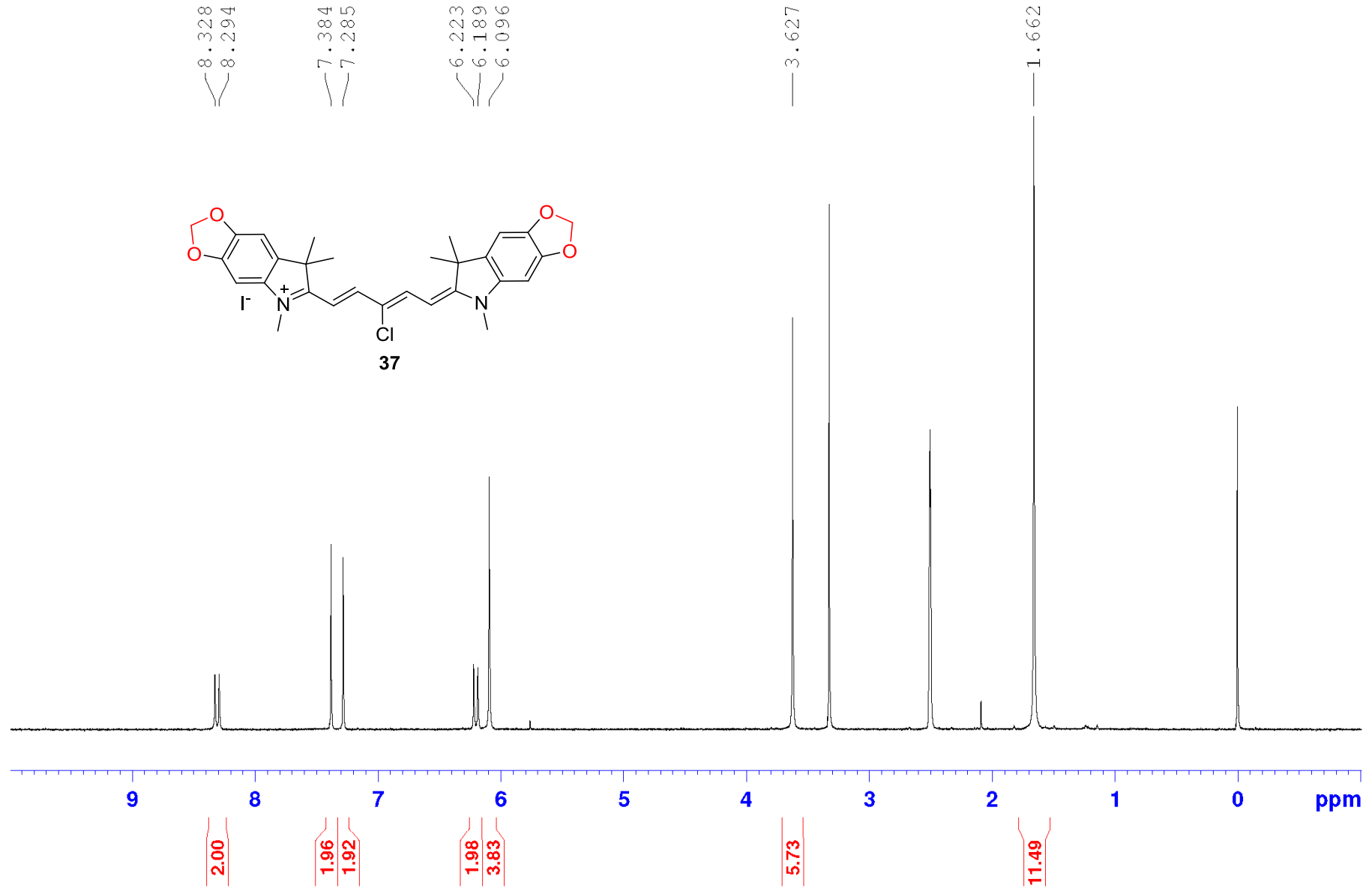


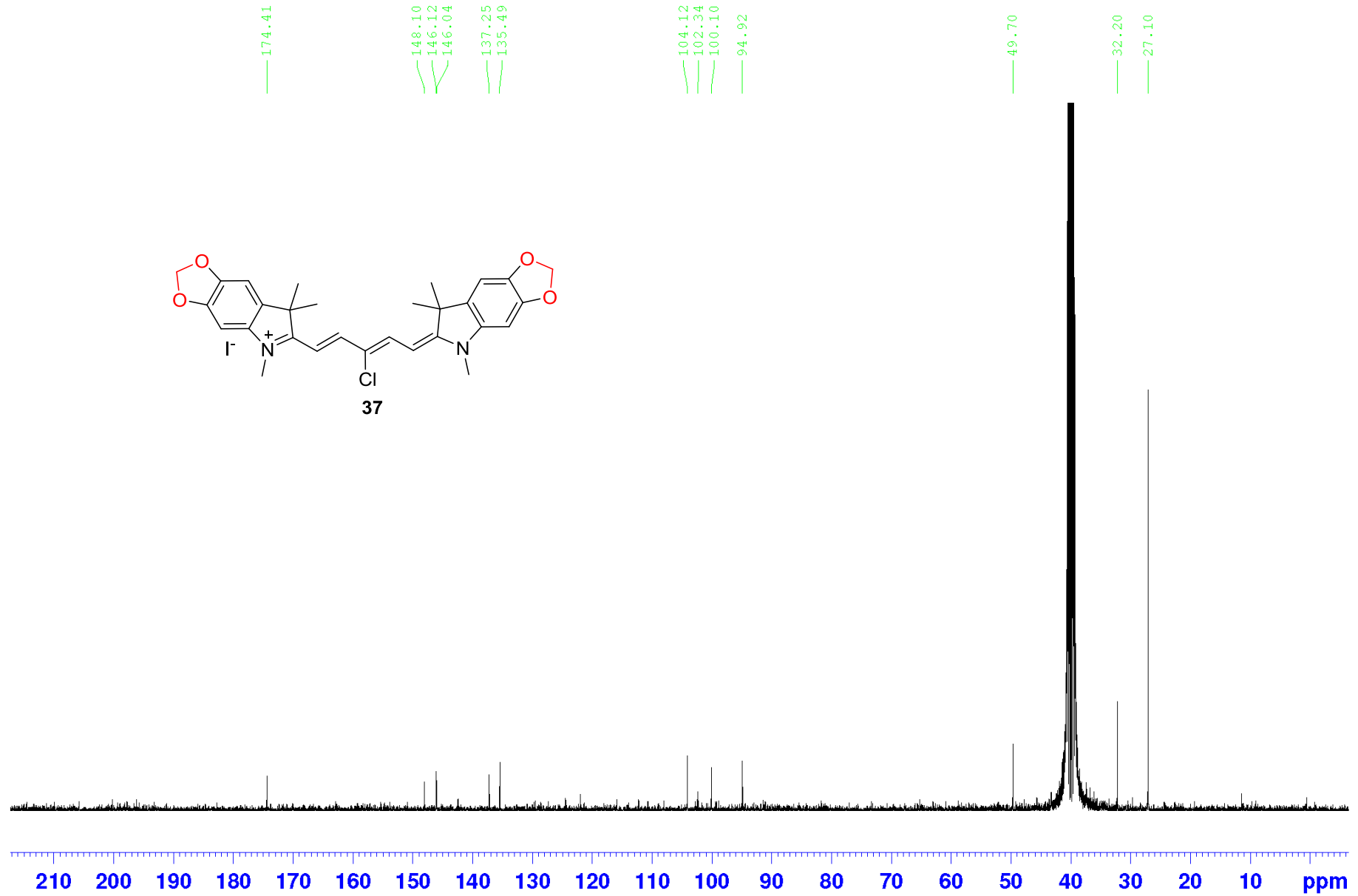
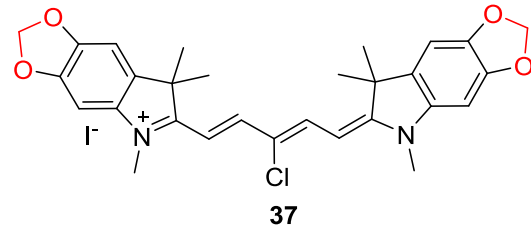
FLARE Parameters				Study Info.				Measurement	
Model	F-FLARE™	Channel	700 nm	Chemical	36	Formulation	30% FBS	FOV	7 / 3.5 / 2 cm
Fluence rate	2.8 mW at 660 nm	Filter	660-20/710-50	Animal	CD-1	Inj. route	Penile	ROI	10
Working Dt.	13 in	Bit depth	16	Gender	Male	Anesthesia	K+X	Acquisition time	4 h post inj.
Gain	24 dB	Matrix size	512x512	Dose	25 nmol			Exp. Time (msec)	L, M, H



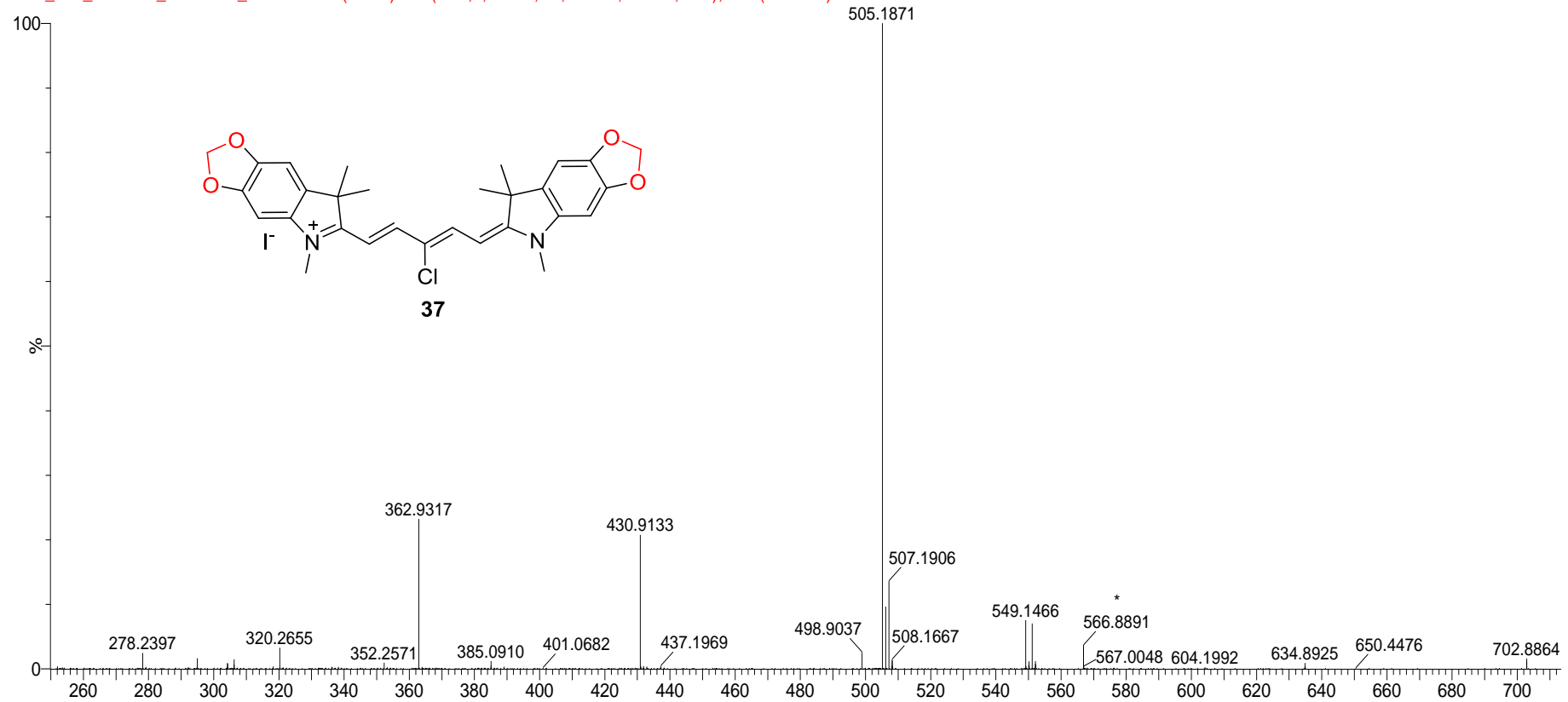
Exact Mass	471.23
LogD at 7.4	2.8
TPSA	43.17
HBD/A	0/5
Total Charge	1
Refractivity	151.05
Rotatable Bond	3
SB pKa	1.43
SA pKa	N/A





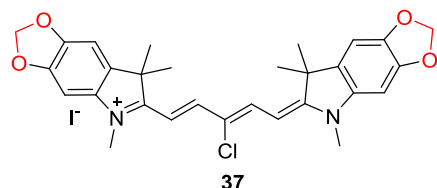


EAO_172_ESIPOS_HENARY_090415 852 (8.438) AM (Gen,2, 80.00, Ht,5000.0,566.89,1.00); Cm (852:862)

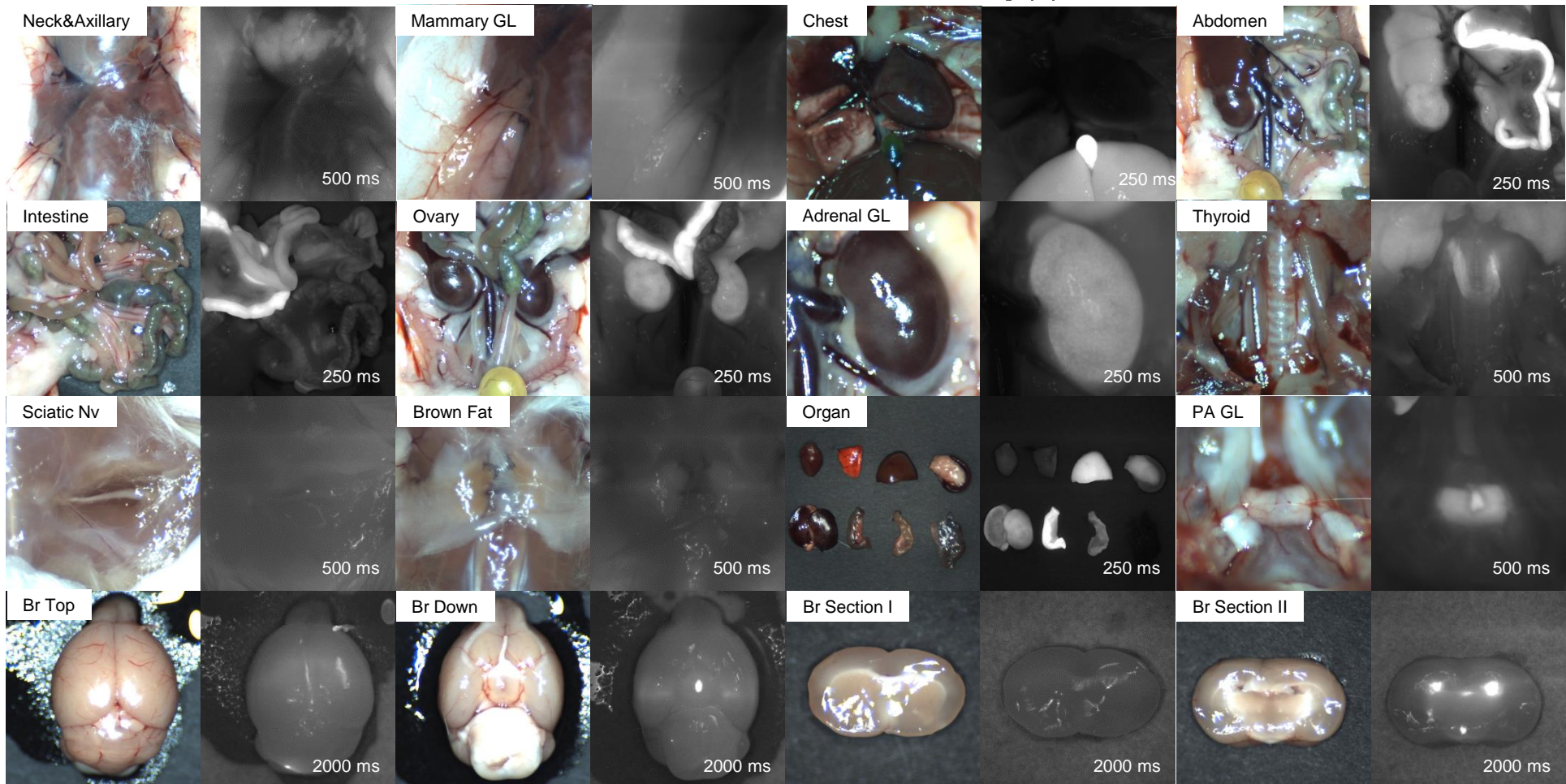
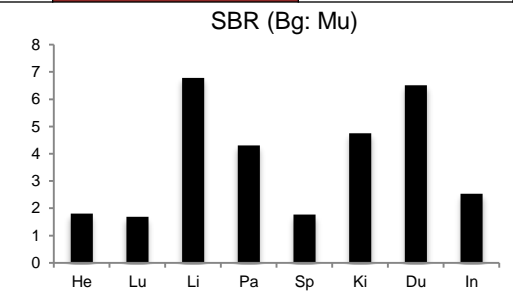
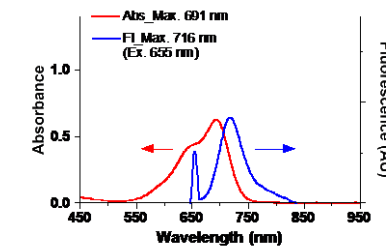


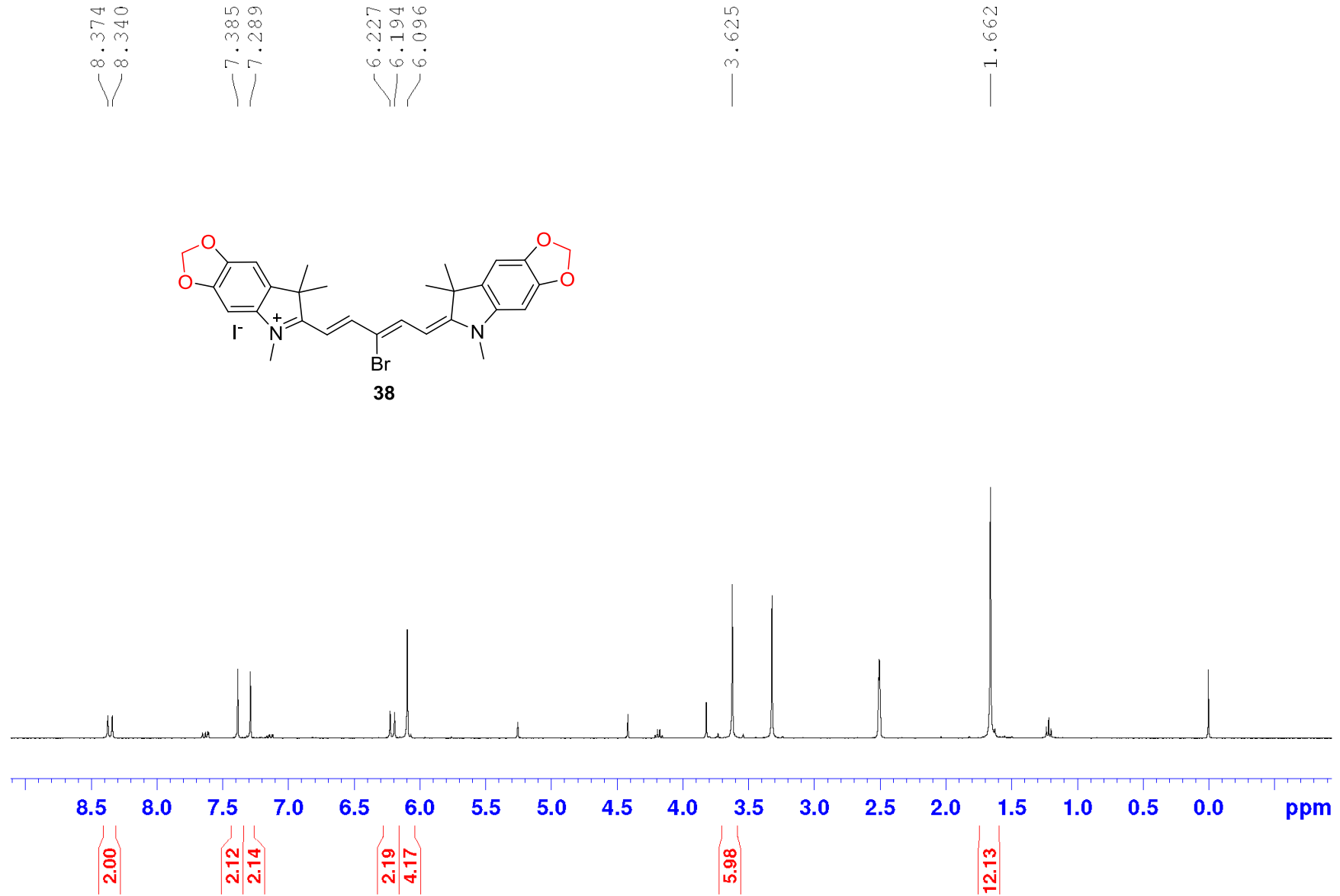
Mass	Calc. Mass	mDa	PPM	DBE	i-FIT	Formula
505.1871	505.1894	-2.3	-4.6	15.5	245.1	C29 H30 N2 O4 Cl

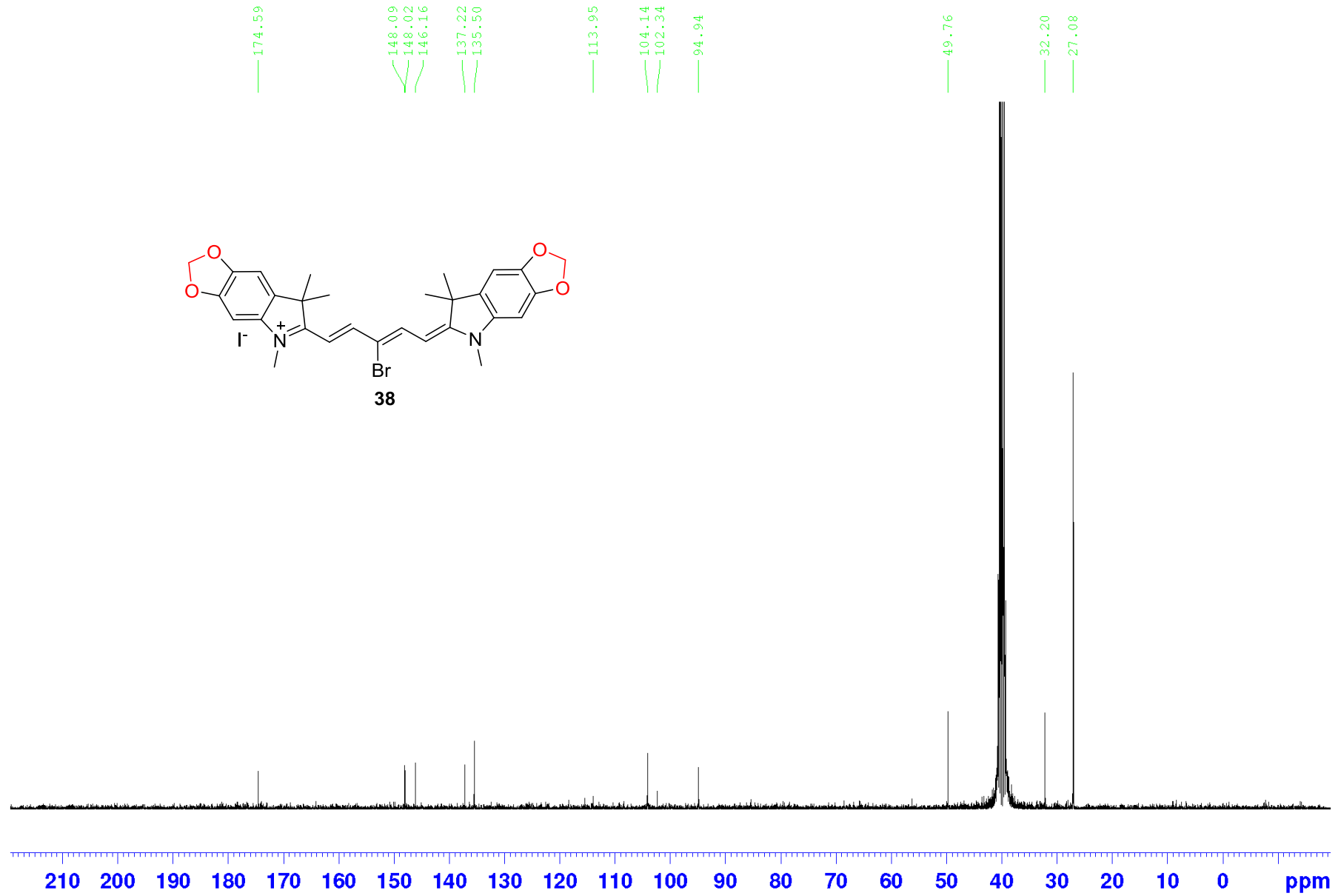
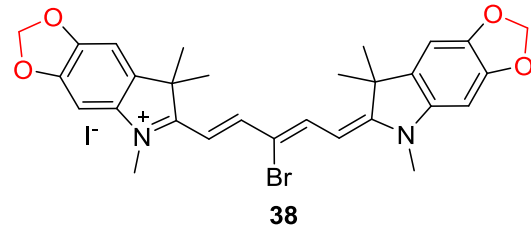
FLARE Parameters				Study Info.				Measurement	
Model	K-FLARE™ Zoom	Channel	700 nm	Chemical	37	Formulation	C-D5W	FOV	5 / 3.3 / 2 cm
Fluence rate	0.54 mW at 660 nm	Filter	660-20/673lpxr/Dual BP (710-50 and 781lp)	Animal	CD-1	Inj. route	R.O.	ROI	13
Working Dt.	9 in	Bit depth	16	Gender	Female	Anesthesia	K+X	Acquisition time	1 h post inj.
Gain	12 dB	Matrix size	512x512	Dose	100 nmol	Body Weight	25-30 g	Exp. Time (msec)	L, M, H



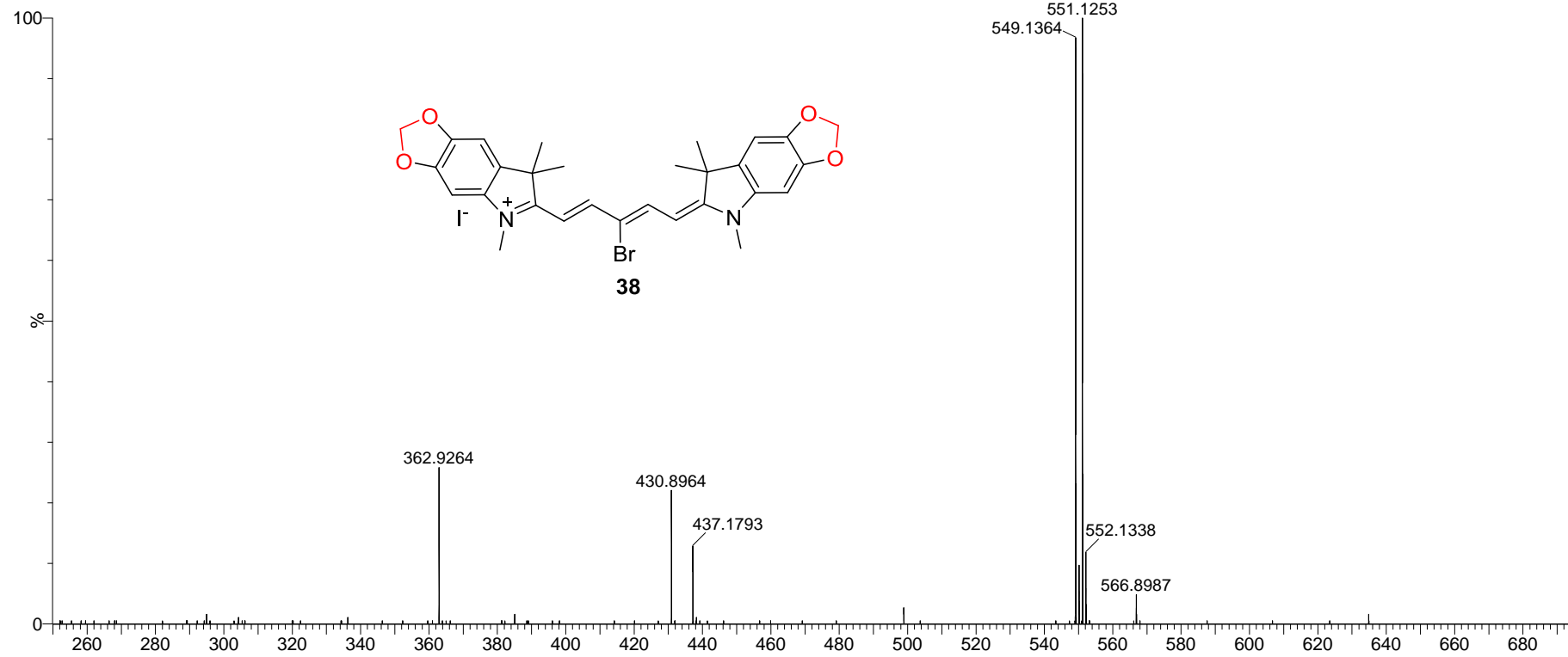
Exact Mass	505.19
LogD at 7.4	3.04
TPSA	43.17
HBD	0.00
HBA	5.00
Total Charge	1.00
Refractivity	155.00
Rotatable Bond	3.00
SB pKa	1.35
SA pKa	





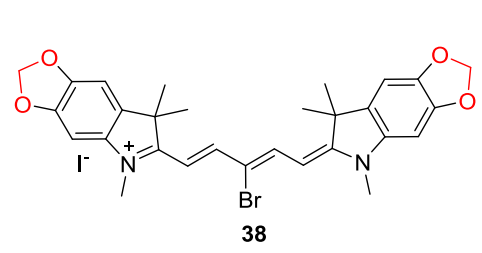


EAO_173_ESIPOS_HENARY_090415 1043 (10.292)

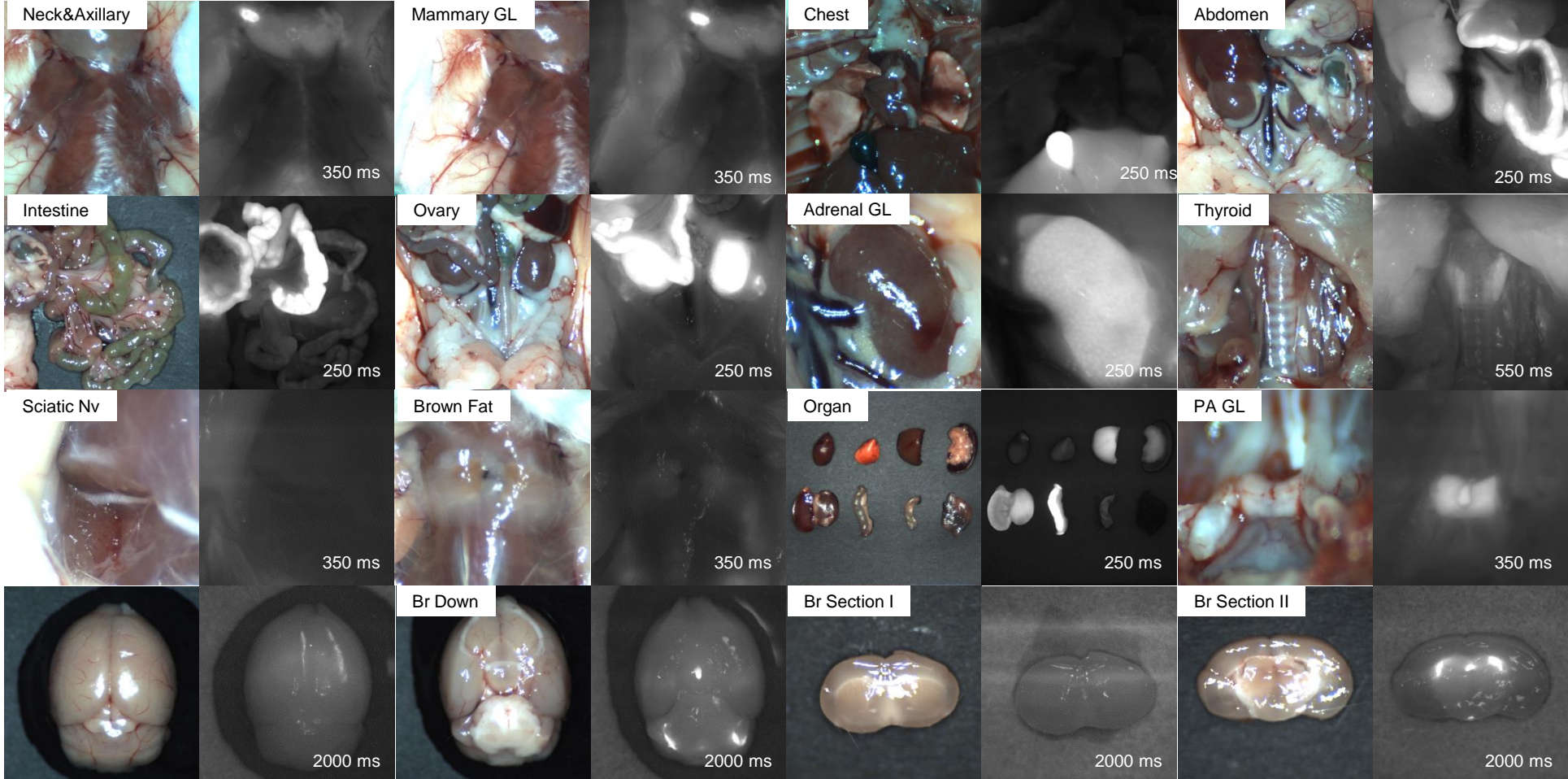
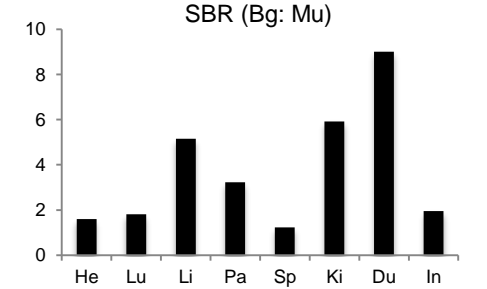
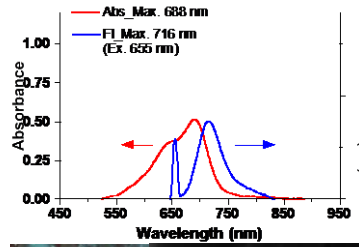


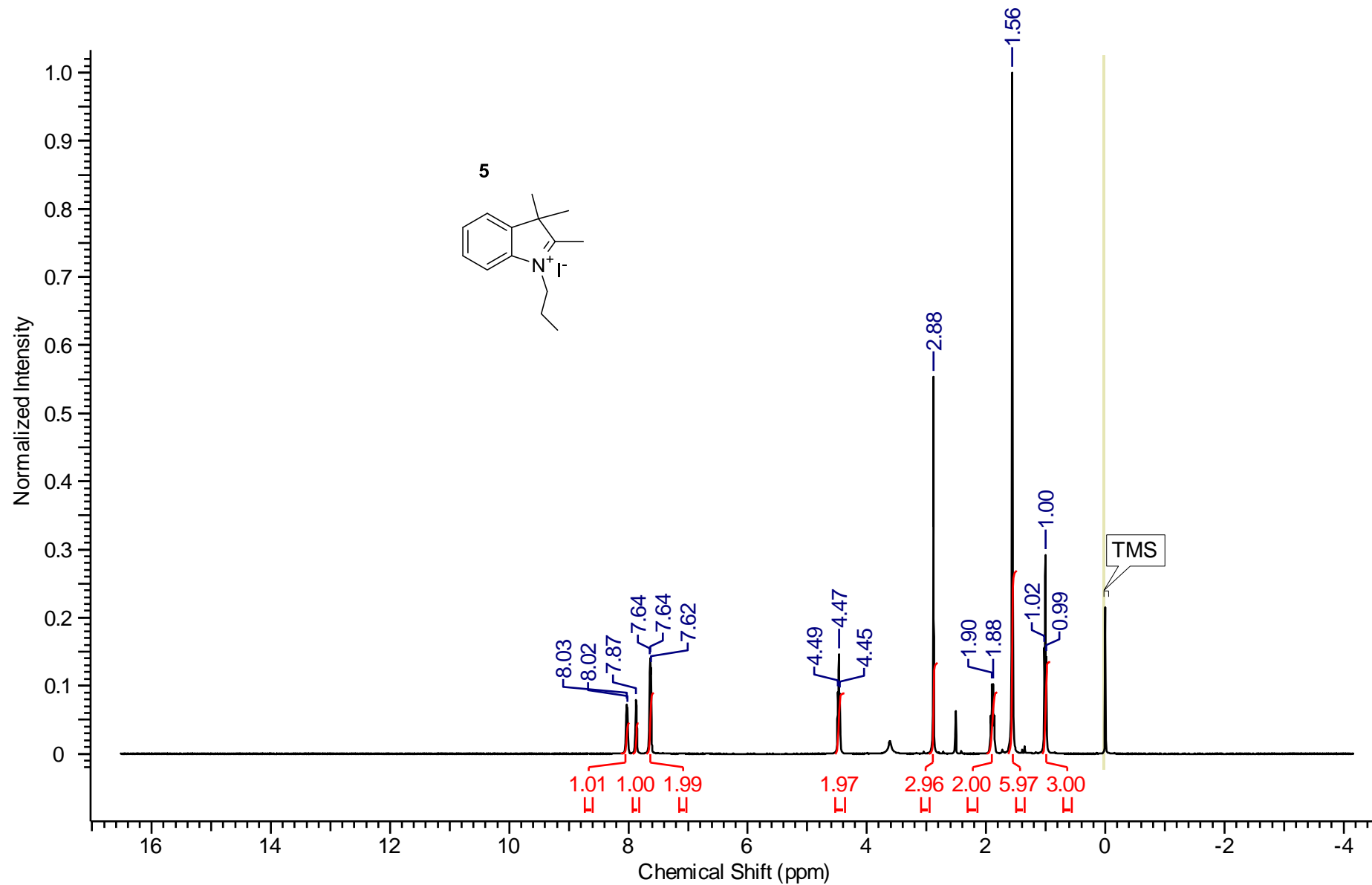
Mass	Calc. Mass	mDa	PPM	DBE	i-FIT	Formula
549.1368	549.1389	-2.1	-3.8	15.5	30.5	C ₂₉ H ₃₀ N ₂ O ₄ Br

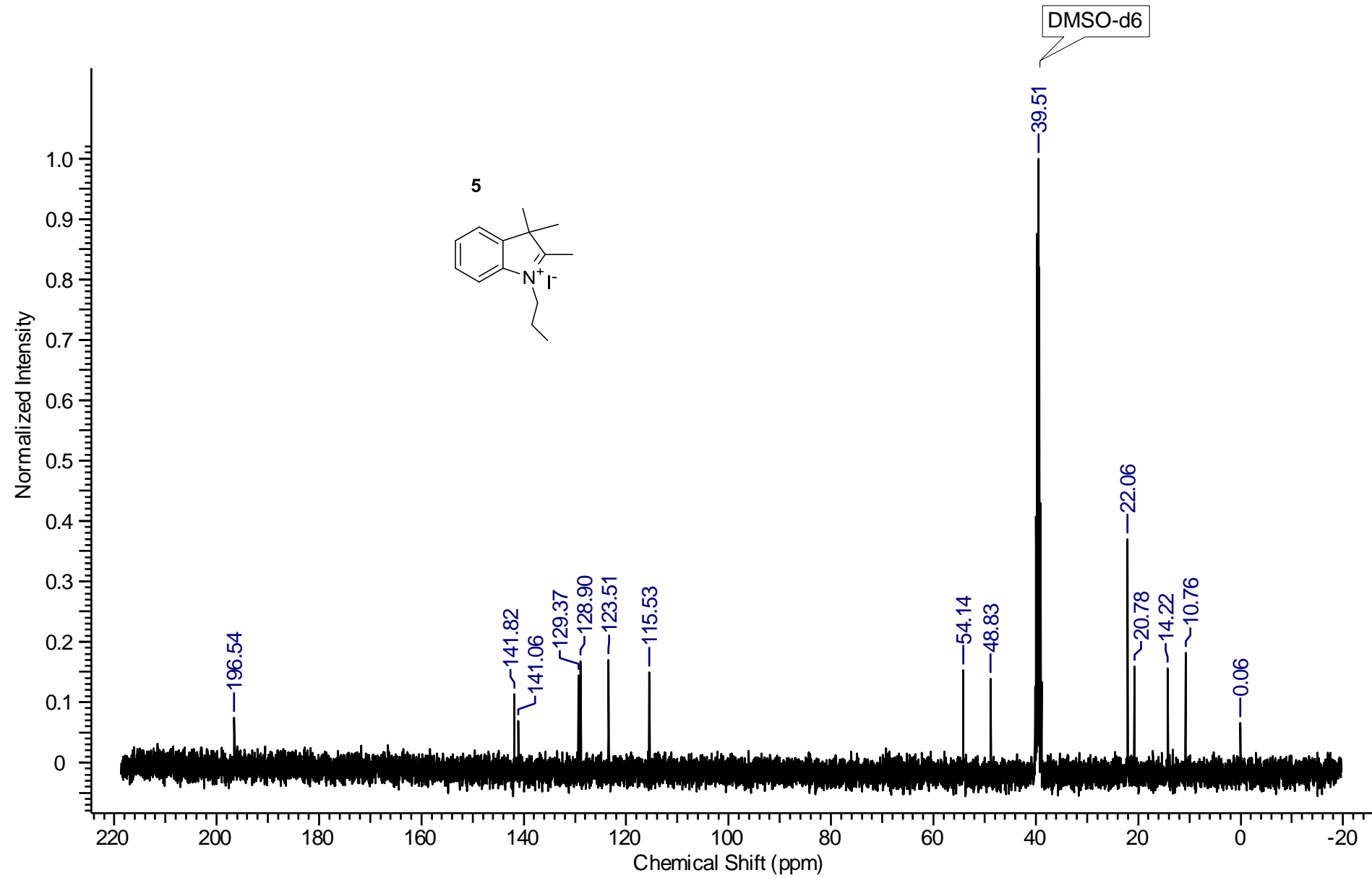
FLARE Parameters				Study Info.				Measurement	
Model	K-FLARE™ Zoom	Channel	700 nm	Chemical	38	Formulation	C-D5W	FOV	5 / 3.3 / 2 cm
Fluence rate	0.54 mW at 660 nm	Filter	660-20/673lpxr/Dual BP (710-50 and 781lp)	Animal	CD-1	Inj. route	R.O.	ROI	13
Working Dt.	9 in	Bit depth	16	Gender	Female	Anesthesia	K+X	Acquisition time	1 h post inj.
Gain	12 dB	Matrix size	512x512	Dose	100 nmol	Body Weight	25-30 g	Exp. Time (msec)	L, M, H

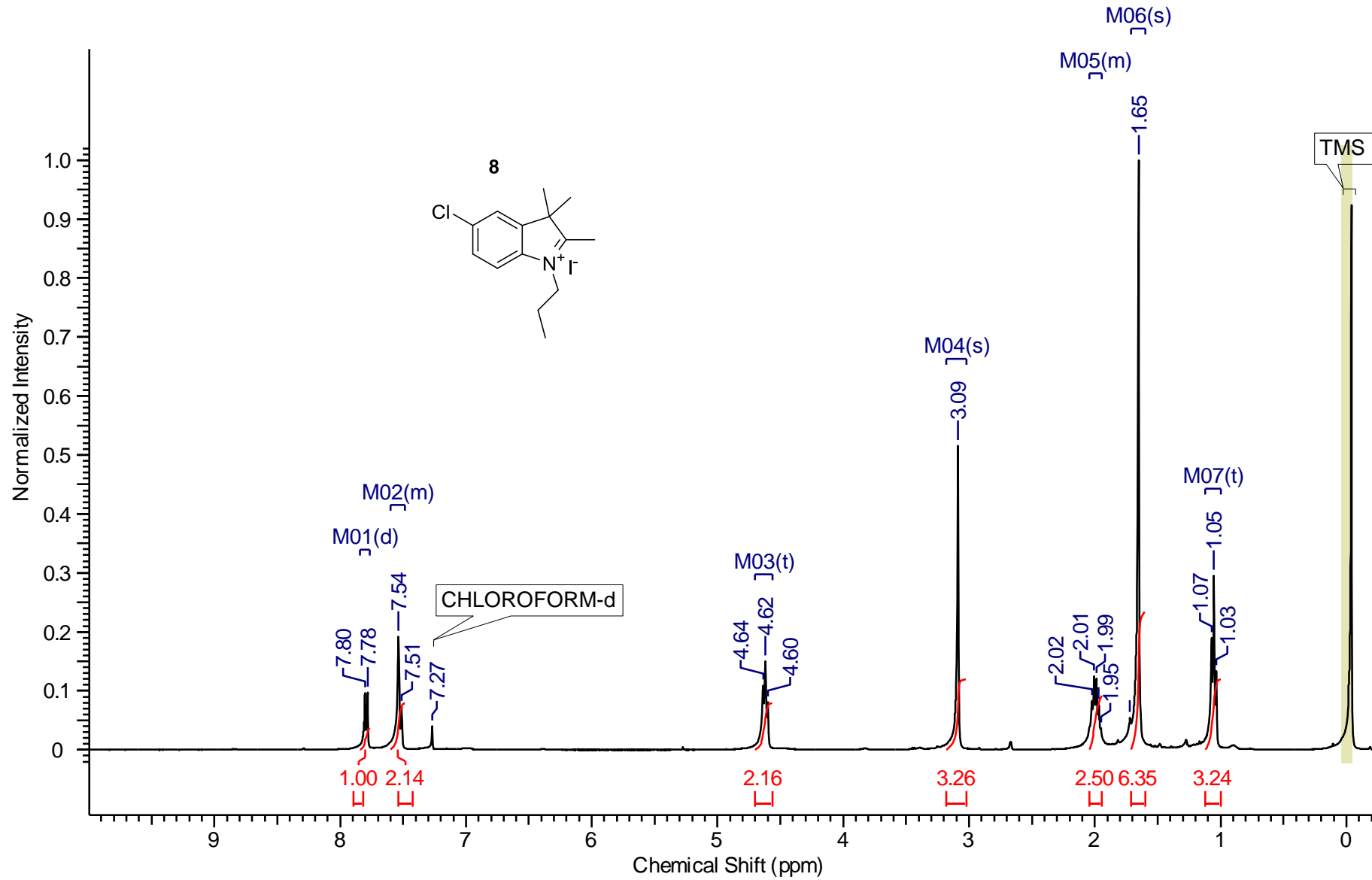


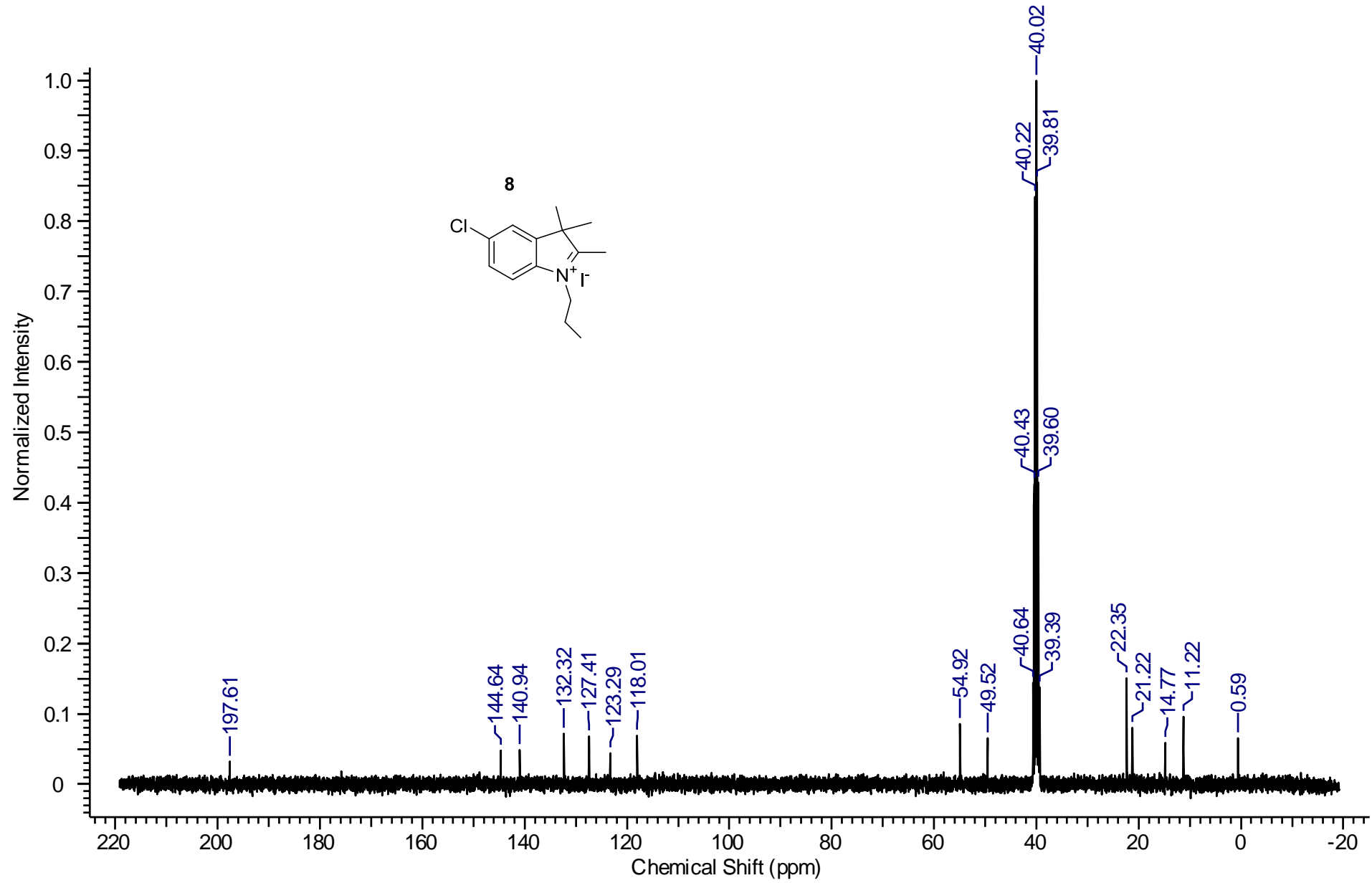
Exact Mass	549.14
LogD at 7.4	3.21
TPSA	43.17
HBD	0.00
HBA	5.00
Total Charge	1.00
Refractivity	158.00
Rotatable Bond	3.00
SB pKa	1.37
SA pKa	0.00

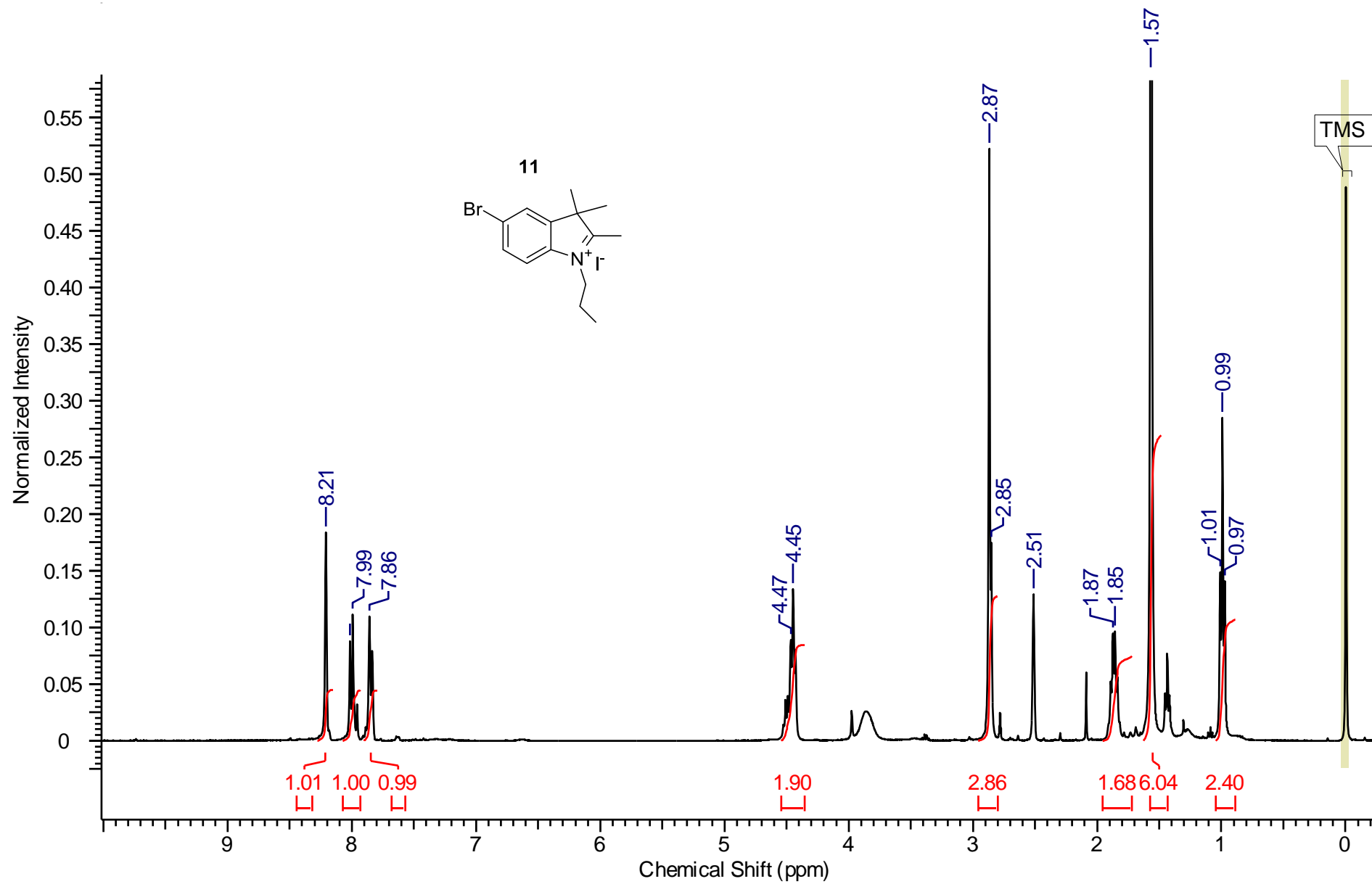


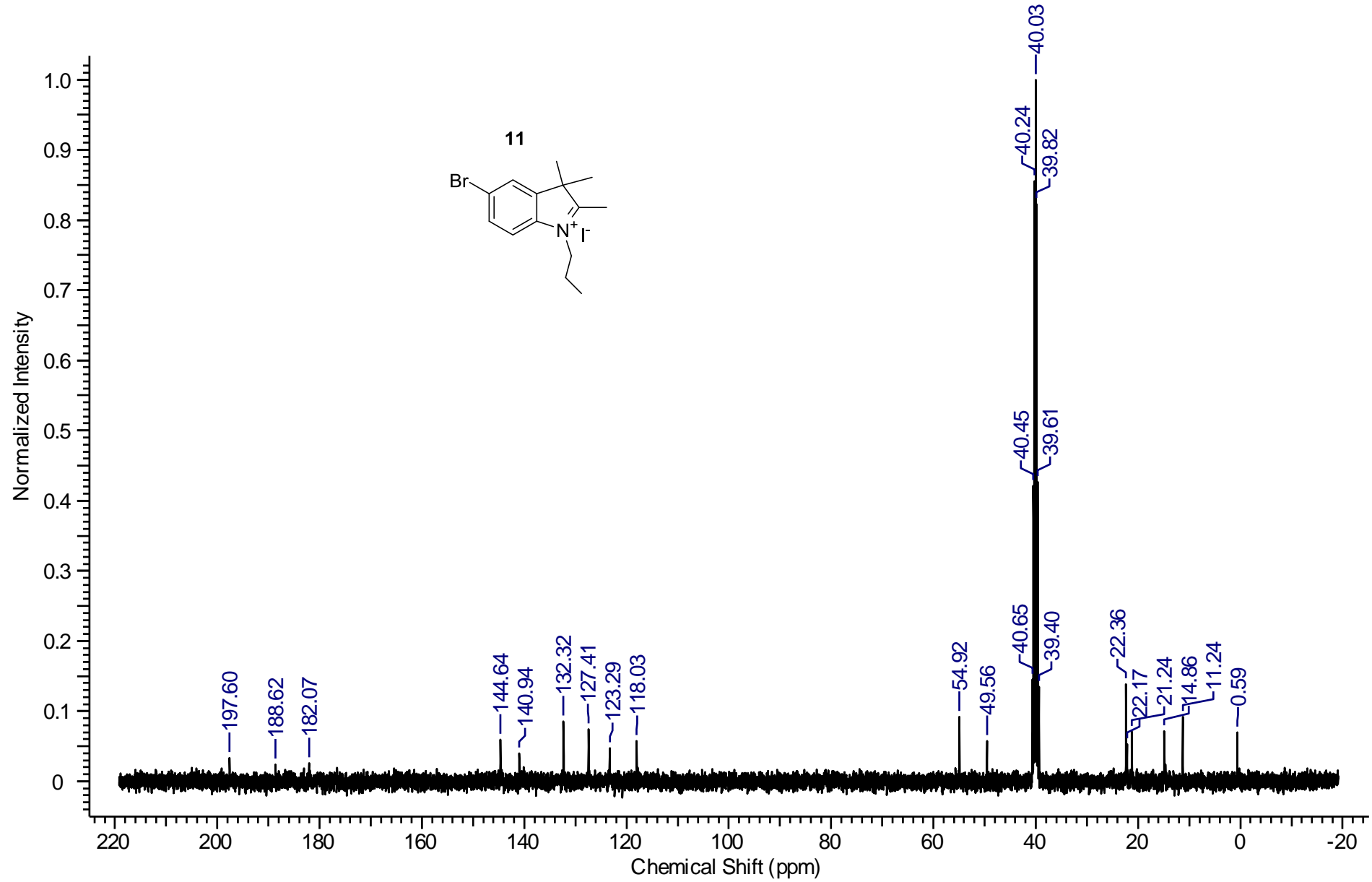


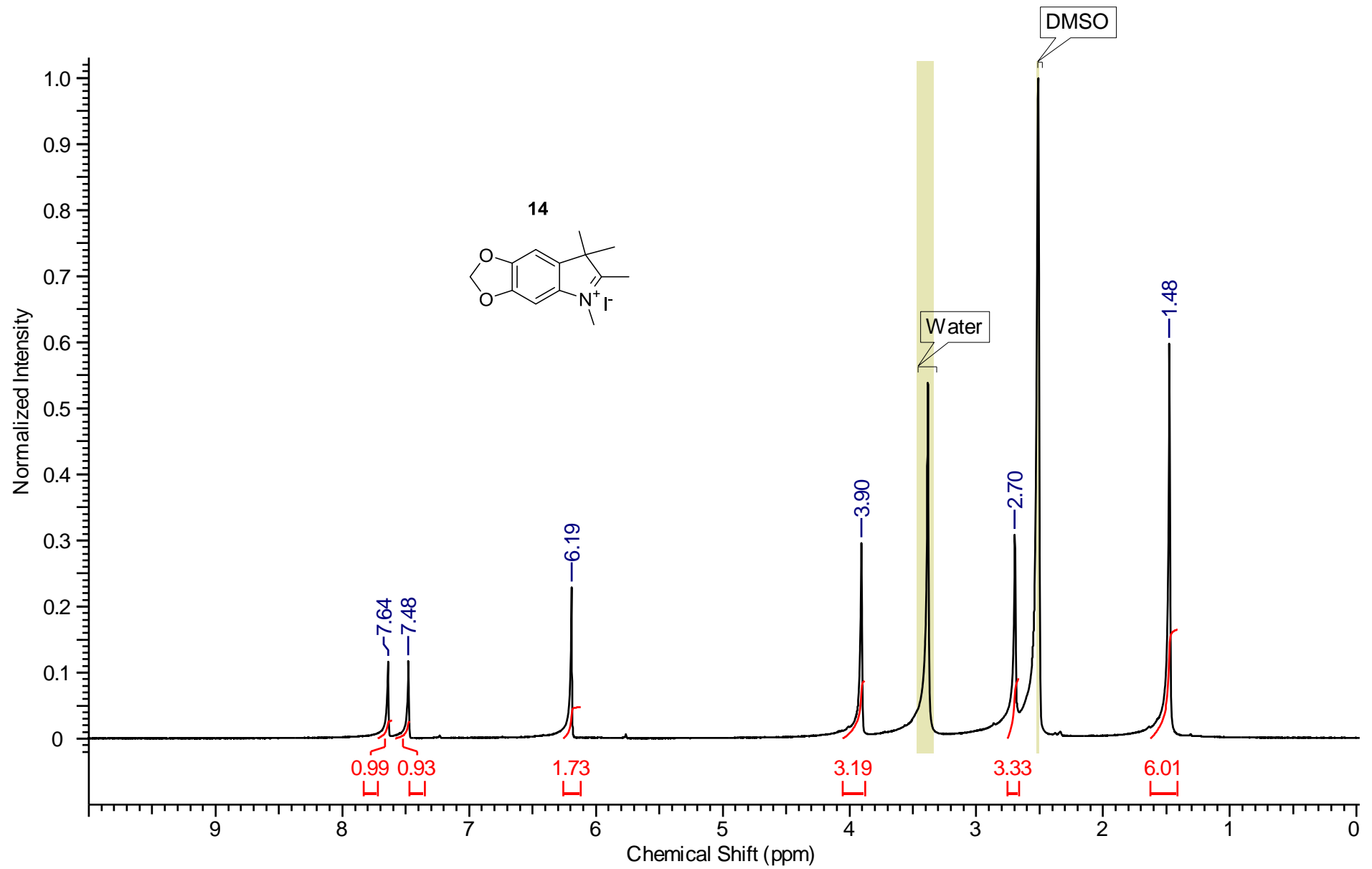


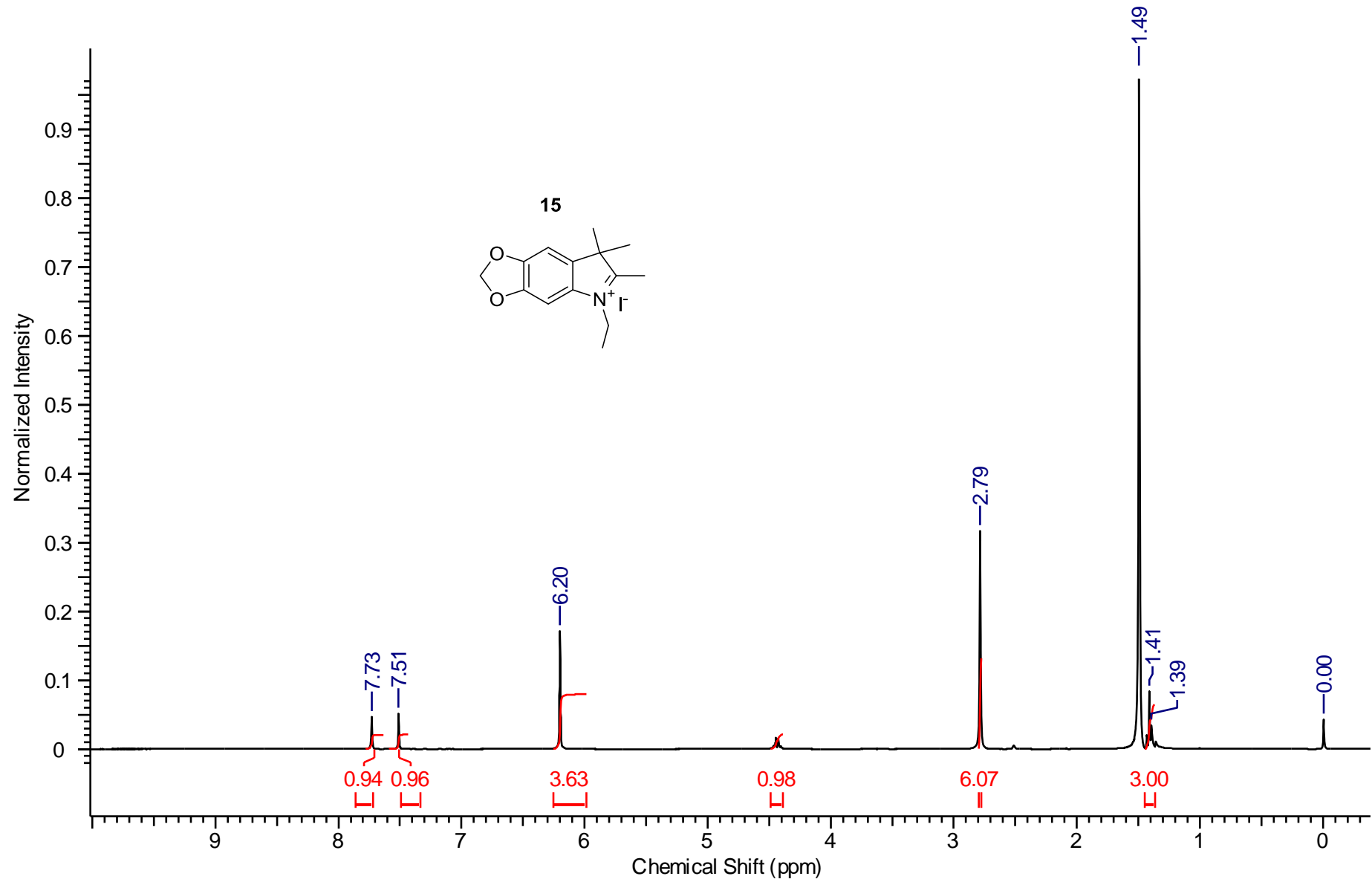


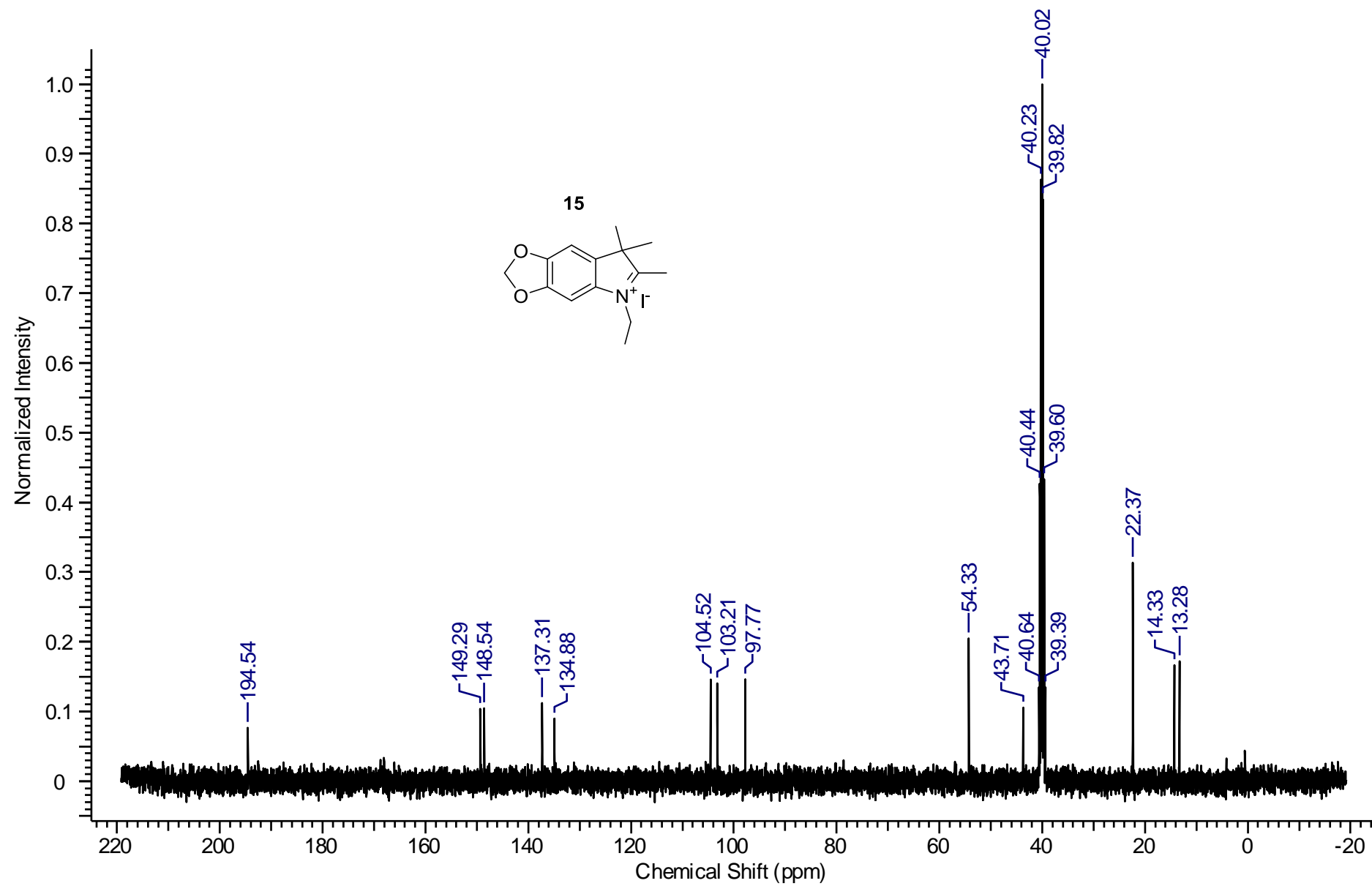


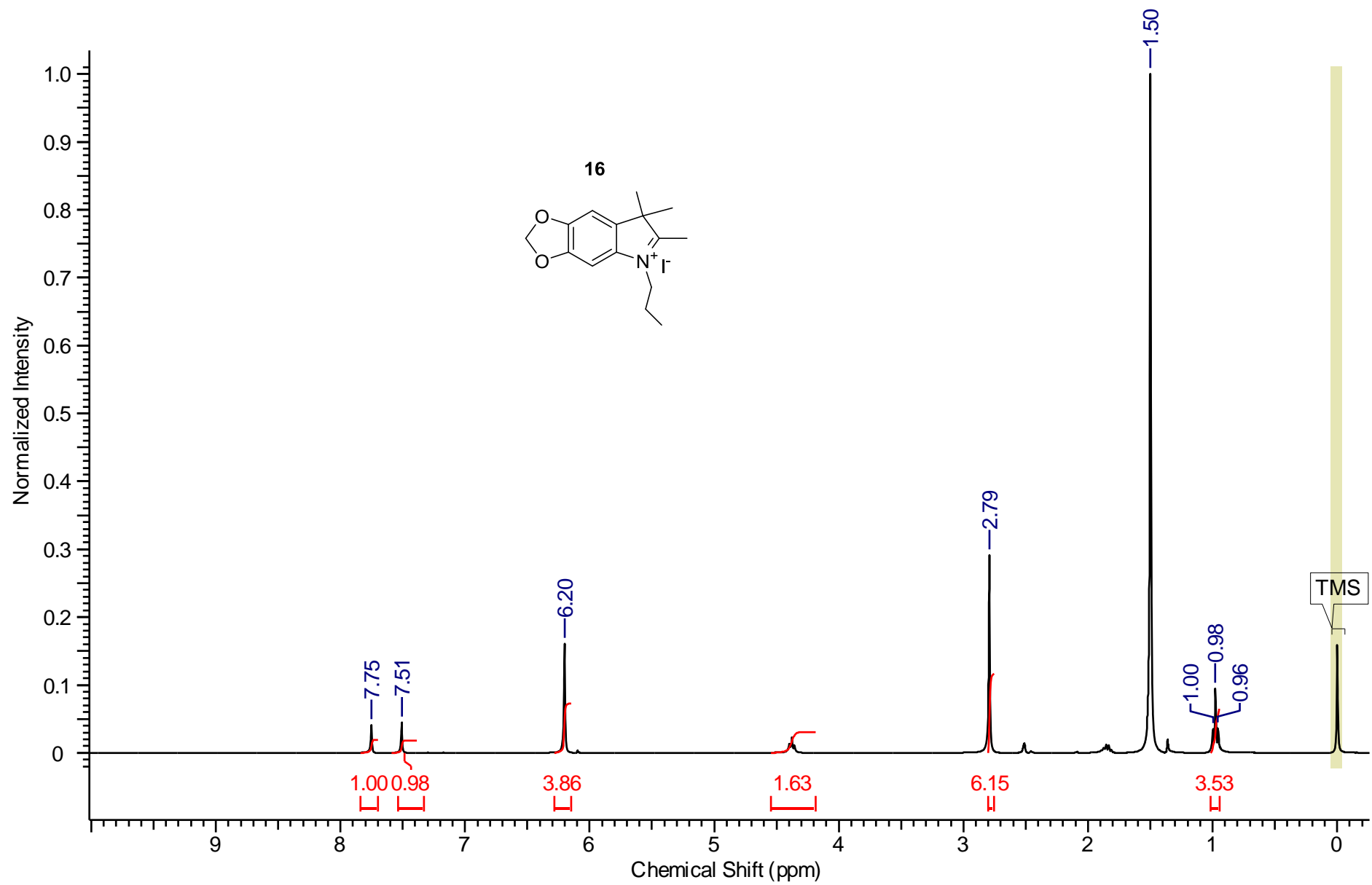


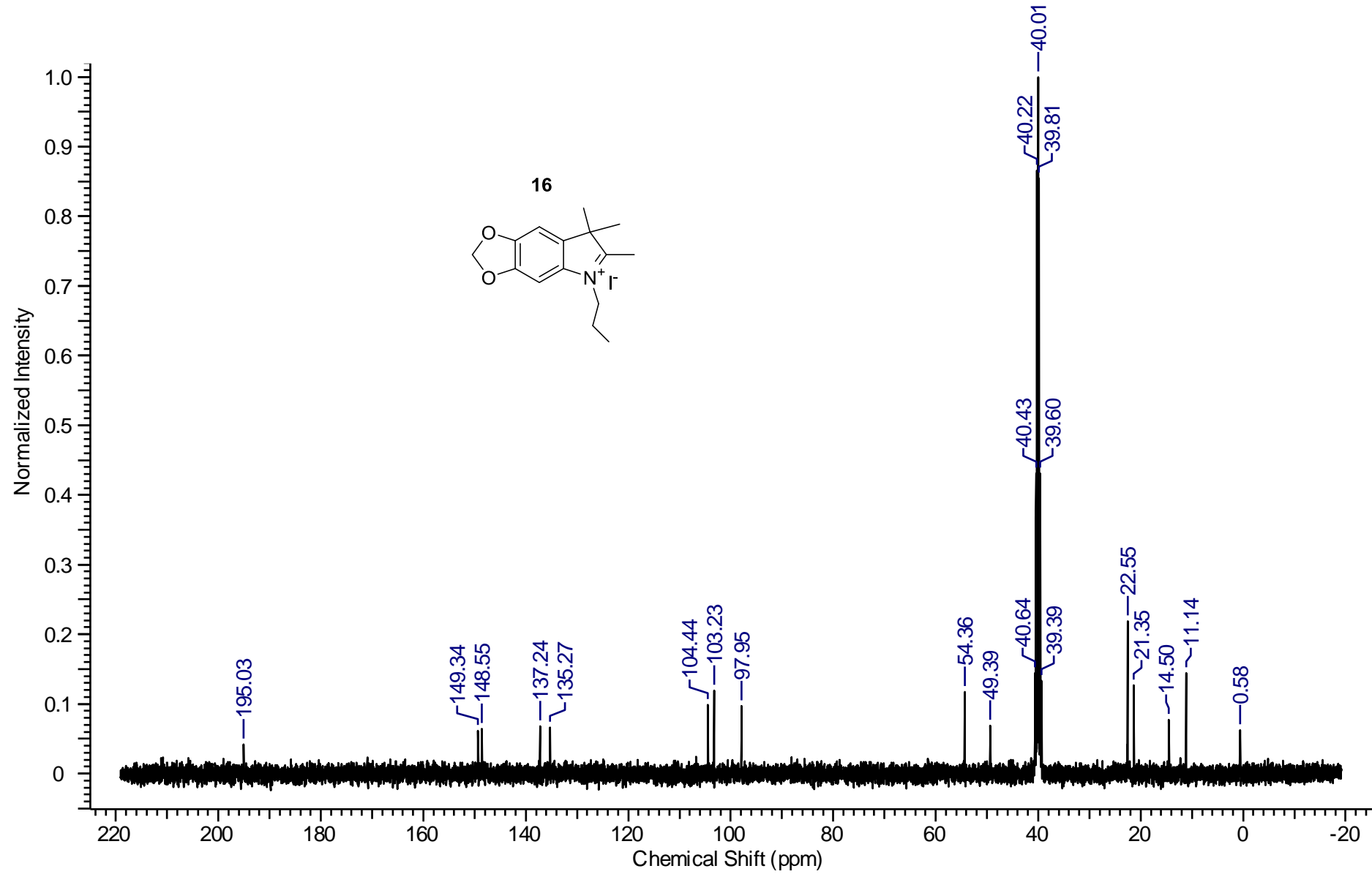


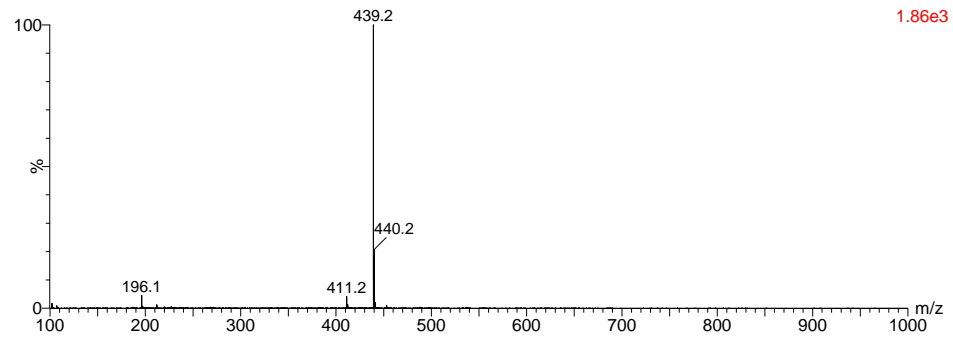




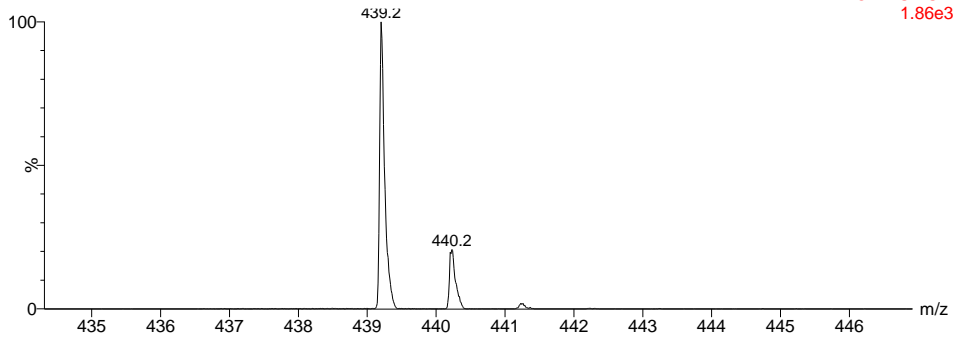


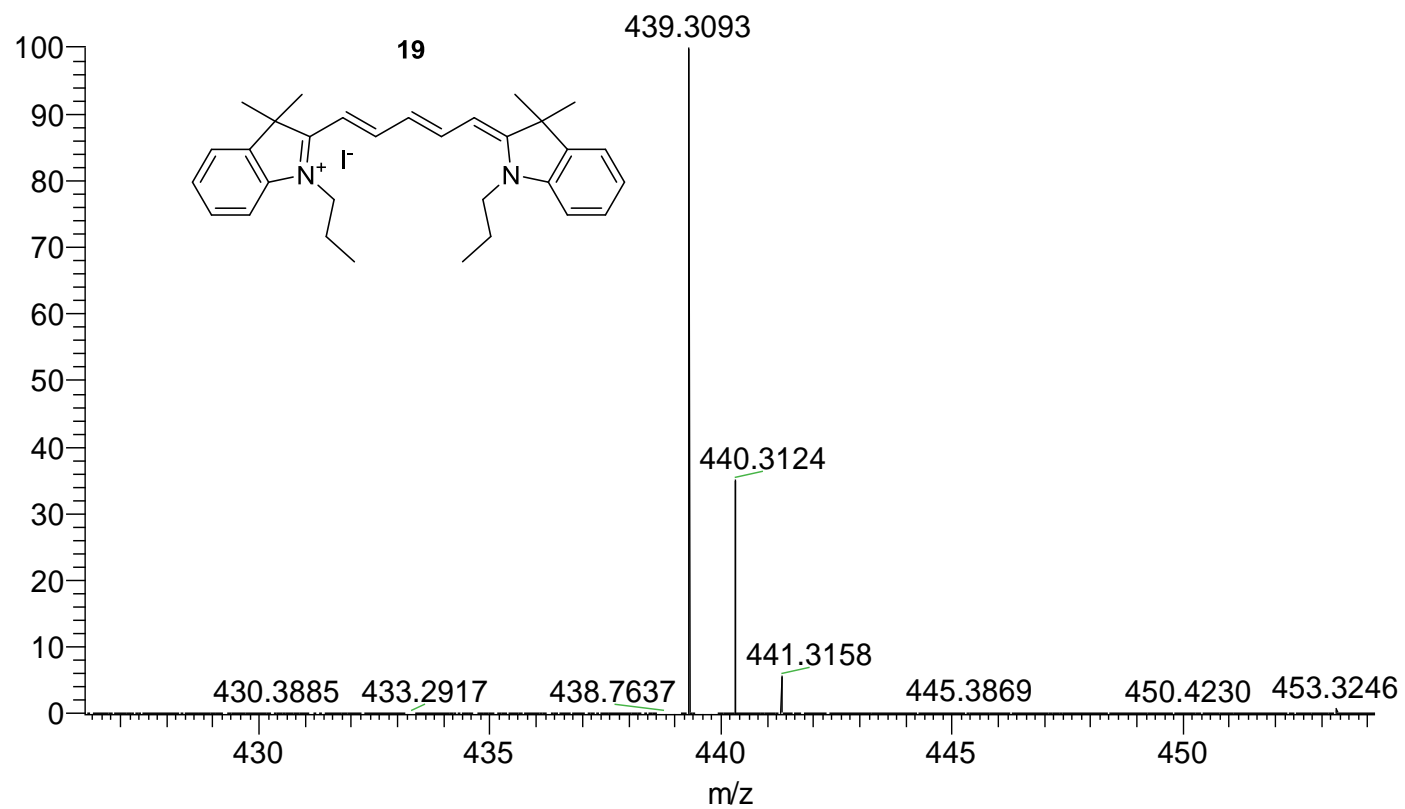




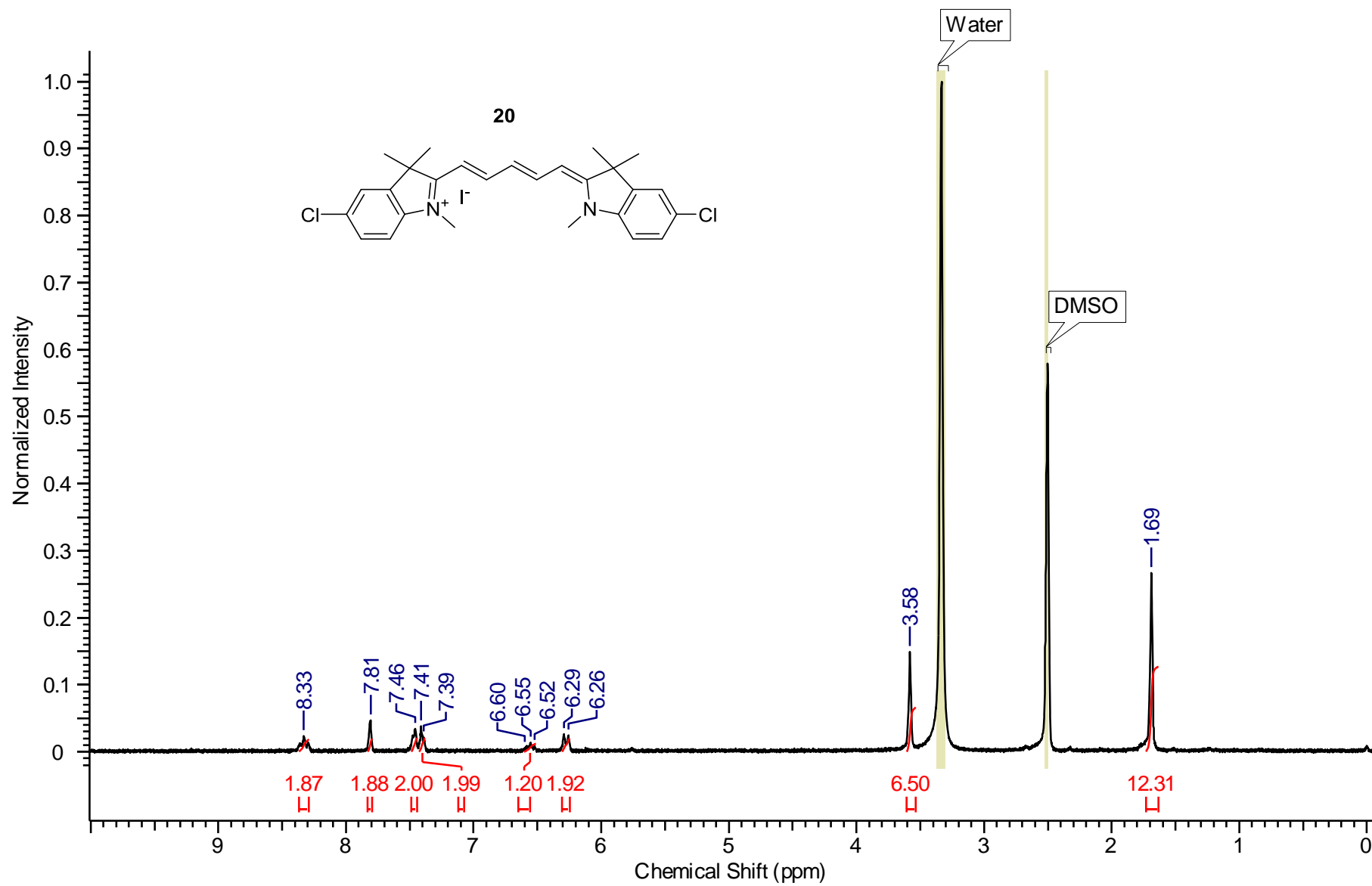


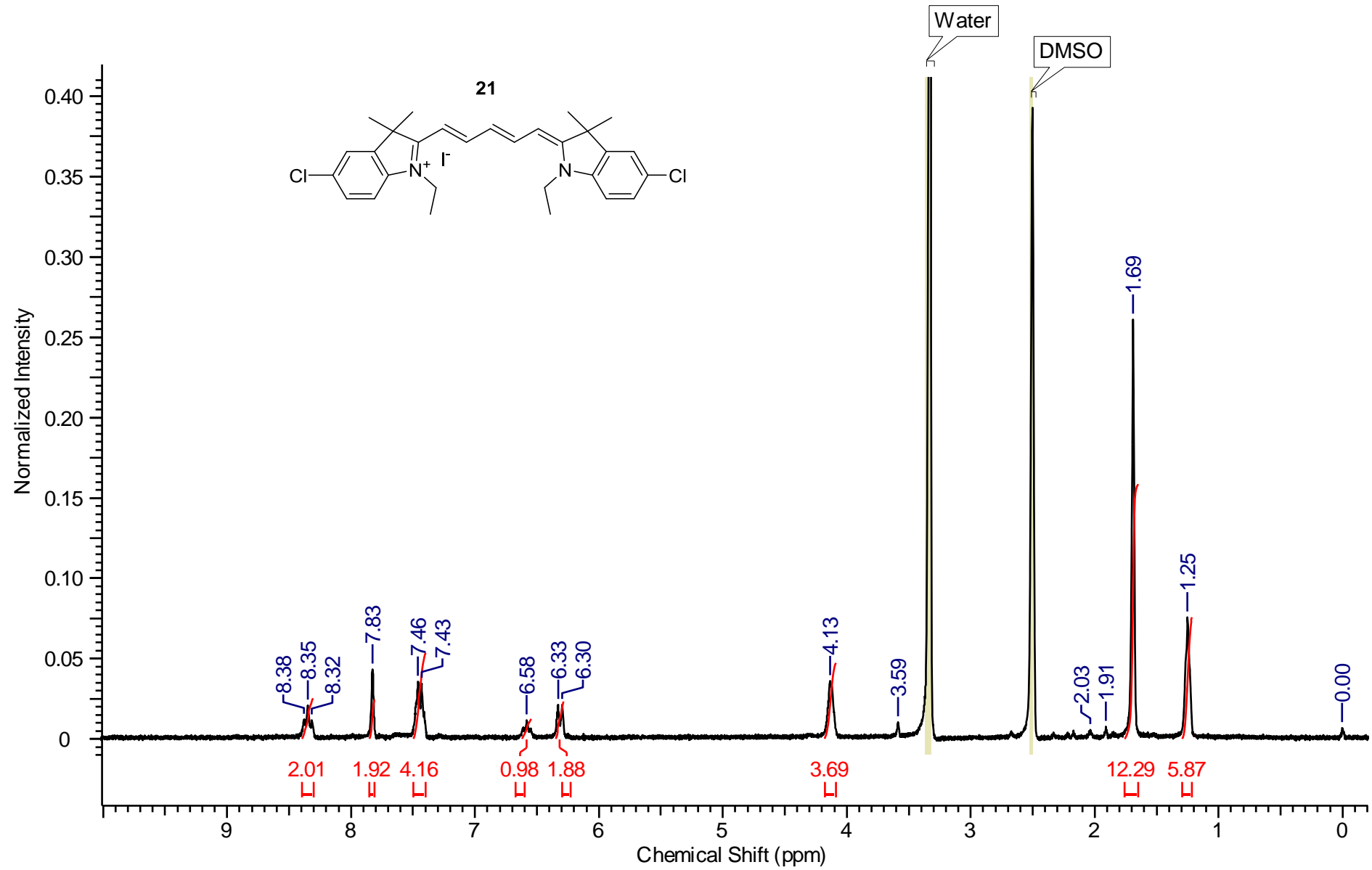
20-Aug-2013 12:20:24
TOF MS ES+
1.86e3

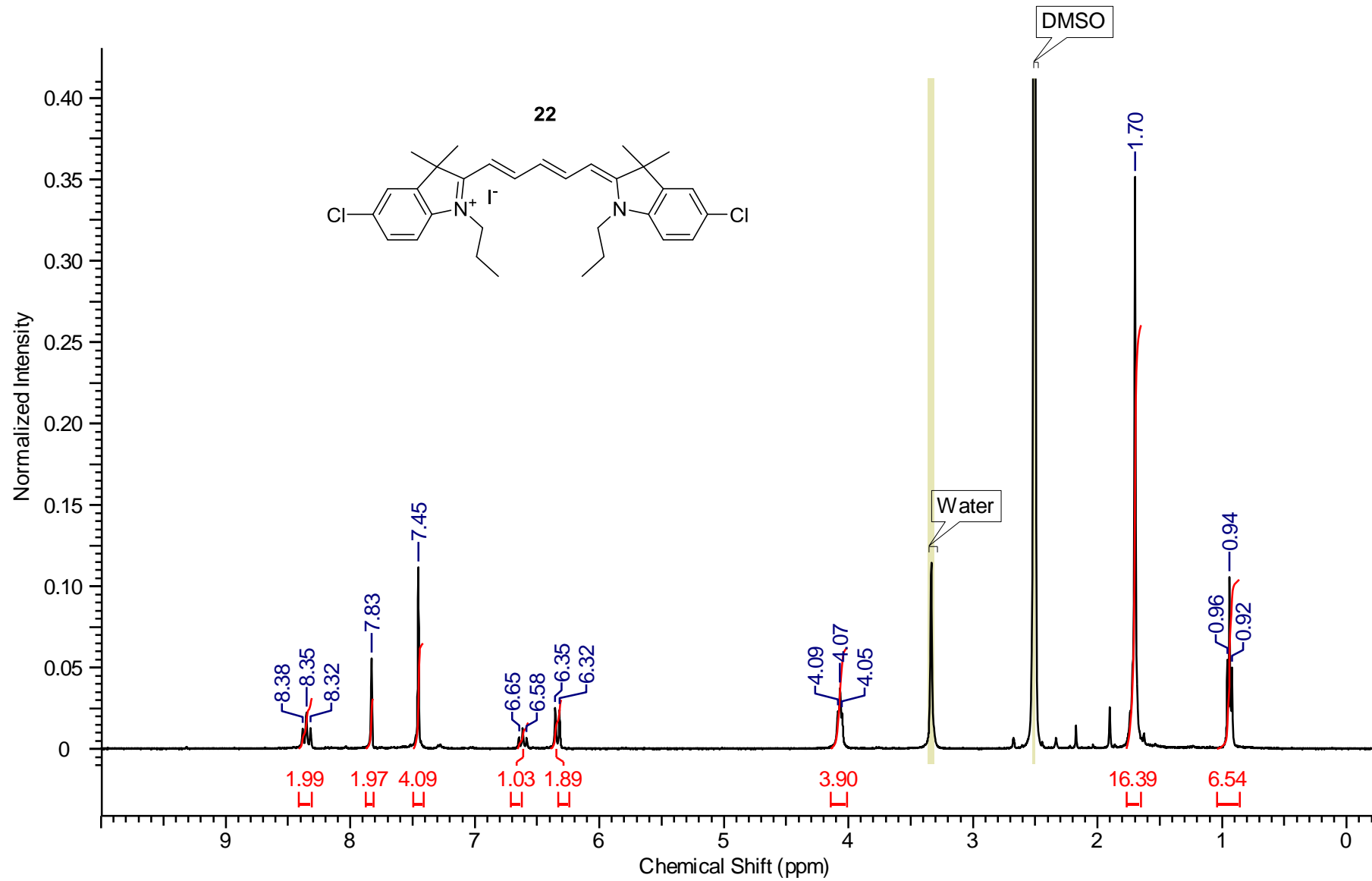


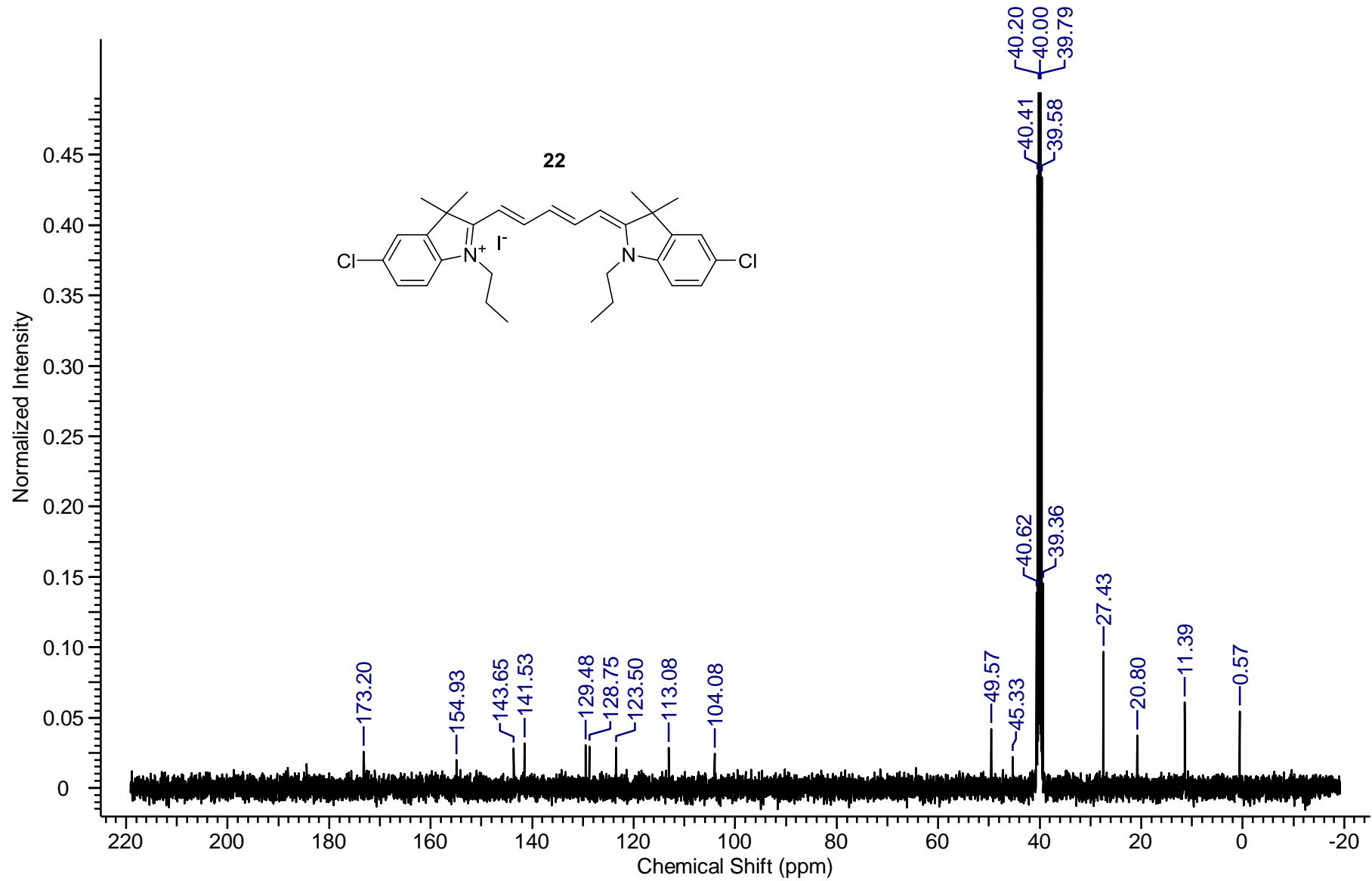


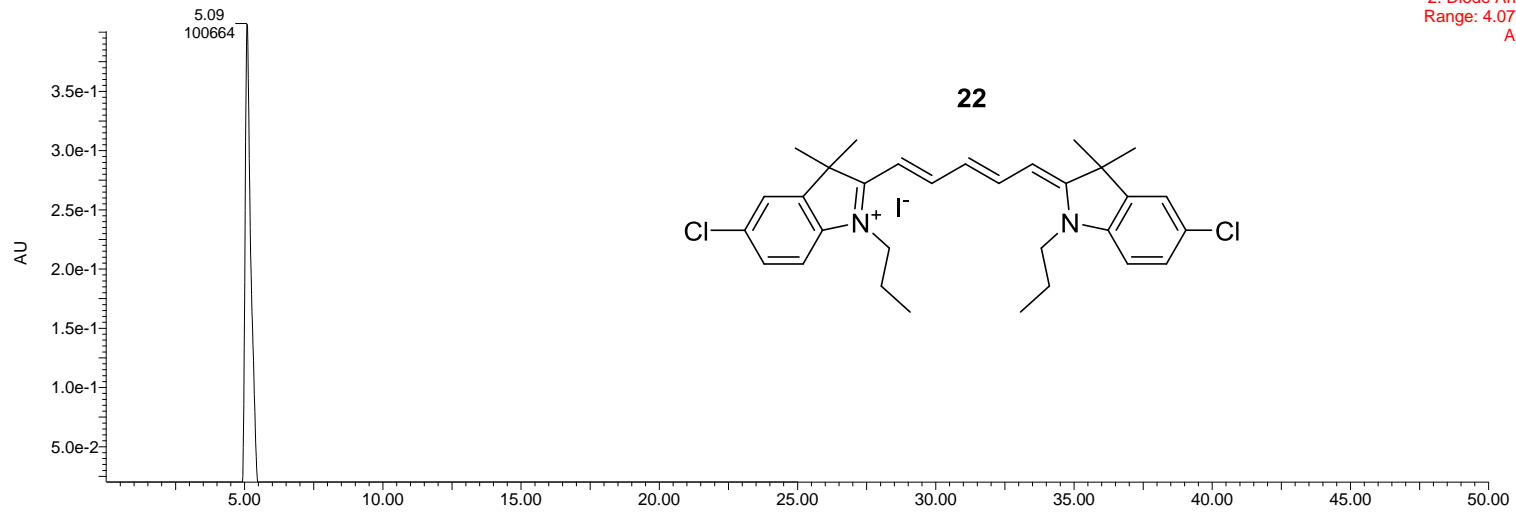
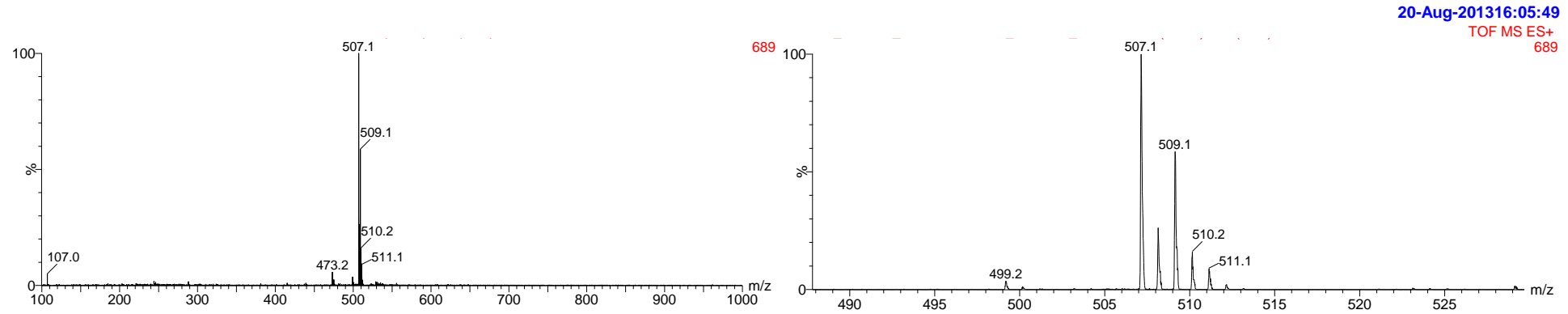
m/z	Theo. Mass	Delta (mmu)	RDB equiv.	Composition
439.3093	439.3108	-1.46	13.5	C31 H39 N2

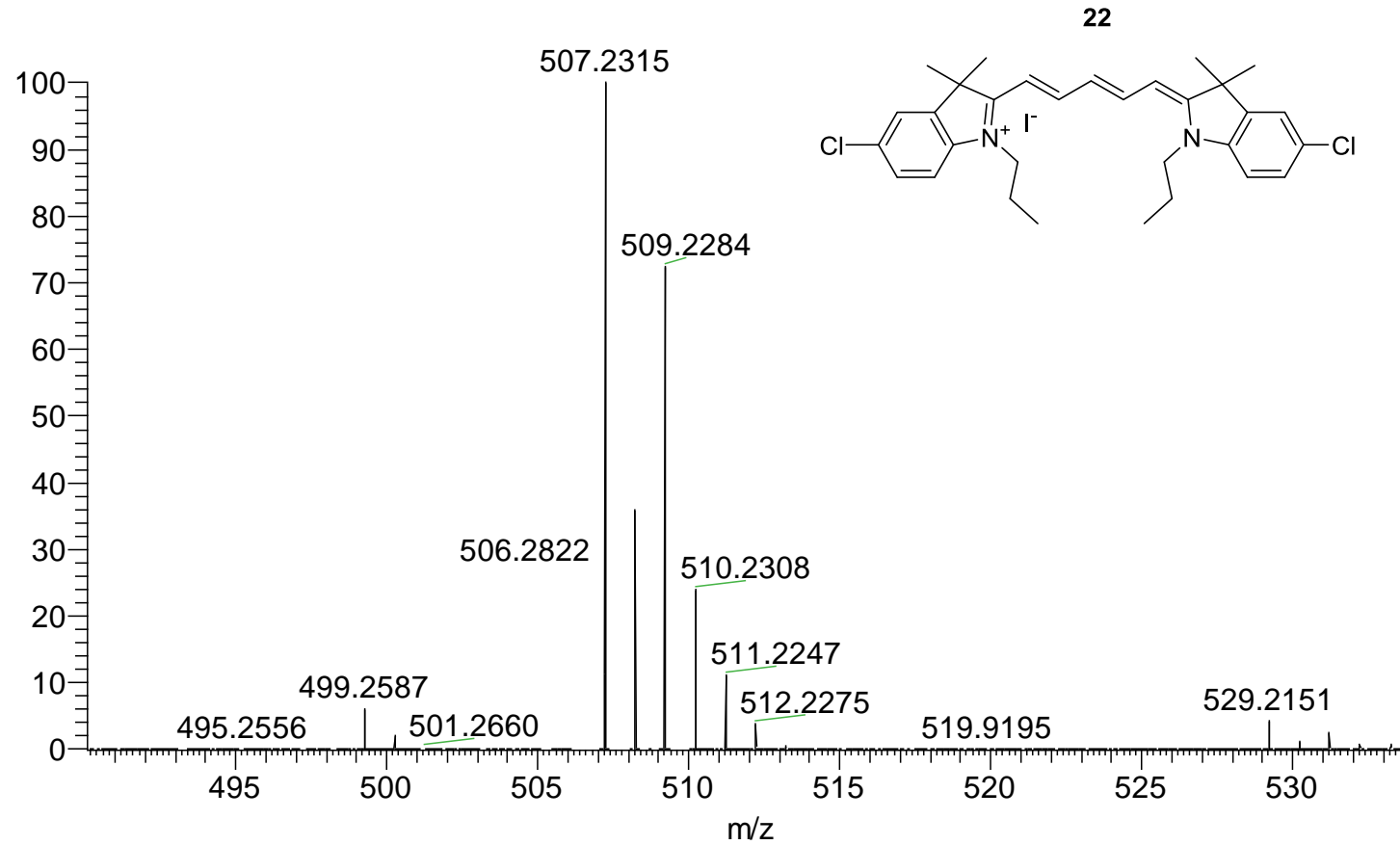




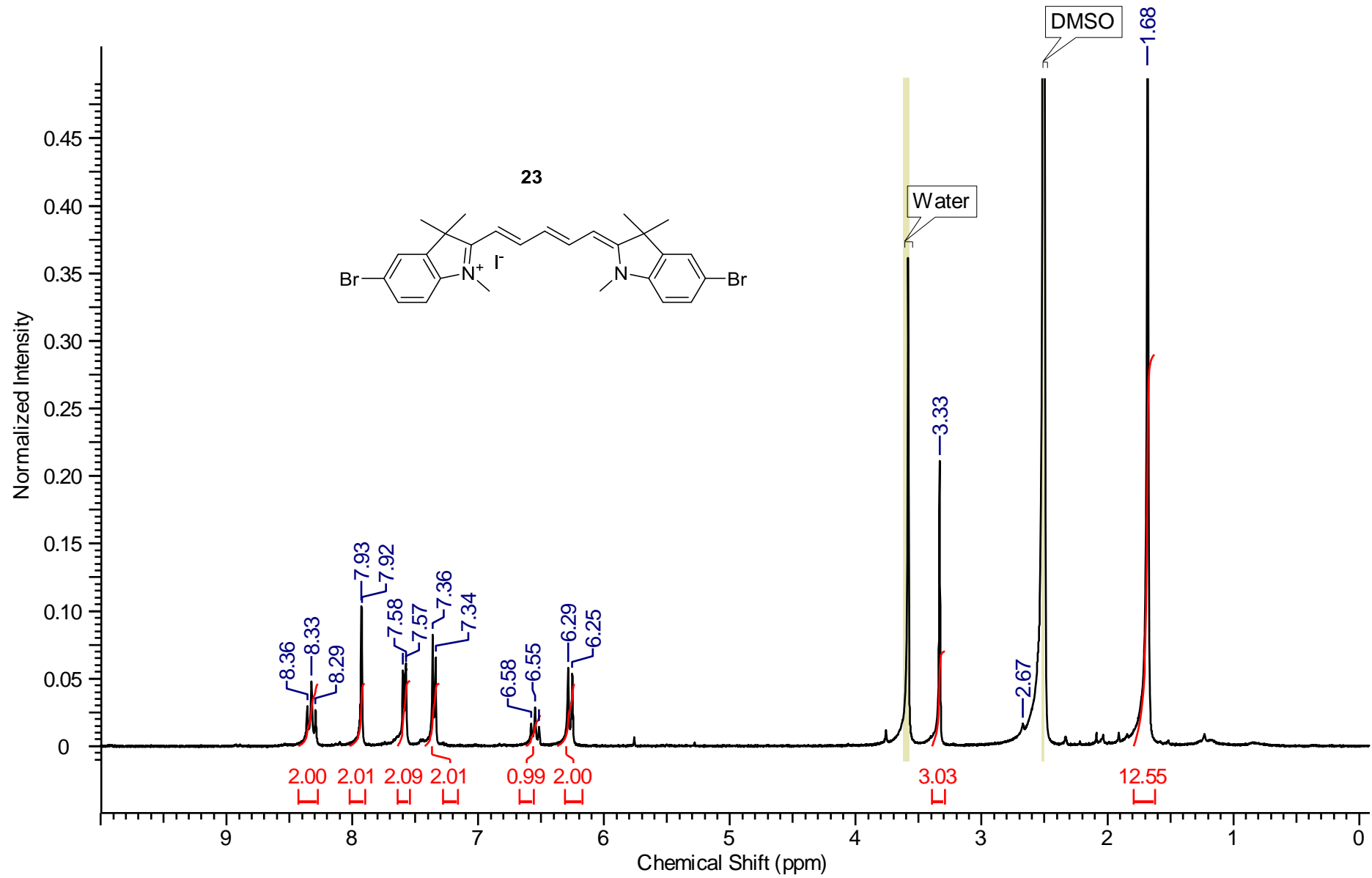


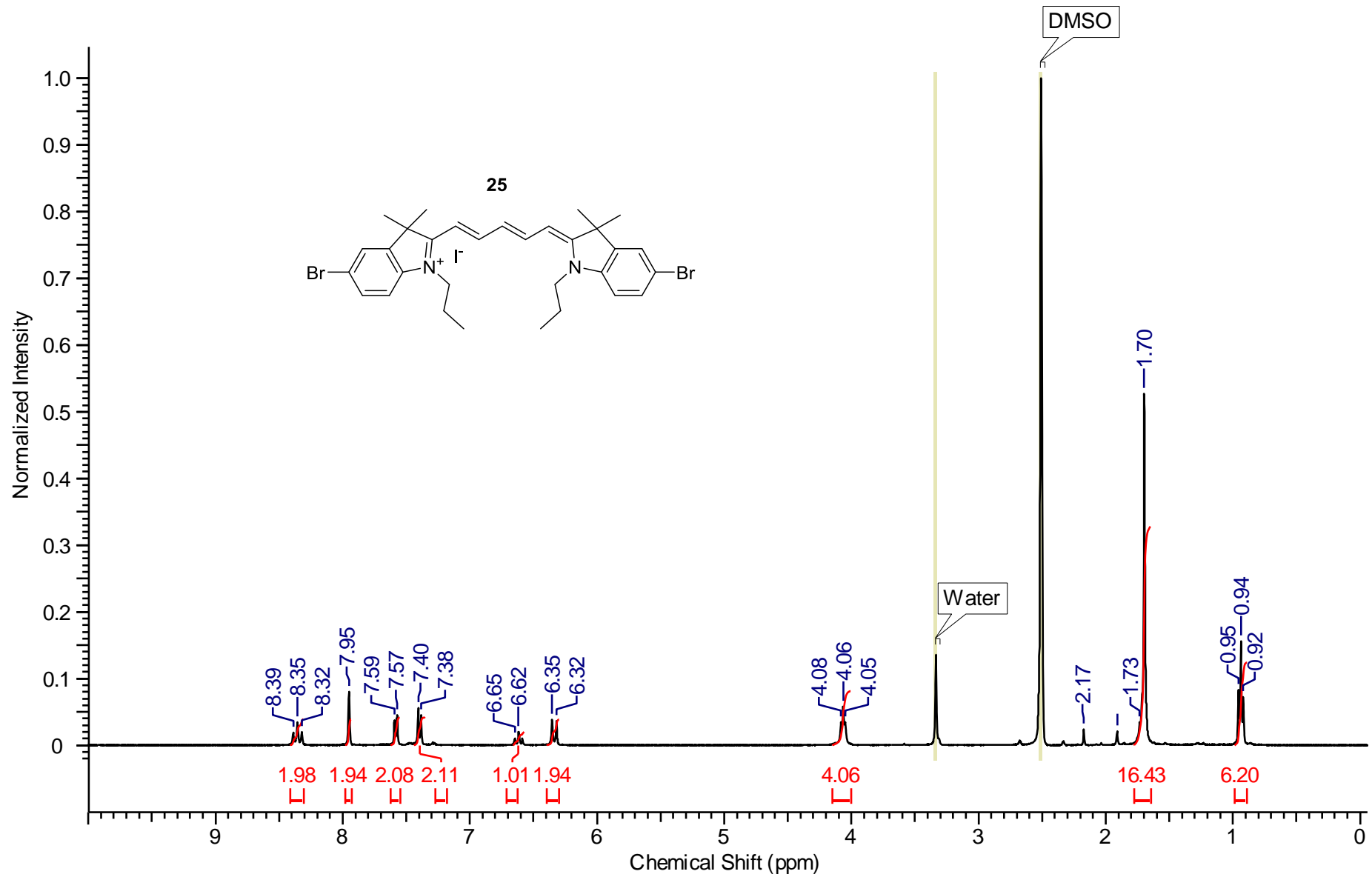


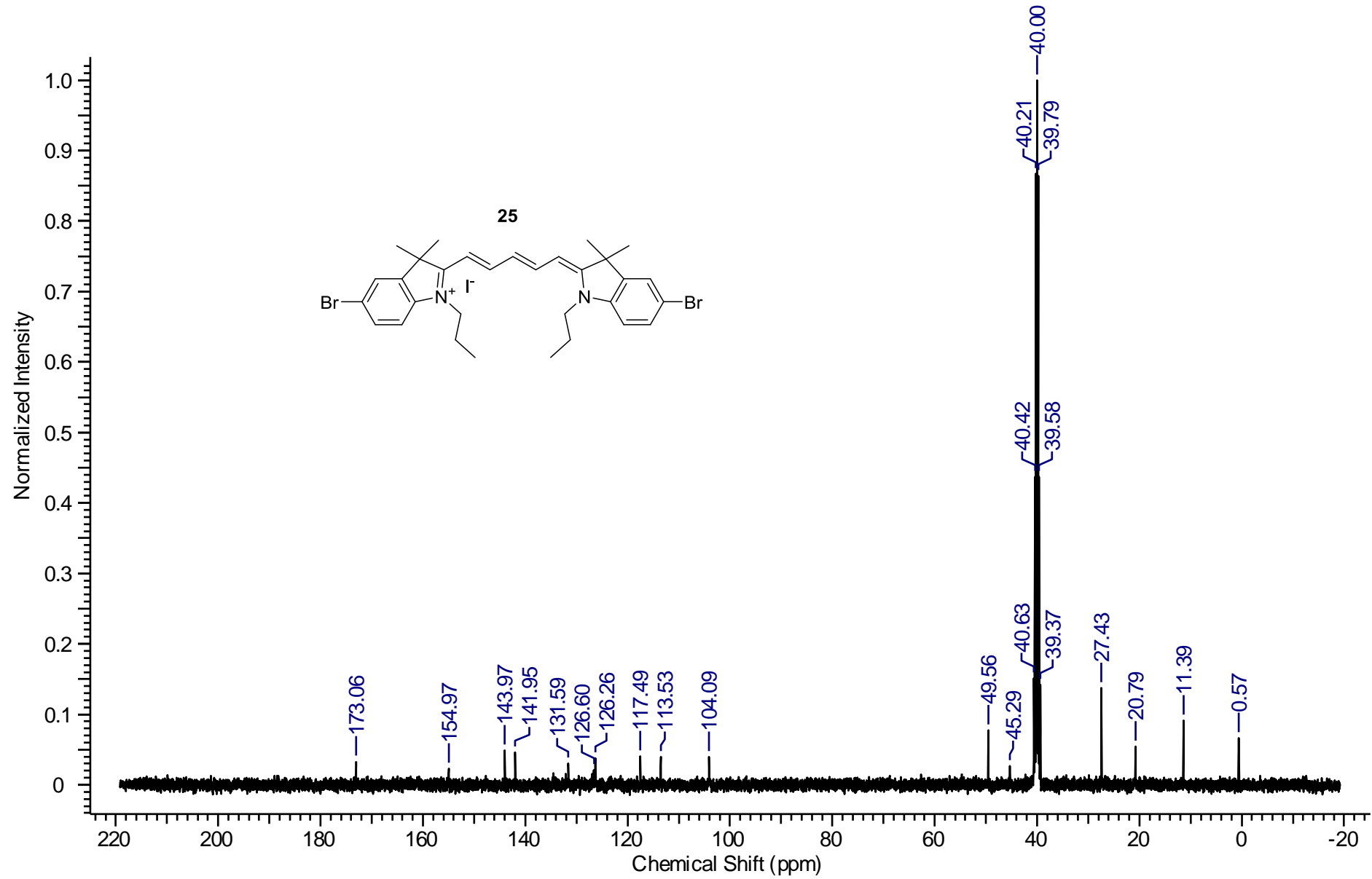


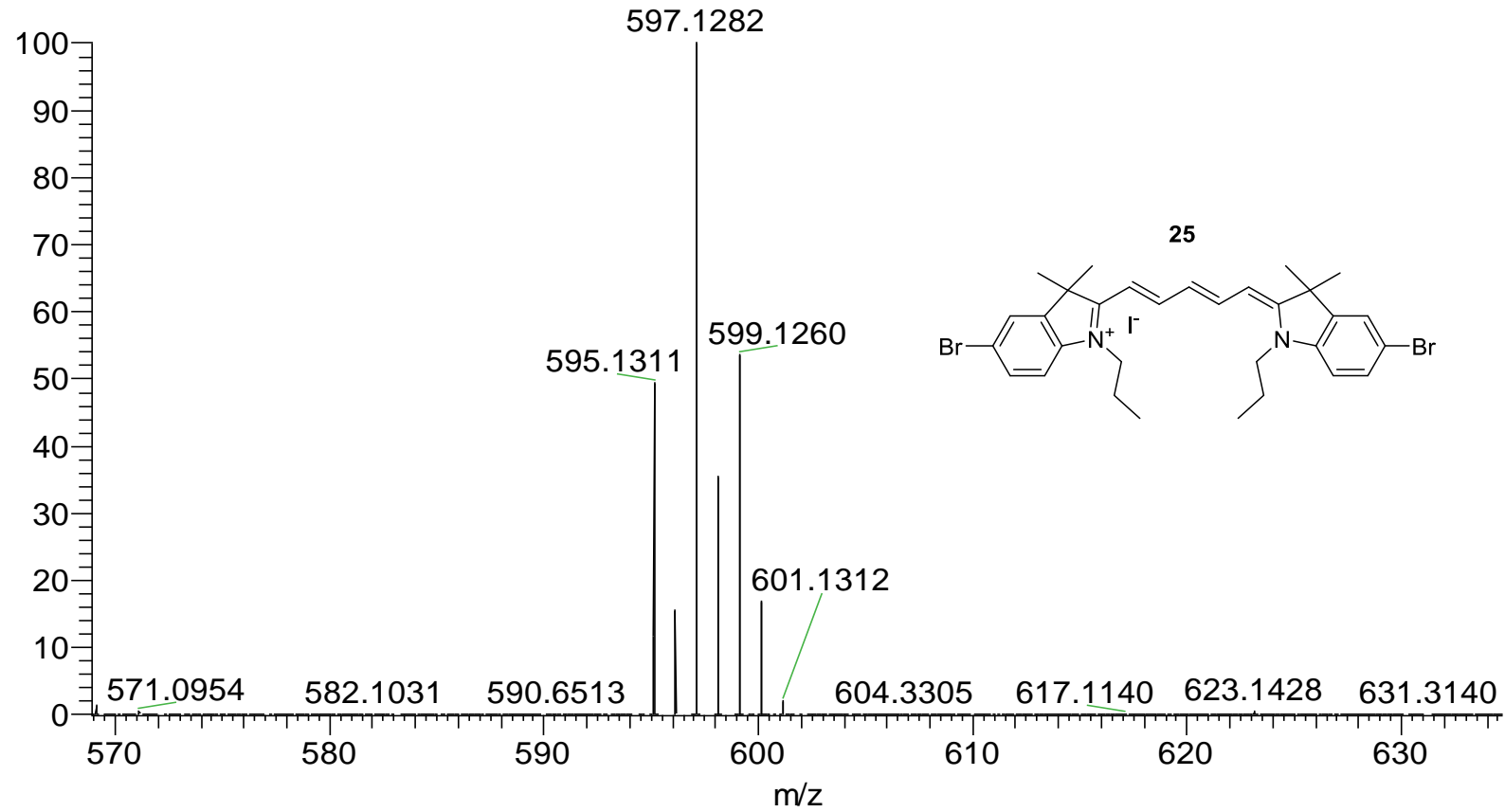


m/z	Theo. Mass	Delta (mmu)	RDB equiv.	Composition
507.2315	507.2328	-1.34	13.5	C31 H37 N2 Cl2

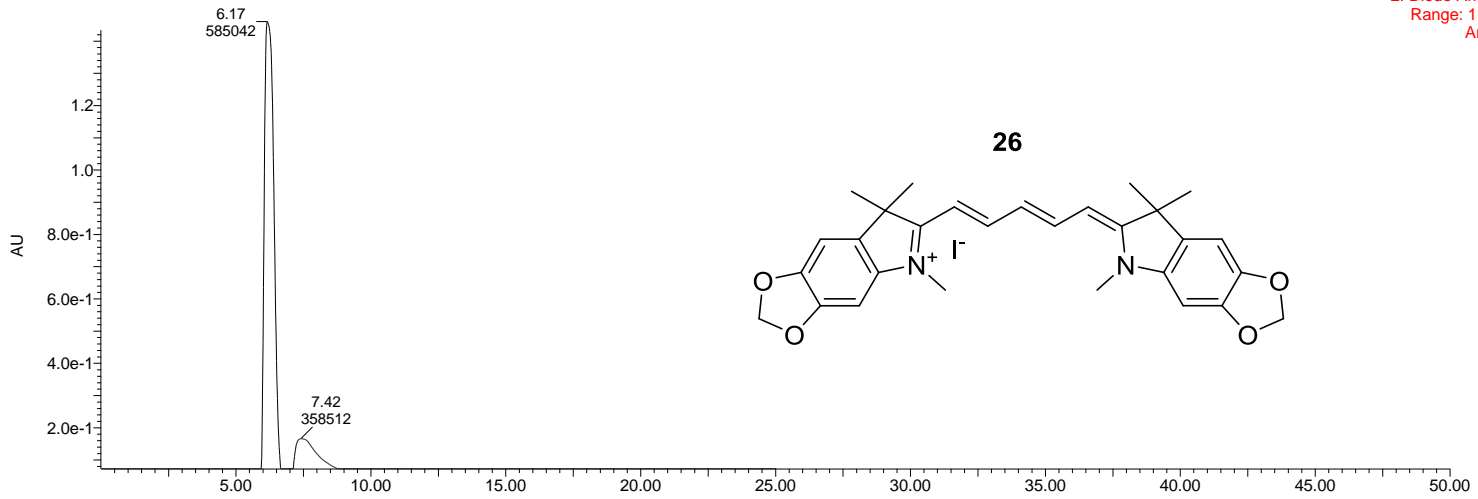
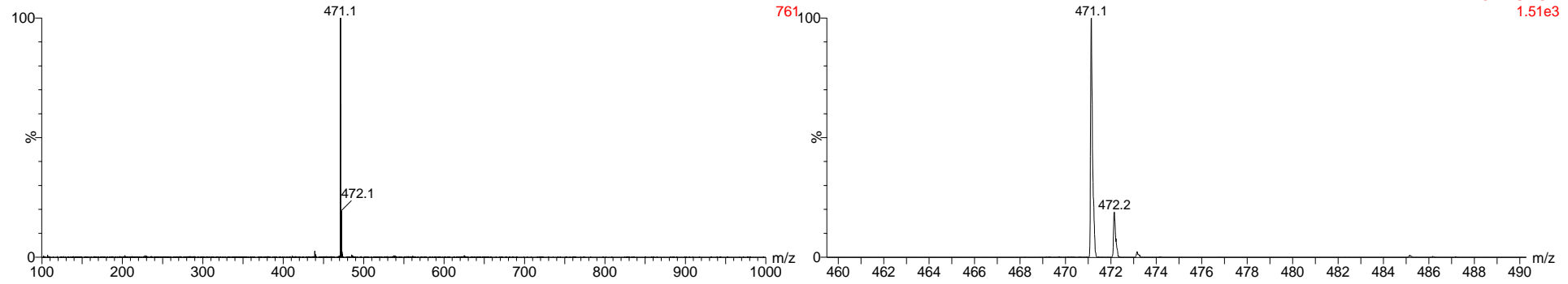


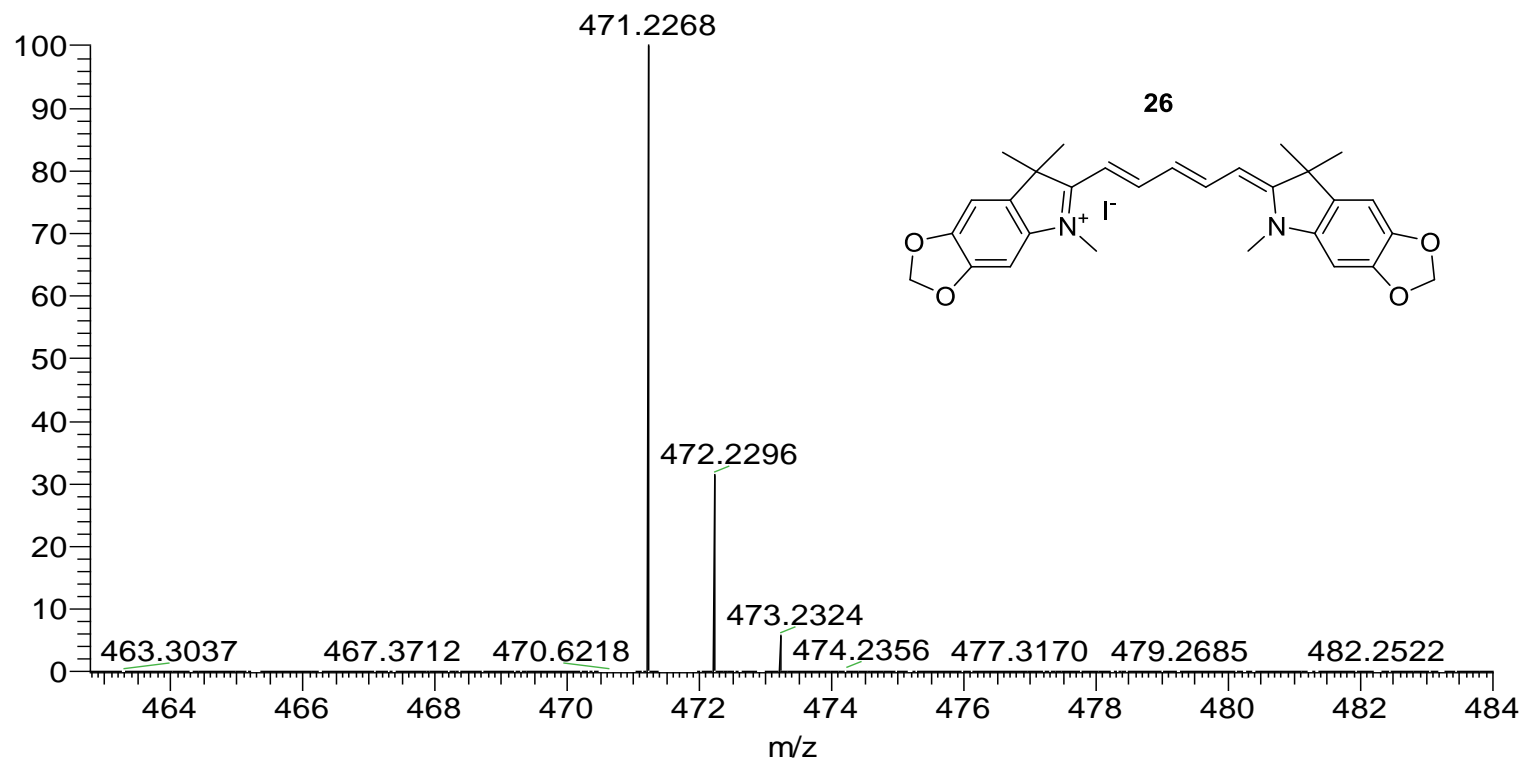




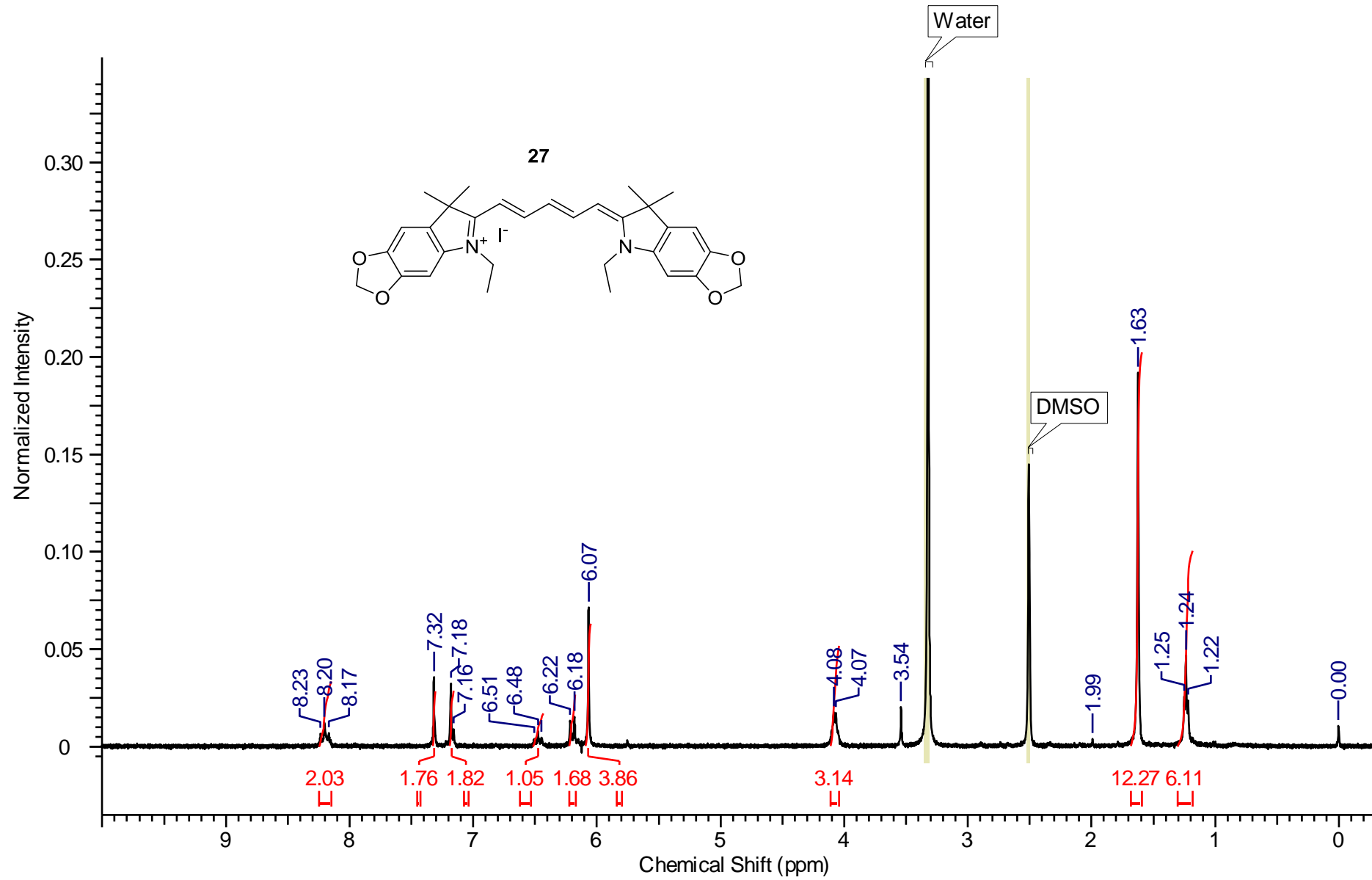


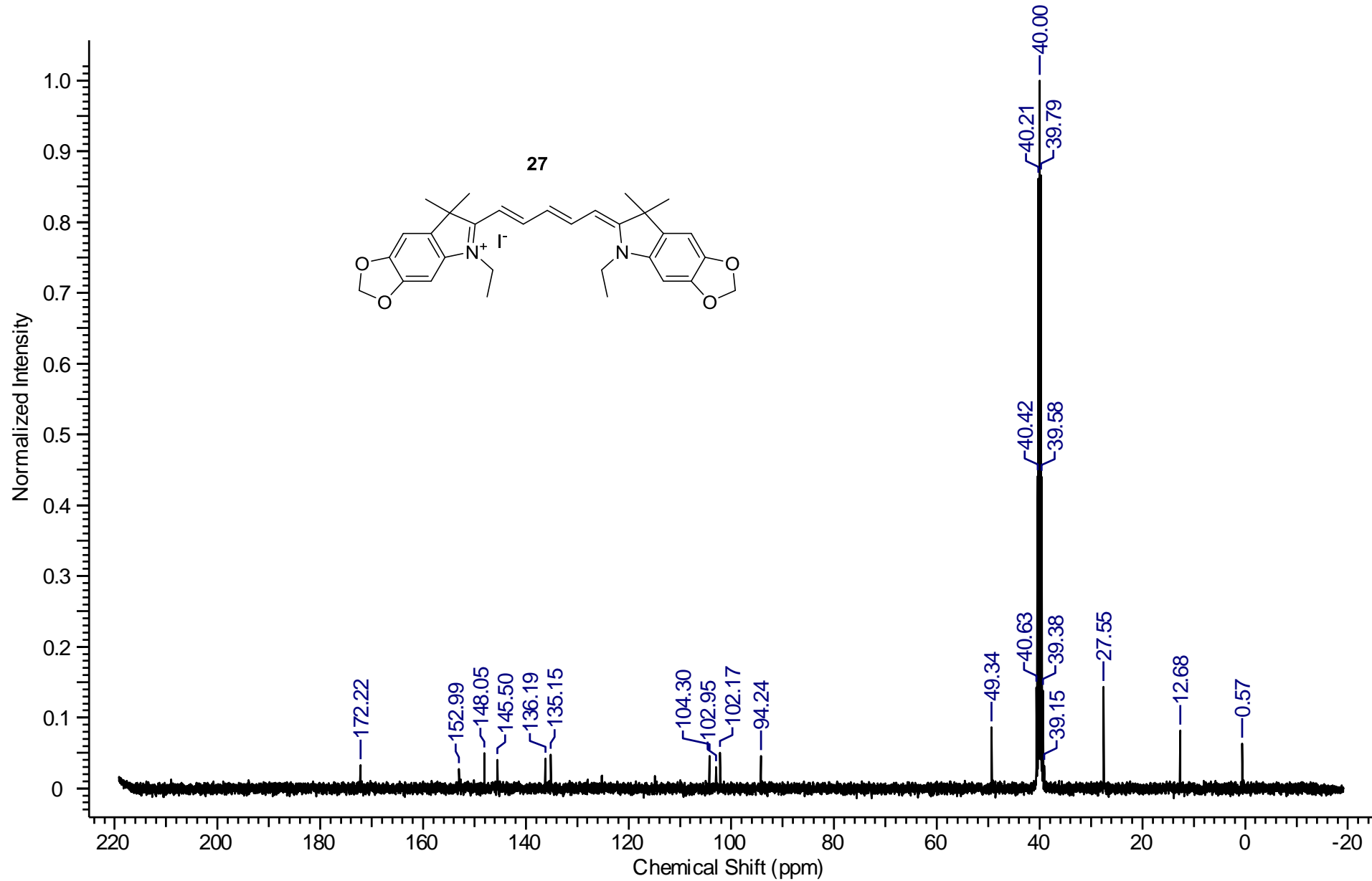
m/z	Theo. Mass	Delta (ppm)	RDB equiv	Composition
595.1311	595.1318	-1.19	13.5	C31 H37 N2 Br2

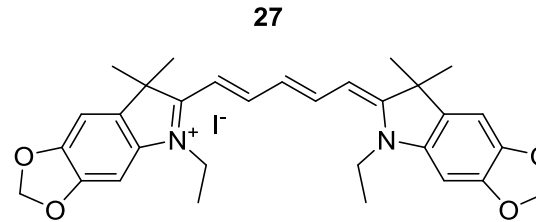
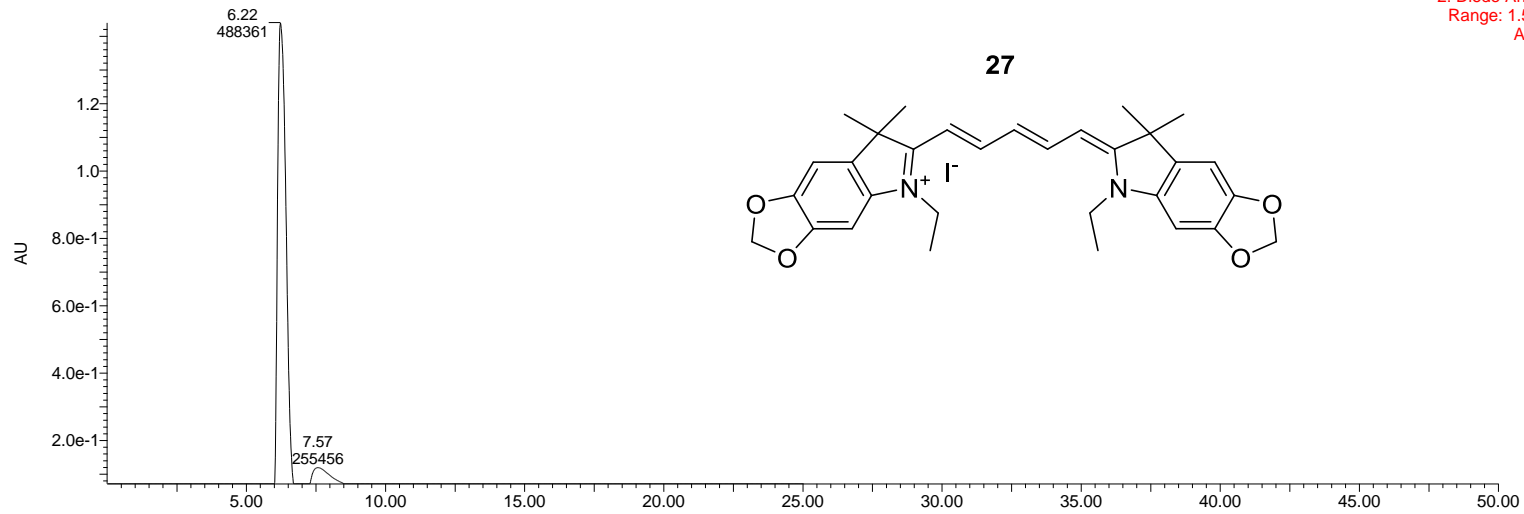
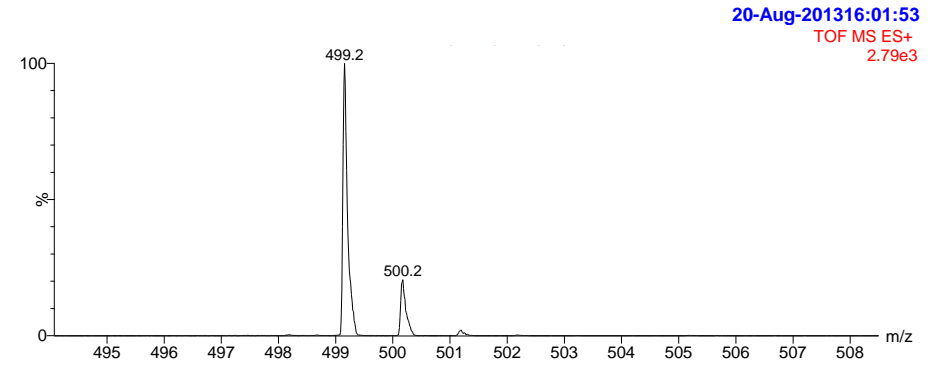
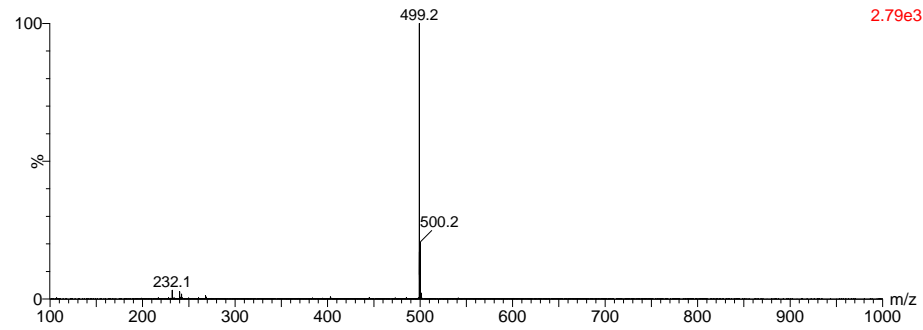


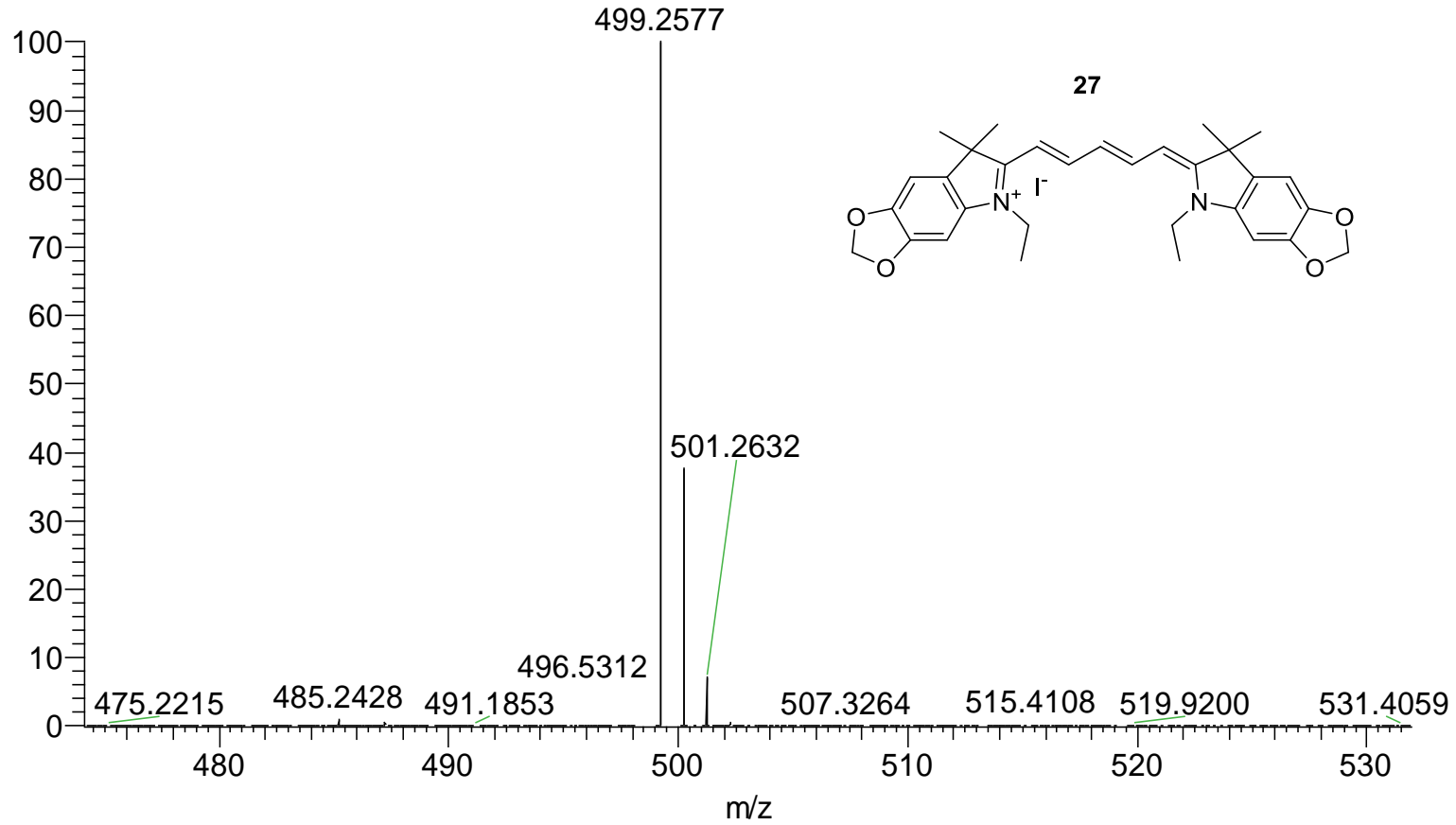


m/z	Theo. Mass	Delta (mmu)	RDB equiv.	Composition
471.2268	471.2278	-1.01	15.5	C ₂₉ H ₃₁ O ₄ N ₂

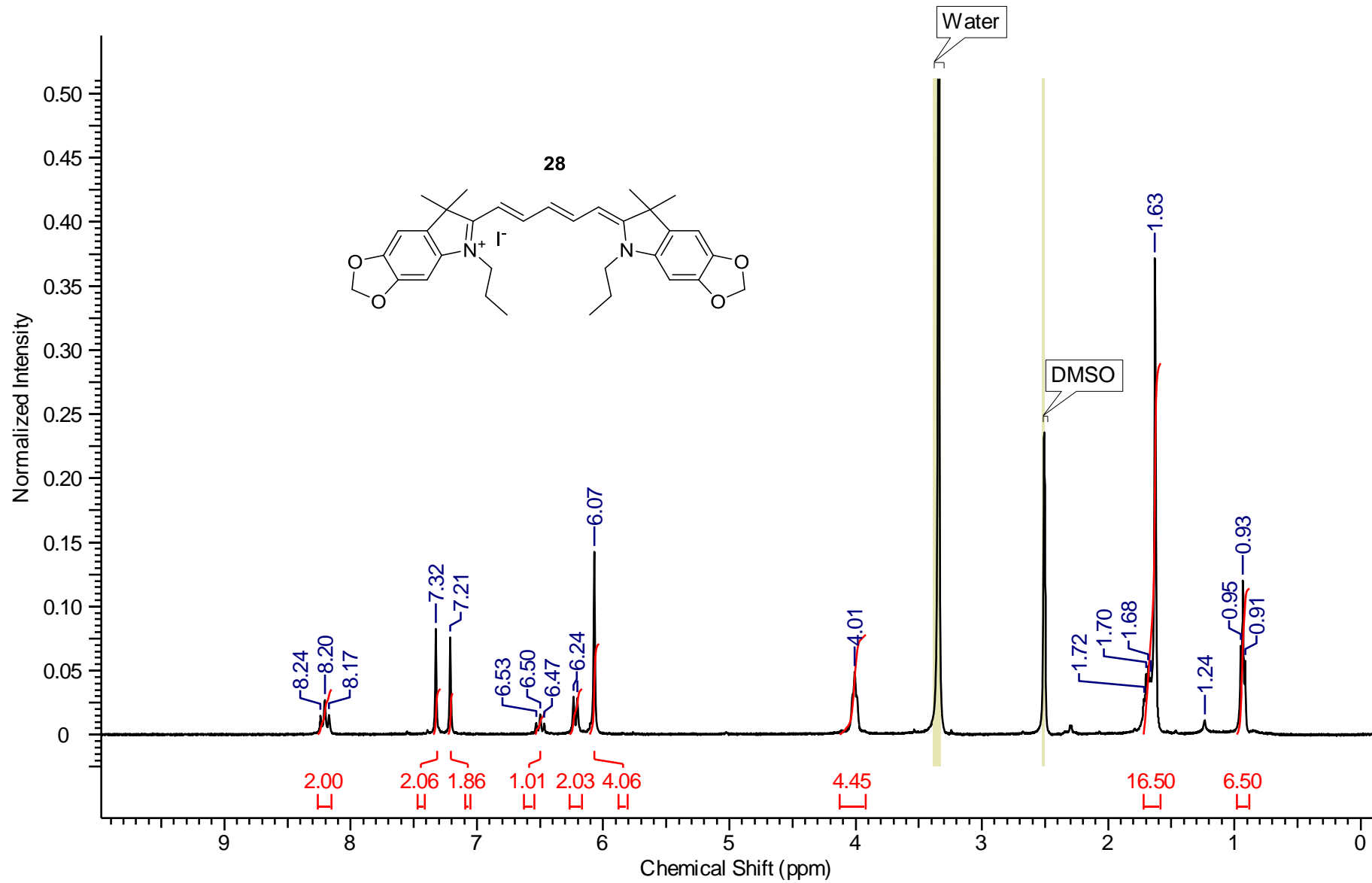


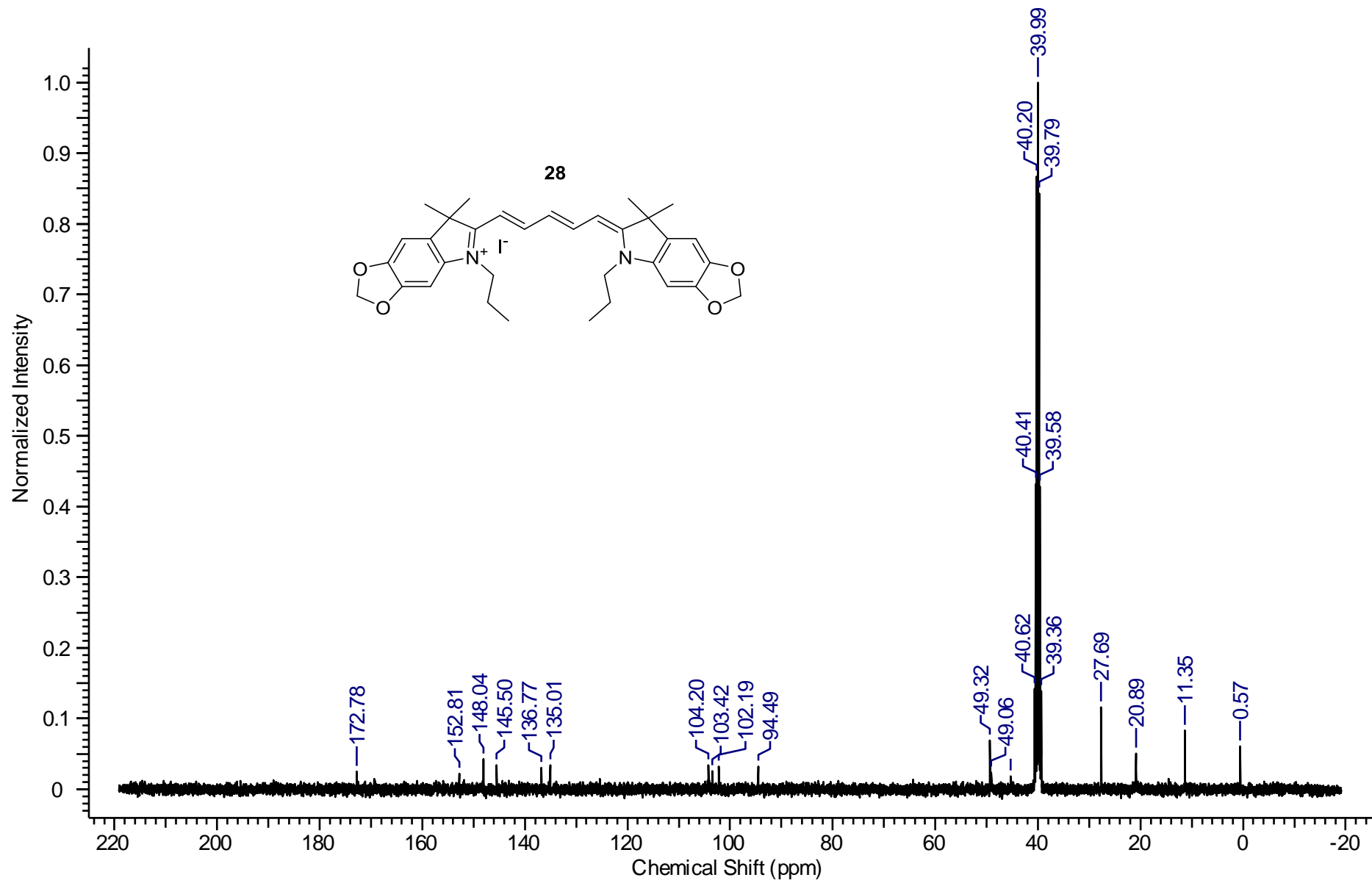


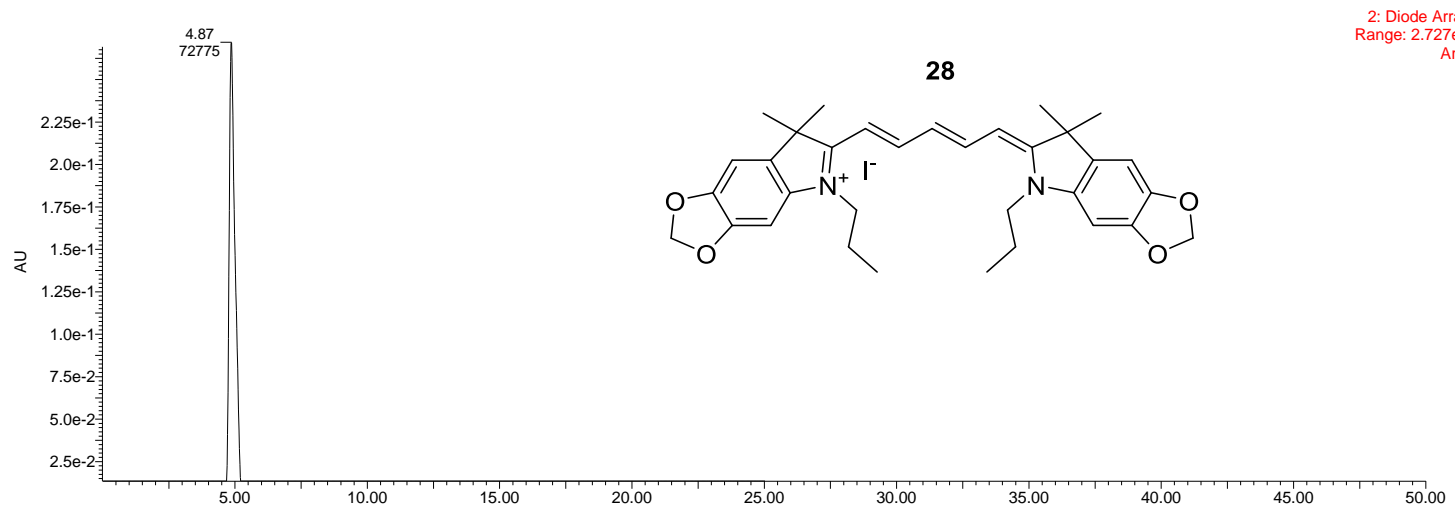
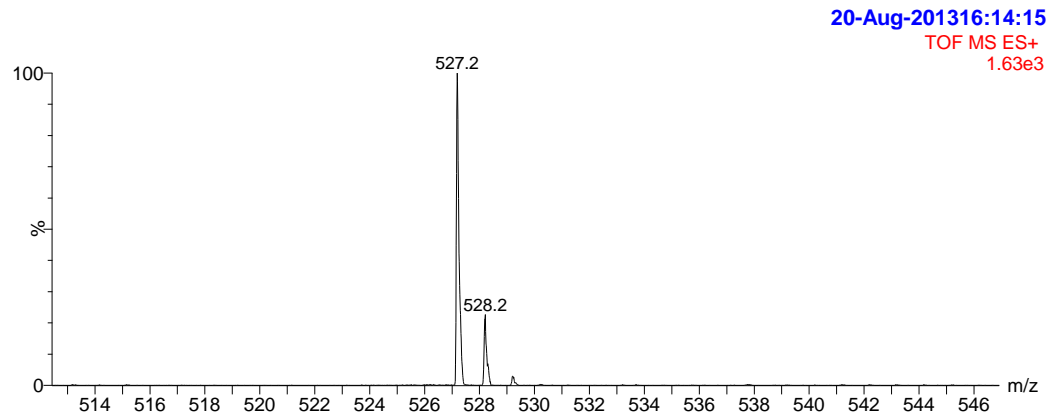


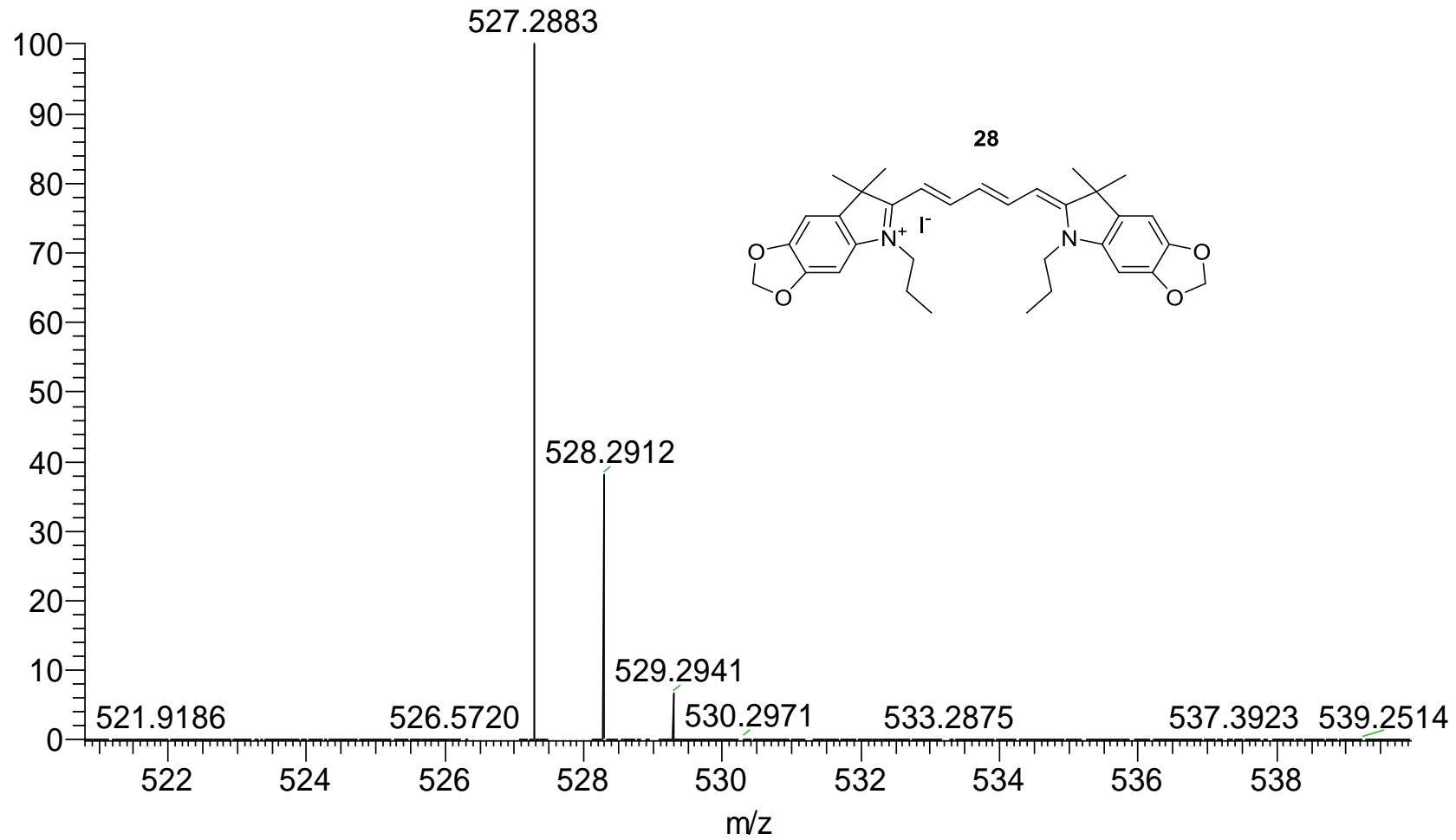


m/z	Theo. Mass	Delta (mmu)	RDB equiv.	Composition
499.2577	499.2591	-1.46	15.5	C31 H35 O4 N2





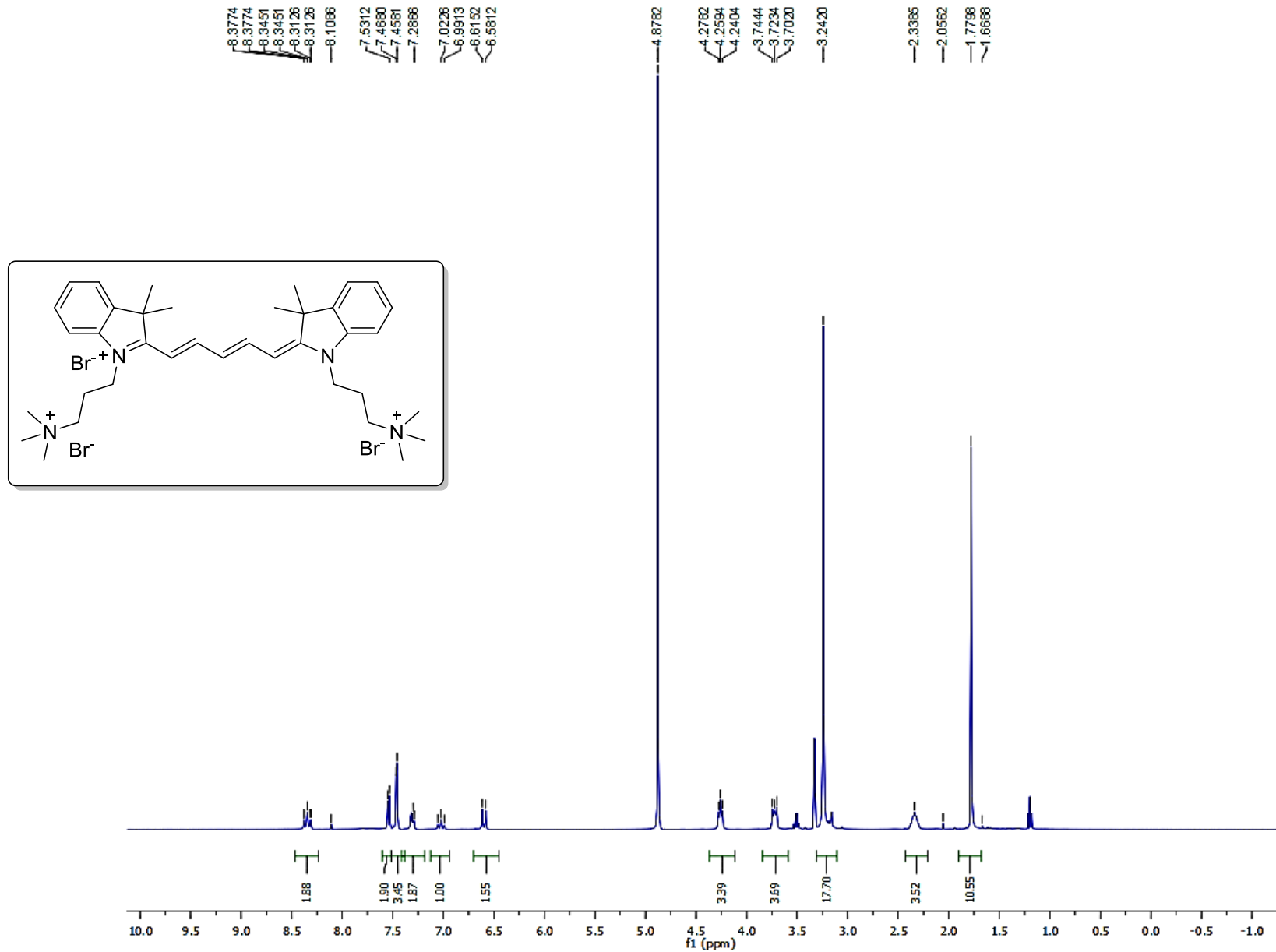


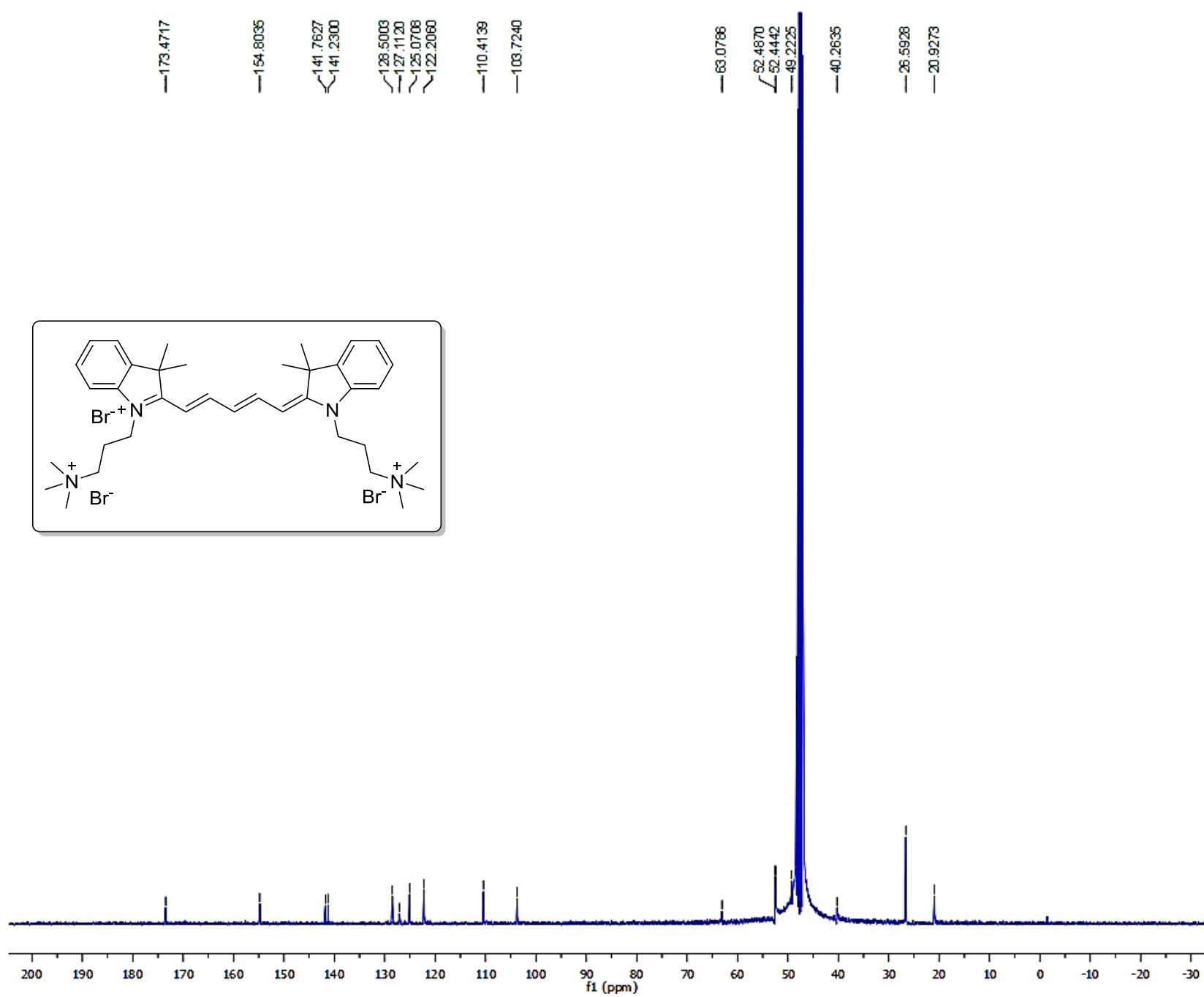


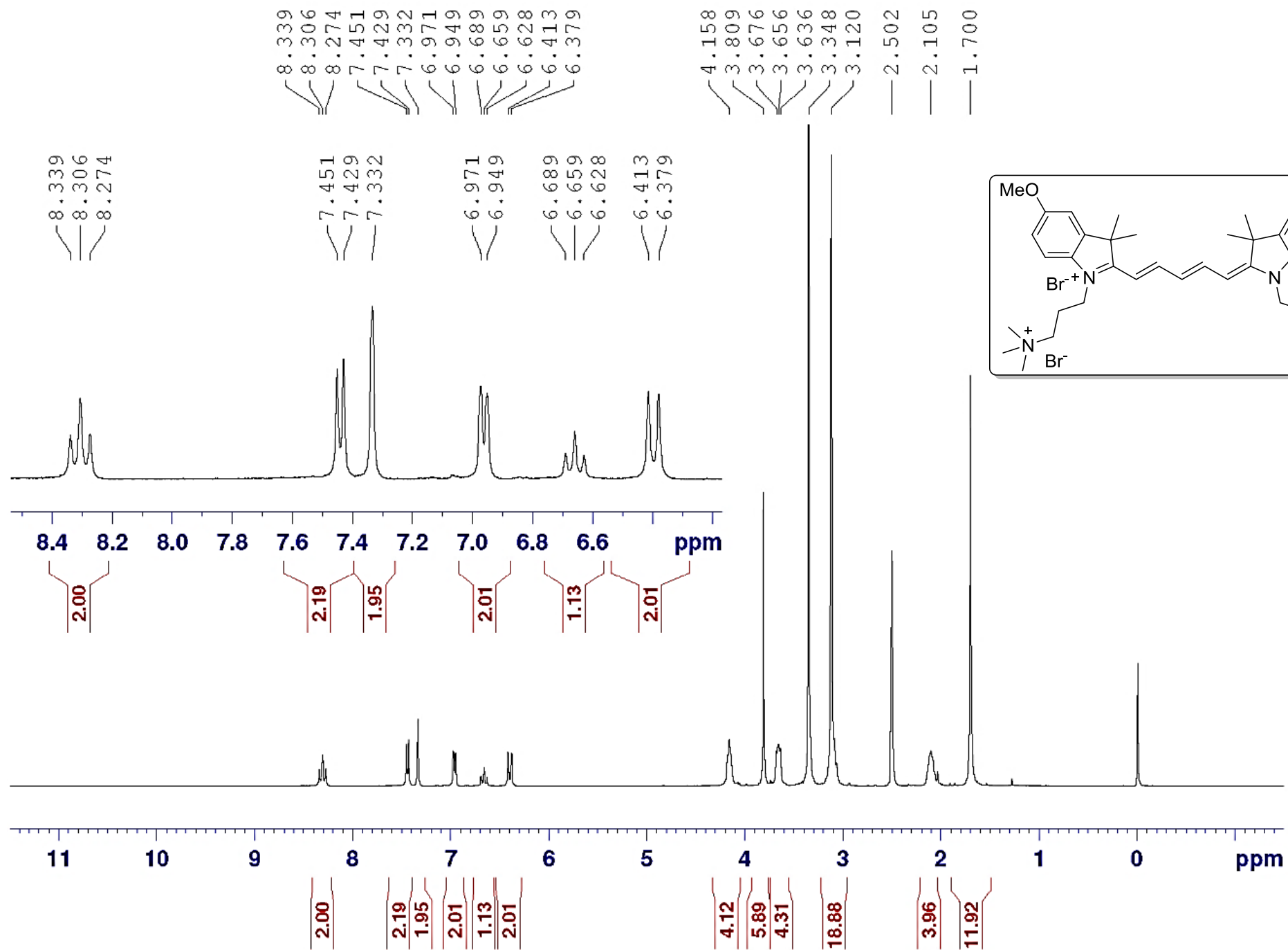
m/z	Theo. Mass	Delta (mmu)	RDB equiv.	Composition
527.2883	527.2904	-2.14	15.5	C33 H39 O4 N2

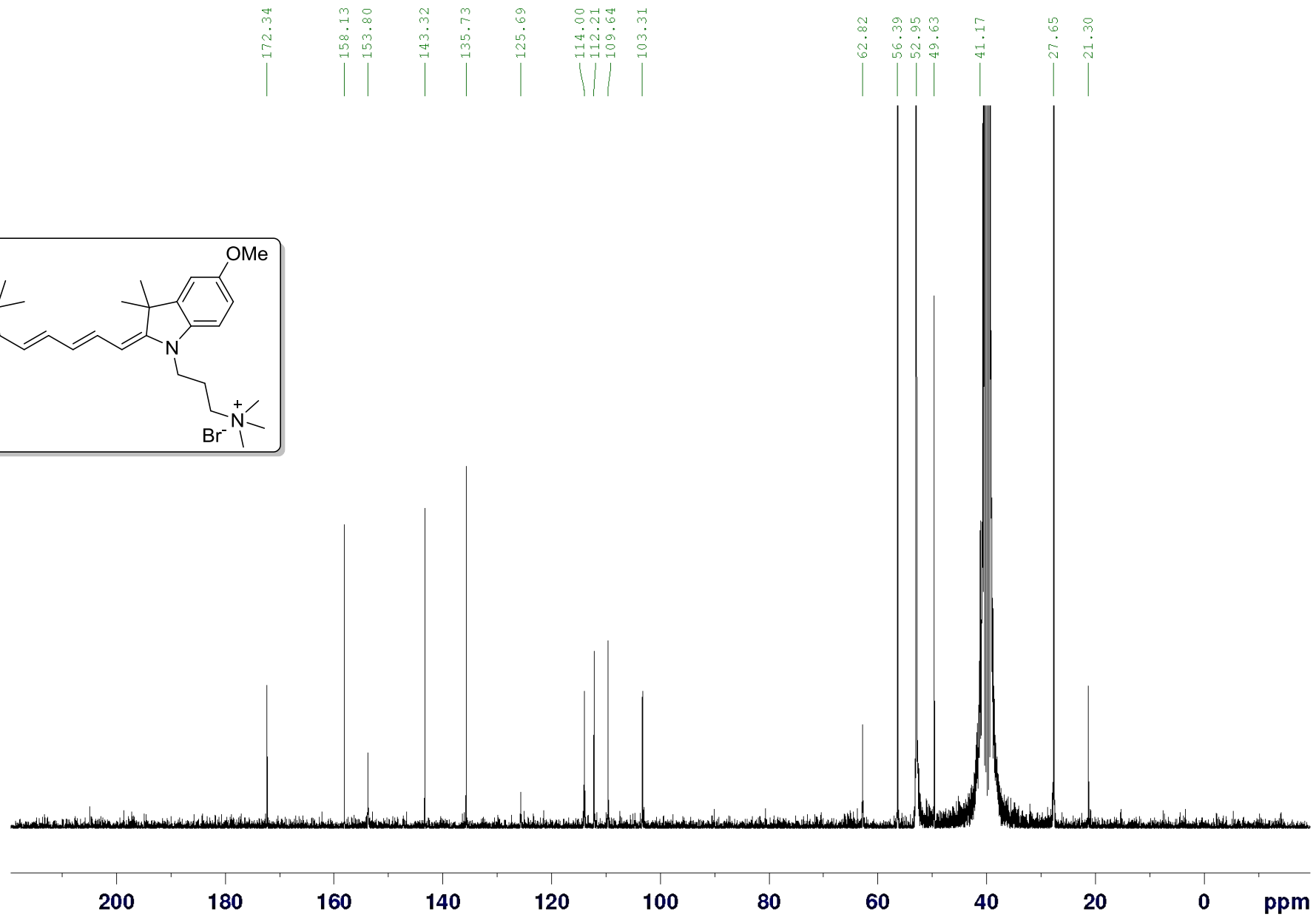
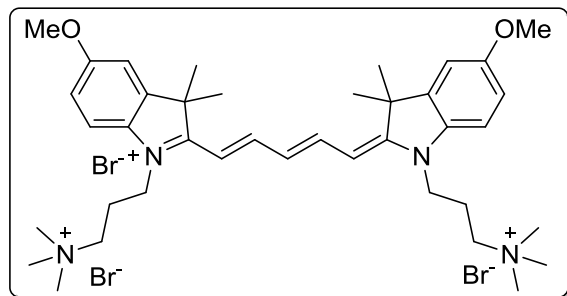
Appendix D

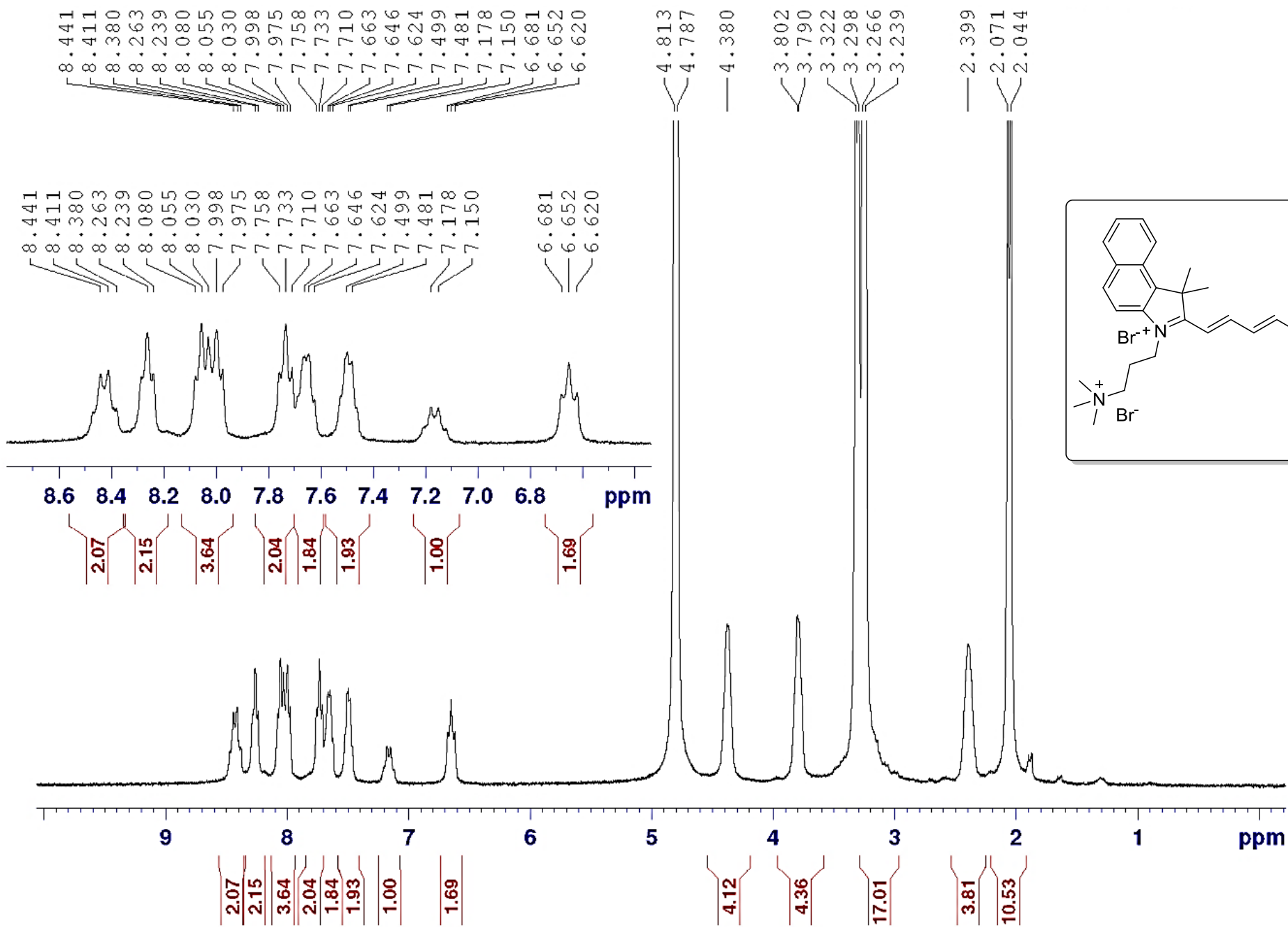
Experimental Data for Chapter 7 -- CARTILAGE AND BONE TARGETING FLUOROPHORES

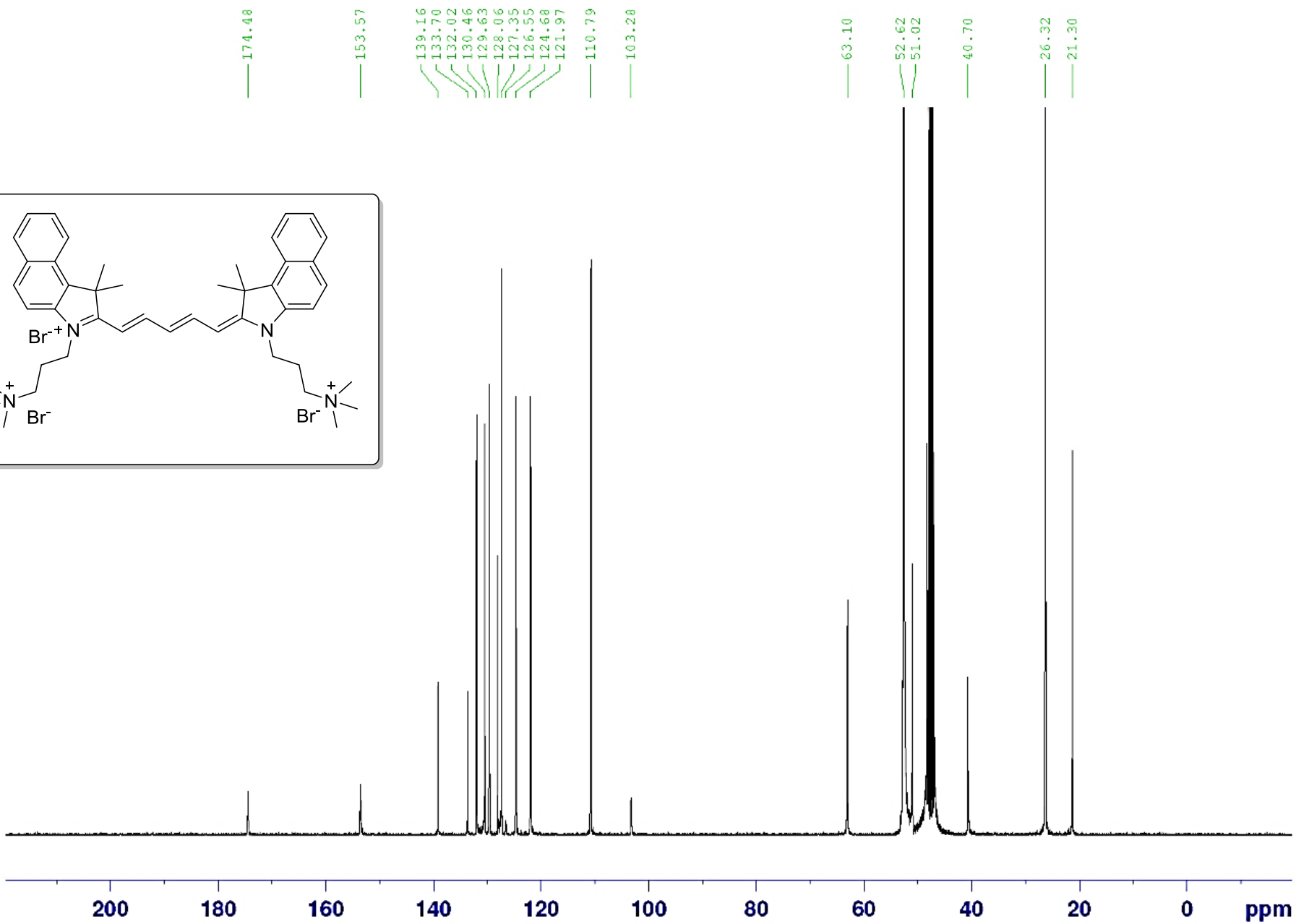
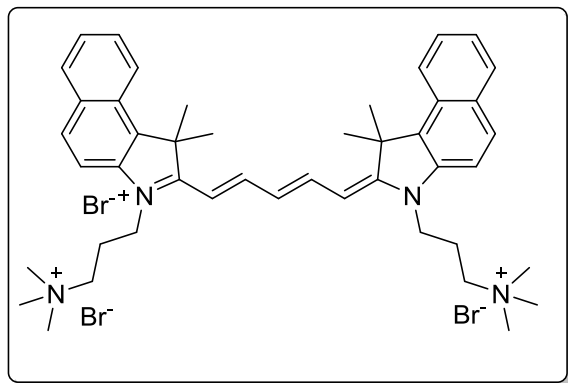


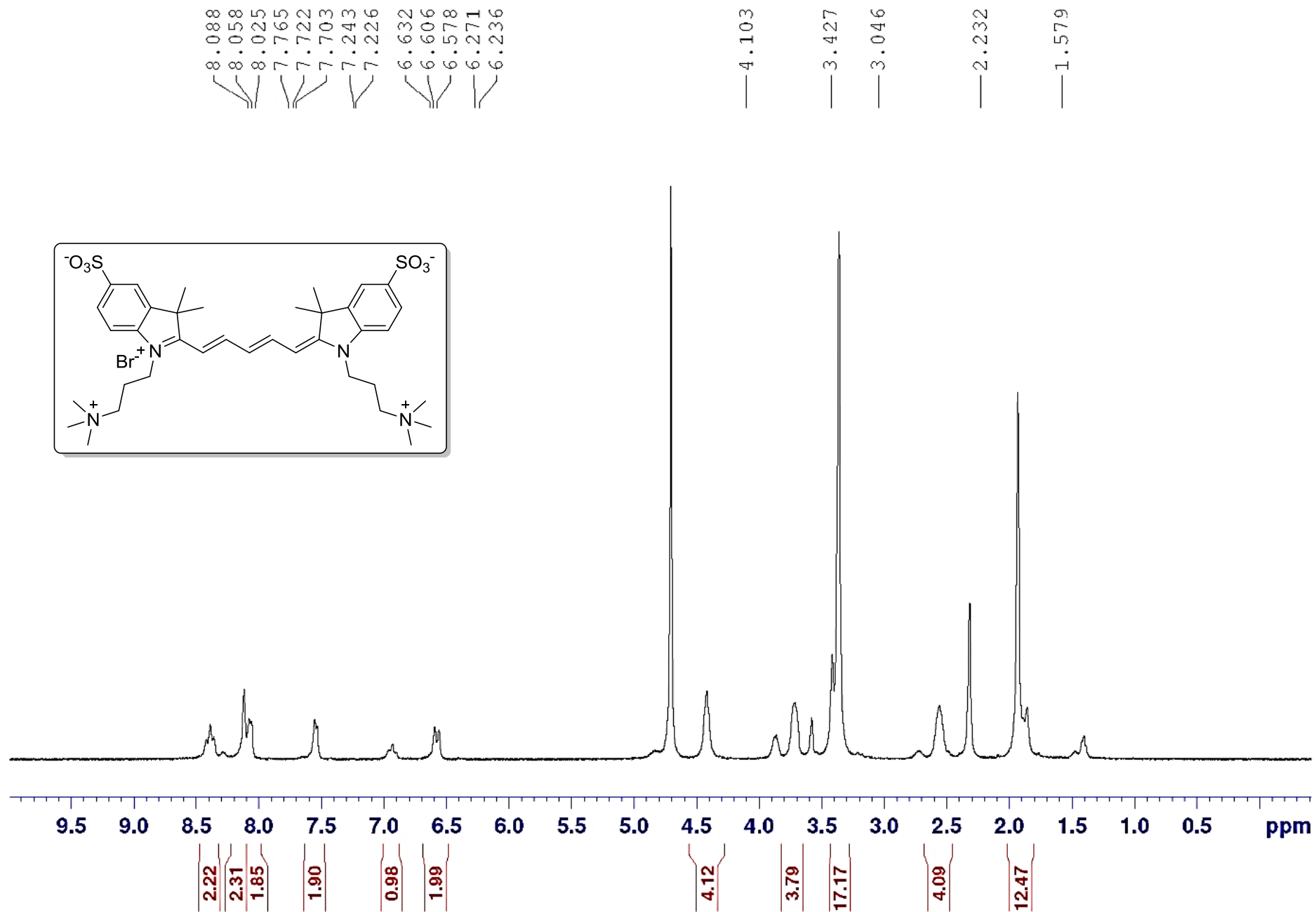


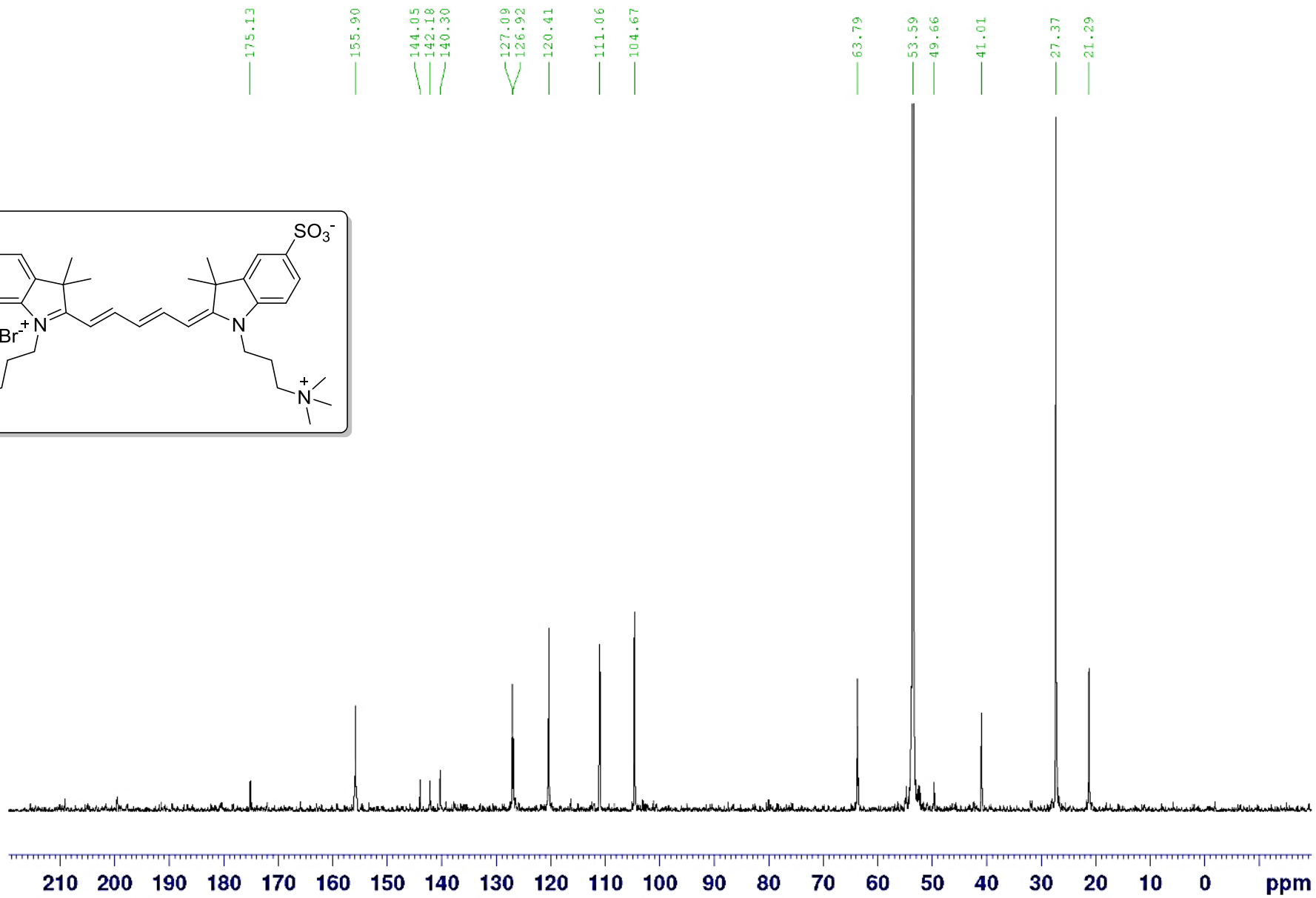
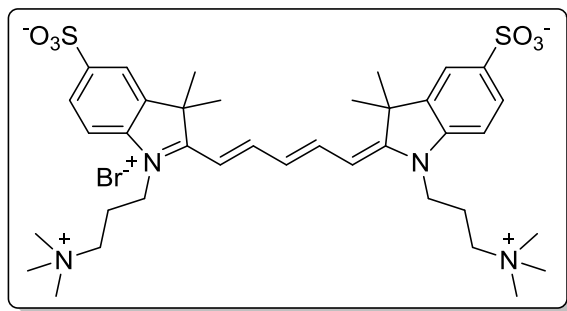


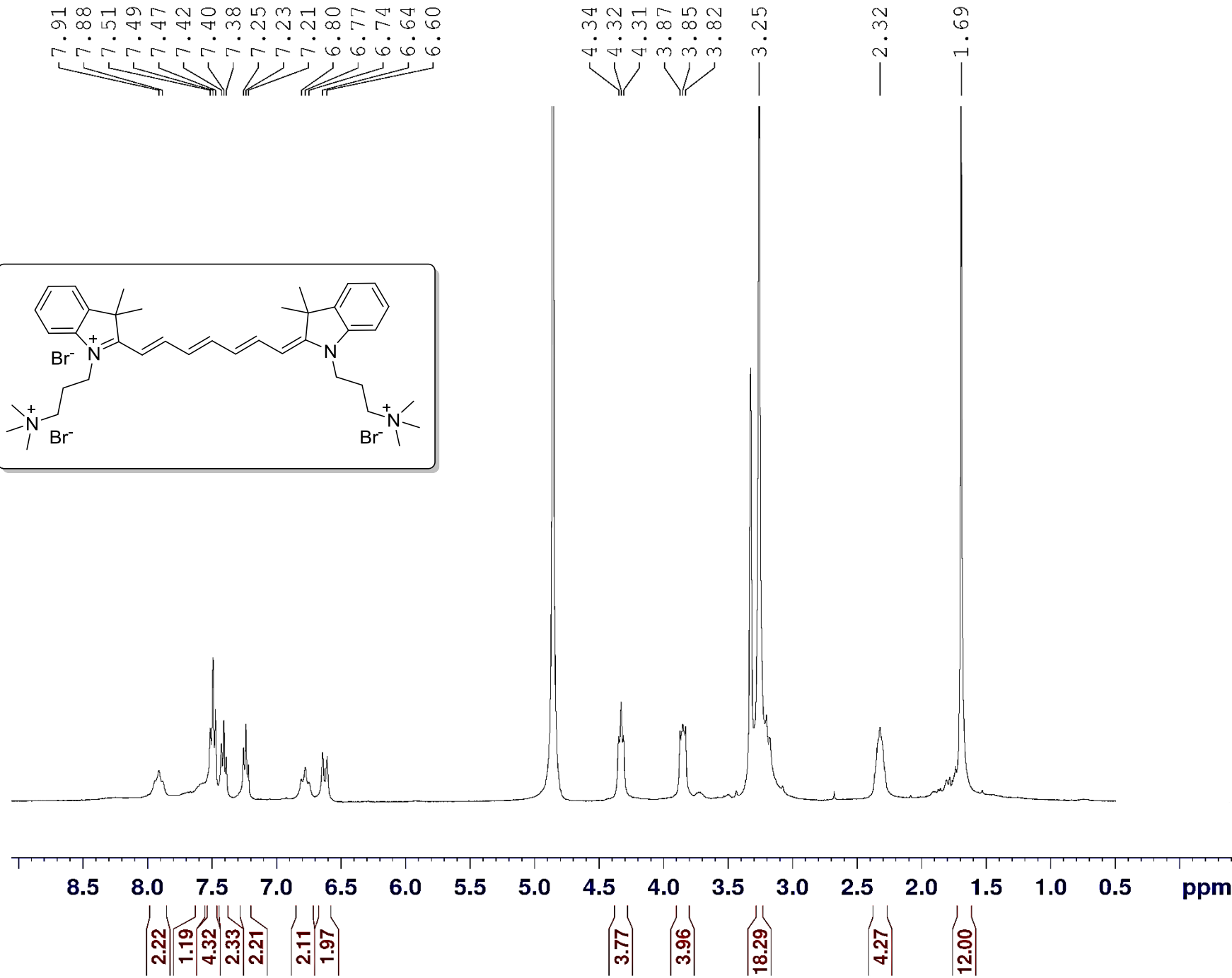
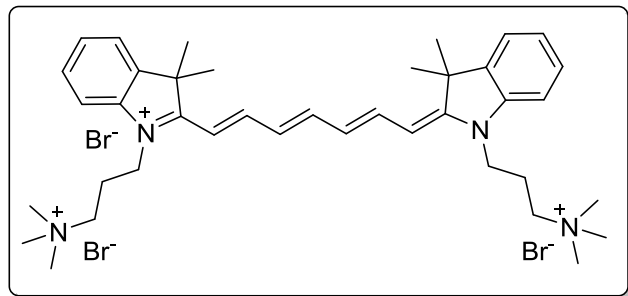


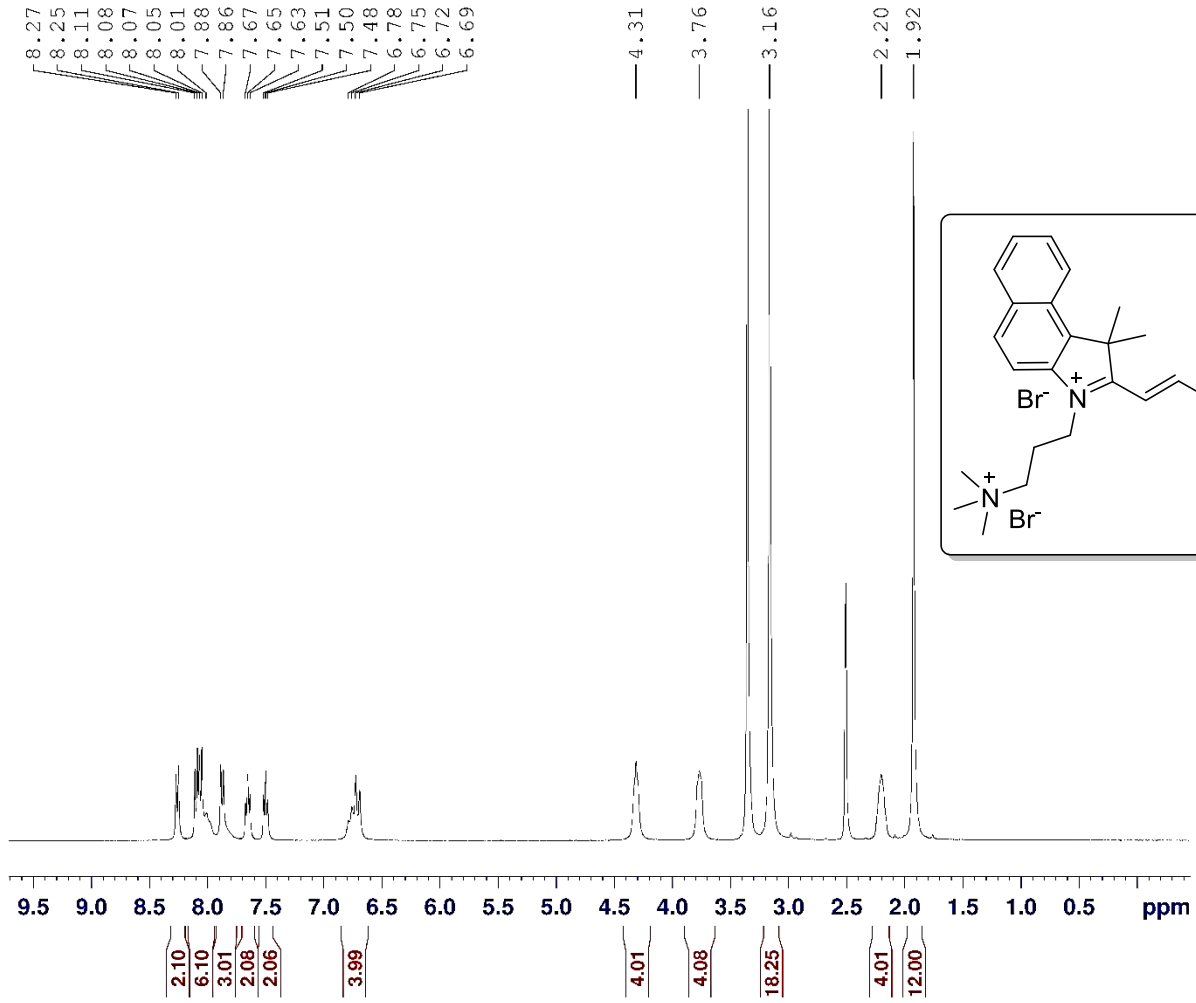


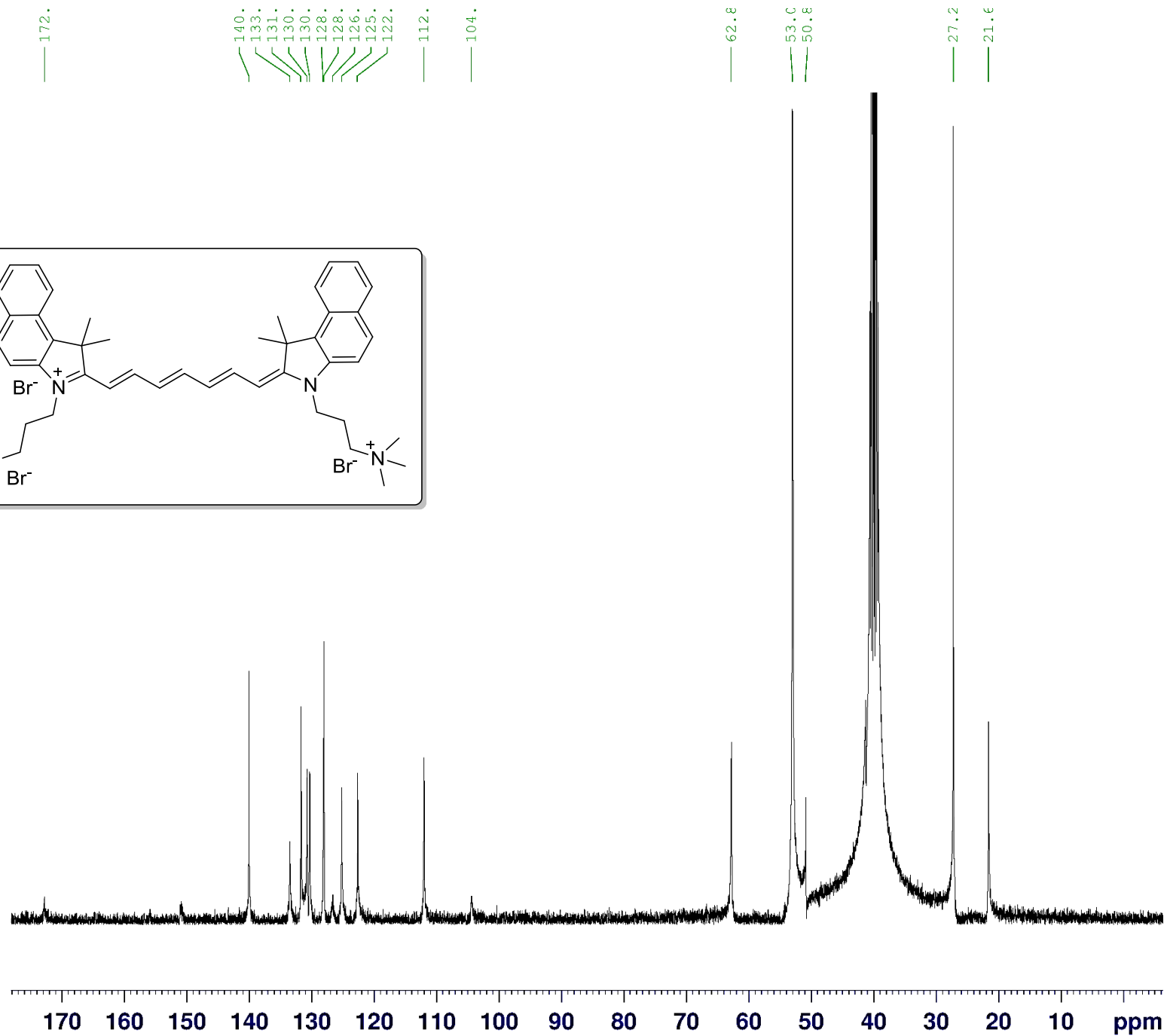
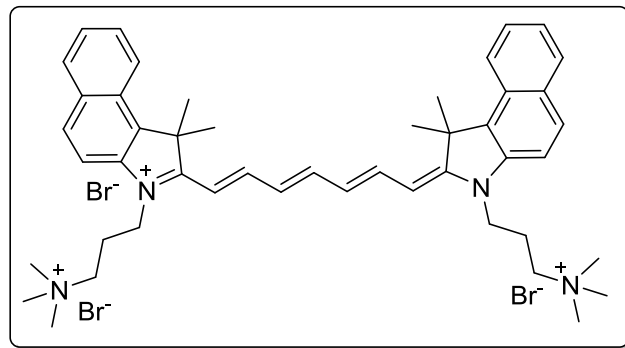


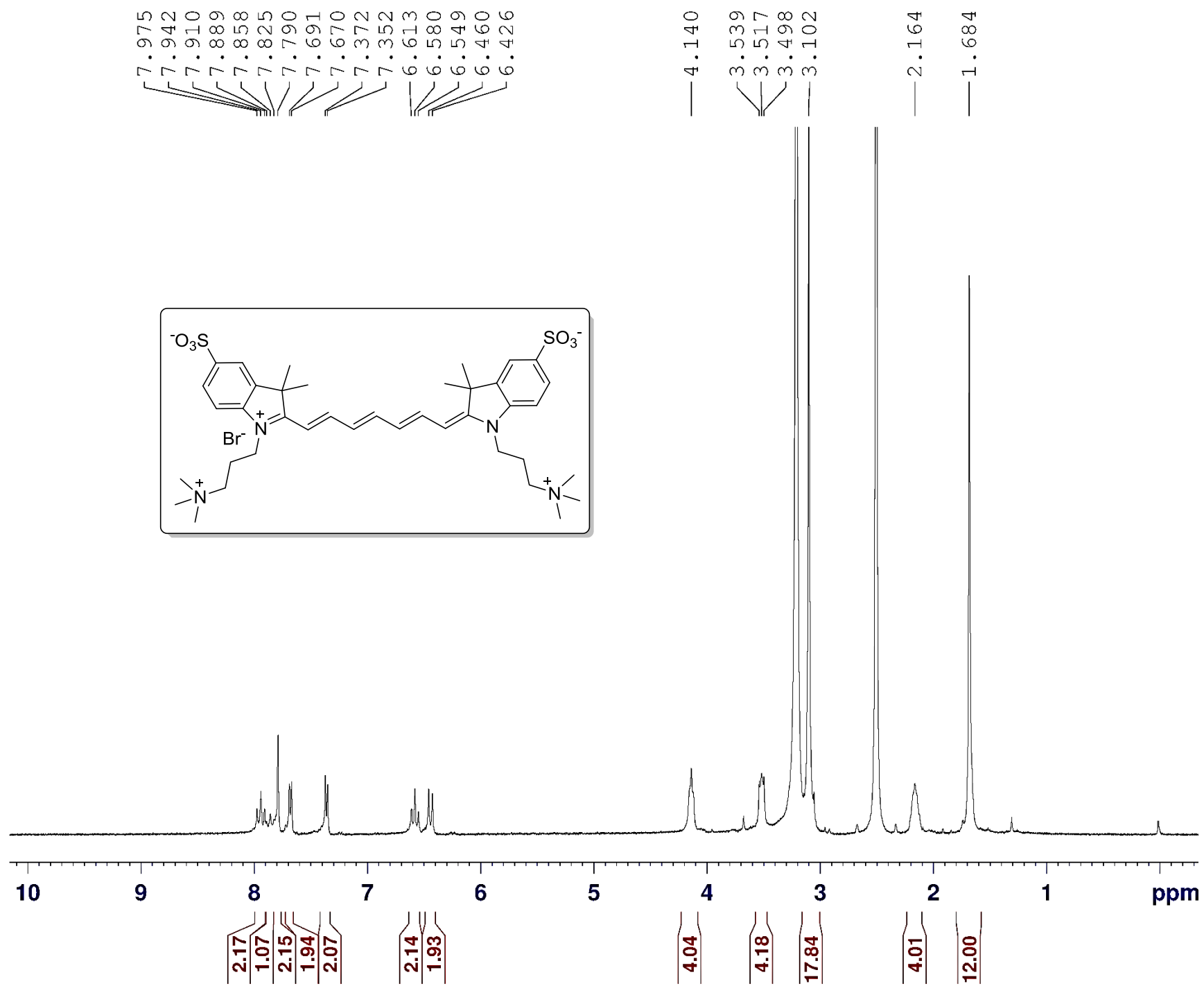


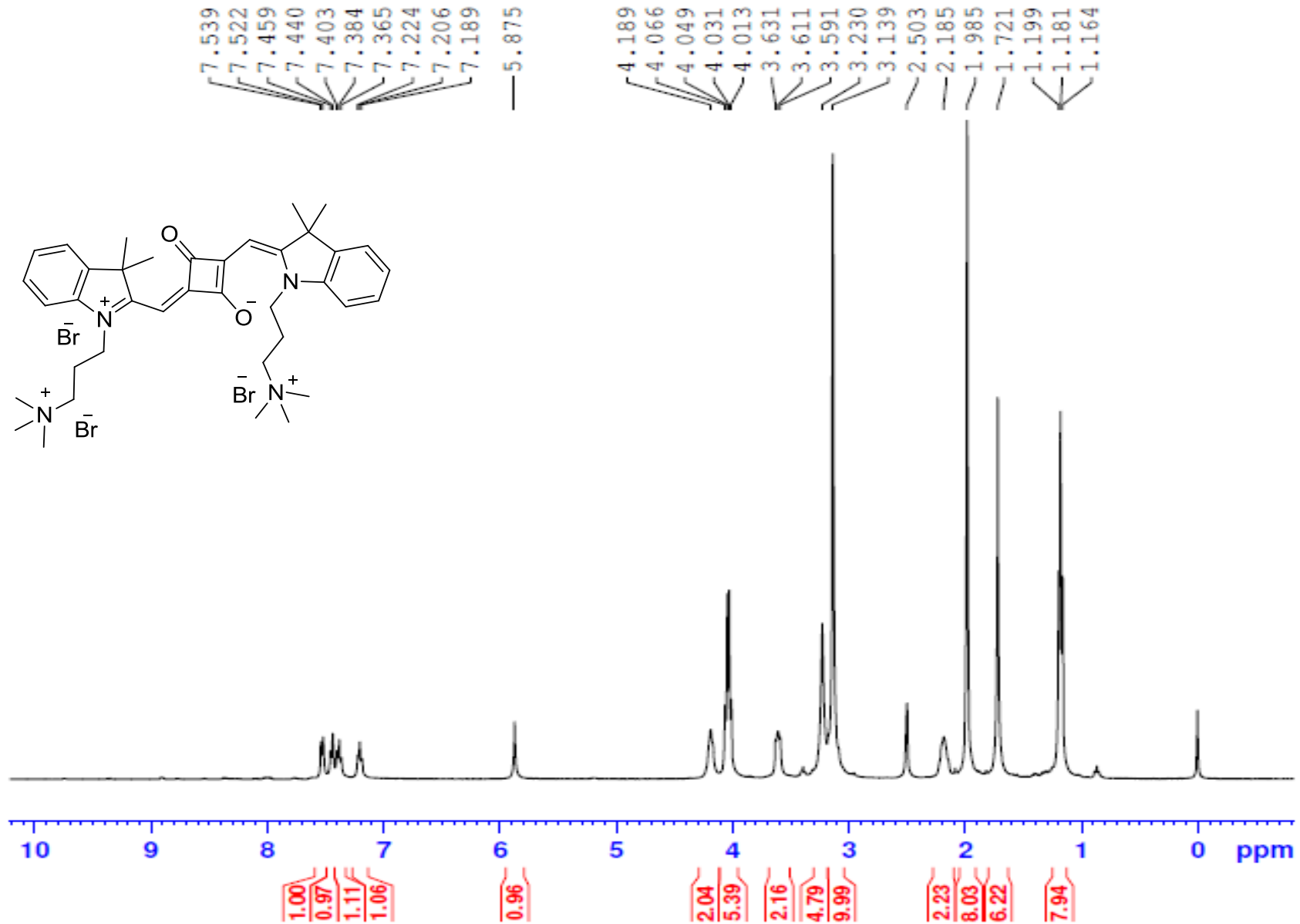


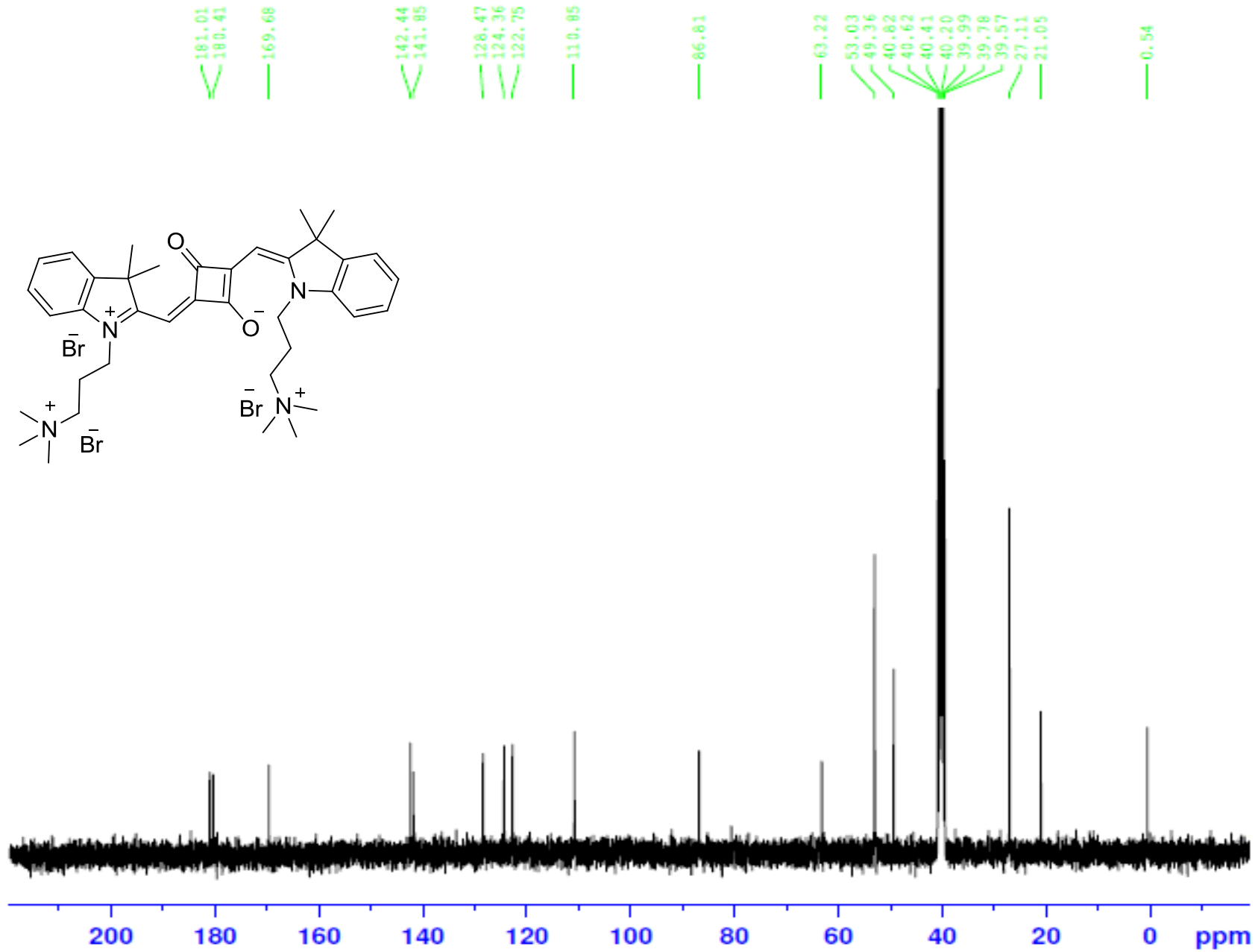


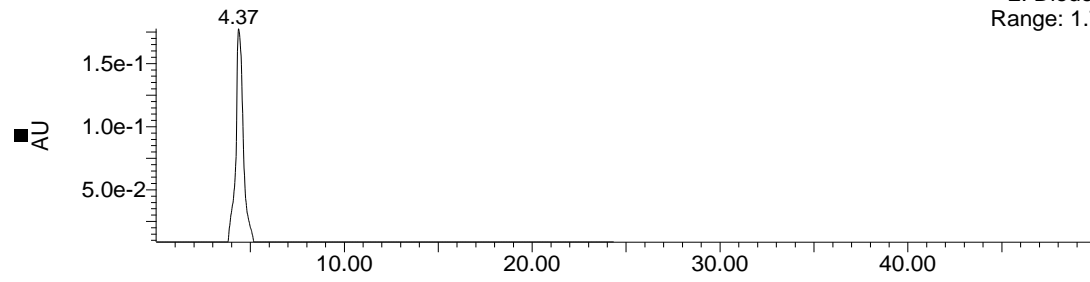




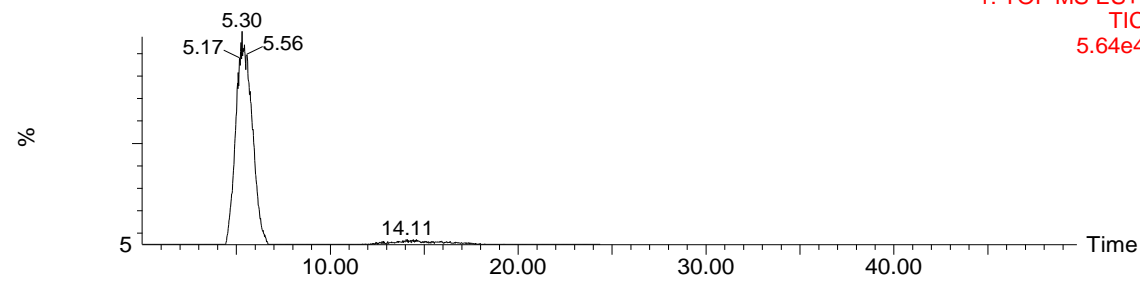
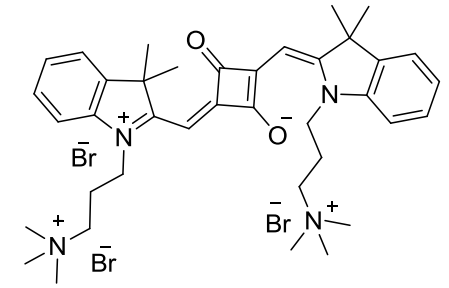








2: Diode Array
Range: 1.776e-1



1: TOF MS ES+
TIC
5.64e4

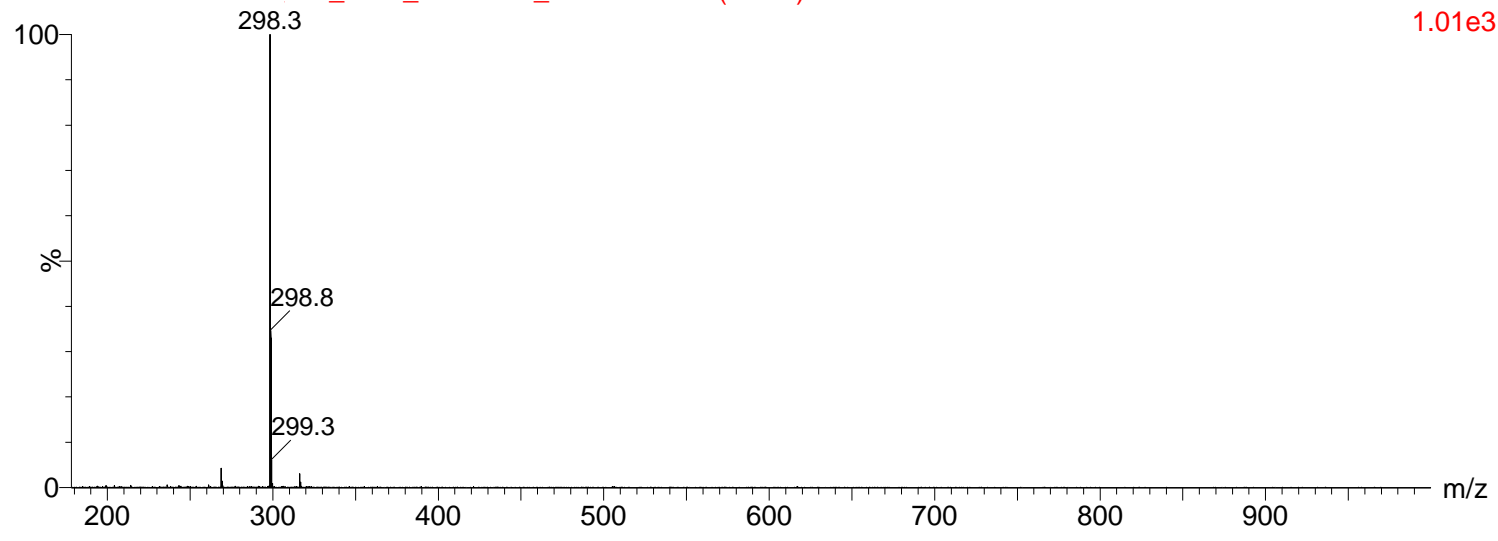
in 50%MeOH+0.1%HCOOH

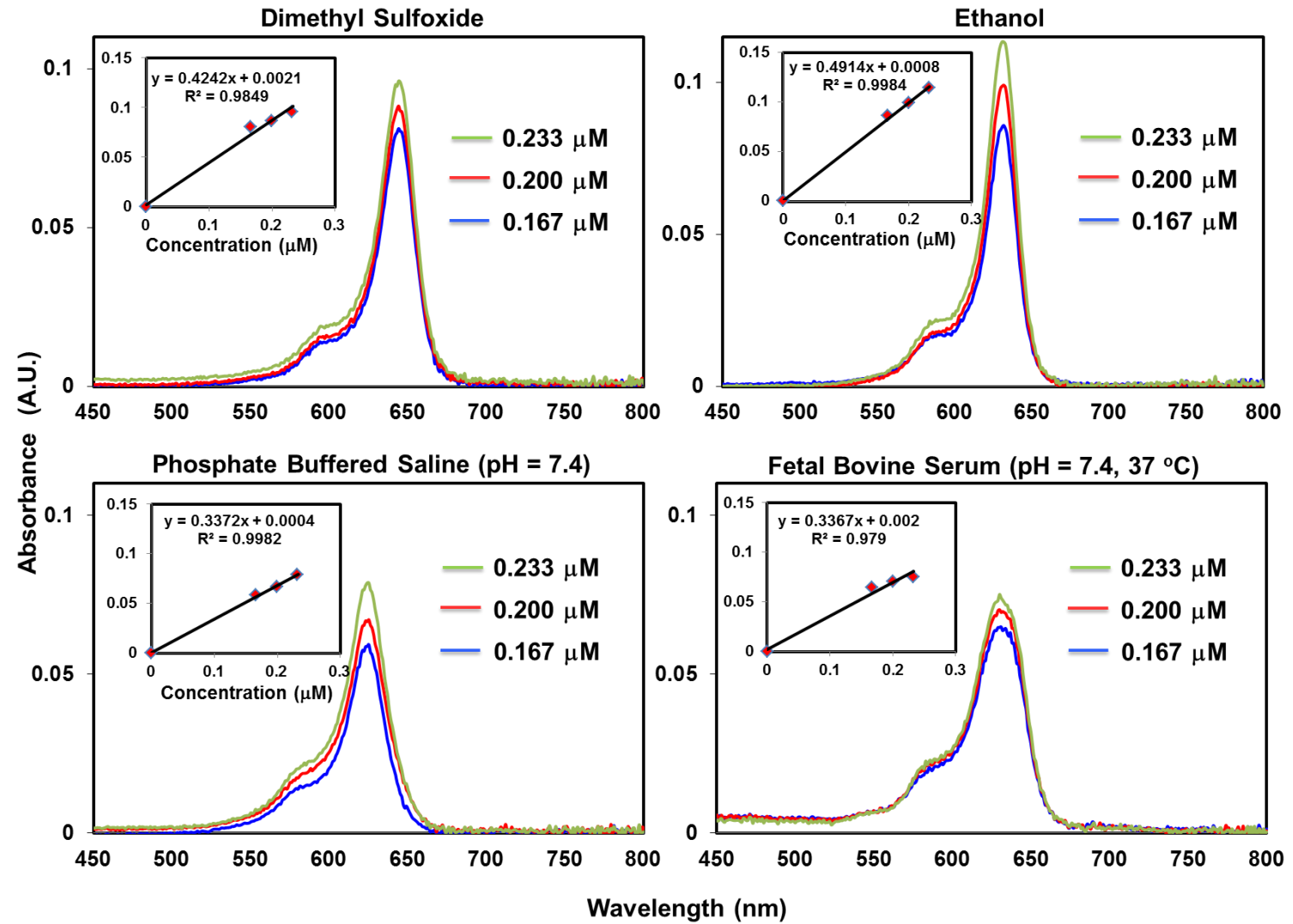
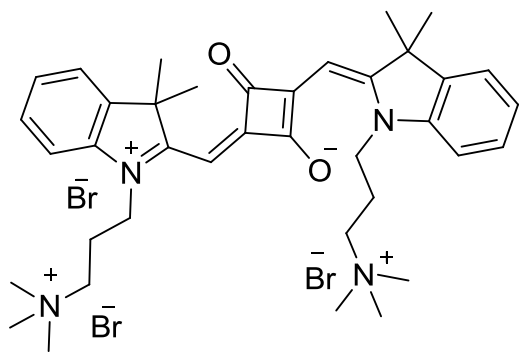
QtofMicro

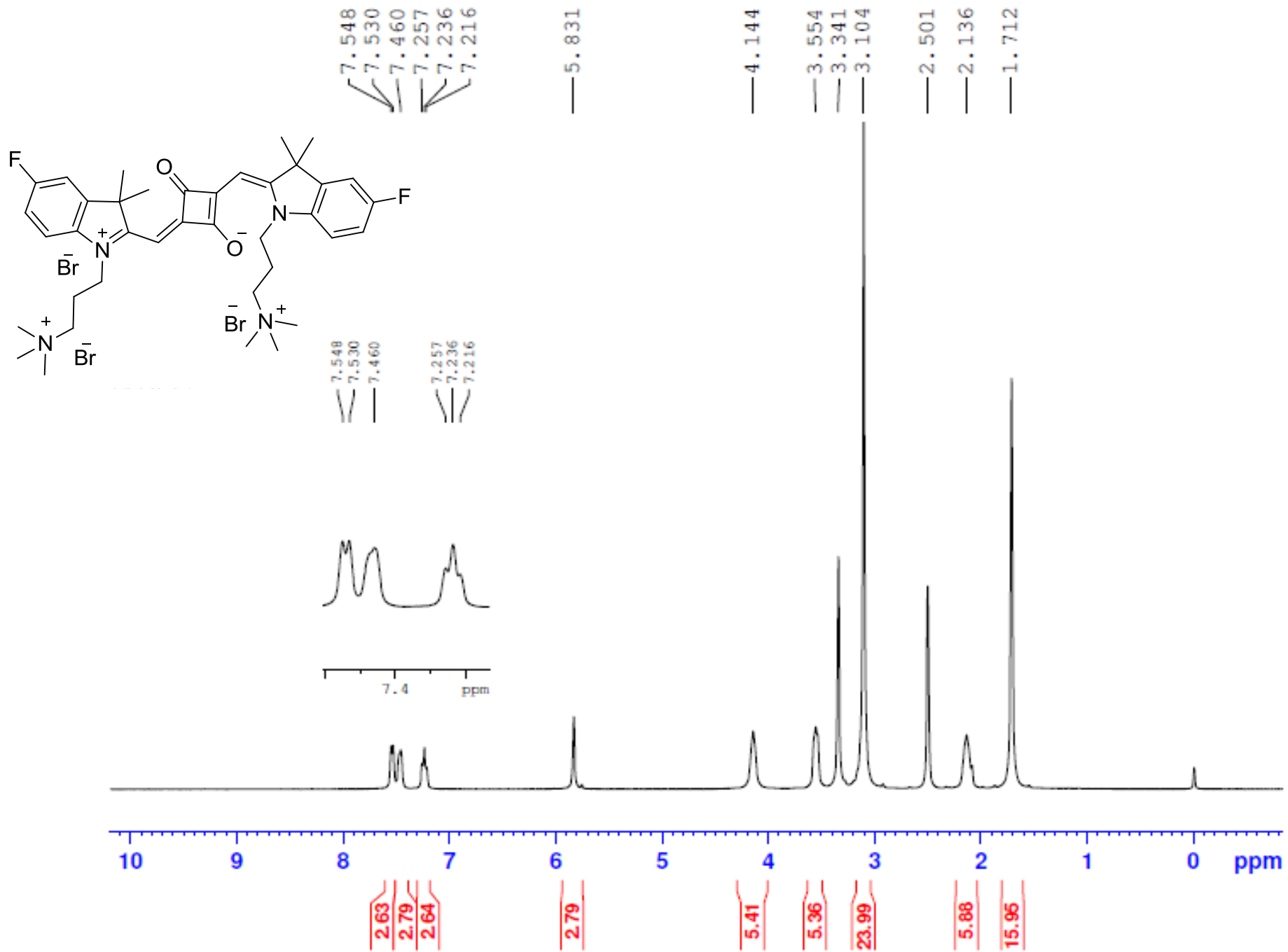
12-Mar-201410:56:12

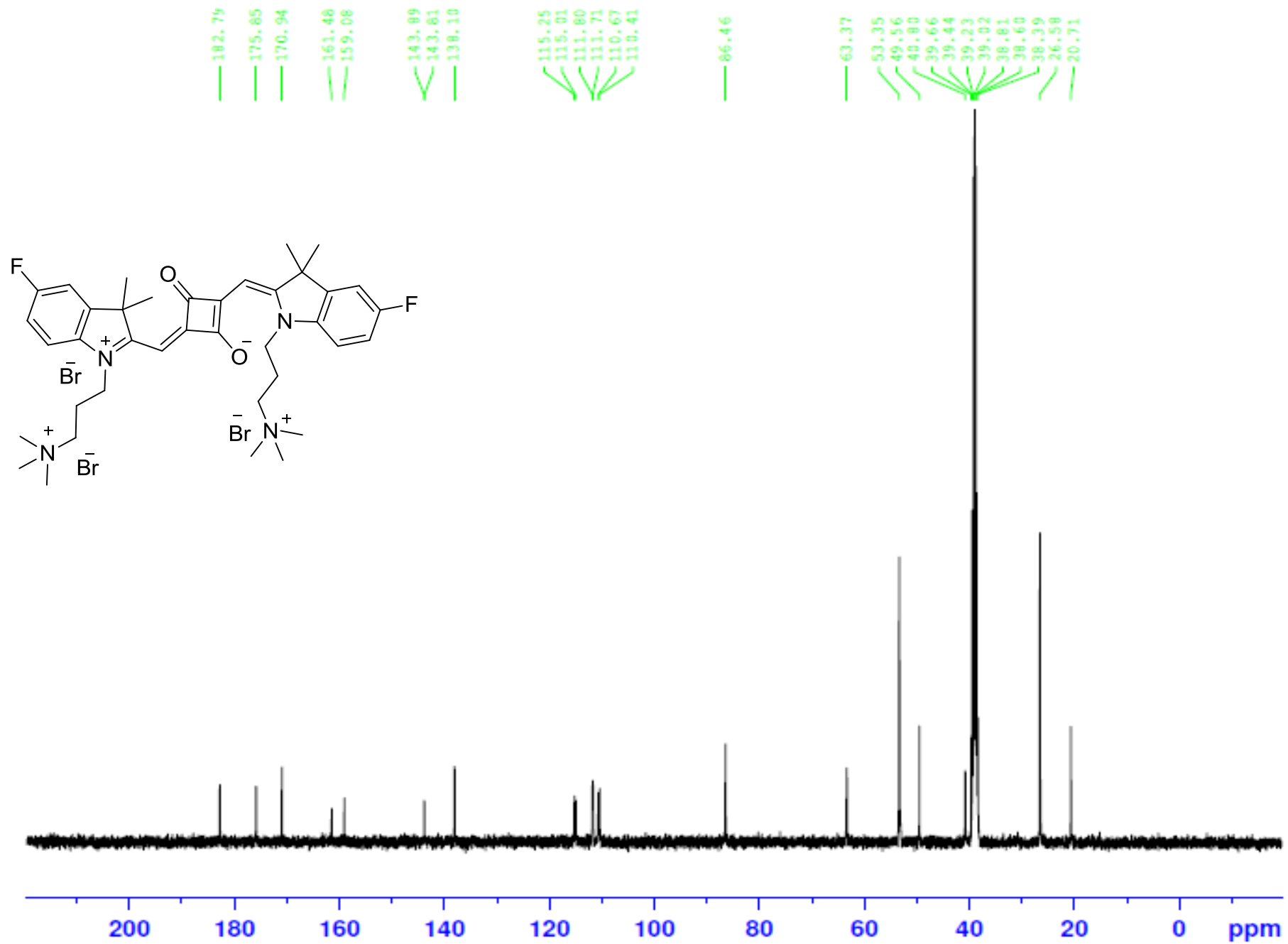
ESI_POS_HENARY_03112014 38 (0.707)

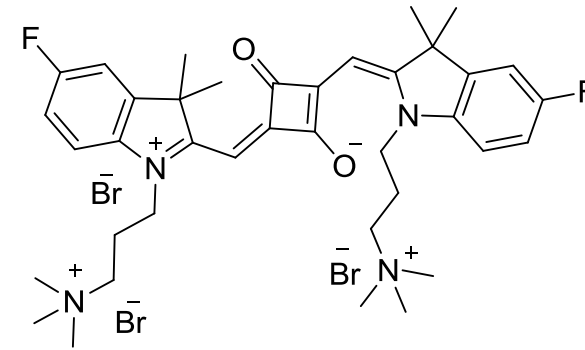
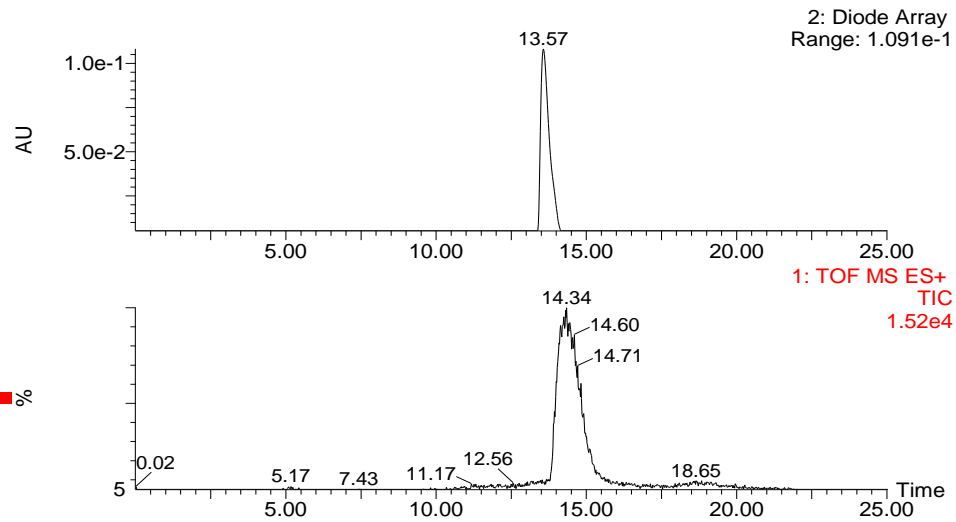
TOF MS ES+
1.01e3











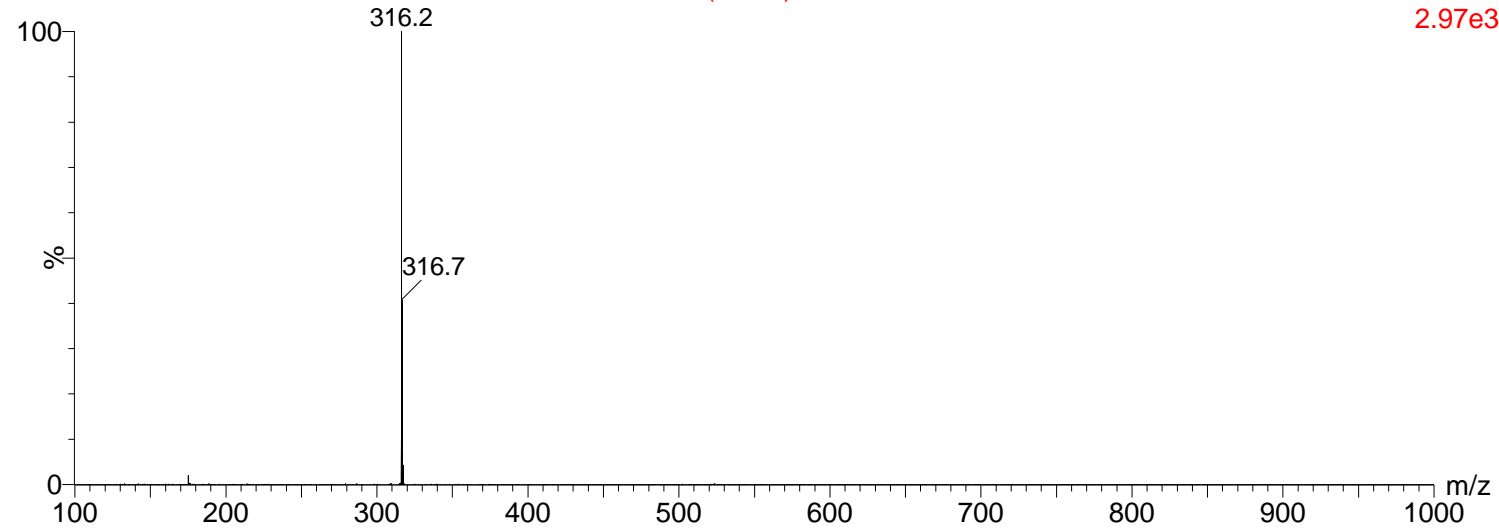
in 50%MeOH+0.1%HCOOH

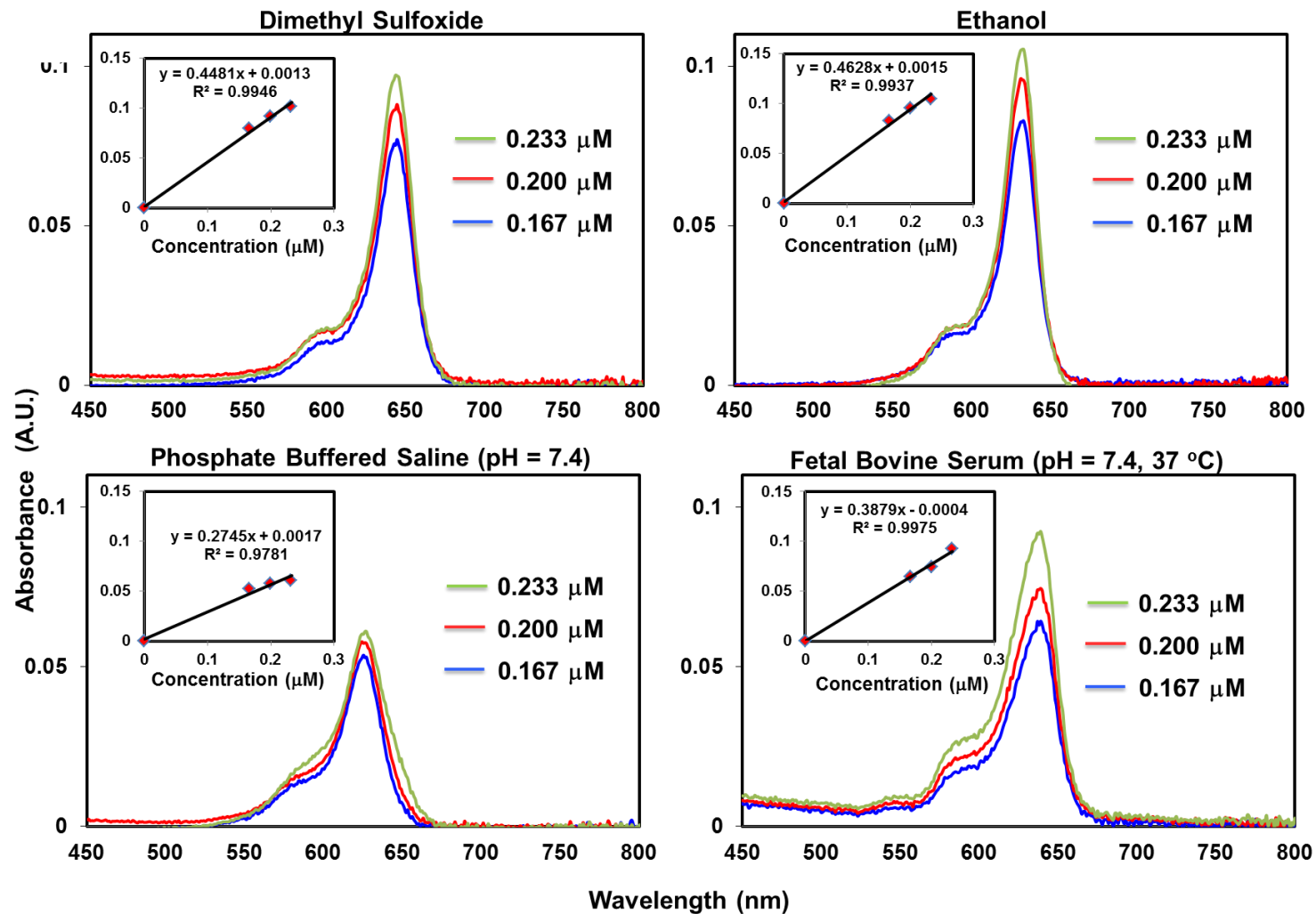
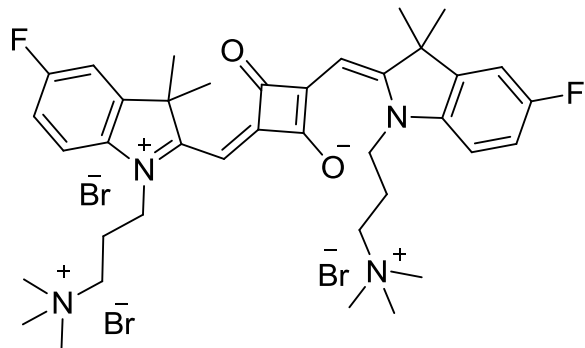
QtofMicro

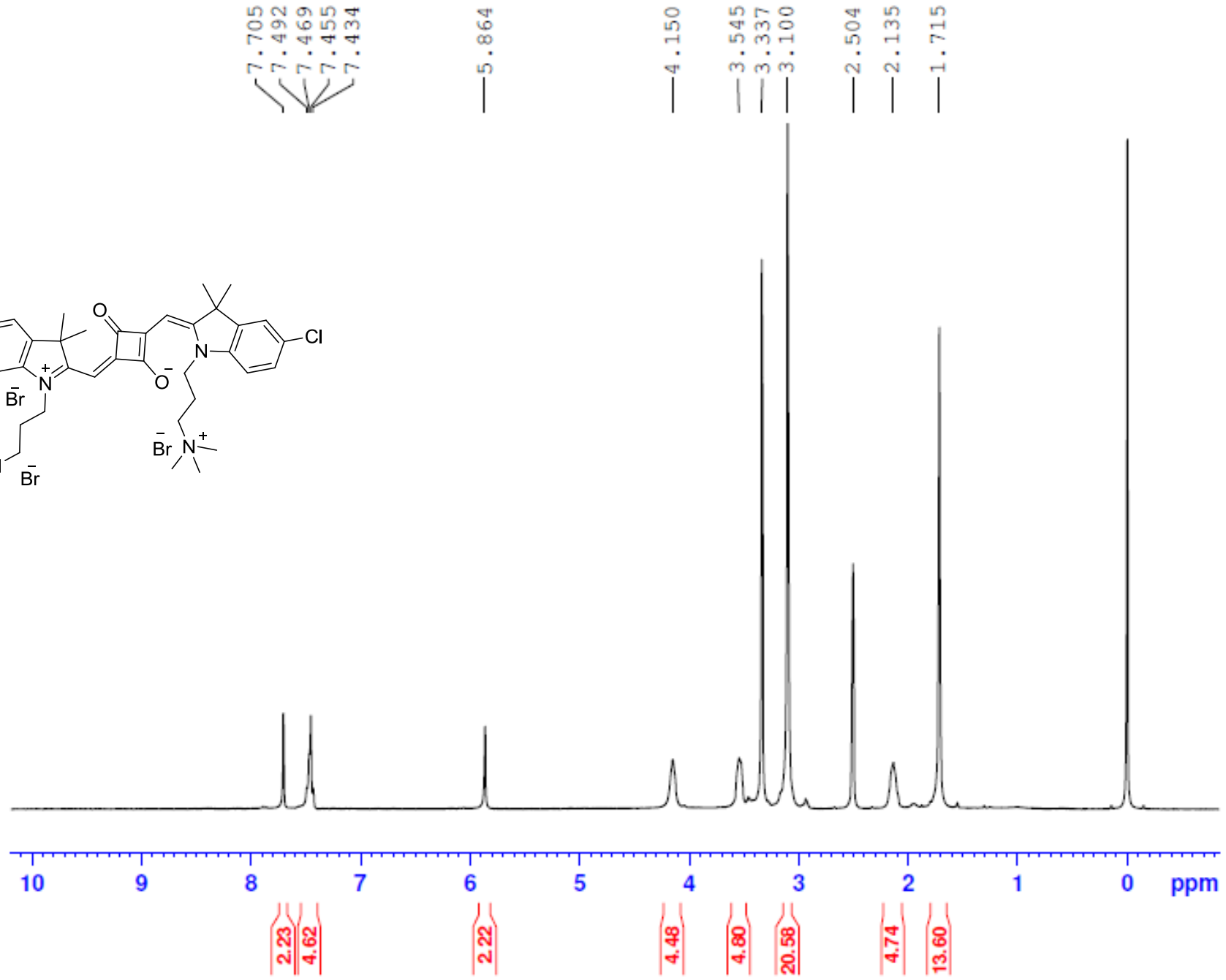
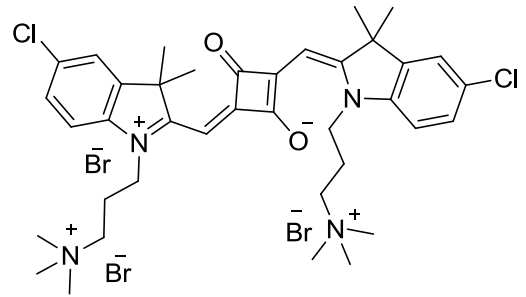
12-Mar-201410:23:38

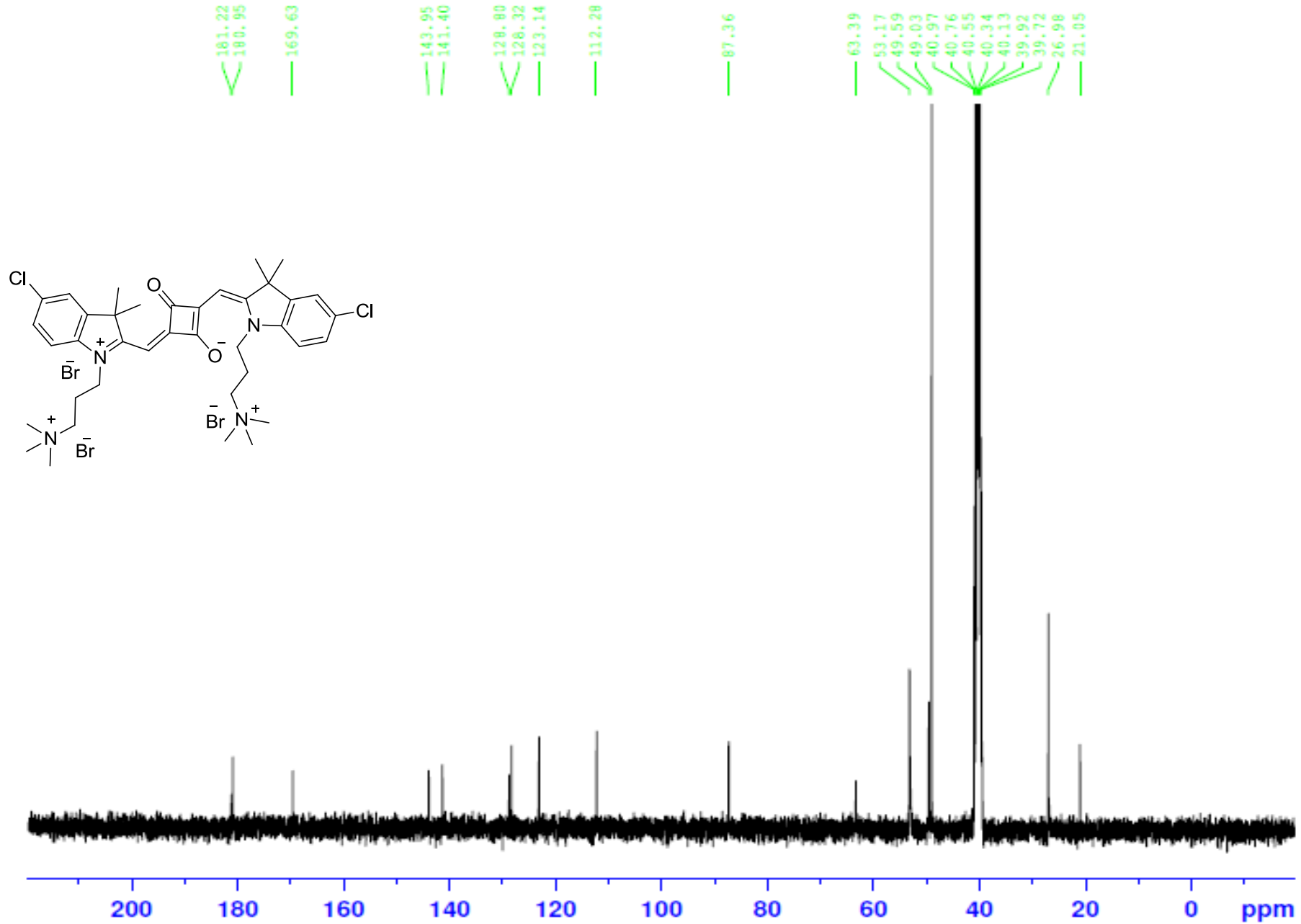
ESI_POS_HENARY_03112014 5 (0.093)

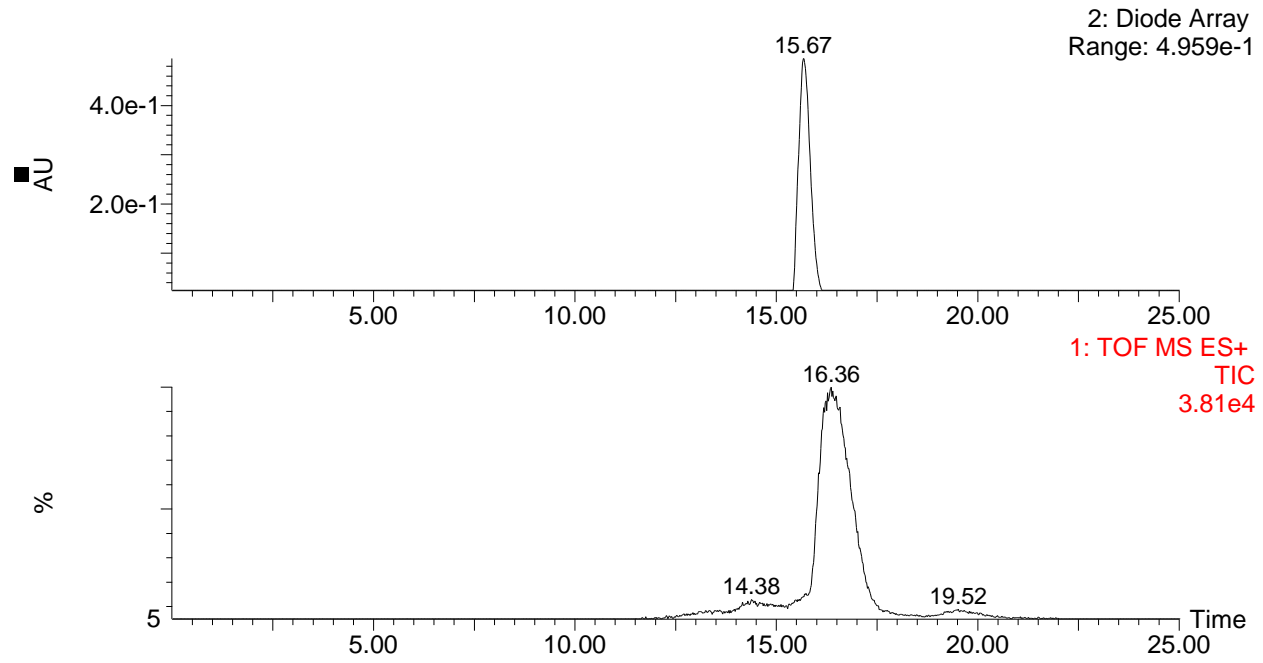
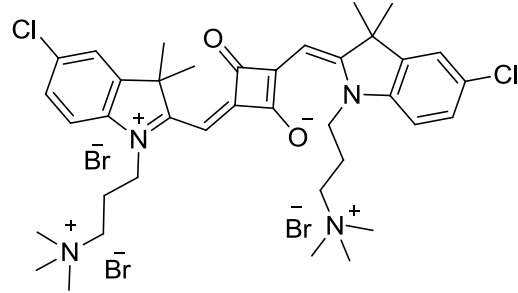
TOF MS ES+
2.97e3

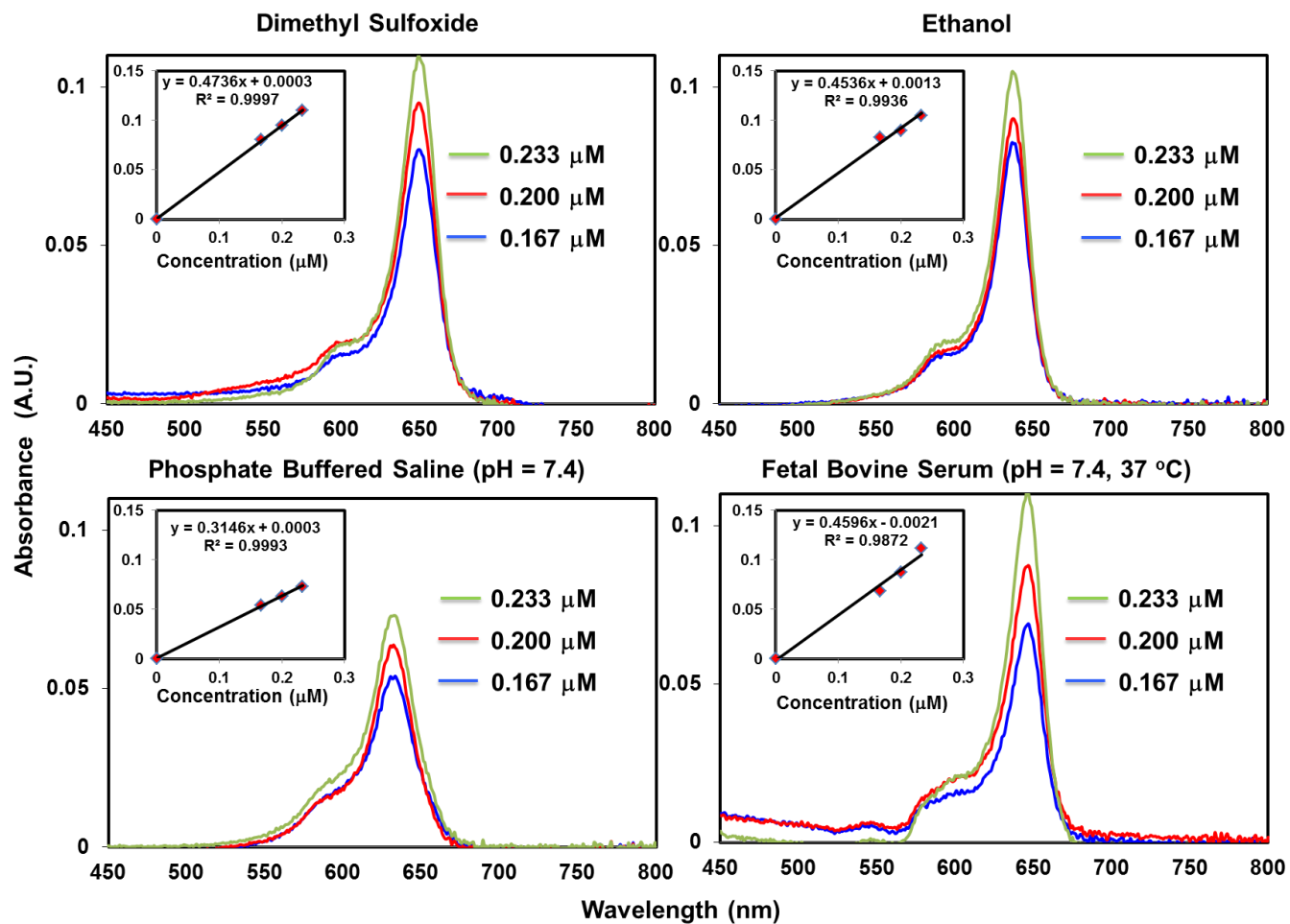
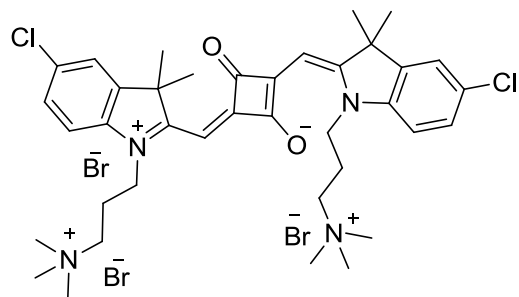


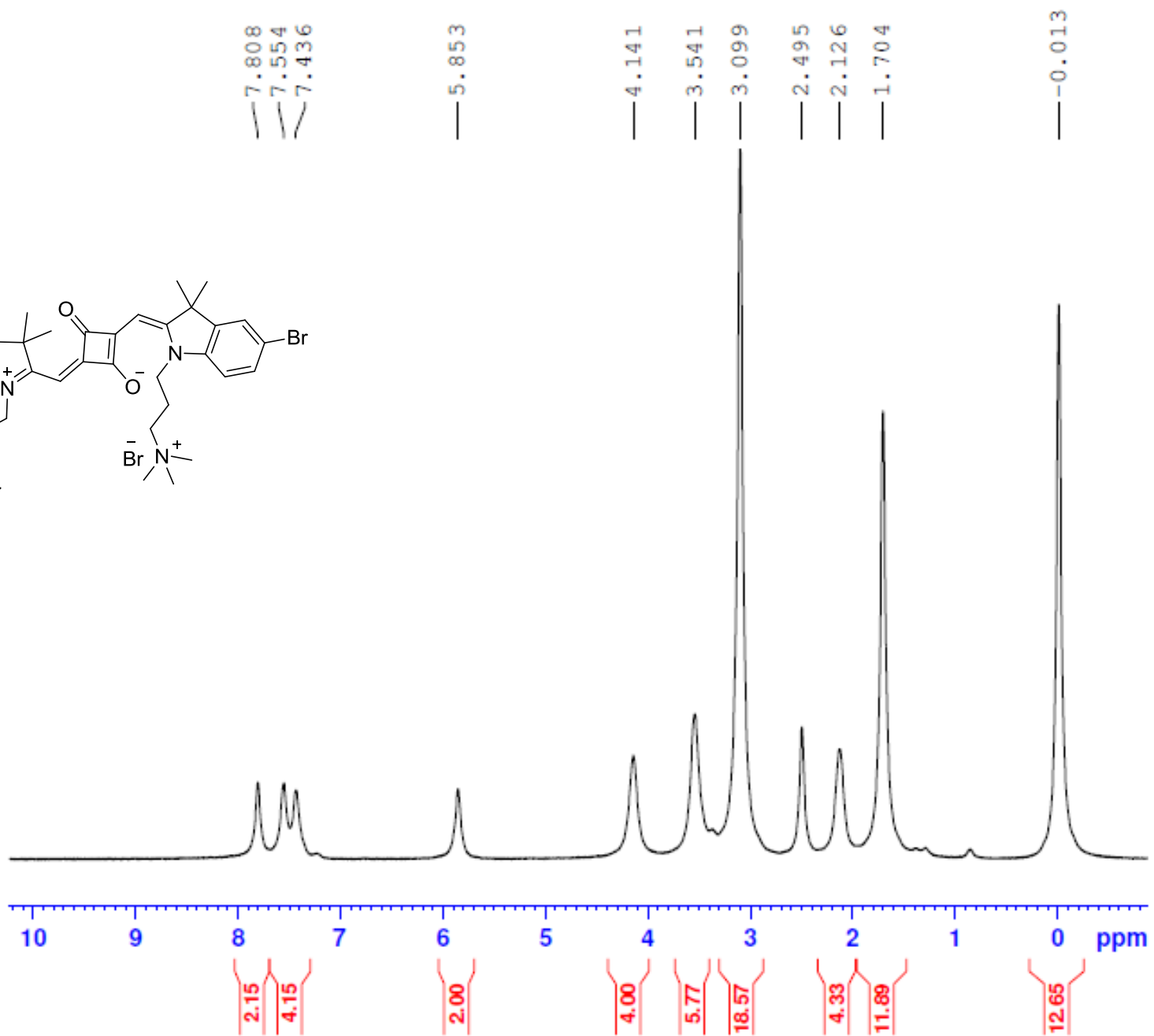
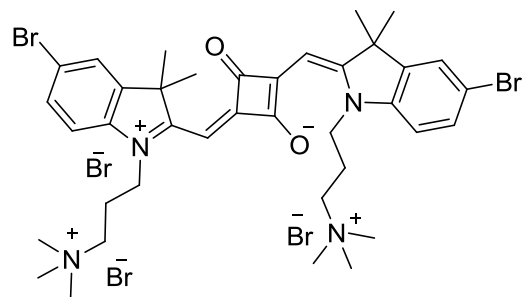


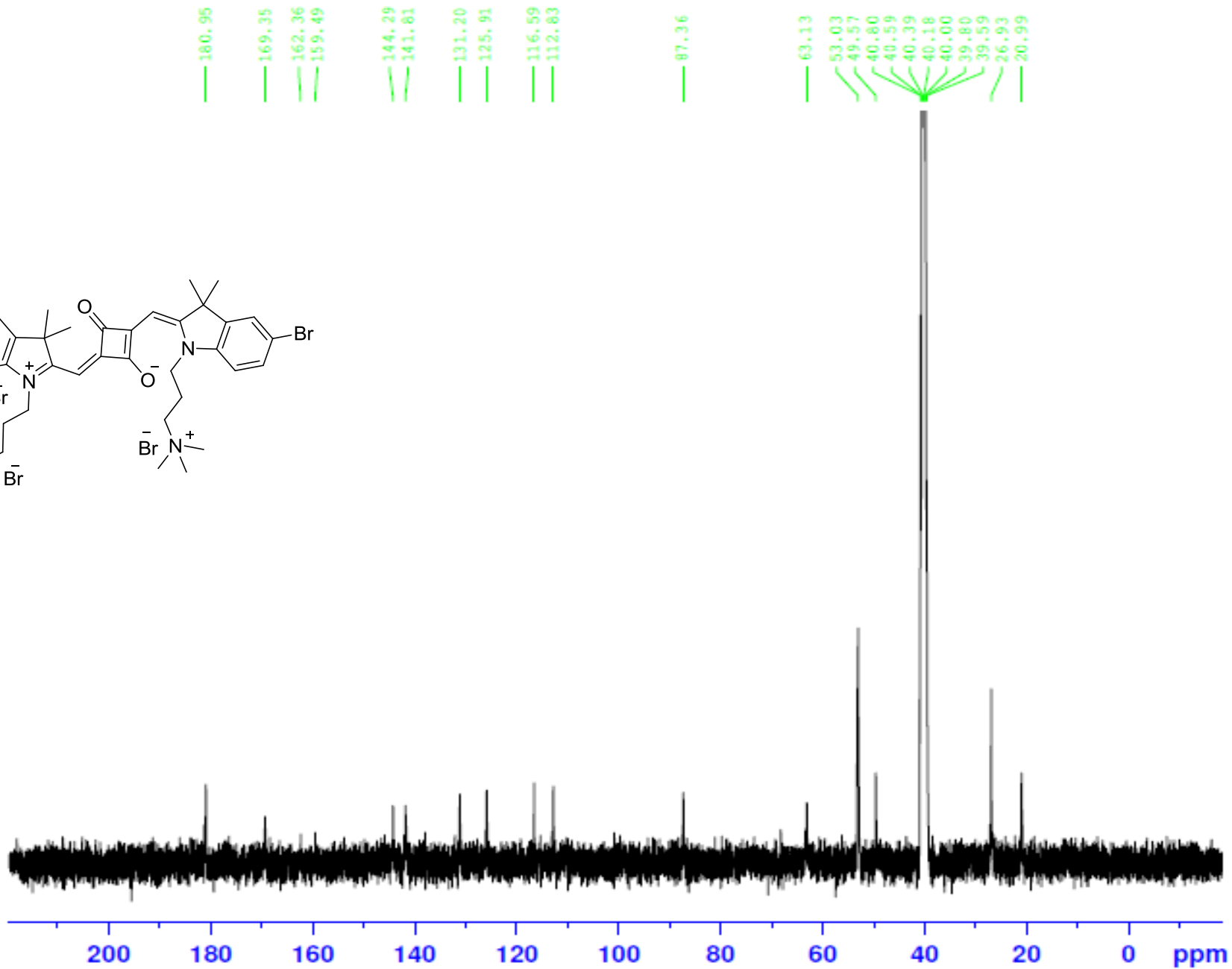
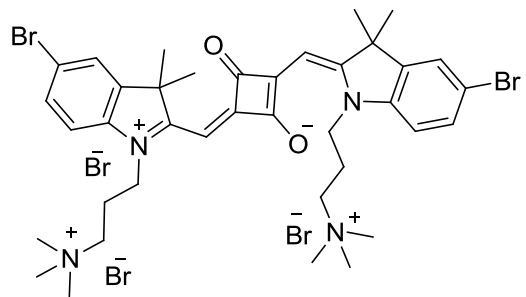


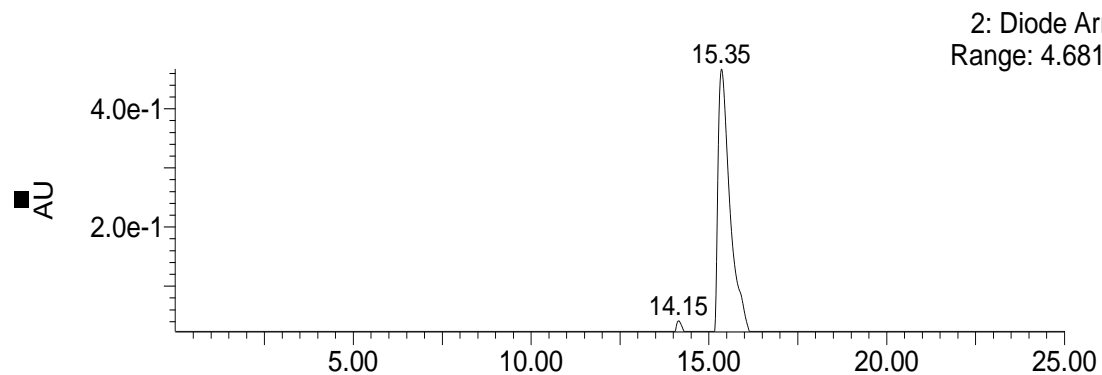
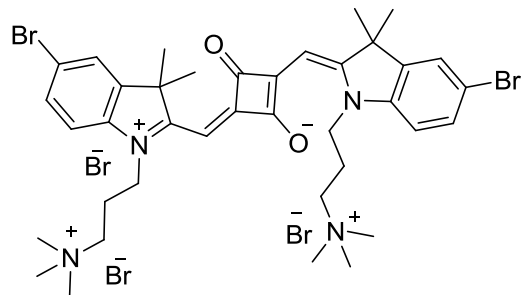












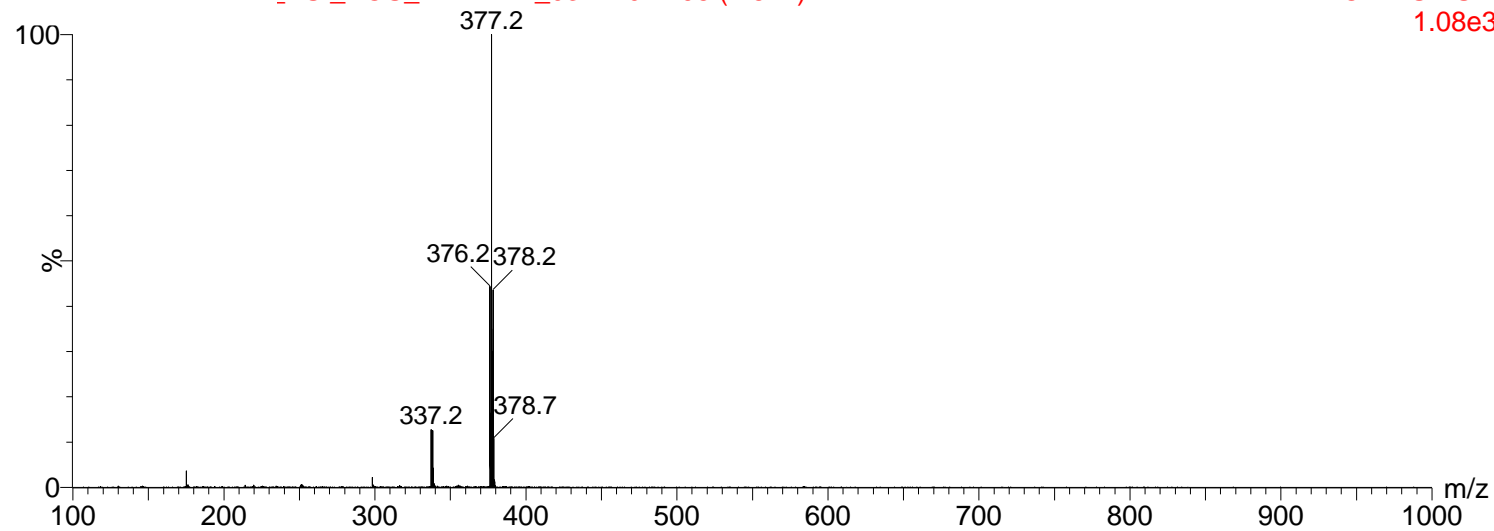
in 50%MeOH+0.1%HCOOH

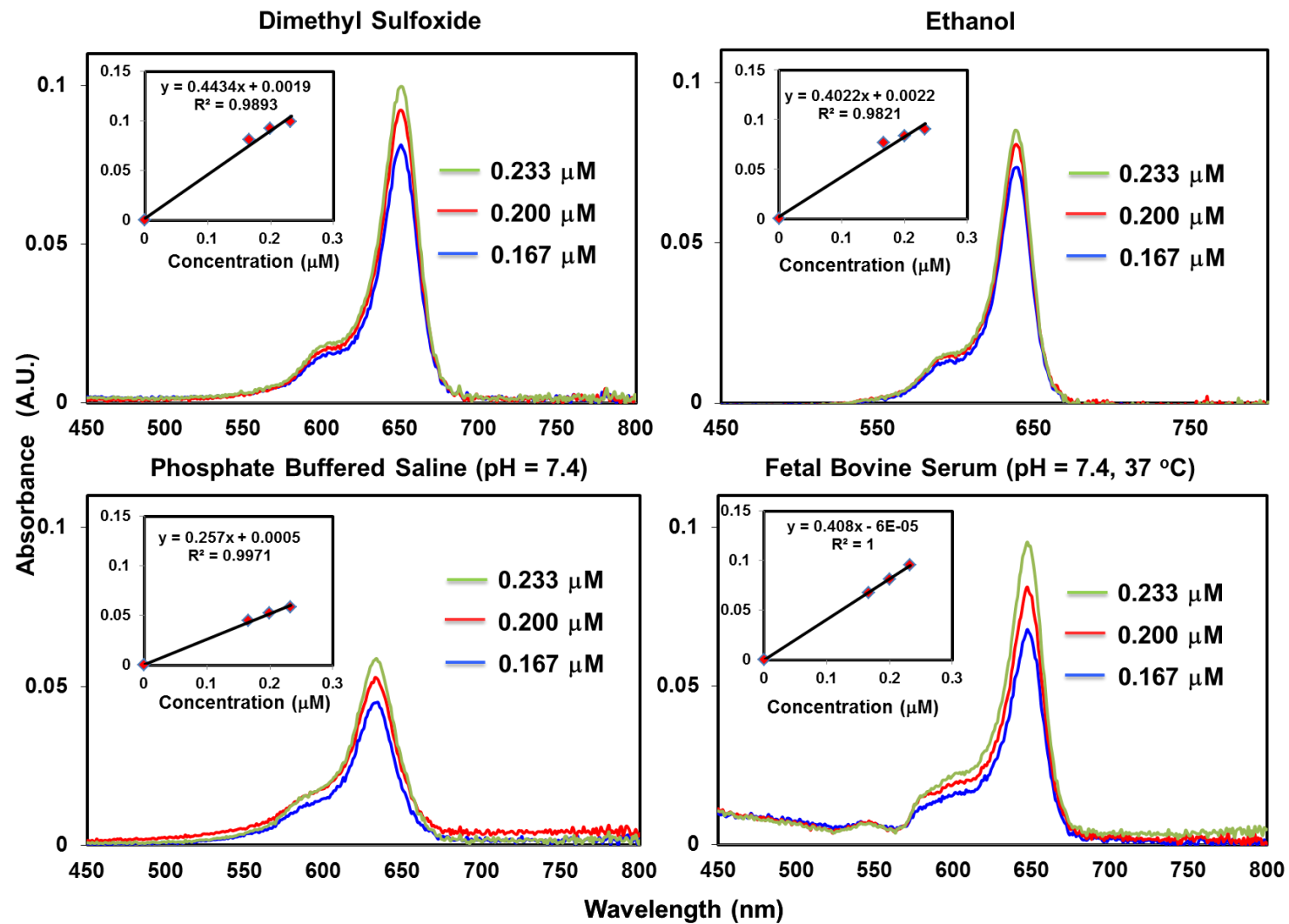
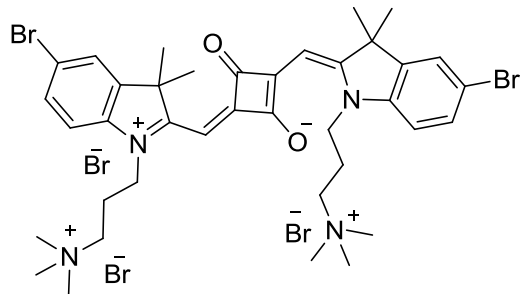
QtofMicro

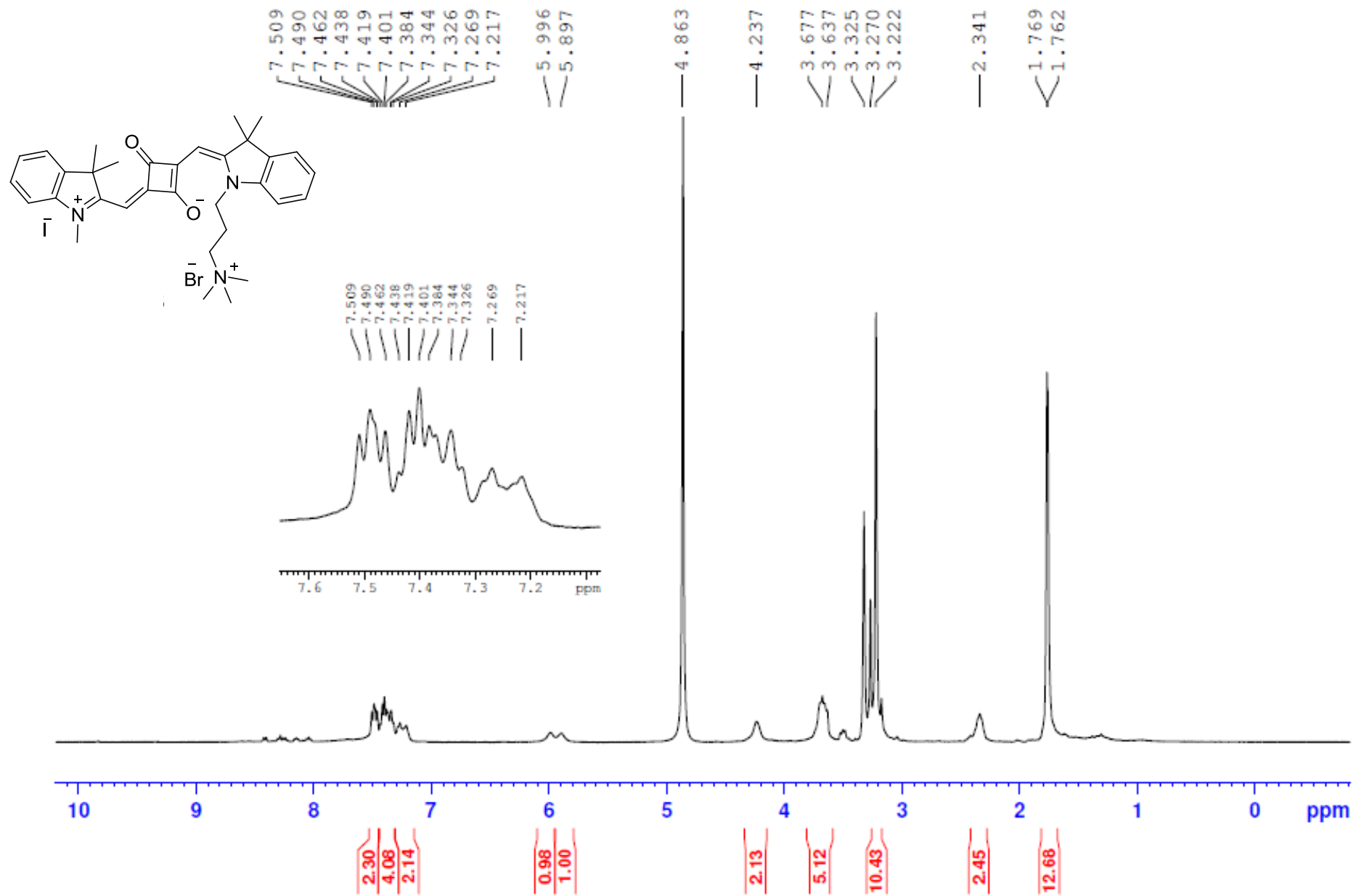
12-Mar-2014 11:16:12

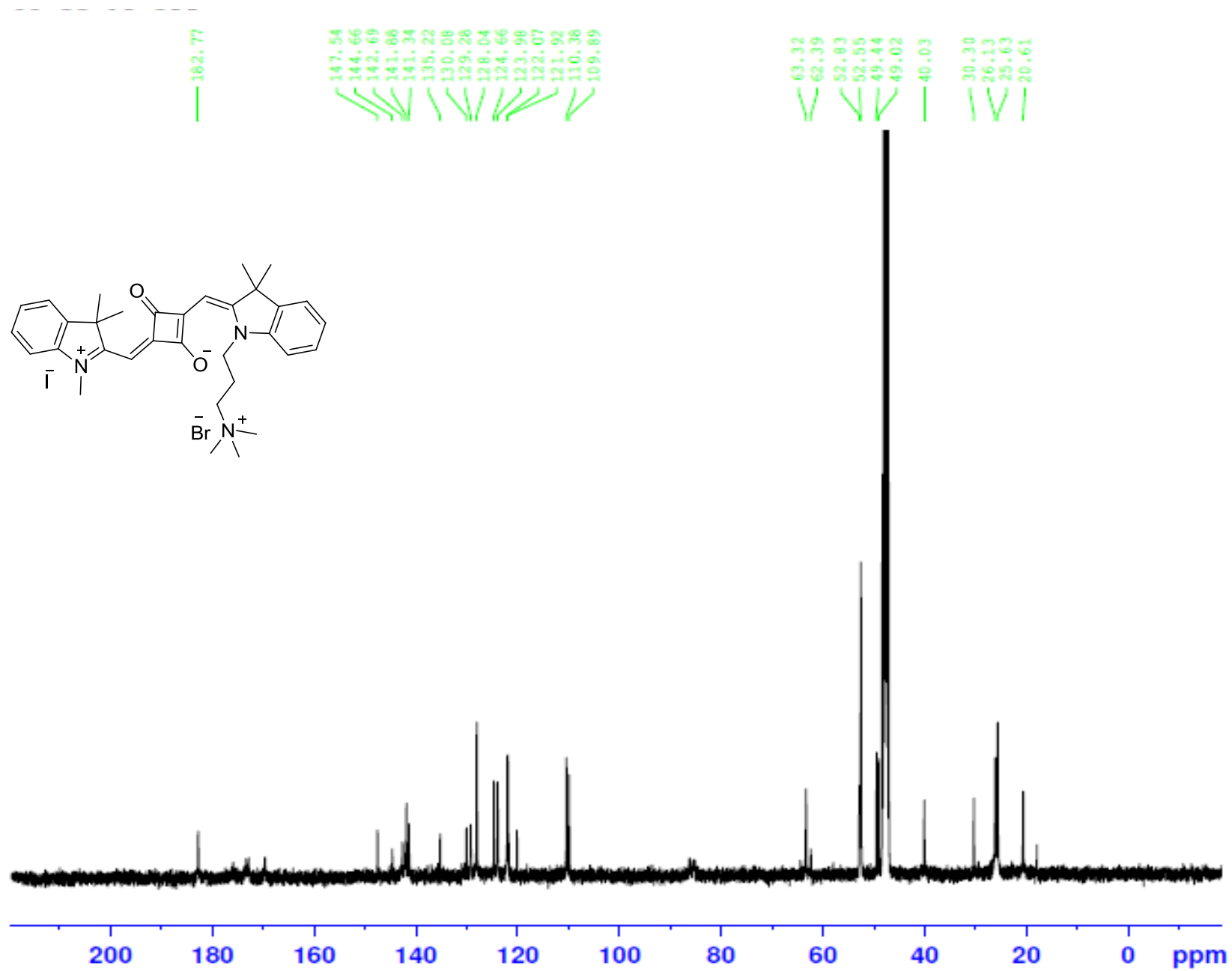
_ESI_POS_HENARY_03112014 98 (1.821)

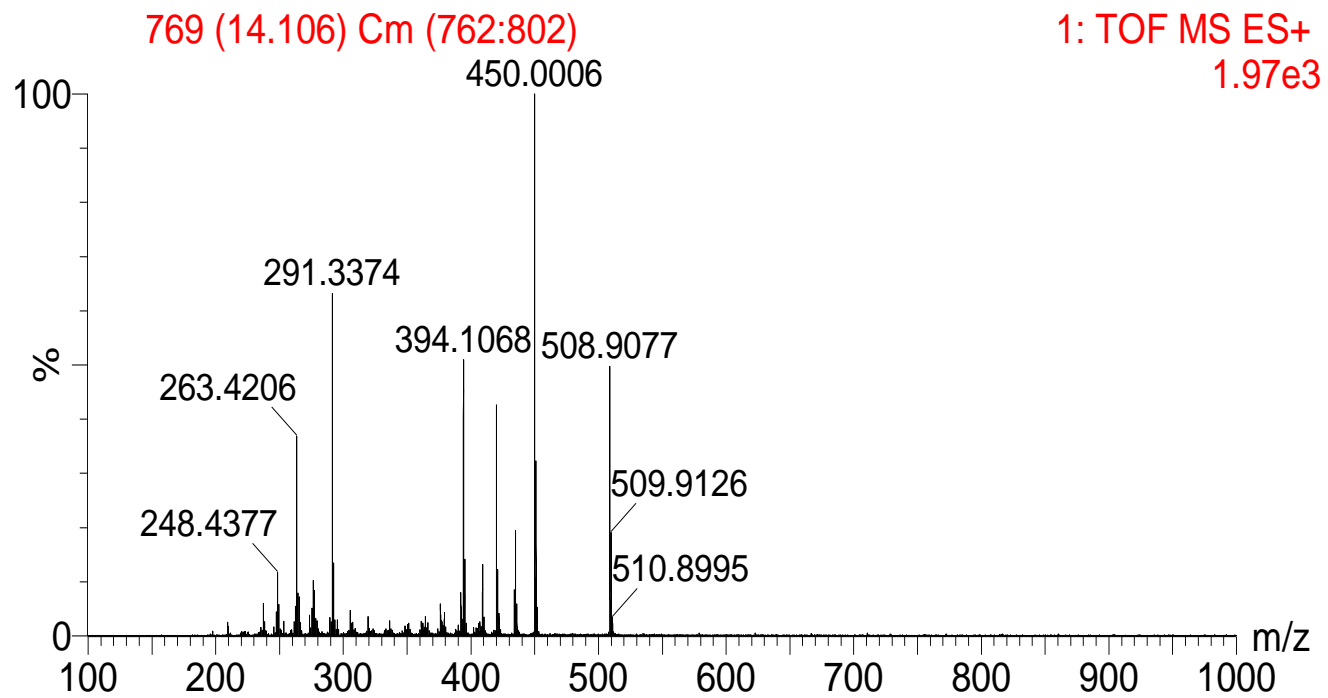
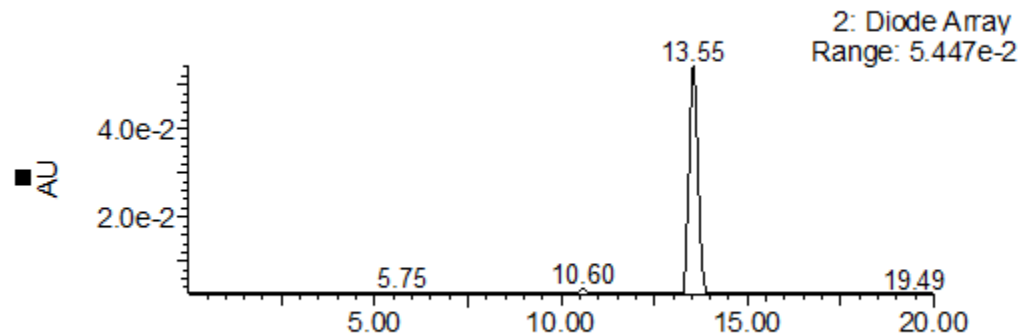
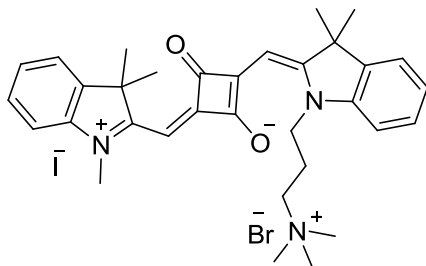
TOF MS ES+
1.08e3

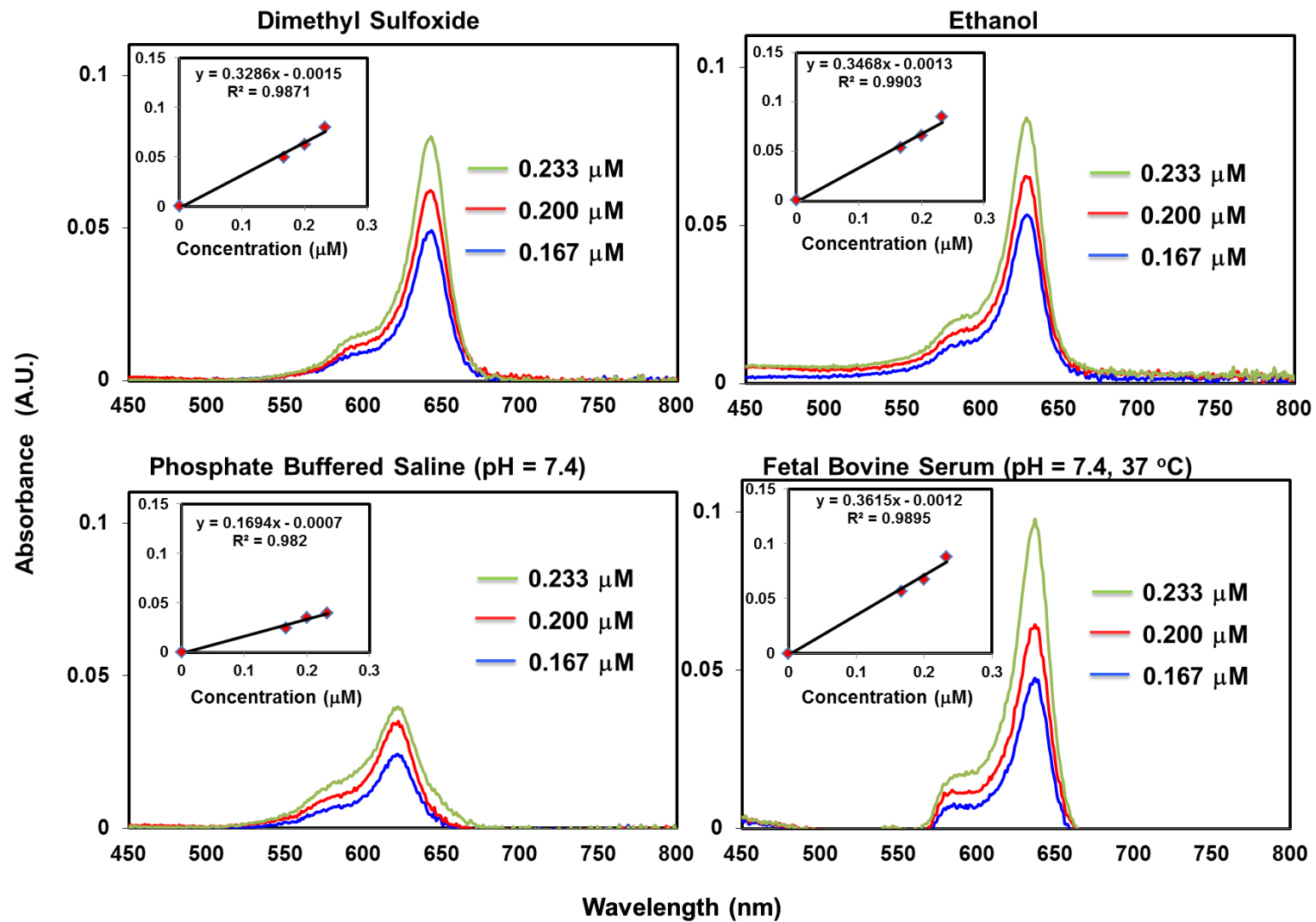
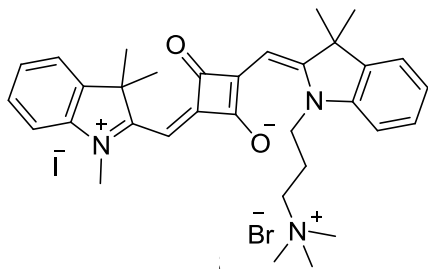


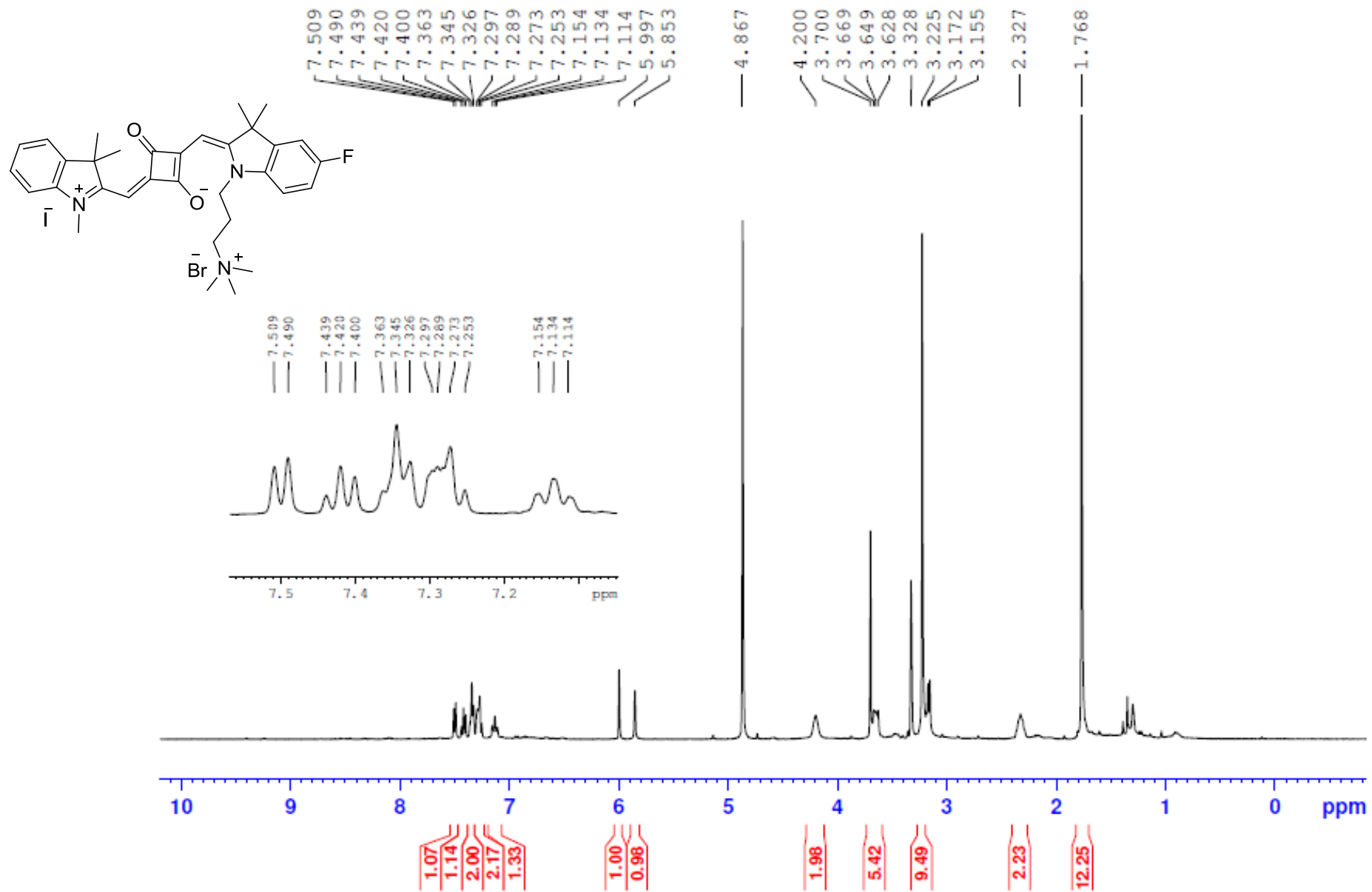


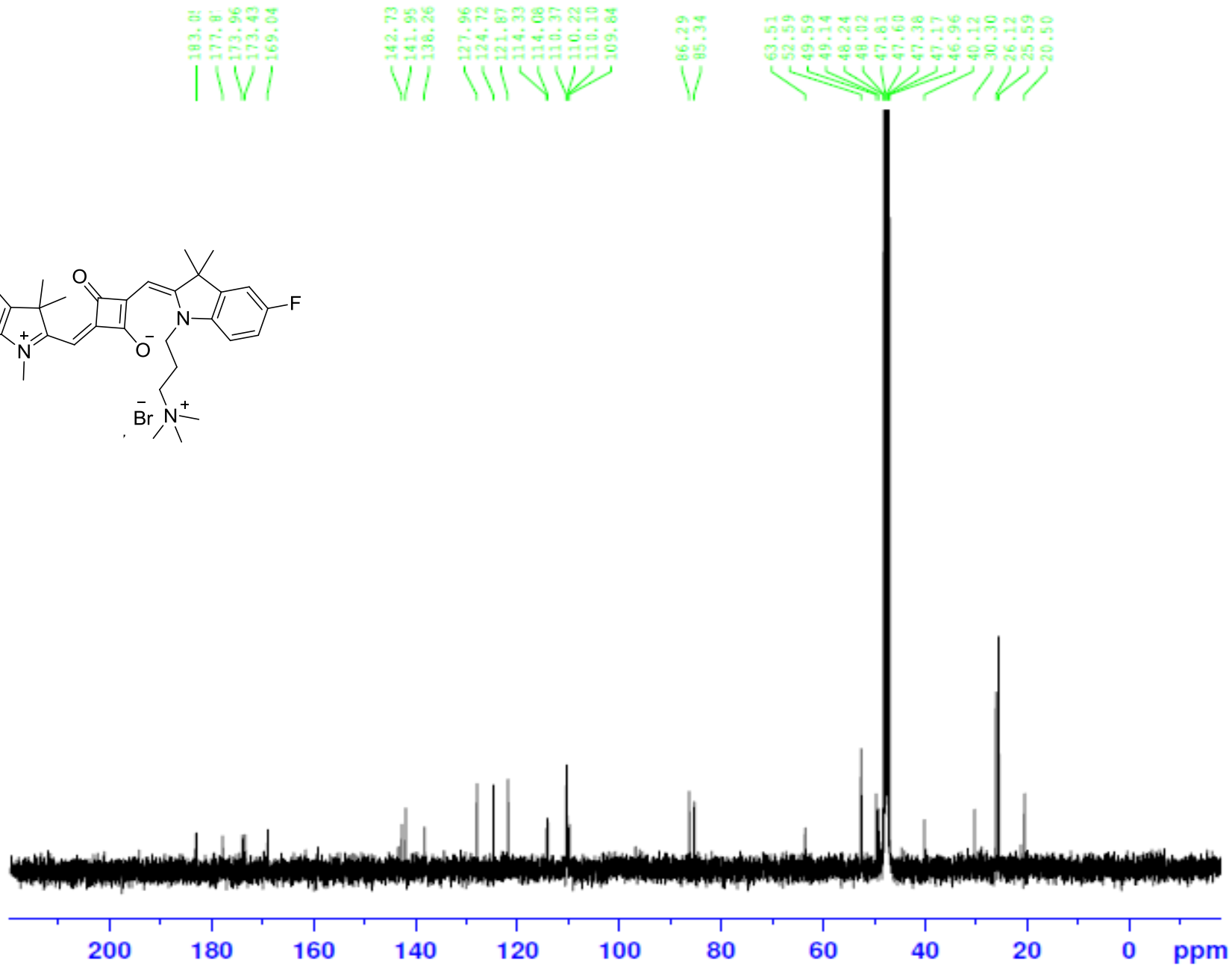
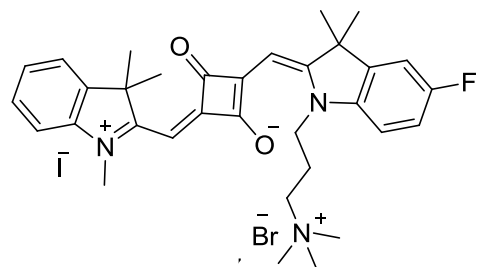


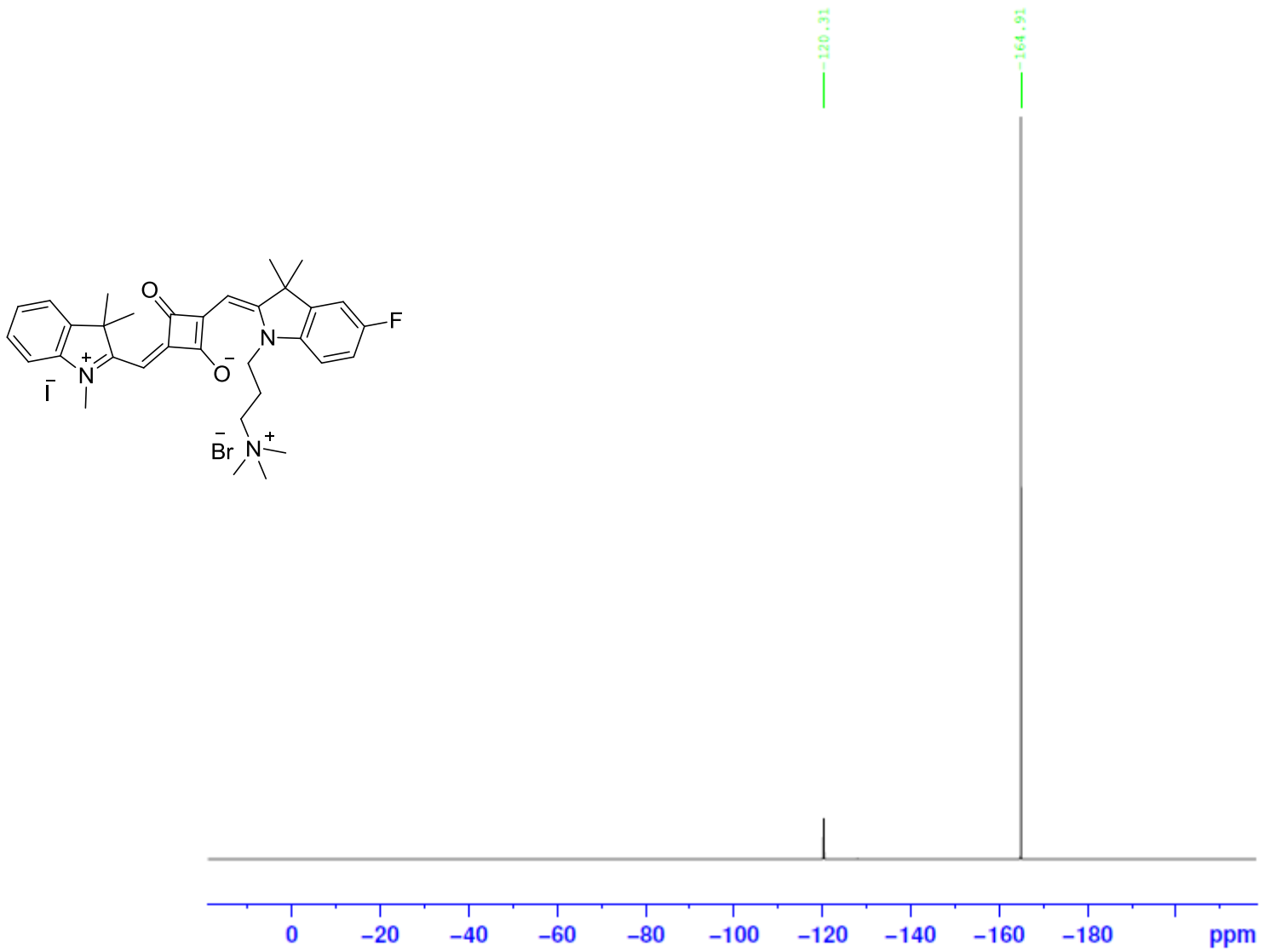


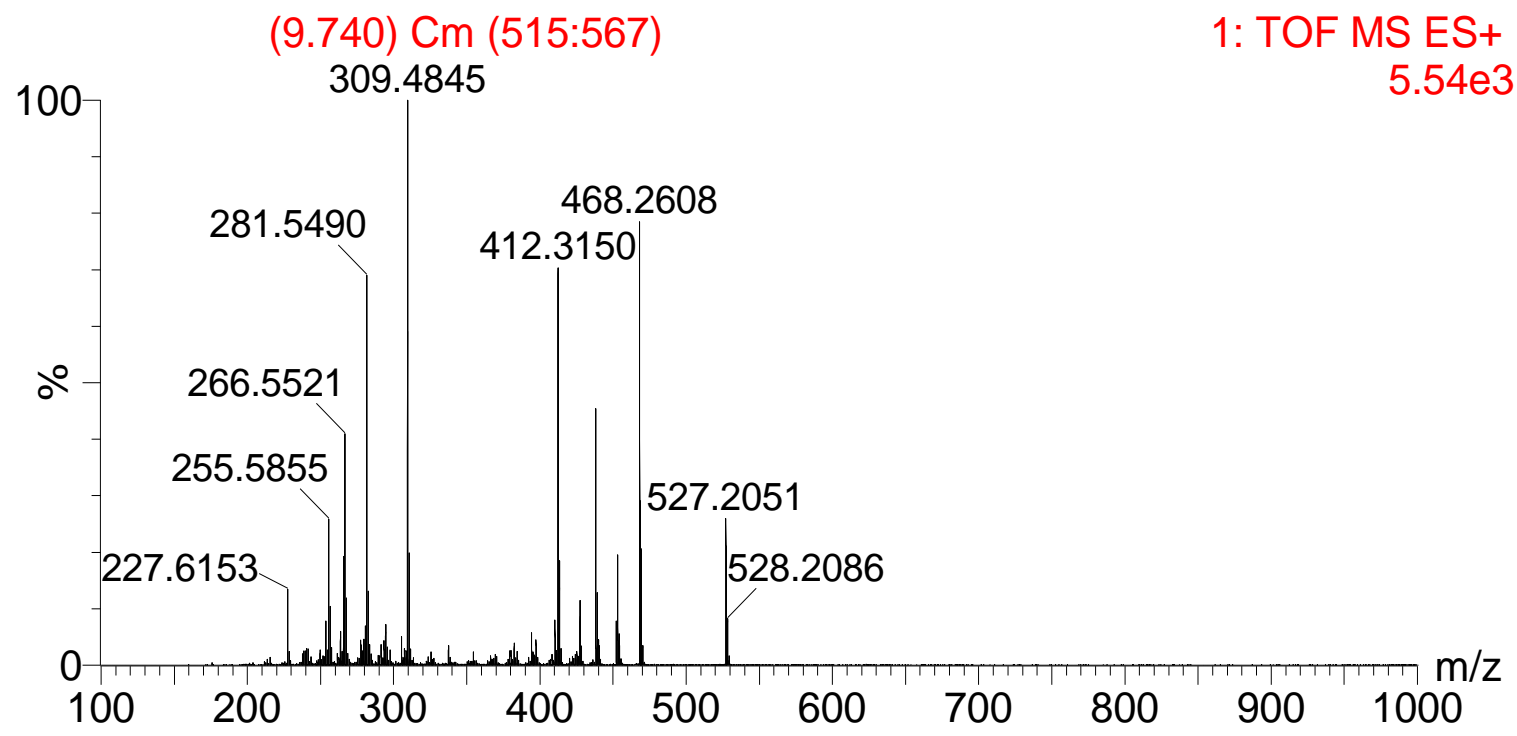
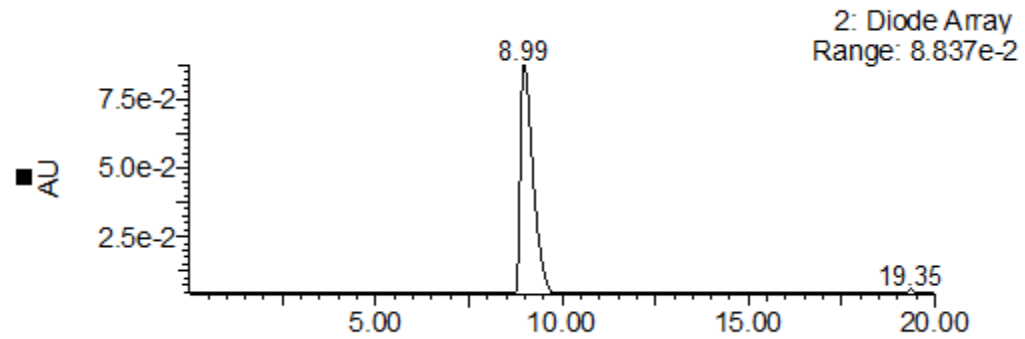
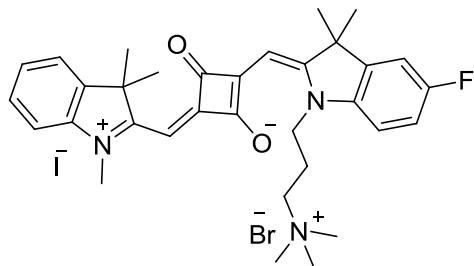


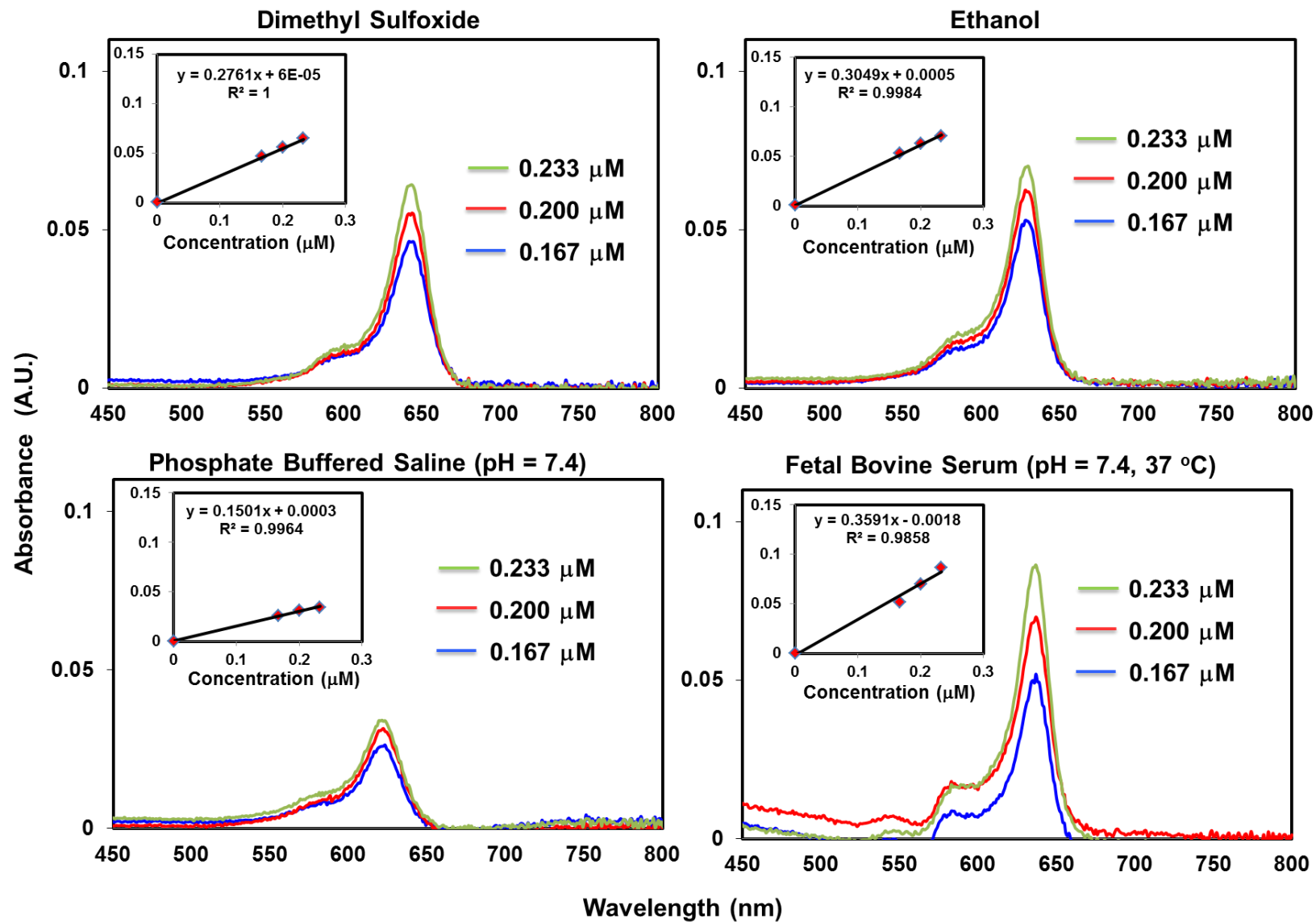
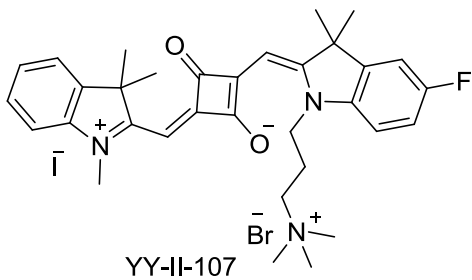


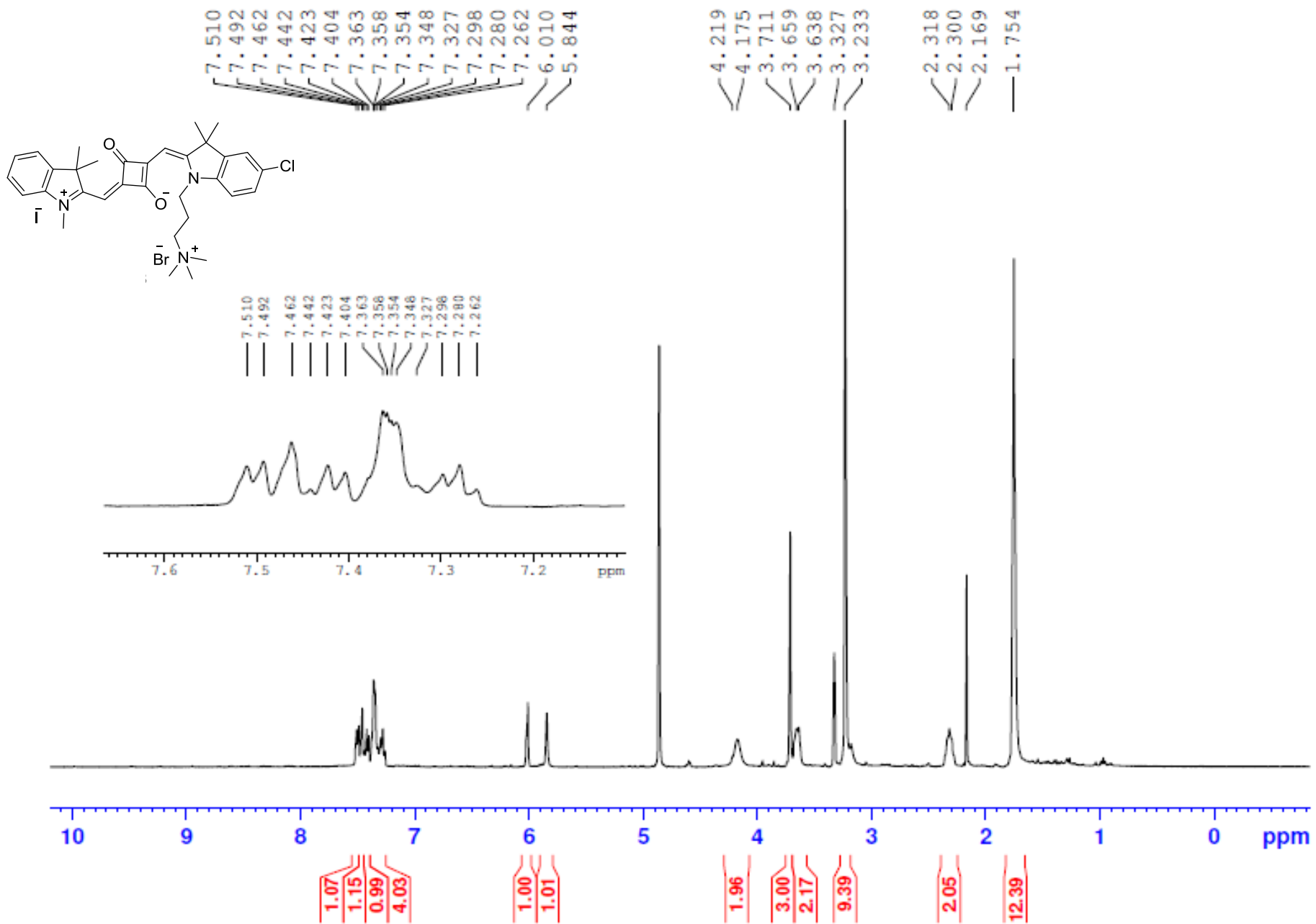


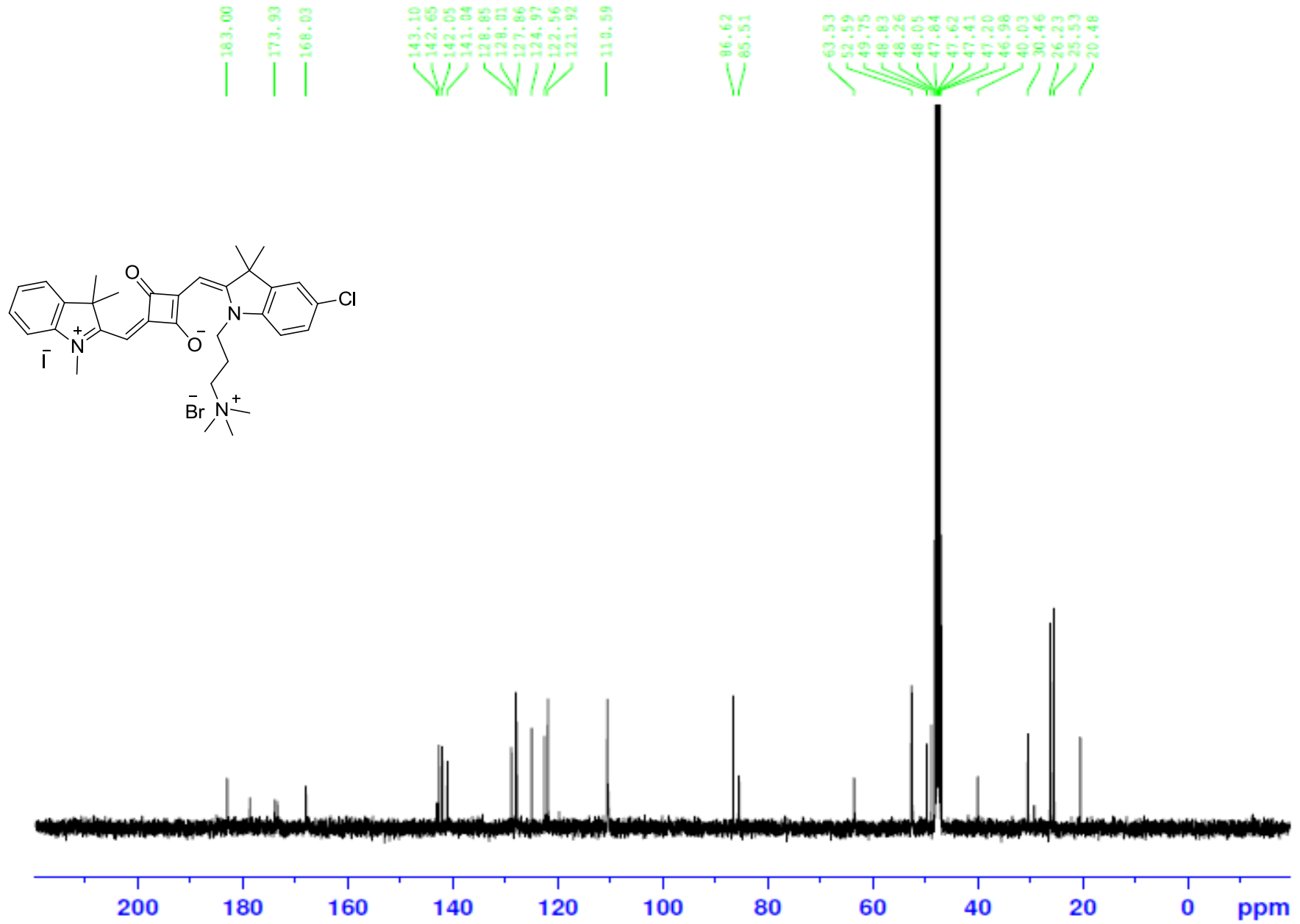


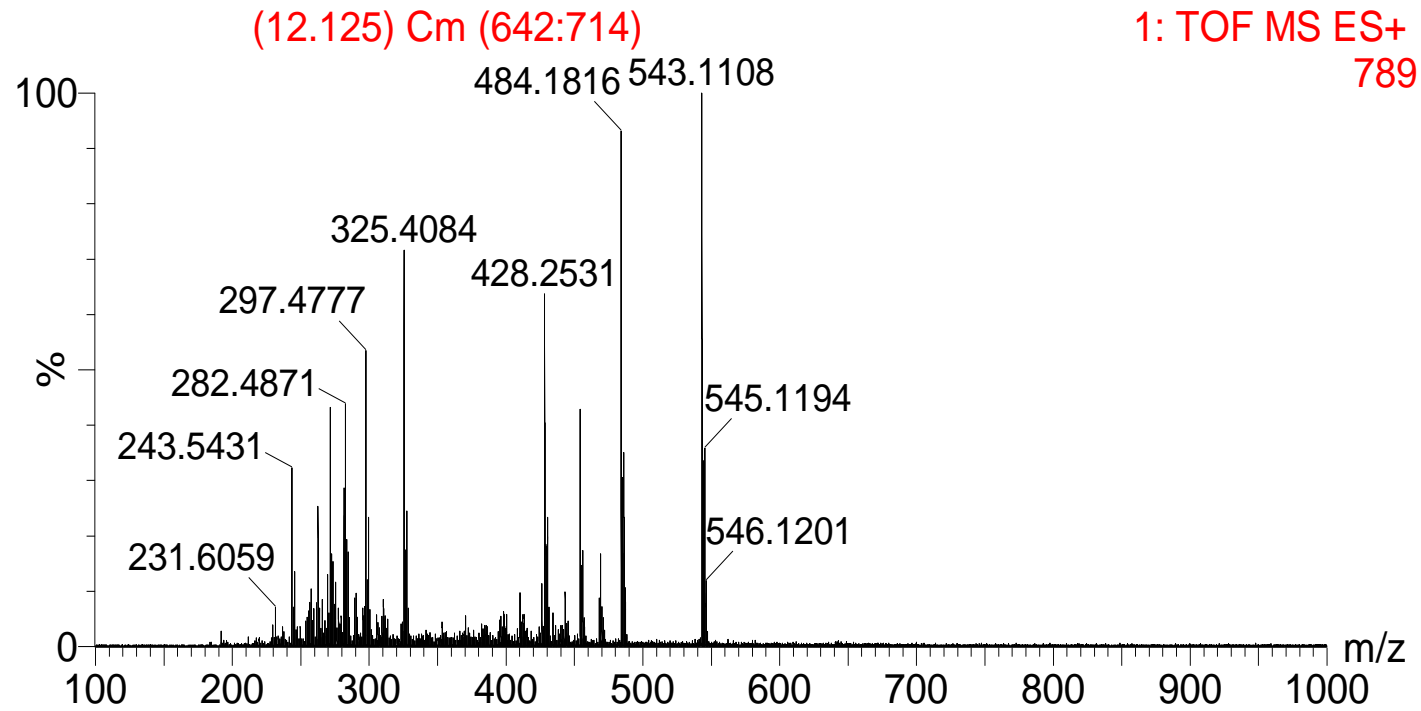
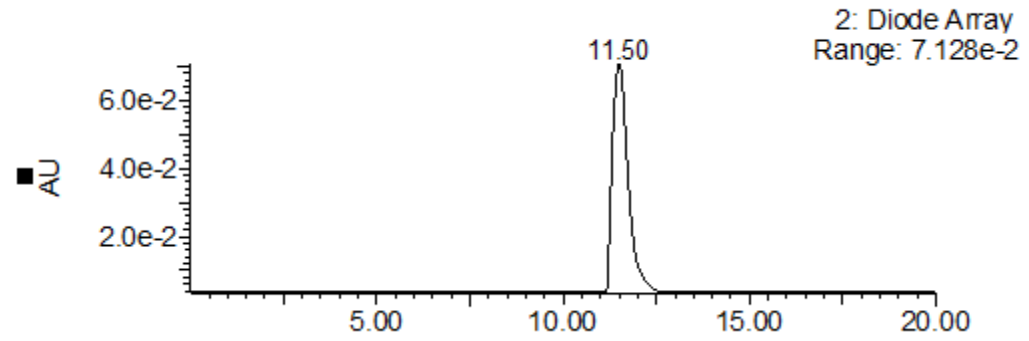
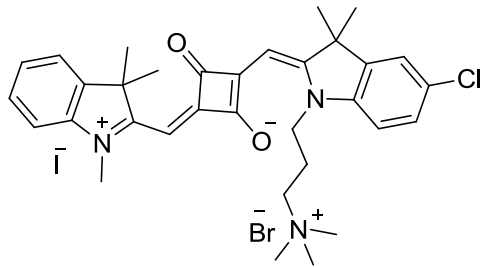


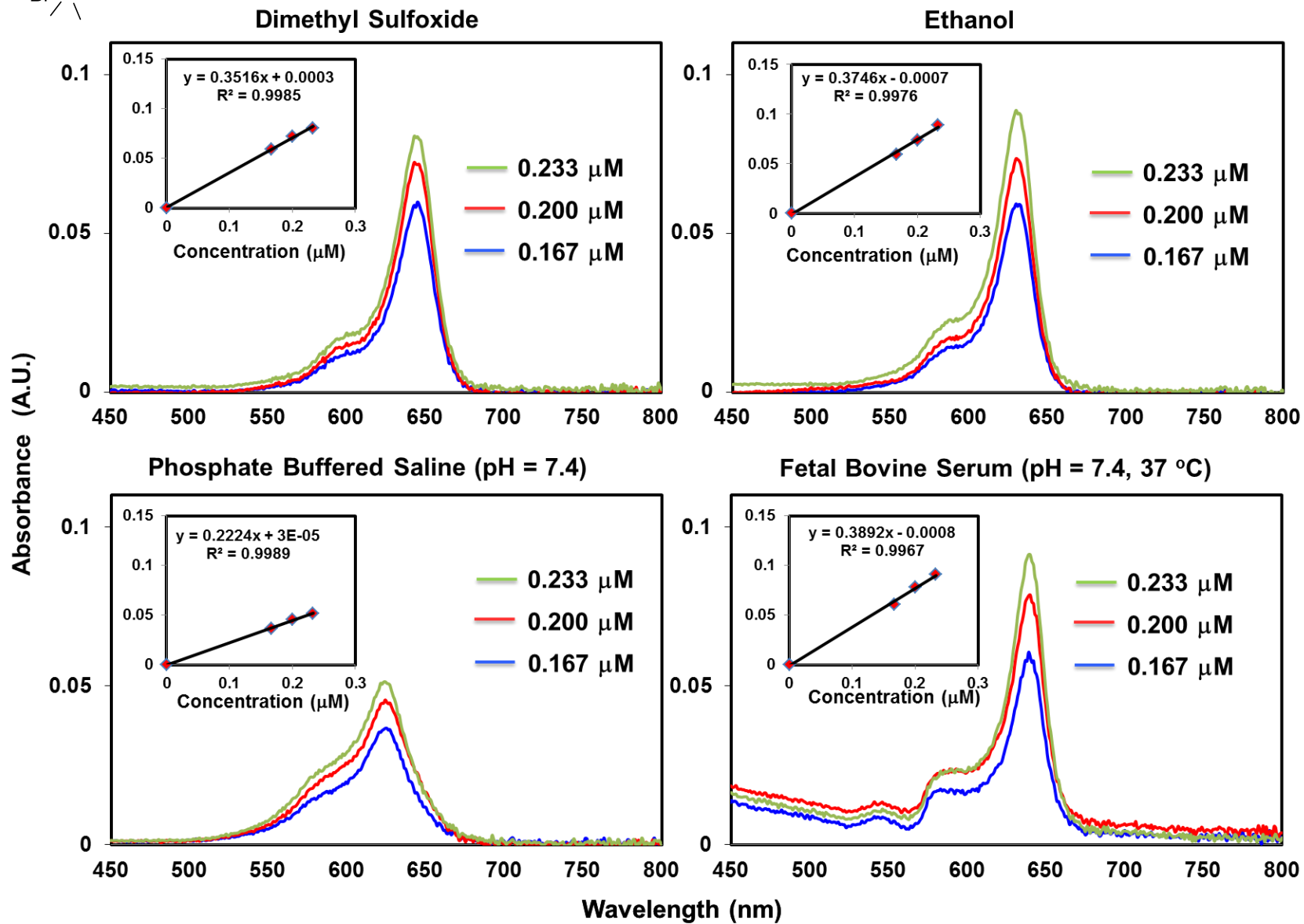
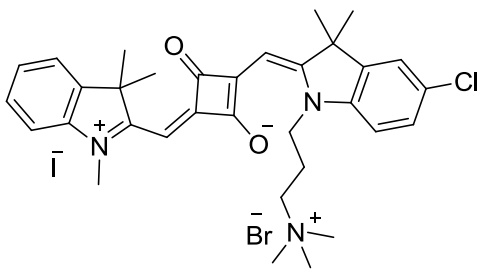


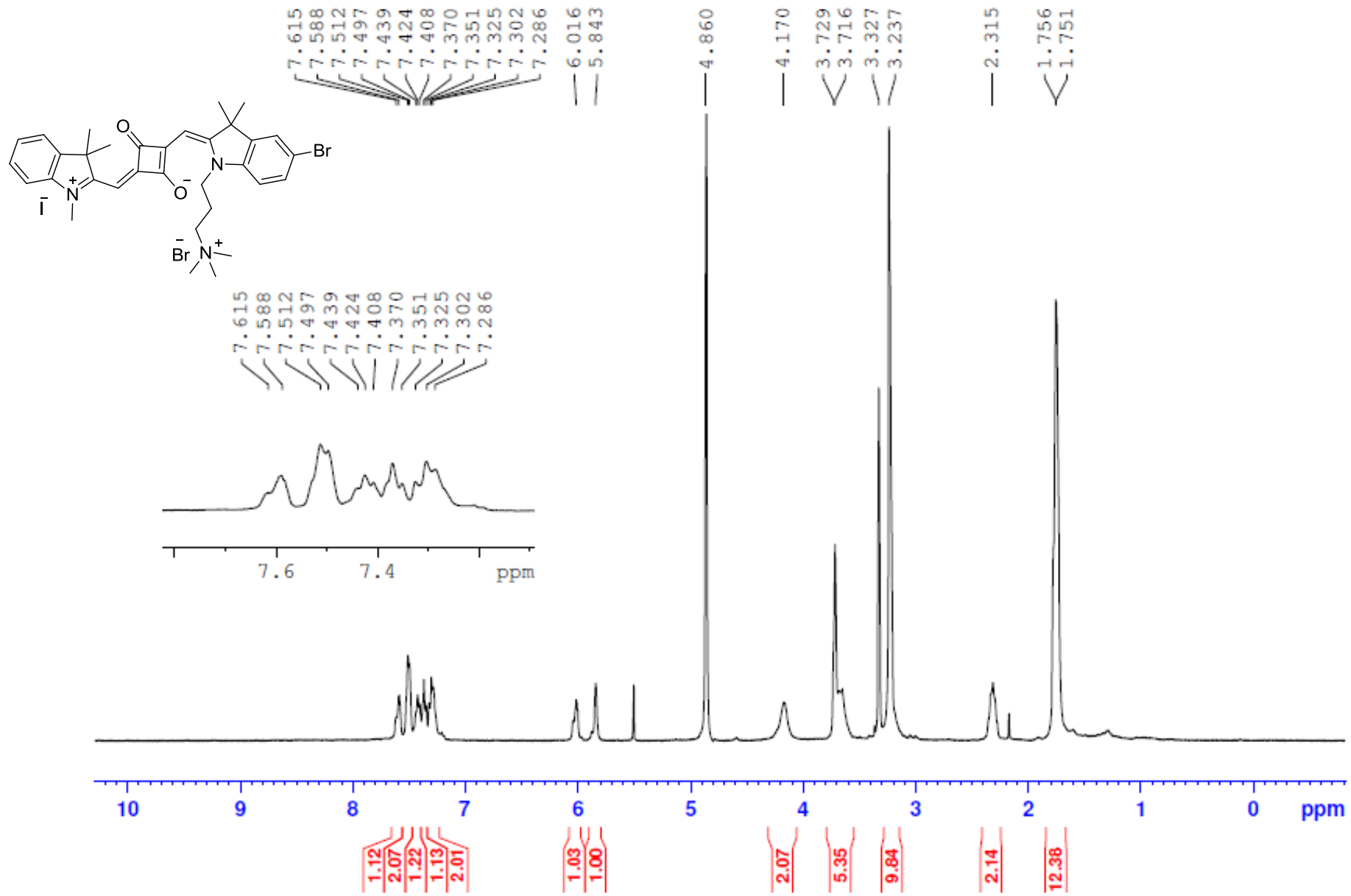


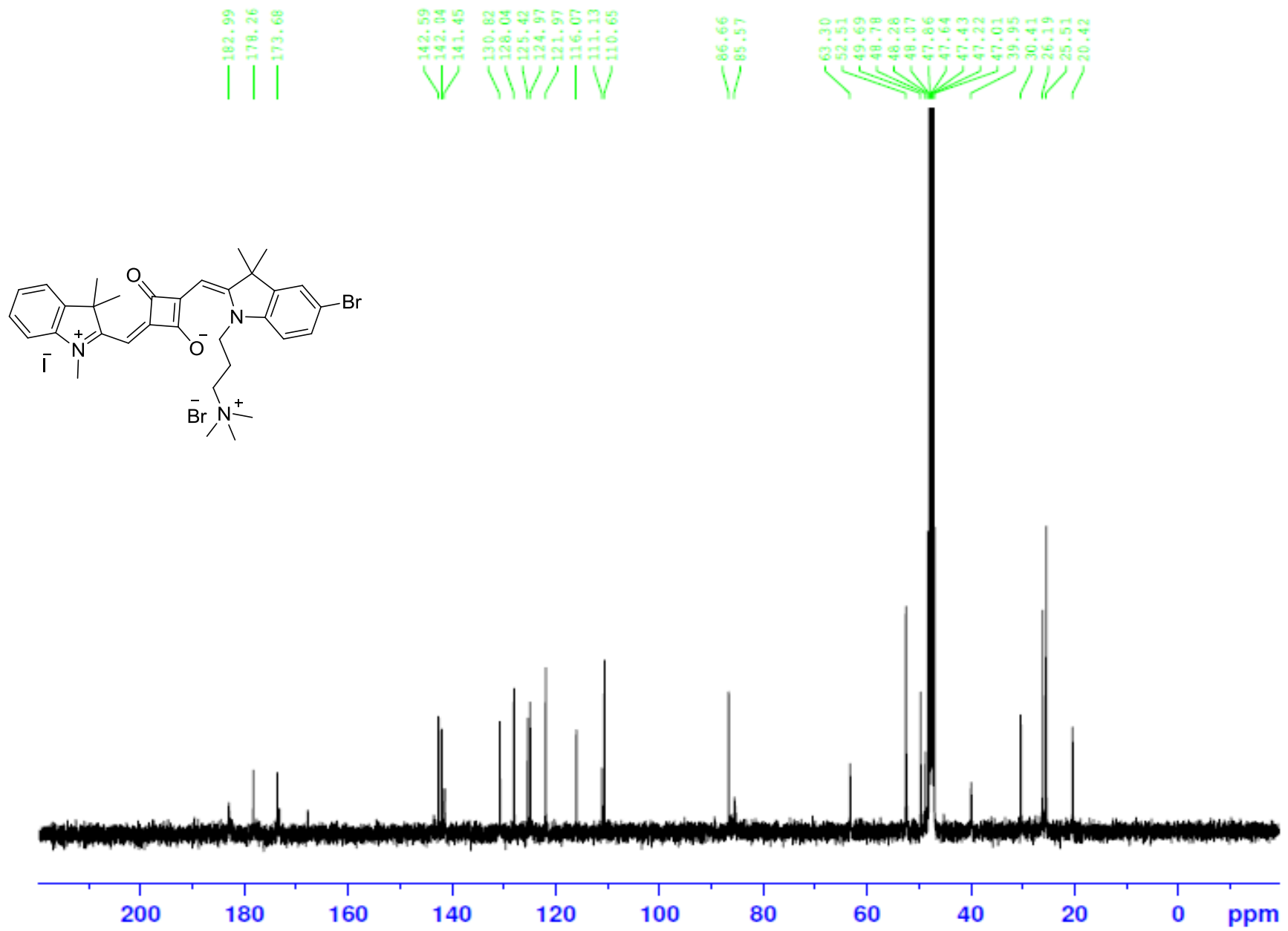


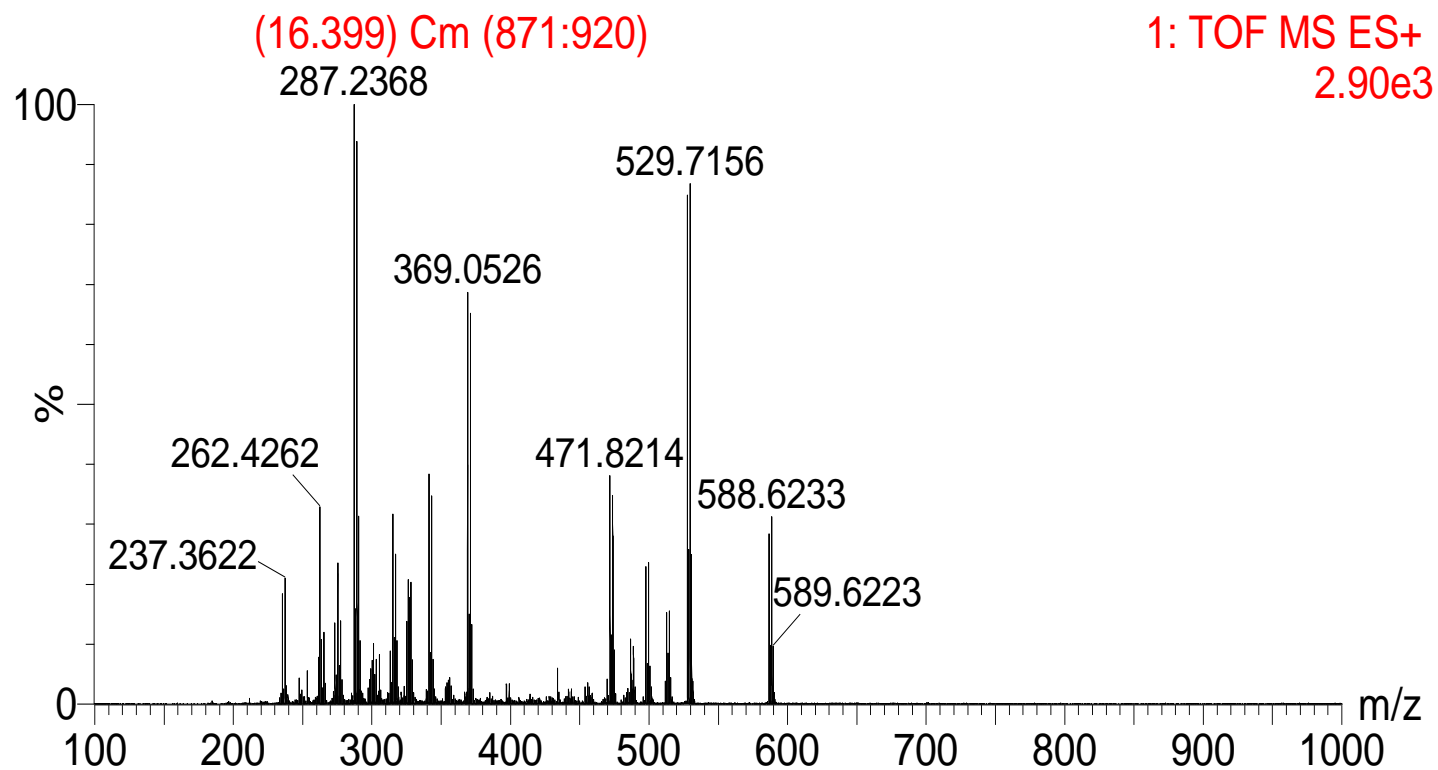
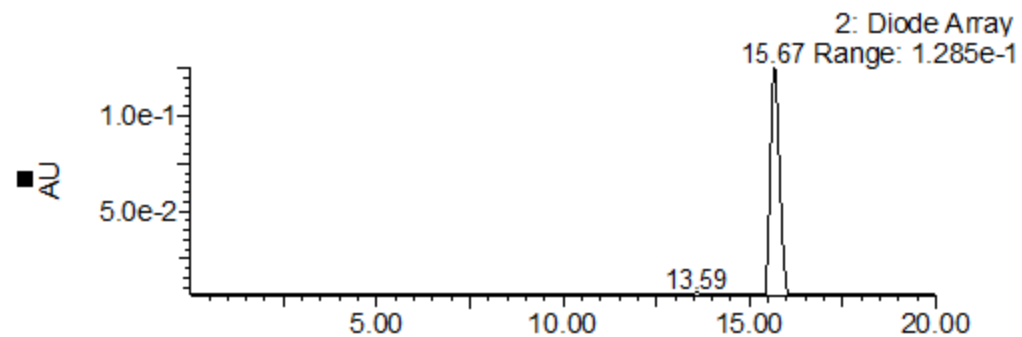
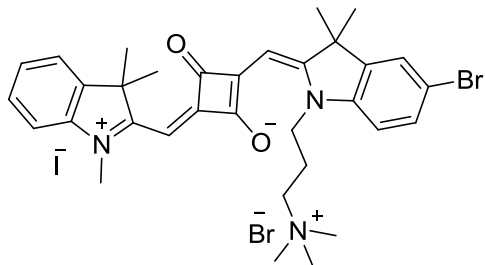


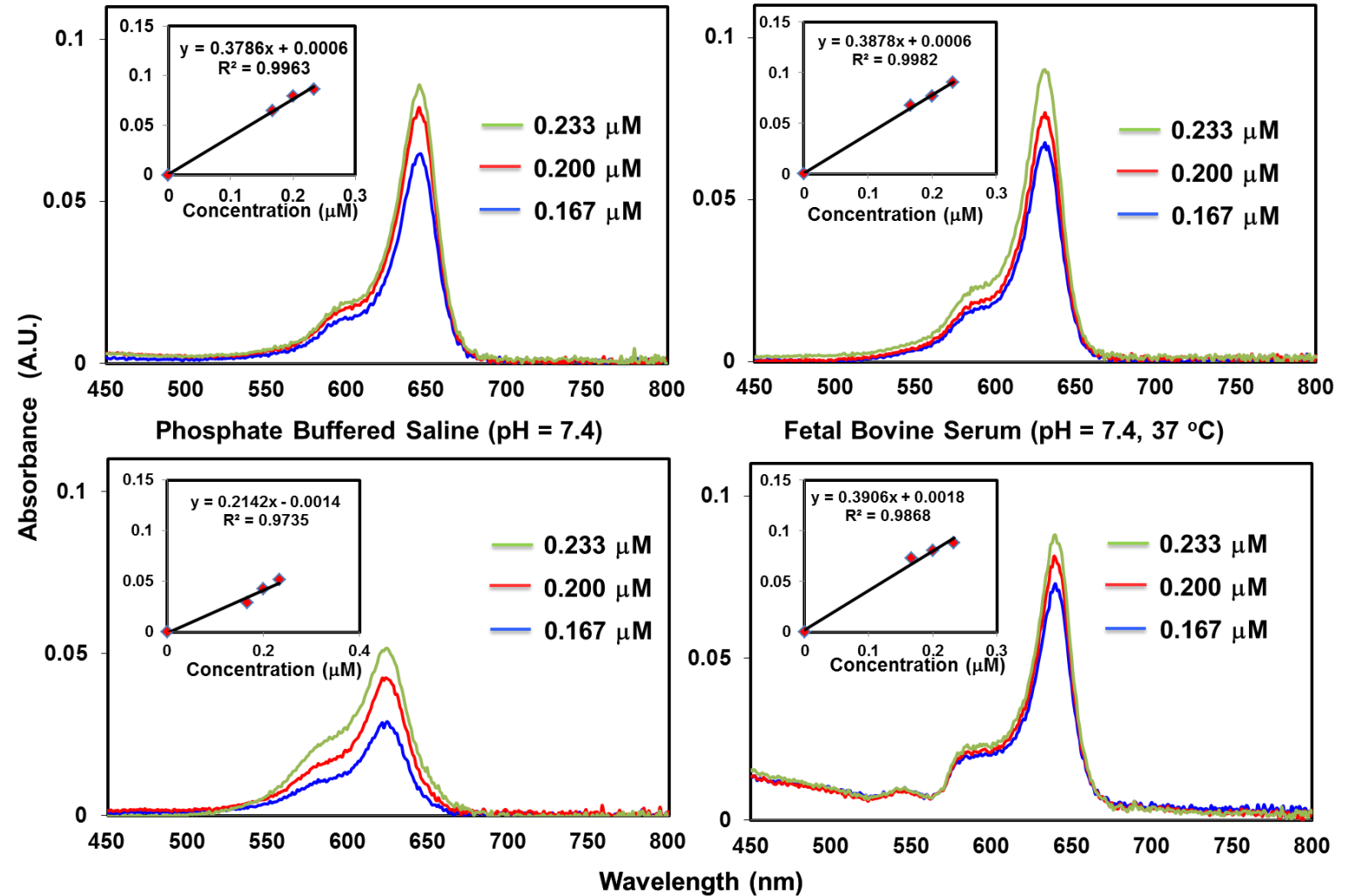
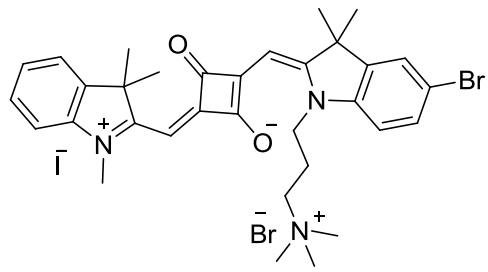






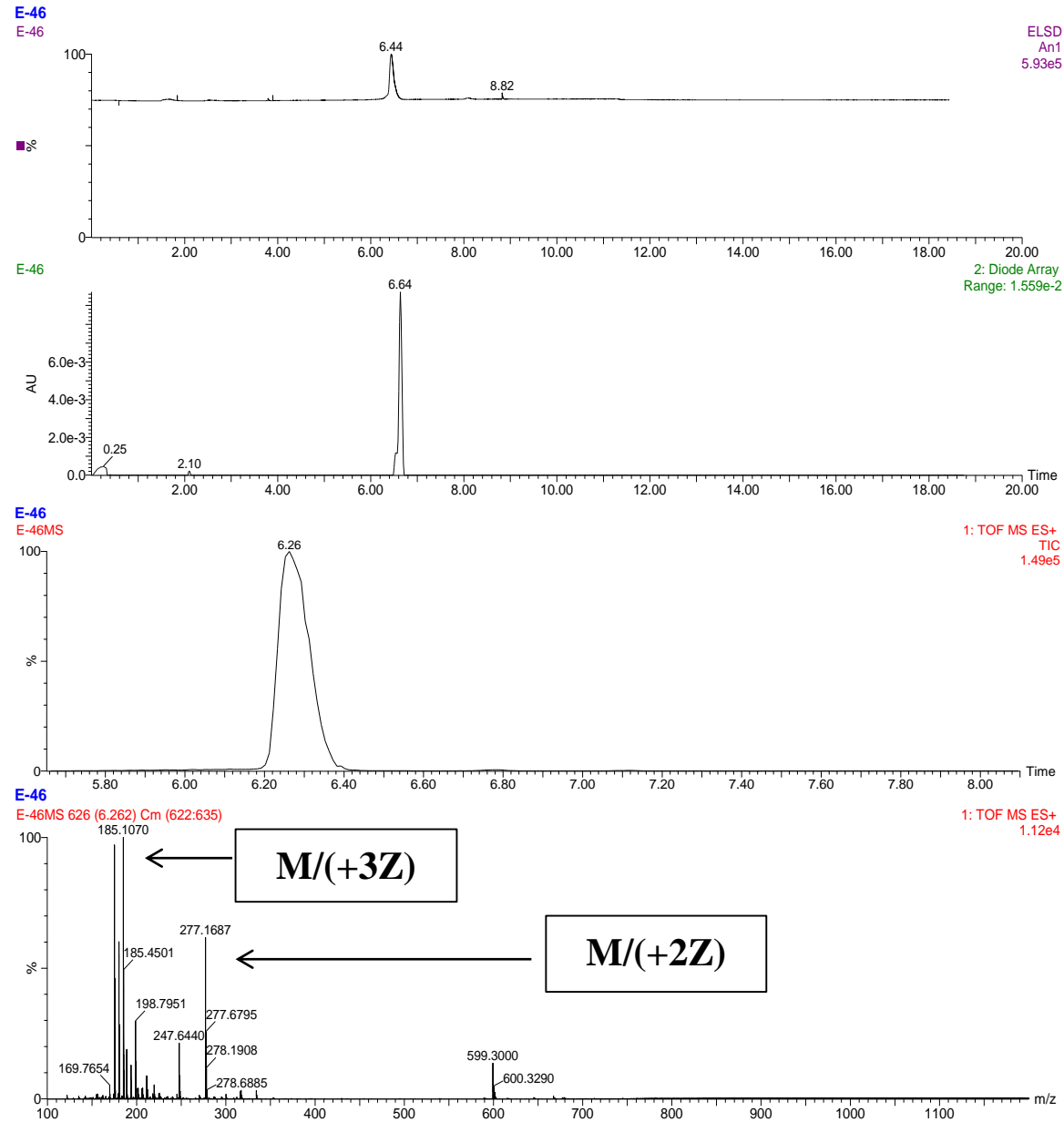
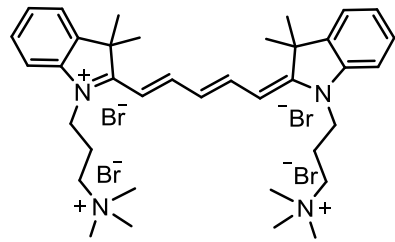


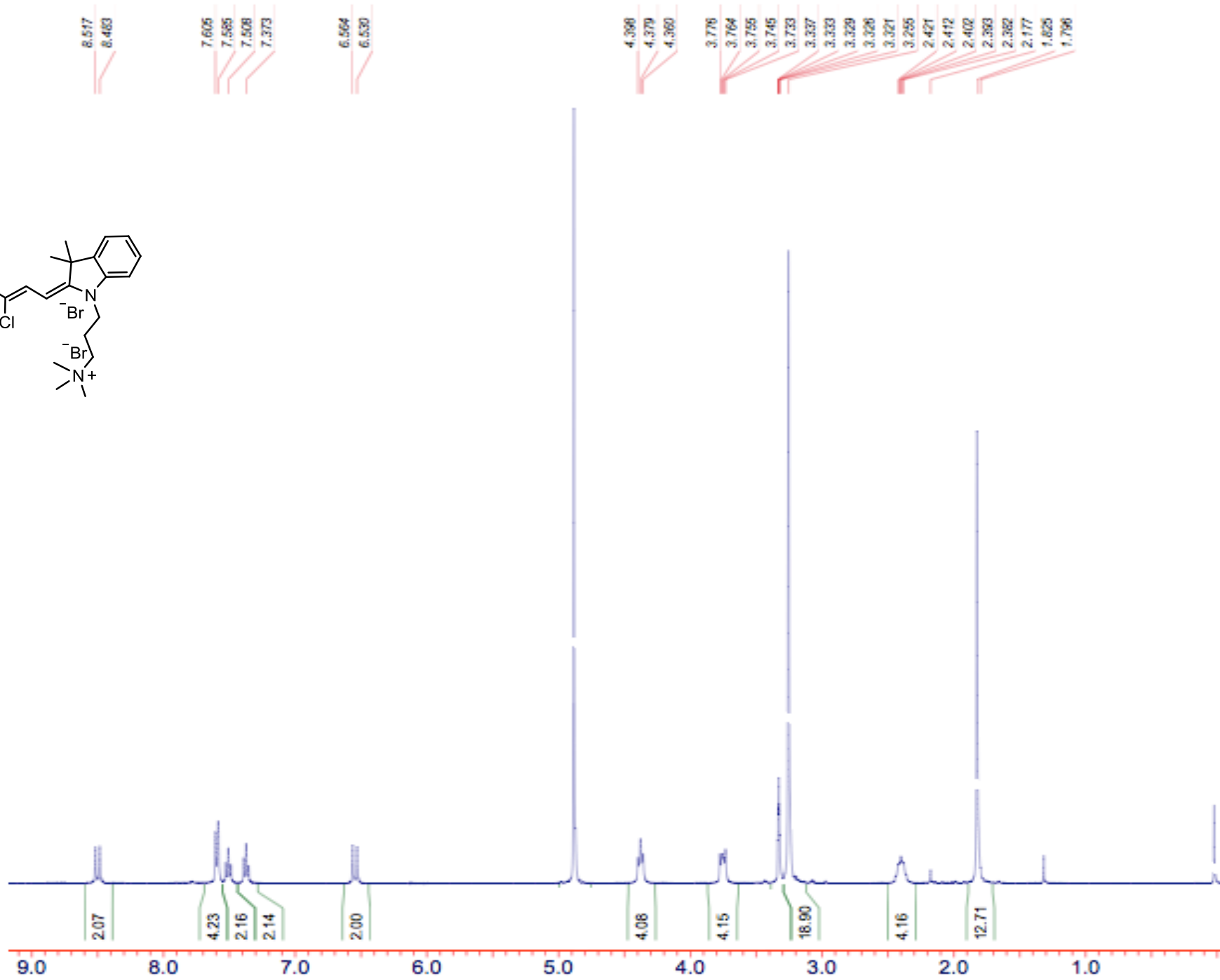
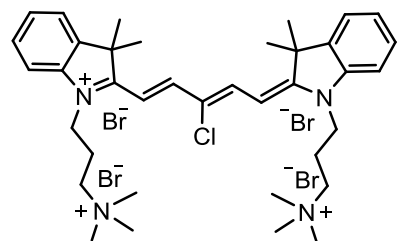


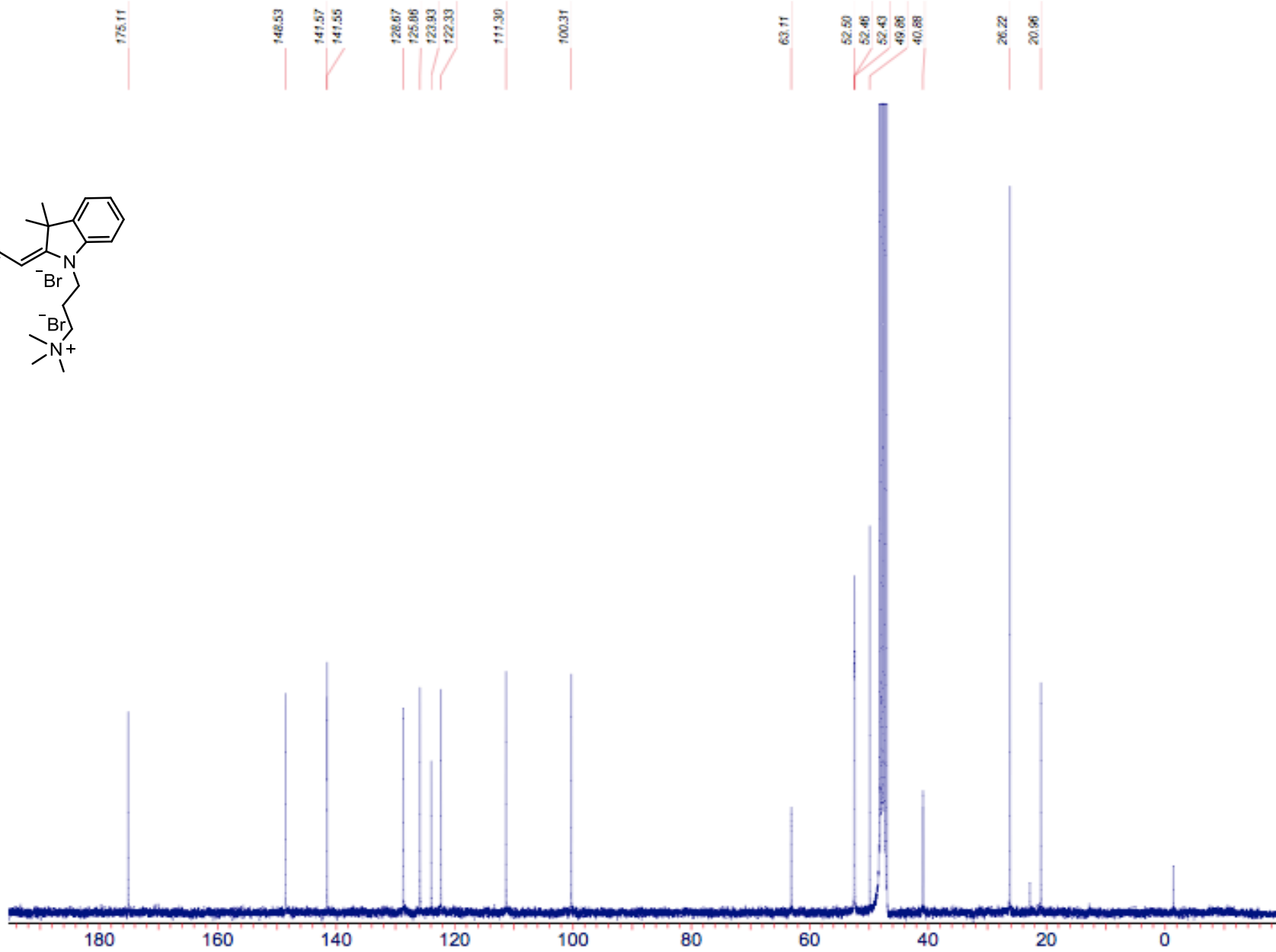
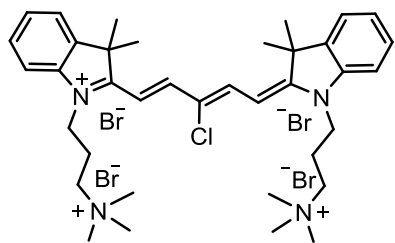


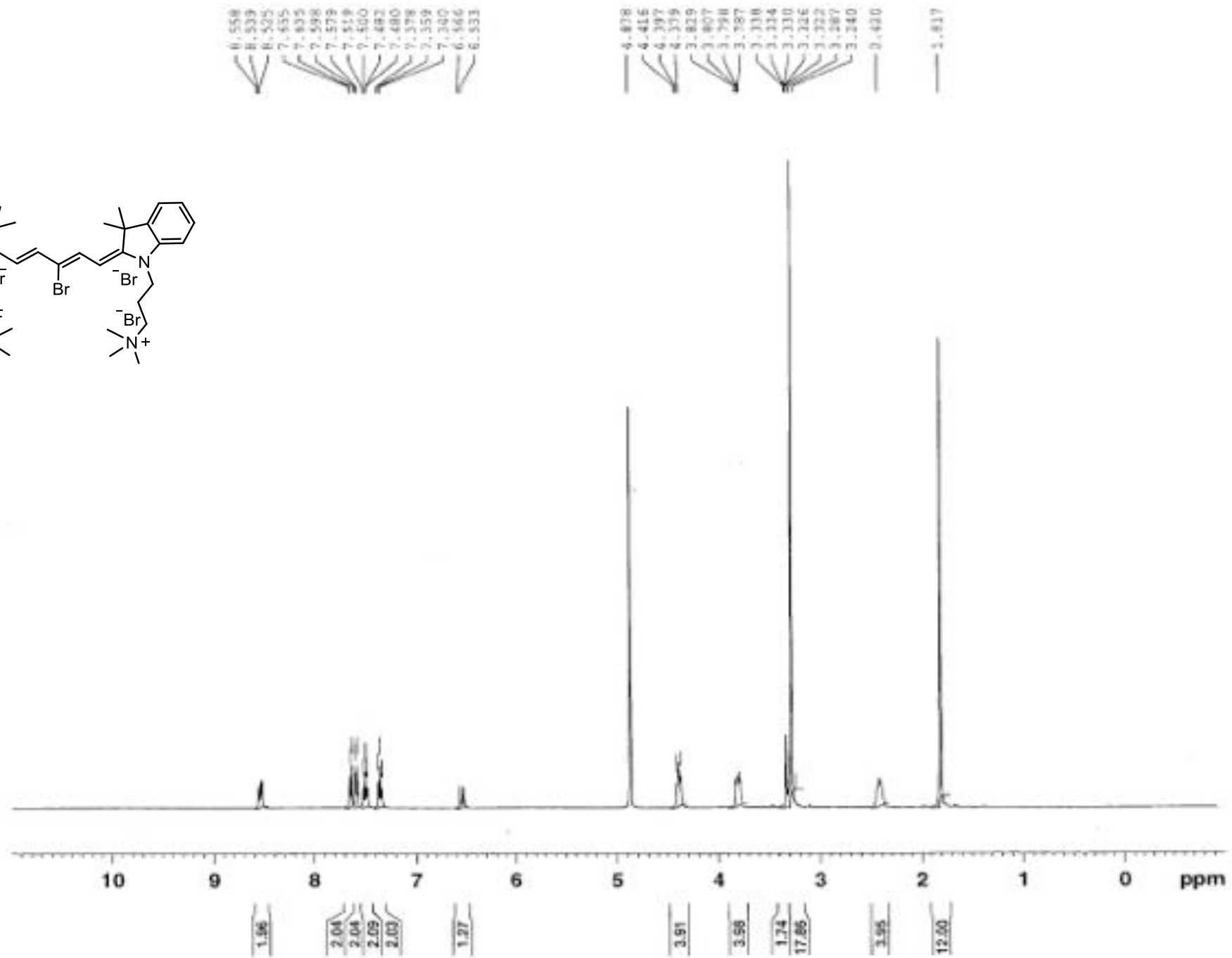
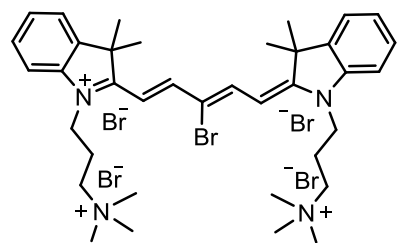
Appendix F

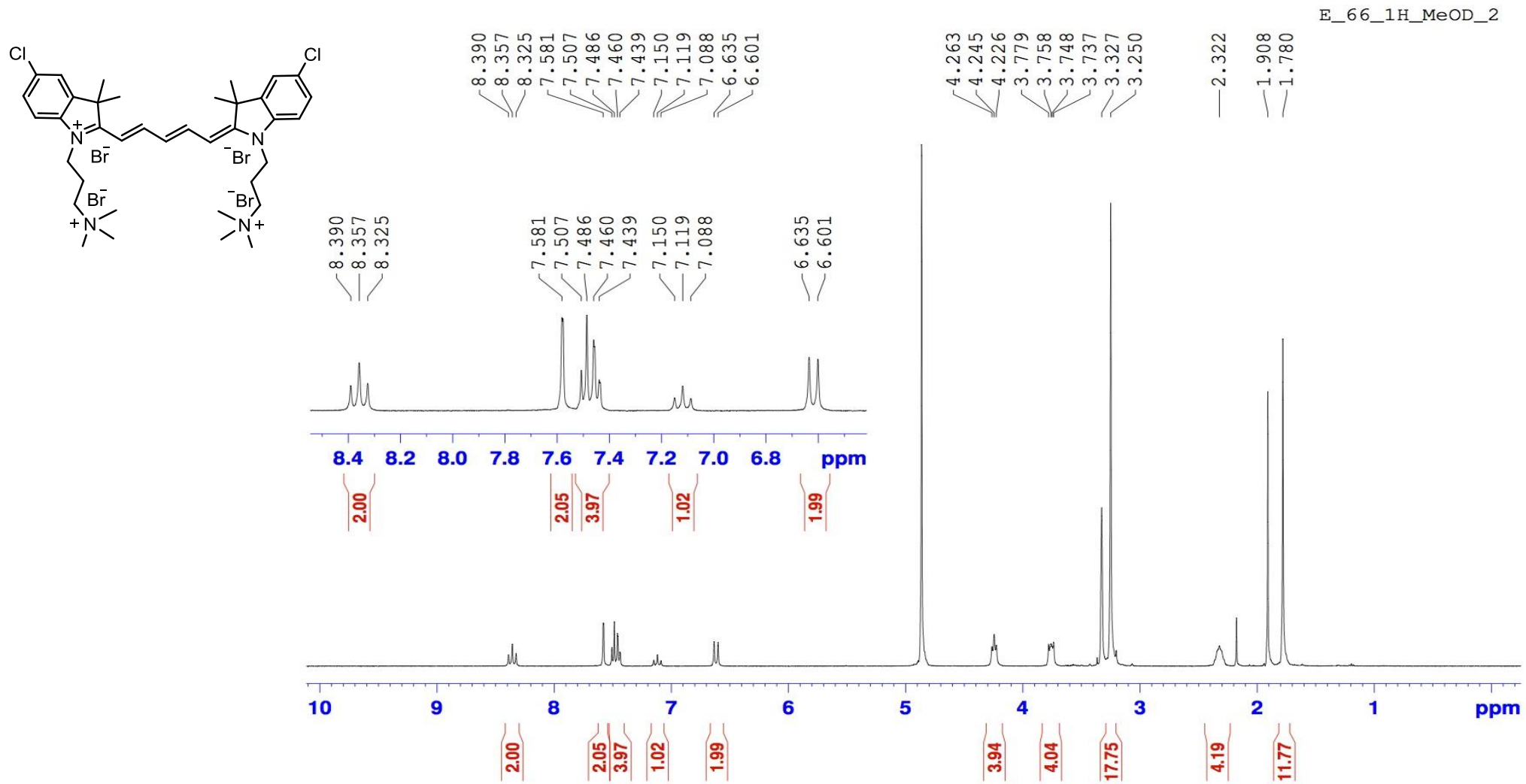
Experimental Data for Chapter 12 – PENTAMETHINE CYANINES WITH HIGH FIDELITY TO QUADRUPLEX DNA

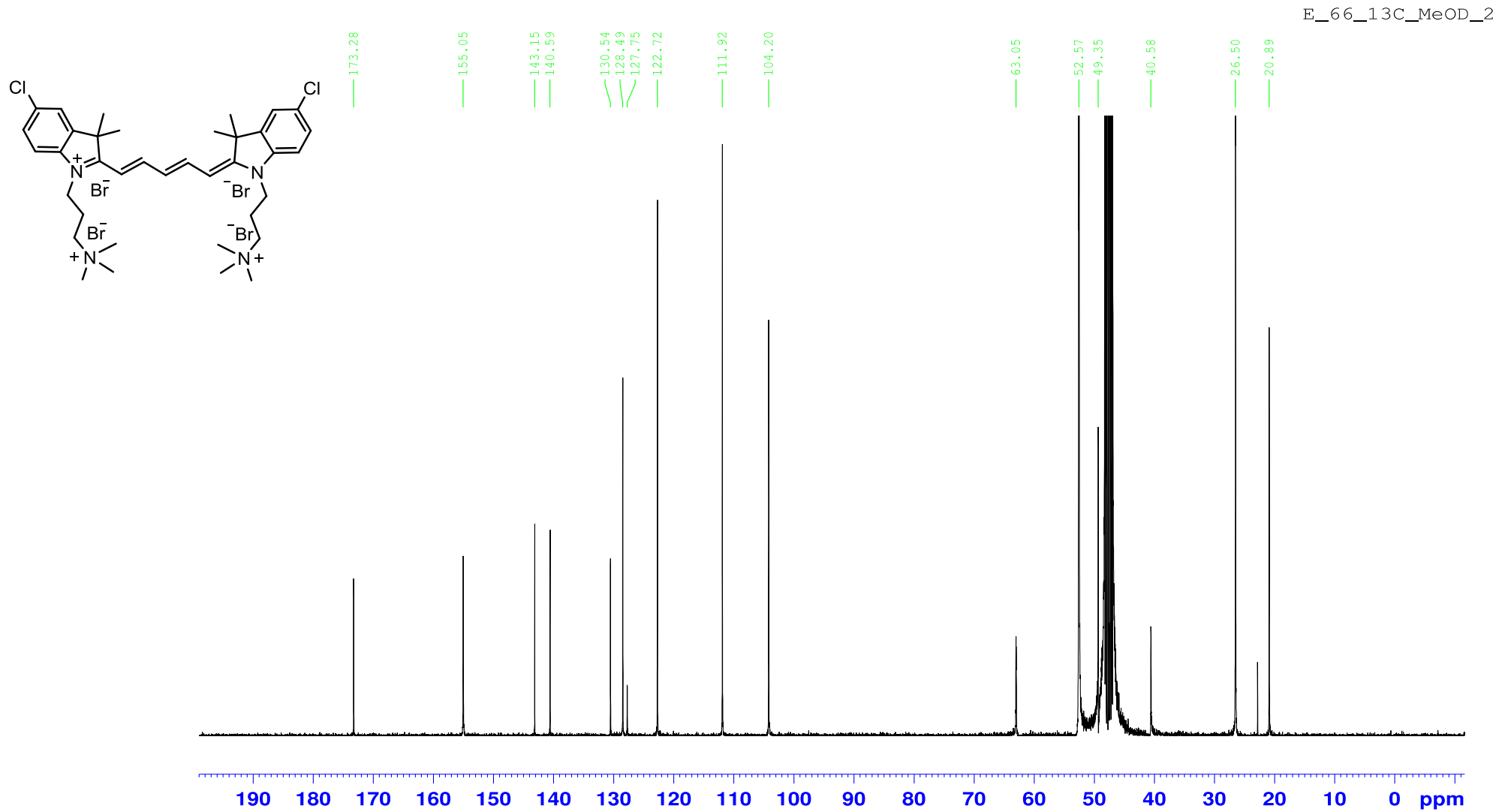


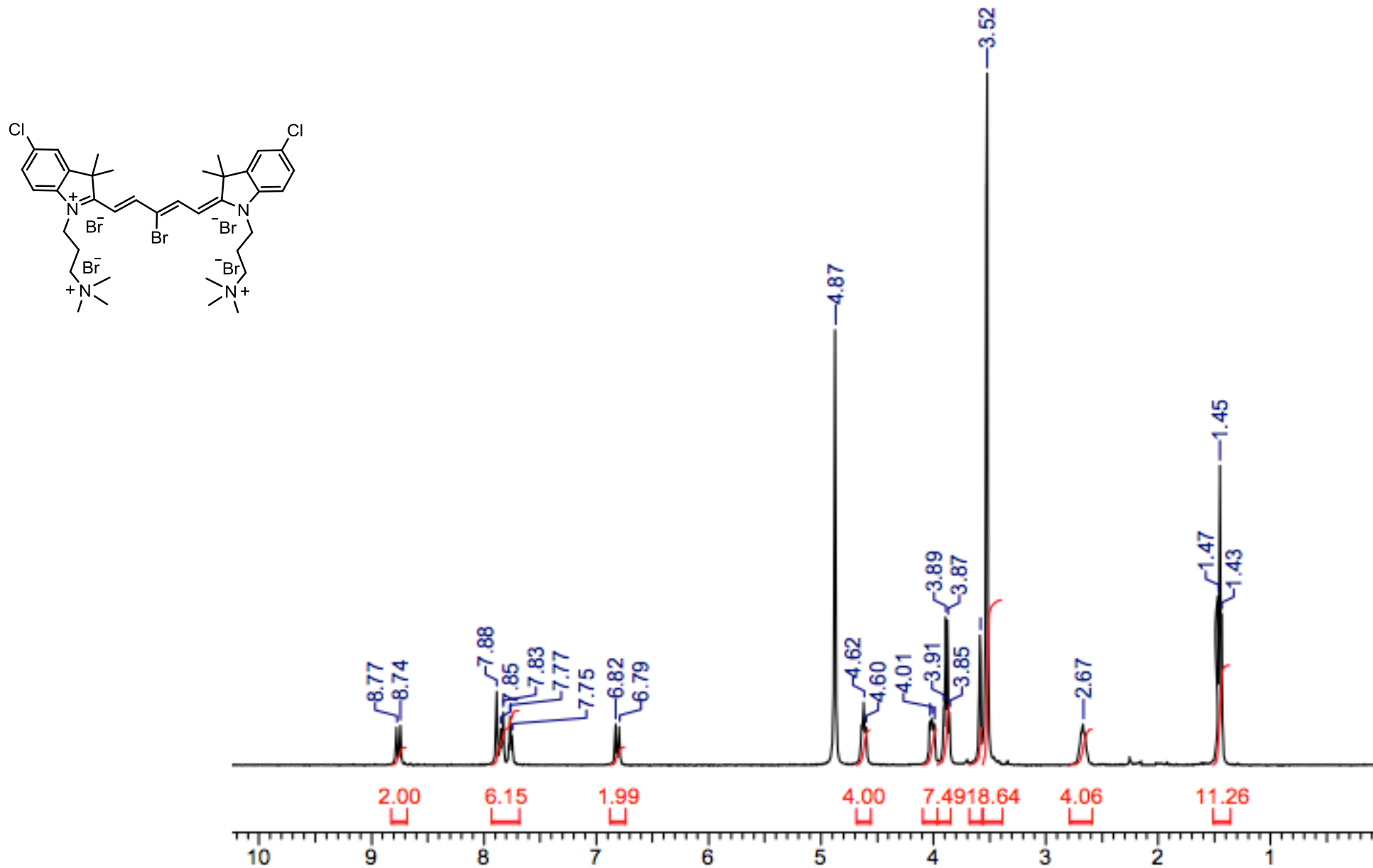


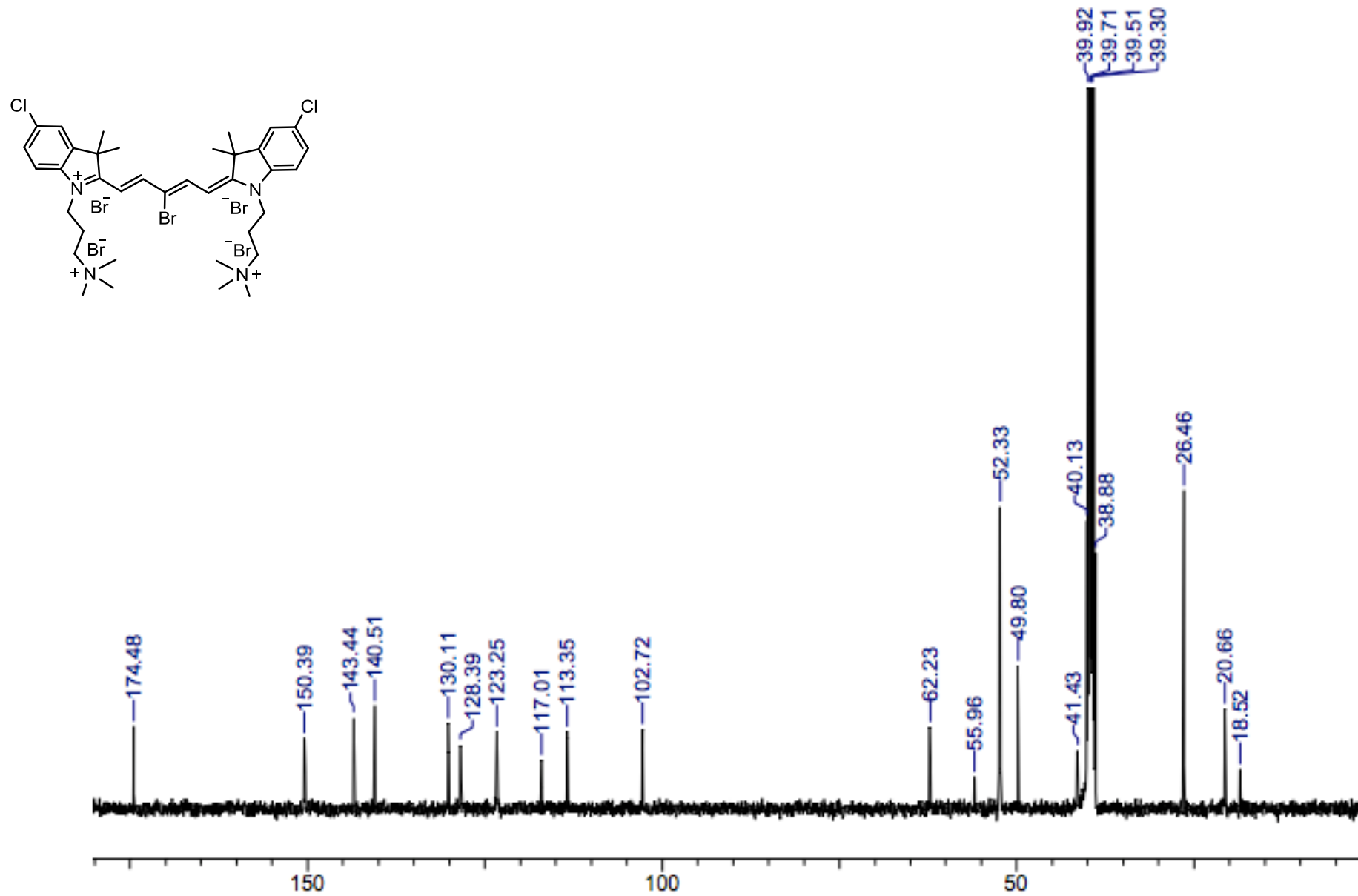


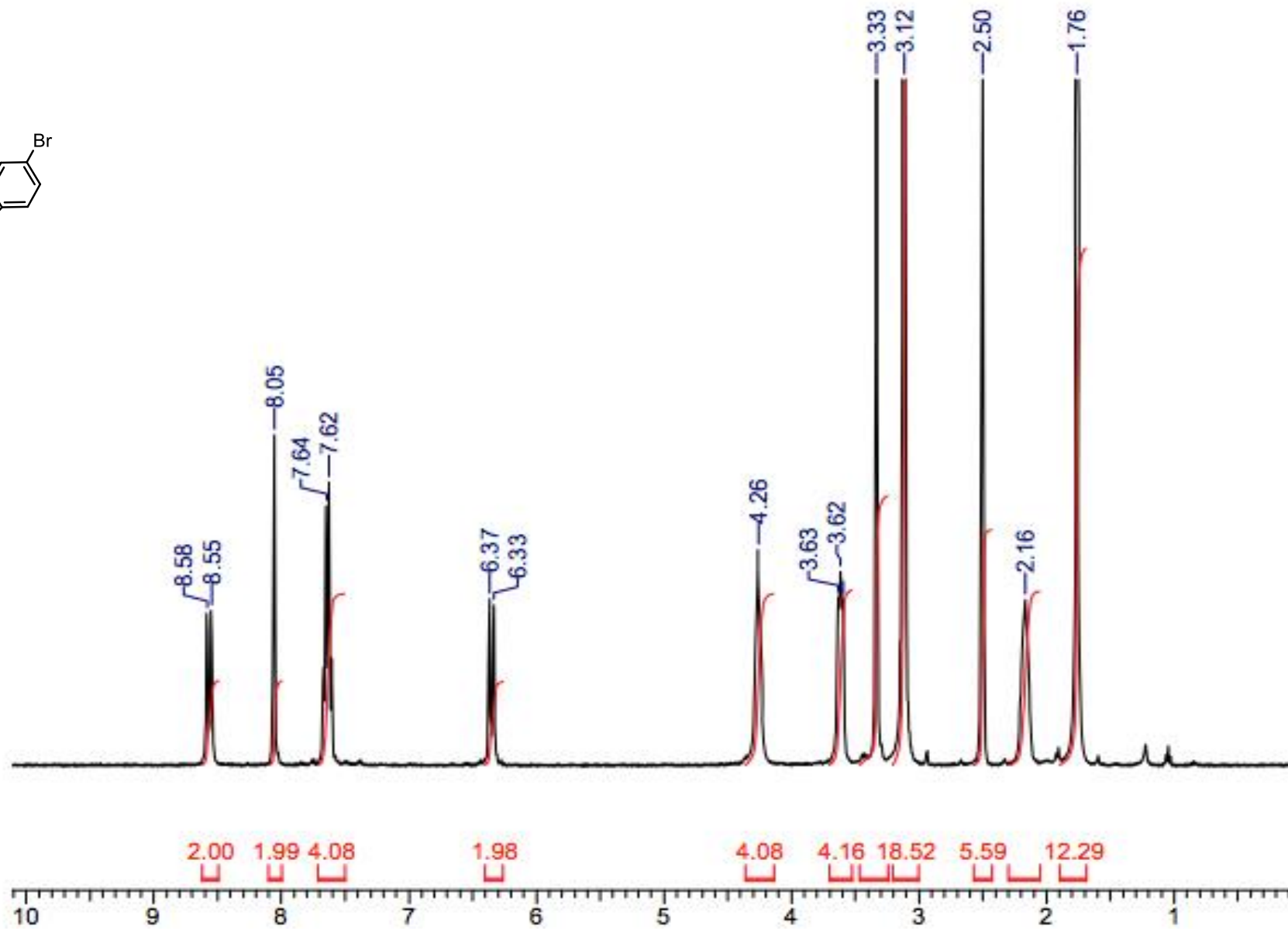
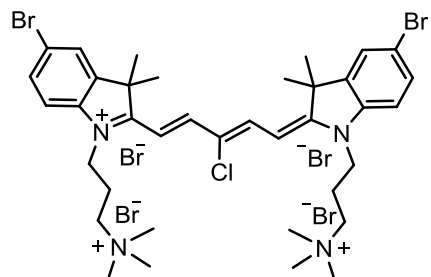


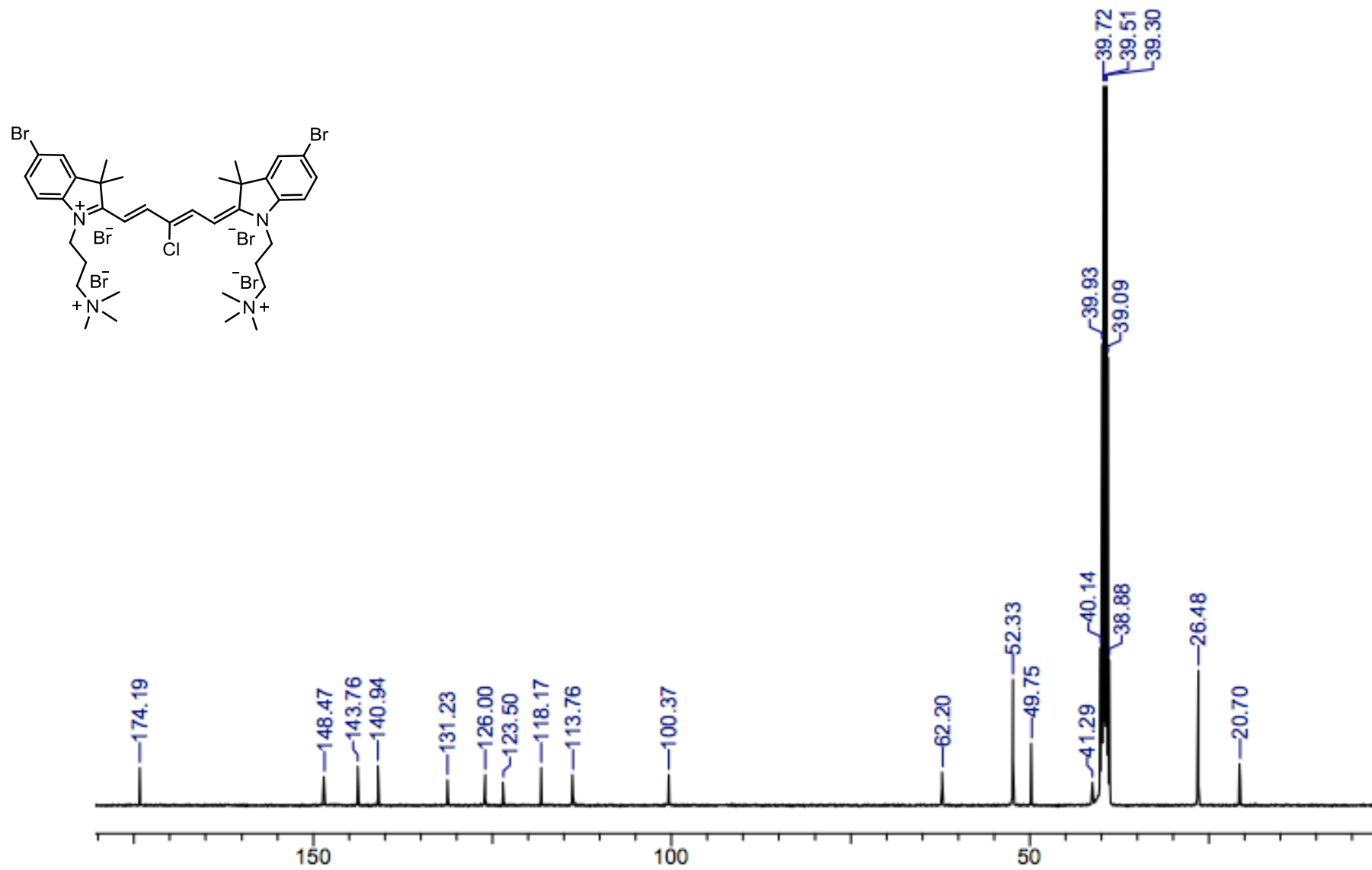


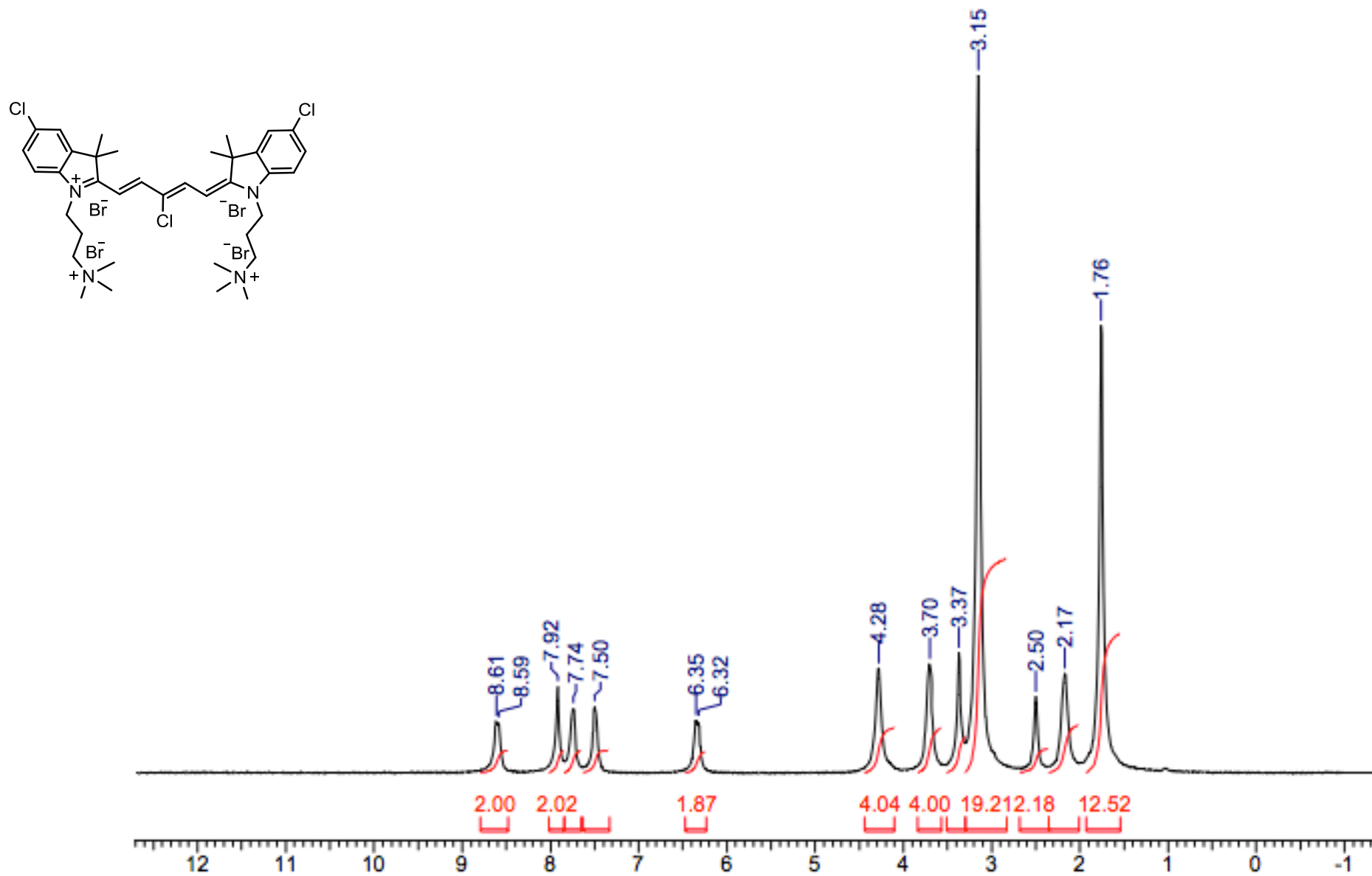


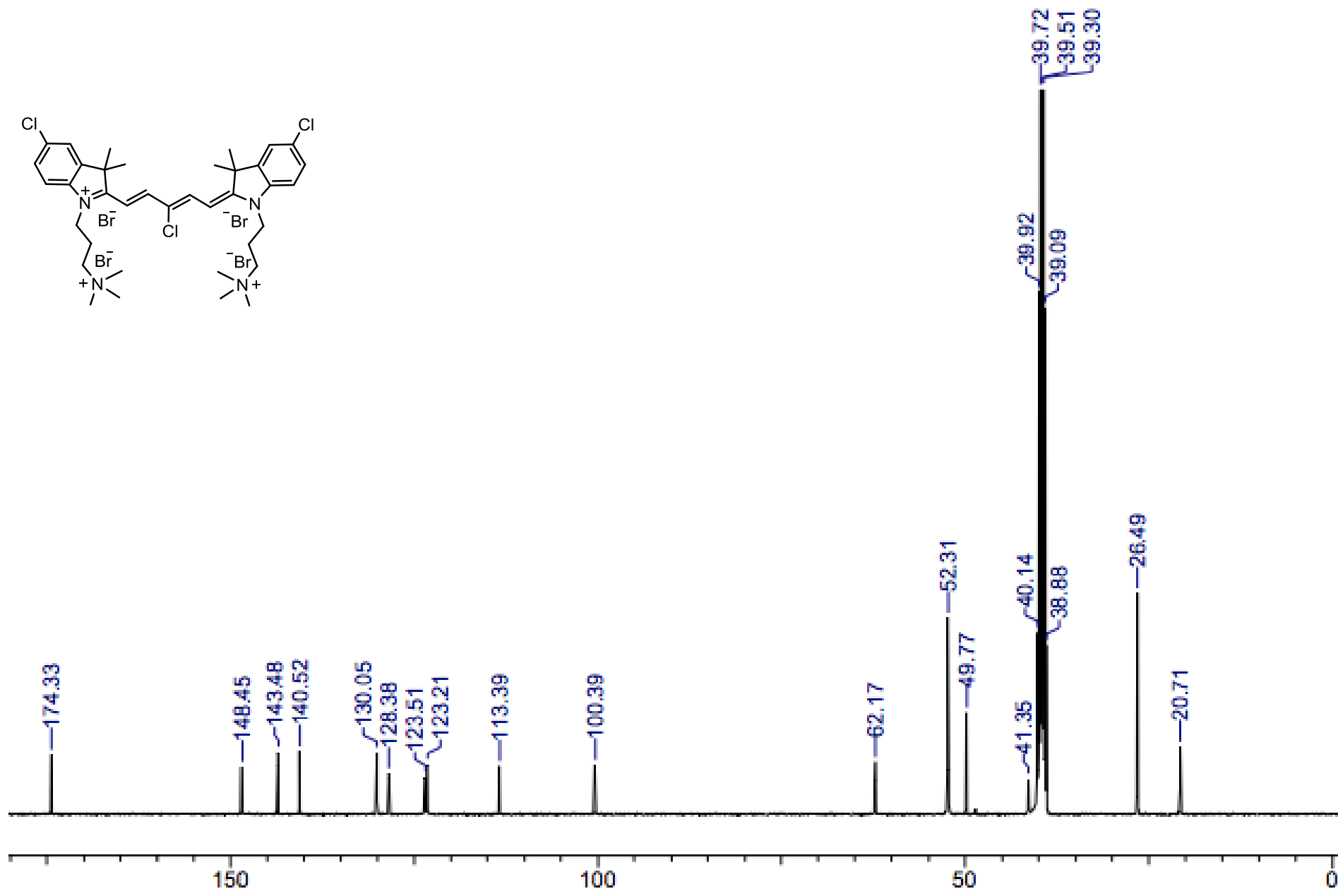


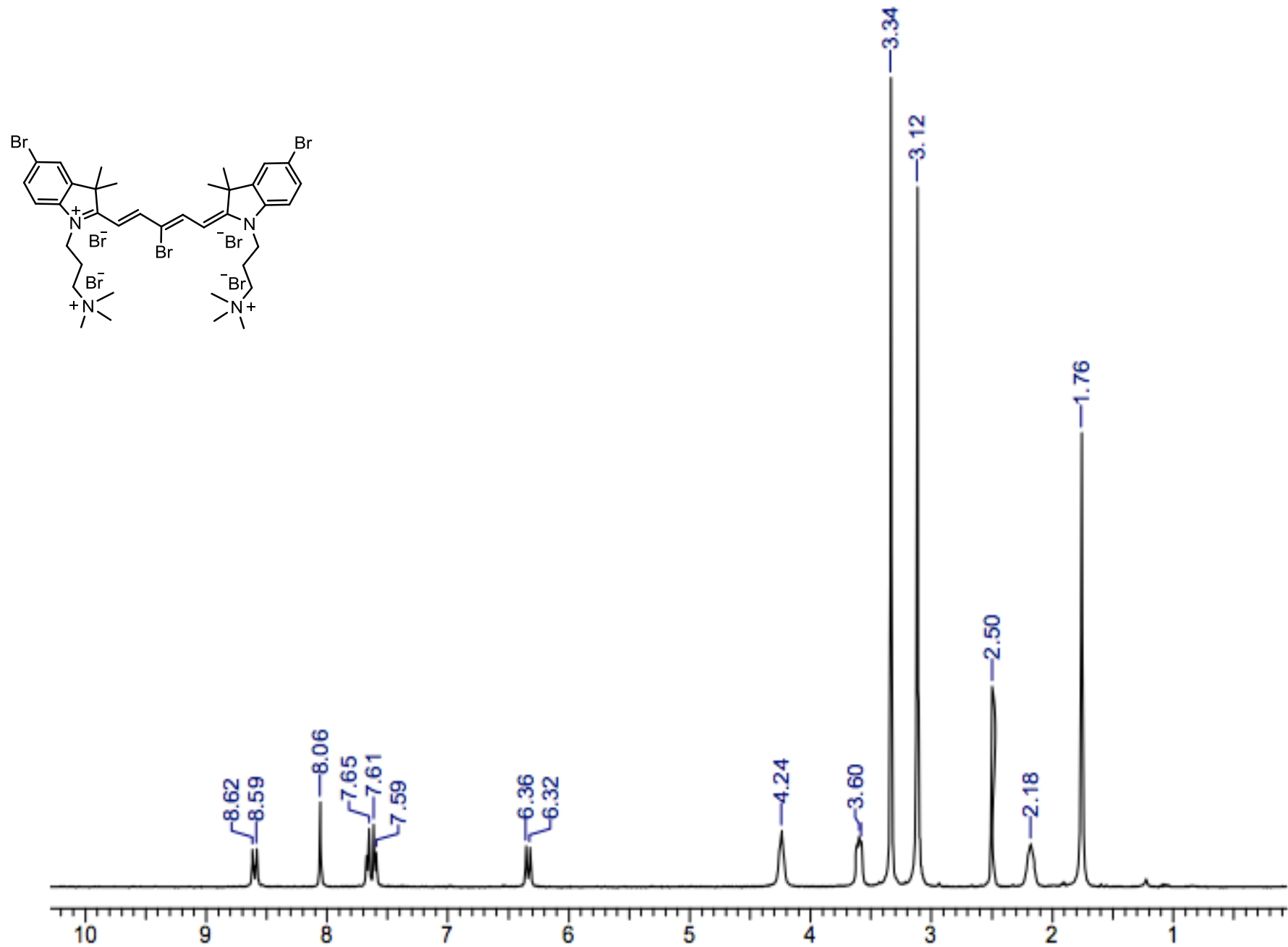


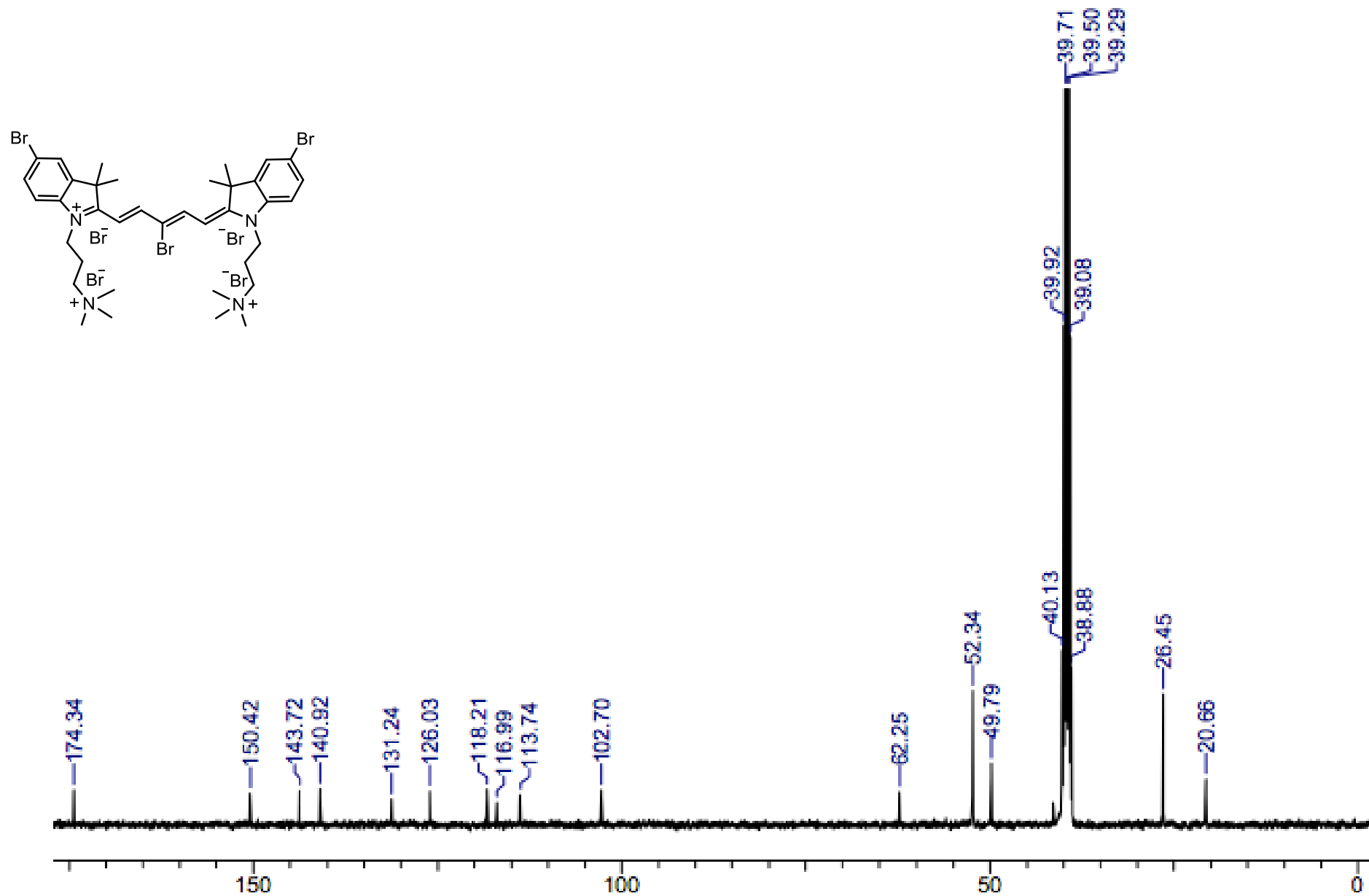




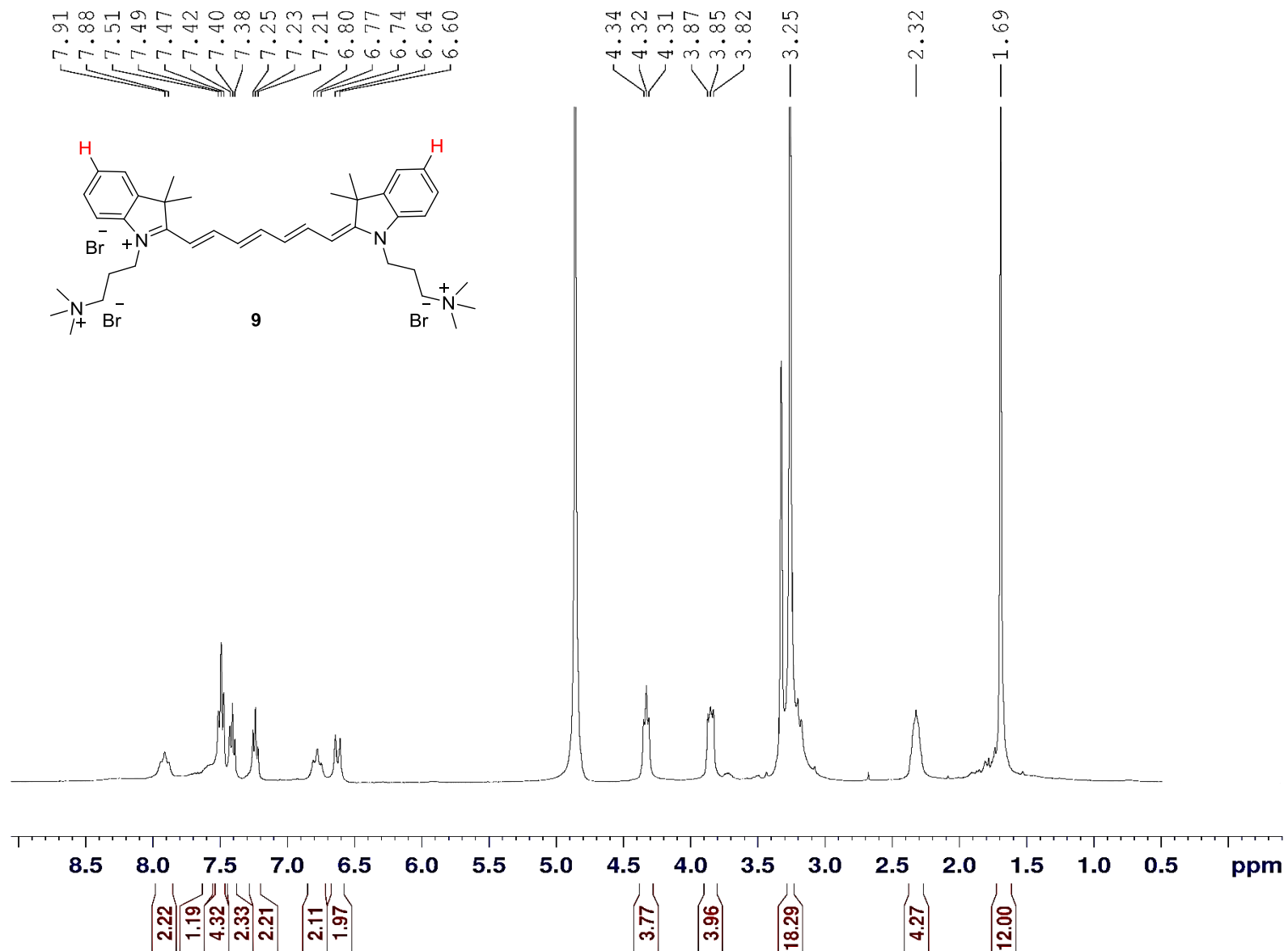


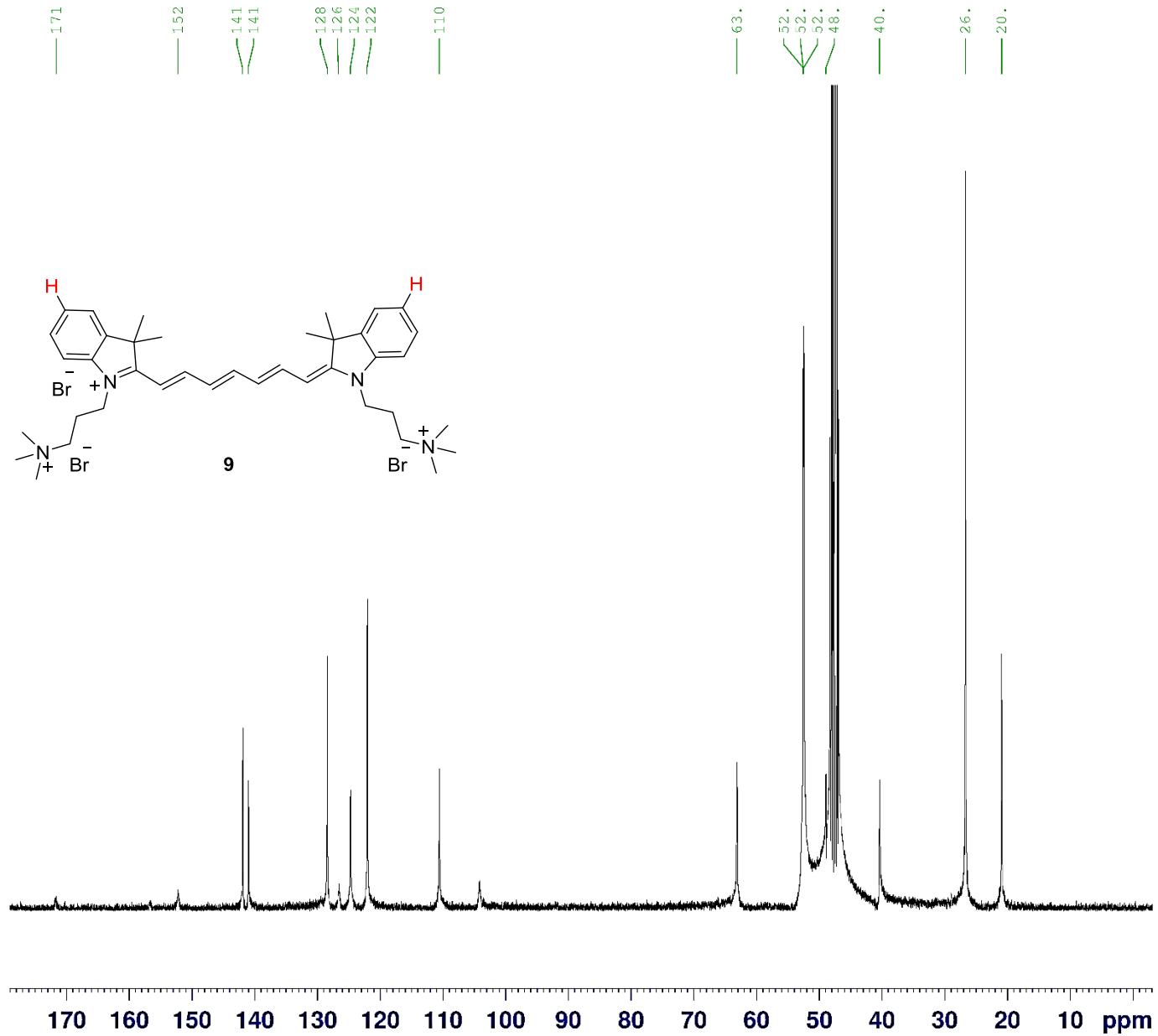


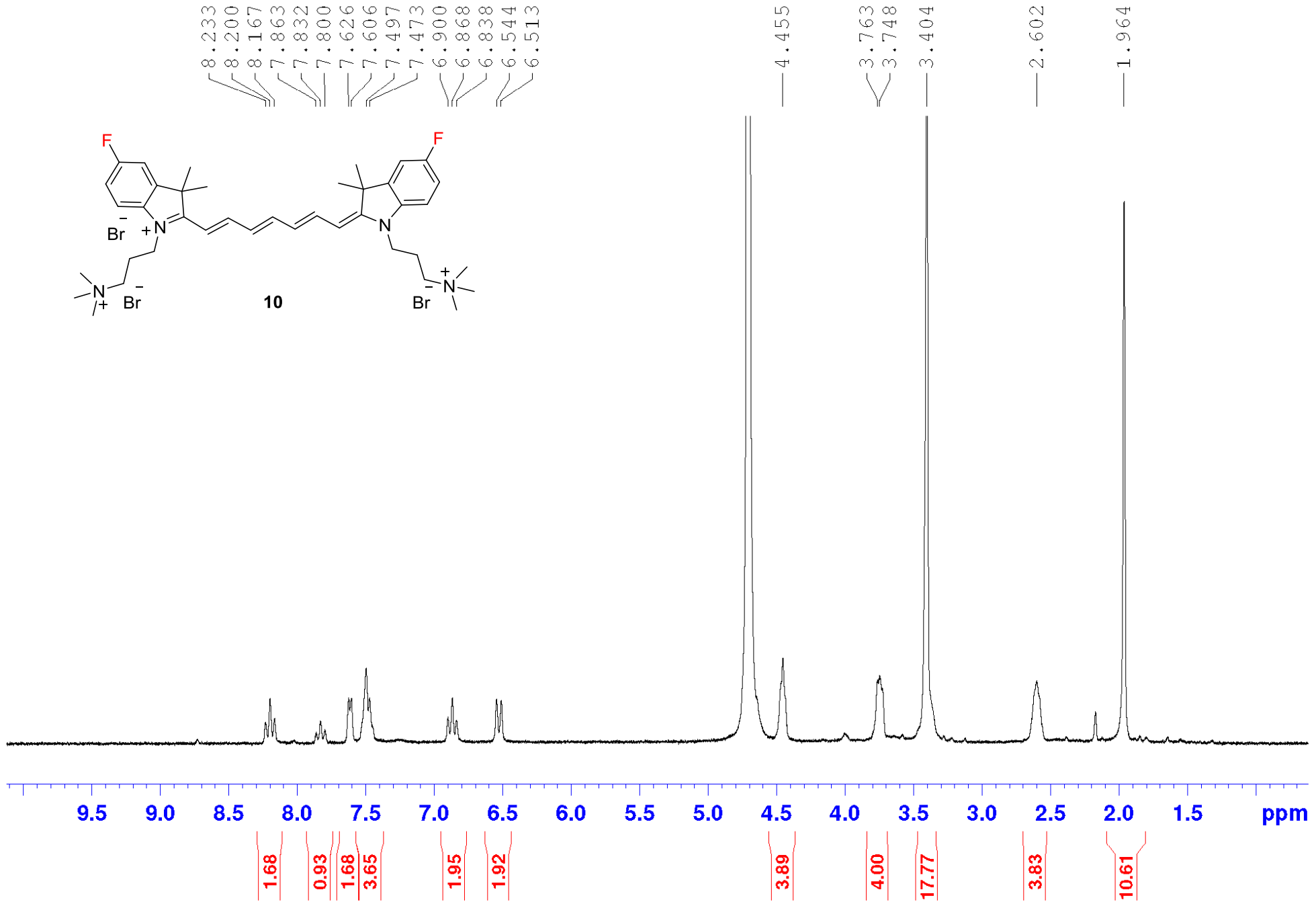


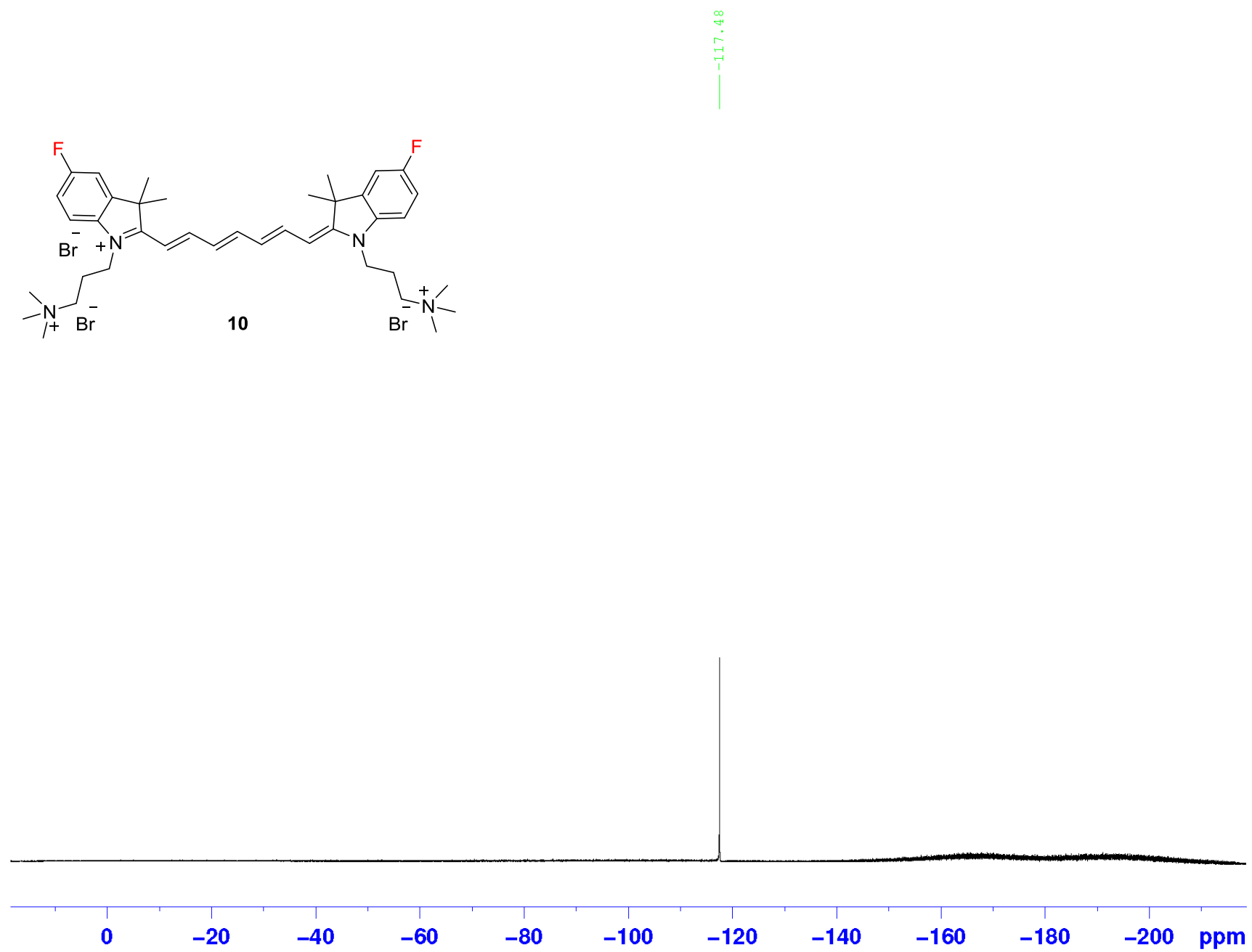
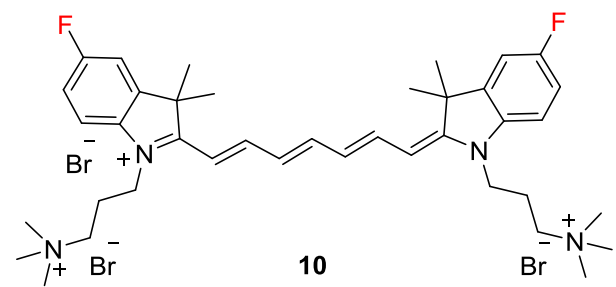


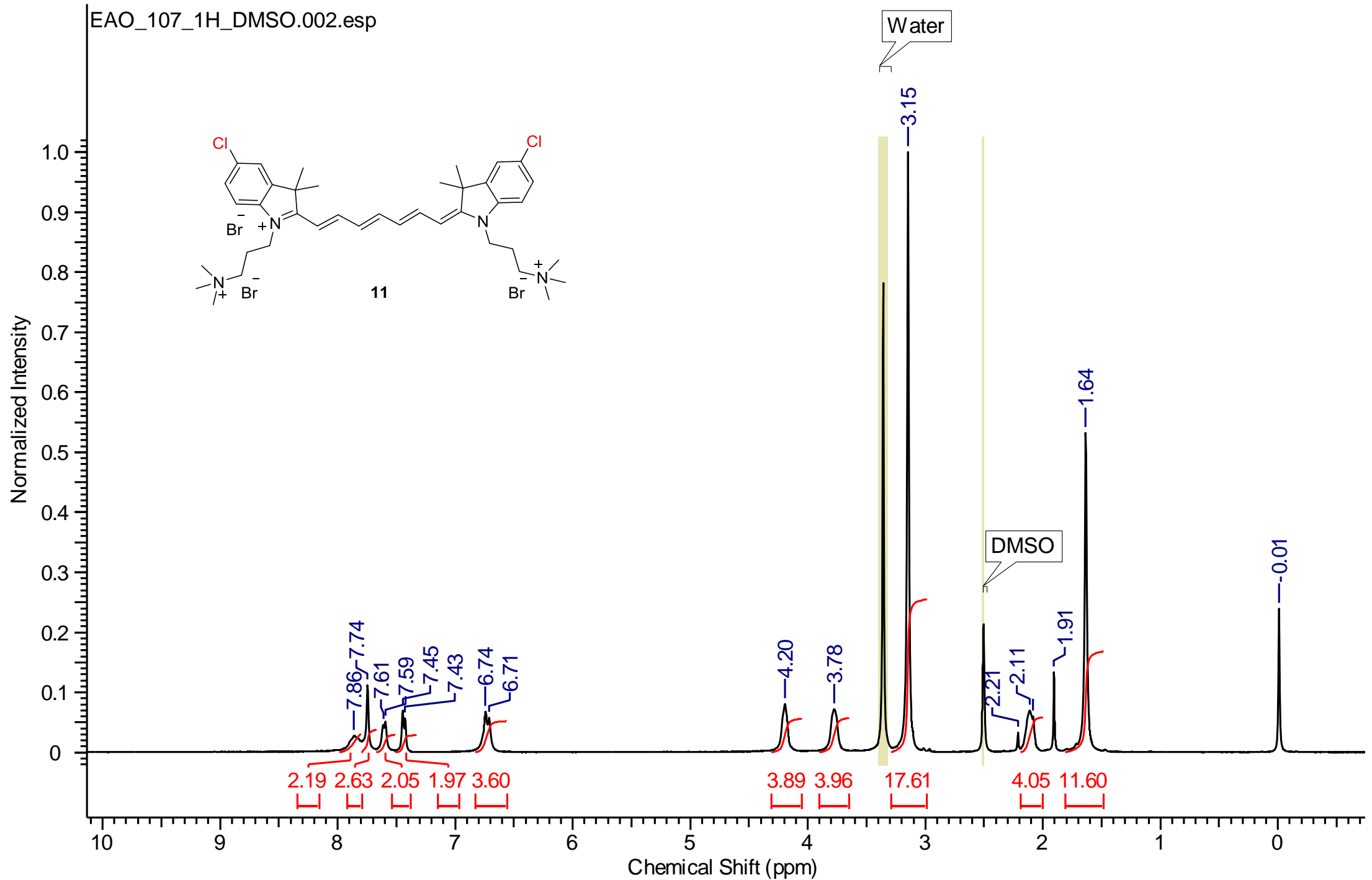
Experimental Data for Chapter 13 – RIGIDITY IN HEPTAMETHINE CYANINES IMPROVES QUADRUPLEX BINDING

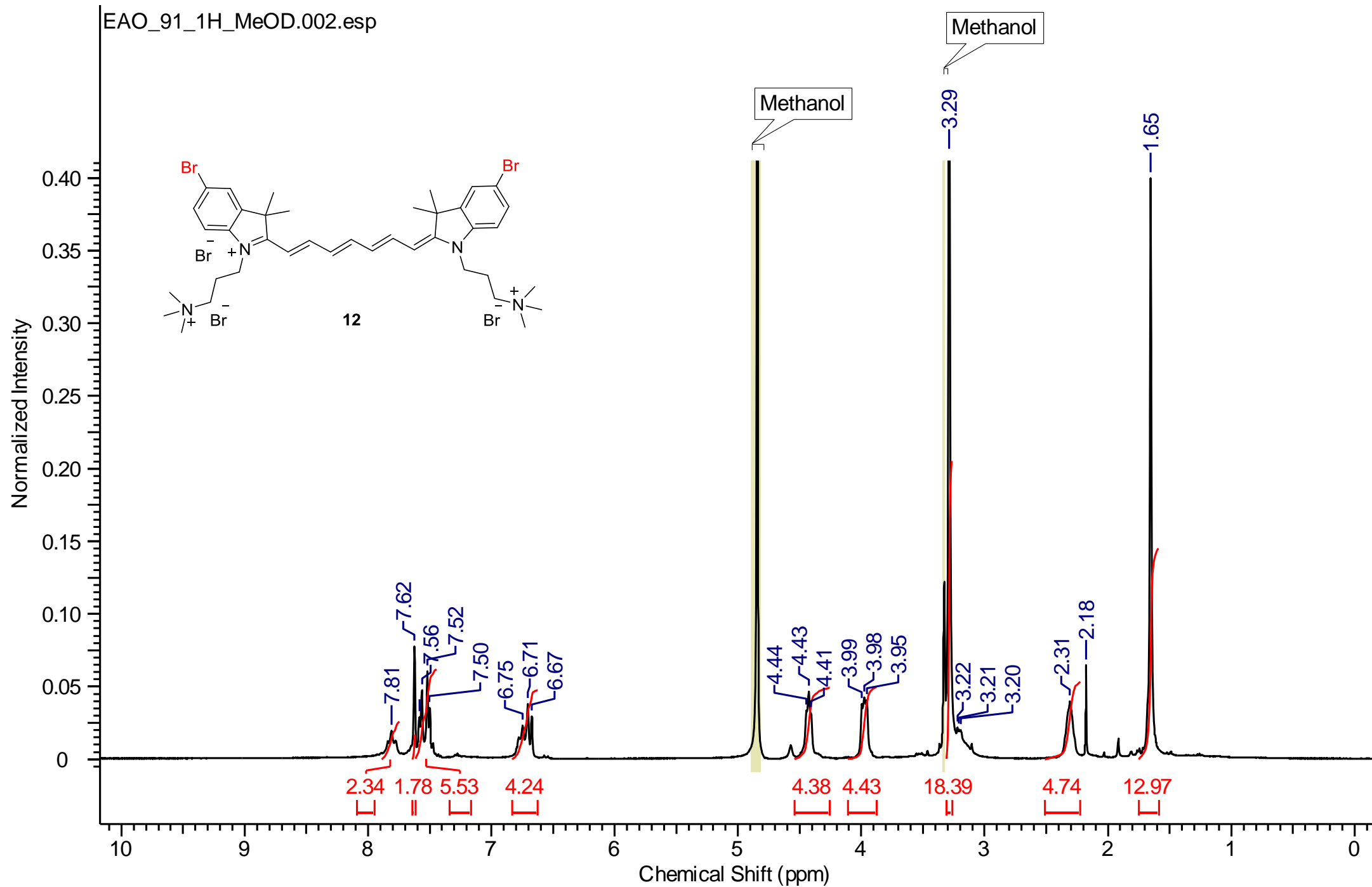


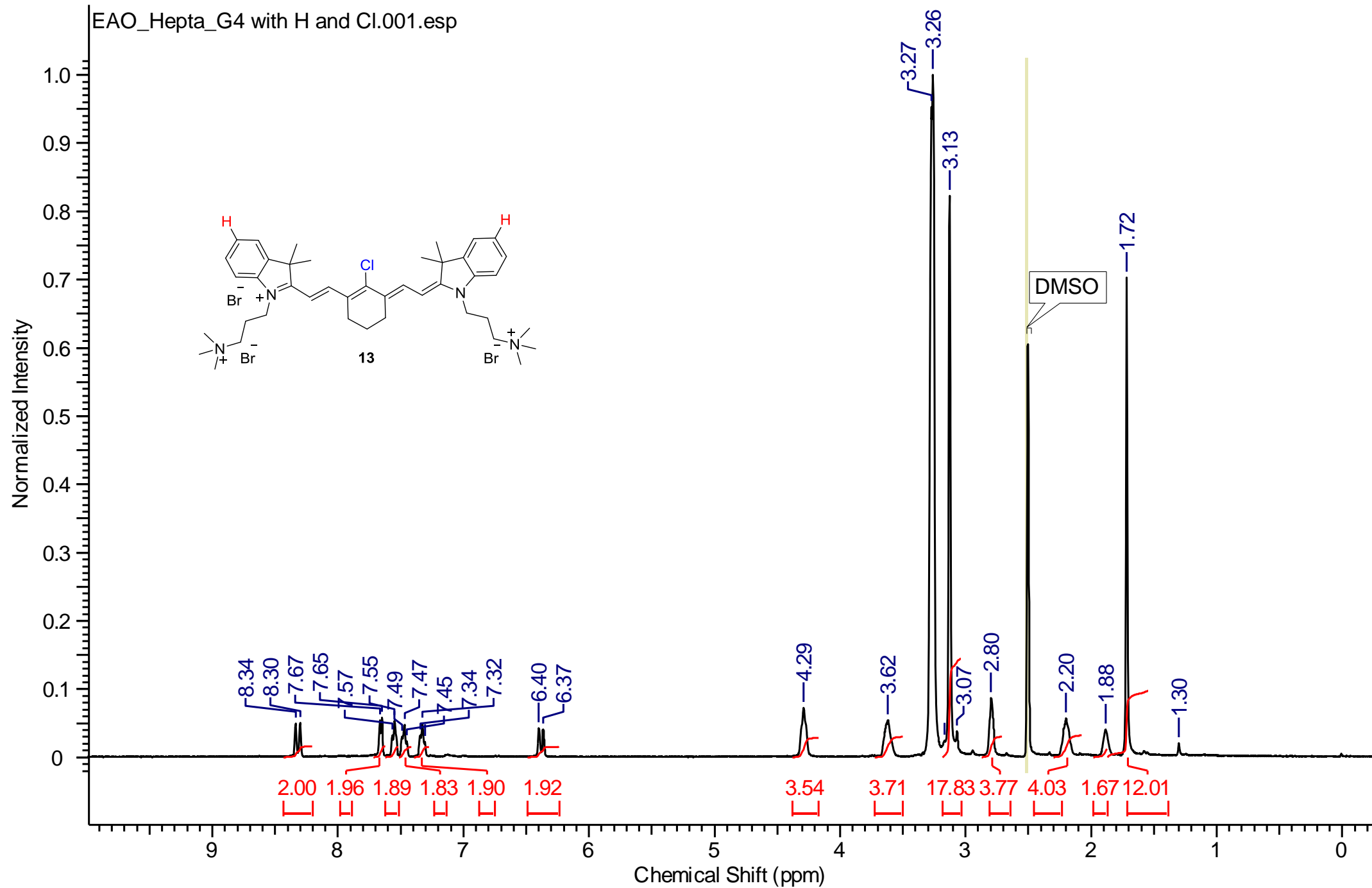




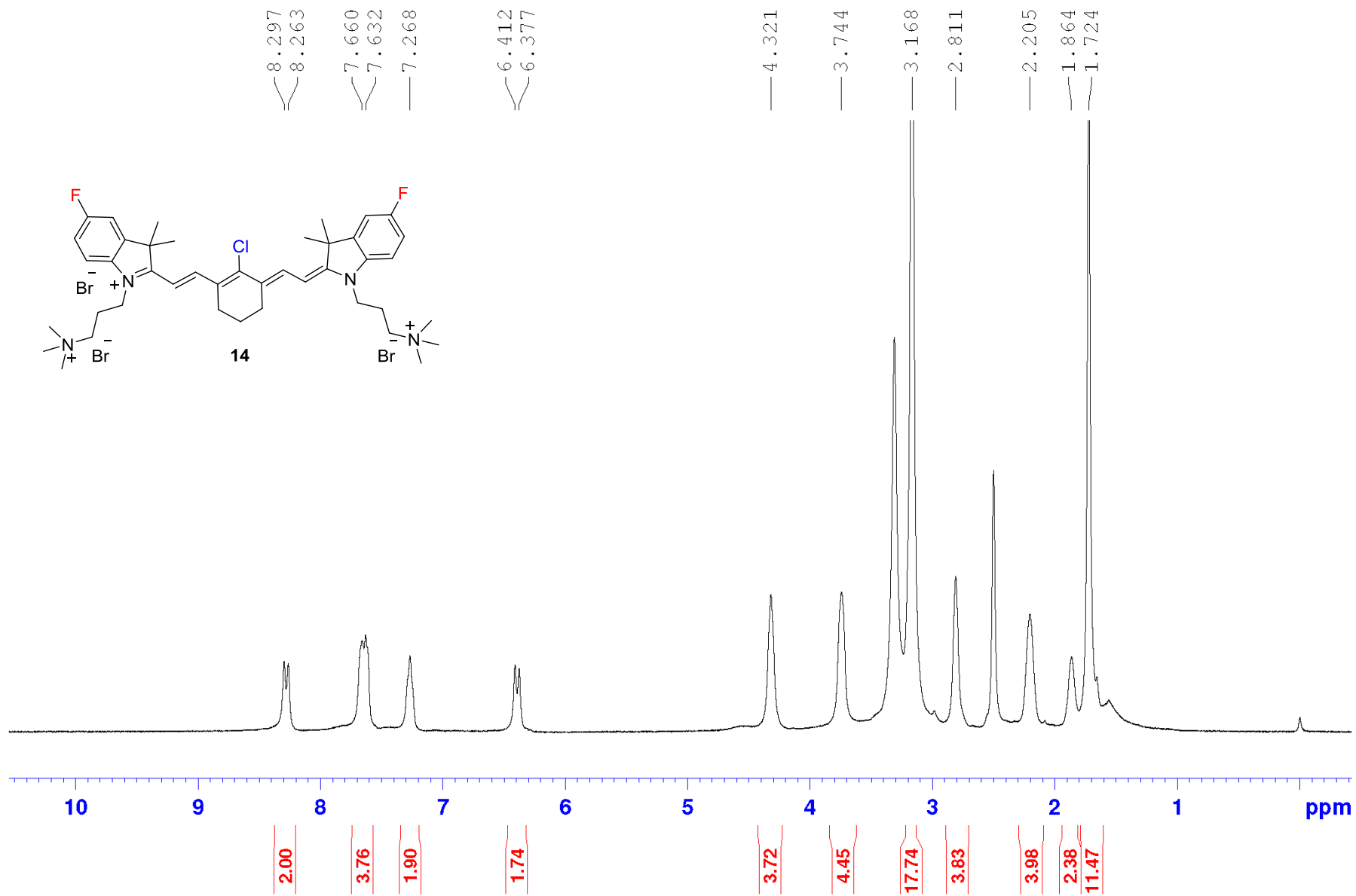


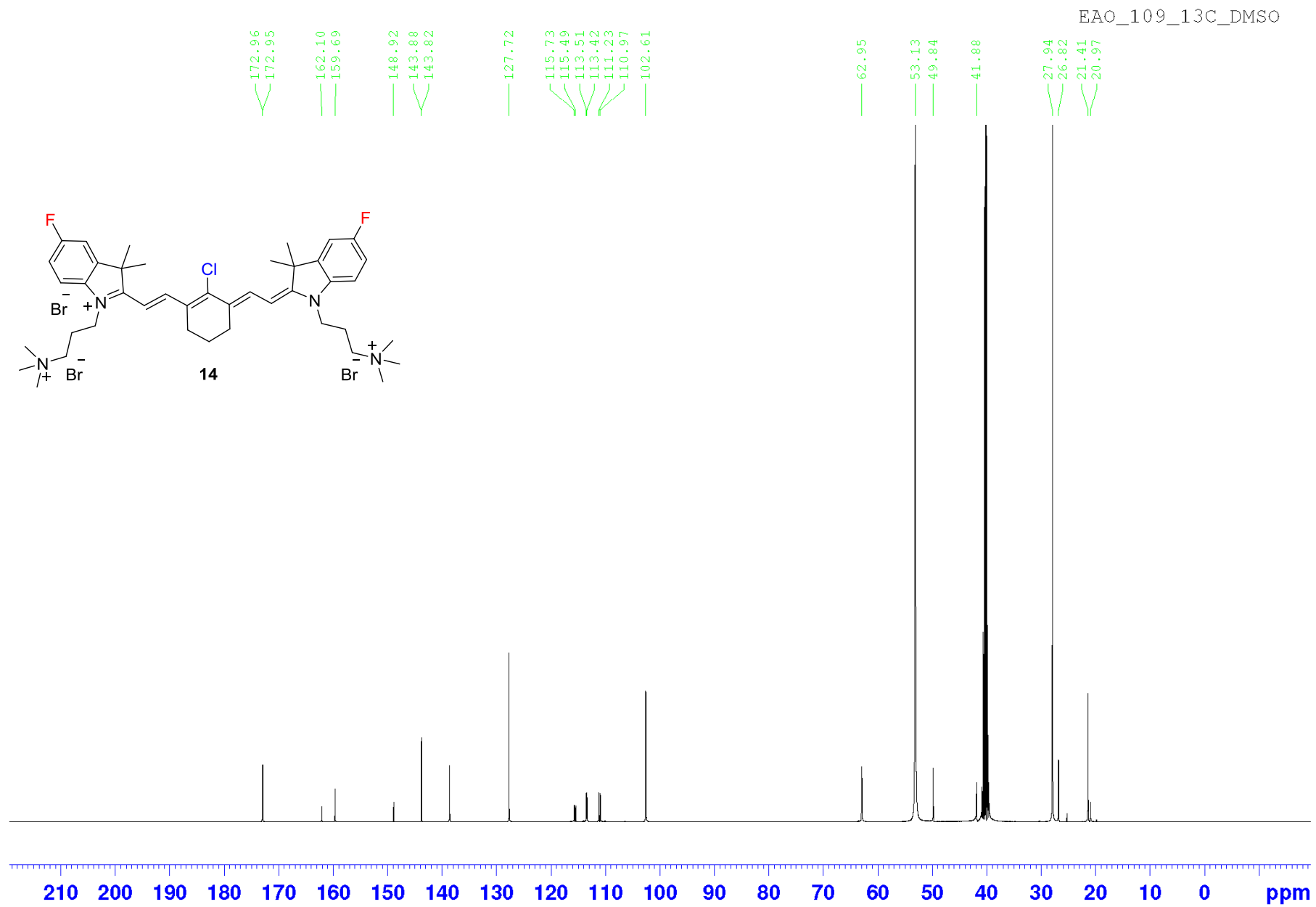




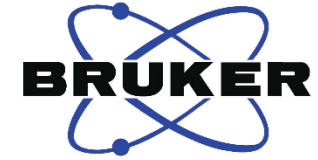
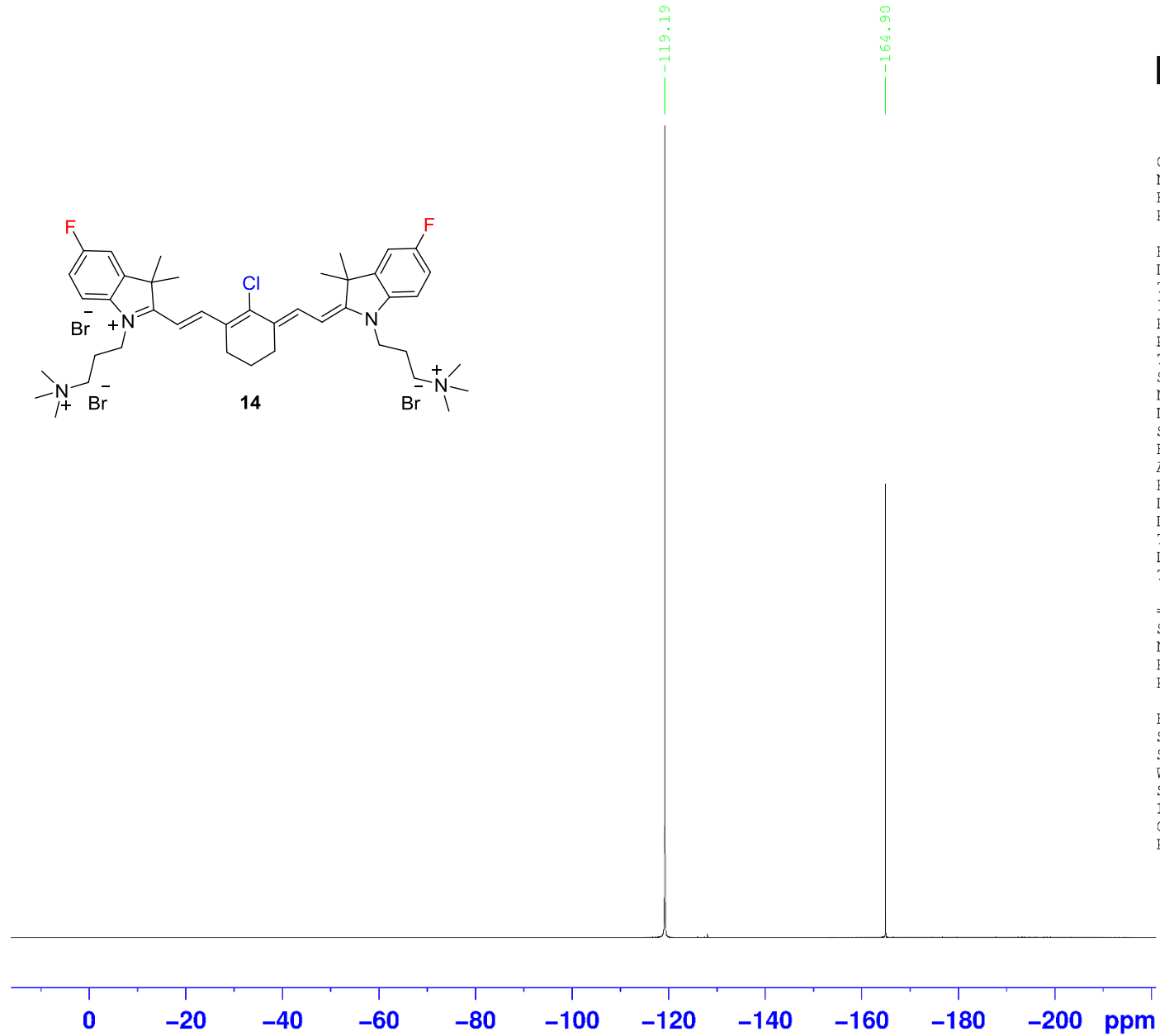
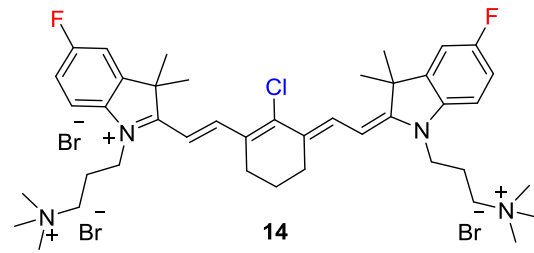


EAO_109_1H_DMSO





F19

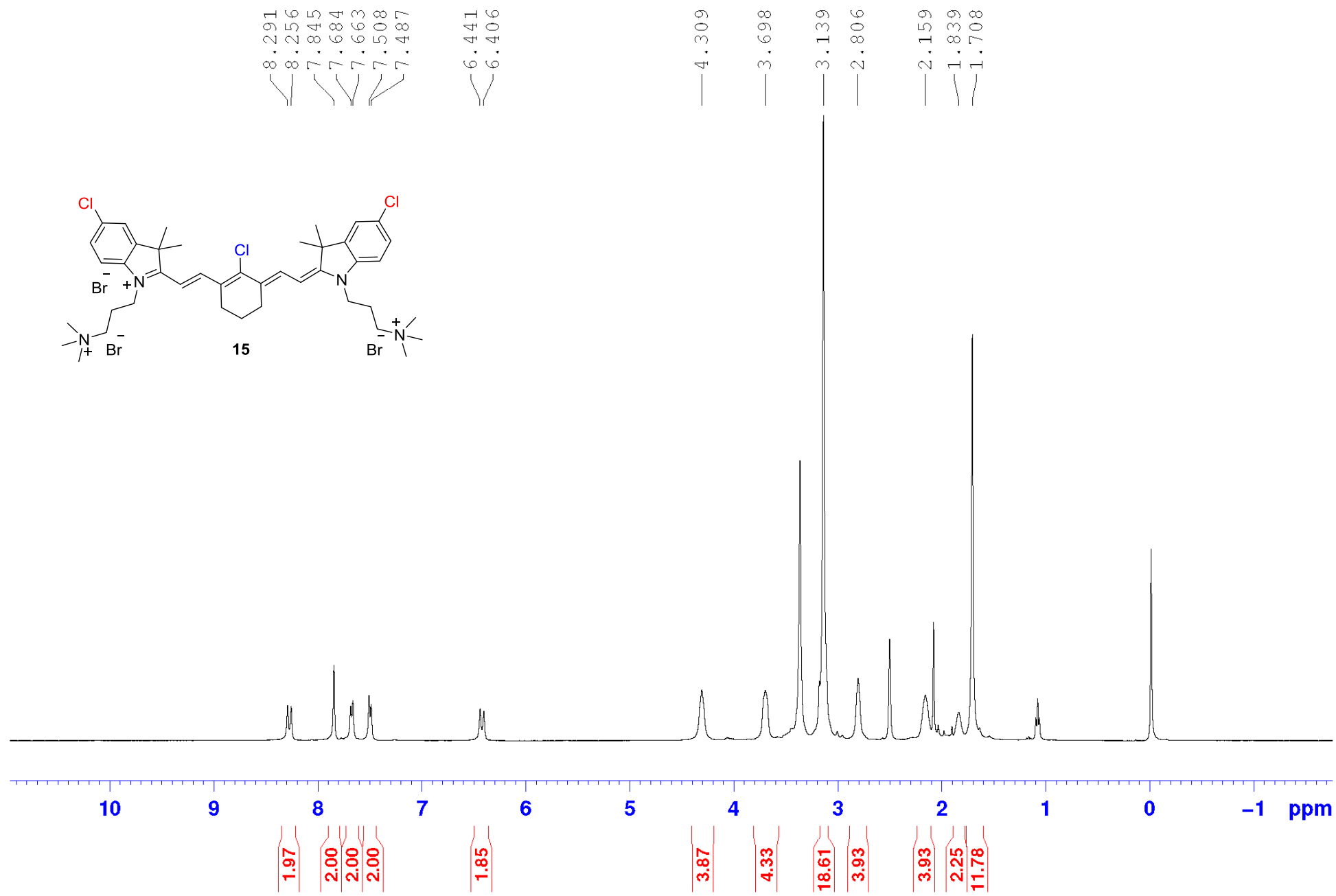


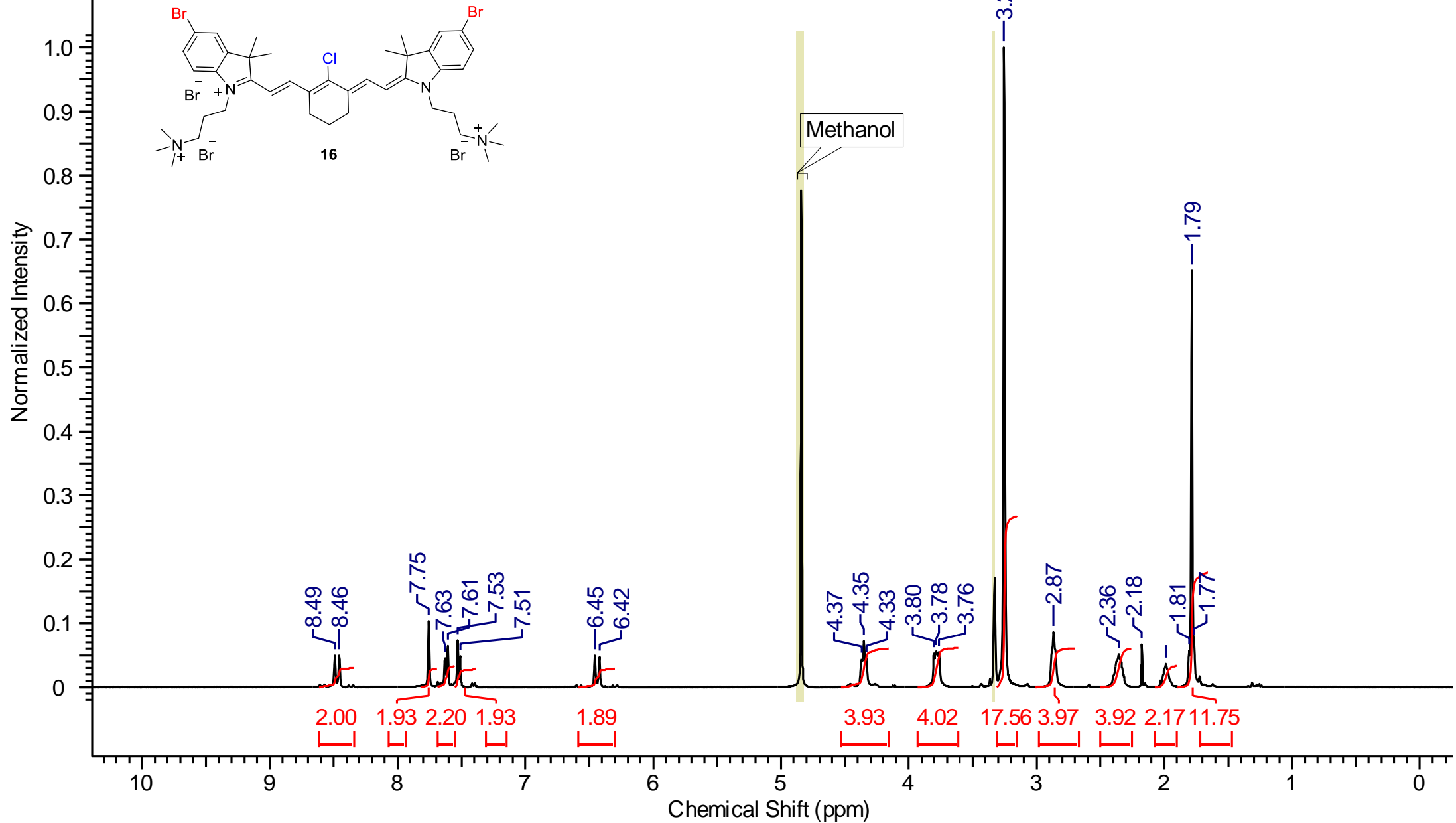
Current Data Parameters
 NAME EAO_109_19F_DMSO
 EXPNO 1
 PROCNO 1

F2 - Acquisition Parameters
 Date_ 20140610
 Time 14.14
 INSTRUM spect
 PROBHD 5 mm PABBO BB-
 PULPROG zgflqn
 TD 131072
 SOLVENT DMSO
 NS 16
 DS 4
 SWH 89285.711 Hz
 FIDRES 0.681196 Hz
 AQ 0.7340032 sec
 RG 203
 DW 5.600 usec
 DE 6.50 usec
 TE 298.0 K
 D1 1.00000000 sec
 TD0 1

===== CHANNEL f1 =====
 SFO1 376.4701248 MHz
 NUC1 19F
 P1 14.00 usec
 PLW1 20.00000000 W

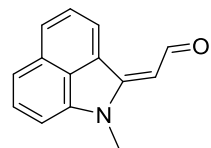
F2 - Processing parameters
 SI 65536
 SF 376.5086668 MHz
 WDW EM
 SSB 0
 LB 0.30 Hz
 GB 0
 PC 1.00



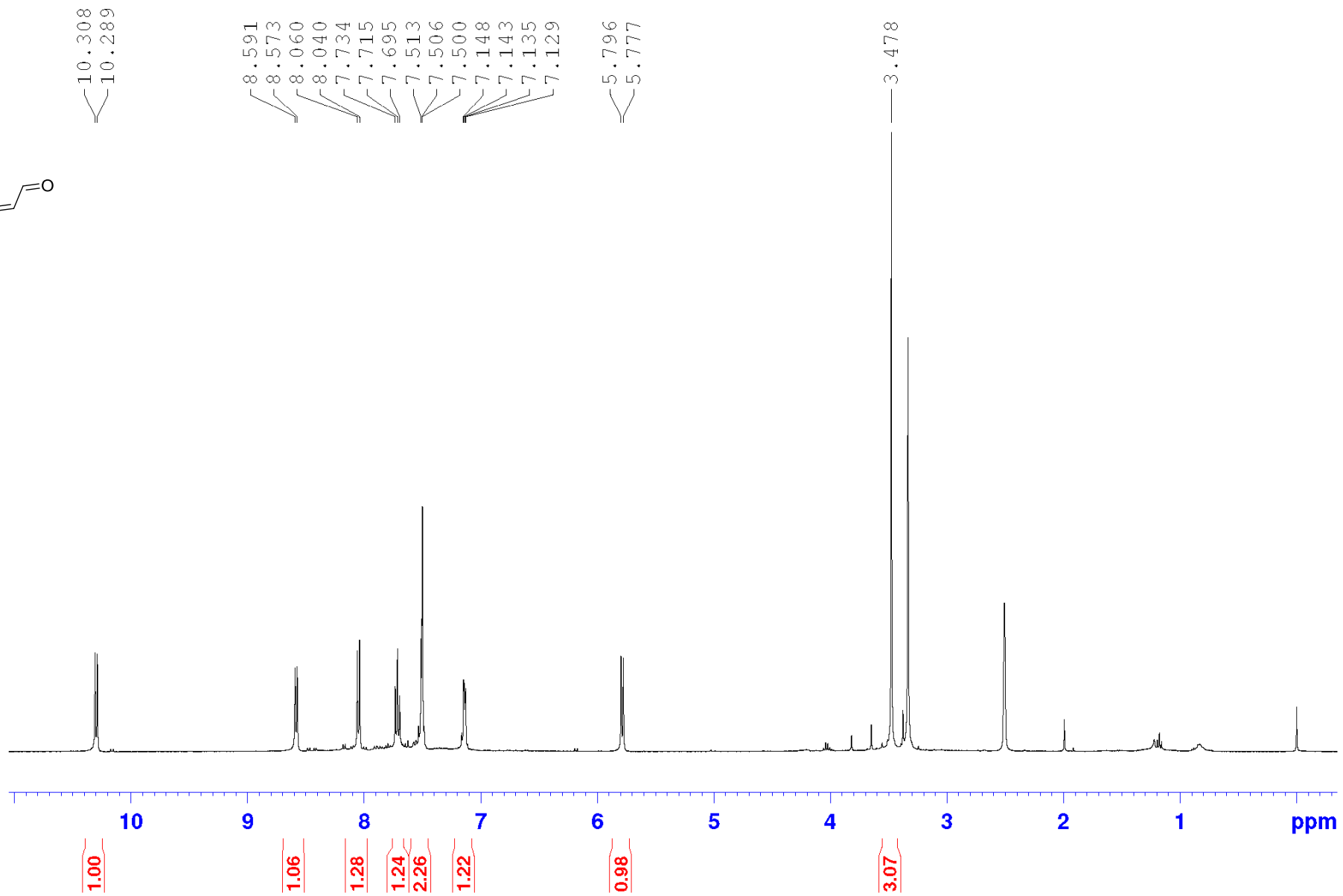


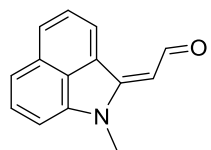
Appendix H

Experimental Data for Chapter 14 – SECOND GENERATION TRIMETHINE CYANINES

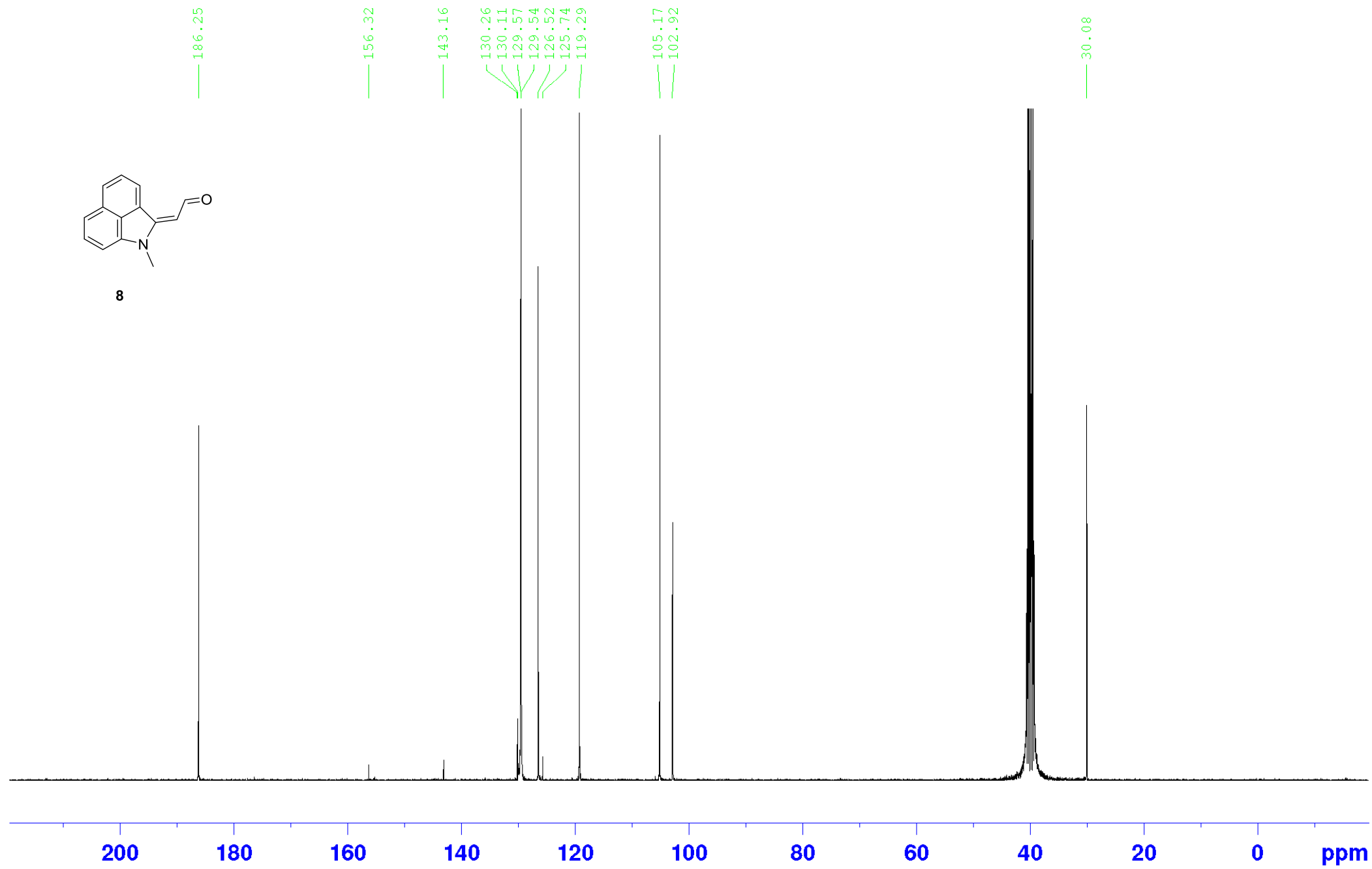


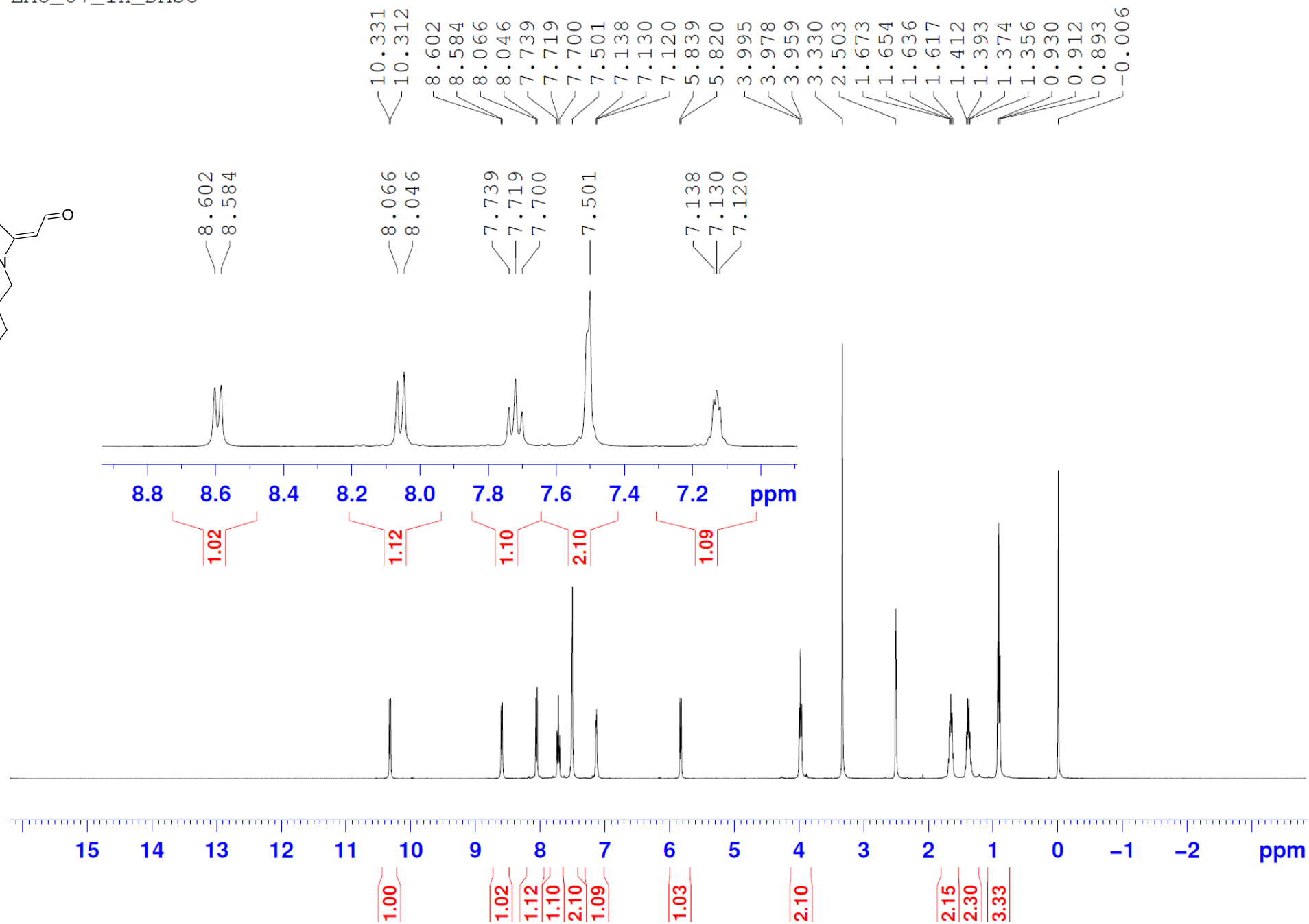
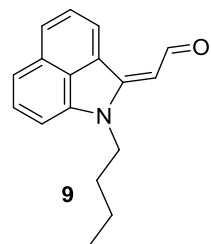
8

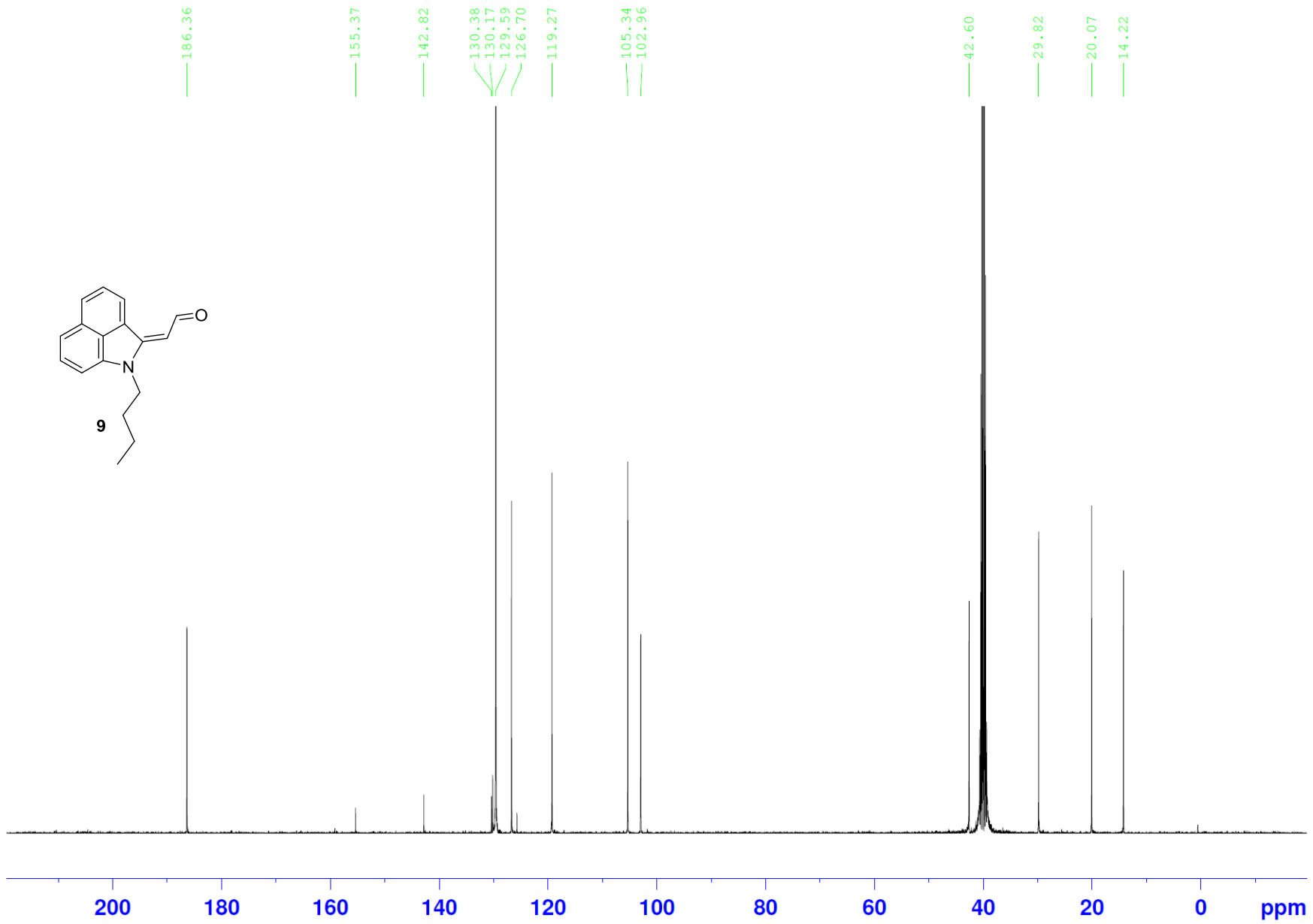


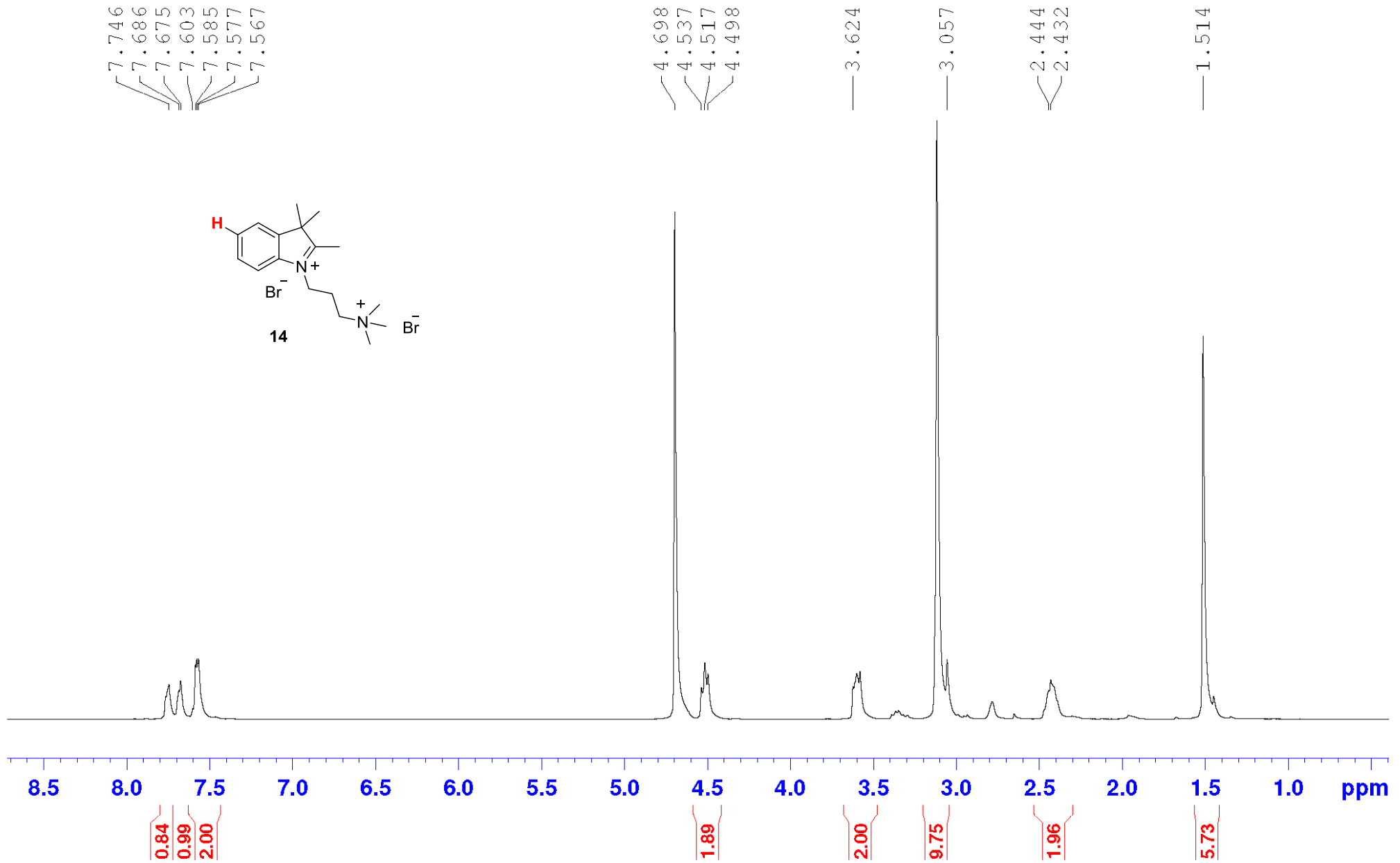


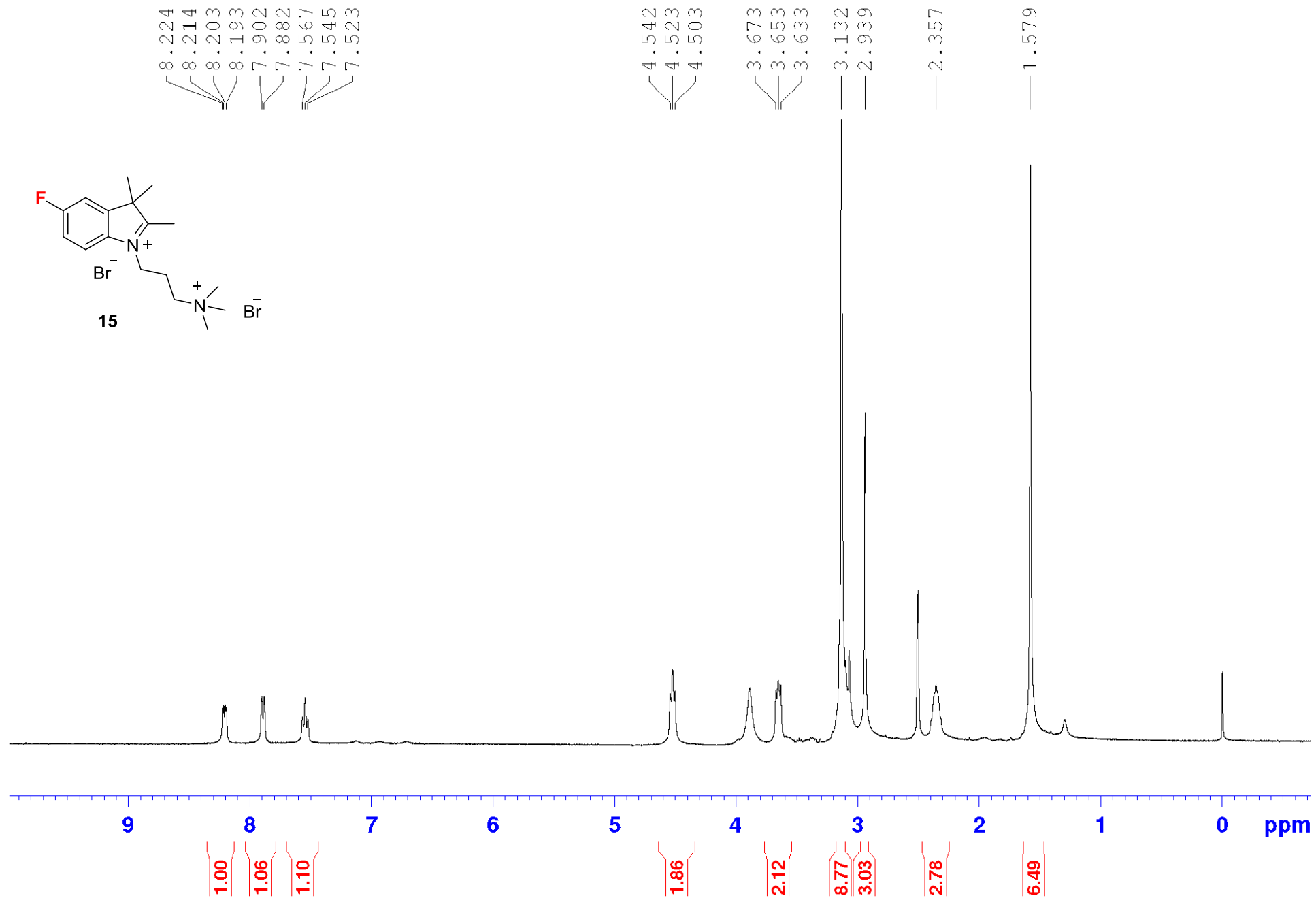
8

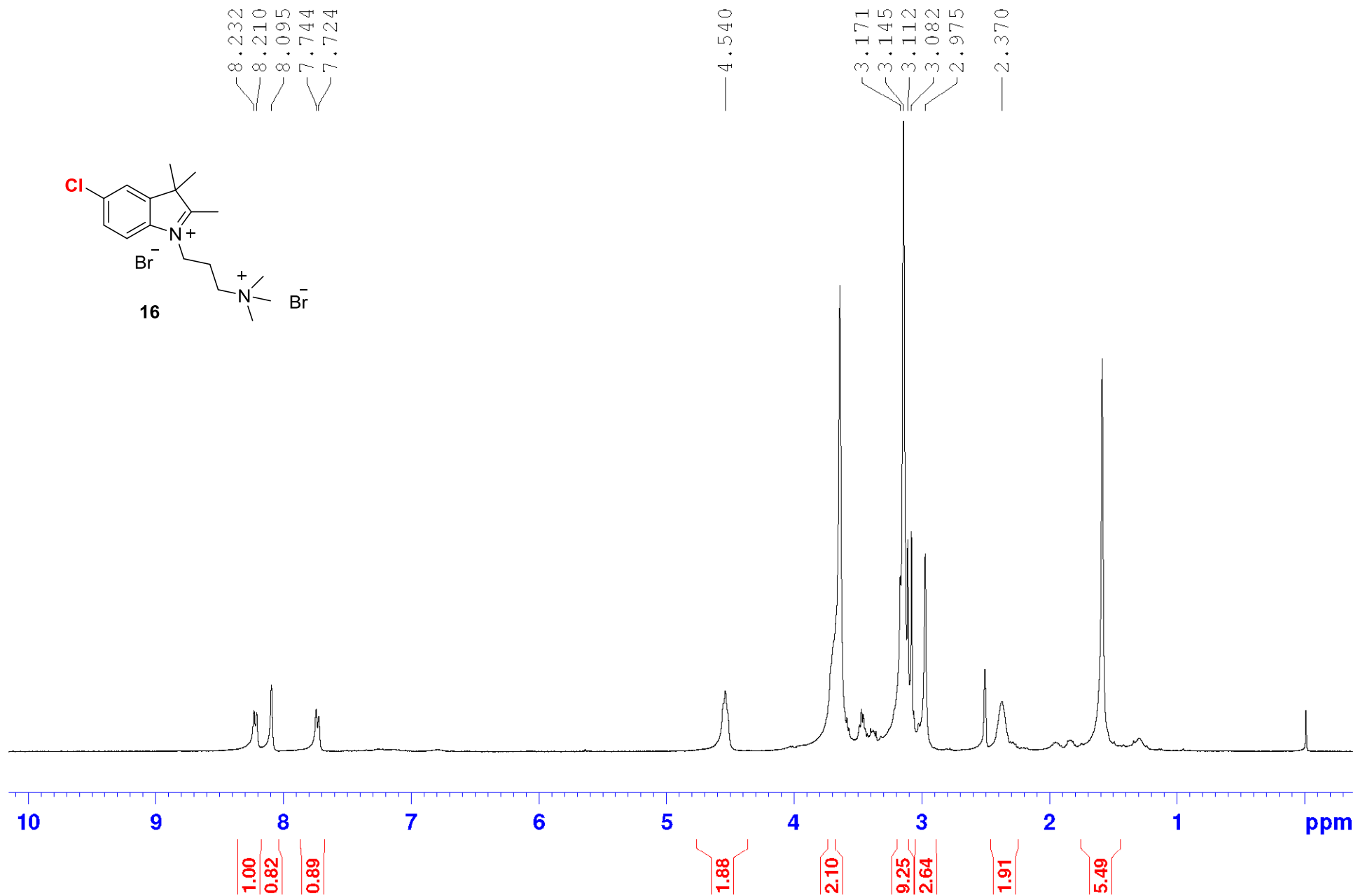


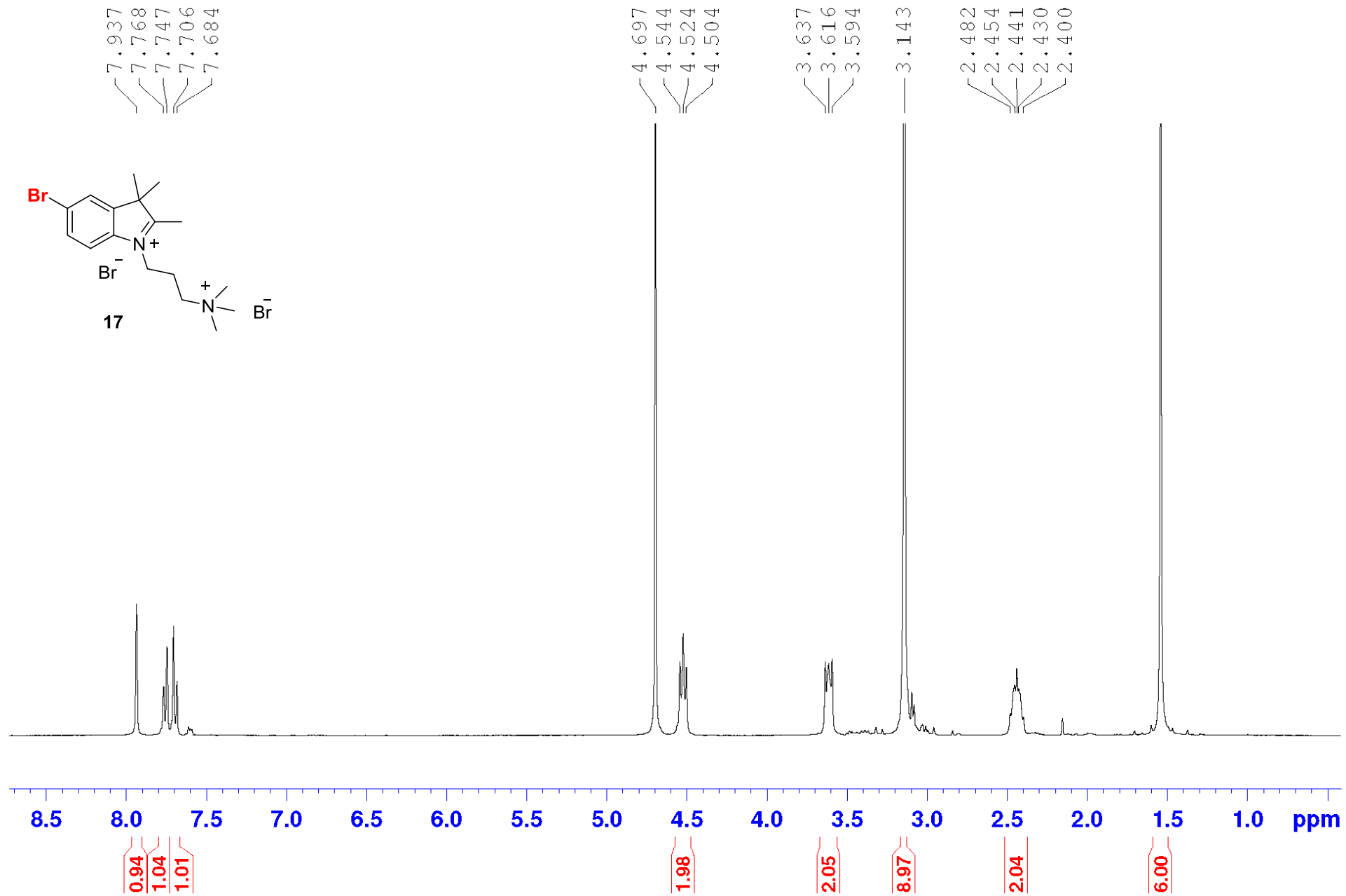


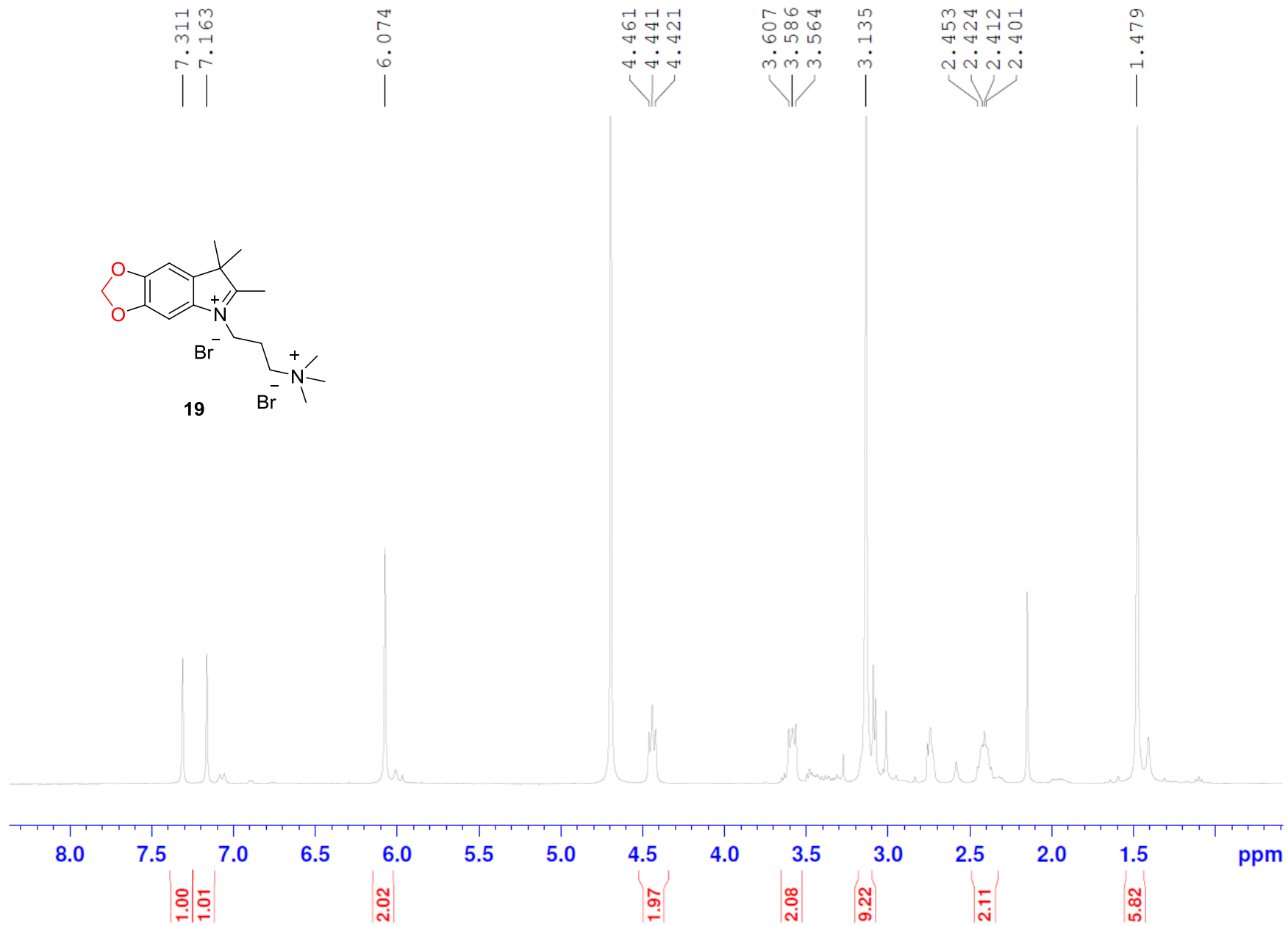


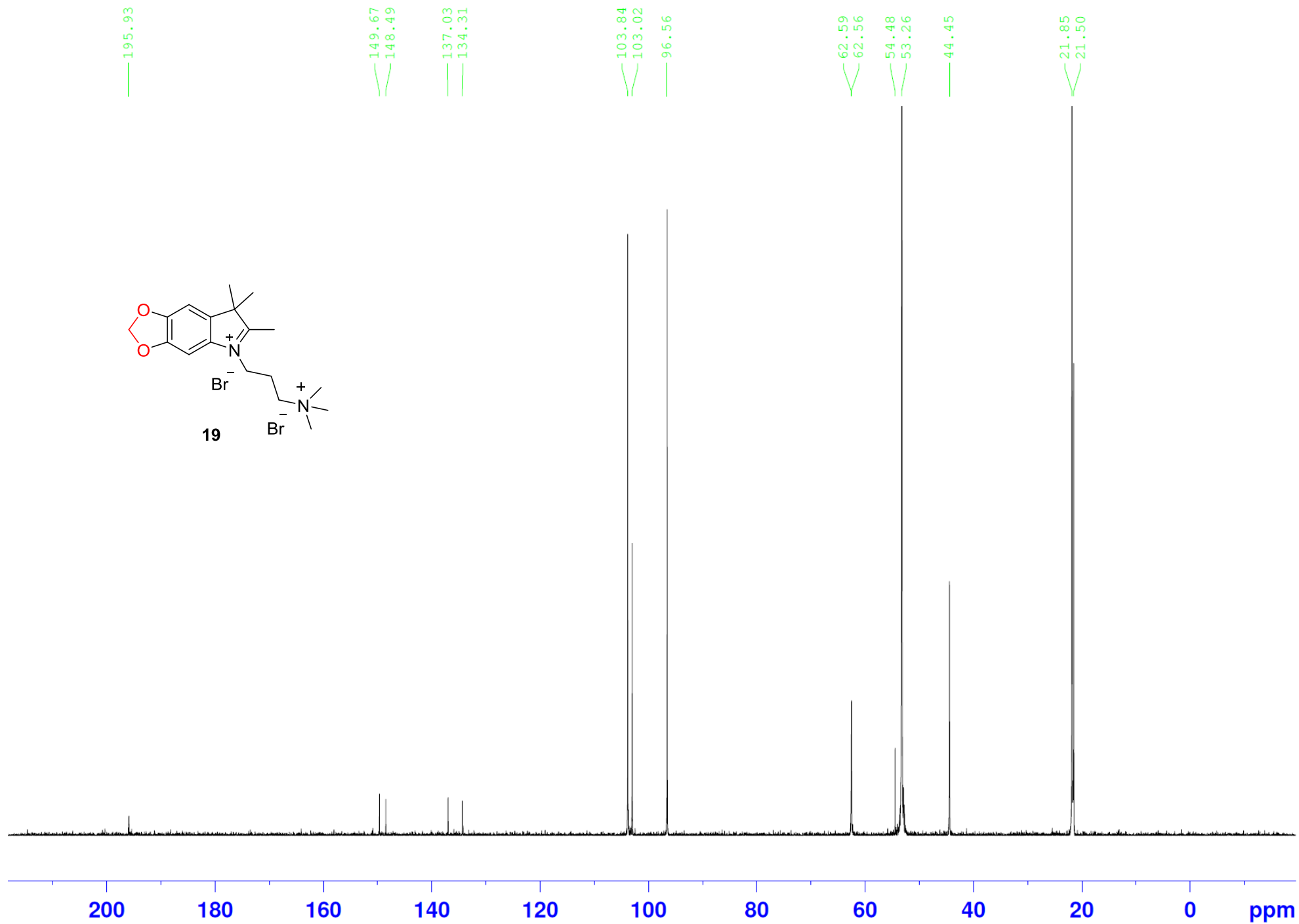
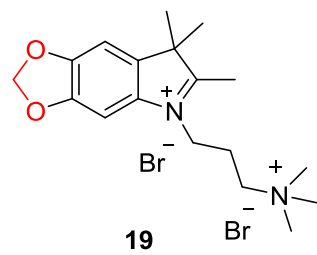


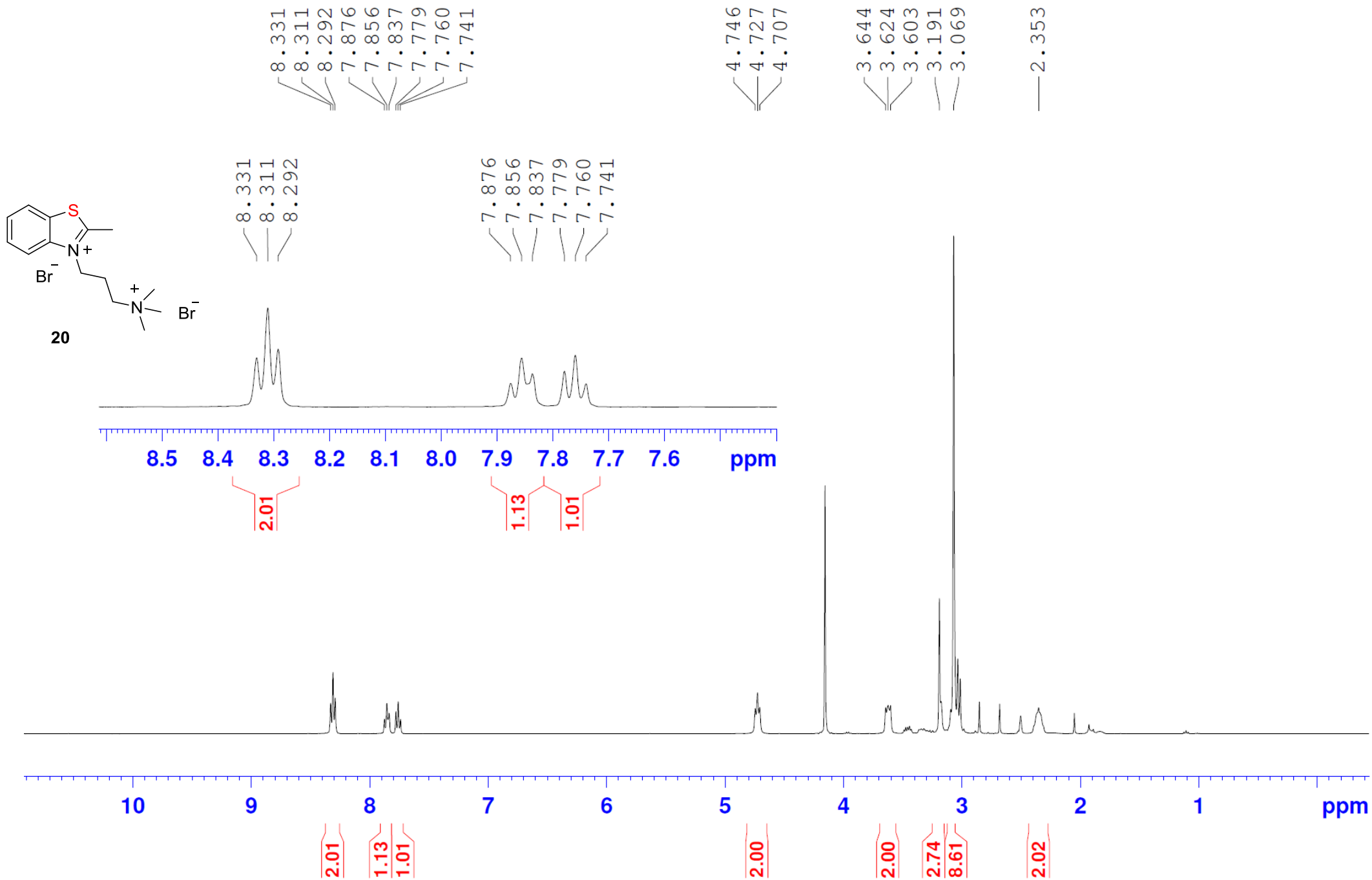


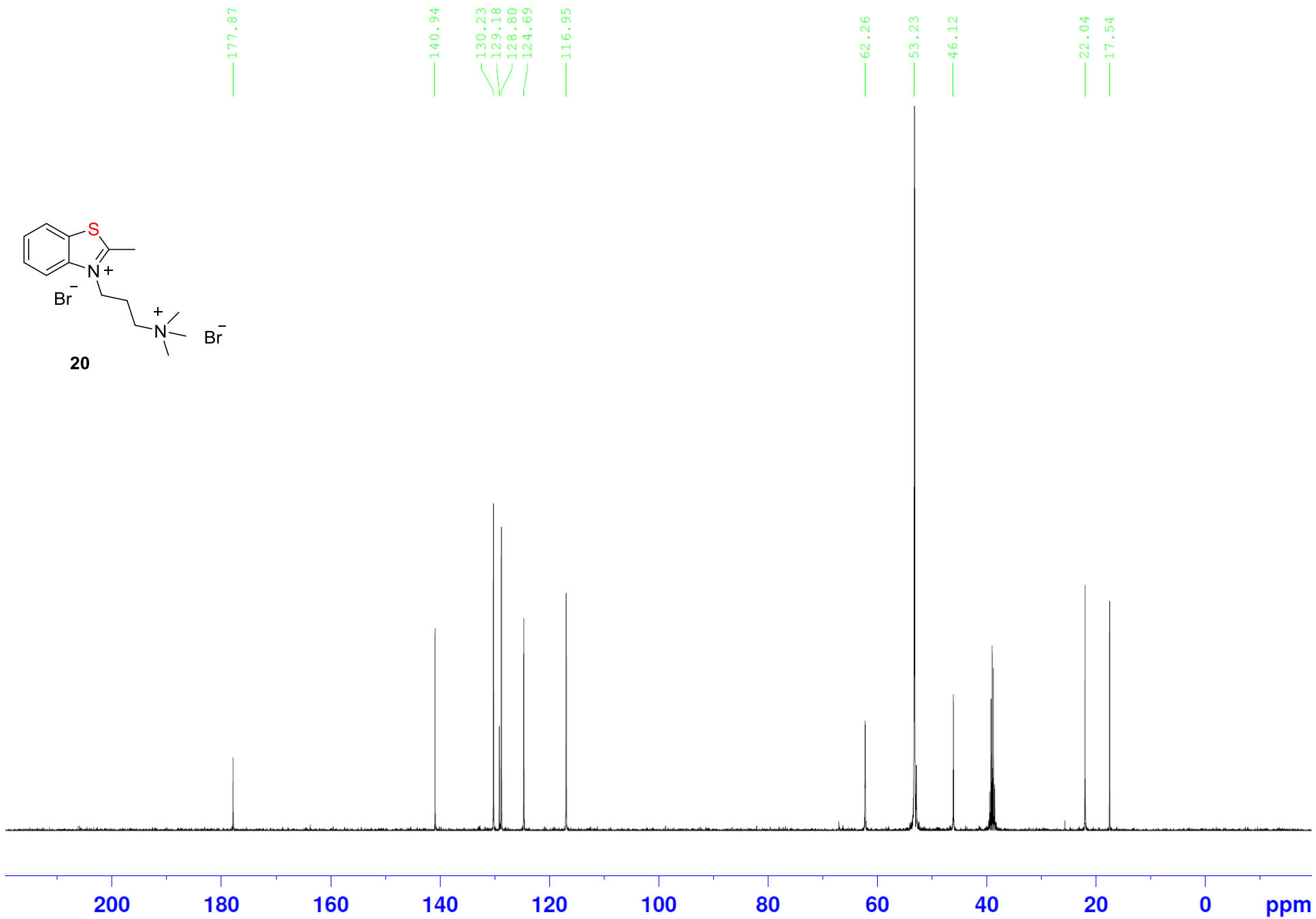
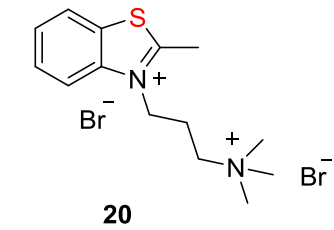




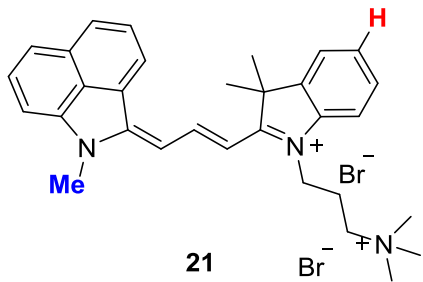








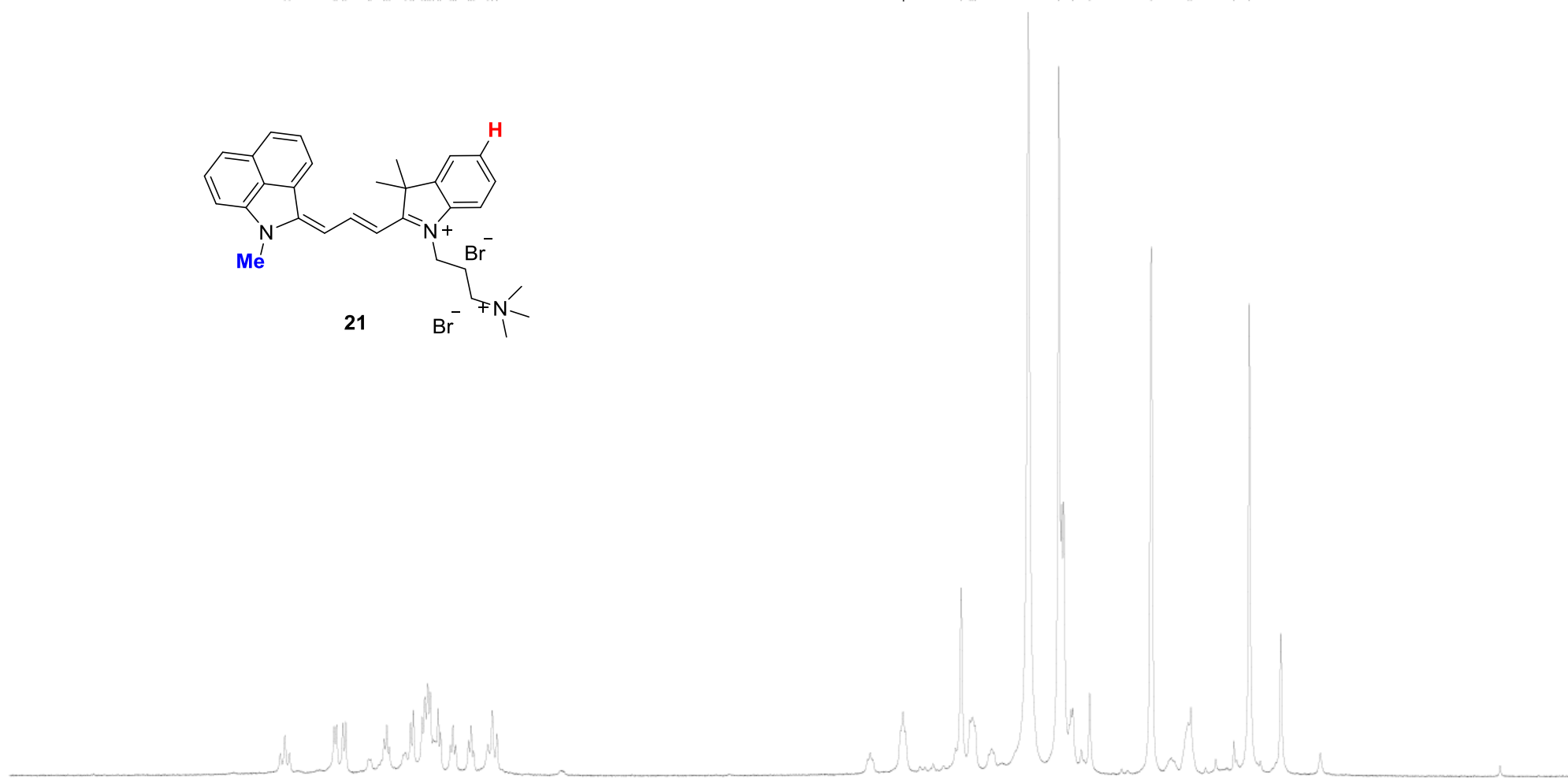
8.732
8.698
8.378
8.360
8.315
8.295
8.128
8.115
8.018
7.999
7.981
7.864
7.828
7.808
7.746
7.726
7.705
7.687
7.665
7.630
7.612
7.542
7.524
7.505
7.411
7.393
7.375
7.272
7.240
7.207



4.288
3.871
3.808
3.790
3.771
3.168
3.068
2.946
2.504
2.237
2.219
1.910
1.799

EAO_165_1H_DMSO

667



10

9

8

7

6

5

4

3

2

1

ppm

1.16

1.14

1.04

1.45

1.33

3.01

1.23

1.15

1.13

1.91

1.96

3.10

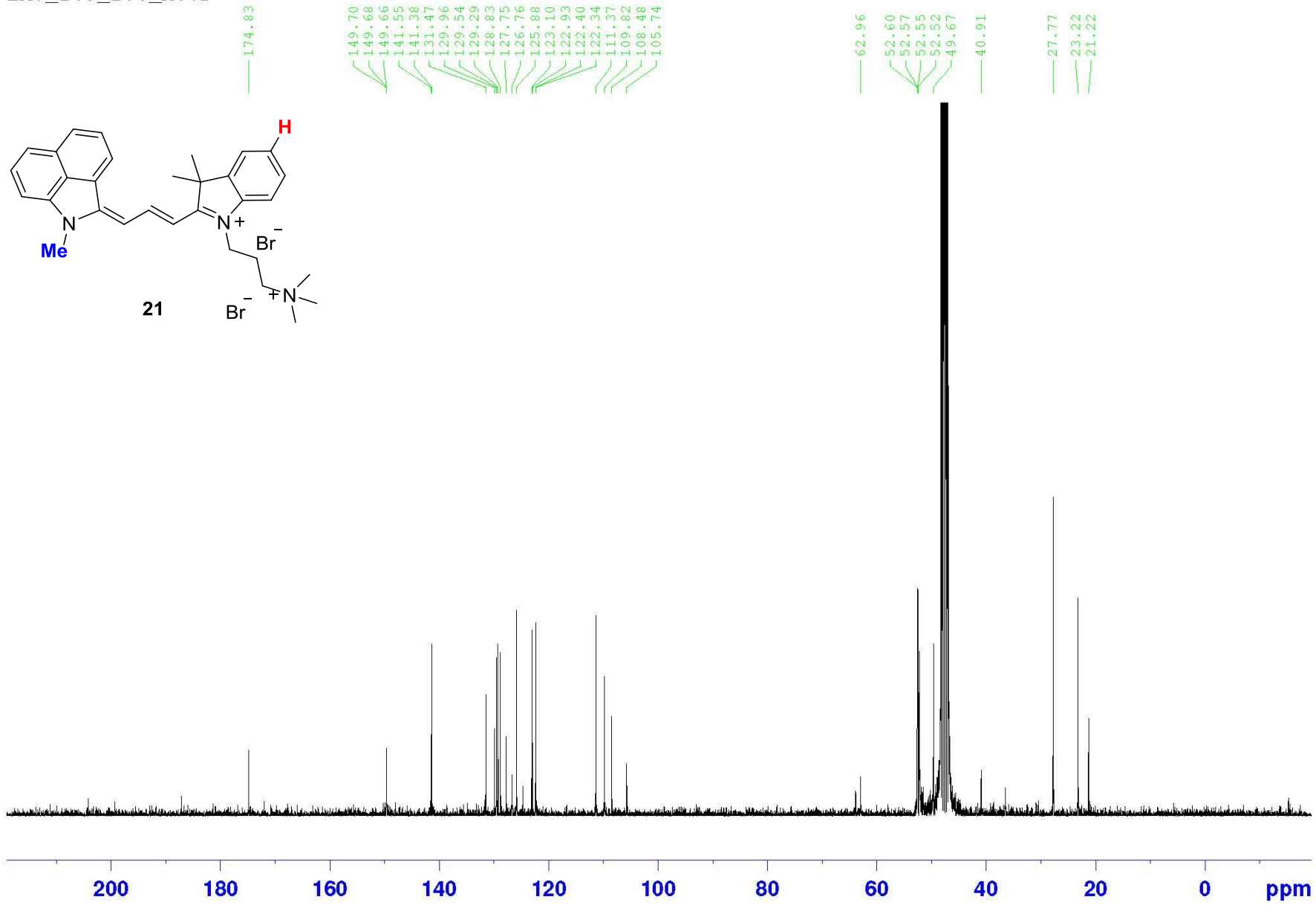
2.09

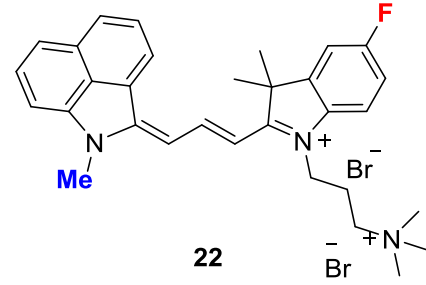
9.26

2.17

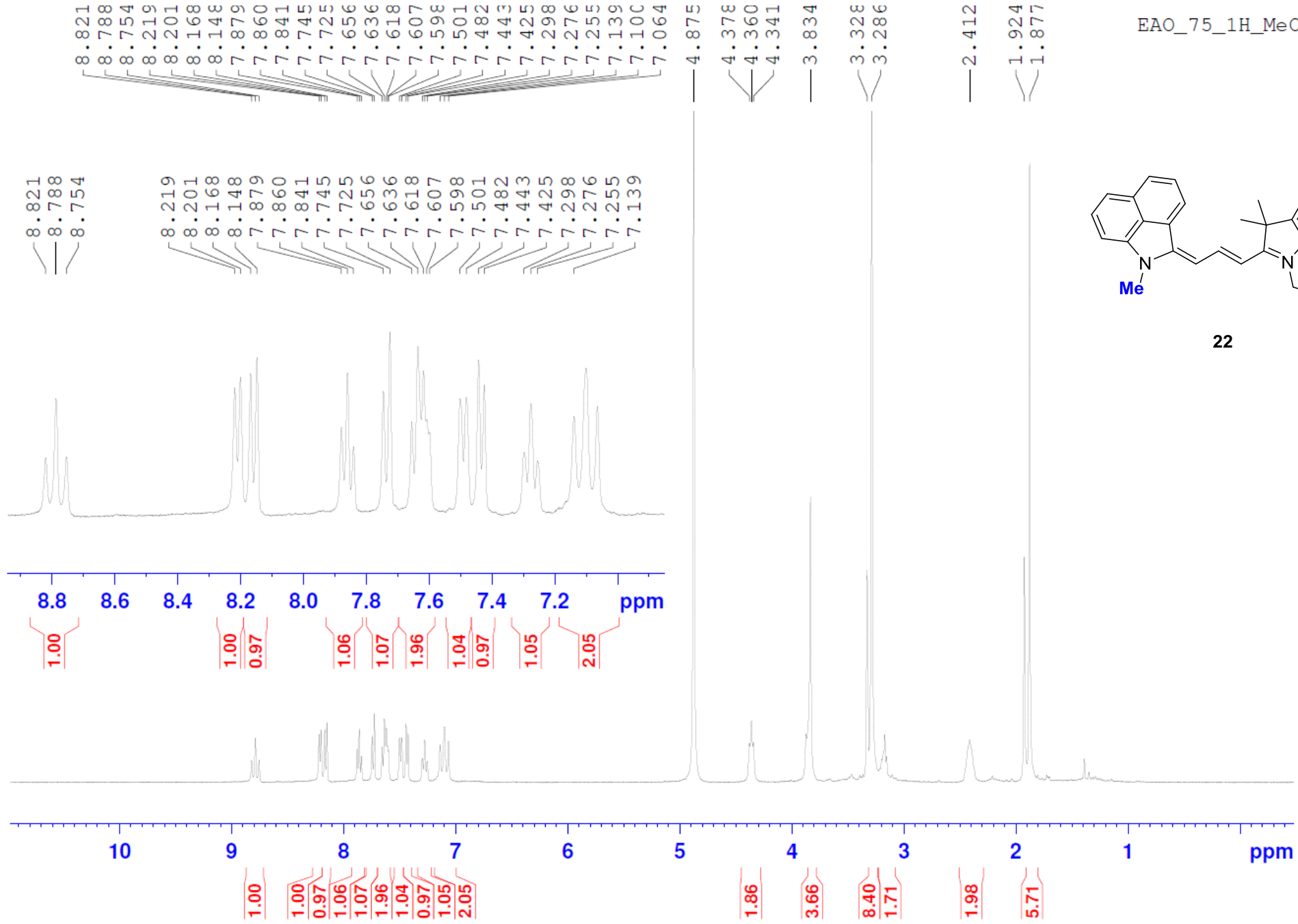
5.59

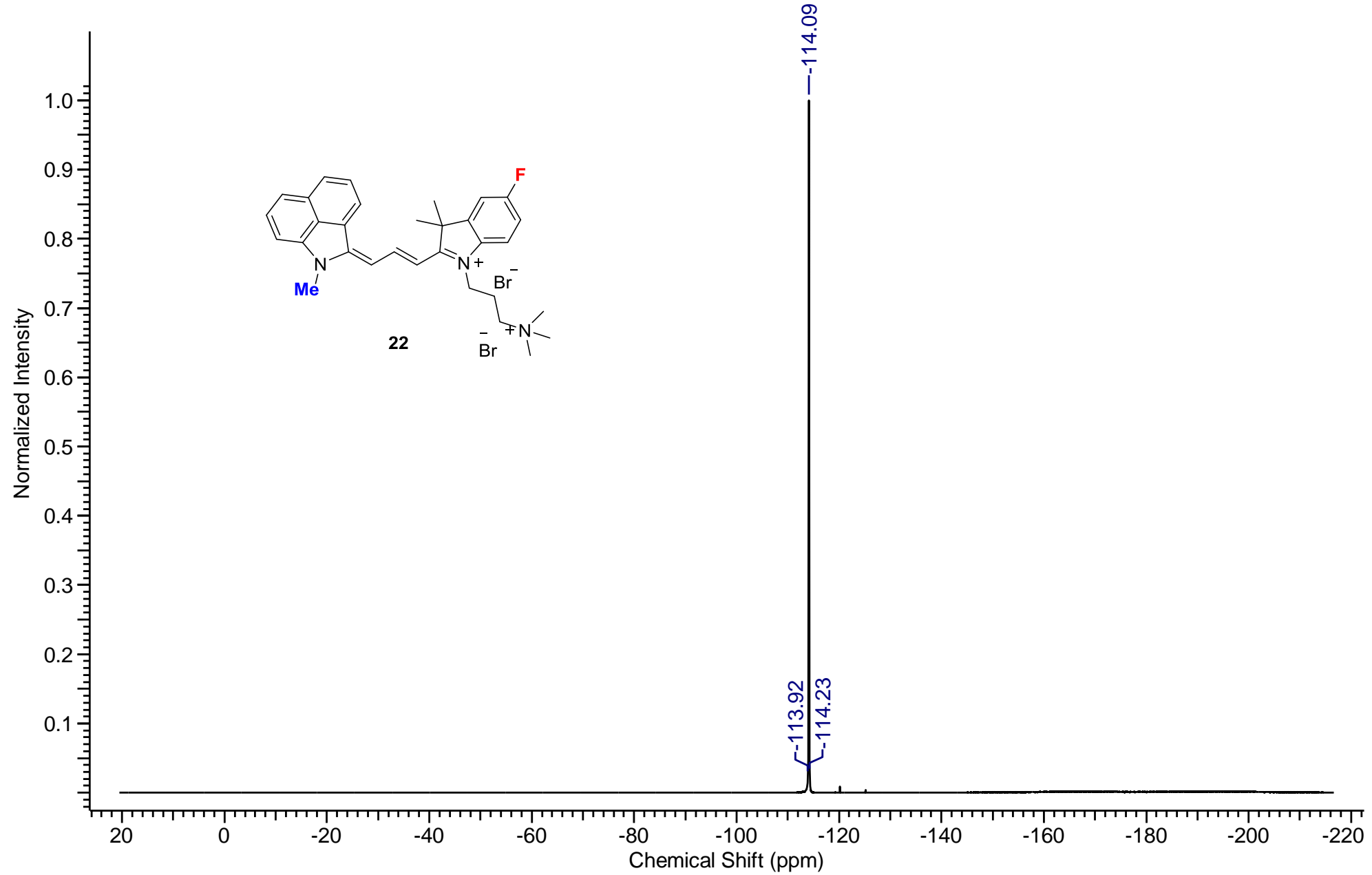
EAO_165_13C_MeOD

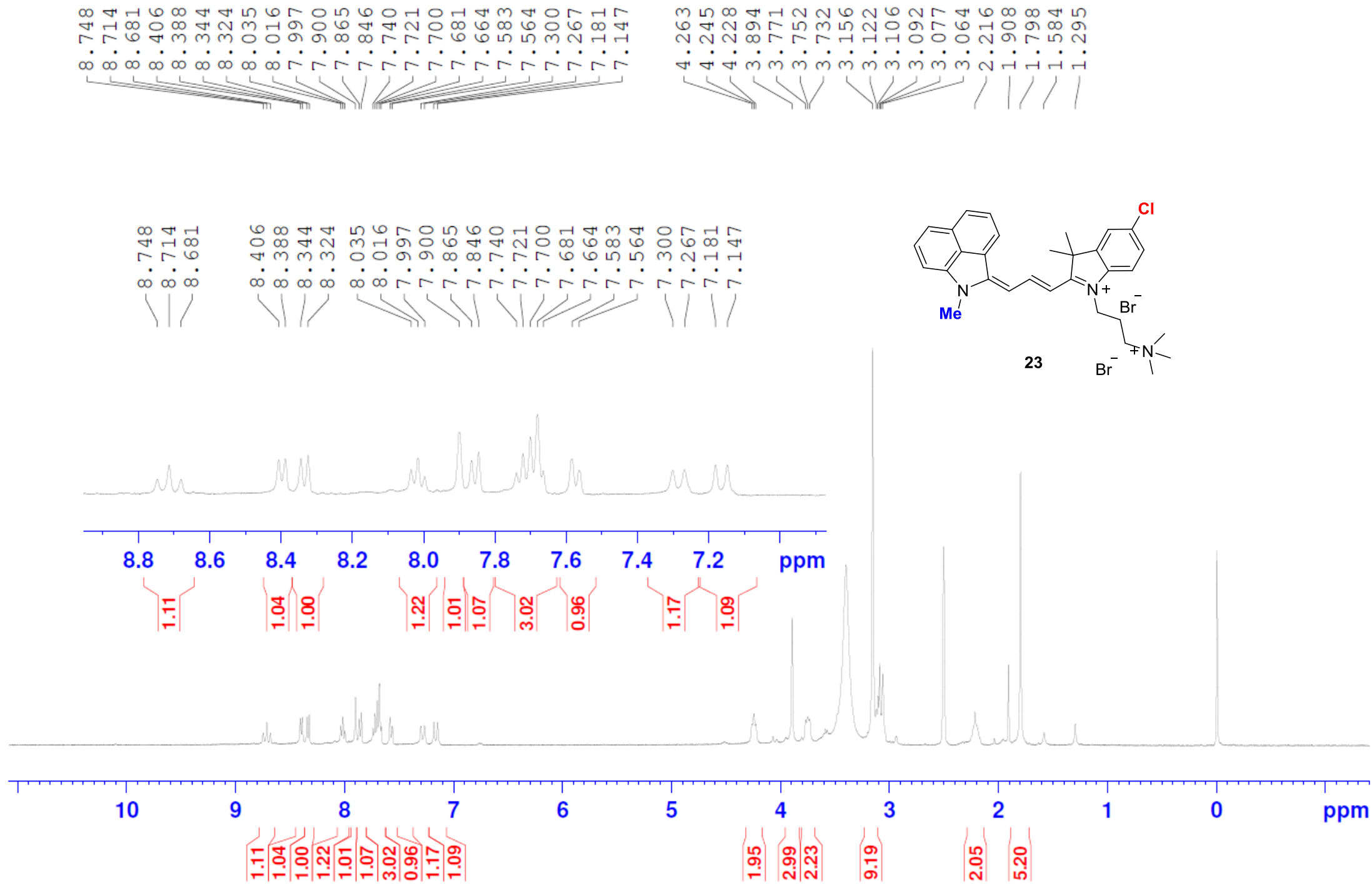


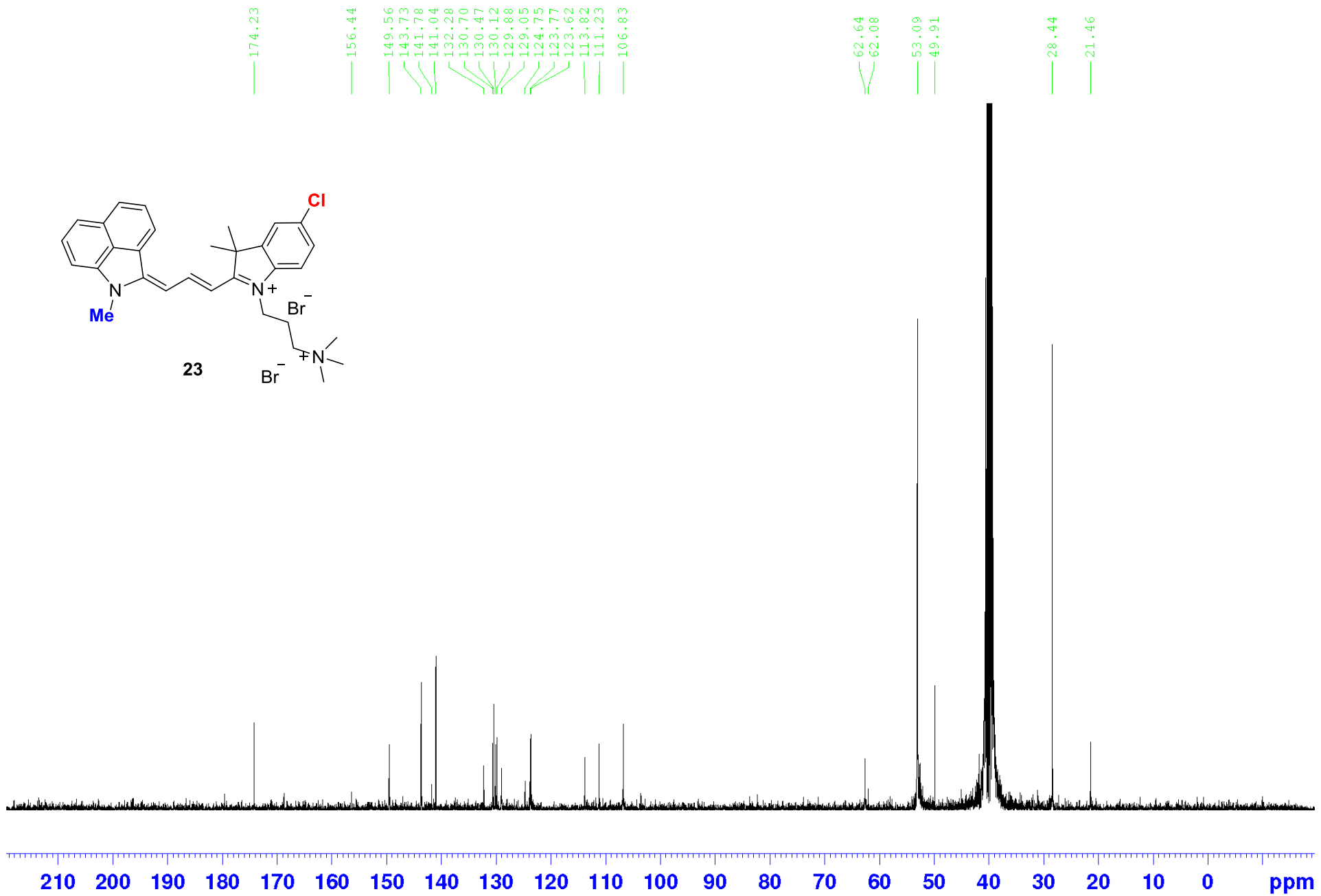


22









8.757
8.724
8.692
8.431
8.413
8.369
8.349
8.056
8.036
8.024
7.887
7.870
7.757
7.739
7.720
7.609
7.587
7.127
7.094
7.049
7.016

— 4.228
— 3.892
— 3.662
— 3.643
— 3.352
— 3.124
— 2.503
— 2.193
— 1.795

LO_14_1H_DMSO

